

Zhizhan Xu · Shengwu Xie
Shi-Yao Zhu · Marlan O. Scully
Editors

Frontiers of Laser Physics and Quantum Optics



Springer

Frontiers of Laser Physics and Quantum Optics

Springer-Verlag Berlin Heidelberg GmbH



<http://www.springer.de/phys/>

Zhizhan Xu Shengwu Xie
Shi-Yao Zhu Marlan O. Scully (Eds.)

Frontiers of Laser Physics and Quantum Optics

Proceedings
of the International Conference
on Laser Physics
and Quantum Optics

With 307 Figures



Springer

Professor Dr. Zhizhan Xu

Shanghai Institute of Optics and Fine Mechanics
P.O.B. 800-211
201 800 Shanghai, China

Professor Dr. Shengwu Xie

Shanghai Jiao Tong University
1954 Huashan Rd.
200 030 Shanghai, China

Professor Dr. Shi-Yao Zhu

Hong Kong Baptist University
Department of Physics
Kowloon
Hong Kong, China

Professor Dr. Marlan Orvil Scully

A & M University, Texas
Department of Physics
TX 77843 College Station, USA

Library of Congress Cataloging-in-Publication Data applied for

Die Deutsche Bibliothek - CIP-Einheitsaufnahme

Frontiers of laser physics and quantum optics : proceedings of the International Conference on Laser Physics and Quantum Optics / Zhizhan Xu ... (ed.). –

ISBN 978-3-642-08644-1 ISBN 978-3-662-07313-1 (eBook)
DOI 10.1007/978-3-662-07313-1

This work is subject to copyright. All rights are reserved, whether the whole or part of the material is concerned, specifically the rights of translation, reprinting, reuse of illustrations, recitation, broadcasting, reproduction on microfilm or in any other way, and storage in data banks. Duplication of this publication or parts thereof is permitted only under the provisions of the German Copyright Law of September 9, 1965, in its current version, and permission for use must always be obtained from Springer-Verlag Berlin Heidelberg GmbH. Violations are liable for prosecution under the German Copyright Law.

© Springer-Verlag Berlin Heidelberg 2000

Originally published by Springer-Verlag Berlin Heidelberg New York in 2000

Softcover reprint of the hardcover 1st edition 2000

The use of general descriptive names, registered names, trademarks, etc. in this publication does not imply, even in the absence of a specific statement, that such names are exempt from the relevant protective laws and regulations and therefore free for general use.

Typesetting: Camera-ready copies by the editors

Cover design: Erich Kirchner, Heidelberg

Printed on acid-free paper

SPIN: 10733299 56/3144/ba - 5 4 3 2 1 0

Preface

Since the advent of the laser about 40 years ago, the fields of laser physics and quantum optics have evolved into a major disciplines. The early studies included optical coherence theory and semiclassical and quantum mechanical theories of the laser. More recently many new and interesting effects have been predicted. These include the role of coherent atomic effects in lasing without inversion and electromagnetically induced transparency, atom optics, laser cooling and trapping, teleportation, the single-atom micromaser and its role in quantum measurement theory, to name a few.

The International Conference on Laser Physics and Quantum Optics was held in Shanghai, China, from August 25 to August 28, 1999, to discuss these and many other exciting developments in laser physics and quantum optics. The international character of the conference was manifested by the fact that scientists from over 13 countries participated and lectured at the conference. There were four keynote lectures delivered by Nobel laureate Willis Lamb, Jr., Profs. H. Walther, A.E. Siegman, and M.O. Scully. In addition, there were 34 invited lectures, 27 contributed oral presentations, and 59 poster papers. We are grateful to all the participants of the conference and the contributors of this volume.

Like any scientific activity of this kind, this conference was generously supported by a number of organizations and funding agencies. Besides the Shanghai Institute of Optics and Fine Mechanics, Shanghai Jiao Tong University and Hong Kong Baptist University, the conference was supported by grants from the National Natural Science Foundation of China, Optical Society of America, International Centre for Theoretical Physics, US Army Research Office, Lee Hysan Foundation, and Epson Foundation. We take this opportunity to express our gratitude to all these organizations for their support.

The Editors

Contents

Super Classical Quantum Mechanics:

The Interpretation of Non-Relativistic Quantum Mechanics

| | |
|---|----|
| <i>Willis E. Lamb, Jr.</i> | 1 |
| 1 A Little Bit of My Early History | 1 |
| 2 Attempts to get to the Schrödinger Equation in Different Ways | 2 |
| 3 Quantum Theory of Measurement | 3 |
| 4 Rewriting the History of Quantum Mechanics | 3 |
| 5 Historical Misunderstandings | 4 |
| 6 What are the Troubles of Classical Mechanics? | 4 |
| 7 Discussion | 5 |
| 8 What are some Troubles with the Determinism of Newtonian Classical Mechanics? | 6 |
| 9 Let's Try Going into the x, p Phase Space | 7 |
| 10 Probability Density in Coordinate Space | 8 |
| 11 Getting a Partial Differential Equation for $\Psi(x, t)$ | 9 |
| 12 I will now show that we can deal with Newtonian Mechanics. Let's test this out with our three simple problems | 10 |
| 13 If it weren't for stationary states, we would not have Quantum Mechanics | 11 |
| 14 We also want to have time-dependent solutions | 11 |
| 15 Method of a complex Gaussian Ψ function | 12 |
| 16 Free Particle | 13 |
| 17 Free fall in a constant uniform force field | 14 |
| 18 Simple harmonic oscillator | 14 |
| 19 Some properties of a complex Gaussian Ψ function | 14 |
| 20 Non-parabolic Potentials! | 15 |
| 21 More General Potential Functions | 16 |
| 22 Ehrenfest's Theorem Revisited | 16 |
| 23 Stationary States | 17 |
| 24 Extensions to other Problems: Magnetic Fields, Relativity, Spin? | 17 |
| 25 Exchange Degeneracy | 18 |
| 26 Remarks on Spin and Magnetic Moments | 18 |
| 27 In Retrospect | 19 |
| References | 19 |

VIII Contents

| | |
|--|-----|
| The Laser Phase Transition Analogy and the Partition Function for Bose Condensation of N Atoms in a Trap | |
| <i>Marlan O. Scully</i> | 23 |
| References | 25 |
| Appendix | 25 |
| | |
| Excess Quantum Noise in Nonnormal Oscillators | |
| <i>A. E. Siegman</i> | 31 |
| 1 Introduction and Background | 31 |
| 2 Normal and Nonnormal Laser Modes | 32 |
| 3 Consequences of Nonnormal Modes | 34 |
| 4 Derivation of the Excess Noise Factor | 35 |
| References | 37 |
| | |
| Single Atom Masers and Lasers | |
| <i>Herbert Walther</i> | 39 |
| 1 Introduction | 39 |
| 2 Experiments with the One Atom Maser | 40 |
| 3 Ion Trap Experiments | 57 |
| 4 Conclusions | 64 |
| References | 65 |
| | |
| Quantum Entanglement: from Popper's Experiment to Quantum Eraser | |
| <i>Yanhua Shih, Yoon-Ho Kim</i> | 71 |
| 1 Introduction | 71 |
| 2 Popper's Experiment | 72 |
| 3 Delayed Choice Quantum Eraser | 80 |
| 4 Conclusion | 87 |
| References | 89 |
| | |
| Sub-Shot-Noise Measurements and Quantum-repeater Using Quantum Correlated Twin Beams | |
| <i>Kunchi Peng, Hai Wang, Jiangrui Gao, Yun Zhang, Hong Su, Xiaoying Li, Qing Pan, Changde Xie</i> | 91 |
| 1 Introduction | 91 |
| 2 Sub-Shot-noise optical measurements | 92 |
| 3 Quantum-repeater | 92 |
| References | 96 |
| | |
| Mirrorless Oscillation Based on Resonantly Enhanced 4-Wave Mixing: All-Order Analytic Solutions | |
| <i>M. Fleischhauer</i> | 97 |
| 1 Introduction | 97 |
| 2 Model and Atomic Polarizations | 98 |
| 3 Stationary field equations and analytic solutions | 101 |

| | |
|---|-----|
| 4 Summary | 106 |
| References | 106 |
| Recent Progress in High-Field Laser Physics Research at SIOFM | |
| <i>Zhizhan Xu, Ruxin Li, Zhong Li, Yingsong Wang, Wei Yu, Ya Cheng</i> | 107 |
| 1 Introduction | 107 |
| 2 The 5TW/46fs Laser System | 108 |
| 3 High-Order Harmonic Generation in Gases | 108 |
| 4 Ion Emission from Laser Heated Clusters | 113 |
| 5 Conclusions | 115 |
| References | 116 |
| Spatial Electron Clouds at Fractional and Multiple Magneto-optical Resonances | |
| <i>Q. Su, R.E. Wagner, P.J. Peverly, R. Grobe</i> | 117 |
| References | 122 |
| Aspect of Harmonic Generation from Solid Surface Plasma by Using Picosecond Laser | |
| <i>Hiroto Kuroda, Atsushi Ishizawa, Tsuneyuki Ozaki, Teruto Kanai</i> | 125 |
| 1 Introduction | 125 |
| 2 Experimental Setup | 127 |
| 3 Experimental Results | 128 |
| 4 Harmonic Yield Dependence on Pump Polarization | 133 |
| 5 Harmonic Yield Dependence on Pump Intensity | 135 |
| 6 Conclusion | 135 |
| References | 136 |
| Generation of Short X-ray Pulse from Femtosecond Laser Produced Plasma and its Application | |
| <i>Hidetoshi Nakano, Peixiang Lu, Tadashi Nishikawa, Naoshi Uesugi</i> | 139 |
| 1 Introduction | 139 |
| 2 X-ray emissions from metal plasma created by a femtosecond laser pulse | 140 |
| 3 Pump-probe spectroscopy in soft x-ray region | 143 |
| 4 Summary | 147 |
| References | 147 |
| Multiple-Scattering Effects in the Second Harmonic Light Generated at Randomly Rough Metallic Interfaces | |
| <i>E. R. Méndez, M. Leyva-Lucero, T. A. Leskova, A. A. Maradudin</i> | 149 |
| 1 Introduction | 149 |
| 2 Theoretical Formulation | 151 |
| 3 Results and Discussion | 157 |
| 4 Summary and Conclusions | 169 |
| References | 170 |

Pump-Probe Spectroscopy - Revisited

| | |
|--|-----|
| <i>P. R. Berman</i> | 173 |
| 1 Introduction | 173 |
| 2 Density Matrix Result | 175 |
| 3 Amplitude Calculation | 176 |
| 4 Open System | 180 |
| 5 Recoil-Induced Resonances | 181 |
| 6 Collective Atomic Recoil Laser | 183 |
| 7 Conclusion | 185 |
| References | 186 |

**Electromagnetically Induced Waveguides
and Propagation in Forbidden Zone**

| | |
|---|-----|
| <i>G.S. Agarwal</i> | 187 |
| 1 Electromagnetic Field Induced Propagation in Forbidden Zone | 187 |
| 2 Electromagnetic Field Induced Wave Guides | 191 |
| References | 194 |

**Photon Localization and Exponential Scaling
of Intensity Variance**

| | |
|---|-----|
| <i>Andrey A. Chabanov, Azriel Z. Genack</i> | 197 |
| References | 201 |

**Coherence and Fluctuation of Light
from Rough Surface Scattering**

| | |
|--|-----|
| <i>Zu-Han Gu, Jun Q. Lu, Mikael Ciftan</i> | 203 |
| 1 Introduction | 203 |
| 2 Theory | 204 |
| 3 Angular correlation effects | 209 |
| 4 Summary | 219 |
| References | 222 |

**Multiple-Scattering Phenomena in the Scattering of Light
from Randomly Rough Surfaces**

| | |
|--|-----|
| <i>E. I. Chaikina, E. E. García-Guerrero, Zu-Han Gu, T. A. Leskova, Alexei A. Maradudin, E. R. Méndez, A. V. Shchegrov</i> | 225 |
| 1 Introduction | 225 |
| 2 Enhanced Backscattering | 226 |
| 3 Satellite peaks | 240 |
| 4 Surface Enhanced Spectral Shifts of Scattered Light | 249 |
| 5 Design of Band-Limited Uniform Diffusers | 253 |
| 6 Some Directions for Future Research | 256 |
| References | 257 |

**Stimulated Raman Scattering of Solid Hydrogen
in the Strong-Coupling Regime**

| | |
|---|-----|
| <i>K. Hakuta, M. Katsuragawa, J.Z. Li, J. Q. Liang, M. Suzuki</i> | 261 |
| 1 Introduction | 261 |
| 2 SRS Process in Solid Hydrogen | 261 |
| 3 Preparation of Solid Hydrogen | 263 |
| 4 Evolution of Anti-Phased State Coherence | 263 |
| 5 Coherence Decay for the Raman transition | 265 |
| 6 Concluding Remarks | 266 |
| References | 267 |

Femtosecond Soliton Propagation in an Optical Fiber

| | |
|---|-----|
| <i>Sien Chi, Chi-Feng Chen</i> | 269 |
| 1 Introduction | 269 |
| 2 Derivation of the Wave Equation | 270 |
| 3 Numerical Results | 274 |
| 4 Conclusions | 280 |
| References | 281 |

Control of Spontaneous Processes

| | |
|---|-----|
| <i>S. Swain, Peng Zhou</i> | 283 |
| 1 Introduction | 283 |
| 2 Phase dependent spectra in a stochastic field | 283 |
| 3 Cavity Induced Quantum Interference | 287 |
| References | 291 |

**Tests on Nonlinear Polymeric Waveguides
for All-Optical Processing**

| | |
|---|-----|
| <i>Stefano Sottini, Francesca Gelli</i> | 293 |
| 1 Introduction | 293 |
| 2 Preparation and linear characterization of guided-wave structures based on third-order organic molecules | 294 |
| 3 Nonlinear tests with polydiacetylene films | 301 |
| 4 Conclusions | 303 |
| References | 305 |

**Spectroscopic Methods for Atom Localization
and Quantum State Measurement**

| | |
|---|-----|
| <i>Sajid Qamar, M. Suhail Zubairy</i> | 307 |
| 1 Introduction | 307 |
| 2 Subwavelength atom localization | 308 |
| 3 Quantum state measurement | 312 |
| References | 318 |

| | |
|---|-----|
| Teleporting an Atomic Wavepacket | |
| <i>Scott Parkins, Jeff Kimble</i> | 321 |
| 1 Introduction | 321 |
| 2 Motion-light coupling | 322 |
| 3 Teleportation Procedure | 324 |
| 4 Discussion | 328 |
| References | 328 |
| | |
| Photon Bunching and Multi-photon Interference between Independent Parametric Down-Conversion Processes | |
| <i>Z. Y. Ou, J. -K. Rhee, L. J. Wang</i> | 331 |
| 1 Introduction | 331 |
| 2 Photon Bunching Effect in Parametric Down-Conversion | 332 |
| 3 Interference of Independent Parametric Down-Conversion fields .. | 335 |
| 4 Four-photon multi-path interference | 339 |
| 5 Discussion and Summary | 342 |
| References | 342 |
| | |
| High Efficiency Frequency Up-Conversion Enhanced by Electromagnetically Induced Transparency | |
| <i>C. Dorman, I. Kucukkara, M. Anscombe, R. Semaoune, J.P. Marangos</i> | 345 |
| 1 Introduction | 345 |
| 2 Calculation of Susceptibilities and Non-Linear Mixing | 347 |
| 3 Experimental Details | 349 |
| 4 Results and Discussion | 352 |
| 5 Conclusion | 355 |
| References | 356 |
| | |
| On the way to Bose-Einstein Condensates in Optical and Electro-Magnetic Traps | |
| <i>Q. Long, S. Y. Zhou, L. F. Xu, J. P. Yin, Y. Z. Wang</i> | 357 |
| 1 Experimental Work | 357 |
| 2 Theoretical Work | 359 |
| References | 361 |
| | |
| Creation of Fock States in an Optical Cavity via Phonon-Photon Interaction | |
| <i>Eduardo Massoni, Miguel Orszag</i> | 363 |
| 1 Introduction | 363 |
| 2 The model | 364 |
| 3 Information Transfer | 365 |
| 4 Numerical Simulation | 369 |
| 5 Discussion | 372 |
| References | 373 |

| | |
|--|-----|
| Spectral and Spatial Coherence in Solid State Raman Lasers | |
| <i>D.D. Smith, A. Oien, G.T. Bennett, T. Monarski</i> | 375 |
| 1 Introduction | 375 |
| 2 Results | 375 |
| 3 Conclusions and Remarks | 379 |
| References | 379 |
| The Hole-Burning Phenomenon under the Action of a Coherent Field | |
| <i>Po Dong, Jin-Yue Gao</i> | 381 |
| References | 385 |
| XUV Emissions from Terawatt Femtosecond Laser Produced Plasma Columns in Gases | |
| <i>Peixiang Lu, Hidetoshi Nakano, Tadashi Nishikawa, Naoshi Uesugi</i> | 387 |
| 1 Introduction | 387 |
| 2 Experiment | 387 |
| 3 OFI in a Strong Linearly Polarized Light Field | 388 |
| 4 Experimental Results and Discussions | 390 |
| 5 Summary | 392 |
| References | 392 |
| Spectral, Temporal and Spatial Characteristics of Few Cycle Optical Pulsed Beam | |
| <i>Zhong-yang Wang, Zhi-zhan Xu</i> | 393 |
| 1 Spectral shift on propagation of ultrashort pulse in the far zone | 393 |
| 2 Scaling law on propagation of ultrashort pulse | 394 |
| 3 Spectral properties of a truncated pulsed Gaussian beam | 396 |
| 4 An analytical form of an ultrashort pulsed Gaussian beam | 396 |
| 5 Summary | 398 |
| References | 398 |
| Quantum Measurement of the State of a Coherently Coupled Dot Device | |
| <i>He-Bi Sun, Howard M. Wiseman, Dian W. Utami, Gerard J. Milburn</i> | 399 |
| References | 402 |
| Controlling Magneto-Optical Rotation via Quantum Coherences | |
| <i>Anil K. Patnaik, G. S. Agarwal</i> | 403 |
| 1 Introduction | 403 |
| 2 The Model Scheme and Determination of χ_{\pm} | 404 |
| 3 Laser Field Induced Enhancement of MOR | 405 |
| 4 Realization of a Magneto-Optical Switch | 406 |
| 5 Conclusion | 407 |
| References | 407 |

| | |
|---|-----|
| Theoretical and Experimental Investigation on Twin Beams Generation by Non-degenerate Optical Parametric Amplifier | |
| <i>Yun Zhang, Hai Wang, Xiaoying Li, Hong Su, Changde Xie, Kunchi Peng</i> | 409 |
| 1 Introduction | 409 |
| 2 Theory | 410 |
| 3 Experiment | 411 |
| References | 414 |
| | |
| Line-Shape Variations of Two-Photon Transition in Molecular Rhomb-Type System Based on Quantum Interference | |
| <i>Weisheng Wang, Le Deng, Zhenrong Sun, Liang'en Ding.....</i> | 415 |
| 1 Introduction | 415 |
| 2 Theoretical work in Rhomb-type system | 415 |
| 3 The result of experiment | 418 |
| 4 Conclusion | 419 |
| References | 419 |
| | |
| Population Oscillation in Two-band Photonic Crystals Via Quantum Interference | |
| <i>Yaping Yang, Shi-Yao Zhu, Hong Chen</i> | 421 |
| 1 Introduction | 421 |
| 2 The model | 421 |
| 3 The properties of the populations | 423 |
| References | 426 |
| | |
| Two Dimensional Nonlinear Dynamics of Cold Atoms in Hollow Fiber | |
| <i>X. M. Liu, G. J. Milburn</i> | 427 |
| 1 The optical potential and Hamiltonian | 427 |
| 2 Classic chaotic dynamics and 2D distribution | 428 |
| 3 Two dimensional quantum nonlinear dynamics | 429 |
| References | 430 |
| | |
| Atomic-State Teleportation Using GHZ State | |
| <i>Shang-qing Gong, Zhong-yang Wang, Xun-li Feng, Zhi-zhan Xu</i> | 433 |
| References | 436 |
| | |
| Experimental Implementation of Quantum Computing with Macroscopic Ensemble of Quantum Spins | |
| <i>Xiwen Zhu, Ximing Fang, Mang Feng, Fei Du, Kelin Gao, Xi'an Mao</i> | 437 |
| 1 Introduction | 437 |
| 2 The network of quantum dense coding | 438 |
| 3 The experimental procedure and result | 438 |
| References | 440 |

Fabrication and Characterization**of Proton-Exchanged Lithium Niobate**

| | |
|--|-----|
| <i>X.F.Chen, Q.Li, S.W.Xie, Y.X.Xia, Y.L.Chen, S.Sottini, E.Giorgetti, A.Carta, R.Ramponi, R.Osellame, M.Marangoni</i> | 443 |
| 1 Introduction | 443 |
| 2 Fabrication and Characterization of PE Waveguides | 444 |
| 3 Fabrication of PE Waveguides for Cerenkov SHG | 446 |
| 4 Conclusion | 447 |
| References | 448 |

A Statistic Model for Ion Clouds in Paul Traps

| | |
|--|-----|
| <i>Jidong Hou, Yiqiu Wang, Donghai Yang</i> | 449 |
| 1 Some Problems of ion clouds in Paul traps | 449 |
| 2 Assumptions and method in our model | 451 |
| 3 Comparison between calculated and experimental results | 452 |
| 4 Discussing laser cooling on ion clouds in a Paul trap | 453 |
| References | 454 |

Single-Mode Self-Homodyne Tomography with Empty Cavity

| | |
|--|-----|
| <i>Jing Zhang, Junxiang Zhang, Tiancai Zhang, Changde Xie, Kunchi Peng</i> | 455 |
| 1 Introduction | 455 |
| 2 The model | 456 |
| 3 Conclusion | 459 |
| References | 459 |

**Narrowing Central Line of Resonance Fluorescence Spectrum
of the V-configuration of a Four-level Atom
via Quantum Interference**

| | |
|--|-----|
| <i>Fu-Li Li, Shi-Yao Zhu</i> | 461 |
| 1 Introduction | 461 |
| 2 Description of the Model | 462 |
| 3 Results and Discussions | 463 |
| 4 Summary | 465 |
| References | 466 |

**A Proposal for Realizing BEC of ^{133}Cs Atoms in Blue-Detuned
 Ar^+ Hollow-Beam Trap**

| | |
|---|-----|
| <i>Jianping Yin, Weijian Gao, Yiqiu Wang</i> | 467 |
| 1 Introduction | 467 |
| 2 PHB cooling and trapping of Cs atoms | 468 |
| 3 Ar^+ HLB GOT and Raman cooling of Cs atoms | 469 |
| 4 The possibility of an optically trapped Cs BEC | 471 |
| 5 Conclusion | 472 |
| References | 472 |

| | |
|--|-----|
| Realization of the Long-Term Continuous Output for an Atom Laser: A Proposal | |
| <i>Yiqiu Wang, Xiaoji Zhou, Donghai Yang</i> | 473 |
| References | 476 |
| | |
| Dynamics of Atom-Cavity system and Elimination of Momentum Elimination | |
| <i>Li-Xiang Cen, Shun-Jin Wang</i> | 477 |
| 1 Introduction | 477 |
| 2 Dynamics of the system | 477 |
| 3 Elimination of recoil effect | 478 |
| 4 Conclusion | 480 |
| References | 480 |
| | |
| Influence of Squeezed Vacuum on Bistable Behavior | |
| <i>Chen Zhaoyang, Zhang Jingtao, Feng Xunki, Xu Zhizhan</i> | 481 |
| 1 Fixed-Period Problems: The Sublinear Case | 481 |
| References | 484 |
| | |
| Numerical Analysis of Wavelength Conversion Based on a Nonlinear Optical Loop Mirror | |
| <i>Chi Nan, Chen Shuqiang, Guan Kejian</i> | 485 |
| 1 Introduction | 485 |
| 2 Principle and System Model | 485 |
| 3 Result and Discussion | 486 |
| References | 488 |
| | |
| Emission Spectrum of Two-Atom Two-Mode Multiphoton Raman Coupled Model | |
| <i>Feng Jian, Gao Yun-feng, Song Tong-qiang</i> | 489 |
| 1 Model and Emission Spectra | 489 |
| 2 Results and Discussion | 490 |
| References | 491 |
| | |
| DFB X-Ray Laser Gain Per Unit in Deformed Crystals | |
| <i>M. M. S. Gualini</i> | 493 |
| 1 Introduction | 493 |
| 2 Semi-empirical approach | 494 |
| 3 Conclusions | 496 |
| References | 496 |
| | |
| Statistical Properties of Fundamental and Second Harmonic Light with Multiplicative Noise | |
| <i>Jing Hu, Xiaoqin Luo, Shiqun Zhu</i> | 497 |
| 1 Introduction | 497 |
| 2 Theoretical analysis | 497 |

| | |
|---|-----|
| 3 Comparison of theory and experiment | 499 |
| 4 Effect of multiplicative noise | 500 |
| 5 Discussion | 500 |
| References | 500 |

Measurement of the Wigner Function via Atomic Beam Deflection

| | |
|---|-----|
| <i>Ashfaq Hussain Khosa, Shi-Yao Zhu, M. Suhail Zubairy</i> | 503 |
| 1 Introduction | 503 |
| 2 Wigner function of radiation field | 505 |
| References | 508 |

Projection Pattern Reducing with Magnetic Lens in Atom Lithography

| | |
|---|-----|
| <i>Zeng Qinglin, Li Chuanwen, Cai Weiquan, Huo Yunsheng, Wang Yuzhu</i> | 509 |
| 1 Introduction | 509 |
| 2 Magnetic Lens | 509 |
| 3 Analysis of the Spherical and Chromatic Aberration | 510 |
| 4 Projection Reducing of Arbitrary Pattern | 511 |
| 5 Conclusion | 512 |
| References | 512 |

Atoms in the Magnetic Atomic Wave-Guide

| | |
|--|-----|
| <i>Daijun Li, Xiaji Liu, Hu Huang, Shiqun Li, Yuzhu Wang</i> | 513 |
| 1 The idea of magnetic tube for atom guidance | 513 |
| 2 The quantum atomic motion | 514 |
| References | 516 |

Study of the Time-Resolved Spectra of $C^1\Pi_1$ State for the InCl Molecule

| | |
|---|-----|
| <i>Yunjing Li, Meirong Lin, Wenli Zou, Baozheng Zhang, Wenju Chen</i> | 517 |
| 1 Introduction | 517 |
| 2 Experiment | 517 |
| 3 Theory | 518 |
| 4 Result and Discussion | 518 |
| References | 520 |

Emission Spectrum of a Three-Level Atom in a Photonic Crystal

| | |
|--|-----|
| <i>Zhixin Lin, Yaping Yang, Hong Chen, Weiguo Feng</i> | 521 |
| 1 Introduction | 521 |
| 2 Basic Theory | 521 |
| 3 Spectrum and spectral analysis | 523 |
| References | 524 |

XVIII Contents

Reduction of Light Speed in One-Dimensional Photonic Band-Gap Structures with a Defect

| | |
|--|-----|
| <i>Nian-hua Liu, Shi-yao Zhu</i> | 525 |
| References | 528 |

Influence of the Kerr Medium on the Fidelity of Quantum State

| | |
|---|-----|
| <i>Liu Tang-Kun, Wang Ji-Suo, Zhan Ming-Sheng</i> | 529 |
| 1 Introduction | 529 |
| 2 The model | 529 |
| 3 Influence of the Kerr medium on the fidelity of quantum state | 531 |
| 4 Conclusion | 532 |
| References | 532 |

Some Anomalous Phenomena of ^{87}Rb Atoms Fluorescence in a Quadrupole Magnetic Field

| | |
|--|-----|
| <i>Q. Long, S.Y Zhou, Y.Z Wang</i> | 533 |
|--|-----|

The Properties of the Macro-Quantum Superposition States Involving Three Elements

| | |
|--|-----|
| <i>Ma Aiqun, Qian Yan, Xie Hongwei, Jiang Zhuohong</i> | 537 |
| 1 Introduction | 537 |
| 2 Free evolution and mean photon number of the optical cat state | 538 |
| 3 The second-order coherence of the optical cat state | 539 |
| 4 The distribution of the optical cat state | 539 |
| References | 540 |

Gain in Autler-Townes Doublet due to Interference in Decay Channels

| | |
|--|-----|
| <i>Sunish Menon and G. S. Agarwal</i> | 541 |
| 1 Introduction | 541 |
| 2 The Model | 542 |
| 3 Quasi-Trapped-States From Interference of Decay Channels | 544 |
| 4 Conclusions | 545 |
| References | 545 |

Short-Wavelength Three-dimensional Photonic Crystals

| | |
|--|-----|
| <i>Ouyang Zhengbiao, Li Jingzhen, Sun Yiling, Lin Min</i> | 547 |
| 1 Introduction | 547 |
| 2 Ideas and Examples of Configuration of Practical 3-D Photonic Crystals | 547 |
| 3 Conclusion | 549 |
| References | 550 |

| | |
|---|-----|
| Diode-laser-based High Resolution Spectroscopy in Sm I | |
| <i>Hyunmin Park, Miran Lee, E. C. Jung, Jonghoon Yi, Yongjoo Rhee, Jongmin Lee</i> | 551 |
| 1 Introduction | 551 |
| 2 Experiment | 551 |
| 3 Results and Discussions | 552 |
| 4 Conclusions | 554 |
| References | 554 |
| QND-Like Quantum Measurement with a Photon-Number Squeezed Light Beam | |
| <i>Peng Fanglin, Zhang Jing, Dong Ruifang, Zhang Tiancai</i> | 555 |
| References | 558 |
| The Dynamics of 1D H_2^+ Interacting with Ultrashort Laser Pulse | |
| <i>Weixing Qu, Zhaoyang Chen, Wei Yu, Wenqi Zhang, Shiqi Jin, Zhizhan Xu</i> | 559 |
| References | 562 |
| 3D Monte-Carlo Simulation of Zeeman Slower System with Two Level Atoms | |
| <i>Min-Gyu Kim, K.S. Lee, D.Y. Jeong, J.M. Han, Yong-joo Rhee, Jongmin Lee</i> | 563 |
| 1 Introduction | 563 |
| 2 Light pressure to an atom | 564 |
| 3 The Simulation and Result | 565 |
| References | 566 |
| The Enhancement of Spontaneous and Stimulated Emission by a Bose-Einstein Condensate | |
| <i>Tan Weihan, Yan Kezhu, Liu Renhong</i> | 567 |
| References | 570 |
| The Small Phase Shift Measurement Using Frequency-Degenerated Twin Beams | |
| <i>Hai Wang, Yun Zhang, Xiaoying Li, Jing Jietai, Changde Xie, Kunchi Peng</i> | 571 |
| 1 Introduction | 571 |
| 2 The principle of measurement | 572 |
| References | 574 |
| Quantum Nondemolition Measurements in Degenerate Optical Parametric Oscillator | |
| <i>Wang Kaige, Wang Danling, Yang Guojian</i> | 575 |
| 1 Introduction | 575 |

XX Contents

| | |
|---|-----|
| 2 Description of DOPO model | 575 |
| 3 QND performance | 577 |
| 4 Conclusion | 580 |
| References | 580 |
| Production of Subfemtosecond Pulses Directly through High-order Harmonic Generation | |
| <i>Yingsong Wang, Zhizhan Xu</i> | 581 |
| References | 584 |
| Spontaneous Emission from a Driven Atom Embedded in a Photonic Crystal | |
| <i>Shuangyuan Xie, Yaping Yang, Hong Chen, Shi-Yao Zhu, Xiang Wu</i> .. | 587 |
| 1 Introduction | 587 |
| 2 Basic theory | 587 |
| 3 The properties of the population | 588 |
| References | 590 |
| AC Magnetic Guide for Cold Atoms in an Ioffe Tube | |
| <i>Lifang Xu, Jianping Yin, Yuzhu Wang</i> | 591 |
| References | 594 |
| Bose-Einstein Condensation of Neutral Atoms with Attractive Interaction in a Harmonic Trap | |
| <i>Yan Kezhu, Tan Weihan</i> | 595 |
| References | 598 |
| Influence of Spontaneous Emission on Two-Atom Dark State Inside a Quantized Standing Wave Cavity | |
| <i>Guojian Yang, Weiqiao Zhen, Jian Wang</i> | 599 |
| 1 Introduction | 599 |
| 2 Two-atom master equation | 599 |
| 3 Two-atom dark states | 600 |
| 4 The effects of spontaneous emission on dark state | 601 |
| 5 Conclusion | 603 |
| References | 605 |
| Spectroscopic Study of Gadolinium Energy Levels by Resonant Multi-Photon Ionization | |
| <i>Jonghoon Yi, Jin Tae Kim, Huynmin Park, Jaemin Han, Yongjoo Rhee, Jongmin Lee</i> | 607 |
| 1 Introduction | 607 |
| 2 Experiment and Results | 608 |
| 3 Conclusions | 609 |
| References | 610 |

| | |
|--|-----|
| Near-Field Optical Trap by Tapered Fibre Probe | |
| <i>Guoping Zhang, Zhuming Huang, Hai Ming</i> | 611 |
| 1 Introduction | 611 |
| 2 Theory | 611 |
| 3 Results and Discussions | 612 |
| 4 Conclusions | 613 |
| References | 614 |
| | |
| Frequency Tunable Nonclassical Light Generation | |
| <i>Lingxiang He, Junmin Wang, Tiancai Zhang, Changde Xie, Kunchi Peng</i> | 615 |
| 1 Introduction | 615 |
| 2 Theoretical analysis | 615 |
| 3 Experimental setup | 616 |
| 4 Experimental result | 617 |
| 5 Conclusion | 618 |
| References | 618 |
| | |
| An Analytic Expression of Enhanced Spontaneous Emission in Semiconductor Microcavity Lasers | |
| <i>Xiaoxia Zhang, Wei Pan, Bin Luo, Hongchang Lü, Jianguo Chen</i> | 619 |
| 1 Introduction | 619 |
| 2 Analytic Resolution of Steady-state Rate Equations | 620 |
| 3 Results and Discussions | 620 |
| References | 621 |
| | |
| Quantum Theory of the 3-Level-Atom Maser | |
| <i>Zhi-Ming Zhang, Xiao-Xia Zhong, Chang-Huan Liao, Ai-Qun Ma, Shi-Kang Zhou</i> | 623 |
| 1 Introduction | 623 |
| 2 General Theory | 624 |
| 3 Emission Probability | 624 |
| 4 Transmission Probability and Velocity Selection | 624 |
| 5 Photon Statistics | 625 |
| 6 Spectrum | 625 |
| 7 Summary | 625 |
| References | 626 |
| | |
| Optical Wave Mixing of Interacting Charge-Transfer Excitons in Organic Crystalline Films | |
| <i>Ka-Di Zhu, Wai-Sang Li</i> | 627 |
| 1 Introduction | 627 |
| 2 Theory | 627 |
| 3 Conclusions | 629 |
| References | 630 |

Synchronization of Chaos in a Coupled Laser System

| | |
|--|-----|
| <i>Shiqun Zhu, Xianfeng Chen, Xiang Lu, K. Scott Thornburg, Jr., Gregory D. Van Wiggeren, Rajarshi Roy</i> | 631 |
| 1 Introduction | 631 |
| 2 Theoretical analysis | 631 |
| 3 Loss of synchronization | 632 |
| 4 Conclusion | 634 |
| References | 634 |

Controlling the Time Evolution of an Atom–Cavity System

via Atomic Feedback

| | |
|--|-----|
| <i>X.-L. Feng, S.-Q. Gong, Z.-Y. Wang, Z.-Z Xu</i> | 635 |
| References | 638 |

Super Classical Quantum Mechanics: The Interpretation of Non-Relativistic Quantum Mechanics

Willis E. Lamb, Jr.

Optical Sciences Center and Department of Physics, University of Arizona
Tucson, AZ 85721, U. S. A

Abstract. Newtonian Classical Mechanics (NCM) suffers from several kinds of chaotic indeterminacy. These shortcomings can be repaired in a simple and obvious manner. The NCM theory is thereby transformed into a new (probabilistic) theory which is fully equivalent to the Non-relativistic Quantum Mechanics of Heisenberg, Schrödinger, and Dirac with the Max Born probabilistic interpretation of the state function built in from the start. I call this new theory Super Classical Quantum Mechanics, (SCQM). With the help of Paul Ehrenfest's 1927 theorem, the **classical limit** of the new theory, SCQM, gives exactly the results expected of an improved Newtonian theory of Classical Mechanics. This approach offers enormous advantages, not only for a physically reasonable interpretation of Quantum Mechanics, but also for its contribution to the Quantum Theory of Measurement, and for the avoidance of all of the so-called paradoxes of traditional non? relativistic Quantum Mechanics.

1 A Little Bit of My Early History

As a 17 year old Freshman at Berkeley in 1930, I took a course on Classical Mechanics, Physics 1A. It mostly dealt with Sir Isaac Newton's Second Law of Motion. This Law seemed to work wonderfully well with massive objects, called "particles", sliding down smooth inclined planes or bouncing up and down at the end of an ideal spring.

After eight years in Berkeley, with short visits to other Universities at Ann Arbor, Michigan, and two closer ones: Stanford University near Palo Alto, and the California Institute of Technology in Pasadena, California, I had learned a lot from Robert Oppenheimer, and others, including William H. Williams, Robert Serber, Felix Bloch, Arnold Nordsieck, George Uhlenbeck, Enrico Fermi, Victor Weisskopf, J. H. Van Vleck and I. I. Rabi. I received a Berkeley Ph. D. in Theoretical Physics in 1938. The second part of my thesis [1] gave a 1930's version of a meson theoretic description of the structure of neutrons and protons.

I liked the use of Quantum Mechanics very much. On balance, it has been very good to me. I owe it a lot. If I had not been able to use and understand the material in Hans Bethe's 1933 Handbuch der Physik article on one- and two- electron problems, I would never have been able to participate in the

1945-1951 study of the fine structure of the hydrogen atom. I have given lectures on Quantum Mechanics at seven universities since 1946: Columbia, Stanford, Harvard, Oxford, Yale, Simon Fraser, and Arizona. For five decades, I never understood the meaning of Quantum Mechanics. I stopped teaching the subject entirely in the mid eighties. Since then, I have learned much more about the Foundations of Quantum Mechanics than I ever knew before. I deeply wish that I could have taught the subject better in lectures to nearly four decades of graduate students.

In 1930, I wondered how Newton's laws of motion could give such a good account of phenomena studied in the undergraduate laboratory of Physics 1A. After some fruitless speculation, I decided that the most important object of physics was to study interesting phenomena in a laboratory, and to try to make a mathematical model in which the mathematical symbols behaved, in some way or another, like the physical system. It was a game, to be taken seriously only if it worked well. The thought occurred to me that there might be several different mathematical models which would more or less imitate the same physical behavior. If that happened, some kind of value judgment would have to be made, perhaps based on criteria such as beauty, accuracy or elegance of the theory.

In later years, I saw two examples of this sort of thing. About 1940, Richard Feynman, then a student of John A. Wheeler's at Princeton, proposed an "absorber theory" as an alternative to Maxwell's theory of electromagnetism. In 1951, David Bohm, who had a Berkeley degree from Oppenheimer in the early forties, and for a short time, was an Assistant Professor at Princeton, proposed a "hidden variable" theory which, he thought, overcame some difficulties of Quantum Mechanics. In each case, the new form of theory was very different from the older form, but it gave equivalent results for simple test problems. On each occasion, I had no difficulty in making my personal choice which favored the older version of theory, for reasons of simplicity and beauty. However, I gave both Feynman and Bohm good marks for trying new things, and my belief in the important role of this kind of model building in physics was strengthened.

In the present paper, I am going to show an example of model building for simple nonrelativistic quantum mechanical problems, like that of the falling apple of Newton, which is taken to be a "particle" in the quaint way used by physicists. As far as possible, I will consider only one dimensional problems.

2 Attempts to get to the Schrödinger Equation in Different Ways

I have made several attempts to think of ways to get to the Schrödinger equation in a non historical manner. One of these, "Suppose Newton had discovered the Schrödinger equation" [2], involved an imagined instance of divine inspiration. Another, entitled "The Borderland between Quantum and

Classical Mechanics" [3], relied on human guess work. The present paper has an improved version of the latter method.

3 Quantum Theory of Measurement

A substantial amount of my work during the last forty years has involved the Quantum Theory of Measurement. During those years, my ideas on the subject evolved considerably. My 1969 paper[4], in Physics Today, which arose from a 1968 Lindau lecture, (with Heisenberg, Dirac and Born in the audience!), dealt with a model for preparation of a quantum state. Measurements of momentum and position were also discussed in simple minded ways. Measurements of some other observable made use of an idealized Stern-Gerlach meter apparatus. At that time, I did not know of the von Neumann meter method (for coordinates) described in the last two pages of the last Chapter, 6, of his 1933 book[5]. I did know of his discussion in Chapter 3 on what is often called the "Collapse" or "Reduction" of the wave function. Very similar ideas had been expressed in first Chapter of Dirac's 1930 book on Quantum Mechanics. I first tried to read this in the summer of 1932 in the Science Reading Room of the Los Angeles Public Library. I found his discussions to be absurdly naive, and could not imagine that anybody would take it seriously. When I found that many people did take it very seriously, I wrote a few papers critical of the collapse of the wave function:[6–8].

In the early eighties, I learned from Melvin Lax of the 1965 Bell System Technical Journal paper by Arthurs and Kelly[9] who made use of the von Neumann meter for measurement of position. They also devised a similar meter model for simultaneous measurement of momentum.

By the time of the 1986 meeting at the New York Academy of Sciences [10], I had learned how to use and improve upon the von Neumann meter method for position measurements. I presented more refined methods at later meetings in 1986 at Tokyo[11] and at Como[12], in 1989 at College Park, Md.[13], and at Turin[14] in 1990.

The most important defect of these papers was that, in discussing the measurement process, I had to change back and forth between a quantum and a classical description of the meter measurement system. The present paper provides a better method for dealing with this transition problem because the classical and quantum theories are brought together into one theory.

4 Rewriting the History of Quantum Mechanics

One of the purposes of the present work is to show how much simpler the History of Quantum Mechanics could have been, than it actually was. The teaching of the subject will be greatly simplified by this approach. The well understood Classical Mechanics is recast into an equivalent, but more general, form. Almost automatically, the theory turns out to be an improvement

of the familiar non-relativistic Quantum Mechanics, It is free of most of the baggage of historical misunderstandings that the traditional Quantum Mechanics developed during much of the twentieth century.

5 Historical Misunderstandings

One of the advantages gained by our treatment is that one can forget (and, or, forgive?) many of the fuzzy ideas[15,16], that cluttered the path from Classical Mechanics to Quantum Mechanics. These include: Planck's theory of black body radiation, Einstein's photon and treatment of the photoelectric effect of 1905, Bohr's 1913 quantization, Bohr's 1918 Correspondence Principle, de Broglie's waves of 1924, Heisenberg's matrix mechanics of 1925, Schrödinger's wave equation of 1925, Dirac's Quantum Mechanics of 1926, Heisenberg's Uncertainty Principle of 1927, Bohr's Principles of Complementarity and Wave-particle Duality, Dirac's and von Neumann's notions of the Collapse of Wave Packets, and the excessive use of Hilbert Space. We might have been spared much of the agony needlessly suffered with the Two Slit Diffraction Pattern Paradoxes, the Einstein-Podolsky-Rosen Paradoxes, and the Schrödinger Cat Paradox[17,18]. Also unnecessary were Bohm's Quantum Mechanics and Hidden Variable Theories, and Bell's Inequalities. Other variations abound in the pages of Physics Today[19] and Physics World[20]: DH (Decoherent Histories), with words like "reality" and "non-locality", SL (Spontaneous Localization), and BQM (Bohmian Quantum Mechanics). It is widely rumored that the Editors of the Physical Review find that papers on measurement theory are too troublesome to edit.

Delayed Choice Experiments[21] have never been adequately discussed using any systematic theory of Quantum Mechanical Measurement. The same can be said of Quantum Computers and Quantum Cryptography[22]. The bulk of papers on these subjects lack any understanding of the intrinsic probabilistic nature of Quantum Mechanics. Papers on teleportation are beneath contempt.

In my opinion, the above troubles can easily be avoided if we derive the probabilistic features of Quantum Mechanics properly by "repairing" the non-deterministic Classical Mechanics. The resulting theory contains Dirac's constant $\hbar \cong 10^{-34}$ joule seconds with dimensions of an "action", i.e., an energy multiplied by a time (or a distance multiplied by a momentum). Physical problems which are characterized by actions very large compared to \hbar can, in suitable cases, be treated by Classical Mechanics, and problems with smaller action will automatically be dominated by quantum features.

6 What are the Troubles of Classical Mechanics?

We have been claiming that NCM is non-deterministic. The following paragraphs describe several types of non-deterministic behavior. Consider the

motion of one particle of mass m moving along a straight line. The particle's position, x , is a function $x(t)$ of time t . Its velocity v is $v(t) = \frac{dx(t)}{dt}$, its acceleration a is $\alpha(t) = \frac{dv(t)}{dt} = \frac{d^2x(t)}{dt^2}$. In a typical application, the force F might be a function of time, $F(t)$, or a function $F(x(t), t)$ of $x(t)$ and t . For the case of a potential energy field $V(x, t)$, one would have $F(x, t) = -\frac{\partial V(x, t)}{\partial x}$. Extensions to many body problems are fairly straightforward.

Newton's classical equation of motion is

$$m \frac{d^2x}{dt^2} = -\frac{dV(x, t)}{dx}. \quad (1)$$

There are some simple analytically solvable one-dimensional problems for potential functions such as $V(x) = \text{constant}$, x , x^2 , and with more trouble, x^4 , etc. Thus, for $V(x)$ proportional to x we get uniformly accelerated motion; for a quadratic, x^2 , we get trigonometric motion. For a quartic potential, x^4 , we are led to elliptic functions. Examples of the simplest potential energy functions are:

1. $V(x) = 0$, for a free particle at x , moving along the x axis,
2. $V(x) = mgx$, for a body falling in a uniform gravitational field,
3. $V(x) = \frac{1}{2}kx^2$, simple harmonic oscillator, with Hooke's law of restoring force exerted by an ideal spring. In these cases, Newton's equation can be solved in terms of elementary functions. For most potential functions, no analytic solutions can be found, and one must use numerical integration, preferably with help from a computer.

7 Discussion

Some important questions arise. How deterministic is the theory based on Newton's equations? What is its range of validity? For how long a time can one expect to have a valid description of the motion of a system? In any case, the longer the time elapsed, the more the motion will be disturbed by remote objects or by forces originating from outside the system.

One might seem to get a pretty good treatment of long time motion if the system of interest is well isolated from the rest of the universe. Then one should have a high degree of determinism. However, in his Nobel Lecture of 1954, Max Born [23], pointed out the mismatch between mathematics and physics. (I had no thoughts of this idea in 1930.) In mathematics, numbers are imagined to be capable of infinitely high precision. In physics, the position of a particle can only be specified by numbers of finite precision. This mismatch might not seem too troublesome for problems of interest, except after very long times.

Another point that Born might have made, but did not: The Newtonian concept of a particle was only a convenient fiction. There probably are no elementary particles anywhere in nature. Galileo had a lamp swinging in a cathedral, or a block of wood sliding down an inclined plane. For Newton,

it might have been a stone, an apple or a heavenly body. Newton probably realized that these objects were composite structures, but did not follow that idea further. Electrification of some bodies by friction was known, but not much studied in the seventeenth century. The discovery of electrons required more than two centuries.

Although, in Newtonian mechanics, the two quantities: coordinate $x(t)$ and momentum $p(t) = mv(t) = m \frac{dx(t)}{dt}$ involve very different concepts, it was tempting to treat them as equally important elements of the theory. This tendency was much encouraged by the beautiful transcription of Newton's equations into Hamiltonian form in the nineteenth century. However, I think that finding a better formulation of Quantum Mechanics is even a more important task.

There are problems involving classical measurement and state preparation: How do we know that a particle is at $x = 0$ at $t = 0$? Or how do we know that a particle has a velocity v at time $t = 0$? In the 1660's, the position of a particle could be measured with a microscope having a suitable distance scale. It took three centuries from about 1660 to 1960 before velocity could be measured with a Doppler laser (speed trap) apparatus. Both of these instruments are optical instruments, and cannot be readily treated with the laws of mechanics. At the time of Newton, position could be measured, but velocity or momentum determination would ordinarily require two position measurements at closely separated times.

It would be nice to have a mechanical model for the measurement processes of Classical Mechanics which could be analyzed using only the laws of Newtonian Mechanics. Heidi Fearn and I [24] have given an indication of how position measurements can be carried out in Newtonian Mechanics. My papers on the Quantum Theory of Measurement, [10], [11], [12] and [14] are, in effect, just quantum transcriptions of this classical discussion. Later papers will return to this problem.

8 What are some Troubles with the Determinism of Newtonian Classical Mechanics?

Consider the free motion of a particle on a straight line. Suppose that we want to have its initial position to be $x(0) = 0$ and its initial velocity $v(0) = \left[\frac{dx(t)}{dt} \right]_0 = 0$. The traditional Newtonian result is that x would remain at $x(0) = 0$ for all later times. However, in a physical world, both of the starting values $x(0)$ and $\left[\frac{dx(t)}{dt} \right]_0 = 0$ would be somewhat out of our control. For a long term solution, we might ignore the effect of a slight offset in position $x(0)$, but a very small value of the initial velocity $v(0)$, when multiplied by a large value of time, could lead to a flagrant discrepancy between theory and experiment for $x(t)$.

Another example: Consider a particle, initially near a position $x = 0$, acted upon by a force derived from a peaked potential energy function curve called the Witch of (Luisa) Agnesi[25].

$$V(x) = \frac{V_0}{1 + \frac{x^2}{x_0^2}} \quad (2)$$

where the peak potential V_0 height is positive, and the distance parameter x_0 gives a measure of the peak width. For coordinate x values much smaller in magnitude than x_0 , this potential function $V(x)$ is like an “upside down” parabolic function of x . If the initial x value were exactly zero, a long term solution of Newton’s equation would be $x(t) = 0$. To try to confirm this, we use the best efforts of a highly skilled person to put the particle at rest with $x = 0$ at $t = 0$. Even so, the long term behavior of the system will be very strongly dependent on the initial values of x and v . When I was younger, this state of affairs was called unstable equilibrium. Now, it is one of the simplest forms of a chaotic problem[26].

There are many other problems in Newtonian mechanics that have similar bifurcation features. One of the first to meet them, without much contemporary notice being taken, was Maxwell, in his kinetic theory of gases, (1865). A good deal of the trouble that Ludwig Boltzmann had in a conflict between mechanics and thermodynamics came from similar chaos. Just think of the chaotic consequences associated with nearly head-on collisions in a gas of two spherical molecules. See also Maxwell’s 1871 Inaugural Lecture as Cavendish Professor [26] at Cambridge. Such things also occur in the 1996 work on Celestial Mechanics by Henri Poincare[27], and in my lecture “Quantum Chaos and the Theory of Measurement”[28] in a 1983 Como Conference on Quantum Chaos, and in a 1986 Royal Society Lecture: “The Recently Recognized Failure of Predictability in Newtonian Dynamics” by the late Sir James Lighthill [29] Other examples of such problems can be found in a 1918 book by Georg Duffing [30], in his early treatise on nonlinear mechanics. As one goes to problems of higher dimensionality, most classical dynamical systems have chaotic behavior, as in the long term motion of particles in the Fermi-Pasta-Ulam [31] and Toda [32] lattices.

9 Let’s Try Going into the x, p Phase Space

I draw from the previous paragraph the conclusion that Classical Mechanics should not be formulated in terms of the ordinary differential equations of NCM which determine trajectories as $x = x(t)$. Instead, one should have a probabilistic description of some kind. I have in mind the early 1900’s work of Willard Gibbs on Statistical Mechanics. Consider also the 1949 Waynflete Lectures of Born[33] at Magdalen College, Oxford. He moved from a trajectory approach with $x(t)$ in coordinate space to a description in a two

dimensional phase space with coordinate x , and momentum p . He made use of the probabilistic concept of a phase space density $\rho(x, p, t)$. This density $\rho(x, p, t)$ obeys the Liouville equation

$$\frac{\partial \rho(x, p, t)}{\partial t} = \{H(x, p, t), \rho(x, p, t)\} \quad (3)$$

involving the Poisson Bracket expressions

$$\{H, \rho\} = \frac{\partial H}{\partial x} \frac{\partial \rho}{\partial p} - \frac{\partial H}{\partial p} \frac{\partial \rho}{\partial x} \quad (4)$$

formed from $\rho(x, p, t)$ and the Hamiltonian function

$$H(x, p, t) = \frac{p^2}{2m} + V(x, t). \quad (5)$$

This kind of approach would put the usual Newtonian results in probabilistic form. It could have helped Born overcome his arithmetic precision problems. It makes use of an x, p phase space, and does not recognize that Newtonian coordinates and momenta really have enormous physical differences. It is not the road to Quantum Mechanics.

10 Probability Density in Coordinate Space

We return to the Newtonian treatment, with the idea of using a probability density only for the time dependent particle position coordinate x , as in a “position pointing function” $W(x, t)$. As a first guess, one could try to find an equation determining $W(x, t)$. This might have to be some kind of partial differential equation since W has to be a function depending on two independent variables x and t . For example, the equation

$$\frac{\partial W(x, t)}{\partial t} + v \frac{\partial W(x, t)}{\partial x} = 0 \quad (6)$$

could describe the motion of a probability density function $W(x, t)$ in free particle motion with constant velocity v . The general solution of this equation is

$$W(x, t) = f(x - vt), \quad (7)$$

where f is an arbitrary normalized function of its argument, $x - vt$. The spatial dependence of the function $W(x, t)$ would determine the probability distribution for the x location of the particle at time t . A well localized free particle at time t would be described by a function

$$W(x - vt) \quad (8)$$

which was sharply confined in the argument $x - vt$.

Of course, our main object is to be able to describe more complicated motions for which forces are acting on the particle. At this point, we have a possible clue: We should look for a partial differential equation for $W(x, t)$ for cases where forces are acting on the particle.

However, solutions of such a partial differential equation could easily become negative for some values of x . I do not want to introduce a nonsensical concept like negative probability into physics. A simple way out of the difficulty is to use a complex probability amplitude function $\Psi(x, t)$ and to assure that $W(x, t)$ remains positive by setting $W(x, t) = |\Psi(x, t)|^2$. Then we can try to find a partial differential equation for $\Psi(x, t)$.

11 Getting a Partial Differential Equation for $\Psi(x, t)$

Looking for a partial differential equation to determine $\Psi(x, t)$ might seem like looking for a needle in a haystack. However, it turns out that two guiding principles can take us a long way to a unique solution. These are (1) simplicity, and (2) dimensional correctness. In an earlier paper [3], I have shown that this approach leads almost uniquely to the Schrödinger equation and Born's probability interpretation of the Ψ function. To save time in this paper, I skip this derivation here and assume the Schrödinger equation, (complete with its "i" and " \hbar "),

$$-\frac{\hbar}{i} \frac{\partial \Psi(x, t)}{\partial t} = -\frac{\hbar^2}{2m} \frac{\partial^2 \Psi(x, t)}{\partial x^2} + V(x, t) \Psi(x, t), \quad (9)$$

to be already known, together with the probabilistic interpretation of $\Psi(x, t)$.

It is strongly recommended that the function $\Psi(x, t)$ should be called a $\Psi(x, t)$ function or a probability amplitude function with NO mention of a Schrödinger, or (Dirac) wave function or wave equation. This advice might help to reduce unnecessary duelling between waves and particles.

The Ψ function can be normalized by providing it with a multiplicative factor so that the integral

$$\int dx W(x, t) = \int dx |\Psi(x, t)|^2 \quad (10)$$

is unity when the integration over x runs from $x = -\infty$ to $x = +\infty$.

Just as in the historical development, we can derive a probability conservation law from the Ψ equation. We can also calculate the time rate of change of the time dependent x -centroid $\langle x(t) \rangle$ or other functions of x . The centroid of the x distribution is

$$\langle x(t) \rangle = \int dx x W(x, t) = \int dx \Psi^*(x, t) \Psi(x, t) \quad (11)$$

and the corresponding time rate of change of $\langle x(t) \rangle$ i.e., velocity, is

$$\langle v(t) \rangle = \frac{d}{dt} \langle x(t) \rangle = \frac{d}{dt} \int dx \Psi^*(x, t) x \Psi(x, t). \quad (12)$$

The time differentiation is now taken under the x integration sign. Use is made of the Ψ and Ψ^* equations, and some partial integrations are performed assuming that the functions Ψ, Ψ^* vanish as x approaches infinity. The result is a time dependent velocity

$$\langle v(t) \rangle = \frac{d}{dt} \langle x(t) \rangle = \left[\frac{1}{m} \int dx \Psi^*(x, t) \frac{\hbar}{i} \frac{\partial \Psi(x, t)}{\partial x} \right]. \quad (13)$$

From this we see that an operator p for the momentum in the x direction, familiar in conventional Quantum Mechanics, can be taken as $p = \frac{\hbar}{i} \frac{\partial}{\partial x}$, which corresponds to the equation $p = m \frac{dx}{dt}$ of classical mechanics.

At this stage, we could, if desired, begin to work with non-commuting x , p , and other operators, as in the familiar forms of Quantum Mechanics.

A further differentiation with respect to t of the above integral expression for $\langle v(t) \rangle$ and use of the Ψ equations for the time derivatives of Ψ and Ψ^* , and some more partial integration, leads to the 1927 Ehrenfest[34] theorem

$$m \frac{d^2 \langle x(t) \rangle}{dt^2} = - \int dx \Psi(x, t)^* \frac{\partial V(x, t)}{\partial x} \Psi(x, t), \quad (14)$$

which is the quantum version of the second law of motion of NCM when the “spatial width” of $\Psi(x, t)$ is sufficiently small. This equation is vital for an understanding of how classical mechanics emerges from Quantum Mechanics in the classical limit.

It may be well to point out that Ehrenfest’s theorem is here derived as an integral relationship from the probability amplitude equation and hence it does not necessarily have any connection to the classical mechanics of a particle. To get such a connection, we must have a situation where $\Psi(x, t)$ and hence $\Psi(x, t)^* \cdot \Psi(x, t)$, is a sufficiently “narrow” function of x . In many cases the width of the Ψ function may increase in time, and the application to classical mechanics is no longer valid. Further discussion of such matters will appear elsewhere.

12 I will now show that we can deal with Newtonian Mechanics. Let’s test this out with our three simple problems

It remains to be seen how well the y equation can imitate the results usually obtained from Newton’s equation of motion for the three problems listed above.

The use of a time-dependent WKB (Wentzel, Kramers and Brillouin) method will prove helpful. We substitute $\Psi(x, t)$ as an exponentiated expression

$$\Psi(x, t) = \exp \left[-\frac{S(x, t)}{\hbar} \right], \quad (15)$$

into the probability amplitude equation and get a time-dependent Riccati equation

$$-i \frac{\partial S}{\partial t} = -\frac{1}{2m} \left[\frac{\partial S}{\partial x} \right]^2 + \left[\frac{\hbar}{2m} \right] \left[\frac{\partial^2 S}{\partial x^2} \right] + V \quad (16)$$

for the complex “action”, or “Hamilton-Jacobi function”, $S(x, t)$.

13 If it weren't for stationary states, we would not have Quantum Mechanics

Most of the applications of the W. K. B. approximation in a well known Quantum Mechanics text book, for instance[35], aim at finding approximate solutions for stationary states. The left hand side of the time dependent Riccati equation is replaced by the product of E and S , the energy eigenvalue of the stationary state. Then, with suitable approximations, one gets the usual W. K. B. expressions for classically allowed and forbidden parts of the eigenfunction for a stationary state with energy E . With the Kramers-Airy function, or the Zwaan connection, one gets good approximations for energy eigenvalues. The emphasis on stationary states came historically from the spectroscopic studies of the nineteenth century.

Most traditional text books on Quantum Mechanics deal with steady, or stationary, states. Moving Ψ packet solutions are harder to treat. This widens the gap between Classical and Quantum Mechanics, and has seriously undermined the unity of the science of mechanics.

14 We also want to have time-dependent solutions

In the present work, we want to get solutions for the time dependent probability amplitude packet for problems 1, 2 and 3, which have different powers 0, 1, and 2 of x in their potential functions. The Riccati equation contains a second order differentiation of S with respect to x , and the square of a first order differentiation of S with respect to x . As a result, we can get simple exact particular solutions of a wide class of time dependent equations. To bring the various possibilities into a compact form, we consider a potential function $V(x, t)$ in the form of a time dependent linear and quadratic (parabolic) function of x

$$V(x, t) = V_1(t)x + V_2(t)x^2 \quad (17)$$

or more explicitly,

$$V(x, t) = -F(t)x + \frac{1}{2}m\omega(t)^2x^2 \quad (18)$$

For such a parabolic polynomial in x , the action function $S(x, t)$ will also be a quadratic polynomial in x . For potentials V with other kinds of x dependence,

we will soon be outlining an efficient way to get useful approximate solutions of Ψ packet problems.

The quantities $F(t)$ and $\omega(t)$ have simple intuitive interpretations, and can have arbitrary time dependence. A way of describing the notation is to say that the force $F(t)$ characterizes the slope of the potential energy $V(x, t)$, i.e., represents a spatially uniform, but time variable, force field $F(t)$, and the coefficient $\frac{1}{2}m\omega(t)^2$ corresponds to the x^2 curvature of the potential function $V(x, t)$, i.e., we have a time dependent Hooke's law spring force constant.

15 Method of a complex Gaussian Ψ function

A quite general expression for the solution of the Riccati equation for the action function S is of the form

$$S(x, t) = \alpha(t)x^2 - 2\beta(t)x. \quad (19)$$

This choice of the action function makes Ψ into a complex Gaussian function.

The quantities $\alpha(t)$ and $\beta(t)$ are complex functions of the time and are still to be determined. The action function $S(x, t)$ could also have a term in x^0 , which would serve to renormalize the probability amplitude function Ψ . I prefer to work now with unnormalized Ψ functions, and will be careful to allow for proper normalization when calculating expectation values. Hence, the x^0 terms will now be omitted from $S(x, t)$.

For this $S(x, t)$ to be a solution of the Riccati equation it is necessary that $\alpha(t)$ and $\beta(t)$ obey the two coupled nonlinear ordinary differential equations

$$\frac{d\alpha(t)}{dt} = i \left[V_2(t) - \frac{2\alpha(t)^2}{m} \right], \quad (20)$$

$$\frac{d\beta(t)}{dt} = i \left[V_1(t) - \frac{2\alpha(t)\beta(t)}{m} \right]. \quad (21)$$

I repeat these equations for the more intuitive explicit representation of the polynomial $V(x, t)$ with x and x^2

$$\frac{d\alpha(t)}{dt} = i \left[m \frac{\omega(t)^2}{2} - \frac{2\alpha(t)^2}{m} \right], \quad (22)$$

$$\frac{d\beta(t)}{dt} = i \left[F(t) - \frac{2\alpha(t)\beta(t)}{m} \right], \quad (23)$$

There is far more generality in these two sets of two equations than we will need, since they are still valid when F, ω , and m , and even \hbar , can be arbitrary functions of time. In earlier years, one could have solved the differential equations in simple but important cases. Nowadays, one might use computer analysis even for the soluble cases.

To sum up, for the class of potentials with linear (and (or)) quadratic x dependence, there are relatively simple complex gaussian Ψ function solutions. As discussed below, these can be used as a starting basis for approximate solutions of a much wider class of x dependent potentials.

16 Free Particle

Case (1) is that of a free particle. F and ω are both zero. The equation for $\frac{d\alpha(t)}{dt}$, does not depend on $\beta(t)$: We have

$$\frac{d\alpha(t)}{dt} = -2i \frac{\alpha(t)^2}{m} \quad (24)$$

with solution given by

$$\frac{1}{\alpha(t)} = \frac{1}{\alpha_0} + \frac{2i\hbar t}{m} \quad (25)$$

or

$$\alpha(t) = \frac{\alpha_0}{1 + \frac{2i\alpha_0 t}{m}} \quad (26)$$

where α_0 is the initial value of $\alpha(t)$ at $t = 0$. The corresponding equation for $\frac{d\beta(t)}{dt}$ is

$$\frac{d\beta(t)}{dt} = -i \left[\frac{2\alpha(t)\beta(t)}{m} \right] \quad (27)$$

One solution is $\beta(t) = 0$. The general solution for $\beta(t)$ is a constant multiple of $\alpha(t)$. If the constant is real, the particle centroid remains at rest. If the constant is pure imaginary, the particle moves with constant velocity.

A free particle $\Psi(x, t)$ packet solution is

$$\Psi(x, t) = \exp(-\alpha(t)x^2 + 2\beta(t)x) \quad (28)$$

The corresponding probability density is

$$W(x, t) = \exp(-2Re(\alpha(t)x^2) + 4Re(\beta(t)x)) \quad (29)$$

The centroid of this Gaussian exponential distribution is at

$$\langle x(t) \rangle = \frac{Re(\beta)}{Re(\alpha)}. \quad (30)$$

That this packet moves with uniform velocity is also easily seen from the integrals in the Ehrenfest relation for a free particle.

17 Free fall in a constant uniform force field

With a constant $F = mg$, (and $\omega = 0$), the $\alpha(t)$ is just that for a free particle, and $\beta(t)$ obeys the easily solved equation

$$\frac{d\beta(t)}{dt} = -i \left[mg + \frac{2\alpha(t)\beta(t)}{m} \right] \quad (31)$$

Again an application of Ehrenfest's theorem shows that in the classical limit of \hbar approaching zero the centroid has the correct constant acceleration g .

18 Simple harmonic oscillator

Case (3) is that of a simple harmonic oscillator. Again, the use of Ehrenfest's theorem shows that, in the classical limit, the centroid $\langle x(t) \rangle$ has the correct Hooke's force law motion.

There is an important special case when $\alpha(t)$ is a constant. According to the differential equation for $\frac{d\alpha}{dt}$ this occurs when $\alpha = \frac{1}{2} \frac{m\omega}{\hbar}$. This α value is that describing the mean square width of the Gaussian ground state simple harmonic oscillator function for the values of m , ω and \hbar . With use of the complex Gaussian method, one could, much earlier and more easily, have found the time dependent states discovered by Schrödinger[36] in Zurich in 1926, generalized by Earle Kennard[37] of Cornell in 1927, and called "coherent" by Roy Glauber[38] of Harvard in the mid 1960's. The time dependent wave packet solutions for a harmonic oscillator have been given in a book on laser physics[39].

19 Some properties of a complex Gaussian Ψ function

This (unnormalized) Ψ function is

$$\Psi(x, t) = \exp \left[-\frac{S(x, t)}{\hbar} \right], \quad (32)$$

The unnormalized probability density $WU(x, t)$ is

$$WU(x, t) = |\Psi(x, t)|^2 = \exp \left[-\frac{S(x, t) + S(x, t)^*}{\hbar} \right] \quad (33)$$

With the action function

$$S(x, t) = \alpha(t)x^2 - 2\beta(t)x, \quad (34)$$

we get

$$WU(x, t) = \exp(-2Re(\alpha)x + 4Re(\beta)x). \quad (35)$$

The peak of the probability distribution is at $x_p = \frac{Re(\beta)}{Re(\alpha)}$. The standard deviation is

$$\sigma = \sqrt{\frac{1}{2Re(\alpha)}} \quad (36)$$

20 Non-parabolic Potentials!

It would seem at first sight that one could only treat problems with potential functions made up of linear and quadratic powers of x . However, in many cases, a very good approximation can be used for a much wider class of potential functions $V(x)$. At each temporal stage of the integration procedure, the values of $\alpha(t)$ and $\beta(t)$ determine the peak coordinate x_p of the Gaussian probability distribution function $W(x, t)$, which occurs at

$$x_p = \frac{Re(\beta)}{Re(\alpha)}. \quad (37)$$

The corresponding inverse squared width parameter is

$$\sigma = 2Re(\alpha) \quad (38)$$

One could then make a Taylor's expansion of the potential function $V(x)$ around the point

$$x = x_p, \quad (39)$$

keeping only linear and quadratic terms in displacements of x from the current peak position. The coefficients of this Taylor's expansion of the potential function V would give the quantities "slope" F and "curvature" $m\omega^2$ that enter into our differential equations for $\alpha(t)$ and $\beta(t)$. The α, β equations could then be integrated numerically for a short time step to give a new configuration expressed in terms of $\alpha(t)$ and $\beta(t)$. From these, a new peak position x_p for the later time could be calculated. After this, a new Taylor's expansion could be made about the new peak location x_p , where new values for F and ω^2 would be calculated, and so on. The process is similar to that used in analytic continuation in the theory of functions of a complex variable.

I list a few more problems which will be treated in later publications.

- (4) A freely swinging simple pendulum (or anharmonic oscillator),
- (5) A periodically forced anharmonic oscillator (Duffing [30] problem),
- (6) A Kepler problem, as in the motion of the Moon around the Earth for which the potential energy varies with the inverse first power of the distance between the Earth and the Moon.
- (7) A charged spinless particle moving in a magnetic field.
- (8) Measurement problems in Quantum Mechanics and Optics.

21 More General Potential Functions

So far, we have considered problems in one Cartesian coordinate x for a single particle in a potential no more complicated than parabolic in form. The method can easily be extended to apply to more complicated potentials and to two or three Cartesian coordinates for a single particle, or to any number of such particles. We begin by assuming that $V(x, y, z, \dots)$ has linear and quadratic terms in x, y, z, \dots and also allow terms in xy, xz, yz, \dots . We merely have to devise a convenient notation for parameters to replace the $\alpha(t)$ and $\beta(t)$ of the earlier treatment. For one coordinate, one needs only two complex functions, $\alpha(t)$ and $\beta(t)$. For two degrees of freedom there are five. In the case of n degrees of freedom, there are

$$\frac{n(n+1)}{2} + n = \frac{n(n+3)}{2} \quad (40)$$

functions of time. The method analogous to analytic continuation is readily available as before. Hence, it is simple to treat the orbits of Kepler for the $\frac{1}{r}$ potential. The Ψ function $\Psi(x, t)$ of x at t now becomes a function $\Psi(x, y, t)$ in a two dimensional space of x and y . At the cost of more numerical work, systems with many particles could be treated. Nowadays, a computer can make large systems easy to treat.

Other applications of this work are to find the ways in which Gaussian Ψ functions spread and are deformed in anharmonic potentials, to discuss chaotic phenomena and the Quantum Theory of Measurement. For lack of time and space, I will have to pass up such topics in the present discussion.

Many problems in electromagnetic theory and quantum optics can be reduced to the dynamical problem of a system consisting of a large number of mechanical simple harmonic oscillators. Each oscillator coordinate is associated with the electric field of one of the normal modes of a cavity resonator. Hence, the method of complex Gaussian Ψ functions can be applied to many problems in the Quantum Theory of Radiation. In case you don't know it already, despite what many other people[40] think, there are NO PHOTONS of a particle-like nature in Quantum Electrodynamics.

22 Ehrenfest's Theorem Revisited

Ehrenfest's theorem of 1927 showed that a sufficiently narrow Ψ packet would follow the Newtonian classical trajectory for a problem with a potential energy $V(x)$. In a later paper, we will show that a Gaussian packet remains Gaussian as time advances if and only if the potential energy $V(x)$ is parabolic in its x -dependence. If the potential is non-parabolic, a Gaussian Ψ function will become non Gaussian as time advances. The time required for this transition becomes longer in the classical limit, i.e., as \hbar approaches zero. It seems that this behavior has not been previously noticed.

23 Stationary States

The Ψ equation has many solutions that are not in the form of narrow packets. There are even solutions which are periodic in time,

$$\Psi(x, t) = u(x) \exp\left(-\frac{iEt}{\hbar}\right) \quad (41)$$

with a circular frequency, $\frac{E}{\hbar}$ where E is a constant with dimensions of an energy. These are called stationary solutions, since their probability distribution functions

$$W(x, t) = |\Psi(x, t)|^2 \quad (42)$$

do not depend on time. They would not have seemed to have any physical application before the time of Planck. They are the stationary states of the twentieth century. The concept of a space-time orbital trajectory naturally has no validity for such a state.

24 Extensions to other Problems: Magnetic Fields, Relativity, Spin?

The above methods can also be applied to the motion of a charged particle in a spatially variable, magnetic field, (described by a vector potential A), and also to the motion of a particle in special relativity mechanics. In the cases treated so far, the quantum theory has a classical, i.e., a non-quantum, limit. However, the Dirac relativistic theory does not have a simple W. K. B. approximation[41], or classical limit. In fact, the case of a particle with a spin magnetic moment can not be treated by the simple methods of this paper. I have been considering the theory of a spinless particle. Spin phenomena are very important for chemistry and physics. For the conventional form of Quantum Mechanics, a Pauli two component probability amplitude function is easily incorporated into the nonrelativistic quantum mechanics. The magnetic moment associated with spin is of some considerable interest, but usually does not dominate the problems of chemical binding. However, the spin itself plays a vital role in the theory of chemical binding, in the proper enumeration of states, and the whole structure of the periodic system of elements. A failure to get that right might literally be a matter of life and death for us. It is much more difficult to extend the theory of probability distribution functions to particles with spin, either in the Pauli approximation or with the Dirac relativistic electron theory. Historically, a nuclear atom with orbiting and spinning electrons seemed very similar to a planetary system with spinning planets in orbital motion about a star. However, in classical theory, the spinning planet is a many body system. The Dirac relativistic wave equation was intended to be a one particle theory, but it was unexpectedly forced to become a many body (or field) theory because of the possibility of

negative energy states in relativistic mechanics. It is possible, but fairly complicated, to apply the method of this paper to a rotating object consisting of several particles. However, the spin of the electron is not treated in Quantum Mechanics in anything like that manner. but rather with multi-component wave functions.

25 Exchange Degeneracy

Another interesting problem concerns exchange phenomena. We easily extended our treatment from a one body to a many body problem. A suitable generalization of Quantum Mechanics is obtained, but nothing is being said about the particle exchange symmetry of the Ψ function. It is easily possible to impose Fermi-Dirac or Bose-Einstein statistics. We are no worse off then in we were in the twenties. The Newtonian classical theory from which we start contains no hints for dealing with the problem of particle exchange. Berry [42] has recently discussed similar problems from a different point of view.

26 Remarks on Spin and Magnetic Moments

The magnetic moment of the electron could be associated with a very rapid small scale circular motion of the electron. The magnetic moment μ associated with a point charge e moving in a circle of radius R with a speed v is $\mu = eR\frac{v}{2}$. If R is taken to be the Dirac length $\frac{\hbar}{mc}$. Note that R is about $\frac{1}{137}$ of the Bohr radius a_0 . One finds

$$\mu = \frac{e\hbar}{mc} v, \quad (43)$$

so that to obtain a magnetic moment of one Bohr magneton,

$$\mu_0 = \frac{e\hbar}{mc} \quad (44)$$

one would have to have $v = c$!!!

This argument is not meant to be quantitative, but just to show that a spinning electron is a strange thing. If the electron were not point-like, but string-like, or a distributed line-charge with a length as long as $\frac{\hbar}{mc}$, the theoretical energy levels of the hydrogen atom would be very different from the observed values.

The trouble is that the theory is built on the concept of point particles which can, in principle, be considered as isolated. An electron is inevitably in interaction with the quantum electromagnetic field. As suggested by Welton[43] this means that the position of the over-idealized point electron is effectively smeared out over a distance an order of magnitude larger than the classical electron radius. The resulting departure from the Coulomb inverse square law force contributes, in large part, to the electromagnetic level shift.

Nuclei also have a finite size. A proton has turned out to be a highly complex particle. At present, it seems to be that the most reliable measure of the proton size comes from studies of the atomic hydrogen levels [44].

27 In Retrospect

The most obvious success of our theory is in the field of Non-Relativistic Quantum Mechanics, and the very clear understanding of the statistical interpretation of quantum theory it gives in that domain. The so-called paradoxes of traditional Quantum Mechanics are all to be found in the non relativistic domain. The most obvious failure involves spin. The easiest way to include spin would be to imitate the Pauli-Dirac methods of multi-component wave function. However, Gaussian exponential factors play a big role in our work, and the four components of a Dirac relativistic wave functions have different exponential factors. The Gaussian exponential functions do not cancel out as nicely as they do in the non-relativistic theory.

It would have been much better for the history of physics if Newton had discovered probability theory, and applied it to the laws of mechanics. A similar remark about Einstein: He was probably the first physicist to use probability theory to discuss a specific physical problem, i.e., for Brownian motion. Unfortunately, Einstein did not believe that the use of probability theory was essential for radioactive decay [45], Brownian motion, and other microscopic problems, and not merely a convenient recipe for the avoiding tedious details.

References

1. W. E. Lamb, Jr. "On the Electromagnetic Properties of Nuclear Systems", Part 2 of Ph. D. Thesis, U. C., Berkeley, Phys. Review, 53, 651-656, (1938).
2. W. E. Lamb, Jr. "Suppose Newton had invented Wave Mechanics", Am. J. Phys. 62, 201-206 (1994).
3. W. E. Lamb, Jr. "The Borderland between Quantum and Classical Mechanics", Physica Scripta T70, 7-13 (1997).
4. W. E. Lamb, Jr., "An Operational Interpretation of Non-relativistic Quantum Mechanics", Physics Today, 22, 23-28, (1969).
5. J. von Neumann, "Mathematical Foundations of Quantum Mechanics", English Translated by R. T. Beyer, (Princeton University Press, Princeton, N. Y.)
6. W. E. Lamb, Jr., "Von Neumann's Reduction of the Wave Function", in The Centrality of Science and Absolute Values, Proceedings of the Fourth International Conference on the Unity of the Sciences, pp. 297-303 (ICF Press, N.Y., N.Y. 1975).
7. W. E. Lamb, Jr., "Remarks on the Interpretation of Quantum Mechanics," in Science of Matter, ed. S. Fujita, pp. 1-8, (Gordon and Breach, New York, 1979).
8. W. E. Lamb, Jr., "A Letter to Kip Thorne", in CCNY Physics Symposium, in Celebration of Melvin Lax's Sixtieth Birthday, ed. H. Falk, pp. 40-43, (City University of New York, 1983).

9. E. Arthurs and J. Kelly, "On the Simultaneous Measurement of a Pair of Conjugate Observables", *Bell System Technical Journal* 44, 725-729 (1965).
10. W. E. Lamb, Jr., "Quantum Theory of Measurement", *Annals, New York Academy of Sciences*, 480, pp. 407-416 (1986).
11. W. E. Lamb, Jr., "Theory of Quantum Mechanical Measurements" in *Proceedings of the 2nd International Symposium on the Foundations of Quantum Mechanics: In the light of new technology*, ed. M. Namiki, pp. 185-192 (Japan Physical Society, 1987).
12. W. E. Lamb, Jr., "Sequential Measurements in Quantum Mechanics". Lecture at Como NATO Advanced Research Workshop in Quantum Optics, September, 1986. In *Quantum Measurement and Chaos*, ed. E. R. Pike and S. Sarkar, pp. 183-193 (Plenum Press, New York and London, 1987).
13. W. E. Lamb, Jr., "Classical Measurements on a Quantum Mechanical System" in *Proceedings of the International Symposium on Spacetime Symmetries*, eds. Y. S. Kim and W. M. Zachary, pp. 197-201, reprinted from *Nuclear Physics B (Proc. Suppl.)* 6, 1989 (North-Holland, Amsterdam, 1989).
14. W. E. Lamb, Jr., "Quantum Theory of Measurement", Lecture at Turin NATO Advanced Research Workshop on Noise and Chaos in Nonlinear Dynamical Systems, March, 1989, eds. F. Moss, L. Lugiato, W. Schleich, pp. 1-14, (Cambridge University Press, 1990).
15. J. A. Wheeler and W. H. Zurek, eds. "Quantum Theory and Measurement", (Princeton University Press, 1983).
16. S. Goldstein, in *Physics Today*, vol. 22, March and April Issues, 1996.
17. Schrödinger Cat Paradox: Translated to English in Ref. 15, pp. 152-167.
18. W. E. Lamb, Jr., "Schrödinger's Cat" in "Paul Adrian Maurice Dirac", eds. B. N. Kursuoglu and E. P. Wigner (Cambridge University Press, 1987).
19. Physics Today
20. Physics World
21. Delayed Choice
22. "Comments by W. E. Lamb", in *Workshop on Quantum Cryptography and Quantum Computing, Proceedings*, February 15, 1995, edited by H. Everitt, U. S. Army Research Office, pp. 24-25.
23. Max Born, "On the Interpretation of Quantum Mechanics", in *Les Prix Nobel en 1954*, Stockholm.
24. W. E. Lamb, Jr. and H. Fearn, "Classical Theory of Measurement: A Big Step Toward the Quantum Theory of Measurement", in "Amazing Light": A Volume Dedicated to Charles Hard Townes on his 80th Birthday, (Edited by R. V. Chiao) Springer-Verlag, New York, N.Y.).
25. See biography of Luisa Agnesi, and article on special functions in *Encyclopedia Britannica*.
26. J. G. Crowther, "Maxwell's Inaugural Lecture", *New Scientist and Science Journal*, (4 March, 1971), pp. 478-481.
27. H. Poincare "New Methods of Celestial Mechanics", in 3 vols., ed. by D. L. Goroff, (A. I. P., 1993).
28. W. E. Lamb, Jr., "Quantum Chaos and the Theory of Measurement", NATO Advanced Research Workshop on "Quantum Chaos", Como, June, 1983. In "Chaotic Behavior in Quantum Systems. Theory and Applications", ed. G. Casati, pp. 253-261. (Plenum Press, New York, 1985).
29. J. Lighthill, "The Recently Recognized Failure of Predictability in Newtonian Dynamics", *Proc. Roy. Soc. A* 407, 35-50 (1936).

30. G. Duffing, "Forced Vibrations at Various Frequencies and their Technical Significance", Sammlung 41-42 (F. Vieweg, Braunschweig, 1918).
31. E. Fermi, J. R. Pasta, and S. Ulam, "Studies of Nonlinear Problems", in Los Alamos Report LA-1940, 1955.
32. M. Toda, J. Phys. Soc. Japan 21, 431 (1967).
33. M. Born, Waynflete Lecture, Magdelen College, Oxford, 1949.
34. P. Ehrenfest, "Notes on the Approximate Validity of Quantum Mechanics", Z. Physik, 455-457 (1927).
35. L. I. Schiff, "Quantum Mechanics", 3rd ed., pp. 28-30, 178-182, (Mc-Graw-Hill, 1955).
36. E. Schrödinger, "Collected Papers on Wave Mechanics", (Blackie, London, 1928).
37. E. H. Kennard, "The Quantum Mechanics of Simple Types of Motion", Z. Phys. 44, 326-352 (1927).
38. R. J. Glauber, "Coherent and Incoherent States of the Radiation Field", Phys. Rev. 2766-2788 (1964).
39. M. Sargent, M. O. Scully and W. E. Lamb, Jr., "Laser Physics", in Appendix H, "The Coherent State", (Wiley, 1977). Largely based on Kennard's approach. Many results are simpler to get using the complex Gaussian method of this paper.
40. W. E. Lamb, Jr. "Anti-Photon", Applied Physics B, Lasers and Optics, 60, 77-84 (1995).
41. J. Bolte and S. Keppeler, "Semiclassical Time Evolution and Trace Formula for Relativistic Spin-2 1 Particles" Phys. Rev. Letters, 81, 1987-1990 (1998).
42. M. V. Berry. From a Lecture in May, 1999, at the University of Arizona.
43. T. A. Welton, "Some Observable Effects of the Quantum Mechanical Fluctuation of the Electromagnetic Field", Phys. Rev. 74, 1157-1167 (1948).
44. S. Bourzeix, et al, "High Resolution Spectroscopy of the Hydrogen Atom: Determination of the 1S Lamb Shift.", Phys. Rev. Letters, 76, 384-387 (1996).
45. See Einstein's Remarks on Radioactive Decay in "Albert Einstein: Philosopher-Scientist", pp. 665-688, edited by P. A. Schilpp. (Open Court Publishing, La Salle, IL, 1970).

The Laser Phase Transition Analogy and the Partition Function for Bose Condensation of N Atoms in a Trap

Marlan O. Scully

Department of Physics and Institute for Quantum Studies, Texas A & M University, TX 77843 and

Max-Planck Institute für Quantenoptik, 85748 Garching, Germany

Abstract. In Ref. [1] [PRL **82**, 3927, (1999)] the first analytical calculation of the partition function for the N -atom Bose-Einstein Condensate (BEC) was carried out. At the conference the question was raised: Is the partition function thus obtained the same as the usual statistical mechanical one? We here show that it is and also present recent improvements of the theory.

Consider a trap having $n_0, n_1, \dots, n_k, \dots$ atoms in levels with energies $\varepsilon_0, \varepsilon_1, \dots, \varepsilon_k, \dots$. The expression for the probability of finding this state of affairs is

$$P_{n_0, n_1, \dots, n_k, \dots} = \frac{1}{Z_N} e^{-\beta(\varepsilon_0 n_0 + \varepsilon_1 n_1 + \dots + \varepsilon_k n_k + \dots)}, \quad (1)$$

where Z_N is the canonical partition function for N bosons and $\beta = 1/k_B T$. Therefore the probability of finding all N atoms in the ground state is

$$P_{n_0=N, n_1=0, \dots, n_k=0, \dots} = \frac{1}{Z_N} e^{-\beta\varepsilon_0 N}. \quad (2)$$

and if we define the ground state energy ε_0 to be zero we have the useful result

$$P_N = \frac{1}{Z_N}. \quad (3)$$

In Ref. [1] we used such ideas to calculate the sum on states, and these considerations have been extended and refined in a more recent paper [2]. In particular in [2] we derive a condensate master equation containing two nontrivial parameters \mathcal{H} and η :

$$\begin{aligned} \frac{dp_{n_0}}{dt} = & -\kappa\{(1+\eta)[(N-n_0)(n_0+1)p_{n_0} - (N-n_0+1)n_0 p_{n_0-1}] \\ & + [\mathcal{H} + (N-n_0)\eta]n_0 p_{n_0} - [\mathcal{H} + (N-n_0-1)\eta](n_0+1)p_{n_0+1}\}. \end{aligned} \quad (4)$$

where

$$\mathcal{H} = \sum_{k>0} (e^{\hbar\varepsilon_k/T} - 1)^{-1}. \quad (5)$$

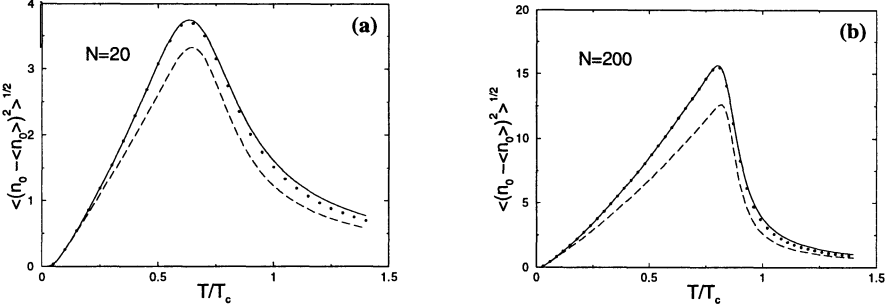


Fig. 1. The variance the number of atoms in the ground level of a harmonic trap, $\Delta n_0^2/\langle n_0 \rangle$, versus normalized temperature, T/T_c , under various approximations (dashed lines for the low temperature approximation ref [1], solid lines for the quasithermal approximation ref [2], and dots for the exact numerical simulation.) Harmonic isotropic trap with (a) $N = 20$, and (b) $N = 200$ atoms.

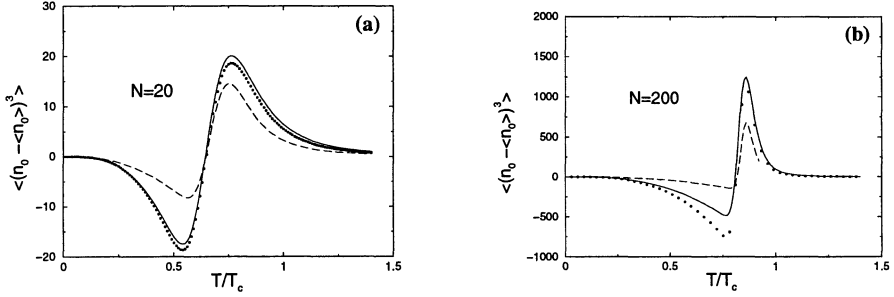


Fig. 2. The third centered moment, $\langle (n_0 - \bar{n}_0)^3 \rangle$, versus normalized temperature, T/T_c , (dashed lines for the low temperature approximation [1], solid lines for the quasithermal approximation [2], and dots for the numerical simulation). Harmonic isotropic trap with (a) $N = 20$, and (b) $N = 200$ atoms.

$$\eta = \frac{1}{\mathcal{H}} \sum_{k>0} \frac{1}{(e^{\epsilon_k/T} - 1)^2}. \quad (6)$$

The steady state of Eq. (4) is given by

$$\begin{aligned} p_{n_0} &= \frac{1}{Z_N} \frac{(N - n_0 + \mathcal{H}/\eta - 1)!}{(\mathcal{H}/\eta - 1)!(N - n_0)!} \left(\frac{\eta}{1 + \eta} \right)^{N - n_0} \\ &= \frac{1}{Z_N} \binom{N - n_0 + \frac{\mathcal{H}}{\eta} - 1}{N - n_0} \left(\frac{\eta}{1 + \eta} \right)^{N - n_0}, \end{aligned} \quad (7)$$

where the canonical partition function $Z_N = 1/p_N$ is

$$Z_N = \sum_{n_0=0}^N \binom{N - n_0 + \mathcal{H}/\eta - 1}{N - n_0} \left(\frac{\eta}{1 + \eta} \right)^{N - n_0}. \quad (8)$$

Using these results we obtain excellent agreement with numerical simulations as per the figures.

Acknowledgments The author wishes to thank K. Kapale, V. Kocharovsky, S.-Y. Zhu and M. S. Zubairy for helpful discussions. This work is supported by the Office of Naval Research, The National Science Foundation and the Welch Foundation.

References

1. M. O. Scully, Phys. Rev. Lett. **82**, 3927 (1999)
2. V. Kocharovsky, M. O. Scully, S.-Y. Zhu, M. S. Zubairy, Phys. Rev. A, Feb. (2000).

Appendix

Reprint of [1] M.O. Scully: Condensation of N Bosons and the Laser Phase Transition Analogy, Phys. Rev. Lett. **82**, 3927 (1999) with permission of The American Physical Society.

PHYSICAL REVIEW LETTERS

VOLUME 82

17 MAY 1999

NUMBER 20

Condensation of N Bosons and the Laser Phase Transition Analogy

Marlan O. Scully

*Physics Department and Institute for Quantum Studies, Texas A&M University, College Station, Texas 77843
and Max-Planck Institute Für Quantenoptik, 85748 Garching, Germany*

(Received 6 April 1998; revised manuscript received 14 July 1998)

A simple analytic expression for the ground state of a dilute gas of N ideal bosons in a 3D harmonic potential at temperature T is derived from the steady state solutions of nonequilibrium equations of motion. The N particle constraint plays the important role of introducing the essential nonlinearity yielding a Ginzburg-Landau free energy. The present analysis has much in common with the quantum theory of the laser, and with the laser phase transition analogy. [S0031-9007(99)09008-0]

PACS numbers: 03.75.Fi, 05.30.Jp

Bose-Einstein condensation (BEC) in dilute ultracold gases has become a laboratory reality, notably the three pioneering experiments reporting BEC in rubidium [1(a)], lithium [1(b)], and sodium [1(c)] and independent confirmation [2]. Furthermore, BEC experiments on dilute He^4 in porous media [3], excitons in Cu_2O [4], demonstration of interference between condensates [5], and the condensate time development [6] are exciting developments.

It is important, therefore, to understand the connection between BEC [7] and the ideal Bose gas [8], and the quantum theory of the laser [9,10], etc. In the latter context, we recall that the saturation nonlinearity in the radiation matter interaction is essential for laser coherence [11]. Is the corresponding nonlinearity in BEC due solely to atom-atom scattering, or is there a coherence generating nonlinearity even in an ideal Bose gas? We shall see that the latter is the case; the laser phase transition analogy [12] provides insight into such questions.

With the above in mind, and stimulated by a recent article [13], we here extend our previous laser-phase transition analogy to the problem of N ideal bosons in a 3D harmonic potential coupled to a thermal reservoir. This “simple” problem turns out to be surprisingly rich. For example, we obtain, for the first time, a simple analytic expression for the ground state density matrix for N ideal bosons in contact with a thermal reservoir [see Eq. (2)]. The N particle constraint is included naturally in the present formulation and introduces the essential nonlinearity [14].

We emphasize that the present work provides another example [15] in which steady state (detailed balance) solutions to nonequilibrium equations of motion provide a supplementary approach to conventional statistical mechanics (e.g., partition function calculations). This is of interest since, for example, the partition sums in the canonical ensemble are complicated by the restriction to N particles. Stated differently, the present approach lends itself to different approximations, yielding, among other things, a simple (approximate) analytic expression for the ground state density matrix for N trapped bosons [see Eq. (2)].

Thus, we derive a nonequilibrium master equation for the ground state of an ideal Bose gas in a 3D harmonic trap coupled to a thermal reservoir; writing only the diagonal elements (the off-diagonal elements will be presented elsewhere), we find

$$\begin{aligned} \frac{1}{\kappa} \dot{\rho}_{n_0, n_0} = & - [(N + 1)(n_0 + 1) - (n_0 + 1)^2] \rho_{n_0, n_0} \\ & + [(N + 1)n_0 - n_0^2] \rho_{n_0-1, n_0-1} \\ & - \left(\frac{T}{T_c} \right)^3 N [n_0 \rho_{n_0, n_0} - (n_0 + 1) \rho_{n_0+1, n_0+1}], \end{aligned} \quad (1)$$

where $|n_0\rangle$ is the eigenstate of n_0 bosons, κ is a rate constant, N is the total number of bosons, T is the temperature of the heat bath, and T_c is a transition temperature, the precise meaning of which is discussed later.

The steady state solution for Eq. (1) is

$$\rho_{n_0, n_0} = \frac{1}{Z_N} \left[N \left(\frac{T}{T_c} \right)^3 \right]^{N-n_0} \frac{N!}{(N-n_0)!}, \quad (2)$$

where the N boson normalization state function Z_N is an incomplete gamma function which is conveniently expressed as

$$Z_N = \left(\frac{T}{T_c} \right)^{3(N+1)} \int_0^\infty dt e^{-t(T/T_c)^3} (t+N)^N. \quad (3)$$

Equation (2) is a main result of this paper; we note that ρ_{n_0, n_0} is not a Poisson distribution as would be expected for a coherent state.

Proceeding further to glean the physics from Eq. (2), we note that it yields the following analytical expressions for the average and the variance [16] of the number of bosons in the ground state (see Fig. 1):

$$\langle n_0 \rangle = \left[1 - \left(\frac{T}{T_c} \right)^3 \right] N + \left(\frac{T}{T_c} \right)^3 N / Z'_N, \quad (4)$$

$$\Delta n_0^2 = \langle n_0^2 \rangle - \langle n_0 \rangle^2 = \left(\frac{T}{T_c} \right)^3 N [1 - (\langle n_0 \rangle + 1) / Z'_N], \quad (5)$$

where $Z'_N = Z_N [N(T/T_c)^3]^{-N}$.

In the limit that $T \rightarrow T_c$, we find (by a steepest-descent approximation) $Z'_N \rightarrow \sqrt{2/N\pi}$; therefore $\langle n_0(T_c) \rangle \approx \sqrt{2N/\pi}$, and $\Delta n_0^2(T_c) \approx N - N(2/\pi + \sqrt{2/N\pi})$.

In developing the laser phase transition analogy the “touch stone” was the Glauber-Sudarshan P distribution. Thus, when we expand the density matrix in terms of coherent (i.e., eigenstates of the annihilation operator)

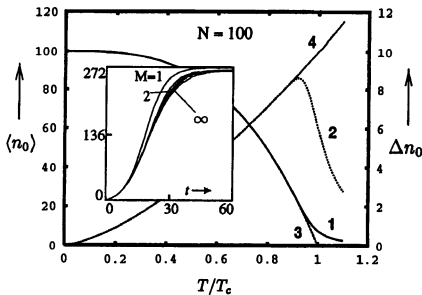


FIG. 1. At sufficiently low temperatures, $\langle n_0 \rangle \approx N[1 - (T/T_c)^3]$ (curve 3) and $\Delta n_0 \approx N^{1/2}(T/T_c)^{3/2}$ (curve 4). Near T_c , corrections are appreciable (of order \sqrt{N} ; see curves 1 and 2). Inset: time evolution of average number given by integration of Eq. (12) truncated according to Ref. [20] (see text). Parameters are $N = 1600$, $T/T_f = 0.94$, vertical axis $\langle n_0 \rangle$, horizontal axis time in units of κ^{-1} .

states $|\Delta\rangle$ using $\rho_{n_0, n_0'} = \int d\Delta P(\Delta) \langle n_0 | \Delta \rangle \langle \Delta | n_0' \rangle$, we find for $T \approx T_c$, $P(\Delta) = \exp[-\beta G(\Delta)]/Z$, with the Ginzburg-Landau-type free energy $G(\Delta) = a(T, T_c) \times |\Delta|^2 + b(T, T_c) |\Delta|^4$.

The correspondence between the expression for $P(\Delta)$ and its laser analog is very close, in accord with Ref. [12]. The bosonic ground state is indeed much “like a laser”; and in this context we note that the off-diagonal generalization of Eq. (1) yields a finite “phase diffusion” linewidth for Δ . This will be discussed elsewhere.

Having presented the master equation, Eq. (1), and some of the physics it contains, we sketch its derivation and limitations. Our reservoir consists of an ensemble of simple harmonic oscillators having a large frequency spread so as to ensure Markovian dynamics.

Defining $\rho_{n_0, n_0'} = \sum_{\{n_k\}} \text{Tr}_{\text{Res}} \rho_{n_0, \{n_k\}, n_0' \{n_k\}}$, where $\{n_k\} = \{n_1, n_2, \dots, n_k, \dots\}$ and Tr_{Res} denotes the trace over the reservoir, we seek the equation of motion for $\rho_{n_0, n_0'}$ as it evolves due to interaction with the reservoir [17], which is governed by the interaction Hamiltonian,

$$V(t) = \sum g_{j,k} b_j^\dagger(t) a_k(t) a_0^\dagger(t) + \text{adj.}, \quad (6)$$

where $g_{j,k}$ is the coupling strength between the j th reservoir oscillator and a gas atom being cooled from the k th level of the trap into its ground state. The raising operator for the j th reservoir oscillator is $b_j^\dagger(t) = b_j^\dagger(0) \exp(i\omega_j t)$. The boson annihilation operator is given by $a_k(t) = a_k(0) \exp(-i\omega_k t)$, where $\hbar\omega_k$ is the energy of the k th state of the 3D trap, and $a_0^\dagger(t)$ is the ground state creation operator.

We proceed via the exact dynamical equation

$$\dot{\rho}_{n_0, n_0} = - \int_{-\infty}^t dt' \sum_{\{\eta_j\}, \{n_k\}} \langle \{\eta_j\}, \{n_k\}, \{n_j\} \rangle [V(t), [V(t'), \rho(t')]] |n_0, \{n_k\}, \{n_j\}\rangle, \quad (7)$$

where $|\{\eta_j\}\rangle = |\eta_1, \eta_2, \dots, \eta_j, \dots\rangle$ is the reservoir state with η_1 quanta in the first oscillator, η_2 in the second, etc., and the summation excludes the ground state.

Inserting Eq. (6) into Eq. (7), we convert the sum over reservoir states to an integral, and note that oscillators for which $\omega_j \approx \omega_k$ dominate. Hence, slowly varying quantities such as the density of states factor W_j , matrix elements g_{jk} , and Bose factors η_j may be evaluated at $j = k$. The resulting integration over ω_j yields a temporal delta function, since $\int d\omega_j \exp(i\omega_k - \omega_j)(t - t') = 2\pi\delta(t - t')$, and the master equation becomes Markovian. We further note that the reservoir is only weakly coupled to the Bose gas and take the reservoir oscillators and the excited states of the Bose gas to be populated according to equilibrium statistical mechanics. Proceeding along these lines we find

$$\begin{aligned} \dot{\rho}_{n_0, n_0} = & -K_{n_0}(n_0 + 1)\rho_{n_0, n_0} + K_{n_0-1}n_0\rho_{n_0-1, n_0-1} \\ & - H_{n_0}n_0\rho_{n_0, n_0} + H_{n_0+1}(n_0 + 1)\rho_{n_0+1, n_0+1}. \end{aligned} \quad (8)$$

The cooling and heating coefficients K_{n_0} and H_{n_0} are given by $K_{n_0} = \sum_k 2\pi W_k g_k^2 \langle \eta_k + 1 \rangle \langle n_k \rangle_{n_0}$ and $H_{n_0} = \sum_k 2\pi W_k g_k^2 \langle \eta_k \rangle \langle n_k + 1 \rangle_{n_0}$, where $\langle \eta_k \rangle$ is the average occupation number of the k th heat bath oscillator as in Eq. (11), and $\langle n_k \rangle_{n_0}$ is the average number of atoms in the k th excited state, given n_0 atoms in the condensate. We evaluate K_{n_0} and H_{n_0} in varying degrees of rigor. One of the most illuminating is to note that for the bulk of the excited states the factors $\langle n_k + 1 \rangle$ and $\langle \eta_k + 1 \rangle$, as they appear in H_{n_0} and K_{n_0} , can be replaced by unity. For simplicity, we take $2\pi W_k g_k^2 = \kappa$; in later work k dependence will be presented.

Then the heating term is approximately

$$H_{n_0} \approx \kappa \sum_k \langle \eta(\epsilon_k) \rangle = \kappa \sum_{\ell, m, n} \frac{1}{e^{\beta \hbar \Omega(n+\ell+m)} - 1} \equiv \mathcal{H}.$$

In the weak trap limit $\mathcal{H} \approx \kappa(k_B T / \hbar \Omega)^3 \zeta(3)$, where $\zeta(3)$ is the Riemann zeta function, and Ω is the trap frequency.

Likewise, the cooling term in Eq. (8) is governed by the total number of excited state bosons,

$$K_{n_0} \approx \kappa \sum_k \langle n_k \rangle_{n_0} = \kappa(N - n_0). \quad (9)$$

The preceding suggests new ways to motivate the critical temperature for small N . By writing the equation of motion for $\langle n_0 \rangle$ from Eq. (8), using \mathcal{H} in the weak trap limit, and (9) for K_{n_0} , we find

$$\langle \dot{n}_0 \rangle = \kappa \left[N \langle n_0 \rangle - \langle n_0^2 \rangle - \zeta(3) \left(\frac{k_B T}{\hbar \Omega} \right)^3 \langle n_0 \rangle \right]. \quad (10)$$

We may obtain T_c in two ways.

Proceeding dynamically, we note that, near T_c , $\langle n_0 \rangle \ll N$, and we may neglect $\langle n_0^2 \rangle$ compared to $N \langle n_0 \rangle$. Then Eq. (10) becomes $\langle \dot{n}_0 \rangle = \kappa[N - \zeta(3)(k_B T / \hbar \Omega)^3] \langle n_0 \rangle$. We now define the critical temperature (in analogy with the laser threshold) such that cooling (gain) equals heating (loss) and $\langle \dot{n}_0 \rangle = 0$ at $T = T_c$; this yields $T_c = [\hbar \Omega / k_B] (N / \zeta(3))^{1/3}$.

Alternatively, from a statistical mechanical point of view, we may define T_c as the temperature at which $\langle n_0 \rangle$ vanishes when neglecting fluctuations. That is, replacing $\langle n_0^2 \rangle \approx \langle n_0 \rangle^2$ in Eq. (10), the steady state solution is $N - \langle n_0 \rangle = \zeta(3)(k_B T / \hbar \Omega)^3$; and $\langle n_0 \rangle$ vanishes when $T_c = [\hbar \Omega / k_B] (N / \zeta(3))^{1/3}$.

In terms of T_c , the heating rate is then $H_{n_0} = \kappa N(T/T_c)^3$. Inserting this and (9) for K_{n_0} into Eq. (8) yields Eq. (1). For other potentials [18], the sum in \mathcal{H} changes and the results will be presented elsewhere.

When we do not go to the weak trap limit, but keep the entire sum in H_{n_0} , we have

$$\tilde{\rho}_{n_0, n_0} = \frac{1}{Z_N} \mathcal{H}^{-n_0} \frac{N!}{(N - n_0)!}. \quad (11)$$

Equation (11) is plotted for a 3D oscillator trap in Fig. 2, as is the distribution from the (1997) papers of Wilkens, Weiss, Grossmann, and Holthaus (WWGH) [8]. We conclude that the simple analytic (but approximate) expression (11) describes the ground state quite well even for $N = 100$. Numerical analysis shows that, for $N \geq 10^5$, ρ_{n_0, n_0} and $\tilde{\rho}_{n_0, n_0}$ given by Eqs. (2) and (11) converge; for $N = 10^2$, their peaks differ by some 10%.

For small N , the critical temperature should now be redefined by modifying Eq. (10) so that $\zeta(3)(k_B T / \hbar \Omega)^3 \rightarrow \mathcal{H}$, and then the modified critical temperature \tilde{T}_c is defined by $\mathcal{H}(\tilde{T}_c) = \sum \{\exp(\hbar \Omega) (\ell + m + n) / k_B \tilde{T}_c\} - 1\}^{-1} = N$, in agreement with Ketterle and van Druten [19].

We remark in closing that, as for the laser, Eq. (1) implies a coupled hierarchy of moment equations which are useful in analysis of the time evolution; we find

$$\begin{aligned} \frac{d}{dt} \langle n_0^\ell \rangle &= \sum_{i=0}^{\ell-1} \binom{\ell}{i} \left[\langle n_0^{i+1} \rangle \kappa N \left[1 - (-1)^{\ell-1-i} \left(\frac{T}{T_c} \right)^3 \right] \right. \\ &\quad \left. + \langle n_0^i \rangle \kappa N - \kappa [\langle n_0^{i+2} \rangle + \langle n_0^{i+1} \rangle] \right]. \end{aligned} \quad (12)$$

Equation (12) can be solved numerically when a proper truncation scheme is devised. This has been carried out in Ref. [20]. See the inset of Fig. 1 for the present problem. When truncating the third moment, only $\langle n_0 \rangle$ and $\langle n_0^2 \rangle$ are involved (i.e., $M = 2$ in the inset of Fig. 1); and the truncation prescription is $\langle n_0^3 \rangle = [2\langle n_0^2 \rangle^{1/2} - \langle n_0 \rangle]^3$.

The present paper is largely devoted to equilibrium questions, and such results are relatively insensitive to the details of the model. For example, Eq. (2) should describe

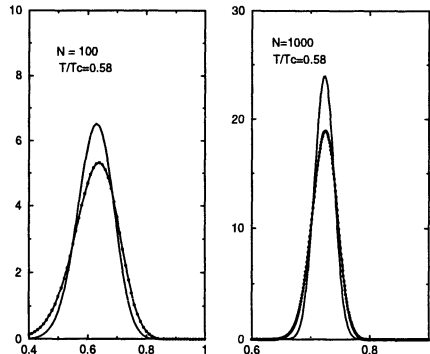


FIG. 2. Equation (11) (solid line) for probability of having n_0 bosons in ground state of 3D harmonic trap compared with WWGH (dot-dashed line), for 100 and 1000 atoms with $T/T_c = 0.58$, vertical axis: $N \times \rho_{n_0, n_0}$ and horizontal axis n_0/N for both graphs.

N atoms in a harmonic trap at steady state reasonably well. However, the dynamics of evaporative cooling is conceptually different from the present heat bath model. The present model would be rather closer to the dilute He⁴ gas in porous gel experiments [3] in which phonons in the gel would play the role of the heat bath. Nevertheless, a master equation having the form of Eq. (8) would be expected for any cooling mechanism, and the structure of Eq. (1) has a certain aesthetic appeal.

In summary, (i) We derive a master equation for the cooling of N bosons towards the ground state via energy exchange with a "phonon" heat bath, which incorporates the N particle constraint in a simple and natural fashion. In the weak trap limit the master equation takes an aesthetically pleasing form. The steady state solution yields a simple analytic expression for (ii) the N boson state function Z_N , (iii) the ground state boson statistics ρ_{n_0, n_0} , and (iv) a quasiprobability density for the order parameter Δ in terms of a Ginzburg-Landau free energy deriving from the fact that the N particle constraint introduces a nonlinear effective interaction. (v) Simple analytic expressions are obtained for $\langle n_0 \rangle$ and Δn_0^2 . (vi) A new "derivation" of the critical temperature valid for small N is developed dynamically and statistically. (vii) Time dependence relevant to experiments such as the porous gel/He⁴ experiments can be obtained via laser calculational techniques.

The author wishes to thank Daniel Kleppner and Willis Lamb for suggesting he write a paper, C. Bednar, K. Kapale, and P. Polynkin for their help in preparing the figures and the manuscript, and G. Baym, S. A. Chin, R. Glauber, M. Girardeau, C. R. Hu, K. Huang, R. Hulet, W. Ketterle, V. Kocharovskiy, W. Lamb, P. Meystre, V. Pokrovsky, M. Wilkens, C. N. Yang, S.-Y. Zhu, and M. Zubairy for helpful discussions. The support of the ONR, the NSF, the Welch Foundation, and the U.S. Air Force is gratefully acknowledged.

see also A. Röhrl, M. Naraschewski, A. Schenzle, and H. Wallis, Phys. Rev. Lett. **78**, 4143 (1997). For a discussion of the "phase" of a Bose condensate, see A. Leggett, in *Bose Einstein Condensation* (Ref. [4]), p. 452.

[6] See especially the time evolution experiments by H.-J. Miesner, D. Stamper-Kurn, M. Andrews, D. Durfee, S. Inouye, and W. Ketterle [Science **279**, 1005 (1998)] and the theoretical work of D. Jaksch, C. Gardiner, K. Gheri, and P. Zoller [Phys. Rev. A **58**, 1450 (1998)] and C. Sackett, H. Stoff, and R. Hulet [Phys. Rev. Lett. **80**, 2031 (1998)].

[7] The classic works in Bose gas physics by Bogoliubov, Huang, Lee, and Yang are well presented by K. Huang [*Statistical Mechanics* (Wiley, New York, 1987), Chap. 19]. See also R. Arnowitt and M. Girardeau, Phys. Rev. **113**, 745 (1959). For more recent work, see G. Baym and C. Pethick [Phys. Rev. Lett. **76**, 6 (1996)] and the forthcoming review article by S. Stringari *et al.* (<http://www.lanl.gov>).

[8] For fluctuations in a Bose gas, see H. Politzer, Phys. Rev. A **54**, 5048 (1996); S. Grossmann and M. Holthaus, Phys. Rev. E **54**, 3495 (1996); C. Herzog and M. Olshanii, Phys. Rev. A **55**, 3254 (1997); P. Navez, D. Bitoux, M. Gajda, Z. Idziaszek, and K. Rzaaewski, Phys. Rev. Lett. **79**, 1789 (1997); M. Wilkens and C. Weiss, J. Mod. Opt. **44**, 1801 (1997); S. Grossmann and M. Holthaus, Phys. Rev. Lett. **79**, 3557 (1997).

[9] For the quantum theory of the laser as developed by Haken and Risken using Fokker-Planck techniques, that of Lax and Louisell using a quantum noise approach, and the density matrix treatment of Lamb and Scully, see, for example, M. Scully and S. Zubairy, *Quantum Optics* (Cambridge University, Cambridge, England, 1997).

[10] Insightful "atom-laser" papers include M. Holland, K. Burnett, C. Gardiner, J. Cirac, and P. Zoller, Phys. Rev. A **54**, R1757 (1996); A. Guzman, M. Moore, and P. Meystre, Phys. Rev. A **53**, 977 (1996); H. Wiseman, A. Martins, and D. Walls, Quantum Semiclass. Opt. **8**, 737 (1996); U. Janicke and M. Wilkens, Europhys. Lett. **35**, 561 (1996); M. Olshanii, Y. Castin, and J. Dalibard, in *Proceedings of the 12th International Conference on Laser Spectroscopy*, edited by M. Inguscio, M. Allegrini, and A. Lasso (World Scientific, Singapore, 1995).

[11] As R. Glauber taught us [Phys. Rev. **130**, 2529 (1963)], pure coherent light is characterized by Poissonian photon statistics. The quantum theory of lasers shows that partially coherent laser light also has a sharp photon distribution (with width several times Poissonian for a typical He-Ne laser). Laser coherence is due to the fact that after emission the atoms become absorbers and this saturation nonlinearity is essential for producing a sharply peaked photon distribution.

[12] V. DeGiorgio and M. Scully, Phys. Rev. A **2**, 1170 (1970); R. Graham and H. Haken, Z. Phys. **237**, 31 (1970).

[13] Daniel Kleppner, Phys. Today **50**, No. 8, 11 (1997).

[14] We agree with Wilkens and Weiss, Ref. [8], who point out that "an ideal Bose gas with a fixed total number of particles must in fact be considered weakly interacting if one prefers to work in the grand-canonical ensemble."

[15] J. Goldstein, M. Scully, and P. Lee, Phys. Lett. **35A**, 317 (1971) contains another example.

- [1] (a) M. Anderson, J. Ensher, M. Matthews, C. Wieman, and E. Cornell, Science **269**, 198 (1995); (b) C. Bradley, C. Sackett, J. Tollett, and R. Hulet, Phys. Rev. Lett. **75**, 1687 (1995); (c) K. Davis, M. Mewes, M. Andrews, N. van Druten, D. Durfee, D. Kurn, and W. Ketterle, Phys. Rev. Lett. **75**, 3969 (1995).
- [2] BEC has been confirmed by the groups of Hänsch, Hau, Heinzen, Kasevich, Phillips, and Rempe.
- [3] In the experiments of the J. Reppy group at Cornell [see, e.g., Phys. Rev. Lett. **61**, 1950 (1988)], they prepare a dilute Bose gas by confining He⁴ in a porous medium.
- [4] See, e.g., J. Wolfe, J. Lin, and D. Snoke, in *Bose Einstein Condensation*, edited by A. Griffin, D. Snoke, and S. Stringari (Cambridge University, Cambridge, England, 1995), p. 281.
- [5] M. Andrews, C. Townsend, H.-J. Miesner, D. Durfee, D. Kurn, and W. Ketterle, Science **275**, 637 (1997);

- [16] The leading term (6) $\Delta n_0 = \sqrt{N} (T/T_c)^{3/2}$ in the case of a harmonic trap. Politzer, Ref. [8], finds $\Delta n_0 = [\zeta(2)/\zeta(3)]^{1/2} \sqrt{N} (T/T_c)^{3/2}$. The prefactor $[\zeta(2)/\zeta(3)]^{1/2} \approx 1.2$. We consider the agreement to be satisfactory for the present purposes. However, in a future paper we will present analysis including the prefactor.
- [17] We do not consider the dynamics of the Bose atoms as they are shuffled between excited states, but rather assume that they are in thermal equilibrium with the reservoir. That is, we assume that the excited states of the trap are adequately thermalized so as to allow this simplifying assumption. This should be a good approximation for the majority of atoms in the excited states.
- [18] For a useful summary of BEC in various external potentials, see V. Bagnato, D. Pritchard, and D. Kleppner, Phys. Rev. A **35**, 4354 (1987).
- [19] In an important paper, W. Ketterle and N. van Druten [Phys. Rev. A **54**, 656 (1996)] show that for “1000 particles the transition temperature is lowered to 79%” of the usual definition.
- [20] M. Sargent, M. Scully, and W. Lamb, Appl. Opt. **9**, 2423 (1970).

Excess Quantum Noise in Nonnormal Oscillators

A. E. Siegman

Ginzton Laboratory, Stanford University, CA 94305-4085, USA
e-mail: siegman@stanford.edu

Abstract. The eigenmodes or “normal modes” of many common laser cavities are in fact eigensolutions of nonhermitian or non-self-adjoint operators, and this unfamiliar circumstance leads to distinctly “nonnormal” behavior for such lasers. Elementary examples include the transverse modes in gain-guided diode lasers and geometrically unstable optical resonators, the longitudinal modes in lasers with large output coupling at one end, and the polarization modes of twisted birefringent cavities. The modes of these systems are all nonorthogonal in the usual power-orthogonal or energy-orthogonal sense, and as a consequence many of the conventional conclusions of classical and quantum noise theory must be substantially modified. Laser oscillators having nonnormal cavity modes are subject in particular to a so-called Petermann excess noise factor or a large excess spontaneous emission per mode. These excess noise properties have been decisively confirmed by observations of greatly increased Schawlow-Townes linewidths in such lasers.

1 Introduction and Background

In 1958 Schawlow and Townes [1] derived an expression for the linewidth of an ideal quantum-limited laser oscillator which can be written in the (slightly simplified) form

$$\Delta f_{\text{osc}} = \frac{\pi h f \Delta f_{\text{cav}}^2}{P_{\text{osc}}} = \frac{1}{4\pi\tau_{\text{cav}}^2} \frac{hf}{P_{\text{osc}}} \quad (1)$$

where Δf_{cav} is the resonant bandwidth and τ_{cav} the ringdown time for the empty laser cavity and P_{osc} is the laser power output. This linewidth is caused by spontaneous emission from the inverted laser atoms into the lasing mode of the oscillator. Its value is therefore closely linked to basic concepts of quantum noise theory [2], as well as to blackbody radiation, the Johnson-Nyquist noise formulation, and thermal-equilibrium and fluctuation-dissipation concepts.

In 1979 Petermann [3] used an approach based on semiconductor laser theory to predict that the fraction of the total spontaneous emission going into the oscillating mode of a gain-guided semiconductor laser would be larger than the usual value by a numerical factor $K_p \geq 1$. He noted that this excess noise factor could be significantly greater than unity in some cases, and that the Schawlow-Townes linewidth would be increased by this same factor. Petermann’s prediction raised serious conceptual difficulties, however, since

applying his analysis to loss-guided systems also predicts an excess thermal energy per mode, in violation of fundamental thermodynamic concepts.

These difficulties were resolved in 1985 by Haus and Kawakami [4] who confirmed that loss-guided systems should indeed have excess spontaneous emission rates into their eigenmodes. They noted, however, that there would also be correlations between the spontaneous emission into different modes with just the necessary values to make the total noise power or energy agree with the predictions of conventional thermodynamics.

Using a semiclassical noise analysis the present author showed in 1989 [5] that these excess noise properties are not directly associated with loss or gain guiding, but result instead from the nonorthogonal (nonhermitian, non-self-adjoint, “nonnormal”, biorthogonal) character of the transverse eigenmodes in such systems. Directly comparable Petermann excess noise factors should thus occur in other nonnormal eigenmode systems, particularly including unstable optical resonators and laser resonators employing variable-reflectivity output mirrors. Hamel and Woerdman soon afterwards confirmed [6] that a previously known increase in the Schawlow-Townes linewidth associated with large and asymmetric output coupling from one end of a laser cavity can also be interpreted in terms of the nonorthogonality of the axial or longitudinal modes in such cavities.

Since 1991 experiments on a variety of different lasers done at Stanford [7], Leiden [8], and Rennes [9] have confirmed that these excess noise factors do exist in nonnormal laser systems. The magnitudes of these effects can be large, and the results are in good agreement with a nonnormal mode analysis which says that the excess noise depends primarily on the nonorthogonality properties of the laser cavities rather than simply on their losses.

There has also been substantial progress toward the quantum analysis of these excess noise effects [10–16], for example in the work of Grangier and Poizat [13]. Perhaps the most striking recent result has been the realization that a large degree of nonorthogonality can exist not only for the transverse and longitudinal modes of laser cavities but also for the polarization modes of conventional cavities containing internal birefringence or Faraday rotation [17,18]. This form of polarization nonorthogonality also leads to large and readily measurable increases in Schawlow-Townes linewidths.

In the remainder of this paper I will give a brief summary of how this excess noise factor arises and how it is based on the nonorthogonality of laser cavity modes rather than on their losses or any alternative properties.

2 Normal and Nonnormal Laser Modes

The “normal modes” in many familiar wave-propagating or resonant electromagnetic systems including closed metal waveguides, index-guided optical fibers, and so-called stable optical lensguides or laser resonators are all eigen-solutions of a hermitian operator \mathcal{L} which is in essence the vector or scalar

wave equation plus a set of boundary conditions. These operators are thus self-adjoint, i.e., they satisfy the condition that $\mathcal{L} \equiv \mathcal{L}^\dagger \equiv \mathcal{L}^{*T}$ where the dagger indicates hermitian conjugation, the asterisk indicates complex conjugation, and the superscript T indicates transpose. Such an operator will have a complete set of eigenmodes, i.e. solutions of the equation $\mathcal{L} \tilde{u}_n = \tilde{\gamma}_n \tilde{u}_n$ with the orthonormality property $\int \tilde{u}_n^* \tilde{u}_m = \delta_{nm}$ where the integral is over the appropriate spatial (or polarization) coordinates of the system.

If the electromagnetic field in the system is expanded in the usual normal-mode fashion $\mathcal{E} = \sum_n \tilde{c}_n \tilde{u}_n$, the optical power flow in a propagating system or the stored energy in a resonant system can be written with appropriate normalization as

$$\mathcal{H} \equiv \int |\mathcal{E}|^2 = \sum_{n,m} \tilde{c}_n^* \tilde{c}_m \int \tilde{u}_n^* \tilde{u}_m = \sum_n \tilde{c}_n^* \tilde{c}_n \quad (2)$$

where the orthogonality of the eigenmodes reduces the double summation to a single sum over the powers or energies of the individual modes. Converting the classical \tilde{c} -number coefficients for the individual modes into creation and annihilation operators \tilde{a}_n^\dagger and \tilde{a}_n then allows this to be written as

$$\mathcal{H} = \sum_n \tilde{c}_n^* \tilde{c}_n = \sum_n \tilde{a}_n^\dagger \tilde{a}_n \cdot \hbar\omega_n. \quad (3)$$

In this form the quantity \mathcal{H} can be interpreted as the hamiltonian for a set of independent simple harmonic oscillators, each corresponding to a single mode of the wave-propagating or resonant structure. The full quantum theory of the laser as developed for example by Lamb and co-workers [2], along with the concept of the “photon” and the standard expressions for blackbody radiation and the Johnson-Nyquist noise formulation, all stem from this approach of normal-mode expansion followed by second quantization of the independent radiation oscillators.

There are, however, a number of common wave-propagating and resonant systems whose radiation modes are not governed by hermitian operators or may, depending on the formulation, be governed by a hermitian operator but with nonhermitian boundary conditions. Examples include gain-guided or loss-guided waveguides as in certain semiconductor lasers; so-called unstable optical resonators used in high-energy or high-power lasers; laser cavities employing variable-reflectivity (VRM) mirrors; “twisted” laser resonators containing a combination of anisotropic polarization loss plus birefringence or Faraday rotation; and in general any linear electrical or electromagnetic system described by a nonhermitian scattering matrix.

The operator governing the electromagnetic or optical modes in such a system will then be nonhermitian or non-self-adjoint, so that $\mathcal{L} \neq \mathcal{L}^\dagger$. Operators of this character are not commonly considered in quantum optics or quantum electronics texts. Systems of this type will, however, have both a

set of system eigenmodes \tilde{u}_n and a matching set of adjoint modes \tilde{v}_n which are solutions of the paired equations

$$\mathcal{L} \tilde{u}_n = \tilde{\gamma}_n \tilde{u}_n \text{ (eigenmodes)} \quad \text{and} \quad \mathcal{L}^\dagger \tilde{v}_n = \tilde{\gamma}_n^* \tilde{v}_n \text{ (adjoint modes).} \quad (4)$$

That is, the eigenvalues for the two operators are the same except for complex conjugation but the eigenfunctions are different, in some cases substantially different, so that $\tilde{v}_n \neq \tilde{u}_n^*$. (In many cases such as periodic lensguides or ring laser cavities, the adjoint modes correspond physically to waves propagating in the opposite direction inside the same physical system.)

The eigenmodes of such nonnormal systems can still be scaled to unit power or energy, so that $\int \tilde{u}_n^* \tilde{u}_n = 1$, but they will no longer be orthogonal to each other, so that $\int \tilde{u}_n^* \tilde{u}_m \neq 0$ for $n \neq m$. The individual eigenmodes \tilde{u}_n will instead be *biorthogonal* to the adjoint modes \tilde{v}_n in the form

$$\int \tilde{v}_n^* \tilde{u}_m = \delta_{nm} \quad (\text{biorthogonality}). \quad (5)$$

The combination of eigenmode normalization plus biorthogonality means that the adjoint modes will have normalization factors greater than unity. In fact, the normalization integrals for individual adjoint modes \tilde{v}_n will correspond directly to the Petermann excess noise factors for the corresponding eigenmodes, as given by

$$K_{pn} \equiv \int \tilde{v}_n^* \tilde{v}_n > 1 \quad (n = m). \quad (6)$$

The off-diagonal products for the adjoint modes will also be non-zero, i.e.,

$$K_{p,nm} \equiv \int \tilde{v}_n^* \tilde{v}_m \neq 0 \quad (n \neq m). \quad (7)$$

These off-diagonal values in fact correspond directly to the correlation factors between the excess noise emission into different eigenmodes.

3 Consequences of Nonnormal Modes

The “nonnormal” properties associated with nonhermitian cavity modes lead to major changes in the mathematical, conceptual and quantum-mechanical characteristics of lasers using such cavities. As a starting point, the field hamiltonian for such a laser now has the form

$$\mathcal{H} \equiv \int |\mathcal{E}|^2 = \sum_n \tilde{c}_n^* \tilde{c}_n + \sum_{n \neq m} \tilde{c}_n^* \tilde{c}_m \int \tilde{u}_n^* \tilde{u}_m. \quad (8)$$

Because the cross-product terms no longer vanish, the total power or energy in the system is no longer the sum of the powers or energies in individual eigenmodes; and the hamiltonian can no longer be separated into the sum of individual harmonic oscillators. A list of changes arising from the loss of the usual normal mode picture in fact includes:

1. The Rayleigh-Ritz procedure for estimating eigenvalues can no longer be guaranteed to give accurate values.
2. There is a loss of second quantization, at least in its usual form, and this leads in turn to a considerable muddying of the photon concept [19,20].
3. One must introduce the concept of “adjoint coupling” [5,19,20] in addition to the usual “matched coupling” into the nonorthogonal waveguide propagation modes or cavity resonant modes. As one perhaps surprising consequence of adjoint coupling, one can couple more energy into the initial excitation of one individual eigenmode than the total energy available in the incident signal.
4. Eigenmode expansions of the system fields in the form $\mathcal{E} = \sum_n \tilde{c}_n \tilde{u}_n$ can still be carried out, but a major revision in the expansion procedure is required because, contrary to what one might expect, simple projection onto the adjoint space no longer gives a minimum-error expansion [21]. The coefficient values \tilde{c}_n also change as one increases the number of terms included in the expansion.
5. Significant changes must be made in the Johnson-Nyquist noise formulation and perhaps also in the fluctuation-dissipation theorem for such systems [22].
6. Finally and perhaps of greatest physical significance, the quantum-limited or Schawlow-Townes linewidths in laser oscillators employing these non-normal modes will be increased by the Petermann excess noise factors introduced earlier.

I will outline in the following section an abbreviated derivation showing how this Petermann excess noise factor emerges from a semiclassical analysis of laser oscillator noise.

4 Derivation of the Excess Noise Factor

In the conventional approach to laser noise theory as developed for example in reference [2], one begins with the wave equation for the fields in the laser cavity, together with an assumption that the laser can be made to oscillate in a single lowest-loss eigenmode only. As a result the cavity fields are given in suitably normalized form by $\mathcal{E}(\mathbf{r}, t) = \tilde{c}_n(t) \times \tilde{u}_n(\mathbf{r})$ where n is the index of the single oscillating mode. The cavity equation can then be reduced to a van der Pol oscillator form, i.e.

$$\left[\frac{d}{dt} - (\alpha - \alpha_n)c \right] \tilde{c}_n(t) = -j\tilde{p}_n(t) \quad (9)$$

in which α is the amplitude gain coefficient for an ideal laser medium that fills the cavity; α_n is the total loss plus output coupling coefficient for the cavity so that the cavity eigenmode is $\tilde{\gamma}_n \equiv \exp[-(\alpha_n + j\beta_n)p]$; p is the

round-trip distance around the laser cavity; c is the velocity of light; and $\tilde{p}_n(t)$ is a Langevin noise term associated with spontaneous emission from the active medium. One also assumes that in steady-state oscillation the laser gain coefficient α will saturate down to equal the cavity loss factor α_n .

In the semiclassical approach to laser noise as followed in reference [5], one then assumes that spontaneous emission from the laser atoms can be represented by a classical noise polarization $\tilde{\mathcal{P}}_N(\mathbf{r}, t)$ whose magnitude squared is proportional to the upper-level population density in the laser medium. The Langevin noise term $\tilde{p}_n(t)$ is then given by

$$\tilde{p}_n(t) = \frac{\omega c \eta_0}{2p} \int e^{-j(\omega_q t - q2\pi z/p) - (\alpha_n - j\beta_n)(z-p)} \tilde{\mathcal{P}}_N(\mathbf{r}, t) \tilde{v}_n^*(\mathbf{r}) d\mathbf{r} \quad (10)$$

where the integration is over the volume of the laser cavity. For the idealized case of a fully inverted transition with a wide atomic linewidth, the noise polarization will be essentially delta-correlated in both space and time and related to the gain coefficient α by

$$\langle \tilde{\mathcal{P}}_N^*(\mathbf{r}, t) \tilde{\mathcal{P}}_N(\mathbf{r}', t') \rangle = \frac{16\hbar\alpha}{\omega\eta_0} \delta(\mathbf{r} - \mathbf{r}') \delta(t - t'). \quad (11)$$

Integration over the cavity volume will then give the correlation function of the Langevin noise term in the form

$$\langle \tilde{p}_n^*(t') \tilde{p}_n(t) \rangle = K_{pn} \times \frac{1 - |\tilde{\gamma}_n|^2}{2\alpha_n |\tilde{\gamma}_n|^2} \times \frac{4c^2 \omega \eta_0 \hbar \alpha}{p^2} \delta(t - t'). \quad (12)$$

This expression contains all the factors necessary to calculate the phase diffusion of the electric field or the mode coefficient $\tilde{c}_n(t)$ and thus the Schawlow-Townes linewidth of the laser oscillator. The final term on the right-hand side (after the second \times sign) is the usual value for the Langevin noise term in a conventional laser cavity with orthogonal modes and low output coupling; this term by itself will lead to the standard expression for the Schawlow-Townes linewidth given in Eq. (1).

The middle term on the right-hand side (between the two \times signs) represents a *longitudinal* excess noise factor; its value will remain close to unity unless the output coupling from the laser cavity is both very large and longitudinally asymmetric. As first noted by Hamel and Wordman [6], this term can also be calculated from the nonorthogonality of the longitudinal or axial mode resonances in the case of large output coupling concentrated at one end of the cavity (i.e., a low-reflectivity end mirror). Note that a laser cavity in which the output coupling is very large but uniformly distributed along its length will not display a significantly increased value for this longitudinal excess noise factor.

Finally, the term K_{pn} on the right-hand side of Eq. (12) represents the Petermann excess noise factor associated with the *transverse* (or possibly the polarization) eigenmodes of the laser cavity, as given in Eq. (6). Even

the brief derivation given here should be adequate to demonstrate that this factor arises because the Langevin noise term $\tilde{p}_n(t)$ must be evaluated by projecting the atomic noise polarization $\hat{P}_N(\mathbf{r}, t)$ onto the adjoint function $\tilde{v}_n(\mathbf{r})$ rather than onto the normalized eigenmode $\tilde{u}_n(\mathbf{r})$. This consequence of the nonorthogonality or biorthogonality of the cavity eigenmodes is the primary source of the excess noise factor K_{pn} . The value of K_{pn} can become very large in realistic laser resonators, especially near certain critical points in unstable optical resonators, as has recently been confirmed in considerable detail by the Leiden group [8].

Acknowledgements. The author appreciates the many contributions to this work made by Jean-luc Doumont, Paul Mussche, Yuh-Jen Cheng, Geoff Fanning and Ad Kostenbauder, and also the continuing support for this research provided by the U.S. Air Force Office of Scientific Research.

References

1. A. L. Schawlow and C. H. Townes: Infrared and optical masers. *Phys. Rev.* **112**, 1940–1949 (1958).
2. M. Sargent, III, M. O. Scully, W. E. Lamb, Jr.: *Laser Physics*. Addison-Wesley Publishing Company (1972).
3. K. Petermann: Calculated spontaneous emission factor for double heterostructure injection lasers with gain-induced waveguiding. *IEEE J. Quantum Electron.* **QE-15**, 566–570 (1979).
4. H. A. Haus and S. Kawakami: On the excess spontaneous emission factor in gain-guided laser amplifiers. *IEEE J. Quantum Electron.* **QE-21**, 63–69 (1985).
5. A. E. Siegman: Excess spontaneous emission in nonhermitian optical systems. I. Laser amplifiers. II. Laser oscillators. *Phys. Rev. A* **39**, 1253–1268 (1989).
6. W. A. Hamel and J. P. Woerdman: Nonorthogonality of the longitudinal modes of a laser. *Phys. Rev. A* **40**, 2785–2791 (1989); also W. A. Hamel and J. P. Woerdman: Observation of enhanced fundamental linewidth of a laser due to nonorthogonality of its longitudinal eigenmodes. *Phys. Rev. Lett.* **64**, 1506–1509 (1990).
7. Y.-J. Cheng, P. L. Mussche, A. E. Siegman: Measurement of laser quantum frequency fluctuations using a Pound-Drever stabilization system. *IEEE J. Quantum Electron.* **QE-30**, 1498–1504 (J1994); and Y.-J. Cheng, G. Fanning, A. E. Siegman: Experimental observation of a large excess quantum noise factor in the linewidth of a laser oscillator using nonorthogonal modes. *Phys. Rev. Lett.* **77**, 627–630 (1996).
8. M. A. van Eijkelenborg, A. M. Lindberg, M. S. Thijssen, J. P. Woerdman: Resonance of quantum noise in an unstable cavity laser. *Phys. Rev. Lett.* **77**, 4314–4317 (18 November 1996); and M. A. Van Eijkelenburg, A. M. Lindberg, M. S. Thijssen, J. P. Woerdman: Higher order transverse modes of an unstable-cavity laser. *IEEE J. Quantum Electron.* **QE-34**, 955–965 (1998).
9. O. Emile, M. Brunel, F. Bretenaker, A. Le Floch: Direct measurement of the excess noise factor in a geometrically stable laser resonator. *Phys. Rev. A* **57**, 4889–4893 (1998).

10. I. H. Deutsch, J. C. Garrison and E. M. Wright: Excess noise in gain-guided amplifiers. *J. Opt. Soc. Am. B* **8**, 1244–1251 (1991).
11. P. Goldberg, P. W. Milonni, B. Sundaram: Theory of the fundamental laser linewidth. *Phys. Rev. A* **44**, 1969–1985 (1 August 1991); also P. Goldberg, P. W. Milonni, B. Sundaram: Laser linewidth: amplification of vacuum fluctuations and effects of spatial hole burning. *J. Modern Opt.* **38**, 1421–1427 (1991).
12. H. Wenzel and H.-J. Wunsche: An equation for the amplitudes of the modes in semiconductor lasers. *IEEE J. Quantum. Electron.* **QE-30**, 2073–2080 (1994).
13. P. Grangier and J.-P. Poizat: A simple quantum picture for the Petermann excess noise factor. *Eur. Phys. J. D* **1**, 97–104 (1998).
14. K. C. Ho, P. T. Leung, A. M. Vandenbrink, K. Young: 2nd quantization of open systems using quasi-normal modes. *Phys. Rev. E* **58**, 2965–2978 (1998).
15. C. Lamprecht and H. Ritsch: Quantized atom-field dynamics in unstable cavities. *Phys. Rev. Lett.* **82**, 3787–3790 (1999).
16. P. J. Bardroff and S. Stenholm: Quantum theory of excess noise. Private communication (1999).
17. A. N. van der Lee et al.: Excess quantum noise due to nonorthogonal polarization modes. *Phys. Rev. Lett.* **79**, 4357–4360 (1997).
18. O. Emile, M. Brunel, A. Le Floch, F. Bretenaker: Vectorial excess noise factor in common lasers. *Europhys. Lett.* **43**, 153–157 (1998).
19. A. E. Siegman: Lasers without photons — or should it be lasers with too many photons? *Appl. Phys. B* **60**, 247–257 (1995).
20. A. E. Siegman: Lasers Without Photons. In *Coherence and Quantum Optics VII*, J. H. Eberly, L. Mandel, E. Wolf (Eds.) (Plenum Press, University of Rochester, New York 1995); pp. 229–238.
21. A. Kostenbauder, Y. Sun, A. E. Siegman: Eigenmode expansions using biorthogonal eigenfunctions: complex-valued Hermite gaussians. *J. Opt. Soc. Amer. A* **14**, 1780–1790 (1997).
22. A. E. Siegman: Nyquist noise formulation for nonhermitian linear systems. Manuscript in preparation (1999).

Single Atom Masers and Lasers

Herbert Walther

Sektion Physik der Universität München and
Max-Planck-Institut für Quantenoptik
85748 Garching, Germany

Abstract. In this paper recent experiments performed in our laboratory are reviewed dealing with the investigation of quantum phenomena in the radiation interaction of single atoms. The first part describes experiments in single mode cavities using the one-atom maser or micromaser and in the second part experiments with ion traps are summarized. The latter experiments concentrate on the investigation of resonance fluorescence. In addition new experimental proposals using ultracold atoms in cavities and traps are discussed. In those future experiments the interplay between atomic waves and light waves is important leading to new phenomena in radiation-atom interaction such as the modification of the Rabi vacuum splitting.

1 Introduction

Using the modern techniques of laser spectroscopy it got possible to observe the radiation interaction of single atoms. The techniques thus made it possible to investigate the radiation-atom interaction on the basis of single atoms. The most promising systems in this connection seem to be single atoms in cavities and also single atoms in traps. The studies in cavities allow to select one interacting mode and thus represent the ideal system with respect to a quantum treatment. In high Q cavities a steady state field of photons can be generated displaying non-classical photon statistics. It thus gets possible to study the interaction also in the limit of non-classical or sub-Poissonian fields. Single trapped ions allow to observe among other phenomena quantum jumps and antibunching in fluorescence radiation. The fluorescent channel represents the interaction with many modes, however, it is also possible to combine single mode cavities with trapped atoms as it is e.g. the case in the proposed ion-trap laser.

A new and interesting twist in radiation-atom interaction can be added when ultracold atoms are used in both cavities and traps. In this case the distribution of the matter wave plays an important role besides the standing electromagnetic wave in the cavity and their interaction is determined by their respective overlap leading to new effects.

In the following we will review experiments of single atoms in cavities and traps performed in our laboratory. Furthermore new proposals for experiments with ultracold atoms will be discussed. We start with the discussion of the one-atom maser.

2 Experiments with the One Atom Maser

The one-atom maser or micromaser uses a single mode of a superconducting niobium cavity [1–4]. In the experiments values of the quality factor as high as 3×10^{10} have been achieved for the resonant mode, corresponding to an average lifetime of a photon in the cavity of 0.2 s. The photon lifetime is thus much longer than the interaction time of an atom with the maser field; during the atom passes through the cavity the only change of the cavity field that occurs is due to the atom-field interaction. Contrary to other strong coupling experiments in cavities (optical or microwave), see e.g. H. J. Kimble et al. [5] for a comparison between the different setups, it is possible with our micromaser to generate a steady state field in the cavity which has nonclassical properties so that the interaction of single atoms in those fields can be investigated. Furthermore the generation process of those fields has been studied and is well understood. The experiment is quite unique in this respect; this also holds in comparison with the one-atom laser [6] which has been omitted in the survey given in Table 1 of [5].

The atoms used in our micromaser experiments are rubidium Rydberg atoms pumped by laser excitation into the upper level of the maser transition, which is usually induced between neighboring Rydberg states. In the experiments the atom-field interaction is probed by observing the population in the upper and lower maser levels after the atoms have left the cavity. The field in the cavity consists only of single or a few photons depending on the atomic flux. Nevertheless, it is possible to study the interaction in considerable detail. The dynamics of the atom-field interaction treated with the Jaynes-Cummings model was investigated by selecting and varying the velocity of the pump atoms [2]. The counting statistics of the pump atoms emerging from the cavity allowed us to measure the non-classical character of the cavity field [3,4] predicted by the micromaser theory. The maser field can be investigated in this way since there is entanglement between the maser field and the state in which the atom leaves the cavity [7,8]. It also has been observed that under suitable experimental conditions the maser field exhibits metastability and hysteresis [9]. The first of the maser experiments have been performed at cavity temperatures of 2 or 0.5 K. In the more recent experiments the temperature was reduced to roughly 0.1 K by using an improved setup in a dilution refrigerator [9]. For a review of the previous work see Raithel et al. [11].

In the following we give a brief review of recent experiments which deal with the observation of quantum jumps of the micromaser field [9] and with the observation of atomic interferences in the cavity [10]. New experiments on the correlation of atoms after the interaction with the cavity field will be briefly mentioned. Furthermore we will discuss the generation of number or Fock states and we will also describe new possibilities opening up when ultracold atoms are used for the experiments.

2.1 Quantum jumps and atomic interferences in the micromaser

Under steady-state conditions, the photon statistics $P(n)$ of the field of the micromaser is essentially determined by the pump parameter, $\Theta = N_{\text{ex}}^{1/2} \Omega t_{\text{int}}/2$ [11,13]. Here, N_{ex} is the average number of atoms that enter the cavity during the decay time of the cavity field τ_{cav} , Ω the vacuum Rabi floppy frequency, and t_{int} is the atom-cavity interaction time. The quantity $\langle \nu \rangle = \langle n \rangle / N_{\text{ex}}$ shows the generic behavior shown in Fig. 1.

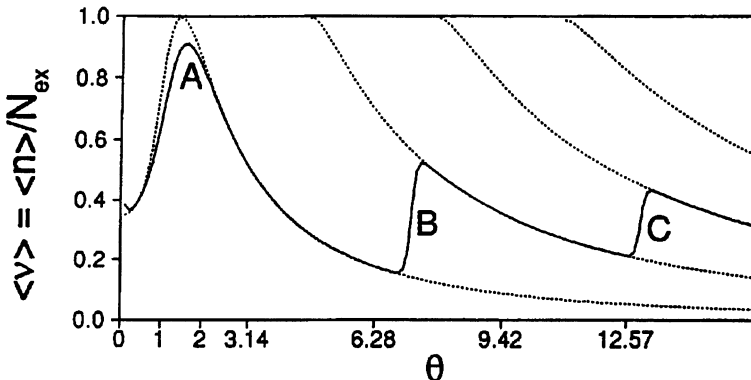


Fig. 1. Mean value of $\nu = n/N_{\text{ex}}$ versus the pump parameter $\Theta = \Omega t_{\text{int}} \sqrt{N_{\text{ex}}}/2$, where the value of Θ is changed via N_{ex} . The solid line represents the micromaser solution for $\Omega = 36$ kHz, $t_{\text{int}} = 35$ s, and temperature $T = 0.15$ K. The dotted lines are semiclassical steady-state solutions corresponding to fixed stable gain=loss equilibrium photon numbers [14]. The crossing points between a line $\Theta = \text{const}$ and the dotted lines correspond to the values where minima in the Fokker-Planck potential $V(\nu)$ occur (details see in the text)

It suddenly increases at the maser threshold value $\Theta = 1$, and reaches a maximum for $\Theta \approx 2$ (denoted by A in Fig. 1). At threshold the characteristics of a continuous phase transition [12,13] are displayed. As Θ further increases, $\langle \nu \rangle$ decreases and reaches a minimum at $\Theta \approx 2\pi$, and then abruptly increases to a second maximum (B in Fig. 1). This general type of behavior recurs roughly at integer multiples of 2π , but becomes less pronounced with increasing Θ . The reason for the periodic maxima of $\langle \nu \rangle$ is that for integer multiples of $\Theta = 2\pi$ the pump atoms perform an almost integer number of full Rabi flopping cycles, and start to flip over at a slightly larger value of Θ , thus leading to enhanced photon emission. The periodic maxima in $\langle \nu \rangle$ for $\Theta = 2\pi, 4\pi$, and so on can be interpreted as first-order phase transitions [12,13]. The field strongly fluctuates for all phase transitions being caused by the presence of two maxima in the photon number distribution $P(n)$ at photon numbers n_l and n_h ($n_l < n_h$).

The phenomenon of the two coexisting maxima in $P(n)$ was also studied in a semiheuristic Fokker-Planck (FP) approach [12]. There, the photon number distribution $P(n)$ is replaced by a probability function $P(\nu, \tau)$ with continuous variables $\tau = t/\tau_{\text{cav}}$ and $\nu(n) = n/N_{\text{ex}}$, the latter replacing the photon number n . The steady-state solution obtained for $P(\nu, \tau), \tau \gg 1$, can be constructed by means of an effective potential $V(\nu)$, showing minima at positions where maxima of $P(\nu, \tau), \tau \gg 1$, are found. Close to $\Theta = 2\pi$ and multiples thereof, the effective potential $V(\nu)$ exhibits two equally attractive minima located at stable gain-loss equilibrium points of maser operation [14] (see Fig. 1). The mechanism at the phase transitions mentioned is always the same: A minimum of $V(\nu)$ loses its global character when Θ is increased, and is replaced in this role by the next one. This reasoning is a variation of the Landau theory of first-order phase transitions, with $\sqrt{\nu}$ being the order parameter. This analogy actually leads to the notion that in the limit $N_{\text{ex}} \rightarrow \infty$ the change of micromaser field around integer multiples $\Theta = 2\pi$ can be interpreted as first-order phase transitions.

Close to first-order phase transitions long field evolution time constants are expected [12,13]. This phenomenon was experimentally demonstrated in [9], as well as related phenomena, such as spontaneous quantum jumps between equally attractive minima of $V(\nu)$, bistability, and hysteresis. Some of those phenomena are also predicted in the two-photon micromaser [15], for which qualitative evidence of first-order phase transitions and hysteresis is reported.

The experimental setup used is shown in Fig. 2. It is similar to that described by Rempe and Walther [4] and Benson, Raithel and Walther [9]. As before, ^{85}Rb atoms were used to pump the maser. They are excited from the $5S_{1/2}, F=3$ ground state to $63P_{3/2}, m_J = \pm 1/2$ states by linearly polarized light of a frequency-doubled c.w. ring dye laser. The polarization of the laser light is linear and parallel to the likewise linearly polarized maser field, and therefore only $\Delta m_J = 0$ transitions are excited. Superconducting niobium cavities resonant with the transition to the $61D_{3/2}, m_J = \pm 1/2$ states were used; the corresponding resonance frequency is 21.506 GHz. The experiments were performed in a $^3\text{He}/^4\text{He}$ dilution refrigerator with cavity temperatures $T \approx 0.15$ K. The cavity Q values ranged from 4×10^9 to 8×10^9 . The velocity of the Rydberg atoms and thus their interaction time t_{int} with the cavity field were preselected by exciting a particular velocity subgroup with the laser. For this purpose, the laser beam irradiated the atomic beam at an angle of approximately 82° . As a consequence, the UV laser light (linewidth $\approx 2\text{MHz}$) is blueshifted by 50-200 MHz by the Doppler effect, depending on the velocity of the atoms.

Information on the maser field and interaction of the atoms in the cavity can be obtained solely by state-selective field ionization of the atoms in the upper or lower maser level after they have passed through the cavity. For different t_{int} the atomic inversion has been measured as a function of the

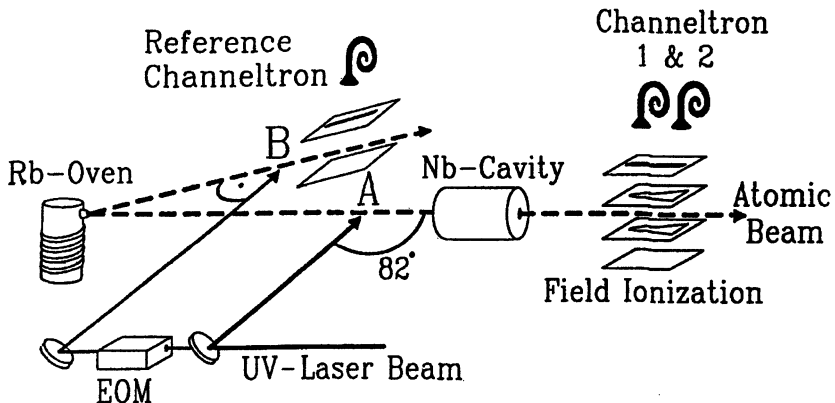


Fig. 2. Sketch of the experimental setup. The rubidium atoms emerge from an atomic beam oven and are excited at an angle of 82° at location A. After interaction with the cavity field, they enter a state-selective field ionization region, where channeltrons 1 and 2 detect atoms in the upper and lower maser levels, respectively. A small fraction of the UV radiation passes through an electro-optic modulator (EOM), which generates sidebands of the UV radiation. The blueshifted sideband is used to stabilize the frequency of the laser onto the Doppler-free resonance monitored with a secondary atomic beam produced by the same oven (location B)

pump rate by comparing the results with micromaser theory [12,13], the coupling constant Ω is found to be $\Omega = (40 \pm 10)$ krad/s.

Depending on the parameter range, essentially three regimes of the field evolution time constant τ_{field} can be distinguished. Here we only discuss the results for intermediate time constants. The maser was operated under steady-state conditions close to the second first-order phase transition (C in Fig. 1). The interaction time was $t_{\text{int}} = 47\mu\text{s}$ and the cavity decay time $\tau_{\text{cav}} = 60$ ms. The value of N_{ex} necessary to reach the second first-order phase transition was $N_{\text{ex}} \approx 200$. For these parameters, the two maxima in $P(n)$ are manifested in spontaneous jumps of the maser field between the two maxima with a time constant of ≈ 5 s. This fact and the relatively large pump rate led to the clearly observable field jumps shown in Fig. 3. Because of the large cavity field decay time, the average number of atoms in the cavity was still as low as 0.17. The two discrete values for the counting rates correspond to the metastable operating points of the maser, which correspond to ≈ 70 and ≈ 140 photons. In the FP description, the two values correspond to two equally attractive minima in the FP potential $V(\nu)$. If one considers, for instance, the counting rate of lower-state atoms (CT2 in Fig. 3), the lower (higher) plateaus correspond to time intervals in the low (high) field metastable operating point. If the actual photon number distribution is av-

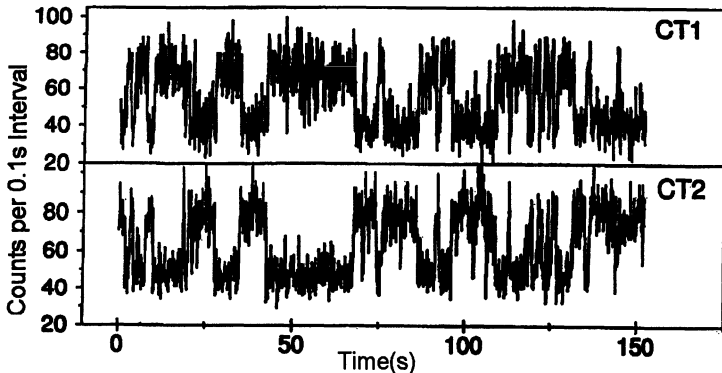


Fig. 3. Quantum jumps between two equally stable operation points of the maser field. The channeltron counts are plotted versus time (CT1= upper state and CT2= lower state signals). The signals of the two different detectors show a counterphase behavior; this makes it easy to discriminate between signal and noise

eraged over a time interval containing many spontaneous field jumps, the steady-state result $P(n)$ of the micromaser theory is recovered.

In the parameter ranges where switching occurs much faster than in the case shown in Fig. 3 the individual jumps cannot be resolved, therefore different methods have to be used for the measurement. Furthermore hysteresis is observed at the maser parameters for which the field jumps occur. Owing to lack of space these results cannot be discussed here. For a complete survey on the performed experiments it is referred to [9].

As next topic we would like to discuss the observation of atomic interferences in the micromaser [10]. Since a non-classical field is generated in the maser cavity, we were able for the first time to investigate atomic interference phenomena under the influence of non-classical radiation; owing to the bistable behavior of the maser field the interferences display quantum jumps, thus the quantum nature of the field gets directly visible in the interference fringes. Interferences occur since a coherent superposition of dressed states is produced by mixing the states at the entrance and exit holes of the cavity. Inside the cavity the dressed states develop differently in time, giving rise to Ramsey-type interferences [16] when the maser cavity is tuned through resonance.

The setup used in the experiment is identical to the one described before [9]. However, the flux of atoms through the cavity is by a factor of 5-10 higher than in the previous experiments, where the $63P_{3/2} - 61D_{5/2}$ transition was used. For the experiments the Q-value of the cavity was 6×10^9 corresponding to a photon decay time of 42 ms.

Figure 4 shows the standard maser resonance in the uppermost plot which is obtained when the resonator frequency is tuned. At large values of N_{ex} (N_{ex}

> 89) sharp, periodic structures appear. These typically consist of a smooth wing on the low-frequency side, and a vertical step on the high-frequency side. The clarity of the pattern rapidly decreases when N_{ex} increases to 190 or beyond. We will see later that these structures have to be interpreted as interferences. It can be seen that the atom-field resonance frequency is red-shifted with increasing N_{ex} , the shift reaching 200 kHz for $N_{ex} = 190$. Under these conditions there are roughly 100 photons on the average in the cavity. The large red-shift cannot be explained by AC Stark effect, which for 100 photons would amount to about one kHz for the transition used. Therefore it is obvious that other reasons must be responsible for the observed shift.

It is known from previous maser experiments that there are small static electric fields in the entrance and exit holes of the cavity. It is supposed that this field is generated by patch effects at the surface of the niobium metal caused by rubidium deposits caused by the atomic beam or by microcrystallites formed when the cavities are tempered after machining. The tempering process is necessary to achieve high quality factors. The influence of those stray fields is only observable in the cavity holes; in the center of the cavity they are negligible owing to the large atom-wall distances.

When the interaction time t_{int} between the atoms and the cavity field is increased the interference structure disappears for $t_{int} > 47 \mu s$ [10]. This is due to the fact that there is no non-adiabatic mixing any more between the substates when the atoms get too slow.

In order to understand the observed structures, the Jaynes-Cummings dynamics of the atoms in the cavity has to be analyzed. This treatment is more involved than that in connection with previous experiments, since the higher maser field requires detailed consideration of the field in the periphery of the cavity, where the additional influence of stray electric fields is more important.

The usual formalism for the description of the coupling of an atom to the radiation field is the dressed atom approach [17], leading to splitting of the coupled atom-field states, depending on the vacuum Rabi-flopping frequency Ω , the photon number n , and the atom-field detuning δ . We face a special situation at the entrance and exit holes of the cavity. There we have a position-dependent variation of the cavity field, as a consequence of which Ω is position-dependent. An additional variation results from the stray electric fields in the entrance and exit holes. Owing to the Stark-effect these fields lead to a position-dependent atom-field detuning δ .

The Jaynes-Cummings-Hamiltonian only couples pairs of dressed states. Therefore, it is sufficient to consider the dynamics within such a pair. In our case, prior to the atom-field interaction the system is in one of the two dressed states. For parameters corresponding to the periodic substructures in Fig. 4 the dressed states are mixed only at the beginning of the atom-field interaction and at the end. The mixing at the beginning creates a coherent superposition of the dressed states. Afterwards the system develops adiabati-

cally, whereby the two dressed states accumulate a differential dynamic phase Φ which strongly depends on the cavity frequency. The mixing of the dressed states at the entrance and exit holes of the cavity, in combination with the

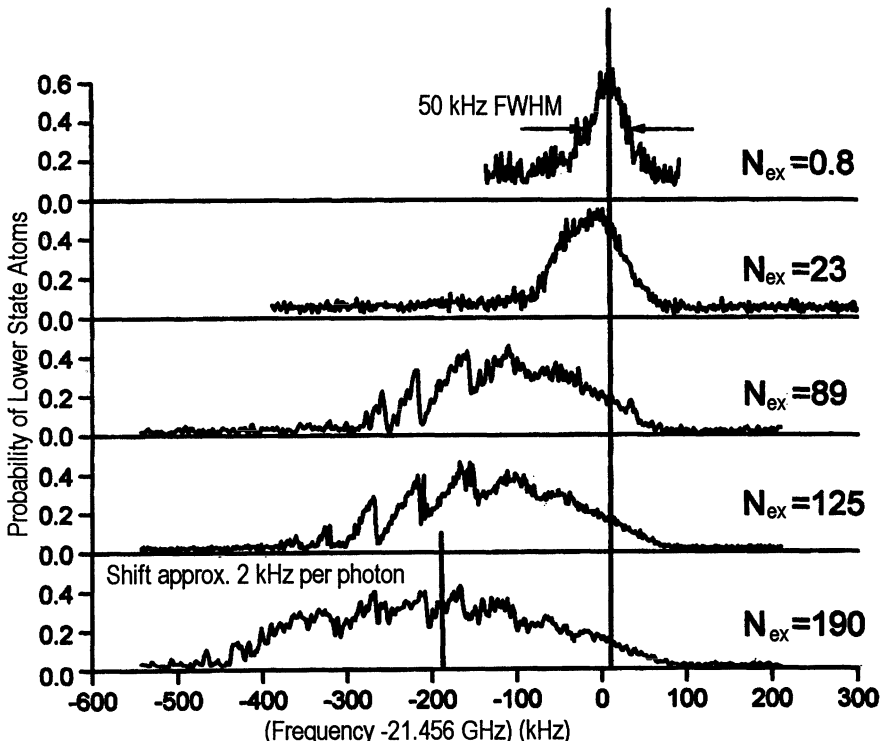


Fig. 4. Shift of the maser resonance $63\text{ P}_{3/2} - 61\text{ D}_{5/2}$ for fast atoms ($t_{\text{int}} = 35$ s). The upper plot shows the maser line for low pump rate ($N_{\text{ex}} < 1$). The FWHM linewidth (50 kHz) sets an upper limit of ≈ 5 mV/cm for the residual electric stray fields in the center of the cavity. The lower resonance lines are taken for the indicated large values of N_{ex} . The plots show that the center of the maser line shifts by about 2 kHz per photon. In addition, there is considerable field-induced line broadening which is approximately proportional to $\sqrt{N_{\text{ex}}}$. For $N_{\text{ex}} \geq 89$ the lines display periodic structures, which are discussed in the text

intermediate adiabatic evolution, generates a situation similar to a Ramsey two-field interaction.

The maximum differential dynamic phase Φ solely resulting from dressed-state coupling by the maser field is roughly 4π under the experimental conditions used here. This is not sufficient to explain the interference pattern of Fig. 4, where we have at least six maxima corresponding to a differential phase of 12π . This means that an additional energy shift differently affecting

upper and lower maser states is present. Such a phenomenon can be caused by the above mentioned small static electric fields present in the holes of the cavity. The static field causes a position-dependent detuning δ of the atomic transition from the cavity resonance; as a consequence we get an additional differential dynamic phase Φ . In order to interpret the periodic substructures as a result of the variation of Φ with the cavity frequency, the phase Φ has to be calculated from the atomic dynamics in the maser field.

The quantitative calculation can be performed on the basis of the micromaser theory. The calculations reproduce the experimental finding that the maser line shifts to lower frequencies when N_{ex} is increased [10]. The mechanism for that can be explained as follows: the high-frequency edge of the maser line does not shift with N_{ex} et all, since this part of the resonance is produced in the central region of the cavity, where practically no static electric fields are present. The low-frequency cutoff of the structure is determined by the location where the mixing of the dressed states occurs. With decreasing cavity frequency those points shift closer to the entrance and exit holes, with the difference between the particular cavity frequency and unperturbed atomic resonance frequency giving a measure of the static electric field at the mixing locations. Closer to the holes the passage behaviour of the atoms through the mixing locations gets non-adiabatic for the following reasons: firstly, the maser field strength reduces towards the holes. This leads to reduced repulsion of the dressed states. Secondly, the stray electric field strongly increases towards the holes. This implies a larger differential slope of the dressed state energies at the mixing locations, and therefore leads to a stronger non-adiabatic passage. At the same time the observed signal extends further to the low frequency spectral region. Since the photon emission probabilities are decreasing towards lower frequencies their behaviour finally defines the low-frequency boundary of the maser resonance line. With increasing N_{ex} the photon number n increases. As for larger values of n the photon emission probabilities get larger, also increasing N_{ex} leads to an extension of the range of the signal to lower frequencies. This theoretical expectation is in agreement with the experimental observation.

In the experiment it is also found that the maser line shifts towards lower frequencies with increasing t_{int} . This result also follows from the developed model: the red-shift increases with t_{int} since a longer interaction time leads to a more adiabatic behavior in the same way as a larger N_{ex} does.

The calculations reveal that on the vertical steps displayed in the signal the photon number distribution has two distinctly separate maxima similar to those observed at the phase transition points discussed above. Therefore, the maser field should exhibit hysteresis and metastability under the present conditions as well. The hysteresis indeed shows up when the cavity frequency is linearly scanned up and down with a modest scan rate [10]. When the maser is operated in steady-state and the cavity frequency is fixed to the

steep side of one of the fringes we also observe spontaneous jumps of the maser field between two metastable field states.

The calculations also show that on the smooth wings of the more pronounced interference fringes the photon number distribution $P(n)$ of the maser field is strongly sub-Poissonian. This leads us to the conclusion that we observe Ramsey-type interferences induced by a non-classical radiation field. The sub-Poissonian character of $P(n)$ results from the fact that on the smooth wings of the fringes the photon gain reduces when the photon number is increased. This feedback mechanism stabilizes the photon number resulting in a sub-Poissonian photon distribution.

2.2 Entanglement in the micromaser

Owing to the interaction of the Rydberg atom with the maser field there is an entanglement between field and the state in which a particular atom is leaving the cavity.

This entanglement was studied in several papers, see e.g. [18] and [8]. Furthermore there is a correlation between the states of the atoms leaving the cavity subsequently. If e.g. atoms in the lower maser level are studied [19] an anticorrelation is observed in a region for the pump parameter Θ where sub-Poissonian photon statistics is present in the maser field. Recently measurements [20] of these pair correlations have been performed giving a rather good agreement with the theoretical predictions by Briegel et al. [21]. Since the cavity field plays an important role in this entanglement the pair correlations disappear when the time interval between subsequent atoms get larger than the storage time of a photon in the cavity.

2.3 Trapping states

The trapping states are a steady-state feature of the micromaser field peaked in a single photon number, they occur in the micromaser as a direct consequence of field quantisation. At low cavity temperatures the number of blackbody photons in the cavity mode is reduced and trapping states begin to appear [22,23]. They occur when the atom field coupling, Ω , and the interaction time, t_{int} , are chosen such that in a cavity field with n_q photons each atom undergoes an integer number, k , of Rabi cycles. This is summarised by the condition,

$$\Omega t_{\text{int}} \sqrt{n_q + 1} = k\pi . \quad (1)$$

When (1) is fulfilled the cavity photon number is left unchanged after the interaction of an atom and hence the photon number is “trapped”. This will occur over a large range of the atomic pump rate N_{ex} . The trapping state is therefore characterised by the photon number n_q and the number of integer multiples of full Rabi cycles k .

The build up of the cavity field can be seen in Fig.5, where the emerging atom inversion is plotted against interaction time and pump rate. The inversion is defined as $I(t_{\text{int}}) = P_g(t_{\text{int}}) - P_e(t_{\text{int}})$ where $P_{e(g)}(t_{\text{int}})$ is the probability of finding an excited state (ground state) atom for a particular

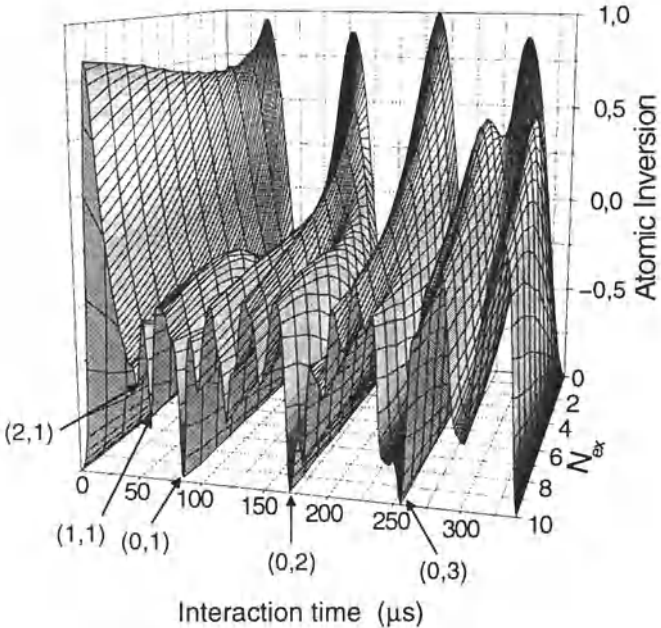


Fig. 5. Inversion of the micromaser field under conditions that the trapping states occur. The thermal photon number is 10^{-4} . As the pump rate increases, the formation of the trapping states from the vacuum show up. See also Fig. 6. The trapping states are characterized by (n_q, k) whereby n_q is the photon number and k the number of Rabi cycles

interaction time t_{int} . At low atomic pump rates (low N_{ex}) the maser field cannot build up and the maser exhibits Rabi oscillations due to the interaction with the vacuum field. At the positions of the trapping states, the field builds up until it reaches the trapping state condition. This manifests itself as a reduced emission probability and hence as a dip in the atomic inversion. Once in a trapping state the maser will remain there regardless of the pump rate. The trapping states show up therefore as valleys in the N_{ex} direction. Figure 6 shows the photon number distribution as the pump rate is increased for the special condition of the five photon trapping state. The photon distribution develops from a thermal distribution towards higher photon numbers until the pump rate is high enough for the atomic emission to be affected by

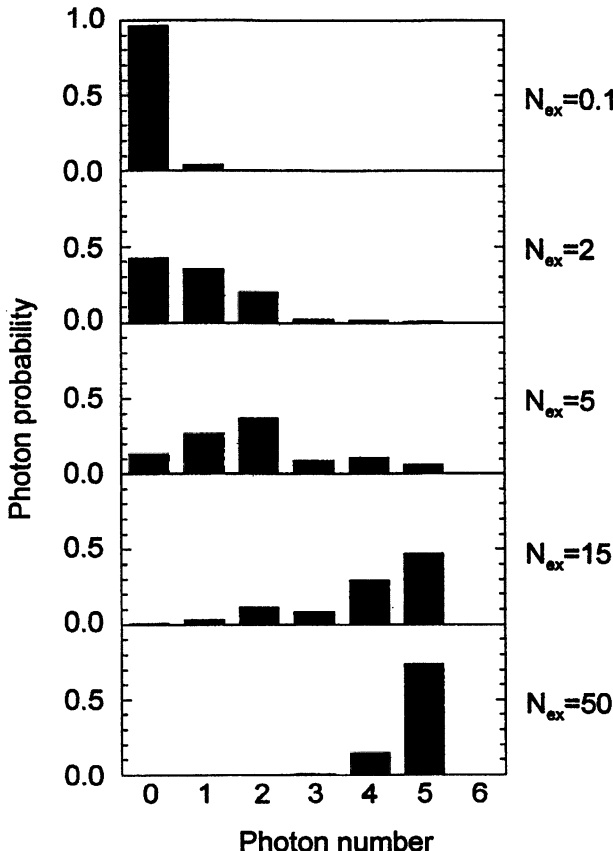


Fig. 6. Photon number distribution of the maser field as a function of the atomic flux N_{ex} . Shown is a numerical simulation. At $N_{ex} = 50$ a Fock state with rather high purity is achieved

the trapping state condition. As the pump rate is further increased, and in the limit of a low thermal photon number, the field continues to build up to a single trapped photon number and the steady-state distribution approaches a Fock state. There is in general a slight deviation from a pure Fock state resulting from photon losses. Therefore the state with the next lower photon number has a small probability. A lost photon will be replaced by the next incoming atom, however, there is a small time interval until this actually happens depending on the availability of an atom.

Owing to blackbody radiation at finite temperatures, there is a probability of having thermal photons enter the mode. The presence of a thermal photon in the cavity disturbs the trapping state condition and an atom can emit a photon. This causes the photon number of the field to jump to a value

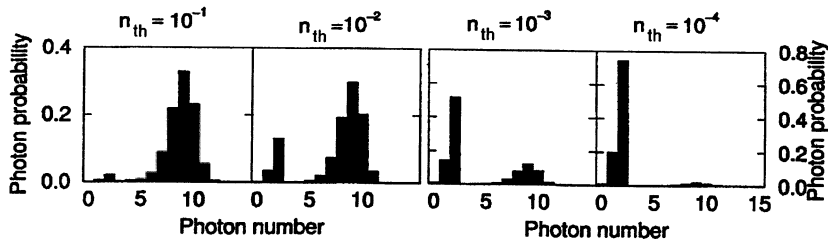


Fig. 7. Photon number distribution of the maser field. This simulation shows the strong influence of thermal photons on the steady-state photon number distribution ($N_{ex} = 25$)

above the trapping condition n_q and a cascade of emission events will follow resulting in a build up of a new photon distribution with an average photon number $n > n_q$ (Fig. 7). The steady state behaviour of the maser field thus reacts very sensitively on the presence of thermal photons and the number of lower state atoms increases.

Note that under readily achievable experimental conditions, it is possible for the steady-state field in the cavity to approach Fock states with a high fidelity. Figure 8 summarizes results of simulations of the micromaser field

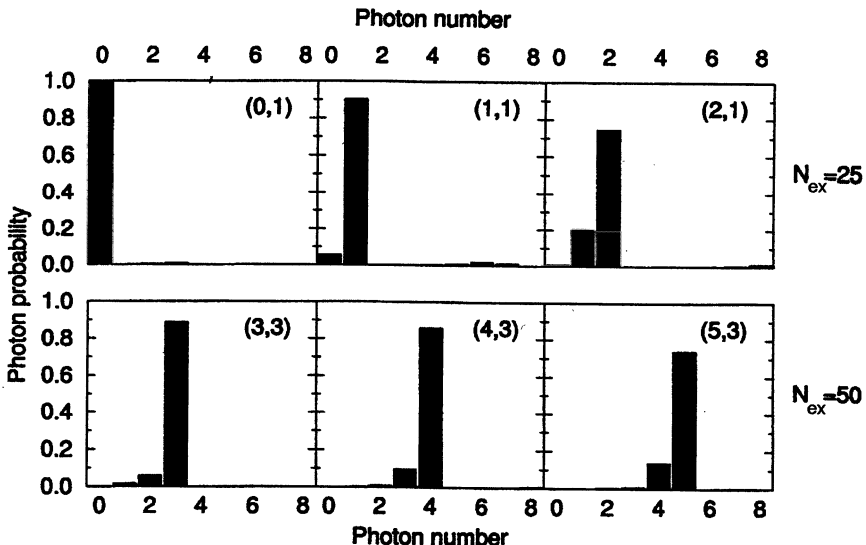


Fig. 8. Purity of Fock states generated in the micromaser under trapping state conditions. Shown are computer simulations for Fock states between $n = 0$ and $n = 5$. The thermal photon number is $n_{th} = 10^{-4}$

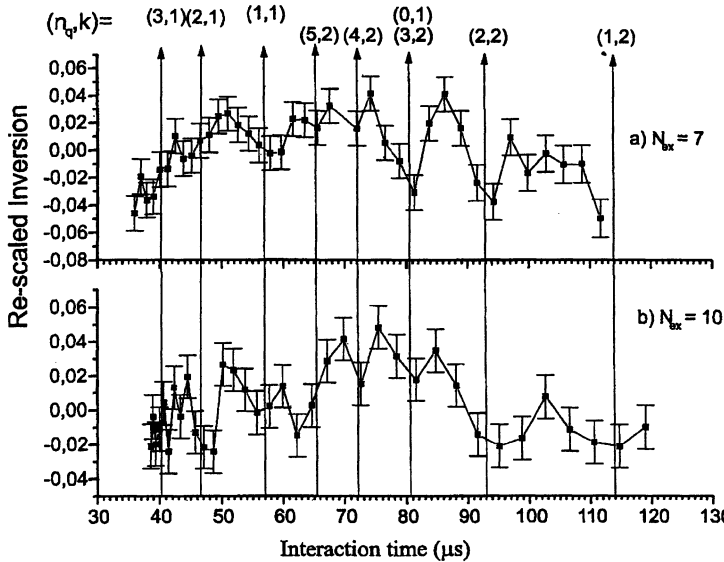


Fig. 9. Experimental measurement of trapping states in the maser field (Weidinger et. al. [23]). Trapping states appear in a reduced probability of finding ground state atoms. The rescaling considers the decay of the Rydberg states on their way from preparation to detection

corresponding to Fock states from $n = 0$ to $n = 5$. The experimental realisation requires pump rates of $N_{\text{ex}} = 25$ to $N_{\text{ex}} = 50$, a temperature of about 100 mK, and a high selectivity of atomic velocity [23].

The results displayed in Fig. 8 show again the phenomenon which is also evident in Fig. 6: the deviation from the pure Fock state is mainly caused by losses, therefore a contribution of the state with the next lower photon number is also present in the distribution. This is caused by the fact that a finite time is needed in the maser cavity to replace a lost photon.

Experimental evidence that trapping states can be achieved is shown in Fig. 9a and 9b (see [23] for details). The measurement was taken at a cavity temperature of 0.3 K corresponding to a thermal photon number of 0.054. The plot shows a rescaled inversion which takes the increasing loss of Rydberg atoms at longer interaction times into account. The shown result gives a good qualitative agreement with the Monte-Carlo simulations performed in [11].

In Fig. 9a which displays the results for smaller N_{ex} the trapping states corresponding to the vacuum (n_q, k) = (0,1), one photon (1,1) and two photons (2,1), and (2,2) are clearly visible while at higher N_{ex} (Fig. 9b) the vacuum and one photon trapping states become less visible. With increasing N_{ex} the width of the trapping states decreases [22] and the influence of detuning and velocity averaging get larger. At higher pump rates it is also im-

portant that the proportion of two atom events grows, reducing the visibility of trapping states.

In the following we would like to mention another method which can be used to generate Fock states of the field of the one-atom maser. When the atoms leave the cavity of the micromaser they are in an entangled state with the cavity field [20]. A method of state reduction was suggested by Krause et al. [24] to observe the build up of the cavity field to a known Fock state. By state reduction of the outgoing atom also the field part of the entangled atom-field state is projected out and the photon number in the field either increases or decreases depending on the state of the observed outgoing atom. If the field is initially in a state $|n\rangle$ then an interaction of an atom with the cavity leaves the cavity field in a superposition of the states $|n\rangle$ and $|n+1\rangle$ and the atom in a superposition of the internal atomic states $|e\rangle$ and $|g\rangle$.

$$\Psi = \cos(\phi)|e\rangle|n\rangle - i \sin(\phi)|g\rangle|n+1\rangle \quad (2)$$

where ϕ is an arbitrary phase. The state selective field ionisation measurement of the internal atomic state, reduces also the field to one of the states $|n\rangle$ or $|n+1\rangle$. State reduction is independent of interaction time, hence a ground state atom always projects the field onto the $|n+1\rangle$ state independent of the time spent in the cavity. This results in an *a priori* probability of the maser field being in a specific but unknown number state [24]. If the initial state is the vacuum, $|0\rangle$, then a number state created is equal to the number of ground state atoms that were collected within a suitably small fraction of the cavity decay time.

In a system governed by the Jaynes-Cummings Hamiltonian, spontaneous emission is reversible and an atom in the presence of a resonant quantum field undergoes Rabi oscillations. That is the relative populations of the excited and ground states of the atom oscillate at a frequency $\Omega\sqrt{n+1}$, where Ω is the atom field coupling constant. Experimentally we measure again the atomic inversion, $I = P_g - P_e$. In the presence of dissipation a fixed photon number n in a particular mode is not observed and the field always evolves into a mixture of such states. Therefore the inversion is generally given by,

$$I(n, t_{\text{int}}) = - \sum_n P_n \cos(2\Omega\sqrt{n+1}t_{\text{int}}) \quad (3)$$

where P_n is the probability of finding n photons in the mode, t_{int} is the interaction time of the atoms with the cavity field.

The experimental verification of the presence of Fock states in the cavity takes the form of a pump-probe experiment in which a pump atom prepares a quantum state in the cavity and the Rabi phase of the emerging probe atom measures the quantum state. The signature that the quantum state of interest has been prepared is simply the detection of a defined number of ground state atoms. To verify that the correct quantum state has been projected onto the cavity field a probe atom is sent into the cavity with a variable,

but well defined, interaction time. As the formation of the quantum state is independent of interaction time we need not change the relative velocity of the pump and probe atoms, thus reducing the complexity of the experiment. In this sense we are performing a reconstruction of a quantum state in the cavity using a similar method to that described by Bardoff et al. [25]. This experiment reveals the maximum amount of information that can be found relating to the cavity photon number. We have recently used this method to demonstrate the existence of Fock states up to $n=2$ in the cavity [26].

2.4 Generation of GHZ states

The following proposal for the creation of states of the Greenberger-Horne-Zeilinger (GHZ) type [28,29] is an application of the vacuum trapping state. By the use of the vacuum trapping state a field determination during the measurement is not necessary which simplifies strongly the preparation of the GHZ-states. We assume that the cavity is initially empty, and two excited atoms traverse it consecutively. The velocity of the first atom, and its consequent interaction time, is such that it emits a photon with probability $(\sin \varphi_1)^2 = 51.8\%$, where $\varphi_1 = 0.744 \pi$ is the corresponding Rabi angle ϕ of (2) for $n = 0$. The second atom arrives with the velocity dictated by the vacuum trapping condition; for $n = 0$ it has $\phi = \pi$ in (2), so that $\phi = \sqrt{2} \pi$ for $n = 1$. Assuming that the duration of the whole process is short on the scale set by the life time of the photon in the cavity, we thus have

$$\begin{aligned} |0, e, e\rangle &\xrightarrow[\text{atom}]{\text{first}} |0, e, e\rangle \cos(\varphi_1) - i|1, g, e\rangle \sin(\varphi_1) \\ &\xrightarrow[\text{atom}]{\text{second}} -|0, e, e\rangle \cos(\varphi_1) - |2, g, g\rangle \sin(\varphi_1) \sin(\sqrt{2}\pi) \\ &\quad - i|1, g, e\rangle \sin(\varphi_1) \cos(\sqrt{2}\pi), \end{aligned} \quad (4)$$

where, for example, $|1, g, e\rangle$ stand for “one photon in the cavity and first atom in the ground state and second atom excited.” With the above choice of $\sin(\varphi_1) = 0.720$, we have $\cos(\varphi_1) = \sin(\varphi_1) \sin(\sqrt{2}\pi) = -0.694$, so that the two components with even photon number ($n = 0$ or $n = 2$) carry equal weight and occur with a joint probability of 96.3%. The small 3.7% admixture of the $n = 1$ component can be removed by measuring the parity of the photon state [30] and conditioning the experiment to even parity. The two atoms and the cavity field are then prepared in the entangled state

$$\Psi_{GHZ} = \frac{1}{\sqrt{2}} (|0, e, e\rangle + |2, g, g\rangle), \quad (5)$$

which is a GHZ state of the Mermin kind [31] in all respects.

2.5 The one-atom maser and ultracold atoms

In the following chapter we discuss the case that the micromaser is pumped by ultracold atoms; in this limit the center of mass motion has to be treated

quantum mechanically, especially when the kinetic energy $(\hbar k)^2 / 2M$ of the atoms is of the same order or smaller than the atom-field [32] interaction energy $\hbar\Omega$.

For simplicity, we here consider the situation where an atom in the excited state $|e\rangle$ is incident upon a cavity that contains n photons so that the combined atom-field system is described by the state $|e,n\rangle = (|\gamma_{n+1}^+\rangle + |\gamma_{n+1}^-\rangle)/\sqrt{2}$. The dressed-state components $|\gamma_{n+1}^+\rangle$ and $|\gamma_{n+1}^-\rangle$, which are the eigenstates of the atom-field interaction Hamiltonian, encounter different potentials giving rise to different reflection and transmission of the atom. Appropriate relative phase shifts between the dressed-state components during the atom-field interaction may result in the state $(|\gamma_{n+1}^+\rangle - |\gamma_{n+1}^-\rangle)/\sqrt{2} = |g, n+1\rangle$, which corresponds to the emission of a photon and a transition to the lower atomic level $|g\rangle$. Likewise, changes in the relative reflection and transmission amplitudes may lead to a de-excitation of the atom.

For thermal atoms, the emission probability shown in Fig. 10 displays the usual Rabi oscillations as a function of the interaction time τ . For very slow atoms, however, the emission probability is a function of the interaction length L and shows resonances such as the ones observed in intensity transmitted by a Fabry-Perot resonator. The resonances occur when the cavity length is an integer multiple of half the de Broglie wavelength of the atom inside the potential well.

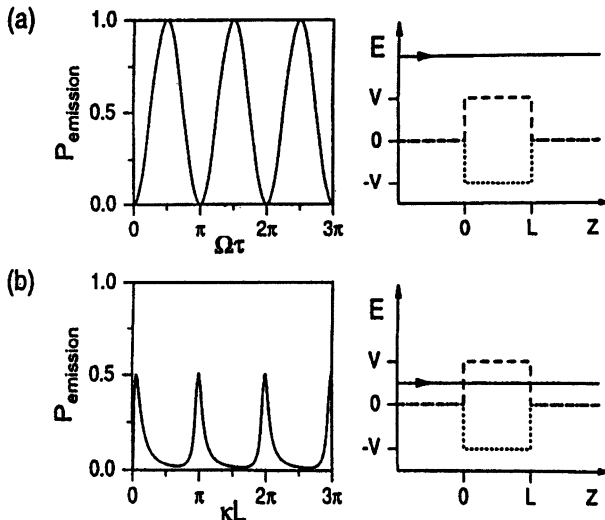


Fig. 10. Emission probability for (a) thermal atoms with $k/\kappa=10$ versus the interaction time $\Omega\tau$ and (b) ultracold atoms with $k/\kappa=0.1$ versus the interaction length κL , and the corresponding repulsive (dashed) and attractive (dotted) atom-field potential. The constant κ is defined by $(\hbar\kappa)^2/2m = \hbar\Omega$

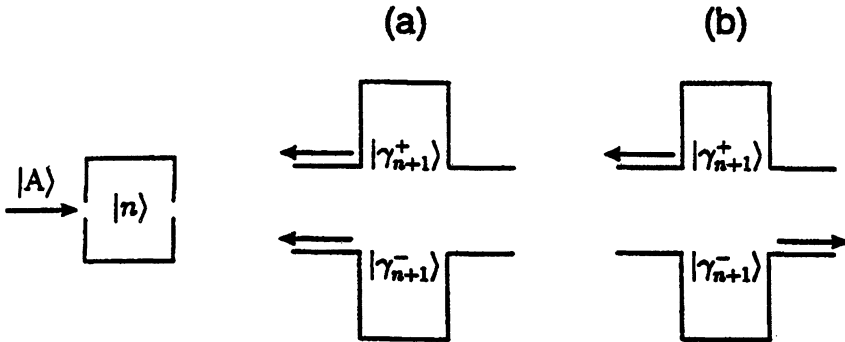


Fig. 11. Reflection and transmission of the atoms at the potential barrier for the $|\gamma_{n+1}^+\rangle$ and at the potential well for the $|\gamma_{n+1}^-\rangle$ component (a) out of the mazer resonance and (b) on resonance

Figure 11 illustrates the reflection and transmission of the atom for a cavity whose mode function is a mesa function, which approximates the lowest TM mode of a cylindrical cavity. For very cold atoms, the dressed-state component that encounters the potential barrier is always reflected. In general, the other dressed-state component is also reflected at the well. The situation changes dramatically if the cavity length is an integer multiple of half the de Broglie wavelength. In this case, the $|\gamma_{n+1}^-\rangle$ is completely transmitted, which implies a 50% transmission probability for the atom. A detailed calculation [32] shows that in such a situation the emission probability for a photon is 1/2 for each of the two dressed-state components, yielding an overall emission probability $P_{\text{emission}} = 1/2$.

So far, we have discussed the motion and atom-field interaction of a single atom incident upon the cavity. Due to the unusual emission probability, a beam of ultracold atoms can produce unusual photon distributions such as a shifted thermal distribution. For details about this microwave amplification by z-motion induced emission of radiation (mazer), the reader is referred to the trilogy [33–35].

In order to see the mazer resonances for atoms with a certain velocity spread, the interaction length L has to be small. Whereas in the usual cylindrical micromaser cavities the smallest cavity length is given by half the wavelength of the microwaves, cavities of the reentrant type, as depicted in Fig. 12, allow for an interaction length much smaller than the wavelength. With such a device, an experiment with realistic parameters seems possible [34].

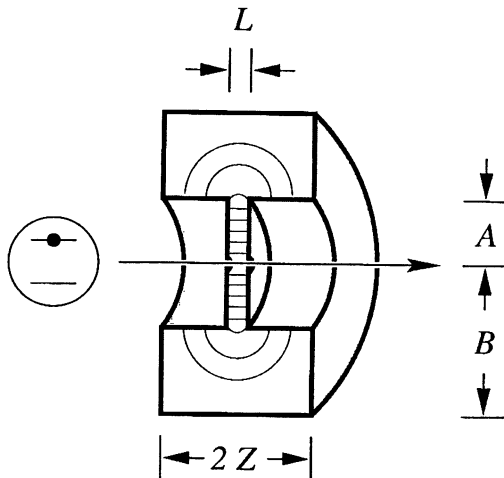


Fig. 12. Possible experimental setup with a reentrant cavity

3 Ion Trap Experiments

Besides the experiments performed with atoms in a cavity the trapped ion techniques provide another way to investigate quantum phenomena in radiation atom interaction. In the following recent experiments and new proposals for experiments will be reviewed.

3.1 Resonance fluorescence of a single atom

Resonance fluorescence of an atom is a basic process in radiation-atom interactions, and has therefore always generated considerable interest. The methods of experimental investigation have changed continuously due to the availability of new experimental tools. A considerable step forward occurred when tunable and narrow band dye laser radiation became available. These laser sources are sufficiently intense to easily saturate an atomic transition. In addition, the lasers provide highly monochromatic light with coherence times much longer than typical natural lifetimes of excited atomic states. Excitation spectra with laser light using well collimated atomic beam lead to a width being practically the natural width of the resonance transition, therefore it became possible to investigate the frequency spectrum of the fluorescence radiation with high resolution. However, the spectrograph used to analyze the reemitted radiation was a Fabry-Perot interferometer, the resolution of which did reach the natural width of the atoms, but was insufficient to reach the laser linewidth, see e.g. Hartig et al. [36] and Cresser et al. [37]. A considerable progress in this direction was achieved by investigating the fluorescence spectrum of ultra-cold atoms in an optical lattice in a heterodyne experiment

[38]. In these measurements a linewidth of 1 kHz was achieved, however, the quantum aspects of the resonance fluorescence such as antibunched photon statistics cannot be investigated under these conditions since they wash out when more than one atom is involved.

Thus the ideal experiment requires a single atom to be investigated. Since some time it is known that ion traps allow to study the fluorescence from a single laser cooled particle practically at rest, thus providing the ideal case for the spectroscopic investigation of the resonance fluorescence. The other essential ingredient for achieving a high resolution is the measurement of the frequency spectrum by heterodyning the scattered radiation with laser light as demonstrated with many cold atoms [38]. Such an optimal experiment with a single trapped Mg^+ ion is reviewed in the following. The measurement of the spectrum of the fluorescent radiation at low excitation intensities is presented. Furthermore, the photon correlation of the fluorescent light has been investigated under practically identical excitation conditions. The comparison of the two results shows a very interesting aspect of complementarity since the heterodyne measurement corresponds to a “wave” detection of the radiation whereas the measurement of the photon correlation is a “particle” detection scheme. It will be shown that under the same excitation conditions the wave detection provides the properties of a classical atom, i.e. a driven oscillator, whereas the particle or photon detection displays the quantum properties of the atom. Whether the atom displays classical or quantum properties thus depends on the method of observation.

The spectrum of the fluorescence radiation is given by the Fourier transform of the first order correlation function of the field operators, whereas the photon statistics and photon correlation is obtained from the second order correlation function. The corresponding operators do not commute, thus the respective observations are complementary. Present theory on the spectra of fluorescent radiation following monochromatic laser excitation can be summarized as follows: fluorescence radiation obtained with low incident intensity is also monochromatic owing to energy conservation. In this case, elastic scattering dominates the spectrum and thus one should measure a monochromatic line at the same frequency as the driving laser field. The atom stays in the ground state most of the time and absorption and emission must be considered as one process with the atom in principle behaving as a classical oscillator. This case was treated on the basis of a quantized field many years ago by Heitler [39]. With increasing intensity upper and lower states become more strongly coupled leading to an inelastic component, which increases with the square of the intensity. At low intensities, the elastic part dominates since it depends linearly on the intensity. As the intensity of the exciting light increases, the atom spends more time in the upper state and the effect of the vacuum fluctuations comes into play through spontaneous emission. The inelastic component is added to the spectrum, and the elastic component goes through a maximum where the Rabi flopping frequency $\Omega = \Gamma / \sqrt{2} (\Gamma$

is the natural linewidth) and then disappears with growing Ω . The inelastic part of the spectrum gradually broadens as Ω increases and for $\Omega > \Gamma/2$ sidebands begin to appear [37,40].

The experimental study of the problem requires, as mentioned above, a Doppler-free observation. In order to measure the frequency distribution, the fluorescent light has to be investigated by means of a high resolution spectrometer. The first experiments of this type were performed by Schuda et al. [41] and later by Walther et al. [42], Hartig et al. [36] and Ezekiel et al. [43]. In all these experiments, the excitation was performed by single-mode dye laser radiation, with the scattered radiation from a well collimated atomic beam observed and analyzed by a Fabry-Perot interferometer.

Experiments to investigate the elastic part of the resonance fluorescence giving a resolution better than the natural linewidth have been performed by Gibbs et al. [44] and Cresser et al. [37].

The first experiments which investigated antibunching in resonance fluorescence were also performed by means of laser-excited collimated atomic beams. The initial results obtained by Kimble, Dagenais, and Mandel [45] showed that the second-order correlation function $g^{(2)}(t)$ had a positive slope which is characteristic of photon antibunching. However, $g^{(2)}(0)$ was larger than $g^{(2)}(t)$ for $t \rightarrow \infty$ due to number fluctuations in the atomic beam and to the finite interaction time of the atoms [46,47]. Further refinement of the analysis of the experiment was provided by Dagenais and Mandel [47]. Rateike et al. [48] used a longer interaction time for an experiment in which they measured the photon correlation at very low laser intensities (see Cresser et al. [37] for a review). Later, photon antibunching was measured using a single trapped ion in an experiment which avoids the disadvantages of atom number statistics and finite interaction time between atom and laser field [49].

As pointed out in many papers photon antibunching is a purely quantum phenomenon (see e. g. Cresser et al. [37] and Walls [50]). The fluorescence of a single ion displays the additional nonclassical property that the variance of the photon number is smaller than its mean value (i.e. it is sub-Poissonian) [49,51].

The trap used for the present experiment was a modified Paul-trap, called an endcap-trap [52]. The trap consists of two solid copper-beryllium cylinders (diameter 0.5 mm) arranged co-linearly with a separation of 0.56 mm. These correspond to the cap electrodes of a traditional Paul trap, whereas the ring electrode is replaced by two hollow cylinders, one of which is concentric with each of the cylindrical endcaps. Their inner and outer diameters are 1 and 2 mm, respectively and they are electrically isolated from the cap electrodes. The fractional anharmonicity of this trap configuration, determined by the deviation of the real potential from the ideal quadrupole field is below 0.1% (see Schrama et al. [52]). The trap is driven at a frequency of 24 MHz with typical secular frequencies in the xy-plane of approximately 4 MHz. This

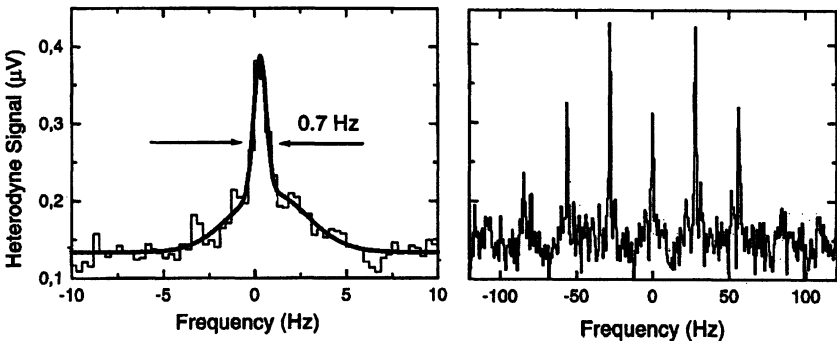


Fig. 13. Heterodyne spectrum of a single trapped 24 Mg^+ -ion. Left side: Resolution bandwidth 0.5 Hz. The solid line is a Lorentzian fit to the experimental data; the peak appears on top of a small pedestal being 4 Hz wide. The latter signal is due to random phase fluctuations in the spatially separated sections of the light paths of local oscillator and fluorescent light; they are generated by variable air currents in the laboratory. Right side: Heterodyne spectrum of the coherent peak with sidebands generated by mechanical vibrations of the mount holding the trap. The vibrations are due to the operation of a rotary pump in the laboratory. For details see [54]

required a radio-frequency voltage with an amplitude on the order of 300 V to be applied between the cylinders and the endcaps.

The measurements were performed using the $3^2S_{1/2} - 3^2P_{3/2}$ transition of 24 Mg^+ - ion at a wavelength of 280 nm. The heterodyne measurement is performed as follows. The dye laser excites the trapped ion while the fluorescence is observed in a direction of about 54° to the exciting laser beam. However, both the observation direction and the laser beam are in a plane perpendicular to the symmetry axis of the trap. A fraction of the laser radiation is removed with a beamsplitter and then frequency shifted (by 137 MHz with an acousto-optic modulator (AOM)) to serve as the local oscillator. An example of a heterodyne signal is displayed in Fig. 13. The signal is the narrowest optical heterodyne spectrum of resonance fluorescence reported to date. Thus our experiment provides the most compelling confirmation of Weisskopf's prediction of a coherent component in resonance fluorescence. The linewidth observed implies that exciting laser and fluorescent light are coherent over a length of 400 000 km. Further details on the experiment are given in [53] and [54]. Investigation of photon correlations employed the ordinary Hanbury-Brown and Twiss setup. The setup was essentially the same as described by Diedrich and Walther [49]. The results are shown and discussed in [53] also.

The presented experiment describes the first high-resolution heterodyne measurement of the elastic peak in resonance fluorescence of a single ion.

At identical experimental parameters we also measured antibunching in the photon correlation of the scattered field. Together, both measurements show that, in the limit of weak excitation, the fluorescence light differs from the excitation radiation in the second-order correlation but not in the first order correlation. However, the elastic component of resonance fluorescence combines an extremely narrow frequency spectrum with antibunched photon statistics, which means that the fluorescence radiation is not second-order coherent as expected from a classical point of view [55]. The heterodyne and the photon correlation measurement are complementary since they emphasize either the classical wave properties or the quantum properties of resonance fluorescence, respectively.

3.2 The ion-trap laser

There have been several theoretical papers on one-atom lasers in the past [56–59,66]. This system provides a testing ground for new theoretical concepts and results in the quantum theory of the laser. Examples are atomic coherence effects [60] and dynamic (i.e. self-generated) quantum-noise reduction [59,61,62]. All these aspects are a consequence of a pump process whose complex nature is not accounted for in the standard treatment of the laser. So far there is one experiment where laser action could be demonstrated with one atom at a time in the optical resonator [6]. A weak beam of excited atoms was used to pump this one-atom laser.

A formidable challenge for an experiment is to perform a similar experiment with a trapped ion in the cavity. Mirrors with an ultrahigh finesse are required, and a strong atom-field coupling is needed. After the emission of a photon, the ion has to be pumped before the next stimulated emission can occur. Similar as in the resonance fluorescence experiments which show antibunching [45,49], there is a certain time gap during which the ion is unable to add another photon to the laser field. It has been shown [59] that this time gap plays a significant role in the production of a field with sub-Poissonian photon statistics.

We have investigated the theoretical basis for an experimental realization of the ion-trap laser. Our analysis takes into account details such as the multi-level structure, the coupling strengths and the parameters of the resonator. It has been a problem to find an ion with an appropriate level scheme. We could show that it is possible to produce a laser field with the parameters of a single Ca^+ ion. This one-atom laser displays several features, which are not found in conventional lasers: the development of two thresholds, sub-Poissonian statistics, lasing without inversion and self-quenching. The details of this work are reported in [63,64]. In a subsequent paper [65] also the center-of-mass motion of the trapped ion was quantized. This leads to additional features of the ion trap laser, especially a multiple vacuum Rabi-splitting is observed.

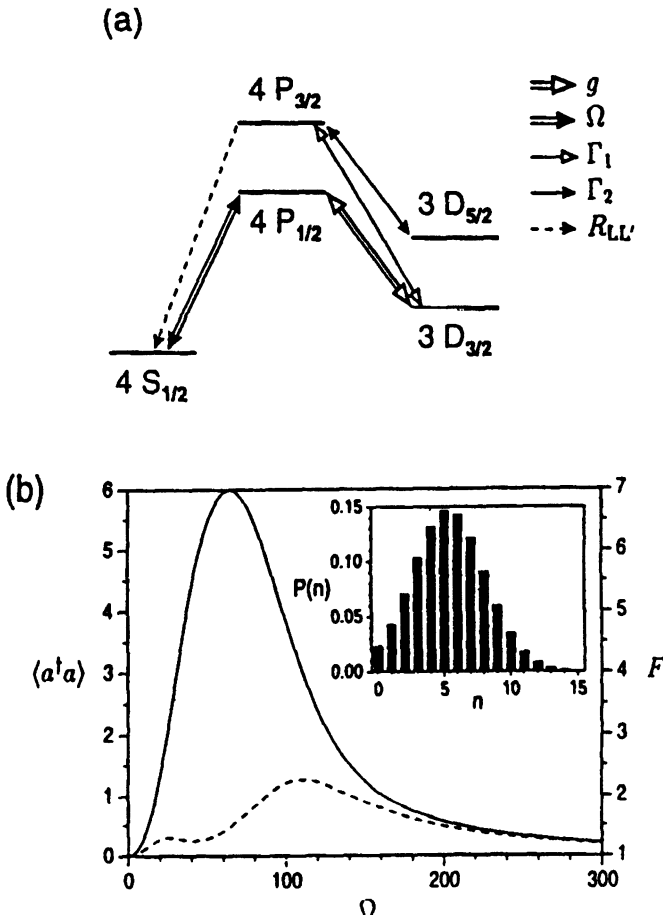


Fig. 14. (a) Schematic representation of the Ca^+ scheme for the ion-trap laser. (b) Mean photon number $\langle a^\dagger a \rangle$ (solid) and Fano factor F (dashed) versus the coherent pump strength Ω . The parameters are $A = 1$, $g = 14.8$, $\Gamma_1 = 40$, and $\Gamma_2 = 100$. The inset shows the photon distribution for $\Omega = 50$. All rates are in MHz

The Ca^+ scheme is sketched in Fig. 14(a). It contains a Λ -type subsystem: the ion is pumped coherently from the ground state to the upper laser level $4\text{P}_{1/2}$, stimulated emission into the resonator mode takes place on the transition to $3\text{D}_{3/2}$ at a wavelength of 866 nm. Further pump fields are needed to close the pump cycle and to depopulate the metastable levels.

Although spontaneous relaxation from the upper laser level to the ground state takes place at a relatively large rate of 140 MHz and suppresses the atomic polarization on the laser transition, laser light is generated for realistic experimental parameters due to atomic coherence effects within the Λ subsystem. The occurrence of laser action is demonstrated in Fig. 14(b)

for a resonator with a photon damping rate $A=1$ MHz and a vacuum Rabi frequency $g=14.8$ MHz on the laser transition. For the numerical calculation of the realistic scheme, the Zeeman substructure and the polarizations of the fields have to be taken into account. With increasing coherent pump Ω , the mean photon number inside the resonator first increases and then decreases. Both the increase and decrease of the intensity are accompanied by maxima in the intensity fluctuations, which can be interpreted as thresholds. Laser action takes place in between these two thresholds. This is confirmed by the Poissonian-like photon distribution given in the inset of Fig. 14(b). In addition, the linewidth of the output spectrum is in the laser region up to ten times smaller than below the first and beyond the second threshold [64]. Note that for a thermal distribution the solid and dashed curves in Fig. 14(b) for the intensity and the intensity fluctuations would coincide.

For a nonvanishing Lamb-Dicke parameter η , higher vibrational states will be excited during the pump and relaxation processes; the amplitude of the atomic motion will increase. Therefore, the ion will in general not remain at an antinode of the resonator mode, and the strength of the atom-field coupling will decrease. However, the atom can be prevented from heating up by detuning a coherent pump field. The coupling strength is given by the product of a constant g_0 depending on the transition probability and a motion-dependent function that is determined by an overlap integral involving the motional wave function of the atom and the mode function of the field [65].

In a simple two-level laser model with decay rate R_{AB} and pump rate R_{BA} , the cooling process may be incorporated by coupling the atomic motion to a thermal reservoir with cooling rate B and thermal vibron number μ . Already in such a simple model, the discrete nature of the quantized motion shows up below threshold in a multiple vacuum Rabi splitting of the output spectrum [65]. This is illustrated in Fig. 15. The pairs of peaks correspond to different vibrational states with different atom-field coupling.

The cooling mechanism is most transparent in the special case of resolved-sideband cooling. The coherent pump may be detuned to the first lower vibrational sideband so that with each excitation from $4S_{1/2}$ to $4P_{1/2}$ one vibron is annihilated and the CM motion is cooled. Eventually, all the population will collect in the motional ground state of the atomic ground state $4S_{1/2}$ and cannot participate in the lasing process. The coherent pump strength is now given by Ω_0 times a motion-dependent function. In order to maintain laser action in the presence of the cooling, an additional broadband pump field Γ may be applied to the cooling transition. Figure 16 indicates that a field with a mean photon number $\langle a^\dagger a \rangle = 2.3$ is generated while the mean vibron number is restricted to a value of $\langle b^\dagger b \rangle = 0.5$. If a larger mean vibron number is acceptable, the pump rate Γ can be increased and more population takes part in the laser action. This leads to considerably larger mean photon numbers. The calculation shows that it is possible to incorporate a cooling

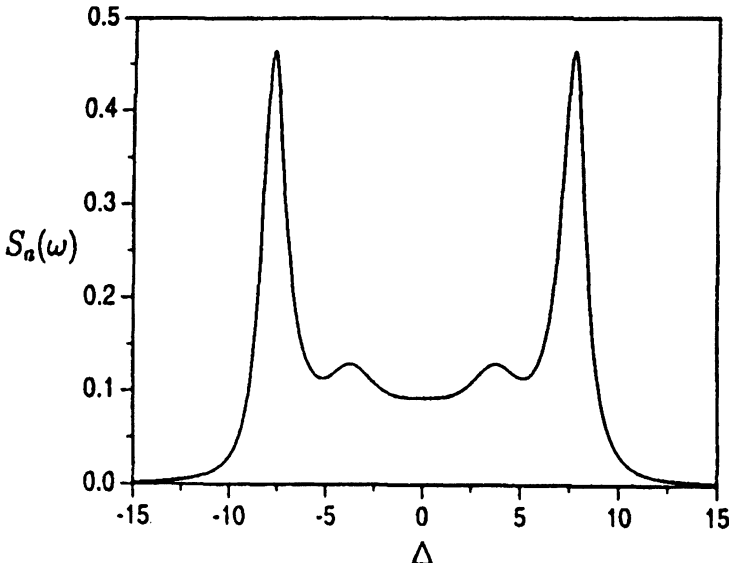


Fig. 15. Multiple vacuum Rabi splitting in the output spectrum $S_a(\omega)$ for the two-level atom with quantized CM motion. The parameters are $A = 0.1$, $B = 0.05$, $\mu = 0.5$, $R_{AB} = 0.1$, $R_{BA} = 0.001$, and $\eta = 0.7$. All rates are in units of g_0

mechanism in a multilevel one-atom laser scheme and to obtain significant lasing also for nonperfect localization of the atom. Although it is difficult to reach the resolved-sideband limit in an experiment, cooling may still be achieved in the weak-binding regime by detuning a coherent pump field.

4 Conclusions

In this paper recent experiments with single atoms in cavities and traps are reviewed. It is especially pointed out that using ultracold atoms will lead to new interesting aspects in atom-matter interaction. The possibility that now ultracold atoms are available bring such experiments into reach in the near future.

The quantum-mechanical CM motion of the atoms incident upon a micromaser cavity is equivalent to a scattering problem that involves both a repulsive and an attractive potential. The emission probability for an initially excited ultracold atom exhibits sharp resonances when the de Broglie wavelength fits resonantly into the cavity. These resonances may be observed experimentally with the help of a reentrant cavity. Whereas the eigenstates of the atomic motion are continuously distributed for the maser, the motion is confined to a trapping potential in the one-atom laser. The discrete nature of the CM motion in the trap is reflected below threshold by multiple vacuum Rabi splitting. In order to prevent the atom from being continuously

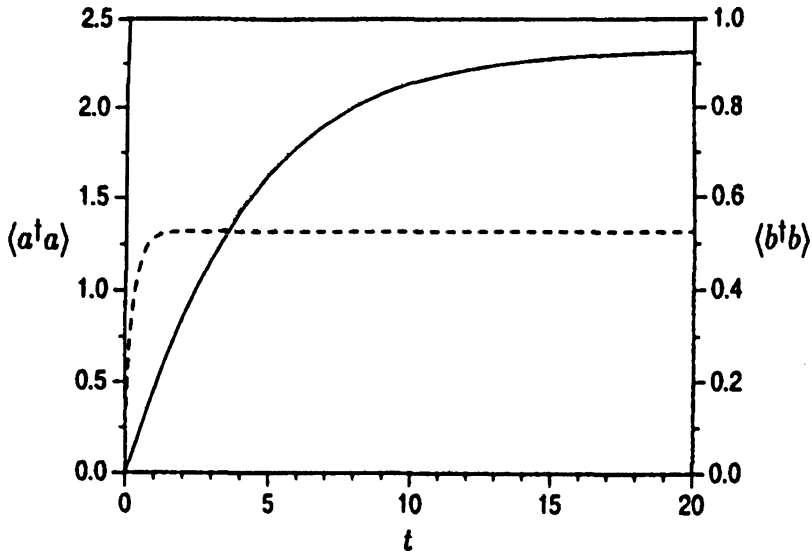


Fig. 16. Time evolution of the mean photon number (*solid*) and the mean vibron number (*dashed*) in the Ca^+ ion-trap laser with sideband cooling. The parameters are $A = 0.5$, $g_0 = 14.8$, $\Omega_0 = 100$, $\Gamma = \Gamma_1 = 40$, $\Gamma_2 = 100$, and $\eta = 0.1$ on the laser transition. Initially, the atom is in the ground state and the vibronic distribution is thermal with $\langle b^\dagger b \rangle = 0.1$. All rates are in MHz

heated by the pump and relaxation processes, sideband cooling has been incorporated into the model. The recently proposed Ca^+ ion-trap laser is used to illustrate the possibility of one-atom lasing in the presence of a cooling mechanism.

There is one very interesting application of the “mazer” which should be briefly mentioned here: the device can act as a filter for matter waves and can thus be used to increase the coherence length of an atomic beam; in the same way as a Fabry-Perot can be used to increase the coherence length of a light wave. This application is discussed in Ref. [67].

References

1. D. Meschede, H. Walther, and G. Müller: The one-atom maser. Phys. Rev. Lett. **54**, 551–554 (1985)
2. G. Rempe, H. Walther, and N. Klein: Observation of quantum collapse and revival in the one-atom maser. Phys. Rev. Lett. **58**, 353–356 (1987)
3. G. Rempe, F. Schmidt-Kaler, and H. Walther: Observation of sub-Poissonian photon statistics in a micromaser. Phys. Rev. Lett. **64**, 2783–2786 (1990)
4. G. Rempe and H. Walther: Sub-Poissonian atomic statistics in a micromaser. Phys. Rev. A **42**, 1650–1655 (1990)

5. H.J. Kimble, O. Carnal, N. Georgiades, H. Mabuchi, E.S. Polzik, R.J. Thompson, and Q.A. Turchette: Quantum optics with strong coupling. In: *Atomic Physics*, D.J. Wineland, C.E. Wieman, S.J. Smith (Eds.), Vol. 14 (American Institute of Physics, New York 1995) pp. 314–335
6. K. An, J.J. Childs, R.R. Dasari, M.S. Feld: Microlaser: a laser with one atom in an optical resonator. *Phys. Rev. Lett.* **73**, 3375–3378 (1994)
7. C. Wagner, R.J. Brecha, A. Schenzle, and H. Walther: Phase diffusion, entangled states and quantum measurements in the micromaser. *Phys. Rev. A* **47**, 5068–5079 (1993)
8. M. Löffler, B.-G. Englert, and H. Walther: Testing a Bell-type inequality with a micromaser. *Appl. Phys. B* **63**, 511–516 (1996)
9. O. Benson, G. Raithel, and H. Walther: Quantum jumps of the micromaser field – dynamic behavior close to phase transition points. *Phys. Rev. Lett.* **72**, 3506–3509 (1994)
10. G. Raithel, O. Benson, and H. Walther: Atomic interferometry with the micromaser. *Phys. Rev. Lett.* **75**, 3446–3449 (1995)
11. G. Raithel, C. Wagner, H. Walther, L.M. Narducci, and M.O. Scully: The micromaser: a proving ground for quantum physics. In: *Advances in Atomic, Molecular, and Optical Physics*, Supplement 2, P. Berman (Ed.) (Academic Press, New York 1994) pp. 57–121
12. P. Filipowicz, J. Javanainen, and P. Meystre: Theory of a microscopic maser. *Phys. Rev. A* **34**, 3077–3087 (1986)
13. L.A. Lugiato, M.O. Scully, and H. Walther: Connection between microscopic and macroscopic maser theory. *Phys. Rev. A* **36**, 740–743 (1987)
14. P. Meystre: Cavity quantum optics and the quantum measurement process. In: *Progress in Optics*, Vol. 30, E. Wolf (Ed.) (Elsevier Science Publishers, New York 1992) pp. 261–355
15. J.M. Raimond, M. Brune, L. Davidovich, P. Goy, and S. Haroche: The two-photon Rydberg atom micromaser. *Atomic Physics* **11**, 441–445 (1989)
16. N.F. Ramsey: In: *Molecular Beams* (Clarendon Press, Oxford 1956) pp. 124–134
17. C. Cohen-Tannoudji, J. Dupont-Roc, and G. Grynberg: In: *Atom-Photon Interactions* (John Wiley and Sons, Inc., New York 1992) pp. 407–514
18. C. Wagner, A. Schenzle, and H. Walther: Atomic waiting-times and correlation functions. *Optics Communications* **107**, 318–326 (1994)
19. H. Walther: Experiments on cavity quantum electrodynamics. *Phys. Reports* **219**, 263–281 (1992)
20. B.-G. Englert, M. Löffler, O. Benson, B. Varcoe, M. Weidinger, and H. Walther: Entangled atoms in micromaser physics. *Fortschritte der Physik* **46**, 897–926 (1998)
21. H.J. Briegel, B.-G. Englert, N. Sterpi, and H. Walther: One-atom maser: statistics of detector clicks. *Phys. Rev. A* **49**, 2962–2985 (1994)
22. P. Meystre, G. Rempe, and H. Walther: Very-low temperature behavior of a micromaser. *Opt. Lett.* **13**, 1078–1080 (1988)
23. M. Weidinger, B.T.H. Varcoe, R. Heerlein, and H. Walther: Trapping states in the micromaser. *Phys. Rev. Lett.* **82**, 3795–3798 (1999)
24. J. Krause, M.O. Scully, and H. Walther: State reduction and $|n\rangle$ -state preparation of a high-Q micromaser. *Phys. Rev. A* **36**, 4547–4550 (1987)
25. P.J. Bardou, E. Mayr, and W.P. Schleich: Quantum state endoscopy: measurement of the quantum state in a cavity. *Phys. Rev. A* **51**, 4963–4966 (1995)

26. B.T.H. Varcoe, S. Brattke, M. Weidinger, and H. Walther, *Nature* *in print*
27. M. Brune, F. Schmidt-Kaler, A. Maali, J. Dreyer, E. Hagley, J.M. Raimond, and S. Haroche: Quantum Rabi oscillation: a direct test of field quantization in a cavity. *Phys. Rev. Lett.* **76**, 1800–1803 (1996)
28. D. M. Greenberger, M. Horne, and A. Zeilinger: In *Bell's Theorem, Quantum Theory, and Conceptions of the Universe*, M. Kafatos, (Ed.) (Kluwer, Dordrecht 1989)
29. D.M. Greenberger, M. Horne, M. Shimony, and A. Zeilinger: Bell's theorem without inequalities. *Am. J. Phys.* **58**, 1131–1143 (1990)
30. B.-G. Englert, N. Sterpi, and H. Walther: Parity states in the one-atom maser. *Opt. Commun.* **100**, 526–535 (1993)
31. N.D. Mermin: What's wrong with these elements of reality. *Physics Today*, **43**(6), 9–11 (1990)
32. M.O. Scully, G.M. Meyer, and H. Walther: Induced emission due to the quantized motion of ultra-cold atoms passing through a micromaser cavity. *Phys. Rev. Lett.* **76**, 4144–4147 (1996)
33. G.M. Meyer, M.O. Scully, and H. Walther: Quantum theory of the maser: I. General theory. *Phys. Rev. A* **56**, 4142–4152 (1997)
34. M. Löffler, G.M. Meyer, M. Schröder, M.O. Scully, and H. Walther: Quantum theory of the maser: II. Extensions and experimental conditions. *Phys. Rev. A* **56**, 4153–4163 (1997)
35. M. Schröder, K. Vogel, W.P. Schleich, M.O. Scully, and H. Walther: Quantum theory of the maser: III. Spectrum. *Phys. Rev. A* **57**, 4164–4174 (1997)
36. W. Hartig, W. Rasmussen, R. Schieder, and H. Walther: Study of the frequency distribution of the fluorescent light induced by monochromatic excitation. *Z. Physik A* **278**, 205–210 (1976)
37. J.D. Cresser, J. Häger, G. Leuchs, F.M. Rateike, and H. Walther: Resonance fluorescence of atoms in strong monochromatic laser fields. *Topics in Current Physics* **27**, 21–59 (1982)
38. P.S. Jessen, C. Gerz, P.D. Lett, W.D. Philipp, S.L. Rolston, R.J.C. Spreeuw, and C.I. Westbrook: Observation of quantized motion of Rb atoms in an optical field. *Phys. Rev. Lett.* **69**, 49–52 (1992)
39. W. Heitler: In: *The Quantum Theory of Radiation*, Third Edition (University Press, Oxford 1954) pp. 196–204
40. B.R. Mollow: Power spectrum of light scattered by two-level systems. *Phys. Rev.* **188**, 1969–1975 (1969)
41. F. Schuda, C. Stroud, Jr., and M. Hercher: Observation of the resonant Stark effect at optical frequencies. *J. Phys. B* **1**, L198–L202 (1974)
42. H. Walther: Atomic fluorescence induced by monochromatic excitation. *Lecture Notes in Physics* **43**, 358–369 (1975)
43. F.Y. Wu, R.E. Grove, and S. Ezekiel: Investigation of the spectrum of resonance fluorescence induced by a monochromatic field. *Phys. Rev. Lett.* **35**, 1426–1429 (1975); R.E. Grove, F.Y. Wu, and S. Ezekiel: Measurement of the spectrum of resonance fluorescence from a two-level atom in an intense monochromatic field. *Phys. Rev. Lett. A* **15**, 227–233 (1977)
44. H.M. Gibbs and T.N.C. Venkatesan: Direct observation of fluorescence narrower than the natural linewidth. *Opt. Comm.* **17**, 87–94 (1976)
45. H.J. Kimble, M. Dagenais, and L. Mandel: Photon antibunching in resonance fluorescence. *Phys. Rev. Lett.* **39**, 691–695 (1977)

46. E. Jakeman, E.R. Pike, P.N. Pusey, and J.M. Vaughan: The effect of atomic number fluctuations on photon antibunching in resonance fluorescence. *J. Phys. A* **10**, L257–L259 (1977)
47. H.J. Kimble, M. Dagenais, and L. Mandel: Multiatom and transit-time effects in photon correlation measurements in resonance fluorescence. *Phys. Rev. A* **18**, 201–207 (1978); M. Dagenais and L. Mandel: Investigation of two-atom correlations in photon emissions from a single atom. *Phys. Rev. A* **18**, 2217–2218 (1978)
48. F.M. Rateike, G. Leuchs, and H. Walther, results cited in Ref. 27
49. F. Diedrich and H. Walther: Non-classical radiation of a single stored ion. *Phys. Rev. Lett.* **58**, 203–206 (1987)
50. D.F. Walls: Evidence for the quantum nature of light. *Nature* **280**, 451–454 (1979)
51. R. Short and L. Mandel: Observation of sub-Poissonian photon statistics. *Phys. Rev. Lett.* **51**, 384–387 (1983)
52. C.A. Schrama, E. Peik, W.W. Smith, and H. Walther: Novel miniature ion traps. *Opt. Comm.* **101**, 32–36 (1993)
53. J.T. Höffges, H.W. Baldauf, T. Eichler, S.R. Helmfrid, and H. Walther: Heterodyne measurement of the fluorescent radiation of a single trapped ion. *Opt. Communications* **133**, 170–174 (1997)
54. J.T. Höffges, H.W. Baldauf, W. Lange, and H. Walther: Heterodyne measurement of the resonance fluorescence of a single ion. *Journal of Modern Optics* **55**, 1999–2010 (1997)
55. R. Loudon: Non-classical effects in the statistical properties of light. *Rep. Prog. Phys.* **43**, 913–949 (1980)
56. Y. Mu and C.M. Savage: One-atom lasers. *Phys. Rev. A* **46**, 5944–5954 (1992)
57. C. Ginzel, H.J. Briegel, U. Martini, B.-G. Englert, and A. Schenzle: Quantum optical master equations: the one-atom laser. *Phys. Rev. A* **48**, 732–738 (1993)
58. T. Pellizzari and H.J. Ritsch: Photon statistics of the three-level one-atom laser. *Mod. Opt.* **41**, 609–623 (1994); Preparation of stationary Fock states in a one-atom Raman laser. *Phys. Rev. Lett.* **72**, 3973–3976 (1994); P. Horak, K.M. Gheri, and H. Ritsch: Quantum dynamics of a single-atom cascade laser. *Phys. Rev. A* **51**, 3257–3266 (1995)
59. H.-J. Briegel, G.M. Meyer, and B.-G. Englert: Dynamic noise reduction in multilevel lasers: nonlinear theory and the pump-operator approach. *Phys. Rev. A* **53**, 1143–1159 (1996); Pump operator for lasers with multi-level excitation. *Europhys. Lett.* **33**, 515–520 (1996)
60. For a recent review see E. Arimondo: Coherent population trapping in laser spectroscopy. In: *Progress in Optics*, vol. XXXV, E. Wolf (Ed.) (Elsevier, Amsterdam 1996) pp. 257–354
61. A.M. Khazanov, G.A. Koganov, and E.P. Gordov: Macroscopic squeezing in three-level laser. *Phys. Rev. A* **42**, 3065–3069 (1990); T.C. Ralph and C.M. Savage: Squeezed light from a coherently pumped four-level laser. *Phys. Rev. A* **44**, 7809–7814, (1991); H. Ritsch, P. Zoller, C.W. Gardiner, and D.F. Walls: Laser light by dynamic pump-noise suppression. *Phys. Rev. A* **44**, 3361–3364 (1991)
62. K.M. Gheri and D.F. Walls: Squeezed lasing without inversion or light amplification by coherence. *Phys. Rev. A* **45**, 6675–6686 (1992); H. Ritsch and M.A.M. Marte: Quantum noise in Raman lasers: effects of pump bandwidth and super- and sub-Poissonian pumping. *Phys. Rev. A* **47**, 2354–2365 (1993)

63. G.M. Meyer, H.-J. Briegel, and H. Walther: Ion-trap laser. *Europhys. Lett.* **37**, 317–322 (1997)
64. G.M. Meyer, M. Löffler, and H. Walther: Spectrum of the ion-trap laser. *Phys. Rev. A* **56**, R1099–R1102 (1997)
65. M. Löffler, G.M. Meyer, and H. Walther: One atom laser with quantized centre-of-mass motion. *Europhys. Lett.* **40**, 263–268 (1997)
66. M. Löffler, G.M. Meyer, and H. Walther: Spectral properties of the one-atom maser. *Phys. Rev. A* **55**, 3923–3930 (1997)
67. M. Löffler and H. Walther: Velocity selection for ultracold atoms using a micromaser. *Europhys. Lett.* **41**, 593–598 (1998)

Quantum Entanglement: from Popper's Experiment to Quantum Eraser

Yanhua Shih and Yoon-Ho Kim

Department of Physics, University of Maryland, Baltimore County,
Baltimore, MD 21250, U.S.A.

Abstract. Uncertainty, being perhaps the most basic principle of quantum mechanics, distinguishes the world of quantum phenomena from the realm of classical physics. Quantum entanglement, being perhaps the most surprising consequence of quantum mechanics, on the other hand apparently suggests paradoxes relating to or violations of the quantum mechanical uncertainty principle in some experimental situations. Popper's experiment and quantum eraser are two examples. Is this a paradox? Are we confronted by a violation of the uncertainty principle? These questions are addressed in this paper.

1 Introduction

Uncertainty, being perhaps the most basic principle of quantum mechanics, distinguishes the world of quantum phenomena from the realm of classical physics. Quantum mechanically, one can never expect to measure both the precise position and momentum of a quantum at the same time. It is prohibited. We say that the quantum observables "position" and "momentum" are "complementary" because the precise knowledge of the position (momentum) implies that all possible outcomes of measuring the momentum (position) are equally probable. Furthermore, one can never observe both the wave and particle behaviors of a quantum in the same measurement, the wave-like and particle-like properties of a quantum are mutually exclusive.

Quantum entanglement, being perhaps the most surprising consequence of quantum mechanics, on the other hand apparently suggests paradoxes relating to or violations of quantum mechanical uncertainty principle in some experimental situations. One classic example of the paradox is shown in the 1935 *gedankenexperiment* of Einstein-Podolsky-Rosen [1]. Popper's experiment, in which Popper intended to show that a quantum must have position and momentum at the same time, is another early example [2]. A recent example of "quantum eraser" was proposed by Scully and Drühl in 1982 exploring the possibility of observing both the wave and particle behaviors of a quantum in the same measurement [3].

Are there paradoxes? Are we faced with possible violations of uncertainty principle?

We have realized the historical Popper's thought experiment and the delayed choice quantum eraser recently by means of an entangled two-photon

state of Spontaneous Parametric Down Conversion (SPDC). The experimental data show that there appears to be a violation of the uncertainty principle. This is, however as we shall argue in this paper, only an illusion provided that we take the teachings of quantum mechanics seriously. The quantum formalism asserts that the measurement for an entangled two-particle system cannot be considered as that for two individual particles. Once again, it calls our attention to the important message: the physics of the entangled two-particle system is inherently different from that of two individual particles.

2 Popper's Experiment

Karl Popper, being a “metaphysical realist”, took a complete different point of view on the uncertainty principle. In Popper’s opinion, the quantum formalism could and should be interpreted realistically: a particle must have precise position and momentum. In this regard he invented a thought experiment in the early 1930’s which aims to support the realistic interpretation of quantum mechanics and undermine Copenhagen [2]. What Popper intended to do in his experiment was to show that a particle can have both precise position and momentum at the same time which is similar to what EPR *gedankenexperiment* of 1935 [1] seeks to conclude. But different from EPR’s *gedankenexperiment*, Popper’s experiment was somehow ignored by the physics community.

It is indeed astonishing to see that the experimental results agree with Popper’s prediction. Through quantum entanglement one may learn the precise knowledge of a photon’s position and would therefore expect a greater uncertainty in its momentum. However, upon first glance of the results, it may appear that the momentum of this photon does not experience a corresponding increase in uncertainty. Is this a violation of the uncertainty principle?

As a matter of fact, one should not be surprised with the experimental result and should not consider this question as a new challenge. Similar results have been demonstrated in EPR type of experiments and the same question has been asked in EPR’s 1935 paper [1]. In the past decades, we have been worrying about problems concerning causality, locality, and reality more than the “crux” of the EPR paradox itself: the uncertainty principle.

Similar to the EPR’s *gedankenexperiment*, Popper’s experiment is also based on *two-particle entanglement*. Quantum mechanics allows the entangled EPR type state, a state in which if the position or momentum of particle 1 is known the corresponding observable of its twin, particle 2, is then 100% determined [1].

Popper’s original thought experiment is schematically shown in Fig. 1. A point source S, positronium for example, is placed at the center of the experimental arrangement from which entangled pairs of particles 1 and 2 are emitted in opposite directions along the positive and negative x -axis towards two screens A and B respectively. There are slits on both screens,

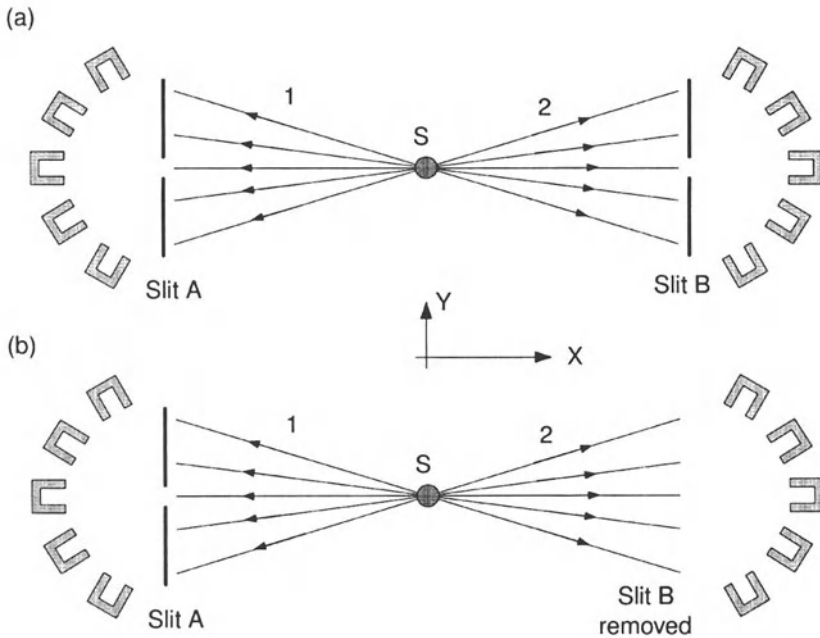


Fig. 1. Popper's thought experiment. An entangled pair of particles are emitted from a point source with momentum conservation. A narrow slit on screen A is placed in the path of particle 1 to provide the precise knowledge of its position on the y axis and this also determines the precise y position of its twin, particle 2 on screen B. (a) Slits A and B are adjusted both very narrowly. (b) Slit A is kept very narrow and slit B is left wide open.

parallel to the y -axis, and the slits may be adjusted by varying their widths Δy . Beyond the slits on each side an array of Geiger counters are arranged for the coincidence measurements of the particle pairs as shown in the figure. The entangled pair could be emitted to any direction in 4π solid angles from the point source. However, if particle 1 is detected in a certain direction, particle 2 is known to be in the opposite direction, due to the momentum conservation of the quantum pair [4].

First let us imagine the case in which slits A and B are adjusted both very narrowly, then counters should come into play which are higher up and lower down, as viewed from the slits. The firing of these counters is indicative of the fact that the wider the scattering angles, i.e., the greater the Δp_y , for each particle due to the narrower the slits, i.e., smaller Δy . There seems to be no disagreement in this situation between the orthodox Copenhagen camp and Popper, and both sides can provide a reasonable explanation based on their own philosophy.

Next imagine that we keep the slit at A very narrow and leave the slit at B wide open. The use of the narrow slit A provides the precise knowledge

of the position y of particle 1 and as a consequence determines the precise position of its twin (particle 2) on side B due to entanglement. Does particle 2 experience a greater uncertainty in Δp_y due to the precise knowledge of its position? If not, there comes a serious problem: the product of Δy and Δp_y of particle 2 could be smaller than h ($\Delta y \Delta p_y < h$). To avoid this problem, it seems that particle 2 going to the left must scatter like its twin which has passed through slit A, even though slit B is wide open. However, based on his “statistical-scatter” theory, Popper provides a different prediction: *particle 2 must not experience a greater Δp_y unless a real physical narrow slit B is applied.*

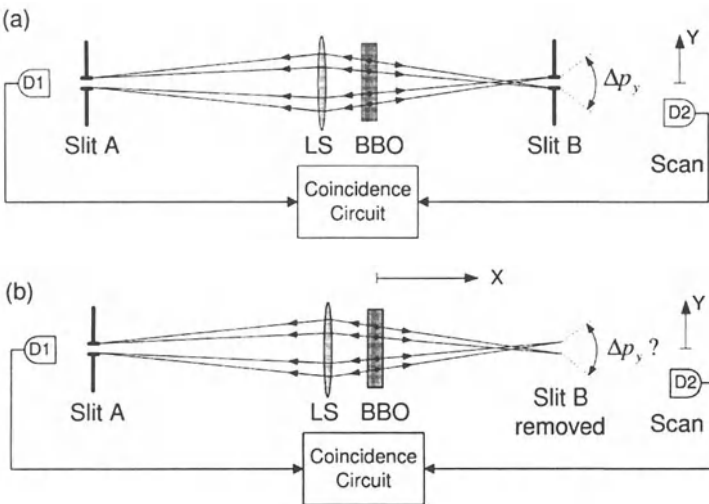


Fig. 2. Modified version of Popper’s experiment. An EPR photon pair is generated by SPDC. A lens and a narrow slit A are placed in the path of photon 1 to provide the precise knowledge of its position on the y axis and also determines the precise y position of its twin, photon 2 on screen B due to the “ghost image” effect. Two detectors D_1 and D_2 are used to scan in the y directions for coincidence counts. (a) Slits A and B are adjusted both very narrowly. (b) Slit A is kept very narrow and slit B is left wide open.

We have realized Popper’s experiment with the use of the entangled two-photon state of spontaneous parametric down conversion (SPDC) [5] [6]. In order to clearly demonstrate all aspects of Popper’s original and the modern experimental concerns in a practical manner, Popper’s original design is slightly modified as in Fig. 2. The two-photon source is a CW Argon ion laser pumped SPDC which provides a two-photon entangled state preserving momentum conservation for the signal-idler photon pair in the SPDC process.

By taking advantage of the entanglement nature of the signal-idler pair (also labeled “photon 1” and “photon 2”) one could make a “ghost image” of slit A at “screen” B, see Fig. 3. The physical principle of the two-photon “ghost image” has been demonstrated in Ref. [7].

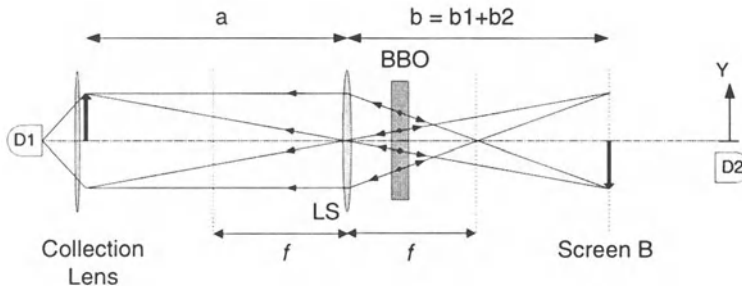


Fig. 3. The unfolded schematic of the experiment. This is equivalent to assume $k_s + k_i = 0$ but without losing the important entanglement feature of the momentum conservation of the signal-idler pair. It is clear that the locations of slit A, lens LS, and the “ghost image” must be governed by the Gaussian thin lens equation, bearing in mind the different propagation directions of the signal-idler by the small arrows on the straight-line two-photon paths.

The experimental condition specified in Popper’s experiment is then achieved: when slit A is adjusted to a certain narrow width and slit B is wide open, slit A provides the precise knowledge about position of photon 1 on the y axis up to an accuracy Δy , which equals the width of slit A, and the corresponding “ghost image” of pinhole A at “screen” B determines the precise position y of photon 2 to within the same accuracy Δy . Δp_y of “photon 2” can be independently studied by measuring the width of its “diffraction pattern” at a certain distance from “screen” B. This is obtained by recording coincidences between detectors D_1 and D_2 while scanning detector D_2 along its y axis, which is behind “screen” B at a certain distance. Instead of a battery of Geiger counters, in our experiment only two photon counting detectors D_1 and D_2 placed behind the respective slits A and B are used for the coincidence detection. Both D_1 and D_2 are driven by step motors and so they can be scanned along their y axis. $\Delta y \Delta p_y$ of “photon 2” is then readily calculated and compared with h [8].

The use of a “point source” in the original proposal has been considered as the fundamental error that Popper committed [9] [10]. The basic criticism is that a point source can never produce a pair of entangled particles which preserves momentum conservation. However, a “point source” is not a necessary requirement for Popper’s experiment. What is needed is the position entanglement of the two-particle system, i.e., if the position of particle 1 is precisely known, the position of particle 2 is also 100% determined. So that one can learn the precise knowledge of a particle’s position through quantum

entanglement. Quantum mechanics does allow the position entanglement for an entangled system (EPR state) and there are certain practical mechanisms, such as that the one shown in our experiment, that can be used for its realization.

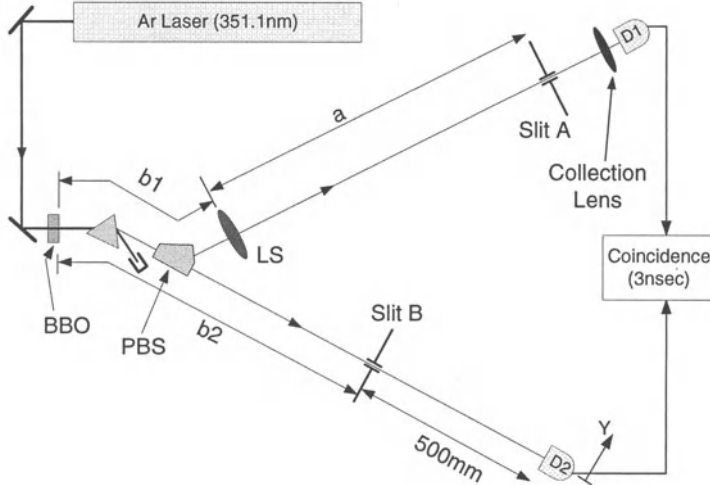


Fig. 4. Schematic of the experimental setup. The laser beam is about 3mm in diameter. The “momentum conservation” is well reinforced. Slit A (0.16mm) is placed 1000mm = 2f behind the converging lens, LS ($f = 500\text{mm}$). The one-to-one “ghost image” (0.16mm) of slit A is located at B. The optical distance from LS, which is in the signal beam, back through PBS to the SPDC crystal ($b_1 = 255\text{mm}$) and then along the idler beam to “screen B” ($b_2 = 745\text{mm}$) is 1000mm = 2f ($b = b_1 + b_2$), see figure 3 in “unfolded” scheme.

The schematic experimental setup is shown in Fig. 4 with detailed indications of distances. A CW Argon ion laser line of $\lambda_p = 351.1\text{nm}$ is used to pump a 3mm long beta barium borate (BBO) crystal for type-II SPDC [11] to generate an orthogonally polarized signal-idler photon pair. The laser beam is about 3mm in diameter with a diffraction limited divergence. It is important not to focus the pump beam so that the phase matching condition, $\mathbf{k}_s + \mathbf{k}_i = \mathbf{k}_p$, is well reinforced in the SPDC process [6], where \mathbf{k}_j ($j = s, i, p$) is the wavevectors of the signal (s), idler (i), and pump (p) respectively. The collinear signal-idler beams, with $\lambda_s = \lambda_i = 702.2\text{nm} = 2\lambda_p$ are separated from the pump beam by a fused quartz dispersion prism, and then split by a polarization beam splitter PBS. The signal beam (“photon 1”) passes a converging lens LS with a 500mm focal length and a 25mm diameter. A 0.16mm slit is placed at location A which is 1000mm (= 2f) behind the lens LS. The use of LS is to achieve a “ghost image” of slit A (0.16mm) at “screen” B, which is at the same optical distance 1000mm (= 2f) from LS,

however in the idler beam (in the path of “photon 2”). The signal and idler beams are then allowed to pass through the respective slits A and B (a real slit B or a “ghost image” of slit A) and to trigger the two photon counting detectors D_1 and D_2 . A short focal length lens is used with D_1 for collecting the signal beam which passes through slit A. A point like detector D_2 is located 500mm behind “screen” B. The detectors are Geiger mode avalanche photodiodes which are $180\mu m$ in diameter. $10nm$ band-pass spectral filters centered at $702nm$ are used with each of the detectors. The output pulses from the detectors are sent to a coincidence circuit. During the measurement, detector D_1 is fixed behind slit A, while detector D_2 is allowed to scan along the y axis, by a step motor.

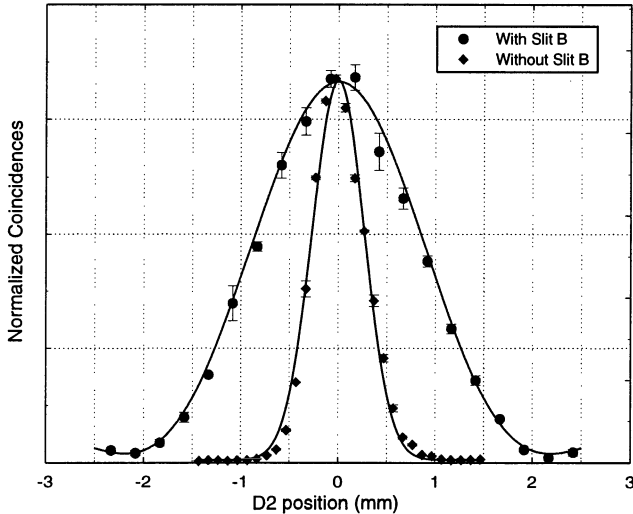


Fig. 5. The observed coincidence patterns. The y coordinate of D_1 was chosen to be 0 (center) while D_2 was allowed to scan along its y axis. Circled dot points: *Slit A = Slit B = 0.16mm*. Diamond dot points: *Slit A = 0.16mm, Slit B wide open*. The width of the *sinc* function curve fitted by the circled dot points is a measure of the minimum Δp_y determined by a $0.16mm$ slit.

Measurement 1: we first studied the case in which both slit A and B were adjusted to be $0.16mm$. The y coordinate of D_1 was chosen to be 0 (center) while D_2 was allowed to scan along its y axis. The circled dot data points in Fig. 5 show the coincidence counting rates against the y coordinate of D_2 . It is a typical single-slit diffraction pattern with $\Delta y \Delta p_y = h$. Nothing is special in this measurement except that we have learned the minimum uncertainty in the width of Δp_y [8]. We should remark at this point that the *single* detector

counting rates of D_2 is basically the same as that of the coincidence counts except for a higher counting rate.

Measurement 2: we kept the same experimental conditions except that slit B was left wide open. This measurement is a test of Popper's prediction. The y coordinate of D_1 was chosen to be 0 (center) while D_2 was allowed to scan along its y axis. Due to the entanglement nature of the signal-idler photon pair and the coincidence measurement, only those twins which have passed through slit A and the "ghost image" of slit A at "screen" B with an uncertainty of $\Delta y = 0.16mm$, which is the same width as the real slit B we have used in measurement 1, would contribute to the coincidence counts through the triggering of D_1 and D_2 . The diamond dot data points in Fig. 5 report the measured coincidence counting rates against the y coordinates of D_2 . The measured width of the pattern is narrower than that of the diffraction pattern shown in measurement 1. In addition, the width of the pattern is also much narrower than the actual size of the diverging SPDC beam at D_2 . It is interesting to notice that the single counting rate of D_2 keeps constant in the entire scanning range, which is very different from that in measurement 1. The experimental data has provided a clear indication of $\Delta y \Delta p_y < h$ in the coincidence measurements.

Given that $\Delta y \Delta p_y < h$, is this a violation of uncertainty principle? Before drawing any conclusions, let us first examine what quantum mechanics predicts. If quantum mechanics does provide a solution with $\Delta y \Delta p_y < h$ for "photon 2". Indeed, we would be forced to face a paradox as EPR had pointed out in 1935.

We begin with the question: how does one learn the precise position knowledge of photon 2 at "screen" B quantum mechanically? Is it $0.16mm$ as determined by the width of slit A? It will be easier then to understand the important physics behind Popper's experiment. The answer is in the positive. Quantum mechanics predicts a "ghost" image of slit A at "screen" B which is $0.16mm$ for the above experimental setup. The crucial point is we are dealing with an entangled two-photon state of SPDC [5][12],

$$|\Psi\rangle = \sum_{s,i} \delta(\omega_s + \omega_i - \omega_p) \delta(\mathbf{k}_s + \mathbf{k}_i - \mathbf{k}_p) a_s^\dagger(\omega(\mathbf{k}_s)) a_i^\dagger(\omega(\mathbf{k}_i)) |0\rangle \quad (1)$$

where ω_j , \mathbf{k}_j ($j = s, i, p$) are the frequencies and wavevectors of the signal (s), idler (i), and pump (p) respectively, ω_p and \mathbf{k}_p can be considered as constants while a_s^\dagger and a_i^\dagger are the respective creation operators for the signal and the idler. As seen in the above state, the entanglement in state (1) can be thought of as the superposition of an infinite number of "two-photon" states, corresponding to the infinite numbers of ways the SPDC signal-idler can satisfy the energy and momentum conservation, see the δ functions of the state which is also called phase matching conditions:

$$\omega_s + \omega_i = \omega_p, \quad \mathbf{k}_s + \mathbf{k}_i = \mathbf{k}_p \quad (2)$$

It is interesting to see that even though there is no precise knowledge of the momentum for either the signal or the idler, the state does give precise knowledge of the *momentum correlation* of the pair. In EPR's language: the momentum for neither the signal photon nor the idler photon is determined; however, if measurement on one of the photons yields a certain value, then the momentum of the other photon is 100% determined.

To simplify the physical picture, we "unfold" the signal-idler paths in the schematic of Fig. 4 into that shown in Fig. 3, which is equivalent to assume $\mathbf{k}_s + \mathbf{k}_i = 0$ but without losing the important entanglement feature of the momentum conservation of the signal-idler pair. This important peculiarity selects the only possible optical paths of the signal-idler pairs that result in a "click-click" coincidence detection, which are represented by *straight lines* in this unfold version of the experimental schematic and therefore the "image" of slit A is well produced in coincidences as shown in the figure. It is similar to an optical imaging in the "usual" geometric optics picture, but bear in mind the different propagation directions of the signal-idler indicated by the small arrows on the *straight lines*. It is easy to see that a "clear" image requires the locations of slit A, lens LS, and screen B to be governed by the Gaussian thin lens equation [7],

$$\frac{1}{a} + \frac{1}{b} = \frac{1}{f}. \quad (3)$$

In our experiment, we have chosen $a = b = 2f = 1000\text{mm}$, so that the "ghost image" of slit A at "screen" B must have the same width as that of slit A. The measured size of the "ghost image" agree with the theory.

In Fig. 3 we see clearly these two-photon paths (*straight lines*) that result in a "click-click" joint detection are restricted by slit A, lens LS as well as the momentum conservation, so that any signal-idler pair that passes through the 0.16mm slit A would be "localized" within $\Delta y = 0.16\text{mm}$ at "screen" B. One does learn the precise position knowledge of photon 2 through the entanglement of the two-photon system.

One could also explain this "ghost image" in terms of conditional measurement: conditioned on the detection of "photon 1" by detector D_1 behind slit A, its corresponding twin, "photon 2" can only be found in a certain position. In other words, "photon 2" is localized only upon the detection of photon 1. However, this "conditionally localized" photon" does not follow ordinary uncertainty relation as shown in Fig. 5.

Now let us go further to examine Δp_y of photon 2 which is conditionally "localized" within $\Delta y = 0.16\text{mm}$ at "screen" B. In order to study Δp_y , the photon counting detector D_2 is scanned 500mm behind "screen" B to measure the "diffraction pattern". Δp_y can be easily estimated from the measurement of the width of the diffraction pattern [8]. The two-photon paths, indicated by the *straight lines* reach detector 2 which is located 500mm behind "screen" B so that detector D_2 will receive "photon 2" in a much narrower width under

the condition of the “click” of detector D_1 as shown in measurement 2, unless a real physical slit B is applied to “disturb” the *straight lines*.

Apparently we have a paradox: quantum mechanics provides us with a solution which gives $\Delta y \Delta p_y < h$ in measurement 2 and the experimental measurements agree with the prediction of quantum mechanics.

3 Delayed Choice Quantum Eraser

In 1927, Niels Bohr illustrated complementarity with the “wave-like” and “particle-like” attributes of a quantum mechanical object [16]. Since then, complementarity is often superficially identified with the “wave-particle duality of matter”. Over the years the two-slit interference experiment has been emphasized as a good example of the enforcement of complementarity. Feynman, in discussing the two-slit experiment, remarked that this wave-particle dual behavior contains the basic mystery of quantum mechanics [8]. The actual mechanisms that enforce complementarity vary from one experimental situation to another. In the two-slit experiment, the common “wisdom” is that the position-momentum uncertainty relation $\delta x \delta p \geq h$ makes it impossible to determine which slit the photon (or electron) passes through without at the same time disturbing the photon (or electron) enough to destroy the interference pattern. However, it has been shown [3] that under certain circumstances this common “uncertainty relation” interpretation may not be applicable. In particular, Scully and Drühl had shown how internal atomic states could be used as “which-path” markers. To be sure the interference pattern disappears when which-path information is obtained. But it can reappear when we erase (quantum erasure) the which-path information [3]. It is especially interesting to see that “quantum eraser” can be combined with “delayed choice” [17]. One could even erase or mark the which-path information after the registration of the quantum and still determine its earlier behavior to be either wave or particle. Since 1982, quantum eraser has been reported in several experiments [18]; however, the original scheme has not been fully demonstrated.

One proposed quantum eraser experiment very close to the 1982 proposal (and our present experiment) is illustrated in Fig.6. Two atoms labeled by A or B is excited by a weak laser pulse: Only one atom, either A or B, is excited by the weak laser pulse. A pair of entangled quanta, “photon” 1 and “photon” 2, is then emitted from either atom A or atom B by atomic cascade decay. Photon 1, propagating to the right, is registered by detector D_0 , which can be scanned by a step motor along its x -axis for the observation of interference fringes. Photon 2, propagating to the left, is injected into a beam splitter. If the pair is generated in atom A, photon 2 will follow the A path meeting BSA with 50% chance of being reflected or transmitted. If the pair is generated in atom B, photon 2 will follow the B path meeting BSB with 50% chance of being reflected or transmitted. In view of the 50% chance of being

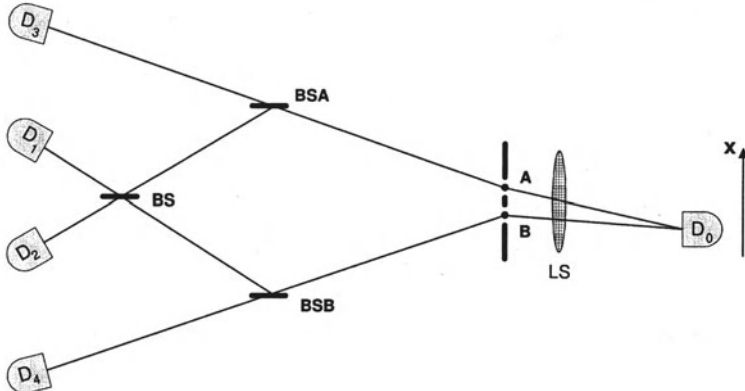


Fig. 6. A proposed quantum eraser experiment. A pair of entangled photon is emitted from either atom A or atom B by atomic cascade decay. “Clicks” at D_3 or D_4 provide the which-path information and “clicks” at D_1 or D_2 erase the which-path information.

transmitted by either BSA or BSB , photon 2 is detected by either detector D_3 or D_4 . The registration of D_3 or D_4 provides which-path information (path A or path B) on photon 2 and in turn provides which-path information for photon 1 because of the entanglement nature of the two-photon state generated by atomic cascade decay. Given a reflection at either BSA or BSB photon 2 will continue to follow its A or B path to meet another 50-50 beam splitter BS and then be detected by either detectors D_1 or D_2 of Fig. 6. The triggering of detectors D_1 or D_2 erases the which-path information. So that either the absence of the interference or its restoration can be arranged via an appropriately contrived photon correlation arrangement.

The experiment is designed in such a way that L_0 , the optical distance between atoms A, B and detector D_0 , is much shorter than L_A (L_B) which is the optical distance between atoms A, B and the beam splitter BSA (BSB). Thus after D_0 is triggered by photon 1, photon 2 is still on its way to the first beam splitter and does not “know” “where” to go yet. After the registration of photon 1, we look at these “delayed” detection events of D_1 , D_2 , D_3 , and D_4 which have constant time delays, $\tau_i \simeq (L_i - L_0)/c$, relative to the triggering time of D_0 . Where L_i is the optical distance between atoms A, B and detectors D_1 , D_2 , D_3 , and D_4 , respectively. It is easy to see these “joint detection” events must have resulted from the same photon pair. It was predicted that the “joint detection” counting rate R_{01} (joint detection rate between D_0 and D_1) and R_{02} will show interference pattern as a function of D_0 ’s position on its x -axis. This reflects the wave nature (both-path) of photon 1. However, no interference will be observed in the joint detection counting events R_{03} and R_{04} during the same scanning of detector D_0 along its x -axis. This is clearly expected because we have now inferred the particle

(which-path) property of photon 1. It is important to emphasize that all four joint detection rates R_{01} , R_{02} , R_{03} , and R_{04} are recorded at the same time during one scanning of D_0 . That is, in the present experiment we “see” both wave (interference) and which-path (particle-like) in the same measurement process.

Different from the early “delayed choice” experiments [19], the “choice” in this experiment is not actively switched by the experimentalist during the measurement. The “delayed choice” to observe either the wave or particle behavior of photon 1 is “randomly” made by photon 2. One simply choose to look at detectors $D_1 \sim D_4$ triggered by photon 2 for the observation of either wave or particle property of photon 1 after the registration of photon 1.

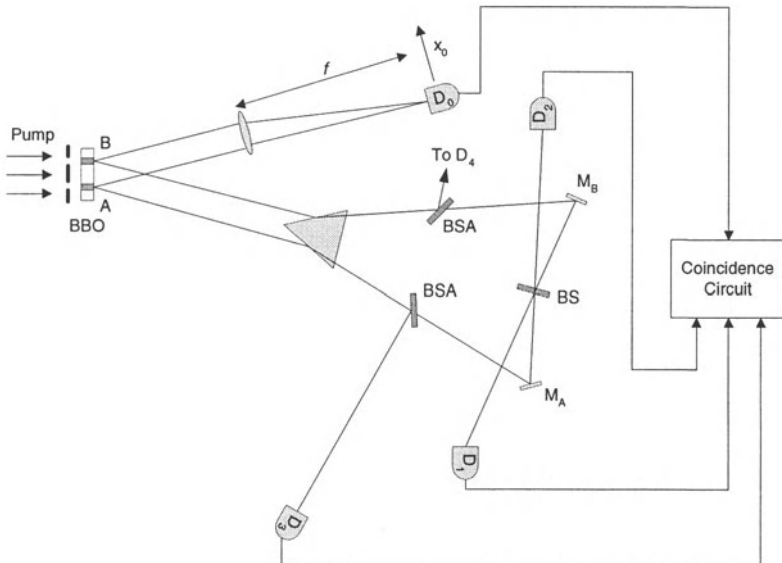


Fig. 7. Schematic of the experimental setup. The pump laser beam of SPDC is divided by a double-slit and incident onto a BBO crystal at two regions A and B. A pair of signal-idler photon is generated either from A or B region. The detection time of the signal photon is 7.8ns earlier before the idler photon decides “which way” to go at BSA or BSB.

Our recent experimental realization of the above quantum eraser is slightly different. The schematic diagram of the experimental setup is shown in Fig. 7. Instead of atomic cascade decay, spontaneous parametric down conversion (SPDC) is used to prepare the entangled two-photon state. SPDC is a spontaneous nonlinear optical process from which a signal-idler photon pair is generated when a pump laser beam is incident on a nonlinear optical crystal.

In our experiment, the 351.1nm Argon ion pump laser beam is divided by a double-slit and directed onto a type-II phase matching nonlinear optical crystal BBO ($\beta - \text{BaB}_2\text{O}_4$) at regions A and B. A pair of 702.2nm orthogonally polarized signal-idler photon is generated either from A or B region. The width of the SPDC slit is about 0.3mm and the distance between the center of A and B is about 0.7mm . A Glen-Thompson prism is used to split the orthogonally polarized signal and idler. The signal photon (photon 1, coming either from A or B) propagates through lens LS to detector D_0 , which is placed on the Fourier transform plane (focal plane for collimated light) of the lens. The use of lens LS is to achieve the “far field” condition, but still keep a short distance between the slit and the detector D_0 . Detector D_0 can be scanned along its x -axis by a step motor. The idler photon (photon 2) is sent to an interferometer with equal-path optical arms. The interferometer includes a prism PS , two 50-50 beam splitters BSA , BSB , two reflecting mirrors M_A , M_B , and a 50-50 beam splitter BS . Detectors D_1 and D_2 are placed at the two output ports of the BS , respectively, for erasing the which-path information. The triggering of detectors D_3 and D_4 provides which-path information for the idler (photon 2) and in turn which-path information for the signal (photon 1). The detectors are fast avalanche photodiode with less than 1ns rise time and about 100ps jitter. A constant fractional discriminator is used with each of the detector to register a single photon whenever the leading edge of the detector output pulse is above the threshold. Coincidences between D_0 and D_i ($i = 1 \sim 4$) are recorded, yielding the joint detection counting rates R_{01} , R_{02} , R_{03} , and R_{04} .

In the experiment the optical delay ($L_{A,B} - L_0$) is chosen to be $\simeq 2.3\text{m}$, where L_0 is the optical distance between the output surface of BBO and detector D_0 , and L_A (L_B) is the optical distance between the output surface of the BBO and the beam splitter BSA (BSB). This means that any “path” information one can infer from photon 2 must be at least 7.7ns later than the registration of photon 1. Compared to the 1ns response time of the detectors, 2.3m delay is thus enough for “delayed erasure”. Although there is an arbitrariness about when a photon is detected, it is safe to say, the “choice” of photon 2 is delayed respect to the detection of photon 1 at D_0 since the entangled photon pair is created simultaneously.

Fig. 8, 9, and 10 report the experimental results, which are all consistent with prediction. Fig. 8 and 9 show the joint detection rates R_{01} and R_{02} against the x coordinates of detector D_0 . It is obvious we have observed the standard Young’s double-slit interference pattern. However, there is a π phase shift between the two interference fringes. The π phase shift is explained in the following. Fig. 10 reports a typical R_{03} measurement, joint detection counting rate between D_0 and “which-path” “marker” D_3 , against the x coordinates of detector D_0 . An absence of interference is clearly demonstrated. Similar results are obtained for D_4 . There is no significant difference between R_{03} and R_{04} from the theoretical prediction.

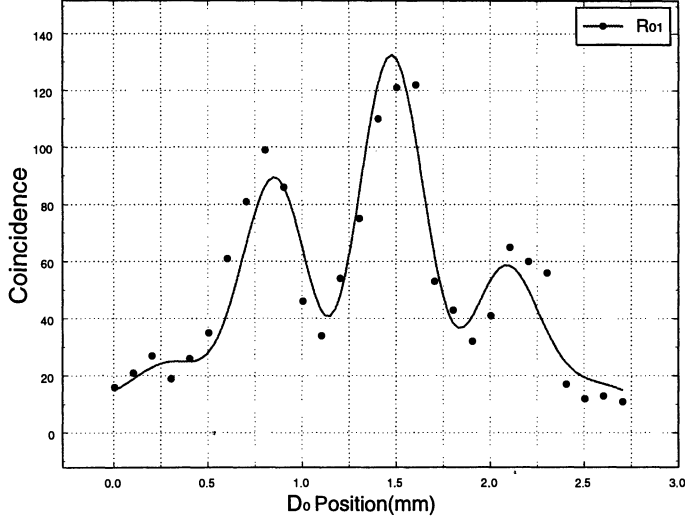


Fig. 8. R_{01} (joint detection rate between detectors D_0 and D_1) against the x co-ordinates of detector D_0 . A standard Young's double-slit interference pattern is observed.

To explain the experimental results, a standard quantum mechanical calculation is presented as follows. The joint detection counting rate, R_{0i} , of detector D_0 and detector D_j , on the time interval T , as given by Glauber [20], reads:

$$\begin{aligned} R_{0j} &\propto \frac{1}{T} \int_0^T \int_0^T dT_0 dT_j \langle \Psi | E_0^{(-)} E_j^{(-)} E_j^{(+)} E_0^{(+)} | \Psi \rangle \\ &= \frac{1}{T} \int_0^T \int_0^T dT_0 dT_j | \langle 0 | E_j^{(+)} E_0^{(+)} | \Psi \rangle |^2, \end{aligned} \quad (4)$$

where T_0 is the detection time of D_0 , T_j is the detection time of D_j ($j = 1, 2, 3, 4$) and $E_{0,j}^{(\pm)}$ are positive and negative-frequency components of the field operators at detectors D_0 and D_j , respectively. $|\Psi\rangle$ is the SPDC entangled state,

$$|\Psi\rangle = \sum_{s,i} C(\mathbf{k}_s, \mathbf{k}_i) a_s^\dagger(\omega(\mathbf{k}_s)) a_i^\dagger(\omega(\mathbf{k}_i)) |0\rangle, \quad (5)$$

where $C(\mathbf{k}_s, \mathbf{k}_i) = \delta(\omega_s + \omega_i - \omega_p) \delta(\mathbf{k}_s + \mathbf{k}_i - \mathbf{k}_p)$, for SPDC in which ω_j and \mathbf{k}_j ($j = s, i, p$) are the frequency and wavevectors of the signal (s), idler (i), and pump (p), respectively, ω_p and \mathbf{k}_p can be considered as constants since the pump is a single mode laser. In eq. (5), a_s^\dagger and a_i^\dagger are creation operators for signal and idler photons, respectively. For the case of two scattering atoms,

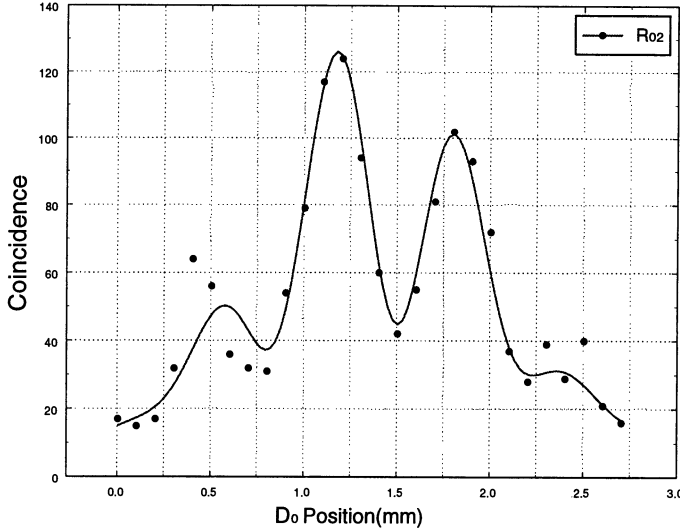


Fig. 9. R_{02} (joint detection rate between detectors D_0 and D_2) Note, there is a π phase shift as compared to R_{01} shown in Fig. 9

see ref. [3], and in the case of cascade radiation, see ref. [21], $C(\mathbf{k}_s, \mathbf{k}_i)$ has a similar structure but without the momentum delta function. We introduce the two-dimensional function $\Psi(t_0, t_j)$ as in eq. (4),

$$\Psi(t_0, t_j) \equiv \langle 0 | E_j^{(+)} E_0^{(+)} | \Psi \rangle. \quad (6)$$

$\Psi(t_0, t_j)$ is the joint count probability amplitude (“effective two-photon wavefunction” or “biphoton wavepacket” for short), where $t_0 \equiv T_0 - L_0/c$, $t_j \equiv T_j - L_j/c$, $j = 1, 2, 3, 4$, L_0 (L_j) is the optical distance between the output point on the BBO crystal and D_0 (D_j). It is straightforward to see that the four wavefunctions $\Psi(t_0, t_j)$, correspond to four different joint detection measurements, having the following different forms:

$$\Psi(t_0, t_1) = A(t_0, t_1^A) + A(t_0, t_1^B), \quad \Psi(t_0, t_2) = A(t_0, t_2^A) - A(t_0, t_2^B), \quad (7)$$

$$\Psi(t_0, t_3) = A(t_0, t_3^A), \quad \Psi(t_0, t_4) = A(t_0, t_4^B), \quad (8)$$

where as in Fig. 6 the upper index of t (A or B) labels the scattering crystal (region A or B) and the lower index on t indicates the different detectors. The different sign between the two amplitudes $\Psi(t_0, t_1)$ and $\Psi(t_0, t_2)$ is caused by the transmission-reflection unitary transformation of the beamsplitter BS , see Fig. 6 and Fig. 7. To simplify the calculations [12], we consider the longitudinal integral only and write the two-photon state in terms of the integral of k_e and k_o :

$$|\Psi\rangle = A'_0 \int dk_e \int dk_o \delta(\omega_e + \omega_o - \omega_p) \Phi(\Delta_k L) a_{k_e}^\dagger a_{k_o}^\dagger |0\rangle, \quad (9)$$

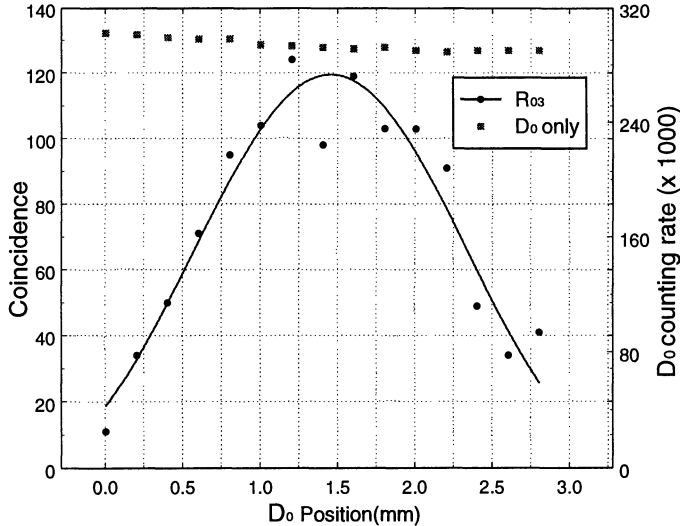


Fig. 10. R_{03} (joint detection rate between detectors D_0 and D_3) and R_0 (single detector counting rate of D_0). An absence of interference in R_{03} is clearly demonstrated. A constant R_0 indicates a much wider size of the “signal” field at D_0

where a type-II phase matching crystal with finite length of L is assumed. $\Phi(\Delta_k L)$ is a sinc-like function, $\Phi(\Delta_k L) = (e^{i(\Delta_k L)} - 1)/i(\Delta_k L)$. Using eqs. (6) and (9) we find,

$$A(t_i, t_j) = A_0 \int dk_e \int dk_o \delta(\omega_e + \omega_o - \omega_p) \Phi(\Delta_k L) f_i(\omega_e) f_j(\omega_o) e^{-i(\omega_e t_i^e + \omega_o t_j^o)}, \quad (10)$$

where $f_{i,j}(\omega)$ is the spectral transmission function of an assumed filter placed in front of the k_{th} detector and is assumed Gaussian to simplify the calculation. To complete the integral, we define $\omega_e = \Omega_e + \nu$ and $\omega_o = \Omega_o - \nu$, where Ω_e and Ω_o are the center frequencies of the SPDC, $\Omega_e + \Omega_o = \Omega_p$ and ν is a small tuning frequency, so that $\omega_e + \omega_o = \Omega_p$ still holds. Consequently, we can expand k_e and k_o around $K_e(\Omega_e)$ and $K_o(\Omega_o)$ to first order in ν :

$$\begin{aligned} k_e &= K_e + \nu \frac{d\omega_e}{dk_e} \Big|_{\Omega_e} = K_e + \frac{\nu}{u_e}, \\ k_o &= K_o - \nu \frac{d\omega_o}{dk_o} \Big|_{\Omega_o} = K_o - \frac{\nu}{u_o}, \end{aligned} \quad (11)$$

where u_e and u_o are recognized as the group velocities of the e-ray and o-ray at frequencies Ω_e and Ω_o , respectively. Completing the integral, the biphoton wavepacket of type-II SPDC is thus [12]:

$$A(t_i, t_j) = A_0 \Pi(t_i - t_j) e^{-i\Omega_i t_i} e^{-i\Omega_j t_j}, \quad (12)$$

where we have dropped the e, o indices. The shape of $\Pi(t_1 - t_2)$ is determined by the bandwidth of the spectral filters and the parameter DL of the SPDC crystal, where $D \equiv 1/u_o - 1/u_e$. If the filters are removed or have large enough bandwidth, we obtain a rectangular pulse function $\Pi(t_1 - t_2)$.

$$\Pi(t_0 - t_j) = \begin{cases} 1 & \text{if } 0 \leq t_0 - t_j \leq DL, \\ 0 & \text{otherwise.} \end{cases} \quad (13)$$

It is easy to show that the two amplitudes in $\Psi(t_0, t_1)$ and $\Psi(t_0, t_2)$ are indistinguishable (overlap in both $t_0 - t_j$ and $t_0 + t_j$), respectively, so that interference is expected in both the coincidence counting rates, R_{01} and R_{02} ; however, with a π phase shift, hence we find,

$$R_{01} \propto \cos^2(x\pi d/\lambda f), \quad \text{and} \quad R_{02} \propto \sin^2(x\pi d/\lambda f). \quad (14)$$

If we consider slits A and B both have a finite width, an integral is performed to sum all the possible amplitudes passing through slit A or slit B. We thus have the standard interference-diffraction pattern for R_{01} and R_{02} ,

$$\begin{aligned} R_{01} &\propto \text{sinc}^2(x\pi a/\lambda f) \cos^2(x\pi d/\lambda f), \\ R_{02} &\propto \text{sinc}^2(x\pi a/\lambda f) \sin^2(x\pi d/\lambda f), \end{aligned} \quad (15)$$

where a is the width of slit A and B (equal width), d is the distance between the centers of slit A and B, $\lambda = \lambda_s = \lambda_i$ is the wavelength of the signal and idler, and f is the focal length of lens LS . We have also applied the “far field approximation”. Finally, after we have taken into account the finite size of the detectors and the divergence of the pump beam, the interference visibility is found to be in satisfactory agreement with observation.

For the joint detection rates R_{03} and R_{04} , it is seen that the “wavefunction” in eq. (8) (which clearly provides the “which-path” information) has only one amplitude and no interference is expected.

The experimental results demonstrated the possibility of simultaneous observation of both the particle-like and wave-like behaviors of a light quantum via quantum mechanical entanglement. The which-path or both-paths information of a quantum can be erased or marked by its entangled twin even after the registration of the quantum. Wave? Or particle? One can make a delayed determination of what the quantum had been even after the registration of the quantum!

4 Conclusion

First, we should not be surprised by the experimental results. Similar experimental results have been demonstrated in EPR type experiments. In fact, the uncertainty principle was the major issue of the 1935 EPR paradox [1]. We therefore consider the following discussions may apply to both Popper and EPR problems.

Popper and EPR were correct in the prediction of the physical outcomes of their experiments. However, Popper and EPR made the same error by applying the results of two-particle physics to the explanation of the behavior of an individual particle. The two-particle entangled state is not the state of two individual particles. Our experimental results are emphatically NOT a violation of the uncertainty principle which governs the behavior of an individual quantum.

(1) It is clear that the measurements associated with Popper's experiment and quantum eraser (EPR experiments as well) are "joint detection" between two detectors applied to entangled states. Quantum mechanically, an entangled two-particle state only provides the correlation of the pair. Neither of the subsystems is determined by the state. A "click-click" joint measurement of the two-particle entangled state projects out the two-particle amplitudes and only these two-particle amplitudes feature in the quantum formalism. It can be clearly seen from our above analysis of Popper's experiment that this kind of measurements is only useful to decide on how good the correlation is between the entangled pair. In the above analysis we never consider "photon 1" or "photon 2" *individually* although the "clicks" of the detectors occur at considerably large distances. Popper's question about the momentum uncertainty of photon 2 is then inappropriate. The correct question to ask in these measurements should be: what is the Δp_y for the signal-idler pair which are "localized" within $\Delta y = 0.16\text{mm}$ at "screen" B and at "screen" A and governed by the momentum conservation? This is indeed the central point for this experiment. There is no reason to expect the "conditionally localized photon 2" will follow the familiar interpretation of the uncertainty relation as shown in Fig. 5.

(2) In Popper's experiment, the measured pattern is the result of the straight-line two-photon paths which have contributed to a "click-click" event. Of course, the measured "pattern" will be limited in width as we have observed in our measurement 2. However, $\Delta y \Delta p_y < h$ does not mean anything except the two-particle entanglement.

(3) One may also consider the measurements in these two experiments as "conditional" measurements. There the behavior of "photon 2" ("photon 1") observed in our experiment is "conditional" upon the condition of the detection of "photon 1" ("photon 2"). If one believes that the conditional behavior of a particle has no difference from the behavior of a particle, one would conclude the results of these two experiments really imply a violation of uncertainty principle. However, the "conditional" behavior of a particle is surely different from the behavior of a particle. A quantum must obey the uncertainty principle, but the "conditional behavior" of a quantum in an entangled two-particle system is different. The uncertainty principle is not for "conditional" behavior. We believe paradoxes are unavoidable if one insists the *conditional behavior of a particle* is the *behavior of a particle*. This is the central problem of both Popper and EPR.

(4) Two-photon is not two photons. As a matter of fact, the two-photon entangled state, see Eq. (1) for example, does not provide any knowledge for either photon 1 or photon 2 individually. Quantum mechanically, as the result of the superposition of the two-photon amplitudes, the pair is described by a non-factorizable two-dimensional *biphoton* wavepacket [14][15][12] instead of two individual wavepackets associated with photon 1 and photon 2. The biphoton concept is clearly shown in the analysis of the quantum eraser experiment.

Once again, the recent demonstrations of Popper's thought experiment and Scully's quantum eraser call our attention to the important message: the physics of the entangled two-particle system must inherently be very different from that of individual particles. In the spirit of the above discussions, we conclude that it has been a long-standing historical mistake to mix up the uncertainty relations governing an individual single particle with an entangled two-particle system.

Acknowledgement. The authors acknowledge important suggestions and encouragement from T. Angelidis, A. Garuccio, C.K.W. Ma, and J.P. Vigier for the realization of Popper's thought experiment. We specially thank C.K.W. Ma from LSE for many helpful discussions. The delayed choice quantum eraser was performed in collaboration with M.O. Scully and S.P. Kulik. This research was partially supported by the U.S. Office of Naval Research and the U.S. Army Research Office - National Security Agency grants.

References

1. A. Einstein, B. Podolsky, and N. Rosen, Phys. Rev., **47**, 777 (1935).
2. K.R. Popper, *Zur Kritik der Ungenauigkeitsrelationen*, Die Naturwissenschaften, 22, Helft, 48, 807 (1934); K. R. Popper, *From the Postscript to the Logic of Scientific Discovery*, edited by E.I. Bitsakis and N. Tambakis, Gutenberg Publishing, (1984); K. Popper, *Quantum Theory And The Schism In Physics*, edited by W.W. Bartly, Hutchinson, London, 28 (1983). Amongst the most notable opponents to the "Copenhagen School" were Einstein-Podolsky-Rosen, de Broglie, Landé, and Karl Popper. One may not agree with Popper's philosophy (EPR classical reality as well) but once again, Popper's thought experiment gives yet another way of understanding the foundations of quantum theory.
3. M.O. Scully and K. Drühl, Phys. Rev. A **25**, 2208 (1982).
4. The use of a "point source" in the original Popper's proposal has been criticized. The basic argument is that a point source can never produce a pair of entangled particles which preserves two-particle momentum conservation. However, a "point source" is not a necessary requirement for Popper's experiment. What we need is to learn the precise knowledge of a particle's position through quantum entanglement. This is achieved in our experiment by the "ghost image".
5. D.N. Klyshko, *Photon and Nonlinear Optics*, Gordon and Breach Science, New York, (1988).
6. A. Yariv, *Quantum Electronics*, John Wiley and Sons, New York, (1989).

7. T.B. Pittman, Y.H. Shih, D.V. Strekalov, and A.V. Sergienko, Phys. Rev. A, **52**, R3429 (1995).
8. R.P. Feynman, R. Leighton, and M. Sands, *The Feynman Lectures on Physics*, Vol. III, (Addison-Wesley, Reading, Massachusetts, 1965).
9. For criticisms of Popper's experiment, see for example, D. Bedford and F. Selleri, Lettere al Nuovo Cimento, **42**, 325 (1985); M.J. Collett and R. Loudon, Nature, **326**, 671 (1987); A. Sudbery, Philosophy of Science, **52**, 470 (1985). Basically the criticisms concern the validity of a point source for entangled two-particles. However, a "point source" is not a necessary requirement for Popper's experiment. What is essential is to learn the precise knowledge of a particle's position through quantum entanglement. This is achieved in our experiment by the "ghost image".
10. The effects of source size for entanglement, see for example, M. Horne, *Experimental Metaphysics*, ed. R.S. Cohen, M. Horne, and J. Stachel, Kluwer Academic, 109 (1997).
11. In type-I SPDC, signal and idler are both ordinary rays of the crystal; however, in type-II SPDC the signal and idler are orthogonal polarized, i.e., one is the ordinary ray and the other is the extraordinary ray of the crystal.
12. M.H. Rubin, D.N. Klyshko, and Y.H. Shih, *Phys. Rev. A* **50**, 5122 (1994).
13. D. Bohm, *Quantum Theory*, Prentice Hall Inc., New York, (1951).
14. E.Schrödinger, Naturwissenschaften **23**, 807, 823, 844 (1935); translations appear in *Quantum Theory and Measurement*, ed. J.A. Wheeler and W.H. Zurek, Princeton University Press, New York, (1983).
15. Y.H. Shih, A.V. Sergienko, and M.H. Rubin, Phys. Rev. A, **50**, 23 (1994).
16. N. Bohr, Naturwissenschaften, **16**, 245 (1928).
17. See Wheeler's "delayed choice", in *Quantum Theory and Measurement*, edited by J.A. Wheeler and W.H. Zurek, Princeton Univ. Press (1983).
18. A.G. Zajonc *et al.*, Nature, **353**, 507 (1991); P.G. Kwiat *et al.*, Phys. Rev. A **49**, 61 (1994); T.J. Herzog *et al.*, Phys. Rev. Lett., **75**, 3034 (1995); T.B. Pittman *et al.*, Phys. Rev. Lett., **77**, 1917 (1996).
19. C.O. Alley, O.G. Jakubowicz, and W.C. Wickes, Proceedings of the 2nd International Symposium on Foundations of Quantum Mechanics, Tokyo 1986, M. Namiki, *et al.* (eds.), Kokubunji, Tokyo, Japan: Physical Society of Japan (1987); T. Hellmuth, H. Walther, A. Zajonc, and W. Schleich , Phys. Rev. A **35**, 2532 (1987).
20. R.J. Glauber, Phys. Rev. **130**, 2529 (1963); **131**, 2766 (1963).
21. M.O. Scully and M.S. Zubairy, *Quantum Optics*, Cambridge Univ. Press, Cambridge, UK (1997).

Sub-Shot-Noise Measurements and Quantum-repeater Using Quantum Correlated Twin Beams

Kunchi Peng, Hai Wang, Jiangrui Gao, Yun Zhang, Hong Su, Xiaoying Li,
Qing Pan, Changde Xie

Institute of Opto-Electronics, Shanxi University, Taiyuan, Shanxi, 030006,
P.R.China

Abstract. The applications of quantum correlated twin beams on the sub-shot-noise measurements and a quantum-repeater have been experimentally accomplished. The experimental results are in agreement with the calculations based on the semi-classical theory to a reasonable extent.

1 Introduction

Recent years the quantum correlated twin beams produced from the Non-degenerate Optical Parametric Oscillator (NOPO) operating above oscillation threshold have been recognized as an useful nonclassical light for the precisely optical measurements with the sensitivity beyond the Standard Quantum Limit (SQL). Nabors and Shelby realized the sub-shot-noise signal recovery in doubly resonant OPO in 1990[1]. Successively, P.Kumer et.al. completed the photo-noise reduction experiments with a Q-switched Nd:YAG laser[2] and P.R. Tapster et.al. performed sub-shot-noise measurement of modulation absorption using twin beams[3]. Later, the two-photon absorption spectroscopy with the improvement of 1.9dB in the Signal-to-Noise Ratio (SNR) with respect to the SQL's that of the total light was reached by Fabre's group in 1997[4].

Through a noncritical phase-matching frequency-down-conversion process in the NOPO including a type-II α -cut KTP crystal we obtained high quantum correlated twin beams. The generation system of bright non-classical light operates stably and robustly. Due to the quantum correlation of intensity fluctuation between twin beams the intensity difference noise spectrum of that is squeezed below the SQL[5,6]. Employing of twin beams we developed the sub-shot-noise optical measurement for the weak absorption of unmodulated sample[7,8] and the quantum-repeater for intensity difference fluctuation[9] .In this paper the applications of twin beams finished by our lab will be summarized.

2 Sub-Shot-noise optical measurements

Usually in the optical measurements with twin beams one of that is used as the carrier of measured information (signal light), the measured signal is modulated on it as an artificial “noise” at a certain modulation frequency, while other one of twin beams serves as the reference light. Then the noise spectrum of the intensity difference fluctuation between the signal and reference light is analyzed by the spectrum analyzer, on that the measured signal emerges from the noise background. Since the intensity difference fluctuation between the quantum correlated twin beams is squeezed below the SQL. the signal-to-noise ratio of measurement must be increased with respect to that using classical light. If $R(\Omega)$ stands for the noise spectrum factor of the intensity difference fluctuation, the minimum detectable signal with twin beams $[\delta]_{\min}$ equals [10]:

$$[\delta]_{\min} = [\delta]_{SQL} \sqrt{R(\Omega)} \quad (0 \leq R(\Omega) \leq 1) \quad (1)$$

Here $[\delta]_{SQL}$ is the minimum detectable signal measured with the coherent state light, that is the standard Quantum Limit. To the perfect correlated twin beams $R=0$, the minimum detectable signal goes to zero too. Without any quantum correlation $R=1$. the result goes back to the SQL. The better the quantum correlation, the better the measurement sensitivity.

With the twin beams of near degenerate frequency around 1.08um and nondegenerate frequency at 1.090um and 1.039um we accomplished the sub-shot-noise measurements, the improvements of signal-to-noise ratio in that are 2.5dB and 7dB with respect to the SQL of total light of twin beams respectively and for the first time to our knowledge the sub-shot-noise measurement related to the SQL of a signal beam (half of twin beam) was experimentally demonstrated[7,8].

3 Quantum-repeater

As will-known, a precise measurement in the microscopic world is not possible without the introduction of a perturbation or “back action” due to the restriction of Heisenberg’s uncertainty relations. To overcome the obstacle Braginsky, Caves and others introduced the strategy of ”Quantum Non-Demonlition:(QND) measurement in the 1970s[11,12], in which the back-action noise is kept entirely within unwanted observables, without being coupled back onto the quantity of interest. The quality of a QND measurement is quantitatively evaluated by three criteria: 1. the signal transfer coefficient T_s , which characterizes the quantum correlation between the output and input observable and namely the nondemolition property of the measurement. 2. The meter transfer coefficient T_m , which quantifies the quantum correlation between the output meter and input signal observable and namely the

efficiency of measurement. 3. The conditional variance $V_{s/m}$, which involves with the quantum correlation between the output signal and output meter observable and characterizes the quantum noise of the input signal corrected by the information of the output meter wave. To an quantum QND measurement[13]:

$$1 < (T_s + T_m) \leq 2 \quad (2)$$

$$0 \leq V_{s/m} < 1 \quad (3)$$

i.e. in this case the QND device has both abilities of quantum signal transfer and quantum state preparation. If $0 \leq (T_s + T_m) \leq 1$ and $1 \leq V_{s/m} < 2$ the device operates in the classical region. $(T_s + T_m) = V_{s/m} = 1$ is the boundary of classical and quantum measurement.

The original QND measurement requires the unitary gain of the observable through measurement device besides fulfilling the criteria of inequalities (2) and (3). If the measurement satisfies all QND criteria in quantum domain (2) and (3), but the signal gain is not unity, i.e. the observable may be enlarged or attenuated linearly, the quantum measurement is named as the “QND-like” measurement or quantum-repeater[13].

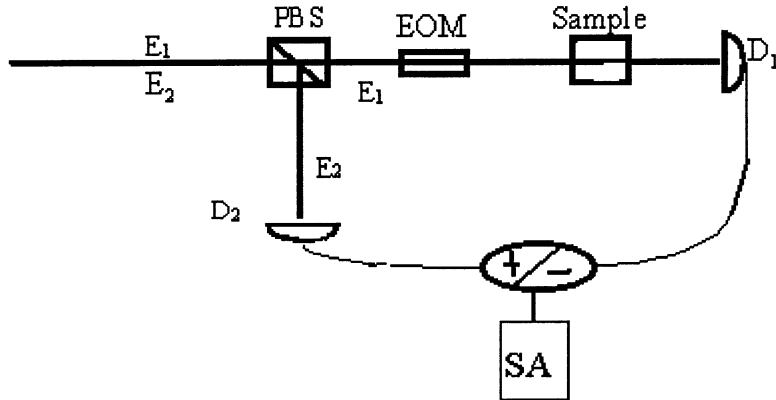


Fig. 1. Scheme for sub-shot-noise measurement with twin beams (E_1 and E_2 —twin beams; PBS—Polarized beam splitter; EOM—Electro-opto modulator; Sample—measured sample; D_1 and D_2 —Photodiode; \pm —power combiner; SA—spectrum analyzer)

We designed and experimentally demonstrated a quantum-repeater, in which the intensity difference fluctuations between the two orthogonal polarized modes in a light wave are the measured obsevables and a 50/50 beam

splitter(BS) is used as the coupling device. The measurement principle is shown in Fig.1. The input signal (S^{in}) and meter wave (M^{in}) consist of two orthogonal polarized modes (S- and P-polarization) of equal mean intensity. The phase and the frequency of S- and P-polarization modes in S^{in} are same as that in M^{in} , respectively. S^{out} and M^{out} are the corresponding signal and meter outputs. D_{in} , D_1 and D_2 are the balanced self-homodyning detectors to measure the noise power spectrum of intensity difference fluctuation between the orthogonal polarized components in the input signal, output signal and output meter.

The derived T_s , T_m and $V_{s/m}$ from the semiclassical theoretical calculation for our system are[9]:

$$T_s = \frac{R}{R + T \langle |\delta r_m^{in}(\omega)|^2 \rangle + \frac{1-\eta}{\eta}} \quad (4)$$

$$T_m = \frac{T}{T + R \langle |\delta r_m^{in}(\omega)|^2 \rangle + \frac{1-\eta}{\eta}} \quad (5)$$

$$V_{s/m} = \frac{1 - \eta + \eta \langle |\delta r_m^{in}(\omega)|^2 \rangle}{\eta [T + R \langle |\delta r_m^{in}(\omega)|^2 \rangle] + 1 - \eta} \quad (6)$$

Where, T and $R = 1 - T$ are the power transmission and reflectivity of BS. η is the detection efficiency of detectors. $\delta\gamma^{in}(\omega)$ is the normalized noise power spectrum of the amplitude difference fluctuation between two orthogonal polarized modes in the input meter wave. When the quantum correlated twin beams is used as the input meter. We have:

$$0 \leq |\delta\gamma^{in}(\omega)| \leq 1 \quad (7)$$

$|\delta\gamma^{in}(\omega)| = 0$ for the perfect quantum correlated light and $|\delta\gamma^{in}(\omega)| = 1$ for the coherent state light without the quantum correlation. It is obvious from eqs. (4)–(6), when $|\delta\gamma^{in}(\omega)| < 1$, the QND criteria in quantum measurement domain can be satisfied.

Using a homemade intracavity frequency-doubled and frequency-stabilized ring Nd:YAP laser as the pump source and an NOPO involved α -cut KTP crystal, we obtained the intensity quantum correlated twin beams, the noise reduction in the intensity difference between that at BS is 6.2dB, i.e. the corresponding noise power spectrum is $|\delta\gamma^{in}(\omega)|^2 = 0.24$. To our system $T = 50\% \pm 1\%$, $\eta = 0.89$ the experimentally measured T_s and T_m from the Signal-to Noise Ratio(SNR) of output signal, output meter and input signal are 0.66 and 0.65 respectively and the measured $V_{s/m}$ from the lowest noise power spectrum of the photo current difference between the output signal and output meter[9] is -2.1dB.

Fig.2 and Fig.3 are the function of $T_s + T_m$ and $V_{s/m}$ versus η and $\delta\gamma_m$ from the eqs. (4)–(6), in which the dark dots (\bullet) are the experimentally measured values. $(T_s + T_m) = 1.31$ is in good agreement with the calculation,

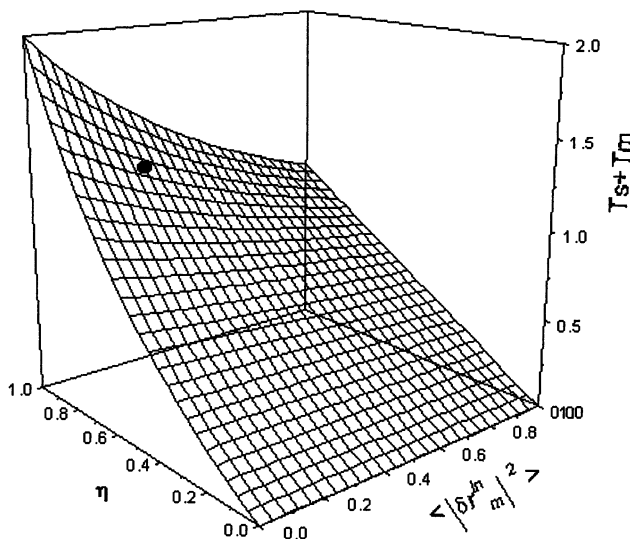


Fig. 2. The dependence of $T_s + T_m$ on $\delta\gamma_m$ and η

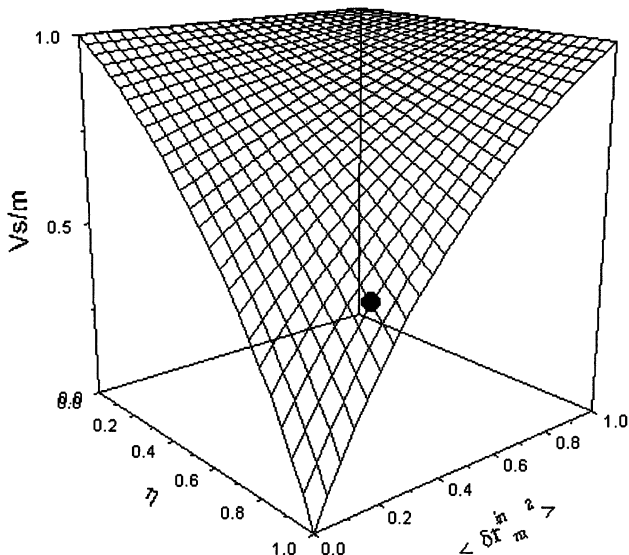


Fig. 3. The dependence of $V_{s/m}$ on $\delta\gamma_m$ and η

but $V_{s/m} = -2.1\text{dB}$ is worse than the calculated value because the desire lowest noise power spectrum was not reached due to that the less sensitiv attenuator and phase-shifter was employed in the experiment. From Fig. and Fig.4 we can see that the higher the η and lower the $\delta\gamma_m$, the better th QND measurement.

In conclusion, we have finished the sub-shot-noise optical measuremen and quantum repeater with the quantum correlated twin beams. These pre sented stable and robust systems are suitable for the practical applications i optical measurements and optical signal transfer with the sensitivity beyond the SQL.

Acknowledgments. This work was supported by the National Natural Scienc Foundation of China (Approval No.69837010) and the Shanxi Provincial Sci ence Foundation.Foundation

References

1. C.D. Nabors and R.M.Shelby, Phys.Rev., **42**,556(1990)
2. P.Kumer et.al., SPIE, **1376**, 192(1990)
3. P.R.Tapster et.al., Phys.Rev., **44**, 3266(1991)
4. P.H.Souto Ribeiro et.al., Opt. Lett., **22**, 1893(1997)
5. A.Heidmann et. al.. Phys.Rev.Lett., **59**, 2555(1987)
6. K.C.Peng et.al., Appl. Phys. **B66**, 755-758(1998)
7. Hai Wang et.al., Proceeding of the Third International Conference on Quantur Communication and Measurement, held September 25-30,1996, in Shznoka Japan, edited by Hirota et.al., Plenum Press, New York, 1997, p445-453
8. Jiangrui Gao et.al., Opt.Lett. **23**, 870(1998)
9. Hai Wang et.al., Phys.Rev.Lett. **82**, 1414(1999)
10. Hai Wang et.al., Science in China (Series A) **41**, 534(1998)
11. V.B.Braginsky et.al., Sov. Phys. Vsp.**17**, 644 (1975)
12. C.M.Caves et.al., Rev.Mod. Phys. **52**, 341 (1980)
13. P. Grangier et.al., Nature, **396**, 537(1998)

Mirrorless Oscillation Based on Resonantly Enhanced 4-Wave Mixing: All-Order Analytic Solutions

M. Fleischhauer

Sektion Physik, Universität München, D-80333 München, Germany
e-mail: mfleisch@theorie.physik.uni-muenchen.de

Abstract. The phase transition to mirrorless oscillation in resonantly enhanced four-wave mixing in double- Λ systems are studied analytically for the ideal case of infinite lifetimes of ground-state coherences. The stationary susceptibilities are obtained in all orders of the generated fields and analytic solutions of the coupled nonlinear differential equations for the field amplitudes are derived and discussed.

1 Introduction

The possibility to cancel the linear absorption in resonant atomic systems by means of electromagnetically induced transparency (EIT) [1] lead in recent years to fascinating new developments in nonlinear optics [2,3]. For example coherently driven, resonant atomic vapors under conditions of EIT allow for complete frequency conversion in distances short enough, such that phase matching requirements become irrelevant [4]. Furthermore the large nonlinearities of these systems may lead to a new regime of nonlinear quantum optics on the few-photon level [5,6] with potential applications to single-photon quantum control [7,8] and quantum information processing.

One particularly interesting nonlinear process based on EIT is the resonantly enhanced 4-wave mixing in a double- Λ system with counterpropagating pump modes [9]. It has been shown experimentally [10] and theoretically [11,12] that this system can show a phase transition to mirrorless oscillations for rather low pump powers. Close to the threshold of oscillation an almost perfect suppression of quantum fluctuations of one quadrature amplitude of a combination mode of the generated fields occurs [13,14]. Also sufficiently above threshold light fields with beat-frequencies tightly locked to the atomic Raman-transition and extremely low relative bandwidth are generated [15].

All previous studies of resonantly enhanced 4-wave mixing were done in the perturbative regime of small amplitudes of the generated fields. In the present paper I want to discuss the case of arbitrary amplitudes. Using a simplified open-system model I will derive stationary propagation equations for the field amplitudes and present analytic solutions of these equations. It will be shown that in an ideal case complete conversion can be achieved within a relatively small interaction length.

2 Model and Atomic Polarizations

I here consider the propagation of four electromagnetic waves in a medium consisting of double- Λ atoms (see Fig.1). These waves include two counter-propagating driving fields with equal frequencies ν_d and Rabi-frequencies Ω_1 and Ω_2 , and two probe fields (anti-Stokes and Stokes) described by the complex Rabi-frequencies E_1 and E_2 , with carrier frequencies $\nu_1 = \nu_d + \omega_0$ and $\nu_2 = \nu_d - \omega_0$, where $\omega_0 = \omega_{b1} - \omega_{b2}$ is the ground-state frequency splitting. The fields interact via the long-lived coherence on the dipole-forbidden transition between the metastable ground states b_1 and b_2 . We assume that the driving field Ω_1 is in resonance with the $b_2 \rightarrow a_1$ transition, whereas the second driving field Ω_2 has a detuning $\Delta \gg |\Omega_2|$ from the $b_1 \rightarrow a_2$ transition. In this case linear losses of the fields due to single-photon absorption processes are minimized.

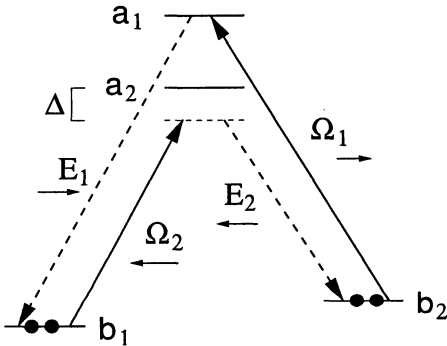


Fig. 1. Atoms in double Λ configuration interacting with two driving fields ($\Omega_{1,2}$) and two generated fields ($E_{1,2}$)

Due to coherent Raman-scattering the pump fields generate counter-propagating anti-Stokes and Stokes fields. For a sufficiently large density-length product of the medium and for a certain pump field intensity, the system shows a phase-transition to self-oscillations [10]. The feedback mechanism required for an oscillation is provided here by the gain medium: A Stokes photon spontaneously generated on the $a_2 \rightarrow b_2$ transition propagates in the $-z$ direction and stimulates the generation of an anti-Stokes photon. This anti-Stokes photon has a different frequency but a fixed relative phase and propagates in the $+z$ direction. It stimulates the generation of another Stokes photon upstream. The second Stokes photon will be in phase with the first one, provided that the system is approximately phase matched and that there has been no decay of the Raman coherence. The phase-locked emission of the second Stokes photon then closes the feedback loop. We have shown in [15] that phase-matching enforces a strong pulling of the beat-note of generated and pump fields to the atomic Raman transition. I will therefore assume here that both Λ systems are in perfect two-photon resonance.

In order to calculate the medium response to the fields, one would have to solve the atomic density matrix equations to all orders in all fields taking into account all relaxation rates. Although this is in principle possible it leads to extremely involved expressions. Instead I here use a simplified open-system model which allows to derive rather compact expressions for the atomic susceptibilities.

Since the effects of spontaneous emission are negligible in the present system, we may model all relaxations out of the excited states a_1 and a_2 by rates γ out of the system. In thermal equilibrium, i.e. in the absence of all fields, both lower states b_1 and b_2 are equally populated. I therefore assume – within the open-system approach – that the atoms are pumped into states b_1 or b_2 with 50% probability respectively. The corresponding rate is denoted as r and will later be determined by the requirement that the total probability to find an atom in any of the states is unity. The finite lifetime of the lower-level coherence will here be described by a decay out of all states with rate γ_0 . Thus the open-system model corresponds to the experimentally relevant situation of an atomic beam or a finite-temperature vapor with time-of-flight broadening. In this case the system can be described by generalized Schrödinger-equations for field amplitudes instead of density-matrix equations.

The interaction Hamiltonian of an atom at position z with the fields can be written in the form

$$H_{\text{int}} = -\hbar \left[\Omega_1(z) e^{-i\nu_a t} |a_1\rangle\langle b_2| + \Omega_2(z) e^{-i\nu_d t} |a_2\rangle\langle b_1| + E_1(z) e^{-i\nu_1 t} |a_1\rangle\langle b_1| + E_2(z) e^{-i\nu_2 t} |a_2\rangle\langle b_2| + \text{adj.} \right]. \quad (1)$$

If we denote the state vector of the atom as

$$|\Psi\rangle = a_1 e^{-i\nu_{a1} t} |a_1\rangle + a_2 e^{-i(\nu_{a2}-\Delta)t} |a_2\rangle + b_1 e^{-i\nu_{b1} t} |b_1\rangle + b_2 e^{-i\nu_{b2} t} |b_2\rangle, \quad (2)$$

where $\hbar\nu_\mu$ are the energies of the corresponding states, we find the following equations of motion of the slowly-varying state amplitudes for an atom at position z

$$\dot{a}_1 = -(\gamma_0 + \gamma) a_1 + i\Omega_1 b_2 + iE_1 b_1, \quad (3)$$

$$\dot{a}_2 = -(\gamma_0 + \gamma + i\Delta) a_2 + i\Omega_2 b_1 + iE_2 b_2, \quad (4)$$

$$\dot{b}_1 = r_1 - \gamma_0 b_1 + i\Omega_2^* a_2 + iE_1^* a_1, \quad (5)$$

$$\dot{b}_2 = r_2 - \gamma_0 b_2 + i\Omega_1^* a_1 + iE_2^* a_2. \quad (6)$$

Here I have introduced the rates r_1 and r_2 to distinguish the cases of pumping into b_1 ($r_1 = r, r_2 = 0$) and into b_2 ($r_1 = 0, r_2 = r$). Note that simultaneously setting $r_1 = r_2 = r$ corresponds to a *coherent* preparation of the atoms in a 50–50 superposition of b_1 and b_2 . In order to describe an *incoherent* preparation in these levels one has to consider the two cases separately and add the density matrix elements following from both cases.

Solving (3–6) in steady state for the case of injection into b_1 , i.e. for $r_1 = r$ and $r_2 = 0$ one finds

$$a_1^{(1)} = -ir \frac{\Omega_1 \Omega_2 E_2^* - E_1 |E_2|^2}{|\Omega_1 \Omega_2 - E_1 E_2|^2}, \quad (7)$$

$$a_2^{(1)} = ir \frac{|\Omega_1|^2 \Omega_2 - \Omega_1^* E_1 E_2}{|\Omega_1 \Omega_2 - E_1 E_2|^2}, \quad (8)$$

$$b_1^{(1)} = ir \frac{\Delta |\Omega_1|^2}{|\Omega_1 \Omega_2 - E_1 E_2|^2}, \quad (9)$$

$$b_2^{(1)} = -ir \frac{\Delta \Omega_1^* E_1}{|\Omega_1 \Omega_2 - E_1 E_2|^2}, \quad (10)$$

where I have used that $\Delta \gg \gamma \gg \gamma_0$ and have kept only the leading terms. Similarly one finds for injection into b_2 , i.e. for $r_1 = 0$ and $r_2 = r$:

$$a_1^{(2)} = ir \frac{\Omega_1 |\Omega_2|^2 - E_1 E_2 \Omega_2^*}{|\Omega_1 \Omega_2 - E_1 E_2|^2}, \quad (11)$$

$$a_2^{(2)} = -ir \frac{\Omega_1 \Omega_2 E_1^* - |E_1|^2 E_2}{|\Omega_1 \Omega_2 - E_1 E_2|^2}, \quad (12)$$

$$b_1^{(2)} = -ir \frac{\Delta \Omega_1 E_1^*}{|\Omega_1 \Omega_2 - E_1 E_2|^2}, \quad (13)$$

$$b_2^{(2)} = ir \frac{\Delta |E_1|^2}{|\Omega_1 \Omega_2 - E_1 E_2|^2}. \quad (14)$$

Taking into account only the leading order contribution in the above expressions is essentially equivalent to assuming an infinitely long lived ground-state coherence between b_1 and b_2 . In vapor cells with coated walls or by using buffer gases, lifetimes of Hyperfine coherences in alkali vapors in the millisecond regime are possible. Hence neglecting contributions from finite values of γ_0 seems justified. However, in this case also linear absorption losses are neglected. As a consequence the threshold condition becomes independent on the pump intensity and an arbitrarily small flux of pump photons is sufficient to maintain oscillations [15]. If on the other hand a small but finite ground-state dephasing rate is taken into account, the threshold condition does depend on the pump intensity leading to a lower limit of the pump-photon flux. In the present paper I am interested only in the analytic behavior of the fields in the ideal limit and therefore the small but finite linear losses associated with the ground-state dephasing will be ignored.

The pump rate r can be determined from the normalization condition $\sum_\mu \varrho_{\mu\mu}^{(1)} + \varrho_{\mu\mu}^{(2)} = 1$. One finds $r = (|\Omega_1 \Omega_2 - E_1 E_2|^2) / [\Delta(|\Omega_1|^2 + |E_1|^2)]$. With this one obtains for the non-diagonal density matrix elements $\varrho_{a_\mu b_\nu} = a_\mu^{(1)} b_\nu^{(1)*} + a_\mu^{(2)} b_\nu^{(2)*}$:

$$\varrho_{a_1 b_1} = -\frac{|\Omega_1|^2 \Omega_1 \Omega_2 E_2^* - E_1^2 E_2 \Omega_1^* \Omega_2^*}{\Delta (|\Omega_1|^2 + |E_1|^2)^2} - \frac{|\Omega_1|^2 (|\Omega_2|^2 - |E_2|^2)}{\Delta (|\Omega_1|^2 + |E_1|^2)^2} E_1, \quad (15)$$

$$\varrho_{a_1 b_2} = \frac{\Omega_1^2 \Omega_2 E_1^* E_2^* - |E_1|^2 E_1 E_2 \Omega_2^*}{\Delta (|\Omega_1|^2 + |E_1|^2)^2} + \frac{|E_1|^2 (|\Omega_2|^2 + |E_2|^2)}{\Delta (|\Omega_1|^2 + |E_1|^2)^2} \Omega_1, \quad (16)$$

$$\varrho_{a_2 b_1} = -\frac{(|\Omega_1|^2 + |E_1|^2) E_1 E_2 \Omega_1^*}{\Delta (|\Omega_1|^2 + |E_1|^2)^2} + \frac{|\Omega_1|^2 (|\Omega_1|^2 + |E_1|^2)}{\Delta (|\Omega_1|^2 + |E_1|^2)^2} \Omega_2, \quad (17)$$

$$\varrho_{a_2 b_2} = -\frac{(|\Omega_1|^2 + |E_1|^2) \Omega_1 \Omega_2 E_1^*}{\Delta (|\Omega_1|^2 + |E_1|^2)^2} + \frac{|E_1|^2 (|\Omega_1|^2 + |E_1|^2)}{\Delta (|\Omega_1|^2 + |E_1|^2)^2} E_2. \quad (18)$$

first terms in these expressions describe the nonlinear coupling between modes and the second ones ac-Stark shift induced changes in the refractive indices. It should be noted that there are no imaginary linear susceptibilities, there is no linear dissipation despite the fact, that Ω_1 and E_1 are in single-photon resonance.

Stationary field equations and analytic solutions

in the slowly-varying amplitude and phase approximation, the field amplitudes satisfy the following equation of motion

$$\frac{d}{dz} E_1 = ik_1 E_1 + i \frac{\wp^2 k_1}{2\hbar\varepsilon_0} N \varrho_{a_1 b_1}, \quad (19)$$

$$\frac{d}{dz} E_2^* = ik_2 E_2^* + i \frac{\wp^2 k_2}{2\hbar\varepsilon_0} N \varrho_{a_2 b_2}^*, \quad (20)$$

$$\frac{d}{dz} \Omega_1 = ik_d \Omega_1 + i \frac{\wp^2 k_d}{2\hbar\varepsilon_0} N \varrho_{a_1 b_2}, \quad (21)$$

$$\frac{d}{dz} \Omega_2^* = ik_d \Omega_2^* + i \frac{\wp^2 k_d}{2\hbar\varepsilon_0} N \varrho_{a_2 b_1}^*, \quad (22)$$

where k_1 , k_2 and k_d are the free-space wavenumbers of the generated and pump fields, N is the atomic number density and \wp are the dipole moments for the corresponding transitions, which have been assumed to be equal for simplicity. Since the wavenumbers of the fields differ only slightly, one may approximate the coupling parameter in all equations by $\kappa \equiv \wp^2 k_d N / 2\hbar\varepsilon_0$. Introducing field amplitudes which are slowly varying in space, $E_1 = \tilde{E}_1 e^{ik_1 z}$, $E_2 = e^{-ik_2 z}$, $\Omega_1 = \tilde{\Omega}_1 e^{ik_d z}$ and $\Omega_2 = \tilde{\Omega}_2 e^{-ik_d z}$ one eventually arrives at

$$\begin{aligned} \frac{d}{dz} E_1 &= -i\kappa \frac{|\Omega_1|^2 \Omega_1 \Omega_2 E_2^* - E_1^2 E_2 \Omega_1^* \Omega_2^*}{\Delta (|\Omega_1|^2 + |E_1|^2)^2} \\ &\quad - i \left[\Delta k + \kappa \frac{|\Omega_1|^2 (|\Omega_2|^2 - |E_2|^2)}{\Delta (|\Omega_1|^2 + |E_1|^2)^2} \right] E_1, \end{aligned} \quad (23)$$

$$\begin{aligned} \frac{d}{dz} E_2^* &= -i\kappa \frac{(|\Omega_1|^2 + |E_1|^2) \Omega_1^* \Omega_2^* E_1}{\Delta (|\Omega_1|^2 + |E_1|^2)^2} \\ &\quad + i\kappa \frac{|E_1|^2 (|\Omega_1|^2 + |E_1|^2)}{\Delta (|\Omega_1|^2 + |E_1|^2)^2} E_2^*, \end{aligned} \quad (24)$$

$$\begin{aligned} \frac{d}{dz} \Omega_1 &= i\kappa \frac{\Omega_1^2 \Omega_2 E_1^* E_2^* - |E_1|^2 E_1 E_2 \Omega_2^*}{\Delta (|\Omega_1|^2 + |E_1|^2)^2} \\ &\quad + i\kappa \frac{|E_1|^2 (|\Omega_2|^2 + |E_2|^2)}{\Delta (|\Omega_1|^2 + |E_1|^2)^2} \Omega_1 \end{aligned} \quad (25)$$

$$\begin{aligned} \frac{d}{dz} \Omega_2^* &= -i\kappa \frac{(|\Omega_1|^2 + |E_1|^2) E_1^* E_2^* \Omega_1}{\Delta (|\Omega_1|^2 + |E_1|^2)^2} \\ &\quad + i\kappa \frac{|\Omega_1|^2 (|\Omega_2|^2 + |E_2|^2)}{\Delta (|\Omega_1|^2 + |E_1|^2)^2} \Omega_2^*, \end{aligned} \quad (26)$$

where I have dropped the tildes again for notational simplicity, and $\Delta k = k_2 - k_1$ is the free-space phase mismatch. Expanding these expressions into third order of the generated fields E_1 and E_2 reproduces the equations of [15]. Equations (23–26) together with the boundary-conditions

$$E_1(0) = 0, \quad E_2(L) = 0, \quad \Omega_1(0) = \Omega_{10}, \quad \text{and} \quad \Omega_2(L) = \Omega_{20}, \quad (27)$$

where L is the length of the interaction region and Ω_{10} and Ω_{20} are the given input amplitudes, form a nonlinear boundary-value problem. One easily verifies that the set of differential equations has always the trivial solution $E_1 \equiv E_2 \equiv 0$, and $\Omega_1(z) \equiv \Omega_{10}$ and $\Omega_2(z) \equiv \Omega_{20}$.

As has been discussed in detail in [15], the phase mismatch is easily compensated in an optically dense vapor by a small detuning from the two-photon resonance. Oscillation occurs at frequencies such that the phase-matching condition is automatically fulfilled. I therefore set this term equal to zero in the following.

Constants of Motion: The field equations have the following constants of motion. From the energy-momentum conservation follow the Manley-Rowe relations

$$\frac{d}{dz} (|\Omega_1|^2 + |E_1|^2) = 0, \quad (28)$$

$$\frac{d}{dz} (|\Omega_2|^2 + |E_2|^2) = 0, \quad (29)$$

which state that each photon taken out of the pump fields Ω_1 or Ω_2 is put into the anti-Stokes and Stokes fields E_1 and E_2 respectively. Furthermore one finds that the total intensity of the pump field is constant in space

$$\frac{d}{dz} (|\Omega_1|^2 + |\Omega_2|^2) = 0. \quad (30)$$

The same is true for the generated fields, which however follow already from the above constants of motion.

$$\frac{d}{dz} (|E_1|^2 + |E_2|^2) = 0. \quad (31)$$

Without the phase terms in (23–26), which represent contributions due to ac-Stark shifts, also the quartic expression $\text{Re}[\Omega_1\Omega_2E_1^*E_2^*]$ would be a constant of motion. In fact the boundary conditions for the generated fields imply that $\text{Re}[\Omega_1\Omega_2E_1^*E_2^*] \equiv 0$. It will be shown later on that $\text{Re}[\Omega_1\Omega_2E_1^*E_2^*]$ is in any case to a very good approximation a constant of motion.

Amplitude-Phase Equations: It is convenient to rewrite the field equations in terms of amplitudes and phases. Introducing $E_n = e_n e^{-i\phi_n}$ and $\Omega_n = a_n e^{-i\psi_n}$ ($n = 1, 2$) one obtains

$$\frac{d}{dz}e_1 = \frac{\kappa}{\Delta} \frac{a_1 a_2 e_2}{a_1^2 + e_1^2} \sin \psi, \quad (32)$$

$$-\frac{d}{dz}e_2 = \frac{\kappa}{\Delta} \frac{a_1 a_2 e_1}{a_1^2 + e_1^2} \sin \psi, \quad (33)$$

$$-\frac{d}{dz}a_1 = \frac{\kappa}{\Delta} \frac{a_2 e_1 e_2}{a_1^2 + e_1^2} \sin \psi, \quad (34)$$

$$\frac{d}{dz}a_2 = \frac{\kappa}{\Delta} \frac{a_1 e_1 e_2}{a_1^2 + e_1^2} \sin \psi, \quad (35)$$

where $\psi = \phi_1 + \phi_2 - \psi_1 - \psi_2$ is the relative phase between the fields. It obeys the equation

$$\begin{aligned} \frac{d}{dz}\psi = & \frac{\kappa}{\Delta} \left[\frac{a_1 a_2 e_2 (a_1^2 - e_1^2)}{e_1 (a_1^2 + e_1^2)^2} - \frac{a_1 a_2 e_1}{e_2 (a_1^2 + e_1^2)} + \frac{a_2 e_1 e_2 (a_1^2 - e_1^2)}{a_1 (a_1^2 + e_1^2)^2} \right. \\ & \left. - \frac{a_1 e_1 e_2}{a_2 (a_1^2 + e_1^2)} \right] \cos \psi + \frac{\kappa}{\Delta} \left[\frac{e_1^4 - a_1^4 + 2e_1^2 a_2^2}{(a_1^2 + e_1^2)^2} \right]. \end{aligned} \quad (36)$$

Solution for Equal Input Intensities: Let me now consider the case of equal input intensities of both pump fields, i.e. $a_1(0) = a_{10} = a_{20} = a_2(L)$. Making use of the constants of motion one can write

$$e_1(z) = e \sin \vartheta(z), \quad a_1(z) = \sqrt{a_{10}^2 - e^2 \sin^2 \vartheta(z)}, \quad (37)$$

$$e_2(z) = e \cos \vartheta(z), \quad a_2(z) = \sqrt{a_{10}^2 - e^2 \cos^2 \vartheta(z)}, \quad (38)$$

with the output amplitude of the generated fields e and the mixing angle $\vartheta(z)$ as the only remaining variables. The boundary conditions are now $\vartheta(0) = 0$ and $\vartheta(L) = \pi/2$, if $e \neq 0$, i.e. for the non-trivial solutions.

Substituting the above expressions into (32) yields the nonlinear equation

$$\frac{d}{dz}\vartheta(z) = \frac{\kappa}{\Delta} \left[1 - \varepsilon^2 + \frac{\varepsilon^4}{4} \sin^2 [2\vartheta(z)] \right]^{1/2} \sin \psi(z), \quad (39)$$

where $\varepsilon \equiv e/a_{10}$. In order to solve (39) one can in principle introduce a nonlinear stretch of the spatial coordinate according to

$$\xi(z) = \int_0^z dz' \sin \psi(z'), \quad \text{and} \quad d\xi = \sin \psi(z) dz \quad (40)$$

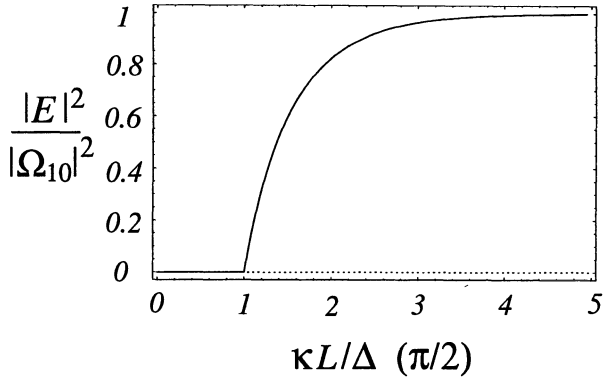


Fig. 2. Output intensity of generated fields $E \equiv E_1(L) = E_2(0)$ normalized to input intensity of pump fields as function of effective interaction length, $\Omega_1(0) = \Omega_2(L) \equiv \Omega_{10}$

which removes the term $\sin \psi(z)$ on the r.h.s. of (39). I will show later on, however, that to a very good approximation $\sin \psi(z) \equiv 1$. Thus $\xi = z$ and $\sin \psi(z) = 1$ is used in the following.

Integrating (39) from $z = 0$ to $z = L$ leads to an equation for the normalized output amplitude $\varepsilon = e/a_{10}$:

$$K \left[\frac{\varepsilon^4}{4(\varepsilon^2 - 1)} \right] = \frac{\kappa L}{\Delta} \sqrt{1 - \varepsilon^2}, \quad (41)$$

where K is the complete elliptic integral of the first kind [16]. One easily verifies that (41) has only a real-valued solution ε , if $\kappa L/\Delta \geq \pi/2$, which is the threshold condition for mirrorless oscillations [10,12]. For smaller values of $\kappa L/\Delta$ the equations of motion have only the trivial solution. Figure 2 shows the output intensity of the generated fields normalized to the input intensity of the pump fields as a function of the effective density length product κL . One clearly recognizes that for a sufficiently large product κL complete conversion can be achieved.

The spatial behavior of the field strength inside the vapor cell can be obtained from incomplete elliptical integrals following from (39). Figure 3 shows the field amplitudes inside the medium for $\varepsilon = 0.2$, i.e. just above threshold and for $\varepsilon = 0.98$ i.e. for almost complete conversion.

Not too far above threshold, the square root in (39) can be expanded and one recovers the third-order solution obtained in [15]:

$$\vartheta(z) \approx \frac{\kappa z}{\Delta} \left(1 - \frac{1}{2} \varepsilon^2 \right) \quad (42)$$

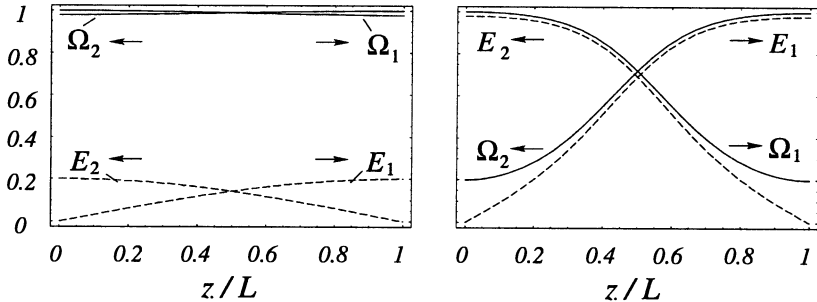


Fig. 3. Field amplitudes inside interaction region for small conversion $\varepsilon = E/\Omega_{10} = 0.2$ (left) and large conversion $\varepsilon = E/\Omega_{10} = 0.98$ (right)

with

$$\varepsilon = \sqrt{2} \left[1 - \frac{\pi}{2} \frac{\Delta}{\kappa L} \right]^{1/2} \quad \text{for} \quad \frac{\kappa L}{\Delta} \geq \frac{\pi}{2}. \quad (43)$$

In order to verify the approximation $\sin \psi(z) \equiv 1$, I have numerically integrated the differential equation (36) with the above solutions. Figure 4 shows the comparison between the nonlinear coordinate $\xi(z)$ and z for the case $\varepsilon = 0.98$. One recognizes that ξ deviates from z by at most 1%. For smaller conversions an even smaller difference shows up. Therefore the approximation $\sin \psi = 1$ is very well justified. This also implies that $\text{Re} [\Omega_1 \Omega_2 E_1^* E_2^*]$ is to a very good approximation a constant of motion.

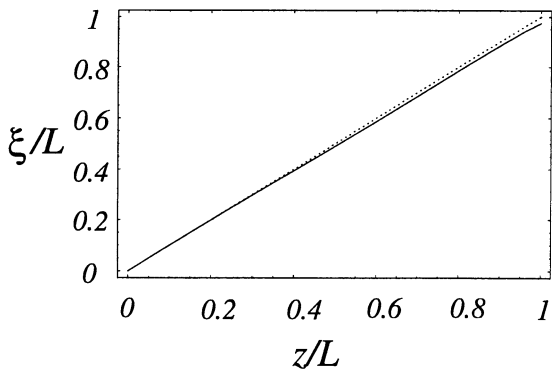


Fig. 4. Effective interaction distance ξ versus physical interaction distance z for large conversion ($\varepsilon = E/\Omega_{10} = 0.98$). Dotted line corresponds to $\xi = z$

4 Summary

In the present paper all-order atomic susceptibilities for resonantly enhanced 4-wave mixing are presented and field equations derived. The coupled nonlinear differential equations are solved analytically for the case of infinitely long-lived ground-state coherences and under the assumption of negligible phase changes due to ac-Stark shifts. Below a certain critical value of the density-length product only the trivial solution exists, where the generated Stokes and anti-Stokes components have vanishing amplitude. Above the threshold to mirrorless oscillations the photon conversion efficiency increases very rapidly and at a density-length product of about 3 times the threshold value, 95% conversion is achieved.

Acknowledgement. The author would like to thank the organizers of the International Conference on Laser Physics and Quantum Optics, ICLPQO'99, in particular Prof. Shi-Yao Zhu for the invitation and the hospitality in China. The financial support of the German Science Foundation is gratefully acknowledged.

References

1. for a review on EIT see: S. E. Harris, Physics Today **50**, 36 (1997)
2. S. E. Harris, J. E. Field, and A. Imamoğlu, Phys. Rev. Lett. **64**, 1107 (1990)
3. K. Hakuta, L. Marmet, and B. P. Stoicheff, Phys. Rev. Lett. **66**, 596 (1991)
4. M. Jain, H. Xia, G. Yin, A. J. Merriam und S. E. Harris, Phys. Rev. Lett. **77**, 4326 (1996)
5. H. Schmidt and A. Imamoğlu, Opt. Lett. **21**, 1936 (1996), A. Imamoğlu, H. Schmidt, G. Woods, and M. Deutsch, Phys. Rev. Lett. **79**, 1467 (1997)
6. S. E. Harris and L. V. Hau, Phys. Rev. Lett. **82**, 4611 (1999)
7. S. Harris and Y. Yamamoto, Phys. Rev. Lett. **81**, 3611 (1998)
8. M. Werner, and A. Imamoğlu, preprint quant-ph/9902005
9. P. R. Hemmer, D. P. Katz, J. Donoghue, M. Cronin-Golomb, M. S. Shahriar and P. Kumar, Opt. Lett. **20**, 982 (1995)
10. A. S. Zibrov, M. D. Lukin, and M. O. Scully, Phys. Rev. Lett. **83** (1999), in press
11. M. D. Lukin, P. Hemmer, M. Loeffler, and M. O. Scully, Phys. Rev. Lett. **81**, 2675 (1998)
12. M. D. Lukin, P. R. Hemmer, M. O. Scully, in *Adv. At. Mol. and Opt. Physics*, **42B**, 347 (Academic Press, Boston, 1999)
13. H. P. Yuen and J. H. Shapiro, Opt. Lett. **4**, 334 (1979)
14. M. D. Lukin, A. B. Matsko, M. Fleischhauer, M. O. Scully Phys. Rev. Lett. **82**, 1847 (1999)
15. M. Fleischhauer, M. D. Lukin, A. B. Matsko, and M. O. Scully, preprint quant-ph/9907032
16. M. Abramowitz and I. A. Stegun, “*Handbook of Mathematical Functions*”, (Thun, Frankfurt/Main, 1984)

Recent Progress in High-Field Laser Physics Research at SIOFM

Zhizhan Xu, Ruxin Li, Zhong Li, Yingsong Wang, Wei Yu, Ya Cheng

Laboratory for High Intensity Optics, Shanghai Institute of Optics and Fine Mechanics, Chinese Academy of Sciences, P. O. Box 800-211, Shanghai 201800, China

e-mail: zzxu@mail.shcnc.ac.cn

Abstract. The recent progress in high-field laser physics research at Shanghai Institute of Optics and Fine Mechanics (SIOFM) is reviewed. Some high-field laser physics experiments based on a 5 TW/46 fs laser system have been carried out and the results are reported here, which include the high-order harmonic generation in gas atoms and the energetic ion emission from the laser irradiated argon clusters.

1 Introduction

Recent years have found that high field laser matter interactions is one of the most rapidly progressing areas in physics [1-5]. The development of compact ultra-high- intensity lasers makes it possible to offer novel experimental methods and to create extreme physical conditions, which can previously be found only at the center of nuclear explosion, in stellar interiors or close to the horizon of a black hole [5]. Under the extremely strong and ultra-fast optical field generated by the rapidly developing ultra-intense ultra-short laser technology, the interaction between laser and various kinds of matter is entering an unprecedented highly nonlinear and relativistic high- field ultra-fast regime [1-7].

The attainable peak laser intensities has been well in excess of 10^{19} W/cm² in a modest-size laboratory, and this value is soon to increase by a few orders of magnitude before the present technological limits will be reached [7,8]. As a rapidly evolving frontier of physics, high field laser interaction yields completely new phenomena and creates a stimulating atmosphere for pioneering interdisciplinary research which can only be compared to few other periods in the recent history of modern sciences. In addition, this field promises a wealth of novel applications. Research and development on short wavelength sources is one of them. For example, high order harmonic generation has been regarded as a very promising method for the board application field of coherent x-ray source [9,10].

The research in high-field laser physics at Shanghai Institute of Optics and Fine Mechanics (SIOFM) mainly focuses on the development of novel ultra-intense ultra-short laser technology, the interaction physics between ultra-intense ultra-short laser and matter, and their applications in creative

interdisciplinary and related high-tech research fields. Limited by space, we will not cover the whole activities and only review the most recent progress in this talk. We describe several high-field laser physics experiments based on a 5 TW/46 fs laser system, which include the high-order harmonic generation in gas atoms and the energetic ion emission from the laser irradiated clusters.

2 The 5TW/46fs Laser System

The laser system was upgraded from a 2 TW laser system [11], which outputs 120 mJ/43 fs pulses with a focusable intensity of $>10^{18}$ W/cm². The 5.4 TW laser system consists of an oscillator, a pulse stretcher, a regenerative amplifier, a pre-amplifier, a main amplifier and a pulse compressor. The final laser energy per pulse after the compressor is about 250 mJ. The measured pulse duration is <46 fs (FWHM), with a time-bandwidth product $\Delta\nu\Delta t \simeq 0.375$. The peak power is 5.4 TW with a $\pm 3\%$ pulse to pulse energy stability. The pulse contrast is measured by using a high-dynamic-range third-order auto-correlator based on third harmonic generation. The intensity contrast of 10^6 in a 6 ps window is obtained [12].

3 High-Order Harmonic Generation in Gases

With the development of the short-pulse high-intensity laser systems, harmonic radiation has attracted great attention for its promising application in coherent XUV and soft x-ray regime. In recent years, considerable progresses have been achieved in both experiments and theoretical analysis on harmonic generation [1,13,14].

The most energetic harmonic photons observed experimentally are about 460 eV, which corresponds to the 297th order harmonic of the Ti:sapphire laser centered at 800 nm and is almost the wavelength limit of harmonic generation in neutral atoms [13]. Nevertheless, under appropriate conditions, the harmonics generated from ions can comparatively contribute to high order harmonics or even higher order harmonics which can not be produced in neutrals because of their cutoff [4,9,13-16]. Another important topic is to increase the harmonic conversion efficiency that is related to harmonic phase matching, addressed in terms of the variation of the phase of the interfering fields throughout the nonlinear medium [4,10].

We present in this section an investigation on the harmonic generation in argon and neon. In addition to the observation of the shortest wavelength harmonic in argon, we will discuss the important role the ions play in their contribution to higher order harmonic generation at a considerable high driving intensity level and report the effects of free electrons on the process of

harmonic generation [16]. And finally we will report a first observation of spectral splitting of harmonics when the driving intensity is very high.

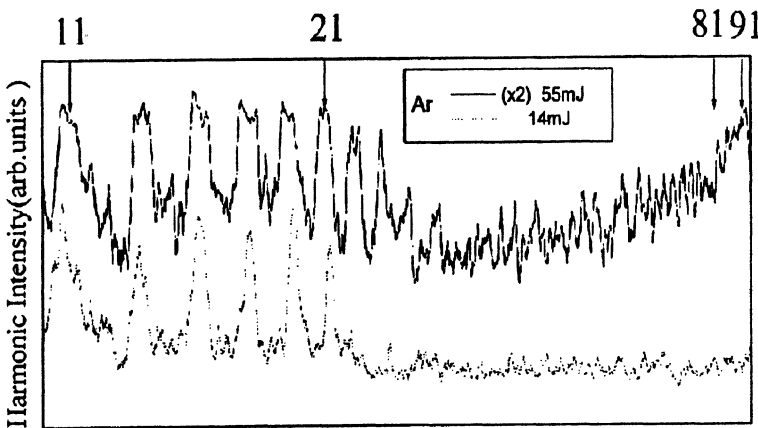
The details of the experimental arrangement can be found elsewhere [16]. The laser beam is linearly polarized and focused by a convex lens of 50 cm focal length. In order to increase the conversion efficiency of harmonic generation, we focused the pump laser 3 mm ahead of the gas target. The beam diameter is about 150 μm at the gas target with a diameter of 0.5 mm. The vertical distance between the focus and the nozzle exit is approximately 2 mm. In the experiment, the laser pulse energy is limited to 1~82 mJ, and the corresponding laser intensity at the gas target ranges from $1.2 \times 10^{14} \text{ W/cm}^2$ to $1.1 \times 10^{16} \text{ W/cm}^2$. The laser pulse energy was in-situ measured and the energy fluctuation was less than 5%. The gas target was provided by an electromagnetically driving vacuum valve. Argon and neon atoms are injected through the nozzle to the interaction region with the densities ranging from 10^{16} to 10^{19} cm^{-3} depending on the backing pressure. Every spectrum was obtained by averaging the signals over 300 shots and is not corrected for the spectral response of the detection system.

In Fig.1 we show two typical spectra obtained in argon with different pumping laser energies. The 55 mJ driving laser pulse induced harmonic signals are shown in the upper part of Fig.1. We could observe harmonic emission corresponding to the 91st order harmonic (8.6 nm). One can see an obvious decrease in the intensity of the harmonics beyond the 25th order. To exclude the possibility that the high frequency signal comes from the scattering lights of the intense low order harmonics, we reduced the laser intensity and found that the signal intensity of the higher order harmonics reduces rapidly and submerges into the noise while the intensity of the lower harmonics remains almost unchanged. It indicates that the signals beyond the 25th order harmonic are not from the scattered light of the lower order harmonics, since the intensity of the scattered light should vary with the laser intensity in the same way as the lower order harmonics do.

In the lower part of Fig.1 we show the harmonic spectrum obtained with 14 mJ laser pulse energy. The harmonic signals beyond the 21st order are very weak. Contrary to this, with the 55 mJ pulses, the harmonic signals beyond the 21st order are relatively strong and superimposed upon a rising background which is due to the response of the grating (blazing at 6.09 nm). Under the applied laser intensity which is high enough to ionize argon atoms, the argon atoms are ionized substantially and the ionized media may emit intense plasma radiation which might contribute to the signal corresponding to the high frequency region observed in our experiment. We have checked this point experimentally. We found that the signals corresponding to the very high order harmonics are reduced rapidly and disappear finally when we gradually move the detection system away from the optical axis by less than 10 mrad. It means that the short wavelength radiation is well collimated. This effect indicates that the plasma radiation is not the main origin of the

signal in the high frequency region, because the plasma should radiate in an isotropical pattern. All these facts reinforce our inference that the short-wavelength emission is due to the high-order harmonic radiation.

As far as we know, the highest harmonic order achieved experimentally in argon is the 65th, by using a Ti:sapphire laser of 150 fs at 794 nm [15]. In that experiment, the applied laser intensity was far above the saturation intensity for argon atoms, and the observed harmonic cutoff was well above the order described by the cut-off law of $I_P + 3.17U_P$. The authors attributed the observed high order harmonics to the harmonic generation from ions. Another experiment using a Ti:sapphire laser with a pulse duration of 26 fs demonstrated harmonic yields up to the 61st order in argon, which were attributed to the harmonic emission wholly from neutral argon atoms, because atoms can survive higher laser intensity for shorter laser pulses [17].



Harmonic Order

Fig. 1. The typical spectra of high order harmonics obtained in argon with 55 mJ and 14 mJ pumping laser energies

The spectrum shown in the upper part of Fig.1 was produced with the 55 mJ laser energy, corresponding to a peak intensity of about $6.9 \times 10^{15} \text{ W/cm}^2$. It is much higher than that required to produce the ions Ar^+ [16], and there should be a possibility that the high order harmonic radiation comes from ions. To check this point, it is necessary to determine the saturation intensity of argon for the 46 fs laser pulses. Following the method developed by B. Chang et al. [18] and assuming Ammosov-Delone-Krainov ionization rates [19], the saturation intensity for argon atoms is about $4.2 \times 10^{14} \text{ W/cm}^2$ for the 46 fs pulse in the experiment. The corresponding highest harmonic order that can be achieved in neutral argon atoms is about the 57th, which is well beneath the highest harmonics observed in our experiments.

When we reduce the laser intensity, the intensity of the very high order harmonic decreases rapidly and finally submerges into noise, while the intensity of the lower order harmonic remains almost unchanged, indicating a different laser intensity-dependence for the lower order harmonics and the higher order harmonics. Please see the well-resolved harmonics, e. g. order 23~29, which have an obviously different intensity-dependence from that of the lower order harmonics as shown in Fig.1. It is a reasonable inference that the higher order harmonics arise from the harmonic generation by argon ions. The sudden decrease in the intensity for harmonics beyond the 25th order can also be attributed to the contribution from the harmonics generated by the ions instead of the neutrals. One can find a similar feature in the published results [15].

In addition to achieve higher order harmonic radiation, another important subject concerning harmonic generation is how to increase the conversion efficiency of the generated harmonics. The conversion process depends on the interplay between the single atom response to the external laser, and the macroscopic propagation effects, i. e., phase matching effects. One factor should be stressed when one considers the effects of phase matching is the dispersion in nonlinear media [4], especially when laser intensity is sufficiently high to ionize the media and hence plasma is formed in the focal volume.

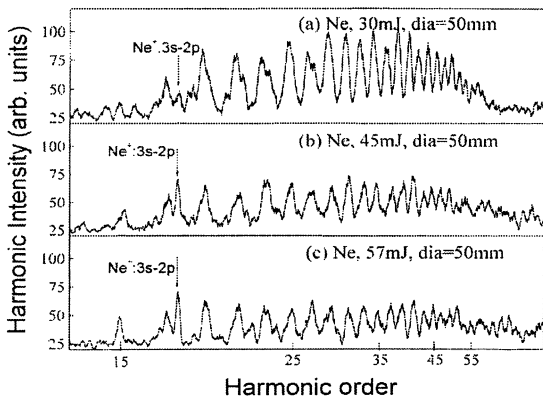


Fig. 2. The typical spectra of high order harmonics obtained in neon with different pumping laser energies.(a) 30 mJ. (b) 45 mJ. (c) 57 mJ

Figure 2 shows the harmonic spectra obtained in neon with different laser energies. An interesting feature is that the intensity of lower order harmonics decreases with the increase in laser intensity, differing from what higher order harmonics do. This can be related to the phase mismatching induced by the generated free electrons in this intensity regime. Phase mismatching induced by free electrons might dominate the process of harmonic generation,

and there have been extensive experimental and theoretical studies on this point [4]. One would expect that the harmonic radiation decreases with the increase in electron density. However, no investigation has been reported on how the intensity of harmonic radiation scales with the electron density. In our experiment, we found that in the observed spectra there appears a line in the vicinity of the 17th order harmonic in neon, as shown in Fig.2. After carefully checking its wavelength, we determined that this is a characteristic emission line of $\text{Ne}^+ : 3s - 2p$ at 44.7 nm and we found that with a definite laser intensity enough to ionize neon atoms, the intensity of this characteristic line depends linearly on the gas density. Since the $\text{Ne}^+ : 3s - 2p$ line is incoherent, there must be a linear dependence of this emission on the Ne^+ ion density or the electron density in the observed spectrum. This can be used to show the effects of phase mismatching due to the generated electrons on harmonic generation [16].

Figure 2 shows that the intensity of the $\text{Ne}^+ : 3s - 2p$ line increases with the laser intensity, which means that the generated electron density increases with the laser intensity. The intensity of the lower order harmonics, which is saturated in this intensity regime, is supposed to decrease due to the phase mismatching induced by the free electrons. It is consistent with the experiment results. However, the higher order harmonics do not saturate in this laser intensity regime and can still increase rapidly with the laser intensity as discussed above, which will partially cancel the effects of phase mismatching induced by the free electrons. This is clearly shown in Fig.2 and it excludes the possibility that the degenerated harmonic radiation is caused mainly by the decreased laser intensity due to the ionization-induced defocusing of the laser beam. Since the lower order harmonics (e.g., the 31st order) saturate at a lower incident laser intensity compared with the higher order harmonics (e.g., the 63rd order), if the decrease in the laser intensity causes the decrease in the lower order harmonic radiation, one would expect the higher order harmonics which are far from saturation compared to the low order harmonics at a fixed laser intensity will also decrease with the decreased laser intensity. Nevertheless, when the laser intensity is increased, the ionization-induced defocusing can only decrease the increment of the laser intensity in the interaction volume and can not decrease the intensity to the level before the incident laser intensity is increased. Another factor must be mentioned in the interpretation of the results shown in Fig.2. That is, the ionization may cause the depletion of the media, which also reduces the atomic density and hence the intensity of the lower order harmonics.

This is the first direct experimental evidence on how the harmonic generation scales with the electron density. However, the decrease in harmonic intensity resulting from the effects of free electrons would not be more than 1 order of magnitude [4]. This is proved to be true in our experiments, since the laser intensity used to obtain the spectra in Fig.2 is well above the saturation intensity for neon ($1.3 \times 10^{15} \text{ W/cm}^2$ for $\lambda = 785 \text{ nm}$ and $\tau = 45 \text{ fs}$),

which produces a considerable electron density. The results shown in Fig.2 also indicate that shorter laser pulses are more favorable for efficient harmonic generation. An atom has less probability to be ionized in shorter pulse excitation, this helps to suppress the depletion of the media and to reduce the phase mismatching and the laser beam defocusing induced by free electrons.

When the driving laser energy is increased further, we find some interesting phenomena again. Fig.3 shows that the spectral splitting of the harmonics in argon occurs when the laser energy is increased to 82 mJ/pulse from 6 mJ/pulse. The backing pressure in the gas nozzle is 0.25 MPa. The relative position of laser focus and the nozzle was the same as that mentioned above. There is no observable splitting when the laser energy is reduced to less than 55 mJ or when the relative position of laser focus and the nozzle is changed while keeping the laser energy as 82 mJ. These results indicate that the spectral splitting is related to the driving laser intensity and the propagation effects in ionized media. According the semi-classical physical explanation of high order harmonic generation [20], the origin of the spectral splitting in the harmonic peaks is the rapid ionization of the atoms and the strong intensity-dependence of the harmonic phase. The rapid change in laser intensity during one optical cycle in the rising edge of the laser pulse with a very high peak intensity is the main origin of the spectral splitting, the splitting is also influenced by the propagation of harmonics in ionized media.

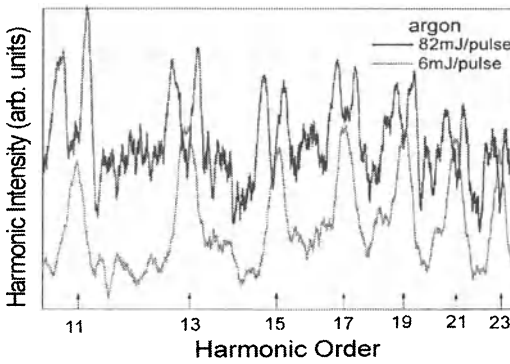


Fig. 3. The comparison of typical spectra of high order harmonics obtained in argon with different pumping laser energies, showing the spectral splitting of the harmonics

4 Ion Emission from Laser Heated Clusters

The research field of laser interaction with matter has extended in recent years from atoms, molecules and solids to clusters [21-24]. Atomic clusters bridge the gap between gaseous atoms, molecules and solids. Existing studies show that the large size atomic clusters can absorb laser energy much more efficiently than gaseous atoms, molecules and solids do. With clusters, one

can produce high temperature and highly charged plasmas which emit bright short-wavelength x-rays, hot electrons, energetic highly charged ions, and even neutrons. These then give rise to impacts on the studies in astronomy physics, plasma physics, inertial confinement fusion and the development of novel x-ray sources.

Most of the published results are so far concerning the x-ray emission, and the ionic energy spectra were measured mainly for Kr and Xe [21-24]. We report in this section the energy spectra of Ar ions ejected from Ar clusters irradiated by laser pulses with a peak intensity of about $2 \times 10^{16} \text{ W/cm}^2$ and a pulse duration of 46 fs. The details of the experimental setup can be found elsewhere [25]. In the experiments atomic clusters formed during the adiabatic expansion of Ar gas at high backing pressures into vacuum. The backing pressure was adjustable in the range of 0.6 to 4.5 MPa. The cluster size was measured to be about 3000 atoms per cluster at 2.0 MPa backing pressure in a separate Rayleigh scattering experiment. The cluster size at 4.5 MPa backing pressure was estimated to be over 10000 atoms per cluster. The details of the Rayleigh scattering measurement will be published elsewhere [26]. The ions emitted from the interaction area were detected by a time-of-flight (TOF) energy spectrometer with a micro-channel plate (MCP) detector. The ion energy was determined by the time-of-flight of ions. The output of the 10 Hz Ti:Sapphire laser is 20 mJ/46 fs in the experiments. The laser beam was focused onto the clusters 2 mm from the nozzle exit by an F/10 aspherical lens. The size of the focus was estimated to be 50 μm in diameter. This corresponds to a laser intensity of about $2 \times 10^{16} \text{ W/cm}^2$ at the focus.

Each spectrum was obtained by the accumulation for 500 shots. A typical energy spectrum of Ar ions at the backing pressure of 2.5 MPa is shown in Fig.4. The average energy $\langle E \rangle$ is about 15 KeV. We should point out that we have not made any correction in the ion energy spectrum to account for the variation in the detection efficiency for different ion energies.

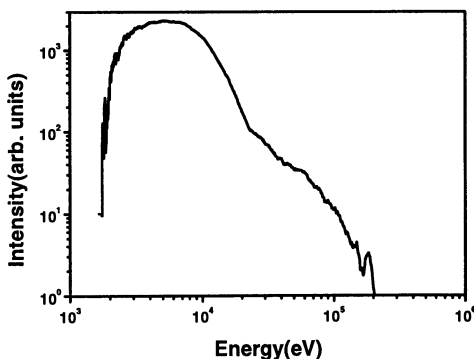


Fig. 4. A typical energy spectrum of Ar ions at the backing pressure of 2.5 MPa

The experimental results indicate that the interaction of Ar atomic clusters with ultra-short intense laser pulses was much more energetic than that of single atomic and small molecular gases and solids. The maximum and the average energies of Ar ions can be up to 0.2 MeV and 15 KeV, respectively. Ditmire et al. [22-25] reported that, at the same laser intensity as that in this experiment the maximum and the average energies of ions were 0.35 MeV and 28 KeV for Kr clusters at a backing pressure of 6 bar, and 1 MeV and 41 KeV for Xe clusters at a backing pressure of 5 bar, respectively. They also reported that the maximum and the average energies of Kr ions and Xe ions change slightly with the backing pressure. Our experimental results together with those of Ditmire et al. [22,23] indicated that the maximum and the average ion energies decreases with reducing atomic number, i.e. from Xe, Kr to Ar [25].

We have investigated the ionic energy spectra as a function of the driving laser intensity. Fig.5 shows the spectra of argon ions generated by laser pulses of different intensities ranging from 5×10^{15} to $6 \times 10^{16} \text{ W/cm}^2$ when the backing pressure is kept as 2.5 MPa. Argon clusters generated with the same backing pressure condition yield similar ionic energy distribution when the clusters are irradiated by the laser pulses of different intensities in this range. The ion yield increases with the laser intensity. When the laser intensity becomes higher than $6 \times 10^{16} \text{ W/cm}^2$, the ion yield almost saturates.

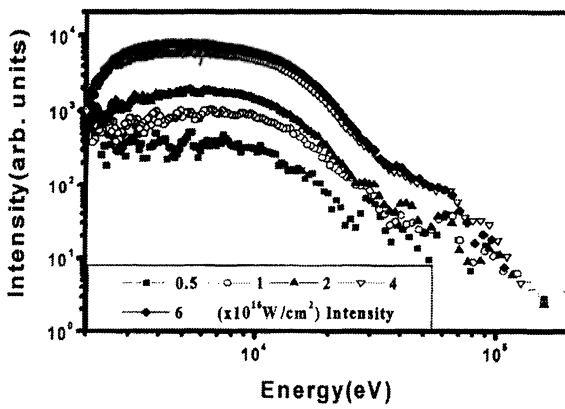


Fig. 5. The energy spectra of argon ions generated by laser pulses of different intensities ranging from 5×10^{15} to $6 \times 10^{16} \text{ W/cm}^2$ when the backing pressure is kept as 2.5 MPa

5 Conclusions

We have constructed a 5 TW/46 fs laser system capable of creating relativistic intensity for the research of high-field laser physics. We have observed the high order harmonic emission up to the 91st order in argon, which corresponds to a wavelength of 8.6 nm and is the highest harmonic order observed

in argon up to date. We have obtained for first time a direct experimental evidence of unfavorable effects of free electrons on harmonic generation. We have also observed for the first time the spectral splitting in the high order harmonic generation in argon. We have investigated the energy spectra of Ar ions ejected from intense femtosecond laser irradiated Ar atomic clusters. Under similar laser conditions, the maximum and average energies of the Ar ions from Ar clusters are lower than those of the Kr and Xe ions from Kr and Xe clusters, respectively.

Acknowledgment. This work is supported by the National Climb Project of China and the Major Fundamental Research Project of Chinese Academy of Sciences. The contributions of Prof. Z. Q. Zhang and Dr. X. D. Yang to some part of this work are highly appreciated.

References

1. M. D. Perry and G. Mourou: *Science* **269**, 917 (1994)
2. C. J. Joshi and P. B. Corkum: *Physics Today* Jan., 36 (1995)
3. D. Umstadter et al.: *Science* **273**, 472(1996)
4. M. Protopapas, C. H. Keitel, and P. L. Knight: *Rep. Prog. Phys.* **60**, 389 (1997), and references therein.
5. G. A. Mourou, C. P. J. Barty and M. D. Perry: *Physics Today* Jan., 22(1998)
6. E. Krausz, T. Brabec, M. Schnurer, and C.Spielmann: *Optics and Photonics News* July, 46 (1998)
7. D. Umstadter et al.: *Optics and Photonics News* July, 41 (1998)
8. C. Rouyer, N. Blanchot, N. Allais et al.: *J. Opt. Soc. Am. B* **13**, 55 (1996)
9. Ch. Spielmann et al.: *Science* **278**, 661 (1997)
10. A. Rundquist, C. G. Durfee III, Z. Chang et al.: *Sciences* **280**, 1412 (1998)
11. Z. Xu, L. Vigroux, F. Saviot et al.: *Science in Chinese(A)* **27**, 640 (1997)(in Chinese)
12. Y. Wang, X. Yang, Z. Zhang: *Acta Optica Sinica* **19**, 261(1999)
13. Z. Chang, A. Rundquist, H. Wang et al.: *Phys. Rev. Lett.* **79**, 2967 (1997)
14. S. G. Preston, A. Sanpera, M. Zepf et al.: *Phys. Rev. A* **53**, R31 (1996)
15. A. G. Wahlstrom, J. Larsson, A. Persson et al.: *Phys. Rev. A* **48**, 4709 (1993)
16. Z. Xu, Y. Wang, K. Zhai et al.: *Opt. Comm.* **158**, 89 (1998)
17. J. Zhou et al.: *Phys. Rev. Lett.* **76**, 752 (1996).
18. B. Chang, P. R. Bolton, and D. N. Fittinghoff: *Phys. Rev. A* **47**, 4193 (1993)
19. M. V. Ammosov, N. B. Delone, and V. P. Kranov: *Sov. Phys. JETP* **64**, 1191 (1986)
20. C. Kan, C. E. Capjack, and R. Rankin: *Phys. Rev. A* **52**, R4336(1995)
21. A. McPherson et al.: *Appl. Phys. B* **57**, 337 (1993)
22. T. Ditmire, J. W. G. Tisch, E. Springate et al.: *Nature* **386**, 54 (1997)
23. T. Ditmire, J. Zweiback, V. P. Yanovsky et al.: *Nature* **398**, 489 (1999)
24. M. Lezius, S. Dobosz, D. Normand et al.: *Phys. Rev. Lett.* **80**, 261 (1998)
25. Z. Li, A. Lei, G. Ni et al.: *Chin. Phys. Lett.* (in press)(1999)
26. A. Lei, G. Ni, Z. Li et al.: *Chin. Phys. Lett.* (submitted)(1999)

Spatial Electron Clouds at Fractional and Multiple Magneto-optical Resonances

Q. Su, R.E. Wagner, P.J. Peverly, R. Grobe

Intense Laser Physics Theory Unit and Department of Physics
Illinois State University, Normal, IL 61790-4560, USA
e-mail: qcsu@ilstu.edu

Abstract. We solve numerically the relativistic Liouville equation for the phase space density of an atom in a uniform static magnetic field and a laser field. If the cyclotron frequency that is associated with the magnetic field is tuned slightly above a multiple or a fraction of the frequency of the laser field, the electron's dynamics becomes resonant and its velocity can approach the speed of light. We compare the spatial electron distributions at these resonances with those obtained from the corresponding non-relativistic calculations and find the formation of stable ring-shaped distributions at the multiple resonances. The fractional resonances are characterized by figure-eight or propeller-shaped distributions.

One of the long term goals of our research work is to explore new phenomena that occur during the interaction of atoms with external fields in the high-speed regime in which dynamical relativistic effects become important. Our main interest is to investigate atomic dynamics that are both relativistic and quantum mechanical, e.g., phenomena that do not have a counterpart in relativistic classical mechanics. This task is from a theoretical point of view extremely challenging, as in the quantum relativistic regime there are only a very few non-perturbative exact solutions available [1] and one has to rely on numerical solutions to the time-dependent Dirac equation. Even though progress has been made in obtaining non-perturbative solutions for reduced dimensional systems in the last few years [2–5], our long term goal has not yet been achieved. Several new relativistic effects however were found in recent studies that do have classical counterparts when phase space density and correspondence principle are employed [6–10].

The natural spreading rate of a wave packet in the presence of intense static or alternating electro-magnetic fields when moving at a fraction of the speed of light, as an example, will be significantly suppressed in both the field as well as the perpendicular directions [6,7]. Classical phase space solution of the relativistic electron motion has confirmed the prediction of Dirac equation. The subnatural spreading has been related to the narrowing of velocity distribution due to the speed limit as well as due to the coupling between velocity components.

Recently, we have begun to explore the interaction of atoms in laser fields that are subjected to a static magnetic field [8–10]. The new dynamical fea-

tures that relativity can bring to the time evolution of the high-speed cyclotron motion of electrons has been demonstrated in a work by *Kim* and *Lee* [11]. They showed that chaotic signatures such as nonlinear resonances, stochastic layers near resonance separatrices, bifurcations of fixed points and reconnection phenomena can be associated with the interaction. We discovered that in addition to the well-known cyclotron resonance, there are additional resonances that can occur if the cyclotron frequency of the magnetic field is a multiple or a fraction of the laser frequency. Each of these resonances can accelerate the electron to velocities close to the speed of light thus requiring a fully relativistic treatment. The existence of these resonances is based on the nonlinearity due to the magnetic field component of the laser [9,10]. If the laser field is treated under the dipole approximation and the magnetic field component of the laser is neglected none of these resonances would be present.

To model the quantum mechanical distribution we have used a classical ensemble with a time-dependent phase space distribution $\rho(r, p, t)$. The initial state $\rho(r, p, t = 0)$ was chosen to crudely mimic the properties of the quantum mechanical ground state of a hydrogenic atom. To obtain the time evolution of the phase-space density, the relativistic Liouville equation [12] was solved numerically using a Monte-Carlo method:

$$\frac{\partial}{\partial t} \rho(r, p, t) = \sum_{i=1}^3 \left[\frac{\partial H}{\partial x_i} \frac{\partial}{\partial p_i} \rho(r, p, t) - \frac{\partial H}{\partial p_i} \frac{\partial}{\partial x_i} \rho(r, p, t) \right]. \quad (1)$$

In atomic units, the relativistic Hamilton function is given by

$$H = \sqrt{c^4 + c^2 \left[p + \frac{1}{c} A(r, t) \right]^2} + V(r) \quad (2)$$

with the Coulombic binding potential $V(r)$ and the vector potential

$$A(r, t) = -\frac{cE_0}{\omega_L} f\left(t - \frac{y}{c}\right) \sin(\omega_L t - ky) e_x + \frac{1}{2} (c\Omega e_z) \times r. \quad (3)$$

The cyclotron frequency Ω is the (scaled) magnetic field strength ($\Omega = B/c$). One (electric) atomic unit of Ω corresponds to a field strength of 1715 Tesla. The first part of the vector potential models the laser field with a pulse envelope $f(t - y/c)$, a frequency ω_L and a peak electric field strength E_0 . The static B-field is aligned in parallel to the laser's alternating magnetic field component.

The general solution of the Liouville equation can be written as

$$\rho(r, p, t) = \iint d^3 r_0 d^3 p_0 \rho(r_0, p_0, t = 0) \delta[r - r(r_0, p_0, t)] \delta[p - p(r_0, p_0, t)], \quad (4)$$

where the functions $r(r_0, p_0, t)$ and $p(r_0, p_0, t)$ denote single trajectory solutions to the corresponding Hamilton's equations with the initial conditions $r(r_0, p_0, t = 0) = r_0$ and $p(r_0, p_0, t = 0) = p_0$. Unfortunately, there are no known closed-form analytical solutions to either the relativistic or the non-relativistic problem. These trajectories can be obtained numerically from the equations of motion and need to be averaged according to the initial phase space density in order to obtain $\rho(r, p, t)$. In practice, the singular delta functions $\delta[\dots]$ can be replaced with narrow Gaussian functions, whose width is large enough to provide smooth densities but not too large to "wash out" important structures in the distribution.

The simultaneous interaction of the static magnetic field and the laser's alternating electric and magnetic fields can lead to a variety of resonances roughly characterized by the condition

$$M \Omega = N \omega_L \quad (5)$$

which brings M magnetic cycles and N laser cycles into resonance in a non-relativistic calculation. For a free electron, the resonance for $N = M = 1$ is, of course, related to the well-known cyclotron resonance that is exploited in synchro-cyclotron particle accelerators. Its surprising dynamical properties which lead to the formation of the so-called cycloatoms in the relativistic regime, have been described recently [10].

The occurrence of the resonances for other pairs of integers $(M, N) \neq (1, 1)$ can be directly associated with the magnetic field component of the laser. In the spirit of a perturbation theory let us investigate first a simple spiral-type (non-closed) orbit that has omitted the atomic potential, the magnetic field component of the laser, relativity and the smooth laser- turn on:

$$\begin{aligned} x^{(0)}(t) &= x_0 + \frac{V_{0x}}{\Omega} \sin(\Omega t) + \frac{V_{0y}}{\Omega} [\cos(\Omega t) - 1] \\ &\quad + F [\cos(\Omega t) - \cos(\omega_L t)], \\ y^{(0)}(t) &= y_0 + \frac{V_{0y}}{\Omega} \sin(\Omega t) - \frac{V_{0x}}{\Omega} [\cos(\Omega t) - 1] \\ &\quad + F \left[\sin(\Omega t) - \frac{\Omega}{\omega_L} \sin(\omega_L t) \right], \\ z^{(0)}(t) &= z_0 + V_{0z}t \end{aligned} \quad (6)$$

with the resonant amplitude $F = E_0/m(\omega_L^2 - \Omega^2)$. The solution $y^{(0)}(t)$ can be inserted back into the vector potential $A(r, t)$ from (3). This corresponds to replacing $\sin(\omega_L t - ky)$ by $\sin[\omega_L t - ky^{(0)}(t)] = \sin\{\omega_L t - F[\sin(\Omega t) - \Omega/\omega_L \sin(\omega_L t)]\}$, where for simplicity we have assumed $r_0 = p_0 = 0$. Using the Jacobi-Anger expansion for trigonometric functions in the exponent: $e^{ia \sin(t)} = \sum_{n=-\infty}^{\infty} J_n(a) e^{int}$, where $J_n(a)$ is the ordinary Bessel function of integer order, it can be seen that the electric field vector of the laser oscillates not just with ω_L but contains effectively various discrete frequencies $M\Omega + N\omega_L$ with an effective amplitude given by sums over Bessel functions.

We will now use the static magnetic field Ω to probe these discrete frequencies. The motion should become resonant if the cyclotron frequency ω_L is commensurate with the laser frequency ω_L as described by (5). To verify this hypothesis we have computed the electron's maximum velocity $\beta \equiv v/c$ during the interaction with the laser pulse and the static magnetic field and repeated these simulations for various magnetic field strengths Ω . Figure 1 proofs the existence of these resonances.

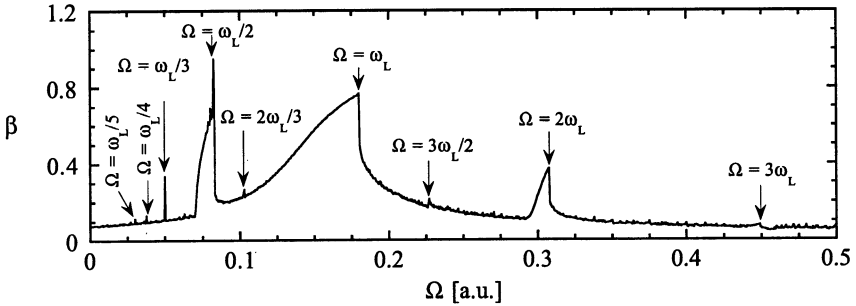


Fig. 1. The maximum speed of the atomic electron during the interaction as a function of the magnetic field strength Ω . The fractional resonances correspond to the peaks close to $\Omega = \omega_L/2$, $\Omega = \omega_L/3$, $\Omega = 3\omega_L/2$, and the multiple resonances are close to $\Omega = \omega_L$, $\Omega = 2\omega_L$, and $\Omega = 3\omega_L$... Parameters are $E_0 = 1.5$ a.u., $\omega_L = 0.15$ a.u., and pulse length is 600 cycles

The multiple resonances close to $\Omega = \omega_L$, $\Omega = 2\omega_L$, and $\Omega = 3\omega_L$ are clearly resolved. Even though with much less amplitude, some of the fractional resonances close to $\Omega = \omega_L/2$, $\Omega = \omega_L/3$ and $\Omega = 3\omega_L/2$ are present.

In Fig. 2 a and b we present the time-evolution of the spatial widths $\Delta x(t)$ of the electron distribution for the multiple resonance close to $\Omega = 3\omega_L$ and the fractional resonance close to $\Omega = \omega_L/3$. Both graphs are characterized by the several time scales, the laser frequency, the cyclotron frequency, the relative detuning between the frequencies and also a longer time scale that corresponds to the formation of steady states that are examined below in more detail. The lower lines were obtained from the corresponding calculation according to a non-relativistic theory but with the laser magnetic field included. The width remains very small, practically comparable to that of the initial state. Superimposed is only the breathing motion as described in more detail in [13].

Figure 3 a-c displays the final spatial probability density $\rho(x, y, t)$ in the x-y-plane for the multiple resonances $\Omega = N\omega_L$ for $N = 1, 2, 3$. Computer movies of the time evolution of the distribution function can be viewed in [14].

In each case the spatial probability density evolves into a ring-like structure in the plane that is perpendicular to the static magnetic field.

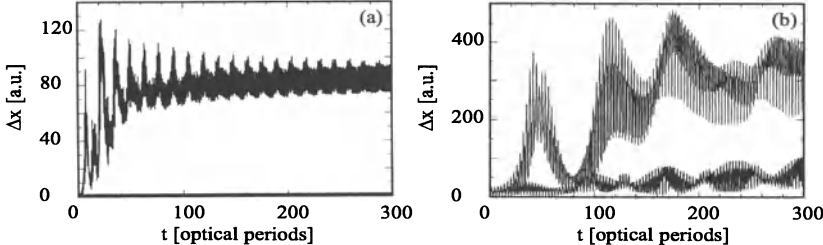


Fig. 2. The spatial width of the electron distribution $\Delta x(t)$ as a function of time at a multiple and fractional resonance. The lower line corresponds to the predictions according to a non-relativistic theory but with the laser magnetic field included. (a) multiple resonance at $\Omega \sim 3\omega_L$, $E_0 = 10$ a.u., $\Omega = 0.486$ a.u., $\omega_L = 0.15$ a.u. (b) fractional resonance at $\Omega \sim \omega_L/3$, $E_0 = 2.7$ a.u., $\Omega = 0.502$ a.u., $\omega_L = 0.15$ a.u.

The center of this steady state ring rotates around the nucleus with a frequency given by that of the laser. This genuinely relativistic effect can be attributed to a dephasing-mechanism (discussed in more detail in [9,10]) associated with velocity dependent cyclotron frequencies in the relativistic regime. The corresponding prediction of this model is shown in Fig. 3d.

For the fractional resonances ($\Omega \approx \omega_L/M$), however, much more complicated steady state distributions of a different type occur. In Fig. 3e and f we show snapshots of the spatial probability density $\rho(x, y, t)$ close to the $\Omega = \omega_L/2$ and $\Omega = \omega_L/3$ resonance. The formation of the steady state “figure eight” electron distribution in (e) and that of a three-leaf propeller in (f) is apparent. This steady state figure rotates around the nucleus with half and a third of the frequency of the laser which clearly is different from the time scale for rotation of the ring-shaped distribution found for the integer multiple resonances at $\Omega \approx N\omega_L$.

The figure-8 pattern discussed here should not be confused with the well-known [15] one from the motion of a free-electron in a electromagnetic plane wave laser field without any static magnetic field that can only be seen in the average rest frame drifting with the electron in the plane associated with the laser’s polarization and propagation direction.

Clearly much more work is needed to understand the details of the formation of the electron clouds. There is no hope to find any analytical solution to this system as relativity makes the dynamics non-integrable and even chaotic [11]. We have begun to analyze these clouds also from a quantum mechanical point of view. Another open question that has to be addressed in future work is to explore the relation of the formation of the steady state

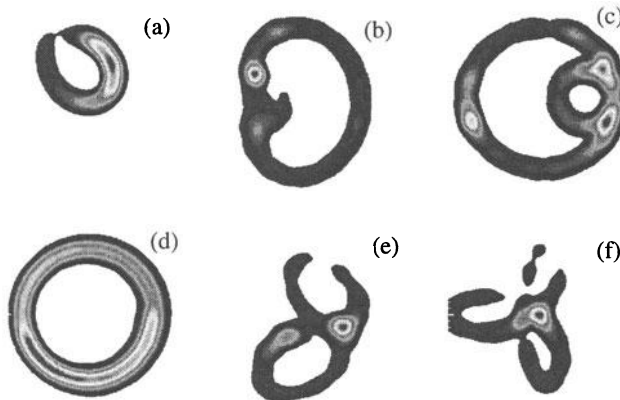


Fig. 3. The final steady state electron distribution in the x-y plane obtained from the numerical solution of the time-dependent relativistic Liouville equation. (a) resonance at $\Omega \sim \omega_L$, $E_0 = 1$ a.u., $\Omega = 0.174$ a.u., $\omega_L = 0.15$ a.u., $T = 1856$ a.u. (b) multiple resonance at $\Omega \sim 2\omega_L$, $E_0 = 5$ a.u., $\Omega = 0.32$ a.u., $\omega_L = 0.15$ a.u., $T = 4147$ a.u. (c) multiple resonance at $\Omega \sim 3\omega_L$, $E_0 = 10$ a.u., $\Omega = 0.486$ a.u., $\omega_L = 0.15$ a.u., $T = 3854$ a.u. (d) analytical solution based on the relativistic dephasing model. (e) fractional resonance at $\Omega \sim \omega_L/2$, $E_0 = 1.5$ a.u., $\Omega = 0.08$ a.u., $\omega_L = 0.15$ a.u., $T = 2090$ a.u. (f) fractional resonance at $\Omega \sim \omega_L/3$, $E_0 = 2.7$ a.u., $\Omega = 0.0502$ a.u., $\omega_L = 0.15$ a.u., $T = 7540$ a.u.

electron configuration and the emission of the high frequency light. One can easily show that charges that rotate along the same circular orbit can inhibit any scattering of light due to destructive interference. In our case, however, the steady state electron distributions in cycloatoms keep oscillating with the laser or cyclotron period. Obviously, more work is needed to identify the peak photon emission times with those characterizing the formation of the steady state electron clouds.

Acknowledgement. We acknowledge helpful conversations with M.V. Fedorov, C.C. Gerry, P. Krekora, R.F. Martin and H. Wanare. This work has been supported by the NSF under grant PHY-9970490. We acknowledge the support from ARO under the grant DAAD19-99-C-0032. We also acknowledge support from the Research Corporation for Cottrell Science Awards and ISU for URGs. REW and PJP thank the Illinois State University Undergraduate Honors Program for support of their research work. The numerical work has been performed at NCSA in Illinois.

References

1. V.G. Bagrov, D.M. Gitman, *Exact Solutions of Relativistic Wave Equations* (Kluwer Academic, Dordrecht 1990)

2. U.W. Rathe, C.H. Keitel, M. Protopapas, P.L. Knight, J. Phys. B **30**, L531 (1997)
3. N.J. Kylstra, A.M. Ermolaev, C.J. Joachain, J. Phys. B **30**, L449 (1997)
4. C. Szymanowski, C.H. Keitel, A. Maquet, Laser Phys. **9**, 133 (1999)
5. J.W. Braun, Q. Su, R. Grobe, Phys. Rev. A **59**, 604 (1999)
6. Q. Su, B.A. Smetanko, R. Grobe, Opt. Express **2**, 277 (1998)
7. Q. Su, B.A. Smetanko, R. Grobe, Laser Phys. **8**, 93 (1998)
8. R.E. Wagner, Q. Su, R. Grobe, Phys. Rev. A **60**, 3233 (1999)
9. P.J. Peverly, R.E. Wagner, Q. Su, R. Grobe, Laser Phys. (in press)
10. R.E. Wagner, Q. Su, R. Grobe, Phys. Rev. Lett. (submitted)
11. J.H. Kim, H.W. Lee, Phys. Rev. E **54**, 3461 (1996)
12. H. Goldstein, *Classical Mechanics*, 2nd ed. (Addison-Wesley, New York 1980)
13. J.C. Cseszneki, G.H. Rutherford, Q. Su, R. Grobe, Laser Phys. **9**, 41 (1999)
14. See several computer animations in <http://www.phy.ilstu.edu/ILP/>
15. J.H. Eberly, in Prog. Opt. **7** (North-Holland, Amsterdam 1969); E.S. Sarachik, G.T. Schappert, Phys. Rev. D **1**, 2738 (1970); J. Krüger, M. Bovyn, J. Phys. A **9**, 1841 (1976)

Aspect of Harmonic Generation from Solid Surface Plasma by Using Picosecond Laser

Hiroto Kuroda, Atsushi Ishizawa, Tsuneyuki Ozaki, Teruto Kanai

Institute for Solid State Physics, University of Tokyo, Minato-ku, Tokyo, Japan
e-mail:ishizawa@ludwig.issp.u-tokyo.ac.jp

Abstract. Investigations have been performed on harmonic generation from solid-vacuum interfaces using a prepulse-free 2.2 ps, 1054 nm laser pulse at maximum intensities of $\sim 2 \times 10^{17} \text{ W} \cdot \text{cm}^{-2}$. We observed, for the first time, that the divergence of harmonics decreases as the order of the harmonic increases when irradiated at the same pump intensity. We also measured that the third harmonics emission is more specular when using a shorter pulse. The harmonic intensities were stronger for p-polarized pump than s-polarized pumps. It has been found that the conversion efficiency of higher harmonic decreases gradually.

1 Introduction

Recent developments in generating ultra-high peak power lasers have made possible a new range of experiments on laser-matter interactions. High brightness, coherent XUV sources may eventually find application in such areas as ultrahigh resolution biological holography [1], plasma interferometry [2], and the probing of targets relevant to inertial confinement fusion [3]. Harmonics have been observed up to the 141st order of Nd:glass lasers(1053 nm) at 7.4 nm [4], the 109th order of Ti:sapphire lasers(800 nm) at 7.3 nm [5] and the 37th order of KrF lasers(249 nm) at 6.7 nm [6]. The wavelength region was recently extended into the water window (2.3-4.4 nm) using ultrashort 5 fs lasers [7].

In addition to harmonic generation from gas targets, there has recently been a renewal in interest in generating high order harmonic from the interaction of high intensity lasers with solids. First observation of high-order harmonics generated from solid surface plasmas was performed by Carman et al. back in 1981 [8,9]. In this experiment, up to the 46th harmonic was reported when a 1.0 ns pulse width, $10.6 \mu\text{m}$ wavelength CO₂ laser was used to irradiate a Cu target, at an intensity of $I\lambda^2 = 6 \times 10^{16} \text{ W} \cdot \text{cm}^{-2} \cdot \mu\text{m}^2$. A cutoff in the higher harmonics was also observed, which depends on the upper shelf density of the plasma. This cutoff was confirmed by a simple model proposed by Bezzerides [10], which seems to sufficiently explain experiments using nanosecond pump lasers.

However, simulations have shown that the situation is quite different for a picosecond pump [11-14]. S.C.Wilks et al. analyzed the harmonics generated by the $\mathbf{v} \times \mathbf{B}$ force experienced by electrons in a steep density profile [11]. The

calculated results by Gibbon suggest a smooth roll off in the harmonics, without a cutoff. It was suggested that the harmonic efficiencies for p-polarized light at 45° incidence can be mostly determined by $I\lambda^2$. Harmonic yield was one to two orders of magnitude stronger for p-polarized driving lasers, as compared with s-polarized ones [12]. These calculations, showing the lack of cutoff in the harmonic spectra, were supported by the detailed theoretical analysis of Lichten et al. [13]. However, when a density ramp was applied to their PIC simulations in a later work, a cutoff was again observed, but only for a very narrow region around a specific density scale length [14].

Several experiments have been reported on the observation of high-order harmonics from surface plasmas pumped by picosecond and femtosecond lasers[15]-[20]. In the first of a series of experiments performed by Kohlweyer et al., the high harmonics were measured using maximum laser intensities of $I\lambda^2 = 6 \times 10^{16} \text{ W} \cdot \text{cm}^{-2} \cdot \mu\text{m}^2$, and up to the 7th harmonic was observed using various targets [15]. Von der Linde et al. observed high-order harmonics up to the 15th by using a 130 fs pulse width, 800 nm wavelength Ti:sapphire laser system. In this experiment, both an optical flat coated with a 200 nm layer of Al and bare glass were used as targets, and the maximum pump intensity was $I\lambda^2 = 6 \times 10^{17} \text{ W} \cdot \text{cm}^{-2} \cdot \mu\text{m}^2$. In their experiment, a cutoff was observed which was in good agreement with the predictions of Bezzerides et al.. Harmonic generation occurred only for p-polarized laser pulses at oblique incidence, and s-polarized light was ineffective. Moreover, a smooth, approximately exponential roll-off of the higher harmonics was observed. From observations with the bare eye, conspicuous second harmonic emission was observed to be confined within a narrow cone in the specular direction [16] [17]. In the experiment by Földes et al., up to the third harmonic was reported by using a 700 fs pulse width, 248 nm wavelength KrF laser, which irradiated a plastic target at an intensity of $I\lambda^2 = 3 \times 10^{14} \text{ W} \cdot \text{cm}^{-2} \cdot \mu\text{m}^2$. In their result, no difference in harmonic emission was observed for s- and p-polarized pump lasers. They also observed that the third harmonic is confined within a narrow cone in the specular direction [20]. The results of Földes et al. and of von der Linde et al. agree in that the harmonics are confined in the specular direction, but disagree on the harmonic yield dependence on pump polarization. The observation of high-order harmonics generated from solid surface plasmas were also performed by Norreys et al. [18]. In this experiment, Norreys et al. found up to the 75th harmonics at 14.0 nm in the second-order diffraction. In their experiment, a 2.5 ps pulse width, 1053 nm wavelength Nd:glass laser system was used to irradiate a plastic target at an intensity of $I\lambda^2 = 1 \times 10^{19} \text{ W} \cdot \text{cm}^{-2} \cdot \mu\text{m}^2$. The harmonics generated in this experiment was found to be isotropic, differing from those reported by von der Linde et al. and Földes et al.. It is thought that this reason is due to Rayleigh-Taylor-like instability at the critical surface. No difference in the harmonic emission was observed between s- and p-polarizations, which agree with the result of Földes et al., but disagree with those of von der Linde et al.,

in which the harmonics were predominant for p-polarized pumps. Recently, Chambers et al. pointed out that the spectral bandwidth of the harmonic source was large and that they were observed to be isotropic at an intensity of $I\lambda^2 = 4 \times 10^{18} \text{ W} \cdot \text{cm}^{-2} \cdot \mu\text{m}^2$ [21]. It was also shown that with the use of an ultraviolet laser, there is a transition from specular to isotropic emission at $I\lambda^2 > 5 \times 10^{15} \text{ W} \cdot \text{cm}^{-2} \cdot \mu\text{m}^2$. However, this result disagrees with those of von der Linde et al., where specular emission has been observed for 130 fs pulses up to $I\lambda^2 = 6 \times 10^{17} \text{ W} \cdot \text{cm}^{-2} \cdot \mu\text{m}^2$. These various results with different pumps reveal a different tendency in the presence of cutoff, the efficiency dependence on pump polarization and pedestal, and on the divergence of the harmonics.

Although the experiment by Norreys et al. is impressive, it also made clear some problems when generating harmonics using Nd:glass lasers. One of the problems is the loss in the collimation of the harmonics. Another disagreement with simulations is that the polarization of the pump does not influence the conversion efficiency. In the present paper, we attempt to clarify the above characteristics of harmonic generation with Nd:glass lasers, using pump intensities where the effects of pre-plasma are negligible. We investigate the spatial distribution of the harmonic dependence on the intensity and the pulse width of the driving laser. We also measure the harmonic yield dependence on pump polarization and intensity, and the efficiency of the harmonic.

2 Experimental Setup

A detailed description of the experimental setup was published in [23]. In our experiment, a chirped pulse amplification (CPA) neodymium-doped phosphate glass (Nd:glass) laser system is used for the driving laser [24]. The CPA laser produces pulses of 2.2 ps duration and energies of about 1 J on the target at a wavelength of 1054 nm. The contrast ratio of the pedestal was measured to be better than 10^{-5} using an autocorrelator. The laser pulse is point focused onto the target set within a vacuum chamber by using a 100-mm focal length achromatic lens. The resulting divergence of the driving laser reflected from the target is 0.25 radian. The driving laser is p-polarized, and the incidence angle of the laser onto the deposited Al target is 75° , resulting in an oval spot with a dimension of $5 \mu\text{m} \times 19 \mu\text{m}$, and a maximum peak intensity of $2 \times 10^{17} \text{ W} \cdot \text{cm}^{-2}$. As a result of the laser irradiation, a plasma is produced on the Al target, and harmonics generated from the plasma surface are spectrally dispersed by a monochromator and detected using a fast rise time photomultiplier (Hamamatsu R2496, 0.7 ns rise time). A crystal depolarizer is placed just before the slit of the monochromator to eliminate any polarization dependence of the monochromator system. The temporal profile of the output signal of the photomultiplier is measured with a 1.5 GHz frequency bandwidth digital oscilloscope (Lecroy 9362).

3 Experimental Results

In our experiments, we measured the dependence of spatial distribution of harmonics on the pump intensity and pulse width of the driving laser, and conversion efficiency of harmonics.

3.1 The Spatial Distribution of Harmonics

Transverse Intensity Profile of the Harmonics. Chambers et al. [21] observed the two-dimensional image of the harmonic source at the peak pump intensity of $I\lambda^2 = 4 \times 10^{18} \text{ W} \cdot \text{cm}^{-2} \cdot \mu\text{m}^2$, which were found to be generated in an isotropic angle. However, there has been no example of an actual observation of the spatial distribution of the coherent harmonics and the divergence of the harmonic, dependence on the pump intensity. Therefore we quantitatively measured the spatial distribution of the harmonic and compared it with those for the driving laser.

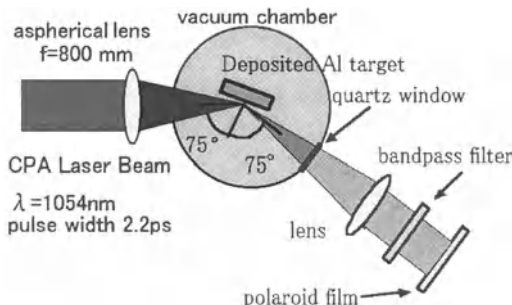


Fig. 1. Experimental arrangement for the observation of transverse intensity profile of the harmonics

The experimental setup is shown in Fig.1. In order to observe the transverse mode of the third harmonics, we used a bandpass filter to spectrally select the wavelength of interest, and recorded the intensity profile on a highly sensitive instant film (Polaroid 612). A lens was placed before the bandpass filter to collimate the harmonics and assure a uniform transmission within the clear aperture of the bandpass filter. We show in Fig.2 the image of the two-dimensional intensity distribution of the third harmonic obtained at a pumping intensity of $6 \times 10^{14} \text{ W} \cdot \text{cm}^{-2}$. One can see that the third harmonic is confined in a narrow cone in the specular direction. The elliptical shape of the third harmonic closely resembles the mode of the driving laser at the time of this experiment. In order to evaluate the divergence of the third harmonic, we moved the monochromator and the detector system along the horizontal

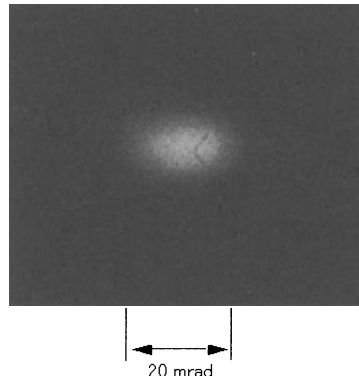


Fig. 2. The two-dimensional spatial distribution of the third harmonic recorded by an instant film

direction of Fig.2 to scan the image and obtain the two-dimensional spatial intensity profile.

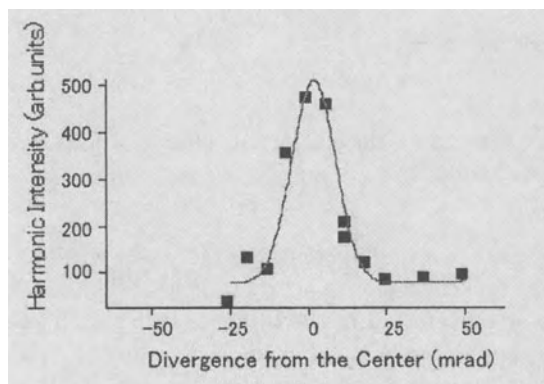


Fig. 3. The one-dimensional spatial intensity profile of the third harmonic. The solid line in the figure is the result of a least mean-squares fitting of the data to the Gaussian function. The evaluated divergence of 0.02 rad, is in good agreement with that of the driving laser.

The result is shown in Fig.3. The solid line in the figure represents a least mean-squares fitting of the data to the Gaussian function. Its full width at half-maximum, which is 0.02 rad, is consistent with that of the driving laser. The divergence of the second, fourth, and fifth harmonics have a similar divergence. These results suggest that the divergence of the harmonics is similar to that of the driving laser at pump intensities of $I\lambda^2 = 3 \times 10^{14} \sim 1 \times 10^{15} \text{ W} \cdot \text{cm}^{-2} \cdot \mu\text{m}^2$.

The Dependence of Spatial Distribution of Harmonics on the Intensity of the Driving Laser. Chambers et al. pointed out that the bandwidth of the harmonics were large and that they were observed to be isotropic at an intensity of $I\lambda^2 = 4 \times 10^{18} \text{ W} \cdot \text{cm}^{-2} \cdot \mu\text{m}^2$ [21]. It was also shown that with the use of an ultraviolet laser, there is a transition from specular to isotropic emission at $I\lambda^2 > 5 \times 10^{15} \text{ W} \cdot \text{cm}^{-2} \cdot \mu\text{m}^2$ [22]. However, this result disagrees with those of von der Linde et al., where specular emission has been observed for 130 fs pulses with intensities as high as $I\lambda^2 = 6 \times 10^{17} \text{ W} \cdot \text{cm}^{-2} \cdot \mu\text{m}^2$ [17]. The schematic diagram of the experimental arrangement is shown in Fig. 4.

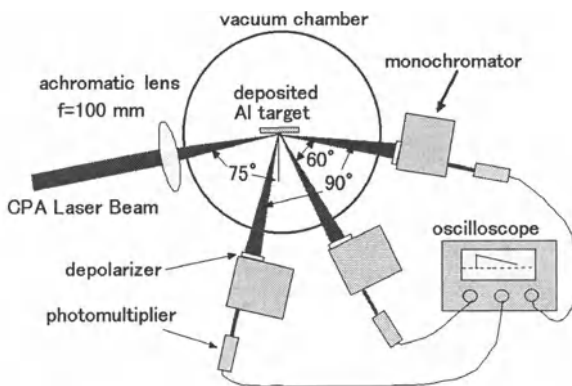


Fig. 4. Experimental setup for the spatial distribution of harmonics depending on the intensity of the driving laser

The laser pulse is point focused onto the target set within a vacuum chamber by using a 100-mm focal length achromatic lens. The resulting divergence of the driving laser reflected from the target is 0.25 rad. The driving laser is p-polarized, and the incidence angle of the laser onto the deposited Al target is 75°. The monochromometer is set up in the direction of 0°, 60°, or 90° from the specular direction. Fig. 5 shows the result of the divergence measurement for the third harmonics at driving laser intensities of (a) 3×10^{15} , (b) 6×10^{15} , (c) 9×10^{15} , and (d) $3 \times 10^{16} \text{ W} \cdot \text{cm}^{-2} \cdot \mu\text{m}^2$. We also show in the figure error bars corresponding to the standard deviation of the shot-to-shot variation in the harmonic intensity. The solid line in the figure represents a least mean-squares fitting of the data to the Gaussian function. As a result, it was found that the divergence of the third harmonic increases gradually with an increase in the driving laser intensity between $I\lambda^2 = 1 \times 10^{15}$ and $1 \times 10^{16} \text{ W} \cdot \text{cm}^{-2} \cdot \mu\text{m}^2$. At $I\lambda^2 = 2 \times 10^{17} \text{ W} \cdot \text{cm}^{-2} \cdot \mu\text{m}^2$, harmonic emission is nearly isotropic. The divergences of the other harmonics are also found to gradually increase. This result, which clearly shows the change in the harmonics from specular to non-specular emission occurring between 10^{15} and $10^{16} \text{ W} \cdot \text{cm}^{-2} \cdot \mu\text{m}^2$, is in agreement with those of Chambers et al. [22]. However, the gradual increase

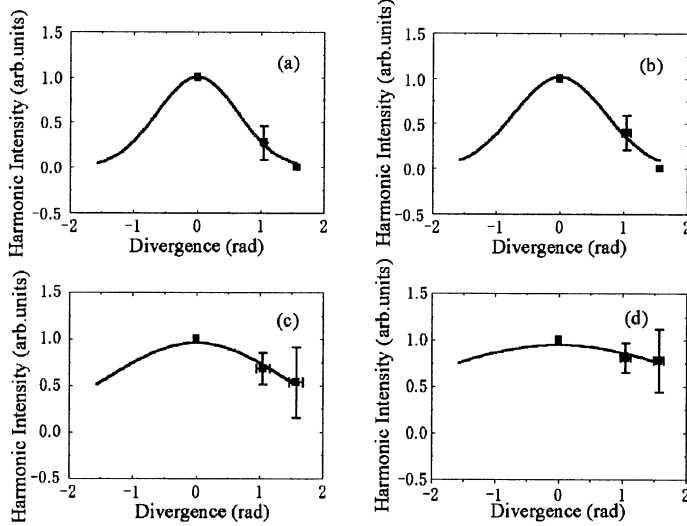


Fig. 5. The divergence of the third harmonics at intensities of (a) 3×10^{15} , (b) 6×10^{15} , (c) 9×10^{15} , and (d) $3 \times 10^{16} \text{W} \cdot \text{cm}^{-2} \cdot \mu\text{m}^2$.

in the divergence of the harmonics observed in the present work differs from their results, who predicted a sudden increase in the divergence at the intensity of $I\lambda^2 = 5 \times 10^{15} \text{W} \cdot \text{cm}^{-2} \cdot \mu\text{m}^2$. When the pump intensity is increased, the factor which causes the divergence of the harmonics to gradually increase is thought to be Rayleigh-Taylor-like instability at the critical surface [11]. At an intensity lower than $I\lambda^2 = 1 \times 10^{15} \text{W} \cdot \text{cm}^{-2} \cdot \mu\text{m}^2$, the harmonics are generated in the specular direction and the divergence is comparable to the driving laser because the plasma surface is still free from Rayleigh-Taylor-like instability and hole boring. The plasma surface will gradually show rippling when the pump intensity is increased. Consequently, the divergence of the harmonics becomes wider than the divergence of the driving laser. Furthermore, it is found that the higher the order of the harmonic is, the smaller the divergence of the harmonic becomes at the same intensity of the driving laser. This result is shown in Fig. 6 as the function of the number of the harmonic. For a Gaussian laser beam, the far-field intensity angular distribution can be written as

$$I(\theta) \propto \exp \left\{ -2 \left(\frac{\theta}{\theta_0} \right)^2 \right\}, \quad (1)$$

where θ_0 is the divergence of the driving laser. Under perturbative conditions, where $I_n \propto (I)^n$ the harmonic intensity would be given by

$$I_n(\theta) \propto \exp \left\{ -2 \left(\frac{\theta}{\theta_0 n^{-1/2}} \right)^2 \right\}, \quad (2)$$

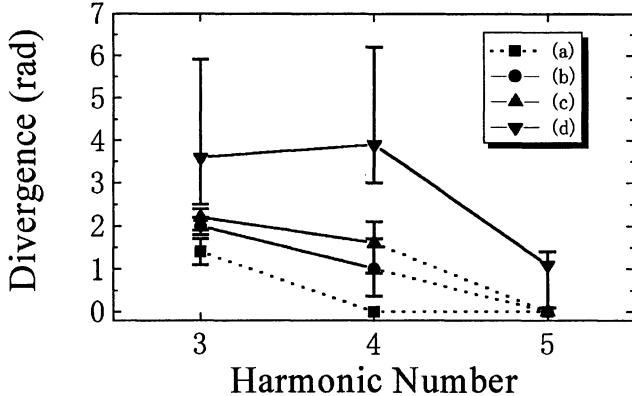


Fig. 6. The divergence of the harmonics as a function of harmonic number at intensities of (a) 2×10^{15} , (b) 6×10^{15} , (c) 8×10^{15} , and (d) $2 \times 10^{16} \text{W} \cdot \text{cm}^{-2} \cdot \mu\text{m}^2$.

with the divergence decreasing relatively weakly with harmonic order as $n^{-1/2}$ [25] [26]. However, the decrease in the divergence on the harmonic order shown in Fig.6 is larger than $n^{-1/2}$, which can be attributed to a dependence of I_n on I different from the perturbation theory.

The Spatial Distribution of Harmonics Depending on the Pulse Width of the Driving Laser. We investigate how the divergence of the harmonics depends on the pulse width of the driving laser. We compared the divergence of the harmonics generated using Nd:glass lasers with pulse width of 2.2 ps, described, above with those generated using 100 ps lasers. The typical energy of the 100 ps pulse is about 5 J, which is point focused onto the target set within a vacuum chamber by using an 800-mm focal length aspherical lens. The driving laser is p-polarized. The incidence angle of the laser onto the deposited Al target is 75° , resulting in an oval spot with a dimension of $56 \mu\text{m} \times 216 \mu\text{m}$, and a peak intensity of $6 \times 10^{14} \text{W} \cdot \text{cm}^{-2}$. The monochromometer is set up in the direction of 0° , 30° , or 60° from the specular direction, as in the experiments with the 2.2 ps lasers. This result is shown in Fig.7. In Fig. 7, we show the divergence of the third harmonics using a 100 ps master oscillator power amplifier (MOPA) Nd:glass laser pulse. We also show in the figure a typical error bar corresponding to the 99 % confidence interval. The solid line in the figure represents a least mean-squares fitting of the data to the Gaussian function. The full width at half-maximum of the divergence of the third harmonics, which is about 0.5 rad, is five times larger than that of the driving laser. We find that the third harmonics generated using 2.2 ps lasers have a divergence closer to specular emission compared with those using 100 ps pulse width lasers. Such tendency can be explained by the fact that the rippling based on Rayleigh-Taylor-like instability grows with time. Therefore, strong rippling of the plasma surface can develop for

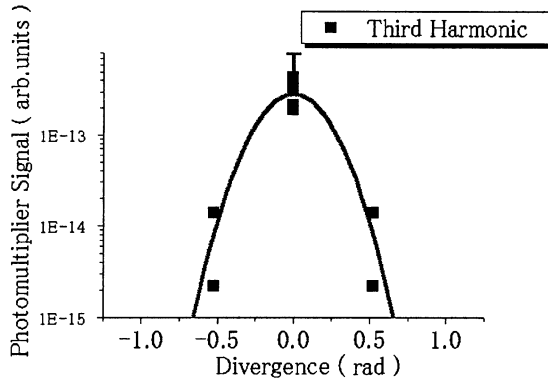


Fig. 7. The divergence of the third harmonics as the function of pump intensity at the intensity of $6 \times 10^{14} \text{W} \cdot \text{cm}^{-2} \cdot \mu\text{m}^2$ for a 100 ps laser pulse.

the longer pulses by the time the plasma interacts with the peak of the pulse. Therefore, one possibility to keep the harmonics collimated even at high intensities is to use driving lasers with shorter pulse width and with high contrast ratios. Futher discussions of this phenomena will require simulations using 2-dimensional PIC codes.

4 Harmonic Yield Dependence on Pump Polarization

Analysis [10] and simulation [12] shows that the efficiencies of the harmonics are stronger for p-polarized driving lasers, as compared with s-polarized ones. On the otherhand, various experimental results showed contradictions, with some results in agreement with theory [17], and some revealing no dependence in the harmonic yield with pump polarization. In our previous work, it is found that the harmonic intensities were strongest for p-polarized pump, and dropped to about 50 % in the case of s-polarized pumps [23]. This result is qualitatively in agreement with the simulations [10] [12], but are contradictory in that simulations predict p- polarization pumps to produce harmonics one to two orders stronger than for the s-polarization. One possible explanation to this disagreement is the effect of the Faraday rotation effect due to the influence of the spontaneous magnetic fields generated within the plasma [27]. Stamper et al. has measured a rotation angle of 22.5° for a linearly polarized $1.06 \mu\text{m}$, 100 ps laser pulse reflected from an Al slab target at a peak intensity of $1 \times 10^{15} \text{W} \cdot \text{cm}^{-2}$. This rotation angle corresponds to a magnetic field strength of 1.6 MG.

The Faraday rotation of the pump laser is investigated using the experimental arrangement shown in Fig.8. The driving laser is focused on an Al deposited target at an incidence angle of 75°. Laser light specularly reflected from the critical surface is thus centered at an angle of 150° to the incident beam. A 100-mm focal length convex lens was used to collimate the

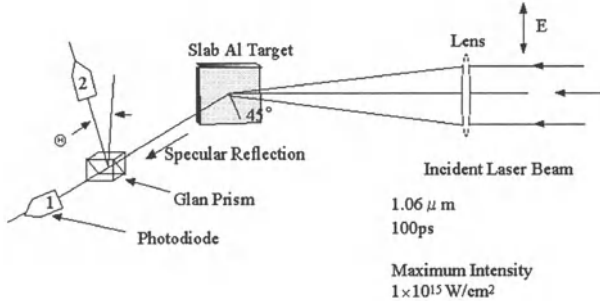


Fig. 8. Experimental arrangement in order to investigate the effect of Faraday rotation effect

driving laser and assure a uniform transmission within the clear aperture of the bandpass filter. A polarizing prism is set after the bandpass filter, and the intensity of each polarization component of the driving laser is measured with a polarizing prism. Each component of polarization is measured with a PIN photodiode equipped with an oscilloscope. The data are temporally integrated intensities, due to the shown response of the photodiode used. The experimental results are shown in Fig.9(a)(b). It is found that the polarization of the driving laser reflected from the target surface is not rotated. This can be attributed to the fact that at a few picosecond after the interaction, the spontaneous magnetic field is still too small to observe Faraday rotation[28][29]. At present, the cause for weak dependence of harmonic yield on pump polarization is not understood. It is therefore necessary to elucidate the cause of this contradiction between experimental and numerical results by performing further investigations.

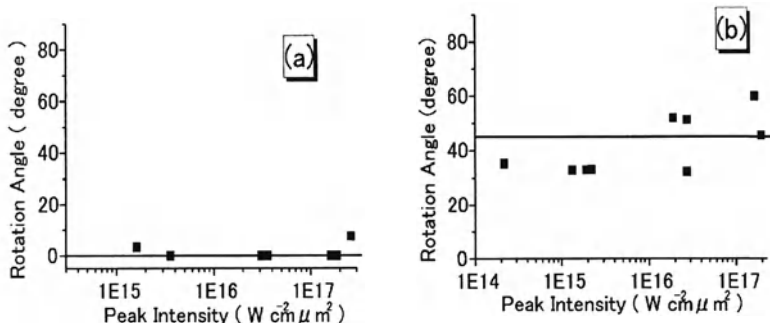


Fig. 9. (a) The rotation angle of the Glan prism is 0 degree. (b) The rotation angle of the Glan prism is 45 degree.

5 Harmonic Yield Dependence on Pump Intensity

The intensities of the third to the fifth harmonics are measured at various pumping laser intensities. We used p-polarized pumping laser for this measurement.

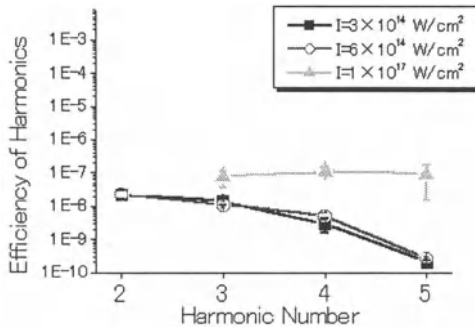


Fig. 10. The conversion efficiency $I_{m\omega}/I_\omega$ of the harmonics as a function of the harmonic order, for a peak pump intensity of $3 \times 10^{14} \text{ W} \cdot \text{cm}^{-2}$ (a), $6 \times 10^{14} \text{ W} \cdot \text{cm}^{-2}$ (b), and $(2 \times 10^{17} \text{ W} \cdot \text{cm}^{-2})$ (c)

In Fig.10, we plot the conversion efficiency $I_{m\omega}/I_\omega$ of the harmonics as a function of harmonic order m . At a peak pump intensity of $2 \times 10^{17} \text{ W} \cdot \text{cm}^{-2}$, the conversion efficiencies of the third and fifth harmonics are $(7.5 \pm 4.1) \times 10^{-8}$ and $(9.0 \pm 7.5) \times 10^{-8}$, respectively. The intensity ratio $I_{5\omega}/I_{3\omega}$ between the two harmonics are about similar. This is a relatively large ratio in comparison with the predicted value of about 0.05 from simulations for the same pump intensity [12]. These results show that the actual conversion efficiency does not closely follow scaling law derived from simulations.

6 Conclusion

We have systematically measured the divergence of harmonics up to the fifth order at 210.8 nm, produced by 2.2 ps duration Nd:glass lasers. It was found that the divergence of the harmonics starts to increase at intensities between $I\lambda^2 = 2 \times 10^{15}$ and $2 \times 10^{16} \text{ W} \cdot \text{cm}^{-2} \cdot \mu\text{m}^2$, depending on the harmonic number. We observed, for the first time, that the divergence of the harmonics decreases as the order of the harmonic increases when irradiated at the same pump intensity. We also measured that the third harmonics emission when using 2.2 ps pulse width for the driving laser is more specular than when using 100 ps pulse from a Nd:glass laser MOPA system. The intensity of

the harmonics were stronger for a p-polarized driving laser, than for an s-polarized one. At a driving laser intensity of $2 \times 10^{17} \text{ W} \cdot \text{cm}^{-2}$, the intensity ratio between the fifth and the third harmonics was found to be about similar. This intensity ratio is higher than that predicted by simulation [12].

Presently, we are performing experiments using double pulses to compare the results with those of the present work. Preliminary results shown that it is possible to generate harmonics much more efficiently if we can control the plasma density profile by double pulse.

References

1. R. A. London, M. S. Rosen, and J. E. Trebes, *Appl. Opt.* **28**, 3397–3404 (1989).
2. L. B. Da Silva, T. W. Barbee, Jr. R. Cauble, P. Celliers, D. Ciarlo, S. Libby, R. A. London, D. L. Matthews, S. Mrowka, J. C. Moreno, D. Ress, J. E. Trebes, A. S. Wan, and F. Weber, *Phys. Rev. Lett.* **74**, 3991–3994 (1995).
3. D. H. Kalantar, M. H. Key, L. B. Da Silva, S. G. Glendinning, J. P. Knauer, B. A. Remington, F. Weber, and S. V. Weber, *Phys. Rev. Lett.* **76**, 3574–3577 (1996).
4. M. D. Perry and G. Mourou, *Science* **264**, 917–924 (1994).
5. J. J. Macklin, J. D. Kmetec, and C. L. Gordon III, *Phys. Rev. Lett.* **70**, 766–769 (1993).
6. Y. Nagata, K. Midorikawa, M. Obara, and K. Toyoda, *Opt. Lett.* **21**, 15–17 (1996).
7. Ch. Spielmann, N. H. Burnett, S. Sartania, R. Koppitsch, M. Schnurer, C. Kan, M. Lenzner, P. Wobrauschek, and R. Krausz, *Science* **278**, 661–664 (1997).
8. R.L.Carman, D.W.Forslund, and J.M.Kindel, *Phys. Rev. Lett.* **46**, 29–32 (1981).
9. R.L.Carman, C.K.Rhodes, and R.F.Benjamin, *Phys.Rev.A.* **24**, 2649–2663 (1981).
10. B.Bezzerides, R.D.Jones, and D.W.Forslund, *Phys.Rev.Lett.* **49**, 202–205 (1982).
11. S. C. Wilks, W. L. Kruer, M. Tabak, and A. B. Langdon, *Phys. Rev.Lett.* **69**, 1383–1386 (1992).
12. P. Gibbon, *Phys.Rev.Lett.* **76**, 50–53 (1996).
13. R.Lichters, J.Meyer-ter-Vehn and A.Pukhov, *Phys.Plasmas* **3**(9) 3425–3437 (1996)
14. R.Lichters and J.Meyer-ter-Vehn, *Inst. Of Phys. Conf. Series* **154**, 221–230 (1997)
15. S. Kohlweyer, G. D. Tsakiris, G. -G. Wahlström, C. Tillman, and I. Mercer, *Opt. Commun.* **117**, 431–438 (1995).
16. D.von der Linde , T.Enger, and G.Jenke, *Phys.Rev.A.* **52**, R25–R27 (1995).
17. D.von der Linde, T.Enger, and G.Jenke, *SPIE* **2770**, 98–105 (1996).
18. P.A.Norreys, M.Zepf, S.Moustaizis, A.P.Fews, J.Zhang, P.Lee, M.Bakarezos, C.N.Danson, A.Dyson, P.Gibbon, P.Loukakos, D.Neely, F.N.Walsh, J.S.Wark, and A.E.Dangor, *Phys. Rev. Lett.* **76**, 1832–1835 (1996).
19. J.Zhang, M.Zepf, P.A.Norreys, A.E.Dangor, M.Bakarezos, C.N.Danson, A.Dyson, A.P.Fews, P.Gibbon, M.H.Key, P.Lee, P.Loukakos, S.Moustaizis, D.Neely, F.N.Walsh, and J.S.Wark, *Phys.Rev.Lett.* **54**, 1597–1603 (1996).

20. I.B.Földes, J.S.Bakos, G.Veres, Z.Bakonyi, T.Nagy, and S.Szatmári, IEEE J. Sel. Top. Quantum Electron. **2**, 776–781 (1996).
21. D. M. Chambers, S. G. Preston, M. Zepf, M. Castro-Colin, M. H. Key, J. S. Wark, A. E. Dangor, A. Dyson, D. Neely, and P. A. Norreys, J. Appl. Phys. **81**, 2055–2058 (1997)
22. D. M. Chambers, P. A. Norreys, A. E. Dangor, R. S. Marjoribanks, S. Moustaijis, D. Neely, S. G. Preston, J. S. Wark, I. Watts, M. Zepf, Opt Commun. **148**, 289–294 (1998).
23. A. Ishizawa, K. Inaba, T. Kanai, T. Ozaki, and H. Kuroda, IEEE J. Quantum Electron. **35**, 60–65, (1999).
24. J. Itatani, T. Kanai, T. Ozaki, and H. Kuroda, Prog. Cryst. Growth Charact. Mater. **33**, 281–284 (1996).
25. J. W. G. Tisch, R. A. Smith, M. Ciarrocca, J. E. Muffett, J. P. Marangos, and M. H. R. Hutchinson, J. Mod. Opt. **41**, 1163–1172 (1994).
26. C. de Lisio, C. Altucci, C. Beneduce, R. Bruzzese, F. De Filippo, S. Solimeno, M. Bellini, A. Tozzi, G. Tondello, and E. Pace, Opt Commun. **146**, 316–324 (1998).
27. J. A. Stamper and B. H. Ripin, Phys.Rev.Lett. **34**, 138–141(1975).
28. M. Borghesi, A. J. Mackinnon, R. Gaillard, and O. Willi, Phys.Rev.Lett. **80**, 5137–5140(1998).
29. M. Borghesi, A. J. Mackinnon, A. R. Bell, R. Gaillard, and O. Willi, Phys.Rev.Lett. **81**, 112–115(1998).

Generation of Short X-ray Pulse from Femtosecond Laser-Produced Plasma and its Application

Hidetoshi Nakano, Peixiang Lu, Tadashi Nishikawa, Naoshi Uesugi

NTT Basic Research Laboratories, 3-1 Morinosato Wakamiya, Atsugi, Kanagawa 243-0198, Japan
e-mail: hnakano@will.brl.ntt.co.jp

Abstract. X-ray emission properties of femtosecond laser-produced plasmas, especially, their dependence on the atomic numbers of target materials, are reported. The plasma emits an ultrashort x-ray pulse that is synchronized to a femtosecond laser pulse. Utilizing this feature, we demonstrate time-resolved soft x-ray absorption measurements of optically pumped silicon near its $L_{II,III}$ absorption edge by means of pump-probe spectroscopy. As a result, we observe more than a 10% increase in the absorption near the absorption edge caused by laser pulse irradiation, which means that the transition of core-electrons is rapidly modified by the excitation of valence electrons. The measured recovery time constant of this change is about 20 ps.

1 Introduction

High-density plasmas created near a solid surface by an intense femtosecond laser pulse have become more attractive for their potential use as ultrafast bright x-ray sources with the recent development of high-power ultrafast laser technologies [1–10]. These plasmas emit x-rays with ultrashort durations in the energy range from sub-keV to MeV. These x-rays not only have short duration, but also synchronize to the femtosecond laser pulse. These features are extremely important when the x-ray pulses are used as diagnostic probes to realize pump-probe-type experiments for observing dynamic response of materials pumped by ultrashort laser pulse on an atomic scale and with high temporal resolution. From this point of view, efforts have been made to demonstrate time-resolved diffraction [11,12] and absorption [13,14] measurements using femtosecond laser-produced plasma x-rays. To date, more attention has been paid to diffraction measurements, since x-ray diffraction provides direct information on atomic positions and molecular structure. However, x-ray absorption measurements are also important in material study. From the x-ray absorption spectrum, we can extract microscopic information on the material such as the electronic states of atoms, chemical bonds, and local structures. In addition, pump-probe absorption spectroscopy using short x-ray probe pulses is expected to be able to probe

the dynamics of core-electrons in optically pumped materials instead of that of valence electrons, which have been well studied by laser spectroscopy.

The first half of this paper describes x-ray emission properties of femtosecond laser-produced plasmas, especially, their dependence on atomic numbers of target materials. The latter half demonstrates time-resolved absorption measurements in soft x-ray region by means of pump-probe spectroscopy [15]. We observed the rapid absorption change induced by a femtosecond laser pulse irradiation in silicon membrane near its $L_{II,III}$ absorption edge for the first time.

2 X-ray emissions from metal plasma created by a femtosecond laser pulse

For practical use, intense x-ray pulses are needed. From this point of view, we tried several ways to improve the efficiency of conversion into x-rays. There are three basically approaches to improving conversion efficiency. One is modifying the conditions of the laser pulse to create plasma. Using a pre-pulse before the intense main pulse is the most powerful and controllable scheme [5,6,8,16–20] though there is some pulse broadening. Another way is choosing appropriate target materials or modifying them. Metals with higher Z , composite materials such as doped glasses [7,8,21], nano-structured targets [10,22–25] are examples. The other approach involves controlling the plasma. In this scheme, plasma confinement in grooved targets [26] has been reported. In this section, the x-ray emission properties from Al-plasma created by femtosecond laser pulses are reviewed and the dependence of the soft x-ray emission on the atomic number of the target materials will be described.

2.1 X-ray emissions from Al-plasma

The light source was a Ti:sapphire laser system that provides 100-fs optical pulses at the wavelength of 790 nm. The extinction ratio between the main pulse and undesirable satellite pulses that preceded the main pulse by more than 1 ns was better than 10^6 , which was high enough to ignore the influence of the satellites. The laser pulses were focused on the target at normal incidence with a 200-mm focal length MgF_2 lens. The spot size was about 30 μm , and the peak intensity was $1.6 \times 10^{16} \text{ W/cm}^2$. As a target, we used a 1- μm thick aluminum film deposited on a silicon wafer to avoid effects due to surface irregularities. The target was mounted on a motorized stage and scanned to expose a fresh surface for each laser shot. To measure soft x-rays in the sub-keV region, we used a grazing incidence flat-field spectrograph and a single-shot time-resolved spectrograph [6]. A spherically bent mica crystal ($2d = 1.994 \text{ nm}$) with a bending radius of 100 mm [27] was used to measure x-ray emission spectra in the keV region.

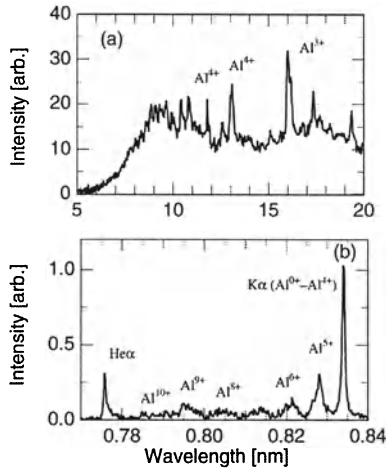


Fig. 1. X-ray spectra in (a) sub-keV and (b) keV regions emitted from Al-plasma created by a $1.6 \times 10^{16} \text{ W/cm}^2$, 100-fs laser pulse

Figure 1 shows time-integrated x-ray emission spectra in the sub-keV and keV regions. The unit of the vertical axis in Fig. 1(b) was of the order of 10^6 photons/Å sr/pulse. In both regions, one can find fine structures corresponding to line emissions, which are dominated by emissions from $\text{Al}^{0+} - \text{Al}^{5+}$, on broad continuum-like pedestals. We estimated the electron density of the plasma at emitting zone to be $8 \times 10^{22} \text{ cm}^{-3}$ ($\sim 45n_c$, where n_c is the critical electron density) from the intensity ratio among Li-like dielectric satellite lines. The efficiency of conversion into soft x-rays at a wavelength of 14 nm was measured to be $4 \times 10^{-4} \text{ %}/(\text{\AA sr})$ using a multi-layered mirror combined with a MCP detector.

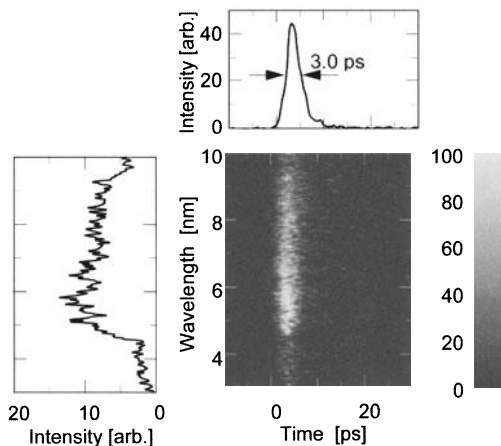


Fig. 2. Temporal evolution of x-rays in the sub-keV region emitted from Al plasma created by a femtosecond laser pulse with an intensity of $1.6 \times 10^{16} \text{ W/cm}^2$.

Figure 2 shows temporal evolution of soft x-ray emission in the sub-keV region. This result shows that soft x-ray emission at 4–10-nm wavelengths started almost simultaneously and lasted almost the same amount of time. The measured duration of the soft x-ray pulse was 3.0 ps, which is almost the instrumental limit.

2.2 Dependence of soft x-ray emissions atomic number of target

Figure 3 shows soft x-ray emission spectra from femtosecond laser-produced plasmas created on Si, Ti, Sn, and Au. In all cases, the intensity of the laser pulse on the target surface was $1.6 \times 10^{16} \text{ W/cm}^2$. With increasing atomic number of a target material, the emission spectrum becomes less structured, due to numerous transitions that give emissions in this range. Figure 4 shows the dependence of the conversion efficiency into soft x-rays

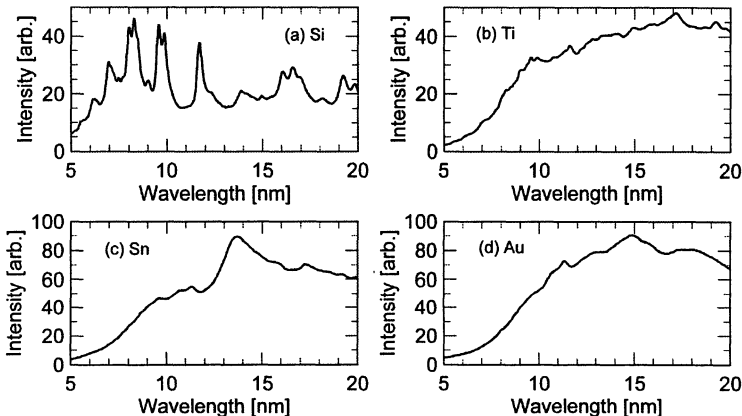


Fig. 3. Time-integrated spectra of soft x-rays in the sub-keV region emitted from (a) Si, (b) Ti, (c) Sn, and (d) Au. In all cases, the intensity of a femtosecond laser pulse was $1.6 \times 10^{16} \text{ W/cm}^2$.

on the atomic number of target materials. We measured conversion efficiencies at 8 and 14 nm using multi-layered mirrors combined with a microchannel plate (MCP) detector. In both cases, the efficiency increased gradually with some undulation as the atomic number increased. This trend is the same as that of ns-laser plasma x-rays [28]. The humps in Fig. 4 correspond to maximum emissivity for L -, M -, N -, and O -shell ions. Therefore, we can select the optimum target material providing intense x-ray emissions in the wavelength range suitable for the applications. For example, for x-ray absorption spectroscopy, broadband x-rays without fine structures are required. Therefore, we should choose a high- Z material as a target. The conversion efficiency into

14-nm soft x-ray was of the order of $10^{-3}\%$. For all materials, the duration of soft x-ray pulses was 3–10 ps, which is close to the instrumental limit. In the case of a broadened pulse, which was obtained at higher pumping intensity, particularly in higher- Z materials, soft x-ray emission at longer wavelength stayed a longer period of time.

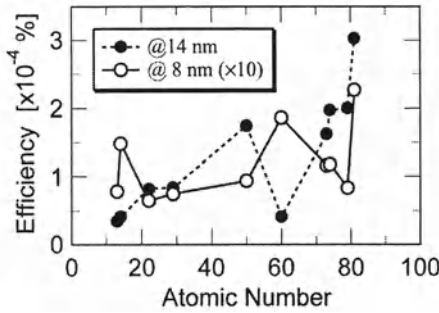


Fig. 4. Dependence of efficiency of conversion from a femtosecond laser pulse with an intensity of $1.6 \times 10^{16} \text{ W/cm}^2$ into soft x-rays on atomic number Z of target materials. Closed and open circles represent efficiencies into 14 nm and 8 nm, respectively.

3 Pump-probe spectroscopy in soft x-ray region

We carried out time-resolved measurement of soft x-ray absorption in optically pumped silicon membrane by means of pump-probe spectroscopy. The dynamic change in the $L_{II,III}$ absorption edge induced by a 100-fs laser pulse was probed by synchronized soft x-ray pulse from femtosecond laser-produced plasma. As shown in Fig. 5, the experiments were carried out using a 100-fs, 10-Hz Ti:sapphire laser system operating at a wavelength of 790 nm. The 50-mJ laser pulses were sent into a beam splitter, where 80% of the energy

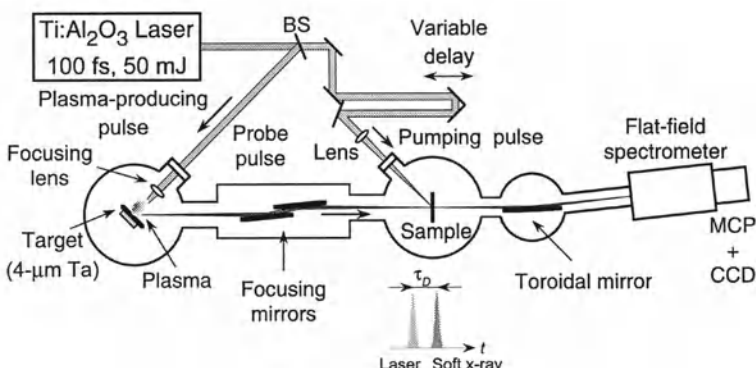


Fig. 5. Experimental setup for time-resolved soft x-ray absorption measurements by means of pump-probe spectroscopy.

was reflected. Reflected light was focused onto a flat target using a 200-mm focal length MgF₂ lens at normal incidence to generate broadband soft x-ray pulses. The intensity of the focused light was 1.5×10^{16} W/cm². We used a 4-μm-thick Ta film deposited on a Si wafer as a target, and scanned it to expose fresh surface for each laser shot. The emitted soft x-rays were focused by grazing-incidence concave mirrors onto a 100-nm-thick silicon membrane without any supporting structures. The sample was set on a pinhole with a diameter of 100 μm. Soft x-rays that passed through the sample were again focused onto the entrance slit of a flat-field grazing incidence spectrograph. The spectrograph had a ruled unequally-grooved grating with a nominal groove number of 1200 mm⁻¹. The soft x-rays (10–15 nm) were detected with a microchannel plate detector combined with a cooled CCD. The remaining 10 mJ of laser light was sent into an optical variable delay line and a variable attenuator, and then softly focused onto the sample by a 500-mm focal length lens. To ensure the spatial overlapping, the spot size of the focused laser beam was set at 5 mm in diameter. Incidence angles of soft x-ray and laser light to the sample were 0° and 45°, respectively. The estimated soft x-ray photon flux at the detector was 100–1000 photons/Å in each pulse. The spectral resolution of our setup is higher than 250 (in $\lambda/\Delta\lambda$) near 12 nm. Figure 6 shows the spectral and temporal characteristics of the soft x-ray

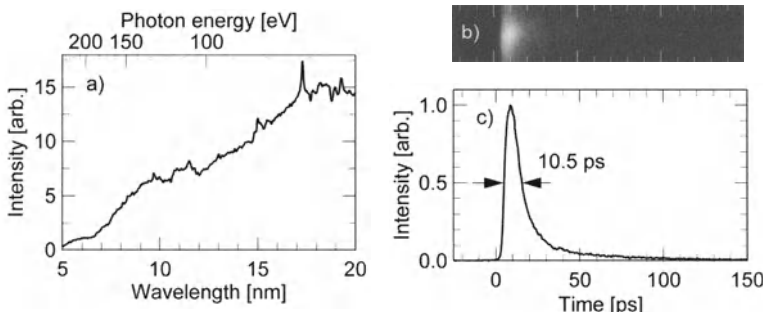


Fig. 6. Time-integrated spectrum (a), streak image (b), and line trace of the streak image (c) of the soft x-ray pulse emitted from Ta-plasma created by a 100-fs Ti:sapphire laser pulse. The intensity of the laser pulse on the Ta target was 3.2×10^{16} W/cm².

pulse used as a probe. The soft x-ray pulse duration was measured by an x-ray streak camera having a temporal resolution of 3 ps. This figure shows that the temporal resolution of our system is ~10 ps.

Figure 7 shows typical transmission spectra with and without laser pulse irradiation. In each curve, 45 shots were accumulated. In this case, the time interval between laser and soft x-ray pulses was almost 0. Curve a, the thick dotted one, shows the transmission spectrum when the pumping laser light

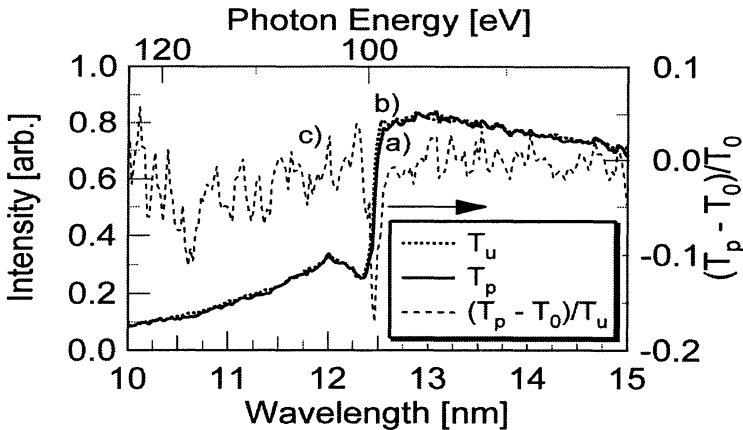


Fig. 7. Transmission spectra of the Si membrane near the $L_{II,III}$ absorption edge. Thick solid and dotted curves [(a) and (b)] represent transmission spectra observed with and without laser pulse irradiation, respectively. The thin broken curve (c) shows the differential transmission spectrum, which is included to show the difference induced by the femtosecond laser pulse irradiation. The intensity of the laser pulse on the Si membrane was $3 \times 10^{10} \text{ W/cm}^2$. To get each spectrum, 45 shots were accumulated.

was blocked. Curve b, the thick solid curve, was obtained when the sample was irradiated by a laser pulse with intensity of $3 \times 10^{10} \text{ W/cm}^2$, which was well below the damage threshold ($\sim 0.1 \text{ J/cm}^2$) [29]. The thin dotted curve, curve c, shows the normalized difference between curves a and b. The differential transmittance T_D is defined as $T_D = (T_p - T_u)/T_u$, where T_p and T_u represent the transmittance of the sample with and without laser pulse irradiation, respectively. Curve c shows that a significant change in transmittance only appeared near the $L_{II,III}$ absorption edge. The most significant dip in the differential transmittance appeared at 99.5 eV (12.46 nm), which corresponds to the energy difference between the $L_{II,III}$ level and the top of the valence band [30].

Figure 8(a) shows the differential transmission spectra at various time delays τ_D between pump and probe pulses when the intensity of the pump pulse was $3 \times 10^{10} \text{ W/cm}^2$. The delay step is 6.6 ps. At each step, 45 shots were accumulated. Change in transmission was observed only at the delay $-20 \text{ ps} < \tau_D < 10 \text{ ps}$. Here, τ_D represents the time delay of the arrival of the probe pulse at the sample surface. In obtaining these curves, we confirmed at each step that there was no big difference among transmission spectra measured without a pumping laser pulse. Therefore, we can exclude the possibility of irreversible processes induced by strong laser pulse irradiation on the sample, such as destruction. In Fig. 8(b), the depth of the dip in the differential transmission at 99.5 eV is plotted as a function of delay time τ_D .

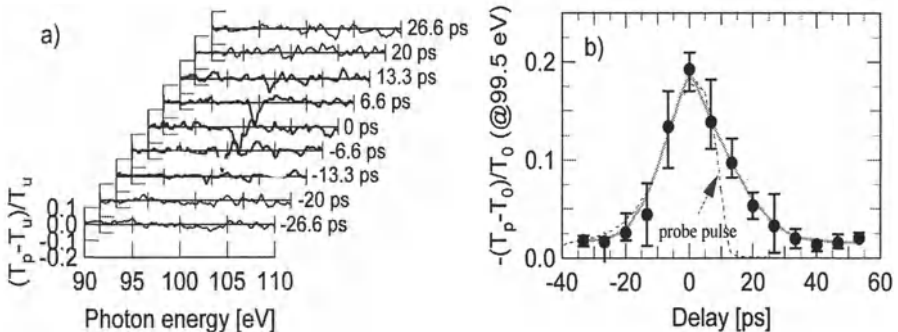


Fig. 8. (a) Differential transmission spectra of the Si membrane induced by laser pulse irradiation at various soft x-ray probe pulse delays. (b) Depth of differential transmission at 99.5 eV as a function of soft x-ray pulse delay time. The dotted curve represents the temporal profile of the soft x-ray probe pulse, which was observed with an x-ray streak camera. The intensity of the laser pulse on the Si membrane was $3 \times 10^{10} \text{ W/cm}^2$.

In this figure, the dependence of the relative increase in absorption on time delay at $\tau_D < 0$ ps fits the pulse shape of the soft x-ray within the error bars. This means that the absorption change built up almost instantaneously (< 10 ps). On the other hand, in the positive delay region, we can clearly see the recovery of the absorption change at 99.5 eV. By fitting this result to an exponential function, we obtained the recovery time constant of about 20 ps.

The most likely reason for the absorption change is a shift of the absorption edge. Since the $L_{II,III}$ absorption edge is sharp, a sharp dip near the absorption edge can appear in the differential transmittance if the edge shifts. We observed that the absorption edge shifted about 0.3 eV toward the lower energy side when the sample was pumped by a $3 \times 10^{10} \text{ W/cm}^2$ -laser pulse. The initial density of the photo-induced electron-hole plasma was estimated to be 10^{19} cm^{-3} , which is high enough to modify the band edge. It is well known that in highly excited semiconductors, the band edge shifts downward due to renormalization of the band energy [31]. Downer et al. observed the temporal evolution of absorption in the visible region modified by $2 \times 10^{11} \text{ W/cm}^2$ -laser pulse irradiation [32]. In their paper, the strong absorption change was reported to recover within tens of picoseconds. They concluded that the initial change was due to light absorption in high-density electron-hole plasma. In our case, the soft x-ray absorption change was observed within the period of electron-hole plasma decay time. When the high-density electron-hole plasma exists, the electronic structure of the silicon is modified. Therefore, the L-absorption edge corresponding to the ionization potential could have shifted when the plasma existed. Clarifying the origin of absorption change will require further studies.

4 Summary

In summary, femtosecond laser-produced plasmas are attractive ultrafast x-ray sources for time-resolved x-ray spectroscopy. They emit x-ray pulses in the energy range from sub-keV to keV with durations of less than 10 ps. By using a femtosecond laser-produced plasma x-ray, we demonstrated time-resolved soft x-ray absorption measurements of optically pumped silicon by means of pump-probe spectroscopy. As a result, we observed, for the first time, that more than 10% increase in soft x-ray absorption near the $L_{II,III}$ absorption edge in silicon was induced by irradiating with a $3 \times 10^{10} \text{ W/cm}^2$ femtosecond laser pulse. This absorption change recovered within about 20 ps. The origin of this absorption change is most likely an absorption edge downward shift related to the band gap renormalization due to the creation of high-density photo-induced electrons and holes.

Potential applications of ultrafast x-rays from femtosecond laser-produced plasmas include the study of the dynamics of core-electrons, photo-induced phase changes, and chemical changes in material.

References

1. M. Murnane, H. C. Kapteyn, S. P. Gordon, and R. W. Falcone, *Appl. Phys. B* **58**, 261 (1994).
2. J. C. Kieffer, M. Chaker, J. P. Matte, H. Pépin, C. Y. Côté, Y. Beaudoin, T. W. Johnston, C. Y. Chien, S. Coe, G. Mourou, and O. Peyrusse, *Phys. Fluids B* **5**, 2676 (1993),
3. J. D. Kmetec, C. L. Gordon III, J. J. Macklin, B. E. Lemoff, G. S. Brown, and S. E. Harris, *Phys. Rev. Lett.* **68**, 1572 (1992).
4. A. Rousse, P. Audebert, J. P. Geindre, F. Fallière, J. C. Gauthier, A. Mysyrowicz, G. Grillon, and A. Antonetti, *Phys. Rev. E* **50**, 2200 (1994).
5. D. Kühlke, U. Herpers, and D. von der Linde, *Appl. Phys. Lett.* **50**, 1785 (1989).
6. H. Nakano, T. Nishikawa, H. Ahn, and N. Uesugi, *Appl. Phys. Lett.* **69**, 2992 (1996).
7. H. Nakano, T. Nishikawa, and N. Uesugi, *Appl. Phys. Lett.* **70**, 16 (1997).
8. H. Nakano, T. Nishikawa, and N. Uesugi, *Appl. Phys. Lett.* **72**, 2208 (1998).
9. M. Yoshida, Y. Fujimoto, Y. Hironaka, K. G. Nakamura, H. Ohtani, H. Tsunemi, and K. Kondo, *Appl. Phys. Lett.* **73**, 2393 (1998).
10. T. Nishikawa, H. Nakano, N. Uesugi, and M. Nakao, in *CLEO/Pacific Rim '99*, (IEEE Log 99TH8464, 1999), pp. 39-40.
11. C. Rischel, A. Rousse, I. Uschmann, P.-A. Albouy, J.-P. Geindre, P. Audebert, J.-C. Gauthier, E. Förster, J.-L. Martin, and A. Antonetti, *Nature* **390**, 490 (1997).
12. T. Guo, C. R. Petrucci, R. Jimenez, F. Ráksi, J. Squier, B. Walker, K. R. Wilson, and C. P. J. Barty, *Proc. SPIE* **3157**, 84 (1997).
13. M. H. Sher, U. Mohideen, H. W. K. Tom, O. R. Wood II, G. D. Aumiller, R. R. Freeman, and T. J. McIlrath, *Opt. Lett.* **18**, 646 (1993).
14. J. Workman, M. Nantel, A. Maksimchuk, and D. Umstadter, *Appl. Phys. Lett.* **70**, 312 (1997).

15. H. Nakano, Y. Goto, P. Lu, T. Nishikawa, and N. Uesugi, in *Applications of High Field and Short Wavelength Sources VIII*, OSA Technical Digest (Optical Society of America, Washington DC, 1999), pp. 116-118. H. Nakano, Y. Goto, P. Lu, T. Nishikawa, and N. Uesugi, to be published in *Appl. Phys. Lett.* **75** (1999).
16. H. W. K. Tom and O. R. Wood, II, *Appl. Phys. Lett.* **54**, 517 (1989).
17. U. Teubner, G. Kühnle, and F. P. Schäfer, *Appl. Phys. B* **63**, 493 (1992).
18. J. C. Kieffer, M. Chaker, J. P. Matte, C. Y. Côté, Y. Beaudoïn, Z. M. Jiang, C. Y. Chien, S. Coe, G. Mourou, O. Peyrusse, and D. Gilles, *Proc. SPIE* **1860**, 127 (1993).
19. H. Nakano, T. Nishikawa, H. Ahn, and N. Uesugi, *Appl. Phys. B* **63**, 107 (1996).
20. H. Nakano, P. Lu, T. Nishikawa, and N. Uesugi, in *X-ray Lasers 1998*, edited by Y. Kato, K. Takuma, and H. Daido (IOP Publishing, Bristol, 1999), pp. 535-538.
21. H. Nakano, T. Nishikawa, and N. Uesugi, *Proc. SPIE* **3157**, 22 (1997).
22. S. P. Gordon, T. Donnelly, A. Sullivan, H. Hamster, and R. W. Falcone, *Opt. Lett.* **19**, 484 (1994).
23. C. Wülker, W. Theobald, D. R. Gnass, F. P. Schäfer, J. S. Bakos, R. Sauerbrey, S. P. Gordon, and R. W. Falcone, *Appl. Phys. Lett.* **68**, 1338 (1996).
24. T. Nishikawa, H. Nakano, H. Ahn, N. Uesugi, and T. Serikawa, *Appl. Phys. Lett.* **70**, 1653 (1997).
25. T. Nishikawa, H. Nakano, N. Uesugi, and T. Serikawa, *Appl. Phys. B* **66**, 567 (1998).
26. T. Nishikawa, H. Nakano, and N. Uesugi, in *X-ray Lasers 1998*, edited by Y. Kato, K. Takuma, and H. Daido (IOP Publishing, Bristol, 1999), pp. 539-542.
27. J. P. Geindre, P. Audebert, A. Rousse, J. C. Gauthier, A. Faenov, T. A. Pikuz, S. A. Pikz, and T. A. Shelkovenko, *Physica Scripta*, **53**, 645 (1996).
28. R. C. Spitzer, T. J. Orzechowski, D. W. Phillion, R. L. Kauffman, and C. Cerjan, *J. Appl. Phys.* **79**, 2251 (1996).
29. C. V. Shank, R. Yen, and C. Hirlimann, *Phys. Rev. Lett.* **50**, 454 (1983).
30. W. Eberhardt, G. Kalkhoffen, C. Kunz, D. Aspens, and M. Cardona, *Phys. Stat. Sol. (B)* **88**, 135 (1978).
31. I. Balslev, *Phys. Rev. B* **30**, 3203 (1984).
32. M. C. Downer and C. V. Shank, *Phys. Rev. Lett.* **56**, 761 (1986).

Multiple-Scattering Effects in the Second Harmonic Light Generated at Randomly Rough Metallic Interfaces

E. R. Méndez¹, M. Leyva-Lucero², T. A. Leskova³, A. A. Maradudin⁴

¹ División de Física Aplicada, Centro de Investigación Científica y de Educación Superior de Ensenada, Apartado Postal 2732, Ensenada, Baja California, 22800 México.

² Escuela de Ciencias Físico-Matemáticas, Universidad Autónoma de Sinaloa, Ciudad Universitaria, Culiacán, Sinaloa, 80000 México.

³ Institute of Spectroscopy, Russian Academy of Sciences, Troitsk 142092, Russia.

⁴ Department of Physics and Astronomy, and Institute for Surface and Interface Science, University of California, Irvine, California, 92717, U. S. A.

Abstract. We study theoretically the generation and scattering of second harmonic light at randomly rough metallic interfaces. For surfaces with relatively large roughness and slopes, we find that the angular distribution of the scattered light at the harmonic frequency displays well-defined minima in the backscattering direction, and show that this effect is due to destructive interference between waves that have been multiply scattered in the valleys of the surface. It is also shown that the complex amplitudes obtained at the frequency 2ω when the positions of the source and detector are exchanged exhibit some degree of anticorrelation.

1 Introduction

The multiple scattering of electromagnetic waves by random surfaces and disordered media has attracted much attention in recent years. An important consequence of multiple scattering is the appearance of coherent effects within the waves diffusely scattered by the medium. The enhanced backscattering phenomenon [1–14], which appears as a peak in the backscattering direction in the angular distribution of light scattered by a random medium, is the best known feature due to these effects but coherence effects are known to have other manifestations [15–18].

For randomly rough metallic surfaces, the multiple scattering that gives rise to the enhancement in the backscattering direction may contain processes that involve the excitation of surface polaritons [3,13,14] or the multiple scattering of volume waves [6,7,10]. The former is the main mechanism involved for the case of weakly rough surfaces, and the latter appears to be the dominant mechanism for the case of strongly rough surfaces.

The main ideas associated with these effects have also been applied to nonlinear optical phenomena in disordered media. In particular, it has been suggested that the second harmonic generation of light diffusely scattered by

a randomly rough metallic surface not only presents interesting features in the backscattering direction, but also in the direction normal to the mean surface [19]. Those predictions are based on a perturbative theory that applies only to weakly rough surfaces. Not surprisingly, surface polaritons play a prominent role in the formation of the predicted features, and it is known that the backscattering effects are due to the nonlinear excitation of surface polaritons at the second harmonic frequency (2ω). Subsequent work [20,21] has shown that, depending on the values of the phenomenological constants that describe the nonlinear interaction at the surface, it is possible to have peaks or dips in the backscattering direction. Apart from the fact that only dips (no peaks) have been observed in the experiments, these numerical calculations [20,21] are in qualitative agreement with the results reported by O'Donnell, Torre, and West [22].

More recently, O'Donnell and Torre [23] have reported measurements of the diffusely scattered second harmonic light from a strongly rough metal surface. Again, backscattering dips were observed, and a possible explanation for these features was put forward [23,24]. For surfaces as rough as the one used in that experimental work, the scattering problem cannot be treated by means of perturbation theory, and the multiple-scattering processes that give rise to the backscattering effects in the second harmonic angular scattering distribution are of a different nature from those occurring at weakly rough surfaces.

In the present work, we report rigorous numerical calculations of second harmonic generation at one-dimensional, strongly rough metal-vacuum interfaces. Our main objectives in this paper are to provide some insight into the physical processes that give rise to the observed backscattering effects and to study the correlation between the scattered amplitudes obtained when the source and detector are interchanged.

In Sect. 2, the theoretical approach is described in some detail. An inhomogeneous integral equation for the fundamental field (at the frequency ω) is obtained by the use of Green's second integral identity. To reduce the size of the computational problem, a local impedance boundary condition is employed, and the resulting integral equation is transformed into a matrix equation that is solved numerically for each of the several hundreds of realizations of the surface profile function, which are generated numerically and all possess the same Gaussian statistics and Gaussian power spectrum. For a given realization of the profile, the computed fundamental source functions (the field and its unnormalized normal derivative on the surface) are used to calculate the surface nonlinear boundary conditions at the frequency 2ω . These boundary conditions involve a jump discontinuity for the field and its normal derivative at the interface and are at the root of the generation of the second harmonic field. The inhomogeneous integral equation for the second harmonic field, obtained in the same manner but without the use of the impedance boundary condition, is solved for each of the same realizations of

the surface profile function. The contribution to the angular intensity distribution from the incoherent component of the generated second harmonic light is averaged over these realization of the surface profile.

The results are presented in Sect. 3, together with a discussion of the processes that give rise to the observed backscattering effects. Employing an iterative technique to solve the scattering equations at the fundamental frequency, it is shown that the backscattering dips in the angular distribution of the mean second harmonic intensity are due to destructive interference between waves that have been multiply scattered by the surface. Also in this section we present results for the angular amplitude correlations of the field. Finally, in Sect. 4, we present our conclusions.

2 Theoretical Formulation

The scattering system we consider is shown in Fig. 1. A monochromatic p-polarized plane wave, propagating in the (x_1, x_3) -plane, illuminates a one-dimensional interface defined by the surface profile function $\zeta(x_1)$. The incidence medium ($x_3 > \zeta(x_1)$) is vacuum, and the region $x_3 < \zeta(x_1)$ is assumed to be an isotropic and homogeneous material characterized by a frequency-dependent dielectric constant $\varepsilon(\omega)$ and some nonlinear parameters that are yet to be specified. Under these circumstances, only the x_2 component of the incident and scattered magnetic field at the fundamental frequency is nonzero. Here, we consider only the p-polarized component of the second

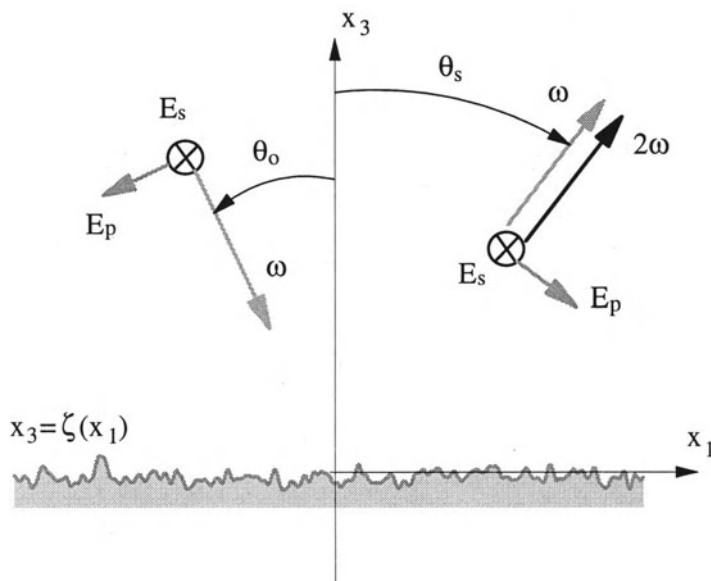


Fig. 1. Geometry of the scattering problem considered.

harmonic field, which constitutes the main contribution. It is assumed that the nonlinearities that give rise to the second harmonic field arise in a thin region in the vicinity of the interface. It is also implicit in our formulation of the problem that the second harmonic field, being small, has no influence on the fields or the scattering problem at the fundamental frequency. Then, the x_2 components of both the ω and 2ω fields satisfy Helmholtz equations above and below the interface. By applying Green's second integral theorem to these regions the following equations are established

$$\begin{aligned} H_2^>(\mathbf{R}|\Omega) &= H_0(\mathbf{R}|\Omega) + \\ &+ \frac{1}{4\pi} \int_{-\infty}^{\infty} dx'_1 \left\{ H_0^{(\Omega)}(\mathbf{R}|\mathbf{R}') H(x'_1|\Omega) - L_0^{(\Omega)}(\mathbf{R}|\mathbf{R}') L(x'_1|\Omega) \right\}, \end{aligned} \quad (1)$$

$$0 = \frac{1}{4\pi} \int_{-\infty}^{\infty} dx'_1 \left\{ H_\varepsilon^{(\Omega)}(\mathbf{R}|\mathbf{R}') H^<(x'_1|\Omega) - L_\varepsilon^{(\Omega)}(\mathbf{R}|\mathbf{R}') L^<(x'_1|\Omega) \right\}, \quad (2)$$

where it is understood that $H_2^>(\mathbf{R}|\Omega)$ represents the 2-component of the total magnetic field on a point $\mathbf{R} = (x_1, x_3)$ that lies above the surface, and $\mathbf{R}' = (x'_1, \zeta(x'_1))$ represents a point on the surface. In these expressions Ω stands for either ω or 2ω ,

$$H_{0,\varepsilon}^{(\Omega)}(\mathbf{R}|\mathbf{R}') = \frac{\partial}{\partial N'} G_{0,\varepsilon}^{(\Omega)}(\mathbf{R}|x'_1, x'_3) \Big|_{x'_3=\zeta(x'_1)}, \quad (3)$$

$$L_{0,\varepsilon}^{(\Omega)}(\mathbf{R}|\mathbf{R}') = G_{0,\varepsilon}^{(\Omega)}(\mathbf{R}|\mathbf{R}'), \quad (4)$$

with $\partial/\partial N = \phi(x_1)\partial/\partial n$, $\phi(x_1) = \sqrt{1 + (\zeta'(x_1))^2}$, and

$$H_0(\mathbf{R}|\Omega) = \begin{cases} H_2(\mathbf{R}|\omega)_{\text{inc}} & \text{if } \Omega = \omega \\ 0 & \text{if } \Omega = 2\omega \end{cases}. \quad (5)$$

The source functions $H(x_1|\Omega)$ and $L(x_1|\Omega)$ are defined by

$$H(x_1|\Omega) = H_2^>(\mathbf{R}|\Omega)|_{x_3=\zeta(x_1)}, \quad (6)$$

$$L(x_1|\Omega) = \frac{\partial}{\partial N} H_2^>(\mathbf{R}|\Omega)|_{x_3=\zeta(x_1)}, \quad (7)$$

with similar expressions for $H^<(x_1|\Omega)$, and $L^<(x_1|\Omega)$. The propagator functions $G_0^{(\Omega)}(\mathbf{R}|\mathbf{R}')$ and $G_\varepsilon^{(\Omega)}(\mathbf{R}|\mathbf{R}')$ represent, respectively, the Green's functions in vacuum or the metal at frequencies ω or 2ω . The incident field is represented by $H_2(\mathbf{R}|\omega)_{\text{inc}}$, and the scattered field in the vacuum region is given by the second term on the right hand side of Eq. (1).

By taking the limit as the point of observation approaches the surface from above, one can derive the following two equations

$$H(x_1|\Omega) = H_0(x_1|\Omega) + \frac{1}{4\pi} \lim_{|\eta| \rightarrow 0+} \int_{-\infty}^{\infty} dx'_1 \left\{ H_0^{(\Omega)}(\mathbf{R} + \boldsymbol{\eta}|\mathbf{R}') H(x'_1|\Omega) - L_0^{(\Omega)}(\mathbf{R} + \boldsymbol{\eta}|\mathbf{R}') L(x'_1|\Omega) \right\}, \quad (8)$$

$$0 = -\frac{1}{4\pi} \lim_{|\eta| \rightarrow 0+} \int_{-\infty}^{\infty} dx'_1 \left\{ H_{\varepsilon}^{(\Omega)}(\mathbf{R} + \boldsymbol{\eta}|\mathbf{R}') H^<(x'_1|\Omega) - L_{\varepsilon}^{(\Omega)}(\mathbf{R} + \boldsymbol{\eta}|\mathbf{R}') L^<(x'_1|\Omega) \right\}, \quad (9)$$

where $H_0(x_1|\Omega) = H_0(\mathbf{R}|\Omega)|_{x_3=\zeta(x_1)}$ and $\boldsymbol{\eta}$ is a vector in the x_3 direction. These equations provide the starting point for the calculations that lead to the determination of the source functions. We now proceed with the treatment of the fields at ω and 2ω separately.

2.1 The Linear Scattering Equations

From the continuity of the tangential components of the fields across the interface we have that

$$H(x_1|\omega) - H^<(x_1|\omega) = 0, \quad (10)$$

$$L(x_1|\omega) - \frac{1}{\varepsilon^<(\omega)} L^<(x_1|\omega) = 0. \quad (11)$$

These continuity conditions couple Eqs. (8) and (9), which we can now write as

$$H(x_1|\omega) = H(x_1|\omega)_{\text{inc}} + \frac{1}{4\pi} \lim_{|\eta| \rightarrow 0+} \int_{-\infty}^{\infty} dx'_1 \left\{ H_0^{(\omega)}(\mathbf{R} + \boldsymbol{\eta}|\mathbf{R}') H(x'_1|\omega) - L_0^{(\omega)}(\mathbf{R} + \boldsymbol{\eta}|\mathbf{R}') L(x'_1|\omega) \right\}, \quad (12)$$

$$0 = -\frac{1}{4\pi} \lim_{|\eta| \rightarrow 0+} \int_{-\infty}^{\infty} dx'_1 \left\{ H_{\varepsilon}^{(\omega)}(\mathbf{R} + \boldsymbol{\eta}|\mathbf{R}') H(x'_1|\omega) - \varepsilon(\omega) L_{\varepsilon}^{(\omega)}(\mathbf{R} + \boldsymbol{\eta}|\mathbf{R}') L(x'_1|\omega) \right\}. \quad (13)$$

These two coupled integral equations can be converted into matrix equations by the following procedure. The infinite range of integration is truncated

to the finite range $(-L/2, L/2)$, and this length L is divided into N equal intervals of length $\Delta x = L/N$. Finally, the method of moments is used to obtain equations for the values of $H(x_1|\omega)$ and $L(x_1|\omega)$ at the midpoints x_n of these intervals, where $x_n = -L/2 + (n - 0.5)\Delta x$, with $n = 1, 2, \dots, N$. The resulting matrix equations can be written as [10]

$$H(x_m|\omega)_{\text{inc}} = \sum_{n=1}^N \left[\left(\frac{1}{2}\delta_{nm} - \frac{1}{2}\mathcal{H}_{mn}^{(0)} \right) H(x_n|\omega) + \frac{1}{2}\mathcal{L}_{mn}^{(0)} L(x_n|\omega) \right], \quad (14)$$

$$0 = \sum_{n=1}^N \left[\left(\frac{1}{2}\delta_{nm} + \frac{1}{2}\mathcal{H}_{mn}^{(\varepsilon)} \right) H(x_n|\omega) - \varepsilon(\omega) \frac{1}{2}\mathcal{L}_{mn}^{(\varepsilon)} L(x_n|\omega) \right]. \quad (15)$$

Explicit expressions for the matrix elements $\mathcal{H}_{mn}^{(0,\varepsilon)}$ and $\mathcal{L}_{mn}^{(0,\varepsilon)}$ are given in [10]. The source functions $H(x_n|\omega)$ and $L(x_n|\omega)$ can be determined from these equations using standard numerical techniques. To simplify the calculations, however, we use a local impedance boundary condition to relate the two source functions at frequency ω . We have that

$$L(x_1|\omega) = \frac{K^{(0)}(x_1|\omega)}{\varepsilon(\omega)} H(x_1|\omega). \quad (16)$$

The function $K^{(0)}(x_1|\omega)$ is given as an expansion in powers of the product of the skin depth of the metal $d(\omega)$ and the second derivative of the surface profile function [25],

$$K^{(0)}(x_1|\omega) = \frac{\phi(x_1)}{d(\omega)} \left\{ 1 + \frac{d(\omega)}{2} \frac{\zeta''(x_1)}{\phi^3(x_1)} - \frac{d^2(\omega)}{8} \frac{[\zeta''(x_1)]^2}{\phi^6(x_1)} + \dots \right\}, \quad (17)$$

with

$$d(\omega) = \frac{c}{\omega\sqrt{-\varepsilon(\omega)}}. \quad (18)$$

The impedance boundary condition is known to represent a good approximation for the case of highly reflecting metals [26,27] and has been used successfully in recent numerical work [27,28]. This approximation makes Eq. (15) redundant, simplifying the numerical problem. For plane wave illumination, the differential reflection coefficient (the fraction of the total incident power on the surface that is scattered per unit angle) is given by

$$\frac{\partial R_p(\theta_s|\omega)}{\partial \theta_s} = \frac{|r_p(\theta_s|\omega)|^2}{8\pi (\omega/c) L \cos \theta_0}, \quad (19)$$

where the scattering amplitude is given by

$$r_p(\theta_s|\omega) = \int_{-\infty}^{\infty} dx_1 \left[i\frac{\omega}{c} [\zeta'(x_1) \sin \theta_s - \cos \theta_s] - \frac{K^{(0)}(x_1|\omega)}{\varepsilon(\omega)} \right] \times \\ \times H(x_1|\omega) \exp \left\{ -i\frac{\omega}{c} (x_1 \sin \theta_s + \zeta(x_1) \cos \theta_s) \right\}. \quad (20)$$

In these expressions, θ_0 is the angle of incidence and θ_s the angle of scattering.

2.2 The Scattering Equations at 2ω

It is well known that homogeneous and isotropic metals have inversion symmetry and, thus, the dipole contribution to the bulk nonlinear polarization is absent. The presence of the interface breaks the inversion symmetry and provides the necessary elements to generate a large optical nonlinearity. Both, the electromagnetic fields and the material constants vary rapidly across the interface. The second harmonic radiation we calculate is generated in a thin layer that surrounds the metal-vacuum interface, while the contribution due to the bulk is neglected. Although the nonlinear layer has finite thickness on the microscopic scale, it can be assumed to be infinitely thin. Then, its effects can be accounted for in the boundary conditions for the fields at 2ω . In our formulation, then, the fields are discontinuous across the nonlinear interface layer and the strength of the discontinuity is determined by the nonlinear polarization. Integrating Maxwell's equations across the interface, one can write the nonlinear boundary conditions at a rough metal surface in the form

$$H_2^>(x_t, 0) - H_2^<(x_t, 0) = \frac{2i\omega}{c} 4\pi \lim_{\delta \rightarrow 0} \int_{-\delta}^{\delta} dx_n P_t(x_t, x_n), \quad (21)$$

$$E_t^>(x_t, 0) - E_t^<(x_t, 0) = -4\pi \frac{\partial}{\partial x_t} \lim_{\delta \rightarrow 0} \int_{-\delta}^{\delta} dx_n \frac{P_n(x_t, x_n)}{\varepsilon(2\omega, x_n)}, \quad (22)$$

where we are using a local coordinate system (x_t, x_n) , and the subscripts t and n denote components that are tangential and normal to the local surface, respectively. These equations express the nonlinear boundary conditions in terms of the nonlinear polarization. As δ tends to zero, only the singular parts of the nonlinear polarization will give nonzero contributions to the integrals.

We can then write the relation between the source functions above and below the interface as follows

$$H(x_1|2\omega) - H^<(x_1|2\omega) = A(x_1), \quad (23)$$

$$L(x_1|2\omega) - \frac{1}{\varepsilon(2\omega)} L^<(x_1|2\omega) = B(x_1), \quad (24)$$

where the functions $A(x_1)$ and $B(x_1)$ can be obtained from Eqs. (21) and (22) and are yet to be specified. These expressions provide the required coupling between Eqs. (8) and (9). Then, we can write

$$\begin{aligned} H(x_1|2\omega) = & \frac{1}{4\pi} \lim_{|\eta| \rightarrow 0+} \int_{-\infty}^{\infty} dx'_1 \left\{ H_0^{(2\omega)}(\mathbf{R} + \eta|\mathbf{R}') H(x'_1|2\omega) - \right. \\ & \left. - L_0^{(2\omega)}(\mathbf{R} + \eta|\mathbf{R}') L(x'_1|2\omega) \right\}, \end{aligned} \quad (25)$$

$$0 = \frac{1}{4\pi} \lim_{|\boldsymbol{\eta}| \rightarrow 0+} \int_{-\infty}^{\infty} dx'_1 \left\{ H_{\varepsilon}^{(2\omega)}(\boldsymbol{R} + \boldsymbol{\eta}|\boldsymbol{R}') [H(x'_1|2\omega) - A(x_1)] - \right. \\ \left. - \varepsilon(2\omega) L_{\varepsilon}^{(2\omega)}(\boldsymbol{R} + \boldsymbol{\eta}|\boldsymbol{R}') [L(x'_1|2\omega) - B(x_1)] \right\}. \quad (26)$$

With the discretization procedure described in the previous section, the following matrix equations can be derived

$$0 = \sum_{n=1}^N \left[\left(\frac{1}{2} \delta_{nm} - \frac{1}{2} \mathcal{H}_{mn}^{(0)} \right) H(x_n|2\omega) + \frac{1}{2} \mathcal{L}_{mn}^{(0)} L(x_n|2\omega) \right], \quad (27)$$

$$\mathcal{Q}_m = \sum_{n=1}^N \left[\left(\frac{1}{2} \delta_{nm} + \frac{1}{2} \mathcal{H}_{mn}^{(\varepsilon)} \right) H(x_n|2\omega) - \varepsilon(2\omega) \frac{1}{2} \mathcal{L}_{mn}^{(\varepsilon)} L(x_n|2\omega) \right], \quad (28)$$

where

$$\mathcal{Q}_m = \sum_{n=1}^N \left[\left(\frac{1}{2} \delta_{nm} + \frac{1}{2} \mathcal{H}_{mn}^{(\varepsilon)} \right) A(x_n) - \varepsilon(2\omega) \frac{1}{2} \mathcal{L}_{mn}^{(\varepsilon)} B(x_n) \right], \quad (29)$$

and the matrix elements have the same functional form as those appearing in Eqs. (14) and (15) but, here, they are evaluated at 2ω instead of ω .

If the functions $A(x_1)$ and $B(x_1)$ are known, these equations may be used for the determination of the nonlinear source functions $H(x_1|2\omega)$ and $L(x_1|2\omega)$ at 2ω . By comparing Eqs. (27) and (28) with (14) and (15), we note that \mathcal{Q}_m plays the role of a source, or a fictitious incident field.

In order to calculate the functions $A(x_1)$ and $B(x_1)$ we must now assume a model for the nonlinear polarization. The results presented here are based on the free electron model [29–31]. We write the nonlinear polarization in the form

$$\boldsymbol{P}(x, z) = \frac{1}{4\pi} [\gamma \nabla(\boldsymbol{E} \cdot \boldsymbol{E}) + \beta \boldsymbol{E}(\nabla \cdot \boldsymbol{E})], \quad (30)$$

where

$$\beta = \frac{e}{8\pi m \omega^2}, \quad \gamma = \frac{e^3 n_0(x_n)}{8m^2 \omega^4},$$

$n_0(x_n)$ is the electron number density, x_n is the coordinate in the direction normal to the local surface, and e and m are the electron charge and mass.

It can then be shown that with this model, the functions $A(x_1)$ and $B(x_1)$ appearing in the nonlinear boundary conditions (Eqs. (23) and (24)) may be written as follows

$$A(x_1) = \frac{2ic}{\omega} \mu_3(\omega) \frac{1}{\phi^2(x_1)} L(x_1, \omega) \frac{d}{dx_1} H(x_1, \omega), \quad (31)$$

$$B(x_1) = \frac{2ic}{\omega} \mu_1(\omega) \frac{d}{dx_1} \left[\frac{1}{\phi(x_1)} \frac{d}{dx_1} H(x_1, \omega) \right]^2, \quad (32)$$

with the constants $\mu_1(\omega)$, and $\mu_3(\omega)$ given by

$$\mu_1(\omega) = -\frac{2}{3}\beta \left[\frac{(\varepsilon(\omega) - 1)(\varepsilon(\omega) - 3)}{2\varepsilon^2(\omega)} - \frac{2}{3} \ln \left(\frac{\varepsilon(\omega)}{\varepsilon(2\omega)} \right) \right], \quad (33)$$

$$\mu_3(\omega) = \beta \left(\frac{\varepsilon(\omega) - 1}{\varepsilon(\omega)} \right). \quad (34)$$

The total power scattered by the sample at the second harmonic frequency is proportional to the square of the irradiance on the surface (incident power per unit area) and to the size of the effective source (illuminated area). It is convenient to normalize the scattered power in such a way that the results are independent of the incident power and the illuminated area. We then define the normalized second harmonic scattered power as

$$p_{sc}^{(2\omega)} = \frac{P_{sc}^{(2\omega)}}{\left(P_{inc}^{(\omega)} \right)^2} A_s, \quad (35)$$

where $A_s = LL_2$, and L_2 is the length of the surface along x_2 . Then, for plane wave illumination, the normalized second harmonic scattered intensity (power scattered per unit angle) may be written as

$$I_p(\theta_s|2\omega) = \frac{|r_p(\theta_s|2\omega)|^2}{2\omega L \cos^2 \theta_0 |\mathcal{H}_0|^4}, \quad (36)$$

where \mathcal{H}_0 is the amplitude of the incident plane wave, and the second harmonic scattering amplitude is given by

$$r_p(\theta_s|2\omega) = \int_{-\infty}^{\infty} dx_1 \left[i \frac{2\omega}{c} [\zeta'(x_1) \sin \theta_s - \cos \theta_s] H(x_1|2\omega) - L(x_1|2\omega) \right] \times \\ \times \exp \left\{ -i \frac{2\omega}{c} (x_1 \sin \theta_s + \zeta(x_1) \cos \theta_s) \right\}. \quad (37)$$

3 Results and Discussion

We present results for a silver surface whose profile constitutes a Gaussian random process with a Gaussian correlation function. To compare with the experimental results reported by O'Donnell and Torre [23], the statistical parameters that characterize the random profile are chosen as $a = 3.4 \mu\text{m}$ and $\delta = 1.81 \mu\text{m}$, where a represents the correlation length (e^{-1} value of the normalized height correlation function) and δ is the standard deviation of heights.

First, in Fig. 2 we show the results of linear scattering calculations at the fundamental wavelength, $\lambda = 1.06 \mu\text{m}$, for the case of normal incidence. The curve has the typical shape of the scattering patterns produced by high-sloped, randomly rough surfaces. The most noteworthy feature in the curve is the presence of pronounced and well-defined enhanced backscattering peak in the $\theta_s = 0^\circ$ -direction. Note that since we are showing only the incoherent component of the mean differential reflection coefficient, the coherent or specular component has been excluded and the peak shown in the figure is not a specular effect. Moreover, for the parameters employed in the simulation, the coherent component is negligible and would not be visible in the figure. These theoretical results for the linear problem are in good agreement with the experimental results of O'Donnell and Torre [23].

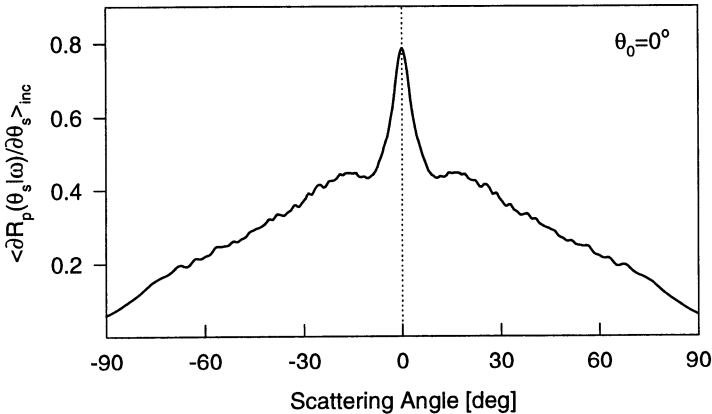


Fig. 2. The incoherent component of the mean differential reflection coefficient as a function of the scattering angle θ_s for the scattering of p-polarized light of wavelength $\lambda = 1.064 \text{ m}$ from a random silver surface characterized by the roughness parameters $a = 3.4 \text{ m}$, and $\delta = 1.81 \text{ m}$, and a dielectric constant $\varepsilon(\omega) = -56.25 + i0.60$. The sampling on the surface, of length $L = 40\lambda$, was $\Delta x = \lambda/20$ and the curve shows the result of averaging over $N_p = 2000$ realizations of the surface. The angle of incidence is $\theta_0 = 0^\circ$.

It is known that for high-sloped surfaces, the backscattering enhancement phenomenon is due to the multiple (mainly double) scattering of waves within the valleys of the surface [6,7,10,33]. The situation is shown schematically in Fig. 3. In the far field, the waves that follow multiple scattering paths such as those shown in Figs. 3(a) and (b) are phase coherent in the vicinity of the backscattering direction, where they interfere constructively. According to this picture the angular width of the backscattering peak is of the order of λ/a .

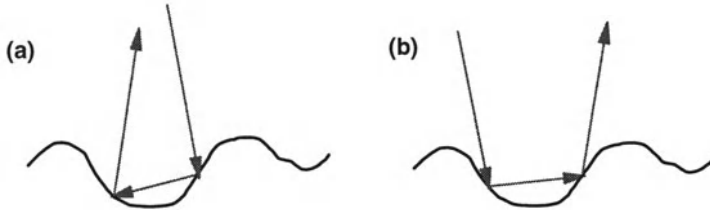


Fig. 3. Illustrative diagram of the double scattering processes in the valleys of the

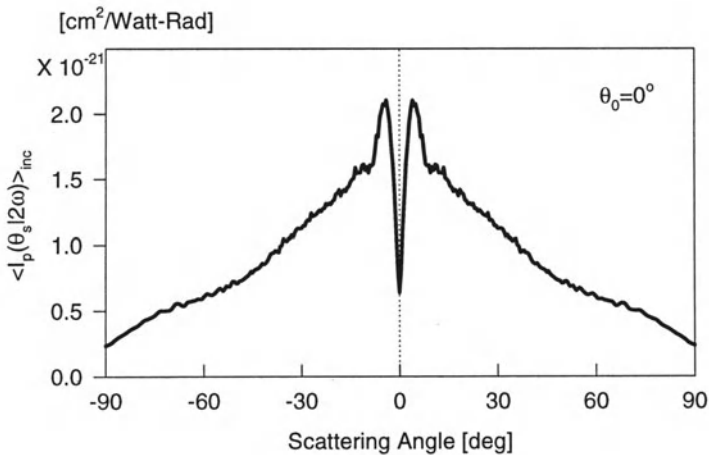


Fig. 4. The incoherent component of the mean normalized second harmonic intensity as a function of the scattering angle θ_s for the scattering of p-polarized light from a random silver surface characterized by the roughness parameters $a = 3.4$ m, and $\delta = 1.81$ m, and dielectric constants $\varepsilon(\omega) = -56.25 + i0.60$ and $\varepsilon(2\omega) = -11.56 + 0.37$. The incident plane wave has a wavelength $\lambda = 1.064$ m and the surface, of length $L = 40\lambda$, was sampled with an interval $\Delta x = \lambda/20$. The curve shows the result of averaging over $N_p = 2000$ realizations of the surface. The angle of incidence is $\theta_0 = 0^\circ$.

Computer simulation results for the mean normalized second harmonic scattering intensity are shown in Fig. 4. It can be verified that they are in good agreement with the experimental results of O'Donnell and Torre [23]. Given the relative simplicity of the model assumed for the nonlinear polarization, and the fact that there are no fitting parameters, this could be even a bit surprising. We note also that the scattering curve has some similarities with the one shown in Fig. 2 but, significantly, instead of a peak there is now a dip in the backscattering direction. In this respect, the results are similar to those found with weakly corrugated surfaces [20,22]. However, in that case, with the same model for the nonlinear polarization as the one employed here, the dips become peaks as the angle of incidence is increased. We have not observed any peaks in the case of strongly corrugated surfaces.

3.1 Single and Multiple Scattering Solutions

It has been suggested [23] that the origin of the dip observed in the backscattering direction lies in the destructive interference between waves multiply scattered within the valleys of the surface. We now turn our attention to this matter and provide some support for the suggestion. For this, we first calculate the angular distribution of the scattered light at the fundamental and harmonic frequencies in a single scattering approximation. Assuming an incident plane wave and a locally flat surface (tangent plane model), we can calculate the linear and nonlinear source functions involved. For the fundamental frequency we can write (Kirchhoff approximation):

$$H_K(x_1|\omega) = [1 + \varrho_p(x_1)] H(x_1|\omega)_{\text{inc}}, \quad (38)$$

$$L_K(x_1|\omega) = -i \frac{\omega}{c} [1 - \varrho_p(x_1)] \phi(x_1) \cos \theta_l H(x_1|\omega)_{\text{inc}}, \quad (39)$$

where $\varrho_p(x_1)$ represents the Fresnel reflection coefficient for p-polarized light from a planar vacuum-metal interface corresponding to the local angle of incidence $\theta_l(x_1)$, defined as the angle of incidence measured from the normal to the surface at the point $(x_1, \zeta(x_1))$. The Fresnel reflection coefficient is given by

$$\varrho_p(x_1) = \frac{\varepsilon(\omega) \cos \theta_l - \sqrt{\varepsilon(\omega) - \sin^2 \theta_l}}{\varepsilon(\omega) \cos \theta_l + \sqrt{\varepsilon(\omega) - \sin^2 \theta_l}}, \quad (40)$$

with

$$\sin \theta_l = \frac{1}{\phi(x_1)} [\sin \theta_0 - \zeta'(x_1) \cos \theta_0], \quad (41)$$

$$\cos \theta_l = \frac{1}{\phi(x_1)} [\cos \theta_0 + \zeta'(x_1) \sin \theta_0]. \quad (42)$$

Once the linear source functions are known, the functions $A(x_1)$ and $B(x_1)$ can be determined from Eqs. (31) and (32). We find that

$$A(x_1) = \frac{2i\omega}{c} \mu_3(\omega) \cos \theta_l \sin \theta_l [1 - \varrho_p^2(x_1)] [H(x_1|\omega)_{\text{inc}}]^2, \quad (43)$$

$$B(x_1) = \left(\frac{2\omega}{c} \right)^2 \mu_1(\omega) \phi(x_1) \sin^3 \theta_l [1 + \varrho_p(x_1)]^2 [H(x_1, |\omega)_{\text{inc}}]^2. \quad (44)$$

Now, for a tilted flat surface, the second harmonic source functions may be found by first writing the second harmonic fields above and below the interface as plane waves multiplied by some coefficients (of reflection and transmission). These coefficients can be determined by requiring that the fields and their unnormalized normal derivatives satisfy the nonlinear boundary

conditions given by Eqs. (23) and (24). Finally, the nonlinear source functions are found by evaluating the vacuum field and its normal derivative on the surface. In our tangent plane approximation, we find that

$$H_K^>(x_1|2\omega) = \varrho^{(2\omega)}(x_1) [H(x_1|\omega)_{\text{inc}}]^2, \quad (45)$$

$$L_K^>(x_1|2\omega) = \frac{2i\omega}{c} \phi(x_1) \cos \theta_l \varrho^{(2\omega)}(x_1) [H(x_1|\omega)_{\text{inc}}]^2, \quad (46)$$

where $\varrho^{(2\omega)}(x_1)$ represents the amplitude of the second harmonic plane wave reflected from a flat, tilted surface illuminated by a unit amplitude plane wave, and is given by

$$\begin{aligned} \varrho^{(2\omega)}(x_1) = & \frac{2i\omega}{c} \sin \theta_l \left[\varepsilon(2\omega) \cos \theta_l + \sqrt{\varepsilon(2\omega) - \sin^2 \theta_l} \right]^{-1} \times \\ & \times \left[\mu_3(\omega) \sqrt{\varepsilon(2\omega) - \sin^2 \theta_l} \cos \theta_l [1 - \varrho_p^2(x_1)] - \right. \\ & \left. - \mu_1(\omega) \varepsilon(2\omega) \sin^2 \theta_l [1 + \varrho_p(x_1)]^2 \right]. \end{aligned} \quad (47)$$

The physical processes taken into account in this approximation are illustrated in Fig. 5, and can be summarized as follows. Light of frequency ω hits the surface. The nonlinearities of the locally flat surface generate light of frequency 2ω that is then scattered into the local specular direction as shown in Fig. 5(a). Further interactions of the second harmonic radiation with the surface are neglected, which may lead to unphysical situations, such as the one illustrated in Fig. 5(b). So, the approximation is the equivalent of the Kirchhoff approximation in linear scattering. The mean normalized second harmonic intensity calculated on the basis of the nonlinear source functions (45) and (46) produces results that are very different from those obtained with the full calculations; we conclude, then, that the observed effects are not due to single scattering.

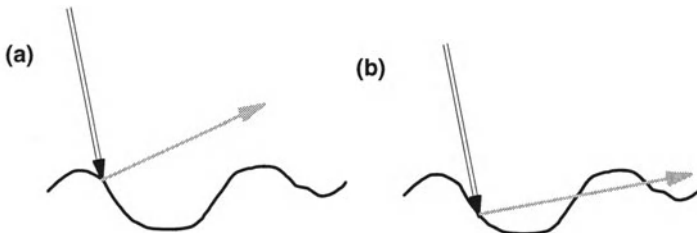


Fig. 5. Illustrative diagram of the single scattering processes that produce the second harmonic scattered light. The double line black arrows represent light of frequency ω , while the thick gray arrows represent light of frequency 2ω .

We now turn our attention to the multiple scattering contributions to the mean second harmonic intensity distribution. For this, we first consider

the single and double scattering contributions to the mean differential reflection coefficient at the fundamental frequency. It is known that solving the scattering equations iteratively one can calculate separately, according to the order of scattering, the different contributions to the scattered field. The iterative method of solution was studied in detail by Liska and McCoy [32] for a case that corresponds to a perfectly conducting one-dimensional surface in s polarization. The technique has been used to show that the backscattering enhancement phenomenon is due to multiple scattering [10]. An extension of this method, applicable to metallic and dielectric surfaces has been proposed by Sentenac and Maradudin [34]. Following these authors, we proceed by subtracting Eq. (15) from Eq. (14) and manipulating the result to write

$$\begin{aligned} H(x_m|\omega) = & [1 + \varrho_p(x_m)]H(x_m|\omega)_{\text{inc}} + \\ & + \frac{1}{2} \sum_{n=1}^N \left\{ [1 + \varrho_p(x_m)]\mathcal{H}_{mn}^{(0)} - [1 - \varrho_p(x_m)]\mathcal{H}_{mn}^{(\varepsilon)} \right\} H(x_n|\omega) + \\ & + \frac{1}{2} \sum_{n=1}^N \left\{ -[1 + \varrho_p(x_m)]\mathcal{L}_{mn}^{(0)} + [1 - \varrho_p(x_m)]\varepsilon(\omega)\mathcal{L}_{mn}^{(\varepsilon)} \right\} L(x_n|\omega). \end{aligned} \quad (48)$$

As before, $\varrho_p(x_m)$ represents the Fresnel reflection coefficient corresponding to a planar surface that is tangent to the rough surface at the point x_m . The first term on the right hand side of the equation represents the Kirchhoff approximation. Employing the local impedance boundary condition (Eq. (16)) we can write the following matrix equation,

$$\begin{aligned} H(x_m|\omega) = & [1 + \varrho_p(x_m)]H(x_m|\omega)_{\text{inc}} + \\ & + \frac{1}{2} \sum_{n=1}^N \left\{ [1 + \varrho_p(x_m)] \left[\mathcal{H}_{mn}^{(0)} - \mathcal{L}_{mn}^{(0)} \frac{K^{(0)}(x_n|\omega)}{\varepsilon(\omega)} \right] - \right. \\ & \left. - [1 - \varrho_p(x_m)] \left[\mathcal{H}_{mn}^{(\varepsilon)} - \mathcal{L}_{mn}^{(\varepsilon)} K^{(0)}(x_n|\omega) \right] \right\} H(x_n|\omega). \end{aligned} \quad (49)$$

A solution to this equation can be written in the form of a Neumann-Liouville series,

$$H(x_m|\omega) = H^{(1)}(x_m|\omega) + H^{(2)}(x_m|\omega) + H^{(3)}(x_m|\omega) + \dots, \quad (50)$$

where

$$H^{(1)}(x_m|\omega) = [1 + \varrho_p(x_m)]H(x_m|\omega)_{\text{inc}}, \quad (51)$$

$$\begin{aligned} H^{(s)}(x_m|\omega) = & \frac{1}{2} \sum_{n=1}^N \left\{ [1 + \varrho_p(x_m)] \left[\mathcal{H}_{mn}^{(0)} - \mathcal{L}_{mn}^{(0)} \frac{K^{(0)}(x_n|\omega)}{\varepsilon(\omega)} \right] - \right. \\ & \left. - [1 - \varrho_p(x_m)] \left[\mathcal{H}_{mn}^{(\varepsilon)} - \mathcal{L}_{mn}^{(\varepsilon)} K^{(0)}(x_n|\omega) \right] \right\} H^{(s-1)}(x_n|\omega). \end{aligned} \quad (52)$$

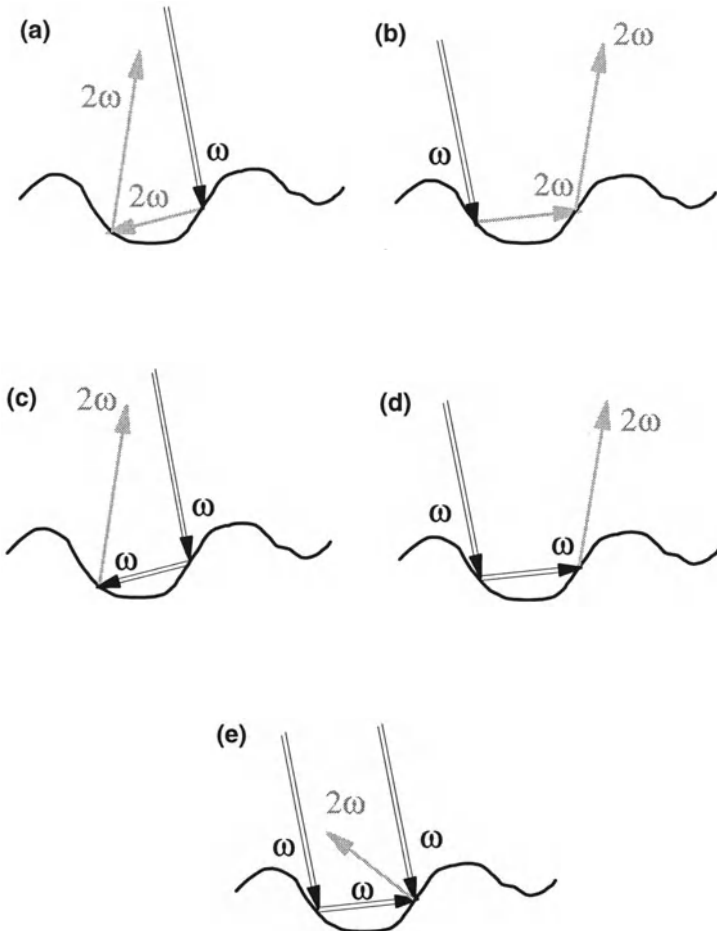


Fig. 6. Illustrative diagram of some of the multiple scattering processes that produce the second harmonic scattered light. The double line black arrows represent light of frequency ω , while the thick gray arrows represent light of frequency 2ω .

If we denote by $r_p^{(s)}(\theta_s)$ the contribution to the scattering amplitude $r_p(\theta_s)$ calculated from $H^{(s)}(x_m|\omega)$, it represents, in the geometrical optics limit, the contribution of s scattering events to the scattering amplitude.

Let us now consider the consequences of making this kind of approximations for the source functions at the fundamental frequency on the calculations of the scattering distribution at the second harmonic frequency. Some of the multiple scattering processes that give rise to the second harmonic scattering pattern are shown in Fig. 6. As far as the linear part of the scattering is concerned, the Kirchhoff approximation is sufficient to describe the processes shown in Figs. 6(a) and (b). However, in contrast with our previous

approximation (see Fig. 5(a)), a multiple scattering solution for the second harmonic field is required to account for these processes. In Fig. 7(a), we present results for the mean normalized second harmonic intensity based on a single scattering approximation for the linear scattering problem and the complete solution of the scattering equations for the second harmonic field. In other words, for each realization of the profile, we use the Kirchhoff approximation to determine the source functions at the frequency ω , and solve the full system of matrix equations given by Eqs. (27) and (28) to determine the source functions at 2ω . This procedure takes into account the processes illustrated in Figs. 6(a) and (b). It may be seen in Fig. 7(a) that when these multiple scattering processes are incorporated into the solution, a sharp minimum in the backscattering direction appears in the angular distribution of the mean second harmonic intensity.

The processes shown in Figs. 6(c) and (d) contain double scattering processes at the fundamental frequency. So, to include these processes we use a double scattering approximation for the source functions at the frequency ω and solve the full system of equations at 2ω . Calculations of the mean normalized second harmonic intensity based on this procedure are shown in Fig. 7(b). The contribution of these processes to the mean second harmonic scattering pattern also leads to a minimum in the backscattering direction. The curve with the thick line shown in Fig. 7(c) contains single and double scattering processes in the linear scattering calculations and a full solution in the second harmonic calculations.

The results shown in Figs. 7 demonstrate that, as suggested by O'Donnell and Torre [23], the minimum in the backscattering direction in the angular distribution of the mean second harmonic intensity is a consequence of multiple scattering (and nonlinear mixing of the light) within the valleys of the surface. As in the case of linear optics, it is also natural to expect that some of these processes are coherent, and that the backscattering effects are due to the interference between multiply scattered waves. However, in contrast with the linear case, in the second harmonic light the interference appears to be destructive.

Since the dependence of the second harmonic wave with the incident one is quadratic, the accumulated phase of the wave of frequency ω is doubled at the point where the second harmonic wave is generated. Thus, apart from the phase shifts acquired by the wave on the reflections, the relative phase difference between the processes illustrated in Figs. 6(a) and (b) should be zero in the backscattering direction. That interference effects are indeed a plausible explanation for the dip may be recognized from the fact that the amplitude reflection coefficient for second harmonic generation (Eq. (47)) is an odd function of the local angle of incidence on the surface. We conclude, then, that the processes depicted in Figs. 6(a) and (b) are phase coherent in the backscattering direction, and that the waves that follow these two paths are π radians out of phase, producing destructive interference in the far field.

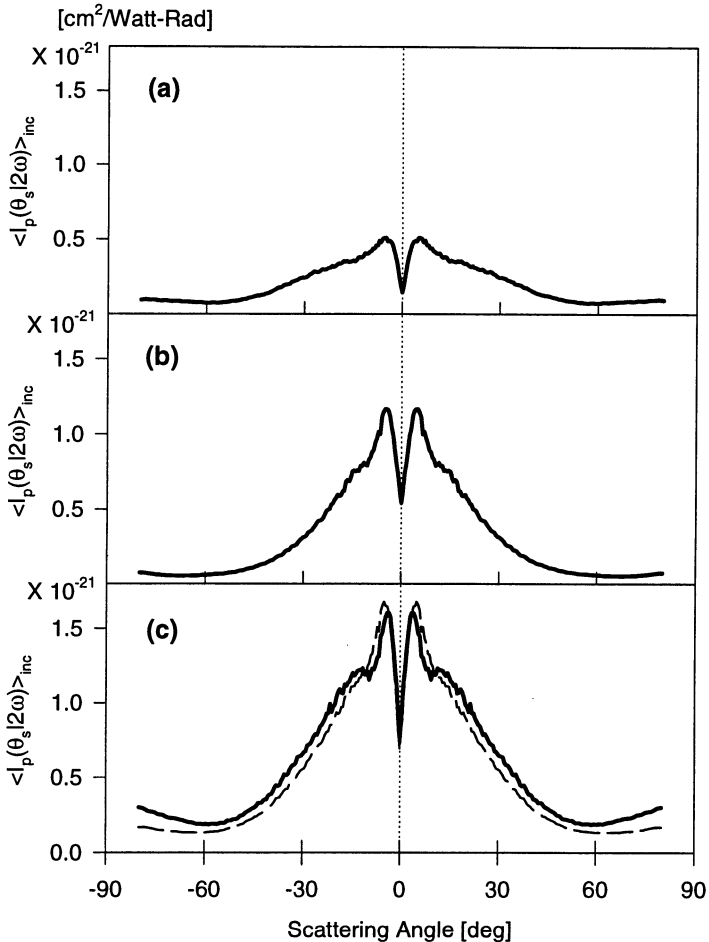


Fig. 7. Calculations of the incoherent part of the mean normalized second harmonic intensity as a function of the scattering angle θ_s based on the iterative solutions of the linear problem, for the scattering of p-polarized light from a random silver surface characterized by the roughness parameters $a = 3.4$ m, and $\delta = 1.81$ m. Other parameters of the simulation are as in Fig. 4, and the angle of incidence is $\theta_0 = 0^\circ$. The curves have, (a) the single scattering contributions in the linear scattering and all contributions at the harmonic frequency, (b) pure double scattering contributions in the linear scattering and all contributions at the harmonic frequency, and (c) the single and double scattering contributions in the linear scattering and all contributions at the harmonic frequency. In (c), the curve shown with the dashed line represents the sum of the curves shown in (a) and (b).

In the linear problem the interference is constructive because the pairs of paths illustrated in Figs. 3(a) and (b) become reciprocal in the backscattering direction. On the other hand, in the case of second harmonic generation reciprocity does not apply and, moreover, there seems to be some degree of antireciprocility when source and detector are interchanged.

The arguments given above can be repeated and applied to the processes shown in Figs. 6(c) and (d). Again, we conclude that these processes are coherent with each other and that the corresponding scattered waves interfere destructively. We also make the remark that there seems to be no coherency between the paths shown in Figs. 6(a) and (c) or (d), or between the paths shown in (b) and (c) or (d).

However, to the order of scattering considered, the processes shown in Figs. 6(a) to (d) are not the only ones that contribute to the second harmonic scattering distribution. The process depicted in Fig. 6(e) is also possible, and it is worth noting that its contribution is already included in the results shown with the thick line in Fig. 7(c). However, we also notice that this process involves the generation of second harmonic light in a direction that is near normal to the local tangent plane, making its contribution relatively small. Furthermore, paths such as this one (Fig. 6(e)) do not seem to have a coherent partner.

To substantiate our arguments and statements we show with the dashed line curve of Fig. 7(c), the sum of the scattering intensities shown in (a) and (b). The curve represents, then, the incoherent sum of the contributions from the pairs of processes shown in Figs. 6(a) and (b), and those shown in (c) and (d). It contains no contributions due to the interference between these two pairs of processes. The two curves presented in Fig. 7(c) are very similar, and present only minor differences in the region that surrounds the backscattering dip. The similarity between these two curves implies that, as expected, the processes of Fig. 6(e) do not contribute significantly. In addition, these curves demonstrate the relative lack of coherence between the contributions from the pairs of processes illustrated in Figs. 6(a) and (b), and those illustrated in (c) and (d).

Our results indicate that, to the order of multiple scattering considered, the main contributions to the second harmonic scattering pattern comes from the processes shown in Figs. 6(a) to (d), and that only the contributions corresponding to the pair of processes shown in (a) and (b), and those corresponding to the pair (c) and (d) are coherent with each other.

3.2 Angular Correlations

We have seen that the destructive interference effects observed in the backscattering direction are due to the fact that the amplitude reflection coefficient for second harmonic generation (Eq. (47)) from a flat interface is an odd function of the angle of incidence. This is a remarkable fact that contrasts

with the more usual situation encountered in linear optics. Moreover, in linear optics, even for an irregular surface, the reciprocity theorem [35] implies that the optical signals obtained upon an exchange of source and detector are identical. In the case of second harmonic generation from a flat surface the signals could be called antireciprocal. It is then interesting to consider the question of the possible existence of some general property analogous to the reciprocity theorem. With this motivation, we study more general situations involving rough surfaces in which the positions of a source radiating at the frequency ω and a detector of 2ω radiation are exchanged.

In Fig. 8, we show the speckle patterns produced by a realization of a rough surface for two different angles of incidence. The black and gray filled circles indicate the specular intensities for angles of incidence $\theta_0 = 10^\circ$ and $\theta_0 = -10^\circ$, respectively. These two intensities correspond to the optical signals that would be obtained by an exchange in the positions of the source and detector. Since these two intensities are different we conclude that there seems to be no general relation analogous to the reciprocity theorem of linear optics. However, the question of whether there is some kind of average reciprocity or antireciprocity is worth exploring. To investigate this issue, we have conducted some studies of the angular correlation of the second harmonic speckle patterns produced by randomly rough metallic surfaces.

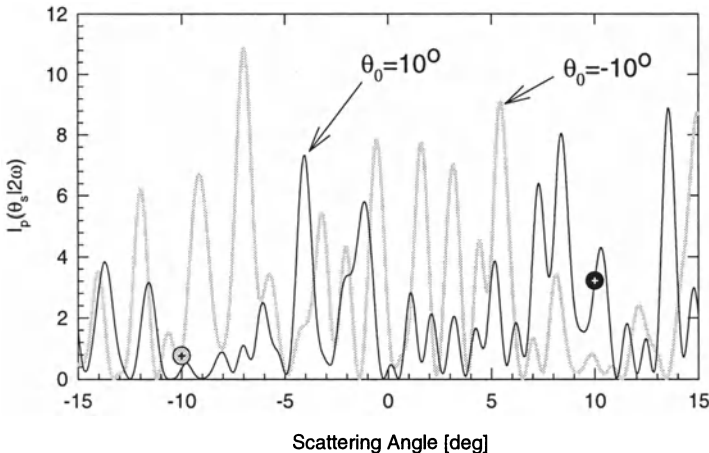


Fig. 8. P-polarized second harmonic speckle patterns generated by a realization of a random silver surface characterized by the roughness parameters $a = 3.4 \text{ m}$, and $\delta = 1.81 \text{ m}$ when the angles of incidence are $\theta_0 = 10^\circ$ (black curve) and $\theta_0 = -10^\circ$ (gray curve).

The general amplitude angular correlation function may be written as

$$C(\theta_{01}, \theta_{s1}, \theta_{02}, \theta_{s2} | \Omega) = \langle A(\theta_{01}, \theta_{s1} | \Omega) A^*(\theta_{02}, \theta_{s2} | \Omega) \rangle , \quad (53)$$

where the amplitude $A(\theta_0, \theta_s|\Omega)$ is given, in normalized form, by

$$A(\theta_0, \theta_s|\omega) = \frac{r_p(\theta_s|\omega)}{\sqrt{8\pi (\omega/c) L \cos \theta_0}}, \quad (54)$$

$$A(\theta_0, \theta_s|2\omega) = \frac{r_p(\theta_s|2\omega)}{\sqrt{2\omega L \cos \theta_0 |\mathcal{H}_0|^2}}, \quad (55)$$

and the angle brackets represent an average over an ensemble of realizations of the surface.

We note now that the general form of the correlation given by Eq. (53) is a function of four variables (the angles of incidence θ_{01} and θ_{02} , and those of scattering, θ_{s1} and θ_{s2}). However, for the information required in our study it is sufficient to consider only the dependence of the correlation function on two of these variables; the other two can be fixed. We then concentrate our efforts on the following form of the complex amplitude correlation at the harmonic frequency:

$$C(\theta_1, \theta_2|2\omega) = \langle A(\theta_1|2\omega) A^*(\theta_2|2\omega) \rangle, \quad (56)$$

where, to simplify the notation we have written $A(\theta_1|2\omega) = A(\theta_{01}, \theta_{01}|2\omega)$ and $A^*(\theta_2|2\omega) = A^*(\theta_{02}, \theta_{02}|2\omega)$. The amplitudes $A(\theta_1|2\omega)$ and $A(\theta_2|2\omega)$ represent the second harmonic complex amplitudes obtained in the specular direction for the angles of incidence θ_1 and θ_2 , respectively, for a given realization of the rough surface. The correlation function we study describes, then, the motion of the “speckle” in the specular direction as the angle of incidence is changed (memory effect). More specifically, we are interested in the behavior of the correlation function $C(\theta_1, \theta_2|2\omega)$ in the parameter space (θ_1, θ_2) along two particular lines. First, along the line $\theta_2 = \theta_1$ this function represents the evolution of the specular signal as the angle of incidence is changed (the so-called memory line). On the other hand, along the line $\theta_2 = -\theta_1$ this function represents the correlation between the signals obtained by an exchange of source (ω) and detector (2ω). In linear optics this is the so-called time-reversed or reciprocal memory line.

Numerical results for the correlation $C(\theta_1, \theta_2|2\omega)$ estimated from $N_p = 2000$ realizations of the rough surface are shown in Fig. 9. It can be seen in the figure that for the real part of $C(\theta_1, \theta_2|2\omega)$ there is a maximum along the line $\theta_2 = \theta_1$, indicating that the “specular speckle” tends to follow the specular direction as the angle of incidence is modified. However, along the line $\theta_2 = -\theta_1$, the real part of the correlation is negative, indicating a degree of anticorrelation between the signals obtained by an exchange of source and detector. The absolute strength of the correlation is not as high as the one obtained along $\theta_2 = \theta_1$, which shows that the anticorrelation is not perfect. In Fig. 9, we can also see that the imaginary part of the correlation $C(\theta_1, \theta_2|2\omega)$ has an oscillatory behavior in a direction perpendicular to both, the lines $\theta_2 = \theta_1$ and $\theta_2 = -\theta_1$. Although this may not be clearly appreciated from the

figure, we have found that the imaginary part of the correlation is practically zero along these two lines. We then conclude that the signals obtained by an exchange of source and detector are partially anticorrelated.

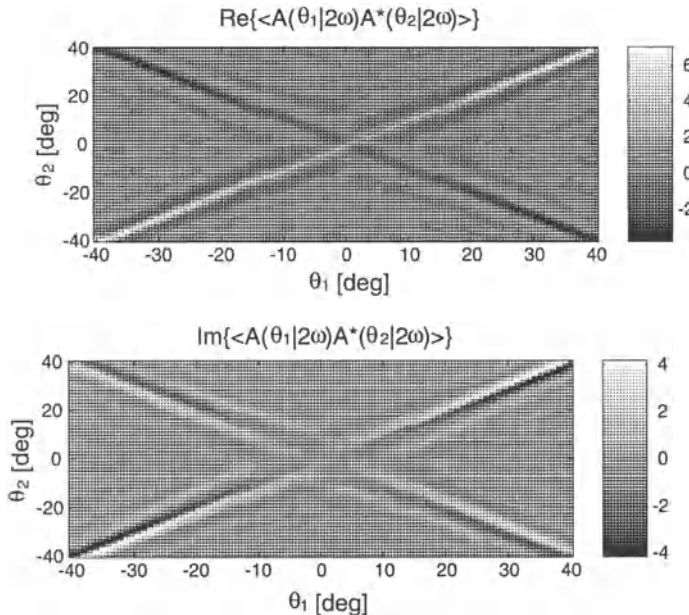


Fig. 9. Calculations of the amplitude correlation for the scattering of p-polarized light from a random silver surface characterized by the roughness parameters $a = 3.4$ m, and $\delta = 1.81$ m.

4 Summary and Conclusions

We have presented a theoretical study of the generation and scattering of second harmonic light at randomly rough metallic interfaces. The study is based on a Monte Carlo-type computer simulation of the problem. The numerical technique employed in the calculations of the fundamental and second harmonic scattered intensities is fairly rigorous. On the other hand, the nonlinearities of the surface were modeled using a free-electron model for the polarizability of the metal. We have found that the angular distribution of the scattered light at the harmonic frequency displays well-defined dips in the backscattering direction, and the results are in quantitative agreement with the experimental results of O'Donnell and Torre [23]. Using an iterative procedure to solve the scattering equations, we have shown that the observed

features are due to destructive interference between waves that have been multiply scattered in the valleys of the surface.

In addition, we have studied the correlation between the second harmonic complex amplitudes obtained when the directions of incidence and detector are exchanged. We have shown that these optical signals are at least partially anticorrelated, which suggests some kind of average antireciprocitity.

Acknowledgment. This work has been supported by the Army Research Office through Grants DAAD 19-99-C-0032 and DAAD 19-99-1-0321, and by the Consejo Nacional de Ciencia y Tecnología (CONACYT, México).

References

1. Yu. A. Kravtsov and A. I. Saichev, Sov. Phys. Usp. **25** 494 (1982).
2. Y. Kuga and A. Ishimaru, J. Opt. Soc. Am. A **1** 831 (1984).
3. A. R. McGurn, A. A. Maradudin, and V. Celli, Phys. Rev. B **31** 4866 (1985).
4. M. P. van Albada and A. Lagendijk, Phys. Rev. Lett. **55** 2692 (1985).
5. P. E. Wolf, and G. Maret, Phys. Rev. Lett. **55** 2696 (1985).
6. E. R. Méndez and K. A. O'Donnell, Opt. Comm. **61** 91 (1987).
7. K. A. O'Donnell and E. R. Méndez, J. Opt. Soc. Am. A **4** 1194 (1987).
8. E. Jakeman, J. Opt. Soc. Am. A **5** 1638 (1988).
9. A. A. Maradudin, E. R. Méndez, T. Michel, Opt. Lett. **14** 151 (1989).
10. A. A. Maradudin, T. Michel, A. R. McGurn, and E. R. Méndez, Ann. Phys. (N. Y.) **203** 255 (1990).
11. M. J. Kim, J. C. Dainty, A. T. Friberg, and A. J. Sant, J. Opt. Soc. Am. A **7** 569 (1990).
12. M. E. Knotts and K. A. O'Donnell, Opt. Commun. **99** 1 (1993).
13. A. A. Maradudin and E. R. Méndez, Appl. Opt. **32** 3335 (1994).
14. S. West and K. A. O'Donnell, J. Opt. Soc. Am. A **12** 390 (1995).
15. A. R. McGurn, A. A. Maradudin, Opt. Commun. **72** 279 (1989).
16. J. A. Sánchez-Gil, A. A. Maradudin, Jun Q. Lu, V. D. Freilikher, Phys. Rev. B **51** 17100 (1995).
17. J. A. Sánchez-Gil, A. A. Maradudin, Jun Q. Lu, V. D. Freilikher, M. Pustilnik, and I. Yurkevich, Phys. Rev. B **50** 15353 (1994).
18. J. A. Sánchez-Gil, A. A. Maradudin, Jun Q. Lu, and V. R. Freilikher, J. Mod. Opt. **43** 435 (1995).
19. A. R. McGurn, V. M. Agranovich, and T. A. Leskova, Phys. Rev. B **44** 11441 (1991).
20. M. Leyva-Lucero, E. R. Méndez, T. A. Leskova, A. A. Maradudin, and J. Q. Lu, Opt. Lett. **21** 1809 (1996).
21. T. A. Leskova, A. A. Maradudin, M. Leyva-Lucero, and E. R. Méndez, in preparation for Ann. Phys. (N.Y.).
22. K. A. O'Donnell, R. Torre, and C. S. West, Opt. Lett. **21** 1738 (1996).
23. K. A. O'Donnell and R. Torre, Opt. Comm. **138** 341 (1997).
24. M. Leyva-Lucero, E. R. Méndez, T. A. Leskova, and A. A. Maradudin, Opt. Commun. **161** 79 (1999).
25. R. García-Molina, A. A. Maradudin, and T. A. Leskova, Phys. Rep. **194** 351 (1990).

26. R. A. Depine, Optica Acta **34** 1135 (1987).
27. M. E. Knotts, T. R. Michel and K. A. O'Donnell, J. Opt. Soc. Am. A **10** 928 (1993).
28. E. R. Méndez, A. G. Navarrete and R. E. Luna, J. Opt. Soc. Am. A **12** 2507 (1995).
29. N. Bloembergen, R. K. Chang, S. S. Jha, and C. H. Lee, Phys. Rev. **174** 813 (1968).
30. D. Maystre and M. Nevière, Appl. Phys. A **39** 115 (1986).
31. M. Nevière, P. Vincent, D. Maystre, R. Reinisch, and J. L. Coutaz, J. Opt. Soc. Am. B **5** 330 (1988).
32. E. G. Liska and J. J. McCoy, J. Acoust. Soc. Am. **71** 1093 (1982).
33. A. A. Maradudin, E. R. Méndez and T. Michel; Backscattering effects in the elastic scattering of p-polarized light from a large-amplitude random metallic grating. In *Scattering in Volumes and Surfaces*, M. Nieto-Vesperinas, J. C. Dainty (Eds.), (North-Holland, Amsterdam, 1990) pp. 157-174.
34. A. Sentenac and A. A. Maradudin, Waves in Random Media **3** 343 (1993).
35. D. S. Saxon, Phys. Rev. **100** 1771 (1955).

Pump-Probe Spectroscopy - Revisited

P. R. Berman

Physics Department, University of Michigan, Ann Arbor, MI 48109-1120 USA;
(1) (734) 763-7762; FAX (1) (734) 764-5153;
email: pberman@umich.edu

Abstract. A theory of pump probe spectroscopy is carried out using an amplitude approach in a bare state basis. The interplay between absorption and emission is clearly defined in this approach. Both closed and open systems are considered. The theory is applied to a calculation of the dispersion-like structure that appears when the probe frequency is nearly equal to the pump frequency, in the limit of large pump field detuning. The theory is extended to include a class of problems in which the recoil atoms undergo on the absorption or emission of radiation leads to resonance structures. The relationship of these *recoil-induced resonances* to the collective atomic recoil laser is discussed. The probe gain which occurs without level inversion in these systems cannot be viewed as a parametric process, in its normal sense.

1 Introduction

Of fundamental interest in nonlinear spectroscopy is the response of an atomic vapor to the simultaneous application of a pump and a probe field. The pump electric field is given by

$$\mathbf{E}(\mathbf{r}, t) = \hat{\mathbf{x}} E \cos(\mathbf{k} \cdot \mathbf{r} - \Omega t) \quad (1)$$

and the probe electric field by

$$\mathbf{E}'(\mathbf{r}, t) = \hat{\mathbf{x}} E' \cos(\mathbf{k}' \cdot \mathbf{r} - \Omega' t), \quad (2)$$

where E and E' are the pump and probe electric field amplitudes, Ω and Ω' their frequencies, and \mathbf{k} and \mathbf{k}' their propagation vectors. These fields interact with an ensemble of two-level atoms, having ground state $|1\rangle$, excited state $|2\rangle$, and transition frequency ω . The atoms are assumed to be stationary at this point. For a given pump frequency Ω and pump field detuning

$$\Delta = \Omega - \omega, \quad (3)$$

one measures the probe field absorption as a function of the probe-pump detuning

$$\delta = \Omega' - \Omega. \quad (4)$$

The probe absorption spectrum can be calculated for probe fields of arbitrary strength [1], but the present discussion is limited to probe absorption or gain that is linear in the probe field intensity.

A calculation of the probe field absorption is relatively straightforward [2,3]. For a pump field detuning $|\Delta| \gg \Gamma, \chi$, where Γ is the upper state decay rate and χ is a pump-field Rabi frequency, one finds the spectrum to consist of three components. There is an absorption peak centered near $\delta = -\Delta$ ($\Omega' = \omega$), an emission peak centered near $\delta = \Delta$ ($\Omega' = 2\Omega - \omega$) and a dispersive like structure centered near $\delta = 0$. Experimentally, a spectrum exhibiting all these features was first obtained by Wu *et al.* [4]. The absorption and emission peaks can be given a simple interpretation in a dressed-atom picture [5], but the non-secular structure centered at $\delta = 0$ is somewhat more difficult to interpret. In a density matrix approach, one can view the pump and probe fields as forming a matter grating which is out of phase with the light grating formed by the pump and probe fields [6]. The pump field scatters off this grating and is amplified or absorbed at the expense of the probe field, depending on the phase shift between the matter and light gratings. In this picture, gain or absorption centered near $\delta = 0$ appears to be a parametric process, but this is not actually the case. The probe field absorption or gain is always at a frequency different than that of the pump field, there is no phase matching requirement, and spontaneous emission plays a critical role in the overall process.

A different picture of the origin of the dispersive structure arises when one considers the interaction of the fields with a *single* atom and calculates directly the probability that the probe field is amplified or absorbed. Such a calculation has the added advantage of allowing one to separate the individual contributions to absorption and emission, a separation that is not possible using a semiclassical density matrix approach. A beautiful calculation of this nature, using an amplitude approach and a dressed-state basis was carried out by Grynberg and Cohen-Tannoudji [7]. They showed that the dispersion-like resonance arises from an interference term that appears in absorption but not emission. The dressed-atom approach has the advantage of using quasi-stationary states of the atom and the pump field, allowing one to apply Fermi's Golden Rule to the calculation of transition probabilities. It is also possible to explain the central resonance within the context of a single atom, density matrix calculation in the dressed basis where the resonance can be attributed to dressed-state coherences created by the pump field [8].

In this contribution, the probe field absorption is calculated using an amplitude approach and a bare state basis. The bare state basis calculation involves more terms than the dressed-state calculation and cannot be carried out using quasi-stationary states. However, the bare state calculation reveals interesting atom-field dynamics which become more complex with increasing pump field strength. The origin of the dispersion-like resonance is still associated with interference effects in the bare state calculation. In both the bare and dressed state calculations, it is possible to reinterpret the resonance as originating from a radiative shift of the absorption line.

Calculations are carried out for both "open" and "closed" systems. In the closed system, all atomic state population resides in the two atomic levels coupled by the radiation fields. In the open system considered in this work, there is an additional ground state level to which the excited state can decay. This additional level is *not* coupled to the excited state by the fields so that population can leak out of the two states that *are* coupled by the field. For the closed system, the width of the dispersion-like resonance is of order of the excited state decay rate and its amplitude is proportional to the pump intensity squared. For the open system, the width of the dispersion-like resonance is determined by transit-time broadening and its amplitude is proportional to the pump intensity to the first power. A dressed state approach could also be used for the open system, but it must be modified to allow for time dependence of the "quasi-stationary" states.

Following the discussion of open and closed systems involving stationary atoms, I will examine the pump-probe spectroscopy of an atomic vapor cooled below the recoil limit. A central resonance appears that is linear in the pump field intensity, but it is not dispersive in shape and does not necessarily involve processes in which spontaneously emitted photons play a role. The origin of the central resonance can be traced to the recoil atoms undergo on the absorption or emission of radiation - it has been termed a *recoil-induced resonance* [9]. The relationship of the recoil-induced resonances to the *collective atomic recoil laser* [10–12] will also be discussed.

2 Density Matrix Result

It is useful to recall the result for the probe absorption obtained from a density matrix approach. For the moment, I consider a closed two-level atom, in which state 1 is stable and state 2 decays only to state 1. The probe absorption rate is proportional to a quantity A defined as [2]

$$A = N_0 \operatorname{Re} \left\{ \frac{1}{\mu'_{12}} \left[1 - \frac{2\chi^2}{\mu'_{12}\mu_{21}^p(1+B)} \right] \right\} \quad (5)$$

where

$$N_0 = \left[1 + \frac{2\chi^2}{\gamma^2 + \Delta^2} \right]^{-1}, \quad (6a)$$

$$\mu'_{12} = \gamma + i(\delta + \Delta), \quad (6b)$$

$$\mu_{21}^p = \gamma - i\Delta, \quad (6c)$$

$$B = \frac{4\chi^2\mu_{12}}{\mu'_{12}\mu_2\bar{\mu}'_{12}}, \quad (6d)$$

$$\bar{\mu}'_{12} = \gamma + i(\delta - \Delta), \quad (6e)$$

$$\mu_2 = \Gamma + i\delta, \quad (6f)$$

$$\delta = \Omega' - \Omega, \quad (6g)$$

$$\chi = -\varphi E/2\hbar, \quad (6h)$$

$$\gamma = \Gamma/2 \quad (6i)$$

and φ is a dipole moment matrix element taken to be real. This expression is valid for arbitrary pump field detunings and pump field strengths. In this paper, I am interested in situations in which it is possible to isolate the structure centered near $\delta = 0$. To accomplish this, one must have

$$|\chi/\Delta|, |\Gamma/\Delta|, |\delta/\Delta| \ll 1. \quad (7)$$

In this limit, for detunings $|\delta|$ less than or of order Γ , Eq. (5) can be approximated as

$$A = \frac{2\gamma}{\Delta^2} \left(1 - \frac{4\chi^2}{\Delta^2} + \frac{8\chi^4}{\Gamma\Delta^3} \frac{\delta\Gamma}{\Gamma^2 + \delta^2} \right) \quad (8)$$

revealing the dispersion-like structure. If $8\chi^4/\Gamma|\Delta|^3 \gg 1$, gain occurs for $\delta \simeq -\Gamma$ if $\Delta > 0$ and for $\delta \simeq \Gamma$ if $\Delta < 0$. For reasons that will become apparent, the lowest order nonvanishing contribution to probe absorption in this spectral region is of order χ^4 .

3 Amplitude Calculation

I now proceed with an amplitude calculation. In an interaction representation, the amplitude equations are

$$\dot{a}_{1\{k\}} = -i\chi a_{2\{k\}} e^{i\Delta t} - i\chi' e^{i\Delta' t} a_{2\{k\}} \quad (9a)$$

$$\dot{a}_{2\{k\}} = -i\chi a_{1\{k\}} e^{-i\Delta t} - i\chi' e^{-i\Delta' t} a_{1\{k\}} - \gamma a_{2\{k\}} \quad (9b)$$

$$\dot{a}_{1\{k\};k'} = -i\chi a_{2\{k\};k'} e^{i\Delta t} - i\chi' e^{i\Delta' t} a_{2\{k\};k'} - ig_k e^{i\Delta_k t} a_{2\{k\}}, \quad (9c)$$

where $\chi' = -\varphi E'/2\hbar$ is the probe field Rabi frequency, $\Delta' = \Omega' - \omega$ is the probe field detuning from resonance, g_k is a coupling constant for the interaction of the atom with mode k of the vacuum field,

$$\Delta_k = \omega_k - \omega, \quad (10)$$

and ω_k is the frequency of a spontaneously emitted photon. The subscript $\{k\}$ refers to an arbitrary state of the radiation field that has been created by the pump and probe fields. For example, if the atom has scattered the pump field into a mode k_1 , then $\{k\} = k_1$. Equations (9a) are solved using time-dependent perturbation theory starting at $t = 0$ from the state in which there are no photons in the field and the atom is in its ground state [13]. Only those times are considered for which

$$\gamma t \gg 1, \quad (11)$$

allowing for a constant absorption rate.

To *zeroth* order in the pump field, one finds the standard result for linear absorption of a field. The absorption rate is proportional to a quantity $A^{(0)}$ given by

$$A^{(0)} = \frac{2\gamma}{\gamma^2 + \Delta'^2} \simeq \frac{2\gamma}{\Delta'^2}, \quad (12)$$

where the last equality follows from the fact that $\Delta' \simeq \Delta$ and $|\Delta| \gg \gamma$.

For terms involving higher powers of the pump field intensity, it is straightforward to use a diagrammatic technique to write down integral expressions for various orders of perturbation theory [14]. Since I work to lowest order in the probe field, I need consider only diagrams that are *linear* in the probe field Rabi frequency χ' . Although I use classical fields, one can think of the probe and pump as quantized fields, starting with a given number of photons in each field. It is then clear that diagrams resulting in a different number of absorbed or emitted photons for either field correspond to distinct final states that cannot interfere.

Each distinct final state amplitude for probe absorption or gain is represented by a *sum* of diagrams, with successive diagrams in the sum containing an additional power of the pump field intensity χ^2 . To calculate the square of an amplitude to order χ^{2n} ($n = 1, 2, \dots$), it is usually necessary to include diagrams of order higher than χ^n , owing to interference between various terms in the sum. The rate for probe field absorption (gain) is proportional to the time derivative of the absolute square of amplitudes corresponding to probe absorption (gain). This implicitly involves a trace over the internal states of the atom, requiring one to consider final state amplitudes terminating on both the ground and excited states. Solid arrows represent the probe field, block arrows the pump field, and dashed arrows represent spontaneously emitted modes of the vacuum field.

The diagrams in Fig. 1 lead to absorption or emission rates that are linear in the pump field intensity. Figure 1 (a) corresponds to probe absorption and pump gain while Fig. 1 (b) to probe gain and pump absorption, both without change in the vacuum field. One might think that the difference of the absolute squares of the diagrams represented by Figs. 1 (a),(b), is responsible for the dispersion like resonance, as proposed in an earlier paper [3]. However it turns out that the contributions from these diagrams *exactly cancel one another* [15].

When one sums all the contributions from the remaining diagrams in Fig. 1, one finds an absorption rate proportional to a quantity $A^{(1)}$ given by [15]

$$A^{(1)} = -8 \frac{\gamma \chi^2}{\Delta^4}, \quad (13)$$

which agrees with the density matrix calculation (8). In this bare state calculation, terms involving the emission of 0, 1, and 2 photons contribute to the total result (13). Moreover, one must include final states in which the atom is either in state 1 *or* in state 2. In the corresponding dressed state calculation

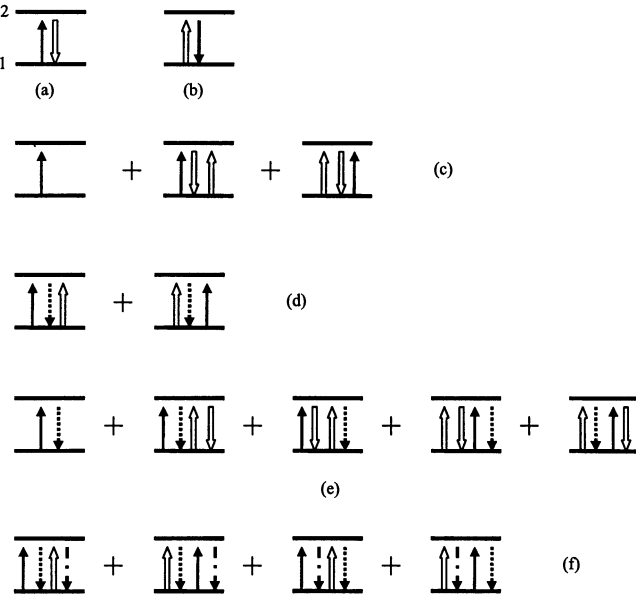


Fig. 1. A diagrammatic representation of the contribution to the ground and excited state amplitudes leading to probe absorption that is first order in the pump field intensity. Each diagram or sum of diagrams corresponds to a specific final state amplitude. Block arrows represent the pump field. Diagram (b) represents probe emission and the remaining diagrams probe absorption. Dashed arrows represent spontaneously emitted photons.

[7], one need consider only final states connected adiabatically to state 1, and evaluate terms involving the emission of 1 or 2 spontaneous photons.

As can be seen from Eq. (13), *there is no dispersion-like resonance to order χ^2 .* the absence of the resonance can be traced to a cancellation from the third and fifth diagrams of Fig. 1(e). For an open system, this cancellation does not occur, as is discussed below.

For closed systems, the dispersion-like resonance near $\delta = 0$ occurs to second order in the pump field intensity. The dominant contribution to the absorption resonance near $\delta = 0$ can be associated with the partial amplitude [7] represented schematically in Fig. 2 (a) and that for emission with that shown in Fig. 2 (b). where I have used the fact that $\Delta + \Delta' - \Delta_{k_1} - \Delta_{k_2} \approx 0$. When the term represented in Fig. 2 (a) is squared and summed over all modes of the radiation field, there are terms of order χ^2 [already considered in Fig. 1 (f)], χ^4 , and χ^6 . The χ^4 term is an interference term, providing a contribution

$$A^{(4)} = \frac{16\gamma\chi^4}{\Delta^5} \frac{\delta}{(2\gamma)^2 + \delta^2}, \quad (14)$$

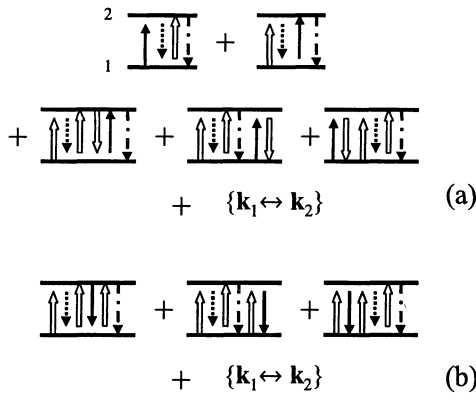


Fig. 2. A diagrammatic representation of the contribution to the ground state amplitude that leads to the dominant contribution to the resonant structure centered near $\delta = 0$. (a) probe absorption (b) probe gain. The symbol $\{\mathbf{k}_1 \leftrightarrow \mathbf{k}_2\}$ indicates that terms in which the order of spontaneously emitted photons is interchanged must be added to the diagrams.

in agreement with the density matrix result (8), The sixth order term,

$$A^{(6)} = \frac{16\gamma\chi^6}{\Delta^6} \frac{1}{(2\gamma)^2 + \delta^2}, \quad (15)$$

is greater than the fourth order term in the limit that $\chi^2/\gamma|\Delta| > 1$. However, the sixth order term is *canceled* exactly by the corresponding contribution to probe field amplification in this region, represented schematically in Fig. 2 (b) [7]. The sixth order terms represent the largest contribution to absorption and emission separately for the $\delta = 0$ resonance, while the fourth order term provides the dominant contribution to the overall absorption or gain. This is an interesting case, analogous to situations in which the second Born approximation can be larger than the first. In our case it arises owing a resonant channel that opens for processes involving the emission of two spontaneous photons; for one-photon processes the spectrum of spontaneously emitted radiation is peaked near $\omega_k = \Omega$, but for two photon processes there is a resonant channel with $\omega_{k_1}, \omega_{k_2} \approx (\Omega + \Omega' - \omega), \omega$. No new additional resonances appear when processes involving the emission of three or more spontaneous photons are considered which is why the maximum contribution to the net absorption peaks at the χ^4 term. New resonant channels *would* appear if higher order probe interactions were included [1].

As pointed out by Grynberg and Cohen-Tannoudji [7], the dispersion-like resonance at $\delta = 0$ can be attributed to an interference channel that occurs for absorption, but not emission. An alternative interpretation can be given. Combining Eqs. (14) and (15) in the limit $\chi^2/\gamma|\Delta| \gg 1$, one can rewrite the absorption as

$$A^{(6)} \approx \frac{16\gamma\chi^6}{\Delta^6} \frac{1}{(2\gamma)^2 + (\delta - S)^2}, \quad (16)$$

where

$$S = \frac{2\gamma\Delta}{\chi^2} \gamma; \quad |S| \ll \gamma, \quad (17)$$

appears to be a type of radiative shift. The emission is peaked at $\delta = 0$ and the difference between absorption and emission gives rise to the dispersive shape.

4 Open System

It is possible to extend the amplitude calculation to include the effect of collisions [7,14] or additional decay channels for the excited state. I consider an open system in which level 2 can decay to an additional ground state sublevel 0, but state $|0\rangle$ is *not* coupled to state $|2\rangle$ by the pump and probe fields. Additional amplitude diagrams are now needed in which spontaneous emission to level 0 is allowed. Since any population arriving in state $|0\rangle$ via spontaneous emission is decoupled from the fields, the only new diagrams that need be considered are those in which the *final* spontaneous emission is to level 0. Thus, instead of getting a full complement of diagrams involving state $|0\rangle$ such as those in Fig. 1, the only new diagrams that appear giving rise to probe absorption to order χ^2 are those shown in Fig. 3 (a). There is no diagram in Fig. 3 (a) analogous to the last diagram in Fig. 1 (e); as a consequence there is no longer a cancellation of the disperion-like resonance to order χ^2 .

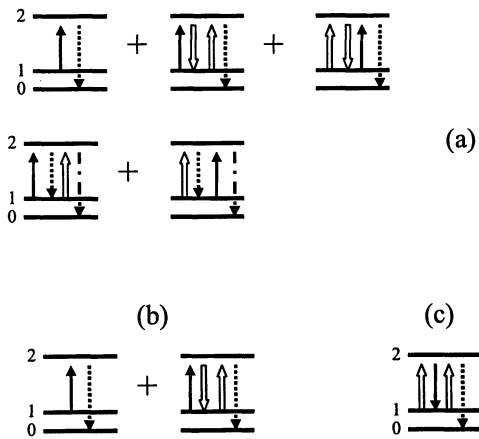


Fig. 3. (a) Additional diagrams that must be considered for an open system when calculating probe absorption to first order in the pump field intensity. (b) and (c) Diagrammatic representations of the contributions to the ground state amplitudes that lead to the dominant contribution to the resonant structure centered near $\delta = 0$ for the open system considered in this work; (b) probe absorption, (c) probe gain.

The dominant contribution to the dispersion-like resonance near $\delta = 0$ can be associated with the partial amplitudes represented schematically in Figs. 3 (b),(c) plus the contribution from linear absorption,

$$A^{(0)} + A^{(2)} + A^{(4)} \sim \frac{2(\gamma + \gamma')}{\Delta^2} + \frac{4\gamma'\chi^2 t \sin^2 y}{\Delta^3 y} + \frac{2\gamma'\chi^4 t^2 \sin^2 y}{\Delta^4 y^2}, \quad (18)$$

where

$$y = \delta t/2 \quad (19)$$

and γ (γ') is one half the partial decay rate from level 2 to level 1 (0). There are a few interesting points to note. If $\chi^2 t / |\Delta| \gg 1$, the term in Eq. (18) of order χ^4 is dominant; however, this term is exactly canceled by the corresponding emission term arising from the diagram of Fig. 6 (c). In this limit, the probe absorption or gain profile near $\delta = 0$ can be approximated as

$$A^{(2)} = \frac{4\gamma'\chi^2 t \sin^2 y}{\Delta^3 y} \quad (20)$$

and is of order χ^2 rather than χ^4 found for closed systems. For fixed t , the dispersion-like line shape, which is plotted in Fig. 4, has a width of order t^{-1} . The width is determined by the time the atoms spend in the field interaction zone or by the observation time, whichever is shorter [14]. The absorption "rate" is not constant, since the effective ground state lifetime depends on t . The corresponding result from a density matrix calculation in which level 1 is incoherently pumped and both ground state levels decay with a phenomenological decay constant, $\Gamma_0 \ll 2(\gamma + \gamma')$, is

$$A = \frac{4\gamma'\chi^2}{\Delta^3} \frac{\delta}{\Gamma_0^2 + \delta^2}, \quad (21)$$

which is also shown in Fig. 4, with $\Gamma_0 = t^{-1}$. For fixed Δ , it is possible to observe probe gain for much lower pump field intensities with open systems than with closed ones.

5 Recoil-Induced Resonances

Up to now the central resonance has involved the emission of spontaneous radiation. It is possible to have a central resonance involving only stimulated processes if one considers pump-probe spectroscopy of an ensemble of atoms cooled below the recoil limit. The recoil limit corresponds to energies less than $\hbar\omega_q$, where $\omega_q = \hbar\kappa^2/2m$ and $\mathbf{q} = \mathbf{k}' - \mathbf{k}$, is the difference in propagation vectors of the probe and pump fields. This condition can be achieved, for example, in a Bose condensate or in a highly collimated atomic beam. Since the center-of-mass energy of the atoms is comparable with the energy associated

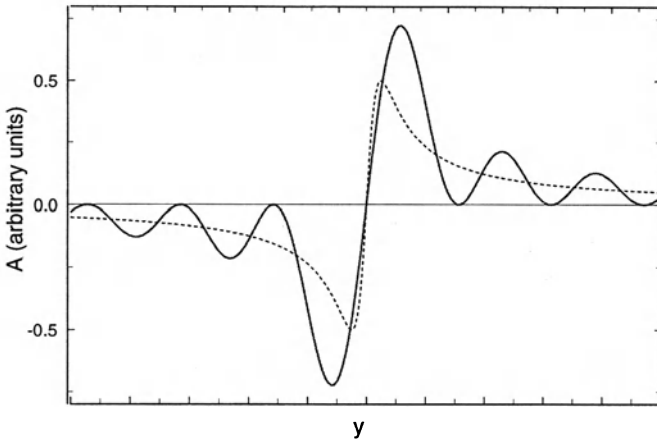


Fig. 4. Probe absorption line shape A as a function of $y = \delta t / 2$. The solid line is the result of the amplitude calculation. The dashed line is the result of a density matrix calculation in which the ground state is given a phenomenological decay constant Γ_0 , $y = \delta / 2\Gamma_0$, and Γ_0 is set equal to t^{-1} .

with a single photon of the pump or probe fields, it is necessary to quantize the momentum states of the atoms. Inclusion of *external* (e.g. center-of-mass) state energies lifts the degeneracy for the processes of (a) probe absorption and pump emission and (b) pump absorption and probe emission. As a result, the central resonance results from the difference in probabilities for these two processes.

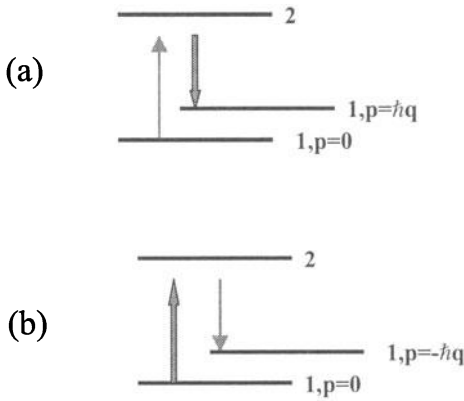


Fig. 5. A diagrammatic representation of the amplitudes that contribute to recoil-induced resonances. The center-of-mass momentum must now be included in the state labels. The vector \mathbf{q} is equal to the difference between the probe and pump field propagation vectors. (a) probe absorption, (b) probe gain.

The diagrams representing these amplitudes are shown in Fig. 5. The probe absorption rate associated with these diagrams, given by

$$A = 2 \frac{\chi^2}{\Delta^2} \left\{ \frac{\sin[(\delta - \omega_q)t]}{\delta - \omega_q} - \frac{\sin[(\delta + \omega_q)t]}{\delta + \omega_q} \right\}, \quad (22)$$

is plotted in Fig. 6. For this quantity to be larger than the linear absorption rate one must have $\chi^2 t / \gamma > 1$. This central resonance is not dispersion-like in shape (the absorption and emission profiles are resolved) and the absorption rate is an even function of Δ , rather than the odd function found in Eqs. (14) and (21). It may be possible to observe absorption profiles of this type in the pump-probe spectroscopy of Bose condensates [16].

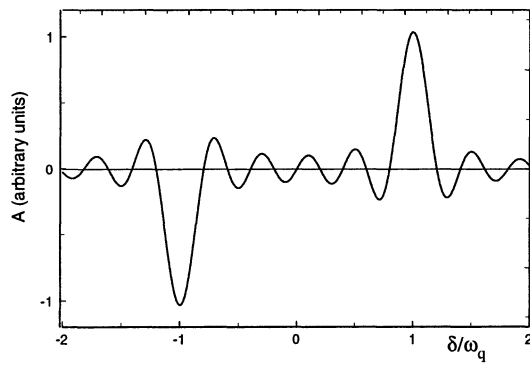


Fig. 6. Probe absorption line shape A for the recoil induced resonances. The width of the resonances is of order t^{-1} so that they are resolved for $\omega_q t > 1$.

In samples, such as laser-cooled vapors, which are cold, but not cooled below the recoil limit, it is necessary to average over the atomic velocity distribution. If $qu > \omega_q$ (u is the most probable atomic speed), the recoil-induced resonance line shape becomes the derivative of the velocity distribution, evaluated at $v = -\delta/q$ [9]. In this way, the probe absorption spectrum can be used to measure the velocity distribution of a laser-cooled sample without significantly perturbing the atoms [17].

6 Collective Atomic Recoil Laser

Bonifacio and De Salvo proposed a type of pump-probe spectroscopy in which the gain coefficient was a nonlinear function of the atomic density [10]. The atomic sample is placed in a cavity which is tuned to the probe frequency, such that the probe field builds up as a function of time. They referred to the overall device as a *collective atomic recoil laser* (CARL). The relationship between the recoil-induced resonances and CARL has been discussed in detail [12].

To illustrate the origin of the nonlinear dependence on atomic density, it is convenient to compare the field evolution for a "normal" laser with the

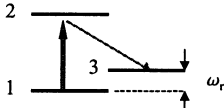


Fig. 7. Level scheme for a Raman laser. Levels 1 and 3 are ground state sublevels having the same parity.

corresponding theory for a Raman laser. In Lamb's theory of the laser [18], the linear gain of the field is described by an equation of the form

$$\frac{d\chi'}{dt} = C_L \gamma^2 \int_0^t \chi'(t') e^{-\gamma(t-t')} \cos[\Delta'(t-t')] dt',$$

while for the Raman laser with level scheme shown in Fig. 7, in which ω_r is the Raman transition frequency, the corresponding equation is

$$\frac{d\chi'}{dt} = C_r \chi^2 \int_0^t \chi'(t') \cos[(\delta - \omega_r)(t-t')] dt'.$$

The constants C_L and C_r are proportional to the atomic density.

In Lamb theory it is possible to evaluate $\chi'(t')$ at $t' = t$ provided the field builds up on a time scale long compared with γ^{-1} . This leads to a *local* relationship between $d\chi'/dt$ and $\chi'(t)$ - that is, $d\chi'/dt$ is proportional to $\chi'(t)$. In the Raman case, this adiabatic elimination may not be justified and one must retain an integral equation for $\chi'(t)$. For $\delta = \omega_r$ and $(C_r \chi)^{1/2} t > 1$, $\chi'(t)$ grows as $\exp[C_r \chi^{1/2} t]$; that is, with a gain coefficient that varies as the square root of the density.

In the case of the recoil-induced resonances, it may also be necessary to retain an integral expression for the field build-up, although the equations differ slightly. One finds an equation of the form [10–12]

$$\frac{d\chi'}{dt} = iQ \omega_q^2 \int_0^t \chi'(t') e^{i\delta(t-t')} \sin[\omega_q(t-t')] dt',$$

where Q is a constant proportional to the atomic density. In this limit the theory is that of the CARL. For a given δ , exponential gain occurs if the atomic density exceeds a critical value. It is in this sense that CARL is a collective effect. The gain coefficient can be proportional to the square root of the density if $\delta = -\omega_q$ and the cube root of the density for other values of δ [10–12]. Recent experiments involving Bose condensates [19] may offer the possibility for measuring CARL gain.

One interesting feature of CARL is that gain occurs at $\delta = 0$ if $Q > 2/2\sqrt{3}$, whereas the gain coefficient vanishes identically at $\delta = 0$ for the central resonance in the pump-probe spectroscopy discussed in Secs. II and III. This feature can also be understood within the context of an amplitude calculation. The probe gain is proportional to $d/dt [|a_-(t)|^2 - |a_+(t)|^2]$, where

the amplitudes $a_-(t)$, $a_+(t)$, are given by [12]

$$a_-(t) = -i\Delta^{-1}\chi \int_0^t [\chi'(t')]^* e^{-i\omega_q(t-t')} dt';$$

$$a_+(t) = -i\Delta^{-1}\chi \int_0^t \chi'(t') e^{-i\omega_q(t-t')} dt'.$$

If $\chi'(t')$ can be evaluated at $t' = t$ then $|a_-(t)|^2 = |a_+(t)|^2$ and there is no gain. In general, however, the phase of the probe field leads to different values for $|a_-(t)|^2$ and $|a_+(t)|^2$. For example, if $\chi'(t')$ varies as $e^{i\alpha t}$ with α real and positive, the integrand for $a_-(t)$ varies more slowly than that for $a_+(t)$, leading to $|a_-(t)|^2 > |a_+(t)|^2$, and probe gain.

7 Conclusion

The subject of pump-probe spectroscopy has been revisited using an amplitude approach. While much more algebraically complicated than a density matrix approach, the amplitude approach provides additional insight into the atom-field dynamics. The origin of the central dispersion-like resonance has been studied for both open and closed systems. An amplitude approach enables one to understand why the amplitude of the central resonance varies as the pump intensity squared for closed systems, but linearly with the pump intensity for open systems. To my knowledge, this type of gain behavior has yet to be observed in open systems of the type described in this paper. It should be observable using atoms in a vapor cell if nearly copropagating pump and probe fields are used to minimize the Doppler effect. Problem involving atomic recoil, such as recoil-induced resonances and CARL, have also been discussed using an amplitude approach.

One can legitimately consider the gain that occurs near $\delta = 0$ for the closed system as amplification without level inversion, since there is no inversion in the bare or dressed basis [7,20]. From Fig. 2 (c), one sees that probe gain near $\delta = 0$ involves the transformation of *three* pump photons into a probe photon and two photons emitted into modes \mathbf{k}_1 and \mathbf{k}_2 . Although this could be viewed as a parametric process for the emission of these three photons, this characterization does not seem appropriate when one considers amplification of the probe field only, with an average over modes \mathbf{k}_1 and \mathbf{k}_2 . The contribution to probe gain from Fig. 2 (c), which varies as $[(2\gamma)^2 + \delta^2]^{-1}$, is maximum for $\delta = 0$, but is nonvanishing over a range of detunings determined by the excited state decay rate. Such behavior is not typical of parametric processes. Moreover it implies that if the pump field has a bandwidth less than or on the order of γ , this pump field energy can be converted into narrowband probe emission, characteristic of lasing processes.

Acknowledgments. This research is supported by the National Science Foundation under Grants No. PHY-9800981 and PHY-9876915, and by the U. S.

Army Research Office under Grants Nos. DAAG55-97-0113 and DAAD19-99-C-0032. I would like to thank G. Grynberg and T. Mossberg for helpful discussions. I should also like to thank Shi-Yao Zhu for his tireless efforts in organizing this Conference and helping the participants with their arrangements.

References

1. See, for example, G. S. Agarwal and N. Nayak, *J. Opt. Soc. Amer. B* **1** (1984) 164; H. Friedman and A. P. Wilson-Gordon, *Phys. Rev. A* **36** (1987) 1333; N. B. Manson, C. Wei, and J. P. D. Martin, *Phys. Rev. Lett.* **76** (1996) 3943; H. S. Freedhoff and Z. Ficek, *Phys. Rev. A* **58** (1998) 1296.
2. B. R. Mollow, *Phys. Rev. A* **5** (1972) 2217.
3. Haroche and Hartmann [S. Haroche and F. Hartmann, *Phys. Rev. A* **6** (1972) 1280] obtained the probe absorption spectrum in the context of velocity-tuned resonances in the theory of saturated absorption. They interpreted the structure centered near $\delta = 0$ as a competition between the two processes shown in Fig. 3 (a),(b) (which cancel exactly in our model). In the context of the relaxation model used in their paper, their amplitude interpretation does not appear to be justified.
4. F. Y. Wu, S. Ezekiel, M. Ducloy, and B. R. Mollow, *Phys. Rev. Lett.* **38** 1077 (1977).
5. C. Cohen-Tannoudji and S. Reynaud, *J. Phys. B* **10** (1977) 345.
6. G. Khitrova, P. R. Berman, and M. Sargent III, *J. Opt. Soc. Amer. B* **5** (1988) 160; P. R. Berman, V. Finkelstein, and J. Guo, in *Laser Spectroscopy X*, edited by M. Ducloy, E. Giacobino, and G. Camy (World Scientific, Singapore, 1992) pps. 15-20.
7. G. Grynberg and C. Cohen-Tannoudji, *Optics Comm.* **96** (1993) 150.
8. P. R. Berman, *Phys. Rev. A* **53**, 2627 (1996).
9. J. Guo, P. R. Berman, B. Dubetsky, and G. Grynberg, *Phys. Rev.* **46**, 1426 (1992).
10. R. Bonifacio and L. De Salvo, *Nucl. Instrum Methods Phys. Res. A* **341**, 360 (1994).
11. M. Moore and P. Meystre, *Phys. Rev. A* **58**, 3248 (1998).
12. P. R. Berman, *Phys. Rev. A* **59**, 585 (1999).
13. It is also possible to carry out the calculations using fields that are turned on adiabatically. The final steady state results are identical, but the contributions from *individual* diagrams differ for the two approaches.
14. B. Dubetsky and P. R. Berman, *Phys. Rev. A* **47** (1993) 1294.
15. P. R. Berman and G. Khitrova, *Opt. Comm.*, to appear.
16. D. M. Stamper-Kurn, A. Chikkatur, A. Görlitz, S. Inouye, S. Gupta, D. Pritchard, and W. Ketterle, cond-matter/9906035; *Phys. Rev. Lett.*, to appear.
17. J. Y. Courtois, G. Grynberg, B. Lounis, and P. Verkerk, *Phys. Rev. Lett.* **72**, 3017 (1994).
18. W. E. Lamb, Jr., *Phys. Rev.* **134**, A1429 (1964).
19. S. Inouye, A. Chikkatur, D. Stamper-Kurn, J. Stenger, D. Pritchard, and W. Ketterle, *Science* **285**, 571 (1999).
20. N. Lu and P. R. Berman, *Phys. Rev. A* **44** (1991) 5965.

Electromagnetically Induced Waveguides and Propagation in Forbidden Zone

G.S. Agarwal

Physical Research Laboratory, Navrangpura,
Ahmedabad-380 009, India
E-mail: gsa@prl.ernet.in

Abstract. We demonstrate how an intense resonant electromagnetic field can be used to allow propagation in otherwise forbidden region. We further show how a weak probe beam can be guided through a medium whose properties are spatially modified by a donut beam.

In recent years considerable progress has been made in achieving control of the optical properties of a medium [1]. In particular the control of the dispersive properties of a medium is especially significant in several contexts. Scully and co-workers proposed enhancement of refractive index and its subsequent usage in enhancing the sensitivity of magnetometers[2]. Harris et al.[3] recognised the possibility of slowing the group velocity [4] of light and this has been demonstrated in recent experiments of Hau et al. [5] and Scully et al. [6]. In early works Tewari and Agarwal [7] and Harris et al. [8] had demonstrated the enhancement of the efficiency of VUV generation by the modifications in the absorptive and dispersive properties of a medium. These ideas have been extended to other nonlinear processes[9].

My group has undertaken studies in several directions involving : (a) detailed considerations of polarization and anisotropies[10]; (b) Considerations of the role of near-l-by levels and breakdown of the usual secular approximation[11]; (c) Considerations of dense media[12]; (d) Considerations of diffraction and propagation effects which is especially challenging as the spatial structure makes the medium highly inhomogeneous [13].

In what follows, I describe the latter two of the above two aspects.

1 Electromagnetic Field Induced Propagation in Forbidden Zone

It is well-known [14] that electromagnetic waves with wavevector \mathbf{k} cannot propagate in the frequency region where the dielectric function $\epsilon(\omega)$ of the medium is negative. This conclusion follows from the standard dispersion relation $k^2 = \frac{\omega^2}{c^2} \epsilon(\omega)$. By way of illustration, let us consider a material system characterized by a dielectric function of the form

$$\epsilon(\omega) = \epsilon_0 \left(1 + \frac{\omega_L^2 - \omega_0^2}{\omega_0^2 - \omega^2} \right). \quad (1)$$

Here ϵ_0 is the background dielectric constant, ω_L is a parameter (defined by $\epsilon(\omega_L) = 0$) that characterizes the strength of the optical response, and we ignore the effects of damping. We see from Eq. (1) that $\epsilon(\omega)$ is negative in the frequency region $\omega_0 < \omega < \omega_L$. This region corresponds to a band gap – a region in which only evanescent waves are possible. This band gap occurs even though in our model $\epsilon(\omega_L)$ is a real quantity. It is also known that the optical properties of a medium can be modified significantly by the application of resonant electromagnetic fields. In particular, resonant absorption can be made very small by the application of a control field leading to electromagnetically induced transparency (EIT)[17]. The question thus arises – Is it possible to eliminate the band gap region by the application of electromagnetic fields? We examine this question in detail and produce an answer in the affirmative. We examine a model system which is of relevance in many applications and which could be generalized easily in several ways depending on need. We take full account of local field effects [15] because band gaps can occur only in dense systems. We demonstrate that such a bandgap can occur in alkali vapors and can be removed by the application of a strong control field, although because of self broadening effects alkali vapors are not an ideal system for studying such effects. This part of the work is done jointly with Prof. R. W. Boyd of the University of Rochester.

It should be noted that the situation considered here is very different from those under which EIT has been previously studied. EIT is usually used to minimize absorption at frequencies for which $\text{Im}[\epsilon(\omega)]$ is large. In contrast, we consider the possibility of allowing propagation at frequencies where $\text{Im}[\epsilon(\omega)]$ is small but where propagation is usually prevented by the fact $\text{Re}[\epsilon(\omega)]$ is negative. We also note that earlier Harris [16] showed how the application of an additional electromagnetic field can produce propagation at a frequency below the cut-off frequency in an ideal plasma. Harris utilised collective effects arising from nonlinearities in a plasma to produce EIT in plasma.

Let us now consider a more detailed theoretical model based on the coupling scheme shown in the inset to Fig. 1. We consider first the optical response to a single applied field at frequency ω ; we will later see how this response is modified by the application of an additional control field of frequency ω_c . The linear response at frequency ω is given by the standard ‘two-level’ model as [17].

$$\chi = \frac{n|\mathbf{d}_{13}|^2}{\hbar(\Delta - i\Gamma)}; \quad \Delta = \omega_{13} - \omega. \quad (2)$$

Here, as usual, n is the atomic number density of the medium, \mathbf{d}_{13} is the transition dipole matrix element and Γ is the half width at half maximum of the transition $|1\rangle \leftrightarrow |3\rangle$. The susceptibility as modified by local field effects is given in Gaussian units by

$$\chi_l = \frac{\chi}{(1 - \frac{4\pi}{3}\chi)}. \quad (3)$$

Let us introduce the *local-field parameter* δ with dimensions of frequency

$$\delta = \frac{4\pi n|d|^2}{3\hbar}. \quad (4)$$

On using Eqs.(2)-(4), the dielectric function with the inclusion of local field effects can be expressed as

$$\epsilon_l(\omega) \equiv 1 + 4\pi\chi_l = 1 + \frac{3\delta}{\Delta - i\Gamma - \delta}. \quad (5)$$

For Γ sufficiently small (in particular, for $\Gamma/\delta < \frac{3}{2}$), Eq. (5) predicts the existence of a band gap region in which $\epsilon_l(\omega)$ is negative. For the limiting case in which Γ is negligibly small, $\epsilon_l(\omega)$ is negative in the region

$$-2\delta < \Delta < \delta. \quad (6)$$

Note that the frequency ω_L of Eq. 1) for the response described by Eq. (5) is determined by the condition $\epsilon_l(\omega_L) = 0$ and hence is given by $\omega_L = \omega_0 + 2\delta$.

We next demonstrate that the band gap can be removed by the application of a resonant electromagnetic field [13] on a suitably chosen transition of the material system, such as the $|1\rangle \leftrightarrow |2\rangle$ transition shown in the inset to Fig. 1. Let us denote by $2G_c$ and Δ_c the Rabi frequency and the detuning of the electromagnetic control field of frequency ω_c on the transition $|1\rangle \leftrightarrow |2\rangle$. Let Γ_d be the dephasing rate of the dipole forbidden transition $|2\rangle \leftrightarrow |3\rangle$. The modification of the susceptibility given by Eq. (2) as a result of the control field on has been derived earlier [1] and is given by

$$\tilde{\chi} = \frac{n|d|^2}{\hbar(\Delta - i\Gamma - \frac{i|G_c|^2}{\Gamma_d + i\Delta - i\Delta_c})}, \quad \Delta_c = \omega_{12} - \omega_c. \quad (7)$$

It should be borne in mind that we are concerned with a region that is distinct from the usual region of electromagnetic induced transparency (which for large $|G_c|$ and $\Delta_c \sim 0$ occurs in the region $\Delta \sim 0$). Using Eq. (7) in Eq. (3), we obtain the control-field-modified susceptibility and the dielectric response with local field corrections given by

$$\tilde{\epsilon}_l(\omega) = 1 + \frac{3\delta}{(\Delta - i\Gamma - \frac{i|G_c|^2}{\Gamma_d + i\Delta - i\Delta_c} - \delta)}. \quad (8)$$

Note that if local field corrections were ignored, then δ would not appear in the denominator in (8). Using Eq. (8), we can study the extent to which the band gap given by Eq. (6) can be eliminated by the application of a control field on the transition $|1\rangle \leftrightarrow |2\rangle$.

In Fig. 1 we show the regions of the parameter space where $\text{Re}[\tilde{\epsilon}_l]$ takes positive and negative values. The plot is shown as functions of the strength of the controlling field. The band gap is removed when $\text{Re}[\sqrt{\tilde{\epsilon}_l}] > 0$ and the region where $\text{Im}[\sqrt{\tilde{\epsilon}_l}]$ remains small is specially of interest.

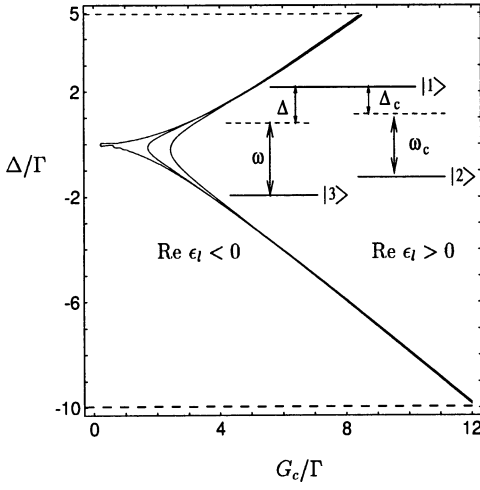


Fig. 1. Contour plots of $\text{Re}[\tilde{\epsilon}_l(\omega)] = 0$, in the band-gap region [indicated by dashed line] defined by relation (6). The three curves from left to right are for increasing values of the collisional parameter $\Gamma_d/\Gamma = 0, 0.5$ and 1.0 . The region to the right of the plot corresponds to positive values of $\text{Re}[\tilde{\epsilon}_l]$, where electromagnetic propagation is allowed. The region to the left of the plot corresponds to negative values of $\text{Re}[\tilde{\epsilon}_l]$, where no electromagnetic propagation is allowed. The inset shows the two level scheme and its modification by the application of a control laser of frequency ω_c . We choose $\delta/\Gamma = 5$.

Let us now explore the experimental feasibility of observing these effects. The primary experimental requirement is that there exist some region near the atomic resonance in which the dielectric function is negative. From Eq. (5) we deduce that the real part of the dielectric function reaches its minimum value for $(\Delta - \delta) = -\Gamma$, at which frequency its value is given by

$$\text{Re}[\epsilon_l(\min)] = 1 - \frac{3\delta}{2\Gamma}. \quad (9)$$

For sufficiently large atomic number density n the line width Γ will be dominated by self-broadening effects such that $\Gamma = C_s n$, where C_s is the self broadening coefficient. For atomic sodium, $C_s = 1.5 \times 10^{-7} \text{ cm}^3/\text{s}$; the value for other alkali atoms is comparable[18]. Thus for sodium vapor, for $n > 6 \times 10^{14} \text{ cm}^{-3}$ the collisional linewidth will exceed the natural linewidth of 10 MHz, and for $n > 1 \times 10^{17} \text{ cm}^{-3}$ the collisional linewidth will exceed the typical 2 GHz Doppler linewidth. Note from Eq. (4) that δ is also proportional to n , and hence for sufficiently large number density $\text{Re} \epsilon_l(\min)$ attains a density-independent value. If we evaluate Eqs. (4) and (9) in this limit, using $d = 5.5 \times 10^{-18} \text{ esu}$ (the value for the sodium resonance line), we find that the ratio Γ/δ (mentioned above in connection with Eq. (5)) has the value 1.25 and that $\text{Re} \epsilon_l(\min) = -0.21$, which hence shows that a band gaps exists under these circumstances. Note, however, that unlike in the idealized situation discussed above where damping was neglected, here the imaginary part of ϵ_l is substantial. To study the influence of damping effects, in the Fig.2 we show the real and imaginary parts of $\sqrt{\epsilon_l}$. We notice the important prediction that in the region $G_c/\Gamma \sim 1$, $\text{Im} \sqrt{\epsilon_l} \approx 0$, whereas the real part is positive leading to the propagation of electromagnetic waves. Note that in order to obtain a Rabi frequency as large as 2 GHz so that the condition $G_c/\Gamma \approx 1$ can be satisfied for a medium in which the collisional broadening is

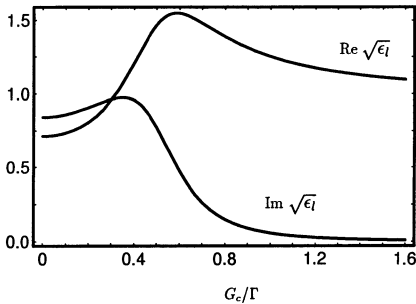


Fig. 2. Control-field-induced propagation for the situation described by Eq. (12) with $\Gamma_d/\Gamma = 0$, $\Delta = \delta - \Gamma$, $\Gamma/\delta = 1.25$, $\Delta_c = 0$. Note that for G_c/Γ greater than approximately 0.4, the real part of $\sqrt{\epsilon_l}$ is greater than unity. Note also that for G_c/Γ greater than approximately 0.7 the imaginary part of $\sqrt{\epsilon_l}$ becomes quite small. Under these conditions the propagation of optical fields has been induced

comparable to Doppler broadening, the laser intensity need be only as large as 600 W/cm^2 .

2 Electromagnetic Field Induced Wave Guides

In a recent experiment Truscott et al. [19] demonstrated yet another important application of the modified dispersive properties of a medium. They produced an optically written waveguide in an atomic vapor. In their experiment a weak Gaussian probe beam was tuned close to the rubidium D_2 line (780 nm, $5^2S_{1/2} \rightarrow 5^2P_{3/2}$), while a strong donut shaped pump beam was tuned close to the rubidium D_1 resonance (795 nm, $5^2S_{1/2} \rightarrow 5^2P_{1/2}$). The two beams interact because the two transitions share a ground state. They used a simplified model for the susceptibilities to argue how the waveguiding can be produced. In collaboration with Dr. R. Kapoor, we develop an explanation based on full density matrix equations and propagation equations in slowly varying envelop approximation. Our work includes all coherence effects. Our simulations for Doppler broadened systems produce results in excellent agreement with the work of Truscott et al. Our simulations also show guiding behavior at different positions inside the cell.

We now present a theoretical model for guiding of one optical beam with another optical beam. We consider the example of the relevant energy levels of Rb. The transitions are shown in Fig. 3. The D_1 and D_2 transition of Rb can be described as a V-type atomic system. The 2γ 's represent the rate of spontaneous decay. The field on the D_2 transition $|1\rangle \rightarrow |3\rangle$ is the probe field while the field on D_1 transition $|2\rangle \rightarrow |3\rangle$ is the pump field. Δ 's represent various detunings: $\Delta_1 = \omega_{13} - \omega_1$ and $\Delta_2 = \omega_{23} - \omega_2$, and $2G$'s denote the Rabi frequencies. $G_1 = d_{13} \cdot E_1 / \hbar$, $G_2 = d_{23} \cdot E_2 / \hbar$. This type of atomic system can be described by the following set of density matrix equations

$$\dot{\rho}_{11} = -2\gamma_1\rho_{11} + iG_1\rho_{31} - iG_1^*\rho_{13} \quad (10)$$

$$\dot{\rho}_{12} = -(\gamma_1 + \gamma_2 + i(\Delta_1 - \Delta_2))\rho_{12} + iG_1\rho_{32} - iG_2^*\rho_{13}$$

$$\dot{\rho}_{13} = -(\gamma_1 + i\Delta_1)\rho_{13} - iG_2\rho_{12} - iG_1(\rho_{11} - \rho_{33})$$

$$\dot{\rho}_{22} = -2\gamma_2\rho_{22} + iG_2\rho_{32} - iG_2^*\rho_{23}$$

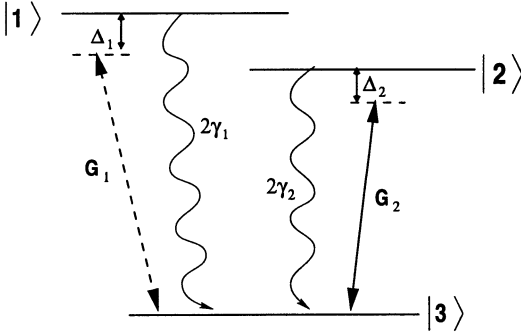


Fig. 3. A typical V -system corresponding to the studies in Ref.[19].

$$\dot{\rho}_{23} = -(\gamma_2 + i\Delta_2) \rho_{23} - iG_1 \rho_{21} - iG_2 (\rho_{22} - \rho_{33})$$

$$\dot{\rho}_{33} = +2\gamma_1 \rho_{11} + 2\gamma_2 \rho_{22} - iG_1 \rho_{31} + iG_1^* \rho_{13} - iG_2 \rho_{32} + iG_2^* \rho_{23}$$

All the fast dependences of $\rho_{\alpha\beta}$ have been removed by canonical transformation. Thus ρ_{13} in Schrödinger picture will be obtained by multiplying the solution of (10) by $e^{-i\omega_1 t}$. A Gaussian probe beam is tuned near to D_2 transition and a donut shaped Laguerre-Gaussian pump beam of charge three is tuned near to D_1 transition. Thus the Rabi frequencies for pump and probe beams are given by

$$G_1 = \left(\frac{G_{01}}{w_1(z)} \right) \sqrt{\frac{2}{\pi}} \exp \left(-\frac{i k r^2}{2 q_1} \right) e^{i k z - i w_1 t}, \quad (11)$$

$$G_2 = \left(G_{02} / \sqrt{3\pi} w_2(z) \right) \left(\frac{\sqrt{2} r}{w_2(z)} \right)^3 \exp \left(-\frac{i k r^2}{2 q_2} - 3i \theta \right) e^{i k z - i w_2 t}, \quad (12)$$

$$r^2 = x^2 + y^2, \theta = \tan^{-1} \left(\frac{y}{x} \right), w(z) = w_{02} \sqrt{1 + \left(\frac{z - z_o}{z_R} \right)^2}. \quad (13)$$

The complex parameter q in these equations can be written as $q_{1,2} = iz_{R1,2} - z + z_0$ where $z_{R1,2} = \pi w_{01,2}^2 / \lambda_{1,2}$ is the Rayleigh range and the beam waist of both the beam is located at $z = z_0$. $w_{01,2}$ is the waist radius. The induced polarization for probe beam due to both the beams is taken as

$$\mathbf{P} = N \mathbf{d}_{13} \rho_{13}, \quad (14)$$

where \mathbf{d}_{13} is the dipole matrix element for the D_2 transition and N is the number density. We solved the density matrix equations for steady state with the assumption of a weak probe beam and strong pump beam. Therefore in the expression for ρ_{13} the higher order terms of G_1 were neglected while keeping all orders of G_2 . The value of ρ_{13} obtained with these assumptions is to be used in the wave equation for the probe field, which in slowly varying envelop approximation can be written as

$$\frac{\partial G_1}{\partial z} = \frac{ic}{2\omega} \nabla_\perp^2 G_1 + i\alpha \rho_{13}, \quad (15)$$

$$\nabla_{\perp}^2 = \left(\frac{\partial^2}{\partial x^2} + \frac{\partial^2}{\partial y^2} \right),$$

where the Rabi frequency is scaled in terms of γ_1 and α is the absorption coefficient at line centre

$$\alpha = \frac{4\pi n d_{13}^2 \omega}{\hbar c \gamma}. \quad (16)$$

ω is the angular frequency of the transition and c is the velocity of light. In principle we should account also for the absorption and diffraction of the pump field. The equation for the pump is obtained from (15) by using the replacements $G_1 \rightarrow G_2$, $\rho_{13} \rightarrow \rho_{23}$. We assume that the absorption coefficient for the two transitions are approximately equal. The density matrix element ρ_{23} can be computed to zeroeth order in G_1 but to all orders in G_2 .

It should be noted that the spatial transverse structure of the pump makes ρ_{13} dependent on spatial coordinate r which we have studied extensively in many different planes of the medium. Thus Eq.(15) becomes inhomogeneous. The inhomogeneities can produce Hermite - Gaussian (or Laguerre-Gauss) modes of higher order. This can be seen by expanding the inhomogeneous term in (15) in a complete set of modes. The appearance of the ring structure in the Fig.4 is due to the excitations of modes of higher order. The experiment of Truscott *et al.* shows that there is no significant change in the pump beam while propagating through the medium. Therefore while the probe beam propagation was done numerically using Eq.(15), the pump beam propagation computations were done using the analytical expressions in Eq.(12). For hot system the average value of $\langle \rho_{13} \rangle$ was calculated numerically. Both the input beams are generated with an aperture large enough to pass 99% of the beam energy at its highest diameter. When both the beams were focussed at center a mesh size 256 x 256 was found to be sufficient. When the probe was focussed at the entrance a larger aperture size was needed. In the latter case we used a mesh size 512 x 512. We consider the Rb cell of length 10 cm. First we do simulations for a hot Rb atomic vapor with Doppler broadening $\nu_D = 120$. This corresponds to a Doppler width of about 690 MHz. We further take $\alpha = 5100 \text{ cm}^{-1}$ corresponding to a density of about $5 \times 10^{12} \text{ cm}^{-3}$. Here it was assumed that 75% ground state population was in ${}^{85}\text{Rb}$ and it was equally distributed among the two hyperfine levels of two isotopes. *The pump beam was focussed at the center of the cell with beam radius of 50 μm and the probe beam was focussed at the entrance of the cell with beam radius of 25 μm .* The parameter G_0 in the beam profiles has dimensions of cm/sec. and is related to the power P measured in Watts via the relation

$$(G_0/\gamma) \equiv \sqrt{\frac{3\lambda^3 P \times 10^7}{8\pi^2 \hbar \gamma c}}. \quad (17)$$

For the power levels used in the experiment [19] we get $G_{02}/\gamma = 11.29 \text{ cm}$ ($P = 400 \text{ mw}$), and $G_{01}/\gamma = 1.78 \text{ cm}$ ($P = 10 \text{ mw}$). The simulations were done

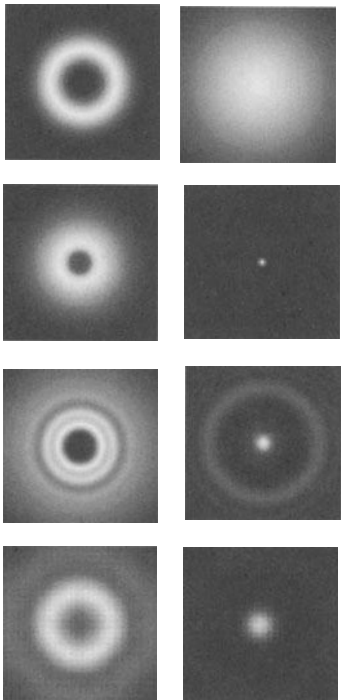


Fig. 4. The profile of the probe beam under different conditions. In the first row, left is the free propagating pump beam at the exit plane. The right part of the first row shows the probe beam at the exit plane in the absence of pump beam but in presence of the medium with $\Delta_1/\gamma = 833$. The second to fourth rows show probe beam profiles for different values of Δ_1 in a hot atomic system with $\nu_D/\gamma = 120$ and $\Delta_2 = 0$, $G_{02}/\gamma = 11.3$ cm and $G_{01}/\gamma = 1.787$ cm. The second row recorded at 5 cm from the entrance window and third row was recorded at the exit plane. In the first three rows $\alpha = 5100 \text{ cm}^{-1}$ and the probe beam was focussed at the entrance. The fourth row shows the probe profile for a different set of parameters $\alpha = 3400 \text{ cm}^{-1}$ and both pump and probe are focussed at the center of the cell. In second to fourth rows $\Delta_1/\gamma = -1267$ in the left column and at $\Delta_1/\gamma = 833$ in the right column

for $\Delta_1 = -1267$ corresponding to 3.8 GHz of detuning towards blue and $\Delta_1 = 833$ corresponding to 2.5 GHz of detuning towards red. The pump beam was tuned to the peak of the D_1 transition, therefore $\Delta_2 = 0$. The probe beam profile was recorded at a plane 5cm. inside the cell and at the exit plane. The results are shown in Fig.4. It can be seen that the red shifted probe beam gets guided into the hole of the donut while the blue shifted probe takes the shape of a ring. These results are in excellent agreement with the experimental results of Truscott and coworkers in a Doppler broadened system. We also show in Fig.4 that the wave guiding occurs rather generally. This is shown by carrying out simulations for a different set of parameters.

In conclusion we have shown how the ideas of quantum interference can be used to get electromagnetic wave propagation in the region in which it is normally forbidden. We have also shown how the waveguiding can be produced by laser induced spatial inhomogeneities of the refractive index.

References

1. S.E. Harris, Phys. Today, **50**(7), 36 (1997).
2. M.O. Scully, Phys. Rev. Lett. **67**, 1855, (1991); M.O. Scully and M. Fleischhauer, Phys. Rev. Lett. **69**, 1360 (1992); A.S. Zibrov *et al* Phys. Rev. Lett. **76**, 3935 (1996).

3. S.E. Harris, J.E. Field and A. Kasapi, Phys. Rev. A **46**, R29 (1992).
4. M.Xiao, Y.Q. Li, S.Z. Jin and J. Gea-Banacloche, Phys. Rev. Lett. **74**, 666 (1995); R. Grobe, F.T. Hioe and J.H. Eberly, Phys. Rev. Lett. **73**, 3183 (1994); A. Kasapi, M. Jain, G.Y. Yin and S.E. Harris, Phys. Rev. Lett. **74**, 2447 (1995).
5. L.V. Hau, S.E. Harris, Z.Dutton and C.H. Behroozi, Nature **397**, 594 (1999).
6. M.M. Kash, V.A. Sautenkov, A.S. Zibrov, L. Hollberg, G.R. Welch, M.D. Lukin, Yuri Rostovtsev, E.S. Fry and Marlan O. Scully, Phys. Rev. Lett. **82**, 5229 (1999).
7. S.P. Tewari and G.S. Agarwal, Phys. Rev. Lett. **56**, 1811 (1986); see also G.S. Agarwal and S.P. Tewari, Phys. Rev. Lett. **70**, 1417 (1993).
8. S.E. Harris, J.E. Field and A. Imamoğlu, Phys. Rev. Lett. **64**, 1107 (1990); M.Jain, G.Y. Lin, J.E. Field and S.E. Harris, Opt. Lett. **18**, 998 (1993).
9. H. Schmidt and A. Imamoğlu, Opt. Lett. **21** 1936 (1996); G.S. Agarwal and W. Harshawardhan, Phys. Rev. Lett. **77**, 1039 (1996).
10. A.K. Patnaik and G.S. Agarwal, Opt. Commun. in press.
11. S. Menon and G.S. Agarwal, Phys.Rev. **A59**, 740 (1999); Phys. Rev. **A** in press.
12. G.S. Agarwal and R.W. Boyd, Phys. Rev. **A60**, R2681 (1999)
13. R. Kapoor and G.S. Agarwal, sub. Phys. Rev.**A**.
14. R.S. Knox, Theory of Excitons (Academic Press, New York, 1963), Sec.8, see especially Fig.21.
15. J.J. Maki, M.S. Malcuit, J.E. Sipe, and R.W. Boyd, Phys. Rev. Lett. **67**, 972 (1991). R.Friedberg, S.R. Hartmann, and Jamal T. Manassah, Phys. Rev. A **40**, 2446 (1989); **42**, 494 (1990); V.A. Sautenkov, H. van Kampen, E.R. Eliel and J.P. Woerdman, Phys. Rev. Lett. **77**, 3327 (1996); I.V. Jyotsna and G.S. Agarwal, Phys. Rev. A**53**, 1690 (1996); G.S. Agarwal, Opt. Express **1**, 44 (1997). J.P. Dowling and C.M. Bowden, Phys. Rev. Lett. **70**, 1421 (1993); A.S. Manka, J.P. Dowling, and C.M. Bowden,*ibid.* **73**, 1789 (1994).
16. S.E. Harris, Phys. Rev. Lett. **77**, 5357 (1996).
17. R.W. Boyd, *Nonlinear Optics* (Academic Press, New York, 1992), Sec.5.3.
18. R.B. Miles and S.E. Harris, IEEE J. Quantum Electronics, 9, 470, (1973).
19. A.G. Truscott, M.E.J. Friese, N.R. Heckenberg and H. Rubinsztein-Dunlop, Phys. Rev. Lett. **82**, 1438 (1999).

Photon Localization and Exponential Scaling of Intensity Variance

Andrey A. Chabanov and Azriel Z. Genack

Queens College of the City University of New York, Flushing NY 11367, USA
e-mail: achqc@qcunix1.acc.edu

Abstract. We show that the extent of photon localization can be characterized by the relative size of fluctuations of intensity or of total transmission, even in absorbing samples. We find that above a value of approximately unity, the variance of normalized total transmission scales exponentially. Using this approach, we identify the spectral range for localization of microwave radiation in an ensemble of random configurations of alumina spheres contained in a copper tube at a volume fraction of 0.068.

The pursuit of photon localization encompasses the investigation of novel strong scattering environments and entails the search for a comprehensive description of statistical optics in terms of the proximity to the localization threshold. This subject is poles apart from the focus of this conference. In most presentations on laser physics and quantum optics, inhomogeneity is banished at the outset since scattering, which is often easily eliminated, suppresses nonlinear optical effects and destroys spatial coherence. Moreover, incorporating impurities clutters up calculations and in any case produces generally systems that cannot be replicated. However, the role of disorder in optics will likely become increasingly important in the years ahead. Not only in traditional fields such as imaging and communications but also in the recent development of random lasers and of quantum optics and energy transfer in doped periodic and nearly periodic photonic band gap materials. Here we will report on the development of a statistical means for identifying photon localization and discuss localization in collections of resonant spheres.

Anderson localization was first studied in the electronic context [1] in which disorder is widespread. Ioffe and Regel [2] argued that the electrons wave function would fall exponentially on average when its transport mean free path became significantly smaller than its wavelength. The realization that electron localization is at root a wave phenomenon [2,3] has led to the conjecture that photons could also be localized [3]. Achieving photon localization would allow a detailed study of the Anderson localization transition undisturbed by the Coulomb interaction and would open up a range of new optical and microwave phenomena.

Microwave measurements such as those reported here are particularly well suited to provide a full description of universal aspects of transport. Microwave field spectra can be measured with high spectral and spatial resolu-

tion for an *ensemble* of random samples. Rearranging the positions of macroscopic scatterers by momentarily tumbling the sample produces a collection of samples with equivalent disorder. This is in contrast to electronic studies, in which the conductance, a highly averaged quantity, is ordinarily measured in a single sample. In order to observe multiple scattering phenomena in samples larger than the dephasing length, electronic samples are generally cooled below 1 K [4,5]. Such samples, with dimensions ~ 1 mm are termed mesoscopic because they are intermediate in size between the microscopic atomic scale and the macroscopic scale. In contrast, temporal coherence is readily achieved for classical waves in static macroscopic samples.

Reports of three-dimensional photon localization have been based upon observations of the exponential decay of the electromagnetic wave [6–10]. These reports have come under close scrutiny because of the possibility that the decay observed may be due to residual absorption [11–13], and because absorption itself may suppress localization [3]. Here we show that the extent of photon localization can be characterized by the relative size of fluctuations of transmission quantities, and that the variance of relative fluctuations properly reflects the extent of localization even in the presence of absorption. Using this approach, we demonstrate microwave localization in samples of randomly positioned alumina spheres contained in a copper tube.

In the absence of inelastic and phase-breaking processes, the ensemble average of the dimensionless conductance $\langle g \rangle \equiv \langle G \rangle / (e^2/h)$ is the universal scaling parameter [14] of the electron localization transition. Here $\langle \dots \rangle$ represents the average over an ensemble of random sample configurations, G is the electronic conductance, e is the electron charge, and h is Planck's constant. The dimensionless conductance g can be defined for classical waves as the transmittance, i.e. the sum over transmission coefficients connecting all input modes a and output modes b , $g \equiv \sum_{ab} T_{ab}$ [15]. In the absence of absorption, $\langle g \rangle$ not only determines the scaling of average transmission quantities, such as T_{ab} and $T_a = \sum_b T_{ab}$ that we will refer to as the intensity and total transmission, respectively, but it also determines their full distributions [16–18]. In electronically conducting samples or for diffusing classical waves, Ohm's law holds, $\langle g \rangle = N\ell/L$, where N is the number of transverse modes at a given frequency, ℓ is the transport mean free path, and L is the sample length. But beyond the localization threshold, at $\langle g \rangle \sim 1$ [14,19], the wave function or classical field is exponentially small at the boundary and $\langle g \rangle$ falls exponentially with L . Localization can be achieved in a strongly scattering three-dimensional sample with a sufficiently small value of ℓ [2], or even in weakly scattering samples in a quasi-one-dimensional geometry of fixed N , once L becomes greater than the localization length, $\xi = N\ell$ [19].

In the presence of absorption, however, $\langle g \rangle$ cannot serve as a universal localization parameter since both the small values of $\langle g \rangle$ and its exponential scaling can be dominated by absorption rather than localization. Nor can the value of $\langle g \rangle$ determine the distributions of transmission quantities. We

find, however, that for $L \leq \xi$, the full distribution of the intensity and total transmission normalized to their ensemble averages, $s_{ab} = T_{ab}/\langle T_{ab} \rangle$ and $s_a = T_a/\langle T_a \rangle$, respectively, can be well expressed in terms of a single parameter, the variance of the normalized total transmission [20,21]. Since the width of these distributions are indicators of the proximity to the localization threshold [22], this suggests that $\text{var}(s_a)$ might serve as a localization parameter even in the presence of absorption. The localized state is characterized by sharp transmission spectra that naturally have large values of $\text{var}(s_a)$. Since $\text{var}(s_a) = 2/3\langle g \rangle$ for $L \ll \xi, L_a$, where L_a is the absorption length, and since the localization threshold occurs at $\langle g \rangle \sim 1$ in the absence of absorption, we make the conjecture that localization is achieved when $\text{var}(s_a) \geq 2/3$. This localization condition may be expressed in a familiar form by defining a new localization parameter $g' \equiv 2/3\text{var}(s_a)$, which reduces to $\langle g \rangle$ in the absence of absorption in the limit $\text{var}(s_a) \ll 1$. Localization is then achieved for $g' \leq 1$ whether absorption is present or not. Since the magnitude of relative fluctuations of total transmission and of intensity are simply related by, $2\text{var}(s_a) = \text{var}(s_{ab}) - 1$, [17] measurements of intensity fluctuations can be used to study the localization transmission.

The sample studied here is composed of alumina spheres (diameter $d_a = 0.95$ cm, dielectric constant $\epsilon_a = 9.8$) embedded in Styrofoam shells ($d_S = 1.9$ cm, $\epsilon_S = 1.05$) at an alumina volume fraction of 0.068 and is contained in a 7.3-cm-diam. copper tube. A Hewlett-Packard vector network analyzer is used to obtain field transmission coefficient. The squared amplitude of the field is then computed to give intensity spectra. A typical spectrum of the normalized intensity s_{ab} near the first Mie resonance of the alumina spheres for a sample length $L = 1$ m is shown in Fig. 1.

Statistics are obtained from 5,000 spectra of different sample configurations. The measured distribution contains intensity values that are as large as 300 times the average intensity. This intensity distribution is used to compute the value of $\text{var}(s_{ab})$ from which $\text{var}(s_a)$ is found. The scaling of $\text{var}(s_a)$ averaged over the indicated frequency interval is shown in Fig. 2. Above a value of approximately unity, $\text{var}(s_a)$ increases exponentially.

The variation with frequency of the total transmission and of $\text{var}(s_{ab})$ is shown in Fig. 3. Dips in the total transmission occur near each of the lower Mie resonances shown. However, $\text{var}(s_{ab})$ only rises above the localization limit near the first Mie resonance. The localization condition in terms of the variance of the intensity is indicated by the horizontal line. At the localization threshold, $\text{var}(s_a) = 2/3$ and $\text{var}(s_{ab}) = 2(2/3) + 1 = 7/3$. These results show that total transmission is not a reliable indicator of localization since it can be dramatically affected by absorption.

In conclusion, we have shown that the variance of the normalized transmission is a reliable guide in the search for photon localization. Scattering is strong near the first Mie resonance of individual spheres in our sample, and localization is achieved once the length of the tube is approximately twice its

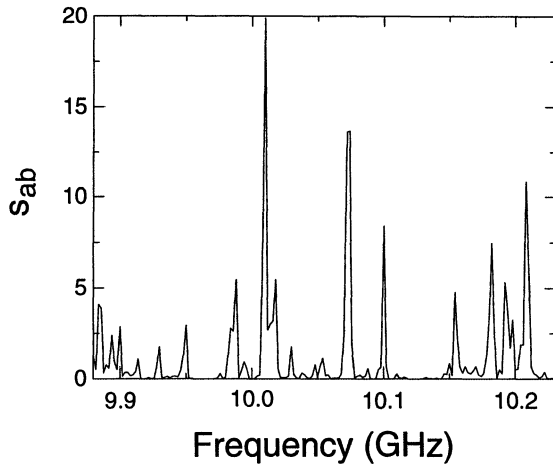


Fig. 1. Typical spectrum of the normalized intensity s_{ab} near the first Mie resonance of the alumina spheres. The narrow-line spectra and giant fluctuations shown are unlike corresponding spectra in diffusive samples

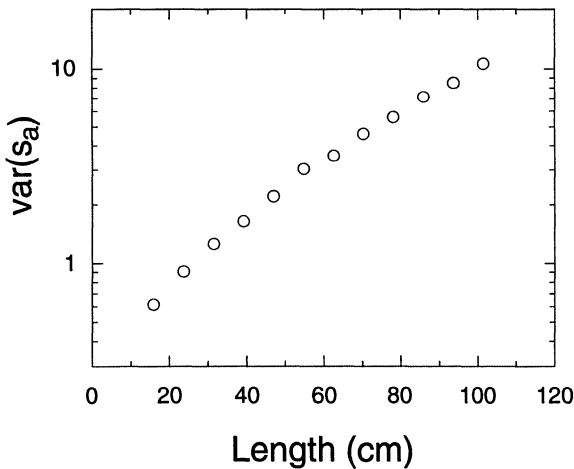


Fig. 2. Scaling of $\text{var}(s_a)$ in alumina samples. The values of $\text{var}(s_a)$ averaged over the frequency interval $f = 9.98 - 10.24$ GHz are obtained from the relation $2\text{var}(s_a) = \text{var}(s_{ab}) - 1$. Above a value of order unity, $\text{var}(s_a)$ increases exponentially

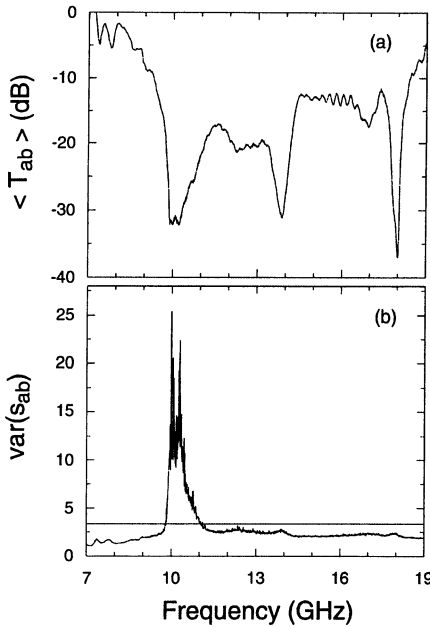


Fig. 3. Frequency dependence of average transmission coefficient (a) and $var(s_{ab})$ (b) in alumina sample with $L = 0.8$ m. Only near the first Mie resonance is $var(s_{ab}) \geq 7/3$. The critical value of $7/3$ is shown as the horizontal line in (b). Dips in the transmission at higher Mie resonances do not indicate localization

diameter. This indicates that wave confinement by the reflecting boundary plays a role in localizing the wave. In a three-dimensional sample without reflecting transverse boundaries the wave would be delocalized but in the critical regime near the localization threshold. Nonetheless, studies in this sample allow us to establish a localization criterion and to study the statistics of localized waves. In future work on this system, the density of alumina spheres and the degree of ordering of the spheres will be varied to achieve localization in open three-dimensional samples.

References

1. P. W. Anderson: Absence of diffusion in certain random lattices. *Phys. Rev.* **109**, 1492–1505 (1958)
2. A. F. Ioffe, A. R. Regel: Non-crystalline, amorphous and liquid electronic semiconductors. *Prog. Semicond.* **4**, 237–291 (1960)
3. S. John: Electromagnetic absorption in a disordered medium near a photon mobility edge. *Phys. Rev. Lett.* **53**, 2169–2172 (1984)
4. B. L. Altshuler, P. A. Lee, R. A. Webb (Eds.): *Mesoscopic Phenomena in Solids* (Elsevier, Amsterdam 1991)
5. R. A. Webb, S. Washburn, C. P. Umbach, and R. B. Laibowitz: Observations of h/e Aharonov-Bohm oscillations in normal-metal rings. *Phys. Rev. Lett.* **54**, 2696–2700 (1985)

6. N. Garcia, A. Z. Genack: Anomalous photon diffusion at the threshold of the Anderson localization transition. *Phys. Rev. Lett.* **66**, 1850–1853 (1991)
7. A. Z. Genack, N. Garcia: Observations of the Anderson transition for electromagnetic radiation. *Phys. Rev. Lett.* **66**, 2064–2067 (1991)
8. D. S. Wiersma, P. Bartolini, A. Lagendijk, R. Righini: Localization of light in a disordered medium. *Nature*, **390**, 671–673 (1997)
9. D. S. Wiersma, J. G. Rivas, P. Bartolini, A. Lagendijk, R. Righini: *Nature*, **398**, 207 (1999)
10. Ya. A. Vlasov, M. A. Kaliteevski, V. V. Nikolaev: Different regimes of light localization in a disordered photonic crystal. *Phys. Rev. B* **60**, 1555–1562 (1999)
11. F. Scheffold, R. Lenke, R. Tweer, G. Maret: *Nature*, **398**, 206 (1999)
12. R. L. Weaver: Anomalous diffusivity and localization of classical waves in disordered media: The effect of dissipation. *Phys. Rev. B* **47**, 1077–1080 (1993)
13. M. Yosefin: Localization in absorbing media. *Europhys. Lett.* **25**, 675–680 (1994)
14. E. Abrahams, P. W. Anderson, D. C. Licciardello, T. V. Ramakrishnan: Scaling theory of localization: absence of quantum diffusion in two dimensions. *Phys. Rev. Lett.* **42**, 673–676 (1979)
15. R. Landauer: Electrical resistance of disordered one-dimensional lattices. *Phil. Mag.* **21**, 863–867 (1970)
16. M. C. W. van Rossum, Th. M. Nieuwenhuizen: Multiple scattering of classical waves: microscopy, mesoscopy, and diffusion. *Rev. Mod. Phys.* **71**, 313–372 (1999)
17. E. Kogan, M. Kaveh: Random-matrix-theory approach to the intensity distributions of waves propagating in a random medium. *Phys. Rev. B* **52**, R3813–3815 (1995)
18. S. A. van Langen, P. W. Brouwer, C. W. J. Beenakker: Nonperturbative calculation of the probability distribution of plane-wave transmission through a disordered waveguide. *Phys. Rev. E* **53**, R1344–1347 (1996)
19. D. J. Thouless: Maximum metallic resistance in thin wires. *Phys. Rev. Lett.* **39**, 1167–1169 (1977)
20. M. Stoytchev, A. Z. Genack: Measurement of the probability distribution of total transmission in random waveguides. *Phys. Rev. Lett.* **79**, 309–312 (1997)
21. M. Stoytchev, A. Z. Genack: Observations of non-Rayleigh statistics in the approach to photon localization. *Opt. Lett.* **24**, 262–264 (1999)
22. B. L. Altshuler, V. E. Kravtsov, I. V. Lerner: Distribution of mesoscopic fluctuations and relaxation processes in disordered conductors. In: *Mesoscopic Phenomena in Solids* B. L. Altshuler, P. A. Lee, R. A. Webb (Eds.) (Elsevier, Amsterdam 1991) pp. 449–521

Coherence and Fluctuation of Light from Rough Surface Scattering

Zu-Han Gu¹, Jun Q. Lu², Mikael Cififtan³

¹ Surface Optics Corporation, 11555 Rancho Bernardo Road,
San Diego, CA 92127, USA

² Department of Physics, East Carolina University Greenville,
NC 27858, USA

³ U.S. Army Research Office, P.O. Box 12211, Research Triangle Park, NC 27709

Abstract. The subject of scattering of electromagnetic waves from a rough surface has been an active research area for a long time. Simple results have been obtained only in two limiting cases. One occurs when the radii of curvature of the surface structure are much larger than the wavelength and the angle of incidence is not large. In this case Beckmann's theory, which is based on the Kirchhoff approximation, has been successfully used. The other case occurs when the surface is almost, but not quite flat (shallow roughness). In this case perturbation theory yields reliable answers. Recently, one of the most interesting phenomena associated with coherence in rough surface scattering is the enhanced backscattering. Similarly there are enhanced reflection and enhanced transmission.

We have also studied the angular correlation function of speckles, which shows another example of coherence and fluctuations of light from rough surface scattering and verifies the property given by the enhanced backscattering phenomena.

1 Introduction

One of the most interesting phenomena associated with the scattering of light from a randomly rough surface is that of enhanced backscattering. This is the presence of a well-defined peak in the retroreflection direction in the angular distribution of the intensity of the incoherent component of the light scattered from such a surface, which results primarily from the coherent interference of each multiply reflected optical path with its time-reversed partner[1-6].

Not all manifestations of localization in the interaction of light with randomly rough surfaces are in enhanced backscattering. Several additional enhancement phenomena in the scattering of light from or in its transmission through randomly rough surfaces have been investigated: (a) enhanced reflection, defined as a peak in the specular direction in the angular dependence of the intensity of the diffuse component of the scattered light; (b) enhanced transmission, defined as a peak in the antispecular direction in the angular distribution of the intensity of the light that has been transmitted diffusely through a film with a randomly rough surface; and (c) enhanced refraction, defined as a peak in the forward direction in the angular distribution of the

intensity of the diffuse component of the light transmitted through a film with a randomly rough surface (see Fig. 1)[7-9].

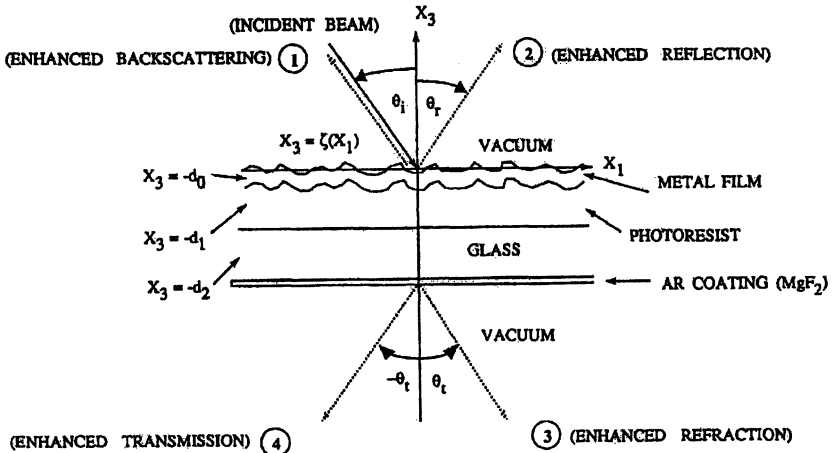


Fig. 1. Schematic of Four Kinds of Enhancement

In this paper we will summarize the observation of rough surface enhanced scattering. We will also report the angular correlation from rough surface scattering. Section 2 introduces the theory for numerical simulation followed by the experimental results. Section 3 talks about the angular correlation function of speckles. The Summary derived from this work is presented in Sec. 4.

2 Theory

In this section we will outline the methods we used in obtaining our numerical results. More details on the development of these methods can be found in Refs. [10] and [11].

In this paper, we consider light scattering from one-dimensional random rough surfaces of two different physical systems: semi-infinite metal or dielectric medium; dielectric film of thickness d on a metal or dielectric substrate. For the first case, the scattering system consists of a vacuum in the region $x_3 > \zeta(x_1)$ (region 1), and a metal or dielectric medium in the region $x_3 < \zeta(x_1)$ (region 2). For the second case, the scattering system consists of a vacuum in the region $x_3 > \zeta(x_1)$ (region 1), a dielectric medium in the region $\zeta(x_1) > x_3 > -d$ (region 2), and a metal or transparent substrate in the region $x_3 < -d$ (region 3). The medium in region 2 for both cases is characterized by an isotropic, frequency-dependent, complex dielectric constant $\varepsilon_2(\omega) = \varepsilon_{21}(\omega) + i\varepsilon_{22}(\omega)$. If the medium is a dielectric, the real part

and imaginary part of the dielectric constant satisfy $\varepsilon_{21}(\omega), \varepsilon_{22}(\omega) > 0$ and $\varepsilon_{21}(\omega) \gg \varepsilon_{22}(\omega)$. If the medium is a metal, the real and imaginary part of the dielectric constant satisfy $\varepsilon_{21}(\omega) < 0$ and $|\varepsilon_{21}(\omega)| \gg \varepsilon_{22}(\omega)$. The substrate in the film case is depicted by an isotropic, frequency-dependent, complex dielectric constant $\varepsilon_s(\omega)$.

The profile function of the one-dimensional random rough surface $\zeta(x_1)$, which defines the vacuum/metal or vacuum/dielectric interface through the equation $x_3 = \zeta(x_1)$, is only a function of x_1 in the x_1x_2 -plane. In this paper the function $\zeta(x_1)$ is a stationary, Gaussian, stochastic process defined by the properties $\langle \zeta(x_1) \rangle = 0$ and $\langle \zeta(x_1)\zeta(x'_1) \rangle = \delta^2 \exp[-(x_1 - x'_1)/a^2]$, where the angle brackets denote an average over the ensemble of realizations of the surface profile, $\delta = \langle \zeta(x_1)^2 \rangle^{1/2}$ is the rms departure of the surface from flatness, and a is the correlation length. The way to generate such kind surface numerically is described in Ref. [10].

We will use a finite beam of light defined in Ref. [10] as our incident field, and this beam is incident from the vacuum side on the rough vacuum/dielectric interface with the incident plane (i.e. x_1x_3 -plane) perpendicular to the grooves of the surface.

2.1 P-polarization

For p-polarization, the magnetic field has the form

$$H(\mathbf{x}; t) = [0, H_2(x_1, x_3|\omega), 0] \exp(-i\omega t), \quad (1)$$

and the single, non-zero component of the magnetic field of the incident beam is given by [10]

$$\begin{aligned} H_2^{(1)}(x_1, x_3|\omega)_{inc} &= \exp\left\{i\frac{w}{c}(x_1 \sin \theta_i - x_3 \cos \theta_i)[1 + w(x_1, x_3)]\right\} \\ &\times \exp[-(x_1 \cos \theta_i + x_3 \sin \theta_i)^2/w^2], \end{aligned} \quad (2)$$

where $w(x_1, x_3) = (c/\omega w)^2[(2/w^2)(x_1 \cos \theta_i + x_3 \sin \theta_i)^2 - 1]$. Here θ_i is the angle of incidence measured from the normal to the mean surface $x_3 = 0$ and $w = g \cos \theta_i$, where g is the half-width of the intercept of the beam with the plane $x_3 = 0$.

In any region of the scattering (say i^{th} region) with dielectric constant $\varepsilon(\omega)$, the only nonzero component of the magnetic field $H_2^{(i)}(x_1, x_3|\omega)$ satisfies the Helmholtz equation:

$$\left(\frac{\partial^2}{\partial x_1^2} + \frac{\partial^2}{\partial x_3^2} + \varepsilon(\omega) \frac{\omega^2}{c^2}\right) \times H_2^{(i)}(x_1, x_3|\omega) = 0, \quad (i^{th} \text{ region}) \quad (3)$$

The boundary conditions on the field components at the interfaces are that the tangential components of the magnetic and electric vectors be continuous. Through the use of the Green's second integral theorem we can express the scattered field in the far-field region in the form

$$H_2^{(1)}(x_1, x_3|\omega)_{sc} = \int_{-\infty}^{\infty} \frac{dk}{2\pi} R_p(k\omega) e^{ikx_1 + i\alpha_0(\omega)x_3}, \quad (4)$$

where $\alpha_0(\omega) = (\frac{\omega^2}{c^2} - k^2)^{\frac{1}{2}}$ for $k^2 < \frac{\omega^2}{c^2}$ and $i(k^2 - \frac{\omega^2}{c^2})^{\frac{1}{2}}$ for $k^2 > \frac{\omega^2}{c^2}$, and the scattering amplitude $R_p(k\omega)$ is given by

$$R_p(k\omega) = \frac{i}{2\alpha_0(\omega)} \int_{-\infty}^{\infty} dx_1 e^{-ikx_1 - i\alpha_0(\omega)\zeta(x_1)} \\ \times [i(k\zeta'(x_1) - \alpha_0(\omega))H^{(1)}(x_1|\omega) - L^{(1)}(x_1|\omega)] \quad (5)$$

where the source functions $H^{(1)}(x_1|\omega)$ and $L^{(1)}(x_1|\omega)$ are defined as [10]

$$H^{(1)}(x_1|\omega) = H_2^{(1)}(x_1, x_3|\omega)|_{x_3=\zeta(x_1)} \quad (6)$$

$$L^{(1)}(x_1|\omega) = \{(-\zeta'(x_1)\frac{\partial}{\partial x_1} + \frac{\partial}{\partial x_2}) \times H_2^{(1)}(x_1, x_3|\omega)\}|_{x_3=\zeta(x_1)} \quad (7)$$

where $H_2^{(1)}(x_1, x_3|\omega)$ is the total magnetic field in the vacuum region.

Our object is to calculate the differential reflection coefficient (*drc*) of the scattered light, which gives the fraction of the total energy incident on the surface that is scattered into an angular interval $d\theta_s$ about the scattering direction defined by the scattering angle θ_s , measured from the normal to the plane $x_3 = 0$. The incoherent contribution to the mean *drc* of the scattered light is given by [10]

$$\langle \frac{\partial R_p}{\partial \theta_s} \rangle_{incoh} = \frac{1}{2(2\pi)^{3/2}} \frac{c}{\omega w} \times \frac{\langle |r_p(\theta_s)|^2 \rangle - |\langle r_p(\theta_s) \rangle|^2}{1 - (1/2)(c/\omega w)^2(1 + 2\tan^2 \theta_i)} \quad (8)$$

where $r_p(\theta_s)$ is the scattering amplitude given by [10,11]

$$r_p(\theta_s) = \int_{-\infty}^{\infty} dx_1 \exp\{-i\frac{\omega}{c}(x_1 \sin \theta_s + \zeta(x_1) \cos \theta_s)\} \\ \times [i\frac{\omega}{c}(\zeta'(x_1) \sin \theta_s - \cos \theta_s)] \times [H^{(1)}(x_1|\omega) - L^{(1)}(x_1|\omega)] \quad (9)$$

Semi-infinite medium. In the semi-infinite medium case, $H^{(1)}(x_1|\omega)$ and $L^{(1)}(x_1|\omega)$ in Eq. (9) are the solutions of a pair of coupled, inhomogeneous integral equations

$$H^{(1)}(x_1|\omega) = H^{(1)}(x_1|\omega)_{inc} + \int_{-\infty}^{\infty} dx'_1 [H_0(x_1|x'_1)H^{(1)}(x'_1|\omega) \\ - L_0(x_1|x'_1)L^{(1)}(x'_1|\omega)], \quad (10)$$

$$0 = \int_{-\infty}^{\infty} dx'_1 [H_{\epsilon}(x_1|x'_1)H^{(1)}(x'_1|\omega) - \epsilon_2(\omega)L_{\epsilon}(x_1|x'_1)L^{(1)}(x'_1|\omega)], \quad (11)$$

where $H^{(1)}(x_1|\omega)_{inc} = H_2^{(1)}(x_1, x_3|\omega)_{inc}|_{x_3=\zeta(x_1)}$, and the kernels that appear in these equations are defined in Ref. 10.

Dielectric film on a metal or dielectric substrate. In the case of light scattering from a dielectric film on a substrate, $H^{(1)}(x_1|\omega)$ and $L^{(1)}(x_1|\omega)$ in Eq. (9) are the solutions of a set of coupled, inhomogeneous integral equations [11]

$$H^{(1)}(x_1|\omega) = H^{(1)}(x_1|\omega)_{inc} + \int_{-\infty}^{\infty} dx'_1 \times \\ [H_0(x_1|x'_1)H^{(1)}(x'_1|\omega) - L_0(x_1|x'_1)L^{(1)}(x'_1|\omega)] \quad (12)$$

$$0 = \int_{-\infty}^{\infty} dx'_1 [H_\epsilon(x_1|x'_1)H^{(1)}(x'_1|\omega) - \epsilon_2(\omega)L_\epsilon(x_1|x'_1)L^{(1)}(x'_1|\omega) \\ - H_{12}(x_1|x'_1)H^{(2)}(x'_1|\omega) + L_{12}(x_1|x'_1)L^{(2)}(x'_1|\omega)] \quad (13)$$

$$H^{(2)}(x_1|\omega) = \int_{-\infty}^{\infty} dx'_1 [-H_{21}(x_1|x'_1)H^{(1)}(x'_1|\omega) + \epsilon_2 L_{21}(x_1|x'_1)L^{(1)}(x'_1|\omega) \\ + H_{22}(x_1|x'_1)H^{(2)}(x'_1|\omega) - L_{22}(x_1|x'_1)L^{(2)}(x'_1|\omega)] \quad (14)$$

$$0 = \int_{-\infty}^{\infty} dx'_1 [H_s(x_1|x'_1)H^{(2)}(x'_1|\omega) - \epsilon_s(\omega)/\epsilon_2(\omega)L_s(x_1|x'_1)L^{(2)}(x'_1|\omega)], \quad (15)$$

where the new source functions $H^{(2)}(x_1|\omega)$ and $L^{(2)}(x_1|\omega)$ are defined as

$$H^{(2)}(x_1|\omega) = H_2^{(2)}(x_1, x_3|\omega)|_{x_3=-d} \quad (16)$$

$$L^{(2)}(x_1|\omega) = \frac{\partial}{\partial x_2} H_2^{(2)}(x_1, x_3|\omega)|_{x_3=-d} \quad (17)$$

respectively, where $H_2^{(2)}(x_1, x_3|\omega)$ is the magnetic field in the dielectric film. The other kernels that appear in these equations are defined in Ref. 11.

2.2 S-polarization

For *s*-polarization, the electric field has the form

$$E(\mathbf{x};t) = [0, E_2(x_1, x_3|\omega), 0] \exp(-i\omega t) \quad (18)$$

and the single, non-zero component of the electric field of the incident beam is given by [10]

$$E_2^{(1)}(x_1, x_3|\omega)_{inc} = \exp\{i\frac{w}{c}(x_1 \sin \theta_i - x_3 \cos \theta_i)[1 + w(x_1, x_3)]\} \\ \times \exp[-(x_1 \cos \theta_i + x_3 \sin \theta_i)^2/w^2], \quad (19)$$

When a finite beam of light is incident from the vacuum side, the incoherent contribution to the mean differential reflection coefficient of the scattered light is given by [10]

$$\left\langle \frac{\partial R_s}{\partial \theta_s} \right\rangle_{incoh} = \frac{1}{2(2\pi)^{3/2}} \frac{c}{\omega w} \times \frac{\langle |r_s(\theta_s)|^2 \rangle - \langle r_s(\theta_s) \rangle^2}{1 - (1/2)(c/\omega w)^2(1 + 2 \tan^2 \theta_i)} \quad (20)$$

where the scattering amplitude $r_s(\theta_s)$ is given by [10]

$$r_s(\theta_s) = \int_{-\infty}^{\infty} dx_1 \exp\left\{-i\frac{\omega}{c}(x_1 \sin \theta_s + \zeta(x_1) \cos \theta_s)\right\} \\ \left\{ i\frac{\omega}{c} [\zeta'(x_1) \sin \theta_s - \cos \theta_s] E^{(1)}(x_1|\omega) - F^{(1)}(x_1|\omega) \right\} \quad (21)$$

where the source functions $E^{(1)}(x_1|\omega)$ and $F^{(1)}(x_1|\omega)$ are defined as

$$E^{(1)}(x_1|\omega) = E_2^{(1)}(x_1, x_3|\omega)|_{x_3=\zeta(x_1)} \quad (22)$$

$$F^{(1)}(x_1|\omega) = \left\{ [-\zeta'(x_1) \frac{\partial}{\partial x_1} + \frac{\partial}{\partial x_2}] \times E_2^{(1)}(x_1, x_3|\omega) \right\}|_{x_3=\zeta(x_1)} \quad (23)$$

where $E_2^{(1)}(x_1, x_3|\omega)$ is the total electric field in the vacuum region.

Semi-infinite medium. In the semi-infinite medium case, $E^{(1)}(x_1|\omega)$ and $F^{(1)}(x_1|\omega)$ in Eq. (21) are the solutions of a pair of coupled, inhomogeneous integral equations [10]

$$E^{(1)}(x_1|\omega) = E^{(1)}(x_1|\omega)_{inc} + \int_{-\infty}^{\infty} dx'_1 [H_0(x_1|x'_1) E^{(1)}(x'_1|\omega) \\ - L_0(x_1|x'_1) F^{(1)}(x'_1|\omega)] \quad (24)$$

$$0 = \int_{-\infty}^{\infty} dx'_1 [H_\epsilon(x_1|x'_1) \times E^{(1)}(x'_1|\omega) - \epsilon_2(\omega) L_\epsilon(x_1|x'_1) F^{(1)}(x'_1|\omega)], \quad (25)$$

where $E^{(1)}(x_1|\omega)_{inc} = E_2^{(1)}(x_1, x_3|\omega)_{inc}|_{x_3=\zeta(x_1)}$.

Dielectric film on a metal or dielectric substrate. In the case of light scattering from a dielectric film on a substrate $E^{(1)}(x_1|\omega)$ and $F^{(1)}(x_1|\omega)$ in Eq. (21) are the solutions of a set of coupled, inhomogeneous integral equations [11]

$$E^{(1)}(x_1|\omega) = E^{(1)}(x_1|\omega)_{inc} + \int_{-\infty}^{\infty} dx'_1 \times \\ [H_0(x_1|x'_1) E^{(1)}(x'_1|\omega) - L_0(x_1|x'_1) E^{(1)}(x'_1|\omega)] \quad (26)$$

$$0 = \int_{-\infty}^{\infty} dx'_1 [H_\epsilon(x_1|x'_1)E^{(1)}(x'_1|\omega) - L_\epsilon(x_1|x'_1)E^{(1)}(x'_1|\omega) \\ - H_{12}(x_1|x'_1)E^{(2)}(x'_1|\omega) + L_{12}(x_1|x'_1)F^{(2)}(x'_1|\omega)] \quad (27)$$

$$E^{(2)}(x_1|\omega) = \int_{-\infty}^{\infty} dx'_1 [-H_{21}(x_1|x'_1)E^{(1)}(x'_1|\omega) + L_{21}(x_1|x'_1)F^{(1)}(x'_1|\omega) \\ + H_{22}(x_1|x'_1)E^{(2)}(x'_1|\omega) - L_{22}(x_1|x'_1)F^{(2)}(x'_1|\omega)] \quad (28)$$

$$0 = \int_{-\infty}^{\infty} dx'_1 [H_s(x_1|x'_1)E^{(2)}(x'_1|\omega) - L_s(x_1|x'_1)F^{(2)}(x'_1|\omega)], \quad (29)$$

where the new source functions $E^{(2)}(x_1|\omega)$ and $F^{(2)}(x_1|\omega)$ are defined as

$$E^{(2)}(x_1|\omega) = E_2^{(2)}(x_1, x_3|\omega)|_{x_3=-d} \quad (30)$$

$$F^{(2)}(x_1|\omega) = \frac{\partial}{\partial x_2} E_2^{(2)}(x_1, x_3|\omega)|_{x_3=-d} \quad (31)$$

respectively, where $E_2^{(2)}(x_1, x_3|\omega)$ is the electric field in the dielectric film.

So the central part of the calculation is to solve the set of integral equations. To do it numerically, we replace the infinite range of integration in the above equations by a finite range $(-L/2, L/2)$, and introduce a set of N equally spaced points $x_n = -L/2 + (n - 1/2)\Delta x$, $n = 1, 2, 3, \dots, N$, with the distance $\Delta x = L/N$ along the rough surface. On the assumption that the source functions are slowly varying functions of x_1 in the interval $(x_n - 1/2\Delta x, x_n + 1/2\Delta x)$, we then convert the above set of integral equations into two matrix equations[10,12]. These matrix equations are then solved numerically to obtain the source functions appeared in the matrix version of Eqs. (9) or (21) and thus to calculate the DRC. We calculated the incoherent contribution to the mean drc in the same way described in Ref. [10] by constructing N_p different surface profiles $\zeta(x_1)$, calculating the scattering amplitude $r_p(\theta_s)$ or $r_s(\theta_s)$ for each profile, and the averaged $|r_p(\theta_s)|^2$ (or $|r_s(\theta_s)|^2$) and $r_p(\theta_s)$ (or $r_s(\theta_s)$) are then input to Eq. (8) (or Eq. 20) to obtain the final results.

3 Angular correlation effects

When a coherent light is reflected from a rough surface, a complex speckle pattern is formed. This is the result of the interference among the scattered wavelets, each arising from a different microscopic element of the rough surface. According to the conventional theory of laser speckle pattern[12], these speckles are not related, and the variations in intensity on a speckle pattern are of the same value as the average intensity itself. However, recent theoretic study in volume scattering[13] shows that there are novel correlations among

the speckle patterns in the multiple-scattering regime and that they can be divided into three types: short-range correlation, long-range correlation, and infinite-range correlation. These three types of correlation play different roles in different scattering-system geometries. The short-range correlation, also known as memory effect, is the dominant part in the system where the dimension in the direction of the light propagation is much smaller than the dimension in the direction perpendicular to it. The memory effect dictates that even though a laser wave suffers many scattering events upon traversing a thick volume scattering sample and therefore its wave front is much distorted and seemingly random, it still “remembers” the wave front of the incoming plane wave so that, as the incoming beam direction changes slightly, the transmitted or reflected speckle pattern will move accordingly[14]. The long-range and the infinite-range correlations will be the dominant part in the system where the dimension in the direction of the light propagation is larger than the dimension in the direction perpendicular to it. These phenomena have been confirmed theoretically and experimentally for volume scattering.[15-20]

Correlation in light scattering from random rough surfaces has been studied [21-24]. Taking into account multiple scattering, McGurn and Maradudin calculated the intensity correlation function for light elastically scattered from a randomly rough metallic grating[21]. In recent theoretical and experimental investigations, the correspondence between the correlation function and the enhanced backscattering peak has been studied for light scattering from randomly rough metallic surfaces that produce multiple scattering[25-26].

We study the angular correlation between the scattered speckle patterns generated by light incident to a rough dielectric film on a glass at different angles of incidence. The surface that separates the dielectric film from the vacuum is a one-dimensional randomly rough grating, and it is rough enough that the specular components are extinguished.

3.1 Angular correlation function

To calculate the angular correlation function, we need the scattered field or intensity at specified scattering angle θ_s for a given angle of incidence θ_i . If we have one scattered speckle intensity $I(\theta_{i1}, \theta_{s1})$ observed at the scattering angle θ_{s1} generated by a incident light at angle of incidence of , and another scattered speckle intensity $I(\theta_{i2}, \theta_{s2})$ observed at the scattering angle θ_{s2} generated by a incident light at angle of incidence of θ_{i2} , the normalized angular correlation between them is defined by:

$$C(\theta_{i1}, \theta_{s1}; \theta_{i2}, \theta_{s2}) = \frac{\langle I(\theta_{i1}, \theta_{s1})I(\theta_{i2}, \theta_{s2}) \rangle - \langle I(\theta_{i1}, \theta_{s1}) \rangle \langle I(\theta_{i2}, \theta_{s2}) \rangle}{[(\langle I(\theta_{i1}, \theta_{s1})^2 \rangle - \langle I(\theta_{i1}, \theta_{s1}) \rangle^2)(\langle I(\theta_{i2}, \theta_{s2})^2 \rangle - \langle I(\theta_{i2}, \theta_{s2}) \rangle^2)]^{\frac{1}{2}}} \quad (32)$$

the symbol $\langle \dots \rangle$ denotes ensemble averaging among the speckles of the speckle distribution. It has been shown that a strong correlation can be observed if the following conditions are satisfied [26]:

$$\sin \theta_{i1} - \sin \theta_{s1} = \sin \theta_{i2} - \sin \theta_{s2} . \quad (33)$$

A correlation exists as long as this quantity is not violated by more than λ/D , where D is the illuminated width of the surface and λ is the wavelength.

3.2 Experimental setup

The sample that we used is a photoresist film deposited on a glass substrate. The interface that separates the film and the vacuum is one-dimensionally rough, and it was fabricated with a variation of the technique described by Gray[27] and modified for a one-dimensional surface[28]. The surface profile of the fabricated sample was measured with a Dektak 3030 stylus machine. Statistical properties of the profile that define the air-dielectric interface were calculated from 10 measured profiles. A total of 1000 points were taken for each trace. The standard deviation of heights σ is estimated to be approximately $1.278\mu\text{m}$, and the $1/e$ value of the correlation length a is approximately $3.85\mu\text{m}$. Both the histogram of heights and the measured correlation function are approximately Gaussian.

The surface profile of the sample is defined through the equation $x_3 = \zeta(x_1)$ such that the grooves and ridges of its one-dimensional surface are parallel to the x_2 axis. The interface between the photoresist film and the glass substrate is approximately plane, which is parallel to the mean of the rough surface. The thickness of the film is approximately $5\mu\text{m}$ and the thickness of the glass substrate is approximately 3 mm. The glass substrate of this sample, however, is wedge shaped so that two surfaces of the substrate are not parallel in either the x_2 direction or in the x_1 direction. In the measurements the light is incident upon the rough surface from the vacuum, and the plane of the incidence is perpendicular to the grooves. For such an experimental setup, owing to the above-mentioned geometry of the substrate, the light scattered from the back surface of the glass substrate will be out of the plane of incidence. Thus the light scattered in the plane of incidence comes from only two surfaces of the photoresist film, i.e., the equivalent scattering system is a rough photoresist film on a semi-infinite glass substrate.

At a wavelength $\lambda = 0.6328\mu\text{m}$, the index of refraction of the photoresist is $n(\omega) = 1.64$ and the approximate index of refraction of the glass is $n_s = 1.51$. Owing to a small difference between $n(\omega)$ and n_s , the reflectance from the interface of the photoresist film and the glass substrate is negligible, thus the in-plane scattering might come mostly from the rough surface of the photoresist film. On the other hand, because of the film structure, there exist some guided waves transmitting along the film[29-30].

The experimental setup can be found in Ref.[6] except we use a CCD camera as a detector; Mirrors and polarizers are indicated by M and P ,

respectively. The sample and the detector arm are mounted separately on two rotational stages run by two stepper motors that are controlled by a PC through a two-axis driver. A He-Ne laser at $0.6328\mu\text{m}$ is used as the light source. The laser beam is directed toward the sample by a folded beam system that collimates it into a 1.27-cm-diameter parallel beam. The beam size on the rough surface was then controlled by an adjustable iris, and the plane of incidence was kept perpendicular to the grooves of the one-dimensional surface. For p polarization the electric vector is perpendicular to the grooves, whereas for s polarization it is parallel to the grooves. Four combinations of polarizations of the input and the receiving beams are used.

The scattered speckle pattern is focused upon the detector by two mirrors attached to the detection arm, and the detector, from Santa Barbara Instruments Group, is a PC-controlled thermoelectrically cooled CCD array of detectors with 375×242 pixels, each pixel being $23\mu\text{m}\times27\mu\text{m}$ in size. The whole array is 8.6×6.5 mm in size, and the data was digitized with 16 bits.

In the measurement the speckle pattern of the scattered light at a defined scattering angle that resulted from a defined angle of incidence is detected by a CCD array in the far-field, and the digitized intensity distribution of the speckle pattern is downloaded to the PC and displayed on the screen; the digitized image is then stored in the PC. An interference filter of $0.6328\mu\text{m}$ is provided to protect the system from external background light. After the images of all desired incident and scattering angles are taken in this way, the obtained images are then transferred into readable numerical format and the correlation among them was obtained through directed computation.

3.3 Dynamic behavior of speckles from rough surface scattering

First we present the speckle trucking in the specular direction. In the experiment we study the correlation function for only $\theta_{i1} = \theta_{s1}$. On the basis of Eq. (32), this condition implies that correlation will be found for only $\theta_{i2} = \theta_{s2}$ which means if you change incident angle, even for multiple scattering, the speckle distribution will remain the same on the specular direction. We present the results for p polarization for both incident light and scattered light, i.e. (p, p) setup. Owing to imperfections in fabricating the sample, the far-field scattering of the one-dimensional random grating is not identical along the direction of the x_2 axis. The nonuniform background causes bias in the correlation function. We have to subtract the background fluctuations from the angular intensity correlation function. Fig. 2 is the angular intensity correlation function derived from the measured speckle patterns: Fig. 2(a) for the angle of incidence $\theta_{i2} = 0.5^\circ$, Fig. 2(b) for the angle of incidence $\theta_{i2} = 10^\circ$, Fig. 2(c) for the angle of incidence $\theta_{i2} = 20^\circ$, and Fig. 2(d) for the angle of incidence $\theta_{i2} = 30^\circ$. These measurements were made through the experimental setup in Fig. 2 with the diameter of the illumination of light on the sample $D = 8$ mm, the temperature of the CCD set at $T = 0^\circ\text{C}$, and with an exposure time of 2 s. Except for Fig. 2(a), for each angle of incidence a pair

of well-defined peaks is observed. The half width of peak is about 8 degrees which implies the dynamic range of specular trucking for this surface.

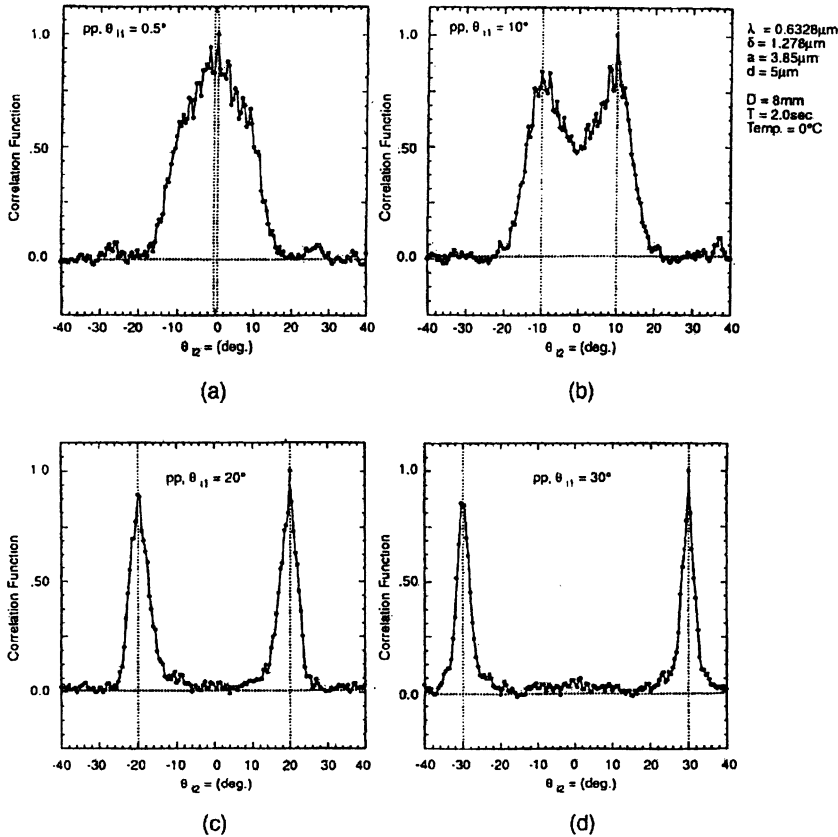


Fig. 2. Angular Intensity Correlation Function Derived from the Measured Speckle Patterns for p-polarization, at an Angle of Incidence (a) $\theta_{i1} = 0.5^\circ$, (b) $\theta_{i2} = 10^\circ$, (c) $\theta_{i3} = 20^\circ$, and (d) $\theta_{i4} = 30^\circ$.

Fig. 3 is the angular intensity correlation function derived from the numerical calculation; For simplicity, we treated the system as a thin photoresist film on a semi-infinite glass substrate. The vacuum-photoresist interface is assumed to be a one-dimensional randomly rough surface characterized by the standard deviation of heights $\delta = 1.278\mu\text{m}$ and the $1/e$ value of the correlation length $a = 3.85\mu\text{m}$. The photoresist-glass interface is assumed to be planar. A finite beam of light is incident from the vacuum side upon the rough surfaces, and the scattered light is collected in vacuum. Other parameters used in the calculation are as follows: wavelength $\lambda = 0.6328\mu\text{m}$;

the indices of refraction of the photoresist film and the glass substrate at this wavelength are 1.64 and 1.51, respectively; the thickness of the photoresist film is $d = 5\mu\text{m}$; a finite length of the rough surface for calculation is $L = 46.2\mu\text{m}$; the surface is sampled at $N = 440$ points; and the total number of surface profiles used in the simulation is $N_p = 500$ for all the results.

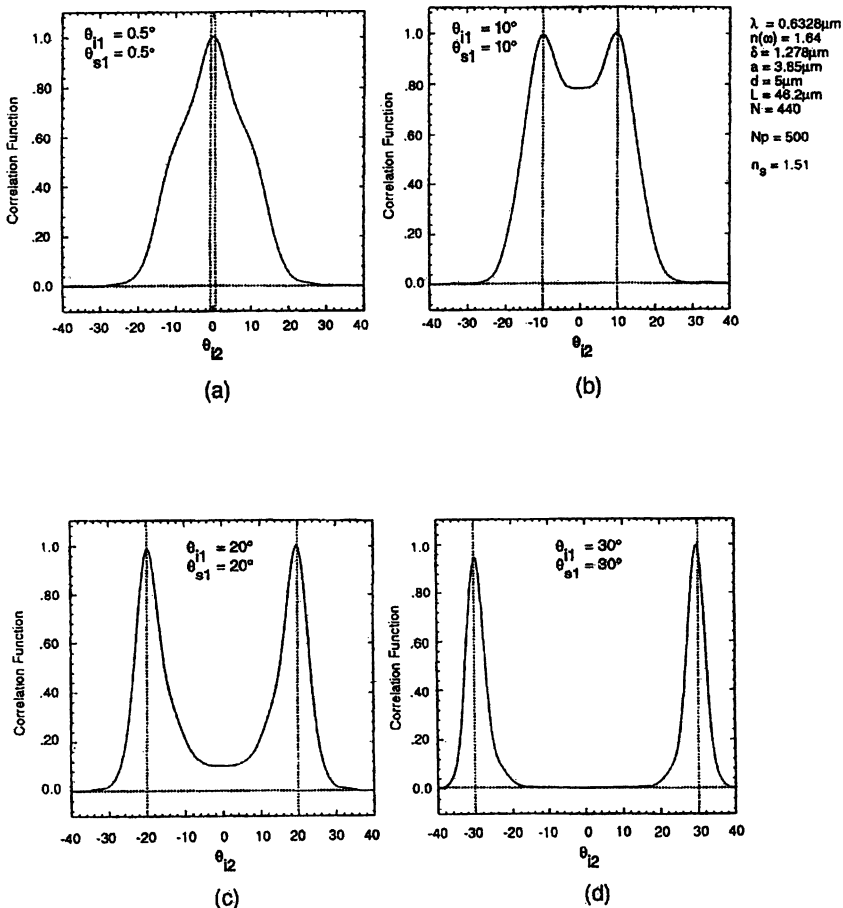


Fig. 3. Calculated Angle Intensity Correlation Function of p- polarization at an Angle of Incidence (a) $\theta_{i1} = 0.5^\circ$, (b) $\theta_{i2} = 10^\circ$, (c) $\theta_{i3} = 20^\circ$, and (d) $\theta_{i4} = 30^\circ$.

Generally speaking, for all the angles of incidence, numerical calculation provides results similar to the experimental measurements of Figure 3, with some minor differences. The angular correlation function in the measurements dropped faster than in the numerical simulation. This may be due to the fact that in experiments the sample is under illumination, i.e., the diameter of the

incident light is smaller than that of the sample. Thus the illuminated area of the surface varies as the angle of incidence changes. In the calculation the intercept of the beam with the rough surface is fixed; therefore the same area is illuminated for all angles of incidence.

Secondly we present the shift invariance of speckles in the $\sin \theta$ domain. For angular memory effect, it has been shown that a strong correlation can be observed based on Eq. (34). If we set $\theta_{i2} = \theta_{i1} + \Delta\theta_i$ and $\theta_{s2} = \theta_{s1} + \Delta\theta_s$ from equation (33) we can find, within a small range of $\Delta\theta_i$ and $\Delta\theta_s$, that

$$\Delta\theta_s = \Delta\theta_i . \quad (34)$$

Fig. 4 shows the angular memory line in the first and third quadrants of the $\Delta\theta_i$ - $\Delta\theta_s$ plane. The experimental results are shown in Fig. 5 for *p*-polarization. The incident angle $\theta_{i1} = 5^\circ$, and the scattering angle $\theta_{s1} = 10^\circ$, the incremental angle is 0.002° . It can be seen that while the scattering angle follows the incident angle, i.e., $\Delta\theta_s = \Delta\theta_i$, the correlation function remains practically unchanged.

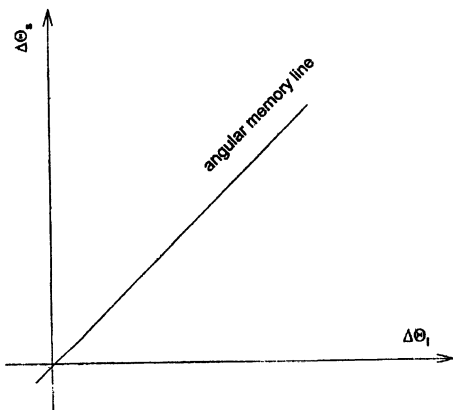


Fig. 4. Relationship Between the Change in the Incident Angle $\Delta\theta_i$ and the Corresponding Change in the Angle of the Scattered Speckle Pattern $\Delta\theta_s$ in Angular Memory Effect.

Thirdly we can see from Fig. 2 the time-reversed memory effect, the peak at $\theta_{i2} = \theta_{i1}$ obviously arises from autocorrelation with itself while the other peak at $\theta_{i2} = -\theta_{i1}$ comes from the reciprocal scattering configuration. Analytical results in Figure 22 show these two peaks are identical equal to one. Due to alignment, the experimental measurement of the reciprocal peak won't reach one.

3.4 Correlation effect for single and multiple scattering ($+45^\circ, +45^\circ$) and ($+45^\circ, -45^\circ$) linear polarization

It is well known that, for a one-dimensional surface, if the incident field is purely *s* or *p* polarized, the scattered field retains the same state of polarization. However, in a more general case in which the incident field is a linear

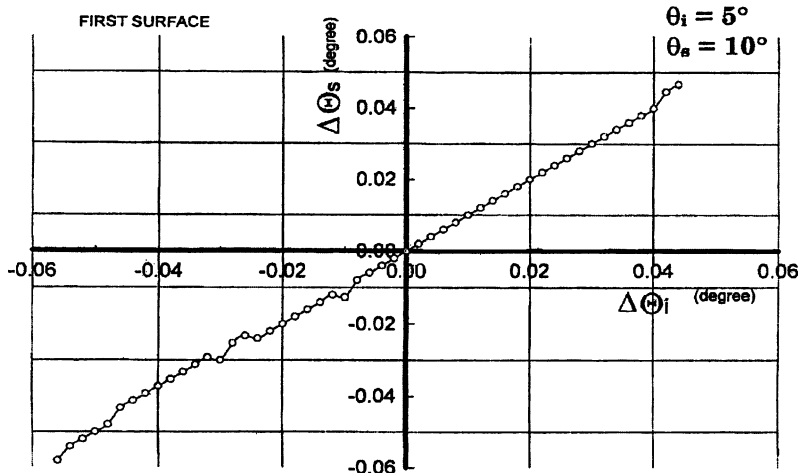


Fig. 5. The Angular Shift of Angular Memory Effect, for p-polarization

combination of s and p states, the state of polarization of the scattered light differs from that of the incident beam, which depends on the angle of scattering. It has been shown that for a rough surface on a semi-infinite medium, if the surface is illuminated with a $+45^\circ$ incident polarization state (equal p and s amplitudes), the mean scattered intensity with -45° polarization contains contributions from single scattering while the mean intensity with $+45^\circ$ polarization contains contributions from double scattering[26].

We measured the far-field scattering of $(+45^\circ, -45^\circ)$ polarization for an angle of incidence $\theta = 5^\circ$. No enhanced backscattering peak is observed. In Fig. 6 the far-field scattering of $(+45^\circ, +45^\circ)$ polarization for an angle of incidence $\theta = 5^\circ$ is presented. A strong, well-defined enhanced backscattering peak is observed in the retroreflection direction $\theta = -5^\circ$. This may be due to the fact that most scattered light comes from double scattering at the rough surface, which causes the enhanced backscattering peak. In these measurements a longer exposure time, 4s, is used to achieve the same speckle pattern quality.

In Fig. 7 we present the derived angular intensity correlation function for $(+45^\circ, -45^\circ)$ polarization from the measured speckle pattern. Although the distinct correlation peaks are observed at each angle of incidence, they are much like those for the p-polarization case. In Fig. 8 we present the derived angular intensity correlation function for $(+45^\circ, +45^\circ)$ polarization, the distinct correlation peaks are accompanied by secondary maxima for small angles of incidence; these secondary peaks decay fast as the angle of incidence increases. Also the width of the correlation peak for $(+45^\circ, +45^\circ)$ is narrower than that for $(+45^\circ, -45^\circ)$.

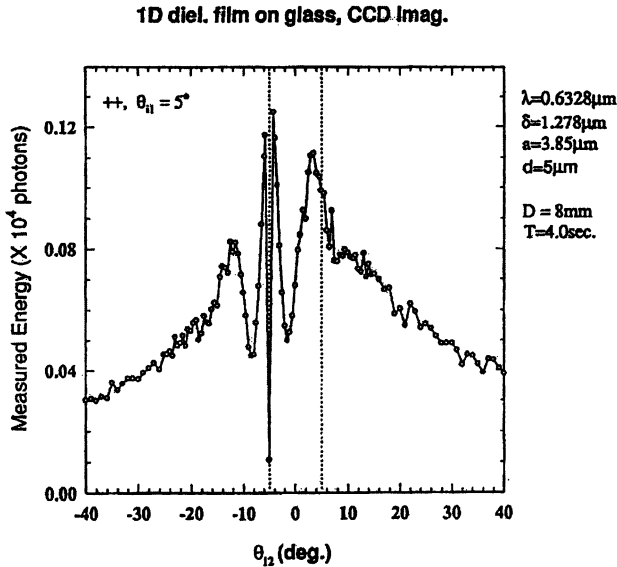


Fig. 6. Measured Far-Field Intensity of Light for $(+45^\circ, +45^\circ)$ Linear Polarization at an Angle of Incidence $\theta = 5^\circ$.

3.5 Symmetry of speckle correlation around the specular direction

Recently, McGurn and Maradudin have predicted an additional short- range correlation C[10], which shows the symmetry of the speckle pattern around the specular direction in the far-field scattering from a rough surface[30-31].

The function C[10] has been overlooked in earlier studies due to the use of the factorization approximation, which presents a new type of memory effect, and its magnitude is comparable with that of C[1]. C[10] can be observed if the following is satisfied:

$$\sin \theta_{i1} + \sin \theta_{i2} = \sin \theta_{s1} + \sin \theta_{s2}. \quad (35)$$

Fig. 9 shows the schematic of the symmetry. If we set θ_{i1} is equal to θ_{i2} , and θ_{s1} is equal to $\theta_{i1} + \Delta\theta$, then θ_{s2} should be $\theta_{i1} - \Delta\theta$ which locates on the other side of the specular direction ($-\theta_{i1}$) and is symmetrical to θ_{s1} around the specular direction. The experimental results are presented to verify the validity of the theoretical analysis. Fig. 10(a) is the angular correlation function for C[1] for a two-dimensional photoresist film on the glass substrate. The incident laser is He-Ne with wavelength at 0.6328 micron, the incident angle θ_{i1} is 20° and the scattering angle is -10° . The surface profile of the sample was measured with the standard deviation of heights σ is approximately 110 Å and the $1/e$ value of the correlation length is approximately 2800 Å. There are two maximum in Fig. 10(a), one for the memory effect

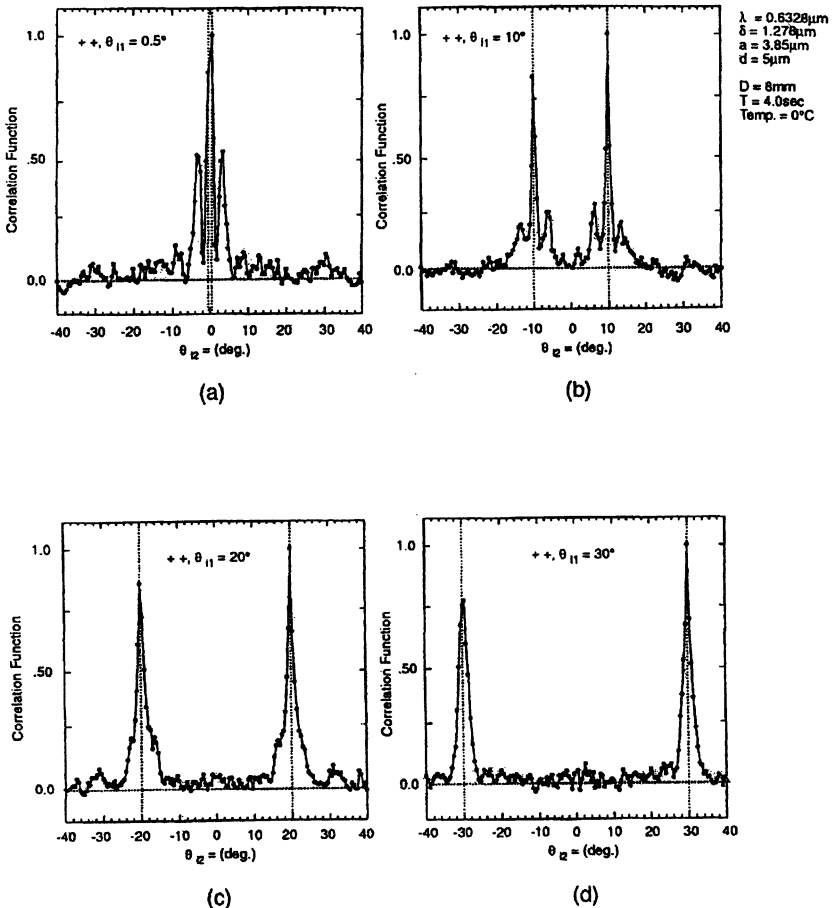


Fig. 7. Angular Intensity Correlation Function for $(+45^\circ, +45^\circ)$ Linear Polarization at an Angle of Incidence (a) $\theta_{i1} = 0.5^\circ$, (b) $\theta_{i1} = 10^\circ$, (c) $\theta_{i1} = 20^\circ$, and (d) $\theta_{i1} = 30^\circ$.

peak at $\theta_{s2} = -10^\circ$, and the other for time-reversed memory effect peak at $\theta_{s2} = -20^\circ$. Fig. 10(b) is the angular correlation function $C[10]$ for the sample. Since the specular direction is at $\theta_{s2} = 20^\circ$, you can find the correlation function $C[10]$ is symmetrical around the specular direction.

Fig. 11 is the far-field intensity distribution for the two-dimensional photoresist film on the glass substrate. The incident angle θ_i is 20° . For a smooth surface, there is a sharp peak on the specular direction and the intensity distribution is symmetrical with respect to the specular direction. Since the far-field low-order scattered amplitude is proportional to the Fourier transform of the real surface profile, which is Hermitian function, therefore the far-field scattered intensity should be symmetrical with respect to the specu-

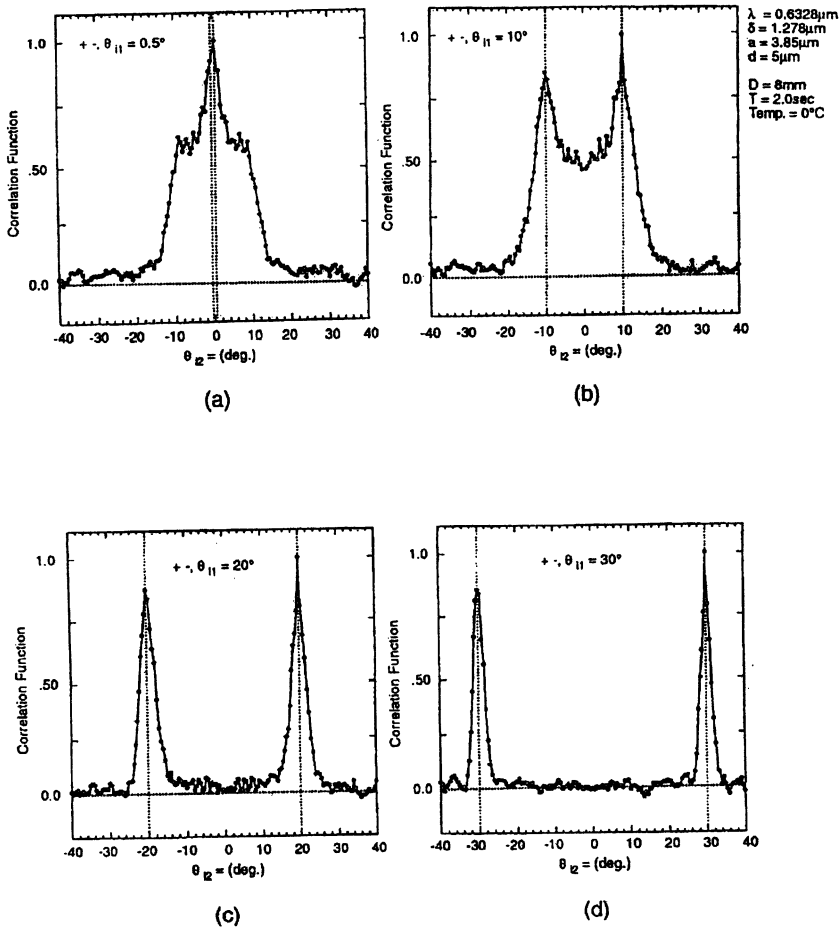


Fig. 8. Angular Intensity Correlation Function for $(+45^\circ, -45^\circ)$ Linear Polarization at an Angle of Incidence (a) $\theta_{i1} = 0.5^\circ$, (b) $\theta_{i1} = 10^\circ$, (c) $\theta_{i1} = 20^\circ$, and (d) $\theta_{i1} = 30^\circ$.

lar direction. The low-order angular correlation function $C[10]$ is proportional to the correlation of the scattered intensity, therefore $C[10]$ is symmetrical around the specular direction.

4 Summary

The results presented in this paper demonstrate the coherence in the scattering from rough surfaces. Four kinds of enhanced scattering from or through dielectric or metal surfaces, such as enhanced backscattering, grazing angle enhanced backscattering, enhanced transmission and enhanced reflection

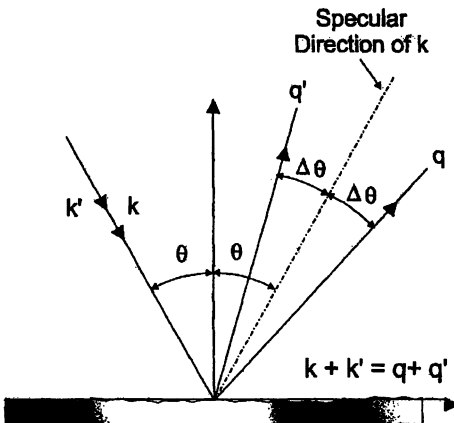


Fig. 9. Schematic of the Symmetry around the Specular Direction

2-D Photoresist on Glass Substrate

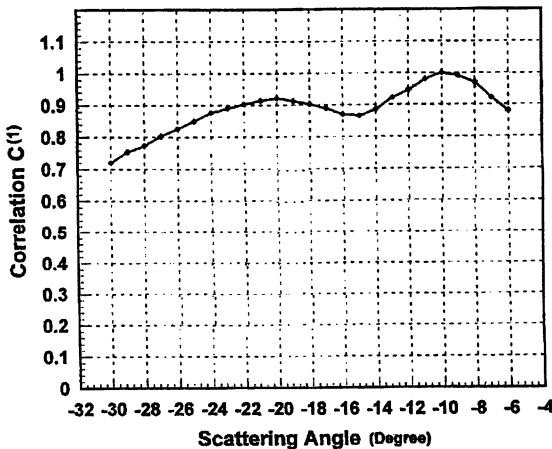


Fig. 10. (a). The Angular Correlation Function $C[1]$ for 2-D Photoresist on Glass Substrate with p-polarization.

of two beam interaction, have been studied. Recent simulation results have shown that for rough surface scattering, the high-sloped nature of the surfaces leads to multiple scattering, and this contribution enhances the scattered light. The enhancement was already significant in a double-scattering approximation. This was done by writing the integral equation for the surface field or its normal derivative for a perfectly conducting, one-dimensional random rough surface in the form of an inhomogeneous Fredholm equation of the second kind. In this equation the inhomogeneous term corresponds to the

2-D Photoresist on Glass Substrate

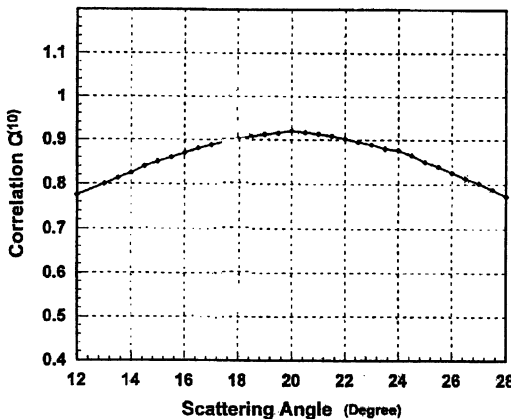


Fig. 10. (b). The Angular Correlation Function $C[10]$ for 2-D Photoresist on Glass Substrate with p-polarization

2-D Photoresist on Glass Substrate

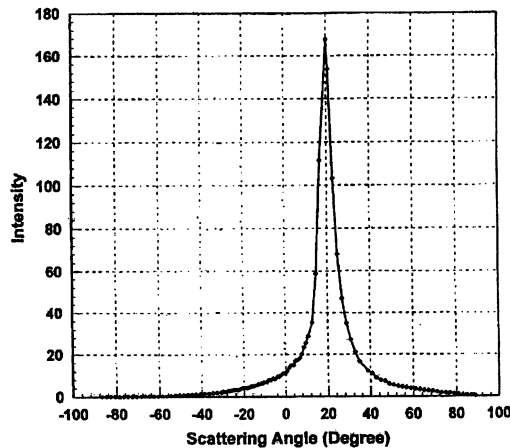


Fig. 11. The Far-Field Intensity Distribution of 2-D Photoresist on Glass Substrate, $\lambda = 0.6328\mu\text{m}$, p-polarization, and $\theta_i = 20^\circ$.

Kirchhoff, or single-scattering, approximation for the surface field, or its normal derivative, depending on the polarization. When this equation is solved iteratively, the n th term in the resulting expansion describes an n -fold scattering process. The first few terms in such a solution have been calculated and averaged with a Monte Carlo computer simulation. The contribution to the mean differential reflection coefficient from the incoherent component of the

scattered light in the single-scattering approximation displays no enhanced backscattering; the contribution from pure double-scattering processes shows a well-defined enhanced backscattering peak. The inclusion of the contribution from triple-scattering processes modifies the sum of the other two contributions from the single- and double-scattering by only a small amount in the vicinity of the enhanced backscattering peak, and is most significant in the region of large scattering angles, where the lower order approximations reproduce the effects of shadowing poorly[10].

We have also studied the angular correlation function of speckles from rough surface scattering . The dynamic behavior of the speckles and the symmetry around the specular direction shows another example of coherence and fluctuation of light from rough surface scattering. It is found that the intensity correlation functions exhibit two distinct maximum: one arises from the autocorrelation and the other from the reciprocity condition. It is also found that different scattering processes give rise to quite different correlation functions: multiple-scattering produces narrow peaks with secondary maxim and single-scattering produces relatively broader peaks. The mapping between two quantities — the enhanced backscattering and the correlation function — gives us a unique tool to verify the information given by the enhanced backscattering peak which is the example of coherence and fluctuations of light from rough surface scattering.

Acknowledgements. The authors wish to express their gratitude to the U.S. Army Research Office for their support under Grants DAAG55-98-C-0034 and DAAD19-99-C- 0032.

References

1. Y. Kuga, L. Tsang, and A. Ishimaru, J. Opt. Soc. Am. **A2**, 616-618 (1985).
2. V. Celli, A.A. Maradudin, A.M. Marvin, and A.R. McGurn, J. Opt. Soc. Am **A2**, 2225-2239 (1985).
3. E. R. Mendez and K.A. O'Donnell, Opt. Commun. **61**(2), 91-95 (1987).
4. Z. H. Gu, R.S. Dummer, A.A. Maradudin, and A.R. McGurn, Appl. Opt. **28**(3), 537-543 (1989).
5. Z. H. Gu, J.Q. Lu and M.M. Tehrani, Opt. Eng. **34**, 1611-1624 (1995).
6. Z. H. Gu, J.Q. Lu, A.A. Maradudin, A. Martinez, and E.R. Mendez, Appl. Opt. **32**(15), 2852-2859 (1993).
7. M. Nieto-Vesperinas and J.M. Soto-Crespo, Phys. Rev. B **38**, 7250-7259 (1988).
8. Z. H. Gu, H. M. Escamilla, E. R. Mendez, A. A. Maradudin, J.Q. Lu, T. Michel, and M. Nieto-Vesperinas, Applied Optics, **31**, 5878-5889 (1992).
9. J. Q. Lu, Z.H. Gu, J. Sanchez-Gil, A.A. Maradudin, and E. Mendez, J. Opt. Soc. Am. **A15**, 185-195 (1998).
10. A. A. Maradudin, T. Michel, A.R. McGurn, and E.R. Mendez, Ann. Phys. (N.Y.) **203**, 155-207 (1990).
11. Zu-Han Gu, J.Q. Lu and A. A. Maradudin, J. Opt. Soc. Am. **A10**, 1753- 1764 (1993).

12. J. W. Goodman, in *Laser Speckle and Related Phenomena*, J.C. Dainty, ed. (Springer-Verlag, Berlin, 1984).
13. S. Feng, C. Kane, P. A. Lee, and A. D. Stone, Phys. Rev. Lett. **61**, 834-837 (1988).
14. I. Freund, M. Rosenbluh, and S. Feng, Phys. Rev. Lett. **61**, 2328-2331 (1988).
15. R. Berkovits, M. Kaveh, and S. Feng, Phys. Rev. B **40**, 737-740 (1989).
16. R. Berkovits and M. Kaveh, Phys. Rev. B **41**, 2635-2638 (1990).
17. M.J. Stephen and G. Cwilich, Phys. Rev. Lett. **59**, 285-287 (1987).
18. R. Berkovits and M. Kaveh, Phys. Rev. B **41**, 7308-7310 (1990).
19. M.P. van Albada, J.F. de Boer, and A. Lagendijk, Phys. Rev. Lett. **64**, 2787-2790 (1990).
20. A.Z. Genack, in *Scattering and Localization of Classical Waves in Random Media*, P. Sheng, ed. (World Scientific, Singapore, 1990).
21. A.R. McGurn and A.A. Maradudin, Phys. Rev. B **39**, 13,160-13,168 (1989).
22. M. Nieto-Vesperinas, J.A. Sanchez-Gil, J. Opt. Soc. Am. A**10**, 150-157 (1993).
23. H.M. Escamilla, E.R. Mendez, and D.F. Hotz, Appl. Opt. **32**, 2734-2743 (1993).
24. M.E. Knotts, T.R. Michel, and K.A. O'Donnell, J. Opt. Soc. Am. A**9**, 1822-1831 (1992).
25. A. Arsenieva and S. Feng, Phys. Rev. B **47**, 13047-13050 (1993).
26. R.E. Luna, E.R. Mendez, J.Q. Lu, and Z.H. Gu, J. Mod. Opt. **42**, 257-269 (1995).
27. P.F. Gray, Opt. Acta **25**, 765-775 (1978).
28. A.A. Maradudin, J.Q. Lu, T. Michel, Z.H. Gu, J.C. Dainty, A.J. Sant, E.R. Mendez, and M. Nieto-Vesperinas, Waves in Random Media **1**, S129- S142 (1991).
29. J.Q. Lu and Z.H. Gu, Appl. Opt. **36**, No. 19, 4562-4569 (1997).
30. V. Malyshkin, A.R. McGurn, T.A. LesKova, A.A. Maradudin and M. Nieto-Vesperinas, Waves in Random Media **7** 479-520 (1997).
31. J.A. Sanchez-Gil, A.A. Maradudin, J.Q. Lu, and V.R. Freilikher, J. Mod. Opt. **43**, 435-452 (1996).

Multiple-Scattering Phenomena in the Scattering of Light from Randomly Rough Surfaces

E. I. Chaikina¹, E. E. García-Guerrero¹, Zu-Han Gu², T. A. Leskova³,
Alexei A. Maradudin⁴, E. R. Méndez¹, A. V. Shchegrov⁵

¹ División de Física Aplicada, Centro de Investigación Científica
y de Educación Superior de Ensenada,
Apartado Postal 2732, Ensenada, Baja California, México

² Surface Optics Corporation, 11555 Rancho Bernardo Road, San Diego, CA
92127 U.S.A.

³ Institute of Spectroscopy, Russian Academy of Sciences, Troitsk, 142092, Russia

⁴ Department of Physics and Astronomy,
and Institute for Surface and Interface Science,
University of California, Irvine, CA 92697, U.S.A.

⁵ Rochester Theory Center for Optical Science and Engineering,
and Department of Physics and Astronomy,
University of Rochester, Rochester, NY 14627-0171, U.S.A.

Abstract. The earliest theories of the scattering of electromagnetic waves from randomly rough surfaces were single-scattering theories, such as small-amplitude perturbation theory and the Kirchhoff approximation. The incorporation of multiple scattering into theories of rough surface scattering has led to the prediction of several new effects, which have now been verified experimentally. The new multiple-scattering effects to be discussed in this paper include enhanced backscattering, which is the presence of a well-defined peak in the retroreflection direction in the angular dependence of the intensity of the diffuse component of the light scattered from a random surface; enhanced transmission, which is the presence of a peak in the antispecular direction in the angular dependence of the intensity of the diffuse component of the light transmitted through a thin metal film with a random surface; satellite peaks that accompany the enhanced backscattering and transmission peaks when light is scattered from, and transmitted through, rough dielectric or metallic films that support two or more surface or guided waves; changes in the spectrum of light scattered from random surfaces (the Wolf shift); and the scattering of light uniformly within a specified angular range and the absence of scattering outside this range. This paper concludes with some suggestions for directions that research in the area of rough surface scattering could take in the next few years.

1 Introduction

The first theoretical study of the scattering of light from a randomly rough surface was carried out by Mandel'shtam in 1913, in the context of the scattering of light from the surface of a liquid[1]. These calculations were carried

out on the basis of a single scattering approximation, and for more than 70 years after the work of Mandel'shtam, single scattering approaches continued to underlie theoretical investigations of rough surface scattering. These approaches consisted either of small-amplitude perturbation theory[2], in which the amplitude of the scattered field was calculated to first order in the surface profile function – the function that gives the departure of a random surface from a planar surface at each point of the latter – or of the Kirchhoff approximation[3], in which the light is assumed to be scattered from and transmitted through the plane tangent to each point of the random surface.

In 1985, however, it was predicted theoretically on the basis of a multiple-scattering calculation of the scattering of p-polarized (transverse magnetic) light from a one-dimensional weakly rough random metal surface that the angular dependence of the intensity of the light scattered incoherently (diffusely) displays a well-defined peak in the retroreflection direction [4], caused by the coherent interaction of the multiply-scattered, p-polarized, surface electromagnetic waves – surface plasmon polaritons – supported by the vacuum-metal interface with their reciprocal partners. This effect was observed experimentally two years later[5], in experiments in which, however, surfaces considerably rougher than those for which the theory of Ref. 4 is valid were used. These results stimulated the development of computational approaches for calculating the scattering of light from large-amplitude, large slope, random surfaces, and searches for additional phenomena that reveal themselves only when multiple scattering is taken into account in these approaches, activities that continue to this day.

In this review some of the techniques that have been used to investigate multiple-scattering phenomena in rough surface scattering are outlined, and effects obtained by their use described. Where experimental confirmations of the latter exist they, too, will be presented.

2 Enhanced Backscattering

The first result showing that taking multiple-scattering into account in theoretical treatments of the scattering of light from a randomly rough surface can lead to new physical effects was the prediction of enhanced backscattering [4]. This is the presence of a well-defined peak in the retroreflection direction in the angular dependence of the intensity of the light that has been scattered incoherently. In this Section we sketch out the approaches that have been used in calculating this effect for one- and two-dimensional surfaces. An explanation of it is deferred to Section 3, where it will be embedded in a discussion of more general multiple-scattering effects occurring in scattering from bounded systems with random surfaces.

2.1 One-Dimensional Surfaces

The earliest calculations of the enhanced backscattering of light from a randomly rough surface were carried out for the scattering of p-polarized light from a one-dimensional random metal surface. They were first carried out by perturbation theory, and subsequently by a computer simulation approach. In what follows we describe two perturbative approaches to this problem, and a computer simulation approach.

2.2 Perturbation Theory

The system considered in the perturbative studies that led to the prediction of enhanced backscattering consisted of vacuum in the region $x_3 > \zeta(x_1)$, and a metal, characterized by an isotropic, frequency-dependent, dielectric function $\epsilon(\omega)$, in the region $x_3 < \zeta(x_1)$. The surface profile function $\zeta(x_1)$ was assumed to be a single-valued function of x_1 that is differentiable as many times as is necessary, and to constitute a zero mean, stationary, Gaussian random process defined by

$$\langle \zeta(x_1)\zeta(x'_1) \rangle = \delta^2 W(|x_1 - x'_1|). \quad (1)$$

The angle brackets here denote an average over the ensemble of realizations of the surface profile function, and $\delta = \langle \zeta^2(x_1) \rangle^{1/2}$ is the rms height of the surface. It is convenient to introduce the Fourier integral representation of $\zeta(x_1)$,

$$\zeta(x_1) = \int_{-\infty}^{\infty} \frac{dk}{2\pi} \hat{\zeta}(k) e^{ikx_1}. \quad (2)$$

The Fourier coefficient $\hat{\zeta}(k)$ also constitutes a zero-mean Gaussian random process defined by

$$\langle \hat{\zeta}(k)\hat{\zeta}(k') \rangle = 2\pi\delta(k + k')\delta^2 g(|k|), \quad (3)$$

where $g(|k|)$, the power spectrum of the surface roughness, is defined in terms of the surface height autocorrelation function $W(|x_1|)$ by

$$g(|k|) = \int_{-\infty}^{\infty} dx_1 W(|x_1|) e^{-ikx_1}. \quad (4)$$

Two forms of $W(|x_1|)$, and of $g(|k|)$, have been assumed in these studies,

$$W(|x_1|) = \exp(-x_1^2/a^2) \quad (5a)$$

$$g(|k|) = \sqrt{\pi}a \exp(-a^2k^2/4), \quad (5b)$$

and

$$W(|x_1|) = \frac{\sin k_{max}x_1 - \sin k_{min}x_1}{(k_{max} - k_{min})x_1} \quad (6a)$$

$$g(|k|) = \frac{\pi}{k_{max} - k_{min}} [\theta(k_{max} - k)\theta(k - k_{min}) + \theta(k_{max} + k)\theta(-k - k_{min})], \quad (6b)$$

where $\theta(z)$ is the Heaviside unit step function. If we define $k_{min} = k_{sp}(\omega) - (\omega/c) \sin \theta_m$ and $k_{max} = k_{sp}(\omega) + (\omega/c) \sin \theta_m$, where $k_{sp}(\omega) = (\omega/c) Re\{\epsilon(\omega)/[\epsilon(\omega)+1]\}^{1/2}$ is the wave number of the surface plasmon polariton of frequency ω supported by a planar vacuum-metal interface, the significance of the angle θ_m is that if p-polarized light of frequency ω is incident on the metal surface from the vacuum side with an angle of incidence θ_0 that lies in the interval $(-\theta_m, \theta_m)$, it can excite forward and backward propagating surface plasmon polaritons of wavenumber $k_{sp}(\omega)$ through the surface roughness[6]. At the same time, the surface plasmon polaritons excited in this way can be converted back into volume electromagnetic waves in the vacuum, through their interaction with the surface roughness, if the scattering angle θ_s lies in the interval $(-\theta_m, \theta_m)$ [6]. Thus, the use of the power spectrum (6b) strongly enhances multiple-scattering processes in which surface plasmon polaritons play the role of intermediate states.

The random surface is illuminated from the vacuum side by a p-polarized plane wave of frequency ω , whose magnetic vector has a single nonzero component, given by

$$H_2(x_1, x_3|\omega)_{inc} = \exp[ikx_1 - i\alpha_0(k, \omega)x_3], \quad (7)$$

where a time dependence $\exp(-i\omega t)$ has been assumed, but not indicated explicitly, and $\alpha_0(k, \omega) = [(\omega/c)^2 - k^2]^{1/2}$ with $Re\alpha_0(k, \omega) > 0$, $Im\alpha_0(k, \omega) > 0$. The wave number k is related to the angle of incidence θ_0 by $k = (\omega/c) \sin \theta_0$. The scattered field is then given by

$$H_2(x_1, x_3|\omega)_{sc} = \int_{-\infty}^{\infty} \frac{dq}{2\pi} R_p(q|k) \exp[iqx_1 + i\alpha_0(q, \omega)x_3]. \quad (8)$$

The scattering amplitude $R_p(q|k)$ plays a central role in this theory. The differential reflection coefficient $\partial R_p / \partial \theta_s$ is defined such that $(\partial R_p / \partial \theta_s)d\theta_s$ is the fraction of the total time-averaged flux of energy incident on the surface that is scattered into the angular interval $(\theta_s, \theta_s + d\theta_s)$. Since we are dealing with scattering from a random surface, it is the average of $(\partial R_p / \partial \theta_s)$ over the ensemble of realizations of the surface profile that will concern us. The contribution to the ensemble average of $\partial R_p / \partial \theta_s$ from the light that has been scattered incoherently (diffusely) is given in terms of $R_p(q|k)$ by

$$\left\langle \frac{\partial R_p}{\partial \theta_s} \right\rangle_{incoh} = \frac{1}{L_1} \frac{\omega}{2\pi c} \frac{\cos^2 \theta_s}{\cos \theta_0} [\langle |R_p(q|k)|^2 \rangle - |\langle R_p(q|k) \rangle|^2], \quad (9)$$

where L_1 is the length of the x_1 -axis covered by the random surface. The wave number q here is related to the scattering angle θ_s by $q = (\omega/c) \sin \theta_s$.

The scattering amplitude $R_p(q|k)$ satisfies the reduced Rayleigh equation[7]

$$\begin{aligned} \int_{-\infty}^{\infty} \frac{dq}{2\pi} \frac{I(\alpha(p, \omega) - \alpha_0(q, \omega)|p - q)}{\alpha(p, \omega) - \alpha_0(q, \omega)} [\alpha(p, \omega)\alpha_0(q, \omega) + pq] R_p(q|k) \\ = \frac{I(\alpha(p, \omega) + \alpha_0(k, \omega)|p - k)}{\alpha(p, \omega) + \alpha_0(k, \omega)} [\alpha(p, \omega)\alpha_0(k, \omega) - pk], \end{aligned} \quad (10)$$

where $\alpha(k, \omega) = [\epsilon(\omega)(\omega/c)^2 - k^2]^{\frac{1}{2}}$, with $Re \alpha(k, \omega) > 0, Im \alpha(k, \omega) > 0$. The function $I(\gamma|Q)$ appearing in Eq. (10) is defined by

$$I(\gamma|Q) = \int_{-\infty}^{\infty} dx_1 e^{-iQx_1} e^{-i\gamma\zeta(x_1)}. \quad (11)$$

In the simplest approach[8] to calculating $\langle \partial R_p / \partial \theta_s \rangle_{incoh}$ we seek the solution of Eq. (10) in the form of an expansion in powers of the surface profile function (small-amplitude perturbation theory [2])

$$\begin{aligned} R_p(q|k) = & 2\pi\delta(q-k)R_0(k, \omega) + \chi_1(q|k)\hat{\zeta}(q-k) \\ & + \frac{1}{2} \int_{-\infty}^{\infty} \frac{dp_1}{2\pi} \chi_2(q|p_1|k)\hat{\zeta}(q-p_1)\hat{\zeta}(p_1-k) \\ & + \frac{1}{6} \int_{-\infty}^{\infty} \frac{dp_1}{2\pi} \int_{-\infty}^{\infty} \frac{dp_2}{2\pi} \\ & \times \chi_3(q|p_1|p_2|k)\hat{\zeta}(q-p_1)\hat{\zeta}(p_1-p_2)\hat{\zeta}(p_2-k) + \dots, \end{aligned} \quad (12)$$

where $R_0(k, \omega) = [\epsilon(\omega)\alpha_0(k, \omega) - \alpha(k, \omega)]/[\epsilon(\omega)\alpha_0(k, \omega) + \alpha(k, \omega)]$ is the Fresnel coefficient for the scattering of a p-polarized plane wave from a planar vacuum-metal interface, and $\chi_1(q|k), \chi_2(q|p_1|k), \dots$, can be calculated recursively. It follows from Eq. (9) that $\langle \partial R_p / \partial \theta_s \rangle_{incoh}$ is given by

$$\begin{aligned} \left\langle \frac{\partial R_p}{\partial \theta_s} \right\rangle_{incoh} = & \frac{\omega}{2\pi c} \frac{\cos^2 \theta_s}{\cos \theta_0} \{ \delta^2 |\chi_1(q|k)|^2 g(|q-k|) \\ & + \frac{1}{4} \delta^4 \int_{-\infty}^{\infty} \frac{dp_1}{2\pi} g(|q-p_1|)g(|p_1-k|) \chi_2(q|p_1|k) \\ & \times [\chi_2^*(q|p_1|k) + \chi_2^*(q|q+k-p_1|k)] \\ & + \frac{1}{3} \delta^4 Re g(|q-k|) \chi_1^*(q|k) \int_{-\infty}^{\infty} \frac{dp_1}{2\pi} [\chi_3(q|p_1|q|k)g(|q-p_1|) \\ & + \chi_3(q|p_1|p_1+k-q|k)g(|q-p_1|) + \chi_3(q|k|p_1|k)g(|p_1-k|)] \\ & + O(\delta^6) \}, \end{aligned} \quad (13)$$

through terms of $O(\delta^4)$. The first term is the single scattering contribution, while the remaining terms are multiple-scattering contributions.

When the result expressed by Eq. (13) is plotted as a function of the scattering angle θ_s for a given value of the angle of incidence, a well-defined peak in $\langle \partial R_p / \partial \theta_s \rangle_{incoh}$ is present in the retroreflection direction $\theta_s = -\theta_0 (q = -k)$ (Fig. 1). It arises from the term containing the product $\chi_2(q|p_1|k)\chi_2^*(q|q+k-p_1|k)$ in the integrand of the first integral on the right hand side of Eq. (13), and is associated with the coherent interference of a doubly-scattered surface plasmon polariton supported by the vacuum-metal interface and its reciprocal partner, in which the surface polariton interacts with the roughness at the same points on the surface, but in the reverse order.

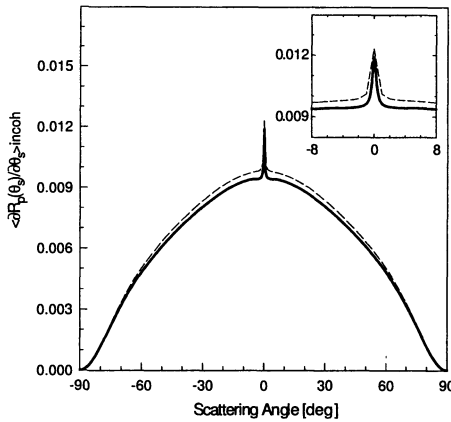


Fig. 1. A plot of $\langle \partial R_p / \partial \theta_s \rangle_{incoh}$ as a function of θ_s for p-polarized light of wavelength $\lambda = 457.9$ nm incident normally on a one-dimensional random silver surface ($\epsilon(\omega) = -7.5 + i0.24$) characterized by the Gaussian power spectrum (5b) with $\delta = 5$ nm and $a = 100$ nm. The calculations are based on Eq. (13) (solid curve) and on Eq. (19) (dashed curve). The inset shows $\langle \partial R_p / \partial \theta_s \rangle_{incoh}$ in the vicinity of the retroreflection direction.

In a second approach to the calculation of $\langle \partial R_p / \partial \theta_s \rangle_{incoh}$ we seek $R_p(q|k)$ in the form[9]

$$R_p(q|k) = 2\pi\delta(q - k)R_0(k, \omega) - 2iG_0(q, \omega)T(q|k)G_0(k, \omega)\alpha_0(k, \omega), \quad (14)$$

where $G_0(k, \omega) = i\epsilon(\omega)/[\epsilon(\omega)\alpha_0(k, \omega) + \alpha(k, \omega)]$ is a Green's function for surface plasmon polaritons at a planar vacuum-metal interface, while the transition matrix $T(q|k)$ is postulated to satisfy

$$T(q|k) = V(q|k) + \int_{-\infty}^{\infty} \frac{dp}{2\pi} V(q|p)G_0(p, \omega)T(q|k). \quad (15)$$

Equations (10), (14), and (15) define the scattering potential $V(q|k)$ which, to first order in the surface profile function (small roughness approximation), is given by

$$V(q|k) = i\frac{\epsilon(\omega) - 1}{\epsilon^2(\omega)} [\epsilon(\omega)qk - \alpha(q, \omega)\alpha(k, \omega)]\hat{\zeta}(q - k). \quad (16)$$

It is also convenient to introduce the Green's function $G(q|k)$ for surface plasmon polaritons at the randomly rough vacuum-metal interface as the solution of

$$G(q|k) = 2\pi\delta(q - k)G_0(k, \omega) + G_0(q, \omega) \int_{-\infty}^{\infty} \frac{dp}{2\pi} V(q|p)G(p|k) \quad (17a)$$

$$= 2\pi\delta(q - k)G_0(k, \omega) + G_0(q, \omega)T(q|k)G_0(k, \omega). \quad (17b)$$

It follows from these equations that $\langle \partial R_p / \partial \theta_s \rangle_{incoh}$ can be written equivalently as

$$\begin{aligned} \left\langle \frac{\partial R_p}{\partial \theta_s} \right\rangle_{incoh} &= \frac{1}{L_1} \frac{2}{\pi} \left(\frac{\omega}{c} \right)^3 \cos^2 \theta_s \cos \theta_0 [\langle |G(q|k)|^2 \rangle - |\langle G(q|k) \rangle|^2] \\ &= \frac{2}{\pi} \left(\frac{\omega}{c} \right)^3 \cos^2 \theta_s \cos \theta_0 |G(q, \omega)|^2 R_{qk} |G(k, \omega)|^2, \end{aligned} \quad (18)$$

where $G(k, \omega)$ is defined by $\langle G(q|k) \rangle = 2\pi\delta(q - k)G(k, \omega)$, and R_{qk} is the reducible vertex function. $G(k, \omega)$ is related to $G_0(k, \omega)$ by $G(k, \omega) = [G_0^{-1}(k, \omega) - M(k, \omega)]^{-1}$ where $M(k, \omega)$ is a self-energy that can be calculated as an expansion in powers of $\zeta(x_1)$. For R_{qk} we take the sum of the contributions from the ladder diagrams and the maximally-crossed diagrams, and obtain

$$\begin{aligned} \left\langle \frac{\partial R_p}{\partial \theta_s} \right\rangle_{incoh} &= \frac{2}{\pi} \left(\frac{\omega}{c} \right)^3 \cos^2 \theta_s \cos \theta_0 |G(q, \omega)|^2 \left[U_{qk}^{(0)} \right. \\ &\quad \left. + \frac{A_{qk}}{4\Delta^2} + \frac{A_{\frac{1}{2}(q-k), \frac{1}{2}(k-q)}}{(q+k)^2 + 4\Delta^2} \right] |G(k, \omega)|^2, \end{aligned} \quad (19)$$

where $U_{qk}^{(0)} = \delta^2 g(|q - k|)[(\epsilon(\omega) - 1)/\epsilon^2(\omega)][\epsilon(\omega)qk - \alpha(q, \omega)\alpha(k, \omega)]|^2$, while A_{qk} is a smoothly varying function of q and k . The parameter Δ is defined by $\Delta^2 = \Delta_\epsilon(\Delta_\epsilon + 2\Delta_{sp})$, where $\Delta_\epsilon = \frac{1}{2}k_{sp}\epsilon_2/[|\epsilon_1|(|\epsilon_1| - 1)]$ is the decay rate of a surface plasmon polariton, whose wave number is $k_{sp} = (\omega/c)[|\epsilon_1|/(|\epsilon_1| - 1)]^{\frac{1}{2}}$, due to ohmic losses in the metal, while $\Delta_{sp} = [|\epsilon_1|^{3/2}/(\epsilon_1^2 - 1)]M(k_{sp}, \omega)$ is the decay rate of a surface plasmon polariton due to its roughness-induced conversion into other surface plasmon polaritons. The first term on the right hand side of Eq. (19) is the single scattering contribution, the second is the contribution from the ladder diagrams, and the third is the contribution from the maximally-crossed diagrams. The latter two terms are equal for scattering into the retroreflection direction, i.e. when $q = -k$ or $\theta_s = -\theta_0$. The prediction of enhanced backscattering in the result given by Eq. (19) is clearly seen through the presence of the denominator $(q+k)^2 + 4\Delta^2$ in the last term on the right hand side of Eq. (19), which is large only when $q \cong -k$. This term is also associated with the coherent interference of multiply-scattered surface plasmon polaritons with their reciprocal partners. It is also seen from Eq. (19) that when $q = -k$ the second and third terms on the right hand side are equal.

The enhanced backscattering peak is clearly visible when the result given by Eq. (19) is plotted as a function of θ_s for a given value of θ_0 (Fig. 1). The result is very close to that obtained for the same random surface by small-amplitude perturbation theory. The chief difference is that the width of the enhanced backscattering peak predicted by Eq. (19) is slightly larger than that predicted by Eq. (13). The first (and so far only) experimental observation of the enhanced backscattering of light from a weakly rough random metal surface, caused by this surface plasmon polariton mechanism, was by West and O'Donnell[6]. These authors scattered p-polarized light from specially fabricated one-dimensional random gold surfaces characterized by the power spectrum (6b). A comparison[10] between their experimental results and the results of the two perturbation theories described in this section with no adjustable parameters in the perturbative calculations, shows that the latter are very accurate (Fig. 2). Perturbative calculations of $\langle \partial R_s / \partial \theta_s \rangle_{incoh}$ carried out for the scattering of s-polarized light from the same random silver surfaces that show enhanced backscattering when illuminated by p-polarized

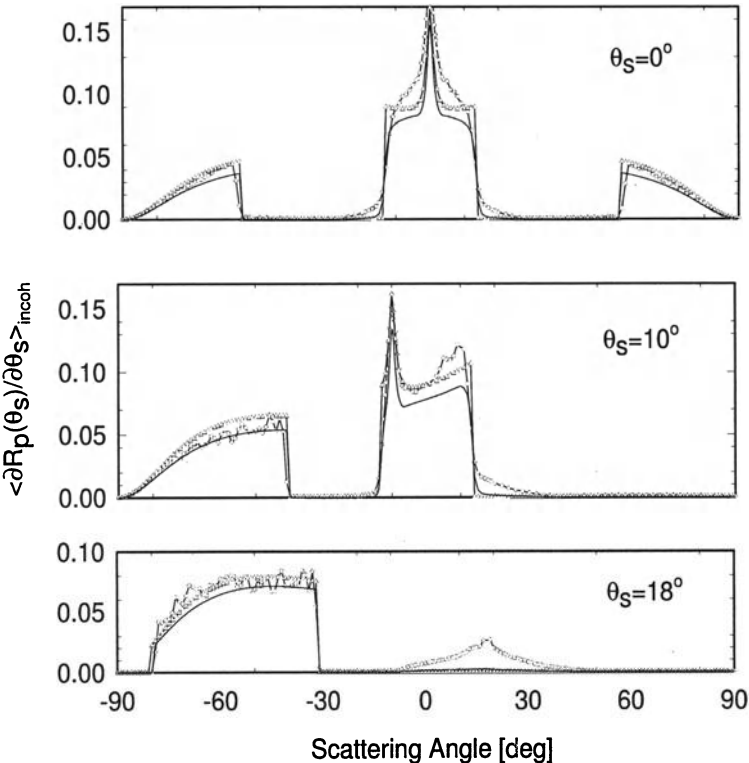


Fig. 2. A plot of $\langle \partial R_p / \partial \theta_s \rangle_{incoh}$ as a function of θ_s for three angles of incidence when p-polarized light of wavelength $\lambda = 0.612\mu\text{m}$ is incident on a one-dimensional random gold surface ($\epsilon(\omega) = -9.00 + i1.29$) characterized by the West-O'Donnell power spectrum (6b) with $\delta = 10.9\text{nm}$, $k_{min} = 8.4815 \times 10^{-3}\text{nm}^{-1}$ and $k_{max} = 13.260 \times 10^{-3}\text{nm}^{-1}$ (0) experimental data of Ref. 9; (-) results based on Eq. (13); (Δ) results based on Eq. (19) [Ref. 10].

light, show no sign of enhanced backscattering. This is because s-polarized surface plasmon polaritons do not exist at a vacuum-metal interface. This result is confirmed by the experimental results of West and O'Donnell[6].

2.3 Computer Simulations

The first experimental observation of the enhanced backscattering of light from a random surface was carried out for metal surfaces that were significantly rougher than those for which the perturbation theories described in Section 2.2 are valid[5]. To deal with such surfaces it became necessary to find a different approach, and the one that has come to be used most frequently is the computer simulation of scattering from random surfaces[11,12].

In this approach a finite segment of a one-dimensional random surface, defined by $x_3 = \zeta(x_1)$, that covers the interval $(-L/2, L/2)$ of the x_1 -axis is generated numerically, for example as in Appendix A of Ref. 13, since computers can't deal with infinitely long surfaces. The region above this surface is vacuum; the region below is a metal or dielectric, characterized by a dielectric function $\epsilon(\omega)$. To minimize end effects this surface is illuminated from the vacuum side by a beam of p- or s-polarized light. In the case of p-polarization the single nonzero component of the magnetic vector of the incident light is given by

$$H_2^>(x_1, x_3|\omega)_{inc} = \frac{w\omega}{2\sqrt{\pi c}} \int_{-\frac{\pi}{2}}^{\frac{\pi}{2}} d\theta e^{-\frac{w^2\omega^2}{4c^2}(\theta-\theta_0)^2} e^{-i\frac{\omega}{c}(x_1 \sin \theta - x_3 \cos \theta)}. \quad (20)$$

Here θ_0 is the angle of incidence, and w is the half-width of the beam. The width of the beam is chosen such that the width of its intercept with the x_1 -axis, $2g = 2w/\cos \theta_0$, is of the order of $L/2$ to $L/2.5$. The total time-averaged flux incident on the surface is

$$P_{inc} = L_2 \frac{cw}{8\sqrt{2\pi}} p_{inc}(\theta_0), \quad (21a)$$

where L_2 is the length of the surface along the x_2 -axis, and

$$p_{inc}(\theta_0) = \frac{1}{2} \left[erf \left(\frac{w\omega}{\sqrt{2c}} \left(\frac{\pi}{2} - \theta_0 \right) \right) + erf \left(\frac{w\omega}{\sqrt{2c}} \left(\frac{\pi}{2} + \theta_0 \right) \right) \right]. \quad (21b)$$

The use of Green's second integral identity in the plane [14] yields the result that the contribution to the mean differential reflection coefficient from the incoherent component of the scattered light is given by[13]

$$\left\langle \frac{\partial R_p}{\partial \theta_s} \right\rangle_{incoh} = \frac{1}{2(2\pi)^{3/2}} \frac{c}{w\omega} \frac{\langle |r_p(\theta_s)|^2 \rangle - |\langle r_p(\theta_s) \rangle|^2}{p_{inc}(\theta_0)}, \quad (22)$$

where

$$r_p(\theta_s) = \int_{-\infty}^{\infty} dx_1 \exp \left(-i \frac{\omega}{c} [x_1 \sin \theta_s + \zeta(x_1) \cos \theta_s] \right) \\ \times \left\{ i \frac{\omega}{c} [\zeta'(x_1) \sin \theta_s - \cos \theta_s] H(x_1|\omega) - L(x_1|\omega) \right\}. \quad (23)$$

The source functions $H(x_1|\omega)$ and $L(x_1|\omega)$ are defined by

$$H(x_1|\omega) = H_2^>(x_1, x_3|\omega) \Big|_{x_3=\zeta(x_1)} \quad (24a)$$

$$L(x_1|\omega) = \left(-\zeta'(x_1) \frac{\partial}{\partial x_1} + \frac{\partial}{\partial x_3} \right) H_2^>(x_1, x_3|\omega) \Big|_{x_3=\zeta(x_1)}, \quad (24b)$$

where $H_2^>(x_1, x_3|\omega)$ is the total magnetic field in the vacuum region $x_3 > \zeta(x_1)$. They satisfy a pair of coupled inhomogeneous integral equations,

$$H(x_1|\omega) = H(x_1|\omega)_{inc} + \int_{-\infty}^{\infty} dx'_1 [H^{(0)}(x_1|x'_1) H(x'_1|\omega)]$$

$$-L^{(0)}(x_1|x'_1)L(x'_1|\omega)] \quad (25a)$$

$$0 = - \int_{-\infty}^{\infty} dx'_1 [H^{(\epsilon)}(x_1|x'_1)H(x'_1|\omega) \\ - \epsilon(\omega)L^{(\epsilon)}(x_1|x'_1)L(x'_1|\omega)], \quad (25b)$$

where $H(x_1|\omega)_{inc} = H_2^>(x_1, x_3|\omega)_{inc}|_{x_3=\zeta(x_1)}$. The kernels $H^{(\epsilon)}(x_1|x'_1)$ and $L^{(\epsilon)}(x_1|x'_1)$ in Eq. (25b) are given by

$$H^{(\epsilon)}(x_1|x'_1) = \frac{1}{4\pi} \left(-\zeta'(x'_1) \frac{\partial}{\partial x'_1} + \frac{\partial}{\partial x'_3} \right) \\ \times G_\epsilon(x_1, x_3|x'_1, x'_3)|_{\begin{array}{l} x'_3 = \zeta(x'_1) \\ x_3 = \zeta(x_1) + \eta \end{array}} \quad (26a)$$

$$L^{(\epsilon)}(x_1|x'_1) = \frac{1}{4\pi} G_\epsilon(x_1, x_3|x'_1, x'_3)|_{\begin{array}{l} x'_3 = \zeta(x'_1) \\ x_3 = \zeta(x_1) + \eta \end{array}}, \quad (26b)$$

where η is a positive infinitesimal, and

$$G_\epsilon(x_1, x_3|x'_1, x'_3) = i\pi H_0^{(1)} \left(\sqrt{\epsilon} \frac{\omega}{c} [(x_1 - x'_1)^2 + (x_3 - x'_3)^2]^{\frac{1}{2}} \right), \quad (27)$$

where $H_0^{(1)}(z)$ is a Hankel function. The kernels $H^{(0)}(x_1|x'_1)$ and $L^{(0)}(x_1|x'_1)$ in Eq. (25a) are obtained by setting $\epsilon(\omega) = 1$ in Eqs. (26)-(27). Equations (25) are solved numerically by converting them into matrix equations by the use of a numerical quadrature scheme. The solutions are then used to calculate $r_p(\theta_s)$. This procedure is carried out for of the order of 1000 different realizations of the surface profile function $\zeta(x_1)$, and the averages $\langle r_p(\theta_s) \rangle$ and $\langle |r_p(\theta_s)|^2 \rangle$ entering $\langle \partial R_p / \partial \theta_s \rangle_{incoh}$ are calculated from the results

The results obtained by this approach display an enhanced backscattering peak not only in p-polarization but in s-polarization as well, in contrast with the results obtained by the use of perturbation theory (Fig. 3). When this approach is applied to the scattering from a randomly rough dielectric surface ($\epsilon = 2.56$), an enhanced backscattering peak is present in the result for the scattering of s-polarized light, but not in the result for the scattering of p-polarized light (Fig. 4). The reason for this difference appears to be that dielectric surfaces reflect s-polarized more strongly than they reflect p-polarized light, and a strongly reflecting surface is required for the existence of this phenomenon in scattering from large rms height, large rms slope random dielectric surfaces[13,15]. When the statistical properties of a random surface are accurately known, and are introduced into a computer simulation calculation of the scattering of light from that surface, the agreement between the theoretical and experimental results is very good[16] (Fig. 5).

2.4 Two-Dimensional Surfaces

The scattering of light from two-dimensional random surfaces is richer in its effects than is scattering from one-dimensional surfaces in that cross-polarized

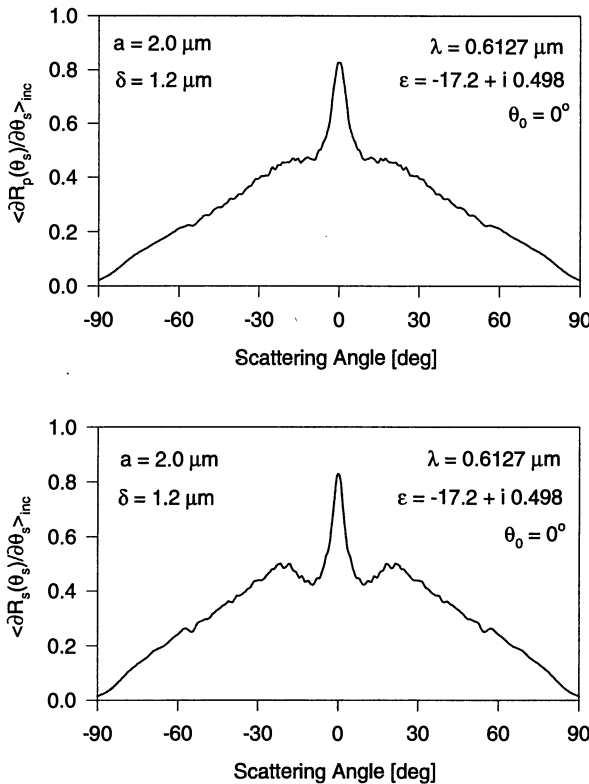


Fig. 3. Computer simulation results for $\langle \partial R_p / \partial \theta_s \rangle_{incoh}$ and $\langle \partial R_s / \partial \theta_s \rangle_{incoh}$ as functions of θ_s , when p- and s-polarized light, respectively, of wavelength $\lambda = 0.6127 \mu\text{m}$ is incident normally on a one-dimensional random silver surface ($\epsilon(\omega) = -17.2 + i 0.498$) characterized by the Gaussian power spectrum (5b) with $\delta = 1.2 \mu\text{m}$ and $a = 2 \mu\text{m}$.

scattering now becomes possible. Thus, incident light of p-polarization can be scattered into light of both p- and s-polarization (with respect to the plane of scattering), while light of s-polarization can also be scattered into light of both p- and s-polarization. This fact can be exploited to eliminate single scattering processes, something that is more difficult to accomplish in scattering from one-dimensional surfaces, so that the effects of only multiple-scattering processes can be investigated experimentally. This is because in in-plane, cross-polarized, scattering the contribution to the scattered intensity from single scattering processes vanishes.

The scattering of light from weakly rough two-dimensional metal surfaces has been calculated perturbatively both by the use of small-amplitude perturbation theory, through terms of fourth-order in the surface profile function

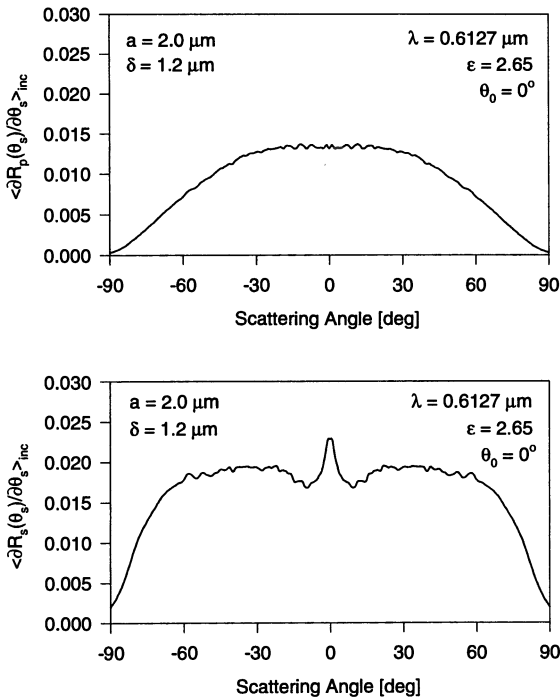


Fig. 4. Computer simulation results for $\langle \partial R_p / \partial \theta_s \rangle_{incoh}$ and $\langle \partial R_s / \partial \theta_s \rangle_{incoh}$ as functions of θ_s when p- and s-polarized light, respectively, of wavelength $\lambda = 0.6127 \mu m$ is incident normally on a one-dimensional random dielectric surface ($\epsilon = 2.65$) characterized by the Gaussian power spectrum (5b) with $\delta = 1.2 \mu m$ and $a = 2 \mu m$.

in the intensity of the scattered light[17], and by many-body perturbation theory[18]. Both approaches predict enhanced backscattering caused by the coherent interference of multiply-scattered surface plasmon polaritons with their reciprocal partners.

A multiple-scattering calculation of the scattering of a scalar plane wave from a weakly rough two-dimensional random surface on which the Dirichlet boundary condition is satisfied, i.e. on which the total field is required to vanish, has been carried out on the basis of phase perturbation theory[19]. The multiple scattering of a scalar plane wave from a weakly rough two-dimensional random surface on which the Neumann boundary condition is satisfied, i.e. on which the normal derivative of the total field is required to vanish, was calculated on the basis of many-body perturbation theory[20]. A result of the latter calculation was the prediction of enhanced backscattering.

In contrast, a computationally tractable numerical simulation approach to the multiple scattering of light from a large rms height, large rms slope,

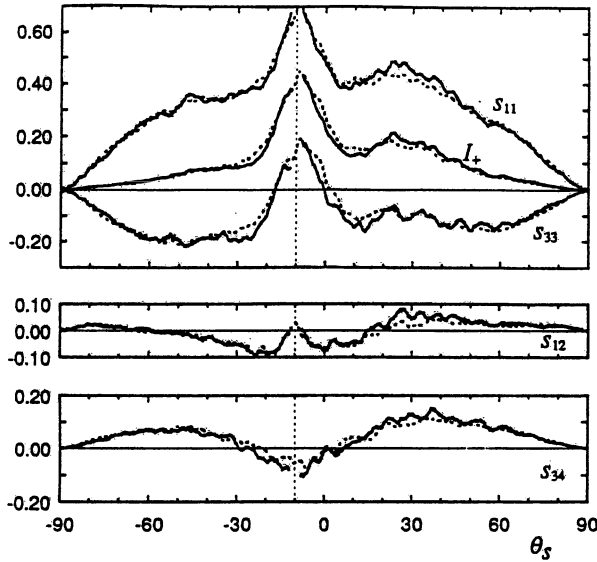


Fig. 5. The elements of the Stokes matrix S_{11} , S_{12} , S_{33} , S_{34} and the $+45^\circ$ -polarized intensity I_+ , when light of wavelength $\lambda = 3.39\mu\text{m}$ is incident on a one-dimensional, randomly rough, gold surface characterized by an rms height $\delta = 1.73\mu\text{m}$ and a transverse correlation length $a = 3.43\mu\text{m}$. The angle of incidence is 10° . Experimental results (solid curves) are compared with computer simulation results obtained by the use of an impedance boundary condition applied to a surface profile obtained directly by contact profilometry [Ref. 16].

two-dimensional, randomly rough surface bounding a penetrable medium, i.e. a metal or a dielectric, has been elusive until recently. The first computer simulation studies of scattering from two-dimensional randomly rough surfaces, which predicted enhanced backscattering from them, were carried out for the scattering of scalar waves from surfaces on which the Dirichlet[21,23] or Neumann[23] boundary conditions were satisfied.

Recently, computer simulation studies have been carried out of the copolarized and cross-polarized in-plane and out-of-plane, scattering of a finite beam of p-polarized light incident normally on large rms height, large rms slope, two-dimensional, randomly rough, perfectly conducting[24,25] and metallic (silver)[25] surfaces. The contribution to the mean differential reflection coefficient from the incoherent component of the scattered light was calculated. In this work the scattered electromagnetic field was expressed in terms of the surface magnetic current, in the case of scattering from a perfectly conducting surface, and in terms of the surface magnetic and electric currents, in the case of scattering from a metallic surface, through the use

of the Franz formulas of electromagnetic theory[26]. Since each of these surface currents is a vector that is tangent to the surface at each point, the scalar product of each with the unit vector normal to the surface at each point vanishes. Consequently, each surface current has only two independent Cartesian components. The inhomogeneous integral equations satisfied by the independent components of the surface currents were obtained by the use of the Stratton-Chu equations[26]. In the case of a perfectly conducting surface a pair of coupled integral equations is obtained for the two independent components of the surface magnetic current vector (because the normal component of the magnetic field vanishes on the surface). In the case of a metallic surface a total of six coupled integral equations was used to obtain the two independent components of each of the surface magnetic and electric currents. This is because they are coupled to the values of the normal components of the vacuum values of the magnetic and electric fields on the surface, and therefore two additional equations are needed to close the system of equations. For either type of surface the corresponding set of integral equations was converted into a set of inhomogeneous, coupled, matrix equations that were solved by the Neumann-Liouville iterative method for each of 100 realizations of the randomly rough, perfectly conducting and metallic surfaces. Although this is the simplest of many iterative methods, it has the advantage of not requiring the storage of the impedance matrix (the kernel of the integral equation): each element was generated anew each time it was used in the calculation. The calculations were carried out on the massively parallel computer MasPar, which possesses $N_p = 4096$ nodes. Because of the highly parallel nature of the Neumann-Liouville iteration scheme (at each iteration the updating of each unknown can be done independently of all the others), the computation time scales as $[\max(1, N^2/N_p)]N^2$, rather than as N^4 , where N^2 is the number of grid points on the surface. The surface profile function was assumed to be a zero-mean, stationary, Gaussian random process with a Gaussian surface height autocorrelation function. These random surfaces were generated numerically on a 128×128 grid covering an area $L^2 = 12.8\lambda \times 12.8\lambda$ of the x_1x_2 -plane, where λ is the wavelength of the incident light. Thus, the $\Delta x_1 (= \Delta x_2)$ used in discretizing the integral equations is $\lambda/10$, which is a commonly accepted value for obtaining good spatial resolution in the results of surface scattering calculations. Consequently, a system of 32,768 equations in 32,768 unknowns had to be solved for scattering from the perfectly conducting surface, while a system of 98,304 equations in 98,304 unknowns had to be solved for scattering from the metallic surface. It was the large sizes of these matrix equations that dictated the use of an iterative method for their solution. The rms height of each rough surface was λ , while the transverse correlation length of the surface roughness was 2λ . The radius of the circular intercept of the incident beam with the mean scattering surface was 3λ . Terms through the 6th iterate were retained in the solution for both the perfectly conducting surface and the metallic surface.

In the calculation for the perfectly conducting surface each iteration required 365 CPU seconds, and the calculation of the scattered field required 360 CPU seconds, for each realization of the surface. In the calculation for the metal surface each iteration required 1210 CPU seconds, and the calculation of the scattered field required 764 seconds, for each realization of the surface.

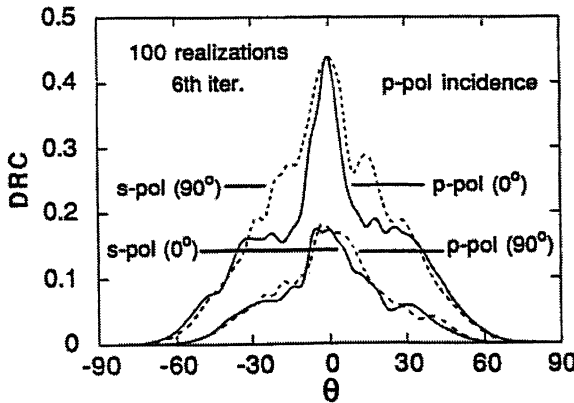


Fig. 6. The contribution to the mean differential reflection coefficient (DRC) from the incoherent component of the co-polarized ($p \rightarrow p$) and cross-polarized ($p \rightarrow s$) scattered light when a beam of p-polarized light of wavelength λ is incident normally on a two-dimensional, randomly rough, perfectly conducting surface, characterized by a Gaussian power spectrum with $\delta = \lambda$ and $a = 2\lambda$. The figure is the average of results for 100 realizations of the surface, when terms through the 6th iterate are retained in the solution for the scattered field. The solid curves give the results for in-plane scattering ($\phi = 0^\circ$), and the dashed curves give the results for out-of-plane scattering ($\phi = 90^\circ$) [Ref. 25].

The results for in-plane ($\phi = 0^\circ$) and out-of-plane ($\phi = 90^\circ$) co-polarized ($p \rightarrow p$) and cross-polarized ($p \rightarrow s$) scattering from the perfectly conducting surface are presented as functions of the polar scattering angle θ in Fig. 6; those for scattering from the silver surface are presented in Fig. 7. In all cases the results display the phenomenon of enhanced backscattering, and there is even the suggestion of subsidiary maxima in some of them. A comparison of the results presented in Figs. 6 and 7 also shows that for the wavelength of light assumed ($\lambda = 457.9\text{nm}$, $\epsilon(\omega) = -7.5 + i0.24$) silver is not well represented by a perfect conductor in surface scattering calculations. The Neumann-Liouville series has a finite radius of convergence. It was found that it stops converging for surfaces with rms slopes of about 1. It should be possible to overcome this restriction by using a more sophisticated iterative method, e.g. the conjugate gradient method.

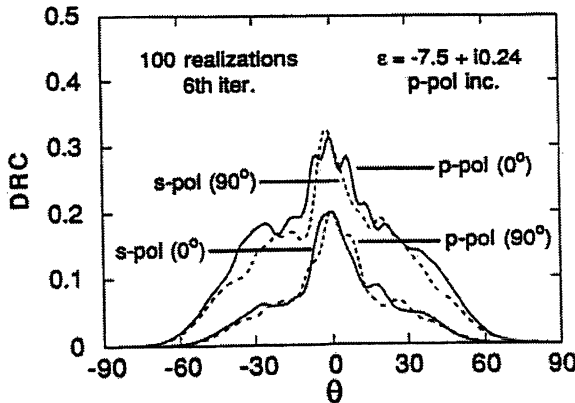


Fig. 7. The contribution to the mean differential reflection coefficient (DRC) from the incoherent component of the co-polarized ($p \rightarrow p$) and cross-polarized ($p \rightarrow s$) scattered light when a beam of p-polarized light of wavelength $\lambda = 0.4579\mu\text{m}$ is incident normally on a two-dimensional, randomly rough, silver surface ($\epsilon(\omega) = -7.5 + i0.24$), characterized by a Gaussian power spectrum with $\delta = \lambda$ and $a = 2\lambda$. The figure is the average of results for 100 realizations of the surface, when terms through the 6th iterate are retained in the solution for the scattered field. The solid curves give the results for in-plane scattering ($\phi = 0^\circ$), and the dashed curves give the results for out-of-plane scattering ($\phi = 90^\circ$) [Ref. 25].

With the feasibility of the calculation of the scattering of light from metallic surfaces established, efforts are now being directed at decreasing the computational time required for them. The system of six coupled integral equations can be reduced to four if the normal components of the vacuum values of the total magnetic and electric fields on the surface are expressed in terms of the surface divergences of the surface electric and magnetic currents. This system of four equations is reduced to a system of two equations if the electromagnetic field inside the metal is eliminated by the use of an impedance boundary condition[27,28]. The use of faster parallel computers will further reduce the computational time required.

3 Satellite peaks

Up to now we have considered the scattering of light from one- and two-dimensional random surfaces that support only a single surface electromagnetic wave. If, instead, we turn our attention to the scattering of light from, or its transmission through, a structure that supports two or more surface or guided waves, new features appear in the angular distribution of the intensity

of the incoherent component of the reflected or transmitted light, not present in the results described so far.

Thus, let us consider a free-standing dielectric or metallic film, characterized by an isotropic, complex, dielectric function $\epsilon(\omega)$ in the region $-d < x_3 < \zeta(x_1)$, with vacuum in the regions $x_3 > \zeta(x_1)$ and $x_3 < -d$ (Fig. 8). We assume that the surface profile function $\zeta(x_1)$ possesses the statistical properties described in Section 2.2. This structure is illuminated from the region $x_3 > \zeta(x_1)$ by a plane wave of p- or s-polarized light, whose plane of incidence is the x_1x_3 -plane. The scattered and transmitted light in this geometry is co-polarized, and the plane of scattering and of transmission is also the x_1x_3 -plane.

We consider the case where this structure supports N guided waves at the frequency ω of the incident light. The wave numbers of these guided waves will be denoted by $q_1(\omega), q_2(\omega), \dots, q_N(\omega)$. Since the illuminated surface of the film is randomly rough, the incident light of p-(s)-polarization can couple into and out of each of these waves of p-(s)-polarization through the breakdown of infinitesimal translational invariance of the structure to which the roughness gives rise. Consider a double-scattering process, in which the incident light excites a given guided wave through the roughness. The wave thus excited propagates through the film, is scattered once more by the roughness, and is converted back into a volume wave in the vacuum, that propagates away from the surface (Fig. 8). We assume that all such double-scattering processes are uncorrelated due to the random nature of

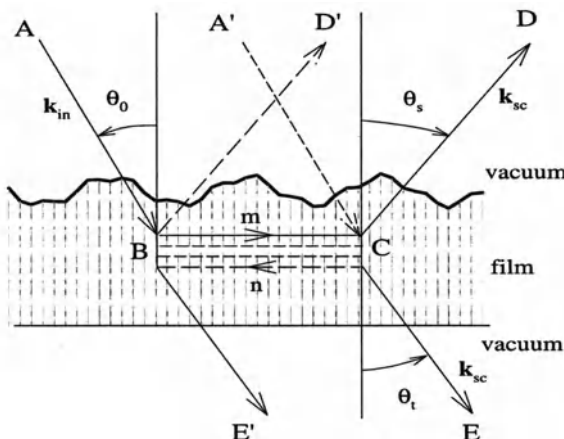


Fig. 8. Double-scattering sequences occurring in the scattering of electromagnetic waves from, and their transmission through, a dielectric or metal film that supports several surface or guided waves, and their reciprocal partners.

the surface. However, to any given sequence there corresponds a reciprocal partner, in which the light and guided waves are scattered from the same points, but in the reverse order. These two sequences interfere constructively when the wave vector of the scattered wave is related to that of the incident wave in special ways. Thus, let us consider a particular double-scattering path ABCD (Fig. 8). To it corresponds a reciprocal partner A'CBD'. Each of these paths is N -fold degenerate in the sense that along the segment BC there are N "channels" with different phase factors. The phase difference between the path $(ABCD)_m$, where the subscript gives the number of the waveguide mode excited by the incident light, and its reciprocal partner $(A'CBD')_n$ is

$$\Delta\phi_{nm} = \mathbf{r}_{BC} \cdot (\mathbf{k}_{in} + \mathbf{k}_{sc}) + |\mathbf{r}_{BC}|[q_n(\omega) - q_m(\omega)], \quad (28)$$

where \mathbf{k}_{in} and \mathbf{k}_{sc} are the wave vectors of the incident and scattered light, respectively, while \mathbf{r}_{BC} is the vector joining the points B and C. We see from Eq. (3.1) that constructive interference ($\Delta\phi_{nm} = 0$) can occur when $n = m$ and $\mathbf{k}_{sc} = -\mathbf{k}_{in}$. The second of these conditions describes scattering into the retroreflection direction. The complex amplitudes of these coherent direct and reciprocal scattering sequences in this case are equal. They must be added, and the modulus of the sum squared, in calculating their contribution to the intensity of the scattered field. For scattering into directions other than the retroreflection direction the two waves have a nonzero phase difference, and very rapidly become incoherent, so that only their intensities add. Consequently, the intensity of scattering into the retroreflection direction is a factor of two larger than it is for scattering into other directions, due to the contribution from the cross-terms in the squared modulus. Of course, the contribution from the single scattering processes has to be subtracted off in obtaining this factor of two enhancement, since it is not subject to coherent backscattering. This increased intensity of scattering into the retroreflection direction is what is called *enhanced backscattering*. This is the only possibility in scattering from a semi-infinite medium bounded by a randomly rough surface, where $q_m(\omega) = q_n(\omega) = q(\omega)$.

However, we see from Eq. (28) that constructive interference can also occur for scattering into other directions $\mathbf{k}_{sc} \neq -\mathbf{k}_{in}$, for some $n \neq m$. The satisfaction of these conditions gives rise to satellite peaks in the angular distribution of the intensity of the incoherent component of the scattered light. Unlike the enhanced backscattering peak, however, the height of a satellite peak has no simple relation to the height of the background at its position, when the contribution of the single scattering processes is subtracted off, because the amplitudes of the two interfering waves are not equal in this case. If we note that the points B and C lie on the scattering surface, so that the vector \mathbf{r}_{BC} is essentially parallel to the mean scattering plane, we find that these satellite peaks occur at scattering angles θ_s related to the angle of incidence θ_0 (Fig. 8) by [29,30]

$$\sin \theta_s = -\sin \theta_0 \pm \frac{c}{\omega}[q_n(\omega) - q_m(\omega)], \quad n \neq m. \quad (29)$$

In transmission we reflect the scattered wave in the mean scattering surface ($\hat{x}_3 \rightarrow -\hat{x}_3$, where \hat{x}_3 is the unit vector normal to the mean scattering surface). The phase difference between the path $(ABCE)_m$ and its reciprocal partner $(A'CBE')_n$ (Fig. 8) is then

$$\Delta\phi_{nm} = \mathbf{r}_{BC} \cdot (\mathbf{k}_{in} + \mathbf{k}_{sc}^*) + |\mathbf{r}_{BC}|(q_n(\omega) - q_m(\omega)), \quad (30)$$

where the vector \mathbf{k}_{sc}^* is defined by $\mathbf{k}_{sc}^* = k_{sc,\parallel}\hat{x}_1 + k_{sc,\perp}(-\hat{x}_3)$, where $k_{sc,\parallel}$ and $k_{sc,\perp}$ are the components of \mathbf{k}_{sc} parallel and perpendicular to the mean scattering surface, respectively. In this case constructive interference ($\Delta\phi_{nm} = 0$) occurs when $n = m$, $\mathbf{k}_{sc}^* = -\mathbf{k}_{in}$. These conditions describe transmission into the antispecular direction, and this gives rise to a peak in the angular distribution of the intensity of the light transmitted incoherently through the film into this direction. This peak is called *enhanced transmission*[31]. However, we see from Eq. (30) that constructive interference can also arise for transmission into other directions $\mathbf{k}_{sc}^* \neq -\mathbf{k}_{in}$ for some $n \neq m$. The satisfaction of these conditions gives rise to satellite peaks in the angular dependence of the incoherent component of the transmitted light. These satellite peaks occur at angles of transmission θ_t related to the angle of incidence θ_0 (Fig. 8) by[32,33]

$$\sin \theta_t = -\sin \theta_0 \pm (c/\omega)(q_n(\omega) - q_m(\omega)) \quad n \neq m. \quad (31)$$

Arguments similar to those made in connection with enhanced backscattering lead to the conclusion that the enhanced transmission peak should be twice as high as the background at its position, when the contribution from the single scattering processes has been subtracted off. No such simple relation exists for the heights of the satellite peaks in transmission.

The maximum number of satellite peaks that can occur, N_s , is just twice the number of combinations of N waves taken in groups of two, namely $N_s = N(N - 1)$. However, it follows from Eqs. (29) and (31) that some of these combinations may not give rise to a satellite peak. This happens when the absolute value of the right-hand side of Eq. (29) or Eq. (31) is larger than unity. Furthermore, among the real satellite peaks that should appear when the absolute value of the right-hand sides of Eqs. (29) and (31) is smaller than unity, not all of them might be intense enough to be observable.

Although the preceding discussion has been based on the double scattering processes depicted in Fig. 8, the conclusions reached, in particular Eqs. (29) and (31) remain valid when all higher-order multiple-scattering processes are taken into account.

We note, however, that the occurrence of satellite peaks in general appears to be limited to the case of the scattering of p- or s-polarized from a one-dimensional random surface of a structure that supports two or more surface or guided waves. In the case of the scattering of light from an isotropic two-dimensional surface of such a structure the ensemble averaging of the scattered intensity restores isotropy in the mean scattering plane, and thereby

eliminates the occurrence of special scattering angles at which satellite peaks could occur[34].

In Fig. 9 we present calculated results for the contribution to the mean

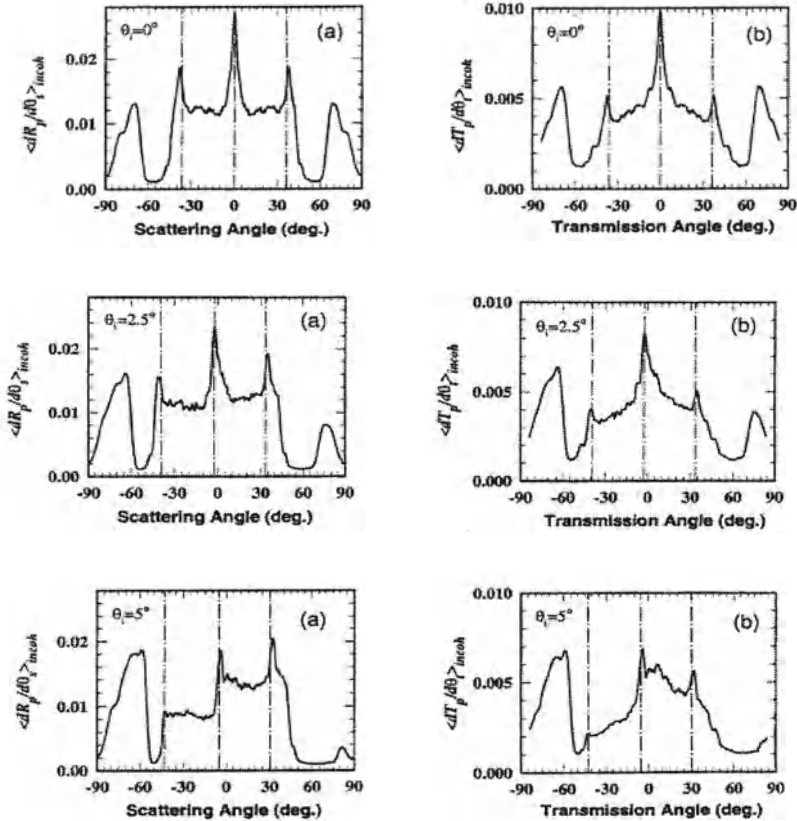


Fig. 9. Computer simulation results for $\langle \partial R_p / \partial \theta_s \rangle_{incoh}$ and $\langle \partial T_p / \partial \theta_t \rangle_{incoh}$ as functions of θ_s and θ_t , respectively, for three angles of incidence, when p-polarized light of wavelength $\lambda = 0.6127\mu\text{m}$ is incident on a silver film ($\epsilon(\omega) = -17.2 + i0.498$) of mean thickness $d = 48\text{nm}$ deposited on the planar surface of a glass substrate ($\epsilon = 2.25$). The illuminated surface of the film is a one-dimensional random surface characterized by the West-O'Donnell power spectrum (6b) with $\delta = 8.8\text{nm}$, $k_{min} = 0.9196(\omega/c)$, and $k_{max} = 1.7406(\omega/c)$. The vertical dash-dot lines give the scattering angles θ_s and transmission angles θ_t at which the enhanced backscattering, enhanced transmission, and satellite peaks are predicted to occur [Jun Q. Lu, private communication].

differential reflection and transmission coefficients from the incoherent components of the scattered and transmitted light, respectively, when p-polarized

light of wavelength $\lambda = 612.7$ nm is incident on a silver film ($\epsilon(\omega) = -17.2 + i0.498$) of mean thickness $d = 48$ nm deposited on the planar surface of a glass substrate ($\epsilon_s = 2.25$). This structure supports two surface plasmon polaritons at the frequency of the incident light, the real parts of whose wavenumbers are $q_1(\omega) = 1.0335(\omega/c)$ and $q_2(\omega) = 1.6266(\omega/c)$. The vacuum-metal interface is a one-dimensional, randomly rough surface characterized by the West-O'Donnell power spectrum (6b) with $k_{min} = 0.9196(\omega/c)$ and $k_{max} = 1.7406(\omega/c)$. Two satellite peaks are expected in reflection and in transmission, in addition to the enhanced backscattering and transmission peaks, and they are clearly visible in the results presented in Fig. 9, where the angular positions at which they are predicted to occur, according to Eqs. (29) and (31), are indicated by vertical dashed lines. The fact that the enhanced transmission peak and the satellite peaks occur at the angles of transmission predicted by Eq. (31) is due to the fact that the glass substrate is assumed to have a finite thickness, so that the transmitted intensity is measured in vacuum.

The enhanced transmission peak has been observed experimentally[35,36]. In Fig. 10,

we present a plot of the bidirectional transmittance of p-polarized light through a silver film on a glass substrate whose dielectric constant is $\epsilon_s = 2.25$. The illuminated surface of the film – the vacuum–silver interface – is a two-dimensional random surface. The plane of transmission coincides with the plane of incidence, and it is the p-polarized component of the transmitted light that is measured. The angle of incidence is $\theta_0 = 20^\circ$. A sharp peak in the bidirectional transmittance is observed at an angle of transmission $\theta_t = 20^\circ$. This is enhanced transmission. The fact that satellite peaks were not observed in this measurement is due to the two-dimensional nature of the surface roughness, which has the effect of washing out the satellite peaks.

The first, and so far only, observation of satellite peaks in the scattering of light from a random surface was carried out for a structure that differs somewhat from the one depicted in Fig. 8[37]. It utilized the double passage of light through a two-dimensional random phase screen placed in front of a mirror, a geometry that is known to give rise to enhanced backscattering [38]. The incident light was in a $+45^\circ$ linear state, i.e. it consisted of a linear superposition of p- and s-polarized components with equal amplitudes. The new feature in the structure employed in Ref. 37 with respect to that of Ref. 38 was the introduction of a piece of birefringent material (calcite), in the form of a beam displacing prism, into the space between the random phase screen and the mirror (Fig. 11). The beam displacing prism was oriented in such a way as to produce a lateral displacement of the p-polarized component of the incident light. This displacement removed the mean rotational symmetry of the random surface that washed out the satellite peaks in the experiment reported in Ref. 34. The birefringence of the calcite prism led to propagation paths that were different for waves polarized along two orthogonal directions,

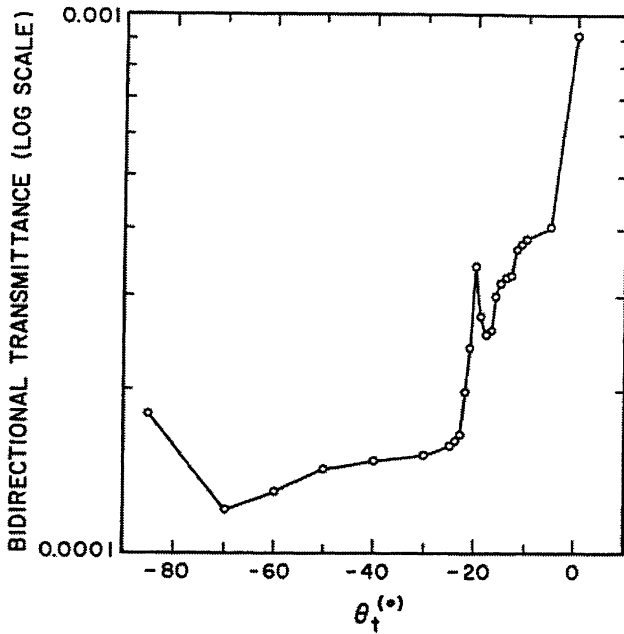


Fig. 10. An experimental result for the bidirectional transmittance of p-polarized light of wavelength $\lambda = 0.6328\mu\text{m}$ through a silver film as a function of the angle of transmission θ_t . The mean thickness of the film is $d = 85\text{nm}$. The angle of incidence is $\theta_0 = 20^\circ$. The illuminated surface of the film is a two-dimensional random surface characterized by a Gaussian power spectrum with $\delta = 11.8\text{nm}$ and $a = 120\text{nm}$. The film is deposited on the planar surface of a glass plate whose index of refraction is $n_d = 1.51$, and whose thickness is 5mm [Ref. 35].

and the inclusion of a linear polarizer between the prism and the mirror mixed these two components of polarization, allowing the interference of waves that had picked up the same random phase (traversing the random phase screen) but that had traveled along different (deterministic) optical paths, when the transmission axis of the polarizer made an angle of 45° with the x-axis.

A theory of the scattering of light from this structure based on the thin random phase screen model[39], in which a delta-correlated random phase screen in contact with a Gaussian aperture was assumed, yields the following expression for the mean scattered intensity in the far field[40]:

$$\begin{aligned} \langle I(q|k) \rangle &= 2 + \exp \left[-\frac{w^2}{4}(k+q)^2 \right] + \exp \left[-\frac{w^2}{4}(k+q \pm p)^2 \right] \\ &\quad + 2 \cos \left(\frac{\omega}{c} \frac{\Delta^2}{4D} \right) \left\{ \exp \left(-\frac{w^2}{4} \frac{p^2}{4} \right) \right. \end{aligned}$$

$$+ \exp \left[-\frac{w^2}{4} (k + q \pm \frac{p}{2})^2 \right] \} . \quad (32)$$

It should be noted that the sign of q in the last three terms of Eq. (32) is opposite to that in the corresponding expression in Ref. 37. This is because we use here the more conventional definitions of the angles of incidence θ_0 and of scattering θ_s , namely those defined by Fig. 8. In Eq. (32) w is the half-width of the Gaussian aperture in the plane of the random phase screen, D is the distance from the random phase screen to the mirror, Δ is the lateral shift of the p-polarized component of the light transmitted through the random phase screen, and $p = (\omega/c)(\Delta/D)$, $k = (\omega/c) \sin \theta_0$, $q = (\omega/c) \sin \theta_s$. The positive sign in the exponentials of the second and third terms applies for the p-polarized component of the scattered light, the negative sign applies for the s-polarized component. In Eq. (32) the first term represents a constant background; the second produces a peak in the retroreflection direction $q = -k$; the third gives rise to satellite peaks at $q = -k \pm p$. The last term produces satellite features at $q = -k \pm (p/2)$ that can be either peaks or dips, depending on the sign of the cosine factor, i.e. on the distance D of the mirror from the random phase screen. No peak in the specular direction is present in the expression for $\langle I(q|k) \rangle$ given by Eq. (32): the “roughness” of the random phase screen was assumed to be sufficiently strong that the coherent component of the scattered light was strongly suppressed, and only the incoherent component contributed to the mean scattered intensity in the far field.

Representative experimental results are shown in Fig. 12 for two different values of D . A situation in which two peaks are obtained on the right of the backscattering peak is shown in Fig. 12(a) for the case of p-polarized detection. The peaks occur on the left of the backscattering peak in the

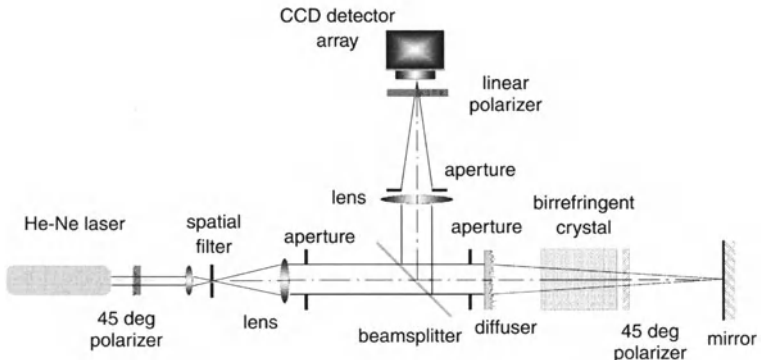


Fig. 11. Schematic diagram of the scattering geometry employed in the observation of satellite peaks through the double passage of light through a random phase screen and a birefringent crystal [Ref. 37].

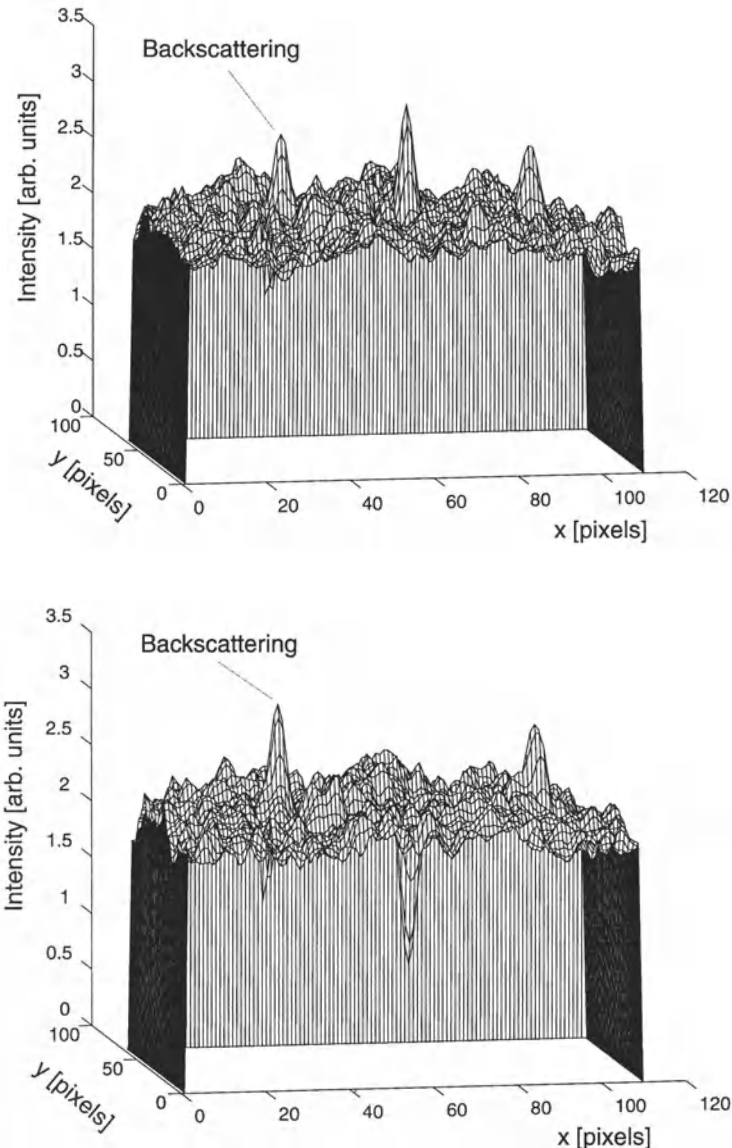


Fig. 12. (a) Experimental results for the p-polarized component of the mean scattered intensity showing two satellite peaks in addition to the enhanced backscattering peak; (b) experimental result for the p-polarized component of the mean scattered intensity showing a satellite peak and a satellite dip, in addition to the enhanced backscattering peak [after Ref. 37].

case of s-polarized detection, and on both sides (four satellite peaks) when no linear analyzer is used in the detection system. The peak closer to the backscattering direction is more intense than the backscattering peak, in agreement with the result given by Eq. (32). When the mirror is moved to another position the middle peak becomes a dip (Fig. 13(b)). In view of the simplicity of the random phase screen model, the agreement between the predicted and observed scattered intensities has to be regarded as quite satisfactory.

4 Surface Enhanced Spectral Shifts of Scattered Light

In a series of papers published about a decade ago, Wolf[41] predicted that the spectrum of the light in the far field emitted by a three-dimensional quasihomogeneous source can be red-shifted or blue-shifted with respect to that of the source, if the degree of spectral coherence of the source is appropriately chosen, even if the light propagates in free space. Because of the close analogy between the processes of radiation and scattering, this prediction stimulated investigations of spectral changes in the light scattered by volume disordered systems[42]. These studies were based on single-scattering approximations, and consequently were applicable only to systems with a low density of scatterers. The first treatment of spectral changes of light scattered by volume disordered media in which multiple-scattering effects were taken into account was given by Lagendijk[43], who pointed out that the enhanced backscattering of light from a strongly scattering random medium, which is due to the coherent interference between multiply-scattered optical paths and their reciprocal partners, can be regarded as being due to the re-emission of light from an extended source in the random medium that possesses just the type of source correlation needed to produce a red shift of the spectrum of the scattered light. However, the magnitudes of the red shifts calculated by Lagendijk for scattering angles close to the backscattering direction were very small, e.g. $\delta\omega/\omega_0 \sim 10^{-5}$, where ω_0 is the central frequency of the incident light, for a linewidth $\Delta\omega/\omega_0 \sim 10^{-2}$. Consequently, these spectral shifts remain unobserved in optical experiments up to the present time. A comprehensive survey of studies of the Wolf shift published prior to 1996 has been provided by Wolf and James[44].

In order to obtain changes in the spectrum of light scattered from a random medium that are large enough to be measured, it is necessary for the angular dependence of the intensity of monochromatic light scattered from the medium to possess features that depend strongly on the frequency of the incident light. The enhanced backscattering peak does not possess this property – it is always in the retroreflection direction. In two recent studies two scattering systems were considered that possess such features[45,46]. The first [45] is a film, either free-standing or supported, that supports two or more guided or surface waves. We have seen in Section 3 that if the illuminated surface of such

a film is a one-dimensional, randomly rough surface, the angular dependence of the intensity of p- or s-polarized light scattered incoherently from it, or transmitted incoherently through it, will display satellite peaks on both sides of the enhanced backscattering and enhanced transmission peaks. The angles of scattering and transmission at which these peaks occur depend on the frequency of the incident light, and this dependence can be quite strong. The second structure considered[46] is a semi-infinite metal with a one-dimensional randomly rough surface that is separated by a sub-wavelength air gap from the planar base of a prism through which the metal surface is illuminated – the Otto attenuated total reflection configuration. The angular intensity of p-polarized light scattered incoherently from this structure displays peaks at scattering angles defined by the wavenumbers of the forward- and backward-propagating surface plasmon polaritons supported by the air-metal interface. These wave numbers, and hence the scattering angles at which these peaks occur, depend strongly on the frequency of the incident light. However, these peaks already occur in the single-scattering approximation, so that the corresponding Wolf shifts are not a multiple-scattering effect, as they are in the case of the film systems described above.

Let us consider, therefore, a film system illuminated from the vacuum side by a p-polarized electromagnetic field, the single nonzero component of whose magnetic vector has the form

$$H_2(x_1, x_3 | t)_{inc} = \int_{-\infty}^{\infty} \frac{d\omega}{2\pi} F(\omega) e^{ikx_1 - i\alpha_0(k, \omega)x_3 - i\omega t}, \quad (33)$$

where $\alpha_0(k, \omega) = [(\omega/c)^2 - k^2]^{\frac{1}{2}}$, with $Re\alpha_0(k, \omega) > 0$, $Im\alpha_0(k, \omega) > 0$. The wave number k is related to the angle of incidence θ_0 by $k = (\omega/c) \sin \theta_0$. The weight function $F(\omega)$ is a random function with the properties $\langle F^*(\omega)F(\omega') \rangle_F = 2\pi\delta(\omega - \omega')S_0(\omega)$, $\langle F(\omega)F(\omega') \rangle_F = 0$, where the angle brackets $\langle \dots \rangle_F$ denote an average over the ensemble of realizations of the field. These relations express our assumption that the field (33) is a zero-mean complex Gaussian random process, which implies that $F(\omega)$ is also a zero-mean complex Gaussian random process. The fluctuation of $|F(\omega)|^2$ as a function of ω , which depends on the integration time of a detector, is below the resolution of a normal spectrograph, so for practical purposes, $F(\omega)$ can be assumed to be delta correlated[47]. The spectral density of the incident field $S_0(\omega)$ will be described by a Gaussian form with central frequency ω_0 and a half-width $\Delta\omega$,

$$S_0(\omega) = \frac{1}{\sqrt{\pi}\Delta\omega} \exp[-(\omega - \omega_0)^2/(\Delta\omega)^2]. \quad (34)$$

The fraction of the total energy incident on the scattering system that is scattered incoherently into the angular interval $(\theta_s, \theta_s + d\theta_s)$ and into the frequency interval $(\omega, \omega + d\omega)$, is then given by[45]

$$\left\langle \left\langle \frac{\partial^2 R}{\partial \omega \partial \theta_s} \right\rangle \right\rangle_{incoh} = S_0(\omega) \left\langle \frac{\partial R_p}{\partial \theta_s} \right\rangle_{incoh}, \quad (35)$$

where the double brackets $\langle\langle \dots \rangle\rangle$ denote an average over both the ensemble of realizations of the surface profile and the ensemble of realizations of the incident field, and $\langle\partial R_p/\partial\theta_s\rangle_{incoh}$ has been defined by Eqs. (9) and (13). Equation (35) defines the function that we will use as the spectral density of light scattered in the direction defined by the scattering angle θ_s .

It should be emphasized that the spectral changes we are considering here involve only a redistribution of spectral weight in the frequency region within which the original spectral density $S_0(\omega)$ is nonzero: no photons are created with frequencies outside this region. This is readily seen if instead of the Gaussian form (34) for $S_0(\omega)$ we take the rectangular form $S_0(\omega) = \theta(\omega_0 + \Delta\omega - \omega) \theta(\omega - \omega_0 + \Delta\omega)/(2\Delta\omega)$, where $\theta(x)$ is the Heaviside unit step function. This spectral density is nonzero only in the frequency range $\omega_0 - \Delta\omega < \omega < \omega_0 + \Delta\omega$. We see from Eq. (35) that the right hand side – the spectral density of the scattered light – is also nonzero only for ω in this range.

Calculations of $\langle\langle \partial^2 R/\partial\omega\partial\theta_s \rangle\rangle_{incoh}$ have been carried out for the case that p-polarized light whose spectral density is described by Eq. (34) is scattered from a ZnS film of mean thickness $d = 475$ nm and dielectric constant $\epsilon_f = 5.6644 + i0.005$, deposited on the planar surface of a perfect conductor. The illuminated surface of the film is a one-dimensional randomly rough surface, characterized by the Gaussian power spectrum (5b) with a transverse correlation length $a = 50$ nm and an rms height $\delta = 10$ nm. The film supports four guided waves that give rise to eight satellite peaks, at $\theta_s = \pm 10.84^\circ, \pm 25.34^\circ, \pm 38.02^\circ, \pm 44.27^\circ$, in the angular dependence of the intensity of the incoherent component of the scattered light, when monochromatic light of wavelength $\lambda_0 = 2\pi c/\omega_0 = 632.8$ nm is incident normally on the film. These satellite peaks give rise to red shifts away from ω_0 of the position of the maximum of the spectrum of the scattered light for scattering angles in their vicinity (Fig. 13)[45]. The magnitude of the relative shift in the position $\omega_m(\theta_s)$ of the maximum of the spectrum of the scattered light as a function of the scattering angle θ_s , $|\omega_m(\theta_s) - \omega_0|/\omega_0$, can reach a value as large as 0.012 for θ_s in the vicinity of the angle at which a satellite peak occurs, when $\Delta\omega/\omega_0 = 0.05$. For narrower bandwidths, corresponding to natural laser sources, the shifts are smaller, e.g. at $\theta_s = 0^\circ$ $(\omega_m - \omega_0)/\omega_0 = -4.4 \times 10^{-4}$ for $\Delta\omega/\omega_0 = 5 \times 10^{-3}$, and the satellite features are narrower. Even so, the Wolf shifts are still about two orders of magnitude larger than those predicted for disordered volume scattering for the same values of $\Delta\omega/\omega_0$.

In the calculations just described the Wolf shifts were calculated from the incoherent components of the scattered light in the far zone, where it is formed by the radiative components of the scattered light. However, in view of the fact that only a source possessing a very special spectral coherence can give rise to radiated light whose spectrum is not shifted from that of the source as it propagates away from the source[48], it was expected that the spectrum of

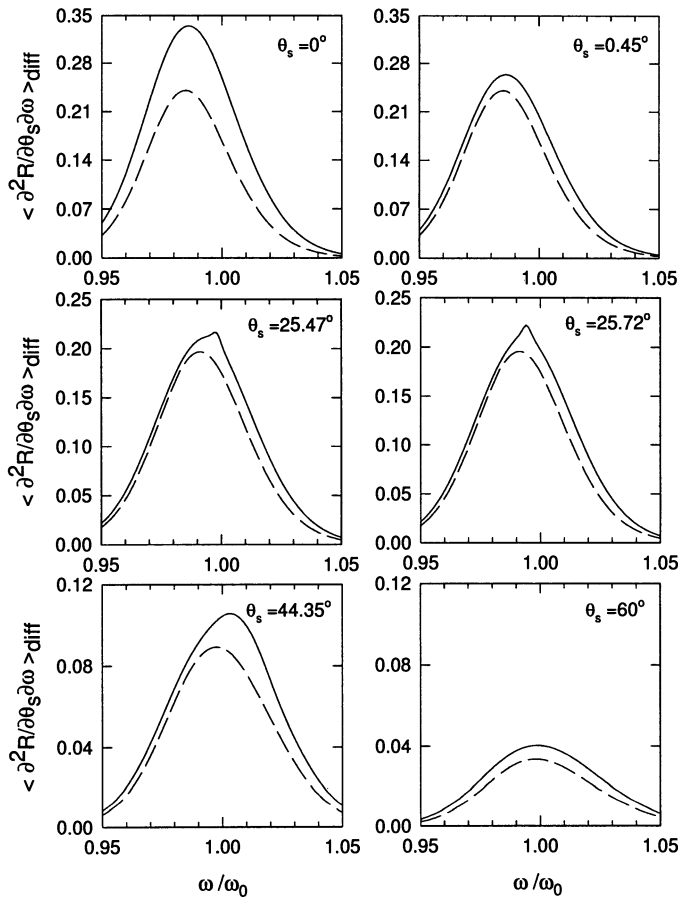


Fig. 13. The spectrum of the incoherent component of p-polarized light scattered from a film of ZnS ($\epsilon = 5.644 + i0.005$) of mean thickness $d = 475\text{nm}$, deposited on the planar surface of a perfect conductor. The angle of incidence is $\theta_0 = 0^\circ$. The central frequency of the incident light is $\omega_0 = 2\pi c/\lambda_0$, with $\lambda_0 = 0.6328\mu\text{m}$, and $\Delta\omega/\omega_0 = 0.05$. The illuminated surface of the film is a one-dimensional random surface characterized by the Gaussian power spectrum (5b) with $\delta = 10\text{nm}$ and $a = 50\text{nm}$. The spectra are plotted for six scattering angles. The contribution through terms of $O(\delta^4)$ is shown as solid curves; the dashed curves show the contribution of $O(\delta^2)$ only [Ref.45].

scattered light measured at any distance from the scattering system should differ from that of the source. In particular, the spectrum of light scattered from a randomly rough surface, measured in the near-field region, i.e. at a sub-wavelength distance from the surface, should be an interesting object of study, because it includes contributions from the evanescent, nonradiative components of the scattered light, which never reach the far field region, as well as from the radiative components, which do.

The evolution of the relative spectral shift on propagation of the scattered light from the near zone to the far zone has been calculated for the case where s-polarized light of central wavelength $\lambda_0 = 2\pi c/\omega_0 = 632.8$ nm was incident normally on a rough BaSO₄ film deposited on the planar surface of a perfect conductor[49]. This structure supports two guided waves which in the far zone give rise to satellite peaks at $\theta_s \cong \pm 25^\circ$, in addition to an enhanced backscattering peak at $\theta_s = 0^\circ$, when monochromatic light of wavelength $\lambda_0 = 632.8$ nm is incident normally on it. It was found that at any distance from the surface the spectrum of the scattered light is red-shifted. At a distance of $0.1\lambda_0$ relative Wolf shifts as large as 0.014 were obtained, and they could be as large as 0.05 in the far zone, for the parameters used in these calculations.

Wolf shifts in the scattering of light from a randomly rough surface have yet to be observed experimentally. Sources with a spectral density given by Eq. (34) with the bandwidth $\Delta\omega/\omega_0 = 0.05$ assumed in the calculations described above can be achieved in the visible range of the optical spectrum by the use of suitably fabricated interference filters. The resulting shifts are large enough to be observable. It is hoped that they soon will be seen.

5 Design of Band-Limited Uniform Diffusers

For many practical applications it is desirable to have optical diffusers whose light scattering properties can be controlled. In particular, a nonabsorbing diffuser that scatters light uniformly within a range of scattering angles, and produces no scattering outside this range, would have applications, for example, to projection systems, where it is important to produce even illumination without wasting light. Such an optical element is called a *band-limited uniform diffuser*. A one-dimensional random surface that acts as a band-limited uniform diffuser can be designed in the following way[50].

We consider a one-dimensional, randomly rough, perfectly conducting surface defined by the equation $x_3 = \zeta(x_1)$, that is illuminated by an s-polarized plane wave of frequency ω . The surface profile function $\zeta(x_1)$ is written in the form

$$\zeta(x_1) = \sum_{\ell=-\infty}^{\infty} c_\ell s(x_1 - \ell 2b), \quad (36)$$

where the $\{c_\ell\}$ are independent, positive, random deviates, b is a characteristic length, and the function $s(x_1)$ is defined by

$$\begin{aligned} s(x_1) &= 0 & x_1 < -(m+1)b \\ &= -(m+1)bh - hx_1 & -(m+1)b < x_1 < -mb \\ &= -bh, & -mb < x_1, mb \\ &= -(m+1)bh + hx_1 & mb < x_1 < (m+1)b \\ &= 0 & (m+1)b < x_1, \end{aligned} \quad (37)$$

where m is a positive integer. Due to the positivity of the coefficient c_ℓ , its probability density function(pdf) $f(\gamma) = \langle \delta(\gamma - c_\ell) \rangle$ is nonzero only for $\gamma > 0$.

It has been shown that for the random surfaces defined by Eqs. (36) and (37) the mean differential reflection coefficient in the geometrical optics limit of the Kirchhoff approximation is given by[50]

$$\begin{aligned} \langle \frac{\partial R}{\partial \theta_s} \rangle &= \frac{1}{2h \cos \theta_0} \frac{[1 + \cos(\theta_0 + \theta_s)]^2}{(\cos \theta_0 + \cos \theta_s)^3} \left[f \left(\frac{\sin \theta_0 - \sin \theta_s}{h(\cos \theta_0 + \cos \theta_s)} \right) \right. \\ &\quad \left. + f \left(\frac{\sin \theta_s - \sin \theta_0}{h(\cos \theta_0 + \cos \theta_s)} \right) \right], \end{aligned} \quad (38)$$

where θ_0 and θ_s are the angles of incidence and scattering, measured counterclockwise and clockwise from the normal to the mean scattering surface, respectively. This result shows that $\langle \partial R / \partial \theta_s \rangle$ is given in terms of the pdf of the coefficient c_ℓ and is independent of the wavelength of the incident light. Equation (38) simplifies greatly in the case of normal incidence ($\theta_0 = 0^\circ$),

$$\left\langle \frac{\partial R}{\partial \theta_s} \right\rangle = \left(1 + \tan^2 \frac{\theta_s}{2} \right) \frac{f(-\frac{1}{h} \tan \frac{\theta_s}{2}) + f(\frac{1}{h} \tan \frac{\theta_s}{2})}{4h}, \quad (39)$$

and we will restrict ourselves to this case in what follows. From Eq. (39) we find that if we wish $\langle \partial R / \partial \theta_s \rangle$ to have the form

$$\left\langle \frac{\partial R}{\partial \theta_s} \right\rangle = \frac{\theta(\theta_m - |\theta_s|)}{2\theta_m}, \quad (40)$$

where $\theta(x)$ is the Heaviside unit step function, we must choose for $f(\gamma)$

$$f(\gamma) = \frac{h}{\tan^{-1} \gamma_m h} \frac{\theta(\gamma)\theta(\gamma_m - \gamma)}{1 + \gamma^2 h^2}, \quad (41)$$

where $\gamma_m = [\tan(\theta_m/2)]/h$. From this form for $f(\gamma)$ a long sequence of $\{c_\ell\}$ can be generated, for example by the rejection method[51], and the surface profile function generated by the use of Eqs. (36) and (37).

The surface profile functions $\zeta(x_1)$ generated in this way are not zero-mean Gaussian random processes, and are not stationary. Indeed, the mean square height of the surface, $\delta^2 = \langle \zeta^2(x_1) \rangle - \langle \zeta(x_1) \rangle^2$, is a periodic function of x_1 with a period $2b$, and for $m = 1$ is given by $\delta^2 = [\langle c^2 \rangle - \langle c \rangle^2]h^2 b^2 [1 + (x_1/b)^2]$

for $-b \leq x_1 \leq b$. The average of this function over a period, $\delta_{av}^2 = [\langle c^2 \rangle - \langle c \rangle^2]4h^2b^2/3$, can be used to estimate the rms height of the surface. Similarly, the mean square slope of the surface is given by $s^2 = \langle (\zeta'(x_1))^2 \rangle - \langle \zeta'(x_1) \rangle^2 = [\langle c^2 \rangle - \langle c \rangle^2]h^2$, from which the rms slope can be determined. The averages $\langle c \rangle$ and $\langle c^2 \rangle$ appearing in these expressions, the first two moments of $f(\gamma)$, are given by

$$\langle c \rangle = \frac{\ell n(1 + \gamma_m^2 h^2)}{2h \tan^{-1} \gamma_m h} \quad (42a)$$

$$\langle c^2 \rangle = \frac{\gamma_m h - \tan^{-1} \gamma_m h}{h^2 \tan^{-1} \gamma_m h}. \quad (42b)$$

The fabrication of one-dimensional surfaces that act as band-limited uniform diffusers has recently been carried out on the basis of the preceding results[50]. An experimental result for the angular dependence of the intensity of s-polarized light of wavelength $\lambda = 632.8$ nm transmitted through a photoresist plate whose illuminated surface has been fabricated on the basis of Eqs. (36) -(37) with $m = 1$ and $b = 6.3\mu\text{m}$ to transmit such light uniformly within the angular range $(-10^\circ, +10^\circ)$ is presented in Fig. 14. The transmission pattern is band-limited, and quite uniform.

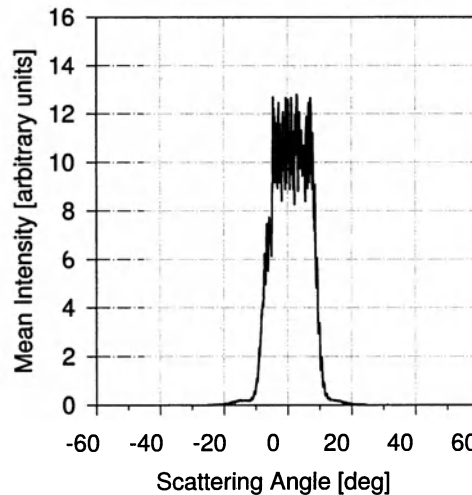


Fig. 14. An experimental result for the angular dependence of s-polarized light transmitted through a photoresist film. The angle of incidence is $\theta_0 = 0^\circ$. The illuminated surface of the film is a one-dimensional random surface that has been designed to transmit light uniformly within the range $-10^\circ < \theta_s < 10^\circ$, and to produce no transmission outside this range.

6 Some Directions for Future Research

To conclude this survey, I would like to indicate some directions that theoretical studies of rough surface scattering could profitably take in the immediate future.

The development of techniques for solving accurately and rapidly the problem of the scattering of electromagnetic waves from two-dimensional randomly rough surfaces would represent a significant advance in this field. These techniques could be purely numerical, and hence formally rigorous, or they could be approximate but accurate and largely analytic in nature, and should be applicable to both metallic and dielectric surfaces.

Much of the work done to date in the area of rough surface scattering has been devoted to the solution of the direct problem, that is, given the statistical properties characterizing a randomly rough surface, to calculate the angular and polarization dependence of the intensity of the scattered field. The inverse problem, namely, given scattering data, to reconstruct the surface profile, or even just such statistical properties as its power spectrum[52], or in some cases, just its rms height, has been less intensively studied until recently and deserves to be more widely pursued.

An interesting recent development that offers the possibility of achieving subwavelength lateral resolution in the determination of the surface profile by exploiting the information contained in the evanescent component of the light scattered from it consists of placing a scatterer, whose dimensions are small compared to the wavelength of the incident light, at distance smaller than the wavelength from the surface, and measuring the intensity of the scattered light in the far field, at fixed angles of incidence and scattering, as the scatterer moves across the surface at a constant height above some reference plane parallel to the mean surface[53–55]. The presence of the scatterer converts the evanescent component of the scattered light into propagating waves whose intensity can be measured in the far field. The chief theoretical problem that has to be solved before this approach can be used for profiling a surface is relating the measured intensity, which includes the effects of the scatterer used in its measurement, to the surface profile being scanned.

A version of the inverse problem that seems to me to deserve more study in the future is the design of random surfaces with specified scattering properties. We have seen one example of how this can be done in Section 5. It would also be desirable to be able to design surfaces with large rms heights, and large rms slopes, that suppress single scattering processes, in order to see multiple-scattering effects such as enhanced backscattering, enhanced transmission, and satellite peaks, more clearly. The design of a random surface that acts as a Lambertian diffuser, namely one that produces a scattered intensity proportional to the cosine of the polar scattering angle, would be useful for calibrating scatterometers, especially in the infrared region of the optical spectrum, where the volume disordered media used as Lambertian diffusers in the visible region are inapplicable[56]. Finally, random surfaces

that suppress leakage, namely the roughness-induced conversion of surface electromagnetic waves into volume electromagnetic waves, would be useful in studies of the Anderson localization of surface electromagnetic waves by random surface roughness[57,59].

Another area that needs to be developed further is that of scattering of electromagnetic waves from the random surface of an inhomogeneous medium. An example of a system to which such a theory would be applicable is a polycrystalline sample of a metal such as beryllium. The optical properties of a beryllium crystallite are anisotropic and the orientations of the crystallites vary randomly across a sample. The earliest efforts to deal with such systems[60,61] used single-scattering approximations in which the effects of the surface roughness and of the dielectric inhomogeneities contributed independently to the intensity of the scattered field. In more recent work[62] a numerical simulation approach was applied to a study of the scattering of light from an inhomogeneous dielectric medium bounded by a one-dimensional random surface. In these calculations multiple scattering was taken into account. The scattering of a scalar wave from a two-dimensional random surface bounding an inhomogeneous dielectric medium was studied by the techniques of many-body perturbation theory, and the use of an impedance boundary condition[63]. However, no results for the mean differential reflection coefficient were presented in this work. A rigorous theory for a two dimensional random surface bounding an inhomogeneous medium that takes into account the vector nature of the scattering problem and can yield numerical results is still lacking.

An important special case of an inhomogeneous medium bounded by a random surface is one in which the dielectric inhomogeneity is due to the presence of a strong reflector, for example, a metal plate or cylinder in an otherwise homogeneous (or even inhomogeneous) substrate. The ability to detect such strong reflectors by ground penetrating radar, especially if one could also characterize their shape and dielectric properties, would have many practical applications.

Acknowledgements. The work of T. A. L. and A. A. M was supported in part by Army Research Office Grant DAAD 19-99-1-0321. A.A.M. would also like to acknowledge support from Army Research Office Grant DAAD19-99-C-0032, which made possible his participation in the International Conference on Laser Physics and Quantum Optics. The work of E. I. C., E. E. G.-G., and E. R. M. was supported in part by CONACYT.

References

1. L. I. Mandel'shtam, Ann. Physik **41**, 609 (1913).
2. S. O. Rice, Commun. Pure Appl. Math. **4**, 351 (1951).
3. P. Beckmann and A. Spizzichino, *The Scattering of Electromagnetic Waves from Rough Surfaces* (Pergamon, Oxford, 1963).
4. A. R. McGurn, A. A. Maradudin, and V. Celli, Phys. Rev. B**31**, 4866 (1985).

5. E. R. Méndez and K. A. O'Donnell, Opt. Commun. **61**, 95 (1987); K. A. O'Donnell and E. R. Méndez, J. Opt. Soc. Am. **A4**, 1194 (1987).
6. C. S. West and K. A. O'Donnell, J. Opt. Soc. Am. **A12**, 390 (1995).
7. F. Toigo, A. Marvin, V. Celli, and N. R. Hill, Phys. Rev. B**15**, 5618 (1977).
8. A. A. Maradudin and E. R. Méndez, Appl. Opt. **32**, 3335 (1993).
9. G. C. Brown, V. Celli, M. Coopersmith, and M. Haller, Surf. Sci. **129**, 507 (1983).
10. A. A. Maradudin, A. R. McGurn, and E. R. Méndez, J. Opt. Soc. Am. **A12**, 2500 (1995).
11. M. Nieto-Vesperinas and J. M. Soto-Crespo, Opt. Lett. **12**, 979 (1987).
12. A. A. Maradudin, E. R. Méndez, and T. Michel, Opt. Lett. **14**, 151 (1989).
13. A. A. Maradudin, T. Michel, A. R. McGurn, and E. R. Méndez, Ann. Phys. (N.Y.) **203**, 255 (1990).
14. See, for example, A. E. Danese, *Advanced Calculus, Volume I* (Allyn and Bacon, Boston, 1965), p. 123.
15. A. A. Maradudin, E. R. Méndez, and T. Michel, in *Scattering in Volumes and Surfaces*, eds. M. Nieto-Vesperinas and J. C. Dainty (North-Holland, Amsterdam, 1990), p. 157.
16. M. E. Knotts, T. R. Michel, and K. A. O'Donnell, J. Opt. Soc. Am. **A10**, 928 (1993).
17. A. R. McGurn and A. A. Maradudin, Waves in Random Media **6**, 251 (1996).
18. A. R. McGurn and A. A. Maradudin, J. Opt. Soc. Am. B**4**, 910 (1987).
19. R. M. Fitzgerald and A. A. Maradudin, Waves in Random Media **4**, 275 (1994).
20. R. M. Fitzgerald, A. A. Maradudin, and F. Pincemin, Waves in Random Media **5**, 381 (1995).
21. P. Tran and A. A. Maradudin, Phys. Rev. B**45**, 3936 (1992).
22. C. Macaskill and B. J. Kachoyan, Appl. Opt. **32**, 2839 (1993).
23. P. Tran and A. A. Maradudin, Appl. Opt. **32**, 2848 (1993).
24. P. Tran, V. Celli, and A. A. Maradudin, J. Opt. Soc. Am. **A11**, 1686 (1994).
25. P. Tran and A. A. Maradudin, Opt. Commun. **110**, 269 (1994).
26. J. A. Kong, *Electromagnetic Wave Theory*, Second Edition (John Wiley and Sons, New York, 1990).
27. T. T. Ong, V. Celli, and A. A. Maradudin, Opt. Commun. **95**, 1 (1993).
28. A. A. Maradudin, Opt. Commun. **116**, 452 (1995).
29. V. Freilikher, M. Pustilnik, and I. Yurkevich, Phys. Lett. A **193**, 467 (1994).
30. J. A. Sánchez-Gil, A. A. Maradudin, Jun Q. Lu, V. D. Freilikher, M. Pustilnik, and I. Yurkevich, Phys. Rev. B**50**, 15353 (1994).
31. A. R. McGurn and A. A. Maradudin, Opt. Commun. **72**, 279 (1989).
32. V. Freilikher, M. Pustilnik, I. Yurkevich, and A. A. Maradudin, Opt. Commun. **110**, 263 (1994).
33. J. A. Sánchez-Gil, A. A. Maradudin, Jun Q. Lu, and V. D. Freilikher, Phys. Rev. B**51**, 17100 (1995).
34. T. Kawanishi, H. Ogura, and Z. L. Wang, Waves in Random Media **7**, 35 (1997).
35. V. Celli, P. Tran, A. A. Maradudin, Jun Lu, T. Michel, and Zu-Han Gu, in *Laser Optics of Condensed Matter, Vol. 2*, eds. E. Garmire, A. A. Maradudin, and K. K. Rebane (Plenum, New York, 1991), p. 315.
36. P. den Outer, Ph. D. Dissertation, University of Amsterdam (1995), Chap 4.
37. E. R. Méndez, E. I. Chaikina, and H. M. Escamilla, Opt. Lett. **24**, 705 (1999).
38. Yu. A. Kravtsov and A. I. Saichev, Sov. Phys. Usp. **25**, 494 (1982); E. Jakeman, J. Opt. Soc. Am. A**5**, 1638 (1988).

39. H. M. Escamilla, E. R. Méndez, and D. F. Hotz, *Appl. Opt.* **32**, 2734 (1993).
40. H. M. Escamilla, E. R. Méndez, and E. I. Chaikina (unpublished work).
41. E. Wolf, *Nature* **326**, 363 (1987); *Phys. Rev. Lett.* **58**, 2646 (1987); *Opt. Commun.* **62**, 12 (1987).
42. E. Wolf, J. T. Foley, and F. Gori, *J. Opt. Soc. Am. A* **6**, 1142 (1989); J. T. Foley and E. Wolf, *Phys. Rev. A* **40**, 588 (1989); E. Wolf, *Phys. Rev. Lett.* **63**, 2220 (1989); D. F. V. James and E. Wolf, *Phys. Lett. A* **146**, 167 (1990).
43. A. Lagendijk, *Phys. Lett. A* **147**, 389 (1990); *Phys. Rev. Lett.* **65**, 2082 (1990).
44. E. Wolf and D. F. V. James, *Rep. Progr. Phys.* **59**, 771 (1996).
45. T. A. Leskova, A. A. Maradudin, A. V. Shchegrov, and E. R. Méndez, *Phys. Rev. Lett.* **79**, 1010 (1997).
46. T. A. Leskova, A. A. Maradudin, A. V. Shchegrov, and E. R. Méndez, *SPIE* **3426**, 81 (1998).
47. J. M. Stone, *Radiation and Optics* (Mc-Graw Hill, New York, 1963), Sec. 12-6.
48. E. Wolf, *Phys. Rev. Lett.* **56**, 1370 (1986).
49. A. V. Shchegrov and A. A. Maradudin, *Phys. Rev. B* **59**, 7732 (1999).
50. E. R. Méndez, G. Martinez-Niconoff, A. A. Maradudin, and T. A. Leskova, *SPIE* **3426**, 2 (1998).
51. W. H. Press, S. A. Teukotsky, W. T. Vetterling, and B. P. Flannery, *Numerical Recipes in Fortran*, 2nd ed. (Cambridge University Press, New York, 1992), pp. 281 and 282.
52. V. Malyshkin, S. Simeonov, A. R. McGurn, and A. A. Maradudin, *Opt.Lett.* **22**, 58 (1997).
53. F. M. P. O'Boyle and H. K. Wickramasinghe, *Appl. Phys. Lett.* **65**, 1623 (1994).
54. F. Zenhausern, Y. Martin, and H. K. Wickramasinghe, *Science* **269**, 1083 (1995).
55. S. A. Zavala, P. Negrete-Regagnon, and E. R. Méndez, *SPIE* **3426**, 76 (1998), and references therein.
56. H. P. Baltes, in *Inverse Scattering Problems in Optics*, ed. H. P. Baltes (Springer-Verlag, New York, 1980), p. 1.
57. D. Sornette, L. Macon, and J. Coste, *J. Phys. (France)* **49**, 1683 (1988).
58. J.-P. Desideri, L. Macon, and D. Sornette, *Phys. Rev. Lett.* **63**, 390 (1989).
59. J. A. Sanchez-Gil and A. A. Maradudin, *Phys. Rev. B* **56**, 1103 (1997).
60. See, for example, J. Merle Elson, Jean M. Bennett, and John C. Stover, *Appl. Opt.* **32**, 3362 (1993).
61. J. M. Elson, *Phys. Rev. B* **30**, 5460 (1984); *Waves in Random Media* **7**, 303 (1997).
62. K. Pak, L. Tsang, and C. H. Chan, *Radio Science* **28**, 331 (1993).
63. S. Mudaliar and J. K. Lee, *J. Electromagnetic Waves and Applications* **9**, 925 (1995).

Stimulated Raman Scattering of Solid Hydrogen in the Strong-Coupling Regime

K. Hakuta, M. Katsuragawa, J.Z. Li, J. Q. Liang, M. Suzuki

Department of Applied Physics and Chemistry, and Institute for Laser Science
The University of Electro-Communications, Chofu, Tokyo 182-8585, Japan
CREST, Japan Science and Technology Corporation (JST), Chofu, Tokyo
182-8585; Japan
e-mail: hakuta@pc.uec.ac.jp

Abstract. Stimulated Raman scattering (SRS) processes are investigated in solid hydrogen in the strong-coupling regime. We show that multi-order SRS processes in solid hydrogen are governed by the anti-phased state coherence, and that the coherence reveals an extremely slow dephasing which may give a concrete basis on the strongly-coupled nonlinear optics using solid hydrogen.

1 Introduction

Recently, there has been increasing interests on the nonlinear optics using electromagnetically-induced transparency (EIT) [1,2], which was first proposed by Harris et al. [3] and was first demonstrated using atomic hydrogen by Hakuta et al. [4]. Essence of the EIT nonlinear optics is to create a strongly-coupled Raman coherence for a three-level system. Although the idea of EIT has started from resonant three-level system, the idea has now been extended to far off-resonant Raman systems. Harris showed theoretically for a far off-resonant Raman three level system that the strong coupling field can control the refractive index and reduce it to unity using the anti-phased state (dark state) coherence [5,6]. Hakuta et al. demonstrated experimentally the strongly-coupled stimulated Raman scattering (SRS) in solid para-hydrogen [7,8]. In order to further explore the EIT physics for the far-off resonant system, the essential issue should be to asses the role of the anti-phased state coherence, and the purpose of the present work is on this point. We investigate experimentally the SRS process in solid hydrogen using two single-frequency pulsed lasers for the coaxial pumping regime. We discuss also on the extremely slow coherence decay behavior for the Raman transition which may give a concrete basis on the strongly-coupled nonlinear optics using solid hydrogen.

2 SRS Process in Solid Hydrogen

Figure 1 illustrates the interaction scheme for the SRS process in solid hydrogen. Solid hydrogen is a molecular crystal consisting of H₂ molecules. Its

remarkable feature is that the molecules consisting of the solid have well-defined vibrational and rotational quantum states as free molecules in the gas phase. One can find the physics of solid hydrogen in the book *Solid Hydrogen* by Van Kranendonk [9]. The SRS process occurs for a pure vibrational transition of $v = 1 - 0$, $J = 0 - 0$ for the ground electronic state $X^1\Sigma_g^+$. The vibrational energy separation is 4149.7 cm^{-1} . The intermediate states for the Raman process locate more than $90,000 \text{ cm}^{-1}$ above the ground state. In solid hydrogen, the $v = 1$ vibrational excited state is well described as a Frenkel exciton described by a Bloch wave, which is termed as vibron. On the other hand, the ground vibrational state is described as a single state without any degeneracy, which is effectively understood as a Bloch-wave of $\mathbf{k} = 0$. This single state nature of the ground state enables the optical transitions from the ground level to pick up selectively the excited levels described by $\mathbf{k} = 0$ Bloch waves, leading the vibration-rotational spectrum to very narrow spectral widths. The Raman width is known to show a very narrow width of less than 14 MHz FWHM [10].

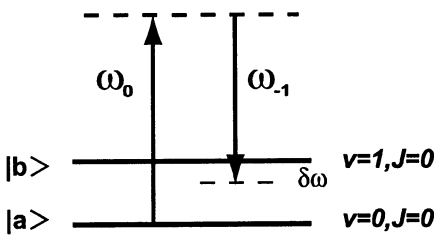


Fig. 1. Energy diagram for the SRS process in solid hydrogen. States $|a\rangle$ and $|b\rangle$ correspond to vibrational-rotational states designated by $v = 0, J = 0$ and $v = 1, J = 0$, in the ground electronic state $X^1\Sigma_g^+$, respectively. Raman resonant two pump laser frequencies are designated as ω_0 and ω_{-1} , respectively. Raman detuning is denoted by $\delta\omega$.

This narrow Raman width can provide an opportunity to realize the strong-coupling condition between fields and medium for the far off resonant Raman system. The strong-coupling may be realized when the two photon-Rabi frequency for the Raman transition has exceeded the dephasing rate (Raman width) for the Raman transition:

$$\frac{\Omega_0 \Omega_{-1}}{2\Delta} > \gamma$$

where γ and Δ are the width of the Raman transition and the effective detuning to the intermediate state, respectively. Assuming the detuning $70,000 \text{ cm}^{-1}$ and the same intensity for the pump and Stokes radiations, it is expected that the strong-coupling can be established with a Stokes Rabi frequency of 6 cm^{-1} which can be obtained for H_2 molecule with reasonably low field intensity of 7 MW/cm^2 . It should be noted that the eigen-state in the strongly coupled system is described by phased or anti-phased linear combination of states $|a\rangle$ and $|b\rangle$. The phased/anti-phased eigenstate is adia-

batically evolved from the ground state by choosing the Raman detuning to positive/negative value.

3 Preparation of Solid Hydrogen

Solid hydrogen crystal (para-hydrogen) was prepared in a cell using the liquid-phase growing method [11]. The cell was attached with two sapphire windows for optical experiments. The parahydrogen was obtained in liquid phase by converting normal hydrogen using catalyst; the purity of parahydrogen was estimated to be greater than 99.9 %. The crystal was grown at a temperature of 15 K under a pressure of 30 atm. After the completion of crystal growth, the temperature of the cell was slowly lowered to 4.2 K and a completely transparent para-hydrogen crystal was prepared without any visible cracks at 4.2 K. The optical interaction length (thickness of the crystal) was determined by the separation of the two windows and was controllable from 20 μm to 1 cm.

4 Evolution of Anti-Phased State Coherence

The experiments were carried out by using two single-longitudinal mode (SLM) pulsed lasers; one was frequency-tripled Nd:YAG laser at 355 nm (ω_0) and the other was frequency-doubled Ti:Sapphire laser at 416 nm (ω_{-1}). The pulse durations were 8 and 16 ns FWHM for the 355 nm and the 416 nm laser outputs, respectively. Both of the laser beams were overlapped temporally and spatially and were focused into solid hydrogen. Maximum incident energy of each of the laser beams was limited to 500 $\mu\text{J}/\text{pulse}$ by the damage of the crystal. The intensities in the crystal were estimated to be 260 MW/cm² and 130 MW/cm² for 355 and 416 nm laser fields, respectively. In order to prepare the large coherence the photon number in a laser pulse must reach to an appreciable amount of the ground state molecules. This requirement poses a condition on setting the interaction length (crystal thickness). We set the interaction length at 60 μm considering both the available maximum photon number (1×10^{15} photons/pulse) and the density of molecules in the solid ($2.64 \times 10^{22} \text{ cm}^{-3}$). The maximum available coherence was estimated to be $|\rho_{ab}| \sim 0.15$.

The SRS characteristics were measured by scanning the Ti:sapphire laser frequency around the Raman resonance. In order to monitor the Raman resonance, we simultaneously measured the SRS tuning characteristics in a weak pump limit for each measurement using by passing a fraction of the pump beams to a different portion of the solid hydrogen from the strongly pumped region. The Raman resonance was detected through the observation of the 2nd Stokes component at 502 nm using a photomultiplier through a monochromator.

Figure 2 displays a typical SRS emission spectrum under maximum pumping conditions, taken by dispersing with a Pellin-Broca prism. Multi-order SRS generation is clearly observed from 2nd anti-Stokes (274 nm) to third Stokes (635 nm) component. Other than the photographed ones, 3rd anti-Stokes (246 nm) and 4th Stokes (862 nm) components were also observed. All SRS components were observed coaxially to the pump beam axis. We did not observe any ring structure which has been believed to be an essential nature due to the phase-matching requirement in parametric SRS processes. The observation means that the present parametric SRS processes based on the prepared Raman coherence in solid hydrogen does not have any serious restriction from the conventional requirement for phase-matching due to the dispersion. This is the unique signature that the observed SRS process should be based on the large coherence, for which multi-order SRS generation occurs within one coherence length [12,13,6].

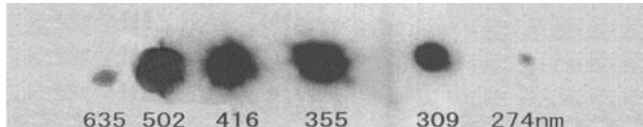


Fig. 2. SRS spectrum under maximum pumping conditions, taken by dispersing a prism. All SRS components are observed coaxially to the two pump beams.

Figures 3(b)-(e) show the tuning characteristics of the 1st anti-Stokes component (309 nm) for the Raman detuning under various pumping conditions. The pump intensities indicated in the figure are for the 355 nm laser pulses and the intensities for the 416 nm pulses are half of the indicated values. Each of the tuning profiles is normalized to its peak value. In Fig. 3(a) is exhibited the tuning curve in the weak pumping limit that is used for the Raman resonance marker is displayed. It should be noted that the spectral width of the resonance marker is 100 MHz FWHM, which corresponds to the instrumental width limited by the Fourier widths for the pump lasers. The traces in Fig. 3 clearly show that the tuning curves become broader and asymmetric to the Raman resonance with the increase of the pump intensities. For the pump intensity of 90 MW/cm², the 1st anti-Stokes radiation is generated over 300 MHz bandwidth with nearly a symmetric profile around a peak near to the resonance. When the pump intensity is increased, the tuning profile became broader and asymmetric, and the peak moves toward the negative detuning-side. For the pump intensity of 260 MW/cm², most of the generation occurs on the negative side with a peak around -0.5 GHz. Tuning behaviors for other SRS components are displayed in Fig. 4 for the pump intensity of 260 MW/cm². The tuning curves appear on the negative side as for the 1st anti-Stokes component, but the tuning width tends to

become narrow for higher order SRS components. These observations reveal that the multi-order SRS in solid hydrogen is based on the *anti-phased state coherence that is evolved from the ground state with the negative two-photon detuning*, or in other words the observations mean that the SRS using solid hydrogen is governed by essentially the same physics as the EIT nonlinear optics demonstrated in gas phase atomic systems [12,13].

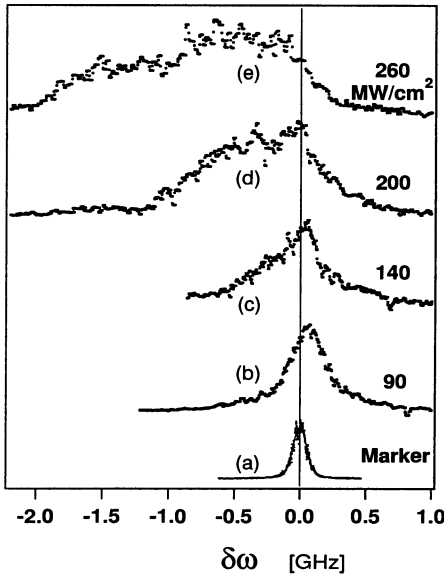


Fig. 3. Tuning characteristics for the SRS process for various pump intensities. Optimum detuning shifts to negative side with the increase of the pump intensities.

5 Coherence Decay for the Raman transition

Next, we describe the direct measurement of the coherence decay for the Raman transition in temporal domain using the time-resolved coherent anti-Stokes stimulated Raman scattering (CARS) method. Three SLM pulsed lasers were used for pumping and probing the coherence, and were introduced to a crystal on the same axis. Here we used a crystal of 1 cm thickness. The Raman coherence was prepared with a frequency-doubled YAG laser at 532 nm (ω_0) and an OPO laser at 683 nm (ω_{-1}). Another laser beam generated with a dye laser at 522 nm was used as a probe beam with various delay times up to 2.5 μ s. Typical intensities at the interaction region were 100-130 MW/cm² and 20 MW/cm² for the pump beams and probe beam, respectively. The probe intensities were kept low enough not to exceed the SRS threshold. The CARS signals were measured using a biplanar phototube through a monochromator.

Figures 4 displays the decay characteristics of the CARS intensities plotted for the delay time with a logarithmic vertical scale. It is clearly seen that the coherence is maintained in a time scale of the order of 100 ns, and that the decay behavior does not show simple exponential decay. Such non-exponential decay behaviors have been reported for molecular crystals [14,15] when the vibrons are excited coherently at the band edge of $k \approx 0$, and the behaviors are understood as those expressed by the curve of $\exp(-\sqrt{t/\tau})$. We fitted the observed decay characteristics with the curve. The fitted curve is displayed in the figure with a solid line showing good agreement with the measured plot. We estimated the Raman width from the observed curve to be 250 kHz HWHM assuming the homogeneous broadening. We should note that this value is very narrow compared to the previously reported value of 7 MHz HWHM measured by the cw Raman gain method [10] in which the resolution was limited by the laser frequency fluctuations. The present direct dephasing measurements reveal that the Raman width in solid hydrogen may exhibit an extremely narrow width of 250 kHz HWHM, giving a concrete basis to the EIT nonlinear optics in far-off resonance scheme using solid hydrogen. But, in order to get further understandings for the Raman dephasing it would be essential to measure the Raman width with the resolution higher than 100 kHz and to compare with the present results.

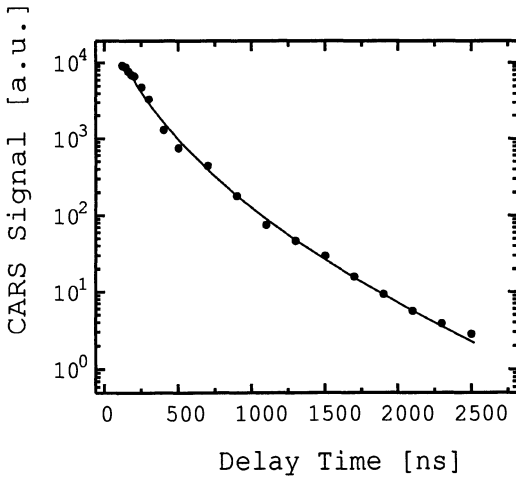


Fig. 4. CARS intensities versus probe delay time up to 2.5 μ s. The plot leads to an effective Raman width of 250 kHz HWHM.

6 Concluding Remarks

We have described the SRS process using solid hydrogen in the strong-coupling regime. We have demonstrated how the anti-phased state coherence

palyss a key role in the multi-order SRS process in solid hydrogen. We have shown through the dephasing measurement using CARS why the solid hydrogen works ideally for the strong coupling regime. The present results reveal that parametric processes using the strongly-coupled Raman coherence in solid hydrogen can become free from the restriction of the phase-matching requirements. Assuming this nature and another inherent nature of solid hydrogen; transparency up to VUV region, one can imagine a fascinating idea of very broad band and super-high-frequency local oscillator which can freely beat with any kind of radiation and can efficiently generate sidebands with the modulation frequency at 124 THz (4149.7 cm^{-1}). The experimental demonstration of such local oscillator has recently been carried out successfully in our group and the results will be published elsewhere.

References

1. S. E. Harris: Physics Today **50**, 36 (1997).
2. M. O. Scully, C. J. Bednar, Y. Rostovtsev, S.-Y. Zhu: Phil. Trans. R. Soc. Lond. A **355**, 2305 (1997).
3. S. E. Harris, J. Field, A. Imamoğlu: Phys. Rev. Lett. **64**, 1107 (1990).
4. K. Hakuta, L. Marmet, B. P. Stoicheff: Phys. Rev. Lett. **66**, 596 (1991).
5. S. E. Harris: Opt. Lett. **19**, 2018 (1994).
6. S. E. Harris, A. V. Sokolov: Phys. Rev. Lett. **81**, 2894 (1998).
7. K. Hakuta, M. Suzuki, M. Katsuragawa, J. Z. Li, Phys. Rev. Lett. **79**, 209 (1997)
8. K. Hakuta, M. Katsuragawa, M. Suzuki, Phil. Trans. R. Soc. Lond. A **355**, 2405 (1997).
9. J. Van Kranendonk: *Solid Hydrogen* (Plenum, New York 1983)
10. T. Momose, D. P. Weliky, T. Oka: J. Mol. Spectrosc. **153**, 760 (1992).
11. M. Suzuki, M. Katsuragawa, R. S. D. Sihombing, J. Z. Li, K. Hakuta: J. Low Temp. Phys. **111**, 463 (1998).
12. M. Jain, H. Xia, G. Y. Yin, A. J. Merriam, S. E. Harris: Phys. Rev. Lett. **77**, 4326 (1996)
13. S. E. Harris, G. Y. Yin, M. Jain, H. Xia, A. J. Merriam: Phil. Trans. R. Soc. Lond. A **355**, 2291 (1997).
14. I. I. Abram, R. M. Hochstrasser, J. E. Kohl, M. Semack, D. White: Chem. Phys. Lett. **71**, 405 (1980)
15. I. I. Abram, R. M. Hochstrasser: J. Chem. Phys. **72**, 3617 (1980).

Femtosecond Soliton Propagation in an Optical Fiber

Sien Chi and Chi-Feng Chen

Institute of Electro-Optical Engineering, National Chiao Tung University,
Hsinchu, Taiwan 30050, Republic of China

Abstract. An accurate wave equation beyond the slowly varying envelope approximation for femtosecond soliton propagation in an optical fiber is derived by the iterative method. The derived equation contains higher nonlinear terms than the generalized nonlinear Schrödinger equation obtained previously. For a silica-based fiber, we have shown that the higher nonlinear terms in the derived equation are negligible for optical pulses in the single cycle regime. The propagations of a 5 fs fundamental soliton and 10 fs and 50 fs second-order solitons in an optical fiber are numerically simulated. We have found that when a 5 fs fundamental soliton propagates in a fiber, it becomes asymmetric with an oscillatory structure near its trailing edge and the main pulse broadens. We have also found that, for the 10 fs second-order soliton, the soliton decay is dominated by the third-order dispersion, and for the 50 fs second-order soliton, the soliton decay is dominated by the delayed Raman response.

1 Introduction

Ultrashort optical pulses containing only a few optical cycles and with pulse-width less than 10 fs have been generated [1]. The propagation of an ultrashort pulse in a fiber is usually described by the generalized nonlinear Schrödinger equation based on the slowly varying envelope approximation (SVEA) [2]. The validity of this equation becomes questionable when the pulse contains only a few optical cycles. To resolve this problem, several approaches which do not make the SVEA have been employed [3-7]. The full-vector nonlinear Maxwell equations have been solved by direct integration [3, 4], but this is very time consuming. By using an operator method and assuming that the nonlinearity is small [5, 6] or by representing the electric field as the superposition of monochromatic waves [7], modified wave equations can be derived. In addition, an iterative method has been used to derive a wave equation for ultrashort pulses [8].

On the other hand, the effects of third-order dispersion, delayed Raman response, and self-steepening terms on the propagations of second-order solitons in a single-mode fiber will lead to the soliton decay [9-16]. When the third-order dispersion parameter exceeds a threshold value, the third-order dispersion leads to the decay of a higher-order soliton[10-12]. The delayed Raman response leads to breakup of a higher-order soliton into its constituents,

of which the main peak shifts toward the trailing side[13-15]. The shift is due to a decrease in the group velocity occurring as a result of the red shift of soliton spectral peak. Even relatively small delayed Raman response effect still leads to the decay of a higher-order soliton. The self-steepening effect breaks the degeneracy of a higher-order soliton and causes the propagating speed of the soliton being different [15, 16].

In this paper, we will derive a wave equation using the electric field expansion of [7], the iterative method of [8] and the order of magnitude considerations of [17]. Through the first iteration, we obtain a wave equation which has four more higher-order nonlinear terms than the equation obtained previously [5-8]. For a silica-based fiber, we will show that these higher order nonlinear terms are negligible for optical pulses in the single cycle regime. We numerically simulate a 5 fs fundamental soliton and 10 fs and 50 fs second-order solitons propagating in an optical fiber. We show that the higher nonlinear terms in the equation are negligible in these cases. We will find that, for the 10 fs second-order soliton, the soliton decay is dominated by the third dispersion and the delayed Raman response has the least effect, and for the 50 fs second-order soliton, the soliton decay is dominated by the delayed Raman response. In addition, we find that the approximation which assumes the Raman gain is a linear function of frequency shift is no longer suitable for the propagation of a 50 fs second-order soliton. The method overestimates the soliton decay. Therefore, it is necessary to use the exact delayed Raman response form when the propagation of a 50 fs second-order soliton is considered.

2 Derivation of the Wave Equation

We will derive the wave equation for a femtosecond pulse propagating in a single-mode fiber with a third-order nonlinearity. The electric field $E(x, y, z, t)$ which propagates in the fiber along the z-direction can be expressed by

$$E(x, y, z, t) = F(x, y) \cdot \phi(z, t), \quad (1)$$

where $F(x, y)$ is the normalized linear eigenfunction of the mode excited in the fiber and $\phi(z, t)$ can be further represented as a superposition of monochromatic waves,

$$\phi(z, t) = \frac{1}{2\pi} \int \varphi(z, \omega) \exp i[\beta(\omega)z - \omega t] d\omega, \quad (2)$$

where $\beta(\omega) = n(\omega)\omega/c$ is the mode propagation constant at frequency ω , c is the velocity of light in vacuum, and $n(\omega)$ is effective refractive index. It is customary to express $\phi(z, t)$ by

$$\phi(z, t) = A(z, t) \exp[i(\beta_0 z - \omega_0 t)], \quad (3)$$

where $A(z, t)$ is the field envelope, ω_0 is the angular frequency of the carrier wave, and $\beta_0 = \beta(\omega_0)$.

From the Maxwell equations, we obtain the wave equation

$$\nabla^2 E - \frac{1}{c^2} \frac{\partial^2 E}{\partial t^2} = -\mu_0 \frac{\partial^2 P_L}{\partial t^2} - \mu_0 \frac{\partial^2 P_{NL}}{\partial t^2}, \quad (4)$$

where μ_0 is the permeability in vacuum, and the linear part P_L and the nonlinear part P_{NL} of the induced polarization are related to electric field $E(x, y, z, t)$ through the following equations:

$$P_L(x, y, z, t) = \epsilon_0 \int_{-\infty}^{\infty} \chi^{(1)}(t - t') E(x, y, z, t') dt', \quad (5)$$

$$P_{NL}(x, y, z, t) = \epsilon_0 \int_{-\infty}^{\infty} \int_{-\infty}^{\infty} \int_{-\infty}^{\infty} \chi^{(3)}(t - t_1, t - t_2, t - t_3) \\ E(x, y, z, t_1) E(x, y, z, t_2) E^*(x, y, z, t_3) dt_1 dt_2 dt_3, \quad (6)$$

where ϵ_0 is the vacuum permittivity, $\chi^{(1)}(t - t')$ is the linear susceptibility response function, and $\chi^{(3)}(t - t_1, t - t_2, t - t_3)$ is the third-order nonlinear susceptibility response function.

Substituting Eqs. (1), (2), (5), and (6) into Eq. (4), we have

$$\frac{\partial \varphi(z, \omega)}{\partial z} = \frac{i\kappa\omega^2}{2c^2\beta(\omega)} \int d\omega' d\omega'' \varphi(z, \omega') \varphi(z, \omega'') \varphi^*(z, \omega' + \omega'' - \omega) \\ \cdot \chi^{(3)}(\omega - \omega') \cdot \exp(i\Delta\beta z) + \frac{i}{2\beta(\omega)} \cdot \frac{\partial^2 \varphi(z, \omega)}{\partial z^2}, \quad (7)$$

where $\kappa = \int |F(x, y)|^4 dx dy / \int |F(x, y)|^2 dx dy$, $\chi^{(3)}(\omega) = \int \chi^{(3)}(t) \exp(i\omega t) dt$ is the third-order susceptibility, and $\Delta\beta = \beta(\omega') + \beta(\omega'') - \beta(\omega' + \omega'' - \omega) - \beta(\omega)$. We expand $\beta(\omega)$ around ω_0 up to the fourth order, we have $\beta(\omega) = \beta_0 + \beta_1 \Delta\omega + \frac{\beta_2}{2} \Delta\omega^2 + \frac{\beta_3}{6} \Delta\omega^3 + \frac{\beta_4}{24} \Delta\omega^4$, where $\Delta\omega = \omega - \omega_0$, $\beta_0 = \beta(\omega_0)$, $\beta_j = \partial^j \beta / \partial \omega^j|_{\omega=\omega_0}$ for $j = 1$ to 4. β_1 is the reciprocal group velocity. β_2 , β_3 , and β_4 are the second-order, third-order, and fourth-order dispersion parameters, respectively. Substituting $\varphi(z, \omega) = \tilde{A}(z, \Delta\omega) \exp\{-i[\beta(\omega) - \beta(\omega_0)]z\}$ into Eq.(7) and taking the inverse Fourier transform $A(z, t) = \frac{1}{2\pi} \int \tilde{A}(z, \omega - \omega_0) \exp[-i(\omega - \omega_0)t] d\omega$, we have

$$\frac{\partial A}{\partial z} = H + \frac{i}{2\beta_0} C_\beta A_h, \quad (8)$$

where

$$H = -\beta_1 \frac{\partial A}{\partial t} - \frac{i\beta_2}{2} \frac{\partial^2 A}{\partial t^2} + \frac{\beta_3}{6} \frac{\partial^3 A}{\partial t^3} + \frac{i\beta_4}{24} \frac{\partial^4 A}{\partial t^4} + \\ i\gamma [1 + i(\frac{2}{\omega_0} - \frac{\beta_1}{\beta_0}) \frac{\partial}{\partial t} - (\frac{1}{\omega_0^2} - \frac{2\beta_1}{\beta_0\omega_0} + \frac{\beta_1^2}{\beta_0^2} - \frac{\beta_2}{2\beta_0}) \frac{\partial^2}{\partial t^2}] N A, \quad (9)$$

$$C_\beta = 1 - i\beta_1 \frac{\partial}{\partial t} + \left(\frac{\beta_2}{2\beta_0} - \frac{\beta_1^2}{\beta_0^2} \right) \frac{\partial^2}{\partial t^2}, \quad (10)$$

$$A_h = \frac{\partial^2 A}{\partial^2 z} + \left(2\beta_1 \frac{\partial}{\partial t} + i\beta_2 \frac{\partial^2}{\partial t^2} - \frac{\beta_3}{3} \frac{\partial^3}{\partial t^3} \right) \frac{\partial A}{\partial z} - \\ [i\beta_1 \frac{\partial}{\partial t} - \frac{\beta_2}{2} \frac{\partial^2}{\partial t^2} - \frac{i\beta_3}{6} \frac{\partial^3}{\partial t^3}]^2 A, \quad (11)$$

where $\gamma = \frac{n_2 \omega_0}{c A_{eff}}$, n_2 is the Kerr coefficient, A_{eff} is effective fiber cross section, $A_{eff} = \frac{\int |F(x,y)|^2 dx dy}{\kappa}$, and the higher order terms are neglected. The response $N(z, t)$ is described by [18]

$$N(z, t) = (1 - \alpha) |A(z, t)|^2 + \alpha \int_{-\infty}^t dt' f(t - t') \cdot |A(z, t')|^2. \quad (12)$$

On the right-hand side of Eq.(12), the first term represents Kerr non-resonant virtual electronic transitions in the order of about 1 fs or less [4], the second term represents delayed Raman response, $f(t)$ is the delayed response function, and $\alpha = 0.18$ parameterizes the relative strengths of Kerr and Raman interactions. In this paper, $f(t)$ is obtained by superposition of 27 Lorentzian lines centered at the different optical phonon frequencies for good fitting of the Raman gain, and

$$f(t) = \sum^{27} \frac{\tau_{1i}^2 + \tau_{2i}^2}{\tau_{1i} \cdot \tau_{2i}^2} \exp(-t/\tau_{2i}) \cdot \sin(t/\tau_{1i}), \quad (13)$$

where the parameters are determined by fitting the imaginary parts of its spectrum to actual Raman gain of fused silica. The fitted Raman gain spectrum is plotted in Fig. 1.

We now use order of magnitude considerations to simplify the calculation. The dispersion and the nonlinear terms in the nonlinear Schrödinger equation are of the same order of magnitude for the fundamental soliton, hence, we have

$$\left| \beta_2 \frac{\partial^2 A}{\partial t^2} \right| \approx \left| \frac{\beta_2 A}{T_0^2} \right| \approx \left| \frac{\gamma |A|^2 A}{N_p^2} \right|, \quad (14)$$

where the parameter $N_p = [\gamma P_0 T_0^2 / |\beta_2|]^{1/2}$ is the order of the soliton and $N_p = 1$ for the fundamental soliton, $T_0 = T_w / 1.763$, T_w is the pulse full width at half maximum, and P_0 is peak power of the incident pulse. In a silica-based weakly guiding single mode fiber, $\beta_0 \approx \frac{n_0 \omega_0}{c}$, $\beta_1 \approx \frac{n_0}{c}$, $\beta_1^2 \gg \beta_0 \beta_2$, and $\beta_1^3 \gg \beta_0 \beta_3$. Defining $\sigma \approx \frac{1}{\omega_0 T_0}$, we obtain from Eq. (14) for the fundamental soliton

$$\left| \frac{\beta_2}{T_0^2} \right| \approx \left| \gamma |A|^2 \right| \approx \omega_0^2 |\beta_2| \sigma^2. \quad (15)$$

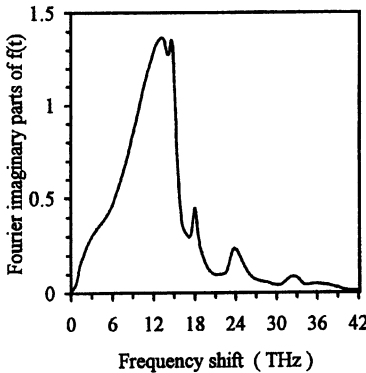


Fig. 1. The imaginary part of the spectrum of delayed Raman response function fitted by 27 Lorentzian lines

By using the iterative technique and the order of magnitude considerations, we first neglect the second term on the right-hand side of Eq.(8) and obtain in the zeroth order approximation

$$\frac{\partial A}{\partial z} = H. \quad (16)$$

From Eq.(16), the first order approximation of A_h is

$$A_h = -\gamma^2 N^2 A - 2\gamma\beta_2 A[(1-\alpha) \left| \frac{\partial A(z, t)}{\partial t} \right|^2 + \alpha \int_{-\infty}^t dt' f(t-t') \cdot \left| \frac{\partial A(z, t')}{\partial t'} \right|^2] - 2\gamma\beta_2 \frac{\partial N}{\partial t} \frac{\partial A}{\partial t}. \quad (17)$$

By substituting Eq.(16) into Eq.(8), the first order approximation of the wave equation is

$$\begin{aligned} \frac{\partial A}{\partial z} = & (-\beta_1 \frac{\partial A}{\partial t} - \frac{i\beta_2}{2} \frac{\partial^2 A}{\partial t^2} + \frac{\beta_3}{6} \frac{\partial^3 A}{\partial t^3} + \frac{i\beta_4}{24} \frac{\partial^4 A}{\partial t^4}) + i\gamma(N A + \\ & i\alpha_1 \frac{\partial}{\partial t} N A) - i\gamma\alpha_2 \frac{\partial^2 N A}{\partial t^2} - \frac{i\gamma\beta_2 A}{\beta_0} [(1-\alpha) \left| \frac{\partial A(z, t)}{\partial t} \right|^2 + \\ & \alpha \int_{-\infty}^t dt' f(t-t') \cdot \left| \frac{\partial A(z, t')}{\partial t'} \right|^2] - \frac{i\gamma\beta_2}{\beta_0} \frac{\partial N}{\partial t} \frac{\partial A}{\partial t} - \\ & \frac{i}{2\beta_0} \gamma^2 N^2 A, \end{aligned} \quad (18)$$

where $\alpha_1 = \frac{2}{\omega_0} - \frac{\beta_1}{\beta_0} \approx \frac{1}{\omega_0}$, $\alpha_2 = \frac{1}{\omega_0^2} - \frac{2\beta_1}{\beta_0\omega_0} + \frac{\beta_1^2}{\beta_0^2} - \frac{\beta_2}{2\beta_0} \approx -\frac{\beta_2}{2\beta_0}$, and retaining all terms to the order of σ^4 . If we make a second iteration, we find that the equation does not change up to the order of σ^4 . On the right-hand side of

Eq.(18), the term with coefficient α_1 is of order σ^3 , and the last five terms representing nonlinear high-order terms of order σ^4 which are newly derived terms. Comparing the σ^4 term with coefficient with the term with coefficient , we have

$$r = \left| \alpha_2 \frac{\partial^2 NA}{\partial t^2} \right|_{\max} / \left| \alpha_1 \frac{\partial NA}{\partial t} \right|_{\max} \approx \frac{|\beta_2|}{\beta_0 T_0^2} / \frac{1}{\omega_0 T_0} \approx \frac{|\beta_2| c}{n_0 T_0}. \quad (19)$$

We consider a single cycle pulse. At the wavelength $\lambda = 1.55$ m, $\beta_2 = -20$ fs²/mm, pulselength $T_w \approx 5.17$ fs and we have $r = 1.4 \times 10^{-3}$. At m, $\beta_2 = 38.5$ fs²/mm, pulselength $T_w \approx 2.67$ fs and we have $r = 5.1 \times 10^{-3}$ [6]. Similarly we can show that other σ^4 terms are much smaller than the σ^3 term. Therefore, all σ^4 terms can be neglected for the single cycle pulse in the low loss window of the fiber.

3 Numerical Results

We now consider the propagations of a 5 fs fundamental soliton and 10 fs and 50 fs second-order solitons in a single-mode fiber. The Equation (18) is used to describe the propagation. In dimensionless soliton units, it can be rewritten as

$$\begin{aligned} \frac{\partial}{\partial \xi} u &= \frac{i}{2} \frac{\partial^2 u}{\partial \tau^2} + \beta \frac{\partial^3 u}{\partial \tau^3} + \frac{i \beta_4}{24 |\beta_2| T_0^2} \frac{\partial^4 u}{\partial \tau^4} + i \bar{N} u - \frac{1}{\omega_0 T_0} \frac{\partial}{\partial \tau} \bar{N} u \\ &\quad - \frac{i \beta_2}{\beta_0 T_0^2} \left\{ \frac{1}{2} \frac{\partial^2 \bar{N} u}{\partial \tau^2} + [(1 - \alpha) \left| \frac{\partial u}{\partial \tau} \right|^2 + \alpha \int_{-\infty}^{\tau} d\tau' \cdot f(\tau - \tau') \cdot \left| \frac{\partial u}{\partial \tau'} \right|^2] \right. \\ &\quad \left. + \frac{\partial \bar{N}}{\partial \tau} \frac{\partial u}{\partial \tau} + \frac{1}{2} \bar{N}^2 u \right\}, \end{aligned} \quad (20)$$

where $\xi = \frac{z}{L_D}$, $\tau = \frac{t - \beta_1 z}{T_0}$, $u = \frac{N_P A}{\sqrt{P_0}}$, $\beta \equiv \frac{\beta_3}{6 |\beta_2| T_0}$, $L_D = \frac{T_0^2}{|\beta_2|}$ is dispersion length , and $\bar{N} = \frac{N_P^2 N}{P_0}$. When the terms of order σ^4 are neglected, Eq. (20) reduces to

$$\frac{\partial u}{\partial \xi} = \frac{i}{2} \frac{\partial^2 u}{\partial \tau^2} + \beta \frac{\partial^3 u}{\partial \tau^3} + \frac{i \beta_4}{24 |\beta_2| T_0^2} \frac{\partial^4 u}{\partial \tau^4} + i \bar{N} u - \frac{1}{\omega_0 T_0} \frac{\partial}{\partial \tau} \bar{N} u. \quad (21)$$

To solve Eq.(20) or Eq.(21), we use the split-step Fourier method and take the typical fiber parameters to be: soliton wavelength $\lambda = 1.55$ m, $\beta_2 = -20$ fs²/mm, $\beta_3 = 100$ fs³/mm, $\beta_4 = 0$ fs⁴/mm, $n_2 = 2.3 \times 10^{-20}$ m²/W, and $A_{eff} = 50$ m².

3.1 The propagation of a 5 fs fundamental soliton

The power evolutions of the 5 fs fundamental soliton propagation simulated by using Eq. (20) are shown in Fig. 2. One can see that the pulse shape

is distorted and becomes asymmetric with an oscillatory structure near the trailing edge of the pulse and the main pulse broadens within two soliton periods. With further propagation inside the fiber, this oscillatory structure gradually disappears. The same propagation is simulated by using Eq. (21), and it is found that the two numerical results differ less than 0.1 %. This means that the higher nonlinear terms proportional to σ^4 in Eq. (20) can be neglected in this case.

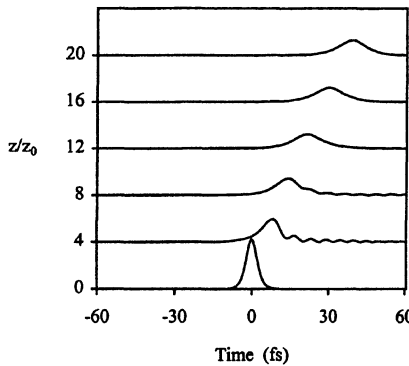


Fig. 2. Power evolution of a 5 fs fundamental soliton over twenty soliton periods along the fiber.

3.2 The propagation of a 10 fs second-order soliton

We simulate the 10 fs second-order soliton propagation by using Eq. (20). The power evolution of the pulse is shown in Fig. 3. It is seen that a stimulated radiation is excited after the first contraction then separates from the main peak, and in the meantime, the pulse is broken into its constituent solitons. Similarly, we compare the numerical results of the propagation of 10 fs second-order soliton obtained by Eq. (20) and Eq. (21), it is found that they differ less than 0.1 percent. These mean that the higher nonlinear terms proportional to σ^4 in Eq. (20) can be also neglected for the propagation of a 10 fs second-order soliton in an optical fiber.

On the other hand, we consider the influence of third-order dispersion, delayed Raman response, and self-steeping on the propagation of the second-order soliton in a single-mode fiber. In Fig. 4, we show the power evolution of the pulse only with the third-order dispersion. One can be seen that the third-order dispersion not only leads to breakup of initial solitons into their constituents but stimulates a radiation within one soliton periods. Then the radiation pulse leaves the main peak in the trailing direction and gradually vanishes[10,11]. Fig. 5 shows the power evolution of the pulse when only the delayed Raman response is considered. It is seen that only small delay occurs

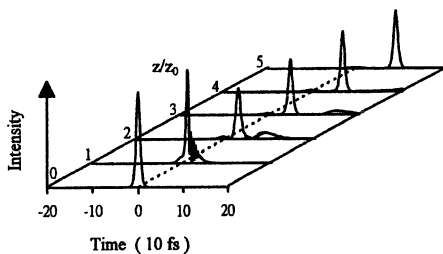


Fig. 3. Power evolution of a 10 fs second-order soliton over five soliton periods along the fiber.

after propagation a distance of five soliton periods. The effect of delayed Raman response is no longer important when the pulse width is short enough. It is because that the spectral width of the input pulse is much larger than the Raman gain spectral width which is about 13.2 THz, and the red spectral components of the pulse can only be amplified by small parts of the blue spectral components. In Fig. 6, we show the power evolution of the pulse when only the self-steepening effect is considered. The two solitons gradually separate from each other at a distance of two soliton periods and both are delayed. One can see that the self-steepening effect is now larger than the delayed Raman response. The power evolution of the pulse when all higher-order effects are included is shown in Fig. 3. By comparing Fig. 3, Fig. 4, Fig. 5, and Fig. 6, it is seen that the third-order dispersion plays the most important role, the next is the self-steepening effect, and the least is the delayed Raman response.

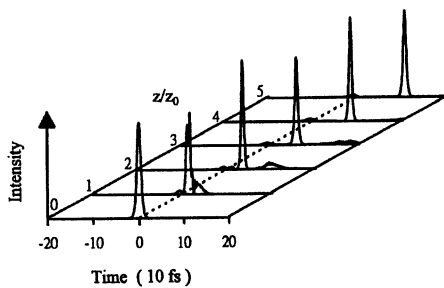


Fig. 4. Power evolution of a 10 fs second-order soliton over five soliton periods along the fiber when only the third-order dispersion is considered.

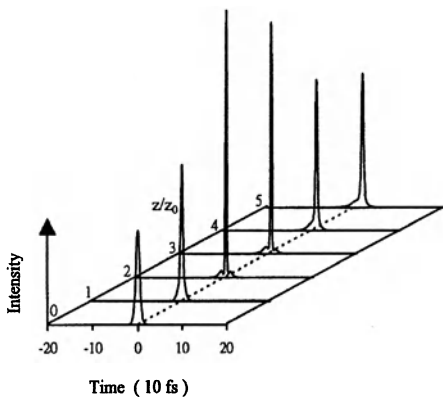


Fig. 5. Power evolution of a 10 fs second-order soliton over five soliton periods along the fiber when only the delayed Raman response is considered.

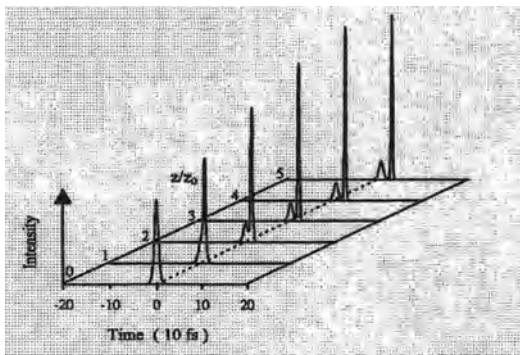


Fig. 6. Power evolution of a 10 fs second-order soliton over five soliton periods along the fiber when only the self-steepening effect is considered.

3.3 The propagation of a 50 fs second-order soliton

Since the higher nonlinear terms proportional to σ^4 can be neglected for a 10 fs second-order soliton propagation, we can simulate the 50 fs second-order soliton propagation by using Eq. (21). Fig. 7 shows the power evolution of the soliton when only the third-order dispersion is considered. It is seen that the soliton decay occurs within two soliton periods. In Fig. 8, we show the power evolution of the soliton when only the delayed Raman response is considered. The soliton decay occurs within two soliton periods, the main peak shifts toward the trailing side at a rapid rate with a further increase in distance and the lower-intensity soliton moves on the leading side. With only the self-steepening effect, the power evolution of the pulse is shown in Fig. 9. Up to five soliton periods, the pulse has no obvious separation. This means that the self-steepening effect is very small compared to the effect of the delayed Raman response. When all the three higher-order effects are considered together, the power evolution of the pulse is shown in Fig. 10. It is seen that the delay of the main peak is about 72 fs after propagating the

distance of five soliton periods. Comparing Fig. 10 with Fig. 8, we can see that they are similar except that the main peak broadens and its delay becomes smaller when all three effects are considered. Among the three effects, it is seen from Fig. 7 to Fig. 10 that the soliton decay is dominated by the delayed Raman response and the self-steepening has the least effect.

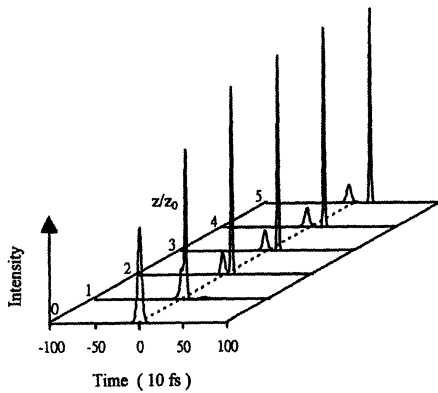


Fig. 7. Power evolution of a 50 fs second-order soliton over five soliton periods along the fiber when only the third-order dispersion is considered.

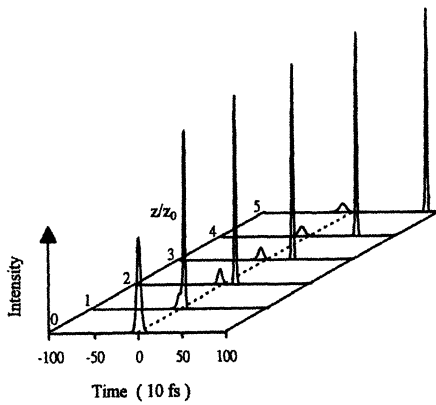


Fig. 8. Power evolution of a 50 fs second-order soliton over five soliton periods along the fiber when only the delayed Raman response is considered.

When the delayed Raman response is approximated by assuming the Raman gain is a linear function of frequency shift, in dimensionless soliton units, Eq. (21) reduces to

$$\frac{\partial u}{\partial \xi} = \frac{i}{2} \frac{\partial^2 u}{\partial \tau^2} + \beta \frac{\partial^3 u}{\partial \tau^3} + \frac{i \beta_4}{24 |\beta_2| T_0^2} \frac{\partial^4 u}{\partial \tau^4} + i |u|^2 u -$$

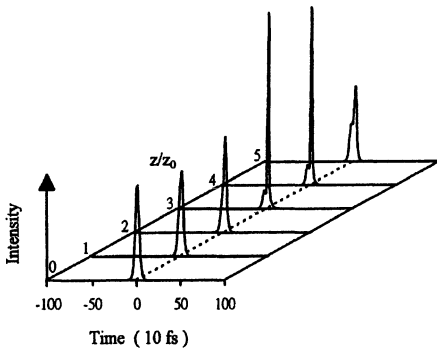


Fig. 9. Power evolution of a 50 fs second-order soliton over five soliton periods along the fiber when only the self-steepening effect is considered.

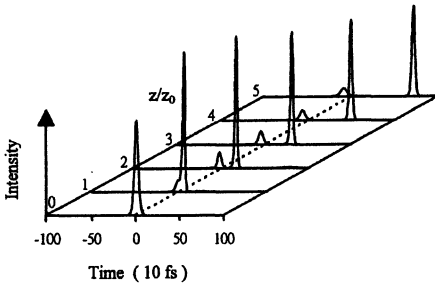


Fig. 10. Power evolution of a 50 fs second-order soliton over five soliton periods along the fiber when all the three effects are considered.

$$i \frac{T_R}{T_0} \frac{u \partial |u|^2}{\partial \tau} - \frac{1}{\omega_0 T_0} \frac{\partial}{\partial \tau} (|u|^2 u), \quad (22)$$

where T_R is the slope of the Raman gain profile at the carrier frequency. Here we take $T_R = 3$ fs [19]. Fig. 11 shows the same pulse propagation as in Fig. 10 when Eq. (22) is used for numerical simulation. The main peak is delayed about 148 fs after propagating the distance of five soliton periods, the delay is much larger than that calculated by Eq. (21). In Fig. 12, we show the averaged frequency shifts obtained by Eq. (21) Eq. (22). After propagating the distance of five soliton periods, the averaged frequency shift obtained by Eq. (22) is about 37 THz and that obtained by Eq. (21) is only about 22 THz. Therefore, Eq. (22) is not suitable for describing the propagation of a second-order solitons whose pulselwidth is equal to or less than 50 fs.

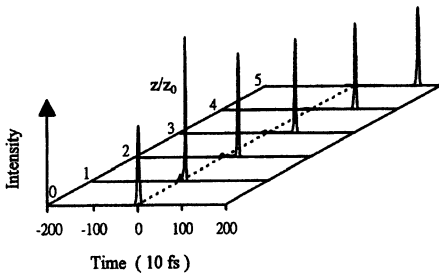


Fig. 11. Same as in Fig. 10, when delayed Raman response is approximated by assuming the Raman gain is a linear function of frequency shift.

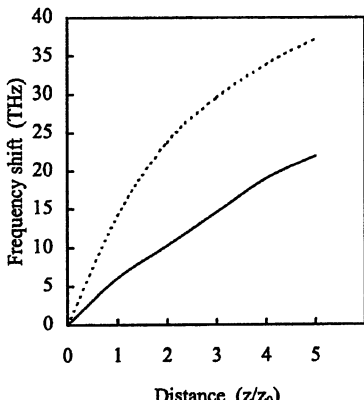


Fig. 12. Averaged frequency shift versus distance for the 50 fs second-order soliton propagation obtained from Fig. 10 (solid curves) and Fig. 11 (dashed curves).

4 Conclusions

In conclusion, we have used iterative method to derive a wave equation for femtosecond soliton propagation in an optical fiber. The derived equation contains higher nonlinear terms than the equation obtained previously. The propagation of a 5 fs fundamental soliton and 10 fs and 50 fs second-order solitons in an optical fiber are numerically simulated. It is found that the higher nonlinear terms in the derived equation are negligible in these cases, which means that the equation obtained previously is valid in these ranges. We have found that when a 5 fs fundamental soliton propagates in a fiber, it becomes asymmetric with an oscillatory structure near its trailing edge and the main pulse broadens. We have also found that for a 10 fs second-order soliton, the soliton decay is dominated by the third-order dispersion, and for a 50 fs second-order soliton, the soliton decay is dominated by the delayed Raman response. In addition, or the propagation of a 50 fs second-

order soliton, we have found that the exact delayed Raman response form must be used.

References

1. R. L. Fork, C. H. Brito Cruz, P. C. Becker, and C. V. Shank, 1987, Opt. Lett., **12**, 483.
2. G. P. Agrawal, Nonlinear Fiber Optics, 2nd edn (Academic Press, New York, 1995) Chap. 2.
3. R. M. Joseph, S. C. Hagness, and A. Taflove, 1992, Opt. Lett., **16**, 1412.
4. P. M. Goorjian, A. Taflove, R. M. Joseph, and S. C. Hagness, 1992, IEEE J. Quantum Electron., **28**, 2416.
5. K. J. Blow and D. Wood, 1989, IEEE J. Quantum Electron., **25**, 2665.
6. T. Brabec and F. Krausz, 1997, Phys. Rev. Lett., **17**, 3282.
7. P. V. Mamyshev and S. V. Chernikov, 1990, Opt. Lett., **15**, 1076.
8. S. Chi and S. Wen, 1996, Opt. and Quantum Electronics, **28**, 1351.
9. E. A. Golovchenko, E. M. Menyuk, A. M. Prokhorov, and V. N. Serkin, 1985, JETP Lett. **42**, 87.
10. P. K. A. Wai, C. R. Menyuk, Y. C. Lee, and H. H. Chen, Opt. Lett. **11**, 464 (1986).
11. P. K. A. Wai, H. H. Chen, and Y. C. Lee, 1990, Phys. Rev. **41**, 426.
12. J. R. Taylor, ED., Optical solitons - theory and experiment (Cambridge University Press, Cambridge, UK, 1992) Chap. 9.
13. W. Hodel and H. P. Weber, 1987, Opt. Lett. **12**, 924.
14. K. Tai, A. Hasegawa, and N. Bekki, 1988, Opt. Lett. **13**, 392.
15. G. P. Agrawal, Nonlinear Fiber Optics, 2nd edn (Academic Press, New York, 1995) Chap. 5.
16. K. Ohkuma, Y. H. Ichikawa, and Y. Abe, 1987, Opt. Lett. **12**, 516.
17. S. Chi and Q. Guo, 1995, Opt. Lett., **20**, 1598.
18. R. H. Stolen and W. J. Tomlinson, 1989, J. Opt. Am. B, **6**, 1159.
19. P. V. Mamyshev and S. V. Chernikov, 1992, Sov. Light. Commun. **2**, 97

Control of Spontaneous Processes

S. Swain and Peng Zhou

Department of Applied Mathematics and Theoretical Physics, The Queen's University of Belfast, Belfast BT7 1NN, The United Kingdom
e-mails: s.swain@qub.ac.uk and pzhou@am.qub.ac.uk

Abstract. We study two novel ways of modifying and controlling spontaneous emission: the first way is by mimicking the properties of a squeezed vacuum reservoir by means of a stochastic field, and the second is by mimicking the effects of quantum interference in a Vee three-level system by exploiting the cavity environment. In the latter case, by pre-selecting the polarization, we ensure that the dipole moments of the two transitions are effectively parallel.

1 Introduction

A major current interest in quantum optics is the modification and control of spontaneous emission. Here, we study two novel ways of achieving this aim. The first method involves mimicking the properties of a squeezed vacuum reservoir by means of a stochastic field, thereby producing resonance fluorescence spectra which depend upon the relative phases of the driving and stochastic fields. The second is by exploiting the cavity environment to mimick the effects of quantum interference in Vee three-level systems. For quantum interference effects to be strong, it is essential that the dipole moments of the two transitions be parallel, or very nearly so. We show how this can be achieved if the cavity polarization is pre-selected. We discuss these two approaches separately. The physics behind them is different but the mathematical techniques used to develop the theory are very similar.

2 Phase dependent spectra in a stochastic field

In 1987, Carmichael et al. [1] showed that the resonance fluorescence from a monochromatically driven two-level atom interacting with a squeezed vacuum exhibits strongly phase-dependent features in resonance fluorescence. The spectra differ greatly from the well-known Mollow triplet which is obtained in the absence of the squeezed vacuum. The Mollow spectrum is a symmetrical triplet, with the side-peaks having one third the height of the central peak, and being separated from it by the Rabi frequency. The central peak has a width γ , and the side-peaks a width $3\gamma/2$, where γ is the natural linewidth. In the presence of the squeezed vacuum, the relative heights and widths of the spectrum triplet vary greatly with the phase of the squeezed vacuum relative

to the phase of the driving laser: some peaks in fact may show subnatural linewidths.

Although these effects were predicted over a decade ago, their experimental verification remains a major challenge in quantum optics. The principal difficulty confronting the experimenter is that the squeezed field modes must occupy the whole 4π solid angle of space.

The squeezed vacuum is a quantum field, and it is tempting to attribute the features described to the quantum nature of the squeezed vacuum. However, in this paper we describe an arrangement using only classical fields which leads to very similar spectra. The only real difference is that subnatural linewidths do not occur, at least in this parameter range, if the fields are all classical¹. Details may be found in the reference [2].

We consider a two-level atom driven by a strong, coherent laser, and in addition, by a weak, amplitude-fluctuating field of wide bandwidth which replaces the squeezed vacuum [3]. We show that the spectra obtained in the stochastic field are qualitatively similar to those obtained in the squeezed vacuum. The experiment should be feasible with current technology, and largely avoids the problem of the 4π angle of squeezing.

The modification of the Mollow triplet, as controlled by the phase difference between the applied coherent and stochastic fields, is studied. The coherent field has a constant amplitude E_c , and the stochastic field a randomly fluctuating amplitude $E_s(t)$. The atom is also damped in the usual way by the electromagnetic vacuum. The frequencies of the atomic transition, of the coherent laser and of the stochastic field are assumed to be identical for simplicity.

The master equation for the density operator ρ of the system is

$$\dot{\rho} = -i[H_{a-c} + H_{a-s}, \rho] + \gamma(2\sigma_- \rho \sigma_+ - \sigma_+ \sigma_- \rho - \rho \sigma_+ \sigma_-), \quad (1)$$

where

$$H_{a-c} = \frac{\Omega}{2}(\sigma_+ + \sigma_-), \quad H_{a-s} = \frac{x(t)}{2}[e^{i\phi}\sigma_+ + e^{-i\phi}\sigma_-]. \quad (2)$$

H_{a-c} and H_{a-s} describe the interaction of the atom with the coherent field and the stochastic field, respectively, γ is the atomic decay constant (natural linewidth), ϕ is the relative phase of the two fields, $\Omega = 2|\mathbf{d} \cdot \mathbf{e} E_c|/\hbar$ is the Rabi frequency of the coherent field, and $x(t) = 2|\mathbf{d} \cdot \mathbf{e} E_s(t)|/\hbar$ represents the stochastic amplitude of the atom/stochastic-field interaction, which is assumed to be a real Gaussian-Markovian random process with zero mean value and correlation function

$$\langle x(t)x(t') \rangle = D\kappa e^{-\kappa|t-t'|}, \quad (3)$$

¹ Subnatural linewidths do occur with classical fields in other parameter ranges (W. S. Smyth and S. Swain, J. Mod. Opt. **46**, 1233 (1999)).

where D and κ are constants. The correlation function (3) describes a field of RMS amplitude $\sqrt{D\kappa}$ undergoing amplitude fluctuations, which result in a finite bandwidth κ .

For simplicity, we assume that the intensity of the coherent part is much greater than that of the stochastic field, and the bandwidth κ of the stochastic field is much greater than the atomic linewidth: $\Omega \gg \sqrt{D\kappa}$ and $\kappa \gg \gamma$. One can then invoke standard perturbative techniques [4,5] to eliminate the stochastic variable $x(t)$. The resultant master equation for the reduced density operator ρ is in general fairly complicated, but in the particular case where $\phi = 0$, it takes the form

$$\begin{aligned}\dot{\rho} = & -i[H_{a-c}, \rho] + \gamma(N+1)(2\sigma_- \rho \sigma_+ - \sigma_+ \sigma_- \rho - \rho \sigma_+ \sigma_-) \\ & + \gamma N(2\sigma_+ \rho \sigma_- - \sigma_- \sigma_+ \rho - \rho \sigma_- \sigma_+) + 2\gamma M(\sigma_+ \rho \sigma_+ + \sigma_- \rho \sigma_-),\end{aligned}\quad (4)$$

where $M = N = D/4\gamma$. The master equation (4) is formally the same as that of a coherently driven two-level atom interacting with a squeezed vacuum. However, the ideal squeezed vacuum (ISV) satisfies $|M| = \sqrt{N(N+1)}$ whereas here we have $M = N$. The latter value of M corresponds to a reservoir in which there is the maximal *classical* correlation between pairs of photons. Such a reservoir is sometimes called a “classically squeezed field” (CSF).

For $\phi = \pi/2$, the master equation again reduces to the form (4), but now with $N = -M = D/4\gamma \times \kappa^2 / (\Omega^2 + \kappa^2)$. (For $\phi \neq 0, \pi/2$ our stochastic system does not correspond exactly to that of a CSF.)

In Figure 1 we present the resonance fluorescence spectra for the stochastic system with $\Omega = 200\gamma$, $\kappa = 100\gamma$ and $D = 10\gamma$ in frames (a) and (b) for $\phi = 0$ and $\pi/2$ respectively, where the strong phase dependence is evident. In frames (c) and (d) we give the spectra for the corresponding ideal squeezed vacuum, with $\Omega = 20$ and $N = 0.25$ in (c), and $N = 0.05$ in (d). (For the squeezed vacuum case we have divided the parameters by a factor of ten, in order to obtain experimentally reasonable values for N .) The spectra for the stochastic system and the spectra for the squeezed vacuum are qualitatively similar. The only essential difference is that the central peak has a subnatural linewidth for $\Phi = 0$ case in the squeezed vacuum case. (It should however, be pointed out that there are parameter ranges where the stochastic field spectra are qualitatively different from the resonance fluorescence spectra produced in a squeezed vacuum [6].)

The physics associated with the modification of the Mollow fluorescence spectrum for arbitrary ϕ is conveniently explored by working in the semi-classical dressed states basis $|\pm\rangle = (|0\rangle \pm |1\rangle)/\sqrt{2}$, which are the eigenstates of H_{a-c} . The condition $\Omega \gg \sqrt{D\kappa}$ ensures the secular approximation to be valid, and consequently, the equations of motion simplify to

$$\dot{\rho}_z = -\Gamma_{||}\rho_z, \quad \dot{\rho}_{+-} = -(\Gamma_\perp + i\Omega')\rho_{+-}, \quad (5)$$

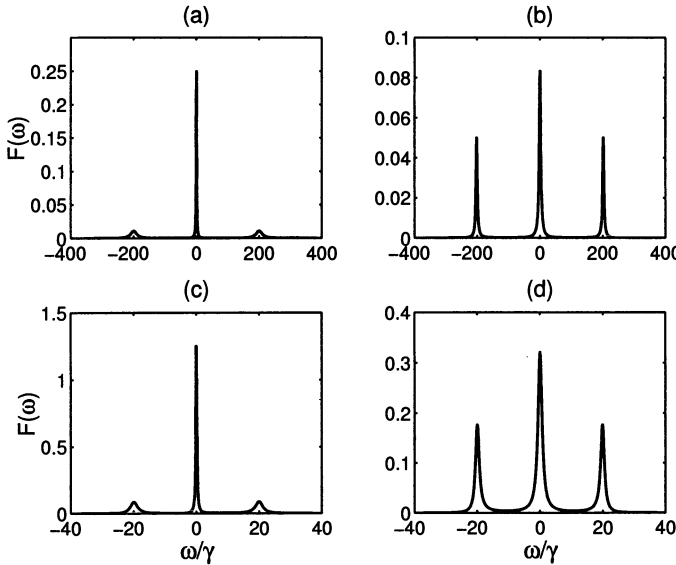


Fig. 1. The resonance fluorescence spectra in a stochastic field with phase $\phi = 0$ in (a) and $\phi = \pi/2$ in (b); and in a squeezed vacuum with $\Phi = \pi$ in (c) and $\Phi = 0$ in (d). In (a) and (b), $\Omega = 200\gamma$, $\kappa = 100\gamma$, $D = 10\gamma$; and $\Omega = 20\gamma$ with $N = 0.5$ in (c) and $N = 0.05$ in (d).

where $\rho_z = (\rho_{++} - \rho_{--})$ and $\rho_{+-} = \langle +|\rho|-\rangle$ are the dressed-state inversion and polarization which have phase-dependent decay rates $\Gamma_{||}$ and Γ_{\perp} respectively, and Ω' is the generalized Rabi frequency. Here

$$\begin{aligned}\Gamma_{||} &= \gamma + \frac{D\kappa^2}{\kappa^2 + \Omega'^2} \sin^2 \phi, & \Gamma_{\perp} &= \Gamma_{||}/2 + \gamma + D \cos^2 \phi, \\ \Omega' &= \Omega \left[1 + \frac{D\kappa}{2(\kappa^2 + \Omega'^2)} \sin^2 \phi \right],\end{aligned}\quad (6)$$

The quantity $\Omega' - \Omega$ represents a dynamical frequency shift due to the additional amplitude-fluctuating field. (In fact, it is consistent with our approximation $\sqrt{D\kappa} \ll \Omega$ to set $\Omega' = \Omega$.) The weak stochastic field modifies the decay rates and level shifts of the dressed states in a manner which depends on the relative phase of the coherent and stochastic fields, the RMS amplitude $\sqrt{D\kappa}$ and the bandwidth κ of the stochastic field.

It follows from (5) that the dressed states $|\pm\rangle$ have the same steady state populations. As a result, the resonance fluorescence spectrum is symmetric:

$$F(\omega) = \frac{\Gamma_{\perp}/8}{\Gamma_{\perp}^2 + (\omega + \Omega')^2} + \frac{\Gamma_{||}/4}{\Gamma_{||}^2 + \omega^2} + \frac{\Gamma_{\perp}/8}{\Gamma_{\perp}^2 + (\omega - \Omega')^2}. \quad (7)$$

The decay of the inversion results in the central peak with linewidth $2\Gamma_{\parallel}$ and height $1/4\Gamma_{\parallel}$, whereas the modulated decays of the coherences give rise to the sidebands with linewidth $2\Gamma_{\perp}$ and height $1/8\Gamma_{\perp}$. When $\phi = 0$, we have $\Gamma_{\parallel} = \gamma$ and $\Gamma_{\perp} = 3\gamma/2 + D$. The central peak is therefore much narrower and higher than the sidebands for $D \gg \gamma$. When $\phi = \pi/2$, however, $\Gamma_{\parallel} = \gamma + D\kappa^2/(\kappa^2 + \Omega^2)$ and $\Gamma_{\perp} = 3\gamma/2 + \frac{1}{2}D\kappa^2/(\kappa^2 + \Omega^2)$. Accordingly, the centre peak widens while the sidebands narrow as the phase varies from 0 to $\pi/2$.

In conclusion, we have reported a scheme to modify the Mollow fluorescence spectra of a two-level atom by applying a stochastic, amplitude-diffusing field. Phase-sensitive spectral features, qualitatively similar to those of a driven atom in a squeezed vacuum, are displayed. Since experiments employing the phase-control of the two-photon excitation spectrum of atoms by a field with coherent and real Gaussian components [7], and of the transient dynamics of bichromatically driven two-level atoms [8], have already been demonstrated, the present model is experimentally accessible. The observation of these features would demonstrate our ability to tailor reservoirs so as to modify atomic radiative properties in fundamental ways, and give an interesting insight into the similarities and differences of quantum and classical noise.

3 Cavity Induced Quantum Interference

There has been a recent rekindling of interest in the phenomenon of quantum interference [9], largely due to the fact that it is the basis of many new effects and applications of quantum optics, such as lasing without population inversion [10], electromagnetically-induced transparency [11], enhancement of the index of refraction without absorption [12], fluorescence quenching [13–16] and spectral line narrowing [14].

The basic system consists of a singlet state connected to a closely-spaced excited doublet by a single-mode laser. Cardimona *et al.* [13,14] studied the effect of quantum interference on the resonance fluorescence of such a system, and found that it can be driven into a dark state in which quantum interference prevents any fluorescence from the excited sublevels, regardless of the intensity of the exciting laser. In the case of a single auxiliary level, quantum interference can lead to the elimination of the spectral line at the driving laser frequency in the spontaneous emission spectrum [15] and transparency in the absorption spectrum [17]. It is important for these effects that the dipole moments of the transitions involved are parallel, so that the *cross-decay terms* are maximal. From the experimental point view, however, it is difficult to find isolated atomic systems which have parallel moments [10,13,18,19].

Various alternative proposals [18,20] have been made for generating quantum interference effects. Here, we propose a scheme to generate quantum interference in realistic, practical situations. We study a Vee-type atom cou-

pled to a single-mode cavity field with a pre-selected polarization in the bad cavity limit, and show that maximal quantum interference (equivalently, two parallel dipole transition moments) can be achieved in such a system [21]. The effects of cavity-induced interference on the probe absorption spectrum, and cavity detuning effects, are also investigated [22].

The Vee-type atom consists of a ground state $|0\rangle$ coupled by the single-mode cavity field to the excited doublet $|1\rangle, |2\rangle$. Direct transitions between the excited sublevels $|1\rangle$ and $|2\rangle$ are dipole forbidden. The master equation for the total density matrix operator ρ_T in the frame rotating with the average atomic transition frequency $\omega_0 = (\omega_1 + \omega_2)/2$ takes the form

$$\dot{\rho}_T = -i[H_A + H_C + H_I, \rho_T] + \mathcal{L}\rho_T, \quad (8)$$

where

$$\begin{aligned} H_C &= \delta a^\dagger a, \quad H_A = \frac{1}{2}\omega_{21}(A_{22} - A_{11}), \quad H_I = i(g_1 A_{01} + g_2 A_{02})a^\dagger - h.c. \\ \mathcal{L}\rho_T &= \kappa(2a\rho_T a^\dagger - a^\dagger a\rho_T - \rho_T a^\dagger a) \end{aligned} \quad (9)$$

with $A_{ij} = |i\rangle\langle j|$, $\delta = \omega_C - \omega_0$, $\omega_{21} = E_2 - E_1$, and $g_j = \mathbf{e}_\lambda \cdot \mathbf{d}_{0j} \sqrt{\hbar\omega_C/2\epsilon_0 V}$, ($j = 1, 2$). Here H_C , H_A and H_I are the unperturbed cavity, the unperturbed atom and the cavity-atom interaction Hamiltonians respectively, while $\mathcal{L}\rho_T$ describes damping of the cavity field by the vacuum electromagnetic modes, characterized by the decay constant κ ; a and a^\dagger are the photon annihilation and creation operators of the cavity mode; δ is the cavity detuning from the average atomic transition frequency, ω_{21} is the splitting of the excited doublet of the atom, g_i is the atom-cavity coupling constant, expressed in terms of \mathbf{d}_{ij} , the dipole moment of the atomic transition from $|j\rangle$ to $|i\rangle$, \mathbf{e}_λ is the polarization of the cavity mode, and V is the volume of the system. For simplicity, we neglect spontaneous emission out of the cavity mode. In the remainder of this work we assume that the polarization of the cavity field is *pre-selected*, i.e., the polarization index λ is fixed to one of two possible directions.

We assume the bad cavity limit, $\kappa \gg g$: that is, we have weak atom-cavity coupling and a low Q cavity so that the cavity field decay dominates. The cavity field response to the continuum modes is much faster than that produced by its interaction with the atom, so that the atom always experiences the cavity mode in the state induced by the vacuum reservoir. Thus one can adiabatically eliminate the cavity-mode variables, giving rise to a master equation for the atomic variables only. After some tedious calculations (see e.g. [23]), we obtain:

$$\begin{aligned} \dot{\rho} &= -i[H_A, \rho] \\ &+ \{L_+ [|g_1|^2(A_{01}\rho A_{10} - A_{11}\rho) + g_1 g_2^*(A_{01}\rho A_{20} - A_{21}\rho)] \\ &+ L_- [|g_2|^2(A_{02}\rho A_{20} - A_{22}\rho) + g_1^* g_2(A_{02}\rho A_{10} - A_{12}\rho)] \\ &+ h.c.\} \end{aligned} \quad (10)$$

where $L_{\pm} = [\kappa + i(\delta \pm \omega_{21}/2)]^{-1}$.

This equation describes the cavity-induced atomic decay into the cavity mode. The real part of $L_{\pm}|g_j|^2$ represents the cavity-induced decay rate of the atomic excited level j ($= 1, 2$), while the imaginary part is associated with the frequency shift of the atomic level resulting from the interaction with the vacuum field in the detuned cavity. In the general case, the cavity-induced decay constants γ_j ($j = 1, 2$) of the excited states have the forms

$$\gamma_1 = \frac{\kappa g_1^2}{\kappa^2 + (\delta + \omega_{21}/2)^2}, \quad \gamma_2 = \frac{\kappa g_2^2}{\kappa^2 + (\delta - \omega_{21}/2)^2}. \quad (11)$$

The other terms, $L_{\pm}g_i g_j^*$, ($i \neq j$) represent the cavity-induced correlated transitions of the atom, i.e., an emission followed by an absorption of the same photon on a different transition, ($|1\rangle \rightarrow |0\rangle \rightarrow |2\rangle$ or $|2\rangle \rightarrow |0\rangle \rightarrow |1\rangle$), which give rise to the effect of quantum interference.

The value of the quantum interference term is very sensitive to the orientations of the atomic dipoles and the polarization of the cavity mode. For instance, if the cavity-field polarization is not pre-selected, as in free space, one must replace $g_i g_j^*$ by the sum over the two possible polarization directions, giving $\sum_{\lambda} g_i g_j^* \propto \mathbf{d}_{0i} \cdot \mathbf{d}_{0j}^*$ [18]. Therefore, only non-orthogonal dipole transitions lead to nonzero contributions, and maximal interference occurs with the two dipoles parallel. As pointed out in Refs. [10,13,18,19] however, it is questionable whether there is an isolated atomic system with parallel dipoles. On the other hand, if the polarization of the cavity mode is fixed, say $\mathbf{e}_{\lambda} = \mathbf{e}_x$, then $g_i g_j^* \propto (\mathbf{d}_{0i})_x (\mathbf{d}_{0j}^*)_x$, which is nonvanishing, regardless of the orientation of the atomic dipole matrix elements. In the following we assume polarization pre-selection.

It is apparent that if $\kappa \gg \delta, \omega_{21}$, the frequency shifts are negligibly small and the cavity-induced decay rates reduce to $\gamma_j = |g_j|^2/\kappa$. The master equation (10) then has the approximate form

$$\begin{aligned} \dot{\rho} \simeq & -i[H_A, \rho] \\ & + \gamma_1(2A_{01}\rho A_{10} - A_{11}\rho - \rho A_{11}) + \gamma_2(2A_{02}\rho A_{20} - A_{22}\rho - \rho A_{22}) \\ & + \sqrt{\gamma_1\gamma_2}(2A_{01}\rho A_{20} - A_{21}\rho - \rho A_{21} + 2A_{02}\rho A_{10} - A_{12}\rho - \rho A_{12}) \end{aligned} \quad (12)$$

– the same as that of a Vee-atom with two parallel transition matrix elements in free space [13,14,22]. Thus, maximal quantum interference in a Vee-type atom can be achieved in a cavity with a pre-selected polarization.

Hereafter, we investigate the effects of quantum interference by studying the steady-state absorption spectrum, defined as

$$A(\omega) = \Re e \int_0^\infty \lim_{t \rightarrow \infty} \langle [P(t + \tau), P^\dagger(t)] \rangle e^{i(\omega_p - \omega_0)\tau} d\tau, \quad (13)$$

where $\omega \equiv \omega_p - \omega_0$, ω_p is the frequency of the probe field and $P(t) = d_1 A_{01} + d_2 A_{02}$ is the component of the atomic polarization operator in the direction

of the probe field polarization vector \mathbf{e}_p , with $d_j = \mathbf{e}_p \cdot \mathbf{d}_{0j}$. The effects of quantum interference are most pronounced in the region where $\omega_{21} \leq 2\gamma_j$.

To monitor quantum interference, we introduce a factor η ($= 0, 1$) in the cross transition terms $g_i g_j^*$. When $\eta = 0$, the cross transitions are switched off, so no quantum interference is present—the dashed curves in the following figures. For $\eta = 1$, the effect of quantum interference is maximal (indicated by the solid curves).

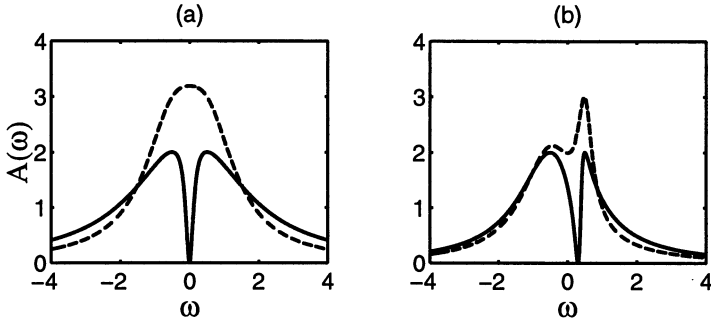


Fig. 2. Absorption spectrum for $\kappa = 100$, $\omega_{21} = 1$, $\delta = 0$, and $g_1 = g_2 = 10$ in (a), $g_1 = 10$, $g_2 = 5$ in (b). The solid curves give the spectrum for maximal interference ($\eta = 1$), and the dashed curves for no interference ($\eta = 0$).

Figure 2 shows the typical effects of quantum interference: narrow resonance at line centre and transparency. The resonance has a Lorentzian-like lineshape and probe transparency occurs at the central frequency ω_0 for two identical atom-cavity coupling constants ($g_1 = g_2 = 10$), as illustrated in Fig. 2(a). However, for $g_1 \neq g_2$, as we see in the frame 2(b) for instance, a Rayleigh-wing-like resonance is evident at line-centre, and the transparency is shifted from the centre frequency. These features are the same as those of a Vee-atom with two parallel dipole moments in free space [22]. In fact, Fig. 2 falls into the limit of $\kappa = 100 \gg \omega_{21} = 1$, where the system obeys the master equation (12).

As we have pointed out, when the level splitting is much greater than the cavity-induced decay rates of the excited levels, the effect of quantum interference disappears. Nevertheless, one can modify the Autler-Townes doublet by tuning the cavity frequency even in this case. In Fig. 3 we take $\omega_{21} = 200$, $\kappa = 100$, $g_1 = g_2 = 20$. When $\delta = 0$ (curve (a)), the spectrum is a well resolved, symmetric, Autler-Townes doublet, whilst when $\delta = 100$ (curve (b)), one component of the doublet is enhanced and the other is suppressed. The enhancement and suppression of the doublet result from changes to the level decay rates produced by tuning the cavity frequency. For example, for $\delta = 0$, $\gamma_1 = \gamma_2 = 2$, whilst for $\delta = 100$, $\gamma_1 = 0.8$ and $\gamma_2 = 4$. The large value of the latter arises because the transition channel $|0\rangle \leftrightarrow |2\rangle$ is resonantly enhanced

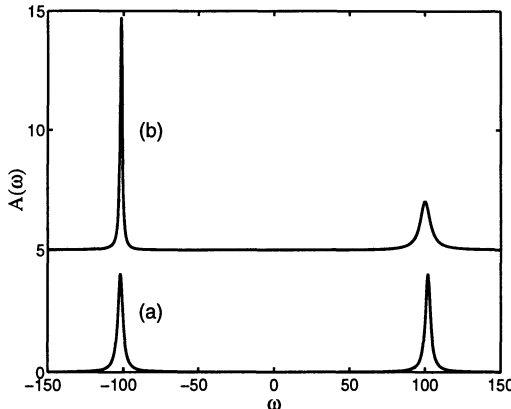


Fig. 3. Absorption spectrum for $\kappa = 100$, $\omega_{21} = 100$, $g_1 = g_2 = 20$, and $\delta = 0$ in (a), $\delta = 100$ in (b). The curve (b) is raised by 5 units for clarity.

by the coupling to the cavity field, which leads to a large decay rate of the level $|2\rangle$. The transition $|0\rangle \leftrightarrow |1\rangle$ is however suppressed, resulting in a small decay rate for level $|1\rangle$. Consequently, the lower-frequency spectral line, originating from the transition $|0\rangle \leftrightarrow |1\rangle$, is very narrow and high, whilst the spectral line resulting from the transition $|0\rangle \leftrightarrow |2\rangle$ is wide and low.

In summary, we have shown that maximal quantum interference can be achieved in a Vee-type atom coupled to a single-mode, frequency-tunable cavity field with a pre-selected polarization in the bad cavity limit. There are no special restrictions on the atomic dipole moments, as long as the polarization of the cavity field is pre-selected.

Acknowledgment. It is a pleasure to acknowledge helpful conversations with G. S. Agarwal, Z. Ficek, C. H. Keitel, S-Y. Zhu and M. S. Zubairy.

References

1. H. J. Carmichael *et al.*, Phys. Rev. Lett. **58**, 2539 (1987);
2. Peng Zhou and S. Swain, Phys. Rev. Lett. **59**, 1603, (1999).
3. G. Vemuri *et al.*, Phys. Rev. A **41**, 2749 (1990); **50**, 2599 (1994); P. Zhou and S. Swain, *ibid.*, **58**, 4705 (1998).
4. N. G. van Kampen, “Stochastic Processes in Physics and Chemistry” (North Holland, Amsterdam, 1981), Chapter XIV; Physics Rep. **24**, 171 (1976), and references therein.
5. P. Zhou and S. Swain, Phys. Rev. A **58**, 1515 (1998).
6. S. Swain, *ibid.* **73**, 1493 (1994); S. Swain and P. Zhou, Phys. Rev. A **52**, 4845 (1995).
7. C. Chen *et al.*, Phys. Rev. A **49**, 461 (1994).
8. Q. Wu *et al.*, Phys. Rev. A **49**, R1519; **50**, 1474 (1994)

9. E. Arimondo, in *Progress in Optics*, North Holland, Amsterdam, 1996, p.257; J. P. Marangos, J. mod. Optics, 45, 471 (1998).
10. S. E. Harris, Phys. Rev. Lett. **62**, 1033 (1989); S. E. Harris and J. J. Macklin, Phys. Rev. A **40**, R4135 (1989); A. Imamoglu, Phys. Rev. A **40**, R2835 (1989).
11. K. J. Boller, A. Imamoglu and S. E. Harris, Phys. Rev. Lett. **66**, 2593 (1991).
12. M. O. Scully, Phys. Rev. Lett. **67**, 1855 (1991).
13. D. A. Cardimona, M. G. Raymer and C. R. Stroud Jr., J. Phys. B **15**, 65 (1982); G. C. Hegerfeldt and M. B. Plenio, Phys. Rev. A **46**, 373 (1992).
14. P. Zhou and S. Swain, Phys. Rev. Lett. **77**, 3995 (1996); Phys. Rev. A **56**, 3011 (1997).
15. S. Y. Zhu and M. O. Scully, Phys. Rev. Lett. **76**, 388 (1996); E. Paspalakis and P. L. Knight, Phys. Rev. Lett. **81**, 293 (1998).
16. H. R. Xia, C. Y. Ye and S. Y. Zhu, Phys. Rev. Lett. **77**, 1032 (1996).
17. E. Paspalakis, N. J. Kylstra, and P. L. Knight, Phys. Rev. Lett. **82**, 2079 (1999).
18. A. K. Patnaik and G. S. Agarwal, Phys. Rev. A **59**, 3015 (1999).
19. P. R. Berman, Phys. Rev. A **55**, 4886 (1998)..
20. M. O. Scully, S. Y. Zhu and A. Gavrielides, Phys. Rev. Lett. **62**, 2813 (1989). M. Fleischauer, C. H. Keitel, L. M. Narducci, M. O. Scully, S. Y. Zhu and M. S. Zubairy, Opt. Commun. **94**, 599 (1992); S. Y. Zhu, L. M. Narducci and M. O. Scully, Phys. Rev. A **52**, 4791 (1995); G. S. Agarwal, Phys. Rev. A **54**, R3734 (1996).
21. P. Zhou and S. Swain, Opt. Commun. – to be published
22. P. Zhou and S. Swain, Phys. Rev. Lett. **78**, 832 (1997); J. Opt. Soc. Am. B **15**, 2583 (1998).
23. P. Zhou and S. Swain, Phys. Rev. A **58**, 1515 (1998), and references therein.

Tests on Nonlinear Polymeric Waveguides for All-Optical Processing

Stefano Sottini and Francesca Gelli

Istituto di Ricerca sulle Onde Elettromagnetiche Nello CARRARA, Via Pancaitichi 64 -50127 Firenze *Italy*

Abstract. All optical devices which utilize nonlinear polymer waveguides result to be simpler and probably more reliable than analogous devices based on second order cascading processes. Here the fabrication and characterization of some polydiacetylene waveguides is described, then nonlinear tests on such guides are reported which are based on four wave mixing. Hybrid organic-glass guides has proved to be of great help in these tests. Finally some preliminary results on a new polycarbazolyldiacetylene are shown. In particular, nonlinear measurements based on surface plasmon resonance, if confirmed by further investigations, are very promising, giving a third order susceptibility which is an order of magnitude better than that of PTS which is probably the most nonlinear known polymer.

1 Introduction

Nonlinear optics is attracting increasing attention in view of practical applications in telecommunications and, more in general, in signal processing. All optical devices, that is devices driven by optical signals instead of electrical ones, are particularly intriguing also as efficient sources of entangled photons for quantum optic applications [1]. They can be based both on a third order process (TOP) and on a cascading of two second order processes (CP's). The latter solution is likely the most studied at the moment because the CP efficiency η depends on an effective third order susceptibility χ_{eff} which is proportional to the square of the second order susceptibility, $[\chi^{(2)}]^2$: whenever a direct comparison is possible, the CP effective susceptibility turns out to be substantially larger than the third order susceptibility $\chi^{(3)}$ of known materials . On the other hand, devices based on CP show also some problems, related to the need of noncentrosymmetric nonlinear materials and to severe phase matching problems since CP usually includes second harmonic generation (SHG).

The previous considerations suggest that the investigation of new materials with higher nonlinearities and the utilization of waveguide configurations to minimize the operating power are fundamental topics of the present research activity. Only few classes of materials show interesting nonlinear properties, among them organics seem very promising. In the case of CP applications, they must be processed to get thin films which have a noncentrosymmetric structure and suitable for waveguiding. The noncentrosymmetry is usually achieved by electric poling (EP), while periodic EP or bleaching

are the techniques currently used to get quasi phase matching (QPM). In the case of TOP, material ordering is not strictly required even if it can help to enhance the nonlinearity. Phase matching conditions are often automatically satisfied. In conclusion, even if waveguide devices based on PC are expected to be more efficient, their fabrication is much more complex and their performances are more critic because of the phase matching, thus the investigation of new third order materials is of great interest to realize simpler and, probably, more reliable devices. Here our activity is reviewed which has been focused to fabricate third order nonlinear polymer waveguides and to characterize them. Our nonlinear tests are usually based on four wave mixing (FWM), but in the last section of this paper some preliminary nonlinear tests are reported on a new polydiacetylene, polycarbazolyldiacetylene (DCHD-HS), which were performed by surface plasmon resonance (SPR).

2 Preparation and linear characterization of guided-wave structures based on third-order organic molecules

The $\chi^{(3)}$ nonlinear waveguides and the related active materials must satisfy several basic requirements in order to be used in all-optical signal processors (AOSP): i) the transverse dimension of the nonlinear waveguide must be large enough to make *self-focusing* effects negligible, and its length must be short enough to avoid the *spectral broadening* of pump pulses and long enough to produce a large nonlinear effect ($\approx 1\text{cm}$); ii) linear losses must be low $\alpha < 0.2\text{cm}^{-1}$; iii) both damage threshold and saturation value for the Kerr-induced refractive index change Δn_{sat} must be large; iv) the material response time τ must be on the subpicosecond time scale; and v) the nonlinearity must exhibit a real component $n_2 > 10^{-6}\text{m}^2/\text{W}$ and a minimum two photon absorption (TPA) coefficient β (cm/GW).

In this sense, organics, in the form of conjugated molecules are promising because, in principle, they allow the full exploitation of fiber bandwidth ($\approx 25\text{Tbit/sec}$), and their processability is expected to reduce both the costs and the integration problems. Table 1 summarizes the most recent results concerning their applications to waveguide AOSP. T and W are figures of merit related to TPA and linear absorption respectively. According to these data, none of the organics available at present can yet be considered as a candidate for the development of operating devices. PTS (p-toluene-sulfonate), which exhibits the best figures of merit is poorly processable, and its nonlinearity ($n_2 = 2 \times 10^{-16}\text{m}^2/\text{W}$ at 1600nm) is still one order of magnitude lower than that required by low power applications [2], however a considerable improvement in the figures of merit of the materials is expected from molecular engineering; for example PDCHD-HS which is currently under investigation by us seems to be very promising: some preliminary tests which confirm this expectations are reported in the last section of this paper. Moreover good

expectations come also from the novel techniques of epitaxial growth, which are aimed at increasing macroscopic nonlinearity through supramolecular ordering.

2.1 Preparation and characterization of thin film polymer waveguides

We have investigated the Langmuir-Blodgett (LB) technique with the aim of obtaining ordered $\chi^{(3)}$ nonlinear films. In particular, we have studied monolayers and LB multilayers of poly-3butoxy-carbonyl-methyl-urethane (P3BCMU), which is a polydiacetylene obtained from the 3BCMU monomer, either by γ - or UV-irradiation: the resulting mean molecular weight is quite different in the two cases, being 375000g/mol and 35000g/mol, respectively.

Table 1. Polymers for third-order nonlinear integrated optics (off-resonance values)

| material | wavelength (μm) | method | n_2 (m^2/W) | β (cm/GW) | $T =$ $2\beta\lambda/n^2$ | $W =$ $\frac{\Delta n_{sat}}{\alpha\lambda_0}$ |
|--------------------|---------------------------|---|----------------------|--------------------|------------------------------|---|
| P-4BCMU (1991) | 1.3 (60ps 10Hz) | SPM (waveguide) | 5×10^{-18} | .25 | ≈ 1 | 0.02 |
| P-3BCMU (1998) | 1.3 (60ps 10Hz) | NDFWM + NL transmission (waveguide) | $\approx 10^{-17}$ | 7 | 8 | 0.2 |
| PPV (1995) | 0.8 (125fs 10Hz) | DFWM (films) | $>10^{-15}$ | 80 | ≈ 1 | / |
| DPOP-PPV (1997) | 0.88-0.99 (2ps 10Hz) | SPM (waveguide) | 10^{-18} | .1 | ≈ 2 | / |
| DANS (1993) | 1.3 (90ps 10Hz) | SPM (waveguide) | 8×10^{-18} | .08 | 0.3 | 1.6 |
| PTS (1994) | 1.06 (35ps 10Hz) | Z-scan (films) | 5×10^{-16} | 100 | 4 | 10 |
| PTS (1994) | 1.6 (65ps 10Hz) | Z-scan (films) | 2×10^{-16} | <0.5 | 0.08 | 6 |

The $\pi - A$ isotherms of the two polymer batches showed a plateau which is related to a first order thermodynamic phase transition. However, apart from some qualitative common trends, the isotherms of the two batches were different. In particular the variation of enthalpy and entropy corresponding to the phase transition resulted to be slightly larger in the γ /P3BCMU: this implies that such transition induces a larger increase in ordering of the γ /P3BCMU monolayers. It is confirmed by the visible spectra of P3BCMU LB films (Fig.1) which showed a peak at 632nm and a large band centered at about 560nm. The peak corresponds to the excitonic transition, which is

related to the high nonlinear response of P3BCMU. The large band is associated with the chains distortions resulting in more localized excitons and in shorter effective conjugation length. The relative intensity of the peak at 632nm increased with increasing transfer pressure and with the number of layers. The excitonic peak at 632nm was more intense in the γ /P3BCMU films. In contrast, as depicted in Fig. 1, the spectra of UV/P3BCMU films transferred at the same surface pressure and with a higher number of layers were more similar to the spectra of disordered spun films, which were obtained from a 20g/l solution of γ /P3BCMU in CHCl₃. Resonance Raman Spectra (RRS) also confirmed these results [3]. On the other hand, spin coated films balance their poorer nonlinear properties with a much higher optical quality up to a thickness of some microns, resulting to be better candidates for waveguide nonlinear tests. In practice, the high scattering losses of P3BCMU LB films prevented both their efficient insertion inside guided-wave structures and a thorough nonlinear characterization.

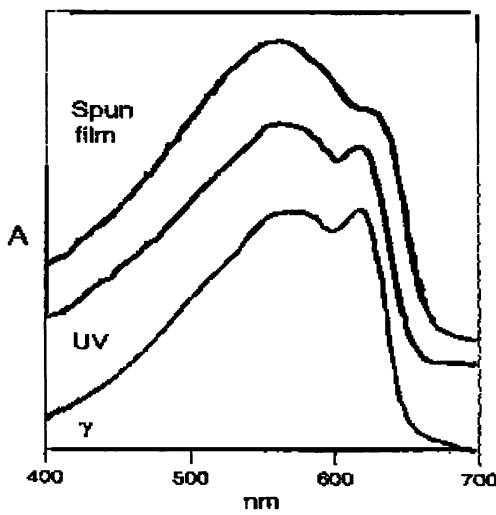


Fig. 1. UV-Vis spectra of LB films of γ /P3BCMU and UV/P3BCMU. For comparison, the spectrum of disordered spun film, obtained from 20 g/l solution of γ /P3BCMU in chloroform is also reported

Waveguides of the soluble conjugated polymers poly-3butoxyl-carbonyl-methyl-urethane (P3BCMU), poly-3-alkylthiophene (P3DT) and poly-carbazoly-diacylene (PDCHD-HS) have been produced using the spin coating technique. Their linear optical properties (TE and TM refractive index and propagation losses) were measured at different wavelengths in the near infrared. The main results are summarized in Table 2.

P3BCMU films were spun from CHCl₃ solutions: the process enabled films to be produced which had a thickness varying between 0.1 and 6.5 μ m and a uniformity, that was better than 10% over 2cm². The electronic spectrum is reported in Fig. 2, dashed line. It is evident from Table 2 that spun P3BCMU

films exhibit birefringence. The high value of n_{TE} suggests that the spinning process results in an alignment of polymer chains in the film plane, where the material is isotropic. This is confirmed by the low n_{TM} , which is very close to that of the P3BCMU monomer, and by its small dispersion. Consequently, nonlinear guided-wave tests on these films require TE propagation for the pump optical fields, since the expected material nonlinearity is negligible for out-of-plane excitation. The linear optical properties of UV- and γ -polymerized P3BCMU were also significantly different. A 1% difference in refractive index was observed (to be compared with the 0.05% experimental error), and the waveguide propagation losses were about 25% larger in the low molecular weight films.

Table 2. Linear optical properties of spin coated polymeric waveguides

| | P3BCMU (CHCl ₃ solution) | P3DT (CHCl ₃ solution) | PDCHD-HS (toluene solution) |
|------------------|---|---|--------------------------------|
| $n_{TE}(849nm)$ | 1.6680 | 1.615 | 1.585 |
| $n_{TM}(849nm)$ | 1.522 | 1.615 | 1.563 |
| $\alpha(849nm)$ | 11dB/cm | | 8.5dB/cm |
| $n_{TE}(1064)$ | 1.622 | | |
| $\alpha(1064nm)$ | 5dB/cm | | |
| $n_{TM}(1321nm)$ | 1.6133 | 1.592 | 1.567 |
| $n_{TE}(1321nm)$ | 1.506 | 1.592 | 1.548 |
| $\alpha(1321nm)$ | 3dB/cm | 6dB/cm | 5dB/cm |
| $n_{TM}(1560nm)$ | 1.5955 | | |
| $n_{TE}(1528nm)$ | 1.5946 | | |

Several batches of P3DT were synthesized at ICM-CNR, Milan by using different catalysts: materials having different molecular weight and dispersivity were obtained, as a result. Solutions of P3DT in CHCl₃ with concentrations ranging between 30 and 60g/l were used for the spin-coating process, and films up to 2 μ m thick were prepared [4]. A typical electronic spectrum is shown by the continuous line of Fig. 2. The waveguide propagation losses were, in general, rather high and often unpredictable, probably because many samples rapidly deteriorated after the spinning. However, the 6 dB/cm value observed at 1321 nm in samples obtained from low molecular weight material, suggests that guided-wave nonlinear tests can actually be performed.

PDCHD-HS is a novel material, that was synthesized at the Chemistry Department of the University of Genova in order to combine the outstand-

ing properties of both the diacetylenic skeleton and the carbazolyl group [5]. The room temperature electronic spectrum of monomer free PDCHD-HS in toluene is reported in Fig. 2 (dash-dotted line). The strong peak at 538 nm originated from a purely excitonic transition, followed by a vibronic broader line. The best films of PDCHD-HS were obtained from toluene solution: their refractive indices and propagation losses are reported in Table 2. Unlike P3BCMU and high molecular weight P3DT, these films show no appreciable birefringence, which indicates a different supramolecular organization of the spun material. This fact suggests that this insensitivity to polarization, which is highly appreciated in telecommunications, also holds in the case of the nonlinearity.

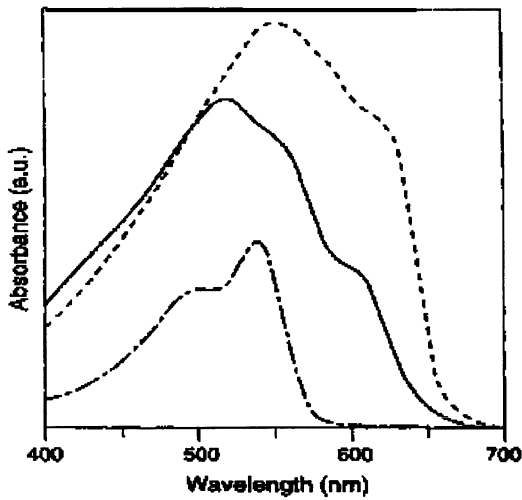


Fig. 2. UV-visible spectra of P3BCMU (dashed line), P3DT (continuous line) and PDCHD-HS (dash-dot line) spin coated films.

2.2 Patterning of polymeric waveguides by photobleaching methods

Future applications require that, in order to develop operating devices, polymer films can be properly patterned. For this reason, the possibility of direct recording of optical elements by means of UV or visible light has been experimentally investigated and subsequently modelled with a two-level picture of the process [6]. This model was verified experimentally with spun P3BCMU films and two different sources: an UV lamp and the 488 nm line of an Ar laser which corresponds to the maximum of the P3BCMU absorption. In the case of blue light exposure, because of the absorption, the effects of the impinging light on the exposed film are localized inside a thin surface layer: the light propagates through such a layer only after its complete bleaching. As

a consequence, the total transmission $T(t)$, which is supposed to be $\ll 1$, becomes:

$$T(t) = \exp[-A(d - vt)] \quad (1)$$

where d is the film thickness, t is the time, A is the initial absorption of the unbleached film and the constant v is the bleaching rate and represents the velocity of propagation inside the film of the sharp interface which separates the bleached and the unbleached material. In general, the photobleaching produces a change in the transmission and refractive index of the material, which is related to a modification of the absorption spectrum. The fine control of the refractive index variation of the exposed material and of the bleaching rate made possible the fabrication of different optical elements on P3BCMU films, such as refractive microlenses (UV exposure), tapers and holographic gratings (blue light exposure). Preliminary experiments were also performed on P3DT and PDCHD-HS samples, which proved to be fully compatible with this processing technique [5,6].

2.3 Hybrid glass/organic waveguide structures

The data on polymer waveguide linear losses which, in the most favourable cases, were of the order of 3 dB/cm , and the observed deterioration of waveguide quality with increasing thickness suggested the development of suitable configurations to reduce propagation inside the polymer as much as possible, to increase the efficiency of coupling with glass fiber networks and to improve field confinement in the nonlinear film. To this end, hybrid glass/polymer waveguides were studied.

Fig. 3 illustrates one example of these hybrid configurations [7]. Linear propagation occurs in a conventional graded-index planar waveguide (GRIN) made by ion-exchange in glass, while the nonlinear interaction is made to occur in the $\chi^{(3)}$ material deposited within a narrow groove, which is perpendicular to the propagation direction of the guided light and is directly etched on the waveguide surface. The functionality of the proposed structure was demonstrated by means of a forward degenerate Four Wave Mixing (FWM) experiment. The results of such experiment, which are in substantially good agreement with the theoretical expectations, suggest that the proposed device can be used to perform efficiently fast all-optical operation in an integrated form (i.e. to develop all-optical AND gates); indeed, it is compatible with different nonlinear materials, and its use is particularly attractive when the active material exhibits large losses (either linear or nonlinear) and low solubility and/or processability, which prevent the fabrication of films of high optical quality. These kinds of devices are expected to gain increasing interest in the near future, provided that cheap and high-resolution replica procedures are developed in order to obtain grooves or other microoptical elements from materials such as sol-gel glass.

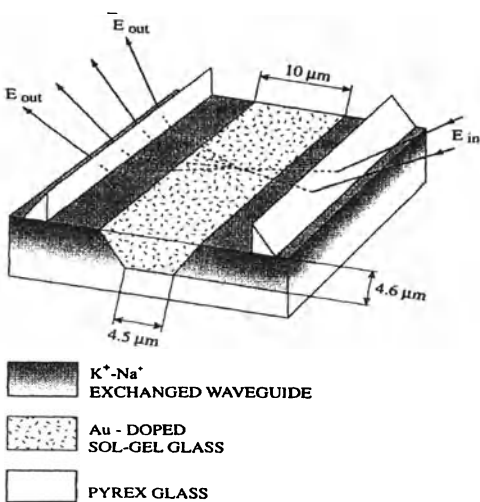


Fig. 3. Sketch of the hybrid structure and of the experimental configuration

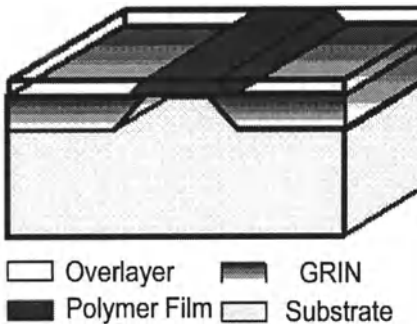


Fig. 4. Sketch of the four-layer tapered coupler (FLTC)

Another example of hybrid waveguiding structure is illustrated in Fig. 4. It can be adopted when the starting polymeric material permits film processing and guided propagation over paths of several millimeters. It is based on two four-layer tapered couplers (FLTC's) that have been especially designed for the efficient transfer of light between a glass waveguide and a polymer film [8]. A nonlinear film is laid on top of a GRIN having a non-constant depth. The GRIN is single mode in the input and output regions, while it disappears completely or, alternatively, is below cutoff, in the central region. These regions are connected by smooth tapers which were designed to maximize the transmission efficiency. The nonlinear film also has tapered edges that were obtained by means of controlled blue light photobleaching. Some

experimental samples containing P3BCMU films were realized for operation at 1300 nm, at this wavelength they were single mode everywhere. Losses $\leq 3\text{dB}$ at each tapered junction were easily achieved with current fabrication procedures; however, a theoretical modelling of the structure showed that a considerable loss reduction, in our case down to 1.5dB, is expected by refining the manufacturing techniques. As a final result, the proposed structure is expected to enable an efficient transfer of light from a large core single mode fiber into a very thin polymeric film ($\leq 1\mu\text{m}$, thus reducing the pulse energy required for the nonlinear operation by a factor of ≈ 5 .

3 Nonlinear tests with polydiacetylene films

Nonlinear tests were performed with P3DT and P3BCMU films in collaboration with Politecnico di Milano and University of Pavia. The first experiments were performed with bulk configurations. The $|\chi^{(3)}|$ of a $2.5\ \mu\text{m}$ thick P3DT film was measured in transmission with a degenerate FWM experiment at $1.3\ \mu\text{m}$, with 60 fs pulses and 1 KHz repetition rate: a value of $7.56 \times 10^{-20}\ \text{m}^2/\text{V}^2$ was obtained, with a response time which was nearly instantaneous on the laser pulse time scale [4]. The same P3DT film and a $6\ \mu\text{m}$ -thick P3BCMU sample were also tested with a nearly degenerate FWM experiment around $1.06\ \mu\text{m}$, with ps pulses and 10 Hz repetition rate: in this case, the $|\chi^{(3)}|$ values were 2.5×10^{-19} and $2.7 \times 10^{-19}\ \text{m}^2/\text{V}^2$, respectively [9].

Successively guided-wave experiments were carried out with a FLTC-based device in the forward degenerate FWM configuration illustrated in Fig. 5 a. The sample was designed for single mode operation at 1053 nm, and consisted of a Na⁺-K⁺ ion-exchanged slab waveguide produced in soda-lime glass and subsequently annealed. The GRIN was $10\ \mu\text{m}$ deep in the input and output regions and $2.5\ \mu\text{m}$ deep in the central region, where it was overlapped by a $0.6\mu\text{m}$ thick and 1.2cm long P3BCMU film. Each taper was 1mm long, and exhibited 3dB coupling losses. The nonlinear experiment was performed with a 50ps Nd:YLF laser, emitting at 1053nm with 1KHz repetition rate and 30MW maximum peak power. The two pump beams were made to overlap inside the P3BCMU film with a lens having 800mm focal length; the interaction angle and the width of the overlap area were varied in the $0.3 - 1^\circ$ and $500-1000\mu\text{m}$ ranges, respectively, in order to obtain gratings with at least 5 lines. A delay line was also introduced, in order to vary the coincidence of pump pulses in the interference region. A typical output signal is shown by the inset of Fig. 5(a). It was obtained with 300KW input power per pump beam. The first order diffraction was clearly visible with the CCD camera; its intensity was $10 - 12\%$ of the pumps. Fig. 5(b) shows the variation of diffracted intensity as a function of the temporal delay between pump pulses: the curve width, which is the same as the pump pulse width, confirms the electronic origin of at least a part of the observed effect [10]. As a consequence, a rough evaluation of material $|\chi^{(3)}|$ was performed by

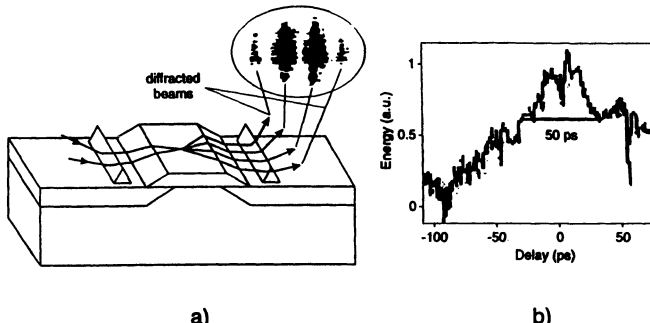


Fig. 5. (a) Experimental configuration adopted for forward degenerate FWM tests with hybrid glass/P3BCMU waveguides. The inset shows the output pump and diffracted beams, as imaged with a CCD camera (b) Diffracted energy versus time delay between pump beams

assuming that only 50% of the observed diffraction efficiency was electronic in origin (that is not thermal). With such diffraction efficiency ($\eta = 6\%$) and an intensity of $1\text{GW}/\text{cm}^2$ confined within the polymeric film, a $|\chi^{(3)}|$ of the order of $3 \times 10^{-19}\text{m}^2/\text{V}^2$ was obtained, in agreement with the bulk measurements reported above.

More recent guided-wave experiments were performed in the nearly degenerate FWM (NDFWM) configuration[11], in order to exclude slow contributions from the nonlinear response. The experiments have been carried out by using two OPO's pumped by the second harmonic of a Nd-YAG laser (10Hz repetition rate, 20ps pulse duration). The strong and weak pump beams were set at $\lambda_1 = 1.27\mu\text{m}$ and $\lambda_2 = 1.29\mu\text{m}$, respectively, and the generation of the new wavelength at $\lambda_3 = 1.25\mu\text{m}$ was monitored. The samples were analogous to the guide structure of Fig.3. A typical experimental result is reported in Fig. 6. After an optical path length of 4.5mm in the polymer waveguide, 1% conversion efficiency for a pump guided intensity of around $100\text{MW}/\text{cm}^2$ was observed, corresponding to a material nonlinearity of $\chi^{(3)} = (1.59 + i0.65) \times 10^{-19}\text{m}^2/\text{V}^2$. The imaginary contribution was too large for practical applications; however, on the basis of the nonlinear transmission experiments reported in [12], the TPA coefficient of poly-3BCMU is expected to become negligible around $1.5\mu\text{m}$, and the development of a practical device seems feasible at this wavelength. Frequency conversion of the order of 1% is inferred at $1.5\mu\text{m}$ with 1W input power (that is, compatible with future possibilities for laser diodes).

The SPR technique was adopted to monitor the Kerr nonlinearity of PDCHD-HS thin films. It is well known that the excitation of a surface electromagnetic wave at the interface between a metallic and a dielectric medium is an angular dependent phenomenon, exhibiting a sharp minimum of the reflected light. Since the position of such minimum is strictly related

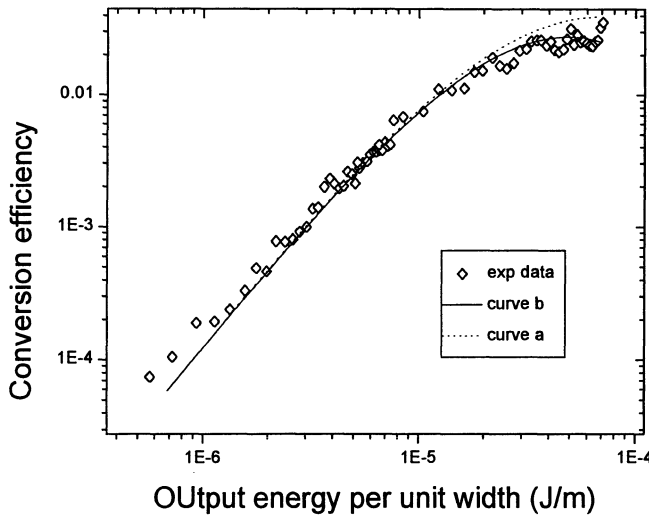


Fig. 6. Conversion efficiency versus pump energy per unit width observed in nearly degenerate FWM performed with glass/P3BCMU hybrid waveguides

to the optical properties of the media, even a weak variation of the refractive index of the dielectric medium can be detected. Therefore, even a small film thickness (10–50nm) is sufficient to demonstrate the Kerr effect, while the thermal contributions can be minimized by using short pulses and low repetition rates. Such tests are in progress, a preliminary result [5], obtained by using the Kretschmann configuration is shown in Fig.7. The thickness of the polymer film was 11.2nm. Two measurements of the coupling angle were performed, at low (8MW/cm^2) and high intensity (0.35GW/cm^2) respectively by using pulses of 20ps. and a repetition rate of 10Hz. A 0.026° angular shift of the reflectivity dip was observed, which is related to the refractive component of $\chi^{(3)}$. While the broadening of the curve and the variation of its minimum are related to its imaginary part. In conclusion, in this experiment the complex $\chi^{(3)}$ resulted to be:

$$\chi^{(3)} = 4.4 \times 10^{-17} + i3.5 \times 10^{-18} m^2/V^2 \quad (2)$$

Even if these preliminary tests need further confirms they seem to be very promising; in particular , the real part of $\chi^{(3)}$ is an order of magnitude higher than that found in the case of PTS, while the imaginary contribution is expected to diminish moving toward longer wavelengths.

4 Conclusions

Some years ago, the high nonlinearities of the push-pull molecules and the promise of an unlimited real nonlinear susceptibility in conjugated polymers

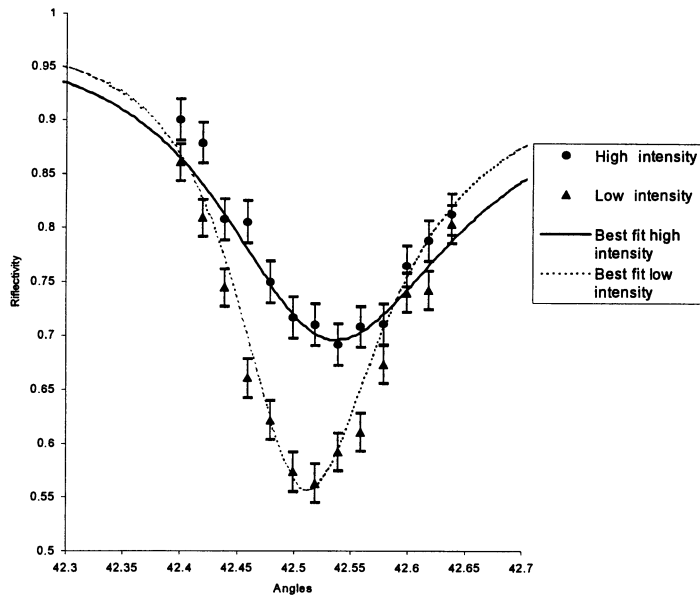


Fig. 7. Angular shift of reflectivity dip due to SPR

gave rise to enthusiastic expectations about the future of organic nonlinear optics. However, a deeper investigation of the materials in terms of modelling, measurements of the nonlinear characteristics and processability, caused a more realistic analysis of the problems to be solved. Nevertheless, taking into account the limited investments on these materials with respect, for example, to inorganic semiconductors, the recent progress of the research in this field is of great interest while the large part of the potentialities of organic materials are still to be explored: the results above reported on PCHD-HS films seem to confirm such expectations. Referring to our nonlinear tests, the combination of organics with glass waveguides within hybrid structures has proved to be quite promising for the nonlinear characterization of organic films, in conditions which are similar to those expected in future devices.

Acknowledgment. The co-operation and scientific support of many people who have contributed to the achievements reported in the present paper are gratefully acknowledged. Particular thanks are due to Emilia Giorgetti, Daniela Grando (presently at CEA, Paris), Luca Palchetti and Giancarlo Margheri (IROE-CNR, Firenze), Sandro De Silvestri (Politecnico and CEQSE-CNR, Milan) and Gianpiero Banfi (University of Pavia).

This research was funded by the Italian Targeted Projects on Special Materials for Advanced Technologies (I and II) and on Telecommunications and RACE 2012 and Brite 7800 Projects of the European Community.

References

1. A. Aspect: Experimental Tests of Bell's Inequalities with Correlated Photons. In: Waves, Information and Foundations of Physics. Pratesi R., Ronchi L (1990) (Eds), Italian Phys. Soc. Conf. Proc., **60**, 345-375.
2. Thakur M., Krol D. M. (1990) Demonstration of all optical phase-modulation in polydiacetylene waveguides. *Appl. Phys. Lett.* **56**, 1213-1215.
3. Grando D., Sottini S. , Gabrielli G.(1998) Monolayers and Langmuir-Blodgett Multilayers of Urethane-Substituted Diacetylene Polymers. *Thin Solid Films*, **327-329**, 336-340.
4. Destri S., Porzio W., Nisoli M., De Silvestri S., Grando D., Sottini S (1994) Poly(3-decylthiophene) as $\chi^{(3)}$ active material in waveguides. *Synthetic Metals* **67**, 293-297.
5. Cravino A., Moggio I., Dell'Erba C., Comoretto D., Cuniberti C., Delle Piane G., Giorgetti E., Grando D., Sottini S.(in press) Linear and Nonlinear Characterization of Poly-DCHD-HS Films. *Synthetic Metals*.
6. Palchetti L., Qu Li, Giorgetti E., Grando D., Sottini S.(1997). Photobleaching of polydiacetylene waveguides: a characterization of the process and patterning of optical elements. *Appl. Opt.*, **36**, 1204-1212.
7. Giorgetti E., Margheri G., Palchetti L., Sottini S., Mennig M.(1998) A guided-wave configuration for two-wave-mixing-based devices containing highly absorbing Au-doped sol-gels. *Appl. Phys. B*, **67**, 587-591.
8. Sottini S., Grando D., Palchetti L., Giorgetti E (1995) Optical Fiber-Polymer Guide Coupling by a Tapered Graded Index Glass Guide. *IEEE Journal of Quantum Electronics*, **QE-31**, 1123-1130.
9. Grando D., Giorgetti E., Palchetti L., Sottini S., Banfi G.P (1996).., Proc. of the International Conf. on Fibre Optics and Photonics, December 9-13, Madras (India), 246-251.
10. Vasil'eva M.A., Vischakas J., Kabelka V., Masalov A.V.(1985) Measurement of relaxation times by phase modulated ultrashort light pulses. *Optics Comm.*, **53**, 412-416.
11. Grando D., Sottini S., Banfi G.P., Fortusini D., Lo Papa M.(1999) Wavelength shifting of optical pulses in a polydiacetylene waveguide. *Appl. Phys. Lett.* **74**, 3601-3603.
12. Banfi G.P., Fortusini D., Dainesi P., Grando D., Sottini S. (1998) Two photon absorption spectrum of 3-butaxy-carbonyl-methyl-urethane polydiacetylene thin films. *J. Chem. Phys.*,**108**, 4319.

Spectroscopic Methods for Atom Localization and Quantum State Measurement

Sajid Qamar and M. Suhail Zubairy

Department of Electronics, Quaid-i-Azam University, Islamabad, Pakistan

Abstract. Entanglement of the atom and field leads towards the measurement of the state of the atom or field depending upon the kind of measurement made. Taking advantage of this fact we suggest spectroscopic techniques based on resonance fluorescence from a two-level atom and Autler-Townes spectrum to localize a single atom and to measure the quantum state of the field.

1 Introduction

When an atom passes through the light field inside a cavity it couples with the field via its dipole moment. This creates an entangled quantum system of atom and field. This entanglement can be used to gain information about the state of the atom or the field depending upon the kind of measurements. In this paper we propose some spectroscopic schemes to find the conditional position distribution of a single atom inside the standing field and also the measurement of the quantum state of the radiation field.

The problem of high resolution position measurement [1] of a single atom is of considerable interest from a theoretical and experimental point of view. This is due to the recent experimental and theoretical progress in fields such as the Bose-Einstein condensation and lithography. Several techniques were proposed in the last decade for the precise information of the position of an atom [2]. In this paper we propose two simple schemes for the atom localization which are based on resonance fluorescence and Autler-Townes spectrum. We show that an atom can be localized within the subwavelength domain of the optical field during its passage through the standing field by making a measurement of the spontaneously emitted photon.

As far as the quantum state measurement is concerned a number of schemes have also been proposed to obtain information about the quantum state of the radiation field [3]. An interest in this subject stems from the possibility of studying nonclassical states of the radiation field, such as the squeezed state [4] and the so-called Schrödinger cat state (which is a coherent superposition of two coherent states) [5]. These states lead to oscillating photon distribution functions. In this article we also show that how the determination of the quantum state, and hence the photon distribution function, from the Autler-Townes spectrum can lead to a direct observation of such nonclassical features.

2 Subwavelength atom localization

In order to understand the concept of the atom localization using spectroscopic methods, we first recall that a two-level atom in an excited state can emit photons spontaneously. The spectrum of the spontaneously emitted photons is a Lorentzian with a width equal to the decay rate. The situation is however different if this atom is driven by a classical field. In that case, the levels experience dynamic Stark shift and the sidebands appear leading to the well-known three-peak spectrum. Similarly in a three level atom in a cascade configuration, where upper two levels are driven by a classical standing field and spontaneous emission takes place due to lower two levels coupling with the reservoir, the response is an Autler-Townes spectrum. In both cases the peaks are located at the Rabi frequency of the driving field. We consider the situation when the Rabi frequency is position dependent therefore the atom-field interaction is position dependent. Hence the spontaneously emitted photons will carry information about the position of the atom inside the standing wave field. This is the basic idea behind the method for atom localization discussed in this section.

We discuss two schemes for atom localization inside the standing field. First scheme utilizes the resonance fluorescence spectrum from a two-level atom [6] and the second scheme is based on the Autler-Townes spectroscopy (driven three-level atom) [7]. In both schemes the atom is driven by a classical standing field.

2.1 Resonance fluorescence spectrum

We consider a two-level atom A with energy levels $|a\rangle$ and $|b\rangle$ and transition frequency ω_{ab} that is described by a center-of-mass wavefunction $f(x)$. The atom is moving along z -axis and interacts with a resonant standing-wave light field of wave-vector $\kappa = \omega_{ab}/c$ aligned along the x direction as shown in Fig.1. The velocity component of the atom along z -axis is considered large enough so that the motion in this direction is treated classically. The driven atom radiates spontaneously and one of the modes of the scattered light interacts with the detector atom B , initially in its ground state. The detector atom consists of the ground level $|\beta\rangle$ and a set of excited levels $|\alpha_k\rangle$. We assume that the scattered light of wave-vector k_0 is absorbed by the detector atom and is excited to an appropriate energy level $|\alpha_{k_0}\rangle$. Our aim is to find the conditional position distribution of the atom A , i.e., the conditional probability $W(x; t | \alpha_{k_0})$ of finding the atom A at position x at time t when the detector atom B is excited to the level $|\alpha_{k_0}\rangle$.

This conditional probability $W(x; t | \alpha_{k_0}) \equiv W(x)$ is then given by

$$W(x) = |f(x)|^2 P(\omega, x, t), \quad (1)$$

with $\omega = |\mathbf{k}_0|/c$ is the frequency of the spontaneously emitted photon and $|f(x)|^2$ is the initial position distribution of the atom. In all of our analysis

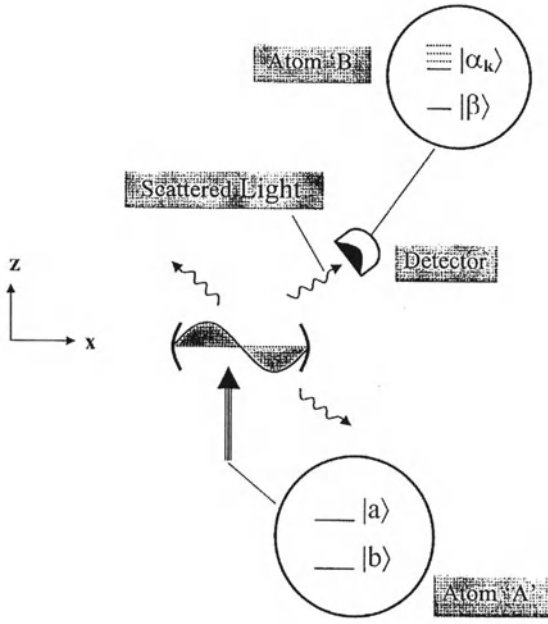


Fig. 1. Two-level atom 'A' moving along z-axis and interacting with a resonant standing wave light field of wave-vector $\kappa = \omega_{ab}/c$ aligned along the x-axis. The driven atom 'A' radiates spontaneously in all directions. The detector atom 'B', consisting of the ground level $|\beta\rangle$ and a set of excited levels $|\alpha_k\rangle$, absorbs the emitted photon in mode k .

for resonance fluorescence spectrum and Autler-Townes spectrum we consider the initial position distribution of the atom, i.e., $|f(x)|^2$, to be constant over many wavelengths of the standing field. Here $P(\omega, x, t)$ is the filter function which is directly proportional to the excitation probability of the detector atom. This excitation probability $P(\omega, x, t)$ is proportional to the power spectrum of the scattered light [8] emitted from the atom A. In the steady state ($t \gg \Gamma^{-1}$) the field emitted by the atom is statistically stationary and we then obtain the power spectrum of fluorescence light [9] for the case when $g(x) \gg \Gamma$ is

$$P(\omega, x, \infty) = \frac{I_0(r)}{8\pi} \left[\frac{3\Gamma/4}{(\Delta + 2g(x))^2 + (3\Gamma/4)^2} + \frac{\Gamma}{\Delta^2 + (\Gamma/2)^2} + \frac{3\Gamma/4}{(\Delta - 2g(x))^2 + (3\Gamma/4)^2} \right] \quad (2)$$

where $I_0(r)$ is a constant and $\Delta = \omega_{ab} - \omega$. This is the well-known three-peak Mollow spectrum, the only difference being the position dependence of the Rabi frequency.

It is evident from Eq. (2) that for zero detuning, $\Delta = 0$, we get peaks for any value of position dependent Rabi frequency and thus for all value of the normalized position κx . These peaks have same heights and thus we expect a

uniform position distribution over the entire wavelength domain. An increase in Δ corresponds to the localization of the atom at different positions inside the standing wave depending on the value of the position dependent Rabi frequency $g(x)$. We obtain four maxima of same heights and widths in the region $0 \leq \kappa x \leq 2\pi$ located at $\kappa x = \pm \sin^{-1}(\Delta/2G) \pm n\pi$ ($n = 0, \pm 1$). For small values of Δ , these maxima are located near the nodes of the standing wave. However with the increased detuning, these peaks move towards the antinodes of the standing wave. For $\Delta = \pm 2G$, four maxima merge into two and lie on the antinodes of the standing wave. There are no resonances for $|\Delta| > 2G$ and we obtain a flat position distribution over the wavelength domain (Fig. 2)[6].

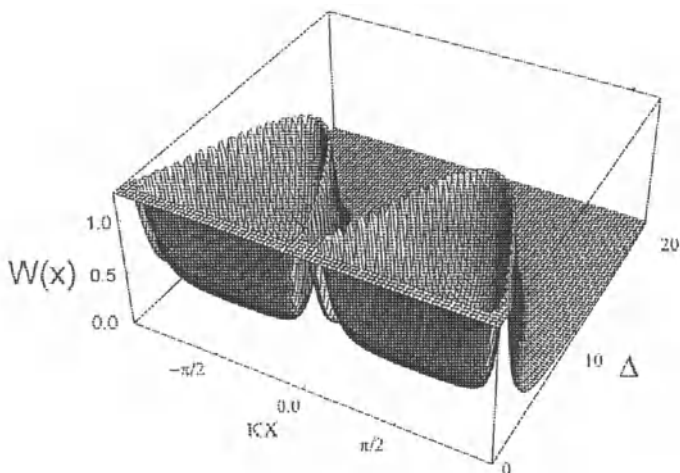


Fig. 2. Conditional position probability distribution $W(x)$ as a function of normalized position κx ($0 \leq \kappa x \leq 2\pi$), and detuning Δ , for $g(x) \gg \Gamma$.

These results indicate a strong correlation between the detuning of the scattered light and the position of the atom. The measurement of a particular frequency corresponds to the localization of the atom in a subwavelength domain of the standing wave.

2.2 Autler-Townes spectroscopy

In our scheme based on the Autler-Townes spectrum we consider the response of a three-level atom, initially in the excited state $|a\rangle$, interacting with the classical standing field. The atomic transition $|c\rangle - |a\rangle$ (upper-level coupling) is detuned with the classical standing field (Fig. 3). The atom with centre

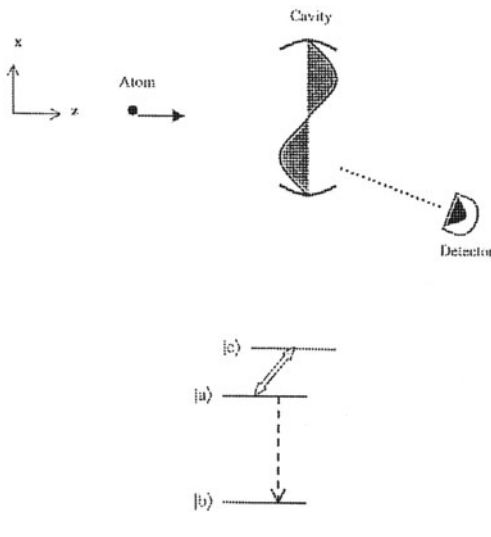


Fig. 3. Three level atom interacting with a nonresonant classical standing field. Spontaneously emitted photon is detected by the detector.

of mass wave-function $f(x)$ decays from the level $|a\rangle$ to the level $|b\rangle$ at a rate γ due to the interaction with the vacuum modes, while we assume that the decay rates from the level $|c\rangle$ and $|b\rangle$ are very small as compared to γ so that we can ignore these. Our aim here is to show that the detuning $\Delta = \omega_{ca} - \omega_0$ can lead to a narrowing of the atom localization peaks in the conditional measurements of the spontaneously emitted photons. The results show a strong narrowing of the peaks for certain values of the detuning present in the upper level coupling case. Hence our proposed modified scheme based on the Autler-Townes spectrum for upper level coupling case increases the precision in the localization of a single atom.

The conditional position probability distribution is now defined as

$$W(x) = \mathcal{F}(x; t | b, 1_k) |f(x)|^2. \quad (3)$$

The steady state ($t \gg \gamma^{-1}$) expression for the filter function $\mathcal{F}(x; t | b, 1_k)$ is

$$\begin{aligned} \mathcal{F}(x; t \rightarrow \infty | b, 1_k) \equiv \mathcal{F}(x) &= |\mathcal{N}|^2 \\ &\left[\frac{|G_{k_o}|^2 (\delta_k + \Delta)^2}{[G^2 \sin^2(\kappa x) - \delta_k^2 - \Delta \delta_k]^2 + (\delta_k + \Delta)^2 \gamma^2 / 4} \right] \end{aligned} \quad (4)$$

where \mathcal{N} is the normalization factor and $\delta_k = \omega_{ab} - \nu_k$.

It is clear from Eq. (4) that the filter function $\mathcal{F}(x)$ depends on the frequency of the spontaneously emitted photon ν_k via δ_k and the detuning Δ present in the atomic transitions $|c\rangle - |a\rangle$. Therefore the atomic transition

from the level $|a\rangle$ to $|b\rangle$ is accompanied by the spontaneous emission of a photon having frequency

$$\nu_k = \omega_{ab} + \frac{\Delta}{2} \mp \frac{1}{2} \sqrt{\Delta^2 + 4G^2 \sin^2(\kappa x)}. \quad (5)$$

This shows that the frequency of the spontaneously emitted photon depends not only on the position dependent Rabi frequency but also on the detuning Δ . By making a measurement of this spontaneously emitted photon we can find out the position distribution of the atom inside the standing field. The peaks in this position distribution are located at the normalized position

$$\kappa x = \pm \sin^{-1} \left(\frac{1}{G} \sqrt{\delta_k(\Delta + \delta_k)} \right) + n\pi, \quad (6)$$

where n is an integer. The widths of all the peaks for a given set δ_k and Δ are equal and are given by

$$w = \left| -\sin^{-1} \left(\frac{1}{G} \sqrt{(\delta_k + \Delta)(\delta_k + \gamma/2)} \right) \right| - \left| \sin^{-1} \left(\frac{1}{G} \sqrt{(\delta_k + \Delta)(\delta_k - \gamma/2)} \right) \right|. \quad (7)$$

For $\delta_k = -\Delta$ we expect a minimum width zero. However at this value the peaks are lying on the nodes of the standing field where the Rabi frequency is zero and the resulting peak is of width $\gamma/2$. As δ_k increases, the peaks move away from the nodes and becomes narrow. The narrow peak is a consequence of quantum interference. For $\delta_k \approx -\Delta$ we get narrow peaks near the nodes of the standing field (Fig. 4. clearly shows this precision localization). A further increase in δ_k however changes the position of the peak maxima away from the node and the width of the peaks starts increasing until $\delta_k = [-\Delta + \sqrt{\Delta^2 + 4G^2}]/2$. At this detuning the peaks have maximum width and they lie at the antinodes.

Therefore we get a much precise position information about the atom in the standing field for $\delta_k \approx -\Delta$ in upper-level coupling case. On contrary in lower-level coupling case the filter function is a superposition of two Lorentzians and no interference term is present. Therefore no quantum interference occurs and we do not expect precision in localization of the single atom[7].

3 Quantum state measurement

As discussed above, when an atom interacts with the intense driving field the splitting of the atomic levels take place which is proportional to the associated Rabi frequency. Thus the spectrum displays peaks which are displaced from the resonance by the Rabi frequency. If the driving field is quantized, the

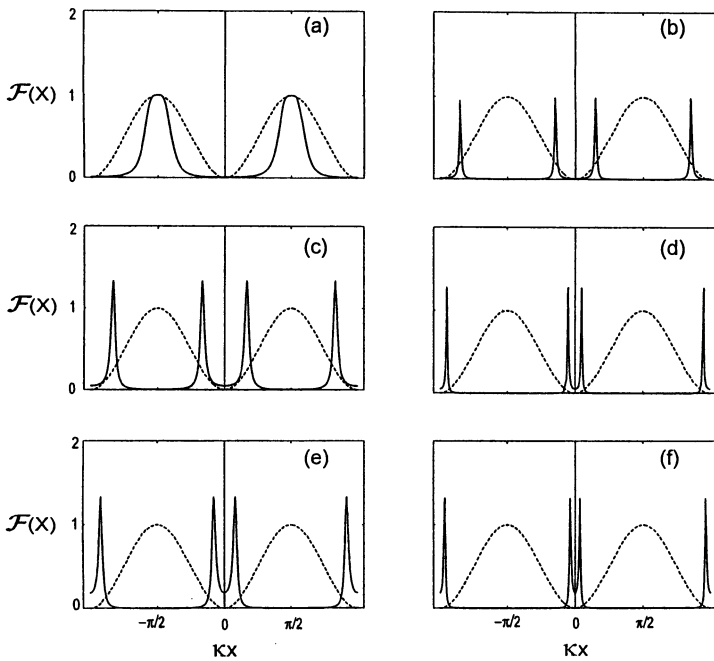


Fig. 4. Strong line narrowing takes place when $\Delta \approx -\delta_k$. Left column shows the spectrum of the filter function $\mathcal{F}(x)$ when $\Delta/G = 0.0$ for (a) $\delta_k/G = 1.0$, (c) $\delta_k/G = 0.5$ and (e) $\delta_k/G = 0.25$. Right column shows the spectrum of the $\mathcal{F}(x)$ when (b) $\delta_k/G = 1.0, \Delta/G = -0.8$, (d) $\delta_k/G = 0.5, \Delta/G = -0.45$, and (f) $\delta_k/G = 0.25, \Delta/G = -0.20$.

associated Rabi frequencies are distributed according to the photon distribution function of the field and the resulting spectrum would mimic the photon distribution function of the driving field. Here we show that the complete Wigner function of a quantum state of the radiation field inside a cavity can be measured via Autler-Townes spectroscopy without resorting to the preparation of coherent superposition of atomic states[10]. We also show that the quantum state of the radiation field can be recovered from the spectrum of the resonance fluorescence from two-level atoms driven by quantized field[11].

3.1 Autler-Townes spectroscopy

The quantum state of the radiation field is described completely by the state vector $|\psi_f\rangle$ for a pure state and by the density operator ρ for a more general mixed state. Equivalent descriptions of the quantum state can be formulated in terms of the quasiprobability distributions such as P -representation,

Q-representation, or the Wigner distribution function. These distributions, which do not have all the properties of a classical probability distribution, allow the evaluation of various correlation functions of the field operators using the methods of classical statistical mechanics. For example, the Wigner distribution function allows the evaluation of symmetrically ordered correlation functions of the creation and destruction operators of the field. Several radiation field states display non-classical features, such as the squeezed state[4] and the so called Schrödinger cat states[5]. These non-classical features are manifested in the quasidistributions such as *P*-representation and the Wigner distribution function.

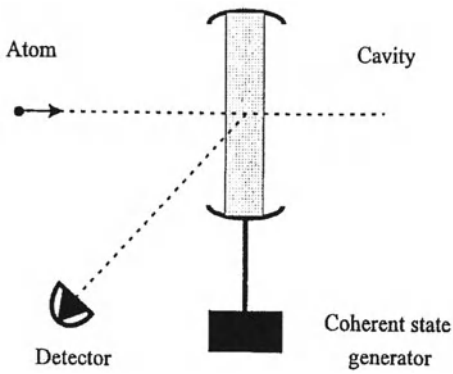


Fig. 5. A three-level atom interacts with the cavity field that contains the quantized field. The cavity is coupled to a resonant classical oscillator such that a coherent state $|\alpha\rangle$ is injected inside the cavity. The spontaneously emitted photon is detected by the detector.

The schematics of our scheme is shown in Fig. 5. A three-level atom initially in the excited state $|a\rangle$ interacts with the cavity field. The atomic transition $|c\rangle - |a\rangle$ is resonant with the cavity field. A source is connected to the cavity such that a coherent state $|- \alpha\rangle$ is injected inside the cavity and the state of the field inside the cavity becomes $D^\dagger(\alpha)|\psi_f\rangle$ where $D(\alpha)$ is the displacement operator given by

$$D(\alpha) = e^{(\alpha a^\dagger - \alpha^* a)}. \quad (8)$$

During the passage of the atom through the cavity, the atom radiates spontaneously from the level $|a\rangle$ to the level $|b\rangle$ at a rate γ . The frequency of the spontaneously emitted photon is measured and the complete spectrum is obtained by repeating the experiment a number of times. The spectrum depends on the complex amplitude α of the coherent state. The experiment is repeated with all possible values of α .

In this scheme we show that the spontaneous emission spectrum yields the photon distribution function when there is no injected field ($\alpha = 0$). In addition the spectrum for each value of α gives the value of the Wigner

function $W(\alpha, \alpha^*)$ in a straightforward way, which in terms of the photon statistics of the displaced state $D^\dagger(\alpha) |\psi_f\rangle$ is defined as

$$W(\alpha, \alpha^*) = \frac{2}{\pi} \sum_n (-1)^n p(n, \alpha). \quad (9)$$

Here $p(n, \alpha)$ is the photon statistics of the displaced state $D^\dagger(\alpha) |\psi_f\rangle$, i.e.,

$$p(n, \alpha) = |\langle n | D^\dagger(\alpha) |\psi_f\rangle|^2. \quad (10)$$

Thus the Wigner function of the field can be found directly if the photon statistics of the displaced state $D^\dagger(\alpha) |\psi_f\rangle$ is known for all values of α .

For our proposed scheme we consider the system of a three-level atom in which the transition $|c\rangle - |a\rangle$ is driven by a quantized field with photon statistics $p(n)$ and transition $|a\rangle - |b\rangle$ is coupled to the vacuum modes. Thus the steady-state ($t \gg \gamma^{-1}$) expression for the spontaneous emission spectrum when there is no injected field ($\alpha = 0$) is given by (apart from a proportionality factor)

$$S(\delta_k) = \sum_{n=0}^{\infty} p(n) \frac{|g_k|^2 \delta_k^2}{(g^2 n - \delta_k^2)^2 + \delta_k^2 \gamma^2 / 4}. \quad (11)$$

To reconstruct the Wigner function from the spontaneous emission spectrum, we inject a coherent state $|-\alpha\rangle$ inside the cavity such that the resulting state inside the cavity is $D^\dagger(\alpha) |\psi_f\rangle$. Now the photon distribution function in the expression of the spectrum corresponds to the displaced state and is given by $p(n) \equiv p(n, \alpha) = |\langle n | D^\dagger(\alpha) |\psi_f\rangle|^2$ and the spectrum $S(\delta_k) \equiv S(\delta_k, \alpha)$ depends on the complex amplitude α . Here the only meaningful values of δ_k^2/g^2 to reconstruct the photon distribution function $p(n, \alpha)$ from the spectrum are the integral values. The reconstructed photon distribution of the displaced state $p_s(n, \alpha)$ is therefore given by those values in the spectrum where $\delta_k = g\sqrt{n}$, and we may write

$$p_s(n, \alpha) \equiv S_N(g\sqrt{n}, \alpha) = \frac{1}{N_u} \sum_{m=0}^{\infty} \frac{p(m, \alpha) n \gamma^2 / 4g^2}{(m - n)^2 + n \gamma^2 / 4g^2}, \quad (12)$$

where $S_N(g\sqrt{n}, \alpha)$ is the appropriately normalized spectrum and N_u is the normalization coefficient that ensures $\sum_n p_s(n, \alpha) = 1$.

Thus the reconstructed Wigner function of the cavity field, using the Eq. 9., is given by

$$W_s(\alpha, \alpha^*) = \frac{2}{\pi N_u} \sum_{m=0}^{\infty} \sum_{n=0}^{\infty} \frac{(-1)^m p(m, \alpha) n \gamma^2 / 4g^2}{(m - n)^2 + n \gamma^2 / 4g^2}. \quad (13)$$

It may be noted that the spectrum for a given value of the injected field $|\alpha\rangle$ gives the Wigner function at a point α in the complex plane and we have to

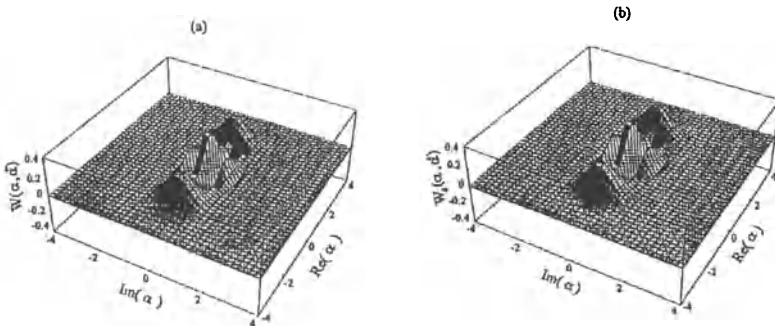


Fig. 6. (a) The Wigner function $W(\alpha, \alpha^*)$ for a Schrödinger cat state with $\alpha_0 = 2$. (b) Reconstructed Wigner function $W_s(\alpha, \alpha^*)$ for $\gamma/g = 0.01$ in the upper-level coupling.

obtain spontaneous emission spectra for different values of α to reconstruct the complete Wigner function.

Fig. 6a, shows the plot of the Wigner function $W_s(\alpha, \alpha^*)$ of the Schrödinger cat state $|\psi_f\rangle = \mathcal{N}(|\alpha_0\rangle + |-\alpha_0\rangle)$ for $\alpha_0 = 2$ where \mathcal{N} is the normalization constant. It is clear from the figure that the Wigner function exhibits two peaks located at $\text{Re}(\alpha) = 2$ and $\text{Re}(\alpha) = -2$. The interference structure observed halfway between the peaks displays the quantum superposition of both amplitudes showing rapid oscillation. The Wigner function also becomes negative in certain regions of α , indicating the nonclassical behavior of the Schrödinger cat state. In Fig. 6b we plot the reconstructed Wigner function $W_s(\alpha, \alpha^*)$ for $\gamma/g = 0.01$. The agreement between the two is excellent.

3.2 Resonance fluorescence spectrum

Going back to the conceptually simplest system in quantum optics, i.e. the resonance fluorescence from a two-level atom, we show that the quantum state of the radiation field can be directly recovered from the spectrum of the resonance fluorescence when the atoms are driven by the quantized field.

Here we again consider the system of two-level atoms with levels $|a\rangle$ and $|b\rangle$ which are now driven by a quantized field inside a high Q cavity [12]. The driven atoms radiate spontaneously in all directions and we look at the spectrum of the radiated light.

For a quantized field, there are four single-photon spontaneous emission lines present in the spectrum. These lines are located at

$$\begin{aligned}\omega &= \omega_{ab} \pm (\Omega_n \pm \Omega_{n-1})/2, \\ &= \omega_{ab} \pm g(\sqrt{n+1} \pm \sqrt{n}).\end{aligned}\quad (14)$$

Thus a plot of the fluorescence spectrum $S(\omega)$ versus δ/g (with $\delta = \omega - \omega_{ab}$) would yield four peaks for each value of n located at $\pm(\sqrt{n+1} \pm \sqrt{n})$ distributed according to the photon distribution function $p(n)$. Thus we should

be able to recover the distribution function of the field from the resonance fluorescence spectrum via the relation

$$p_s(n) = \begin{cases} \frac{1}{N} S(\omega)|_{\delta/g=(\sqrt{n+1}+\sqrt{n})}, & \text{when } n > 0 \\ \frac{1}{2N} S(\omega)|_{\delta/g=1}, & \text{when } n = 0, \end{cases} \quad (15)$$

where N is the normalization factor and $S(\omega)$ is the physical spectrum of the non-stationary fluorescent light at some suitably chosen point \mathbf{r} in the far-field for the condition $g \gg \gamma_d \gg 1/T \gg \Gamma$.

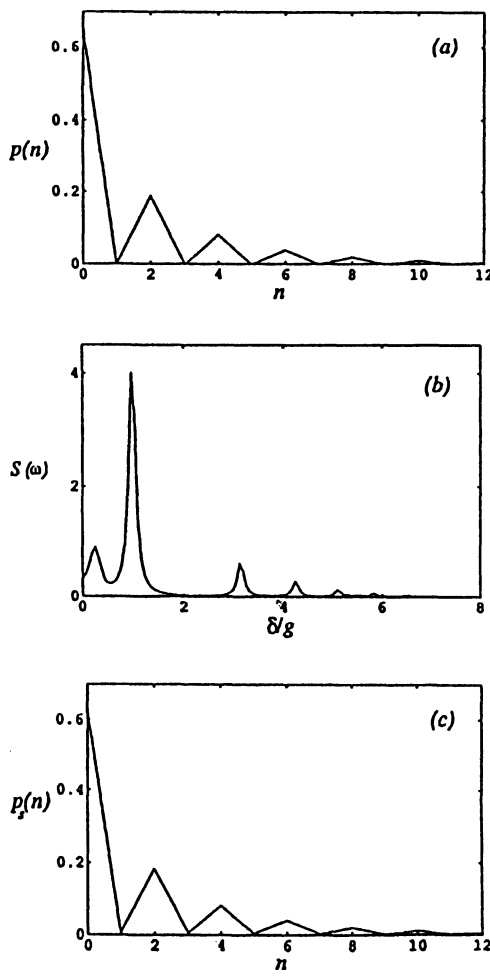


Fig. 7. (a) Photon distribution function $p(n)$ for a squeezed vacuum state with $r = 1$. (b) The spontaneous emission spectrum S (in arbitrary units) vs δ/g for $\gamma_d/g = 0.1$, $gT = 100$, and $\Gamma/g = 0.001$. (c) The photon distribution function $p_s(n)$ recovered from (b) according to Eq. (15).

We now consider an example to illustrate how the photon statistics $p(n)$ can be determined from the spectrum $S(\omega)$. We assume that the driving field is in a squeezed vacuum state whose photon distribution function is highly oscillatory as shown in Fig. 7a. The corresponding spontaneous emission spectrum (S vs δ/g) is shown in Fig. 7b, for $\gamma_d/g = 0.1$, $gT = 100$, and $\Gamma/g = 0.001$. It shows peaks located at $\sqrt{n+1} \pm \sqrt{n}$. The only visible peaks corresponding to $(\sqrt{n+1} - \sqrt{n})$ are located at $\delta/g = 1$ and 0.41 corresponding to $n = 0$ and 1 , respectively, the rest being too close to $\delta/g \simeq 0$. The photon distribution $p_s(n)$ can now be recovered by using Eq. (15). The resulting distribution is shown in Fig. 7c. The agreement between the original photon distribution and the recovered distribution is excellent. Thus a direct evidence of the oscillatory photon distribution can be obtained using this method.

In summary, we present spectroscopic schemes based on resonance fluorescence and Autler-Townes spectrum for the atom localization and the quantum state measurement of the radiation field. These schemes give a direct and rather simple way to get the position information of the single atom during its passage through the standing classical field. This localization of the atom is done within the subwavelength domain of the optical field. The reconstruction of the Wigner function and hence the complete quantum state measurement is done without any cumbersome numerical computation. These schemes, which require direct detection of the scattered field, are independent of the detector efficiency and are experimentally accessible due to the recent development in the field[12–14].

References

1. J. E. Thomas and L. J. Wang, Phys. Rep. **262**, 311 (1995); G. Rempe, Appl. Phys. B **60**, 233(1995).
2. P. Storey, M. Collett, and D. F. Walls, Phys. Rev. Lett. **68**, 472 (1992); P. Storey, M. Collett, and D. F. Walls, Phys. Rev. A **47**, 405 (1993); M. A. M. Marte and P. Zoller, Appl. Phys. B **54**, 477 (1992); A. M. Herkommer, V. M. Akulin, and W. P. Schleich, Phys. Rev. Lett. **69**, 3298 (1992); R. Quadt, M. Collett, and D. F. Walls, Phys. Rev. Lett. **74**, 351 (1995); A. M. Herkommer, H. J. Carmichael, and W. P. Schleich, Quant. Semiclass. Optics **8**, 189 (1996); M. Brune, S. Haroche, V. Lefevere, J. M. Raimond, and N. Zagury, Phys. Rev. Lett. **65**, 976 (1990); M. Brune, S. Haroche, J. M. Raimond, L. Davidovich, and N. Zagury, Phys. Rev. A **45**, 5193 (1992); Fam Le Kien, G. Rempe, W. P. Schleich, and M. S. Zubairy, Phys. Rev. A **56**, 2972 (1997).
3. K. Vogel and H. Risken, Phys. Rev. A **40**, 2847 (1989); D. T. Smithey, M. Beck, M. G. Raymer, and A. Faridani, Phys. Rev. Lett. **70**, 1244 (1993); G. M. D'Ariano, U. Leonhardt, and H. Paul, Phys. Rev. A **52**, R1801 (1995); U. Leonhardt and H. Paul, Phys. Rev. A **52**, 4899 (1995); G. M. D'Ariano, C. Macchiavello, and M. G. Paris, Phys. Lett. A **195**, 31 (1994); S. Schiller, G. Breitenbach, S. F. Pereira, T. Müller, and J. Mlynek, Phys. Rev. Lett. **77**, 2933 (1996); M. S. Zubairy, Phys. Lett. A **222**, 91 (1996); T. Azim and M. S. Zubairy,

- Phys. Lett. A **250**, 344 (1998); H. Paul, P. Törmä, T. Kiss, and I. Jex, Phys. Rev. Lett. **76**, 2464 (1996); P. J. Bardroff, E. Mayr, and W. P. Schleich, Phys. Rev. A **51**, 4963 (1995); M. Brune, F. Schmidt-Kaler, A. Maali, J. Dreyer, E. Hagley, J. M. Raimond, and S. Haroche, Phys. Rev. Lett. **76**, 1800 (1996).
- 4. For a review on squeezed states, see K. Zaheer and M. S. Zubairy, in *Advances in Atomic, Molecular, and Optical Physics*, Vol. 28, edited by D. Bates and B. Bederson, (Academic Press, New York 1991), p. 143.
 - 5. E. Schrödinger, Naturwissenschaften **23**, 807 (1935); **23**, 823 (1935); **23**, 844 (1935) [English translation by J. D. Trimmer, Proc. Am. Phys. Soc. **124**, 3325 (1980)].
 - 6. Sajid Qamar, S. Y. Zhu, and M. S. Zubairy, (to be published).
 - 7. Sajid Qamar, S. Y. Zhu, and M. S. Zubairy, (to be published).
 - 8. J. H. Eberly and K. Wodkiewicz, J. Opt. Soc. Am. **67**, 1252 (1977).
 - 9. See, for example M. O. Scully and M. S. Zubairy, *Quantum Optics*, (Cambridge Press, 1998).
 - 10. M. Mahmoudi, H. Tajalli, and M. S. Zubairy, (to be published).
 - 11. M. S. Zubairy, Phys. Rev. A **57**, 2066 (1998).
 - 12. D. Meschede, H. Walther, and G. Müller, Phys. Rev. Lett. **54**, 551 (1985).
 - 13. See, for example, G. Raithel, C. Wagner, H. Walther, L. M. Narducci, and M. O. Scully, in *Advances in Atomic, Molecular, and Optical Physics*, edited by P. Berman (Academic, New York, 1994).
 - 14. Q. A. Turchette, R. A. Thompson, and H. J. Kimble, Appl. Phys. B: Photophys. Laser Chem. **60**, S1 (1995); C. J. Hood, M. S. Chapman, T. W. Lynn, H. J. Kimble, Phys. Rev. Lett. **80**, 4157 (1998).

Teleporting an Atomic Wavepacket

Scott Parkins¹ and Jeff Kimble²

¹ University of Auckland, Physics Department, Private Bag 92019, Auckland, New Zealand

² California Institute of Technology, Norman Bridge Laboratory of Physics 12-33, Pasadena, CA 91125, USA

Abstract. We outline a scheme for teleporting an unknown atomic center-of-mass wave function between distant locations. This scheme employs interactions in cavity quantum electrodynamics to facilitate a coupling between the motional degrees of freedom of an atom trapped inside a cavity and external propagating light fields. This enables the distribution of quantum entanglement and the realization of the required motional Bell-state analysis.

1 Introduction

Teleportation of unknown quantum states from one location to another is now an experimental science, with initial attempts directed to the teleportation of the polarization state of a photon [1,2] and then the first complete realization performed with optical coherent states [3]. The former experiments were based on the original procedure for finite-dimensional quantum systems (in particular, two-state systems) proposed by Bennett and coworkers [4], and the latter on a continuous variable (i.e., infinite dimensional) adaptation of this procedure put forward by Vaidman [5] (see also [6,7]). In both instances, though, the essential ingredient in the teleportation procedure is quantum entanglement of a bipartite system shared by the sender, Alice, and the receiver, Bob. For experiments with light, this entanglement can be generated via the process of parametric amplification (see, e.g., [8]).

While the experiments performed thus far have dealt exclusively with light, the procedure of Vaidman offers, in principle, the possibility of teleporting the quantum states of massive particles. The required quantum entanglement in this procedure takes the form of the original Einstein-Podolsky-Rosen (EPR) state of two particles; that is, a state in which the positions and momenta of the particles (labelled 2 and 3) are perfectly anticorrelated and correlated, respectively:

$$x_2 + x_3 = 0, \quad p_2 - p_3 = 0. \quad (1)$$

Joint measurements performed on particle 1, whose state is to be teleported, and particle 2 then establish a correlation between particles 1 and 3. In particular, measurements of the quantities $x_1 + x_2$ and $p_1 - p_2$, with outcomes

$$x_1 + x_2 = a, \quad p_1 - p_2 = b, \quad (2)$$

establish the relationship

$$x_3 = x_1 - a, \quad p_3 = p_1 - b, \quad (3)$$

so that, if the initial state of particle 1 is $\Psi(x_1)$, then the state of particle 3 after the measurements is $e^{ibx_3}\Psi(x_3 + a)$. Appropriate shifts of the state in x_3 and p_3 complete the teleportation.

For the teleportation of optical coherent states using this procedure the relevant variables are the quadrature amplitudes of the electromagnetic fields, the entangled state (1) is generated via parametric amplification, and the joint measurements are performed by combining fields at a beamsplitter and using homodyne detection. In the field of quantum optics, these techniques are now quite standard. In contrast, for the teleportation of the wave function of a massive particle one would seem to be faced with serious difficulties in producing the required states and operations.

However, in recent work we have proposed and analyzed a cavity-QED-based system that enables the transfer of quantum states between the external, or motional, degrees of freedom of a trapped atom and propagating light fields [9,10]. This system should lead to new capabilities for the synthesis, control, and measurement of quantum states for both motion and light. A particular example is the possibility of creating an EPR state of the form (1) where (x_2, x_3) and (p_2, p_3) are indeed the positions and momenta of *distantly separated atoms*. This in turn offers a route to achieving the teleportation of an atomic wavepacket [11], which we summarize in this article.

An overview of our proposed teleportation scheme is given in Fig. 1. Each of Alice (\mathcal{A}), Bob (\mathcal{B}), and Victor (\mathcal{V}) possess an atom trapped inside an optical cavity, with the aim being to teleport the (x -dimension) motional state of Victor's atom to Bob's atom. Again, the three basic steps involved are: (i) preparation of quantum entanglement between Alice and Bob's atoms, (ii) joint (or "Bell-state") measurement by Alice on her atom and Victor's atom, and (iii) phase-space displacement $[D(\alpha^*)]$ by Bob (given the classical result α of Alice's measurement). Finally, the state of Bob's atom may be examined by Victor for verification of the quality of the teleportation. Stages (i) and (ii), as illustrated in Fig. 1, employ the cavity-mediated motion-light state transfer scheme of [9], to which we now turn our attention.

2 Motion-light coupling

Briefly, a single two-level atom (or ion) is tightly confined in a harmonic trap located inside a high-finesse optical cavity. The atomic transition of frequency ω_a is coupled to a single mode of the cavity field of frequency ω_c and also to an external (classical) laser field of frequency ω_L and strength \mathcal{E}_L . The physical setup and excitation scheme are depicted in Fig. 2(a). The cavity is aligned along the x -axis, while the field \mathcal{E}_L is incident from a direction in the y - z plane. Both the cavity field and \mathcal{E}_L are far from resonance with the atomic

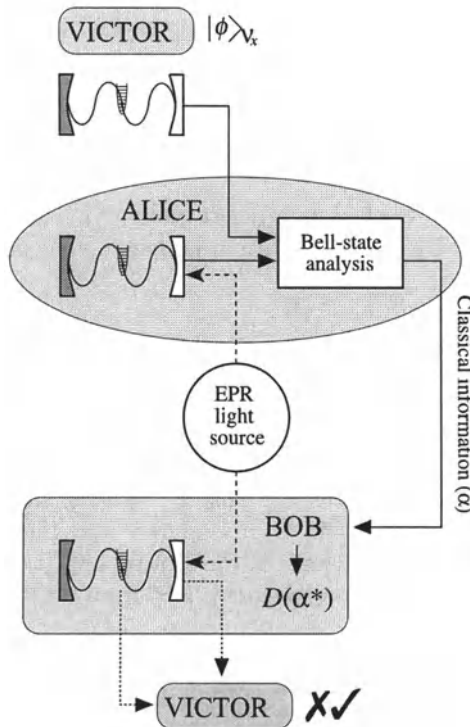


Fig. 1. Schematic of proposed teleportation scheme for atomic wavepackets

transition, but their difference frequency is chosen so that they drive Raman transitions between neighboring motional number states (i.e., $\omega_c - \omega_L = \nu_x$, with ν_x the x -axis trap frequency).

A number of assumptions are made in order to achieve the desired motion-light coupling:

- Atomic spontaneous emission is neglected and the internal atomic dynamics adiabatically eliminated.
- The size of the harmonic trap, located at a *node* of the cavity field, is taken to be small compared to the optical wavelength (Lamb-Dicke regime), enabling the approximations

$$\sin(k\hat{x}) \simeq \eta_x(\hat{b}_x + \hat{b}_x^\dagger), \quad \mathcal{E}_L(\hat{y}, \hat{z}, t) \simeq \mathcal{E}_L(t) e^{-i\phi_L}, \quad (4)$$

where η_x ($\ll 1$) is the Lamb-Dicke parameter and

$$\hat{x} = (\hbar/2m\nu_x)^{1/2}(\hat{b}_x + \hat{b}_x^\dagger). \quad (5)$$

- The trap frequency ν_x and cavity field decay rate κ are assumed to satisfy $\nu_x \gg \kappa \gg |(g_0\eta_x/\Delta)\mathcal{E}_L(t)|$, where g_0 is the single-photon atom-cavity mode coupling strength, and $\Delta = \omega_a - \omega_L$. The first inequality allows a rotating-wave approximation to be made with respect to the trap oscillation frequency, while the second inequality enables an adiabatic elimination of the cavity field mode.

Under these conditions, the motional mode dynamics in the x direction is well described by the simple quantum Langevin equation [9]

$$\dot{\tilde{b}}_x \simeq -\Gamma(t)\tilde{b}_x + \sqrt{2\Gamma(t)} \tilde{a}_{\text{in}}(t), \quad (6)$$

where $\tilde{b}_x = e^{i\nu_x t}\hat{b}_x$ and $\Gamma(t) = [g_0\eta_x|\mathcal{E}_L(t)|/\Delta]^2/\kappa$. The operator $\tilde{a}_{\text{in}}(t)$ obeys the commutation relation $[\tilde{a}_{\text{in}}(t), \tilde{a}_{\text{in}}^\dagger(t')] = \delta(t-t')$ and describes the quantum noise *input to the cavity field* (in a frame rotating at the cavity frequency). From the linear nature of (6), it follows that the statistics of a (continuous) light field incident upon the cavity can be “written onto” the state of the atomic motion. For example, in [9] it is shown how this effect can be used to prepare a (pure) squeezed state of the motion of a trapped atom by driving the cavity with broadband squeezed light from a degenerate parametric amplifier. This also means that entanglement between separate light fields can be transferred to entanglement between the motional states of separate atoms, as we discuss below. From a consideration of the input-output theory of optical cavities (see, for example, [12]), it also follows that measurements on the cavity output field amount to measurements on the motion of the atom. In particular, one can show that

$$\tilde{a}_{\text{out}}(t) \simeq -\tilde{a}_{\text{in}}(t) + \sqrt{2\Gamma(t)} \tilde{b}_x(t). \quad (7)$$

So, for a vacuum input field, homodyne measurements on the cavity output field realize position or momentum measurements (or some mixture, depending on the local oscillator phase) on the trapped atom. This enables the necessary Bell-state analysis to be performed.

3 Teleportation Procedure

3.1 State to be teleported

To begin the teleportation procedure, Victor’s atom is prepared in a particular motional state $|\phi\rangle_{\mathcal{V}x}$ in the x dimension (e.g., by the techniques of [13]). With the motion-light coupling switched off in Victor’s cavity (i.e., $\mathcal{E}_{L\mathcal{V}} = 0$), this state is assumed to remain unchanged until required by Alice for the Bell-state analysis.

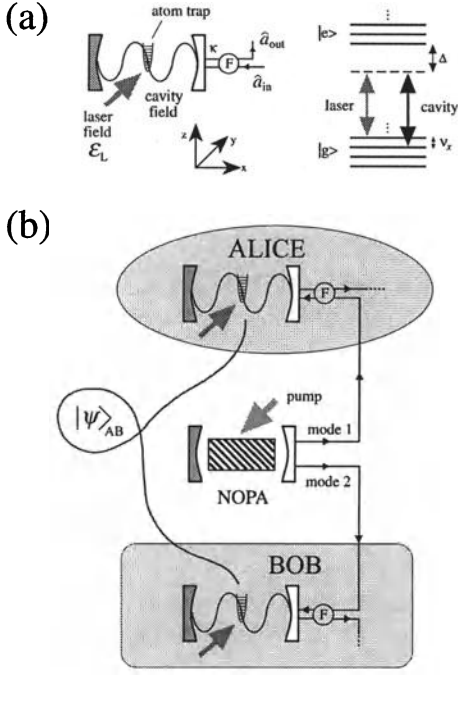


Fig. 2. (a) Proposed setup and excitation scheme for coupling between the motion of a trapped atom and a quantized optical cavity mode, and thence to a freely propagating external field. The cavity is assumed to be *one-sided*, i.e., one mirror is perfectly reflecting. (b) Preparation of a position-momentum EPR state of Alice and Bob's atoms. Faraday isolators (F) facilitate a unidirectional coupling between the entangled light source and the atom-cavity systems

3.2 Preparation of position-momentum EPR state

Next, a position-momentum EPR state of Alice and Bob's atoms is prepared by using the motion-light coupling described in (6), with input light fields from a nondegenerate optical parametric amplifier (NOPA). This preparation, described in detail in [10], is depicted in Fig. 2(b). The two quantum-correlated output light fields from a NOPA (operating below threshold) are separated and made to impinge on Alice and Bob's cavities, respectively. Assuming $\Gamma_A = \Gamma_B = \Gamma$, after a time $t \gg \Gamma^{-1}$, the following *pure* entangled motional state is prepared,

$$|\psi\rangle_{AB} = [\cosh(r)]^{-1} \sum_{m=0}^{\infty} [-\tanh(r)]^m |m\rangle_{Ax} |m\rangle_{Bx}, \quad (8)$$

where $|m\rangle_{A,Bx}$ are Fock states of the motional modes and r is the ‘entanglement’ parameter. The nature of the correlations inherent in the joint state (8) is most clearly expressed through the Wigner function for this state:

$$\begin{aligned} W(x_A, p_A; x_B, p_B) \\ = \frac{4}{\pi^2} \exp \left\{ - \left[(x_A + x_B)^2 + (p_A - p_B)^2 \right] e^{+2r} \right\} \end{aligned}$$

$$\times \exp \left\{ - [(x_A - x_B)^2 + (p_A + p_B)^2] e^{-2r} \right\} \quad (9)$$

$$\rightarrow C \delta(x_A + x_B) \delta(p_A - p_B) \text{ as } r \rightarrow \infty, \quad (10)$$

with C a constant. Once this state has been prepared, the atom-cavity couplings are turned off ($\Gamma_A, \Gamma_B \rightarrow 0$), as is the NOPA pump field. Again, we assume that the entangled state (8) remains unchanged until the next step in the procedure.

3.3 Bell-state analysis

At this stage in the procedure, the total system state is

$$|\Psi_1\rangle = |\phi\rangle_{\nu_x} |\psi\rangle_{AB}. \quad (11)$$

The Bell-state analysis performed by Alice is depicted in Fig. 3. At a predetermined time, Victor switches on his atom-cavity coupling Γ_V via $\mathcal{E}_{LV}(t)$, thus converting the state $|\phi\rangle_{\nu_x}$ to that of a freely propagating field delivered to input beam-splitter BS of Alice's sending station. With due accounting for propagation delay, Alice has likewise switched on the coupling Γ_A from her cavity, where, for simplicity, $\Gamma_V = \Gamma_A = \Gamma$. Note that Victor and Alice's cavities both have vacuum inputs at this stage. The two cavity output fields are combined by Alice at the 50/50 beamsplitter BS, the two outputs of which are incident on homodyne detectors D_{\pm} . Through the input-output relation (7), and through the mixing of the cavity output fields at the beamsplitter, these detectors effect homodyne measurements on the modes $\tilde{c}_{\pm} = 2^{-1/2} (\tilde{b}_{\nu_x} \pm \tilde{b}_{Ax})$. In particular, with suitable choices of the local oscillator phases, the setup realizes measurements of the variables $x_A + x_V$ and $p_A - p_V$, as required by the teleportation protocol.

Mathematically, the effect of these measurements is to project the system state onto quadrature eigenstates of the modes \tilde{c}_{\pm} , and the relevant measurement results, which we denote by χ_{\pm} , are given by the integrated homodyne photocurrents. Note that this projection requires that the local oscillator photon flux matches the temporal shape of the signal flux [which in our case is set by $\Gamma(t)$] [14,15].

Expanding the motional state of Victor's atom, $|\phi\rangle_{\nu_x}$, in terms of the coherent states, i.e.,

$$|\phi\rangle_{\nu_x} = \frac{1}{\pi} \int d^2\beta \nu_x \langle \beta | \phi \rangle_{\nu_x} |\beta\rangle_{\nu_x}, \quad (12)$$

one can show that the motional state of Bob's atom following the Bell-state measurements, $|\varphi\rangle_{Bx}$, is proportional to

$$\frac{1}{\pi} \int d^2\beta \nu_x \langle \beta | \phi \rangle_{\nu_x} \frac{\nu_x \langle \alpha^* | \beta \rangle_{\nu_x}}{\nu_x \langle \Lambda \alpha^* | \Lambda \beta \rangle_{\nu_x}} D_B(-\Lambda \alpha^*) D_B(\Lambda \beta) |0\rangle_{Bx}, \quad (13)$$

where $\alpha = (\chi_+ + i\chi_-)/\sqrt{2}$, $\Lambda = \tanh(r)$, and

$$D_B(\beta) = \exp(\beta \tilde{b}_{Bx}^\dagger - \beta^* \tilde{b}_{Bx}) \quad (14)$$

is the coherent displacement operator for Bob's atom. In the limit of strong squeezing and entanglement ($\Lambda \rightarrow 1$), (13) approaches

$$D_B(-\alpha^*) \frac{1}{\pi} \int d^2\beta \nu_x \langle \beta | \phi \rangle \nu_x |\beta\rangle_{Bx}. \quad (15)$$

That is, $|\varphi\rangle_{Bx}$ approaches a state which, apart from a coherent displacement by $-\alpha^*$, is identical to the initial motional state (in the x dimension) of Victor's atom.

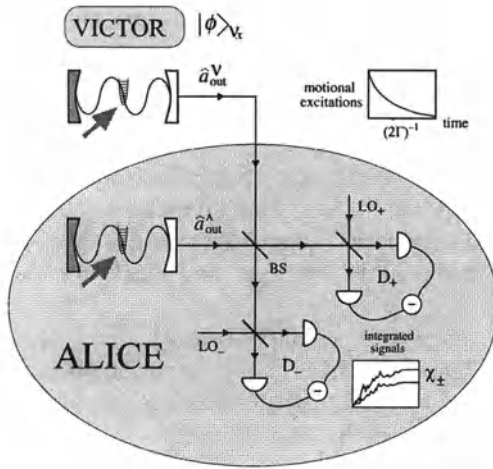


Fig. 3. Schematic of Alice's Bell-state analysis. The output field representing Victor's unknown state is combined by Alice at a 50/50 beam-splitter (BS) with the output field from her cavity. The resulting output fields from the BS are incident on homodyne detectors D_{\pm} . The cavity output fields follow the motional modes, which decay on a timescale Γ^{-1} . The local oscillator fields (LO_{\pm}) are pulsed, with temporal profiles chosen to match that of the cavity output fields

3.4 Phase-space displacement

Given the measurement results χ_{\pm} , transmitted to Bob via a *classical* channel, the final step in the teleportation procedure is for Bob to apply a coherent displacement α^* (assuming $\Lambda \simeq 1$) to the motional state of his atom, i.e.,

$$D_B(\alpha^*)|\varphi\rangle_{Bx} \rightarrow |\phi\rangle_{Bx}. \quad (16)$$

In practice, this might be achieved by applying an electric field (in the case of a trapped ion) along the x -axis which oscillates at the trap frequency ν_x , or, alternatively, by applying off-resonant laser fields which drive stimulated Raman transitions between neighboring trap levels [13]. After this, control of Bob's atom can be passed to Victor, who is free to confirm the overall quality of the teleportation protocol, e.g., along the lines analyzed in [16].

4 Discussion

To realize our teleportation scheme, required conditions are of (i) strong coupling optical cavity QED, such that $g_0^2/(\kappa\gamma) \gg 1$, where γ is the atomic spontaneous decay rate, (ii) strong confinement of the atoms with minimal motional-state decoherence, and (iii) strongly entangled light fields [9–11]. Each of these conditions have been achieved separately (for cavity QED see, e.g., [17–19]; for trapped ions see, e.g., [13,20]; for entangled light fields, see, e.g., [3]), while the first generation of experiments actually trapping atoms in cavity QED have been performed [21].

Much of the interest in quantum teleportation is rooted in its intimate connection to issues in the fields of quantum information and quantum computation. There, indeed, nonclassical light fields and trapped atoms and ions are leading candidates for the implementation of, for example, elementary quantum computers [22,13,23,24], and quantum dense coding [25] and universal quantum computation [26] with continuous quantum variables. The present work points to the exciting possibility of combining these candidate technologies in distributed quantum networks, where, for example, the “distribution” is achieved with light fields, while “storage” and local processing is achieved with trapped atoms.

Acknowledgment. ASP gratefully acknowledges support from the Marsden Fund of the Royal Society of New Zealand. HJK is supported by the National Science Foundation, by DARPA via the QUIC Institute which is administered by ARO, and by the Office of Naval Research.

References

1. D. Bouwmeester, J.-W. Pan, K. Mattle, M. Eibl, H. Weinfurter, A. Zeilinger: *Nature* **390**, 575 (1997)
2. D. Boschi, S. Branca, F. De Martini, L. Hardy, S. Popescu: *Phys. Rev. Lett.* **80**, 1121 (1998)
3. A. Furusawa, J. L. Sørensen, S. L. Braunstein, C. A. Fuchs, H. J. Kimble, E. S. Polzik: *Science* **282**, 706 (1998)
4. C. H. Bennett, G. Brassard, C. Crépeau, R. Jozsa, A. Peres, W. K. Wootters: *Phys. Rev. Lett.* **70**, 1895 (1993)
5. L. Vaidman: *Phys. Rev. A* **49**, 1473 (1994)
6. S. L. Braunstein, H. J. Kimble: *Phys. Rev. Lett.* **80**, 869 (1998)
7. L. Vaidman, N. Yoran: *Phys. Rev. A* **59**, 116 (1999)
8. H. J. Kimble: In *Fundamental Systems in Quantum Optics*, Proceedings of the Les Houches Summer School, Session LIII, 1990, J. Dalibard, J.-M. Raimond, J. Zinn-Justin (Eds.) (Elsevier, New York, 1992) pp. 545–674
9. A.S. Parkins and H.J. Kimble: *J. Opt. B: Quantum Semiclass. Opt.* **1**, 496 (1999)
10. A.S. Parkins and H.J. Kimble: [quant-ph/9907049](#)
11. A.S. Parkins and H.J. Kimble: [quant-ph/9909021](#)
12. D. F. Walls, G. J. Milburn: *Quantum Optics* (Springer-Verlag, Berlin, 1994)

13. D. J. Wineland, C. Monroe, W. M. Itano, D. Leibfried, B. E. King, D. M. Meekhof: Jou. Res. Nat. Inst. Stand. Tech. **103**, 259 (1998)
14. A. M. Herkommer, H. J. Carmichael, W. P. Schleich: Quantum Semiclass. Opt. **8**, 189 (1996)
15. H. M. Wiseman: Quantum Semiclass. Opt. **8**, 205 (1996)
16. S. L. Braunstein, C. A. Fuchs, and H. J. Kimble: J. Opt. B: Quantum Semiclass. Opt., in press
17. C. J. Hood, M. S. Chapman, T. W. Lynn, H. J. Kimble: Phys. Rev. Lett. **80**, 4157 (1998)
18. H. Mabuchi, J. Ye, H. J. Kimble: Appl. Phys. B **68**, 1095 (1999)
19. P. Münstermann, T. Fischer, P. Maunz, P. W. H. Pinkse, G. Rempe: Phys. Rev. Lett. **82**, 3791 (1999)
20. Ch. Roos, Th. Zeiger, H. Rohde, H. C. Nägerl, J. Eschner, D. Leibfried, F. Schmidt-Kaler, R. Blatt: quant-ph/9909038
21. J. Ye, D. W. Verwoerd, H. J. Kimble: quant-ph/9908007
22. J. I. Cirac and P. Zoller: Phys. Rev. Lett. **74**, 4091 (1995)
23. C. Monroe, D. M. Meekhof, B. E. King, W. M. Itano, D. J. Wineland: Phys. Rev. Lett. **75**, 4714 (1995)
24. Q. A. Turchette, C. S. Wood, B. E. King, C. J. Myatt, D. Leibfried, W. M. Itano, C. Monroe, D. J. Wineland: Phys. Rev. Lett. **81**, 3631 (1998)
25. S. L. Braunstein and H. J. Kimble: quant-ph/9910010
26. S. Lloyd and S. L. Braunstein: Phys. Rev. Lett. **82**, 1784 (1999)

Photon Bunching and Multi-photon Interference between Independent Parametric Down-Conversion Processes

Z. Y. Ou¹, J. -K. Rhee², L. J. Wang²

¹ Department of Physics, Indiana University Purdue University
Indianapolis, Indianapolis, IN 46202

² NEC Research Institute, Inc., 4 Independence Way, Princeton, NJ 08540

Abstract. In this paper, we discuss photon bunching effect in parametric down-conversion and its connection to the visibilities of a number of multi-photon interference experiments between independent parametric down-conversion processes. We find that mode matching, especially temporal mode matching, plays an equally important role for photon bunching effect and for two-photon interference between two independent emissions in parametric down-conversion. We extend the discussion further to a four-photon interference effect.

1 Introduction

Photon bunching effect [1], when first discovered, was thought of as the manifestation of Boson nature of photons [2]. But later on, it was revealed that light may also exhibit an opposite effect, namely, photon anti-bunching effect [3]. Nevertheless, as the first higher-order effect in optical physics, it was the starting point for the field of quantum optics. Now it was fully understood both in classical wave theory and with quantum theory of light [4]. Usually it is associated with optical fields with thermal fluctuations. In 1986, Yurke and Potasek [5] discovered that spontaneous parametric down-conversion also exhibits photon bunching effect as far as only one beam in the two conjugate fields is concerned. This is not a surprise if we realize that optical amplifier without input signal exhibits thermal fluctuations – spontaneous emission basically is of thermal nature[6] and parametric down-conversion process is an amplification process. Such an effect has been largely ignored so far in all the higher order photon counting measurement in parametric down-conversion because of the extremely wide bandwidth of down-converted fields (in the Tera Hz range). It was only recently noticed in the large excess quantum noise at the output of a parametric amplifier in narrowband detection [7].

Interference between independent sources was first demonstrated in 1963 with two independent lasers [8]. The variation of such an experiment at low light intensity [9] led to higher-order interference effect (two-photon interference). However, because of the independent nature of the sources, the bandwidth of the sources must be resolved by the optical detectors in order to keep the phases of the sources constant during the period of detection [10]. Because

of this restriction, no further demonstration was made until recently when there is renewed interest in producing multi-photon entanglement by combining two pairs of photons from independent parametric down-conversion processes [11–13]. Especially, when ultrafast pulse is used for pumping the parametric down-conversion process, requirement on the detector response can be relaxed [14,15]. However, because of the dispersive nature of the parametric down-conversion, the down-converted fields are not transform-limited [16] and the consequence is that perfect temporal mode match is hard to achieve so that visibility in these interference experiments is compromised [17–19].

At first glance, there seems to be no connection between photon bunching effect and multi-photon interference effect except that they are both higher order effects. However, as we will show later, photon bunching effect is a result of stimulated emission or amplification of the initial spontaneous emission. Just like in optical interference, mode matching in both space and time is important in amplification process. For photon bunching effect, spatial mode matching is not a problem because the modes are well defined and are the same for both spontaneous and stimulated emission. For temporal mode, on the other hand, because the down-converted fields are not transform-limited, it is impossible to match the temporal mode between spontaneous and stimulated emission. Spectral filtering may be used to achieve transform-limited temporal modes. This can be implemented with fast detection process [10] or with direct optical filtering [15]. Nevertheless, as we shall find out, the photon bunching effect should have same dependence on temporal mode match as the visibility of two-photon interference.

In this paper, we will first discuss photon bunching effect in parametric down-conversion process. Then we will analyze a simple two-photon interference experiment between two signal fields of two independent down-converted fields. In the end, we extend the argument to a four-photon interference experiment.

2 Photon Bunching Effect in Parametric Down-Conversion

Photon bunching effect is a well-known higher order effect associated with thermal fluctuations of light. It was shown that spontaneous emission from an amplifier has such a feature [6]. This can be easily confirmed from a simple model for an amplifier[7]:

$$\hat{a}_{out} = G\hat{a}_{in} + \hat{F}^\dagger, \quad (1)$$

where \hat{a}_{in} and \hat{a}_{out} represent the input and output fields, respectively. G is the amplitude gain of the amplifier. \hat{F} characterizes the internal mode of the amplifier and it satisfies the following commutation relationship

$$[\hat{F}, \hat{F}^\dagger] = G^2 - 1. \quad (2)$$

With vacuum for both input \hat{a}_{in} and internal mode of the amplifier, we have spontaneous emission of the amplifier:

$$\langle \hat{n}_{out} \rangle = \langle \hat{a}_{out}^\dagger \hat{a}_{out} \rangle = G^2 - 1 \quad \text{and} \quad \langle \hat{n}_{out}^2 \rangle = (2G^2 - 1)(G^2 - 1) \quad (3)$$

so that

$$\langle (\Delta \hat{n}_{out})^2 \rangle = \langle \hat{n}_{out} \rangle^2 + \langle \hat{n}_{out} \rangle \quad (4)$$

So the photon number fluctuation from an amplifier without input is exactly same as that of a thermal field and the normalized intensity (two-photon) correlation function is equal to

$$g^{(2)} \equiv \frac{\langle : \hat{n}_{out}^2 : \rangle}{\langle \hat{n}_{out} \rangle^2} = \frac{\langle \hat{n}_{out}^2 \rangle - \langle \hat{n}_{out} \rangle}{\langle \hat{n}_{out} \rangle^2} = 2. \quad (5)$$

which indicates the photon bunching effect. The value of $g^{(2)}$ is exactly same as that of a thermal field [4].

As for parametric down-conversion process, it has the following input-output relationship

$$\hat{a}_{out} = G \hat{a}_{in} + \sqrt{G^2 - 1} \hat{b}_{in}^\dagger, \quad (6)$$

$$\hat{b}_{out} = G \hat{b}_{in} + \sqrt{G^2 - 1} \hat{a}_{in}^\dagger, \quad (7)$$

where a, b denote the signal and idler mode of parametric down-conversion process, respectively. Notice that Eqs.(2.6, 2.7) are exactly of the form of Eq.(2.1). So parametric down-conversion should exhibits photon bunching effect for either of the two fields alone[5].

From Eq.(2.5), we see that the photon bunching in an amplifier is independent of the gain G (or stimulated emission). In other words, one may argue that even if we set $G \rightarrow 1$, we still have $g^{(2)} = 2$. However, it is precisely at this limit that the role of the stimulated emssion becomes obvious. Consider an amplifier with low gain. For single photon events, because the gain is small, the contribution from stimulated emission is neglegible. For two-photon events, however, there are two ways to obtain two photons for coincidence: one is from two independent spontaneous processes and the other is from the amplification or stimulated emission of the first spontaneously emitted photon and it has been shown that the two possibilities have equal strength [20]. While the first possibility sets the background as the accidental two-photon coincidence, the second possibility gives rise to excess coincidence as large as the accidental coincidence hence $g^{(2)} = 1 + 1 = 2$.

The description above is for single mode in each field. In practice, we have multimode fields. Therefore, mode match becomes a problem, especially in time domain. The less than perfect temporal mode match will result in less gain in amplification or equivalently fewer excess two-photon events. So we expect $g^{(2)} < 2$. To demonstrate this, we consider in the following the

parametric amplification process with small gain ($G \sim 1$) and without input signal. The system is described by the following state [16]

$$|\Psi\rangle = (1 - |\eta|^2/2)|vac\rangle + \eta|\Phi_1\rangle + \eta^2|\Phi_2\rangle. \quad (8)$$

up to the second order of η . Here the states $|\Phi_{1,2}\rangle$ have the following form:

$$|\Phi_1\rangle = \int d\Omega_1 d\Omega_2 \Phi(\Omega_1, \Omega_2) \hat{a}_s^\dagger(\Omega_1) \hat{a}_i^\dagger(\Omega_2) |vac\rangle, \quad (9)$$

$$\begin{aligned} |\Phi_2\rangle &= \frac{1}{2} \int d\Omega_1 d\Omega_2 d\Omega'_1 d\Omega'_2 \Phi(\Omega_1, \Omega_2) \Phi(\Omega'_1, \Omega'_2) \\ &\quad \hat{a}_s^\dagger(\Omega_1) \hat{a}_i^\dagger(\Omega_2) \hat{a}_s^\dagger(\Omega'_1) \hat{a}_i^\dagger(\Omega'_2) |vac\rangle. \end{aligned} \quad (10)$$

The information about the pump field and the parametric interaction is contained in the function $\Phi(\Omega_1, \Omega_2)$, which has the explicit form of

$$\Phi(\Omega_1, \Omega_2) = a_p(\Omega_1 + \Omega_2) \phi(\Omega_1 + \Omega_2, \Omega_1 - \Omega_2), \quad (11)$$

where $a_p(\omega)$ describes the pump field spectrum and $\phi(\omega_p, \omega)$ is the two-photon wave amplitude for single-frequency (ω_p) pumped parametric down-conversion. For CW case, $a_p(\omega)$ becomes a δ -function characterizing the single frequency for pump field. For a coherent pulse (transform-limited), $a_p(\omega)$ is a well-behaved deterministic function of ω . Here the pump field is treated as a classical field. With proper normalization for $\Phi(\Omega_1, \Omega_2)$, η is simply the probability amplitude of photon conversion for a single pump photon.

To see photon bunching in either the signal or idler field, let us calculate the two-photon detection probability rate for one of the fields, say, signal field, alone:

$$p_{2s}(t_1, t_2) = ||\hat{E}_s(t_1) \hat{E}_s(t_2) |\Psi\rangle||^2, \quad (12)$$

where the electric field operator is expressed as $\hat{E}_s(t) = \int d\omega \hat{a}_s e^{-i\omega t} / \sqrt{2\pi}$. With some lengthy calculation, Eq.(2.11) becomes

$$\begin{aligned} p_{2s}(t_1, t_2) &= \frac{|\eta|^4}{4(2\pi)^2} \int d\Omega_2 d\Omega'_2 \\ &\quad \left\{ |F(\Omega_2, \Omega'_2)|^2 + F(\Omega_2, \Omega'_2) F^*(\Omega'_2, \Omega_2) \right\} \end{aligned} \quad (13)$$

where

$$\begin{aligned} F(\Omega_2, \Omega'_2) &\equiv \int d\Omega_1 d\Omega'_1 \Phi(\Omega_1, \Omega_2) \Phi(\Omega'_1, \Omega'_2) \\ &\quad \left(e^{-i\Omega_1 t_1 - i\Omega'_1 t_2} + e^{-i\Omega'_1 t_1 - i\Omega_1 t_2} \right) \end{aligned} \quad (14)$$

In the CW case when $\Phi(\Omega_1, \Omega_2) = \delta(\Omega_1 + \Omega_2) \phi(\Omega_1)$, Eq.(2.12) has a simple form of

$$p_{2s}(t_1, t_2) = p_{1s}^2(t_1) [1 + |\gamma(t_1 - t_2)|^2]. \quad (15)$$

Here γ is the normalized second-order coherence function for signal field [4] and $p_{1s}(t)$ is the single photon detection rate. Eq.(2.14) is exactly same as that for a thermal field. The observation of the second term in Eq.(2.14) gives the excess coincidence for photon bunching and requires that the detectors' response is faster than the fluctuations of the fields.

As for the nonstationary case of ultra short pulse pumping, the optical detector is usually slower than the whole process. So we calculate the overall probability for detecting two photons in one pump pulse by integrating the time variables t_1, t_2 over the pulse period (from $-\infty$ to $+\infty$) and we obtain after some manipulation,

$$P_{2s} = \mathcal{A} + \mathcal{E}, \quad (16)$$

where

$$\mathcal{A} \equiv |\eta|^4 \int d\Omega_1 d\Omega'_1 d\Omega_2 d\Omega'_2 |\Phi(\Omega_1, \Omega_2)\Phi(\Omega'_1, \Omega'_2)|^2 = P_{1s}^2 \quad (17)$$

is the accidental two-photon probability with P_{1s} as the single photon probability and

$$\mathcal{E} \equiv |\eta|^4 \int d\Omega_1 d\Omega'_1 d\Omega_2 d\Omega'_2 \Phi(\Omega_1, \Omega_2)\Phi(\Omega'_1, \Omega'_2)\Phi^*(\Omega_1, \Omega'_2)\Phi^*(\Omega'_1, \Omega_2) \quad (18)$$

is the excess two-photon probability due to photon bunching. Notice that $\mathcal{E} \leq \mathcal{A}$ because of the Schwartz inequality. The equality holds if and only if the function $\Phi(\Omega_1, \Omega_2)$ can be factorized into $k(\Omega_1)h(\Omega_2)$. But this is impossible because of the non-transform-limited nature of the down-converted fields [16]. We can also consider the requirement for the equality in the Schwartz inequality as that for the temporal mode match in the stimulated process and the incoherent part in the spontaneously down-converted fields makes perfect mode matching impossible.

However, with the help of narrow band filters before detection, we can force the down-converted fields be transform-limited if the bandwidth of the filters is much smaller than all the bandwidth involved, as demonstrated by Rarity [15]. When this is achieved, $\Phi(\Omega_1, \Omega_2)$ is then factorized and we have the perfect photon bunching:

$$g^{(2)} \equiv P_{2s}/P_{1s}^2 = (\mathcal{A} + \mathcal{E})/\mathcal{A} = 2. \quad (19)$$

The temporal mode matching requirement discussed above for the photon bunching effect plays an equally important role in the interference effect in the following.

3 Interference of Independent Parametric Down-Conversion fields

Quantum interference between the correlated signal and idler fields from parametric down-conversion has been demonstrated to have high visibility

because of the correlated and identical temporal mode for the two conjugate fields [21], even though asymmetric spectra for the two fields in type II parametric down-conversion make it hard to match the temporal mode and result in reduced visibility [22,23]. However, for the interference between two independent parametric sources, the temporal mode matching is similar to the situation discussed in photon bunching. So the visibility should be directly associated with the quantity \mathcal{E}/\mathcal{A} discussed in the preceding section. For the simplicity in arriving at the visibility of the interference, we will only discuss the case of pulsed pumping.

3.1 Two-photon interference without gating

Let us first consider two-photon interference between two signal fields in two parametric processes pumped by a common pulse described by $a_p(\omega)$ (Fig.1). We will leave the idler fields unattended at present. The quantum state of the overall system is given by

$$|\Psi\rangle = |\Psi^{(1)}\rangle \otimes |\Psi^{(2)}\rangle, \quad (20)$$

where $|\Psi^{(1,2)}\rangle$ describes the quantum state from each parametric process and has the form of Eq.(2.1) with \hat{a}_s changed to \hat{a}_{s1} or \hat{a}_{s2} and \hat{a}_i changed to \hat{a}_{i1} or \hat{a}_{i2} .

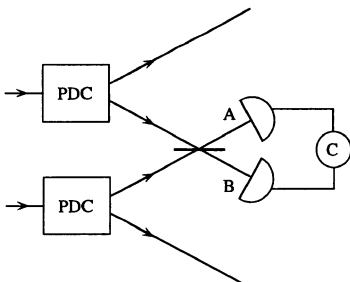


Fig. 1. Interference between two signal fields of two independent parametric processes.

The output fields of the beamsplitter are connected to $s1$ and $s2$ fields by

$$\hat{E}_A(t) = \frac{1}{\sqrt{2}}(\hat{E}_{s1}(t) + \hat{E}_{s2}(t + \tau)), \quad (21)$$

$$\hat{E}_B(t) = \frac{1}{\sqrt{2}}(\hat{E}_{s2}(t) - \hat{E}_{s1}(t - \tau)), \quad (22)$$

where we introduced a time delay τ so that the two fields arrive at the beamsplitter at different times. This time delay is important because when τ is zero, we should have complete overlap of the two fields and maximum

interference effect; but when τ is larger than the coherence time of the two fields, no interference should occur. So by comparing the coincidence at these two values of τ , we can deduce the visibility of the interference.

Two-photon coincidence between \hat{E}_A and \hat{E}_B fields is proportional to

$$p_2(t_1, t_2) = \|\hat{E}_A(t_1)\hat{E}_B(t_2)|\Psi\rangle\|^2. \quad (23)$$

From Eq.(3.2), we find 3 contributions to the two-photon coincidence in Eq.(3.3):

$$\begin{aligned} p_2(t_1, t_2) = & \frac{1}{4} \left\{ \|\hat{E}_{s1}(t_1)\hat{E}_{s1}(t_2 - \tau)|\Psi\rangle\|^2 + \|\hat{E}_{s2}(t_1 + \tau)\hat{E}_{s2}(t_2)|\Psi\rangle\|^2 \right. \\ & \left. + \|\hat{E}_{s1}(t_1)\hat{E}_{s2}(t_2) - \hat{E}_{s2}(t_1 + \tau)\hat{E}_{s1}(t_2 - \tau)|\Psi\rangle\|^2 \right\}. \end{aligned} \quad (24)$$

The first two contributions are directly from individual fields and for pulsed case, we have already obtained them from Eq.(2.15) as $\mathcal{A} + \mathcal{E}$. Notice that these two terms are independent of the time delay τ and provide an unmodulated base line for interference fringe. The contribution from the last term in Eq.(3.4) gives rise to interference. After some lengthy and tedious calculation, we arrive at

$$\begin{aligned} \int dt_1 dt_2 & \|\hat{E}_{s1}(t_1)\hat{E}_{s2}(t_2) - \hat{E}_{s2}(t_1 + \tau)\hat{E}_{s1}(t_2 - \tau)|\Psi\rangle\|^2 \\ & = 2[\mathcal{A} - \mathcal{E}(\tau)] \end{aligned} \quad (25)$$

with

$$\begin{aligned} \mathcal{E}(\tau) \equiv & |\eta|^4 \operatorname{Re} \int d\Omega_1 d\Omega'_1 d\Omega_2 d\Omega'_2 \Phi(\Omega_1, \Omega_2) \\ & \Phi(\Omega'_1, \Omega'_2) \Phi^*(\Omega'_1, \Omega_2) \Phi^*(\Omega_1, \Omega'_2) e^{i(\Omega_1 - \Omega'_1)\tau}. \end{aligned} \quad (26)$$

Notice that $\mathcal{E}(0) = \mathcal{E}$, and $\mathcal{E}(\infty) = 0$ if $\Phi(\Omega_1, \Omega_2)$ has a finite bandwidth. So we find the overall coincidence proportional to

$$P_2(\tau) = \mathcal{A} + \frac{1}{2}[\mathcal{E} - \mathcal{E}(\tau)]. \quad (27)$$

Therefore, as the time delay τ scans through 0 from $-\infty$ to $+\infty$, the coincidence will show a dip at $\tau = 0$ with a minimum value of \mathcal{A} . The baseline for the coincidence is at $\tau = \pm\infty$ with a value of $\mathcal{A} + \mathcal{E}/2$. So the visibility of the interference pattern is

$$v = \frac{P_2(\infty) - P_2(0)}{P_2(\infty)} = \frac{\mathcal{E}}{2\mathcal{A} + \mathcal{E}}. \quad (28)$$

Since $\mathcal{E} \leq \mathcal{A}$, the maximum value of v is $1/3$. This value is consistent with the theory of two-photon interference between two thermal fields [24].

3.2 Two-photon interference with gating

Now let the idler fields get involved. If we gate the coincidence measurement between A and B fields on the detection of the two idler fields in the two parametric process, the gated signal fields will be in a single-photon Fock state [25] and the situation has no difference from the correlated two-photon case [26]. We should expect the visibility of the interference reach 100% in ideal condition.

To show that it is so, we calculate the quadruple coincidence rate of two output fields of the beamsplitter and two idler fields (Fig.2):

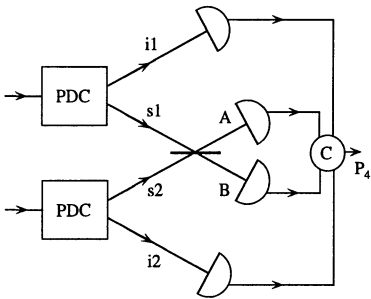


Fig. 2. Interference between two signal fields of two independent parametric processes gated upon the detection of two idler fields.

$$p_4(t_1, t_2, t_3, t_4) = \|\hat{E}_A(t_1)\hat{E}_B(t_2)\hat{E}_{i1}(t_3)\hat{E}_{i2}(t_4)|\Psi\rangle\|^2. \quad (29)$$

There are also 3 contributions as in Eq.(3.4). But it can be easily shown that there is no contribution from the first two terms because of the two-photon nature of $|\Phi_1^{(1,2)}\rangle$ in Eq.(2.2a). The contribution from the last term is similar to Eq.(3.5) and after integrating over time variables and performing some lengthy calculation, we have

$$P_4(\tau) = \frac{1}{2}[\mathcal{A} - \mathcal{E}(\tau)], \quad (30)$$

where \mathcal{A} and $\mathcal{E}(\tau)$ are the quantities defined in Eq.(2.15) and Eq.(3.11), respectively. As expected, the gated detection takes out the extra τ -independent contribution given in Eq.(3.4) to the overall coincidence. Therefore, the visibility of the interference fringe is

$$v = \mathcal{E}/\mathcal{A}. \quad (31)$$

In the ideal case when $\mathcal{E} = \mathcal{A}$, we will have $v = 1$, i.e., 100% visibility, which is exactly what we expect for the interference of two single-photon Fock states. Notice that the visibility is directly connected to the photon bunching quantity \mathcal{E}/\mathcal{A} . This interference scheme together with the one in part A has been recently implemented experimentally by Rhee and Wang [27] and the connection between the visibility of the interference experiment and the quantity \mathcal{E}/\mathcal{A} as in Eqs.(3.8,3.11) has been demonstrated.

3.3 Quantum State Teleportation, Entanglement Swapping and Three-Photon GHZ State

Another type of interference effect between independent fields from parametric down-conversion involves polarization entanglement. Interference occurs by projecting fields with correlated polarization into certain common direction. Quantum superposition stems from projection of fields of different polarizations. There are three different schemes for this sort of polarization interference involving independent parametric down-conversion sources. They are quantum state teleportation[28,17], entanglement swapping [18], and generation of three-photon GHZ state[11]. The underlying principle is same as discussed in the previous part and the results of calculation are similar. For example, the visibility in the three-photon interference scheme for achieving GHZ state is exactly same as Eq.(3.11).

4 Four-photon multi-path interference

So far our discussion has been limited to two-photon interference. Even for the schemes in part B with quadruple coincidence measurement, it is still two-photon amplitudes that are involved in interference. Ever since Greenberger, Horne, and Zeilinger discovered that quantum states with 3 or more-particles can display more dramatic locality violation, there have been several proposals to produce such states based on superposition of independent pairs of photons from parametric down-conversion. As we have seen earlier, stimulated process duplicates the incoming photon. Although it cannot be used for photon cloning because of the accompanying spontaneous process, this process can produce a four-photon state in parametric down-conversion. The extra two photons are stimulated from a pair of spontaneous photons. The four-photon state so produced cannot be used as GHZ multiphoton state because the stimulated photon can never be separated from stimulating photon and the state is in the form of $|2_s, 2_i\rangle$. Nevertheless it can be used to demonstrate a four-photon interference effect, namely, four-photon partition at a 50:50 beamsplitter.

Consider now the situation when two pairs of photons enter a 50:50 beam-splitter (BS) with each pair in one input port (Fig.3). The output state is given by[29]

$$|\Phi\rangle = \sqrt{\frac{3}{8}} \left(|4_A, 0_B\rangle + |0_A, 4_B\rangle \right) + \frac{1}{2} |2_A, 2_B\rangle, \quad (32)$$

where the subscripts {A,B} denote the two output modes. Notice that the states $|3_A, 1_B\rangle$ and $|1_A, 3_B\rangle$ are missing in Eq.(4.1). This can be understood in terms of two-photon interference. Recall that for an input state of $|1_1, 1_2\rangle$ to the BS, the output state is[26]

$$|\Phi\rangle = \frac{1}{\sqrt{2}} \left(|2_A, 0_B\rangle + |0_A, 2_B\rangle \right). \quad (33)$$

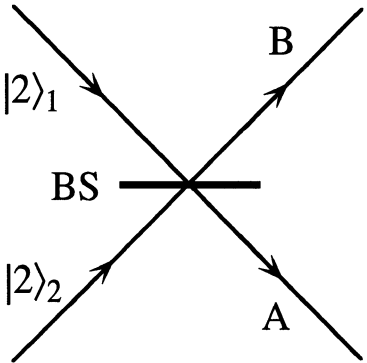


Fig. 3. Scheme of four-photon partition at a 50:50 beamsplitter

If we consider the four photons as two pairs of photon with each pair in the state $|1_1, 1_2\rangle$, then according to Eq.(4.2), only $|4_A, 0_B\rangle$, $|0_A, 4_B\rangle$, and $|2_A, 2_B\rangle$ are possible. The disappearance of $|3_A, 1_B\rangle$ and $|1_A, 3_B\rangle$ terms in Eq.(4.1) is a direct result of the absence of $|1_A, 1_B\rangle$ term in Eq.(4.2) due to two-photon interference. This picture of two pairs of photons is usually referred to as 2×2 situation. However, such a picture is inappropriate in explaining the probability for $|4_A, 0_B\rangle$ and $|0_A, 4_B\rangle$. For, from Eq.(4.2) the probability for $|4_A, 0_B\rangle$ is $1/2$ for one pair, so the probability for $|4_A, 0_B\rangle$ is simply $(1/2)^2 = 1/4$ for two pairs. But Eq.(4.1) gives $3/8$. The difference comes from the fact that the four photons in the 2×2 case are from two independent (uncorrelated) pairs while the four photons for Eq.(4.1) are correlated.

To understand the partition probability for $|4_A, 0_B\rangle$ output state, we notice that classically, the four photons can be thought of as independent particles and follows simply the Bernoulli distribution with $P_4^c = (1/2)^2 = 1/16$. So we have the ratio

$$P_4^q / P_4^c = 6. \quad (34)$$

The six-fold increase for quantum prediction can be understood in terms of four-photon interference: if we consider the two photons entering each side of the BS indistinguishable, then there are 6 possible ways to arrange the four photons (Fig.4). The four numbered slots for the four photons can be viewed as four photodetectors. Since the four photons in the state $|4_A, 0_B\rangle$ are indistinguishable, the amplitudes for the 6 possibilities are added to give an overall amplitude of $6A$ due to constructive four-photon interference. Here A is the probability amplitude for each possibilities. So the overall probability for $|4_A, 0_B\rangle$ is then $P_4^q = (6A)^2 = 36A^2$ for quantum prediction. However, for classical particles, there is no interference and we simply add probability A^2 for each possibility to obtain overall probability $P_4^c = 6A^2$. So we have the

ratio $P_4^q/P_4^c = 36A^2/6A^2 = 6$, or six-fold increase from classical prediction to quantum prediction.

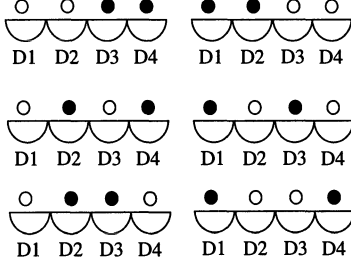


Fig. 4. Six possible ways to arrange 2 pairs of photons with four detectors for multi-path four-photon interference.

The difference between the four-photon interference case and the 2×2 case lies in the correlation between the four photons. As mentioned earlier, besides the stimulated amplification of a spontaneous photon for two-photon event, there is also an equal chance from two spontaneous photons. When applied to parametric down-conversion process, this leads to two correlated pairs from stimulated process and equally probable case of two independent spontaneous pairs. Since the stimulated process requires mode match for multimode field, The enhancement factor for the quadruple coincidence will then depend on the quantity \mathcal{E}/\mathcal{A} . When $\mathcal{E}/\mathcal{A} = 1$, this corresponds to the case when the two pairs of photons are produced via stimulated process and are correlated, we should expect four-photon interference. But if $\mathcal{E}/\mathcal{A} = 0$, there is no mode match and hence no stimulated emission. So we should expect two independent pairs of photons and it gives the 2×2 case.

To confirm the above, we calculate with the multimode state in Eq.(2.8) the quadruple detection probability at one output port (say, port A) of the beamsplitter:

$$p_4(t_1, t_2, t_3, t_4) = \|\hat{E}_A(t_1)\hat{E}_A(t_2)\hat{E}_A(t_3)\hat{E}_A(t_4)|\Psi\rangle\|^2, \quad (35)$$

where

$$\hat{E}_A(t) = \frac{1}{\sqrt{2}}[\hat{E}_s(t) + \hat{E}_i(t + \tau)] \quad (36)$$

with a delay τ between the arrivals of signal and idler fields at the BS. There are 16 terms in the expansion of Eq.(4.4) when we substitute Eq.(4.5) into Eq.(4.4). Among them 10 terms of the form $E_s E_s E_s E_s$, $E_i E_i E_i E_i$, $E_s E_s E_i E_i$, and $E_s E_i E_i E_i$ will be zero. The six nonzero terms correspond to the six possibilities in the simple picture of four-photon interference.

After integrating the time variables over the whole pulse duration, the quadruple detection probability is only a function of τ . Because of the complicated calculation involved, we only present two extreme cases of $\tau = 0$ and

$\tau = \infty$:

$$P_4(\tau = 0) = \alpha(4\mathcal{A} + 8\mathcal{E}), \quad (37)$$

$$P_4(\tau = \infty) = \alpha(\mathcal{A} + \mathcal{E}). \quad (38)$$

Obviously, $\tau = 0$ corresponds to the quantum case described in Eq.(4.1) and $\tau = \infty$ gives the classical result. So the ratio

$$\frac{P_4^q}{P_4^c} = \frac{P_4(0)}{P_4(\infty)} = 4 + \frac{4\mathcal{E}}{\mathcal{A} + \mathcal{E}}, \quad (39)$$

is the multimode result similar to Eq.(4.3). It is interesting to note that

$$\frac{P_4^q}{P_4^c} = \begin{cases} 6, & \text{if } \mathcal{E} = \mathcal{A}, \\ 4, & \text{if } \mathcal{E} = 0. \end{cases} \quad (40)$$

which confirms the intuitive argument earlier.

5 Discussion and Summary

We have analyzed the photon bunching effect in parametric down-conversion process and some two-photon and four-photon interference schemes involving fields from two independent parametric down-conversion processes. We have shown that the photon bunching effect is essentially an amplification (stimulated emission) of an initially spontaneously emitted photon or photon pair. Since amplification process depends on good matching in both space and time between the input mode and amplified mode, the condition for observing photon bunching is exactly same as that of the interference fringe in interference experiment. It turns out that the visibilities in these interference schemes are directly related to the quantity \mathcal{E}/\mathcal{A} , which is also a measure of photon bunching effect for one field (signal or idler) of parametric down-conversion. Photon bunching can be easily measured experimentally: the access coincidence gives rise to \mathcal{E} while the accidental coincidence corresponds to \mathcal{A} when we measure the auto-correlation of intensity. Furthermore, it involves only two-photon coincidence and has relatively higher rate. So by measuring the photon bunching effect or the quantity \mathcal{E}/\mathcal{A} , we can predict what will be the visibility of interference involving four-photon coincidence measurement, which has much lower rate.

Acknowledgments. ZYO is supported by the Office of Naval Research.

References

1. R. Hanbury Brown and R. Q. Twiss, Nature **177**, 27 (1956).
2. E. M. Purcell, Nature **178**, 1449 (1956).
3. H. J. Kimble, M. Dagenais, and L. Mandel, Phys. Rev. Lett. **39**, 691 (1977).

4. L. Mandel and E. Wolf, *Optical Coherence and Quantum Optics* (Cambridge University Press, New York, 1995).
5. B. Yurke and M. Potasek, Phys. Rev. A**36**, 3464 (1987).
6. S. Carusotto, Phys. Rev. A**11**, 1629 (1975).
7. Z. Y. Ou, S. F. Pereira, and H. J. Kimble, Phys. Rev. Lett.**70**, 3239 (1993).
8. G. Magyar and L. Mandel, Nature **198**, 255 (1963).
9. R. L. Pfleegor and L. Mandel, Phys. Lett. **24A**, 766 (1967).
10. Z. Y. Ou, Phys. Rev. A**37**, 1607 (1988).
11. D. M. Greenberger, M. A. Horne, and A. Zeilinger, in *Bell's Theorem, Quantum Theory, and Conceptions of the Universe*, edited by M. Katafias, (Kluwer Academic, Dordrecht, The Netherlands, 1989)
12. B. Yurke and D. Stoler, Phys. Rev. Lett. **68**, 1251 (1992).
13. A. Zeilinger, M. A. Horne, H. Weinfurter, and M. Zukowski, Phys. Rev. Lett. **78**, 3031 (1997).
14. M. Zukowski, A. Zeilinger, and H. Weinfurter, in *Fundamental Problems in Quantum Theory*, edited by D. M. Greenberger and A. Zeilinger, Ann. NY Acad. Sci. **755**, 91 (1995).
15. J. G. Rarity, in *Fundamental Problems in Quantum Theory*, edited by D. M. Greenberger and A. Zeilinger, Ann. NY Acad. Sci. **755**, 624 (1995).
16. Z. Y. Ou, Quantum Semiclass. Opt. **9**, 599 (1997).
17. D. Bouwmeester, J-W. Pan, K. Mattle, M. Eibl, H. Weinfurter, and A. Zeilinger, Nature (London) **390**, 575 (1997).
18. J-W. Pan, D. Bouwmeester, H. Weinfurter, and A. Zeilinger, Phys. Rev. Lett. **80**, 3891 (1998).
19. D. Bouwmeester, J-W. Pan, M. Daniell, H. Weinfurter, and A. Zeilinger, Phys. Rev. Lett. **82**, 1345 (1999).
20. Z. Y. Ou, L. J. Wang and L. Mandel, J. Opt. Soc. B**7**, 211 (1990).
21. P. G. Kwiat, K. Mattle, H. Weinfurter, A. Zeilinger, A. V. Sergienko, and Y. H. Shih, Phys. Rev. Lett. **75**, 4337 (1995).
22. W. P. Grice and I. A. Wamsley, Phys. Rev. Rev. A**56**, 1627 (1997); D. Branning, W. P. Grice, R. Erdmann, and I. A. Wamsley, Phys. Rev. Lett. **83**, 955 (1999).
23. M. Atature, A. V. Sergienko, B. M. Vost, B. Saleh, and M. C. Teich, Phys. Rev. Lett. **83**, 1323 (1999).
24. L. Mandel, Phys. Rev. A**28**, 929 (1983).
25. C. K. Hong and L. Mandel, Phys. Rev. Lett. **56**, 58 (1986).
26. C. K. Hong, Z. Y. Ou, and L. Mandel, Phys. Rev. Lett. **59**, 2044 (1987).
27. J. -K. Rhee and L. J. Wang, personal communication.
28. C. H. Bennett, G. Brassard, C. Crepeau, R. Jozsa, A. Peres, and W. K. Wootters, Phys. Rev. Lett. **70**, 1895 (1993).
29. R. A. Campos, B. E. A. Saleh, and M. C. Teich, Phys. Rev. A**40**, 1371 (1990).

High Efficiency Frequency Up-Conversion Enhanced by Electromagnetically Induced Transparency

C. Dorman, I. Kucukkara, M. Anscombe, R. Semaoune, J.P. Marangos

Physics Department, Blackett Laboratory, Imperial College of Science Technology and Medicine, Prince Consort Road, London SW7 2BZ e-mail:
j.marangos@ic.ac.uk

Abstract. Electromagnetically induced transparency (EIT) can enhance the conversion efficiency of a resonant four-wave mixing scheme. This is demonstrated for a scheme in Kr resulting in the generation of a field at 123.6 nm. The absolute VUV radiation yield was measured using a calibrated photodiode in the limit of a large density-length product. Energies of ~ 30 nJ per pulse were produced, with an energy conversion efficiency from the coupling field of $\sim 1\%$. Higher yields are thought to be achievable by the use of a transform limited UV pulse of the same duration as the coupling field and by increasing the coupling laser intensity and the path length in the medium.

1 Introduction

In 1990 Steve Harris proposed [1] that the phenomenon of electromagnetically induced transparency (EIT) could be used in a resonant frequency mixing scheme to suppress the absorption of the light generated whilst also improving the phase-matching by altering the dispersion. The third-order non-linearity of the medium $\chi^{(3)}$ can be enhanced by resonance (for example 2-photon resonance [2][3]) but normally the generated field must be far from single photon resonance to avoid re-absorption. The dispersion of the medium at a resonance also usually varies steeply, causing disruption to the phase matching. The advantages of this type of EIT scheme are that the non-linear susceptibilities ($\chi^{(3)}$) governing the coupling of light into the generated field are still resonantly enhanced through constructive interference. In contrast the linear susceptibility (governing absorption and dispersion) undergoes destructive interference. Accompanying changes in the dispersion of the medium improve phase matching by increasing the coherence length.

Experiments have followed that demonstrate the viability of this method of wave mixing. In 1993 Jain et al. observed electromagnetically induced phase-matching in a four-wave mixing scheme in lead, with a measured conversion efficiency of 2.4×10^{-8} when referenced to the power of the coupling laser [4]. Recently Merriam et al.[5] achieved near unity conversion efficiency in a lead four-wave mixing scheme using the principles of EIT. This scheme generated a field in the far UV at 186 nm using three near resonantly tuned

transform limited lasers. This type of mixing scheme relies upon the creation of a maximal coherence by a pair of transform limited laser pulses Raman resonant with atomic levels in a Λ configuration. A third field, close to resonance with a fourth energy level, mixes with this coherence to generate a new field with very high efficiency. It is not clear that this kind of scheme can be extended to the generation of significantly higher frequency fields (e.g. < 130 nm) due to the absence of atoms with suitable energy level configurations.

For the generation of shorter wavelength high energy two-photon resonances can be employed in a four-wave mixing scheme (Figure 1(b)), but at the cost of large detunings from any single photon resonance for these two-photon transitions. The detrimental effects of large detuning can be partially compensated by using EIT with high density-length products to enhance frequency mixing. In 1993 Zhang et al.[6] reported their results from a four-wave sum-mixing scheme using electromagnetically induced transparency in atomic hydrogen. The conversion efficiency to the VUV (102.6 nm) was measured to be 1×10^{-4} , limited by the rather low density-length products available in the atomic hydrogen medium [6]. Subsequent work by these authors succeeded in showing conversion efficiencies $> 10^{-3}$ under conditions of larger density-length product. There were, however, other limits in this scheme to achieving higher conversion efficiency for instance the large Doppler broadening (30 GHz) of the hydrogen transitions at the temperatures of the sample. As a consequence further increase in the density-length product did not result in further improvements in conversion efficiency.

Here we report an observation of $\sim 1\%$ conversion efficiency into the VUV at 123.6 nm using a four-wave mixing scheme in room temperature krypton. An advantage compared to hydrogen is the relatively small Doppler width of the transitions involved (1 GHz). Atomic energy levels for Kr involved in this interaction can be reduced to the three levels shown in Figure 1. EIT can occur in this ladder configuration (Figure 1 (a)) comprising a ground-state $4p^6 \ ^1S_0$, ($|1\rangle$), an excited state $4p^5 5s[1, 1/2]$ ($|3\rangle$) dipole coupled to $|1\rangle$, and an excited state $4p^5 5p[0, 1/2]$ ($|2\rangle$) which is dipole coupled to $|3\rangle$ but not to $|1\rangle$. The medium, optically deep at ω_{VUV} (123.6 nm), can be rendered transparent by a field ω_c (758 nm). This basic EIT ladder scheme can be incorporated within a resonant four-wave mixing scheme, Figure 1(b), by the introduction of a two-photon resonant field at 212.55 nm (ω_{VUV}), applied in two photon resonance with the $|1\rangle$ - $|2\rangle$ transition. There is a large single photon detuning of this field from the nearest intermediate state of $33,000$ cm $^{-1}$. For resonant conditions the absorption and coherence length of the medium will be highly dependent on the coupling laser intensity. As the 758nm pulse energy is increased these lengths will become many orders of magnitude larger when the coupling laser Rabi frequency exceeds the Doppler width of the 123.6 nm transition. The absorption at 123.6 nm is suppressed by EIT due to destructive interference on the absorption pathway whilst the mixing process remains resonantly enhanced due to constructive interference

[7]. A significant enhancement in the frequency up-conversion efficiency is therefore expected.

In previous experiments conducted using a Kr gas jet [8], a large ($\sim 10^4$) increase in the VUV yield was demonstrated by using a resonant coupling laser in an optically deep sample. In the experiment reported here a krypton filled cell was used which permitted accurate determination of path-length and density and an increase in the density-length product (NL) of the krypton medium to values much greater than those achievable in the gas jet. The gas jet had densities 10^{15} - 10^{16} cm $^{-3}$ of krypton with path lengths 0.1 to 0.5 cm ($NL \sim 10^{15}$ cm $^{-2}$), approximately the same NL values as the maximum used in earlier four-wave mixing schemes in hydrogen [6]. In contrast the 1 cm gas cell was operated in the pressure range 0 - 10 mbar ($0 < NL < 2.5 \times 10^{17}$ cm $^{-2}$). This increase in NL allowed us to access higher conversion efficiencies.

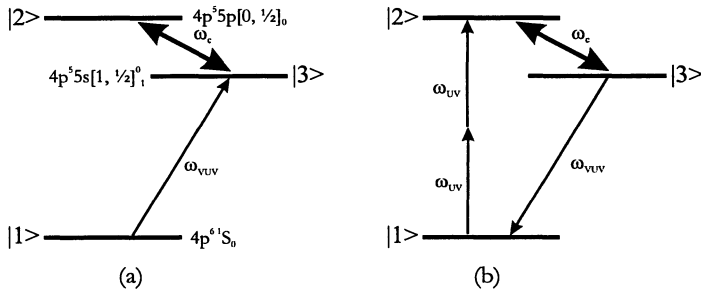


Fig. 1. Level scheme in krypton. (a) Shows a scheme for EIT, giving transparency at 123.6 nm by application of 759 nm coupling field ω_c . (b) Shows the four wave mixing scheme with two-photon pump field at 212.55 nm (ω_{UV}) and 759 nm coupling field (ω_c) with light generated at 123.6 nm (ω_{VUV}).

2 Calculation of Susceptibilities and Non-Linear Mixing

The susceptibilities were found by solving the equations of motion of the density matrices of the atom under steady-state conditions. After Doppler averaging the resulting susceptibilities were used in a propagation calculation to yield the dependence of the generated VUV signal on various parameters that can be compared with the experiment results. A fuller description of the method used can be found in [7], and here we will provide only an outline. The Hamiltonian for the interaction with the electromagnetic fields is V :

$$V = \hbar\Omega_a e^{-i2\omega_a t} |2\rangle\langle 1| + \hbar\Omega_C e^{-i\omega_C t} |2\rangle\langle 3| + \hbar\Omega_g e^{-i\omega_g t} |3\rangle\langle 1| \quad (1)$$

Ω_a is the effective two-photon Rabi frequency arising from the two-photon resonant field at frequency ω_a , Ω_C is the coupling field Rabi frequency and Ω_g is the Rabi frequency of the generated field (where $\hbar\Omega_i = \mu_i |E(\omega_i)|$). The evolution of each density matrix element is described by the Liouville equation:

$$\hbar \frac{\partial \varrho_{nm}(t)}{\partial t} = -i \sum_k H_{nk}(t) \varrho_{km}(t) + i \sum_k \varrho_{nk}(t) H_{km}(t) + \Lambda_{nm} \quad (2)$$

where Λ_{nm} in (2) is a phenomenological decay term. This system of equations can be solved to yield values for each of the matrix elements. The rotating-wave approximation is made and the terms in the equations of motion are transformed into a rotating frame such that all the frequencies are eliminated with the exception of the detunings:

$$\Delta_a = \omega_{13} - 2\omega_a, \quad \Delta_C = \omega_{32} - \omega_C, \quad \Delta_g = \omega_{21} - \omega_g. \quad (3)$$

Further it is assumed that the system is closed so that the population sum $\varrho_{11} + \varrho_{22} + \varrho_{33} = 1$. In the conditions of the experiment $\Omega_C \gg \Omega_a, \Omega_g$, and also in practice, it is always true that $\varrho_{11} \gg \varrho_{22}, \varrho_{33}$. In the calculations considered here the matrix elements are calculated in the steady-state limit. All fields, other than Ω_C , are assumed to be weak so their effects are usually only retained up to first order. But Ω_C is retained to all orders in the calculation. A set of differential equations of the form (2) [7] are obtained. These can be solved in the steady state limit by a straightforward inversion of what reduces to an 8×8 matrix.

The phenomenological dampings in (2) include the spontaneous decay rates appropriate for these states of Kr. The effects of collisions and photoionisation on these damping rates were, however, ignored. The omission of collisional dampings is consistent with their expected values in this system under the density conditions likely ($< 10^{17} \text{ cm}^{-3}$) being at least an order of magnitude less [9] than the leading spontaneous decay rates. Photoionisation of state $|2\rangle$ will occur under the experimental conditions due to the presence of the field at ω_a but is found to be still significantly smaller than spontaneous decay rates of $|3\rangle$. Monochromatic fields are assumed in this calculation of the density matrix. Inserting a laser linewidth into a steady-state calculation, for instance by adding an additional phenomenological decay due to Wiener-Levy phase-diffusion of the fields, is a procedure that will overestimate their effect in this pulsed laser experiment. As a transform-limited coupling laser is employed the amount of dephasing over the laser pulse duration (the interaction time) is not significant.

The inverted matrix yields the steady-state values of the matrix elements. The relevant matrix element for the generation of the field at ω_g is ϱ_{13} . The macroscopic polarisation at ω_g is described in terms of the density matrix by the following expression;

$$P(\omega_g) = 2N\mu_{12}\varrho_{13} \quad (4)$$

The matrix element ϱ_{13} contains, to all orders, the terms relevant for calculating the dressed susceptibilities of the system i.e. $\chi_D^{(1)}(\omega_g; \omega_g)$ and $\chi_D^{(3)}(\omega_g; 2\omega_a, \omega_C)$. It is important to recognise that these quantities (even the "linear" terms $\chi_D^{(1)}$) are inherently non-perturbative since they include the interaction Ω_C to all orders.

In matching the calculations to the experiments, the modifications due to the Doppler effect is incorporated into the susceptibilities. Random Doppler shifts due to the Maxwellian velocity distribution of the Kr atoms cause a distribution in the detunings (defined equation 3) for the ensemble of atoms. The response of the medium, characterized by the susceptibilities, at a given set of applied laser frequencies must therefore include the Doppler broadening via performing the weighted sum over these detunings. Due to the Gaussian form of the Maxwellian velocity distribution, the effect on susceptibilities from atoms in velocity classes significantly larger than the width of the distribution (i.e. giving rise to frequency shifts significantly larger than the Doppler width) will be negligible.

The correct calculation of the intensity generated at ω_g proceeds by the substitution of these dressed and Doppler averaged susceptibilities into the propagation equation derived from Maxwell's equations:

$$\frac{\partial A_g}{\partial z} = i \frac{\omega_g}{4c} \chi_D^{(3)} A_a^2 A_C \exp(-i\Delta k_g z) - \frac{\omega_g}{2c} \text{Im} \left(\chi_D^{(1)} \right) A_g i \frac{\omega_g}{2c} \text{Re} \left(\chi_D^{(1)} \right) A_g \quad (5)$$

where A_i 's are the electric field amplitudes, Δk_g the wavevector mismatch for the generated field defined as $\Delta k_g = k_g + k_C - 2k_a$, where these wavevectors are also derived from the dressed and Doppler averaged susceptibilities. This equation can be solved analytically for a homogenous medium with a well defined length and this operation was carried out to generate a general analytical expression for the intensity of the generated field.

There were limitations to achieving quantitative agreement between these calculations and experiments. These arise from two sources; the lack of a full set of data for the dipole moments of transitions in Kr which prohibits the determination of an absolute value for Ω_P , and the neglect of the finite bandwidth of the UV laser employed on the two-photon transition. Good qualitative agreement is found between calculation and experiment despite these limitations.

3 Experimental Details

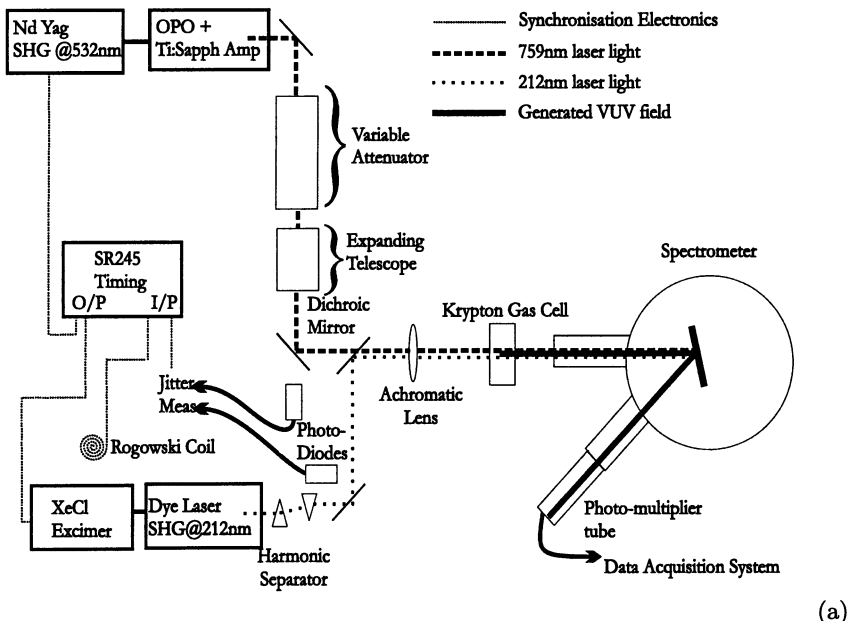
A schematic of the experiment is shown in figure 2(a). The coupling field (at 759 nm), was produced by a titanium-sapphire amplified optical parametric oscillator pumped by a single-mode, frequency-doubled Nd:YAG laser. This 759 nm coupling field was a single mode, near transform-limited pulse (< 250 MHz, 4 ns) which was kept to within ± 1 GHz of the resonance by reference to laser induced fluorescence in a krypton hollow-cathode lamp. The UV field

was produced by a XeCl excimer pumped dye laser, frequency doubled to produce a pulse of length 16ns, energy 150 μ J and 1.5 GHz bandwidth [8]. Two-photon resonance was determined by measurement of photo-ionisation in a separate krypton gas cell. The relative jitter in arrival time of the laser pulses was minimised using computer controlled active feedback to around ± 2.5 ns, which is short compared to the 16ns pulse length of the UV field, and so the IR pulse was timed to coincide within ± 2.5 ns of the peak of the UV intensity.

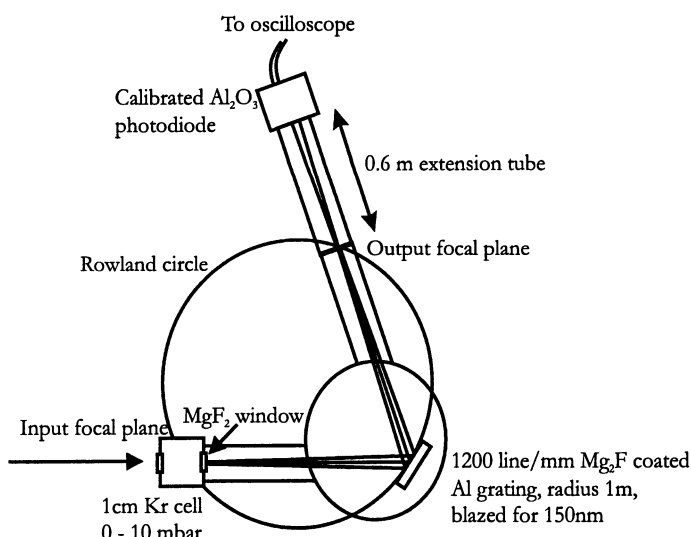
The UV laser field was focussed into a 1cm long cell containing Kr by a 33 cm focal length lens with a confocal parameter of ~ 10 cm. This ensured that the intensity of the UV radiation was uniform throughout the 1cm long cell. At the interaction region the coupling beam diameter was larger (2.3 ± 0.1 mm) to provide uniform intensity throughout the focussed region of the (0.10 ± 0.02 mm) UV beam, with the coupling beam size changing very little over the length of the cell. These beam sizes were measured with a CCD array placed at the interaction plane. The rear window of the cell consisted of a 3mm thick polished MgF₂ disc which transmitted the generated VUV radiation into a 1 m Seya mounted grating spectrometer (See Figure 2(b)). The spectrometer was pumped by an oil diffusion pump and maintained at a pressure of 10^{-5} mbar. The grating was a 1200 lines/mm aluminium coated ruled grating, with a 998.8 mm concave radius and a magnesium fluoride coating to prevent oxidation of the surface (supplied in 1998).

The relative scaling of the VUV pulse intensity (but not the absolute energy) with coupling laser intensity were made using a solar blind photomultiplier tube (PMT). The PMT was used due to its high sensitivity and large dynamic range. To measure the dependence of the VUV intensity on the coupling laser pulse strength the coupling laser energy was varied using an adjustable wave-plate/ polariser combination placed in the beam. The VUV signal data was then recorded on a shot wise basis along with the coupling laser pulse energy measured using a calibrated photodiode.

The absolute VUV radiation intensity was measured using a calibrated photo-diode at the exit slit of the monochromator. The aluminium oxide photodiode was issued by NIST as a transfer standard detector calibrated in 1987 [10]. The detector was essentially solar blind and produced extremely low dark current and noise characteristics. Radiation incident on the photo-cathode generated photoelectrons in the film and an anode biased to 60V generated an electric field that enhanced the collection of the electrons emitted from the surface. The signal was measured on a fast oscilloscope (Tektronix TD620). The sensitivity of the photodiode to light at the generated wavelength, 123.58 nm was extrapolated (from the quantum efficiency curves provided in [10]) to be $0.0075(\pm 0.001)$ electrons per photon. In order to minimise saturation due to space-charge effects a large VUV spot was used. The VUV was nominally focussed at the exit slit of the monochromator and so the photo-cathode was mounted 600 mm back from this plane. The signal



(a)



(b)

Fig. 2. (a)Schematic of experiment showing laser systems and optical arrangement. (b)Schematic of experiment showing the spectrometer, with 60 cm extension on output port. The Rowland circle of the grating is indicated

in this position was seen to increase by a factor of > 100 compared to that with the detector at the exit focal plane of the VUV, indicating the strong saturation that resulted from the small beam area.

In order to determine the actual VUV pulse energy generated in the cell, several factors need to be taken into account, including the efficiency of the grating and the transmission of optics between the region of generation of the VUV and detection. Taking into account the ruling efficiency, the reflectivity of aluminium, and the blaze angle, the efficiency of the grating was calculated to be $10 \pm 5\%$. It should, however, be noted that additional losses might occur due to the deterioration of the grating surface with time and VUV absorbing impurities in the vacuum chamber. The rear window of the cell was made of magnesium fluoride. This material is often used for VUV work, due to its transmission of short wavelength light and non-hygroscopic nature. However, 123.58 nm light is near the limit of its transparency dictating the accurate measurement of the transmission of the window at 123.58 nm. The window was placed in the output arm of the spectrometer and the attenuation of the signal was measured using the photomultiplier operated in the linear regime. The rear window of the cell was replaced for this run by a similar MgF₂ window. The window used in the calibration experiment was found to transmit 15% of the incident VUV radiation.

4 Results and Discussion

A series of experiments were carried out to investigate the dependence of the VUV intensity on the coupling laser energy at a number of different NL values. The NL value was varied by changing the Kr pressure (always at room temperature) within the 1 cm long cell. Values of NL from 10^{15} cm^{-2} to $2.5 \times 10^{17} \text{ cm}^{-2}$ were investigated. The lower NL values coincided with those already investigated for a gas jet [8], and the measured VUV intensity dependence on laser coupling strength was found to be very similar to this previous data. In the low NL region ($NL \sim 10^{15} \text{ cm}^{-2}$) the VUV intensity grows quickly at small coupling strengths to reach a maximum, followed by a plateau, for coupling field Rabi frequencies exceeding the Doppler width ($\sim 1\text{GHz}$). As NL is increased the peak in the VUV intensity increases and is reached at larger coupling laser strength. This is shown in figure 3 for five different pressures of Kr; (a) 0.12 mbar, (b) 0.25 mbar, (c) 0.48 mbar, (d) 0.95 mbar, (e) 1.7 mbar, from which plots the large increase in VUV yield as a function of NL is evident.

This behaviour reflects that expected from our theoretical treatment, as is clear from figure 4. Here the calculation is performed, under the same assumptions outlined earlier, for the NL values corresponding to the same five pressures examined in the experiment. Whilst the relative VUV intensities between these five curves is correct the intensity is not placed on an absolute scale for the reasons already explained. For the high NL products ($> 10^{16}$

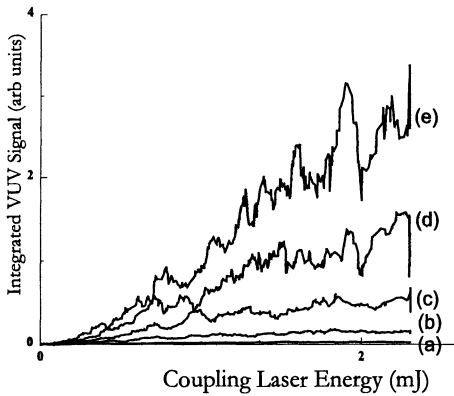


Fig. 3. Experimental dependence of the generated VUV pulse intensity (in relative units) as a function of the coupling laser pulse energy for various krypton pressures; (a) 0.12 mbar, (b) 0.25 mbar, (c) 0.48 mbar, (d) 0.95 mbar, (e) 1.7 mbar. The VUV intensity was measured on a shot to shot basis by a photomultiplier tube. Note that there is substantial shot-to-shot noise due to fluctuations in the UV laser intensity, which accounts for the noise in the plot.

cm^{-2}) the VUV intensity continues to rise, and reaches much higher values, as the EIT is improved with increasing coupling laser energy.

Under the higher NL conditions ($1.7 \text{ mbar} = 5 \times 10^{16} \text{ cm}^{-2}$) of the results shown in Figure 3 it should be noted that the coupling laser energy required to provide a Rabi frequency larger than the Doppler width ($0.5 \mu\text{J}$) is much less than that to satisfy the coupling laser preparation energy [11] (about 0.5 mJ). In the calibration experiment the pulse energy was 4 mJ giving a Rabi frequency of $\sim 10 \text{ cm}^{-1}$ for the coupling laser, as compared to the Doppler width of the VUV transition, which was only 0.03 cm^{-1} . Given the energy limitations of the coupling laser it was found that the maximum VUV intensity, though not necessarily the VUV efficiency, was found at ~ 2 mbar. Above 2 mbar the intensity of the VUV generated falls off again as the increased coupling pulse intensity necessary to overcome the preparation energy requirement and to create transparency leads to a reduction in the non-linear susceptibility, governing the coupling of energy into the VUV field. This complex interplay between the optimum NL product and the coupling intensity will be the subject of further investigation.

The highest VUV signals were found at the highest coupling intensities available. For coupling pulse energies of 4 mJ the optimum VUV generation was found at ~ 2 mbar. The pressure of krypton, 2 mbar, gave an NL value of $5 \times 10^{16} \text{ cm}^{-2}$. Under these conditions the output of the photodiode was a pulse of 10 ns with a pulse height of 2 mV measured into 50Ω . This corresponds to 2.5×10^6 electrons per pulse, giving a VUV pulse energy of 0.5 nJ. When the attenuation of the grating and the window are taken into account the energy of the VUV generated at the interaction region is calculated to be $33 \pm 10 \text{ nJ}$. This value of the VUV pulse energy is probably an underestimate. Absorption by residual oil molecules in the vacuum chamber and on the grating has not been taken into account. Some saturation of the signal at the photodiode is also a possibility. Larger displacements of the photodiode from the focal plane than 600 mm were impractical leaving

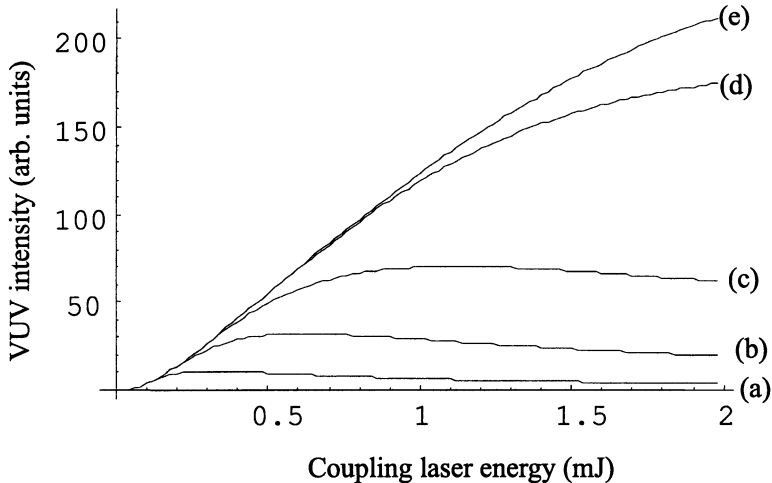


Fig. 4. Theoretical plots for the same conditions as the experiment i.e. 10mm cell and pressures ; (a) 0.12 mbar, (b) 0.25 mbar, (c) 0.48 mbar, (d) 0.95 mbar, (e) 1.7 mbar. The absolute scaling of the VUV signal is arbitrary and has been adjusted to be approximately the same magnitude as the experimental data.

the VUV spot still significantly smaller than the $6 \times 6 \text{ mm}^2$ spot size used for the calibration of the device. Therefore some signal saturation, further reducing the measured VUV energy, cannot be ruled out. The energy of the infrared pulse which interacts in the four-wave mixing scheme is that portion of the infrared light which overlapped the smaller (0.1 mm diameter) region in which the UV pulse was focussed in the cell. This was determined to be 5 μJ , corresponding to a conversion efficiency into the VUV of $\sim 1\%$ from the coupling laser.

The energy of the VUV generated will ultimately be limited by several factors. The first is that the 212.55 nm photoionisation channel can destroy coherence induced by the coupling field [8]. Another limiting factor is the driving of the $|1\rangle - |2\rangle$ coherence due to the generated field as discussed by Deng et al.[12]. They found that the optimum density-length product for a four-wave mixing scheme in rubidium was $6 \times 10^{14} \text{ cm}^{-2}$, limited by the destructive interference effects of the generated field. Our optimum density-length product, $5 \times 10^{16} \text{ cm}^{-2}$ is clearly much greater than that found by Deng et al. and is probably due to the transform limited nature of our coupling laser creating better transparency. There is however a maximum limit to the value of the density-length product of the medium when the preparation energy exceeds that provided by the coupling laser [11].

The most important practical limit to VUV energy will be the available input UV pulse energy. The UV pulse energy at the interaction region was measured to be 60 μJ with a pulse length of over 16 ns. The coupling laser

pulse duration was less than 4ns, therefore the effective UV energy available to the mixing process, within the coupling pulse duration, was only 15 μ J. Given that the generated VUV radiation was estimated to have an energy of 33 nJ, this corresponds to an efficiency, from the UV, of 0.2%. A UV pulse of similar length to the coupling pulse would produce much larger VUV energies. Another shortcoming of our UV laser is its bandwidth, 1.5 GHz, which was not optimally matched to the coupling field. This should also be taken into account when analysing the relative efficiency of the scheme compared to the UV pulse energy, as matched UV and IR pulses are required for optimum conversion efficiency.

In our experiments only 100 μ J UV pulses were available, far higher energy transform limited UV pulse energies are in principle achievable. For example Bergeson et al. [13] produced 3 mJ transform-limited pulses at 210 nm with a pulse length and bandwidth well matched to the requirements of the present experiment. If we use a higher energy transform limited UV pulse, and keep the intensity at the focus at the same as in this work (by increasing the UV beam waist) we would expect to obtain an improved conversion efficiency due to the matched bandwidth. Even assuming no increase in efficiency but increasing the UV pulse energy to say 5 mJ we would expect to obtain VUV pulse energies of 10 μ J. This gives a peak power of 1kW and the pulse would be focusable to yield intensities $> 10^8 \text{ Wcm}^{-2}$ in a bandwidth $< 1 \text{ GHz}$. For a 20 Hz rep-rate system the average coherent VUV power would be 200 μW from this source.

5 Conclusion

In conclusion we have measured substantial VUV energies associated with high conversion efficiencies of about 1%, in an EIT enhanced VUV frequency up- conversion scheme. Future investigation will examine the VUV yield when two temporally-matched transform-limited pulses are used with a longer path-length cell. Conversion efficiencies significantly larger than 1% should be possible, with VUV pulse energies perhaps $> 10 \mu\text{J}$ if higher power transform limited UV pulses are used.

Usually schemes employed to generate coherent radiation at VUV wavelengths have made use of four-wave mixing in atomic gases conducted off-resonance in order to avoid re-absorption of the generated light. Typical conversion efficiencies in the region 10^{-5} - 10^{-6} are obtained with peak powers limited to the order of 1W. These schemes have been widely used in linear spectroscopy but the relatively low pulse energies generated have largely precluded other uses. With the high power VUV pulses available from EIT schemes new applications such as non-linear spectroscopy, photolithography and photochemistry may now become possible in the VUV. We suggest, for instance, that the high power 123.6nm pulse could be used in combination with another tunable transform limited pulse in the VUV/UV wavelength

range to carry out high resolution two photon spectroscopy into the 15-20 eV energy range.

Acknowledgment. We would like to acknowledge the technical help of Peter Ruthven and Shahid Hanif. We are very grateful to Steve Harris and G.Y. Yin for the loan of the calibrated photodiode, and to Steve Harris, Kozho Hakuta and Peter Knight for very useful discussions during this work. This work was funded by the UK EPSRC.

References

1. Harris S. E., J. E. Field, and A. Imamoglu, Phys. Rev. Lett., **64**, 1107, (1990)
2. G. Hilbig, and R. Wallenstein, IEEE J. Quantum Electron., QE-**19**, 194 (1983)
3. J. P. Marangos, N. Shen, H. Ma, M. H. R. Hutchinson and J. P. Connerade, J. Opt. Soc. Am. B., **7**, 1254 (1990)
4. M. Jain, G. Y. Yin, J. E. Field and S. E. Harris, Opt. Lett., **18**, 998 (1993)
5. A. J. Merriam, S. J. Sharpe, H. Xia, D. Manuszak, G. Y. Yin and S. E. Harris, Optics Lett., **24**, 625 (1999)
6. G. Z. Zhang, K. Hakuta, B. P. Stoicheff, Phys. Rev. Lett., **71**, 3099 (1993)
7. J.C.Petch, C.H.Keitel, P.L.Knight and J.P.Marangos, Phys.Rev.A, **53**, 543 (1996)
8. C. Dorman and J. P. Marangos, Phys. Rev. A, **58**, 4121 (1998)
9. W.R.Hindmarsh and J.M.Farr, *Progress in Quantum Electronics*, ed J.H.Sanders and S.Stenholm, (**2**, 141, Pergamon, New York, 1972)
10. U.S Department of Commerce, National Bureau of Standards, Report of Test, P.O. C3XD 9607400 (1987)
11. Harris.S.E and Z.-F.Luo, Phys.Rev.A, **52**, R928 (1995)
12. Lu Deng, W. R. Garret, M. G. Payne, and D. Z. Lee, Optics Letters, **21**, 928 (1996).
13. S. D. Bergesson, A. Balakrishnan, K. G. H. Baldwin, T. B. Lucatorto, J. P. Marangos, T. J. McIlrath, T. R. O'Brian, S. L. Rolston, C. JU. Sansonetti, Jesse Wen, N Westbrook, C. H. Chen and E. E. Eyler, Phys. Rev. Letters, **80**, 3475 (1998)

On the way to Bose-Einstein Condensates in Optical and Electro-Magnetic Traps

Q. Long, S. Y. Zhou, L. F. Xu, J. P. Yin, Y. Z. Wang

Shanghai Institute of Optics and Fine Mechanics of Chinese Academy of Sciences,
P.O.Box 800211, 201800 Shanghai China
e-mail: longq4@kali.com.cn

Abstract. We report in this paper some of our progress, including experimental work and proposals, in trapping and guiding atoms. A convenient method of measuring atomic density by studying the fluorescence interference fringes through CCD has been presented. An ac magnetic atomic guide and trap is proposed. The possibility of some new types of optical trap in realizing Bose-Einstein condensates has been discussed.

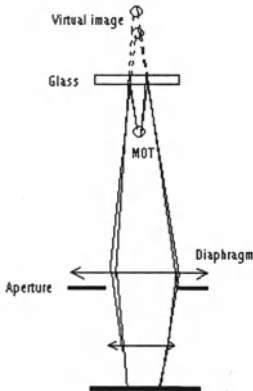
Our current work at Laboratory of Quantum Optics in SIOFM is focused on realizing Bose-Einstein condensates (BEC). We have built a two-vacuum-chamber system and a Rubidium atom beam system. Some experiments have been carried out on these systems. The paper is divided in two parts, experimental and theoretical works.

1 Experimental Work

1.1 Atomic Density Measured by Detection of the Interference Fringe of Fluorescence

To realize BEC it is important to get the information of the cold atomic density. The usual way to measure the density is to use a photodiode through detection of the total fluorescence collected by lens or the absorption of a weak probe beam. We present a convenient and quick one by just using a CCD camera. Although it is more sensitive than a diode [1], the ordinary CCD is easily saturated at the center of the atomic cloud. If adding an attenuator before the lens of CCD, the center peak can be viewed but at the expense of the fluorescence on the brim of the cloud. However, a interference fringe picture caused by the reflection of fluorescence by two surfaces of a plane glass will not saturate the CCD because of small reflection of the glass and limited spatial angle of observation. By recording the interference fringes, we can estimate from the CCD picture not only the total number of trapped atoms but also the magnitude of the atomic cloud.

We have observed the interfering fringes, which are produced by the light emitted from cold atom cloud and reflected by a plane glass window, whose thickness is 1cm, of a low-vapour-pressure cell. The paths of rays are shown

**Fig. 1.****Fig. 2.**

in Fig. 1. Fig. 2 is the image of the interfering fringe. When we change the width of CCD's diaphragm, the diameter of the interfering region changes along with it. If we asymmetrically change electric currents in coils to make cold atom cloud move, the fringes would move but the circle interfering region does not because it is restricted by the adjustable diaphragm (see Fig.1). In experiment we opened the CCD diaphragm to largest, and added an aperture whose diameter is 2cm near the lens to control the spatial angle of observation. The Len of the CCD is placed not directly to the MOT but with a little deviation to make sure the interfering region not be overlapped by the image of cold atom cloud. As the intensity recorded by CCD had been calibrated by using a weak laser beam whose intensity was known, we can count the total flux of interfering region by subtracting intensity of background fluorescence. The number of trapped atoms can be estimated according to

$$N \approx \frac{4\pi H^2 M W_A}{A R} \quad (1)$$

where M is the attenuate multiple, W_A the total flux of interference fringes, A the area of the aperture, H the distance from the virtual image to aperture and R the photon scattering rate[2]

$$R = \frac{(I/I_S)\pi\Gamma}{1 + (I/I_S) + 4(\delta/\Gamma)^2} \quad (2)$$

In the above equation I is total intensity of six laser beam in the trap, I_S is the saturation intensity $4.1\text{mw}/\text{cm}^2$, Γ the natural line width 6MHz for ^{87}Rb atom, and δ the detuning.

From the interference fringes we can also estimate the magnitude of MOT. As the cold atoms approximately obey the Gaussian distribution, a numerical simulation shows that when the half-width of the distribution is larger than

the separation of the fringes, the interference picture will be cancelled. Therefore, in return the separation of interference fringes can tell us the upper limit of the magnitude of MOT defined as the half-width of Gaussian distribution. Consequently, the atomic density can be determined by the total number and the half-width. The result of this method is very close to that obtained by traditional ways.

The conditions of our experiment on trapping ^{87}Rb atoms are listed as follows: the intensity of the trapping beam red detuned to $F = 2 \rightarrow F' = 3$ transition with $\delta = -3\Gamma$ is $17\text{mw}/\text{cm}^2$, it is 2cm in diameter; the repumping beam intensity is $2.5\text{mw}/\text{cm}^2$, tuned to resonance $F=1 \rightarrow F'=2$ transition; the vapor pressure about $1.5 \times 10^{-6}\text{Pa}$, the field gradient of quadrupole magnetic filed in axial direction is $18\text{G}/\text{cm}$. From the above method, we estimate the number of atoms trapped on $F=2$ is 4×10^8 , and a peak density is about $1.3 \times 10^{11}/\text{cm}^3$. However, since there exists strong optical pumping(although a repumping beam is present), the population in ground level $F=1$ is considerable. An extreme example is dark MOT. As the atom in $F=1$ contributes little to fluorescence, in order to get relatively exact number of atoms being trapped in $F=1$ we could do it by detecting the absorption of a weak probe beam whose frequency sweeps over the D_2 -line of ^{87}Rb . From such an absorption spectra, we can therefore determine the population ratio of two levels which is equal to the product of the ratio of two absorption probabilities of each level to excited level and the ratio of two absorption peak heights. We measured the total trapped atoms in both $F=1$ and $F' = 2$ is nearly 1×10^9 .

1.2 Optical Trap obtained by Conical Lens

We have generated a V-type optical trap by using a two-asymmetric-conical-Len system. An experiment on this trap to capture cold atoms from MOT is being carried out.

2 Theoretical Work

2.1 AC Magnetic Ioffe Atomic Guide and Trap

To realize BEC, we shall prepare the cold atoms in one vacuum chamber and then transfer them to another one with a higher vacuum degree. Compared with an optical guiding, the advantage of a magnetic one is that there is no photon scattering heating since there is no spontaneous emission. Several magnetic guidings have been proposed till now, but all of them are dc ones [3]. As we know the static trap is a weak-field-seeker and is unstable when subjected to hyperfine or Zeeman level exchange collisions. We propose an ac magnetic Ioffe guiding, where instead of dc, we use ac in Ioffe bars. The time-changing field will induce a magnetic dipole moment, the interaction of whom with the magnetic field will be analogous to that of a two-level atomic

electric dipole moment with a linearly polarized standing wave laser and will thus make the atom feel an attractive force to the center of the guide. A detail discussion of this new atomic guide will be given in the poster paper by L. F. Xu et al. Moreover, if close the current bars, we can also obtain an ac Ioffe trap.

2.2 Pyramidal Atom Trapping with Dark Hollow Beam Cooling

Instead of an evanescent wave used in gravitational optical trap [4], we adopt a blue detuned Dark Hollow Beam. By changing the Len's focus length, we can adjust the trapping angle. Our calculation of the dependence of the cooling efficient on trapping angle shows that, for continuous loading from a cold atom source, the steady state trapped atomic Densities for different angle are always higher than those needed for BEC under the same balance temperature. For a single load, the observation time of trapped atoms can be as long as from one to above ten seconds. We have also done Monte Carlo simulation to imitate the movement of atoms in the trap. It can be seen that the equilibrium temperature will tend to a value close to the theoretic predict and the atoms will eventually rest along the z axis (gravitational direction) and a small distance above the trap tip. A post paper written by J. P. Yin et al will give a more detailed description.

2.3 Optical Trap with the help of Additional Microwave Field

An optical trap using evanescent wave in gravitational field has been proposed by Soding et al. This kind of trap has overcome many limits in current optical traps, but there is still a problem. To realize BEC, we would like to obtain an equilibrium temperature and loss rate as low as possible. To reduce the loss rate we should reduce the spontaneous emission rates of the dressed atoms. Since they are inversely proportional to the detuning, it may be thought to increase the detuning. This will result in a smaller heating rate but will also reduce the cooling rate and the height of the trap potential, and may consequently enhance the equilibrium temperature. Is there a way to simultaneously reduce the loss rate and the balance temperature or reduce the spontaneous emission rates without changing the detuning? We find it possible if we apply an additional microwave field to couple the two ground levels. A destructive quantum interference induced by the present of both laser field and microwave field may cancel the spontaneous decay rate. Actually, the idea of using two fields to reduce spontaneous emission rate has been widely used in, such as, laser without inversion. From the energy cascade, it can be seen that m.w. may pump the atom from lower ground level to higher ground level and contribute to the cooling while modifies the spontaneous decay rates. By dressing the two ground levels with m.w., we can obtain the equivalent detuning, energy separation, branch ratios, Clebsh-Gordon coefficients and light shifts. Our calculation shows that for suitable parameters,

both the balance temperature and loss rate can be reduced. On the other hand, the geometric cooling induced by repump laser is not much affected by the m.w. field. However, there is a drawback in this proposal. Since the trap potential may be lower than that without m. W. Field, there may be a larger initial (before attaining a balance) loss rate.

Acknowledgement. This work was supported by Chinese National Natural Science Foundation. Q. Long was supported by Postdoctoral Research Aid of China.

References

1. C.G.Townsend, N.H.Edwards et al. (1995) Phase-space density in the magneto-optical trap. *Phys. Rev. A.* **62**, 1423-1440.
2. W.Demtröder, *Laser Spectroscopy* (Springer,New.York,1982) 105-106
3. D. J. Li, H. Huang, Y, H. Lu, S. Q. Li, *Opt. Commun.*, **160** (1999) 72 and references therein.
4. J. Soding, et al, *Opt. Commun.*, **119** (1995) 652.

Creation of Fock States in an Optical Cavity via Phonon-Photon Interaction

Eduardo Massoni and Miguel Orszag

Facultad de Física, Pontificia Universidad Católica.
Casilla 306, Santiago 22, Chile.

Abstract. An initial phonon vibrational distribution of an ion in a Paul trap can be ‘translated’ into a photon distribution in an optical cavity. This is achieved coupling the motion of the center of mass of the ion with a cavity mode via two internal ion levels. In particular, we can generate Fock states in the cavity. We also study the experimental realization of the present scheme.

1 Introduction

Single trapped ions [1] have led to observation of fundamental quantum phenomena such as quantum jumps [2], antibunching in resonance fluorescence [3] and quantum Zeno effect [4]. Also, coupling the ion energy levels with vibrational states, via one or more laser fields, proved the possibility of creating quantum vibrational states, such as Fock, coherent or squeezed states [8]. On the other hand, the creation of quantum states in a cavity has been a very active subject in recent years. For example, Brune *et al.* [5] proposed a model of three-level atom passing through two Ramsey fields and an optical cavity in between. At the exit point of the second Ramsey field, the final state of the atom is measured. These measurements affect the field inside the cavity, producing a decimation of the photon distribution until a Fock state is reached. In the present research, we study a system that is similar to Meyer *et al.* [11], where the trapped ion interacts resonantly with the cavity field. They show that the atom-field coupling and decay channels depend on the vibrational state of the ion. Here, we treat the non-resonant case and through incoherent pumping, we can copy a phonon distribution into the electromagnetic field in the cavity. We should point out that the phonon distribution is transferred without the coherences, so the final state is not a pure state, except for the pure Fock state case. This paper is organized as follows: in Sect. 2 we introduce the model and approximations. Section 3 contains the calculations leading to the phonon-photon transfer and in Sect. 4, we present the numerical results related to the transfer times, decoherence and the effects of atomic and cavity losses. Finally, in Sect. 5 we discuss the possibility of observing these effects in the laboratory.

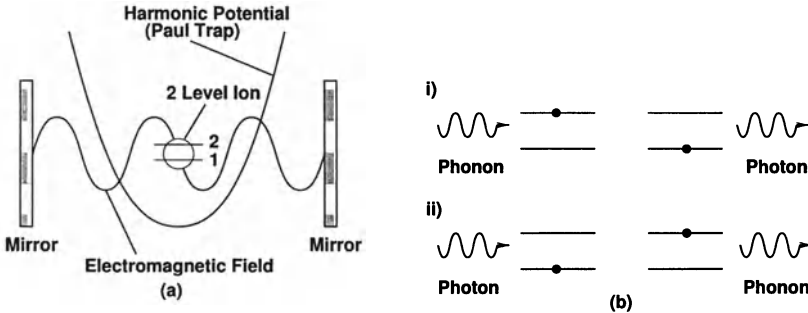


Fig. 1. (a) Schematic diagram of the PPT considered in this paper. (b) Two processes suggested by the Hamiltonian (1): (i) absorption of a phonon followed by the creation of a photon and decay of the ion from level 2 to 1, and the inverse process (ii) absorption of a photon followed by the creation of a phonon and the excitation of the ion.

2 The model

We consider a single trapped ion in a harmonic potential and located inside an optical cavity that consists of two mirrors, as shown in Fig. 1.a. The Hamiltonian of the system is given by

$$H = \hbar\omega_a\sigma_z + \hbar\omega_v b^+b + \hbar\omega_c a^+a + \hbar g \cos(kx + \phi)(a^+ + a)(\sigma^+ + \sigma^-).$$

where b^+ , b , a^+ , a are the creation and annihilation operators associated with the center of mass of the ion and one electromagnetic mode of the cavity respectively. σ_z , σ^+ , σ^- are the usual atomic operators of the two level ion defined in the basis $\{|2\rangle, |1\rangle\}$ as $\sigma_z = (|2\rangle\langle 2| - |1\rangle\langle 1|)/2$, $\sigma^+ = |2\rangle\langle 1|$ and $\sigma^- = |1\rangle\langle 2|$. The position operator is given by $x = x_0(b^+ + b)$, g is the atom-field coupling constant, k is the electromagnetic wavevector and ϕ determines the position of the trap inside the cavity. We consider the case $\omega_c = \omega_a + \omega_v$ that selects two possible processes: (i) a photon is created, a phonon is absorbed and the ion decays from state $|2\rangle$ to $|1\rangle$ and (ii) a photon is absorbed, a phonon is created and the atom is excited from state $|1\rangle$ to $|2\rangle$. These two processes are shown in Fig. 1.b. In the interaction picture, the Hamiltonian reads as follows:

$$H_I = \hbar\Omega(a\sigma^+b^+ + a^+\sigma^-b) \quad (1)$$

where $\Omega \equiv gkx_0\sin(\phi)$. We also introduce an incoherent pump from $|1\rangle$ to $|2\rangle$, with intensity Γ . This pump can be modeled through a process that corresponds to an inverse spontaneous decay [7]. The purpose of the pump is to favour process (i) over (ii), in such a way that the conversion from phonons to photons is achieved. We baptize the present system as the ‘Phonon-Photon

Translator' (PPT). Now, the evolution of the density operator ρ is given by Liouville's equation:

$$\frac{d\rho}{dt} = \frac{1}{i\hbar}[H_I, \rho] + \mathcal{L}_\Gamma \rho, \quad (2)$$

where $\mathcal{L}_\Gamma \rho \equiv \frac{\Gamma}{2}(2\sigma^+ \rho \sigma^- - \sigma^- \sigma^+ \rho - \rho \sigma^- \sigma^+)$ is the pumping term. From (1) and (2) we get the explicit formulas for the time evolution for the various density matrix elements expressed in the $|j\rangle|nc\rangle|nv\rangle$ (atomic, photon and phonon number) basis:

$$\begin{aligned} \dot{\rho}_{11} \frac{mc, mv}{nc, nv} &= -\Gamma \rho_{11} \frac{mc, mv}{nc, nv} \\ &+ \Omega \left\{ \sqrt{mc(mv+1)} \rho_{21} \frac{mc-1, mv+1}{nc, nv} + \sqrt{nc(nv+1)} \rho_{12} \frac{mc, mv}{nc-1, nv+1} \right\} \\ \dot{\rho}_{22} \frac{mc-1, mv+1}{nc-1, nv+1} &= \Gamma \rho_{11} \frac{mc-1, mv+1}{nc-1, nv+1} \\ &- \Omega \left\{ \sqrt{mc(mv+1)} \rho_{12} \frac{mc, mv}{nc-1, nv+1} + \sqrt{nc(nv+1)} \rho_{21} \frac{mc-1, mv+1}{nc, nv} \right\} \\ \dot{\rho}_{12} \frac{mc, mv}{nc-1, nv+1} &= -\frac{\Gamma}{2} \rho_{12} \frac{mc, mv}{nc-1, nv+1} \\ &+ \Omega \left\{ \sqrt{mc(mv+1)} \rho_{22} \frac{mc-1, mv+1}{nc-1, nv+1} - \sqrt{nc(nv+1)} \rho_{11} \frac{mc, mv}{nc, nv} \right\} \\ \dot{\rho}_{21} \frac{mc-1, mv+1}{nc, nv} &= -\frac{\Gamma}{2} \rho_{21} \frac{mc-1, mv+1}{nc, nv} \\ &+ \Omega \left\{ \sqrt{nc(nv+1)} \rho_{22} \frac{mc-1, mv+1}{nc-1, nv+1} - \sqrt{mc(mv+1)} \rho_{11} \frac{mc, mv}{nc, nv} \right\} \end{aligned} \quad (3)$$

with $\rho_{ij} \frac{mc, mv}{nc, nv} \equiv \langle mc | \langle mv | \langle i | \rho | j \rangle | nv \rangle | nc \rangle$. In the above system, we have neglected both the atomic and cavity loss terms, assuming that the corresponding lifetimes are much longer than the translation time. We will further discuss this approximation in Sect. 5. In the next section we study the problem of how to transfer the information of the vibrational state of the ion to the cavity mode.

3 Information Transfer

The PPT works as follows: we initially prepare the cavity in the vacuum state and the ion in a vibrational state $|\psi_v\rangle$. As mentioned in the introduction, the preparation of vibrational Fock, coherent or squeezed states has been achieved experimentally with the interaction of the ion with laser pulses in a Raman Scheme [8]. Also, we choose the initial state of the ion to be $|1\rangle$ for computational convenience. Once the system has been prepared in the

initial state, we turn on the incoherent pump that will convert phonons into photons via the process (i) until the phonons are depleted. At this point, it is clear that a phonon-photon conversion takes place. However, the question is: what is the relation between the initial state of the trap and the final state of the cavity?. In this section, we will show that the initial phonon distribution is identical to the final photon distribution.

Taking the Laplace Transform L of the system (3) for $nc = mc$ y $nv = mv$ we get:

$$\begin{aligned} s\wp_{11}^{nc,nv}(s) - \rho_{11}^{(0)} \frac{nc,nv}{nc,nv} &= G_{nc,nv} \left\{ \wp_{12}(s) + \wp_{21}(s) \right\} \\ &\quad - \Gamma \wp_{11}^{nc,nv}(s), \\ s\wp_{22}^{nc-1,nv+1}(s) - \rho_{22}^{(0)} \frac{nc-1,nv+1}{nc-1,nv+1} &= -G_{nc,nv} \left\{ \wp_{12}(s) + \wp_{21}(s) \right\} \\ &\quad - \Gamma \wp_{11}^{nc-1,nv+1}(s), \\ s\wp_{12}(s) - \rho_{12}^{(0)} \frac{nc,nv}{nc-1,nv+1} &= G_{nc,nv} \left\{ \wp_{22}^{nc-1,nv+1}(s) - \wp_{11}^{nc,nv}(s) \right\} \\ &\quad - \frac{\Gamma}{2} \wp_{12}(s), \\ s\wp_{21}(s) - \rho_{21}^{(0)} \frac{nc-1,nv+1}{nc,nv} &= G_{nc,nv} \left\{ \wp_{22}^{nc-1,nv+1}(s) - \wp_{11}^{nc,nv}(s) \right\} \\ &\quad - \frac{\Gamma}{2} \wp_{21}(s), \end{aligned}$$

where we have used the following definitions: $\wp_{11}^{nc,nv} \equiv L\left(\rho_{11}^{nc,nv}(t)\right)$, $\wp_{22}^{nc-1,nv+1} \equiv L\left(\rho_{22}^{nc-1,nv+1}(t)\right)$, $\wp_{12}(s) \equiv L\left(\rho_{12}^{nc,nv}(t)\right)$, $\wp_{21}(s) \equiv L\left(\rho_{21}^{nc-1,nv+1}(t)\right)$ and $G_{nc,nv} \equiv \Omega\sqrt{nc(nv+1)}$. With the initial conditions described before, the only non-zero initial elements are $\rho_{11}^{(0)} \frac{0,nv}{0,nv}$. After some algebra we find:

$$\wp_{11}^{nc,nv}(s) = \frac{2G_{nc,nv}^2 \Gamma \wp_{11}^{nc-1,nv+1}(s)}{(s + \Gamma/2)(s^2 + \Gamma s + 4G_{nc,nv}^2)}, \quad (4)$$

$$\wp_{22}^{nc-1,nv+1}(s) = \frac{2G_{nc,nv}^2 \wp_{11}^{nc,nv}(s) + \Gamma(s + \Gamma/2) \wp_{11}^{nc-1,nv+1}(s)}{(s(s + \Gamma/2) + 2G_{nc,nv}^2)}, \quad (5)$$

$$\rho_{12}(s) = \frac{G_{nc,nv}(\varphi_{22}^{nc-1,nv+1}(s) - \varphi_{11}^{nc,nv}(s))}{(s + \Gamma/2)} = \varphi_{21}(s), \quad (6)$$

$$\varphi_{11}^{0,nv}(s) = \frac{\rho_{11}^{(o)0,nv}}{(s + \Gamma)}, \quad (7)$$

$$\varphi_{22}^{nc,0}(s) = \frac{\Gamma \varphi_{11}^{nc,0}(s)}{s}. \quad (8)$$

From (4),(7) and (8) we can calculate the final photon distribution $\rho_{22}^{N,\theta}_{N,0}(t)$.

With the initial probability distribution $P_N = \rho_{11}^{(o)0,N}_{0,N}$ of having N phonons in the trap and the recursion relation (4), we obtain $\varphi_{11}^{N,\theta}(s)$. Then from (8), the inverse transform of $\varphi_{22}^{N,\theta}(s)$ gives us the the final probability distribution $\rho_{22}^{N,\theta}_{N,0}(t)$ of having N photons in the cavity. Explicitly we have

$$\varphi_{11}^{N,\theta}(s) = \frac{P_N(2\Omega^2\Gamma)^N(N!)^2}{(s + \Gamma/2)^N(s + \Gamma)} \prod_{i=1}^N \frac{1}{(s - \lambda_i^+)(s - \lambda_i^-)}, \quad (9)$$

$$\rho_{22}^{N,\theta}_{N,0}(t) = \Gamma \int_0^t dt' \rho_{11}^{N,\theta}_{N,0}(t'), \quad (10)$$

with $\lambda_i^\pm = \frac{-\Gamma}{2} \pm \frac{\sqrt{\Gamma^2 - 4\eta_i^2}}{2}$ and $\eta_i^2 = 4\Omega^2 i(N + 1 - i)$. Before doing the inverse transform of (9), we notice that if N is even, there are $N/2$ factors of multiplicity 2 of the type $(s - \lambda_i^+)^2(s - \lambda_i^-)^2$, while if N is odd, there will be $(N - 1)/2$ factors of the same kind plus an extra factor of multiplicity 1 of the type $(s - \lambda_i^+)(s - \lambda_i^-)$. Since both calculations are quite similar we will concentrate in the even N case. We define:

$$F(s) \equiv \frac{1}{(s + \Gamma/2)^N(s + \Gamma)} \prod_{i=1}^{N/2} \frac{1}{(s - \lambda_i^+)^2(s - \lambda_i^-)^2}. \quad (11)$$

For the sake of simplicity we take the limit $\Gamma \gg 4\eta_i^2$. The exact calculation will generate more terms with the same qualitative result in the transfer from a phonon distribution in the trap to a photon distribution in the cavity. In this limit, the factors like $\frac{1}{(s - \lambda_i^-)^2}$ transform to fast decaying exponentials that contribute little to (10), so we can write

$$F(s) = \sum_{i=1}^{N/2} \frac{A_i}{(s - \lambda_i^+)^2} + \frac{B_i}{(s - \lambda_i^+)}, \quad (12)$$

where

$$\begin{aligned} A_i &= F(s)(s - \lambda_i^+)^2 /_{s=\lambda_i^+} \\ &= \frac{-2^N}{\lambda_i^- (\Gamma^2 - 4\eta_i^2)^{N/2+1}} \prod_{i \neq j=1}^{N/2} \frac{1}{(\eta_j^2 - \eta_i^2)^2}, \\ B_i &= \frac{d}{ds} (F(s)(s - \lambda_i^+)^2) /_{s=\lambda_i^+} \\ &= A_i \left\{ \frac{-2(N+1)}{\sqrt{\Gamma^2 - 4\eta_i^2}} + \frac{1}{\lambda_i^-} - 2\sqrt{\Gamma^2 - 4\eta_i^2} \sum_{i \neq j=1}^{N/2} \frac{1}{\eta_j^2 - \eta_i^2} \right\}. \end{aligned}$$

Now taking the inverse transform of (12) and using (9), we get

$$\rho_{11}^{N,\theta}(t) = P_N(2\Omega^2\Gamma)^N (N!)^2 \sum_{i=1}^{N/2} \exp(\lambda_i^+ t) (A_i t + B_i). \quad (13)$$

We still need to comment about the diagonal matrix elements $\rho_{22}^{i,j}(t)$. Evidently $\rho_{22}^{N,\theta}(t)$ will have a non-zero value when the transfer is finished, as seen from (10). However, intermediate elements like $\rho_{22}^{N-j,j}(t)$ ($j = 1..N$) will decay to zero. This result can be seen from (5), rewritten as

$$\rho_{22}^{nc-1,nv+1}(s) = \rho_{11}^{nc,nv}(s) h(s) + \rho_{11}^{nc-1,nv+1}(s) g(s), \quad (14)$$

where $h(s)$ and $g(s)$ are easily read out. If we take the inverse Laplace transform to the last equation and using the convolution theorem, equation (14) takes the following form:

$$\begin{aligned} \rho_{22}^{nc-1,nv+1}(t) &= \\ &\int_0^t du \left(\rho_{11}^{nc,nv}(u) H(t-u) + \rho_{11}^{nc-1,nv+1}(u) G(t-u) \right). \end{aligned} \quad (15)$$

However, the inverse Laplace transforms $H(t)$ and $G(t)$ of h and g respectively are proportional to $\exp(-\Gamma t/4)$, so these terms will vanish for long times.

Now, we go back to the question posed at the beginning of this section. First, we notice that all the matrix elements $\rho_{11}^{nc,nv}(t)$ decay to zero for obvious reasons. In the continuous phonon-photon conversion, we end up with no phonons in the trap, thus inhibiting the process i) which allows the $|2\rangle \rightarrow |1\rangle$ transition. If we continue to incoherently pump the system, there is no way to keep the system in state $|1\rangle$. On the other hand, if for example we start with a vibrational Fock state, that is $P_N = 1$ for a given N , then

according to the recursion relations (4) and (5), the diagonal matrix elements participating in the dynamics are $\rho_{11}^{j,N-j}(t)$, $\rho_{22}^{j,N-j}(t)$ ($j = 0..N$). All the matrix elements of this set that we call the ‘transfer channel of N ’ should add up to one. Since all the elements of this channel decay to zero except for $\rho_{22}^{N,0}$, we conclude that $\rho_{22}^{N,0}(\infty) = 1$ (a Fock state in the cavity). In the general case of an arbitrary distribution P_N , each N has its own independent transfer channel and there is no probability flux between them. Since P_N is just a factor in (13) and using the previously discussed fact that each Fock state is totally transmitted from the trap to the cavity, we arrive to the conclusion that $\rho_{22}^{N,0}(\infty) = P_N$. Figure 2 shows the transmission of an initial Poissonian phonon distribution corresponding to a coherent state with $\alpha = 1.2$. For long times, $t = 20 \Omega^{-1}$, the cavity ends up with the same distribution.

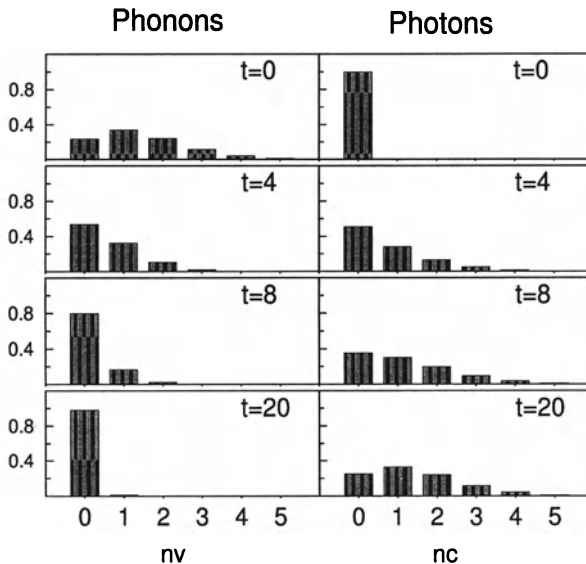


Fig. 2. Time evolution of the phonon (right column) and photon (left column) distributions. The initial Phonon distribution corresponds to a coherent state with $\alpha = 1.2$.

4 Numerical Simulation

We have solved numerically the set of equations (3). Our analytical solutions of the matrix elements show no difference with the numerical solutions with

a high enough pumping rate Γ . As discussed in Sect. 3, we only take this approximation for the sake of simplicity, but exact analytical formulas can be obtained following a similar procedure for all values of Γ . For these reasons, all the following figures are plotted from the numerical calculations. All parameters are scaled by Ω to make them dimensionless. Here, we will compare the effects of cavity and atomic losses in the behaviour of the PPT versus the ideal case where no losses are introduced.

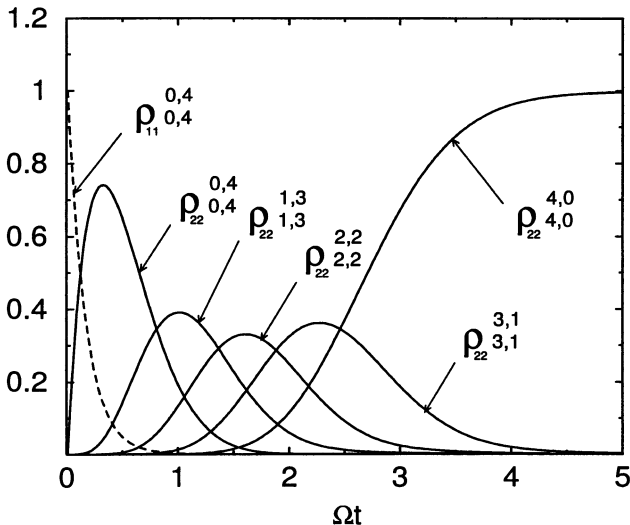


Fig. 3. Time evolution of some density matrix elements corresponding to an initial vibrational Fock state $N = 4$, $\Gamma = 6$ without cavity and atomic losses. The only surviving element for long times is (i.e. phonon vacuum state and photon Fock state $N = 4$).

Ideal PPT

In Fig. 3 we have plotted the time evolution of some diagonal matrix elements corresponding to a transmission channel of an initial vibrational Fock state $N = 4$. We observe that there is not a direct transmission of the probability from $\rho_{11}^{0,4}$ to $\rho_{22}^{4,0}$ but through intermediate elements. As shown in this figure, these intermediate elements appear and decay in an ordered sequence: $\rho_{22}^{1,3}$, $\rho_{22}^{2,2}$ and $\rho_{22}^{3,1}$. The same occurs to the other $\rho_{11}^{i,4-i}$, ($i = 1..4$) and the off-diagonal elements, not plotted here. Physically speaking, this just shows that the conversion of phonons to photons is done gradually. For the specific case of a general phonon state, the initial coherences decay to

zero in a time scale similar to the diagonal elements. To analize when this conversion is finished we define a characteristic time τ_N as the time it takes for $\rho_{22}^{N,0}$ to reach 90% of its final value. We found an optimum pumping rate Γ that produces the fastest phonon-photon conversion. This is shown in Fig. 4, where τ_N is plotted versus Γ for various initial vibrational Fock states with $N = 2, 4, 16$. This dependence shows, for a fixed Γ , that the larger N portion of a general distribution (e.g. a coherent state) is transmitted first and the lower N values take a longer time (Fig. 2).

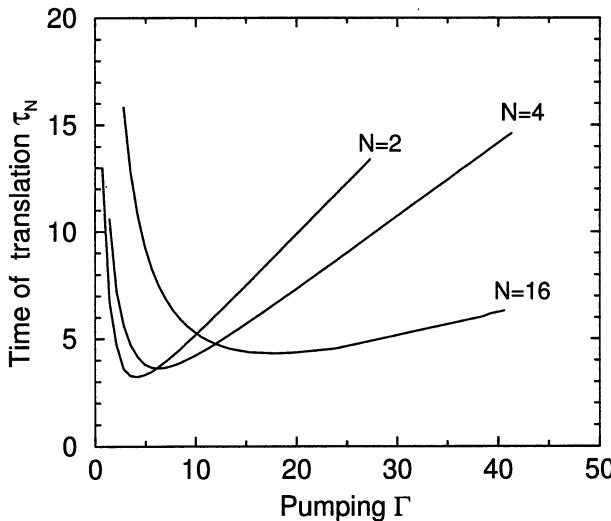


Fig. 4. Translation time versus pumping rate Γ for different initial vibrational Fock states $N = 2, 4, 16$. Each curve has a minimum which gives the optimal pumping rate for a given value of N

Non Ideal PPT

Here, we introduce cavity and atomic losses by adding to (2) the standard Liouville operators $\mathcal{L}_{atom}\rho$ and $\mathcal{L}_{field}\rho$. They are defined as:

$$\begin{aligned}\mathcal{L}_{atom}\rho &\equiv \frac{\gamma_a}{2}(2\sigma^-\rho\sigma^+ - \sigma^+\sigma^-\rho - \rho\sigma^+\sigma^-), \\ \mathcal{L}_{field}\rho &\equiv \frac{\gamma_c}{2}(2a\rho a^\dagger - a^\dagger a\rho - \rho a^\dagger a),\end{aligned}$$

where γ_a is the spontaneous emission rate from level $|2\rangle$ to $|1\rangle$, and γ_c is the cavity damping rate. These losses spoil the final photon distribution in two different ways. The cavity losses will eventually kill the field in the cavity.

On the other hand, spontaneous emission increases the time the ion is in state $|1\rangle$, favouring the conversion of photons to phonons. Fig. 5.a shows the final photon and phonon distribution with an initial vibrational Fock state $N = 4$, $\gamma_a = 2$, $\gamma_c = 0$ and $\Gamma = 10$. We see that spontaneous emission spreads the final distributions, so the trap ends up with some phonons and the field is no longer a Fock state with $N = 4$. To minimize the effect of the spontaneous emission we could increase the pumping rate Γ . However this also increases the transmission time τ_N . For example, varying the pumping rate from $\Gamma = 10$ to 25 with $\gamma_a = 0.2$ raises τ_4 by about a factor 2, as seen in Fig 5.b. This dependence limits the value of Γ to keep τ_N quite below the cavity lifetime. Next, we discuss the experimental realization of the PPT and the possible applications.

5 Discussion

Some realistic values of the parameters are: $g = 10\text{ MHz}$, $\gamma_c = 1\text{ MHz}$ to 10 MHz [11], $\gamma_a = 1\text{ MHz}$ to 100 MHz , and the cavity wavelength $\lambda = 866\text{ nm}$ [10]. We define also the parameter $\eta \equiv kx_0$ such that $\Omega = g\eta$ ($\phi = 0$). If we scale the above frequencies by Ω we get: $\gamma_a = 0.1/\eta$ to $10/\eta$ and $\gamma_c = 0.1/\eta$ to $1/\eta$. A reasonable value for $\eta = 0.5$ can be obtained for trap parameters as in [8]. These parameters allow us to set $\gamma_a = 0.2$ to achieve the transmission of a vibrational Fock state $N = 4$ to a final cavity Fock state $N = 4$ with probability = 0.95 (i.e $\rho_{22}^{4,0} = 0.95$) for $\Gamma = 10$ as in Fig 5.b. However, the transmission time $\tau_4 = 5\Omega^{-1}$ is of the same order as the cavity lifetime $t_c = \gamma_c^{-1} = 5\Omega^{-1}$. This shows that we require an optical cavity with higher quality Q-parameter by at least a factor 10 to observe a good translation.

As an application, we may think about a one atom laser with some novel features. In order to make it work, we would need two kinds of pumping. The atomic pumping to favour phonon to photon conversion, and a phonon pumping to maintain the production of photons. As we have shown in this work, the vibrational state of the ion influences the photon distribution in the cavity. So we could manipulate the field state via the phonon pumping. The phonons can be pumped via Raman coupling, a spatially uniform classical driving field or a parametric driving of the ion [8]. This variety of pumps may lead to new and interesting physics.

In summary, we have shown the possibility of transferring a phonon distribution of an ion in a Paul trap to a photon distribution in a high-Q cavity. This scheme can be used to produce photon Fock states in an optical cavity. *Acknowledgments.* One of us (M.O) would like to thank the support of Fondecyt (#1980807).

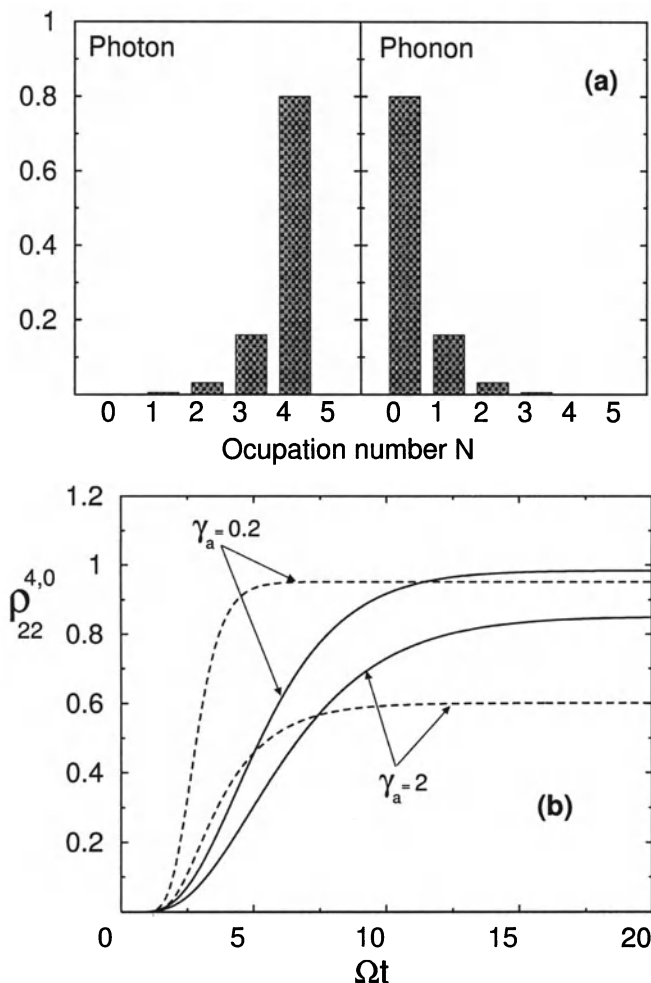


Fig. 5. All plots are for an initial vibrational Fock state $N = 4$. (a) Final Photon and Phonon distributions with $\Gamma = 10$, $\gamma_a = 2$ and $\gamma_c = 0$. (b) Time evolution of ρ_{22} matrix elements with different spontaneous emission rates $\gamma_a = 2$ and $\gamma_a = 0.2$. We observe that as we increase the pumping rate from $\Gamma = 10$ (dashed line) to $\Gamma = 25$ (solid line), τ_N grows.

References

1. The physical discussion of the Paul traps is found in two review papers: Dehmelt, H. (1990) Rev. Mod. Phys. **62**, 525 and Paul, W. (1990) Rev. Mod. Phys. **62**, 531.
2. W. Nagourney, J. Saudherg, H. Dehmelt (1986), Phys. Rev. Lett. **56**, 2797; Th. Sauter, W. Neuhauser, R. Blatt, P. E. Toschek, ibid **57**, 1696, (1986); J. C. Berquist, R. G. Halet, W. M. Itano and D. J. Wineland, ibid **57**, 1699 (1986).

3. F. Dietrich, H. Walther, Phys. Rev. Lett. **58**, 203, (1987; M. Schubert, I. Siemers, R. Blatt, W. Neuhauser, P. E. Toschek, *ibid* **68**, 3016, (1992). The first observation of antibunching in resonance fluorescence from an atomic beam was made by H. J. Kimble, M. Dagenais, L. Mandel, *ibid* **39**, 691 (1977)
4. W. Itano, D. J. Heinzen, J. J. Bollinger, D. J. Wineland, Phys. Rev. A **41**, 2295, (1990)
5. M. Brune, S. Haroche, J.M. Raimond, L. Davidovich and N. Zagury, Phys. Rev. A **45**, 5193, (1992).
6. P. Meystre, Phys. Lett. **219**, 243 (1992).
7. H. Haken, *Light and Matter*, edited by L. Genzel, Handbuch der Physik Vol. XXv/2c (Springer-Verlag, Berlin, 1970).
8. D.M Meekhof, C. Monroe, B.E.King, W.M. Itano and D.J. Wineland Phys. Rev. Lett. **76**, 1796 (1996).
9. M. Löffler, G. M. Meyer, H. Walther, Phys. Rev. A **55**, 3923 (1997).
10. G. M. Meyer, H.-J. Briegel and H. Walther, Europhys. Lett. **37**, 317 (1997).
11. G. M. Meyer, M. Löffler and H. Walther, Phys. Rev A, **56**, R1099, (1997).

Spectral and Spatial Coherence in Solid State Raman Lasers

D.D. Smith, A. Oien, G.T. Bennett, T. Monarski

Coherent Technologies Inc., P.O. Box 7488, Boulder, CO 80306, USA

Abstract. Multiple standing wave and traveling wave Ba(NO₃)₂ Solid State Raman Lasers (SSRLs) have been built and characterized. The Ba(NO₃)₂ SSRLs were pumped by a 1338 nm wavelength Nd:YAG laser resulting in 1556 nm output wavelength. Folded Raman ring resonators have produced near-transform-limited spectral coherence via injection-seeding. Several different resonators have also produced near-diffraction limited spatial coherence, without seeding. A three-mirror ring configuration Ba(NO₃)₂ SSRL produced 1/5 wave peak-to-valley wavefront aberration, 175 mJ/pulse and 30 pulses per second while being pumped by lasers with a beam quality figure of merit M² > 15. The spectral and spatial coherence of the SSRLs is indicative of a rich phenomenology.

1 Introduction

While the coherence properties of nonlinear optical frequency converters such as the Optical Parametric Oscillator (OPO) continue to be investigated, there is comparatively less effort being invested into optical coherence control in Raman shifters and Raman lasers. This work reported here focuses on new results concerning the spectral and spatial coherence characteristics of Ba(NO₃)₂ injection-seeded Solid State Raman Lasers (SSRLs). SSRLs have been existed for over 25 years, with some of the early work being reported in the open literature in the 1970's or earlier[1]. SSRLs have been demonstrated in a range of materials such as LiNbO₃, CaWO₄, CaCO₃, Ba(NO₃)₂, GaP. However, SSRLs have not been as widely developed as other nonlinear optical devices for reasons that may include: (a) fewer materials have been identified or developed with good stimulated Raman scattering gain, and (b) SSRLs lack the continuously tunable frequency agility of OPOs. However, in situations where frequency tunability is not required, SSRLs offer increased robustness (no angle or temperature phase matching requirements) and often lower cost, larger crystals.

2 Results

Figure 1 shows the layout of the guided-wave fiber optic Master Oscillator (MO) used to injection seed Ba(NO₃)₂ SSRL Slave Oscillators (SO's). Without stabilization of the diode pump source, the fiber laser or the erbium doped

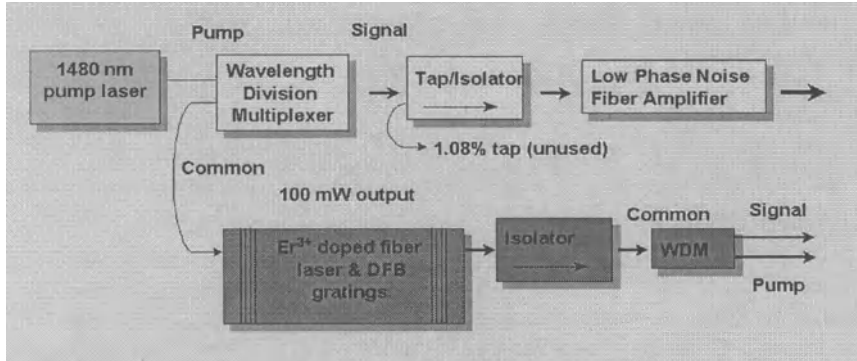


Fig. 1. Block diagram of the optical fiber laser and optical fiber amplifier used as the master oscillator to seed the slave oscillator SSRL.

fiber amplifier, the short term delayed self-heterodyne linewidth (delays up to 22 km, spectrum sweep times up to approximately 1 ms) of the MO is in the few kHz range (see Figure 2). The fiber amplifier phase fidelity contributes only small amplitude sidebands split from the carrier by about 100 Hz and down approximately C20 dB from the carrier (data not shown). The fiber amplifier sidebands are thought to be vestigial relaxation oscillations. Reductions in the pump laser diode intensity noise, introduction of thermal stabilization, and acoustic isolation result in orders-of-magnitude reduction in the MO spectral linewidth. However, those enhancements were not pursued here as they were not central to investigating pulsed SSRL coherence.

The four mirror Raman ring resonator and injection seeder that were utilized in the first injection seeded SSRL experiments are shown in Figure 3. The temporal heterodyne beat note between the injection-seeded oscillator and the frequency shifted MO is shown in Figure 4. The beat note spectrum

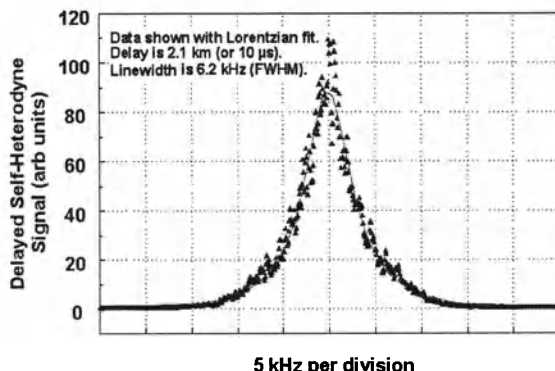


Fig. 2. MO linewidth measured with the delayed self-heterodyne technique.

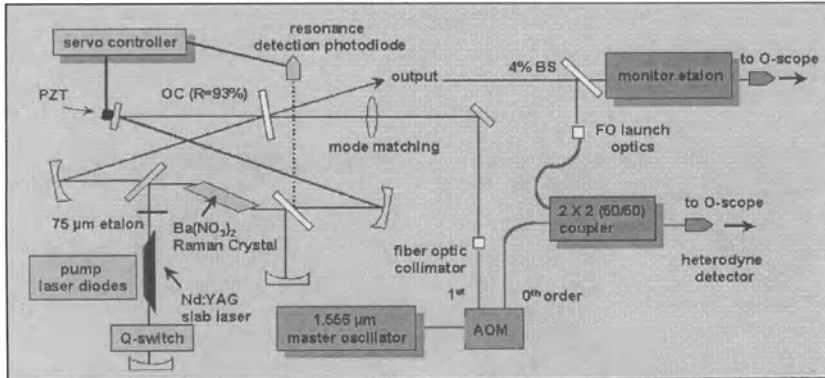


Fig. 3. Injection-seeded SSRL ring resonator and beat-note diagnostic configuration.

is also shown in Figure 4. A slave resonator servo control circuit was used to provide reliable matching of the MO and SO spectral modes. Transform-limited spectral output was obtained with exemplary capture-and-comply characteristics with respect to the injection seeder. When the slave oscillator is not injection seeded, the SSRL tends produce a coherence length of a few cm, as measured by an imaging Michelson interferometer (data not shown here). In Raman gain crystals with narrow spectral gain bandwidths, care

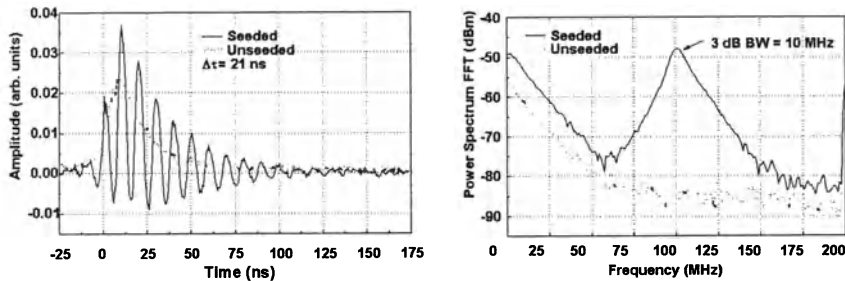


Fig. 4. The left plot shows the temporal beat note of slave oscillator pulse with 100 MHz frequency shifted replica of the MO. The smooth envelope represented by the dotted line is for the unseeded 4 mirror symmetric ring resonator. The solid line for the ringing beat note is for the seeded SO. The right plot is the Fourier transform spectrum of the beat note of the seeded SO with the MO. The apparent concavity on the red side of the spectrum and convexity on the blue side of the spectrum are due to the faster rising edge and slower falling edge of the SO temporal pulse. The dotted line below the spectrum shows the detection noise floor intentionally displaced downward by C3 dB for clarity of presentation. The data illustrate that the seeded SO pulse is transform limited, within the precision of the experimental measurements.

must be exercised not to let the pump laser spectral bandwidth exceed that of the Raman spectral gain bandwidth.

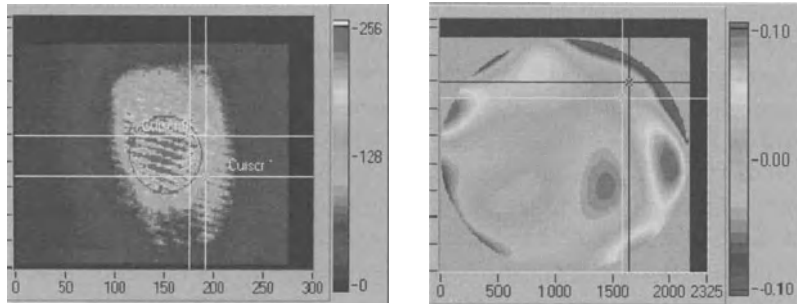


Fig. 5. The left frame is an intentionally sheared interferogram of the SSRL output. The interferogram was acquired with a transient, self-referencing Mach-Zehnder interferometer that utilized an equal-arm path delay and a spatial filter in one arm. The intensity scale resolution is 8 bits (1 part in 256). The right frame is the residual wavefront error after a fit of a parabolic wavefront to the circled area of the interferogram on the left. The vertical axis is in wavelengths at 1556 nm, illustrating a peak-to-valley wavefront aberration of 1/5 wave.

An asymmetric three-mirror Raman ring resonator has been operated with multiple-transverse mode $M^2 \approx 15$ pump laser while producing 175 mJ pulses at 1556 nm with less than 1/5 wave peak-to-valley wavefront aberration over the central 80% of the beam intensity (see Figure 5). The 3-mirror asymmetric ring resonator had a pump beam which was collinear with the Raman beam, so only a modicum of spatial intensity averaging can occur vs. pump-beam “print-through”, especially with the high output coupling fraction present (as much as 60%T). While there are multiple potential mechanisms for the observed Raman beam clean-up, such as the “dominant specklon” or four-wave mixing, the data collected to date do not definitively measure their relative contributions.

3 Conclusions and Remarks

New data on injection-seeded solid state Raman lasers have been presented. In addition to spectral transform-limited performance being obtained from the seeded slave oscillator, Raman beam clean-up has been observed, resulting in near diffraction-limited output beam quality. The spectral and spatial coherence of the SSRLs bode well for future applications.

Acknowledgment. The technical and financial support of Dr. Edward Watson and Dr. Paul McManamon through contract F33615-96-C-1853 is gratefully acknowledged.

References

1. For an early review article, see A.Z. Grasyuk, *Kvant. Elektron.* (Moscow) 1 pgs 485-609, March 1974. Early work on stimulated Raman scattering from phonon-polaritons was reported by S.K. Kurtz and J. A. Giordmaine, *Phys. Rev. Letts.*, **22**, Number 5, pg. 192 (1969).

The Hole-Burning Phenomenon under the Action of a Coherent Field

Po Dong² and Jin-Yue Gao^{1,2,3}

¹ China Center of Advanced Science and Technology (World Laboratory)
P. O. Box 8730, Beijing 100080, China

² Physics Department, Jilin University, Changchun, Jilin 130023, China

³ State Key Laboratory of Photoelectronics, Jilin University,
Changchun, Jilin 130023, China

Abstract. We study a new kind of hole-burning phenomenon where a strong coherent field, which makes an Electromagnetically Induced Transparency (EIT) window, is used to connect the upper level of Hole-burning to the third one in a three-level system. In this scheme, more than one or disappearance of burning Holes in a Doppler broadening medium under different conditions could occur.

One saturating laser could burn a hole into the population distribution of a Doppler-broadened medium, which lead to the production of "Bennet hole" [1] or "Lamb hole" within absorption spectrum of another probe beam. This Doppler-free Saturating Spectroscopy allows one to resolve fine and hyperfine structure even in the presence of a much large Doppler width [2]. Furthermore, the phenomena of persistent spectral hole-burning makes possible to write and read optical data [3]. On the other hand, the absorption of a weak resonant probe beam can be reduced or even eliminated by a strong coherent coupling beam, called Electromagnetically Induced Transparency(EIT) phenomenon[4,5], and the related subjects, such as lasing without inversion (LWI)[6], have attracted much attention over the last few years.

In the present paper, we explore theoretically the hole-burning phenomenon in the presence of a strong coherent field which couples one of the transition levels to the third one in a Ladder three-level configuration of a Doppler broadening medium. The significance of this work lies in the fact that saturating spectrum technology could open up a possible way to the realization of atomic coherence and measuring the Rabi frequency even in the Doppler broadening media, and the potential application in reading and writing optical information as well as one beam controlling two other beams.

Figure(1) shows a cascade scheme used in this letter. In Fig. 1, one frequency tunable probe beam(PB) at frequency ω_p probes the transition $|1\rangle - |2\rangle$, while one saturating beam(SB) at frequency ω_s close or equal to the resonance of $|1\rangle - |2\rangle$ and counterpropagating with PB pumps a particular group of atoms with a definite velocity. At the same time, levels $|2\rangle$ and $|3\rangle$ are coupled by one coupling beam(CB) at frequency ω_c . In such

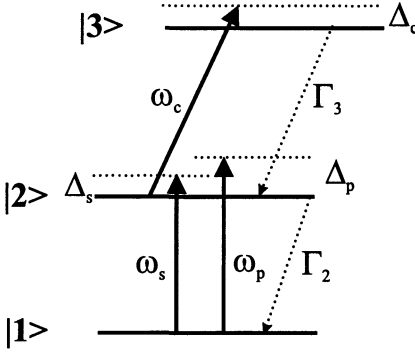


Fig. 1. Energy schematic of a Ladder configuration for hole-burning behind EIT window. Γ_2 is the population decay rate from $|2\rangle$ to $|1\rangle$. Γ_3 is the population decay rate from $|3\rangle$ to $|2\rangle$.

circumstance, the density-matrix equations in rotating-wave approximation will be

$$\begin{aligned}\dot{\rho}_{11} &= \Gamma_2 \rho_{22} + iG_s \rho_{12} - iG_s^* \rho_{21} \\ \dot{\rho}_{22} &= -\Gamma_2 \rho_{22} + \Gamma_3 \rho_{33} - iG_s \rho_{12} + iG_s^* \rho_{21} + iG_c \rho_{23} - iG_c^* \rho_{32} \\ \dot{\rho}_{21} &= -(\gamma_{21} - i\Delta_s) \rho_{21} + iG_s (\rho_{22} - \rho_{11}) - iG_c^* \rho_{31} \\ \dot{\rho}_{31} &= -(\gamma_{31} - i(\Delta_c + \Delta_s)) \rho_{31} - iG_c \rho_{21} + iG_s \rho_{32} \\ \dot{\rho}_{32} &= -(\gamma_{32} - i\Delta_c) \rho_{32} + iG_c (\rho_{33} - \rho_{22}) + iG_s^* \rho_{31} \\ \rho_{11} + \rho_{22} + \rho_{33} &= 1, \quad \rho_{ij} = \rho_{ji}^*\end{aligned}\tag{1}$$

As in the conventional notation, the coupling coefficients are denoted as $G_c = \mu_{23} E_c / \hbar$ and $G_s = \mu_{12} E_s / \hbar$, and the detunings are $\Delta_c = \omega_c - \omega_{21}$ and $\Delta_s = \omega_s - \omega_{32}$, respectively. This set of equations can be written in the matrix form,

$$R = LR + I \tag{2}$$

with

$$\begin{aligned}R_1 &= \rho_{11}, R_2 = \rho_{22}, R_3 = \rho_{21}, R_4 = \rho_{12}, \\ R_5 &= \rho_{31}, R_6 = \rho_{13}, R_7 = \rho_{32}, R_8 = \rho_{23}\end{aligned}$$

The steady state probe absorption spectrum of PB in this system can be written as [8],

$$A(\Delta_p) = \Re \left(\int_0^\infty \lim_{t \rightarrow \infty} \langle [P^-(t + \tau), P^+(t)] \rangle e^{i\Delta_p \tau} d\tau \right) \tag{3}$$

where $\Delta_p = \omega_p - \omega_{21}$ is the detuning of PB, $P^- = \mu_{21}|1\rangle\langle 2|$ is the atomic polarization operator with μ_{21} being the dipole moment of the atomic transition from $|1\rangle$ to $|2\rangle$. By utilizing the quantum regression theory [9], the absorption spectrum of PB can be carried out.

$$A(\Delta_p) = \Re \{ |\mu_{21}|^2 [M_{41}(z) R_3(\infty) + M_{44}(z) R_2(\infty) + M_{46}(z) R_8(\infty) - M_{42}(z) R_3(\infty) - M_{44}(z) R_1(\infty) - M_{47}(z) R_5(\infty)] \} \tag{4}$$

where $M = (z - i\Delta_s - L)^{-1}$ | $z = i\Delta_p$ and $R_i(\infty)$ is the steady state solution of Eq. (1).

For the Doppler broadening medium, if the number of atoms per unit volume with velocity v is $N(v)dv$, the total absorption coefficient will be

$$A(\Delta_p) = \int_{-\infty}^{+\infty} A(\Delta_p, v) N(v) dv = \int_{-\infty}^{+\infty} A(\Delta_p, v) \frac{N_0}{u\sqrt{\pi}} e^{-v^2/u^2} dv \quad (5)$$

where $u/\sqrt{2}$ is the root-mean-square atomic velocity and N_0 is the atomic number per unit volume.

Based on numerical integration, we consider the following three cases:

(1) SB has definite detuning from the resonance, while CB is counterpropagating with PB.

(2) PB and SB come from the same laser beam and CB is counterpropagating with PB.

(3) Both SB and CB are at resonance with the atomic transitions, respectively, and CB is propagating in the same direction with PB.

In case (1), we obtain a result from Eq. (5) and show it in Fig. 2. Under this condition, four burning holes could be produced, which could be derived and understood by Autler-Townes splitting of individual group of atoms with a particular velocity. The absorption peak of those atoms with velocity v seeing CB with frequency detuning $\Delta_c - \omega_{32}v/c$ will be driven to two resonant absorption Autler-Townes peaks. At the same time, this group of atoms will see SB with detuning $\Delta_s - \omega_{21}v/c$. So that, when the following equation is satisfied

$$\Delta_s - \omega_{21}v/c = -\frac{1}{2} \left(\Delta_c - \frac{\omega_{32}v}{c} \right) \pm \frac{1}{2} \left[4|G_c|^2 + \left(\Delta_c - \frac{\omega_{32}v}{c} \right)^2 \right]^{\frac{1}{2}} \quad (6)$$

this group of atoms could be excited to state $|2\rangle$ by SB. It is clear that there are two groups of atoms satisfy this requirement. The two excited groups of atoms with these velocities will give four burning holes in the probe absorption spectrum at the detunings of PB [7]

$$\Delta_p + \omega_{21}v/c = -\frac{1}{2} \left(\Delta_c - \frac{\omega_{32}v}{c} \right) \pm \frac{1}{2} \left[4|G_c|^2 + \left(\Delta_c - \frac{\omega_{32}v}{c} \right)^2 \right]^{\frac{1}{2}} \quad (7)$$

For example, with the parameters in Fig 2, we get $\frac{\omega_{21}v}{c} \approx \pm 140MHz$ from Eq. (6). With Eq. (7) we get $\Delta_p \approx \pm 140, \pm 280MHz$, which are just the hole positions in Fig. 2.

We plot the absorption spectrum for the case (2) in Fig. 3. There are several features visible in this spectrum: one EIT hole in the two-photon resonance, two Lamb holes appearing at the position of Dynamic Stark shift

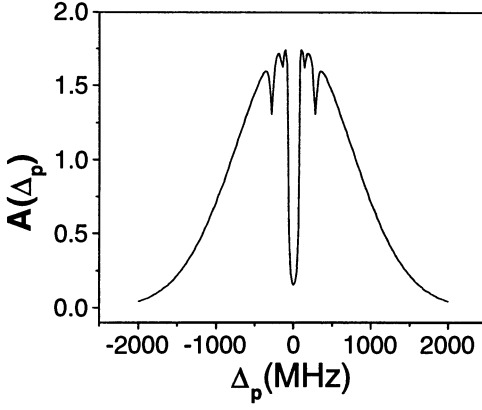


Fig. 2. The dimensionless absorption coefficient A as a function of probe detuning Δ_p under the case (1). The parameters used are $u = 600m/s$, $\Gamma_2 = \Gamma_3 = 20MHz$, $\gamma_{21} = \gamma_{31} = 10MHz$, $\gamma_{32} = 20MHz$, $\lambda_{12} = 589.6nm$, $\lambda_{23} = 568.8nm$, $\Delta_c = 0MHz$, $|G_c| = 200MHz$, $|G_s| = 10MHz$; $\Delta_s = 0MHz$.

($\pm|G_c|$). These are easy to be understood from above discussions. In this case, the hole position can be found by following equations,

$$\left\{ \begin{array}{l} \Delta_s - \omega_{21}v/c = -\frac{1}{2}(\Delta_c - \frac{\omega_{32}v}{c}) \pm \frac{1}{2}\left[4|G_c|^2 + (\Delta_c - \frac{\omega_{32}v}{c})^2\right]^{\frac{1}{2}} \\ \Delta_p = -\frac{\omega_{21}v}{c} - \frac{1}{2}(\Delta_c - \frac{\omega_{32}v}{c}) \pm \frac{1}{2}\left[4|G_c|^2 + (\Delta_c - \frac{\omega_{32}v}{c})^2\right]^{\frac{1}{2}} \\ \Delta_s = \Delta_p \end{array} \right. \quad (8)$$

The equations can be solved, yielding $\Delta_p = \pm|G_c|$ for $\Delta_c = 0$ and other two complicated solutions. It is clear that the former two holes are located at the point of Dynamic Stark shift of ($\pm|G_c|$). Because they are corresponding to the group of atoms with zero velocity and this group of atoms are at resonance with CB, so the two holes are very deep. The later two holes are very weak since they are located at the edge of EIT window. Clearly, above phenomenon could provide a possible way to measure Rabi frequency according to the hole positions even in the Doppler broadening medium.

Fig. 4 shows the results of case (3). Under the condition (3), SB and CB are at frequency resonant with the transitions $|1\rangle - |2\rangle$ and $|2\rangle - |3\rangle$, respectively, and they are propagating in the opposite direction. In Fig. 4, there is no EIT window because each atom sees PB and CB with large total Doppler shift. We note that in fig. 4, burning hole created by SB with the absence of CB disappears because the frequency of SB is just located at the EIT window produced by CB and SB can not be absorbed. In this case CB enhances the absorption of PB and reduces the absorption of SB at the zero detuning of PB. It means that the CB could change the absorption status of SB and PB simultaneously. Clearly, above discussions have provided a way for one beam to control two beams.

In conclusion, we have reported theoretically a new hole-burning phenomenon when the excited state is split into Autler-Townes doublets by the action of a strong coherent beam in a Doppler-broadened ladder system. We remark that in our theoretical derivation both SB and CB are treated as

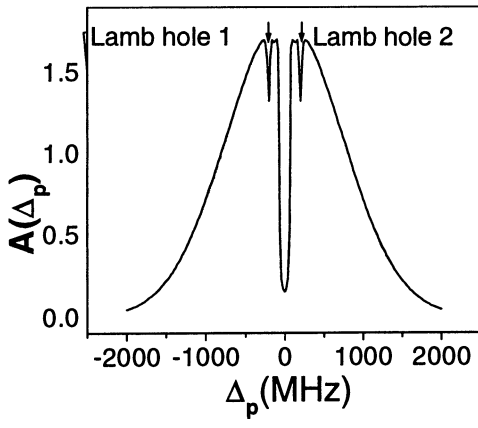


Fig. 3. The dimensionless absorption coefficient A as a function of probe detuning Δ_p under the case (2). The parameters used are the same as in Fig. 2. In this case, $\Delta_s = \Delta_p$.

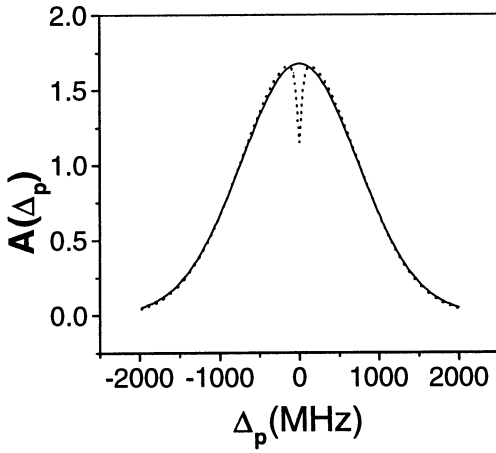


Fig. 4. The dimensionless absorption coefficient A as a function of probe detuning Δ_p under the case (3). The parameters used are the same as in Fig. 2 and Fig. 3. we choose: $\Delta_c = \Delta_s = 0MHz$, $|G_s| = 10MHz$. And $|G_c| = 200MHz$ (solid line), $0MHz$ (dotted line).

strong fields means that the effect of the coherence of SB has been included. However, their values are so carefully chosen that the main role which SB played is the saturation rather than coherence. For this purpose, we chose $|G_c|$ as $200MHz$, while $|G_s|$ as $10MHz$ in the calculation. Under this condition, $|G_s|^2 / \Gamma_2 \gamma_{21} = 0.5$. Thus the hole-burning is mainly from the pump of SB rather than from the coherence of SB.

References

1. W.R Bennet, Phys. Rev. **126**, 580 (1962).
2. T.W. Hansch, M.H. Nayfeh et al., Phys. Rev. Lett. **32**, 1336 (1974);
3. W.E. Moerner, ed., Persistent spectral hole burning; science and application (Springer, Berlin, 1988(and refs. therein)).

4. S.E. Harris, J.E. Field, and A. Imamoğlu, Phys. Rev. Lett. **64**, 1107 (1990).
5. Min Xiao, Yong-qing Li, Shao-Zheng Jin, and Julio Gea-Banacloche, Phys. Rev. Lett. **74**, 666 (1995).
6. S.E. Harris, Phys. Rev. Lett. **62** , 1033 (1989); J. Y. Gao, et. al, Opt. Commun. **93**, 323 (1992).
7. J. R. Boon, E. Zekou, D. J. Fulton, and M. H. Dunn, Phys. Rev. A **57**, 1323 (1998).
8. B. R. Mollow, Phys. Rev. A **5**,2217 (1972).
9. L. M. Narducci et al., Opt. Commun. **86**, 324 (1991).

XUV Emissions from Terawatt Femtosecond Laser Produced Plasma Columns in Gases

Peixiang Lu, Hidetoshi Nakano, Tadashi Nishikawa, Naoshi Uesugi

NTT Basic Research Laboratories, 3-1 Morinosato Wakamiya, Atsugi, Kanagawa 243-0198, Japan

Abstract. Terawatt femtosecond laser pulses were focused into a gas cell to produce plasma columns in gases of N_2 , O_2 , and He. The axial xuv emission spectra that were generated are reported and analyzed. The xuv amplifications on transitions of NIII $3s(^2S) - 2p(^2P)$ at 45.2 nm and OIII $2p3s(^3P) - 2p^2(^3P)$ at 37.4 nm in low-charged nitrogen and oxygen ions were successfully demonstrated by a linearly-polarized 100-fs pump laser pulse of only 25 mJ. Strong axial xuv emission lines from a laser-produced plasma column in helium gas were also observed, however, no amplification was observed for the L_α line at 30.3 nm. High-order harmonics from a helium plasma column were also investigated with different pump energies under the defocusing condition for the laser beam.

1 Introduction

Commercial intense terawatt femtosecond laser systems has led to a great interest in the development of table-top soft x-ray lasers with a high repetition rate based on the optical-field ionization (OFI). The optical-field ionization is one of the most interesting kinds of high-intensity interactions with matter [1–5]. For the linearly polarized ionizing laser pulse, the theory predicts that the temperature of the generated electron could be considerably lower than the ionization potential, resulting in a high rate of three-body recombination. Therefore it has been suggested as a mechanism for creating favorable conditions for inversions on transitions in the xuv and x-ray regions in an overionized plasma [4–11]. Using a small size terawatt femtosecond laser, the first OFI recombination x-ray laser to the ground state at 13.5 nm in LiIII was successfully demonstrated at RIKEN [12], and was further confirmed with a lithium capillary at Princeton [13]. In th is paper, we will present our recent results on xuv amplifications and high-order harmonics emissions from a terawatt femtosecond laser produced plasma column in gases of nitrogen, oxygen, and helium.

2 Experiment

The experimental setup is shown in Fig. 1. The femtosecond laser system used in the experiment is a commercial, high-repetition rate (10-Hz), Ti:sapphire chirped pulse amplification system with a maximum energy output of 100

mJ [14]. In the experiment, we used output energy less than 40 mJ to avoid the air breakdown due to the smaller beam diameter (1 inch) of the laser beam. The 100-fs 790-nm linearly-polarized laser pulse is passed through a 2-in.-diameter, 5-mm-thick MgF_2 window into an evacuated chamber, and is focused by a 400-mm focal length MgF_2 lens into a differentially pumped gas cell. The diameter of the focused spot was estimated to be about $50\mu m$. The measured pulse energy before the gas cell is about 25 mJ and the corresponding peak intensity is about $1.3 \times 10^{16} W/cm^2$. For observing the high-order harmonics in helium, we set the best focused spot 3 mm before the the gas cell center (i.e. the defocusing condition) for a 3-mm long helium plasma co lumn, and the corresponding peak intensity is then estimated to be $3.6 \times 10^{15} W/cm^2$ for a pump energy of 24 mJ. As shown in Fig. 1, the focused laser beam drilled two pinholes ($\leq 500\mu m$) on and through two replaceable 100 – μm – thick stainless steel plates, whose separation can be accurately varied by means of translation stages. These two pinholes provide the entrance for the pump laser and the exit for both the pump and x-ray lasers. The axial plasma emission from the gas cell was spectrally dispersed by means of a transmission grating (5000 lines/mm), with grating bars oriented parallel to a 3-mm-long, $50\mu m$ – wide slit. A MCP (Galileo Co.) combined with an optical CCD was used to record the axial plasma soft x-ray emission spectra.

3 OFI in a Strong Linearly Polarized Light Field

At laser intensities above $10^{14} W/cm^2$, optical field ionization (OFI) becomes a key mechanism for plasma production and heating. With ultrashort pulse laser systems, a plasma with strong nonequilibrium can be created by OFI of a gaseous medium in an intense laser field. For the recombination

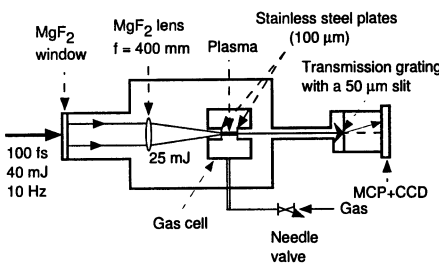


Fig. 1. Schematic diagram of the experimental setup.

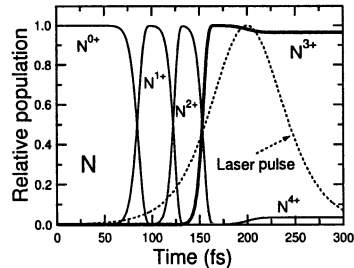


Fig. 2. Evolution of the relative population of the charge state in He for a 100-fs linearly-polarized laser pulse with a peak intensity of $6.5 \times 10^{15} W/cm^2$.

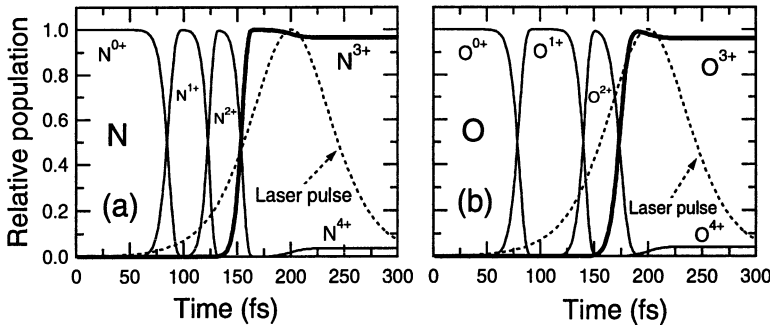


Fig. 3. Evolution of the relative population of the charge state in (a) N_2 and (b) O_2 for a 100-fs linearly-polarized laser pulse with a peak intensity of $6.5 \times 10^{15} \text{ W/cm}^2$.

x-ray laser, a linearly polarized driving laser pulse is required in order to produce cold electrons to create a transient population inversion between excited and ground ion states during the three-body recombination cascade. The level of ionization reached during the laser pulse can be calculated using the tunneling ionization theory of Ammosov, Delone, and Krainov (ADK) [15] to describe laser-atom interactions in strong fields because experiments by Augst et al. [16] confirm that the ADK rates are in better agreement with the data than the Keldysh rates [1]. Considering the actual intensity in the gas cell may be well lower than the estimated intensity of $1.3 \times 10^{16} \text{ W/cm}^2$, we used its half value ($6.5 \times 10^{15} \text{ W/cm}^2$) to be the peak intensity of the pumping pulse for our calculation. This value was confirmed to be near the real intensity by our nitrogen and oxygen experiments.

Fig. 2 shows the evolution of the charge-state populations in He for a 100-fs linearly polarized laser pulse with a peak intensity of $6.5 \times 10^{15} \text{ W/cm}^2$. It is shown in Fig. 2 that after the laser pulse peak the He atoms are stripped to 57% H-like He ions and 43% bare He ions which are required for the recombination L_α x-ray laser. It is clear that the pump laser intensity in our experiment is not enough to produce a high enough bare helium ion abundance for the recombination H-like He ion x-ray laser at 30.3 nm. Maybe this is one of the main reasons why the gain was not observed in our experiment. Also the typical evolutions of the charge-state populations in N_2 and O_2 are shown in Fig. 3 for a 100-fs linearly polarized laser pulse with a peak intensity of $6.5 \times 10^{15} \text{ W/cm}^2$. One can see from Fig. 3 that the N and O atoms are stripped to Be-like N and B-like O ions before the laser peak and there are still with a rather high Be-like N or B-like O ion abundance of 96% after the laser peak. The Be-like N and B-like O ions are basically required for the recombination boron-like N and carbon-like O ion x-ray lasers. Therefore our laser pumping intensity should be near the optimum value for the creation of NIII and OIII ion x-ray lasers.

4 Experimental Results and Discussions

4.1 XUV Amplification in Low-Charged Nitrogen and Oxygen Ions

We demonstrated, for the first time, xuv amplification to the ground state in low-charged nitrogen ions at a 10-Hz repetition rate in a commercial femtosecond laser system. A gain $G = 9.6 \pm 0.5\text{cm}^{-1}$ and gain-length product $\text{GL}=3.84$ on the lasing transition [$\text{NIII } 3s(^2S) - 2p(^2P)$] at 45.2 nm was achieved by a 25-mJ 100-fs linearly-polarized laser pulse at 1.0 torr. As a

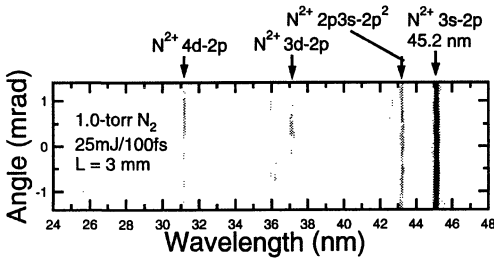


Fig. 4. Typical example of raw data from the CCD read-out of an axial xuv emission spectrum for a 3-mm-long plasma column in 1-torr nitrogen gas.

typical example for the raw data obtained, the CCD read out for the case of 1-torr N_2 with a separation of 3 mm between two stainless steel plates is shown in Fig. 4. In the experiment, we also observed a small gain coefficient of $\sim 2\text{cm}^{-1}$ at 2 torr but we did not observe any gain with nitrogen gas pressures higher than 2.0 torr.

We also carried out a similar experiment to observe the gain of the $2p3s(^3P) - 2p^2(^3P)$ transition in carbon-like oxygen ions, which has been demonstrated by Chichkov et al. [17], at the oxygen gas pressures between 1.0 and 2.0 torr. Fig. 5 shows an example of a plasma spectrum produced in O_2 gas cell at 1.5 torr with a 4-mm plasma length.

A large gain of $G = 11.7 \pm 0.5\text{cm}^{-1}$ and the corresponding gain-length product $\text{GL}= 4.7$ was observed at 1.5 torr. In the experiment, we also observed small gain coefficients of 5.4cm^{-1} and 7.8cm^{-1} on the $\text{OIII } 2p3s(^3P) - 2p^2(^3P)$ transition at 1.0 and 2.0 torr, respectively.

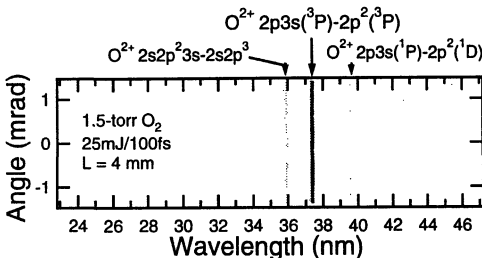


Fig. 5. An example of the raw data from the CCD image of an axial xuv emission spectrum for a 4-mm-long plasma column in 1.5-torr oxygen gas.

4.2 XUV Emission from Helium

It was found that the generation of the atomic lines depended critically on the adjustment of the focus into the gas cell. For a plasma irradiated by a tightly focused laser pulse, strong atomic lines were observed. While high-order harmonics instead of atomic lines were observed from a laser-produced plasma column in helium under the defocusing condition for the laser beam. Under the tightly focusing condition for the laser beam, strong axial atomic spectrum of helium was observed but no strong high-order harmonics at 10 torr, as shown in Fig. 6, the spectrum is dominated by the hydrogenic lines. Most striking is the strong $Lyman-\alpha$ emission in relation to $Lyman-\beta$ and $Lyman-\gamma$, strongly suggesting gain on the $Lyman-\alpha$ transition (30.3 nm). However, the gain on the transition was not observed by a gain measurement based on the plasma length. As we mentioned in the section 3, probably our pumping laser intensity is not high enough, and therefore the produced bare helium ion abundance of only 43% is not high enough for the recombination H-like He L_α x-ray laser. In the experiment, we did not observe any atomic lines as well as high-order harmonics with a pressure lower than 5 torr. On the other hand, only strong high-order harmonics were observed at 10 torr under the defocusing condition for the laser beam, and almost no signal with a pressure lower than 5 torr. Fig. 7 shows xuv emission spectra of high-order harmonics from 10-torr helium gas with different pump energies from 6 mJ to 24 mJ. It is clear that the highest order of the observed harmonics at 24 mJ is much higher than that at 6 mJ, and it can reach 141st for a pump energy of 24 mJ, and 87th for a pump energy of 6 mJ at 10 torr. The higher

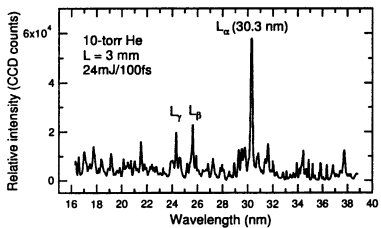


Fig. 6. Typical axial xuv emission spectrum for a 3-mm-long plasma column produced by a 24-mJ, 100-fs linearly-polarized laser pulse in 10-torr helium gas.

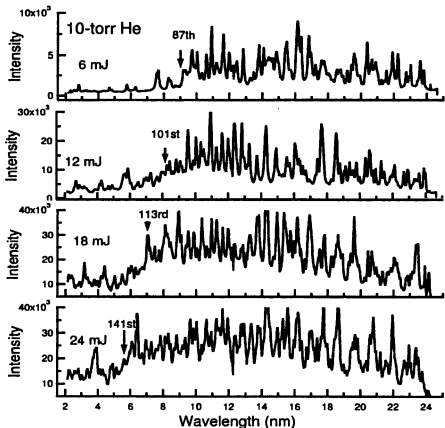


Fig. 7. Axial xuv emission spectra of helium plasma columns with four different pump energies (6, 12, 18, and 24 mJ) under the defocusing condition for the laser beam at 10 torr.

cutoff order of the harmonics observed at a high pumping energy may be from helium ions produced by OFI [18].

5 Summary

In summary, xuv emissions from terawatt femtosecond laser produced plasma columns in N_2 , O_2 , and He were investigated experimentally. The xuv amplifications on transitions of NIII $3s(^2S) - 2p(^2P)$ at 45.2 nm and OIII $2p3s(^3P) - 2p^2(^3P)$ at 37.4 nm in low-charged nitrogen and oxygen ions were successfully demonstrated by a linearly-polarized 100-fs pump laser pulse of only 25-mJ. The strong L_α line from a plasma column in 10-torr helium gas was observed, and also under the defocusing condition for the laser beam, the cutoff order of the observed high-order harmonics can reach 141st for a pump energy of 24 mJ, and 87th for a pump energy of 6 mJ at a helium gas pressure of 10 torr.

References

1. L. V. Keldysh: Sov. Phys. - JETP 20, 1307 (1965).
2. 'DL. Huiller et al., Phys. Rev. Lett. 48, 1814(1982).
3. T. S. Luk et al., Phys. Rev. Lett. 51, 110(1983).
4. P. B. Corkum, N. H. Burnett, and F. Brunel, Phys. Rev. Lett. 62, 1259(1989).
5. M. D. Perry et al., Phys. Rev. Lett. 60, 1270(1988).
6. N. H. Burnett and P. B. Corkum, J. Opt. Soc. Am. B6, 1195 (1989).
7. J. Peyraud and N. Peyraud, J. Phys. 43, 2993(1972).
8. N. H. Burnett and G. D. Enright, IEEE J. Quantum Electron, 26, 1797(1990).
9. P. Amendt, D. C. Eder, and S. C. Wilks, Phys. Rev. Lett. 66, 2589 (1991).
10. E. Fill et al., Phys. Rev. E 51, 6016 (1995).
11. G. Pretzler and E. Fill, Opt. Lett. 22, 733 (1997).
12. Y. Nagata et al., Phys. Rev. Lett. 71, 3774 (1993).
13. D. V. Korobkin, C. H. Nam, and S. Suckewer, Phys. Rev. Lett. 77, 5206 (1996).
14. H. Nakano et al., in "X-ray Lasers 1998", ed. by Y. Kato and H. Takuma, Inst. Phys. Conf. Ser. No. D159, 1999 IOP Publishing, pp535-538
15. M. V. Ammosov et al., Sov. Phys. JETP 64, 1191 (1986).
16. S. Augst et al., Phys. Rev. Lett. 63, 2212 (1989).
17. B. N. Chichkov et al., Phys. Rev. A52, 1629 (1995).
18. J. L. Krause et al., Phys. Rev. Lett. 68, 3535(1992).

Spectral, Temporal and Spatial Characteristics of Few Cycle Optical Pulsed Beam

Zhong-yang Wang and Zhi-zhan Xu

Laboratory for High Intensity Optics, Shanghai Institute of Optics and Fine Mechanics, Chinese Academy of Sciences, Shanghai 201800, China

Abstract. In this paper, the spectral, temporal and spatial properties of few cycle optical pulsed beam on propagation in free space has been studied. We analyze the spectral shifts of the ultrashort pulse in the far zone, and then discuss the scaling law of the pulsed sources. It is found that by the truncation of the pulsed beam, the scaling law may be destroyed. In this case the spectral shifts on propagation of the few cycle pulses may be observed in experiment. On the other hand, we reveal an analytical form of the pulsed Gaussian beam in free space and analyze the space-time coupling on propagation.

The techniques of ultrashort pulse laser have been developed rapidly. Up to date, pulses that are less than 5fs in duration and contain below two cycles can be generated [1]. The physics of the propagation of this extreme short pulse is important for the increasing number of application. In the many previous treatment, the electric fields of the pulse are always considered separable in space and time. But for few cycle optical pulses, its spatial and temporal characteristics interact with each other during propagation. On the other hand, since E.Wolf in 1986 [2] had revealed that light emitted a source which have a certain degree of spectral coherence and violate the called scaling law undergoes spectral shift during its propagation, this properties have been extensively studied for the partially coherent light. For few cycle optical pulse, its spectra is very broad. But how is the change of its spectra on propagation. What is the scaling law of this deterministic sources. In this paper, we will study these problems and discuss the spectral, temporal and spatical properties of few cycle optical pulsed beam on propagation.

1 Spectral shift on propagation of ultrashort pulse in the far zone

Consider an ultrashort pulsed source of the form: $E^0(r, \omega) = s^0(\omega) \exp(-\frac{r^2}{2\sigma_I^2})$, where $s^0(\omega)$ is the spectral amplitude of the pulse and spatial size σ_I is assumed to be independent on the frequency, incident into a circular aperture of radius a in the place $z = 0$. If the radius of the aperture is sufficiently larger than the spatial size σ_I , by using the Rayleigh diffraction formula, we can resolve the normalized far-zone spectra as the form [3]

$$S^\infty(u, \omega) = (\omega^2/M) \exp[-\alpha^2(\omega - \omega'_0)^2], \quad (1)$$

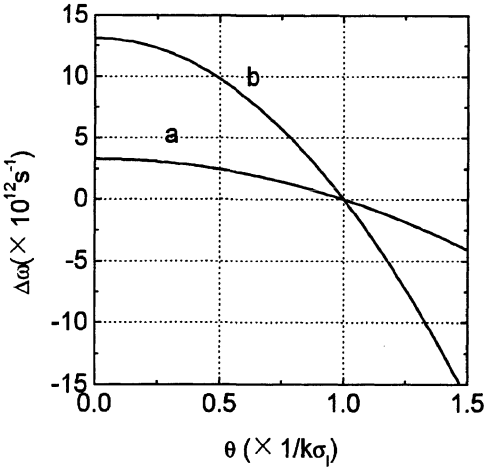


Fig. 1. Plots of the shift $\Delta\omega$ of the peak of the spectra versus the observation direction θ : (a) $t_0 = 10fs$, (b) $t_0 = 5fs$. In this case, $\omega_0 = 3.04 \times 10^{15} s^{-1}$.

where $M = \frac{\sqrt{\pi}}{\alpha}(\omega'_0 + \frac{1}{2\alpha^2})$, $\omega'_0 = \frac{\omega_0}{1+\epsilon^2}$, $\alpha^2 = (1/\delta_0^2)(1+\epsilon^2)$, and $\epsilon = (2\pi\sigma_I/\lambda_0)(\delta_0/\omega_0)\sin\theta$. The initial spectra of the pulse considered here is a Gaussian shape, i.e., $s^0(\omega) = E_0 \exp[-(\omega - \omega_0)^2/2\delta_0^2]$, where δ_0 is the $1/e$ bandwidth and ω_0 is the center frequency. It is found that the far-zone spectra does not have a strictly Gaussian shape. Comparing to the initial spectra, there exists a spectral shift which comes from two parts. One is the term ω^2/M which originates from the dispersive propagator and leads to blue shift in the spectra. The other is the Gaussian distribution in Eq.(1) which is centered at a lower frequency. This red shift is related with the effective spatial size and the direction of observation. For the on-axis point, $\omega'_0 = \omega_0$, hence only the dispersive propagator leads to blue shift. But for the paraxial point, the blue and red shifts interact with each other. So when the distance from the optical axis increases, the blue shift decreases. At a critical angle $\theta = \theta_c$, no shift occurs. We find that this critical angle $\theta_c = \lambda_0/2\pi\sigma_I$ is equal to the far-zone divergence angle of Gaussian beam. After that, there appears red shift. These results are shown in Fig.1. The magnitude of spectral shift also depends on the pulselength. In Table 1, we calculate the spectral shift values of ultrashort pulse at the far field on-axis point (here, the initial center wavelength is 800nm). It is found that for 5 fs pulse the spectral shift in the far-zone is very remarkable. When the duration of the pulse increases, the shift decreases rapidly.

2 Scaling law on propagation of ultrashort pulse

In 1986, E. Wolf [2] revealed that if the complex degree of spectral coherence depends on frequency only through the variable $k(\rho_2 - \rho_1)$, i.e., $\mu^0(\rho_2 - \rho_1, \omega) = h[k(\rho_2 - \rho_1)]$, the spectrum of light source will remain invariant on propagation and the source is said to satisfy the scaling law. Violating

Table 1. The spectral shifts values at the far field on-axis point

| Pulse width (FWHM,fs) | Center wavelength in far zone $\lambda_{max}(\text{\AA})$ | Spectral shift $\Delta\lambda (\text{\AA})$ |
|--------------------------|---|--|
| 3 | 7593.3 | 402.7 |
| 5 | 7845.4 | 154.6 |
| 10 | 7960 | 39.8 |
| 20 | 7990 | 10.0 |
| 50 | 7998.4 | 1.6 |

this scaling law, light will undergoes spectral shift during propagation. These properties have been demonstrated in experiment. For the ultrashort laser pulse considered above, it is a spatial completely coherent source. What is the scaling law for this class of source? In section I, using the initial condition which the FD waist size is independent of frequency, the pulsed beam propagating into far zone undergoes speectral shift. This shows that the source violates scaling law. However, according to the laser resonator theory, the waist size on a cavity resonator depends on the wave number. For the confocal cavity, the waist size is give by $W_0 = \sqrt{L/k}$, where L is the length of the cavity. If using this initial condition of the pulsed source, we immediately find that the spectra of the source will remain invariant on propagation. This condition is also suited for the pulsed beam with Hermite-Gaussian modes. Considering the frequency dependence of the waist size and employing the same calculation as Gamlieil [4], the far-zone spectra of Hermite-Gaussian modes are unchanged comparing with the spectra at the waist. Hence, the scaling law on propagation of ultrashort laser pulse can be expressed by

$$\sigma_I = \alpha \sqrt{\lambda}, \quad (2)$$

i.e., the FD spot size of the pulsed source is directly proportional to the square root of wavelength.

Our scaling law for ultrashort laser pulse can be generalized to any stationary sources. In 1982, E.Wolf [5] developed a new theory of partial coherence in the space-frequency domain (SFD), and showed that the cross-spectral density of a steady-state source of any state of coherence may be expressed in terms of certain new modes of oscillation, each of which represents a completely spatially coherent elementary excitation, i.e., $W(\mathbf{r}_1, \mathbf{r}_2, \omega) = \sum_n \gamma_n(\omega) \phi_n^*(\mathbf{r}_1, \omega) \phi(\mathbf{r}_2, \omega)$. The SFD coherence theory has been applied to analyze laser resonator modes [6]. It is found that the elementary modes of the cross-spectral density in laser resonator is identical to the Fox-Li transverse modes. Hence our scaling law may be regarded as a sort of scaling law of the spatially completely coherent sources. Gori, Starikov and Wolf [7] have found that the cross-spectral density of the Gaussian Schell-model sources may be expanded as the sum of Hermite-Gaussian modes. Thus according

to our scaling law, the scaling law of Gaussian Schell-model sources can be obtained that

$$\sigma_I = \alpha \sqrt{\lambda}, \quad \sigma_\mu = \beta \sqrt{\lambda}, \quad (3)$$

i.e., both spatial size of spectral intensity and degree of coherence depend on the wavelength. That scaling law of Gaussian Schell-model souces is different from the one derived by Agrawal et al. and Gori et al. [8].

From the analysis above, we find that there exists another description of scaling law for any stationary sources: *If the spatial distribution of each natural mode of oscillation of the light sources is directly proportional to the wavelength, the spectrum of light will remain invariant on propagation.*

3 Spectral properties of a truncated pulsed Gaussian beam

The scaling law of the pulsed sources may be easily destroyed by truncation of the pulsed beam, and in this case the spectrum of the pulse will be changed on propagation. Consider the diffraction of a pulsed field by a circular aperture of radius a in the plane $z = 0$. The pulsed field with space-time Gaussian shape and satisfying the scaling law is normally incident into the aperture plane. Using Rayleigh diffraction formulas, the FD field of the pulse in the far zone can be derived by

$$E(\mathbf{r}, \omega) = s^0(\omega) M(\omega), \quad (4)$$

where

$$M(\omega) = -\frac{i\omega}{2\pi c R} \int_0^a \rho \exp[-\rho^2/\sigma_0^2 + ik\rho^2/2R] J_0(k\rho x/R) d\rho, \quad (5)$$

It is noted that the change of spectrum is determined by $M(\omega)$. Fig. 2 illustrates the spectral shift in the far zone versus the radius of circular aperture. It is found that when the aperture is very smaller than the spot size of the pulse, the magnitude of the spectral shift has the same order as the on-axis shift in section I. But when the radius of aperture increases, the magnitude of shift decreases. As the radius of aperture is large than $1.5\sigma_0$, the shift is very small and can be neglected. In addition, for the truncated pulsed beam, the far-zone spectra has steady blue shift whatever for the on-axis or paraxial point. Hence we can conclude that the spectral shift of the few cycle pulse may be observed in experiment, if the pulsed beam is truncated.

4 An analytical form of an ultrashort pulsed Gaussian beam

Consider the initial codition which the FD waist size depends on wave number, and introduce a complex temporal variable $\tau(r, z, t) = t - (z + \frac{r^2}{2R(z)})/c +$

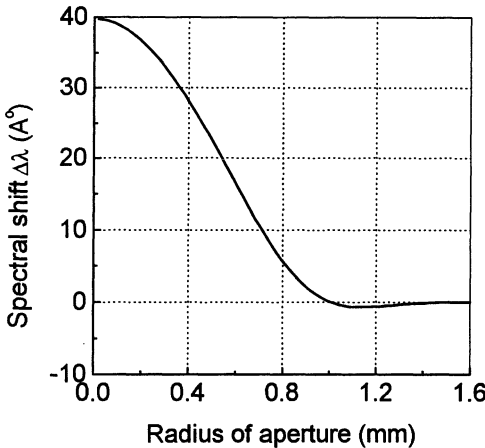


Fig. 2. Illustrate the spectral shift in the far zone due to the truncation of the pulsed beam. In this case, the FWHM of the pulse is 10fs , $\sigma_0 = 0.5\text{mm}$, and $\lambda_0 = 800\text{nm}$.

$i\frac{r^2}{\omega_0\sigma^2(z)}$, we can obtain an analytical expression of the pulsed Gaussian beam in free space [9]

$$U(r, z, t) = \frac{\sigma_0}{\sigma(z)} A(\tau) e^{i[\omega_0\tau + \varphi(z)]}, \quad (6)$$

In this expression, the pulsed Gaussian beam with an arbitrary shape of the spectral amplitude is expressed as a simple wave packet (at a carrier frequency ω_0) along with a complex time τ , which contains all the information about the spatial and temporal behaviors of the pulse.

For a space-time Gaussian pulse, we obtain

$$\begin{aligned} U(r, z, t) &= A_0 \frac{\sigma_0}{\sigma(z)} \exp\left[-\left(t - \frac{r^2}{2cR(z)} - \frac{z}{c}\right)^2 / 2t_0^2\right] \\ &\times \exp\left[-\frac{r^2}{\sigma^2(z)} + \frac{r^4}{2\sigma^4(z)}\left(\frac{\delta_0}{\omega_0}\right)^2\right] \\ &\times \exp\left\{i\omega_0\left[1 - \frac{r^2}{\sigma^2(z)}\left(\frac{\delta_0}{\omega_0}\right)^2\right]\left[t - \frac{r^2}{2cR(z)} - \frac{z}{c}\right]\right\} \\ &\times \exp[i\varphi(z)], \end{aligned} \quad (7)$$

It is noted that there exists a coupling among the beam parameters in space and time. In other words, the spatial variable emerges in the time shape of the pulse, and a coupling term, which is related with the bandwidth of the pulse, exists both in the phase and in the spatial distribution of the pulse. It is found that as the pulse propagates from near to far field, the transverse spatial shape is bent with the wave front. This leads to the difference between the peak intensity profile and energy profile. Hence the intensity-moment formalism for describing the spatial behavior of CW laser beam is not appropriate for the pulsed beam. In addition, the coupling term correlated with the spot size

enlarges the TD spatial size and lessens the carrier frequency of the pulse on the paraxial points. For few cycle pulse, these coupling effects are remarkable.

5 Summary

The spectral, temporal and spatial properties of few cycles optical pulsed beam on propagation have been studied. We find that for few cycle pulse there exists a remarkable spectral shift in the far zone. The scaling law of the pulse can be described that the spatial size of each Fourier components of the pulse depends on the wavelength. This scaling law can be generalized to any stationary sources. But it will be destroyed due to the truncation of the pulsed beam. On the other hand, we find an analytical form of the pulsed Gaussian beam in free space and discuss the space-time coupling on propagation.

References

1. Nisoli, M., et al.(1997) Compression of high-energy laser pulses below 5fs, Opt. Lett. **22**, 522-524
2. Wolf, E.(1986) Invariance of the spectrum of light on propagation, Phys. Rev. Lett. **56**, 1370-1373
3. Zhang-yang Wang, et al. (1996) Spectral and temporal properties of ultrashort light pulse in the far zone, Opt. Comm. **123**, 5-10
4. Gamilie, A. (1990) Mode analysis of spectral changes in light propagation from sources of any state of coherence, J. Opt. Soc. Am. A **7**, 1591-573
5. Wolf, E. (1982) New theory of partial coherence in the space-frequency domain Part I: spectra and cross spectra of steady-state sources, J. Opt. Soc. Am **72**, 343-351
6. Wolf, E., and Agarawl, G. S. (1984) Coherence theory of laser resonator modes, J. Opt. Soc. Am. A **1**, 541-546
7. Gori, F. (1980) Collett-Wolf sources and multimode lasers, Opt. Commun. **34**, 301-305; Starikov, A. and Wolf, E. (1982) Coherent-mode representation of Gaussian Schell-model sources and of their radiation fields, J. Opt. Soc. Am. **72**, 923-928
8. Agrawal, G. P. and Gamilie, A. (1990) Spectrum of partially coherent lights transition from near to far zone, Opt. Commun. **78**, 1-6
9. Zhang-yang Wang, et al. (1997) Space-time profiles of an ultrashort pulsed Gaussian beam, IEEE J. Quantum Electron. **33**, 566-573
10. Zhang-yang Wang, et al. (1997) Diffraction integral formulas of the pulsed wave field in the temporal domain, Opt. Lett. **22**, 354-356

Quantum Measurement of the State of a Coherently Coupled Dot Device

He-Bi Sun¹, Howard M. Wiseman^{1,2}, Dian W. Utami¹, Gerard J. Milburn¹

¹ University of Queensland, Brisbane, QLD 4072, Australia

² Griffith University, Nathan, QLD 4111, Australia

e-mail: sun@physics.uq.edu.au

Abstract. One limit on the performance of a quantum computer is unambiguous readout of data encoded in the qubit states. We analyze a method to measure the states of a coherently coupled dot device (qubit) using a single electron transistor. We derive a master equation to describe the unconditional evolution of the qubit when the measured records are averaged over, and a conditional stochastic master equation describes the conditional evolution of the qubit. The results from both descriptions are consistent.

Coupled electron systems, such as quantum dots, spin-polarized electrons, and Josephson junctions have been proposed as qubits, the basic elements of solid state quantum computers. One limit on performance of a quantum computer is the unambiguous readout of data encoded in the qubit states. We describe the conditional and unconditional dynamics of two coherently coupled quantum dots when one dot (target) is subjected to a measurement of its occupation number using a single electron transistor (SET). Each dot contains a single electron bound state. The charging effects are tuned away by means of the gate voltages [1]. The Hamiltonian of the two-dot system is

$$H = \hbar \sum_{i=1}^2 \omega_i c_i^\dagger c_i + i\hbar \frac{\Omega}{2} (c_1^\dagger c_2 - c_2^\dagger c_1) \quad (1)$$

where c_i^\dagger and c_i represent the Fermi annihilation and creation operators for the i -th dot respectively, and Ω is the coupling rate between two dots. The quiescent rate of current tunnelling through the SET is denoted as D_0 . If the electron is in dot-1 (target), the rate of the tunnelling is $D_0 + D_1$ with $D_1 > 0$. The quantum master equation representing the state of the coupled dot system is [2]

$$\frac{d\rho}{dt} = i[H, \rho] + D_1 \left[c_1^\dagger c_1 \rho c_1^\dagger c_1 - \frac{1}{2} (c_1^\dagger c_1 \rho + \rho c_1^\dagger c_1) \right] \quad (2)$$

The master equation describes the unconditional evolution of the measured system when the results of all measurement records (current) are averaged

over. This gives the rate at which coherence in the target system is destroyed by the measurement. The steady state current through the SET is given by

$$i_\infty = e \left(D_0 + D_1 \left\langle c_1^\dagger c_1 \right\rangle_\infty \right) = e \left(D_0 + \frac{D_1}{2} \right) \quad (3)$$

where the ∞ subscript indicates that the system is at steady-state. The fluctuations in the observed current, $i(t)$ are quantified by the two-time correlation function:

$$G(\tau) = E[i(t)i(t+\tau)]_\infty - i_\infty^2 = \frac{e}{2} i_\infty \delta(\tau) + \langle i(t), i(t+\tau) \rangle_\infty^{\tau \neq 0} \quad (4)$$

To relate these classical averages to the fundamental quantum processes occurring in the well we apply the theory of open quantum system [3] to the present system and calculate correlation function in the stationary state [4]:

$$G(\tau) = \frac{e}{2} i_\infty \delta(\tau) + \frac{e^2 D_1^2}{8} \left(\frac{\Delta_+ e^{\lambda_3 \tau} - \Delta_- e^{\lambda_4 \tau}}{\sqrt{D_1^2 - 16\Omega^2}} \right) \quad (5)$$

where

$$\Delta_\pm = D_1 \pm \sqrt{D_1^2 - 16\Omega^2}, \text{ and } \lambda_{3,4} = \frac{-\Delta_\mp}{4} \quad (6)$$

The first term of $G(\tau)$ represents the shot noise component. The power spectrum of the noise is

$$S(\omega) = e i_\infty + \frac{32 e^2 D_1^2 \Omega^2}{\sqrt{D_1^2 - 16\Omega^2}} \left\{ \frac{1}{\Delta_-^2 + 16\omega^2} - \frac{1}{\Delta_+^2 + 16\omega^2} \right\} \quad (7)$$

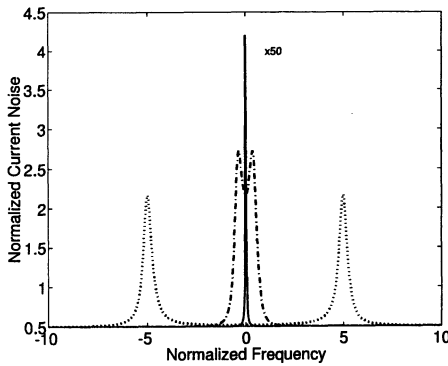


Fig. 1. Current noise power spectra normalized by full short noise (all other parameters are normalized by D_1) for various coherent coupling rates: $\Omega = 0.1$ (solid), $\Omega = 0.5$ (dot-dashed), $\Omega = 5$ (dotted)

We plot the current noise power spectra for various coupling rates in Fig.1. As shown in this figure, when $4\Omega > D_1$ the spectrum will have a double peak

structure indicating coherent tunnelling between the two coupled dots. It is therefore possible to use the noise power spectrum of the current though the SET as a means to measure the tunnel coupling between dots if the coupling is high enough.

In order to determine the signal to noise ratio and other measures of the quality of the measurement we also need to know how the system state depends on the actual current through the device. We use a conditional stochastic master equation which gives the evolution of the measured system, conditioned on a particular realization of the measured current. The state of the target conditions the measured current while the measured current itself conditions the future evolution of the measured system in a self consistent manner. At zero response time limit the current consists of a sequence of δ function spikes. $I(t) = dN/dt$ where $dN(t)$ ($= 0$ or 1) is a classical point process defined by the conditions

$$[dN(t)]^2 = dN(t) \quad (8)$$

$$E[dN(t)]/dt = D_0 + D_1 Tr[c_1^\dagger c_1 \rho] = D_0 + D_1 Tr[c_1^\dagger c_1 \rho c_1^\dagger c_1] \quad (9)$$

The first condition means that $dN(t)$ equals zero or one. The second says that the rate of events is equal to a background rate D_0 plus an additional rate D_1 if and only if the electron is in dot-1 (target). The stochastic master equation conditioned on the observed event in time dt is

$$\begin{aligned} d\rho = dN & \left[\frac{D_0 + D_1 \mathcal{D}[c_1^\dagger c_1] \rho}{D_0 + D_1 Tr[\rho c_1^\dagger c_1]} - 1 \right] \rho \\ & + dt \left[\frac{-D_1}{2} \{c_1^\dagger c_1, \rho\} + D_1 Tr[\rho c_1^\dagger c_1] \rho - i[H, \rho] \right] \end{aligned} \quad (10)$$

where $\mathcal{D}[A]B = ABA^\dagger$ and $\{A, B\} = AB + BA$. To derive the different time scales we use the Bloch representation of the state matrix:

$$\rho = \frac{1}{2} (I + x\sigma_x + y\sigma_y + z\sigma_z) \quad (11)$$

where $\sigma_x = c_1^\dagger c_2 + c_2^\dagger c_1$, $\sigma_y = i(c_2^\dagger c_1 - c_1^\dagger c_2)$, $\sigma_z = c_2^\dagger c_2 - c_1^\dagger c_1$. The moments of the Pauli matrices are given by $\langle \sigma_\alpha \rangle = \alpha$ ($\alpha = x, y, z$). That is, $z = \pm 1$ when the system is in a definite state. Fig.2 shows the trajectories for three tunnel coupling rates between two dots which correspond to those in Fig.1. One can see that when Ω is small ($< D_1/2$), the electron is almost localized in one dot state or the other with a little probability to tunnel. After a long time a transition from dot-2 ($z=-1$) into dot-1 ($z=1$) occurs suddenly. This behaviour corresponds to a Lorentzian noise spectrum as shown in the solid line in Fig.1. For $\Omega >> D_1/2$ the trajectory shows nearly sinusoidal oscillations with jumps occurring at an average rate of $D_1/2$ which corresponds

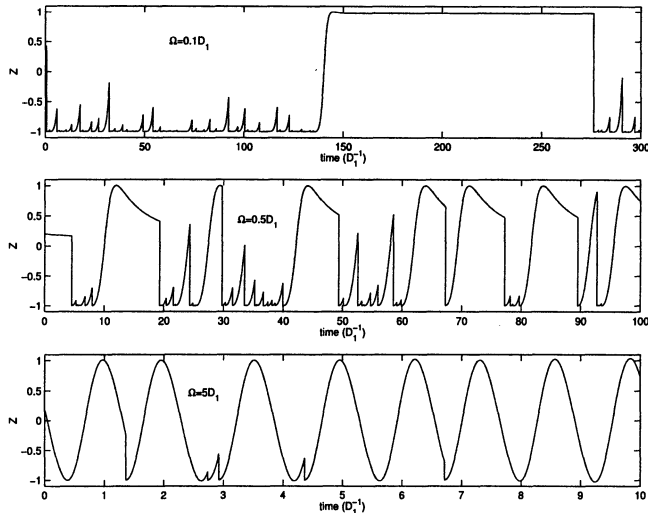


Fig. 2. Trajectories for various coherent coupling rates

to the noise spectrum featuring double peaks at $\omega \sim \pm \Omega$ shown in the dotted line in Fig.1. When the coupling is moderate ($\Omega \sim D_1/2$), the trajectory shows neither well localized nor regular sinusoidal oscillating feature. The non-sinusoidal oscillations give peaks at frequency less than Ω in the noise spectrum of the dot-dashed line in Fig.1.

In summary, we describe the average and dynamic evolution of the states of a coherently coupled dot device using unconditional and conditional quantum master equations respectively. The tunnelling rates D_0 and D_1 can be obtained from the steady state current. The tunnel coupling rate Ω between dots can be measured from noise power spectrum. The quantum trajectory method we used is different from the approach of keeping track of all states of tunneled electrons [5]. The more detailed application of the approach to quantum measurement will be presented in a large publication where we will show the similar results from the two approaches, and how to provide a measure of the purity of the state.

References

1. T. Fujisawa and S. Tarucha, *Superlattices and Microstructures*, **21**, 247 (1997)
2. H.B Sun and G.J. Milburn, *Phys. Rev. B* **57**, 10748 (1999)
3. H. Carmichael, *An Open Systems Approach to Quantum Optics*, (Springer-Verlag, Berlin Heidelberg 1993).
4. H. M. Wiseman and G.J . Milburn, *Phys. Rev. A* **47** , 1652 (1993) (appendix).
5. G. Schön, A. Shnirman, and Y. Makhlin, cond-mat/9811029

Controlling Magneto-Optical Rotation via Atomic Coherences

Anil K. Patnaik and G. S. Agarwal

Physical Research Laboratory, Navrangpura,
Ahmedabad 380 009, India
e-mail: aanil@prl.ernet.in

Abstract. An isotropic medium, having magnetic sublevels, when subjected to a magnetic field or an electromagnetic field can induce anisotropy in the medium; and as a result the plane of polarization of the probe field can rotate. Therefore the rotation due to the magnetic field alone, can be *controlled efficiently* with use of a coherent field. We show, using a control field, significant enhancement of the magneto-optical rotation and demonstrate the possibility of realizing *magneto-optical switch*.

1 Introduction

An isotropic medium having m -degenerate sublevels when subjected to a magnetic field exhibits birefringence in its response to a polarized optical field. This is due to the fact that Zeeman splitting of magnetic sublevels causes asymmetry in the refractive indices for left and right circular polarization components of the optical field. The result is magneto-optical rotation (MOR); i.e., the plane of polarization of the light emerging out of the medium is rotated with respect to that of the incident. For example consider a V -scheme (say ^{40}Ca system) with 4^1S_0 as ground state and 4^1P_1 as its excited states, subjected to a magnetic field \mathbf{B} . We probe it by a linearly polarized light propagating along \mathbf{B} . Let χ_+ and χ_- be the susceptibilities corresponding to the right and left circular polarizations. For small absorption the polarization rotation is given by

$$\theta = \pi k_p l \text{Re}(\chi_- - \chi_+), \quad (1)$$

where k_p corresponds to propagation vector of the probe and l is the length of the medium. We note that χ_{\pm} depend on the number density of atoms and the oscillator strength of the transition.

Production of large magneto optical rotation is important for a number of applications. In a recent experiment, Sautenkov *et al* [1] have shown enhancement of resonant MOR in an optically dense vapor of Rb atom by several order of magnitude. Further, a coherent field can manipulate the susceptibilities χ_{\pm} of the medium, and in particular can modify the dispersion properties of the medium [2]. In another recent experiment on coherence induced anisotropy, Wielandy and Gaeta [3] have demonstrated that when a Rb vapor cell is illuminated by a strong laser beam of a particular polarization,

and is probed by a linearly polarized laser beam, the plane of polarization of the probe is rotated as the control field induces birefringence in the medium.

In this article, we consider the possibility of control of the MOR by using a strong laser beam. We also show that for a chosen configuration, inclusion of Doppler effect in the problem gives significant enhancement in the MOR - that demonstrates the possibility of realizing *Magneto-optical switch*.

2 The Model Scheme and Determination of χ_{\pm}

We consider a model system [see Fig.1] involving say cascade of transitions $|j = 0, m = 0\rangle$ (level $|g\rangle$) \leftrightarrow $|j = 1, m = \pm 1\rangle$ (level $|1\rangle$ and $|2\rangle$) \leftrightarrow $|j = 0, m = 0\rangle$ (level $|e\rangle$). This for example will be relevant for expressing ^{40}Ca . The probe \mathbf{E}_p will act between the levels $|g\rangle$ and $|1\rangle, |2\rangle$. We assume in addition the interaction of a control laser \mathbf{E}_c to be nearly resonant with the transition $|e\rangle \leftrightarrow |1\rangle, |2\rangle$. For simplicity we drop the transition $m = 0 \leftrightarrow m = 0$. We thus assume the loss to $m = 0$ state by spontaneous emission could be pumped back by an incoherent pump. We derive the density matrix equation for the system

$$\frac{\partial \rho}{\partial t} = -\frac{i}{\hbar} [\mathcal{H}, \rho] + \text{spontaneous decay terms}, \quad (2)$$

that describes the dynamics of the system. Where \mathcal{H} defines the Hamiltonian of the system. We solve Eq.(2) and could obtain complete analytical solutions

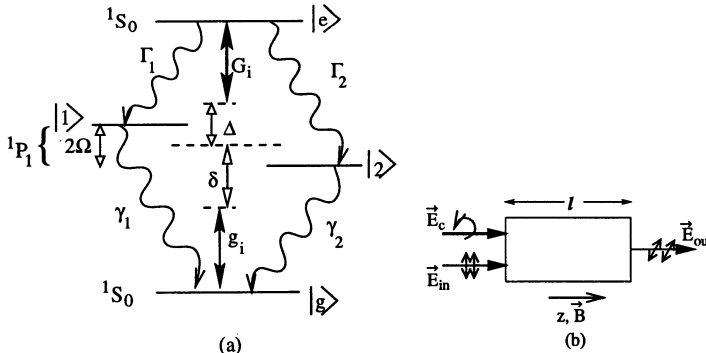


Fig. 1. (a) The four-level model scheme (say of ^{40}Ca) having m -degenerate sub-levels as its intermediate states. The symbols in left hand side denote the energy levels of ^{40}Ca atom. $2\Gamma_i$ and $2\gamma_i$ are the spontaneous decays, $2g_i$ ($2G_i$) is Rabi frequency of the probe (control) field due to coupling of the intermediate state $|i\rangle$ with $|g\rangle$ ($|e\rangle$). The detuning of probe (control) field from the center of $|1\rangle$ and $|2\rangle$ are represented by δ (Δ). 2Ω is the Zeeman split between the intermediate states. (b) A block diagram that shows the configuration under consideration. \mathbf{B} defines the quantization axis z . The input probe \mathbf{E}_{in} is x -polarized and the control field is left circularly polarized. Both the fields propagate along z . After passing through the cell, output is observed through a y -polarized analyzer.

in the steady state. The susceptibilities of the medium, to different circularly polarization components, are proportional to the off-diagonal density matrix element corresponding to the transition the polarized field couples. However, here we do not present the complete analytical results [4].

For an x -polarized input probe beam, after passing through the medium, the transmission at the output through a crossed polarized analyzer (scaled with the input intensity) can be written as

$$T_y = \frac{1}{4} \left| \exp \left(i \frac{\alpha l}{2} \tilde{\chi}_+ \right) - \exp \left(i \frac{\alpha l}{2} \tilde{\chi}_- \right) \right|^2; \quad (3)$$

where $\tilde{\chi}_{\pm}$ represent the normalized susceptibilities. In rest of this article, we drop the tilde for brevity. The quantity αl gives resonant absorption of the medium. For a particularly interesting case of a σ_- polarized control field (i.e., $\mathcal{E}_{c+} = 0$, $\mathcal{E}_{c-} \neq 0$), χ_{\pm} are found to be

$$\chi_- \equiv \frac{i\gamma}{(\gamma + i(\delta - \Omega))}, \quad (4)$$

$$\chi_+ \equiv \frac{i\gamma(\Gamma_1 + \Gamma_2 + i(\Delta + \delta))}{|G_1|^2 + (\gamma + i(\delta + \Omega))(\Gamma_1 + \Gamma_2 + i(\Delta + \delta))}, \quad (5)$$

where the symbols represent the parameters defined in Fig.1. For simplicity, we have assumed $\gamma_i = \gamma$. In all the plots, all frequencies are scaled with γ ($= \Gamma_i$). Clearly, χ_- is independent of control field parameters, where as χ_+ depends strongly on the strength and frequency of the control field. For large $|G_1|$, both real and imaginary part of χ_+ will show Autler-Townes splitting and therefore will cause a large asymmetry between the two polarization components.

3 Laser Field Induced Enhancement of MOR

From Eq.(4) and (5), we note that, $\chi_+(\Omega = 0) \neq \chi_-(\Omega = 0)$ for $G_c \neq 0$. Therefore the birefringence can be induced in the medium by the laser field even in absence of the magnetic field [3]. Thus one observes a large rotation of the polarization of the probe. There are many reports of laser field induced birefringence [5] which had suffered from large absorption, resulting in a very small rotation signal at the output. Further when magnetic field is present, *new frequency regions* are created by application of the control field where significant enhancement of MOR signal is obtained particularly in the regions where the MOR, otherwise, is negligible. For example in Fig.2, at $\delta \sim \pm 50$, there is a large enhancement of MOR. For detuned control fields the MOR could be enhanced further and we also analyze the case of an elliptically polarized control field and identify many interesting parameter domains where large MOR is obtained (results not shown here).

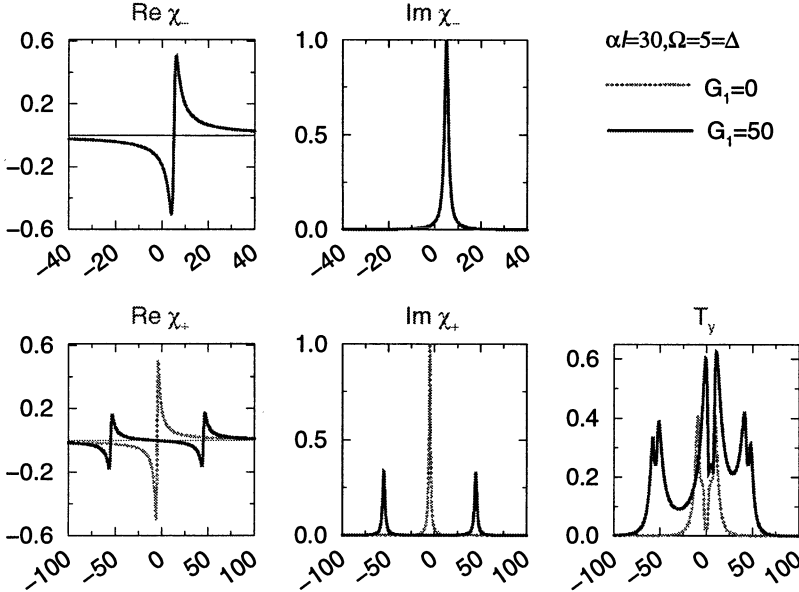


Fig. 2. Large enhancement of MOR for a range of frequencies of the probe beam is shown. The parameters are mentioned above.

4 Realization of a Magneto-Optical Switch

We next consider a Doppler broadened medium where one needs to average χ_{\pm} over the atomic velocity distribution function inside the cell. We have identified a configuration that *takes advantage of the Doppler broadening* to increase the asymmetry between χ_{\pm} , and hence to obtain significantly large enhancement of the MOR signal.

We consider the same configuration as in Fig.1 but with control field (σ_- polarized) and the probe field (x -polarized) counter propagating to each other. The σ_- component of the probe is, thus, Doppler broadened as it does not see the control field, but on the other hand σ_+ component experiences the counter propagating σ_- polarized control field and, therefore, is almost Doppler free. That leads to enhancement of the asymmetry between χ_+ and χ_- . We have derived analytical expressions for the Doppler averaged values of χ_{\pm} and hence for the rotation spectra. In Fig.3, at $\delta \sim 0$, MOR enhancement factor is as large as 3.7×10^4 , compared to that of MOR with no control field case. Such an action of control field can be used as a *magneto-optical switch* that switches the given polarization state of the probe field to its orthogonal component. Several interesting set of parameters are identified where the y -polarized signal intensity at the output is as large as $\sim 92\%$ of the x -polarized input intensity.

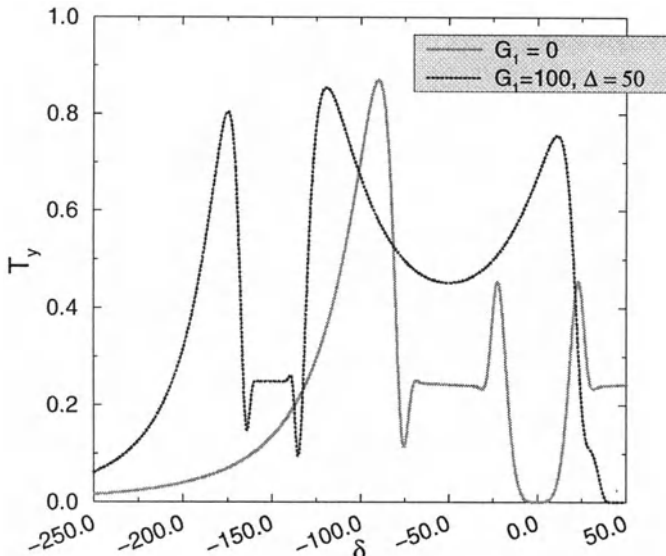


Fig. 3. Significant enhancement of MOR in a Doppler broadened medium. The large enhancement factor at $\delta = 0$ demonstrates the possibility of *Magneto-optical switch*. Here the parameters used are $\alpha l = 300$ and $\Omega = 50$.

5 Conclusion

We have shown how a control field can induce birefringence and enhance MOR. We have also shown that it can create new regions where MOR enhances significantly. In an inhomogeneously broadened medium, we have shown that, the control field enhances MOR to a large order of magnitude, and therefore it demonstrates the possibility of realizing a *magneto-optical switch*.

References

1. V. A. Sautenkov, M. D. Lukin, C. J. Bednar, G. R. Welch, M. Fleischhauer, V. L. Velichansky, and M. O. Scully, quant-ph/9904032; MOR under saturation conditions in a *Ca* system is discussed in: G. S. Agarwal, P. Anantha Lakshmi, J-P Connerade, and S. West, *J. Phys. B* **30**, 5971 (1997).
2. M. O. Scully, *Phys. Rev. Lett.* **67**, 1855 (1991); M. Fleischhauer, C. H. Keitel, M. O. Scully, Su Chang, B. T. Ulrich, and S. Y. Zhu, *Phys. Rev. A* **46**, 1468 (1992).
3. S. Wielandy and A. L. Gaeta, *Phys. Rev. Lett.*, **81**, 3359 (1998).
4. For details see: A. K. Patnaik and G. S. Agarwal, *Opt. Commun.*, in press and to be published.
5. B. Stahlberg, P. Jungner, T. Fellman, K.-A. Suominen, and S. Stenholm, *Opt. Commun.* **77**, 147 (1990); F. S. Pavone, G. Bianchini, F. S. Cataliotti, T. W. Hänsch, M. Inguscio, *Opt. Lett.* **22**, 736 (1997).

Theoretical and Experimental Investigation on Twin Beams Generation by Non-degenerate Optical Parametric Amplifier

Yun Zhang, Hai Wang, Xiaoying Li, Hong Su, Changde Xie, Kunchi Peng

Institute of Opto-Electronics, Shanxi University, Taiyuan 030006, P.R.China

Abstract. Intensity difference variances of signal and idler modes from nondegenerate optical parametric amplifier (NOPA) are theoretically analyzed. The continuous wave twin beams with degenerate frequency at $1.08\mu\text{m}$ and orthogonal polarization have been generated from a double resonant NOPA. The intensity difference fluctuation between the twin beams is 3.7dB(57%) below the shot noise limit at the measurement frequency of 3MHz.

1 Introduction

Over the past twenty years the properties of nonclassical states of light with squeezed quantum fluctuation have been extensively studied, both theoretically and experimentally[1]. The continuous optical parametric oscillator(OPO) without injected subharmonic signal and amplifier(OPA) with injected signal are important schemes to generate squeezed states of light. The degenerate optical parametric oscillator (DOPO) and optical parametric amplifier (DOPA) have been successfully used to produce quadrature squeezed light of single-mode. The two-mode quadrature squeezed vacuum state of light and the quantum correlated twin beams with squeezed intensity difference fluctuation have been generated from continuous Nondegenerate optical parametric oscillators(NOPO) respectively operated below and above the oscillation threshold[2]. Recently, the interests of study on the nonclassical states of light concentrate on improving optical measurement sensitivity to beat the vacuum fluctuation of the electromagnetic field. To practical applications the stability and reliability of nonclassical light generation systems are of great importance. By injecting a seed wave into a type I DOPA, Mlynek's group in Konstanz[3] obtained continuous-wave bright quadrature squeezed state of light with excellent long-term stability over several hours. Later, a series of advanced quantum measurement experiments were accomplished on this DOPA system. It has been well demonstrated that long-term stability of OPA is much better than OPO. On the other hand, the frequency of output wave from OPA can be locked on the frequency of injected signal, so that the investigation on OPA can provide useful information to develop the tunable nonclassical light sources. At last, the frequency of type II NOPA is degenerate, it is very important in using the twin beams. Therefore, it is necessary to study the quantum optical properties of output fields from NOPA.

2 Theory

The NOPA device, which is pumped by harmonic wave of frequency 2ω and injected by two subharmonic waves with degenerate frequency ($\omega_1 = \omega_2 = \omega$) but orthogonal polarization is considered. The harmonic and two subharmonic modes in the cavity are described by α_0 , α_1 and α_2 . We suppose that there are completely identical losses for α_1 and α_2 in the system and $\gamma = \gamma_b + \gamma_c$ denote the total loss rate for each of these modes. The transmission of input-output coupler and extra losses for the pump mode α_0 are taken to be γ_{0b} and γ_{0c} , so that the total loss rate for the pump mode is $\gamma_0 = \gamma_{0b} + \gamma_{0c}$. Assuming zero detuning of the cavity, the equations of motion for the intracavity modes with the rotating wave approximation are as follows[4]

$$\dot{\alpha}_0 = -\gamma_0\alpha_0 - \kappa\alpha_1\alpha_2 + \varepsilon + \sqrt{2\gamma_{0c}}c_0(t) \quad (1a)$$

$$\dot{\alpha}_1 = -(\gamma_b + \gamma_c)\alpha_1 + \kappa\alpha_0\alpha_2^* + \sqrt{2\gamma_b}\alpha_1^{in} + \sqrt{2\gamma_c}c_1(t) \quad (1b)$$

$$\dot{\alpha}_2 = -(\gamma_b + \gamma_c)\alpha_2 + \kappa\alpha_0\alpha_1^* + \sqrt{2\gamma_b}\alpha_2^{in} + \sqrt{2\gamma_c}c_2(t) \quad (1c)$$

where, κ is the nonlinear coupling parameter, $\varepsilon = \sqrt{2\gamma_{0b}}\alpha_0^{in}$ is the coherent field driving pump mode, α_i^{in} and $c_i(t)$ are the incoming fields, associated with the coupling mirror and with the extra loss respectively. In equation(1), we have assumed that the pump and both signal and idler beams triply resonate in a cavity. Choosing a proper phase, we make α_i to be real and take $\dot{\alpha}_i = 0$, the steady state equations are obtained. Here we have assumed that $\alpha_1^{in} = \beta + b_1(t)$, and $\alpha_2^{in} = \beta + b_2(t)$ have the same non-zero mean value β , but different fluctuations ($b_1(t) \neq b_2(t)$) and $c_i(t)$ have zero mean value, i.e. the vacuum fluctuation. Let $\alpha = \alpha_1 = \alpha_2$, the solution of equation (1) is given :

$$\begin{aligned} \alpha_0 &= \frac{\varepsilon - \kappa r^2}{\gamma_0} = \frac{\gamma}{\kappa} - \frac{\sqrt{2\gamma_b}\beta}{\kappa\alpha} \\ 0 &= \alpha^3 - \frac{\kappa\varepsilon - \gamma\gamma_0}{\kappa^2}\alpha - \frac{\gamma_0\sqrt{2\gamma_b}\beta}{\kappa^2} \end{aligned} \quad (2)$$

In the case of $\beta = 0$, we get the parametric oscillation threshold of the cavity $\varepsilon^{th} = \gamma_0\gamma/\kappa$ from eq.(2) and the equations go back to the expressions of NOPO. In the case of non-zero subharmonic input ($\beta \neq 0$), the equation (2) is a cubic equation, the solution of that and the classical behavior of system given from the solution have been discussed by F.E.Harrison et al [5] and S.Schiller et al [6] in detail.

Using a semiclassical input-output formalism, we obtain the fluctuation dynamic equations

$$\begin{aligned} \delta \dot{\alpha}_0(t) &= -\gamma_0\delta\alpha_0(t) - \kappa\alpha[\delta\alpha_1(t) + \delta\alpha_2(t)] \\ &\quad + \sqrt{2\gamma_{0b}}b_0(t) + \sqrt{2\gamma_{0c}}c_0(t), \end{aligned} \quad (3a)$$

$$\begin{aligned}\delta \dot{\alpha}_1(t) = & -\gamma\delta\alpha_1(t) + \kappa[\alpha_0\delta\alpha_2^*(t) + \alpha\delta\alpha_0(t)] \\ & + \sqrt{2\gamma_b}b_1(t) + \sqrt{2\gamma_c}c_1(t),\end{aligned}\quad (3b)$$

$$\begin{aligned}\delta \dot{\alpha}_2(t) = & -\gamma\delta\alpha_2(t) + \kappa[\alpha_0\delta\alpha_1^*(t) + \alpha\delta\alpha_0(t)] \\ & + \sqrt{2\gamma_b}b_2(t) + \sqrt{2\gamma_c}c_2(t).\end{aligned}\quad (3c)$$

The fluctuation of the intensity difference of the signal and idler modes is

$$D(t) = \delta(I_1 - I_2) = \delta(a_1^+a_1 - a_2^+a_2) = \alpha[\delta a_1(t) + \delta a_1^+(t) - \delta a_2(t) - \delta a_2^+(t)] \quad (4)$$

and equation of motion is

$$\dot{D}(t) = -\gamma D(t) - \kappa\alpha_0 D(t) + \sqrt{2\gamma_b}D^b(t) + \sqrt{2\gamma_c}D^c(t). \quad (5)$$

Assuming that the fluctuation of input waves and noise of extra losses are uncorrelated and equal one, we can calculate the output variance in frequency domain:

$$Var(D^{out}, \omega) = \frac{4\gamma_b\gamma_c}{(\gamma + \kappa\alpha_0)^2 + \omega^2} + \frac{(\gamma_b - \gamma_c - \kappa\alpha_0)^2 + \omega^2}{(\gamma + \kappa\alpha_0)^2 + \omega^2} \quad (6)$$

Equation (6) is similar to the result of Ref[4], so we can conclude that the output of the NOPA has the property of intensity difference squeezing.

3 Experiment

A general overview of experimental set-up is shown in Fig.1. A home made intracavity frequency-doubled and frequency-stabilized CW ring Nd:YAP laser serves as the source of both the seed wave and the pump wave of nondegenerate OPA. The heart of the experiment is the NOPA. The NOPA consists of a 10-mm-length KTP crystal and an external mirror. The total length of cavity is 52mm. One face of the crystal as the input coupler is coated with a high reflectivity at $1.08\mu m$ and high transmission ($T > 95\%$) at $0.54\mu m$, the other face is coated antireflection at both $1.08\mu m$ and $0.54\mu m$. The squeezed output wave is extracted from a 50mm radius-of-curvature mirror with a transmission of $T = 5\%$ at $1.08\mu m$ and high reflectivity at $0.54\mu m$. The mirror is mounted on a piezoelectric transducer(PZT) to lock the cavity length on resonance for the two injected modes. The measured finesse for $1.08\mu m$ of the resonator is 90, the total extra intracavity losses are estimated to be 1.3%, the free spectral range is 2.6GHz and the cavity linewidth is 28MHz. The NOPA cavity is pumped at $0.54\mu m$ with a beam polarized along the b-axis that is doubled pass through the cavity. An input beam is injected in KTP crystal at an angle 45° from the crystal axes and undergoes phase-sensitive amplification. So, the output beam(signal and idler) is polarized along b-and c-axes of the crystal(correspond to S-polarized and P-polarized), respectively.

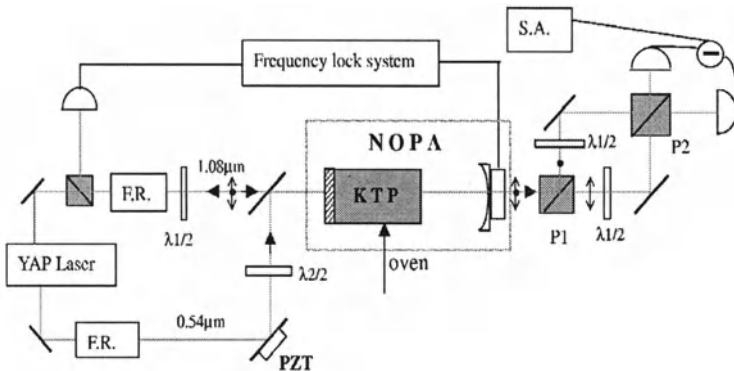


Fig. 1. Scheme of an Optical parametric amplifier

For nondegenerate operation the NOPA cavity must be resonant at the two seed beams. Because the nature of Type II processes, both the b-and c-polarized beams are not usually simultaneously resonant for a given cavity length. However, the b-and c-polarized beams have different temperature dependence for their indices of refraction inside the crystal, so that by fine-tuning of the temperature, we can reach the condition of simulations resonance for the signal and idler. After the double resonance is completed the NOPA is locked on the frequency of injected field via a standard FM-sideband technique, in which the subhrmonic wave is electro-optically phase modulated in the crystal at 60MHz.

To generate the quantum correlated twin beams the relative phase between the subharmonic and harmonic beams corresponds to maximum amplification. This is due to the fact that the signal and idler photons are produced in pairs. When the , maximum parametric deamplification is achieved and quarduture amplitude-squeezed state is generated[3]. Unlike the output from the above the threshold OPO, the signal and idler from the OPA combine a linearly polarized light. So, the detection system is not the one as the same as before. The output from the NOPA resonator are separated into two equal parts by a polarizor (P1) with transmission and reflection axes parallel to the crystal axes. Each beam is rotated by a half-wave plate then combined by another polarizor (P2) to form a balanced homodyne detector. We use detectors with ETX500 InGaAs photodiodes. The outputs of the photodiodes are amplified and combined in a hybrid junction to generate difference currents. These currents are sent to a spectrum analyzer (HP8591). To ensure the balance of the detection system the photodiodes were carefully chosen and electronic compensation is included. The total quantum efficiency of detection system is 86%. When the polarization of the two beams are rotated by an angle of 45°, each beams is separated into two equal parts by the poarizor(P2). So, the noise measured in the intensity difference is the shot

noise limit. When the two beams are rotated by an angle of 0° , each beam is transmitted or reflected by the polarizer(P2). So, the noise measured in the intensity difference is the intensity difference spectrum between the twin beams.

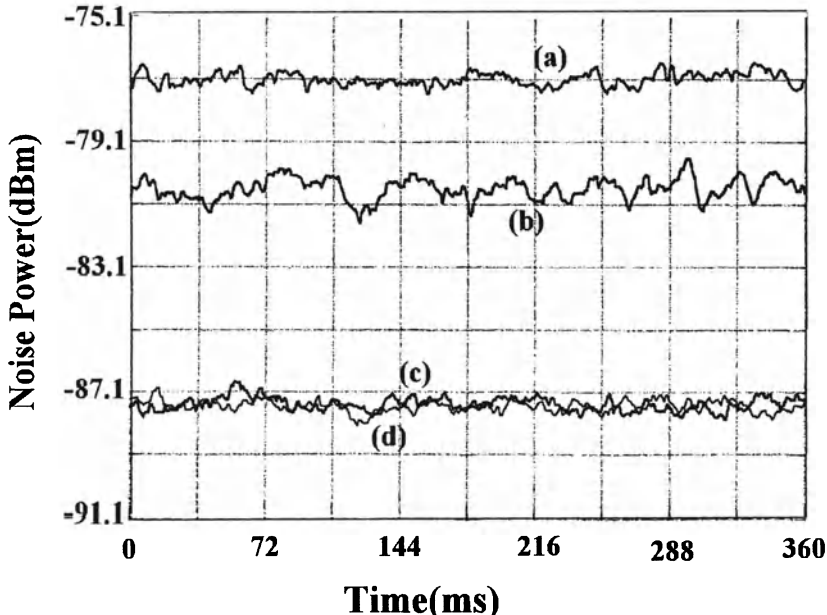


Fig. 2. Measured intensity difference variances

Figure 2 shows the measured intensity difference variances at analysis frequency 3 MHz. The pump power before the NOPA is fixed at 430mW to ensure the NOPA operating below the threshold that is approximately 450mW. Trace(a) and (b) refer to the shot noise limit and the intensity difference, respectively, where the relative phase between subharmonic and harmonic waves has been low scanned. Averaging the noise of both traces determines the squeezing level to be 3.7dB below the shot-noise level. Trace(c) and Trace(d) are the measured the shot noise level and the intensity difference noise for the case when the NOPA is not pumped, respectively.

In the summary, we have investigated in detail the intensity difference noise properties of the output light field from NOPA, theroretically and experimentally. We have built a simple semimonolithic OPA to generate the intensity difference squeezing. The intensity difference noise of twin beams is about 3.7dB below the shot noise limit at the measurement frequency of 3MHz.

Acknowledgment. Supported by the National Natural Science Foundation of China(No.69837010), the Science Foundation of Shanxi Province and the Youth Science Foundation of Shanxi Province.

References

1. J. Opt. Soc. Am. B **4**, 1453-1741 (1987); J. Mod. Opt., **34** (1987); Appl. Phys. B **55** 190-303 (1992).
2. K.C.Peng, Q. Pan, H. Wang, et al, Appl. Phys B **66**, 755 (1998).
3. K.Schneider, et al, Opt. Lett., **21**, 1396 (1996).
4. C.Fabre, et.al., J. Phys., **50**, 1209 (1989).
5. F.E.Harrison and D.F.Walls, Opt.commun, **123**, 331(1996).
6. S.Schiller, et.al. Applied Physics B, **60**, S77(1995).

Line-Shape Variations of Two-Photon Transition in Molecular Rhomb-Type System Based on Quantum Interference

Weisheng Wang^{1,2}, Le Deng¹, Zhenrong Sun¹, Liang'en Ding¹

¹ Department of Physics, East China Normal University Laboratory for Quantum Optics,

East China Normal University Shanghai, 200062, P. R. China

² Department of Electronics, Fuzhou University Fuzhou, 350002, P. R. China

Abstract. Line-shape variations of two-photon transition in rhomb-type system were theoretically investigated. The theoretical results have been experimentally demonstrated.

1 Introduction

In recent years, many novel physical phenomena based on quantum interference have been discovered, such as coherent population trapping [1-3], electromagnetically induced transparency [4-6] and lasing without inversion [4,7,8]. But, the most experiments were carried out in atomic samples. Experiments in molecular samples were seldom reported.

The spin-orbit perturbation between the rotational levels with same J value in the single and triplet states in a diatomic molecule can form a pair of levels, not only close each other but also with their wave-function sharing. The coherent population trapping and some novel spectral effects due to the quantum interference were studied for the four-level system with a pair of mixed levels in our laboratory [9,10].

In this paper we report the line-shape variations of the two-photon transitions in rhomb-type four-level system. The line-shape variations based on quantum interference such as the broadening of Doppler-free peak and of Doppler-broadened pedestal and the asymmetry of line-shape of the two-photon transition are shown. The results quite agree with our experiment in Na_2 .

2 Theoretical work in Rhomb-type system

Fig. 1 shows the level structure of rhomb-type system. Level 1 is ground state. Level 2 and 3 are two close intermediate levels. Level 4 is upper level, it is excited by two-photo transition.

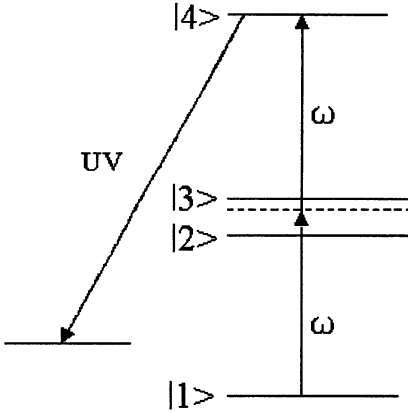


Fig. 1. Level structure of rombl-type system

The density-matrix motion equation describing the interaction of the rhomb type level system with two travelling-wave fields has the following form,

$$i\hbar\left(\frac{\partial}{\partial t} + v\frac{\partial}{\partial z}\right)\rho_{ij} - \hbar(\omega_i - \omega_j)\rho_{ij} + i\hbar\gamma_{ij}\rho_{ij} = i\hbar\Lambda_{ij} - E\sum_{k=1}^4 (\mu_{ik}\rho_{kj} - \rho_{ik}\mu_{kj}) \quad (1)$$

where subscripts $i, j = 1, 2, 3, 4$ corresponding to energy-levels 1, 2, 3 and 4, respectively. $\Lambda_i = \Lambda_{ij}$ ($i = j$) is the thermal excitation rate of level i , $\gamma_i = \gamma_{ij}$ ($i = j$) is the relaxation rate of level i . Ignoring collisional dephasing, $\gamma_{ij} = (\gamma_i + \gamma_j)/2$. We have and $\mu_{12}, \mu_{13}, \mu_{23}, \mu_{24} \neq 0$ and $\mu_{14}, \mu_{23} = 0$ with the dipole-transition approximation, meanwhile $\mu_{23} \neq 0$ with the spin-orbital perturbation between the intermediate enhancing levels 2 and 3.

For the system showed as Fig. 1, the interaction Hamilton can be written as

$$H^I = \begin{bmatrix} 0 & \mu_{12}E & \mu_{13}E & 0 \\ \mu_{21}E & 0 & 0 & \mu_{24}E \\ \mu_{31}E & 0 & 0 & \mu_{34}E \\ 0 & \mu_{42}E & \mu_{43}E & 0 \end{bmatrix}, \quad (2)$$

With the rotating wave and slowly varying envelope approximations and under the steady-state conditions, we can obtain the following expression for the population of the upper level 4

$$\rho_{44} = \frac{\frac{-\rho_{22} + \tilde{\rho}_{14} - \rho_{23}}{\Delta_{24}^p - i\gamma_{24}} - \frac{\rho_{22} + \tilde{\rho}_{41} + \rho_{23}}{-\Delta_{24}^p - i\gamma_{42}} + \frac{-\rho_{33} + \tilde{\rho}_{14} - \rho_{23}}{\Delta_{34}^q - i\gamma_{34}} - \frac{\rho_{33} - \tilde{\rho}_{41} + \rho_{23}}{-\Delta_{34}^q - i\gamma_{43}}}{\frac{\gamma_4}{i\Omega^2} - \frac{1}{\Delta_{24}^p - i\gamma_{24}} - \frac{1}{-\Delta_{24}^p - i\gamma_{42}} - \frac{1}{\Delta_{34}^q - i\gamma_{34}} - \frac{1}{-\Delta_{34}^q - i\gamma_{43}}}, \quad (3)$$

where Ω is the Rabi frequency. The detunings are defined as $\Delta_{ij}^l = \omega + lkv_z + \omega_i - \omega_j$ and $l = p, q$, p and q denote the direction of the travelling waves and have the value 1 and -1, respectively. The sign '̃' denotes the slowly varying

amplitudes of the off-diagonal matrix elements oscillating with the optical frequency.

From Eq. (3) we can obviously see that a nonzero off-diagonal element of the density matrix, ρ_{23} (or ρ_{32} , $\rho_{32} = \rho_{23}^*$), appears in the expression. That is to say, the quantum interference due to the coherent superimposition between the two intermediate levels 2 and 3 has direct contribution to the upper level population.

In order to predict the influence of the coherent superimposition on the upper level population $|\rho_{44}|^2$, we take the full numerical calculations to $|\rho_{23}|^2$ and $|\rho_{44}|^2$. Figure 3 displays the calculated trace of $|\rho_{23}|^2$ and $|\rho_{44}|^2$ against laser detuning δ ($\delta = \omega - \frac{\omega_4}{2}$). The values of all parameters are taken according to the experimental conditions. It is obvious that the trace of $|\rho_{23}|^2$ with line width of $(\omega_3 - \omega_2)$ has a maximum at $\omega = \frac{\omega_2 + \omega_3}{2}$ (center position of the two intermediate mixing levels) and a sharp dip at the intermediate resonant frequency $\frac{\omega_4}{2}$ of the two-photon transition (the same as the maximum position of $|\rho_{44}|^2$).

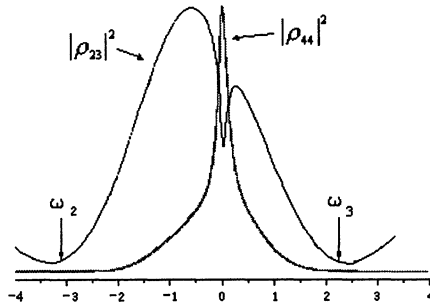


Fig. 2. Theoretical traces of $|\rho_{23}|^2$ and $|\rho_{44}|^2$

Considering the quantum interference characterized by $|\rho_{23}|^2$, the population distribution of the upper level in the considered four-level system has no longer the typical line-shape of a three-level system [10]. Because the line width of $|\rho_{23}|^2$ is the spacing of the intermediate levels, the profile of the upper level population would be broadened when the spacing is larger than the Doppler width. On the other hand, because the Lorentz dip on the trace of $|\rho_{23}|^2$ places just right at the intermediate resonant frequency of the two-photon transition, it would broaden the Doppler-free peak of the UV fluorescence emission from level 4.

Furthermore, it is easy to see that the influence of $|\rho_{23}|^2$ on $|\rho_{44}|^2$ is asymmetric, because the trace center $\frac{\omega_2 + \omega_3}{2}$ of $|\rho_{23}|^2$ is different from the trace center of $\frac{\omega_4}{2}$ of $|\rho_{44}|^2$. In the left side of the intermediate resonant

frequency $\frac{\omega_4}{2}$, the influence of $|\rho_{23}|^2$ is stronger than that in the right side and has the maximum at the central position of the intermediate levels. As a result, the lineshape of the upper level population profile would display an asymmetric feature. While $\omega_4 = \omega_2 + \omega_3$ and $\gamma_2 = \gamma_3$, the line-shape of the upper level population profile will be symmetric.

3 The result of experiment

The used experimental setup of the typical Doppler-free two-photon spectroscopy was similar to that shown in Ref. 10. The output of a single-mode scannable dye laser pumped by an Ar^+ laser was separated into two equal-intensity beams. They were focused and passed through a stainless steel cross-oven operated at $\sim 693K$ in opposite directions. An NO_2 spectrum was recorded simultaneously for measuring the dye laser frequency with an accuracy of $10^{-3}cm^{-1}$. The UV fluorescence of sodium dimmer was detected by a photo-multiplier at a side window of the oven, and a UV band-pass filter was inserted between the photo-multiplier and the window of the oven. The signals were fed to a lock-in amplifier and a PC computer for data processing.

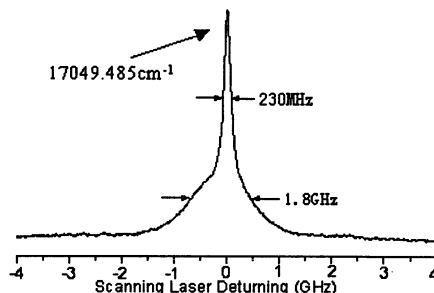


Fig. 3. Recorded trace of UV fluorescence from up level.

Fig.3 shows the recorded trace of UV fluorescence from upper level around scanning laser frequency $17049.485cm^{-1}$. The states of the two intermediate levels are $A^1\Sigma_u^+(22, 12)$ and $b^3\Pi_u(24, 12)$. There are a pair of mixed levels. The ground state is $X^1\Sigma_g^+(0, 13)$. The state of upper level is $2^3\Pi_g$. The spacing of the two intermediate levels is 5.4 GHz. The position of the Doppler free peak corresponds to the scanning laser frequency $17049.485cm^{-1}$. The width of the Doppler free peak and Doppler-broadened pedestal are 230 MHz and 1.8 GHz, respectively. In conventional, they are around 80 MHz and 1.4 GHz in our experimental condition. It is easy to see that the UV fluorescence curve displays an asymmetric feature. The agreement between theoretical results and experiment is quite good.

4 Conclusion

In conclusion, line-shape variations of the two-photon transition in rhomb type level system have been discussed theoretically and experimentally. They are the consequence of quantum interference of the two intermediate levels.

1. Not only the population of intermediate levels can excite the upper level in rhomb-type system, but also the interaction element ρ_{23} .
2. If the spacing of the two intermediate levels is larger than Doppler width, both of Doppler free peak width and spectral background width in rhomb-type system will be broadened by ρ_{23} .
3. If the position of $\frac{\omega_4}{2}$ is different from that of $\frac{\omega_2+\omega_3}{2}$, the UV fluorescence profile will display an asymmetric feature.

References

1. E. Arimondo and S. Reynaud, J. Phys. B10 (1977), 2311.
2. H. R. Gray, R. M. Whyitley, and C. R. Stroud, Opt. Lett. 3 (1978), 218.
3. A. M. Akulshin, A. A. Celikov, and V. L. Velichansky, Opt. Commun. 81 (1991), 364.
4. S. E. Harris, Phys. Rev. Lett. 62 (1989), 1033.
5. K. J. Boller, A. Imamoglu, and S. E. Harris, Phys. Rev. Lett. 66 (1991), 2593.
6. Min Xiao, et. al., Phys. Rev. Lett. 74 (1995), 666.
7. M. O. Scully, S. Y. Zhu and A. Gavrielides, Phys. Rev. Lett. 62 (1989), 2813.
8. A. S. Zibro, et. al., Phys. Rev. Lett. 76 (1996), 3935.
9. H. R. Xia, et. al., NASA CP-3322, 501.
10. Z. G. Wang and H. R. Xia, Molecular and Laser Spectroscopy, (Springer 91)

Population Oscillation in Two-band Photonic Crystals Via Quantum Interference

Yaping Yang^{1,2}, Shi-Yao Zhu², Hong Chen^{1,2}

¹ Department of Physics, Tongji University, Shanghai 200092, China

² Department of Physics, Hong Kong Baptist University, Hong Kong

Abstract. We investigate the spontaneous emission from a V three-level atom embedded in two-band photonic crystals. The dipoles of the two transitions from the two upper levels to the lower level are parallel. Due to the quantum interference between the two decay processes and the existence of two bands, the populations in the excited states display some novel properties, which strongly depend on the initial states and the relative position of the upper levels from forbidden gap.

1 Introduction

In recent years, the study of quantum and nonlinear optical phenomena in atoms embedded in a photonic crystal has attracted much attention. Such as the non-exponential spontaneous decay[1], photon localization and photon-atom bound dressed state[2-4], fractional steady-state atomic population in the excited state[5]. In these studies, only one band for photonic crystals were considered. If the atomic frequency is very close to the edge of one band and the gap is relative large, one band model is a good approximation. If the gap is narrow, we must consider both upper and lower bands.

In this paper, the spontaneous emission from a V three-level atom embedded in two-band photonic crystals is studied. Due to the quantum interference between two transitions and the existence of two bands, the populations trapped in the two upper levels display some novel properties.

2 The model

Let us consider a V three-level atom coupled to the radiation field in photonic crystal with an upper band, a lower band and a forbidden gap. The cut-off frequencies of the upper and lower band edge are ω_{c_1} and ω_{c_2} , respectively. The gap width $\omega_{c_1} - \omega_{c_2}$ is assumed much smaller than $\omega_{c_1}, \omega_{c_2}$. Near the two band edges, the dispersion relation may be expressed approximately by $\omega_k = \omega_{c_1} + A_1(k - k_0)^2$ for $(k > k_0)$, and $\omega_k = \omega_{c_2} - A_2(k - k_0)^2$ for $(k < k_0)$ with $A_1 = \omega_{c_1}/k_0^2$, $A_2 = \omega_{c_2}/k_0^2$. The atom has two upper levels $|a_1\rangle, |a_2\rangle$ and a lower level $|b\rangle$. The frequencies of the two upper levels $|\omega_1\rangle, |\omega_2\rangle$

are $\omega_{a_1 b}$ and $\omega_{a_2 b}$ ($\omega_{a_1 b} > \omega_{a_2 b}$). The interaction Hamiltonian of the system in the interaction picture can be written as

$$V_I = i\hbar \sum_k \left(\sum_{j=1,2} g_k^{(j)} e^{i(\omega_{a_j b} - \omega_k)t} a_k |a_j><b| - H.C. \right), \quad (1)$$

$g_k^{(1,2)}$ are the coupling constants. The two dipoles of the two transitions are parallel to each other. a_k (a_k^+) is the annihilation (creation) operator for k -th mode with frequency ω_k . The wave function at time t may be written as

$$|\psi(t)\rangle = \sum_{i=1,2} A^{(i)}(t) |a_i\rangle |0\rangle_f + \sum_k B_k(t) |b\rangle |1_k\rangle_f. \quad (2)$$

We assume the atom initially in a superposition of the upper levels. $|0\rangle_f$ represent the absence of photons in all vacuum modes; $|1_k\rangle_f$ describes a single photon in k -th mode. The evolution of $|\psi(t)\rangle$ obeys the schrödinger equation. So we have

$$\frac{\partial}{\partial t} A^{(1,2)}(t) = \sum_k g_k^{(1,2)} e^{i(\omega_{a_1,2 b} - \omega_k)t} B_k(t) \quad (3a)$$

$$\frac{\partial}{\partial t} B_k(t) = - \sum_{j=1,2} g_k^{(j)} e^{-i(\omega_{a_j b} - \omega_k)t} A^{(j)}(t). \quad (3b)$$

For simplicity, we consider a special case $g_k^{(1)} = g_k^{(2)} = g_k$. Using the Laplace transform method, we have the Laplace transform of $A^{(1,2)}(t)$,

$$A^{(1)}(s) = (A^{(1)}(0)(s - i\omega_{12}) + (A^{(1)}(0) - A^{(2)}(0))\Gamma)/G(s), \quad (4a)$$

$$A^{(2)}(s - i\omega_{12}) = (A^{(2)}(0)s + (A^{(2)}(0) - A^{(1)}(0))\Gamma)/G(s), \quad (4b)$$

$\Gamma = \{\beta^{3/2}/[\sqrt{i}\sqrt{s - i(\omega_{a_1 b} - \omega_{c_1})}] + \beta^{3/2}\sqrt{i}/\sqrt{s - i(\omega_{a_1 b} - \omega_{c_2})}\}/2$, with $\beta = (\omega_{ab}^{7/2} d_{ab}^2 / 6\pi\epsilon_0\hbar c^3)^{2/3}$, and $\omega_{12} = \omega_{a_1 b} - \omega_{a_2 b}$, $G(s) = s(s - i\omega_{12}) + (2s - i\omega_{12})\Gamma$. The amplitudes can then be obtained by the inverse Laplace transform, $A^{(1,2)}(t) = \frac{1}{2\pi i} \int_{\sigma-i\infty}^{\sigma+i\infty} A^{(1,2)}(s) e^{st} ds$. To perform the integral, we must consider the poles of the integral functions, which are the roots of the equation $G(s) = 0$. The poles depend on the separation of the two band, ω_{12} , and the relative position of the upper levels of atom from the two band edges. We will focus our discussion on the situations, $|a_1\rangle$ in the upper band or in the gap, and $|a_2\rangle$ in the gap. For such situations there are at least two poles, and at most four poles. With the help of residues at poles of the integral function, we have $A^{(1,2)}(t) = \sum_{j=1}^4 A_j^{(1,2)}(t) + A_5^{(1,2)}(t)$. $A_j^{(1,2)}(t)$ ($j = 1, 2, 3, 4$) come from the relevant poles s_j if they exist, and $A_5^{(1,2)}(t)$ result from the integrations along the two cuts of the single valued branch. Note that $|\psi(t)\rangle$ is a wave function in the interaction picture, and consequently if the imaginary part of the pole is b , the oscillation frequency in Schrödinger picture will be $\omega_{a_1 b} - b$. The populations can be obtained.

$$P_{1,2}(t) = \sum_{j=1}^5 |A_j^{(1,2)}(t)|^2 + \sum_{i \neq j} A_i^{(1,2)}(t) (A_j^{(1,2)}(t))^*. \quad (5)$$

$A_j^{(1,2)}(t)$ ($j = 1, 2, 3, 4$) can be written as

$$A_j^{(1)}(t) = \frac{(s_j - i\omega_{12})H(s_j)e^{s_j t}}{(2s_j - i\omega_{12})G'(s_j)}, \quad A_j^{(2)}(t) = \frac{s_j H(s_j)e^{(-i\omega_{12} + s_j)t}}{(2s_j - i\omega_{12})G'(s_j)}. \quad (6)$$

Where $H(s) = (s - i\omega_{12})A^{(1)}(0) - sA^{(2)}(0)$. From Eqs (5,6), we can see that there are two different types of quantum interference: (1) The quantum interference between two dressed states. (2) The quantum interference between two transitions from each upper level to the lower level. To analyse the roles of the quantum interference in the present system, we will pay our attention to the final populations in the two upper levels. As time goes to infinity, the terms related to the pure imaginary roots in Eqs.(5,6) contribute to the population, and other terms go to zero. When $\omega_{a_1 b} - \omega_{c_1} \geq \omega_{12}/2$, there is one pure imaginary root, and the final populations are

$$P_1(\infty) = \frac{|(s_1 - i\omega_{12})H(s_1)|^2}{|G'(s_1)(2s_1 - i\omega_{12})|^2}, \quad P_2(\infty) = \frac{|s_1 H(s_1)|^2}{|G'(s_1)(2s_1 - i\omega_{12})|^2}. \quad (7)$$

When $\omega_{a_1 b} - \omega_{c_1} < \omega_{12}/2$, there are two pure imaginary roots ib_1, ib_2 , and the final populations in the upper levels are

$$P_1(t \rightarrow \infty) = |A_1^{(1)}(t)|^2 + |A_2^{(1)}(t)|^2 + (b_1 - \omega_{12})(b_2 - \omega_{12})Q(t), \quad (8a)$$

$$P_2(t \rightarrow \infty) = |A_1^{(2)}(t)|^2 + |A_2^{(2)}(t)|^2 + b_1 b_2 Q(t), \quad (8b)$$

where $Q(t) = \frac{1}{(2b_1 - \omega_{12})(2b_2 - \omega_{12})} [\frac{H(ib_1)H(ib_2)^*}{G'(ib_1)G'(ib_2)^*} e^{i(b_1 - b_2)t} + H.C.]$. The populations in the upper levels display some new behavior due to the interference.

3 The properties of the populations

3.1 Anti-trapping

When $\omega_{a_1 b} - \omega_{c_1} \geq \omega_{12}/2$, there is one pure imaginary root, and also only one localized mode in the localized field. As time goes to infinity, we only have the quantum interference between two transitions.

For a fixed relative position, the initial atomic coherence affects the quantum interference between two transitions, and then affects the final population trapping in upper levels. If the root is $s_1 = ib_1$, and $A^{(1)}(0), A^{(2)}(0)$ satisfy the relation $A^{(2)}(0)/A^{(1)}(0) = (\omega_{12} - b_1)/b_1$, we will have a complete constructive interference $H(s) = 0$, which will result in no final populations in two upper levels (see Eqs.7). That is to say, the populations in the two upper levels decay totally to the lower level. This complete decay can be also understood from the energy of the localized field, which is also proportional to $|((s - i\omega_{12})A^{(1)}(0) - sA^{(2)}(0))|^2$. If $A^{(2)}(0)/A^{(1)}(0) = (\omega_{12} - b_1)/b_1$, the quantum interference reduces the energy in the localized field to zero. Without a localized field, the populations in the upper levels can decay to the lower

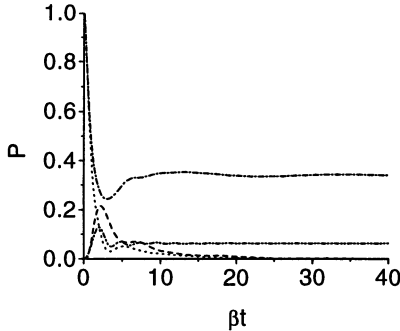


Fig. 1. The time evolution of the upper-level populations. (a) P_1 and P_2 with $\omega_{a_1b} - \omega_{c_1} = 0.8\beta$, $\omega_{12} = \beta$, $\omega_{a_2b} - \omega_{c_2} = 0.3\beta$, $|\psi(0)\rangle = 0.9992|a_1\rangle + 0.0387|a_2\rangle$ (dotted curve and dashed curve, respectively). (b) P_1 and P_2 with $\omega_{c_1} - \omega_{a_1b} = 0$, $\omega_{12} = \omega_{a_2b} - \omega_{c_2} = \beta$, $|\psi(0)\rangle = |a_1\rangle$ (long-short dashed curve and long-short-short dashed curve, respectively).

level, and the population in the lower level can not jump to the upper levels. Consequently, the population will stay in the lower levels for ever (see Fig.1, dotted curve and dashed curve).

If $\omega_{a_1b} - \omega_{c_1} \geq \omega_{12}/2$, and $|a_2\rangle$ is at the center of the band gap, we will have one pure imaginary root equal to $i\omega_{12}$ and complex roots. From Eqs.(7), it can be seen that the final population in $|a_1\rangle$ is equal to zero, and the final population in $|a_2\rangle$ is not equal to zero except for $A^{(2)}(0) = 0$. Such property comes from the change of the quantum interference between the two transition. If the pure imaginary root is $i\omega_{12}$, the term $(s - i\omega_{12})s^* A^{(1)}(0)(A^{(2)}(0))^*$ will be equal to zero, and the second quantum interference will vanish as time goes to infinity. Under such situation, the present system can be regarded as a simple combination of two two-level systems. The contribution to the localized field comes only from $|a_2\rangle$. The dressed state corresponding to the pure imaginary root $i\omega_{12}$ consists only of $|a_2\rangle$, and the amplitude of the localized field is the same as that in two-level system composed of $|a_2\rangle$ and $|b\rangle$. Thus, there is a localized field for the two-level system of $|a_2\rangle$ and $|b\rangle$, and no localized field for the two-level system of $|a_1\rangle$ and $|b\rangle$. The population in the ground state $|b\rangle$ can jump only to the excited state $|a_2\rangle$ by absorbing the photon in such localized field, and no population can jump back to $|a_1\rangle$. So the population in $|a_1\rangle$ decays totally to lower level, and no population is trapped in $|a_1\rangle$.

3.2 fractional steady-state populations in both upper levels

In the following cases, the final populations are constants.

(1) When $\omega_{a_1b} - \omega_{c_1} \geq \omega_{12}/2$, there is one pure imaginary root ib_1 . From Eqs.(7), the populations trapped in the upper levels are constants, which are not equal to zero except for $A^{(2)}(0)/A^{(1)}(0) = (\omega_{12} - b_1)/b_1$ or $\omega_{a_2b} = (\omega_{c_1} + \omega_{c_2})/2$.

Although the population depends on the initial state, it can be proved that the ratio of the populations in the two upper levels is independent of the

initial condition, $P_1(\infty)/P_2(\infty) = |(b_1 - \omega_{12})/b_1|^2$. We can prove analytically that, $P_1(\infty)/P_2(\infty) < 1$, which means that the population inversion does not exist. Due to the quantum interference, the population in $|b\rangle$ may jump back to the both excited states by absorbing the photon in the localized field. If the frequency position of localized field is closer $|a_2\rangle$ ($|a_1\rangle$), more population come back to $|a_2\rangle$ (or $|a_1\rangle$), and the more final population is trapped in the upper level $|a_2\rangle$ (or $|a_1\rangle$). From the range of the pure imaginary root ib_1 , we know that the frequency of localized field, $\omega_{a_1b} - b_1$, is closer to $|a_2\rangle$. So the population inversion does not occur.

(2) When $\omega_{a_1b} - \omega_{c_1} < \omega_{12}/2$, there are two pure imaginary roots. From the Eqs.(8), we can see that, the final populations in the two upper levels will be constants if $A^{(1)}(0), A^{(2)}(0)$ satisfy the relation $A^{(2)}(0)/A^{(1)}(0) = (\omega_{12} - b_j)/b_j$ ($j = 1$ or 2), in which ib_j ($j = 1, 2$) are the poles (See Fig.1, long-short dashed curve and long-short-short dashed curve).

If $A^{(2)}(0)/A^{(1)}(0) = (\omega_{12} - b_2)/b_2$ (or $A^{(2)}(0)/A^{(1)}(0) = (\omega_{12} - b_1)/b_1$), the quantum interference between two transitions will result in a zero amplitude of the localized mode with the frequency $\omega_{a_1b} - b_2$ (or $\omega_{a_1b} - b_1$). In this case, there is only one localized mode with frequency $\omega_{a_1b} - b_1$ (or $\omega_{a_1b} - b_2$) in the localized field, which could trap population in the two upper levels. Consequently, the final populations in upper levels are constants. From the range of the pure imaginary ib_1 (or ib_2), we know that the frequency of the relevant localized field is more closer to $|a_1\rangle$ (or $|a_2\rangle$), and the more population is trapped in the upper level $|a_1\rangle$ (or $|a_2\rangle$). Thus, the population inversion can (or cannot) occur in this case.

3.3 Population oscillation

When $\omega_{a_1b} - \omega_{c_1} < \omega_{12}/2$, there are two pure imaginary roots s_1, s_2 . If ω_{a_2b} is at the center of the band gap, one of the two pure imaginary roots is $s_2 = i\omega_{12}$. From the Eqs.(8), we have that, the final population in $|a_1\rangle$ is a constant, and the population in $|a_2\rangle$ oscillates (See Fig.2, dotted curve and dashed curve). In this case, the frequency of the localized mode related to $i\omega_{12}$ is ω_{a_2b} . From the discussion in Sec. 3.1, we know that, the population in $|b\rangle$ can come back only to $|a_2\rangle$ by absorbing the photon of frequency ω_{a_2b} , and can not come back to $|a_1\rangle$. However, the two upper levels have their contributions to the another localized mode related to the pure imaginary root ib_1 . By absorbing the photon of frequency $\omega_{a_1b} - b_1$, the population in $|b\rangle$ can jump back to both upper levels. So the population can be trapped in $|a_2\rangle$ through two channels (one by absorbing the photon of frequency ω_{a_2b} , and the other one by absorbing the photon of frequency $\omega_{a_1b} - b_1$). The interference between two channels leads to the oscillatory behavior of the final population in $|a_2\rangle$. The population can be trapped in $|a_1\rangle$ by only one channel, and there is no interference. So the final population in $|a_1\rangle$ is a constant. Symmetrically, if ω_{a_1b} is at the center of the band gap, the

final population in $|a_2\rangle$ will be a constant, the final population in $|a_1\rangle$ has oscillation property.

When $\omega_{a_1b} - \omega_{c_1} < \omega_{12}/2$, there are two pure imaginary roots $s_1 = ib_1$ and $s_2 = ib_2$, and there are two localized modes with the frequencies $\omega_{a_1b} - b_1$ and $\omega_{a_1b} - b_2$ in localized field. In general, the frequencies of the localized modes are not equal to ω_{a_1b} or ω_{a_2b} . The population in $|b\rangle$ can come back to both upper levels by absorbing the photon of frequency $\omega_{a_1b} - b_1$ (or $\omega_{a_1b} - b_2$). The population can be trapped in $|a_1\rangle$ (or $|a_2\rangle$) through two channels. The interference between two channels leads to the population oscillation in the two upper levels (See Fig.2, long-short dashed curve and long-short-short dashed curve). The amplitudes of the periodic oscillation do not damped to zero in time. From the Eqs.(8), we can obtain that, (1) The oscillation frequency for the both upper levels is the same, equal to $b_1 - b_2$. (2) The ratio of the amplitudes K_1 (for $|a_1\rangle$) and K_2 (for $|a_2\rangle$) of the oscillations is $K_1/K_2 = |(b_1 - \omega_{12})(b_2 - \omega_{12})/(b_1 b_2)|$, which is independent of the initial atomic state. (3) If the relative positions of the two upper levels and the gap edges satisfy $\omega_{a_1b} - (\omega_{c_1} + \omega_{c_2})/2 < 0$ or $\omega_{a_1b} - (\omega_{c_1} + \omega_{c_2})/2 \geq \omega_{12}$, the phase difference of two periodic oscillations will be π ; when $0 \leq \omega_{a_1b} - (\omega_{c_1} + \omega_{c_2})/2 < \omega_{12}$, the phase difference is 0.

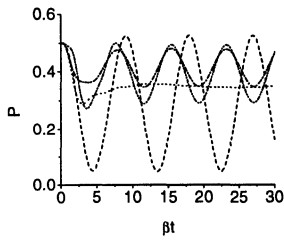


Fig. 2. The time evolution of the upper-level populations. (a) P_1 and P_2 with $\omega_{c_1} - \omega_{a_1b} = 0, \omega_{12} = \omega_{a_2b} - \omega_{c_2} = \beta, |\psi(0)\rangle = \frac{1}{\sqrt{2}}(|a_1\rangle - |a_2\rangle)$ (dotted curve and dashed curve, respectively). (b) P_1 and P_2 with $\omega_{c_1} - \omega_{a_1b} = \omega_{12} = \beta, \omega_{a_2b} - \omega_{c_2} = 1.2\beta, |\psi(0)\rangle = \frac{1}{\sqrt{2}}(|a_1\rangle - |a_2\rangle)$ (long-short dashed curve and long-short-short dashed curve, respectively).

In conclusion, we studied the spontaneous emission from a V three-level atom with two parallel transition dipoles embedded in a two-band isotropic photonic crystal with narrow band gap. The time evolution of the upper-level populations has been investigated.

Acknowledgment. This work was supported in part by Shanghai Educational Committee and FRG from the Hong Kong Baptist University.

References

1. M. Lewenstein, et.al., J. Phys. **B21**, L9(1988).
2. S.John and J.Wang, Phys. Rev. Lett. **64**, 2418(1990).
3. S.John and J.Wang, Phys. Rev. **B43**, 12772(1991).
4. S.-Y.Zhu, H.Chen, and H.Huang, Phys. Rev. Lett. **79**, 205(1997).
5. S. John and T.Quang, Phys. Rev. **A50**, 1764(1994).

Two Dimensional Nonlinear Dynamics of Cold Atoms in Hollow Fiber

X. M. Liu and G. J. Milburn

The Center for Laser Sciences, Department of Physics, The University of Queensland, St. Lucia, Brisbane, Qld 4072, Australia

Abstract. We describe the classical and quantum two dimensional nonlinear dynamics of large blue-detuned evanescent-wave guiding cold atoms in hollow fiber. We show that the atoms will accumulate on several annular regions when the system enters a regime of globally classical chaos. When the atomic flux is very small, a similar distribution will be obtained if we detect the atomic distribution once each the modulation period and integrate the signals. For quantum dynamics, quantum collapses and revivals appear. For periodically modulated optical potential, the variance of atomic position will be suppressed compared to the no modulation case. The atomic angular momentum will influence the evolution of wave function in two dimensional quantum system of hollow fiber.

1 The optical potential and Hamiltonian

A two-level atom interacting with far-off-resonant inhomogeneous laser field has an effective potential[10] of the form

$$U(\mathbf{r}) = \frac{\hbar\Omega(\mathbf{r})^2}{4\Delta}. \quad (1)$$

For light striking the glass-vacuum interface at angle θ , the evanescent intensity profile is

$$I(r) = I(0)\alpha^2 \exp[2\kappa(r - r_1)], \quad (2)$$

where r_1 is the inner radius of fiber , and the factors α and κ are given in terms of the index of refraction n , inner reflection angle θ and laser wavelength λ by $\alpha = 2\sqrt{n^2/(n^2 - 1)} \cos \theta$, and $\kappa = (2\pi/\lambda) \sqrt{(n^2 \sin^2 \theta - 1)}$.

When the laser intensity is periodically modulated, I_0 becomes time dependent, $I_0[1 + \epsilon \cos(\omega t)]$ and the dynamics of the atom can be chaotic for certain initial conditions. There are two factors to consider in treating the two dimensional classic chaotic dynamics for evanescent wave guided atoms in a hollow fibre. Firstly, the boundary of the hollow fiber will limit the divergence of the atomic motion in the radial direction making it easier to simulate the two-dimensional the dynamics of the atomic system (and also easier to probe the two dimensional distribution in experiment). Secondly, due to the small inner radius of a hollow fiber, atoms with a small transverse

velocity will be selected at the entry to the hollow fiber and it is not necessary to pre-cool the transverse temperature.

The effective optical potential depends on the inner radius r_1 and decay coefficient κ . If the r_1 is much larger than wavelength λ or θ is too large, the potential will be very steep on the boundary and decay rapidly away from the inner surface of the fiber. In order to observe two dimensional chaotic dynamics in (x, y) plane, r_1 should be the same magnitude as $1/\kappa$, so that the potential will decay slowly away from the surface of the hollow fiber. It is possible to make the reflection angle approach the critical reflection angle $\sin^{-1}(1/n)$ by using several micro hollow fibers to guide the atoms and polish the incoming end of the hollow fiber at a specific acute angle [3].

The dimensionless Hamiltonian can be rewritten as

$$H(t) = \frac{p_x^2 + p_y^2}{2} + \xi e^{\sqrt{x^2+y^2}-r_1} (1 + \epsilon \cos \omega t), \quad (3)$$

with the canonical commutation relations

$$[q_j, p_k] = ik\delta_{jk}, \quad (4)$$

where q_j, p_k represents x, y and $k = \frac{\hbar(2\kappa)^2}{M\omega_0}$, plays the role of a dimensionless Planck constant. If the dimensionless Planck constant k approaches 1, the atomic motion in small hollow fibers will be correctly described by quantum dynamics.

2 Classic chaotic dynamics and 2D distribution

Although the flux of guided atoms entering the fiber is very small, we still have the possibility to observe classic chaotic dynamics by integrating the signal over many periods of the modulation. The integration length can be taken long enough to ensure that it includes large numbers of atoms.

The choice of modulation frequency ω depends on the frequency of unperturbed periodic motion. For simplicity we assume $y = 0$ and $p_y = 0$, therefore

$$\omega_0 = \frac{\pi}{\int_{-x_M}^{x_M} \{2[H_0 - \xi e^{\sqrt{x^2}-r_1}]\}^{-1/2} dx}, \quad (5)$$

where x_M is determined by $H_0 = \xi e^{\sqrt{x_M^2}-r_1}$.

We can select the modulation frequency ω to control the position of the fixed points.

We use a symplectic integration routine [12],[13] to solve the equations of motion so as to preserve the Poisson bracket relation $\{q_i(t), p_j(t)\} = \delta_{ij}$, and thus maintain the Hamiltonian character of the motion. We plot the stroboscopic portrait of the system at multiples of the period of modulation, $t = (2\pi/\omega)s$, where s is an integer referred to as the strobe number. We can

see that regions of globally chaotic motion will arise when ϵ is large, together with some regular regions. A broad initial phase space distribution of atoms will enable some atoms to become trapped in these stable regions.

We define a classical state to be a probability measure on phase space of the form $Q(x, y, p_x, p_y)dx dy dp_x dp_y$. The probability density satisfies the Liouville equation

$$\frac{\partial Q}{\partial t} = \{H, Q\}_{q_i, p_i}, \quad (6)$$

where $\{, \}_{q_i, p_i}$ is the Poisson bracket.

To simulate an experiment, we assume atoms are initially randomly uniformly distributed on $x^2 + y^2 < r_1^2$. The momentum distributions for p_x and p_y are assumed to be Gaussian distributions. Therefore

$$Q_0(p_i) = \frac{1}{2\pi\sigma_{p_i}} \exp [-(p_i - p_i(0))^2/2\sigma_{p_i}^2]. \quad (7)$$

The variances of p_x and p_y are related to the temperature T_i

$$\sigma_{p_i} = k_B T_i / [M\omega_s^2 / (2\kappa)^2]. \quad (8)$$

We simulated the atomic system of 10^4 numbers and take $\sigma_{p_i} = 0.1$, which corresponds to radical rms velocity 2cm/s for helium if $\theta = 45^\circ$ and $\omega = 2$.

In the case of no modulation, atoms will accumulate around the fix point $x = y = 0$. When the modulation is added the atoms will diffuse in regions of chaotic motion but some will accumulate around several rings corresponding to fixed points at non-zero radius.

Because the inner size of hollow fiber is very small. The flux of guiding atoms entering the fiber will be very small. But we can use a pulsed probe laser, whith a time interval equal to the modulation period, to detect the atomic distribution at diffrent integer strobe numbers and integrate the signals. The simulation shows that this will produce similar results.

3 Two dimensional quantum nonlinear dynamics

If the tranverse temperature of atoms in hollow fiber is very cold, quantum nonlinear dynamics will result. Here we take the same parameters and same definition for dimensionless parameters as the classical dynamics and the dimensionless Plank constant $\frac{\hbar(2\kappa)^2}{M\omega_s} \simeq 1$. The dimensionless 2D Schrödinger equation for atoms in hollow fiber

$$ik \frac{\partial \psi(\mathbf{r}, t)}{\partial t} = \hat{H}(t)\psi(\mathbf{r}, t), \quad (9)$$

where

$$\hat{H}(t) = -\frac{k^2}{2} \left(\frac{\partial^2}{\partial x^2} + \frac{\partial^2}{\partial y^2} \right) + \xi e^{\sqrt{x^2+y^2-r_1}} (1 + \epsilon \cos \omega t), \quad (10)$$

and $x^2 + y^2 \leq r_1^2$.

For simplicity we assume the boundary condition is

$$\psi(x, y, t)|_{\sqrt{x^2+y^2}=r_1} = 0, \quad (11)$$

and at $t = 0$ the wave function is a minimum uncertainty wave function. The initial variance of x, y are the same $\sigma_x = \sigma_y = \sigma$. The expression for this wave function is

$$\psi(x, y) = \frac{1}{\sqrt{2\pi}\sigma} e^{-\frac{(x-x_0)^2}{4\sigma}} e^{-\frac{(y-y_0)^2}{4\sigma}} e^{iP_{0x}x/k} e^{iP_{0y}y/k}. \quad (12)$$

In order to observe genuine quantum nonlinear behaviour we have to wait for a time that is longer than the classical period. Quantum collapses and revivals appear for quantum nonlinear dynamics as expected.

In order to understand the influence of the modulation of the potential, we have calculated the variances of $\langle x^2 \rangle - \langle x \rangle^2$, $\langle p_x^2 \rangle - \langle p_x \rangle^2$ versus strobe numbers. We found at integer strobe numbers, the modulation will increase the variance of momentum, but suppress the variance of position. The fluctuation of variances of positions and momentum are consistent with the Heisenberg uncertainty relationship in this quantum system.

If we rewrite \hat{H} in polar coordinate (r, θ) , we get

$$\hat{H} = -\frac{k^2}{2} \left(\frac{\partial^2}{\partial r^2} + \frac{1}{r} \frac{\partial}{\partial r} + \frac{1}{r^2} \frac{\partial^2}{\partial \theta^2} \right) + V(r, t), \quad (13)$$

The general solution of eq.(19) will be [16]

$$\psi(r, \theta, t) = \sum_m a_m(r, t) e^{im\phi}, \quad (14)$$

where m is angular momentum quantum number. It shows that the evolution of wave function will be related to atomic angular momentum. In general for $t > 0$ the probability $|\psi(x, y)|^2$ will not be symmetric except the initial wavefunction has no angular momentum. Therefore the atomic angular momentum plays an important role in the evolution of wave function.

References

1. H. Ito, K. Sakaki, W. Jhe, M. Ohtsu, Opt. Commun. 141, 43-47(1997).
2. H. Ito, T. Nakata, K. Sakaki, M. Ohtsu, Phys. Rev. Lett. 76, 4500(1996).
3. Michael J. Renn, Elizabeth A. Donley, Eric Cornell, Carl E. Wieman, Dana Z. Anderson, Phys. Rev. A. 53, R648(1996).
4. F.L.Moore, J.C.Robinson, C. Bharucha, P.E.Williams adn M.G.Raizen, Phys. Rev. Lett, 73, 2974 (1994).
5. R.V.Jensen,S.M.Susskind and M.M.Sanders, Phys. Rep. 201, 1 (1991).
6. C.M.MArcus,A.J.Rimberg,R.M.Westervelt,P.F.Hopkins, and A.C.Gossard, Phys. REv. Lett. 69, 506 (1992).

7. R. P. Taylor, R. Newbury, A. S. Sachrajda, Y. Feng, P. T. Coleridge, C. Dettmann, Ningjia Zhu, Hong Guo, A. Delage, P.J. Kelly, and Z. Wasilewski, Phys. Rev. Lett **78**, 1952 (1997).
8. A.R.Kovlosky, Phys. Rev. E **50**, 3569 (1994).
9. Wenyu Chen, S.Dyrting and G.J. Milburn, Australia Journal of Physics, **49**, 777-818 (1996).
10. C. Cohen-Tannoudji, in *Fundamental Systems in Quantum Optics*, Proceedings of the Les Houches Summer School(North-Holland, Amsterdm, 1992).
11. A.J.Lichtenberg, M.A. Lieberman (1983), *Regular and Stochastic motion*, Springer-Verlag, New York ,Heidelberg Berlin.
12. Etienne Forest and Martin Berz. Canonical integration and analysis of periodic maps using non-standard analysis and Lie methods. In Kurt Bernardo Wolf, editor, *Lie Methods in Optics II* , page 47, Berlin Heidelberg, 1989, Springer-Verlag.
13. S.Dyrting. Ph.D thesis (1995), Department of Physics, University of Queensland.
14. X.M. Liu and G.J. Milburn, Phys. Rev. E, **59**, 2842(1999).
15. Ronnie Kosloff, J. Phys. Chem, **92**, 2087(1988).
16. Lothar Collatz (1986), *Differential Equations: An Introduction with Applications* , John Wiley & Sons.
17. William H Press et al (1992), *Numerical Recipes in C* , Cambridge, University Press.

Atomic-State Teleportation Using GHZ State

Shang-qing Gong, Zhong-yang Wang, Xun-li Feng, Zhi-zhan Xu

Laboratory for High Intensity Optics, Shanghai Institute of Optics and Fine Mechanics, Chinese Academy of Sciences, Shanghai 201800, China

Abstract. Following the principle outlined by Karlsson and Bourennane [Phys. Rev. A **56**, 5394(1998)], we propose an experimentally feasible scheme for the teleportation of an unknown atomic state among three high-Q cavities containing a nonlocal quantum superposition of microwave field states, in which the unknown atomic state can be completely teleported to either of two locations. This scheme can also be used for the teleportation of a cavity field in a superposition of zero- and one-photon Fock states.

There has been considerable interest in the study of quantum teleportation in recent years. In 1993, Bennett et al. [1] have shown that an entangled pair of spin-1/2 particles could be used, with the addition of information transmitted through a classical channel, to teleport an unknown quantum state from one observer to another. The process of teleportation involves three steps: preparation of two particles in a maximally entangled state; a joint measurement on one of these particles and the unknown particle; and communication of the measurement result to the other particle of the initially entangled pair and subsequent rotation of this particle.

Following the ideas of Bennett et al. [1], Davidovich et al. [2] have presented an experimentally feasible scheme for the teleportation of an unknown two-level atomic state between two high-Q cavities containing a nonlocal microwave field. Cirac and Parkins [3] have made another cavity QED proposal for the realization of quantum teleportation of an atomic state based on the interaction of the atoms with a cavity mode. Such schemes can also be used for the teleportation of a cavity mode in a superposition of zero- and one-photon of a cavity field. The teleportation schemes mentioned above [1,3] have been demonstrated using two-particle entangled states. By the teleportation process, the unknown quantum state can be teleported from one observer to another (and only one) receiver.

Entangled states of three- or more-particle such as a Greenberger-Horne-Zeilinger (GHZ) state [4] are fascinating quantum system, the experimental realization [5] of such states will open the door to many novel quantum phenomena and application in quantum computer [6], certain types of quantum cryptography [7], etc.. It is nature to expected that such states will have an important application in teleportation of quantum state. Recently, Karlsson and Bourennane [8] have proposed a new scheme for quantum-state teleportation using three-particle entanglement and have shown that one may

teleport an unknown quantum state to either of the two receivers in such a way that, generally, either one of the two, but only one, can fully reconstruct the quantum state conditioned on the measurement outcome of the other. It is clear that it does not permit by any means the faithful transmission of unknown quantum state to two locations. This would be forbidden by no-cloning broadcast theorem [9]. In view of this, Karlsson and Bourennane's scheme is an interesting midway case where both parties have some information about the original state.

In this paper, following the principle outlined by Karlsson and Bourennane [8], we propose an experimentally feasible scheme for the teleportation of an unknown atomic state among three high-Q cavities containing a nonlocal quantum superposition of microwave field states, in which the unknown atomic state can be completely teleported to either of two locations considered. A sketch of the experimental setup for the present scheme is shown in Fig.1. The setup contains three cavities C_1 , C_2 and C_3 , state-selective ionization detectors (D_a , D_b , D_c and D_d), auxiliary microwaves (R_1 , R_2 , R_3 , R_4 , R , R_1^{-1} and R_2^{-1}), microwave zones (P_a , P_b and P_c), and four atomic beams (D , A , B and C) made of identical two-level atoms (levels $|e\rangle$ and $|g\rangle$). $|e\rangle$ and $|g\rangle$ must be circular Rydberg levels with adjacent principal quantum numbers, in order to prepare and to detect long-lived correlations between atom and field states.

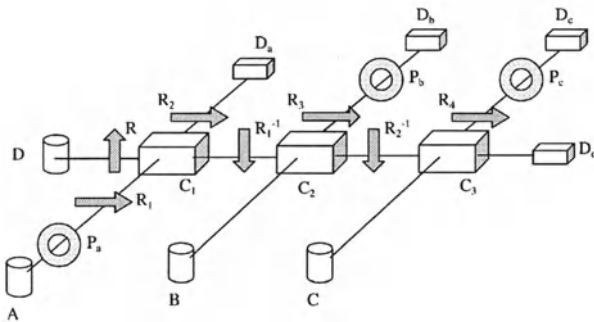


Fig. 1. A sketch of the teleportation experimental setup using GHZ state

The teleportation machine in the setup is a three-cavity entangled state.

$$|\Psi_c\rangle = \frac{1}{\sqrt{2}}(|1\rangle_1|1\rangle_2|1\rangle_3 + |0\rangle_1|0\rangle_2|0\rangle_3). \quad (1)$$

Such GHZ state has been prepared by Bergou and Hillery recently [10]:

Now we investigate the teleportation of quantum state using three-cavity entanglement (1). The atom a to be teleported is assumed to be in an arbit-

trary (e, g) superposition $|\phi_a\rangle = \alpha|e\rangle + \beta|g\rangle$. The combined atom-field state can then be expanded as:

$$|\Psi\rangle = \frac{1}{2}[\psi^+(\alpha|1\rangle_2|1\rangle_3 + \beta|0\rangle_2|0\rangle_3) + \psi^-(-\alpha|1\rangle_2|1\rangle_3 + \beta|0\rangle_2|0\rangle_3) + \phi^+(\alpha|0\rangle_2|0\rangle_3 + \beta|1\rangle_2|1\rangle_3) + \phi^-(-\alpha|0\rangle_2|0\rangle_3 + \beta|1\rangle_2|1\rangle_3)], \quad (2)$$

where

$$\psi^\pm = \frac{1}{\sqrt{2}}(|e\rangle|0\rangle_1 \pm |g\rangle|1\rangle_1), \quad (3)$$

$$\phi^\pm = \frac{1}{\sqrt{2}}(|e\rangle|1\rangle_1 \pm |g\rangle|0\rangle_1) \quad (4)$$

are the Bell's basis states of the atom a and the cavity field in $C1$. Such Bell states (ψ^\pm, ϕ^\pm) can be measured according to the method proposed by Davidovich et al. [2], which requires a twostep approach and involves appropriate atomic manipulations. At last, by measuring atom pair a and a' sent through $R1$, $C1$ and $R2$, one gets the complete information on Bell state characterizing the $a + C1$ system, with following correspondences: $g_a, g_{a'} \rightarrow \psi^+, g_a, e_{a'} \rightarrow \psi^-, e_a, g_{a'} \rightarrow \phi^+, e_a, e_{a'} \rightarrow \phi^-$.

Here we analyze the case in which the Bell state analyzers give the readout ψ^+ , which occurs with a probability $1/4$, all of the other cases can be treated in a similar fashion as was the case of the two-particle teleportation scheme [2]. In this case, the state of cavity-field is

$$|\Psi_{23}\rangle = \alpha|1\rangle_2|1\rangle_3 + \beta|0\rangle_2|0\rangle_3. \quad (5)$$

Let us now show how the original state can be reconstructed in cavity $C2$ or $C3$ in terms of Eq.(5). Here we seek to reconstruct the state in cavity $C3$. We assume that atom b prepared in $|g\rangle$ pass through cavity $C2$, this atom is made resonant with the cavity $C2$ with $\pi/2$ pulse. After the interaction, the state of the atom-cavity system is

$$|\Psi_{b3}\rangle = (\alpha|1\rangle_3|e\rangle + \beta|0\rangle_3|g\rangle), \quad (6)$$

and the cavity $C2$ is left in vacuum state $|0\rangle_2$. Then, the atom passes through a Ramsey zone $R3$ with $\pi/4$ pulse, $|\Psi_{b3}\rangle$ is now

$$|\Psi_{b3}\rangle = (\alpha|1\rangle_3 + \beta|0\rangle_3)|e\rangle + (-\alpha|1\rangle_3 + \beta|0\rangle_3)|g\rangle. \quad (7)$$

If the atom b is detected in the excited state $|e\rangle$, the state of cavity field is projected onto $|\phi_3\rangle = \alpha|1\rangle_3 + \beta|0\rangle_3$; and the state onto $|\phi_3\rangle = -\alpha|1\rangle_3 + \beta|0\rangle_3$ if detected in the ground state $|g\rangle$.

Finally, we can replicate on an atom c the information contained in the $C3$ field state. Let atom c prepared in state $|g\rangle$ pass through $C3$ and interact on resonantly with cavity $C3$ with $\pi/2$ pulse. For the case of $|\phi_3\rangle = \alpha|1\rangle_3 + \beta|0\rangle_3$,

$$(\alpha|1\rangle_3 + \beta|0\rangle_3)|g\rangle \longrightarrow (\alpha|e\rangle + \beta|g\rangle)|0\rangle_3. \quad (8)$$

In this way, the information stored in the field state $|\phi_3\rangle = \alpha|1\rangle_3 + \beta|0\rangle_3$ is completely transferred to atom c . For the case of $|\psi_3\rangle = -\alpha|1\rangle_3 + \beta|0\rangle_3$, the information stored in $C3$ is transferred to the state $-\alpha|e\rangle + \beta|g\rangle$. A completed replication on atom c can also be realized by a known unitary transformation. Then we have realized the complete teleportation from atom a to atom c through cavity C_3 . In a similar way, we can also teleport the state from atom a to another atom d through cavity C_2 . Thus we have successfully teleported the unknown atomic state to either of two locations using the three-cavity entanglement.

In summary, using three-photon entangled (GHZ) state, we have successfully teleported the unknown atom state to one of the two locations (c or d) among three high-q cavities. It should be noted that, this scheme can also be used for the teleportation of a cavity field in a superposition of zero- and one-photon Fock states.

References

1. Bennett, C.H. et.al.(1993) Teleporting an unknown quantum state via dual classical and Einstein-Podolsky-Rosen channels. *Phys. Rev. Lett.* **70**, 1895-1898.
2. Davidovich, L. et.al.(1994) Teleportation of an atomic state between two cavities using nonlocal microwave fields. *Phys. Rev. A***50**, R895-R898.
3. Cirac, J.I. and Parkins, A.S (1994) Schemes for atomic-state teleportation. *Phys. Rev. A***50**, R4441-R4444.
4. Greenberger, D.M. et.al. (1990) Bell's theorem without inequalities. *Am. J. Phys.* **58**, 1131-1143.
5. Bouwmeester, D. et.al. (1999) Observation of three-photon Greenberger-Horne-Zeilinger entanglement. *Phys. Rev. Lett.* **82**, 1345-1348.
6. Vedral, V. and Plenio, M.B. (1999) Basics of quantum computation. *Progress in Quantum Electronics* **22**, 1-39.
7. Ekert, A. (1991) Quantum cryptography based on Bell's Theorem. *Phys. Rev. Lett.* **67**, 661-663.
8. Karlsson, A. and Bourennane, M. (1998) Quantum teleportation using three-particle entanglement. *Phys. Rev. A* **58**, 4394-4400.
9. Wootters, W.K. and Zurek, W.H. (1982) A single quantum cannot be cloned. *Nature (London)***299**, 802-804.
10. Bergou, J.A. and Hillery, M. (1997) Generation of highly entangled field states in multiple micromaser cavities. *Phys. Rev. A* **55**, 4585-4588.

Experimental Implementation of Quantum Computing with Macroscopic Ensemble of Quantum Spins

Xiwen Zhu, Ximing Fang, Mang Feng, Fei Du, Kelin Gao, Xi'an Mao

Laboratory of Magnetic Resonance and Atomic and Molecular Physics,
Wuhan Institute of Physics and Mathematics,
Sciences, Wuhan 430071, P. R. China

Abstract. We have carried out several ensemble quantum computing experiments by NMR spectroscopy with sample of carbon-13 labeled chloroform. Here we mainly demonstrate the experimental realization of quantum dense coding which can transmit two classical bits of information by coding one of the EPR pair. All the experiments were proceeded by preparing the pseudo-pure states, manipulating the qubits according to the algorithms and read out the final outcomes. The extracted data are in good agreement with the expected results.

1 Introduction

Quantum computers[1-5] can outperform classical ones owing to their capabilities of solving classically intractable problems (such as factoring large integers[3]) or finding tractable solutions more rapidly(e. g., searching an unsorted database[6]). The quantum discrete Fourier transform plays a key role in many quantum algorithm, and it can be regarded as the basic procedure in the quantum computing. Besides above mentioned algorithms, another quantum algorithm for a class of highly structured combinatorial searching was proposed recently by Hogg[7]. A few simple SAT, such as the SAT having a logic formula in n variables and all clauses with one variable (1-SAT), needs to be classically solved in $O(n)$ steps, but only even requires a single step with Hogg's algorithm.

The striking power of the quantum computing is originated from the quantum parallelism whose essence is the entanglement and superposition of the quantum states. With revealing and understanding the miraculous properties of the quantum states, people paid more attention to the uses of quantum states for quantum information transmission and processing. Among the major application schemes investigated are cryptography based on Bell's theorem, teleportation and dense coding. As sending more than one bit of information classically requires manipulation of more than one two-state particle, dense coding proposed by Bennett and Wiesner[8] in 1992, which can transmit two bits message by manipulating one of the entangled two-state pair, is seemingly striking. Several alternatives for realizing dense coding

have been suggested. However, only one experiment of dense coding was reported [9] so far, in which polarization-entangled photon pair was exploited for transmitting 3 messages per two-state photon, i. e. 1 'trit' \approx 1.58bit.

We have carried out experimentally the quantum discrete Fourier transform, Hogg's algorithm and quantum dense coding using nuclear magnetic resonance(NMR) scheme[9] with two-qubit sample. In this contribution, we will focus on the demonstration of two-qubit quantum dense coding.

2 The network of quantum dense coding

The network that we use for realizing quantum dense coding in terms of the logic gates and circuits in quantum computation is shown in Fig. 1, where a and b denote two quantum systems with two states $|0\rangle$ and $|1\rangle$. It consists of three parts divided by the dashed lines.

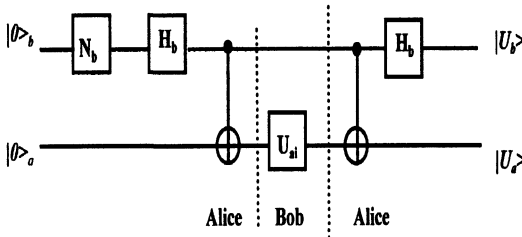


Fig. 1. The network for quantum dense coding.

It can be clearly seen that four messages have been transmitted from Bob to Alice via encoding transformation on one of the entangled pair and decoding measurement of the whole system in terms of the network shown in Fig.1, which is consistent with the original idea of Bennett-Wiesner proposal. No matter from which of the four Bell states the process begins, we always get definite outputs associated with different transformation operations.

3 The experimental procedure and result

The network stated above can be put into practice with NMR techniques. We choose 1H and ^{13}C in the molecule of carbon-13 labeled chloroform $^{13}CHCl_3$ (Cambridge Isotope Laboratories, Inc.) as the two-spin system in the experiment and d6-acetone as a solvent. Their cubic ratio is 1:1(v/v). It is flame sealed in a standard 5-mm NMR sample tube. Spectra were recorded on a Bruker ARX500 spectrometer with a probe tuned at 500.135297 MHz for 1H (denoted by a) and at 125.767969MHz for ^{13}C (denoted by b).

We carried out the experiment in the following procedure. First, the effective pure state $|00\rangle$ was prepared by temporal averaging[11]. Then the

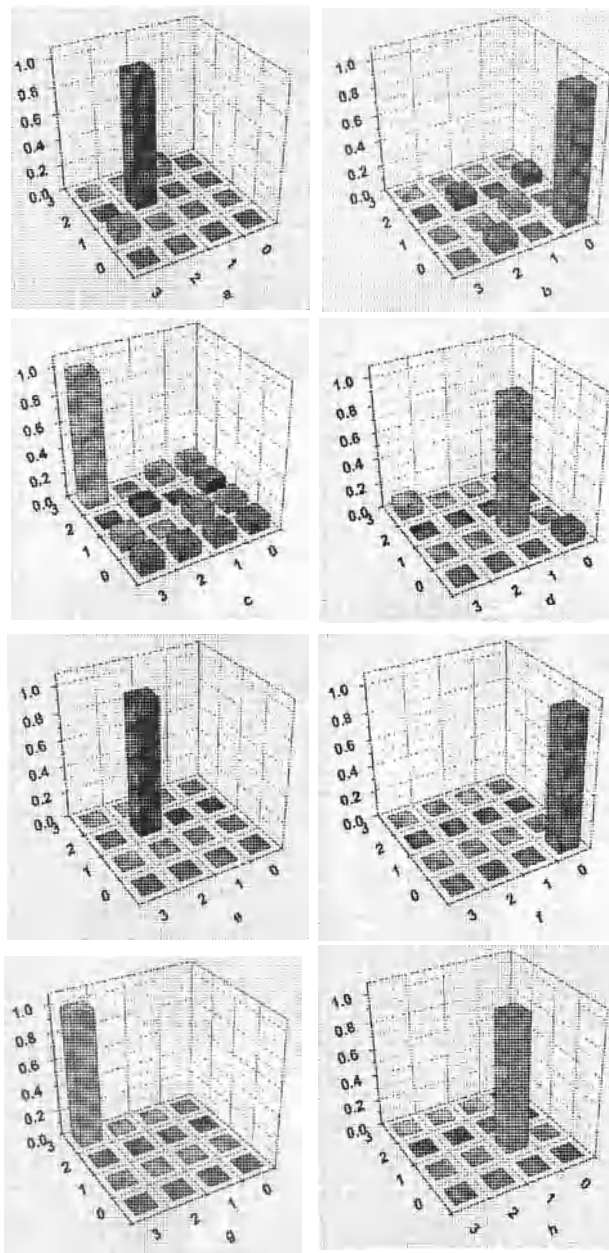


Fig. 2. The distribution of the density matrices of the quantum system. The a, b, c, and d are the dimensionless experimental results. e, f, g and h are dimensionless theoretical ones corresponding to the operations I, σ_z , σ_x and $i\sigma_y$, respectively. See text

operations applied according to the network shown In Fig. 1 were executed by a series of NMR pulses mentioned above. Finally, the outputs experiments expressed by the density matrices $\rho_{out} = |yx\rangle_{ii}\langle yx|$ corresponding to four operations of U_{ai} were reconstructed by the technique of state tomography[11]. The matrices reconstructed by fitting the data from the spectra measured are shown in Fig. 2. The axes of the horizontal plane denote the locations of the elements in the matrix, its values 0, 1, 2 and 3 correspond to the states $|00\rangle$, $|01\rangle$, $|10\rangle$ and $|11\rangle$ respectively, and the vertical axes represents the module of the elements. The theoretical matrices are also shown as a contrast. Comparing the theoretical and experiment matrices, we can find that they are in good agreement. Experimental errors were primarily due to RF field and static magnetic field inhomogeneity, imperfect calibration of pulses and signal decay during the experiment. The largest error is about 10%. These results show that the network actually does the quantum dense coding communication.

Conclusion

We have experimentally implemented quantum dense coding by using quantum logic gates and circuits in quantum computation and NMR techniques, which demonstrated physically the original ideal of Bennett-Wiesner proposal. Principally, dense coding experiment with maximally entangled states for $n > 2$ particles can be performed by utilizing an appropriate NMR sample with n spins and a generalized quantum network.

Acknowledgment. This work was supported by National Nature Science Foundation of China and Chinese Academy of Sciences.

References

1. Feynman R. P., (1982) Simulating physics with computers. Int. J. Theor.Phys. **21**, 467-488
2. Deutsch D., (1985) Quantum theory, the Church-Turing principle and the universal quantum computer. Proc. Soc. Lond. A**400**, 97-117
3. Shor P., (1994) Algorithms for quantum computation:discrete logarithms and factoring. Proc. 35th Annu. Symp. on Found. of Computer Science, 124-134 (IEEE Comp. Soc. Press, Los Alomitos, CA)
4. DiVincenzo D.P., (1995) Quantum computation. Science **270**, 255-261
5. Lloyd S., (1995) Quantum-mechanical computers. Sci. Am. **273**, 44-50
6. Grover L. K.,(1997) Quantum mechanics helps in searching for a needle in a haystack. Phys. Rev. Lett. **79**, 325-328
7. Hogg T., (1998) Highly structured searches with quantum computers. Phys. Rev. Lett. **80**, 2473-2476
8. Bennett C.H. and Wiesner S.J., (1992) Communication via one- and two-particle operations on Einstein-Podolsky-Rosen states. Phys.Rev.Lett., **69**, 2881-2884

9. Mattle K., Weinfurter H., Kwiat P.G. and Zeilinger A., (1996) Dense coding in experimental quantum communication. *Phys.Rev.Lett.*, **76**, 4656-4659
10. Gershenfeld N. and Chuang I.L., (1997) Bulk spin resonance quantum computation. *Science* **275**, 350-356
11. Chuang I.L., Vandersypen L.M.K., Zhou X., Leung D. and Lloyd S., (1998), Experimental realization of a quantum algorithm, *Nature* **393**, 143-146

Fabrication and Characterization of Proton-Exchanged Lithium Niobate

X.F.Chen¹, Q.Li¹, S.W.Xie¹, Y.X.Xia¹, Y.L.Chen¹, S.Sottini², E.Giorgetti²,
A.Carta², R.Ramponi³, R.Osellame³, M.Marangoni³

¹ Department of Applied Physics, Shanghai Jiao Tong University,
Shanghai 200030, P.R. China

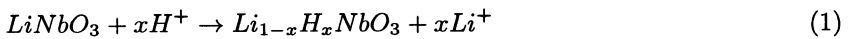
² IROE-CNR, 64 Via Paciatichi, 50127, Firenze, Italy

³ Politecnico di Milano, p.le L. da Vinci, Milano, Italy

Abstract. Proton-exchanged (PE) lithium niobate waveguides have potential value in application of photonics devices. Based on the characterization of PE waveguides and theoretical predication of Cerenkov SHG. We design a PE waveguide that is optimal for Cerenkov SHG in which we experimentally observe effective blue and green SHG.

1 Introduction

Optical waveguides fabricated using proton-exchanged (PE) method in lithium niobate are the basis of many optical components, such as electro-optical modulator [1], waveguide Second harmonic Generation (SHG) devices [2] and polarizers[3].Proton-exchange technique uses a chemical reaction between the lithium niobate and a suitable proton source, such as benzoic acid and pyrophosphoric acid. This reaction can be described as follow[4]:



Proton-exchange is one of the two main methods for fabricating optical waveguides in lithium niobate. Proton-exchange method has some advantages over their titanium diffusion counterpart. First, less optical damage is observed in proton-exchanged process which is more desirable for short wavelength applications. Second, after exchange, only extraordinary index is increased, with large index changes as 0.135 at $\lambda = 0.6328\mu m$, so that the strongly confined waveguides can be easily fabricated. Third, the proton-exchange temperature, typically from $200^\circ C$ to $300^\circ C$, is much lower than Ti-indiffusion temperature.

In this paper, we experimentally studied the fabrication of proton- exchanged waveguide in Z-cut $LiNbO_3$ and establish the relation between the parameter of the guide and the fabrication condition. Based on above results and theoritiaci predication for Cerenkov SHG in PE waveguides, we design and make a wavguide optimal for Cerenkov SHG. Last, we observed effective SHG with blue and green output frnon the PE waveguide.

2 Fabrication and Characterization of PE Waveguides

Fabrication and Measurement of PE Waveguides. The proton source we used is benzonic acid melt diluted by lithium benzoate. Proton-exchange takes place when the $LiNbO_3$ substrate is immersed in the above melts. Under these conditions, lithium diffuses out of the substrate and is replaced with H^+ from the proton source. $H_xLi_{1-x}NbO_3$ strcture is formed in the layer near the crystal surface. Dilution by lithium benzoate is for slowing down the process of proton exchange and enhance the reproductivity of the waveguides. Because evaporation rate of two materials is different, a tight sealed and simple designed tube to hold the acid powers is necessary. We design a tube that can fabricate Proton-exchange waveguide easily and with high reproductivity that is significant for commercial application. In our experiment, exchange temperature is $190^\circ C$ and exchange time is from 1 hour to 24 hours. Content of Lithium Benzoate in the melt is 0.2% to 2%.

TM effective-mode indices were measured with the use of the standard two prism coupling technique at various wavelength. Low powers were used to avoid photorefractive effects. A photodiode was used to improve the precision of the effect index measurement, and care was taken to measure the $LiNbO_3$ substrate refractive index with various wavelength. Reproducibility in the effect indeces was 10^{-4} .

Characterization of PE Waveguides. Proton-exchanged waveguides have step-like index profile, only TM mode can propagate in PE guides. $LiNbO_3$ substrate is anisotropic crystal, index profile can be determined by the dispersive equation in anisotropic media by comparing measurement results of effective index with that of theoretical calculations.

$$\kappa d = m\pi + \tan^{-1}\left(\frac{n_{o,f}}{n_{o,s}} \frac{p}{\kappa}\right) + \tan\left(\frac{n_{o,f}}{n_{o,c}} \frac{q}{\kappa}\right) \quad (2)$$

where $\kappa^2 = \frac{n_{o,f}^2}{n_{e,f}^2}(k^2 n_{e,f}^2 - \beta^2)$, $p^2 = \frac{n_{o,s}^2}{n_{e,s}^2}(\beta^2 - k^2 n_{e,s}^2)$, $q^2 = \frac{n_{o,c}^2}{n_{e,c}^2}(\beta^2 - k^2 n_{e,c}^2)$, in which $n_{o,f}$, $n_{o,s}$ and $n_{o,c}$ are ordinary refractive index in the guided layer, substrate and cladding, respectively; $n_{e,f}$, $n_{e,s}$ and $n_{e,c}$ are extraordinary index in the guided layer, substrate and cladding, respectively, d_e is depth of PE waveguide, k is wave vector in vacuum and β is propagation constant of guided-mode.

In our experiments, exchange time range from 2 to 10 hours and exchange temperature is $190^\circ C$. A beam with wavelength $\lambda = 0.488\mu m$ was used to maximize the number of modes.

Fig. 1 shows the diffusion depth d_e as a function of lithium benzoate content M. Content M ranges from 0.0wt% to 1wt%, all PE waveguides are fabricated with at 2 hours exchange time and temperature $190^\circ C$. The number of guided-mode decrease as the content M increase.

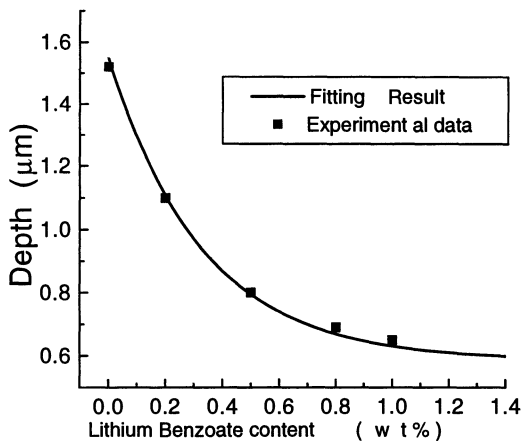


Fig. 1. Plot of depth of PE waveguide vs. Lithium benzoate content M

Exchange in 1% lithium benzoate diluted melt is much slower than that in pure benzoic acid can enhance the reproductivity of the waveguides. Two and five modes can be stimulated at the wavelength $\lambda = 0.488\mu m$ with 4 hours exchange time at the temperature $190^{\circ}C$, respectively, In the following experiments, we fabricate and characterize the proton exchanged waveguides in 1% lithium benzoate diluted melt for SHG waveguide devices.

Depth d_e as a function of exchange time is shown in Fig. 2. From the gradient of the curves, the values for the diffusion coefficient were calculated assuming that the diffusion proton source concentration did not vary during the exchange process. The diffusion coefficient $D(T)$ were calculated assuming the depth d_e various as follow[5]:

$$d_e = 2\sqrt{t \times D(T)} \quad (3)$$

The relation between exchange depth d_e and exchange time is shown in Fig. 2. The fitting curve is obtained to be $d_e = 0.09907 + 0.24467t^{1/2}(A)$ and the diffusion coefficient $D(T) = 0.0156\mu m^2/h$ diffusion coefficient in this case has one magnitude smaller than that in proton source without dilution.

As exchange time increase, extraordinary index can be observed to increase and gets saturation when exchange time is long enough. We fitting the experimental data with exponential function, and the results is $\Delta n_e = 0.1418 \times [1 - 0.1305 \exp(-t/2.908)](B)$. To check the reproductivity of our setup, we fabricate PE waveguides for three times with the same condition ($T=190^{\circ}C$, $t=2$ hours) in 1% diluted melt. The measurement results are 2.33882, 2.33757 and 2.33920 respectively which shows that our setup is stable and suitable for PE fabrication.

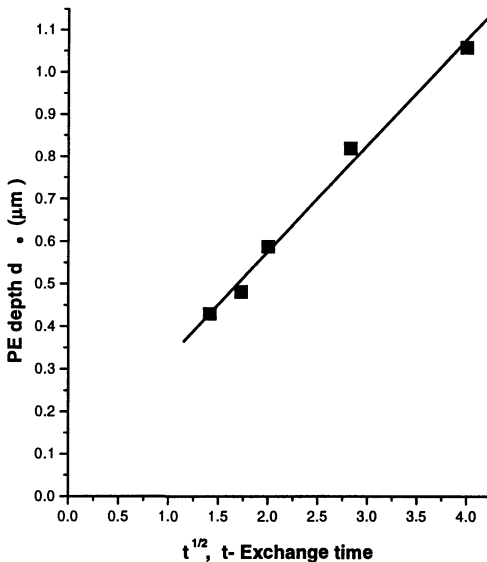


Fig. 2. Plot of depth vs time for proton- exchanged waveguides in 1wt% diluted benzoic acid at 190°C at $\lambda = 0.488\mu\text{m}$

3 Fabrication of PE Waveguides for Cerenkov SHG

In reference 6, a model is developed to calculate the Cerenkov SHG by directly resolving the propagation equation. The results show that Cerenkov radiation strongly depends on the discontinuities at the interface of the forced fields generated by the nonlinear polarization. Proton exchange process generates a guided layer with a step-like index distribution and the reduction of nonlinear coefficient. We calculated Cerenkov SHG efficiency as a function of pump wavelength in Fig. 3 in the case the depth of PE waveguide is $0.54\mu\text{m}$. The efficiency is very sensitive to pump wavelength and two peaks are observed near the pump wavelength $0.78\mu\text{m}$ and $1.00\mu\text{m}$. The SHG radiation $0.39\mu\text{m}$ and $0.50\mu\text{m}$ are blue and green, respectively.

We fabricate the PE waveguide with the depth $0.54\mu\text{m}$ in 1wt% lithium benzoate diluted melt. The small diffusion coefficient enhances the reproducibility and credibility of the fabrication. From formula (A) in Section 2.2, the exchange time 3.25 hours is needed to obtain the PE waveguide with $0.54\mu\text{m}$ depth. The extraordinary index change the guided layer is $\Delta n_e = 0.1357$ by calculating the formula (B) and ordinary index is given as $\Delta n_o = -0.034$ according to our experiments. The sample is immersed in the proton source for 3.25 hours and we measured effect index of the guide-mode after exchange with the wavelength $\lambda = 0.488\mu\text{m}$. The effective index from the measurement and characterization results are shown in Table 1. The results show that our characterization model which establish the relation between fabrication con-

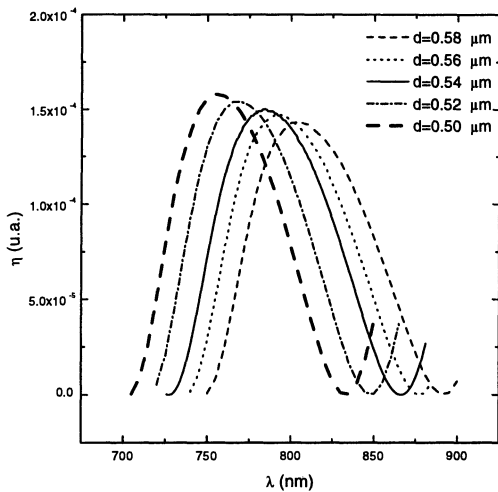


Fig. 3. Cerenkov SHG efficiency as a function of pump wavelength

dition and parameter of the PE waveguides is good for predicating the depth and the index change of the waveguides.

Table 1. Effective Index of PE waveguide with depth $0.54\mu m$

| | TM1 | TM2 |
|---------------------------|---------|---------|
| Characterization results | 2.35802 | 2.27089 |
| Experimental measurements | 2.35853 | 2.26934 |

We observe the Cerenkov SHG with blue and green output in this waveguide, the SHG experimental measurement shows good agreement with theoretical predication. The detailed results will be published later.

4 Conclusion

We fabricate and characterize PE waveguides. After exchange process, index profile is found to be step-like and extraordinary index change is large. With the increase of the content of Lithium benzoate in benzonic acid as proton source, proton-exchange process becomes slower. The relationship between the fabrication condition and waveguide parameters is established which is shown to be agreement with the experiments. The reproducibility of the PE waveguides is good by our fabrication setup. Based on the characterization of PE waveguides, we design and fabricate a waveguide with depth $0.54\mu m$ which is suitable for Cerenkov SHG with blue and green output.

Acknowledgements. This work is supported by Shanghai Education Committee Foundation. Xianfeng CHEN, one of the authors, Thank International Center of Theoretical Physics (ICTP) TRIL program for the financial support to have a chance to visit Institute of Electro-magnetic Wave, CNR, Florence, Italy.

References

1. M. M. Abouelleil and F. J. Leonberger, *J. Am. Ceram. Soc.* 72, 1311(1989)
2. K. Mizuuchi, H. Ohta et al., *Opt. Lett.* 22, 1217(1997)
3. N. Got and Y. L.Yip, *J. Lightwave Technol.* 7, 199 (1989)
4. K. Ito and K. Kawamoto, *Jan. J. Appl. Phys.* 36, 6775(1997)
5. D.F. Clark, A.C. G. Nutt et al., *J. Appl. Phys.* 54, 6218(1983)
6. M. J. Li, M. De. Micheli, et al., *IEEE J. of Quantum Electron.* 26, 1384(1990)

A Statistic Model for Ion Clouds in Paul Traps

Jidong Hou, Yiqiu Wang, Donghai Yang

Dept. of Electronics, Peking University, Beijing, 100871, China

Abstract. This paper present a statistic model for ion clouds in Paul trap. In this model the collision between ions and molecules is a very important factor and space charge effect is considered by self-consist method. Given the parameters of a Paul trap, the properties of ion clouds can be obtained by this model without choosing physical parameters or changing trap parameters.

1 Some Problems of ion clouds in Paul traps

Ion traps have been widely used in spectroscopy for highly precise measurements [1]. There are two types of ion traps, Penning traps and Paul traps. The latter are widely used for their simple structure.

Paul traps are constructed by ring and endcap (up and down) electrodes, they all have a hyperboloidal surface. A DC and AC voltage are applied on the ring and endcap electrodes. Let r_0 denote the radius of the ring electrode and z_0 half of the distance between the up and down caps. Usually the ratio of r_0 to z_0 is $\sqrt{2}$. In Paul traps the movement of ions can be described by a Mathieu equation [2]

$$\frac{d^2u}{dx^2} + (a - 2q \cos 2x) = 0 \quad (1)$$

here $x = \Omega t / 2$ and

$$a_z = -2a_r = 8\left(\frac{eU_0}{mz_0^2}\right)\frac{1}{\Omega^2}, \quad q_z = 2q_r = 4\left(\frac{eU_0}{mz_0^2}\right)\frac{1}{\Omega^2} \quad (2)$$

Here $a_{r,z}, q_{r,z}$ are connected with the parameter of Paul trap. And only in certain regions of the plane formed by a and q can ions be trapped stably. The main region usually used can see ref. [2]

In Paul traps the Doppler effect is the main factor that limits precise measurements. The technique of laser cooling can reduce the frequency shift by decreasing the mean kinetic energy of ions. However, in practice this technique works only when the number of confined ions is small [3], marred low S-N ratio. In order to obtain a high S-N ratio, ion clouds with a large number of ions are still in use today.

Because of the time-dependent potential, the motion of ions in a Paul trap is complicated, Fig.1 is a example of a part of the trajectory of an ion

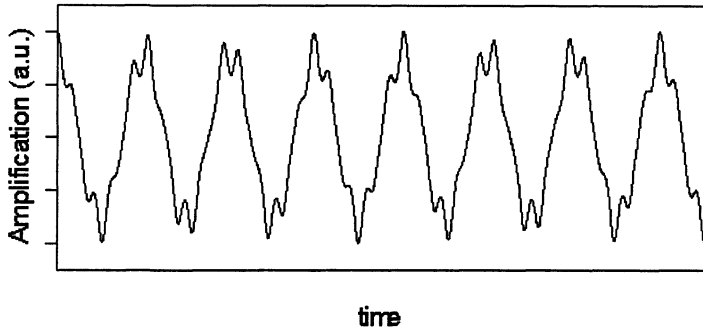


Fig. 1. Example of an ion trajectory of one dimension in a Paul trap.

in one dimension. We can see it is like a harmonic well motion. But it is not a real periodic motion. Usually the complicated motion is divided into a micromotion and macromotion under the limitation of $a \ll q \ll 1$. The latter is related to the 'restoring force' obtained by averaging the time-dependent potential over one oscillation cycle. This restoring force is similar to that of a harmonic well. According to the treatment, a pseudopotential well model [4,5] is proposed. While in experiments q is usually between 0.3 to 0.6.

Beside the complicated motion of ions, another problem is space-charge effect. Ref. [5] assumes a Gaussian distribution of ion clouds, and Ref. [6,7] change the trap parameter in equations to simulate the effect. Ref. [8] presents an analytical model which can be used to describe a Gaussian-like distribution, and the resulting mean kinetic energy is corrected by adding a term related to the micromotion. Ref. [9] presents a perturbation method which just considers the "weak space-charge", and it is applicable when the number of confined ions is less than 2×10^5 . A Brownian-motion model [7,10] has no limitations on the values of a and q . In this model, some equation parameters, such as the damping and diffusion constants, are chosen or adjusted to fit the experimental results. The space-charge potential is introduced by changing the trap parameters.

Here we present a statistical model. In this model neither choice of equation parameters nor changing of the trap parameters in equations is needed. We directly calculate the ion trajectories by solving a Newton equation of motion and the space charge is considered by a self-consistent method. Once real trap parameters are given, the characteristics of an ion cloud can be obtained. In this aspect, the model is deterministic.

2 Assumptions and method in our model

Our model has three assumption. The first one is an ion cloud confined in a Paul trap exchanges its kinetic energy with the molecules of background gases by collisions, and reaches a quasi-stable state. The second is that the motion of confined ions is ergodic, so a time average value of a certain ion in a cloud is equal to the corresponding ensemble average value of the cloud. The third is that the spatial distribution of an ion cloud in a quasi-stable state does not change with time [11]. The first assumption explains why an ion cloud evolves to a quasi-stable state, The two latter give a feasible way to calculate the characteristics of an ion cloud in a quasi-stable state. Usually ion clouds contain several hundred thousands to several millions ions, and precision resolve to this multibody system is almost impossible. The second assumption allows us to calculate the time average values of a certain ion to represent the corresponding ensemble values of an ion cloud. The third allow us treat the other ions as a time-independent ion cloud which interacts with the tracked ion by the Coulomb force. the potential of a Paul trap is supposed to be spherically symmetric to simplify calculations. Therefore, $a_{x,z}$, $q_{x,z}$ are equal, respectively. They are denoted by a and q below. Core to core collision is also supposed. Let v'_i denote the velocity of the tracked ion just after a collision, it can be given as

$$\cdot v'_i = \frac{2}{\beta + 1} v_g + \frac{\beta - 1}{\beta + 1} v_i \quad (3)$$

β is the ratio of the ion mass to the gas molecule mass, v_g and v_i is the velocity of the gas molecules and that of the ion just before the collision, respectively. v_g satisfies a Maxwell distribution Between collisions, the ion trajectory is obtained by solving Eq.4 (see below) Let $f_n(r)$ and $S_n(r)$ denote the ion spatial distribution and the space-charge field amplitude between the (n-1)th and nth collision, respectively, and $E(r, t)$ the trap field amplitude. The equation of motion of the tracked ion between the nth and (n+1)th collisions is

$$\ddot{r} = \frac{e}{m} (E(r, t) + S_n(r)) \quad (4)$$

Here $E(r, t)$ is the trap potential and $S_n(r)$ is the potential of spacial charge, it can be obtained by

$$\begin{aligned} \oint_s S_n(r) ds &= \frac{Q_n}{\epsilon_0}, \\ Q_n &= Ne \frac{\int_0^R \sum_{i=0}^n f_i(r') r'^2 dr'}{\int_0^R \sum_{i=0}^n f_i(r') r'^2 dr'}. \end{aligned} \quad (5)$$

After a certain amount of computing time, the statistical values of an ion cloud tend to constant values. The stability of the mean kinetic energy is the criterion for ending the calculation.

3 Comparison between calculated and experimental results

We calculate ion clouds of Barium with our model for the relevant experiment results are ample. The relevant energy levels of Ba^+ are shown in Fig.2, where the $5\text{D}_{3/2}$ state is a metastable state. To observe the resonant fluorescence between the $6\text{S}_{1/2}$ and $6\text{P}_{1/2}$ state, a repumping light between $6\text{S}_{1/2}$ and $5\text{D}_{3/2}$ is used. Considering the complicate motion of ions in trap(macromotion plus microsmotion, see the fig.1), we ignore the effect of repumping light and consider the Ba^+ as two level system, for a certain ion can be excited and repumped at different times and at different speeds.

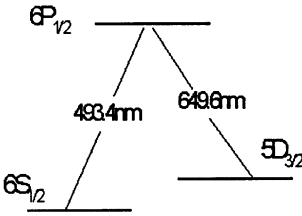


Fig. 2. The scheme of relevant level of Ba^+ .

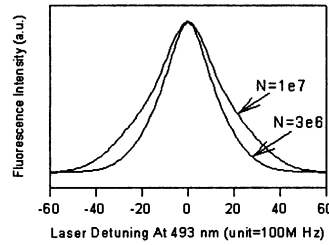


Fig. 3. The spectral profile of ion clouds of Ba^+ at different number of ions.

We firstly calculate the spectral profile of the fluorescence. By our model we can obtain the velocity distribution $p(v)$ directly. According to the equation

$$f(\omega) = \int \frac{p(v)}{(\omega_l - \omega_0 - kv)^2 - (\Gamma/2)^2} \quad (6)$$

fluorescence profile can be obtain. Here ω_l is the laser frequency and ω_0 is the resonant frequency of ions. Γ is the linewidth. Fig.3 shows two fluorescence shaps at different number of ions. The shap of small number is very similar with that of ref.[7], just like Gaussian. But the one of large number can not be discribed as Gaussian.

The spacial distribution of ion clouds can be obtained by this model without other more assumption when the number of ions in cloud is given. We know the distribution of a partical doing Brownian motion in a harmonic well is Gaussian, this is coincident with our calculated result of small number of ions(see Fig.4). Ref. [12] gives similar experiment result. But when the number of ions is big, the interaction of ions becomes important and this fact will affect the motion of ions, the distribution would deviate the Gaussian shape.

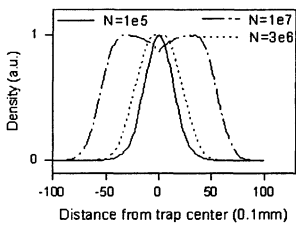


Fig. 4. The spacial distribution of ion clouds at different number of ions.

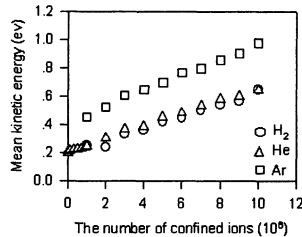


Fig. 5. The effects of different background gases can be evaluated.

Our calculated results show when the number is 10^7 , the distribution is almost uniform, having a shallow pit in its center. And there are transitional distribution between Gaussian and uniform shape.

In Experiments gases are usually used as buffer gases. We evaluate the influence of different background gases on the mean kinetic energy of ion cloud when the ionic number varies(see Fig.5). We can see light gases is better than heavy gasess according to the mean kinetic energy, his is consistent with the experience.

4 Discussing laser cooling on ion clouds in a Paul trap

Laser cooling is a very powerful technique for precision measurement. But for ion clouds in a Paul trap, this technique only works when the number of ions in clouds is small[3]. There are two opinions on this phenomenon. One is that RF-heating hamper the laser cooling. RF-heating is arised from the collisions between the ions and ions to molecules, through the collisions ion's micromotion is transferred to macromotion. Another opinion is that the Coulomb force between the ions expels some ions to the peripheral region and the time-dependent field heats them. Until now there is no model giving the relationship between mean kinetic energy and ionic number of a ion cloud in the present of cooling laser. To study on what extent the spacial charge effect influence the mean kinetic energy, we calculate the relationship between the mean kinetic energy and the ion number. In calculation the cooling power of cooling laser is aggrandized – ions just absorb the photons that decrease their kinetic energy at saturate rate. and the stochastic momentum obtained by fluorescence emission is ignored. The collision between ions and molecule of background gases is infrequent compared with the absord of photons and its damping effect is neglected. The value of v'_i (see Equ.3) decrease P/m_i after each absord. P is the momentum of photon and m_i is the mass of an ion. Fig.6 is the calculated results. Compare this figure to Fig.5, we can see the temperature of ion cloud is decreased by cooling laser when the number of ions is low. But when the ionic number exceed 10^6 ,The temperature with

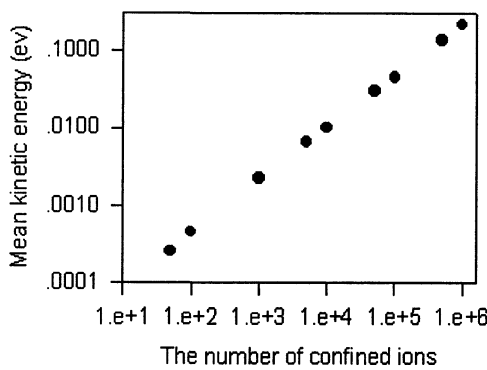


Fig. 6. The relationship between mean kinetic energy and ionic number of ion cloud at the present of laser cooling.

laser cooling is almost the same as that without laser cooling. It should be noted that we assume that cooling effect is the highest and the heating effect of laser is ignored. The result shows spacial charge effect is very important and it can cancel the cooling effect in a Paul trap even if the cooling laser is very powerful.

References

1. R. Blatt and G. Werth, Phys. Rev. A **25**, 1476 (1982).
2. R. F. Wuerker, H. Shelton, and R. V. Langmuir, J. Appl. Phys. **30**, 342 (1959).
3. R. Blatt, P. Gill, R. C. Thompson, J. Mod. Opt. **39**, 193 (1992).
4. H. G. Dehmelt, Adv. Atom. Molec. Phys. **3**, 53 (1967).
5. L. S. Cutler, C.A. Flory, R. P. Giffard and M.D. McGuire, Appl. Phys. B **39**, 251 (1986).
6. E. Fischer, Z. Phys. **156**, 1 (1959).
7. I. Siemers, R. Blatt, Th. Sauter, W. Neuhauser, Phys. Rev. A **38**, 5121 (1988).
8. C. Meis, M. Desaintfuscien, and M. Jardino, Appl. Phys.B **45**, 59 (1988).
9. F. Vedel, and J. Andre, Phys. Rev. A **29**, 2098 (1984).
10. R. Blatt, P. Zoller, G. Holzmuller, and I. Siemers, A. Phys. D **4**, 121 (1986).
11. Once given the original condition, the ion's motion is determined. The ceaseless collisions between ions and gas molecules erase the ions' original conditions endowed at their origin. Therefore it would be impossible that at one moment all ions move in one certain direction.
12. R. D. Knight and H. M. Prior, J. Appl. Phys. **50**, 3044 (1979).

Single-Mode Self-Homodyne Tomography with Empty Cavity

Jing Zhang, Junxiang Zhang, Tiancai Zhang, Changde Xie, Kunchi Peng

Institute of Opto-Electronics, Shanxi University,Taiyuan 030006 P.R.China

Abstract. A self-homodyne detection scheme with empty cavity is proposed to perform quantum tomography of single-mode which have a strong mean field. The local oscillator used in conventional homodyning is not needed in the proposed scheme and the overall quantum efficiency can be improved.

1 Introduction

Optical Homodyne Tomography(OHT) has attracted a lot of research interest in recent years. The significant advances in the theory[1] and experiment have been acquired. In the OHT the set of distributions $\{P_\theta(x_\theta)\}$ is measured by means of Optical Homodyne Detection (OHD) which is based on the interference of the signal field with a strong coherent reference field (local oscillator LO), which has an adjustable phase with value θ . $X_\theta = (ae^{i\theta} + a^+e^{-i\theta})/\sqrt{2}$ is the phase-rotated quadrature amplitude. This scheme encounters the problem of mode matching between the LO and the measured modes[2].The mode matching is determined by their spatiotemporal overlap, and the quality of overlap directly influence the overall quantum efficiency [3] upon which the detected quantum features of light field depend significantly. Moreover, it is difficult to find matched LO in many practical system such as bright squeezed light from frequency doubler ,squeezed states from Kerr medium.

Recently a self-homodyne tomography [4] was developed that creates both the LO and the signal in the same optical parametric amplifier OPA injected with an input field having a strong coherent component at frequency ω_0 . In the direct detection of the output signal field, a strong mean field at the central frequency ω_0 was used as the LO to measure the two sidebands mode at $\omega_0 \pm \Omega$. The relative phase between the LO and the two sidebands mode was varied by scanning the relative phase between input field and the pump field, thus the homodyne tomography of the sidebands was accomplished.

In Ref.[5], the phase of the squeezed state is controlled by Fabry-Perot empty cavity, then the squeezing spectra is measured. In this paper, we develop this scheme to reconstruct the optical quantum state. The input field with a strong coherent component at frequency ω_0 serve as the LO to measure two sidebands mode at $\omega_0 \pm \Omega$. According to the sidebands frequency Ω , the suitable finesse of empty cavity is selected. The relative phase between the LO and the two sidebands mode $\omega_0 \pm \Omega$ is controlled by varying the

cavity length, then the tomographic reconstruction of optical quantum state is performed.

2 The model

The scheme of a self-homodyne tomography with empty cavity is depicted in Fig 1. The input field includes a strong coherent component $\hat{a}_0^{in}(\omega_0)$ and two measured two sidebands mode $\hat{a}_+^{in}(\omega_0 + \Omega)$, $\hat{a}_-^{in}(\omega_0 - \Omega)$, footnote 0 of \hat{a} designates at the center frequency ω_0 and footnote \pm at the sidebands $\omega_0 \pm \Omega$. ω_0 is typically an optical frequency, whereas Ω is a radio frequency. The input coupler is a partly reflecting mirror of amplitude reflection coefficients r and transmission $t(r^2 + t^2 = 1)$. If all losses are neglected, using the boundary conditions the field reflected by the cavity is described by the semi-classical method

$$\begin{aligned} a' &= ra + ta^{in} \\ a^{out} &= ta - ra^{in} \\ a &= a'e^{i\phi} \end{aligned} \tag{1}$$

where a and a' is the intracavity fields just before and just after the reflection on the mirror, which couples them to the output fields a^{in} and a^{out} , ϕ is the cavity round trip propagation phase shift. The following relation is yielded by the Eq(1) between the input and output fields of the central frequency and the two sidebands mode

$$\hat{a}_+^{out}(\omega_0 + \Omega) = \frac{re^{-i(\phi_0 + \Omega L/c)} - 1}{e^{-i(\phi_0 + \Omega L/c)} - r} \hat{a}_0^{in}(\omega_0 + \Omega)$$

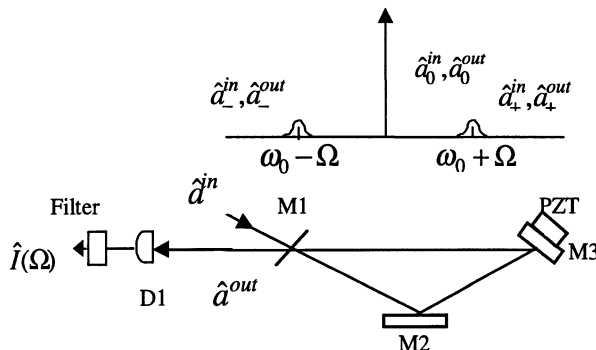


Fig. 1. The scheme of a self-homodyne tomography with empty cavity.

$$\hat{a}_-^{out}(\omega_0 - \Omega) = \frac{re^{-i(\phi_0 - \Omega L/c)} - 1}{e^{-i(\phi_0 - \Omega L/c)} - r} \hat{a}_0^{in}(\omega_0 - \Omega) \quad (2)$$

where phase detune $\phi_0 = \frac{\omega_0 L}{c} + \varphi_r - 2\pi N$ ($N = \text{integer}$), $2\pi N = \frac{\omega_0 L_{res}}{c} + \varphi_r$, L_{res} is the cavity trip length L at resonance, φ_r is the total shift at three cavity mirrors, L is the round trip length of the cavity, c is the speed of light in vacuum. From Eq.(2) we define the phase shift angle of output field

$$\theta(\phi_0) = \text{Arg}\left[\frac{re^{-i\phi_0} - 1}{e^{-i\phi_0} - r}\right] \quad (3)$$

The phase shift angle as a functions of the detuning ϕ_0 is shown in Fig2. When $\theta = \pi - \delta$ ($\delta \rightarrow 0$), the corresponding detune frequency is Ω_π . So the cavity full-width is defined as $2\Omega_\pi$.

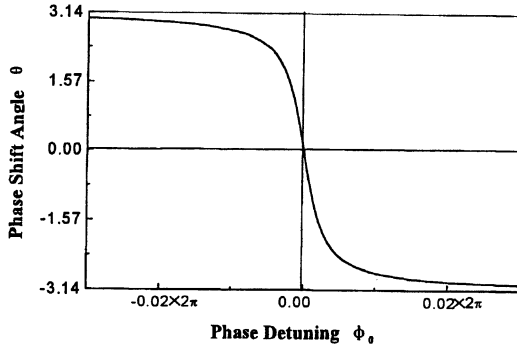


Fig. 2. Phase shift angle θ as funtion of the-phase detuning $\phi_0.r = 0.9998$.

The output field reflected by empty cavity is detected directly by D_1 . Passing the narrow band filter at Ω , the output filtered photocurrents are given by the operators[4]

$$\begin{aligned} \hat{I}(\Omega) &= \int_{-\infty}^{+\infty} dt e^{i\Omega t} : |\hat{\varepsilon}(t)|^2 : \\ &= \int_{-\infty}^{+\infty} d\omega \hat{\varepsilon}^+(\omega + \Omega) \hat{\varepsilon}(\omega) \end{aligned} \quad (4)$$

where $: :$ denote the customary normal ordering with the output field annihilation operator components $\hat{\varepsilon}$ on the right and the creation operator $\hat{\varepsilon}^+$ on the left. Because the field have a strong coherent component only at the center frequency ω_0 , Eq.(4) is simplified:

$$\hat{I}(\Omega) = \hat{a}_0^{out+} \hat{a}_-^{out} + \hat{a}_+^{out+} \hat{a}_0^{out} \quad (5)$$

In the process of direct detection, the highly excited central mode \hat{a}_0 beat with the $\omega_0 \pm \Omega$ sideband modes, thus playing the role of the LO of homodyne and heterodyne detectors. This converts the direct detectors into self-homodyne detectors whose experimental outcomes are measured values of the following rescaled output photocurrents in the limit of strong LO's

$$\hat{i}(\Omega) = \lim_{|\hat{a}_0^{out}| \rightarrow \infty} \frac{\text{Tr}_{LO}[\hat{I}(\Omega)\hat{\rho}_{LO}]}{\sqrt{2}|\hat{a}_0^{out}|} \quad (6)$$

where $\hat{\rho}_{LO}$ represents the density operator of the LO state, Tr_{LO} denotes the partial trace over the LO mode, $|\hat{a}_0^{out}|$ represents the LO average value. thus we obtain

$$\begin{aligned} \hat{i}(\Omega) &= \frac{1}{\sqrt{2}}(e^{i\theta(\phi_0)}\hat{a}_-^{out} + e^{-i\theta(\phi_0)}\hat{a}_+^{out+}) \\ &= \frac{1}{\sqrt{2}}(e^{i[\theta(\phi_0)-\theta(\phi_0-\frac{\Omega L}{c})]}\hat{a}_-^{in} + e^{-i[\theta(\phi_0)-\theta(\phi_0+\frac{\Omega L}{c})]}\hat{a}_+^{in+}) \end{aligned} \quad (7)$$

As shown in Ref[1], reconstruction of optical quantum state need to measure quadrature amplitude distributions of different phase angle by orthogonal phase-rotated transformation. So we must get optical field orthogonal phase-rotated transformation by empty cavity. For the sake of this reason, we will select the suitable cavity full-width $2\Omega_\pi$ that is smaller than the measured sideband frequency Ω . The empty cavity is scanned linearly by the high voltage ramp on the PZT and the detuning frequency range from $-\Omega_\pi$ to Ω_π . Using Eqs.(1) and (2), we obtain

$$\begin{aligned} \theta(\phi_0 - \frac{\Omega L}{c}) &= \pi \\ \theta(\phi_0 - \frac{\Omega L}{c}) &= \pi \quad -\frac{\Omega_\pi L}{c} < \phi_0 < \frac{\Omega_\pi L}{c} \end{aligned} \quad (8)$$

$\theta(\phi_0)$ is varied continuously at $[-\pi, \pi]$. So Eq.(7) become a simple form

$$\hat{i}(\Omega) = \frac{1}{\sqrt{2}}(e^{i\theta(\phi_0)}\hat{a}_-^{in} + e^{-i\theta(\phi_0)}\hat{a}_+^{in+}) \quad (9)$$

Eq.(9)is orthogonal phase-rotated transformation[1] when the phase shift angle $\theta(\phi_0)$ is varied continuously from $-\pi$ to π . Thus given the set of the measured quadrature amplitude distributions for the different phase angle θ , the quantum state of optical field can be reconstructed using empty cavity.

3 Conclusion

we propose a self-homodyne detection scheme using the dispersion characteristics of the empty cavity to perform quantum tomography of single-mode which have a strong mean field. Comparing with normal Optical Homodyne Tomography(OHT), the influence of space-mode-matching between the LO and the measured mode to the quantum efficiency is eliminated, and it can also be used to the optical quantum system where LO field is not available. *Acknowledgment.* This research is supported by the National Natural Science Foundation of China (Approval No.69837010), the Excellent Young Teacher Foundation from Education Department of China and the Shanxi Province Science Foundation.

References

1. K. Vogel and H. Risken, Phys. Rev. A **40**, 2847(1989).
2. J. H. Shapiro and A. Shakeel, J. Opt. Soc. Am. B **14**, 232 (1997).
3. G. M. D'Ariano,U. Leonhardt, and H. Paul, Phys. Rev. A **52**, R1801 (1995).
4. G. M. D'Ariano, M. Vasilyev, and P. Kumar, Phys. Rev. A **58**, 636 (1998).
5. T.C Zhang, J.P Poizat, P Grelu, J.F Roch, P Grangier, F Marin, A Bramati, V Jost, M.D Levenson and E Giacobino, Quantum Semiclass.opt. **7**, 601(1995).

Narrowing Central Line of Resonance Fluorescence Spectrum of the V-configuration of a Four-level Atom via Quantum Interference

Fu-Li Li^{1,2} and Shi-Yao Zhu¹

¹ Department of Physics, Hong Kong Baptist University, Hong Kong

² Université Department of Applied Physics, Xian Jiaotong University,
Xian 710049, P. R. China

Abstract. The interaction of a four-level atom consisting of one excited state, two upper levels and one ground state with two coherent fields is considered. We use one field to drive the transition between the excited state and the ground state, and simultaneously apply another field to couple the ground state to the upper-level doublet. We find that when the dipole moments between the upper doublet and the ground state are parallel the central linewidth of resonance fluorescence spectrum of the driven transition can be much narrower than both the linewidth of spontaneous emission of the excited state and of the upper doublet due to quantum interference between two decay pathways from the upper levels to the ground state of the atom.

1 Introduction

The resonance fluorescence spectra of various configurations of a three-level atom have been extensively studied. For the V-configuration of a three-level atom, Narducci et al.[1] found that resonance fluorescence spectrum of one driven transition can be controlled by applying a coherent field to another transition. In special, linewidths of both the central peak and the sidebands is determined by spontaneous decay rate of the applied transition but not the driven transition itself when the applying field is sufficient strong[1,2]. Therefore, if the applied transition decays very slowly, the linewidth of resonance fluorescence of the driven transition can become much narrow. Gauthier, Zhu and Mossberg[3] have experimentally proved the theoretical prediction. From these previous excellent studies, we realize that in order to make the spectral linewidth narrowing further, for a given decay rate of the applied transition, it is necessary to depress the spontaneous emission through the applied transition channel.

In this paper, we consider the V-configuration of a four-level atom interacting with two coherent fields. We investigate how to control spectral linewidth of the resonance fluorescence spectrum via quantum interference.

2 Description of the Model

The atomic level scheme under consideration is shown in Fig.1. The transition from the excited state $|a\rangle$ to the ground state $|c\rangle$ is driven by a coherent field at frequency ω_{L1} (referred to as "driven transition"). The ground state is also coupled to the upper levels $|b_1\rangle$ and $|b_2\rangle$ by another coherent field at frequency ω_{L2} (referred to as "applied transition"). We suppose that transitions from $|a\rangle$ and $|b_{1,2}\rangle$ to $|c\rangle$ are also coupled by the vacuum modes of electromagnetic field. Meanwhile, we assume that the vacuum modes which couple $|b_1\rangle$ to $|c\rangle$ and $|b_2\rangle$ to $|c\rangle$ are same and the dipole transitions between $|b_{1,2}\rangle$ and $|a\rangle$ are forbidden because of the same parity.

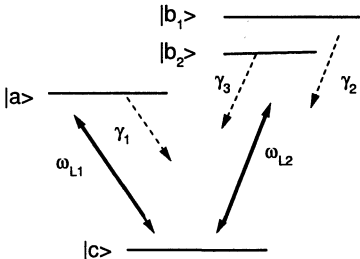


Fig. 1. Schematic representation of the V-configuration of a four-level atom.

With the rotation-wave approximation, we write the model Hamiltonian as

$$\hat{H} = \hat{H}_0 + \hat{V}_C + \hat{V}_{Ra} + \hat{V}_{Rb} \quad (1)$$

where

$$\begin{aligned} \hat{H}_0 = & \hbar\omega_c|c\rangle\langle c| + \hbar\omega_a|a\rangle\langle a| + \hbar\omega_{b_1}|b_1\rangle\langle b_1| \\ & + \hbar\omega_{b_2}|b_2\rangle\langle b_2| + \hbar\sum_q\omega_qa_q^+a_q + \hbar\sum_k\omega_kb_k^+b_k, \end{aligned} \quad (2)$$

$$\begin{aligned} \hat{V}_C = & \hbar\Omega_1e^{-i\omega_{L1}t}|a\rangle\langle c| + \hbar\Omega_2e^{-i\omega_{L2}t}|b_1\rangle\langle c| \\ & + \hbar\Omega_3e^{-i\omega_{L2}t}|b_2\rangle\langle c| + H.c., \end{aligned} \quad (3)$$

$$\hat{V}_{Ra} = \hbar\sum_q[g_qa_q|a\rangle\langle c| + g_q^*a_q^+|c\rangle\langle a|], \quad (4)$$

$$\hat{V}_{Rb} = \hbar\sum_k[g_k^{(1)}b_k|b_1\rangle\langle c| + g_k^{(2)}b_k^+|b_2\rangle\langle c| + H.c.]. \quad (5)$$

In the above, $a_q(a_q^+)$ is the annihilation (creation) operator for the q th mode of the vacuum which couples $|a\rangle$ to $|c\rangle$, and $b_k(b_k^+)$ for the k th mode of the vacuum which couples $|b_{1,2}\rangle$ to $|c\rangle$.

We denote the parallelism of the dipole moment matrix elements $\vec{\mu}_{b_1c}$ and $\vec{\mu}_{b_2c}$ by a parameter p . When $p \neq 0.0$ the two decay pathways from $|b_1\rangle$ and $|b_2\rangle$ to $|c\rangle$ are correlated and thus as the atom decays from the excited sublevel $|b_1\rangle$ it drives the excited sublevel $|b_2\rangle$ decaying and vice versa. In other words, the two decay pathways can have a quantum interference. It is the destructive quantum interference that results in the depression of spontaneous emission[4-7].

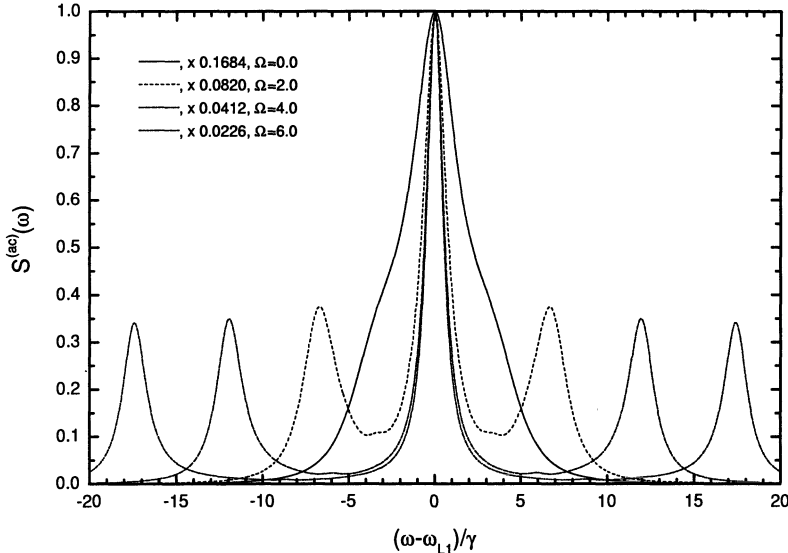


Fig. 2. Resonance fluorescence spectra of the driven transition for $\Omega_1 = 2.0$, $\gamma_1 = 3.0$, $\gamma = 1.0$, $\Delta_1 = 0.0$, $\Delta_2 = -\Delta_3 = \omega_{b_1 b_2}/2$, $\omega_{b_1 b_2} = 1.0$, $p = 0.0$ and different values of Ω as given in the figure.

3 Results and Discussions

The incoherent part of resonance fluorescence spectrum of the driven transition can be calculated by employing the approach given in [1,7]. In our calculations, detunings $\Delta_1 = \omega_a - \omega_c - \omega_{L1}$, $\Delta_2 = \omega_{b_1} - \omega_c - \omega_{L2}$, $\Delta_3 = \omega_{b_2} - \omega_c - \omega_{L2}$, and Rabi frequencies, detunings and decay constants are scaled by the spontaneous emission rate of the upper doublet($\gamma = \gamma_2 = \gamma_3$). Correspondingly, the time is scaled by γ^{-1} and the spectrum of resonance fluorescence of the driven transition is scaled by $|\vec{\mu}_{ac}|^2 \gamma^{-1}$. In Fig.2, the resonance fluorescence spectra of the driven transition for different values of

the Rabi frequency $\Omega (= \Omega_2 = \Omega_3)$ of the applied transition are shown. Here, each of the spectra is rescaled by its highest peak which value is marked in the figure. Unless otherwise specified, in the whole paper, we always plot the spectra in this way. In Fig.2, we observe that the spectrum changes from the wide single peak to the triplet when the applying field is switched on. We notice that both the sidebands and the central peak become narrowing with increasing the Rabi frequency of the applying field. The narrowest width of the central peak is bounded by the natural linewidth of the applied transition[1,2].

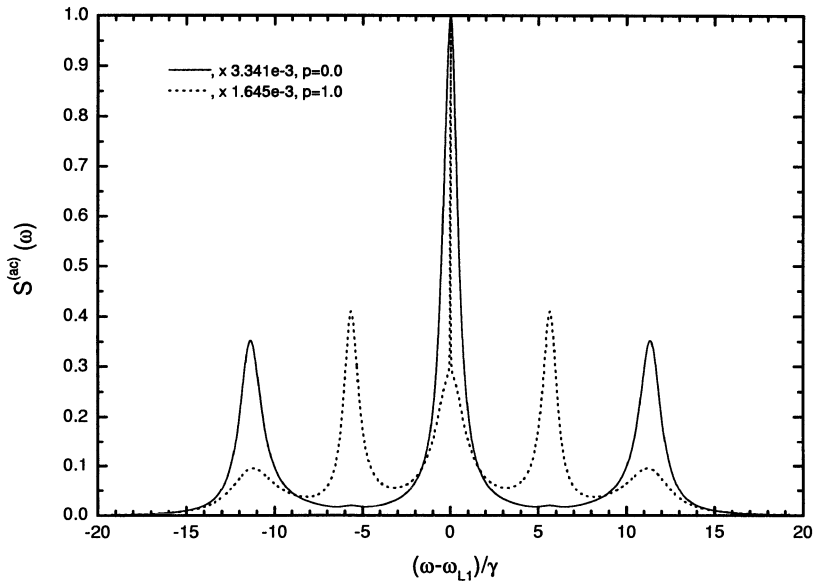


Fig. 3. Resonance fluorescence spectra of the driven transition for $\gamma_1 = 3.0$, $\gamma = 1.0$, $\Delta_1 = 0.0$, $\Delta_2 = -\Delta_3 = \omega_{b_1 b_2}/2$, $\omega_{b_1 b_2} = 1.0$, $\Omega = 4.0$ and $\Omega_1 = 0.5$

In Fig.3, the spectra of the driven transition are shown for both $p = 0.0$ and $p = 1.0$. We observe that when the quantum interference takes place($p = 1.0$) an ultranarrow central peak appears and stands on a wide background in each of the spectra. From this figure, we see that the quantum interference can make the half-maximum-width of the central peak much narrower than the natural linewidth of the applied transition.

The quantum interference is sensitive to the parameter p . In Fig.4, the central peaks of spectra of the driven transition for different values of p are shown. We see that the ultranarrow central peak exists only when p is very close to 1.0.

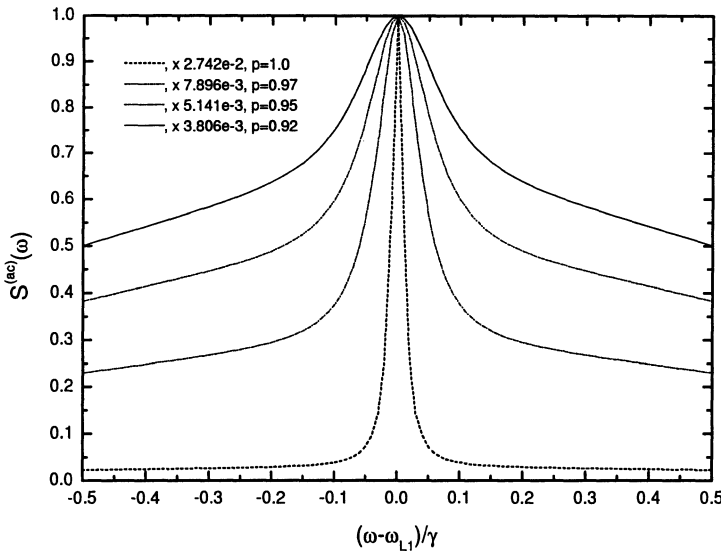


Fig. 4. Central peaks of the resonance fluorescence spectra of the driven transition for different values of p which are marked in the figure. Other parameters are the same as in Figs. 3 but $\Omega_1 = 1.0$ and $\gamma_1 = 10.0$.

Since resonance fluorescence of a driven atom can be explained as decaying of dressed states of the combined atom-field system in vacuum, the above result can be well understood in the dressed state representation. We can show that because of the quantum interference the present system has two dressed states which decay very slowly through the applied transition channel and are well populated at steady state. This is the reason why the ultranarrow central line in the resonance fluorescence spectrum of the driven transition appears when the quantum interference takes place. The detail results will be shown elsewhere.

4 Summary

We have investigated the resonance fluorescence spectrum of the V configuration of a four-level atom. We show that for the parallel or nearly parallel case of the two dipole moments between the upper levels and the ground state, there may exist a destructive quantum interference in the two decay pathways from the upper levels to the common ground state. This destructive quantum interference results in an ultranarrow peak at the center position of the resonance fluorescence spectrum of the driven transition.

Acknowledgments. This work was supported by HKBU and UGC. F.L.Li also acknowledges support from the National Natural Science Foundation of China.

References

1. L. M. Narducci, M. O. Scully, G.-L. Oppo, P. Ru and J. R. Tredicce, Phys. Rev. **A42**, 1630(1990).
2. C. H. Keitel, L. M. Narducci and M. O. Scully, Appl. Phys. **B60**, S153(1995).
3. D. J. Gauthier, Y. F. Zhu and T. W. Mossberg, Phys. Rev. Lett. **66**, 2460(1991).
4. S. Y. Zhu and M. O. Scully, Phys. Rev. Lett. **76**, 388(1996).
5. H. R. Xia, Cen-Yun Ye and S. Y. Zhu, Phys. Rev. Lett. **77**, 1032(1996).
6. P. Zhou and S. Swain, Phys. Rev. Lett. **77**, 3995(1996); Phys. Rev. **A56**, 3011(1997).
7. F. L. Li and S. Y. Zhu, Phys. Rev. **A59**, 2330(1999); Opt. Commun. **162**, 155(1999).

A Proposal for Realizing BEC of ^{133}Cs Atoms in Blue-Detuned Ar^+ Hollow-Beam Trap

Jianping Yin¹, Weijian Gao¹, Yiqiu Wang²

¹ Department of Physics, Suzhou University Suzhou, Jiangsu 215006, P. R. China
Department of Electronics, Peking University Beijing 100871, P. R. China

² Université Department of Electronics, Peking University Beijing 100871, P. R. China

Abstract. We propose an all-optically-cooled and -trapped Cs BEC scheme, which is composed of a pyramidal-hollow-beam gravito-optical trap (PHB GOT) from a diode laser and a conical-hollow-beam (CHB) GOT from an Ar^+ laser. In the PHB GOT, the cold atoms experience an efficient hollow-beam induced Sisyphus cooling and repumping-beam induced geometric cooling, and they will be cooled to a few photon-recoil limits from MOT's temperature ($\sim 60 \mu\text{K}$). Whereas in the Ar^+ hollow-laser-beam trap, cold atoms will be further cooled by Raman cooling and compressed by a blue-detuned cover beam. We have performed Monte-Carlo simulations for PHB cooling process, calculated the optical potential for ^{133}Cs atoms in Ar^+ hollow laser beam, and estimated total atomic loss and density. Our study shows that an optically-trapped Bose-Einstein condensation (BEC) of ^{133}Cs atoms may be observed in our all-optical dipole trap.

1 Introduction

Since the first Bose-Einstein condensation (BEC) was observed by a JILA group in 1995[1], a series of magnetically-trapped and evaporative-cooled BECs in various atomic gases (such as H, ^7Li , ^{23}Na and ^{87}Rb) have been reported by nineteen groups in the world, respectively. But no BEC to date has been realized in a pure optical atom trap except for the transferring a Na BEC from a magnetic trap to a red-detuned optical trap [2]. Due to extremely-unusual elastic and inelastic collision properties of ^{133}Cs atoms in magnetic trap, all attempts to observe a magnetically-trapped cesium BEC by evaporative cooling have been failed so far. It is well known that the BEC of Cs atoms would be an important step in the improvement of primary time and frequency standard. In addition, a blue-detuned, dark optical trap allows all magnetic sub-levels to be both trapped and cooled, and maybe provide a better elastic and inelastic collision property compared with that in a magnetic trap. So it would be interesting and worthwhile to explore the possibility of an optically-trapped Cs BEC by using dark-hollow-beam cooling and trapping.

In this paper, we propose an all-optically-cooling and trapping scheme for Cs atomic BEC, which consisted of a PHB GOT from a diode laser and a CHB

GOT from an Ar⁺ laser. Both blue-detuned PHB and CHB are propagated along the vertical direction towards and overlapped well. First, cold atoms in a standard Cs MOT ($\sim 60 \mu\text{K}$) are loaded into PHB GOT. Due to ac stark effect, cold atoms in the PHB trap will experience an efficient hollow-beam induced Sisyphus cooling and repumping-beam induced geometric cooling, and they will be cooled to a few photon-recoil limits. Secondly, by blocking the PHB, the cold atoms with a temperature of $\sim 2 \mu\text{K}$ are loaded into a far-blue-detuned Ar⁺ hollow-laser-beam GOT. Then, by using Raman cooling, cold atoms in the CHB GOT are further cooled to below one recoil limit, and obtained an ultracold Cs atomic sample with a temperature of $\sim 0.08 \mu\text{K}$. Finally, a blue-detuned cover beam propagated in transverse direction is used to compress the ultracold Cs atomic cloud, and an all-optically-trapped BEC will be explored. We have done Monte-Carlo simulations for PHB cooling process, and calculated the trapping potential for ¹³³Cs atoms in Ar⁺ hollow laser beam. We also have estimated total atomic loss and density, and discussed the possibility of an optically-trapped BEC in our scheme.

2 PHB cooling and trapping of Cs atoms

Fig.1 shows the scheme of pyramidal-hollow-beam GOT for Cs atoms. When the central part of a collimated doughnut hollow beam (DHB) with blue detuning is blocked by a black square plate, and the DHB is focused by a convergent lens with an adjustable focal length f , a dark pyramidal-hollow-beam GOT can be formed above the focal point of the lens. The DHB comes from a diode laser with $p_0 = 500 \text{ mW}$ and $\lambda = 0.852 \mu\text{m}$; When $\delta = 1 \sim 5 \text{ GHz}$, the trapping potential in the lower hyperfine ground state is far higher than the MOT's temperature ($60 \mu\text{K}$); The blue-detuned plug overlaps with the conical DHB, which can be used to manipulate the cold atoms dropped from the MOT by moving up or down.

To introduce an efficient Sisyphus cooling and geometrical cooling, a weak, near-resonant repumping beam (RPB) is propagated down and overlapped with the DHB. Cold atoms are loaded into the PHB GOT from a standard MOT. When the atoms bounce inside the DHB, they will experience the DHB-induced Sisyphus cooling and the RPB-induced geometrical cooling, which can cool directly the atoms to a few photon recoil limit ($\sim 1 \mu\text{K}$) from the Cs MOT's temperature ($60 \mu\text{K}$). Moreover, the cooling rate, the 3D equilibrium temperature, the trapping volume and atomic density in the PHB GOT can be controlled easily by adjusting the divergent angle of the PHB (i.e., by changing the focal length of the lens), or moving the plug beam up or down.

The hollow-beam cooling mechanism of trapped atoms was introduced Ref.[3], and the equilibrium rms momentum is given by:

$$-\frac{1}{3} \frac{\Delta_{hfs}}{\delta + \Delta_{hfs}} \left(\frac{p_{rms}}{\hbar k} \right)^2 - \frac{\sin \theta}{q_{rep}} \frac{p_{rms}}{\hbar k} + \frac{1}{q_{rep}^2} + \frac{1}{1 - q_{PHB}} = 0 \quad (1)$$

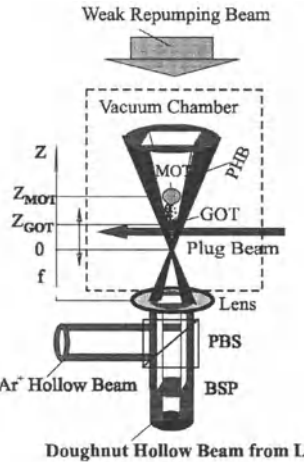


Fig. 1. Pyramidal-hollow-beam GOT of Cs atoms.

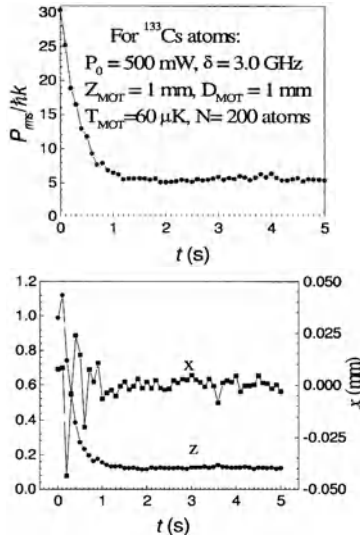


Fig. 2. The results of Monte-Carlo simulations: (a) Equilibrium rms momentum and (b) mean z-position of 200 ^{133}Cs atoms being dropped from 1 mm above the tip of PHB at $t=0$ with an initial momentum of $30 \hbar k$.

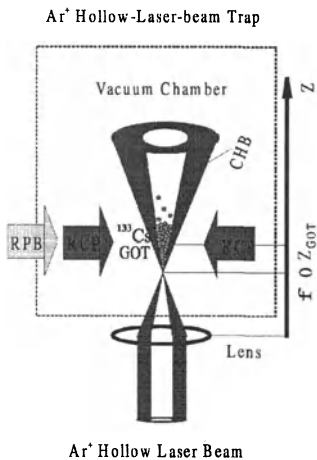
where $q_{rep}(q_{PHB})$ is the transition probability of an atom from $|1, n >$ to $|2, n-1 >$ after absorbing a repumping photon (a PHB photon).

We have performed Monte-Carlo simulations for the dynamical process of PHB cooling, the results are shown in Fig.2. When $N = 200$ ^{133}Cs atoms, $\lambda_A = 0.852 \mu\text{m}$, $T_{MOT} = 60 \mu\text{K}$, $z_{MOT} = 1\text{mm}$, $D_{MOT} = 1\text{mm}$, and the diode laser power $P_0 = 500\text{mW}$, $\delta = 3.0\text{GHz}$, $\theta = 30^\circ$, we have obtained $\langle z_{GOT} \rangle \approx 0.13\text{mm}$, $P_{rms} \approx 5.3\hbar k$ ($T \approx 1.8 \mu\text{K}$), which is consistent with the theoretical result ($P_{rm} = 3.8\hbar k$) from Eq.(1).

3 Ar⁺ HLB GOT and Raman cooling of Cs atoms

After the atomic sample in PHB GOT reach its 3D equilibrium temperature, cold atoms will be loaded into an Ar⁺ hollow-laser-beam GOT (CHB GOT) by removing the PHB and repumping beam.

We have calculated the trapping potential of Ar⁺ conical hollow beam for ^{133}Cs atoms, When $\delta = 2.468 \times 10^5 \text{GHz}$, $P_0 = 20 \text{ W}$ (30 W), and $\theta = 30^\circ$, $z = z_{GOT} = 0.13\text{mm}$, the trapping potential $U_{max} > 70 \mu\text{K}$ (105 μK), which is far higher than $T_{GOT} \approx 1.8 \mu\text{K}$ and also far higher than the gravity potential $mgz/k_B = 20.4 \mu\text{K}$.



GOT--Gravito-optical trap, CHB-- conical hollow beam
RPB -- repumping beam, RCP-- Raman cooling pulse

Fig. 3. Raman cooling scheme of Cs atoms n the Ar^+ CHB GOT.

Optically-trapped Cs BEC

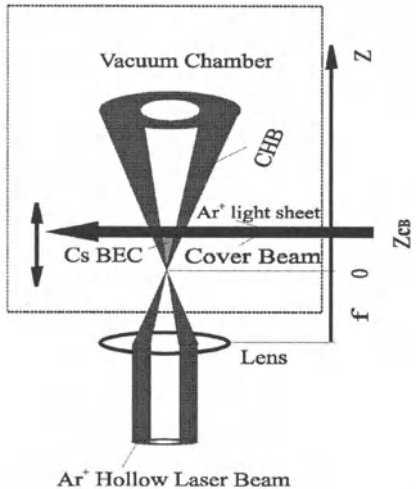


Fig. 4. The compressing scheme of ultracold Cs atoms in the Ar^+ conical-hollow-beam GOT.

The blue detuning of the Ar^+ laser related to the resonant frequency of Cs atom is far larger than the obtainable detuning of the diode laser with $\lambda = 0.852 \mu\text{m}$, and the spontaneous-emission rate of atoms in blue-detuned Ar^+ hollow-laser-beam trap is only about $10^{-3} \sim 10^{-4}/\text{s}$, which is ~ 300 times smaller than that in red-detuned optical dipole trap under the same beam parameters [4]. So the blue-detuned Ar^+ laser trap is very useful and desirable for the exploration of an optically-trapped BEC.

After cold atoms are loaded into the Ar^+ hollow-laser-beam GOT from the PHB GOT with $\lambda_A = 0.852 \mu\text{m}$, they will be further cooled by Raman cooling, the corresponding cooling scheme is shown in Fig.3.

Recently, S. Chu's group demonstrated a Raman cooling of Na atoms in a blue-detuned pyramidal gravito-optical trap (which is composed of four elliptical sheets of light) and obtained an ultracold atomic sample with a temperature of $\sim 1 \mu\text{K}$ ($T \approx 0.4T_{rec}$) [5]. Due to a smaller geometric size ($< 500 \mu\text{m}$) and weaker trapping potential ($\sim 9T_{rec}$), their loading efficiency ($< 5\%$) and atomic density ($\sim 4 \approx 10^{11}/\text{cm}^3$) in the GOT were limited. In our Ar^+ CHB GOT, however, there are not these problems. So we can obtain higher loading efficiency and atomic density. If using the results of Chu's group, $T \approx 0.4T_{rec}$ [5], we can get an ultracold and dense Cs atomic sample with a temperature of $\sim 0.08 \mu\text{K}$.

4 The possibility of an optically trapped Cs BEC

After Raman cooling, we can further compress the ultracold Cs atomic sample in Ar^+ hollow-beam trap by using a blue-detuned cover beam (see Fig.4), which is an elliptical Ar^+ laser sheet with $P_0 = 1000\text{mW}$ and $2a = 1100 \mu\text{m}$ and $2b = 15 \mu\text{m}$ [4–5].

When the temperature of Cs atomic sample is $T = 0.08 \mu\text{K}$ (which is the result of Raman cooling), the BEC density is given by

$$n_{BEC} = 2.612 \left(\frac{P_{rms}^2}{6\pi\hbar^2} \right)^{\frac{3}{2}} = 4.915 \times 10^{12} \quad (\text{atoms/cm}^3) \quad (2)$$

If the height of ultracold Cs atomic cloud is compressed downwards to be $z_{CB} = 20 \mu\text{m}$, the atomic density without considering any atomic collision loss in the trap is shown in Fig.5

In Ar^+ laser trap, we can obtain an ultrahigh atomic density, and it can be adjusted by changing the focal length f of the lens. From Fig.5, the trapped atomic number N should be larger than 10^4 in order to reach BEC. In this Ar^+ hollow-laser-beam trap, when the pressure in the vacuum chamber is lower than 10^{-11} Torr, the hyperfine changing collision between the two different ground-state atoms and the three-body recombination between three ground-state atoms in the dark region of the hollow-beam trap become two dominant losses. The total loss rate can be estimated by [6]

$$\gamma_{HBT} = \frac{1}{n} \frac{dn}{dt} \approx \eta_{ug} \beta_{ggc} n + L n^2 \quad (3)$$

where η_{ug} is the fraction of atoms in upper hyperfine ground state in MOT, β_{ggc} is the rate coefficient of hyperfine changing collision, L is the rate coefficient of three-body recombination. For Cs atoms, $\eta_{ug} \approx 10^{-4} \sim 10^{-5}$, $\beta_{ggc} \approx 10^{-11} \text{cm}^3/\text{s}$, $L \approx 5 \times 10^{-29} \text{cm}^6/\text{s}$. When $N = 10^5$ atoms, $z_{CB} =$

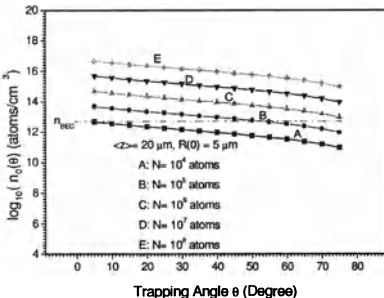


Fig. 5. The dependence of lossless atomic density of Cs atoms in the Ar^+ CHB GOT on the trapping angle.

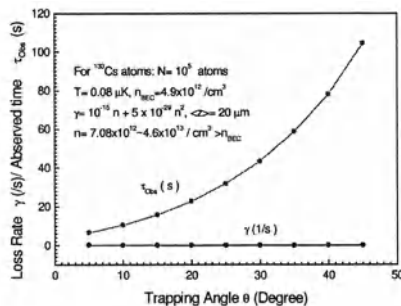


Fig. 6. The dependence of loss rate of Cs atoms in the CHB GOT and its observed time on the trapping angle.

$20 \mu\text{m}$, $n = 7.1 \times 10^{12} \sim 4.6 \times 10^{13}/\text{cm}^3$, and $n > n_{BEC} = 4.915 \times 10^{12}/\text{cm}^3$, the loss rate is shown in Fig.6.

From Fig.6, when trapping angle $\theta = 5^\circ \sim 45^\circ$, and $N \geq 10^5$ atoms, the loss rate $\gamma_{HBT} \approx 0.14 \sim 0.01/\text{s}$ at the density $n \geq n_{BEC}$, the corresponding observed time $\tau_{Obs} > 7 \sim 100\text{s}$, which is long enough to observe an optically-trapped Cs BEC in our Ar^+ laser trap.

5 Conclusion

In this paper, we have proposed and studied a novel scheme of all-optically-cooled and trapped Cs BEC, and found that:

(1) The results of Monte-Carlo simulation show that hollow-beam induced Sisyphus cooling and repumping-beam induced geometric cooling in PHB GOT can cool the Cs atoms from MOT's temperature ($60 \mu\text{K}$) to $2 \mu\text{K}$;

(2) In Ar^+ hollow-beam GOT with a power of 30W , the trapping potential ($> 105 \mu\text{K}$) is high enough to collect and trap all cold atoms loaded from the PHB GOT ($\sim 2 \mu\text{K}$), and spontaneous emission rate is lower than $0.001/\text{s}$. So such Ar^+ laser trap is very useful and desirable in the experiments of Raman cooling and an optically trapped BEC.

(3) By using Raman cooling, an ultracold Cs atomic sample with a temperature of $\sim 80nK$ could be obtained. In the Ar^+ laser trap, when trapped atomic number $N \geq 10^5$, and at the density $n \geq n_{BEC}$, the loss rate $\gamma_{HBT} \approx 0.14 \sim 0.01/\text{s}$, the corresponding observed time $\tau_{Obs} > 7 \sim 100\text{s}$. So it may be possible to realize an optically-trapped Cs BEC in our pure optical trap.

In addition, all of BECs to date were realized by evaporative cooling, the condensed atomic number in magnetic traps is $10^3 \sim 10^6$ atoms so that the output lasting time of CW atom laser with 5×10^5 condensed atoms is only 100ms , whereas it needs about 30s time to prepare a BEC. Therefore, to realize the output of a real CW atom laser, one first need to generate a BEC with more than 5×10^7 condensed atoms, which is difficult to be obtained by using the conventional evaporative cooling in magnetic traps. However, by using Raman cooling in a blue-detuned optical dipole trap, one may obtain a BEC with $\sim 10^8$ condensed atoms when the atomic number in the first MOT is 10^9 atoms. So it is possible to generate a real CW atom laser by using a Raman cooled and optically-trapped BEC.

References

1. M. H. Anderson, et al, Science, **269**, 198 (1995)
2. D. M. Stamper-Kurn, et al, Phys. Rev. Lett., **80**, 2027 (1998)
3. Jianping Yin, et al, Phys. Rev. A, **57**, 1957 (1998)
4. N. Davidson, et al, Phys. Rev. Lett., **74**, 1311 (1995)
5. H. J. Lee, et al, Phys. Rev. Lett., **76**, 2658 (1996)
6. Jianping Yin, et al, Opt. Commun., **152**, 421 (1998)

Realization of the Long-Term Continuous Output for an Atom Laser: A Proposal

Yiqiu Wang, Xiaoji Zhou, Donghai Yang

Department of Electronics, Peking University, Beijing, 100871, China

Abstract. We propose a scheme for realizing the long-term continuous output of an atom laser. The process of the phase unification of the new entered BEC atoms with the remaining atoms in the main BEC trap, the coupling of the atoms from the subsidiary BEC to the main BEC and the time rates of all the different processes are discussed in this scheme. The duration of the continuous output of the atom laser beam is actually unlimited and thus creates the possibilities of their practical application.

In recent years the atom laser has become the most attracting hot point in the area of researches on the optics and atomic physics, since the Bose-Einstein Condensation (BEC) in dilute atomic gases was realized in 1995 [1], and, especially, after the first atom laser appeared in 1997[2]. The pulsed[2], quasi-continuous output [3] or continuous atom laser beam with very short duration in the order of several tens[4] were obtained so far, but this is far away from the practical use of the atom lasers. The main problem for realizing the real long-term continuous wave (cw) output of an atom laser is to refill atoms continuously into the BEC trap to compensate for the output loss. In this paper we present a scheme to realize it, as shown in figure.

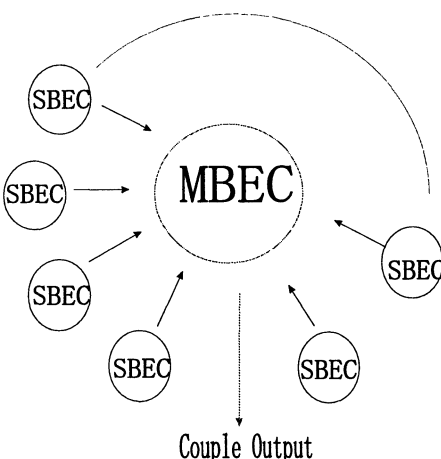


Fig. 1. A scheme for realization of a cw output of atomic matter wave.

A main Bose-Einstein Condensate (MBEC) serves as the source for the useful output beam of atom laser, and several subsidiary Bose-Einstein Condensates (SBEC) around the MBEC are constructed.. The temperature of the SBEC keeps somewhat lower than that of MBEC. The reducing of condensed atoms in MBEC due to extract them outside will be compensated by adding the cold atoms from one of the SBECs, which have been prepared earlier. In the MBEC, the injected atoms will mix with the remaining atoms in it and reach the same phase very rapidly. Before exhausting a part of condensed atoms in MBEC, which has already been filled with the atoms from first SBEC, we couple the atoms in from another SBEC to sustain the process of the cw output of coherent atomic beam. In the meantime, the first SBEC is prepared again for next time use. In this way the MBEC is sequentially refilled by atoms from several SBECs one by one in turn and continuously produces the coherent atomic beam.

To realize this scheme several problems must be considered. First, will the cold atoms newly coupled in from one of the SBECs merge with the remaining ones in the MBEC and are they phase coherent? Secondly, how to guide the atoms from SBEC into the MBEC without changing the phase of the MBEC? The third problem is how many SBEC are needed to construct? We will discuss these problems subsequently.

We can attribute a definite phase to a certain BEC[5,6]. As in the situation of light laser, the atom trap plays the role of cavity and determines the phase, thus the characteristics of coherent atom beam. In our scheme the phase of the MBEC is a phase standard[6]. When the small atomic cloud from SBEC enter into the MBEC trap, a relative phase of zero will be setup between two atomic clouds from two condensates. It can be thought as a process of phase unification. As indicated by J. Javanainen and Yoo[7], phase appears in a condensate instantaneously, no time and no interaction between the atoms are needed to communicate the phase throughout the condensate. So the process of unification of the phase, i.e. the transition of the original phase of atoms from SBEC to that of atoms in the MBEC is the same process of merging two BEC into common one. In the process of formation of BEC there is a Bose stimulation which can lead to matter-wave amplification and constitutes the gain mechanism of an atom laser[8,9]. The condensate grows very rapidly (in the order of several tens to hundreds milliseconds) when there already exists a substantial condensate fraction and the speed is depending upon the original number of condensed atoms in the trap and the sort of atoms. From this concept we may expect, when the atoms from SBEC are being injected into the MBEC(the condensed atoms in MBEC serve as "seeds"), they will quickly merge together into common one, whose characteristics are mainly determined by the MBEC.

The growth of a condensate can be described by a rate equation [7,8],while it has already been formed. But in our particular case we should consider that the new coming atoms from SBEC bring about some kinetic energy (they

come with some velocity) into MBEC. Therefore, to overcome the temperature rising effect we carry out the evaporative cooling during the addition of atoms from SBEC to the MBEC.

Now we discuss the problem of coupling out and guiding the atoms from SBEC into the MBEC without disturbing the state of condensate. Many coupling methods have been proposed, such as radio-frequency[10] , quantum tunneling [11], Raman transition [12], and some guiding techniques, for example, the magnetic guide [13], the evanescent wave hollow fiber [14] have been presented. It seems that they are all plausible for our use. However, considering the trap field requires extremely stable, the most suitable and convenient method maybe is the Raman transition. In Raman transition a coherent, stimulated Raman process extracts atoms from a SBEC trap and gives the output-coupled BEC fraction a well-defined momentum[3]. Furthermore, we can control the direction, speed and number of output atoms. The Raman process plays both the roles of output coupler and guiding the condensed atoms from SBEC to MBEC. The coupling can be made by either pulsed or continuous ways.

The time of constructing a BEC is different with different kinds of atom. This time determines the number of SBECs needed for cw output of the MBEC. The process of extracting of condensed atoms from SBEC, which takes about few milliseconds, is much faster than the process of the BEC formation (seconds)[15]. Let T denotes the constructing time for a SBEC condensate, n is the total number of SBECs, N the number of condensate atoms in one of SBEC and ρ is output rate. The number of SBECs needed for sustain the cw output of an atom laser is then equal to $n = T\rho/(N - 1)$. For sodium suppose $T = 10$ s, $\rho = 10^6$ s, and $N = 10^6$, we need the number of SBECs $n = 10$. In the case of rubidium, we may need more SBECs for maintaining the laser cw output.

In summary, we propose a scheme for realizing the long-term continuous output of an atom laser. In this scheme the exhausting condensed atoms in MBEC, which serves for the continuous coupling out of an atom laser beam, will be prevented by refilling cold atoms from several SBEC one by one in turn. We have clarified that the new coming cold atoms from SBEC will quickly merge with the remaining condensed atoms in MBEC and the phase unification process takes place synchronously with the process of the merging. To overcome the temperature rising in the MBEC the evaporative cooling is carrying out during the process of refilling. The rate equilibrium needed between the atoms coupling' out and the refilling in is discussed and leads to the least number of the subsidiary BECs, necessitated for satisfying the cw output. Thus we realize in principle an unlimited duration of the continuous output of an atom laser beam and create the possibilities of their practical application. The essential of our scheme is to solve the problem of unmatchable time difference between the long formation of a BEC and the short extraction of condensed atoms from BEC trap. Our scheme may be

also referred as a multi-cavity (trap) atom laser. In the view of the present experimental condition our scheme seems a realizable method for cw output of an atom laser.

Acknowledgment. We are grateful to Prof. Liyuan Zhang and Dr. Xuzong Chen for useful discussion. This work is partially supported by National Natural Science Foundation of China.

References

1. M. Anderson, J.R. Ensher, M.R. Mathews *et.al.* *Science* **269**, 189 (1995).
2. M-O. Mewes, M.R. Anderson, D.M. Kurn, *et.al.* *Phys. Rev. Lett.* **78**, 582 (1997).
3. E.W. Hagley, L. Deng, M. Kozuma, *et.al.* *Science* **283**, 1706 (1999).
4. I. Bloch, T.W. Hansch, and T. Esslinger, *Phys. Rev. Lett.* **82**, 3008 (1999).
5. S.M. Barnett, K. Burnett, and J.A. Vaccaro, *J. Res. NIST* **101**, 593 (1996).
6. J.A.Dunningham and K. Burnett, *Phys. Rev. Lett.* **82**, 3729 (1999).
7. J. Javanainen, S. M. Yoo, *Phys. Rev. Lett.* **76**, 161 (1996).
8. H.-J. Miesner, D. M. Stamper-Kurn, M. R. Andrews *et.al.* *Science* **279**, 1005 (1998).
9. C. W. Gardiner, M. D. Lee, R. J. Ballagh *et al.* *Phys. Rev. Lett.* **81**, 5266 (1998); C. W. Gardiner, P. Zoller *et al.* *Phys. Rev. Lett.* **79**, 1793 (1997).
10. R. J. Ballagh, K. Burnet, T. F. Scott, *Phys. Rev. Lett.* **78**, 1607 (1997).
11. M. W. Jack, M. J. Collett, D. F. Walls, *Phys. Rev. A* **54**, R4625 (1996).
12. C. M. Moy, I. J. Hope, C. M. Savage, *Phys. Rev. A* **55**, 3631 (1997).
13. D. J. Li, H. Huang *et al.*, *Opt. Commun.* **160**, 72 (1999).
14. J. P. Yin, Y. F. Zhu and Y. Z. Wang, *Phys. Rev. A* **57**, 1957 (1998).
15. <http://amo.phy.gason.edu/bec.html>.

Dynamics of Atom–Cavity System and Elimination of Momentum Recoil

Li-Xiang Cen¹ and Shun-Jin Wang^{1,2}

¹ Department of Modern Physics, Lanzhou University, Lanzhou 730000,
P.R.China

² Institute of Modern Physics, Southwest Jiaotong University, Chengdu 610031,
P.R.China

Electronic address: gontp@spin.lzu.edu.cn

Abstract. We describe the dynamics of an atom-cavity system of Ξ configuration with the center-of-mass motion included. An linear expression of the Hamiltonian is obtained and by examining the evolution properties of the system, we show that the momentum recoil effect can be eliminated under certain conditions.

1 Introduction

Quantum-optical interactions of atoms with coherent fields may be studied at different levels of sophistication. In early works of quantum optics [1,2] the attention was simply concentrated on the internal atomic transitions without regarding an external motion of the atom. However, with the development of cavity quantum electrodynamic techniques, one needs to describe the system in a more precise standard and the center-of-mass recoil should be taken into account. Such a consideration is also crucial in studies of many fields such as laser cooling of atoms [3,4] and atomic interferometers [5,6].

In this paper, we investigate an atom-cavity system of Ξ configuration with the center-of-mass motion included. We analyze the dynamics of the system and linearize the Hamiltonian in terms of Lie algebraic generators. Then, by examining the evolution properties of the system, we show the momentum recoil of the atom can be eliminated under certain conditions.

2 Dynamics of the system

Consider a three-level atom of Ξ configuration interacting with a two-mode cavity field. Assume energies of the three levels satisfy $E_3 > E_2 > E_1$, and the dipole-induced transitions $|1\rangle \leftrightarrow |2\rangle$ and $|2\rangle \leftrightarrow |3\rangle$ are mediated by photons of the two cavity modes a_1 and a_2 with corresponding frequencies ω_1 and ω_2 . With the atomic motion included, the system is described by the Hamiltonian

$$H = \frac{\mathbf{p}^2}{2m} + \sum_{i=1}^3 E_i \sigma_{ii} + \hbar \omega_1 a_1^\dagger a_1 + \hbar \omega_2 a_2^\dagger a_2 + \hbar(g_1 \sigma_{21} a_1 e^{i\mathbf{k}_1 \cdot \mathbf{r}} + g_2 \sigma_{32} a_2 e^{i\mathbf{k}_2 \cdot \mathbf{r}} + h.c.), \quad (1)$$

where $g_1(g_2)$ is assumed to be real, \mathbf{k}_1 and \mathbf{k}_2 are wave vectors of the two cavity modes. It is easily shown that the system has three invariants

$$N_1 = a_1^\dagger a_1 + 1 - \sigma_{11}, \quad N_2 = a_2^\dagger a_2 + \sigma_{33}, \quad (2)$$

$$\mathbf{P}_i = \mathbf{P}_{tot} - \hbar\mathbf{k}_1(N_1 - 1) - \hbar\mathbf{k}_2N_2 = \mathbf{p} + \hbar\mathbf{k}_1\sigma_{11} - \hbar\mathbf{k}_2\sigma_{33}. \quad (3)$$

Here, N_1 and N_2 are excitation numbers of the two modes, $\mathbf{P}_{tot} = \mathbf{p} + \hbar\mathbf{k}_1a_1^\dagger a_1 + \hbar\mathbf{k}_2a_2^\dagger a_2$ is the total momentum of the system. \mathbf{P}_i is the atomic momentum connected with the intermediate level $|2\rangle$. Introduce notations

$$\begin{aligned} A_{ii}^r &= \sigma_{ii}, \quad A_{12}^r = N_1^{-1/2}\sigma_{12}a_1^\dagger e^{-i\mathbf{k}_1 \cdot \mathbf{r}}, \quad A_{23}^r = N_2^{-1/2}\sigma_{23}a_2^\dagger e^{-i\mathbf{k}_2 \cdot \mathbf{r}}, \\ A_{13}^r &= A_{12}^r A_{23}^r = N_1^{-1/2}N_2^{-1/2}\sigma_{13}a_1^\dagger a_2^\dagger e^{-i(\mathbf{k}_1 + \mathbf{k}_2) \cdot \mathbf{r}}, \quad (A_{ij}^r)^\dagger = A_{ji}^r, \end{aligned} \quad (4)$$

where, $i, j = 1, 2, 3$. One can verify that the above operators span an algebra $\text{su}(3)$ and have the following project property

$$A_{ij}^r A_{kl}^r = \delta_{jk} A_{il}^r, \quad \sum_{i=1}^3 A_{ii}^r = 1. \quad (5)$$

We can now rewrite the Hamiltonian (1) in terms of the operators A_{ij}^r :

$$\begin{aligned} H &= E_0(N_1, N_2, \mathbf{P}_i) + \Delta_1(\mathbf{P}_i)A_{11}^r + \Delta_3(\mathbf{P}_i)A_{33}^r \\ &\quad + [\tilde{g}_1(N_1)A_{12}^r + \tilde{g}_2(N_2)A_{23}^r + h.c.]. \end{aligned} \quad (6)$$

Here, $\tilde{g}_i(N_i) = \hbar\sqrt{N_i}g_i$, $E_0(N_1, N_2, \mathbf{P}_i) = E_2 + \hbar\omega_1(N_1 - 1) + \hbar\omega_2N_2 + \frac{\mathbf{P}_i^2}{2m}$,

$$\begin{aligned} \Delta_1(\mathbf{P}_i) &= \frac{\hbar^2\mathbf{k}_1^2}{2m} - \frac{\hbar\mathbf{P}_i \cdot \mathbf{k}_1}{m} - (E_2 - E_1 - \hbar\omega_1), \\ \Delta_3(\mathbf{P}_i) &= \frac{\hbar^2\mathbf{k}_2^2}{2m} + \frac{\hbar\mathbf{P}_i \cdot \mathbf{k}_2}{m} + E_3 - E_2 - \hbar\omega_2. \end{aligned} \quad (7)$$

Since N_1 , N_2 , and \mathbf{P}_i can be treated as constants in their common eigenspace, the Hamiltonian (6) is a linear expression in terms of the generators A_{ij}^r .

3 Elimination of recoil effect

Generally, atomic transitions between levels will cause a recoil to the atom. However, for a two-photon process the recoil effect can be eliminated in a suitable scheme. The main idea is: the photons of the two modes shall possess equal and opposite momentums; and the detunings of the two transitions $|1\rangle \leftrightarrow |2\rangle$ and $|2\rangle \leftrightarrow |3\rangle$ must be large enough so that the level $|2\rangle$ can be adiabatically eliminated [7]. As a result, the atom will transit between the levels $|1\rangle$ and $|3\rangle$ without changing its momentum. Obviously, these conditions mean that we must tune the wavenumbers as $\mathbf{k}_2 = -\mathbf{k}_1 \equiv k_1\hat{\mathbf{e}}_x$ and the frequencies as $E_3 - E_1 = \hbar\omega_1 + \hbar\omega_2 = 2\hbar\omega_1$. Thus we have: $\Delta_1(\mathbf{P}_i) = \Delta_3(\mathbf{P}_i) \equiv \Delta(P_i)$ (here $\mathbf{P}_i = P_i\hat{\mathbf{e}}_x$). Introduce the following transformation [8]

$$U_g = \exp[\alpha(A_{13}^r - A_{31}^r)] \exp[\beta(A_{23}^r - A_{32}^r)], \quad (8)$$

with $\alpha = \arctan \frac{\tilde{g}_1}{\tilde{g}_2}$ and $\beta = \frac{1}{2} \arctan \frac{2\sqrt{\tilde{g}_1^2 + \tilde{g}_2^2}}{\Delta}$. The dressed Hamiltonian is

$$H' = U_g^{-1} H U_g = E_0 + \Delta A_{11}^r + \lambda_2 A_{22}^r + \lambda_3 A_{33}^r, \quad (9)$$

where, $\lambda_{2,3} \equiv \lambda_{2,3}(N_1, N_2, P_i) = \frac{\Delta}{2} \pm \sqrt{(\frac{\Delta}{2})^2 + \tilde{g}_1^2 + \tilde{g}_2^2}$. Noticing the relation of (5), we can obtain the evolution operator as (setting $\hbar = 1$)

$$U(t) = e^{-iHt} = U_g e^{-iH't} U_g^{-1} = \sum_{i,j=1}^3 U_{ij}(N_1, N_2, P_i) A_{ij}^r, \quad (10)$$

where,

$$\begin{aligned} U_{11}(N_1, N_2, P_i) &= e^{-iE_0 t} [\cos^2 \alpha e^{-i\Delta t} + \sin^2 \alpha (\sin^2 \beta e^{-i\lambda_2 t} + \cos^2 \beta e^{-i\lambda_3 t})], \\ U_{22}(N_1, N_2, P_i) &= e^{-iE_0 t} (\cos^2 \beta e^{-i\lambda_2 t} + \sin^2 \beta e^{-i\lambda_3 t}), \\ U_{33}(N_1, N_2, P_i) &= e^{-iE_0 t} [\sin^2 \alpha e^{-i\Delta t} + \cos^2 \alpha (\sin^2 \beta e^{-i\lambda_2 t} + \cos^2 \beta e^{-i\lambda_3 t})], \\ U_{12}(N_1, N_2, P_i) &= e^{-iE_0 t} \sin \alpha \sin \beta \cos \beta (e^{-i\lambda_3 t} - e^{-i\lambda_2 t}), \\ U_{23}(N_1, N_2, P_i) &= e^{-iE_0 t} \cos \alpha \sin \beta \cos \beta (e^{-i\lambda_3 t} - e^{-i\lambda_2 t}), \\ U_{13}(N_1, N_2, P_i) &= e^{-iE_0 t} \sin \alpha \cos \alpha (\sin^2 \beta e^{-i\lambda_2 t} + \cos^2 \beta e^{-i\lambda_3 t} - e^{-i\Delta t}), \\ U_{ij}(N_1, N_2, P_i) &= U_{ji}(N_1, N_2, P_i), \quad (i, j = 1, 2, 3) \end{aligned} \quad (11)$$

Assume that at $t = 0$ the internal level of the atom is in the ground state, and the density operator of the system can be factorized into three parts

$$\rho(0) = |\Psi_F(0)\rangle \langle \Psi_F(0)| \otimes |\Psi_{p_x}(0)\rangle \langle \Psi_{p_x}(0)| \otimes |1\rangle \langle 1|, \quad (12)$$

where, $|\Psi_F(0)\rangle = \sum_{n_1, n_2} F_{n_1, n_2} |n_1, n_2\rangle$, and $|\Psi_{p_x}(0)\rangle = \int dp_x C(p_x) |p_x\rangle$. To explore the evolution properties of the atomic internal state, we need to investigate two quantities: the population inversion $W(t) = \rho_{33}^A(t) - \rho_{11}^A(t)$ and $\rho_{22}^A(t)$. Here, $\rho^A(t)$ is reduced density operators of the atomic internal state. From Eqs. (10)-(12), one can obtain

$$\begin{aligned} \rho_{22}^A(t) &= \int dp_x \sum_{n_1, n_2} |C(p_x)|^2 |F_{n_1, n_2}|^2 |U_{12}(n_1, n_2, p_x + \hbar k_1)|^2, \\ W(t) &= \int dp_x \sum_{n_1, n_2} |C(p_x)|^2 |F_{n_1, n_2}|^2 [|U_{13}(n_1, n_2, p_x + \hbar k_1)|^2 \\ &\quad - |U_{11}(n_1, n_2, p_x + \hbar k_1)|^2]. \end{aligned} \quad (13)$$

And to investigate the recoil effect of the atom, we need to calculate the momentum distribution function of the atom, $P(p_x, t)$, defined as

$$\begin{aligned} P(p_x, t) &\equiv \rho_{p_x, p_x}^{P_A}(t) \\ &= \sum_{n_1, n_2} |F_{n_1, n_2}|^2 \{ |C(p_x)|^2 |U_{11}(n_1, n_2, p_x + \hbar k_1)|^2 \\ &\quad + |C(p_x - \hbar k_1)|^2 |U_{12}(n_1, n_2, p_x)|^2 \\ &\quad + |C(p_x)|^2 |U_{13}(n_1, n_2, p_x + \hbar k_1)|^2 \}. \end{aligned} \quad (14)$$

As is shown, the above calculations are valid for an arbitrary detuning Δ . To eliminate the middle level $|2\rangle$, we shall consider the large detuning case, namely, $\Delta^2 \gg \tilde{g}_1^2 + \tilde{g}_2^2$. It is easily shown that there is approximate relation: $\sqrt{(\frac{\Delta}{2})^2 + \tilde{g}_1^2 + \tilde{g}_2^2} - \frac{\Delta}{2} \simeq \frac{\tilde{g}_1^2 + \tilde{g}_2^2}{\Delta}$. Hence we can obtain

$$W(t) \simeq \int dp_x \sum_{n_1, n_2} |C(p_x)|^2 |F_{n_1, n_2}|^2 \left[\frac{8\tilde{g}_1^2\tilde{g}_2^2}{(\tilde{g}_1^2 + \tilde{g}_2^2)^2} \sin^2\left(\frac{1}{2}\lambda_2 t\right) - 1 \right],$$

$$\rho_{22}^A(t) \simeq 0, \quad P(p_x, t) \simeq |C(p_x)|^2. \quad (15)$$

As is expected, the atomic internal level $|2\rangle$ has been removed and the population oscillates between levels $|1\rangle$ and $|3\rangle$. Also, the atomic momentum distribution $P(p_x, t)$ retains its initial value during the whole evolution.

4 Conclusion

In conclusion, we have studied the dynamics of an atom-cavity system with atomic motion included. We gave a clear description of the dynamics of the system, and based on it, we show that the elimination of the momentum recoil of the atom is possible under certain conditions.

Acknowledgments. This work was supported in part by the National Natural Science Foundation, the Doctoral Education Fund of the Education Ministry, and the Nuclear Theory Fund of HIRFL of China.

References

1. L. Allen and J.H. Eberly, *Optical Resonance and Two-Level Atoms* (Wiley & Sons, New York, 1975); H.-I. Yoo and J.H. Eberly, Phys. Rep. **118**, 239 (1985); B.W. Shore and P.L. Knight, J. Mod. Opt. **40**, 1195 (1993).
2. J. R. Kuklinski and J. Madajczyk, Phys. Rev. A **37**, 3175 (1988); M. Wilkens, Z. Bialynicka-Birula, and P. Meystre, *ibid.* **45**, 477 (1992).
3. J. Chen, J.G. Story, J.J. Tollet, and R.G. Hulet, Phys. Rev. Lett. **69**, 1344 (1992).
4. T. Zaugg, M. Wilkens, P. Meystre, and G. Lenz, Opt. Commun. **97**, 189 (1993); I. Marzoli, J.I. Cirac, R. Blatt, and P. Zoller, Phys. Rev. A **49**, 2771 (1994).
5. M. Kasevich and S. Chu, Phys. Rev. Lett. **67**, 181 (1991).
6. S. Glasgow, P. Meystre, M. Wilkens, and E.M. Wright, Phys. Rev. A **43**, 2455 (1991).
7. C.C. Gerry and J.H. Eberly, Phys. Rev. A **42**, 6805 (1990); S.-C. Gou, Phys. Lett. A **147**, 218 (1990); M. Alexanian and S.K. Bose, Phys. Rev. A **52**, 2218 (1995).
8. L.-X Cen and S.-J. Wang, *Canonical transformation for three-level system of V configuration and its non-decaying state*, accepted by Phys. Lett. A.

Influence of Squeezed Vacuum on Bistable Behavior

Chen Zhaoyang, Zhang Jingtao, Feng Xunli, Xu Zhizhan

Laboratory for High Intensity Optics

Shanghai Institute of Optics and Fine Mechanics, Chinese Academy of Sciences,
P.O.Box 800-211, Shanghai 201800, China

Abstract. The influence of squeezed vacuum input on the optical bistable behavior of a system of N three-level atoms which are simultaneously coupled to a coherent pump field and a squeezed vacuum input is investigated. It is shown that the squeezed vacuum will significantly increase the range of the optical bistability and this effect is phase-sensitive. The results exhibit that the optical bistability can be controlled by the squeezed vacuum input.

1 Fixed-Period Problems: The Sublinear Case

Since Gardiner [1] first predicted that the squeezed light incident upon a single two-level atom can inhibit its phase decay the interaction of squeezed light with atomic systems has been a topic of significant interest in quantum optics (see, e.g., Ref.2 and references therein). Optical bistability has been extensively investigated (see, e.g. [3]) since Szöke [4] suggested that optical bistability can be realized by a nonlinear medium in a cavity. In the presence of a squeezed vacuum optical bistability has its own distinctive features. The effects of squeezed vacuum input on bistable behavior of a system of two-level atoms have been investigated by Bergou *et al.* [5], Singh *et al.* [6] and Galatola *et al.* [7].

In this paper we examine the optical bistable behavior of the output field from the system of N homogeneously broadened three-level atoms in V configuration which is pumped simultaneously by a coherent input field and a squeezed vacuum field. Our model is similar to that discussed in [5]. Consider a three-level atom, with one ground state $|1\rangle$, and two excited states $|2\rangle$ and $|3\rangle$. The excited state $|2\rangle$ ($|3\rangle$) decays to the ground state $|1\rangle$ by spontaneous emission with rate γ_2 (γ_3). The transition frequencies are ω_2 and ω_3 . These transitions are associated with electric dipole matrix elements μ and μ' (assumed real for simplicity) respectively, whereas the transition between the excited states is forbidden in the electric dipole approximation ($\mu_{23} = 0$). We take $\gamma_{23} = \gamma_{32} = \sqrt{\gamma_2\gamma_3}$ to make the quantum interference effect maximal. The frequency of the coherent input field is ν , and the carrier frequency of the squeezed input field is ω_s . For simplicity, we shall assume that ω_s is equal to ν . The slowly varying amplitude of the coherent field is $E = |E|\exp(i\phi_L)$.

Making use of Scully-Lamb technique [8] and the rotating wave approximation and Born-Markoff approximation, we can derive the Maxwell-Bloch equations as follows,

$$\begin{aligned}\frac{\partial}{\partial t} \rho_{22} &= \gamma_2 \beta n \rho_{11} - \gamma_2 (1 + \beta n) \rho_{22} - \frac{1+\beta n}{2} \gamma_{23} (\rho_{23} + \rho_{32}) \\ &\quad - \frac{i}{\hbar} (\mu \rho_{21} E^* - c.c.), \\ \frac{\partial}{\partial t} \rho_{33} &= \gamma_3 \beta n \rho_{11} - \gamma_3 (1 + \beta n) \rho_{33} - \frac{1+\beta n}{2} \gamma_{23} (\rho_{23} + \rho_{32}) \\ &\quad - \frac{i}{\hbar} (\mu' \rho_{31} E^* - c.c.), \\ \frac{\partial}{\partial t} \rho_{12} &= \left[i(\delta - \Delta) - \frac{1+\beta n}{2} \gamma_2 - \frac{\beta n}{2} (\gamma_2 + \gamma_3) \right] \rho_{12} - \gamma_{23} m \rho_{31} \\ &\quad - \gamma_2 m \rho_{21} - \frac{1+\beta n}{2} \gamma_{23} \rho_{13} + \frac{i}{\hbar} \mu (\rho_{22} - \rho_{11}) E + \frac{i}{\hbar} \mu' E \rho_{32}, \\ \frac{\partial}{\partial t} \rho_{13} &= \left[i(\delta + \Delta) - \frac{1+\beta n}{2} \gamma_3 - \frac{\beta n}{2} (\gamma_2 + \gamma_3) \right] \rho_{13} - \gamma_{23} m \rho_{21} \\ &\quad - \gamma_2 m \rho_{31} - \frac{1+\beta n}{2} \gamma_{23} \rho_{12} + \frac{i}{\hbar} \mu' (\rho_{33} - \rho_{11}) E + \frac{i}{\hbar} \mu E \rho_{23}, \\ \frac{\partial}{\partial t} \rho_{23} &= \left[2i\Delta - \frac{1+\beta n}{2} (\gamma_2 + \gamma_3) \right] \rho_{23} + \frac{i}{\hbar} \mu E \rho_{13} - \frac{i}{\hbar} \mu' E \rho_{21} \\ &\quad - \frac{1+\beta n}{2} \gamma_{23} (\rho_{33} + \rho_{22}) + \gamma_{23} \beta n.\end{aligned}\quad (1)$$

$$\frac{\partial E}{\partial t} + c \frac{\partial E}{\partial z} = 2\pi i \nu N (\mu^2 \rho_{21} + \mu'^2 \rho_{31}). \quad (2)$$

Here the frequency detuning δ and Δ are respectively equal to $2\nu - \omega_2 - \omega_3$ and $\omega_2 - \omega_3$. The parameter c is the light speed. The parameter β , which appears in Eq.(1), depends on the ratio of the number of squeezed modes to the number of all modes enveloping atoms and on the matching of the squeezed modes to the vacuum modes coupled to atoms. The parameters n and m characterize the squeezed vacuum field such that $|m|^2 \leq n(n+1)$, where the equality holds for the minimum-uncertainty squeezed states of the field. φ_s is the phase of the squeezed vacuum. matching.

For perfect resonance and steady state, taking into account $\langle b \rangle = 0$ (b is the annihilation operator of the squeezed vacuum) [2], the boundary condition can be obtained as follows,

$$\begin{aligned}E(L) &= E_T / \sqrt{T}, \\ E(0) &= \sqrt{T} E_I + R E(L),\end{aligned}\quad (3)$$

where E_I and E_T are the input field and the output field respectively, L is the length of the atomic sample. R and T are respectively the reflection and transmission coefficients of mirrors (with $R + T = 1$).

In order to investigate the bistable behavior for this ring cavity, similarly to Ref.3, the absorption coefficient α for the V medium is given as

$$\alpha = \frac{4\pi N \nu \mu^2}{\hbar c \gamma}, \quad (4)$$

where $\gamma = \gamma_2 + \gamma_3$. The usual cooperation parameter C is equal to $\alpha L / 2T$.

In the mean-field limit [7], considering $\mu' = \mu$ and the steady state, we can get the field equation $\partial E / \partial z = 2\pi i \nu N \mu^2 (\rho_{21} + \rho_{31}) / c$. Using the boundary

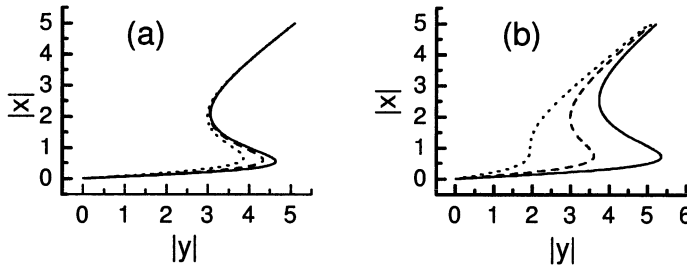


Fig. 1. (a) Input-output relationship for $C = 5$, $\beta = 1$, $\phi_s - 2\phi_L = 0$ and different n : 0.01 (dotted line), 0.05 (dashed line), 0.1 (solid line); (b) Input-output relationship for $n = 0$, and different C : 15 (solid line), 10 (dashed line) and 5 (dotted line).

conditions (3), and normalizing the fields by letting $y = \mu E_I / \gamma \sqrt{T}$, $x = \mu E_T / \gamma \sqrt{T}$, the input-output relationship is obtained

$$y = x + C\gamma(\rho_{21} + \rho_{31}). \quad (5)$$

Next, we will use graphical method to display the features of bistable behavior. For the convenience of comparison, we choose $\gamma_2 = \gamma_3 = \gamma_{23} = 0.5\gamma$, $\delta = 0$, $\Delta = 0$ and $|m| = \sqrt{n(n+1)}$ throughout all figures. Fig.1(a) shows that in the presence of squeezed vacuum field, for small cooperation parameter C such as $C = 5$, bistable hysteresis cycle becomes large as n increases. But Fig.1(b) exhibits that, in the absence of the squeezed vacuum input, when C becomes small (i.e. the number of atoms inside the cavity decreases), the optical bistability tends to disappear. From Fig.1 one can find that for the same cooperation parameter C , the bistable behavior in the absence of squeezed vacuum input is different from that in the presence of the injection of squeezed vacuum field. This is due to strong two-photon correlation presenting in squeezed vacuum field.

The optical bistability is influenced by the parameter β . Fig.2(a) shows that the bistable hysteresis cycle becomes smaller as the parameter β decreases. Obviously, the pronounced bistable behavior is observed when $\beta = 1$. When β decreases, the contribution of the squeezed vacuum field to the bistable behavior is also decreased. In general, the bigger the parameter β , the more obvious the bistable behavior. Fig.2(b) presents the influence of relative phase on bistable behavior. For the same n , due to different value of $\phi_s - 2\phi_L$, the optcial bistable behavior can be switched from existence to disappearance. This reflects the phase-sensitive characteristic of the squeezed vacuum.

In summary, we have investigated the optical behavior of a system of N homogeneously broadened V-type three-level atoms pumped by a coherent input field and coupled to a squeezed vacuum field by treating the optical bistability of such a system as an input-output problem. Our results show that, for small cooperation parameter C , there is no optical bistability in the

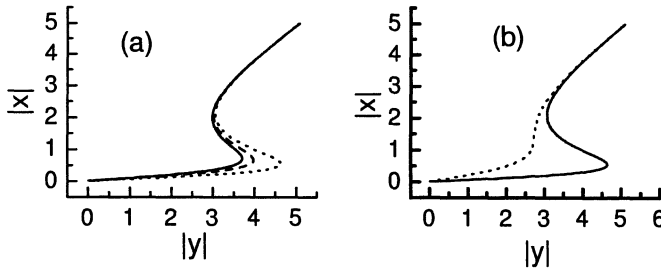


Fig. 2. (a) Input-output relationship for $C = 5$, $n = 0.1$, $\phi_s - 2\phi_L = 0$ and different β : 0.6 (solid line), 0.8 (dashed line) and 1 (dotted line); (b) Input-output relationship for $C = 5$, $n = 0.1$, and different $\phi_s - 2\phi_L$: 0 (solid line), π (dotted line).

absence of the squeezed vacuum field, but in the presence of the squeezed vacuum field, bistability exists. Physically, this is due to the strong two-photon correlation in the squeezed vacuum. It is shown that the bistable hysteresis cycle becomes wider as the average photon number in the squeezed vacuum increases. We have also found that, the effect of the squeezed vacuum on the optical bistability is phase-sensitive, and the degree of matching of the squeezed vacuum to the modes surrounding the atoms obviously influence on the optical bistability. The result indicates that the optical bistability can be controlled by the squeezed vacuum input.

References

1. Garginer, C. W. (1986) Inhibition of atomic phase decays by squeezed light: A direct effect of squeezing. *Phys. Rev. Lett.* **56**, 1917-1920
2. Ferguson, M. R., Ficek, Z., Dalton, B. J. (1997) Phase-dependent fluorescence linewidth narrowing in a three-level atom damped by a finite-bandwidth squeezed vacuum. *Phys. Rev. A* **56**, 4125-4138
3. Lugiato, L. A. (1984) *the Progress in Optics*, vol. XXI, edited by E. Wolf, North Holland, Amsterdam
4. Szöke, A., Daneu, V., Goldhar, J., Kurnit, N. A. (1969) Bistable optical element and its applications. *Appl. Phys. Lett.* **15**, 376-379
5. Bergou, J., Zhao, D. (1995) Effect of a squeezed vacuum input on optical bistability. *Phys. Rev. A* **52**, 1550-1560
6. Singh, S., Rai, J., Bowden, C. M., Postan, A. (1992) Intrinsic optical bistability with squeezed vacuum. *Phys. Rev. A* **45**, 5160-5165
7. Galatola, P., Lugiato, L. A., Porreca, M. G., Tombesi, P. (1991) Optical switching by variation of the squeezing phase. *Opt. Commun.* **81**, 175-178
8. Sargent III, M., Scully, M. O., Lamb, W. E. Jr. (1974) *Laser Physics*, Addison-Wesley, Reading, MA

Numerical Analysis of Wavelength Conversion Based on a Nonlinear Optical Loop Mirror

Chi Nan, Chen Shuqiang, Guan Kejian

Beijing University of Posts and Telecommunications, Beijing 100876, China
e-mail: chinan@bupt.edu.cn

Abstract. The application of NOLM to wavelength conversion may be promising in practical high speed communication systems. This paper gives a numerical analysis of the NOLM based on a mathematical description of the NOLM by the coupled nonlinear Schrödinger equations. The results show that increasing the loop length and working in anomalous-dispersion regime can achieve satisfied output, proper adjusting the relation between initial time delay and walk-off can compensate walk-off induced degradation.

1 Introduction

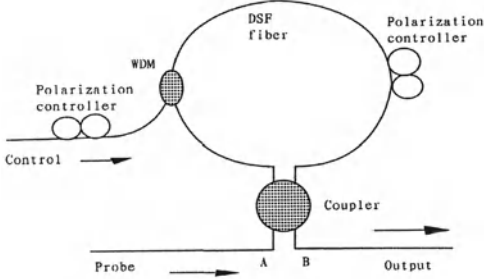
Wavelength conversion techniques are currently subject to a considerable interest. The application of NOLM to wavelength conversion that use the optical Kerr effect in optical fiber are very attractive because of their subpicosecond response and low switching power due to extremely long interaction length [1]. The setup of the NOLM used for our calculation is shown in Fig. 1. A probe beam is split into two by a 50:50 fiber coupler and propagated in both directions. In the absence of nonlinear interaction, the output ports sees no probe beam [2]. An control signal is coupled into the loop via a fiber coupler and propagates in a clockwise direction. This signal causes the phase of the probe beam propagating clockwise to increase relative to that of the counter-clockwise beam. Thus the symmetry between the counter propagating paths is broken due to the induced cross phase modulations, and some part of the input is transmitted.

2 Principle and System Model

The propagation of the parallel polarized signal and control pulses in a fiber with randomly varying birefringence is governed by the coupled nonlinear Schrödinger equations [3]:

$$\frac{\partial U_1}{\partial z} \pm \frac{i}{2} \frac{\partial^2 U_1}{\partial \tau^2} = i \frac{L_d}{L_{nl}} \left(|U_1|^2 + 2|U_3|^2 \right) U_1 - \frac{1}{2} \frac{L_d}{L_g} |U_3|^2 U_1 \quad (1)$$

$$\frac{\partial U_2}{\partial z} \pm \frac{i}{2} \frac{\partial^2 U_2}{\partial \tau^2} = 0 \quad (2)$$

**Fig. 1.** Setup of the NOLM

$$\frac{\partial U_3}{\partial z} + \frac{L_d}{L_w} \frac{\partial U_3}{\partial \tau} \pm \frac{ir}{2} \frac{\partial^2 U_1}{\partial \tau^2} = i \frac{r L_d}{L_{nl}} \left(|U_3|^2 + 2 |U_1|^2 \right) U_3 + \frac{r L_d}{2 L_g} |U_1|^2 U_3 \quad (3)$$

$$L_d = \frac{T_0^2}{|\beta_{21}|}, L_w = \frac{T_0}{d}, L_{nl} = \frac{1}{\gamma_1 P_0}, L_g = \frac{1}{g_R P_0}, r = \frac{\lambda_1}{\lambda_2}$$

Where U_1 , U_2 and U_3 are the normalized amplitudes of the field along the local polarization eigenaxes of the fiber for co-propagating pulses, counter-propagating pulses and control pulses, respectively. d is the inverse group velocity difference called walk-off which is given by $d = \frac{D'}{2} (\lambda_1 - \lambda_2)(\lambda_2 + \lambda_1 - 2\lambda_0)$ [4], Where $D' = 0.055 \text{ps/nm}^2 \cdot \text{km}$, $\lambda_0 = 1550 \text{nm}$. γ is the nonlinear coefficient defined as $\frac{2\pi n_2}{\lambda A_{eff}}$, the mark 1 for probe pulses, 2 for control pulses. ‘±’ is decided by the sign of β_{21} . g_R is the Raman gain coefficient coupling the longer wavelength, $g_R = \frac{\Delta\nu}{1.3 \times 10^{13}} \frac{g_p}{A_{eff}}$ [5]. The output signal intensity of port B is given by $P_B = |U_1(L, t) - U_2(L, t)|^2$. Assume probe pulse and control pulse are Gaussian pulses, T_0 are 1/e pulse width of pulse. T_d is the initial time delay between two beams. The bit rate is 40Gbit/s, NRZ signal.

3 Result and Discussion

In the prior equations, we assume the fiber loss can be neglected. Fig. 2(a) gives the eye-grams of the input and output signal. The loop length L_π is so designed that the variation of the phase shift of the two counter-propagating beams attains π . The converted signal changes to RZ code because of the nonlinear effect. If the fiber loss is considered, the loop length should be replaced by effective length, that is, $L_{eff} = \frac{1 - \exp(-\alpha L)}{\alpha}$. Thus the interacting length decreases due to fiber loss. Fig. 2 (b) shows the eye-grams of input and output signal with loss consideration. It is apparently the converted signal amplitude is degraded since the nonlinear phase shift is not sufficient.

In Fig. 3(a), the loop length is double and the output intensity is enhanced. The reason is that long fiber loop will cause long interacting length, which will compensate the loss induced degradation. However, increasing the

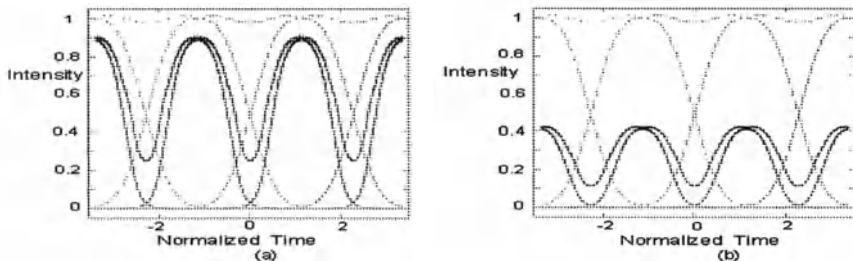


Fig. 2. Influence on the converted signal by fiber loss. (a) Input (dotted line) and output signal (straight line) without loss consideration. (b) The eyegrams of input signal and output signal with loss consideration ($\alpha = 0.2 \text{ dB/km}$)

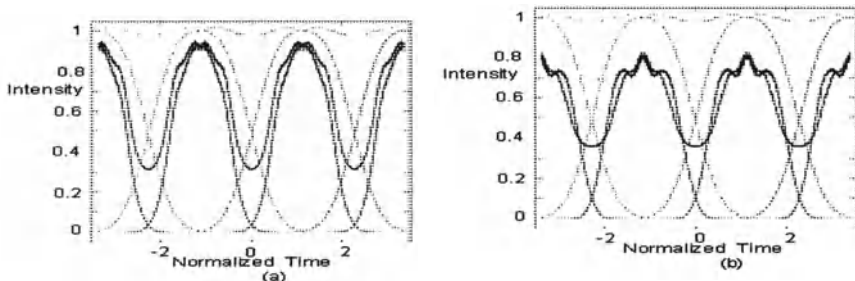


Fig. 3. Enlarge fiber length to compensate insufficient nonlinear effect. (a) Fiber length is double ($2L_\pi$). (b) Fiber length is more than double ($2.2L_\pi$)

fiber length to reduce the switching power enlarges the walk-off between the input signal and the control pulse. This results in a saturation of the switching power reduction [1] and a limitation of the loop length. Fig.3(b) shows continue enlarging the loop length , the waveform is obvious degraded since over-compensation of loss makes $\Delta\phi$ is larger than π and the output pulses appear multi-peaks.

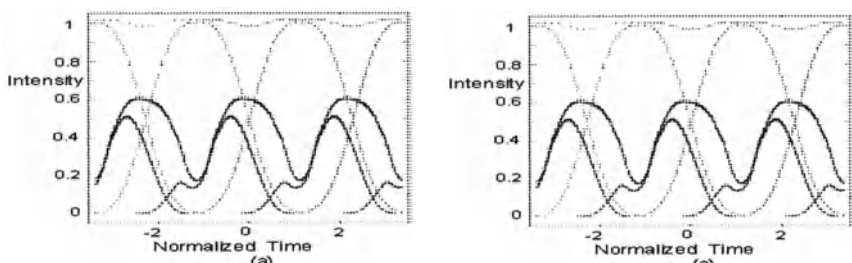


Fig. 4. Intensity of output signal at different values of walk-off d and initial time delay T_d . (a) $d = -2, T_d = 0$. (b) $d = -2, T_d = 1$

Fig. 4 shows the effect of different walk-off and initial time delay. If walk-off has counter sign with initial time delay, the output will be less asymmetric. The explanation for this phenomenon is, when walk-off is minus and no initial delay, probe pulse interact with the trailing edge of control pulse caused by its slower speed, XPM effect is weak. The maximum phase shift is less than π . As the initial delay is induced, control pulse will keep up with the co-propagating probe pulse, and the XPM effect attends all the way so that better output is given as the phase shift is near to π . Thus adjusting initial delay can compensate the walk-off induced degradation.

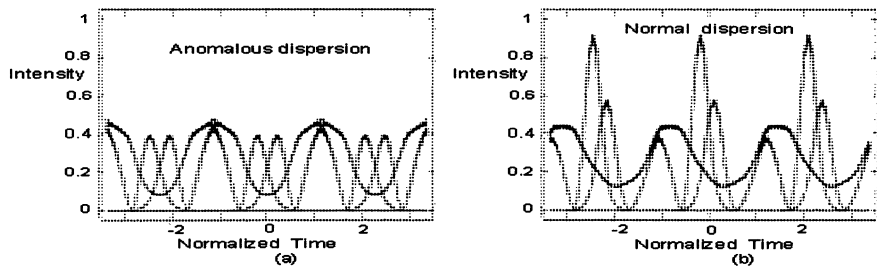


Fig. 5. Waveform of output signal. (a) Anomalous-dispersion regime. (b) Normal-dispersion regime.

In Fig. 5 we simulate evolution of the pulse shape propagating in the normal-dispersion regime ($\beta_2 > 0$) or the anomalous-dispersion regime ($\beta_2 < 0$) of the fiber. If the fiber length is shorter than L_π , output pulses are almost same under the two conditions. Once the fiber length is longer than L_π , pulse with dispersion parameter $\beta_2 < 0$ had larger output intensity. So if we increase the fiber length to compensate walk-off, the pulse should be within the anomalous-dispersion regime.

References

1. T. Morioka, M. Saruwatari: Ultra-fast all-optical switching utilizing the optical Kerr effect in polarization maintaining single-mode fiber. *IEEE J. Select. Areas Commun.* **6**, 1186–1198 (1988)
2. G. L. Abbas, V. S. Chan, et al. : A dual-detector optical heterodyne receiver for local oscillator noise suppression. *IEEE J. Lightwave. Tech.* **5**, 1110–1122 (1985)
3. G. P. Agrawal: *Nonlinear fiber optics* (Rochester, New York, 238–315 1995)
4. S. Bigo, E. Desurvire, et al: All-optical RZ-to-NRZ format conversion at 10 Gbit/s with nonlinear optical loop mirror . *Electron. Lett.* **9**, 1868–1869 (1996)
5. A. R. Chraplyvy: Optical power limits in multi-channel wavelength-division-multiplexed systems due to stimulated Raman scattering. *Electron. Lett.* **20**, 58–59 (1984)

Emission Spectrum of Two-Atom Two-Mode Multiphoton Raman Coupled Model

Feng Jian, Gao Yun-feng, Song Tong-qiang

Department of Communication Engineering
Liaocheng Teachers University
Liaocheng 252059, Shandong Province, P.R. China

Abstract. The emission spectrum of a pair of effective two-level atoms interacting with two modes of the radiation field with different coupling constants through multiphoton Raman process is investigated.

1 Model and Emission Spectra

Our model contains two effective two level atoms, each consisting of an upper level $|+\rangle$ and a lower level $|-\rangle$ and interacting with two modes of the field through multiphoton Raman process, N_1 photons are absorbed in mode 1 and N_2 photons are emitted in mode 2, with an atom making transition $|-\rangle \rightarrow |+\rangle$ through the virtual states $|j\rangle, N_i (i = 1, 2)$ is the nonzero positive integrals. The pump radiation mode (i.e. mode 1) and the Stokes radiation mode (i. e. mode 2) are in exact multiphoton resonance with the transition $|-\rangle$ to $|+\rangle$ (i.e. $\omega_0 = N_1\omega_1 - N_2\omega_2$), where ω_0 and $\omega_i (i = 1, 2)$ are the frequencies of atomic transition and of the ith mode of the radiation field, respectively. In our model, each atom interacts with two modes of the radiation field with different coupling constants. In the rotating wave approximation, by the method of adiabatic elimination of all the intermediate virtual levels and the neglect of Stark shift, the effective Hamiltonian of the whole system reads

$$H = \omega_1 a_1^+ a_1 + \omega_2 a_2^+ a_2 + \frac{1}{2} \omega_0 \sum_{i=1}^2 \sigma_{zi} + \sum_{i=1}^2 g_i (a_1^{N_1} a_2^{+N_2} \sigma_i^+ + \sigma_i a_2^{N_2} a_1^{+N_1}) \quad (1)$$

where $\hbar = 1, a_i, a_i^+$ are the annihilation and the creation operators for the ith mode of the field, $\sigma_{zi}, \sigma_i, \sigma_i^+$ are pseudospin operators for the ith atom, g_i is the effective multiphoton Raman coupling constant of the ith atom with two modes of the field.

Following the definition of the physical spectrum by Eberly and Wodkiewicz[1], the spectrum for the system of the two-atom and two-mode field may be written [2,3]

$$S(\omega) = 2\Gamma \int_0^T dt' \exp[-(\Gamma - i\omega)(T - t')]$$

$$\times \int_0^T dt \exp[-(\Gamma + i\omega)(T-t)] \langle \Phi(0) | D^+(t') D(t) | \Phi(0) \rangle \quad (2)$$

where Γ is the bandwidth of the spectrometer, T is the time at which the measurement takes place and $|\Phi(0)\rangle$ is the initial state of the system of two-atom and two-mode field, $D = \sigma_1 + R\sigma_2$, $D^+ = \sigma_1^+ + R\sigma_2^+$.

We can derive the general analytic expression for the emission spectrum by complicate calculation. The properties of the spectra for the arbitrary photon numbers absorbed in one mode and emitted in the other with the two modes of the field in arbitrary states may be analysed by choosing the values of N_1 and N_2 .

2 Results and Discussion

For the purpose of definiteness, we look at the behaviour of $S_{n_1 n_2}(\omega)$ for $N_1 = 1$ and $N_2 = 1$, i.e., the spectra of two atoms interacting with two modes of the cavity field with different coupling constants through nondegenerate two-photon Raman process when the two modes of the field are in arbitrary number states. We obtain some new results as follows.

- (1) When mode 1 is in vacuum state and mode 2 is in a strong field ($n_2 = 100$). The spectra for $0 < R < 1$ show symmetric ten-peak structure. With increasing R, the position and height of each peak are changed apparently. The spectra for $R = 0, 1$ have symmetric two- and six-peak structures, respectively. This is in marked contrast to the single-mode case [4] and two dipole-dipole coupling identical atoms case [5].
- (2) When mode 1 of the field is in vacuum state and mode 2 is in weak field ($n_2 = 5$), as R increases from 0.25 to 1, the ten- and six-peak structures appear alternately in the spectrum, which indicates that the effects of R on the spectra $S_{0,5}(\omega)$ are remarkable and the spectra reflects the different Raman interacting intensities of two atoms with the cavity field more sensitively than in the case of a single-mode field [4].
- (3) The spectra for $n_1 = n_2 = 100$ show that the effects of R on the spectra are less obvious in the case of two-mode strong fields.
- (4) The remarkable difference between the spectra for $n_1 = 1, n_2 = 50$ and $n_1 = 50, n_2 = 1$ reflects that mode 1 and mode 2 of cavity field have the different positions in the nondegenerate two-photon Raman interaction with two atoms.
- (5) The relative heights of peaks are dependent not only on R but also on n_1 and n_2 . This result is quite different from the emission spectra of two atoms interacting with a single mode of the cavity field with different coupling constants through Raman process [4].

(6) In the case of arbitrary two-mode number states the numerical calculation shows that the spectra are always symmetric about the resonant frequency ω_0 for $N_1 = N_2 = 1$ although two atoms interact with two modes of the field with different coupling constants ($g_1 \neq g_2$). Actually, the emission spectra for arbitrary N_1 and N_2 possess this property. It may be analysed with an analytic method.

References

1. J. H. Eberly and K. Wodkiewicz, J. Opt. Soc. Am. 67 (1977) 1252.
2. Z. F. Luo, L. Xu, and Z. Z. Xu, Phys. Lett. A 164 (1992) 83.
3. J. Feng, T. Q. Song, W. Z. Wang, and J. Z. Xu, J. Phys. B: At.Mol.Opt.Phys.28 (1995) 989.
4. Z. F. Luo, Z. Z. Xu, L. Xu, Acta Phys. Sin. 41 (1992) 1950.
5. J. Feng, T. Q. Song, W. Z. Wang, and J.Z.Xu,Acta Opt. Sin. 14 (1994) 1272.

DFB X-Ray Laser Gain Per Unit in Deformed Crystals

M. M S. Gualini

Pakistan Institute of Lasers and Optics, P.O. Box 1384, Islamabad, Pakistan

Abstract. We find G enhanced (≈ 1) in DFB crystals deformed at anomalous transmission conditions [1] confronting semi-empirical and rigorous complex field analysis. Deformation induces Zeeman splitting of states, thus enabling DFB laser emission of x-rays.

1 Introduction

Relativistic particles, channeled in deformed crystals, fig. 1, stimulate coherent, intense hard x-rays. DFB x-ray stimulated emission excited by relativistic particles was derived rigorously [2] and confirmed by complex continuum potential [3]. Impossibility to achieve $G \approx 1$ was shown [4, 5] even for $F = 200$. Gain enhancement factor, $g(W)$, may be large ($G \approx 1$) in deformed crystals at Borrmann effect conditions [1, 6, 7]. We compare semi-empirical and preliminary results of rigorous approach to verify $G \approx 1$ in deformed crystals.

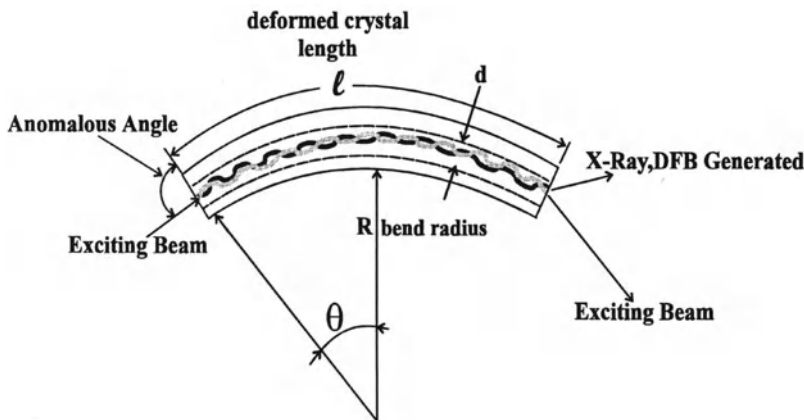


Fig. 1. Plastically deformed crystal

2 Semi-empirical approach

The gain enhancement factor [1] $G = [(3/\pi)\lambda\lambda_{ab}(\Psi_{ab}/\tau\Delta\omega)]g(W)$ is related to the cross sections for stimulated emission, σ_{STIM} , and resonance absorption, σ_{ABS} , the upper (N_U) and lower (N_L) population densities in a two state system. $G = N_U\sigma_{STIM} - N_L\sigma_{ABS} = N_U\sigma_{STIM}[1 - (N_L\sigma_{ABS}/N_U\sigma_{STIM})] \equiv N_U\sigma_{STIM}F$, F inversion factor[4]. But $\sigma_{STIM} = (c^2/8\pi v^2) * (1/\Delta v) * A_{ul}$, where A_{ul} is the transition probability at frequency v . We assume $g(W) \propto F$, at $\lambda = \lambda_{ab}$, because the above σ_{STIM} is general, while for DFB in crystals is derived rigorously. It was proposed [1] for deformed crystals that $g(W)^{-1} = (1/2\pi R^{-1}) \int [\sin(Ry)]^2 dy = 1/2$, @ $W = 0$ (integrated between $2\pi R^{-1}$ and 0). W , resonance error parameter, R curvature radius of the bent crystal of length "1", $0 \cong l/2R$ incidence angle between the critical angle α_c , for anomalous transmission, and θ_c , the critical acceptance angle for bent crystal. Large values [1] of $g(W)$ are possible for $W \neq 0$, where W depends on $\theta \cong l/2R$, $g(W) \equiv g(a, b)$. Double integrating the indefinite form of $g(W)^{-1}$ we find $g(W) = 4/[2ab - \text{SinIntegral}(2ab)]$. Fig. 2 shows the surface graph of $g(W)$ for angular gradients per length, "b" and crystal bent radius of curvature "a". Only "b" values giving total deviation from the Bragg's condition within $\pm 4^\circ$ of arc are of interest. For example for 1\AA , $\tau\Delta\omega \approx 1$, we obtain $G = 9.5493 \cdot 10^{-6} \text{ cm}^{-1}$. To obtain $G \approx 1$ we need $g(W) \geq 10^6$. We find "b" values, $g(W) \gg 1$, like $b = 0.01^\circ/\text{cm}$ so that $\theta = 0.32459 \text{ rad} \pm .6 \text{ mrad}$, bending the crystal by a radius of 0.5 cm and a critical angle across the first order Bragg's angle (.13057 rad@ 1\AA) for $Si(110)$ with $d = 3.84026 \text{\AA}$.

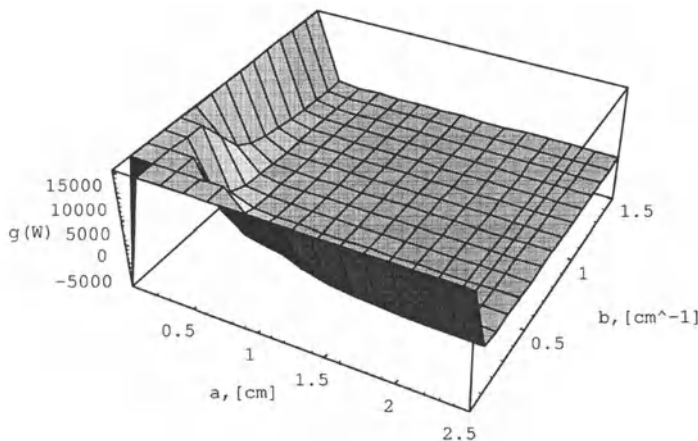


Fig. 2. Surface graphic of semi-empirical $g(W)$

The continuum potential for planar channeling [3, 7] is $U(y) + jC^i(y) \equiv U(y) + j \sum_{g\perp} C_{og\perp}^i \exp(j2g\perp\pi.y_0)$. The imaginary part is derived [3] from Lin-

hard's continuum potential theory, $U(y) = \sum_{g\perp} U_{g\perp} \exp(j2g\perp\pi.y_0)$ with $U_{g\perp}$ scattering potential of systematic reflection for electron diffraction $\mu(y_0) = -(2m/\hbar^2)C^i(y_0)$. The Shroedinger equation [7] is then:

$$-\partial^2\Psi(y)/\partial y^2 + (2m/\hbar^2)[U(y) + jC^i(y)]\Psi(y) = (2m/\hbar^2)E_\perp\Psi(y) \quad (1)$$

$E_\perp = E_{in}\Theta^2$, E_{in} incident exciting radiation energy, Θ Bragg angle. A first solution of Eq.(4) is obtained neglecting the imaginary terms with the reasonable assumption that $U(y) >> C^i(y)$ also in deformed conditions. The continuum potential [7] is $U(y) = V_0 + V' \cos(2\pi y/d)$ where V_0 and V' have suitable values, like $V_0 = -3.24 \cdot 10^{-18} J$ and $V' = -1.58 \cdot 10^{-18} J$ for Au(111). We assume "d", Lindhard's elementary stringe, variable as $d = R_2 - R_1 \equiv l/2\theta$ and $\Phi = (2\pi/d)y$. Then we rewrite Eq.(2) in the classic form of a Mathieu equation, with solution in Mathieu functions of first order [7]:

$$\begin{aligned} \partial^2\Psi(\Phi)/\partial\Phi^2 + (2m/\hbar^2)(d/\pi)^2[(E_\perp - V_0 + V') - 2V' \cos^2\Phi]\Psi(\Phi) = 0 \\ z_M = \cos\Phi; \end{aligned} \quad (2)$$

$Me_\alpha^{(q)}(h, z_M) = \sum B_{2n+1}^{o1} \sin[(2n+1)\Phi] + j\{\sum B_{2n+1}^{e1} \cos[(2n+1)\Phi]\}$ are general solutions of Eq.(3), where $S_{o1}(h, z)$ and $S_{e1}(h, z)$ are the odd and even Mathieu functions of the first order. Sums are from $n = 0$ to ∞ , $B_{2n+1} = a_{2n+1}/[\sum a_{2n+1}]$ are normalized, (q) is the q - branch order in the crystal energy band. Thus the wave function in the crystal is $\Psi(\Phi) = \sum_q \Psi_q \exp(jk_z^{(q)}z) Me_\alpha^{(q)}(h, z_M)$ where Ψ_q results from the boundary conditions at the crystal surface. The averaged channeled absorption coefficient is:

$$\mu_{CH} \approx (1/d) \int_{-d/2}^{d/2} |\Psi(y)|^2 \mu dy \quad (3)$$

$\mu = \mu_0 \pm [\Delta\mu_G/(1+W^2)]^{1/2}$ [1]. This is an approximation because we should consider $\mu(y)$ from complex continuum potential for channeling [3]. Comparing semi-empiric $g(w)^{-1}$ and Eq.(3) we assume $\mu_{CH}^{-1} \approx g(w)$ for $W \neq 0$. Thus $|\Psi(y)|^2 = k_1 \sin^2 ab + k_2 \cos^2 ab$, where $ab \equiv \Phi = (2\pi/d)y$. Solving Eq.(3) as a double integral in a and b we find:

$$g(w) = 4/[2k_1^2 ab + 2k_2^2 ab - k_1^2 \text{SinIntegral}(2ab) + k_2^2 \text{SinIntegral}(2ab)] \quad (4)$$

Surface graphic of Eq(4), fig. 3, is similar to fig. 2 if $1 > k_1 >> k_2$ and $k_1 << k_2 < 1$, since for $k_1 = k_2 \rightarrow g(w)^{-1} \equiv 1$, because $\sum B_{2n+1}^{o1} \sin[(2n+1)\Phi]$ and $\sum B_{2n+1}^{e1} \cos[(2n+1)\Phi]$ are two of the four independent solutions of Eq.(2) and $\sum B_{2n+1}^{o1} \leq 1$, $\sum B_{2n+1}^{e1} \leq 1$ are normalized. Conditions $1 > k_1 >> k_2$, $k_1 << k_2 < 1$ are asymmetrical, which we account to deformation. Larger values of $g(W)$ are obtained for $1 >> k_1 >> k_2$, due to $U(y) >> C^i(y)$ also in deformed conditions.

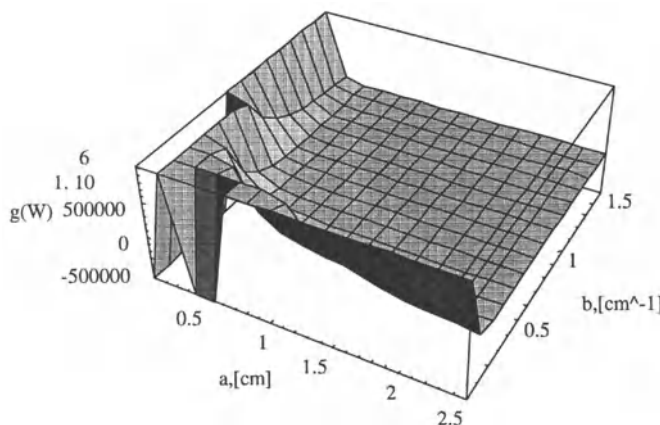


Fig. 3. Surface graphic of rigorous $g(W)$

3 Conclusions

We found $g(W)$ with same behavior either by semi-empirical and rigorous, quantum, approach. Atomic irregularities in crystals produce Zeeman splitting [9]. We suggest that in the above conditions crystals behave like ring lasers [10]. Work is in progress to demonstrate the assumptions with rigorous quantum optic analysis.

References

1. Ohtsuki Y.H., (1984), X-Ray Laser by Channeling Radiation, Nuclear Instr. Methods in Phys. Res.-North-Holland (Amsterdam), B2,80-82,
2. Beloshitskii V.V., Kumakhov M.A., (1978), Quantum theory of spontaneous electrons and induced radiation of channeled positrons, Sov.Phys.JETP47(4),
3. Ohtsuki Y. H., (1973), Complex Continuum Potential for Channeling, J. Phys. Soc. Jap., Vol 34, No. 2, February, pp 473-475,
4. Elton R.C., (1990), X-Ray lasers, Academic Press, Inc.,
5. Fusina R., Production of laser radiation in aligned crystal targets, (unpublished, private communication from Prof. R. C. Elton),
6. Cullity B.D., (1978), Elements of x-ray diffraction, Addison-Wesley Publishing Co. 2nd Ed.,
7. Kubota Y., Ohtsuki Y. H., (1972), Bloch Wave channeling and Extended Lindhard's Theory, Phys. Stat. Sol. (b) 52, pp 271-274,
8. Morse, P.M. and Feshbach, H. (1953) Methods of Theoretical Physics,
9. Hannon J. P., Trammel G. T., (1975), Anomalous Emission Effect and the Possibility of γ -Ray Lasers, Optics Communications, Volume 15, Number 3, November/December, pp 330-334,
10. Sargent III M., Scully M. O., Lamb W. E., Jr., (1977), Laser Physics, Addison-Wesley pp 176-177

Statistical Properties of Fundamental and Second Harmonic Light with Multiplicative Noise

Jing Hu, Xiaoqin Luo, Shiqun Zhu

Department of Physics, Suzhou University, Suzhou, Jiangsu 215006, China
e-mail: szhu@suda.edu.cn

Abstract. The statistical properties of fundamental and second harmonic light in a single mode laser is investigated through a full saturation model. The expressions for the probability distribution function, second and third factorial moments of the photon counting m are presented. Compared to the experimental measurements, good agreement is obtained near threshold. It is shown that the multiplicative noise can enhance the fluctuations of fundamental light, meanwhile it can reduce the fluctuations of the second harmonic light.

1 Introduction

The nonlinear polarization in certain anisotropic media can bring the generation of second-harmonic light. It undergoes the following process with absorption of two photons from an optical beam of frequency ω_1 (the fundamental) followed by the generation of a single photon of frequency $\omega_2 = 2\omega_1$ (the second harmonic) [1]. Though the statistics of second harmonic photons depend on the fundamental beam, in general, they are different from each other. It is necessary to investigate the difference between fundamental and second harmonic light in the statistical properties when the multiplicative noise is included.

In this paper, the expressions of the probability distribution function is derived from a full saturation laser theory [2]. The theoretical results of the second and third factorial moments of the photon counting m are compared with the experimental measurements. Good agreement is obtained. The effects of multiplicative noise in fundamental and second harmonic light are discussed.

2 Theoretical analysis

The single-mode laser model with a full account of the saturation effects follows the Langevin equation:

$$\frac{dE}{dt} = -KE + \frac{FE}{1 + A|E|^2/F} + p(t)E + q(t) \quad (1)$$

where K is the cavity decay rate for the electric field and $F = a + K$ is a gain parameter; a is the net gain and A is the self-saturation coefficient; $q(t)$ is additive noise, $p(t)$ is multiplicative noise. The random fluctuations are Gaussian white-noise processes with

$$\begin{aligned}\langle q(t) \rangle &= \langle p(t) \rangle = 0 \\ \langle q^*(t) q(t') \rangle &= 2P\delta(t - t') \\ \langle p^*(t) p(t') \rangle &= 2P'\delta(t - t')\end{aligned}\quad (2)$$

where P and P' are the noise strength of additive and multiplicative fluctuations respectively.

The corresponding probability density function of the fundamental light is:

$$Q(I_1) = \frac{K(1 + P'I/P)^{\beta_1 - \alpha_1}}{P_2 F_1(\beta_1, 1; \alpha_1; 1 - AP/FP')(1 + AI/F)^{\beta_1}} \quad (3)$$

where $\alpha_1 = K/P' + 1$, $\beta_1 = F^2/(FP' - PA)$, and the hypergeometric function $_2F_1(\alpha_1, \alpha_2; b_1; x) = \sum_{k=0}^{\infty} \frac{\Gamma(\alpha_1+k)\Gamma(\alpha_2+k)\Gamma(b_1)}{\Gamma(\alpha_1)\Gamma(\alpha_2)\Gamma(b_1+k)} \frac{x^k}{k!}$.

The second-harmonic field will be related to the intensity of the fundamental beam by $I_2 = \kappa I_1^2$ where κ is a constant that depends on material constants of the nonlinear medium and various scale factors. The relationship between $Q_2(I_2)$ and $Q_1(I_1)$ is given by [4]:

$$Q_2(I_2)dI_2 = Q_1(I_1)dI_1 \quad (4)$$

In the second-harmonic experiment, the probability that m photo-electric pulses are recorded in a time t is given by:

$$\begin{aligned}P_2(m) &= \frac{K\mu^m}{P_m!} \sum_{n=0}^{\infty} \frac{(-\mu)^n}{n!} B[\alpha_1 - 2m - 2n - 1, 2m + 2n + 1] \\ &\quad \left(\frac{P}{P'}\right)^{2m+2n+1} \left(\frac{AP}{FP'}\right)^{-\beta_1} \frac{{}_2F_1[\beta_1, \alpha_1 - 2m - 2n - 1; \alpha_1; 1 - \frac{FP'}{AP}]}{{}_2F_1[\beta_1, 1; \alpha_1; 1 - \frac{AP}{FP'}]}\end{aligned}\quad (5)$$

where $\mu = \kappa\lambda$, and $\lambda = \lambda't$ is the product of the over-all detection efficiency λ' and the counting interval t . The k th factorial moment of the second-harmonic light is given by:

$$\langle m^{(k)} \rangle = \sum_m \frac{m!}{(m-k)!} P_2(m) \quad (6)$$

So, the second and third normalized factorial moments can be written as:

$$S_2 = \langle m^{(2)} \rangle / \langle m^{(1)} \rangle^2, S_3 = \langle m^{(3)} \rangle / \langle m^{(1)} \rangle^3 \quad (7)$$

Similarly, the counting distribution of the fundamental beam is given by:

$$P_1(m) = \frac{K\eta^m}{Pm!} \sum_{n=0}^{\infty} \frac{(-\eta)^n}{n!} B[\alpha_1 - m - n - 1, m + n + 1] \\ \left(\frac{P}{P'}\right)^{m+n+1} \left(\frac{AP}{FP'}\right)^{-\beta_1} \frac{{}_2F_1[\beta_1, \alpha_1 - m - n - 1; \alpha_1; 1 - \frac{FP'}{AP}]}{{}_2F_1[\beta_1, 1; \alpha_1; 1 - \frac{AP}{FP'}]} \quad (8)$$

where $\eta = \eta' t$ is the product of the overall detection efficiency η' for the fundamental photons and the counting interval t . The second and third factorial moments can be written as:

$$F_2 = \langle m^{(2)} \rangle / \langle m^{(1)} \rangle^2, F_3 = \langle m^{(3)} \rangle / \langle m^{(1)} \rangle^3 \quad (9)$$

Then the statistical properties of the fundamental and the second-harmonic can be compared to the experimental measurements.

3 Comparison of theory and experiment

To check the accuracy of the full saturation laser models, the analytic results have been compared with the experimental measurements from Ref [1]. In the experimental setup, a gas laser had been used. For a gas laser, the additive noise play a major rule while the multiplicative noise can be neglected. Fig.1 shows the measured data and theoretical curves. It is clear that good agreement is obtained between theory and experiment when $P' = 0$ and $K = 50$.

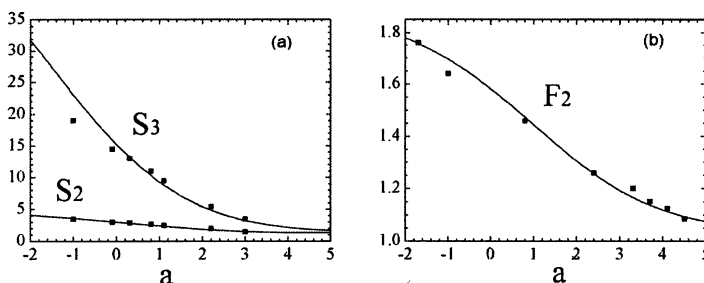


Fig. 1. The factorial moments as a function of the pump parameter a . (a) The normalized second and third factorial moment S_2 and S_3 of the second-harmonic light.(b) The normalized second moment of the fundamental light.

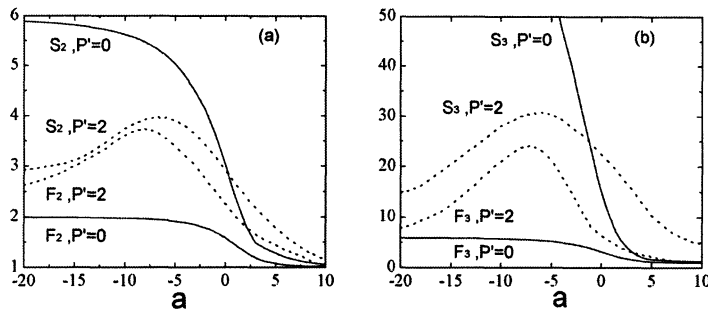


Fig. 2. The normalized second and third factorial moments of the fundamental and second-harmonic light as a function of pump parameter a with different values of multiplicative noise $P', P' = 2$ (dotted line); $P' = 0$ (straight line). (a):the second factorial moment S_2 and F_2 . (b):the third factorial moment S_3 and F_3 .

4 Effect of multiplicative noise

The second and third factorial moments of the fundamental and the second harmonic light with different multiplicative noise are plotted in Fig.2. From Fig.2. it is shown that the fluctuations of the fundamental and second harmonic light exhibit different statistical properties for various multiplicative noise. The increase of multiplicative noise can enhance the fluctuations of fundamental light, meanwhile it can reduce the fluctuations of the second harmonic light.

5 Discussion

It is shown that the statistical properties of the laser intensity depend not only on the process of the light but also on the noise in the system. The fluctuation of fundamental light increases with multiplicative noise while that of second harmonic light decrease with multiplicative noise.

Acknowledgements. The financial supports from the National Natural Science Foundation of China and Natural Science Foundation of Jiangsu Education Commission are gratefully acknowledged.

References

1. Yuiing Qu, and Surendra Singh: Measurements of photon statistics in second-harmonic generation. Phys. Rev. A **51**(3), 2503-2536(March 1995)
2. Shiqun Zhu, and Jianping Yin: Saturation effect in a laser at steady state. Phys. Rev. A **45**(7), 4969-4973(April 1992)

3. Shiqun Zhu: Saturation effect in a laser with multiplicative white noise. Phys. Rev. A **45**(5), 3210–3215(March 1992)
4. A. Yariv, *Quantum Electronics*: Chap. 9(Wiley, New York, 1989)

Measurement of the Wigner Function via Atomic Beam Deflection

Ashfaq Hussain Khosa^{1,2}, Shi-Yao Zhu², M. Suhail Zubairy^{1,2}

¹ Department of Electronics, Quaid-i-Azam University,
Islamabad, Pakistan

² Department of Physics, Hong Kong Baptist University, Hong Kong

Abstract. We show that the Wigner function of a cavity field can be reconstructed by knowing the position distribution of resonant two level atoms on detection screen. The atoms are deflected during their passage through the quantized cavity field, we calculate the momentum distribution of the deflected atoms by taking the Fourier transform of position distribution and show that how the Wigner function can be reconstructed by having the knowledge of momentum distribution. In the proposed method, the Wigner function of the coherent state and Schrodinger cat state is recovered in a straightforward manner, without much mathematical manipulation of the experimental data.

1 Introduction

The concept of a quantum state has always played a key role in discussions treating the foundations of quantum theory. Each physical quantity can be represented by a Hermitian operator which is called an ‘observable’ [1]. A measurement of this observable leaves the system in an eigenstate of the operator. A single measurement performed on a quantum system reveals a certain aspect of its state, and it will not uncover the quantum state completely. It is a basic assumption of the quantum theory that an infinite ensemble of system contains all the information about the quantum system.

In this paper we shall be concerned with the measurement of the quantum state of the radiation field inside a cavity. The quantum state of the radiation field is described completely by the state vector $|\psi\rangle$ for a pure state and by the density operator ρ for a more general mixed state. Equivalent descriptions of the quantum state can be formulated in terms of the quasiprobability distributions such as P -representation, Q -representation, or the Wigner distribution function. These distributions, which do not have all the properties of a classical probability distribution, allow the evaluation of various correlation functions of the field operators using the methods of classical statistical mechanics. For example, the Wigner distribution function affords the evaluation of symmetrically ordered correlation functions of the creation and destruction operators of the field. In recent years, a large class of the states of the radiation field have been studied. Some of them such as a squeezed state [2] or a Schrödinger-cat state [3] exhibit interesting features in

their quantum statistical properties. For example, they may have oscillatory photon distributions.

Several methods have been proposed to measure quantum state of light as well as quantum state of matter. These are, tomographic method [4], dispersive atom-field coupling in a Ramsey method of separated oscillatory fields [5], atomic beam deflection [6], the conditional measurements on the atoms in a micromaser set-up [7]. A class of schemes for the measurement of the quantum state of the radiation field involves the measurement of the absorption and emission spectrum in a driven system [8]. The atom deflection method uses momentum distribution of atoms in order to reveal the quantum state of the light inside the cavity. In this case the atom serves as a tool that probes a quantum state of radiation field.

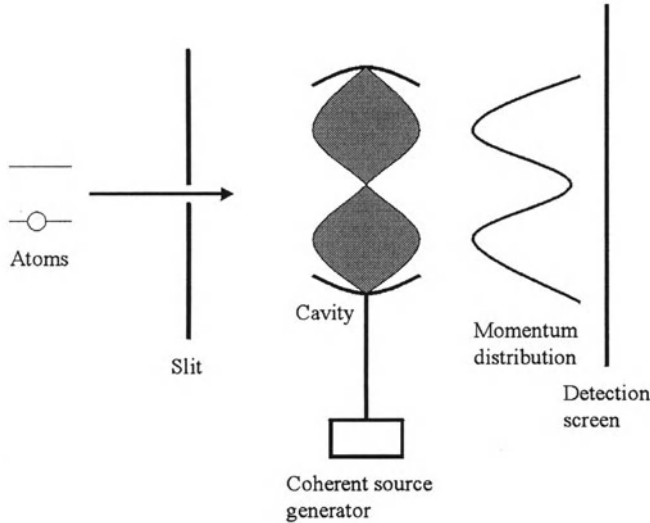


Fig. 1.

Freyberger and Herkommer proposed an interesting scheme to measuring quantized cavity field in Ref. [6]. Their proposed scheme utilize resonant two level atoms. The atoms are made in superposition of coherent state, before interacting with the cavity field. A narrow slit of width much smaller than the wave length of the cavity field is put in front of standing wave (of the cavity field). They look at the momentum distribution of the atoms and find the photon statistics of the cavity field by recursion. It is a nice scheme for the case where the probability amplitudes of photon statistics never go to zero. The method has the limitation that when the probability amplitude w_{m-1}^* become equal to zero, w_m cannot be found. Such is, for example, the case of Schrödinger cat state. Contrary to Freyberger and Herkommer the

method our propose do not requires the atoms in their superposition of states, rather than this we inject a coherent state inside the cavity which cases the displacement of the original photon statistics of the field. Our proposal has the advantage of using mixed state instead of pure state.

2 Wigner function of radiation field

We assume that there is a probability of m photons inside the cavity which we would like to measure. A source is connected to the cavity such that a coherent state is injected inside the cavity and the state of the field inside the cavity is displaced by the displacement operator $D(\alpha)$, which is given by $D(\alpha) = \exp(\alpha a^\dagger - \alpha^* a)$. We recall the definition of the Wigner function, which belongs to a general class of phase-space distribution

$$W(\alpha, \alpha^*) = \frac{1}{\pi} \text{Tr}[\rho T(\alpha, s)], \quad (1)$$

where s is the order of products of field operators. By order we mean the normal ordered, antinormal ordered and symmetric ordered. The $s = 1, -1$, or 0 for normal-, antinormal-, and symmetric-order, respectively. The term $T(\alpha, s)$ given by [9]

$$T(\alpha, s) = \frac{1}{\pi} \int \exp(\beta^* \alpha - \beta \alpha^*) \exp\left(\frac{s |\beta|^2}{2}\right) D(\beta) d^2 \beta, \quad (2)$$

and is the Fourier transform of the displacement operator $D(\beta)$. For $s = 0$ one obtains the Wigner distribution and for $s = -1, 1$, Q -representation and P -representation, respectively. An alternative expression for $T(\alpha, s)$, which is useful for our purpose is [9]

$$T(\alpha, s) = \frac{2}{1-s} D(\alpha) \left(\frac{s+1}{s-1} \right)^{\alpha^\dagger \alpha} D^\dagger(\alpha). \quad (3)$$

For a general state $\rho = |\Psi\rangle \langle \Psi|$ we obtain the following expression for the Wigner function

$$W(\alpha, \alpha^*) = \frac{2}{\pi} \sum_m (-1)^m p(m, \alpha), \quad (4)$$

where $p(m, \alpha)$ is the displaced photon statistics of the cavity field, i.e., $p(m, \alpha) = |\langle m | D^\dagger(\alpha) | \Psi \rangle|^2$. Thus the Wigner function of the field can be found directly if the displaced photon statistics $p(m, \alpha)$ is known for all values of α .

Here we consider the same scheme as in Ref. [6] with two modifications: (a) we inject two-level atoms in the standing wave field initially in their ground state $|b\rangle$ and (b) we displace the state of the field inside the cavity by injecting a coherent state inside the cavity. We assume that the transition

$|a\rangle - |b\rangle$ of the two-level atoms is resonant with the quantized cavity field. A narrow slit of width Δx is put in front of the single mode of cavity field. The interaction Hamiltonian in the dipole and rotating-wave approximations is

$$H = -\mu\varepsilon_0 kx(\sigma_+a + a^\dagger\sigma_-), \quad (5)$$

where k is the wave vector of the cavity field. The terms μ and ε_0 stand for the dipole moment of the atom and the effective electric field per photon, respectively. The atoms are transmitted through the small region Δx such that $\Delta x \ll \lambda$ and is centered around $x = 0$. This has allowed us to replace $\sin(kx)$ dependence by a linear kx dependence. As the atom is initially in the ground state $|b\rangle$, we can write

$$\rho_{am-1,am-1}(x',x,0) = \rho_{am-1,bm}(x',x,0) = \rho_{bm,am-1}(x',x,0) = 0 \quad (6)$$

$$\rho_{bm,bm}(x',x,0) = g(x')g(x)p(m) \quad (7)$$

where $g(x)$ is the distribution function of the atoms and $p(m)$ is the photon statistics of the field inside the cavity. The Fourier transform from position distribution to momentum distribution in normalized coordinates is as

$$\rho(\wp, t) = \frac{1}{2\pi\hbar} \int_{-\infty}^{\infty} \frac{d\theta}{k} \int_{-\infty}^{\infty} \frac{d\theta'}{k} \rho(\theta', \theta, t) e^{i\wp(\theta' - \theta)}. \quad (8)$$

The probability of momentum distribution of atoms on detection screen after taking the trace over the field states and atomic states is $W(\wp) = \sum_m [\rho_{am,am}(\wp, t) + \rho_{bm,bm}(\wp, t)]$. It follows, on substituting for $\rho_{am,am}(\wp, t)$ and $\rho_{bm,bm}(\wp, t)$, that

$$W(\wp) = 2 \sum_m \left[|f(\wp + \kappa\sqrt{m})|^2 + |f(\wp - \kappa\sqrt{m})|^2 \right] p(m). \quad (9)$$

where \wp and θ are normalized momentum and position, and are given by $\wp = p/\hbar k$ and $\theta = kx$, and $\kappa = \mu\varepsilon_0 t/\hbar$. For normalized Gaussian distribution of the atoms at the slit

$$f(\wp \pm \kappa\sqrt{m}) = \left(\frac{\Delta x^2}{16\pi\hbar^2} \right)^{\frac{1}{4}} e^{-k^2\Delta x^2(\wp \pm \kappa\sqrt{m})^2/2}. \quad (10)$$

The plot $W(\wp)$ verses \wp/κ shows that the first term in equation (9) selects the negative side of \wp/κ axis and second term selects the positive side. It is clear from equation (10) that there will be peaks whenever \wp/κ becomes equal to \sqrt{m} . At $\sqrt{m} = 0$, the contribution comes from the both terms, i.e., from $|f(\wp + \kappa\sqrt{m})|^2$ and $|f(\wp - \kappa\sqrt{m})|^2$, so that the peak located at $\wp/\kappa = 0$ has the double height, i.e.,

$$W(\wp) = 2p(m) \left\{ 2|f(\sqrt{m} = 0)|^2 + \sum_{m=1}^{\infty} \left\{ |f(\wp + \kappa\sqrt{m})|^2 + |f(\wp - \kappa\sqrt{m})|^2 \right\} \right\}. \quad (11)$$

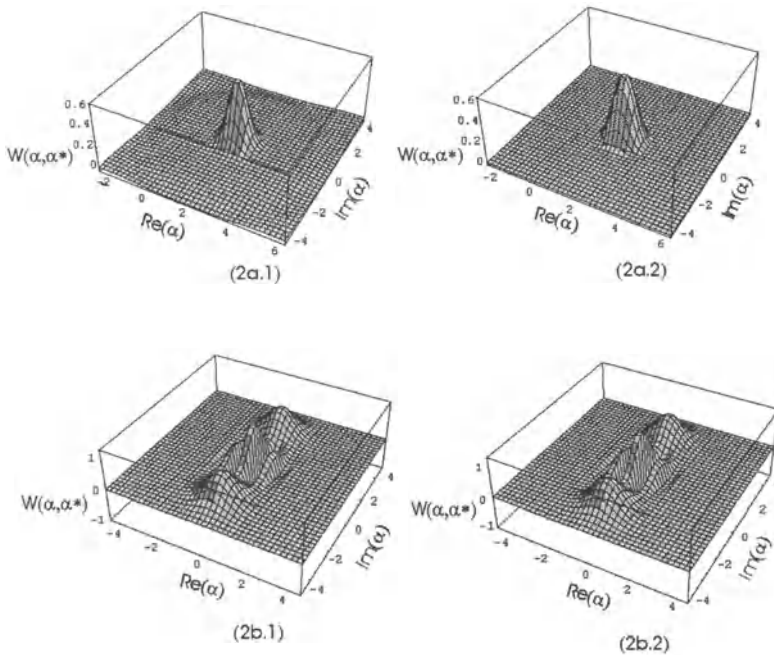


Fig. 2. (a.1) Original Wigner function of coherent state. (a.2) Reconstructed Wigner function of coherent state. (b.1) Original Wigner function of Schrödinger cat state. (b.2) Reconstructed Wigner function of Schrödinger cat state.

It is clear now that, for $k\Delta x \gg 0$, $f(\varphi \pm \kappa\sqrt{m})$ is a sharply peaked function at $\varphi/\kappa = \pm\sqrt{m}$. We can therefore recover the photon statistics of the cavity field $p_r(m, \alpha)$ from the momentum distribution $W(\varphi)$ via

$$p_r(m, \alpha) = \begin{cases} \frac{1}{2N} W(\varphi)|_{\varphi=0} & \text{for } m = 0 \\ \frac{1}{N} W(\varphi)|_{\varphi=\kappa\sqrt{m}} & \text{for } m \geq 1 \end{cases} \quad (12)$$

where N is a normalization constant to ensure $\sum_m p_r(m, \alpha) = 1$. The reconstructed Wigner function is then given by

$$W_r(\alpha, \alpha^*) = \frac{2}{\pi} \sum_m (-1)^m p_r(m, \alpha). \quad (13)$$

As an example we consider Schrödinger cat state $|\Psi\rangle = \mathcal{M}(|\alpha_0\rangle + |-\alpha_0\rangle)$, where $\mathcal{M} = [2(1 + \exp(-2|\alpha_0|^2))]^{-1/2}$ is the normalization constant [10]. In Fig. (2a & 2b) we plot the original Wigner function $W(\alpha, \alpha^*)$ and the reconstructed Wigner function $W_r(\alpha, \alpha^*)$ for coherent state and Schrödinger cat state. The reconstructed Wigner functions are in good agreement with original Wigner functions. *Acknowledgment.* Authors would like to acknowledge the financial support of Pakistan Science Foundation.

References

1. P. A. M. Dirac, *The Principles of Quantum Mechanics* (Clarendon Press, Oxford, 1958).
2. K. Zaheer and M. S. Zubairy, in *Advances in Atomic, Molecular, and Optical Physics*, Vol. 28, ed. by D. Bates and B. Bederson, (Academic Press, New York 1991), p. 143.
3. E. Schrödinger, *Naturwissenschaften* **23**, 807 (1935); **23**, 823 (1935); **23**, 844 (1935) [English translation by J. D. Trimmer, Proc. Am. Phys. Soc. **124**, 3325 (1980)].
4. K. Vogel and H. Risken, *Phys Rev. A* **40**, 2847 (1989); G. M. D'Ariano, U. Leonhardt, and H. Poul, *ibid.* **52**, R1801 (1995). *ibid.* **52**, 4899 (1995).
5. M. Brune, *et al*, *Phys. Rev. Lett.* **65**, 976 (1990).
6. M. J. Holland, D. F. Walls, and P. Zoller, *Phys. Rev. Lett.* **67**, 1716 (1991); A. M. Herkommer, V. M. Akulin and W. P. Schleivh, *ibid.* **69**, 3298 (1992); M. Freyberger and A. M. Herkommer, *ibid.* **72**, 1952 (1994).
7. P. J. Bardroff, E. Mayr, and W. P. Schleich, *Phys. Rev. A* **51**, 4963 (1995); W. Vogel, D.-G. Welsch, and L. Leine, *J. Opt. Soc. Soc. Am. B* **4**, 1633 (1987).
8. M. S. Zubairy, *Phys. Lett.* **A 222**, 91 (1996); T. Azim and M. S. Zubairy, *ibid.* **250**, 344 (1998); M. S. Zubairy, *Phys. Rev. A* **57**, 2066 (1998).
9. K. E. Cahill and R. J. Glauber, *Phys. Rev. A* **177**, 1857 (1969); **177**, 1882 (1969).
10. Mohammad Mahmoudi and M. Suhail Zubairy (submitted)

Projection Pattern Reducing with Magnetic Lens in Atom Lithography

Zeng Qinglin, Li Chuanwen, Cai Weiquan, Huo Yunsheng, Wang Yuzhu

Laboratory for Quantum Optics, Shanghai Institute of Optics and Fine Mechanics, Chinese Academy of Sciences, P. O. Box 800-211, Shanghai 201800, China

Abstract. We analyse the chromatic and spherical aberration of the image formation by a hexapole magnetic lens focusing a cooled Cr beam and forwarded a proposal of projecting arbitrary pattern onto a substrate with reduced magnification. The feature size is determined by the spherical aberration.

1 Introduction

In 1995, W. G. Kaanders et. al.[1] successfully completed an image formation experiment for an object illuminated by laser cooled Rb atomic beam with a hexapole magnetic lens. And this technique has evoked potential application in atom lithography. Here we analyse the properties of a hexapole magnetic lens in atomic beam imaging and propose a method for arbitrary atom lithography – projection pattern reducing with magnetic lens aimed at the fabrication of sub-micron arbitrary patterns.

2 Magnetic Lens

An atom in a hexapole magnetic field is susceptible to a force which can be written as

$$F = -2\mu_{eff}H_0 \left[1 - 8(r/r_0)^2 \right]. \quad (1)$$

When $(r/r_0) \ll 1$, the force has the form of a harmonic oscillation and the magnetic lens has similar imagery characters to the atomic beam as a thin lens to a light beam. The focus length of an ideal magnetic lens should be

$$f = mv_z^2 / \left[\int_0^{l_2} \mu_{eff} \frac{\partial^2 H}{\partial r^2} dz \right], \quad (2)$$

here m is the atom mass, l_2 is the geometric length of the magnetic poles, v_z is the longitudinal velocity of the atom. Fig.1 shows the real experimental situation. An object O is an arbitrary pattern (here a circle on the y-axis with radius $\Delta\delta$) is placed before the lens. The height of the point O is δ_0 . The

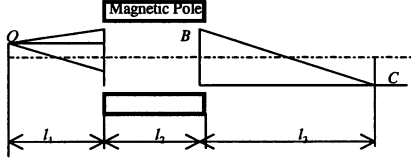


Fig. 1. The formation of an image by an experimental hexapole magnetic lens l_1 is the distance between the entrance of the lens and the object, l_3 is the distance between the exit of the magnetic lens and the imaging plane.

image of this object is formed at C after focused by the magnetic lens. The height of the image and the transverse velocity at relevant points are

$$\begin{aligned}
 R(C) &= R(B) - \frac{v_r(B)l_3}{v}, \\
 R(B) &= \delta_0 \cos \frac{l_2}{l_T} + \theta(l_T \sin \frac{l_2}{l_T} + l_1 \cos \frac{l_2}{l_T}), \\
 v_r(B) &= \omega [\delta_0 \sin \frac{l_2}{l_T} + \theta(l_T \cos \frac{l_2}{l_T} - l_1 \sin \frac{l_2}{l_T})], \\
 l_T &= \frac{v}{\omega}, \\
 \omega &= \sqrt{\frac{2\mu_{eff}H_0}{mr_0^2}}. \tag{3}
 \end{aligned}$$

where l_T is the character length of forming an image, ω is the frequency of the harmonic oscillation, θ is the angle divergence of the beam. The magnification is

$$K = \frac{R(C)}{\delta_0} = \cos \frac{l_2}{l_T} - \frac{(l_T \sin \frac{l_2}{l_T} + l_1 \cos \frac{l_2}{l_T})}{(l_1 \sin \frac{l_2}{l_T} - l_T \cos \frac{l_2}{l_T})} \tag{4}$$

3 Analysis of the Spherical and Chromatic Aberration

Preserving the eighth-order term and using Van der pole approximation, $R(C)$ can be written as

$$\begin{aligned}
 R(C) &= \delta_0 [\cos \frac{l_2}{l_T} - (\frac{l_T \sin \frac{l_2}{l_T} + l_1 \cos \frac{l_2}{l_T}}{l_1 \sin \frac{l_2}{l_T} - l_T \cos \frac{l_2}{l_T}} \sin \frac{l_2}{l_T}) \\
 &\quad \times (1 - 4(\frac{\delta_0}{r_0})^6)(l_T + l_1 \frac{l_T \sin \frac{l_2}{l_T} + l_1 \cos \frac{l_2}{l_T}}{l_1 \sin \frac{l_2}{l_T} - l_T \cos \frac{l_2}{l_T}})]. \tag{5}
 \end{aligned}$$

From Eq.(5), the spherical aberration coefficients are

$$A_{sph}(\delta_0) = 32(\frac{\delta_0}{r_0})^6 (\frac{l_T \sin \frac{l_2}{l_T} + l_1 \cos \frac{l_2}{l_T}}{l_1 \sin \frac{l_2}{l_T} - l_T \cos \frac{l_2}{l_T}} \times \sin \frac{l_2}{l_T})$$

$$\begin{aligned}
& + 24\theta \left(\frac{\delta_0}{r_0} \right)^6 \left(\frac{l_T}{\delta_0} + \frac{l_1}{\delta_0} \frac{l_T \sin \frac{l_2}{l_T} + l_1 \cos \frac{l_2}{l_T}}{l_1 \sin \frac{l_2}{l_T} - l_T \cos \frac{l_2}{l_T}} \right), \\
A_{sph}(\theta) & = 4 \left(\frac{\delta_0}{r_0} \right)^6 \left(l_T + l_1 \frac{l_T \sin \frac{l_2}{l_T} + l_1 \cos \frac{l_2}{l_T}}{l_1 \sin \frac{l_2}{l_T} - l_T \cos \frac{l_2}{l_T}} \right). \quad (6)
\end{aligned}$$

The coefficient of chromatic aberration is

$$\begin{aligned}
A_{chro} & = \frac{\delta_0}{v_z} \left[\frac{l_2}{l_T} \sin \frac{l_2}{l_T} - \frac{l_3}{l_T} \sin \frac{l_2}{l_T} - \frac{l_3 l_2}{l_T^2} \cos \frac{l_2}{l_T} \right] \\
& + \frac{\theta}{v_z} \left[l_T \sin \frac{l_2}{l_T} - l_2 \cos \frac{l_2}{l_T} + \frac{l_1 l_2}{l_T} \sin \frac{l_2}{l_T} \right. \\
& \left. - \frac{l_1 l_3}{l_T} \sin \frac{l_2}{l_T} - \frac{l_2 l_3}{l_T} \sin \frac{l_2}{l_T} - \frac{l_1 l_2 l_3}{l_T^2} \cos \frac{l_2}{l_T} \right] \quad (7)
\end{aligned}$$

Considering focusing a Cr atomic beam at the magnetic sublevel $m_z = 4$, and when $\frac{\partial^2 H}{\partial r^2} = 266 \text{ T/m}^2$, $\Delta\delta = 50 \mu\text{m}$, $\delta_0 = 950 \mu\text{m}$, $l_1 = 80 \text{ mm}$, and $l_2 = 20 \text{ mm}$, $r_0 = 10 \text{ mm}$, $\Delta v = 1 \text{ m/s}$, $v = 100 \text{ m/s}$, $\theta = 0.1 \text{ mrad}$. l_3 is determined by Eq.(5) in [2]. The feature size expanded by the chromatic aberration is $1.32 \mu\text{m}$ and the ones expanded by the angle divergence and the different initial position are at the order nanometer.

4 Projection Reducing of Arbitrary Pattern

The basic idea is shown in Fig.2. The atomic beam is considered as a matter wave, the wave function of the atomic beam after illuminating the object is

$$U(x_0, y_0, v_z) = \frac{f A(v)}{f - d} \exp\left(\frac{x_0^2 + y_0^2}{2(f - d)}\right) t(x_0, y_0). \quad (8)$$

here $A(v)$ is the distribution of the velocity of the atoms, $t(x_0, y_0)$ is pattern distribution of the mask, $A(v)$ is the distribution of the velocity of the atoms, here

$$A(v) = B v^3 \exp\left(\frac{(v - \bar{v})}{\Delta v}\right)^2, \quad (9)$$

where mean velocity is $\bar{v} = 100 \text{ m/s}$, velocity deviation is $\Delta v = 1 \text{ m/s}$ and B is the normal coefficient. Down the stream is placed a substrate on which the patterns is deposited, the wave function at the substrate is

$$\begin{aligned}
U_l(x_l, y_l, v_z) & = \exp(j k l) \exp\left(-jk \frac{x_l^2 + y_l^2}{2l}\right) \\
& \times \int U(x_0, y_0, v_z) \exp[-jk(x_0^2 + y_0^2)/2l] \\
& \times \exp[jk(x_0 x_l + y_0 y_l)] dx_0 dy_0, \quad (10)
\end{aligned}$$

The Fourier limitation is

$$L = 1.22\hbar l / (2\Delta\delta mv). \quad (11)$$

The mean value of L is $\bar{L} = \int A(v)Ldv$, and the size expanded by the velocity is $\Delta L_{chro} = -L\frac{dv}{v}$, the expanded size due to the spheric aberration is $\Delta L_{sph} = ((x_0^2 + y_0^2)^3)_{max}/l^2$. According to Eq.(2) and Eq.(9), $f = 44\text{mm}$. For $d = 5\text{mm}$, $l = 38\text{mm}$, the mean values of the Limitation, the expended sizes are $\bar{L} = 5.6\text{nm}$, $\Delta\bar{L}_{chro} = 14\text{nm}$, $\Delta\bar{L}_{sph} = 0.69\mu\text{m}$ (in the direction of y axis) respectively, and at the same time the mean value of the image spot is $2.56\mu\text{m}$.

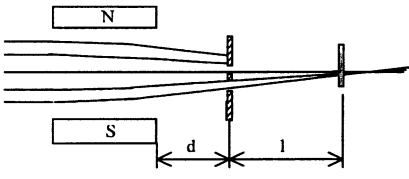


Fig. 2. the basic idea of image formation based on the Fourier optics. d is the distance between the main plane of the lens and the object, l is the distance between the object and the substrate.

From the above numerical results, when $d + l < f$ is satisfied, it is only a process of geometrical image formation. If $d + l = f$, a very small image spot will be attained, this process is just what we proposed. But it also should be noticed that there will be some defects in the symmetry.

5 Conclusion

A new method for arbitrary pattern atom lithography which can obtain sub-micrometer featuresize pattern is proposed, And the resolution is ultimately determined by the spherical aberration. The numerical results show that the method is feasible in theory.

Acknowledgments. This research is supported by the National Science Foundation of China (69678009,19774060) and the Science and Technique Development Foundation of Shanghai.

References

1. Kaonders W.G.,et al.(1995) Imaging with an atomic beam. *Nature* **375**, 214-216.
2. Peng Zu-qin, et al.(1989) The Design and Optimization of Atomic Beam Optics in a Hydrogen Maser. *Acta Metrologica Sinica* **10**, 306-310

Atoms in the Magnetic Atomic Wave-Guide

Daijun Li¹, Xiaji Liu¹, Hu Huang¹, Shiqun Li¹, Yuzhu Wang²

¹ Department of Physics, Tsinghua University, Beijing 100084, China

² Shanghai Institute of Optics and Fine Mechanics, Shanghai 201800, China
e-mail: gjc-dmp@mail.tsinghua.edu.cn

Abstract. In the beginning of this year, we drew a novel model that uses the evanescent magnetic field produced by a period-magnetized magnetic hollow tube to guide cold atoms. In this paper, we simulate the quantum motion of the atoms in the tube and present the magnetic atom wave-guide theory analogous to optic wave-guide.

1 The idea of magnetic tube for atom guidance

Recently, we introduced a new hollow magnetic tube structure as atomic wave-guide[1]. Our idea of the magnetic tube comes from the magnetic mirror[2](Fig. 1).

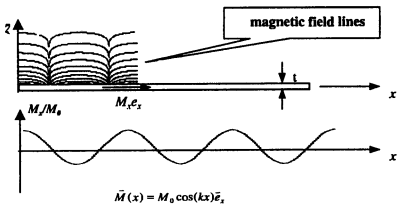


Fig. 1. The magnetic mirror

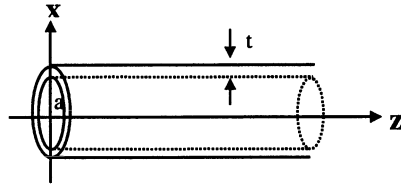


Fig. 2. The magnetic tube

The magnetic mirror is magnetized with sinusoidal magnetization $\vec{M}(x) = \vec{e}_x M_0 \cos kx$. The atom undergoes an elastic specular reflection by the short range perpendicular Stern-Gerlach force of the magnetic mirror. We construct our hollow magnetic tube by *wrapping the planar magnetic mirror into a tube*.(Fig. 2).

The tube is magnetized with sinusoidal magnetization along the z direction. The magnetic fields inside at the plane $y = 0$ are:

$$B_x = -\frac{\mu_0 M_0}{2} \int_0^{+\infty} z \sin(kz) \frac{2}{\pi} \left[\int_0^\pi \left(\frac{a}{r_1^3} - \frac{a+t}{r_2^3} \right) \cos \theta d\theta \right] dz \cdot \sin(kz_0)$$

$$B_z = \frac{\mu_0 M_0}{2} \int_0^{+\infty} \cos(kz) \frac{2}{\pi}$$

$$\left[\int_0^\pi \left(\frac{a(x_0 \cos \theta - a)}{r_1^3} - \frac{(a+t)(x_0 \cos \theta - a - t)}{r_2^3} \right) d\theta \right] dz \cdot \cos(kz_0) \quad (1)$$

The magnitude distributions of the field along the radial direction and the longitudinal direction are Fig. 3(a), (b). In numerical calculation, we adopt $a = 80\mu\text{m}$ (the inner radius), $t = 2.5\mu\text{m}$, $\mu_0 M_0 = 700\text{G}$ and $\lambda = \frac{2\pi}{k} = 14\mu\text{m}$.

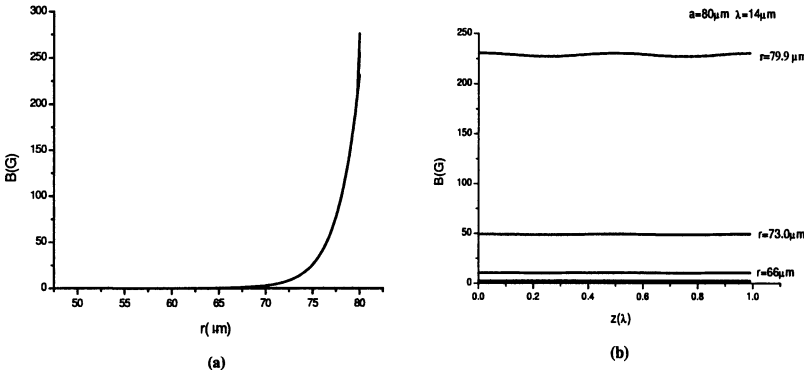


Fig. 3. The distribution of the magnetic field (a) along the radial direction. (b) along the axial direction.

The magnetic tube could be used to guide atoms when some conditions are satisfied, as we have discussed in our paper[1].

In comparison with the hollow fiber, the magnetic tube has a larger aperture. The radius of the magnetic tube we considered is about 0.1mm which is the same size as that of BEC, while the typical radius of the hollow fiber are about 4 – 10 micron. The field distribution in the magnetic tube always has perfect axial symmetry. In the hollow optical fiber, only the HE₁₁ mode is suitable for the atomic guidance[3]. An atom in a optical atomic wave-guide has due to the interaction of the atom and the photons. In magnetic atomic wave-guide, the spontaneous emission loss can be ignored.

2 The quantum atomic motion

We consider the magnetic potential and the van der Waals potential [4] (Fig. 4). The radial potential distribution in the tube :

$$V = V_{mag} + V_{vdw} = \mu_B \cdot B_{max} \exp[k(r - a)] + \frac{C_{vdw}}{(r - a)^3} \quad (2)$$

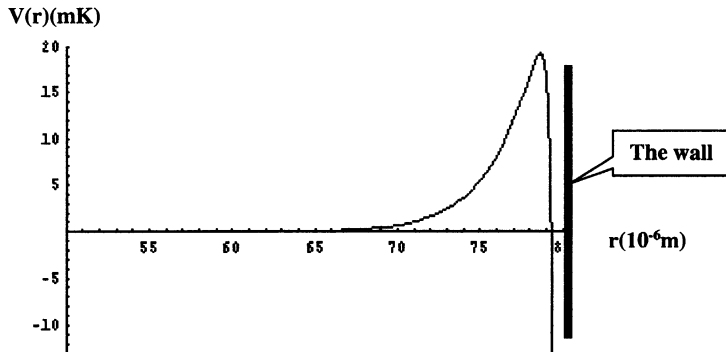


Fig. 4. The radial potential distribution in the tube considering the magnetic potential and the van der Waals potential

The potential can be written approximately:

$$V(r) = \begin{cases} 0 & (r < r_1) \\ V_0 & (r_1 \leq r < r_2) \\ -\infty & (r \geq r_2) \end{cases} \quad (3)$$

Using the cylinder coordinates, the wavefunction has the following form

$$\Psi(r, \theta, z) = R(r) \exp(im\theta) \exp(i\beta z) \quad (4)$$

where the radial wavefunction $R(r)$ satisfy the Bessel equation.

We replace the $-\infty$ potential with a definite potential $-V_m$, then make V_m limit to ∞ and denote $\delta_1 = \frac{2Ma^2}{\hbar^2} \left(E - \frac{\hbar^2\beta^2}{2M} \right)$, $\delta_2 = \frac{2Ma^2}{\hbar^2} \left(V_0 - E + \frac{\hbar^2\beta^2}{2M} \right)$, $\delta_3 = \frac{2Ma^2}{\hbar^2} \left(V_m + E - \frac{\hbar^2\beta^2}{2M} \right)$. The solution of the radial wavefunction is:

$$R(r) = \begin{cases} AJ_m(\sqrt{\delta_1} \frac{r}{a}) & (0 \leq r < r_1) \\ BI_m(\sqrt{\delta_2} \frac{r}{a}) + CK_m(\sqrt{\delta_2} \frac{r}{a}) & (r_1 \leq r < r_2) \\ DH_m^{(1)}(\sqrt{\delta_3} \frac{r}{a}) & (r \geq r_2) \end{cases} \quad (5)$$

The constants A, B, C, D and the energy E can be determined by the boundary condition at $r=r_1$ and r_2 . The wave-function of the basic transverse mode Ψ_{01} is Fig. 5.

When the potential is low, the energy has a imaginary component, that is, the atoms will be attenuated when propagate in the radial direction. But fortunately, the magnetic interaction potential we construct is so high(for ^{87}Rb atom and taking $B_{max} = 300\text{G}$, $V_0 = 20\text{mK}$) that the imaginary component can be ignored when we consider the basic transverse mode.

The energy of the ground state(with $V_0 = 20\text{mK}$) is:

$$E_0 \approx 6.55 \frac{\hbar^2}{2Ma^2} + \frac{\hbar^2\beta^2}{2M} \quad (6)$$

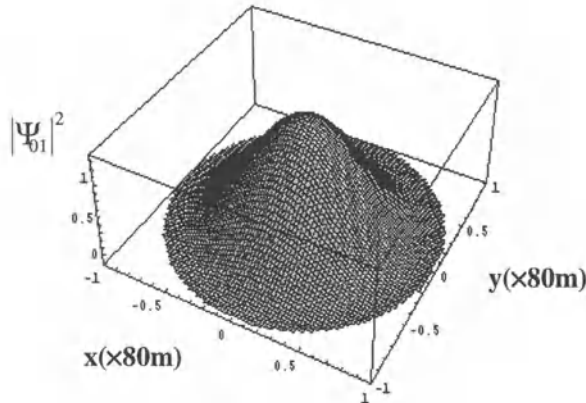


Fig. 5. The absolute value squared of the wave-function of the basic transverse mode

The longitudinal velocity of the atoms is $v_l = \frac{\hbar\beta}{M}$ and the transverse atom velocity of the basic mode is $v_t \approx 2.56 \frac{\hbar}{Ma}$. In case of ^{85}Rb , $M = 1.42 \times 10^{-25} \text{ Kg}$, then $v_t = 2.38 \times 10^{-5} \text{ m/s}$, the corresponding transverse temperature is only 0.006 nK, and the de Broglie wavelength of the basic transverse mode is about $196 \mu\text{m}$. The low transverse temperature of the basic mode is due to the large radii of the tube. When $a = 5 \mu\text{m}$, the temperature of the transverse mode is 1.54 nK. This temperature is feasible to achieve now.

Acknowledgments. This work was supported by the National Natural Science Foundation of China and National Education Committee's Foundation.

References

1. Daijun Li, Hu Huang et al. (1999) A magnetic tube structure for atom guidance. *Optics Comm.* **160**, 72-74
2. T. M. Roach, et al. (1995) Realization of a Magnetic Mirror for Cold Atoms. *Phys. Rev. Lett.* **75**, 629
3. Haruhiko Ito, et al. (1995) Optical potential for atom guidance in a cylindrical-core hollow fiber. *Optics Comm.* **115**, 57-64
4. Victor I.Balykin (1999) Atom Waveguides, *Advances in atomic, molecular, and optical physics*, 4, p181.

Study of the Time-Resolved Spectra of $C^1\Pi_1$ State for the InCl Molecule

Yunjing Li, Meirong Lin, Wenli Zou, Baozheng Zhang, Wenju Chen

Nankai University, Institute of Modern Optics, Opto-electronic Information Science and Technology Laboratory, EMC., Tianjin 300071, P. R. China

Abstract. The laser induced fluorescence spectrum of the $C^1\Pi_1 \rightarrow X^1\Sigma^+$ for InCl molecule has been studied. The emission spectrum of $C^1\Pi_1(v' = 1)$ is observed for the first time, which proved that the predissociation of $C^1\Pi_1$ only occur above the $v' = 1$. The collision-free fluorescence radiative lifetime of $\tau_0 \approx 11$ ns and the electronic transition moment $|Re|^2 \approx 5.95 D^2$ for $C^1\Pi_1(v' = 1)$ are obtained.

1 Introduction

The indium monohalides have attracted people's interest in physical and chemical property for a long time[1-6]. In the development of new semiconductor devices in high frequency and opto-electronic application, they play an important role. In chemical vapor deposition techniques such as the Effer process[3], indium monohalide act as gas phase transporters of semiconductor material[4,5].

The $C^1\Pi_1$ state of InCl molecule is a striking example of predissociation in the upper electronic state. Wehrli and Miescher[1] have studied the $X^1\Sigma^+ \rightarrow C^1\Pi_1$ over the spectral range $265 \sim 282$ nm. Perumalsamy[6] suggested that the complete predissociation of the C state take place only above $v = 3$ and first found the predissociation occurred in the $J = 73$ of $v = 0$ level of $C^1\Pi_1$ state[7]. Jones *et. al.*[8] have observed more new bands up to $v = 6$ in C state from microwave discharge absorption spectra.

In this paper, we present the laser induced fluorescence of $C^1\Pi_1(v' = 1) \rightarrow X^1\Sigma^+(v'' = 1 \text{ to } 7)$ and the time-resolved spectra of $C^1\Pi_1(v' = 1) \rightarrow X^1\Sigma^+(v'' = 4)$ in different pressures. At last we obtained the collision-free lifetime and electronic transition moment of $C^1\Pi_1(v' = 1) \rightarrow X^1\Sigma^+$.

2 Experiment

We use a pulsed Q-switched fourth harmonic YAG (Quanlet YG580). The indium monochloride is produced by heating the indium trichloride (China, 99.999%) in the presence of an excess of mental indium (99.99%) under vacuum ($\times 10^{-5}$ Torr). The other detailed description can be seen in paper[9].

3 Theory

3.1 The theory of collision-free radiative lifetime τ_0 and quenching rate constant k_Q

The relation of the collision-free radiative lifetime $1/\tau_0$ and quenching rate constant k_Q is:

$$\frac{1}{\tau} = \frac{1}{\tau_0} + k_Q P_T \quad (1)$$

where P_T is the pressure of the molecule. In order to obtain the collision-free radiative lifetime τ_0 of the molecule, we need to measure the lifetimes in different pressures. According to the equation of (1), we can get the curve of $\tau \sim P_T$, the Stern-Volmer curve. From it the collision-free radiative lifetime τ_0 and quenching rate constant k_Q are determined by extrapolating the curve to zero pressure.

As the influence of the instruments, the measured fluorescence decay curve is the convolution of the real fluorescence decay curve and the response function of the instruments, which is called the apparent fluorescence decay curve. In order to eliminate the error of the time response of the instruments, the apparent curve will be deconvoluted.

The theory of the electronic transition moment $|\text{Re}|^2$. The radiative lifetime $\tau_{v'}$ of an excited vibration level v' is related to the transition probability $A_{v'v''}$ by the following expression:

$$\frac{1}{\tau_{v'}} = \frac{64\pi^4}{3h} |\text{Re}|^2 \sum_{v''} q_{v'v''} r_{v'v''}^3 \quad (2)$$

where v , $q_{v'v''}$ and $r_{v'v''}$ are, respectively, the transition frequency, Frank-Condon factor, and r-centroid of the (v', v'') band, and $|\text{Re}|^2$ is the square of the electronic transition moment.

Thus we can calculate $|\text{Re}|^2$ from $\tau_{v'}$ by evaluating the simple summation contained in equation (2).

4 Result and Discussion

Figure 1 shows the LIF spectra of the $C^1\Pi_1 \rightarrow X^1\Sigma^+$ transition excited using 266 nm laser. The wavelength of the six bands are 268.4 nm, 270.7 nm, 273.0 nm, 275.4 nm, 277.7 nm, 280.2 nm and 282.5 nm. We assigned these vibration bands to (1-1), (1-2), (1-3), (1-4), (1-5), (1-6), (1-7) based on the band frequencies of Jones[8]. To our knowledge, it is the first time to observe the transition from the $v' = 1$ of $C^1\Pi_1$ state in emission which proved that the predissociation of $C^1\Pi_1$ state only occurs above the $v' = 1$.

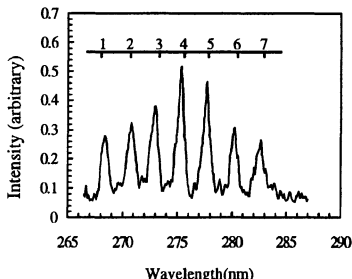


Fig. 1. The laser induced fluorescence in the range of 266.5 – 287.0 nm of InCl

In order to obtain collision-free lifetime, we measured the time-resolved curves of 275.4 nm band of $C^1\Pi_1(v' = 1) \rightarrow X^1\Sigma^+(v'' = 4)$ in $250^\circ\text{C} \sim 290^\circ\text{C}$. The vapor pressures under different temperatures are gotten, according to the Robert equation[10]. Figure 2 shows a typical fluorescence decay curve of InCl in 290°C , where the solid curve represents the apparent fluorescence decay curve, the dotted line represents the deconvoluted fluorescence decay curve.

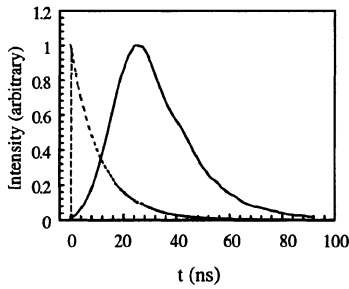


Fig. 2. The fluorescence decay curve of InCl $C^1\Pi_1(v' = 1) \rightarrow X^1\Sigma^+(v'' = 4)$ at 290°C . — The observed fluorescence decay curve; - - - The deconvoluted fluorescence decay curve

Table 1 gives the deconvoluted lifetimes of $C^1\Pi_1(v' = 1) \rightarrow X^1\Sigma^+(v'' = 4)$ for InCl under different pressures. It can be seen from the table that the lifetimes under different pressures could not be distinguished in our experimental precision scope. So we approximately think the collision-free lifetime of $C^1\Pi_1(v' = 1)$ is approximate $11(\pm 1)$ ns.

Table 1. The lifetimes of $C^1\Pi_1(v' = 1) \rightarrow X^1\Sigma^+(v'' = 4)$ for InCl in $0.144 \sim 0.614$ Torr.

| $P(\text{Torr})$ | 0.144 | 0.211 | 0.305 | 0.436 | 0.614 |
|-------------------|-------|-------|-------|-------|-------|
| $\tau(\text{ns})$ | 12 | 10 | 10 | 12 | 11 |

Consider the F-C factors[7] of $C^1\Pi_1(v' = 1) \rightarrow X^1\Sigma^+$, the measurement result of radiate lifetime and the frequency of the molecular transiation, we calculate the electronic transition moment $|Re|^2 \approx 5.95\text{ D}^2$ according to the equation (3). This value has been obtained for the first time.

References

1. M. Wehrli, E. Miescher 1934 Spektroskopische untersuchung dampfformiger indiumhalogenide, Helvetica Physica Acta **7**, 298-330
2. H. M. Froslie, J. G. Winans 1947 The absorption spectrum of InCl, Phys. Rev. **72**, 481-491
3. D. Effer 1965, Epitaxial growth of doped and pure GaAs in an open flow system, J. Electrochem. Soc. **112**, 1020-1025
4. V. M. Donnelly and R. F. Karlicek 1982, Development of laser diagnostic probes for chemical vapor deposition of InP/InGaAsP epitaxial layers, J. Appl. Phys. **53**, 6399-6407
5. R. F. Karlicek, B. Hammarlund and J. Ginocchio 1986, Uv absorption spectroscopy for monitoring hydride vapor-phase epitaxy of InGaAsP alloys, J. Appl. Phys. **60**, 794-799
6. K. Perumalsamy, S. B. Rai, K. N. Upadhyay and D. K. Rai 1985, Study of indium monochloride molecule, Phys. **132C**, 122-140.
7. K. Perumalsamy, S. B. Rai and K. N. Upadhyay 1986, On the $C^1\Pi_1-X^1\Sigma^+$ system of the indium monochloride molecule and its dissociation energy, Phys. **141C**, 315-322
8. W. E. Jones and T. D. Mclean 1991, Spectroscopic investigation of InCl in the ultraviolet: The $C^1\Pi_1-X^1\Sigma$ system, J. Mol. Spec. **150**, 195-200
9. Yunjing Li, Meirong Lin, Baozheng Zhang, Qingchun Zhao, Wenli Zou, and Wenju Chen 1999, Lifetime measurement of the $A^3\Pi_0$ electronic state of InCl by laser induced fluorescence, Mole.Phys. **97**, 606-609
10. O. Kubaschewski and E. LL. Evans, Metallurgical thermochemistry (London, Perga Press, 1955)

Emission Spectrum of a Three-Level Atom in a Photonic Crystal

Zhixin Lin, Yaping Yang, Hong Chen, Weiguo Feng

Department of Physics, Tongji University, Shanghai 200092, China

Abstract. We study the spontaneous emission from a V-type three-level atom embedded in a photonic band gap material. The radiation field may contain zero or one or two travelling pulses by selecting the atom-field coupling constants and changing the relative positions of the upper levels from the band edge. The properties of the localized modes are also displayed by means of spectral analysis. And we get two propagating pulses of similar height in the propagating field.

1 Introduction

With the proposal of photonic band gap materials [1,2], many interesting effects have been predicted when the transition frequencies lying near band edge, such as the formation of photon-atom bound state[3], spectral splitting of spontaneous emission [4] and enhanced quantum interference effects [5].

In this paper, we investigate emission spectrum of a three-level atom in a photonic crystal. Through the spectral analyses of radiation field, we can see the variation of the relative positions of the localized modes. And we find there are two propagating pulses of similar height in spontaneous spectrum, which can be applied to design an active microsized optical switch.

2 Basic Theory

Consider a three-level atom with two upper levels $|a_1\rangle$ and $|a_2\rangle$ and a lower level $|a_3\rangle$. $|a_1\rangle$ and $|a_2\rangle$ are supposed to be near the band edge and coupled by the same vacuum modes to $|a_3\rangle$, the energy of which is assumed to be zero. The resonant transition frequencies from $|a_1\rangle$ and $|a_2\rangle$ to $|a_3\rangle$ are ω_1 and ω_2 . The dispersion relationship in the vicinity of the band edge can be expressed approximately by [3,4] $\omega_k = \omega_c + \omega_c(k - k_0)^2/k_0^2$, where ω_c is the cut-off frequency of the band edge. After carrying out the rotating wave approximation at ω_c , the atom-field Hamiltonian can be written as

$$\hat{H} = \sum_k \hbar \omega_k b_k^\dagger b_k + \sum_m \hbar \omega_m |a_m\rangle \langle a_m| + i\hbar \sum_k \left(\sum_m g_k^{(m)} b_k^\dagger |a_3\rangle \langle a_m| - H.c. \right), \quad (1)$$

where k stands for both momentum and polarization of the vacuum modes. b_k (b_k^\dagger) is the annihilation (creation) operator for the k -th vacuum mode with

frequency ω_k . $g_k^{(m)}$ is the coupling constant between the k -th vacuum mode and the atomic transitions from $|a_m\rangle$ to $|a_3\rangle$ ($m = 1, 2$), and is hypothesized to be real. The wave function of the system at time t can be given by

$$|\Psi(t)\rangle = \sum_{m=1,2} A_m(t) e^{-i\omega_m t} |a_m\rangle_f + \sum_k B_k(t) e^{-i\omega_k t} |a_1\rangle |1_k\rangle_f, \quad (2)$$

with $|A_1(0)|^2 + |A_2(0)|^2 = 1$ and $B_k(0) = 0$.

Assuming that the two transitional dipole moments are parallel to each other and Using the method of Laplace transform, we obtain that as $t \rightarrow \infty$,

$$B_k(\infty) = -g_k^{(1)} \sum_m \frac{F(x_m^{(1)})}{K(x_m^{(1)})G'(x_m^{(1)})} - g_k^{(1)} \sum_m \frac{F(x_m^{(2)})}{K(x_m^{(2)})H'(x_m^{(2)})} + C_k. \quad (3)$$

Here $F(s) = s[A_1(0) + \sqrt{\alpha}A_2(0)] - i\omega_{12}A_1(0)$, $K(x) = i(\omega_k - \omega_1) + x$, $\gamma_m = \frac{\beta_m^{3/2}}{i\sqrt{-is-\omega_{1c}}}$, and $\beta_m = \left[\frac{\omega_m^2 d_m^2 k_0^3}{6\pi\epsilon_0\hbar\omega_c^{3/2}} \right]^{2/3}$ ($m = 1, 2$). We define $\alpha = \beta_2^{3/2}/\beta_1^{3/2} = (g_k^{(2)})^2/(g_k^{(1)})^2$, $\omega_{12} = \omega_1 - \omega_2$, $\omega_{1c} = \omega_1 - \omega_c$, and $\omega_{2c} = \omega_2 - \omega_c$. C_k comes from the integration along the cut of the single valued branchs. $x_m^{(1)}$ is the root of equation $G(s) = s(s - i\omega_{12}) + [(\alpha + 1)s - i\omega_{12}]\gamma_1 = 0$ in the region ($\text{Im}(s) > \omega_{1c}$ or $\text{Re}(s) > 0$), and $x_m^{(2)}$ is the root of $H(s) = s(s - i\omega_{12}) + [(\alpha + 1)s - i\omega_{12}]\beta_1^{3/2}/\sqrt{is + \omega_{1c}} = 0$ in the region ($\text{Im}(s) < \omega_{1c}$ and $\text{Re}(s) < 0$).

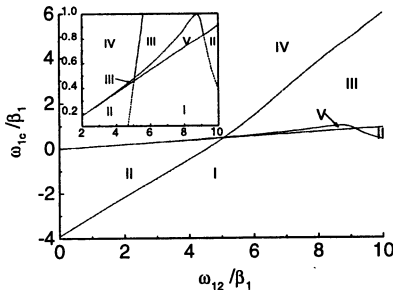


Fig. 1. Five-region distribution for roots with $\alpha = 10$

With the help of numerical calculation, we have found that there are one root at least, and three roots at most, which depends on the atom-field coupling constants and the relative positions of the upper levels from the band gap. When $\alpha = 10$, we can have five cases, as shown in Fig. 1. There are two pure imaginary roots in region I, one complex root and two pure imaginary roots in region II, one complex root and one pure imaginary root in region III, one pure imaginary root and two complex roots in region IV, and only one pure imaginary root in region V. Suppose the imaginary part of the root is b , the corresponding mode's frequency is $\omega_1 - b$ [4]. For the pure imaginary root $x_m^{(1)}$, the corresponding dressed state denotes localized

mode. For the complex root $x_m^{(2)}$ with a negative real part, the corresponding dressed state denotes propagating mode [5].

3 Spectrum and spectral analysis

As the frequency-momentum dispersion relation and the mode density of electromagnetic field in a photonic crystal are strongly altered, the atomic emission spectrum should be drastically modified [1,3]. In this paper, the spontaneous spectrum of the atom $S(\omega_k)$ is the Fourier transform of $\langle E^-(t + \tau)E^\dagger(t) \rangle_{t \rightarrow \infty}$ [6], $S(\omega_k) = |B_k(\infty)|^2 D(\omega_k)$, where $D(\omega_k)$ is mode density.

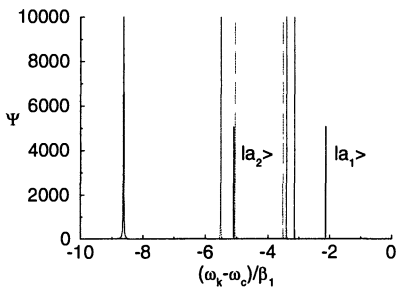


Fig. 2. spectral analysis for $\omega_c = 100\beta_1$, $\omega_{1c} = -3\beta_1$, $\omega_{12} = 2\beta_1$, $|\psi(0)\rangle = \frac{1}{\sqrt{2}}(|a_1\rangle + |a_2\rangle)$, and for various values of the ratio of two coupling constants $\alpha = 0.1$ (dotted curve), $\alpha = 1$ (dashed curve) and $\alpha = 10$ (solid curve).

The localized mode will disappear in the spontaneous spectrum as the mode density is zero when $\omega_k < \omega_c$. Omitting the mode density in the expression of $S(\omega_k)$, we can have $\Psi = |B_k(\infty)|^2$ and study the relation between Ψ and ω_k , which we call spectral analysis. From the expression of the $B_k(\infty)$, we can see that the first term stands for the localized modes, and that the second term is the propagating modes. The number and positions of the localized and propagating modes are obvious in the graph of spectral analysis.

Let the atom initially be in the excited states $|a_1\rangle$ and $|a_2\rangle$ equally. When $\omega_c = 100\beta_1$, $\omega_{1c} = -3\beta_1$, $\omega_{12} = 2\beta_1$, there are two pure imaginary roots for α at the range of 0.1 and 10, The imaginary parts of which are in the regions

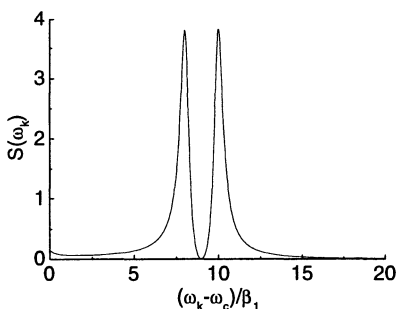


Fig. 3. spontaneous spectrum for $\omega_c = 100\beta_1$, $\omega_{1c} = 10\beta_1$, $\omega_{12} = 2\beta_1$, $\alpha = 0.9$, $|\psi(0)\rangle = \frac{1}{\sqrt{2}}(|a_1\rangle + |a_2\rangle)$;

$[\max(0, \omega_{1c}), \omega_{12}/(\alpha + 1)]$ and (ω_{12}, ∞) , respectively. The radiation field has two localized modes and no propagating mode. In Fig. 2, the position of $|a_1\rangle$ is at -2 in abscissa, and the position of $|a_2\rangle$ is at -5 in abscissa. The position of the upper localized mode is between the levels $|a_1\rangle$ and $|a_2\rangle$, and the ratio of distance to $|a_1\rangle$ and $|a_2\rangle$ is $1 : \alpha$. Another localized mode is below $|a_1\rangle$.

When α increases from 0.1 to 10, $g_k^{(1)}$ is changeless and $g_k^{(2)}$ are increcent, that is to say, the coupling between the atomic radition and the transition from $|a_1\rangle$ to $|a_3\rangle$ remains its intensity, whereas the coupling between the radition and the transition from $|a_2\rangle$ to $|a_3\rangle$ becomes stronger. The lower localized mode, as shown in Fig. 2, becomes farther from $|a_2\rangle$ because it is mainly influenced by $|a_2\rangle$, whereas the upper localized mode influenced partly by $|a_2\rangle$ becomes nearer to $|a_1\rangle$ due to the interference between the two transitions from the two upper levels to the lower level. We can deduce that if $g_k^{(1)}$ increases and $g_k^{(2)}$ reduces or remains invariable (α decreases), the modes will move far away from $|a_1\rangle$.

When $\omega_c = 100\beta_1, \omega_{1c} = 10\beta_1, \omega_{12} = 2\beta_1$, there are two complex roots and one pure imaginary root for α at the range of 0.1 and 10. Here we also let the initial state $|\psi(0)\rangle = (|a_1\rangle + |a_2\rangle)/\sqrt{2}$. The upper levels $|a_1\rangle$ and $|a_2\rangle$ split into dressed states (due to the interference between the two transitions from two upper levels to the lower level. Two of these dressed states represent propagating modes, which can be observed in the spontaneous emission spectrum. From the spectrum graphs as α changes from 0.1 to 10, we know that when $\alpha = 0.9$ there are two propagating pulses of similar height, which can be applied to design an active microsized optical switch.

Studying the expression of $S(\omega_k)$, we find that the spontaneous spectrum is influenced not only by the coupling contants, but also by the initial states. There can also be two similar-height pulses if we adjust the initial states, for example, $|\psi(0)\rangle = 0.6870|a_1\rangle + 0.7266|a_2\rangle$.

In summary, we have derived some features of spontaneous emission from three-level atoms in which two transition frequencies lies near the edge of a photonic band gap. The localized modes' properties and the emission spectrum have been investigated.

Acknowledgment. This work was supported in part by the Shanghai Educational Committee and FRG from Hong Kong Baptist University.

References

1. E. Yablonovitch, Phys. Rev. Lett. **58**, 2059(1987)
2. S. John, Phys. Rev. Lett. **58**, 2486(1987)
3. S. John and J. Wang, Phys. Rev. Lett. **64**, 2418(1990)
4. S. John and T. Quang, Phys. Rev. A **50**, 1764(1994)
5. S.-Y. Zhu, H. Chen and H. Huang, Phys. Rev. Lett. **79**, 205(1997)
6. M. O. Scully and M. S. Zubairy, Quantum Optics (Cambridge University Press, Cambridge, England, 1997), Chap. 10

Reduction of Light Speed in One-Dimensional Photonic Band-Gap Structures with a Defect

Nian-hua Liu^{1,2} and Shi-yao Zhu²

¹ Department of Physics, Nanchang University, Nanchang, 330047, P. R. China

² Department of Physics, Hong Kong Baptist University, Kowloon Tong, Hong Kong

Abstract. The light propagation through one-dimensional photonic band-gap structures with a defect layer embedded at the center was investigated. A multi-scattering model is used to evaluate the average time spent in each layer. The average velocity of light at the defect frequency is greatly reduced.

Ultraslow group velocity of light has been observed recently in an ultracold gas of atoms[1] and in an optically dense hot rubidium gas[2]. This unusual phenomenon may find its potential applications such as optical delay lines[3].

Great time delay was also found in one-dimensional (1D) photonic band gap structures (PBGS)[4,5]. However, the reduction is not so heavy as in the situation of single transmission peak in a completely absorbed background[1].

If a defect is introduced into a PBGS, localized defect modes will appear in the gap[6]. We notice that around the defect mode frequency there is a very narrow transmission peak in a background of strong reflection and expect to have heavy reduction in the light velocity.

Compared with bulk material, the distinguishing feature of the 1D PBGS is the multiple interfaces. As a result of the multiple reflection, a photon after entering the PBGS has to pass very long optical path before it goes out[7]. With the optical path increases, the time spent in the interior increases accordingly. The questions naturally raised are: How long does the optical path be increased in each layer? How much time does a photon spend in each layer before it goes out? In this paper, we will investigate the increased optical path and the traversal time by taking a multiple-reflected photon as a model of light propagation. By means of a statistical method we will investigate the average time spent in each layer.

We consider the normal propagation of light through a finite 1D PBGS which is composed of dielectric layers arranged as “*ABAB* … *ABDBA* … *BABA*”, where *D* is a defect layer embedded at the center. The medium outside is vacuum. The refractive indexes of the layers are n_A , n_B and n_D , and the thicknesses are d_A , d_B and d_D , respectively. We choose $n_A d_A = n_B d_B$, and define a character wavelength $\lambda_0 = 4n_A d_A$ so that the periodic part is a quarter-wave stack.

The propagation of light of frequency ω in the 1D PBGS is described by a photon. The photon is treated as a classical particle when we consider its

optical path. While the reflection and transmission are calculated by wave theory. Consider the situation in the μ th layer. After entering the layer the photon will be reflected frequently by the right interfaces and the left interfaces. It spends time $n_\mu d_\mu/c$ across the layer once. The events of being reflected occur with different probabilities. Assume σ_μ is the probability of entering the μ th layer for the first time, $R_{r,\mu}$ is the reflectivity by the layers on the right side, and $R_{l,\mu}$ is the reflectivity by the layers on the left side. The probabilities of being reflected successively by the right interface and the left interface are in turns equal to $\sigma_\mu R_{r,\mu}$, $\sigma_\mu R_{r,\mu} R_{l,\mu}$, $\sigma_\mu R_{r,\mu}^2 R_{l,\mu}$, $\sigma_\mu R_{r,\mu}^2 R_{l,\mu}^2$, $\sigma_\mu R_{r,\mu}^3 R_{l,\mu}^2 \dots$. Because each event contributes a time $n_\mu d_\mu/c$ with a weight to the total time delay, the time spent in the μ th layer is equal to

$$\tau_\mu = \frac{n_\mu d_\mu \sigma_\mu}{c} (1 + R_{r,\mu} + R_{r,\mu} R_{l,\mu} + R_{r,\mu}^2 R_{l,\mu} + R_{r,\mu}^2 R_{l,\mu}^2 + R_{r,\mu}^3 R_{l,\mu}^2 + \dots) \quad (1)$$

Suppose the total flux of propagation to the right is S_μ . If the photon moves to the right, it makes a positive contribution to the flux. If it moves to the left, it makes a negative contribution to the flux. The total flux is the sum of all contributions of the reflection events,

$$S_\mu = \sigma_\mu [(1 + R_{r,\mu} R_{l,\mu} + R_{r,\mu}^2 R_{l,\mu}^2 + \dots) - (R_{r,\mu} + R_{r,\mu}^2 R_{l,\mu} + R_{r,\mu}^3 R_{l,\mu}^2 + \dots)] \quad (2)$$

If the transmission through the whole system is T , the conservation of the total flux demands $S_\mu = T$, which gives $\sigma_\mu = T(1 - R_{r,\mu} R_{l,\mu})/(1 - R_{r,\mu})$. Substituting σ_μ into Eq.(1) we have

$$\tau_\mu = \frac{n_\mu d_\mu}{c} \frac{T(1 + R_{r,\mu})}{1 - R_{r,\mu}}. \quad (3)$$

The total time of the photon through the whole system is $\tau = \sum_\mu \tau_\mu$, where the sum is over all layers. If the total thickness of the 1D PBGS is L , then the average velocity of the light through the whole system is equal to $v = L/\tau$.

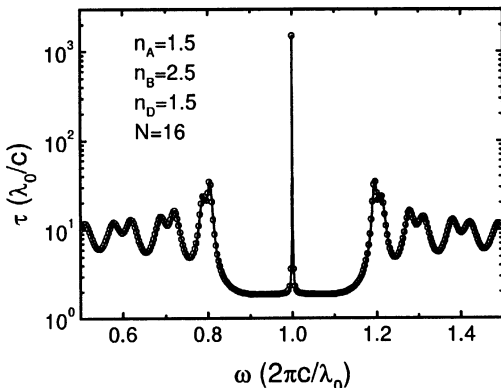


Fig. 1. Total time τ as a function of frequency (solid line) for a 16-period 1D PBGS (quarter-wave stack) with a defect of half-wave embedded at the center. The open circles indicate the result calculated from the group index.

The calculated total time τ as a function of frequency is shown in Fig. 1 (see the solid line) for $n_A = n_D = 1.5$, $n_B = 2.5$, $n_D d_D = \lambda_0/2$ and $N = 16$, where N is the number of periods of the periodic part. We have as well as calculated the time by means of the group index (see the open circles)[5]. The results calculated by two different methods are identical. From the figure we see that the traversal time at the defect frequency is much longer than that in the band and at the band edge.

In the interior of the PBGS, the photon will stay in the defect layer for very long time. The time spent in each layer is plotted in Fig. 2 (see the open circles) for the same structure as in Fig. 1. It is demonstrated that the time is mainly spent around the defect ($\mu = 17$). The long dwell time results in very high energy density around the defect. The localization feature of the defect mode can be understood from the temporal behavior. Such a property of energy localization suggests applications in detectors and nonlinear optics. If a micro-detector is embedded into the defect layer, the sensitivity will be greatly enhanced due to the centered energy.

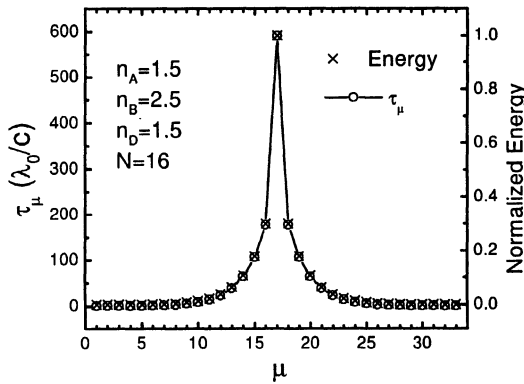


Fig. 2. The time spent in each layer (open circle). The 1D PBGS is the same as in Fig. 1. The cross indicates the distribution of energy for the defect mode of an infinite periodic quarter-wave stack doped with a half-wave defect.

With the similar method as in [8] we have solved the eigenvalue problem of the 1D PBGS with a defect of half-wave doped into an infinite periodic quarter-wave stack. The calculated distribution of energy in each layer is almost the same as the distribution of τ_μ (see the cross in Fig. 2).

The average velocity will be reduced rapidly as we increase the number of the layers, or increase the contrast of the refractive indexes. The dependence of the average velocity on the contrast of the refractive index is shown in Fig. 3 for four different PBGSs. As we see from the figure, the average velocity is reduced to as slow as 10^{-6} of the light speed in vacuum when $n_A = n_D = 1.5$, $n_B \approx 2.5$ for a structure of “16-period + defect + 16-period”.

In summary, we have investigated the temporal behavior of light propagation in 1D PBGS contained a defect layer. Two different methods, one is based on the statistical model of multiple reflection of a photon, the second is derived from the transmission phase shift, give consistent result of the time

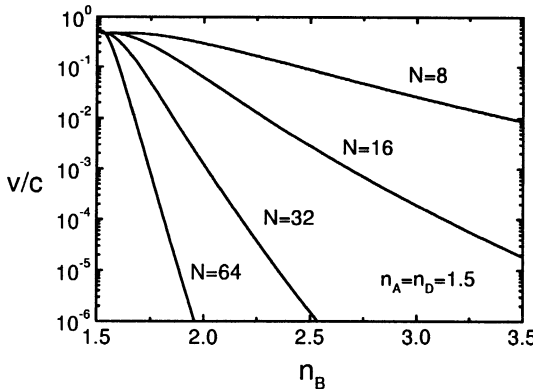


Fig. 3. Average velocity as a function of n_B for fixed $n_A = 1.5$, $n_D = 1.5$. N is the number of periods.

delay. The model of multiple reflection not only gives the average velocity, but also gives the average time spent in each layer. It provides a reasonable physical picture for the time delay. The localization feature of the defect modes can be understood from the temporal behavior. At the frequency of the defect mode, the photon will be trapped in the defect layer for very long time, which leads to a dramatic reduction of the average propagation velocity. It should be noted that the time delay in the ultracold gas of atoms needs very low temperature of nanokelvin. This condition impedes its application. However, the 1D PBGS can work at room temperature, and the attenuation of energy at the transmission peak frequency is negligible. The PBGS could be useful in the devices of optical delay lines.

Acknowledgment. This research was supported by FRG from the Hong Kong Baptist University and UGC from Hong Kong Government. The author Liu was also supported by the Natural Science Foundation of Jiangxi, China.

References

1. L. V. Hau, S. E. Harris, Z. Dutton and C. H. Behroozi, *Nature*, **397**, 594 (1999); S. E. Harris and L. V. Hau, *Phys. Rev. Lett.* **82**, 4611 (1999).
2. M. M. Kash, V. A. Sautenkov, A. S. Zibrov, L. Hollberg, G. R. Welch, M. D. Lukin, Y. Rostovtsev, E. S. Fry, M. O. Scully, *Phys. Rev. Lett.* **82**, 5229 (1999).
3. J. Marangos, *Nature*, **397**, 559 (1999).
4. M. Scalora, R. J. Flynn, S. B. Reinhardt, R. L. Fork, M. J. Bloemer, M. D. Tocci, C. M. Bowden, H. S. Ledbetter, J. M. Bendickson, J. P. Dowling, and R. P. Leavitt, *Phys. Rev. E*, **54**, R1078, (1996).
5. J. M. Bendickson, J. P. Dowling, M. Scalora, *Phys. Rev. E*, **53**, 4107 (1996).
6. E. Yablonovich and T. J. Gmitter, R. D. Meade, A. M. Rappe, K. D. Brommer, and J. D. Joannopoulos, *Phys. Rev. Lett.* **67**, 3380 (1991).
7. J. P. Dowling, M. Scalora, M. J. Bloemer, and C. M. Bowden, *J. Appl. Phys.*, **75**, 1896 (1994).
8. N. H. Liu, *Phys. Rev. B*, **55**, 4097 (1997).

Influence of the Kerr Medium on the Fidelity of Quantum State

Liu Tang-Kun, Wang Ji-Suo, Zhan Ming-Sheng

Laboratory of Magnetic Resonance and Atomic and Molecular Physics,
Wuhan Institute of Physics and Mathematics,
The Chinese Academy of Sciences, Wuhan 430071, P.R.China

Abstract. In this paper, the fidelity in two-photon J-C model of a high Q cavity filled with the Kerr medium is investigated. It is found that the Kerr medium significantly influences the fidelity of quantum states. When the coupling between the medium and the cavity is strong, the fidelity of atom keeps to be 1, the atom is disentangled, which results from the shielding of interaction of the field and the atom by the Kerr medium.

1 Introduction

Fidelity is an important concept in quantum optics. Recently, it was found that fidelity can also play a key role in quantum information and communication theory[1-3]. Twamley[4] has calculated the fidelity for squeezed thermal states. Scutaru[5] proposed an approach to calculate the fidelity for system with a quadratic Hamiltonian. Wang[6] has given a formula of fidelity for displaced squeezed thermal states directly by the displacement and squeezing parameters.

In this paper, we consider a quantum system, in which the cavity is filled with a Kerr medium, and the atom passes the cavity through a hole. We study the influence of the nonlinear coupling of the cavity mode to a Kerr medium on the fidelity of quantum states.

2 The model

We adopt the model similar to Ref.[7]. The model consists of a single two-level atom surrounded by a nonlinear Kerr medium contained inside a very good quality single-mode cavity. The cavity mode is coupled to the Kerr medium as well as to the two-level atom. The atom interacts with the cavity via two-photon transition processes. The effective Hamiltonian in the rotating-wave approximation can be written as [8] ($\hbar = 1$)

$$\hat{H}_{eff} = \omega \hat{a}^+ \hat{a} + \omega_0 \hat{s}_z + \chi \hat{a}^{+2} \hat{a}^2 + g(\hat{a}^{+2} \hat{s}_- + \hat{s}_+ \hat{a}^2) \quad (1)$$

where \hat{a}^+ and \hat{a} are the creation and annihilation operators of the cavity mode of frequency ω , \hat{s}_\pm and \hat{s}_z are the atomic transition and inversion,

respectively; ω_0 is the atomic transition frequency, g is the atom-field coupling constant, and χ is the coupling constant of the field with the Kerr medium. χ is actually the dispersive part of the third-order nonlinearity susceptibility of the Kerr medium. Let us suppose the atom at the initial moment ($t = 0$) to be in the excited state $|e\rangle$ and the cavity mode be prepared in the coherent state $|\alpha\rangle$. The initial state vector $|\psi(0)\rangle$ of the system under consideration can be written as

$$|\psi(0)\rangle = |\alpha\rangle \otimes |e\rangle = \sum_n F(n) |n, e\rangle \quad (2)$$

where $F(n) = \exp(-\frac{1}{2}|\alpha|^2) \frac{|\alpha|^n}{\sqrt{n!}} e^{in\phi}$, $|\alpha| = \sqrt{\bar{n}}$, \bar{n} is the initial average photon number, ϕ is the direction angle of the excitation of the coherent field.

For simplicity, we consider the resonant case (i.e. $\omega_0 = 2\omega$). The solution of the Schrödinger equation

$$i \frac{d}{dt} |\psi(t)\rangle = \hat{H}_{eff} |\psi(t)\rangle \quad (3)$$

for the state vector $|\psi(t)\rangle$ with the initial condition (2) is [8]

$$\begin{aligned} |\psi(t)\rangle &= \sum_n e^{-\bar{n}/2} \left(\frac{\bar{n}^n}{n!}\right)^{1/2} \exp\{-i[\omega(n+1)t - n\phi] - i\chi(n^2 + n + 1)t\} \\ &\quad [A_n(t)|n, e\rangle + B_{n+2}(t)|n+2, g\rangle] \end{aligned} \quad (4)$$

where the coefficients $A_n(t)$ and $B_{n+2}(t)$ are

$$A_n(t) = \cos(\theta_n t) + i \frac{\chi(2n+1)}{\theta_n} \sin(\theta_n t), \quad (5)$$

$$B_{n+2}(t) = -i \frac{[g^2(n+1)(n+2)]^{1/2}}{\theta_n} \sin(\theta_n t). \quad (6)$$

The generalized Rabi frequencies are defined as

$$\theta_n = \{[\chi(2n+1)]^2 + g^2(n+1)(n+2)\}^{1/2} \quad (7)$$

The density operator for the system at time $t = 0$ is assumed to be decoupled, thus it is given by $\rho_s(0) = \rho_f(0) \otimes \rho_a(0)$, where $\rho_f(0) = |\alpha\rangle\langle\alpha|$ and $\rho_a(0) = |e\rangle\langle e|$ describe the initial values for the field and atomic density operator, respectively. Eq.(4) gives the density operator for the system at any time $t > 0$, $\rho_s(t) = |\psi(t)\rangle\langle\psi(t)|$. Thus it is easy to obtain the reduced field density operator $\rho_f(t) = Tr_a \rho_s(t)$ and the reduced atom density operator $\rho_a(t) = Tr_f \rho_s(t)$, respectively.

3 Influence of the Kerr medium on the fidelity of quantum state

The fidelity of quantum state is the degree to keep the information of the initial state in a final state and is given by the relation [4]

$$F(\rho_1, \rho_2) = (Tr \sqrt{\rho_1^{1/2} \rho_2 \rho_1^{1/2}})^2 \quad (8)$$

where ρ_1 and ρ_2 are for two states on a finite dimension Hilbert space. F varies between 0 and 1. When $F = 1$, it indicates that the output state and input state are the same and state has non-distortion; for $F=0$, it means that the quantum state is completely distorted and the output state and input state are orthogonal.

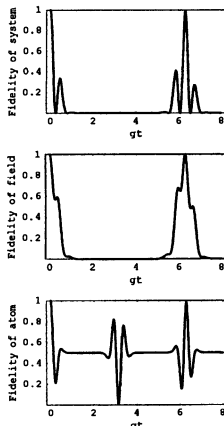


Fig. 1. Fidelities vs gt for $\bar{n} = 5$, $\chi/g = 0$.

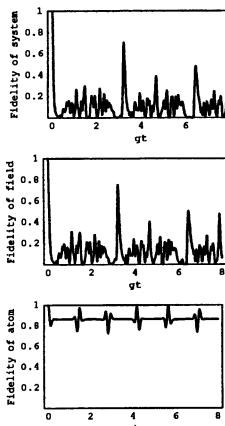


Fig. 2. Fidelities vs gt for $\bar{n} = 5$, $\chi/g = 1$.

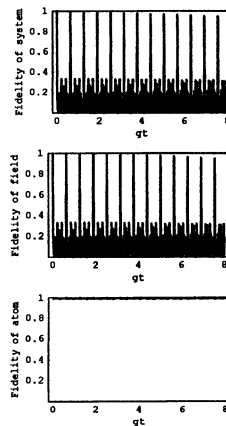


Fig. 3. Fidelities vs gt for $\bar{n} = 5$, $\chi/g = 5$.

If at $t = 0$ the atom is in the excited state and the cavity field is prepared in the coherent state, then the time evolution of the system is described by the state vector (4), the $F_s(t)$, $F_f(t)$ and $F_a(t)$ (s , f and a denote the system, field and atom, respectively) are then

$$F_s(t) = \left| \sum_n e^{-\bar{n}} \frac{\bar{n}^n}{n!} A_n(t) \right|^2, \quad (9)$$

$$F_f(t) = \left| \sum_n e^{-\bar{n}} \frac{\bar{n}^n}{n!} A_n(t) \right|^2 + \left| \sum_n e^{-\bar{n}} \frac{\bar{n}^{n+1}}{n!} e^{-i2\phi} [\sqrt{n+2}\sqrt{n+1}]^{-1} B_{n+2}(t) \right|^2, \quad (10)$$

$$F_a(t) = \sum_n e^{-\bar{n}} \frac{\bar{n}^n}{n!} |A_n(t)|^2. \quad (11)$$

It is obvious that all of the fidelities depend on the coupling constant χ . The numerical results are shown in Figs.1, 2 and 3 for different values of χ . In Fig.1, the special case $\chi = 0$ for the time evolution of the fidelities is considered. It is observed that for $\bar{n} = 5$, there are large peak values for the evolution of the system and field fidelities, and there is oscillation around $F_a = 0.5$. As χ values increases, interaction between the field and the Kerr medium becomes stronger, amplitude of $F_a(t)$ decreases, but values of $F_a(t)$ increases (Fig.2). When $\chi = 5g$, (Fig.3) it is observed that $F_a(t) \approx 1$, there are high fidelity, almost there is no interaction between field and atom, namely the interaction of the field with atom is shielded by the Kerr medium.

4 Conclusion

In summery, we have studied the influence of the Kerr medium on the fidelity of quantum state in the two-photon J-C model. It is shown that the evolution of the fidelity of system, field and atom is very sensitive to the coupling constant χ of the field with the Kerr medium. The fidelity of atom increases when value of the coupling constant χ increases. When χ is equal to $5g$, the fidelity of atom amounts to 1, and the atom is in a disentangled pure state, which result form the shielding of the interaction of the field and the atom by the Kerr medium.

Acknowledgment. The project is supported by the National Natural Science Foundation of China under grant No. 19774069.

References

1. Jozsa R, (1994) Fidelity for mixed quantum states. *J. Mod. Opt.*, **41**, 2315-2323
2. Duan Lu-ming and Guo Guang-can, (1997) Perturbative expansions for the fidelities and spatially correlated dissipation of quantum bits. *Phys. Rev.*, **A56**, 4466-4470
3. Schumacher B, (1995) quantum coding. *Phys. Rev.*, **A51**, 2738-2747
4. Twamley J, (1996) Bures and stetisical distance for squeezed thermal states. *J. Phys.*, **A29**, 3723-3731
5. Scutaru H, (1998) Fidelity for displaced squeezed thermal states and the oscillator semigroup. *J. Phys.*, **A31**, 3659-3663
6. Wang Xiang-bin, Oh C H, and Kwek L C, (1998) Bures fidelity of displaced squeezed thermal states. *Phys. Rev.*, **A58**, 4186-4190
7. Buzeck V and Jex I, (1990) Dynamics of a two-level atom in a Kerr-like medium. *Opt. Commun.*, **78**, 425-435
8. Liu Tang-kun and Peng Jin-sheng, (1997) Time evolution of population number and dipole squeezing of atom in Kerr-like medium. *Acta Optica Sinica* (in Chinese), **17**, 991-996

Some Anomalous Phenomena of ^{87}Rb Atoms Fluorescence in a Quadrupole Magnetic Field

Q. Long, S.Y Zhou, Y.Z Wang

Shanghai Institute of Optics and Fine Mechanics of Chinese Academy of Sciences,
P.O.Box 800211, 201800 Shanghai China
e-mail: longq4@kali.com.cn

Abstract. We report an experimental observation of a decrease in fluorescence intensity near zero-field point in the present of quadrupole magnetic field when atom vapour is excited by a circularly polarized traveling laser. The decrease is due to the magnetic dipole precession which will mostly cancel the orientation induced by optical pumping at zero-field point.

A dark region has been observed in spatial fluorescence distribution, when a low-pressure nature Rubidium vapor (10^{-7} – 10^{-6} Pa) in a vacuum cell is excited by a single traveling circularly polarized laser.

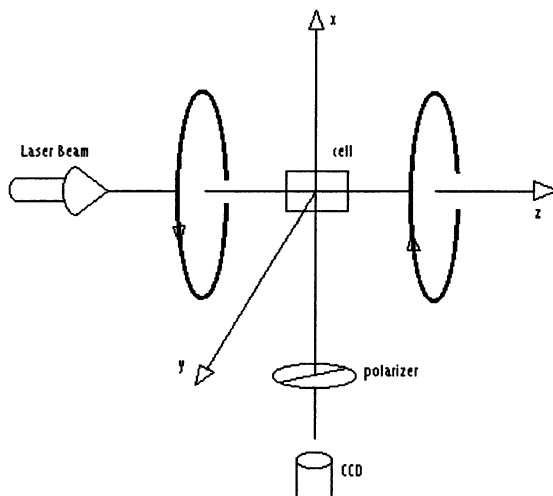


Fig. 1. Experiment set-up

Figure 1 shows the experiment set-up. A pair of Helmholtz coils with anti-currents produces the quadrupole magnetic field. The laser tuned to near the D₂-line's L₃ peak of ^{87}Rb ($5\text{S}_{1/2}, F = 2 \rightarrow F = 3$) is passed through the vacuum chamber (10cm in diameter). The fluorescence emitted in the direction at the right angle to the laser beam is collected by a CCD camera.

From the camera picture it can be seen that, around the zero-field point, there exists a dark region (Fig. 2), where coordinate Z is defined along the beam. If a polarizer is put in front of the camera, the region becomes darker or turns to be bright for Y- or Z- polarized fluorescence.

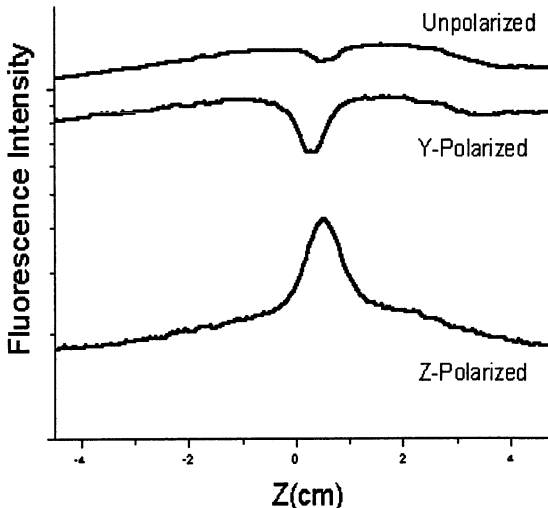


Fig. 2. Flourescence Intensity

It was initially thought that the observation is simply a result of velocity hole, while a calculation considering the longitudinal magnetic field shows that there should be a peak instead of a dip near the zero-field point for unpolarized fluorescence. It was further wondered whether it is caused by an optical pumping of atoms from $F_g = 2 \rightarrow F_e \leq 2$ to $F_g = 1$ which is not coupled with the laser field. These transitions can be made possible by the Doppler shift. Since there is no repump laser, $F_g = 1$ is a dark level. Then it may be expected a most dip at the resonance of L₂ transition $F_g = 2 \rightarrow F_e = 2$, which occur at $Z = -\frac{(\Delta+\delta)}{\alpha[\gamma_e(m+1)-\gamma_g m]}$ with Δ =energy separation between $F_e = 3$ and $F_e = 2$, γ =gyromagnetic ratio and α =magnetic gradient. For $\delta \approx 0$, under the experimental condition we have $Z \approx -10\text{cm}$ which is beyond our cell's magnitude. Moreover, the expression implies that if we scan the laser frequency, the center of the dip should move across the chamber. But what we have observed is that the dip almost rests for varying frequencies. To explain the above strange phenomena, it is found that taking into account of the transverse magnetic field is necessary. In this configuration, the phenomena can be understood as a result of optical double-resonance with a zero rotation frequency of transverse magnetic field. To make a clear physics picture, a

model $J_g = 1/2 \rightarrow J_e = 3/2$ is used. A calculation based on it gives the intensities of un-, Y- and Z- polarized fluorescence:

$$I(ey + ez) = \frac{1}{8\pi} \left(\frac{7}{2} + \langle M_Z \rangle \right) \Gamma_P \quad (1)$$

$$I(ey) = \frac{1}{4\pi} \left(\frac{5}{4} + \langle M_Z \rangle \right) \Gamma_P \quad (2)$$

$$I(ez) = \frac{1}{8\pi} (1 - \langle M_Z \rangle) \Gamma_P \quad (3)$$

where $\langle M_Z \rangle$ represents the orientation of the atom ensemble,

$$\langle M_Z \rangle = 1 - \frac{3/2\omega_r^2}{(\Gamma_P/3)^2 + (\Delta_0 + \omega_Z)^2 + 3/2\omega_r^2} \quad (4)$$

where ω_r, ω_z are precession frequencies of transverse and longitudinal magnetic field. It can be seen obviously from the equations that the dip in $I(ey + ez)$, $I(ey)$ or peak in $I(ez)$ is actually caused by a disorientation, which reaches its maximum near zero-field point, due to the precession induced by the transverse magnetic field. A quantum interference due to the Hanle coherence between two substates with $\Delta m = \pm 2$ taking place at $2\sqrt{\omega_r^2 + \omega_z^2} \leq \Gamma$ also contributes to Y-polarized fluorescence but on a second order. Besides of the case of circularly polarization, we have also investigated those when laser are linearly polarized. It is found that when the plane of polarization is perpendicular (parallel) to the observe direction, the fluorescence near zero-field point is bright (dark). The results are actually the consequence of a combination of classical Hanle effect and optical double-resonance.

Acknowledgments. This work was supported by Chinese National Natural Science Foundation. Q. Long was supported by Postdoctoral Research Aid of China.

The Properties of the Macro-Quantum Superposition States Involving Three Elements

Ma Aiqun¹, Qian Yan², Xie Hongwei³, Jiang Zhuohong⁴

¹ Zhuhai Polytechnic School, Zhuhai 519015, P.R. China

² Harbin College, Harbin 150020, P.R. China

³ Heilongjiang Education College, Harbin 150040, P.R. China

⁴ Heilongjiang University, Harbin 150080, P.R. China

Abstract. In this paper, the mean photon number, the second-order coherence and the distribution of this optical state are derived and some properties of this state are presented. In general the mean photon number is not equal to the sum of the mean photon number of three elements, the distribution is not equal to the sum of the distribution of three elements. The result shows that whether this optical cat state exists bunching effect or an bunching effect is decided by the eigenvalues, superposition coefficients of coherent states they take part in superposition and their relation.

1 Introduction

In recent years, distinguishable Macro-Quantum superposition states Schrödinger Cat makes a lot of people pay attention to it. The light field of Schrödinger Cat state is a kind of nonclassical light field, and has pure quantum action. It has very important applied future in light communication field, fine measurement field and other important fields, and has very high academic value for the research of the Macro-Quantum coherence of light field. The most excited thing is that people have found some methods to make optical cat state[5], and open up a broad future for the experimental research of the optical cat state. In this paper, some properties of the optical cat state which involving three elements are studied.

The expression of the optical cat state which involving three elements is:

$$|\psi\rangle = C_1|\alpha\rangle + C_2|\beta\rangle + C_3|\gamma\rangle \quad (1)$$

where $|\alpha\rangle$, $|\beta\rangle$, and $|\gamma\rangle$ are coherence states, C_1 , C_2 and C_3 are superposition coefficients, and be satisfied $|C_1|^2 + |C_2|^2 + |C_3|^2 = 1$. Every kind of optical cat state have different quantum statistical properties, these statistical properties are decided by the eigenvalues, superposition coefficients of the coherent states they take part in this superposition and their relation.

In this paper, the general expressions of the mean photons number, the second-order coherence and the distribution of the optical cat state which involving three elements, and some properties were discussed, we make farther proving that the quantum statistical properties of Schrödinger Cat state are

decided by the eigenvalues, superposition coefficients of the coherent states they take part in this superposition and their relations.

2 Free evolution and mean photon number of the optical cat state

In the free space, the Hamiltonian of the single mode electromagnetic field reads as follows:

$$H = \omega(a^\dagger a + 1/2) \quad (2)$$

where $\hbar = 1$. Let initial state is the optical cat state which involving three elements which was given by Eq.(1), then from Heisenberg equation, we have

$$\frac{da(t)}{dt} = \frac{1}{i}[a(t), H] = -i\omega a(t) \quad (3)$$

Solving Eq.(3) we have $a(t) = a(0)e^{-i\omega t}$. Let $a(0) = C_1|\alpha\rangle + C_2|\beta\rangle + C_3|\gamma\rangle$ then

$$|\psi(t)\rangle = C_1|\alpha e^{i\omega t}\rangle + C_2|\beta e^{i\omega t}\rangle + C_3|\gamma e^{i\omega t}\rangle \quad (4)$$

Eq.(4) is still Schrödinger Cat State. Eq.(4) shows that the propagating of the single mode Schrödinger Cat State in the free space maitains its original characteristic.

The mean photon number of the Schrödinger cat state which involving three elements [Eq.(4)] is

$$\begin{aligned} \bar{n} &= \langle\psi(t)|a^\dagger a|\psi(t)\rangle \\ &= |C_1|^2\bar{n}_1 + |C_2|^2\bar{n}_2 + |C_3|^2\bar{n}_3 \\ &\quad + 2[\text{Re}(C_1^*C_2\alpha^*\beta) + \text{Re}(C_2^*C_3\beta^*\gamma) + \text{Re}(C_3^*C_1\gamma^*\alpha)] \end{aligned} \quad (5)$$

For simplicity, we let $\beta = Mae^{i\theta}$, $\gamma = Nae^{i\phi}$, $C_2 = KC_1$, $C_3 = JC_1$, then

$$\begin{aligned} \bar{n} &= \bar{n}_1[1 + K^2M^2 + J^2N^2 + 2KM\cos\theta + 2JN\cos\phi \\ &\quad + 2KJMN\cos(\phi - \theta)]/[1 + K^2 + J^2] \end{aligned} \quad (6)$$

The sum of the mean photon number of three elements is

$$\bar{n}_{03} = \frac{1}{1 + K^2 + J^2}\bar{n}_1[1 + K^2M^2 + J^2\bar{n}^2] \quad (7)$$

Comparing Eq.(6) and Eq.(7),we find that in general the mean photon number of optical cat state which involving three elements is not equal to the sum of the mean photon number of three elements, but be decided by the value α, β, γ of and C_1, C_2, C_3 .

3 The second-order coherence of the optical cat state

Be known to every one, the bunching effect of the light field and the antibunching effect are decided by the second-order coherence of the light field. According to the definition of second-order coherence, when light field is in the optical cat state which involving three elements, it's second-order coherence is

$$\begin{aligned} g(z) &= \langle \phi | a^{+2} a^2 | \phi \rangle / \langle \phi | a^+ a | \phi \rangle^2 \\ &= [|C_1|^2 |\alpha|^4 + |C_2|^2 |\beta|^4 + |C_3|^2 |\gamma|^4 \\ &\quad + 2\text{Re}(C_1^* C_2 \alpha^{*2} \beta^2 + C_2^* C_3 \beta^{*2} \gamma^2 + C_3^* C_1 \gamma^{*2} \alpha^2)] / [|C_1|^2 |\alpha|^2 \\ &\quad + |C_2|^2 |\beta|^2 + |C_3|^2 |\gamma|^2 \\ &\quad + 2\text{Re}(C_1^* C_2 \alpha^* \beta + C_2^* C_3 \beta^* \gamma + C_3^* C_1 \gamma^* \alpha)]^2 \end{aligned} \quad (8)$$

For simplicity of discussion, we let $\beta = Mae^{i\theta}$, $\gamma = Nae^{i\phi}$, $C_2 = KC_1$, $C_3 = JC_1$, then

$$\begin{aligned} g(z) &= (1 + K^2 + J^2)[1 + K^2 M^4 + J^2 N^4 + 2KM^2 \cos(2\theta) \\ &\quad + 2JN^2 \cos(2\phi) + 2KJMN \cos 2(\phi - \theta)] / [1 + K^2 M^2 + J^2 N^2 \\ &\quad + 2KM \cos \theta + 2JN \cos \phi + 2KJMN \cos(\phi - \theta)] \end{aligned} \quad (9)$$

When $M = 2, N = 3, K = \frac{1}{4}, J = \frac{1}{6}, \theta = \frac{\pi}{4}$ and $\phi = \frac{\pi}{4}$, $g(z) = (5 \times 157) / [(1.5 + \sqrt{2}) \times 4 \times 144] < 1$. This shows that the existence of the antibunching effect is true under these conditions.

It is very easy to chose the comfortable value of M, N, K and J to make $g(z) > 1$, this shows that the bunching effect is true also.

The above proving shows that whether the optical cat state which involving three elements exists bunching effect or antibunching effect is decided by the eigenvalues, superposition coefficients of coherent states they take part in superposition and their relation.

4 The distribution of the optical cat state

The distribution of photon number reads as $P_n = |\langle n | \psi \rangle|^2$, where

$$\begin{aligned} \langle n | \psi \rangle &= \frac{C_1}{\sqrt{n!}} \alpha^n e^{-\frac{1}{2}|\alpha|^2} + \frac{C_2}{\sqrt{n!}} \beta^n e^{-\frac{1}{2}|\beta|^2} + \frac{C_3}{\sqrt{n!}} \gamma^n e^{-\frac{1}{2}|\gamma|^2} \\ &= \frac{C_1}{\sqrt{n!}} |\alpha|^n [\sin(n\alpha) + i \cos(n\alpha)] e^{-\frac{1}{2}|\alpha|^2} \\ &\quad + \frac{C_2}{\sqrt{n!}} |\beta|^n [\sin(n\beta) + i \cos(n\beta)] e^{-\frac{1}{2}|\beta|^2} \\ &\quad + \frac{C_3}{\sqrt{n!}} |\gamma|^n [\sin(n\gamma) + i \cos(n\gamma)] e^{-\frac{1}{2}|\gamma|^2} \\ &= \frac{1}{\sqrt{n!}} \{ [e^{-\frac{1}{2}|\alpha|^2} |\alpha|^n (C'_1 \sin n\alpha - C''_1 \cos n\alpha) \right. \\ &\quad \left. + e^{-\frac{1}{2}|\beta|^2} |\beta|^n (C'_2 \sin n\beta - C''_2 \cos n\beta) + e^{-\frac{1}{2}|\gamma|^2} |\gamma|^n (C'_3 \sin n\gamma - C''_3 \cos n\gamma)] \} \end{aligned}$$

$$\begin{aligned}
& + e^{-\frac{1}{2}|\beta|^2} |\beta|^n (C'_2 \sin n\beta - C''_2 \cos n\beta) \\
& + e^{-\frac{1}{2}|\gamma|^2} |\gamma|^n (C'_3 \sin n\gamma - C''_3 \cos n\gamma)] \\
& + i[e^{-\frac{1}{2}|\alpha|^2} |\alpha|^n (C'_1 \sin n\alpha - C''_1 \cos n\alpha) \\
& + e^{-\frac{1}{2}|\beta|^2} |\beta|^n (C'_2 \sin n\beta - C''_2 \cos n\beta) \\
& + e^{-\frac{1}{2}|\gamma|^2} |\gamma|^n (C'_3 \sin n\gamma - C''_3 \cos n\gamma)] \}
\end{aligned} \tag{10}$$

Where $C_1 = C'_1 + iC''_1$, $C_2 = C'_2 + iC''_2$, and $C_3 = C'_3 + iC''_3$. Then we have

$$\begin{aligned}
P_n &= |\langle n|\psi \rangle|^2 \\
&= \frac{1}{n!} [e^{-\frac{1}{2}|\alpha|^2} |\alpha|^n (C'_1 \sin n\alpha - C''_1 \cos n\alpha) \\
&\quad + e^{-\frac{1}{2}|\beta|^2} |\beta|^n (C'_2 \sin n\beta - C''_2 \cos n\beta) \\
&\quad + e^{-\frac{1}{2}|\gamma|^2} |\gamma|^n (C'_3 \sin n\gamma - C''_3 \cos n\gamma)]^2 \\
&\quad + \frac{1}{n!} [e^{-\frac{1}{2}|\alpha|^2} |\alpha|^n (C'_1 \sin n\alpha - C''_1 \cos n\alpha) \\
&\quad + e^{-\frac{1}{2}|\beta|^2} |\beta|^n (C'_2 \sin n\beta - C''_2 \cos n\beta) \\
&\quad + e^{-\frac{1}{2}|\gamma|^2} |\gamma|^n (C'_3 \sin n\gamma - C''_3 \cos n\gamma)]^2 \\
&= |C_1|^2 \frac{|\alpha|^{2n}}{n!} e^{-|\alpha|^{2n}} + |C_2|^2 \frac{|\beta|^{2n}}{n!} e^{-|\beta|^{2n}} + |C_3|^2 \frac{|\gamma|^{2n}}{n!} e^{-|\gamma|^{2n}} \\
&\quad + \frac{2}{n!} e^{-(|\alpha|^2+|\beta|^2)} [\text{Re}(C_1 C_2^*) \text{Re}(\alpha^n \beta^{*n}) - \text{Im}(C_1 C_2) \text{Im}(\alpha^n \beta^n)] \\
&\quad + \frac{2}{n!} e^{-(|\beta|^2+|\gamma|^2)} [\text{Re}(C_2 C_3^*) \text{Re}(\beta^n \gamma^{*n}) - \text{Im}(C_2 C_3) \text{Im}(\beta^n \gamma^n)] \\
&\quad + \frac{2}{n!} e^{-(|\gamma|^2+|\alpha|^2)} [\text{Re}(C_3 C_1^*) \text{Re}(\gamma^n \alpha^{*n}) - \text{Im}(C_3 C_1) \text{Im}(\gamma^n \alpha^n)]
\end{aligned} \tag{11}$$

Equation (11) shows that, in general, the distribution of the optical cat state which involving three elements is not equal to the sum of the distribution of three elements.

References

1. B.Yurke, W.Schleich, and D.F.Walls,(1990) Quantum superpositions generated by quantum nondemolition measurements, Phys.Rev.A,42,1703-1711.
2. Shang Song, Carlton M.Caves, and Bernard Yurke,(1990) Generation of superpositions of classically distinguishable quantum states from optical back-action evasion,Phys.Rev.A, 41,5261-5264.
3. K.Tara, G.S.Agarwal, and S.Chaturvedi,(1993) Production of Schrödinger macroscopic quantum-superposition state in a Kerr medium, Phys.Rev.A, 47,5024- 5029.
4. L.Davidorich, A.Maali, J.M.Raimond and S.Herode,(1993)Quantum Switchs and Nonlocal Microwave Fields, Phys.Rev.Lett.71,2360-2363.
5. Wu Jinwei, and Guo Guangcan,(1995) Schrödinger Cat-Marcoscopic quantum-superposition states, Physics (China), 24,269-272

Gain in Autler-Townes Doublet due to Interference in Decay Channels

Sunish Menon and G. S. Agarwal

Physical Research Laboratory, Navrangpura,
Ahmedabad-380 009, India
E-mail: sunish@prl.ernet.in

Abstract. We consider **non-degenerate** pump-probe spectroscopy of V-systems under conditions such that interference among decay channels is important. We demonstrate how this interference can result in new gain features instead on the usual absorption features. We relate this gain to the existence of a new vacuum induced quasi-trapped-states.

1 Introduction

Spontaneous emission is a well known phenomena which occurs in a medium due to vacuum of electromagnetic field. But under certain circumstances interference in spontaneous emission can also arise. Consider two excited atomic or molecular states $|1\rangle$ and $|2\rangle$, decaying to the same ground state $|3\rangle$. If both these excited states can spontaneously emit almost identical photons (identical in energy and polarization), then interference in spontaneous emission can occur.

Let the spontaneous emission rates from levels $|1\rangle$ and $|2\rangle$ to level $|3\rangle$ be denoted as $2\gamma_1$ and $2\gamma_2$ respectively. The spontaneously emitted photons will have almost identical energy when $W_{12} \approx 2\gamma_1, 2\gamma_2$, where $\hbar W_{12}$ is the energy separation between the excited levels. Since polarization of emitted photons are decided by the dipole matrix elements $d_{13}, d_{23}, (d_{ij} = \langle i|er|j\rangle)$ the angle θ between these two vectors is very crucial. For small θ the interference effect is very large and for $\theta = 90^\circ$ the interference is absent. A result of such an interference is that, for certain parameters, a coherence between $|1\rangle$ and $|2\rangle$ is created by spontaneous emission. We refer to it as vacuum induced coherence (VIC). This coherence can *create trapping in a degenerate V-system* [1]. The coherence can also modify significantly the emission spectrum of a near-degenerate V-system [2]. Such coherence effects have been shown to give rise to quantum beats [3] and spontaneous emission quenching [4,5].

In the present article, we show how to probe VIC by using a pump-probe spectroscopy. We demonstrate that the VIC can manifest itself via gain features instead of the traditional absorption features in a V-system.

2 The Model

We study [6] the effect of vacuum induced coherence on the Autler-Townes doublets seen in the pump-probe analysis of a V-system. Consider the pump-probe set-up shown in Fig. 1(a). The transition dipole moments \mathbf{d}_{13} and \mathbf{d}_{23} are non-orthogonal. To study the situation as much parallel to the usual case where the pump and probe fields act on two different arms of the V-system, we consider an arrangement of field polarization as shown in Fig. 1(b). This enables us to study the VIC effects as well as compare with the usual situation. Thus the pump field ($\mathbf{E}_2 = \epsilon_2 e^{-i\omega_2 t} + c.c.$) with a Rabi frequency $2G = 2\mathbf{d}_{23} \cdot \mathbf{\epsilon}_2 / \hbar$ drives $|2\rangle \leftrightarrow |3\rangle$ transition ($\mathbf{d}_{23} \cdot \mathbf{\epsilon}_2 = 0$) and similarly probe field ($\mathbf{E}_1 = \epsilon_1 e^{-i\omega_1 t} + c.c.$) with a Rabi frequency $2g = 2\mathbf{d}_{13} \cdot \mathbf{\epsilon}_1 / \hbar$ drives $|1\rangle \leftrightarrow |3\rangle$ transition ($\mathbf{d}_{13} \cdot \mathbf{\epsilon}_1 = 0$). We note here that for the Fig. 1(b) the Rabi frequencies will also depend on the angle θ . But for convenience in comparison with different values of θ , we will keep the Rabi frequencies same, which in practice can be done by suitably increasing/decreasing the field strength.

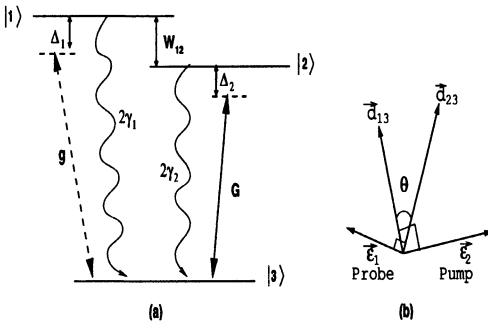


Fig. 1. (a) Schematic diagram of a three-level V-system. The pump and probe fields have a frequency detunings Δ_2 and Δ_1 respectively. The γ 's denote the spontaneous emission rates from the respective levels. (b) The arrangement of field polarization required for single field driving one transition if dipoles are non-orthogonal.

The density matrix equations with the inclusion of all the decay terms will be

$$\begin{aligned}\dot{\rho}_{11} &= -2\gamma_1\rho_{11} - \eta(\rho_{12} + \rho_{21}) + ig e^{-i\delta t}\rho_{31} - ig^* e^{i\delta t}\rho_{13}, \\ \dot{\rho}_{22} &= -2\gamma_2\rho_{22} - \eta(\rho_{12} + \rho_{21}) + iG\rho_{32} - iG^*\rho_{23}, \\ \dot{\rho}_{12} &= -(\gamma_1 + \gamma_2 + iW_{12})\rho_{12} - \eta(\rho_{11} + \rho_{22}) + ig e^{-i\delta t}\rho_{32} - iG^*\rho_{13}, \\ \dot{\rho}_{13} &= -(\gamma_1 + i(\Delta_2 + W_{12}))\rho_{13} - \eta\rho_{23} - iG\rho_{12} + ig e^{-i\delta t}(1 - 2\rho_{11} - \rho_{22}), \\ \dot{\rho}_{23} &= -(\gamma_2 + i\Delta_2)\rho_{23} - \eta\rho_{13} - ig e^{-i\delta t}\rho_{21} + iG(1 - \rho_{11} - 2\rho_{22}),\end{aligned}\quad (1)$$

where $\delta = \omega_1 - \omega_2$ is the probe-pump detuning. The probe detuning $\Delta_1 = W_{13} - \omega_1$ and the pump detuning $\Delta_2 = W_{23} - \omega_2$ are related by $\Delta_1 - \Delta_2 = W_{12} - \delta$. In deriving (1) we have made the canonical transformations so that ρ_{13} and ρ_{23} are obtained by multiplying the solution of (1) by $e^{-i\omega_2 t}$. We also use the trace condition $\rho_{11} + \rho_{22} + \rho_{33} = 1$. Here $\eta = \sqrt{\gamma_1\gamma_2} \cos\theta$ is the

VIC parameter, which is nonzero when $\theta \neq 90^\circ$. Note that for the geometry shown in Fig. 1(b), θ is always nonzero, though it could be small. Due to vacuum coupling of levels $|1\rangle$ and $|2\rangle$, explicit time dependence arise in the equation of motion (1). Since the time dependence is periodic, we can solve these equations by Floquet analysis. The solution can be written as

$$\rho_{ij} = \sum_m \rho_{ij}^{(m)} e^{-im\delta t}. \quad (2)$$

Thus the absorption and emission spectra gets modulated at various harmonics of δ . The dc component in probe absorption spectrum is related to $\rho_{13}^{(+1)}$. The absorption coefficient α per unit length can be shown to be

$$\alpha = \frac{\alpha_0 \gamma_1}{g} \text{Im}(\rho_{13}^{(+1)}), \quad (3)$$

where $\alpha_0 = 4\pi\mathcal{N}|d_{13}|^2\omega_1/\hbar\gamma_1c$ and \mathcal{N} denote the atomic density. Note that in (3) only one term from the entire series (2) contributes. For the case of degenerate pump-probe ($\delta = 0$), all the terms in the series (2) are important.

2.1 Numerical Results

In order to obtain the probe absorption spectra we solve (1) numerically using the series solution (2) and the steady state condition $\dot{\rho}_{ij}^{(m)} = 0$. The situation is much simpler for a weak probe when $\rho_{ij}^{(+1)}$ can be computed to first order in g , otherwise we use Floquet method. In Fig. 2 we plot the probe absorption as a function of probe detuning. We observe that *one of the Autler-Townes component flips sign to give rise to significant gain in the presence of VIC*. The solid curve in Fig. 2(b) shows that the effect of VIC is observed even for

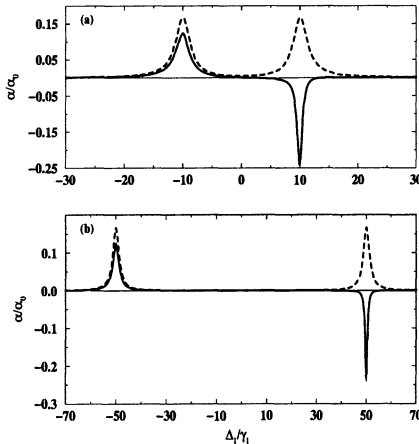


Fig. 2. Effect of interference between decay channels on probe absorption. For both the frames the dashed curves show the usual Autler-Townes components in the absence of VIC ($\theta = 90^\circ$) and the solid curves is for $\theta = 15^\circ$. The common parameters are $g = 0.01\gamma_1$, and $\gamma_2 = \gamma_1$, and $\Delta_2 = 0$. Note that α will depend on W_{12} only when VIC is present and we take $W_{12} = -G$. In frame (a) we have kept $G = 10\gamma_1$ and in frame (b) we take $G = 50\gamma_1$. The solid curve in frame (b) shows that the effect of VIC is retained even for large W_{12}

large W_{12} compared to γ_1, γ_2 . This is in contrast to the situation that exist in the absence of external fields. As can be seen from the Fig. 2(b), for strong pump fields, such a restriction can be relaxed. In the following sections we analyze the origin of gain shown above.

3 Quasi-Trapped-States From Interference of Decay Channels

For a very weak probe field ($g \ll \gamma_1, \gamma_2$) we can solve equations (1) perturbatively with respect to the strength of the probe field. To the lowest order in g , the solution may be written as

$$\rho_{ij} = \sigma_{ij}^0 + g\sigma_{ij}^+e^{-i\delta t} + g^*\sigma_{ij}^-e^{i\delta t}. \quad (4)$$

We first examine the behavior of the system in the presence of pump field alone ($g = 0$). It is clear that field G creates a coherent mixing of states $|2\rangle$ and $|3\rangle$. The new eigenvalues will be $\lambda_{\pm} = \frac{\Delta_2 \pm \sqrt{\Delta_2^2 + 4|G|^2}}{2}$, and the corresponding dressed energy states can be written as

$$\begin{aligned} |+\rangle &= \cos\psi|2\rangle + \sin\psi|3\rangle, \\ |-\rangle &= -\sin\psi|2\rangle + \cos\psi|3\rangle, \end{aligned} \quad (5)$$

where $\tan\psi = -G/\lambda_+$. The crucial point to note is that the level $|1\rangle$ is coupled with $|\pm\rangle$ because of the presence of VIC. Thus the population in $|\pm\rangle$ also depends on the VIC parameter η . An important case arises when $|1\rangle$ is degenerate with either $|\pm\rangle$, i.e. when $W_{12} = \lambda_{\pm}$. The degenerate levels get strongly coupled via VIC, giving rise to trapping. When $|1\rangle$ and $|-\rangle$ are degenerate, we find that the dynamical behavior of the system can be best analyzed in the basis given below:

$$|+\rangle, \quad |c\rangle = \frac{\sqrt{2\gamma_1}|1\rangle + \sqrt{\gamma_2}|-\rangle}{\sqrt{\gamma_2 + 2\gamma_1}}, \quad |uc\rangle = \frac{\sqrt{\gamma_2}|1\rangle - \sqrt{2\gamma_1}|-\rangle}{\sqrt{\gamma_2 + 2\gamma_1}}. \quad (6)$$

Using the transformations (5), (6) and Eqs. (1) with $g = 0$, we numerically compute the steady state population in the states (6). In Fig. 3 we plot the population of these states as a function of pump detuning. Note that in the presence of VIC, σ_{ucuc}^0 approaches unity at $\Delta_2 = 0$ i.e. when the states $|1\rangle$ and $|-\rangle$ are degenerate. Trapping requires θ to be small. Ideally for a perfectly trapped state, at steady state, the population will unity. It can be shown [6] that $\sigma_{ucuc}^0 \neq 1$ for the arrangement in Fig. 1(b). Thus we refer to $|uc\rangle$ as ‘quasi-trapped-state’ (QTS). The QTS $|uc\rangle$ is a result of interference among decay channels of $|1\rangle$ and $|-\rangle$ levels. As a consequence, even if W_{12} is large in bare basis, strong VIC effects can reappear when dressed levels are degenerate with the bare excited levels unconnected by the pump field.

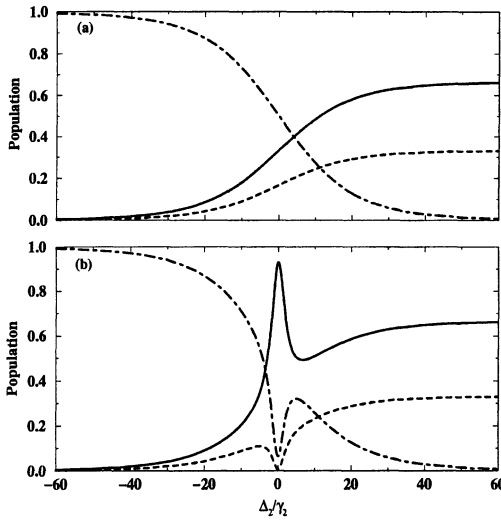


Fig. 3. The atomic population in the basis (6) as a function of pump detuning Δ_2/γ_2 in presence (frame b, $\theta = 15^\circ$) and in absence (frame a, $\theta = 90^\circ$) of VIC. The parameters are $G = 20\gamma_2$, $W_{12} = -G$, and $\gamma_1 = \gamma_2$. The solid curves denote σ_{ucuc}^0 , the dashed curves are for σ_{cc}^0 and the dot-dashed curves denote σ_{++}^0 .

3.1 Origin of Gain Through Quasi-Trapped-States

The origin of the Autler-Townes doublet in the absorption spectrum is well understood. The pump dresses the states $|2\rangle$ and $|3\rangle$. The population in the dressed states $|\pm\rangle$ absorbs a photon from the probe field leading to the Autler-Townes doublet. The situation changes drastically in presence of VIC, where for a suitable choice of parameters, lead to a quasi-trapped-state $|uc\rangle$. For $\Delta_2 = 0$, $W_{12} = -G$, $\gamma_1 = \gamma_2$ and small values of θ the dressed state $|+\rangle$ is almost empty where as $\sigma_{--}^0 > \sigma_{11}^0$. Thus the probe can be absorbed in the transition $|-\rangle \rightarrow |1\rangle$ whereas the probe will experience gain in the transition $|1\rangle \rightarrow |+\rangle$. The population in the states $|\pm\rangle$ and $|1\rangle$ depends on the angle θ between the two dipole matrix elements. For intermediate values of θ 's the population in $|1\rangle$ and $|+\rangle$ can be almost same. This can suppress one of the Autler-Townes component (result not shown).

4 Conclusions

In summary, we have studied the **non-degenerate** pump-probe spectroscopy of V-systems when the presence of interference in decay channels is significant. We have shown the possibility of gain components in Autler-Townes doublet. We present physical interpretation of this gain. We have also shown the possibility of a new quasi-trapped-states due to VIC.

References

1. Agarwal G. S. (1974), *Quantum Optics*, Springer Tracts in Modern Physics Vol. 70. Springer, Berlin. Pg. 95.

2. Agarwal G. S. et al. (1984) Phys. Rev. A **29**, 2565; Agassi D. (1984) Phys. Rev. A **30**, 2449; Zhu S. -Y. et al. (1995), Phys. Rev. A **52**, 710.
3. Hegerfeldt G. C., Plenio M. B. (1992) Phys. Rev. A **46**, 373; (1993) **47**, 2186.
4. Zhu S. -Y., Scully M. O. (1996) Phys. Rev. Lett. **76**, 388; Lee H. et al. (1997) Phys. Rev. A **55**, 4454.
5. Xia H. -R. et al. (1996) Phys. Rev. Lett. **77**, 1032.
6. For detailed discussion see [Menon S., Agarwal G. S. (2000), to appear in Jan. issue of Phys. Rev. A.]

Short-Wavelength Three-dimensional Photonic Crystals

Ouyang Zhengbiao, Li Jingzhen, Sun Yiling, Lin Min

Dept. Opto-Electronic Engg., School of Sci. & Tech.,
Shenzhen Univ., Shenzhen 518060, P. R. China

Abstract. A new kind of three-dimensional photonic crystal, called as *combined three-dimensional photonic crystal*, is presented and shown to be practical. The combined three-dimensional photonic crystal is an enclosed structure made of several pieces of one-dimensional photonic crystals. It is found out that, under present technology, there exists no difficulty in the fabrication of the proposed combined three-dimensional photonic crystals working in short wavelengths, including those in the visible. Three practical schemes are given and discussed.

1 Introduction

Photonic crystals (PCs) are of great interest in recent years for their potential wide application [1-11]. Much progress is made in two- and three-dimensional PCs working in the long wavelength region ranging from microwave to the near infrared [12-21]. Three-dimensional (3-D) PCs operating in optical wavelengths has also been investigated both theoretically and experimentally [22-27]. Yet, until now there still exist plenty of technical difficulties in the fabrication of 3-D PCs operating in the short wavelength region, especially in the visible light wavelength region.

In this paper, we present a new kind of practical scheme for constructing 3-D PCs that may operate in the regions from microwave to the visible light-wave. Each of the proposed new 3-D PCs consists of a number of one-dimensional (1-D) PCs. It is known that there exists no difficult in fabricating 1-D PCs operating both in long wavelengths and in short wavelengths. So our schemes are of practical significance for producing 3-D PCs that may operate in a wide range of wavelengths, especially, in the visible light wavelengths.

2 Ideas and Examples of Configuration of Practical 3-D Photonic Crystals

The essential characteristic of 1-D PCs is that the transmission of photons is prohibited in the directions in one dimension. While in 3-D PCs, the transmission of photons is forbidden in all directions in three dimensions. From these essential characteristics of 1-D and 3-D PCs, we may get the idea that some structures consisted of several pieces of 1-D PC can play the role of 3-D

PCs and can be considered as a new kind of 3-D PC. This new kind of 3-D PCs is advantageous for its simplicity in configuration and fabrication, which is specially useful for obtaining 3-D PCs that operate in the visible, because 1-D PCs working in the visible can be fabricated without much difficulty by conventional techniques.

We find that the necessary and sufficient condition for a structure made of 1-D PCs to behave like a 3-D PC is that the structure is enclosed in space by these 1-D PCs. This can be shown to be true through the analyses of the motions of photons in these structures.

Since any enclosed structure made of several pieces of 1-D PCs can serve as a 3-D PC, a lot of schemes can be obtained according to this principle. Here we just give three examples to save pages, as shown in Figs. 1 - 3.

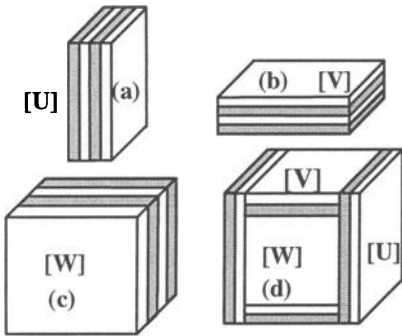


Fig. 1. A cubic structure (d) made of three types of 1-D PCs: [U], [V] and [W], as shown in (a), (b) and (c), respectively

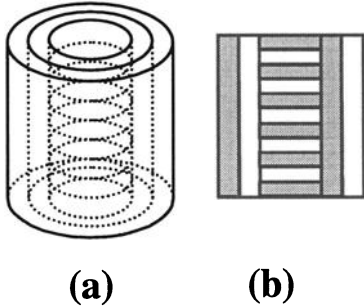


Fig. 2. A cylindrical structure made of two special kinds of 1-D PCs, where (b) is a sectional view of (a)

A cubic structure made of five pieces of 1-D PCs is shown in Fig. 1. It should be pointed out that the effective space for forbidding photons in the structure shown in Fig. 1(d) is the volume of the central 1-D PC block

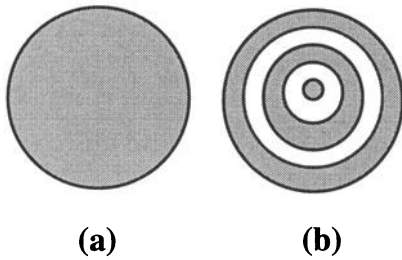


Fig. 3. A spherical structure made of dielectric spherical shells, where (b) is a sectional view of (a)

[W]. This structure can be fabricated according to the following steps: first the central block, then the four outside blocks one by one, either through depositing, growing or film coating techniques.

A cylinder configuration consisted of two pieces of 1-D PCs is presented in Fig. 2. Here the effective space for forbidding photons in this structure is the volume of the central cylinder made of several dielectric discs. The central cylinder of this structure can be obtained through laser cutting of an ordinary 1-D PC. The outside cylinder shell, a special kind of 1-D PC, can be prepared by dielectric growing around the central cylinder. To assure good quality, one may rotate the central cylinder while growing dielectrics around it.

And a spherical structure is given in Fig. 3. The dielectric constant in the structure varies periodically in the radial directions, without any dependence on the other two coordinates. Thus this structure is theoretically a 1-D PC. But it is easily seen that this structure is enclosed and the photons inside the sphere are forbidden in it. Also, photons outside the sphere will not be able to penetrate the sphere. Actually, it can be considered as a structure made of an infinite number of 1-D PC pieces. Thus this structure can serve as a 3-D PC.

Here we point out that, in conventional sense, the structures given above are not 3-D PCs. But they have the same functions as those conventional 3-D PCs. So, for simplicity, we may still call the structures presented above 3-D PCs. To avoid confusion, we may call the new 3-D PCs proposed in this paper as *combined three-dimensional photonic crystal*.

3 Conclusion

A new idea is presented and shown to be useful that an enclosed structure made of several pieces of 1-D PCs, called as a combined 3-D PC, can serve as a 3-D PC. The advantage of the new idea is that it brings technical simplicity in fabrication, being especially meaningful for the production of 3-D PCs operating in short wavelengths as in the visible, because there exists no technical difficulty in the fabrication of 1-D PCs working in short wavelengths.

References

1. S. Fan, et al.: Phys. Rev. Lett. **78**, 3294 (1997)
2. V. I. Kopp, et al.: Opt. Lett. **23**, 1707 (1998)
3. D. R. Smith, et al.: Appl. Phys. Lett. **65**, 645 (1994)
4. A. Mekis, et al.: Phys. Rev. Lett. **77**, 3787 (1996)
5. J. S. Foresi, et al.: Nature (London) **390**, 143 (1997)
6. X. Y. Lei, et al.: Appl. Phys. Lett. **71**, 2889 (1997)
7. M. J. Bloemer, M. Scalora: Appl. Phys. Lett. **72**, 1676 (1998)
8. S. E. Barkou, et al.: Opt. Lett. **24**, 46 (1999)
9. H. -B. Lin, et al.: Opt. Lett. **23**, 94 (1998)
10. S. Enoch and H. Akhouayri: J. Opt. Soc. Am. B **15**, 1030 (1998)
11. P. Tran: J. Opt. Soc. Am. B **16**, 70 (1999)
12. E. Yablonovitch, et al.: Phys. Rev. Lett. **67**, 2259 (1991)
13. C. M. Anderson and K. Giapis: Phys. Rev. Lett. **77**, 2949 (1996)
14. V. Kuzimiak, et al.: Phys. Rev. B **55**, 4298 (1997)
15. G. Feiertag, et al.: Appl. Phys. Lett. **71**, 1441 (1997)
16. S. Gupta, et al.: Appl. Phys. Lett. **71**, 2412 (1997)
17. W. Y. Yeung, et al.: J. Appl. Phys. **84**, 4091 (1998)
18. D. F. Sievenpiper, E. Yablonovitch: Phys. Rev. Lett. **80**, 2829 (1998)
19. Z. Q. Zhang, et al.: Phys. Rev. Lett. **81**, 5540 (1998)
20. J. Q. Fleming and S. -Y. Lin: Opt. Lett. **24**, 49 (1999)
21. H. Kosaka, et al.: Appl. Phys. Lett. **74**, 1370 (1999)
22. S. Fan, et al.: Appl. Phys. Lett. **65**, 1466 (1994)
23. H. Miguez, et al.: Appl. Phys. Lett. **71**, 1148 (1997)
24. Y. A. Vlasov, et al.: Phys. Rev. B **55**, R13357 (1997)
25. B. T. Rosner, et al.: J. Opt. Soc. Am. B **15**, 2654 (1998)
26. H. Mguez, et al.: Phys. Rev. B **59**, 1563 (1999)
27. H. -B. Sun, et al.: Appl. Phys. Lett. **74**, 786 (1999)

Diode-laser-based High Resolution Spectroscopy in Sm I

Hyunmin Park, Miran Lee, E. C. Jung, Jonghoon Yi, Yongjoo Rhee,
Jongmin Lee

Laboratory for Quantum Optics
Korea Atomic Energy Research Institute
P. O. Box 105, Yusong, Taejon, 305-600, Korea

Abstract. The present paper reports more extensive and precise experimental results about the isotope shifts of Sm I in the 635 nm - 690 nm range by Doppler-free saturation absorption spectroscopy using a single-mode diode laser with a small linewidth. We measured newly the isotope shifts and hyperfine structures of 20 transition lines, which are mostly originating from the $[4f^66s^2] \ ^7F_J$ to $[4f^66s6p] \ ^9D_o, \ ^9F_o$ and $\ ^7G_o$ levels, with a resolution better than 8 MHz. The measured isotope shifts were resolved into mass shifts and field shifts by King plot analysis. Finally, we could obtain the changes in mean-square nuclear charge radii from field shifts, and they were compared with the previous results.

1 Introduction

Tunable diode lasers can be used effectively in high resolution laser spectroscopy because of their narrow linewidth, wide tunability and compactness. Spectroscopic studies on Sm I have been of continuing interest because its stable isotopes lie in a region where great changes in the nuclear shapes occur. However, most the previous spectroscopic studies of Sm I were performed with a cw tunable dye laser in the wavelength region of 550 nm-620 nm. The present paper reports more extensive and precise experimental results about the isotope shifts and the hyperfine structures of Sm I in 635 nm - 690 nm wavelength range by Doppler-free spectroscopy using a single-mode diode laser system.

2 Experiment

For an atomic excitation laser, we used a commercial single-mode tunable diode laser with an extra-cavity which is operated in the wavelength range of 635 nm - 690 nm. The oscillator of the diode laser is the Liu and Littmann type. The structure enables the laser to operate in a single longitudinal mode and to be continuously tunable with minimum mode hops. The vacuum wavelength of the laser was measured by a wavemeter. Additionally, a part of the diode laser beam was sent to a confocal Fabry-Perot interferometer of 150 MHz free spectral range to record the frequency marks as the laser was

swept over the atomic transition lines. An atomic vapor of Sm metal was produced in a long metal tube vapor cell which generates an isothermal vapor with constant density. To obtain an isothermal constant density vapor in the atom-laser interaction zone, we made the active length of the tubular vapor cell long enough, about 80 cm. The temperature of the cell was kept at 700 °C to generate enough Sm vapor density, which was about $3 \times 10^{12}/\text{cm}^3$.

After the laser beam was split into a strong pump beam and a weak probe beam, two separated beams were aligned to propagate through Sm vapor in opposite directions. The intensity of the pump beam was modulated by a mechanical chopper to send a modulated signal to a lock-in amplifier. By scanning the diode laser over the range of 635 nm to 690 nm, we could obtain twenty Doppler-free spectra of transition lines where isotope shifts of Sm atom were obtained.

3 Results and Discussions

As an example of experimental results, a Doppler-free spectrum of the transition $[4f^66s^2] ^7F_1$ (292 cm^{-1}) - $[4f^66s6p] ^9F_1$ (14864 cm^{-1}) with the wavelength near 686.093 nm is shown in Fig. 1.

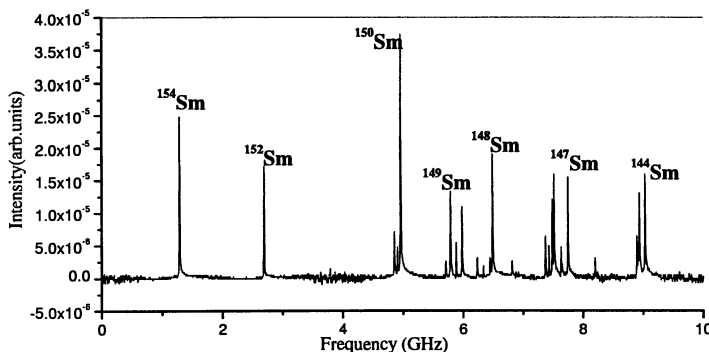


Fig. 1. Doppler-free spectrum of the transition 292 cm^{-1} - 14864 cm^{-1} of Sm atom

The figure shows the typical features of all spectrum measured in this paper. As can be seen well, each even mass isotopes, ^{154}Sm , ^{152}Sm , ^{150}Sm , ^{148}Sm and ^{144}Sm , are well resolved spectrally. Since the odd isotopes ^{147}Sm and ^{149}Sm have the nuclear spin ($I=7/2$) and the total angular momenta of the lower level and upper level are 1 and 1, they have seven peaks and are also well resolved in the spectrum. Each peaks in Fig. 3 have small background Gaussian pedestals which are originated from the velocity-changing collisions in the interaction region. But the background do not affect the accuracy of isotope shifts measurement because each peak in the spectrum has symmetric

lineshape. From the spectra, the magnetic dipole hfs constants A_{hfs} and the electric quadrupole hfs constants B_{hfs} of the states, $4f^66s6p\ ^9F_1$ were determined and they are $A_{149} = -345.7$ MHz, $B_{149} = -3.8$ MHz, $A_{147} = -423.4$ MHz, and $B_{147} = -13.2$ MHz. Additionally, we observed similar spectra for 20 transition lines and measured all isotope shifts between even isotopes of the transition lines. The measured isotope shifts of the even isotopes are summarized in Table 1.

Table 1. Measured isotope shifts of even isotopes for twenty transitions of Sm(MHz)

| Energy(cm ⁻¹) | ¹⁵⁴ Sm- ¹⁵² Sm | ¹⁵² Sm- ¹⁵⁰ Sm | ¹⁵⁰ Sm- ¹⁴⁸ Sm | ¹⁴⁸ Sm- ¹⁴⁴ Sm |
|---------------------------|--------------------------------------|--------------------------------------|--------------------------------------|--------------------------------------|
| 1490-17190 | -1251.5(8.1) | -2340.0(2.9) | -1659.0(3.0) | -2831.0(5.6) |
| 4021-19712 | -1261.6(6.5) | -2352.4(1.8) | -1644.6(4.7) | -2847.3(5.5) |
| 0-15650 | -1241.8(6.5) | -2318.5(3.0) | -1645.8(2.7) | -2807.1(6.1) |
| 293-15650 | -1251.5(0.9) | -2326.8(4.4) | -1657.1(7.6) | -2821.5(7.7) |
| 2273-17587 | -1230.0(1.4) | -2288.5(1.5) | -1626.7(2.5) | -2772.3(9.9) |
| 812-16116 | -1257.6(0.1) | -2331.3(5.5) | -1658.0(1.7) | -2826.8(3.3) |
| 812-16112 | -1256.0(4.5) | -2331.4(9.2) | -1657.4(3.3) | -2827.7(3.4) |
| 2273-17567 | -1253.3(5.3) | -2335.0(4.5) | -1663.6(1.9) | -2833.5(5.5) |
| 293-15567 | -1226.5(3.3) | -2285.7(5.6) | -1621.9(4.8) | -2771.5(5.4) |
| 1490-16748 | -1250.4(8.9) | -2333.2(3.0) | -1664.0(3.1) | -2821.7(3.9) |
| 4021-19006 | -1224.3(2.3) | -2275.2(2.9) | -1620.0(2.7) | -2756.0(1.9) |
| 0-14864 | -1214.8(3.0) | -2265.6(6.4) | -1608.8(6.3) | -2739.5(20.8) |
| 812-15567 | -1234.0(2.6) | -2294.9(3.5) | -1627.6(8.0) | -2782.5(3.8) |
| 293-15040 | -1214.0(1.5) | -2255.5(2.4) | -1602.3(2.1) | -2734.8(1.5) |
| 1490-16211 | -1240.9(0.1) | -2305.6(0.7) | -1641.0(4.8) | -2789.1(5.0) |
| 812-15507 | -1206.6(7.0) | -2240.7(1.5) | -1601.7(5.3) | -2725.4(11.1) |
| 1490-16131 | -1203.0(2.1) | -2230.4(3.4) | -1593.6(7.5) | -2766.3(7.0) |
| 2273-16859 | -1212.8(5.1) | -2249.6(2.6) | -1576.9(9.1) | -2711.6(6.4) |
| 293-14864 | -1218.8(2.6) | -2262.3(4.1) | -1607.9(2.5) | -2737.8(6.9) |
| 3125-17654 | -1169.1(0.3) | -2184.5(11.5) | -1568.2(4.9) | -2676.6(8.7) |

For the analysis of the measured results, we used the King plot method [1]. The method is used for the determination of the changes in mean-square nuclear charge radii, between different isotopes. Isotope shifts can be divided mass shift(MS) and field shift(FS). FS gives the informations about

the change of nuclear charge distribution. Hence, if we derive the field shifts from the measured isotope shifts, we can determine the changes in mean-square nuclear charge radii, directly from the known relation[2] $\delta\nu_i^{FS}/\delta < r^2 > = 5.491 \text{GHz/fm}^2$. The estimated results are listed in Table 2 and compared with the previous results by other groups[2][3][4]. From the table, we can see that the average values are in good agreement with the previous results with a small discrepancy while the experimental accuracy of ours is better than those.

Table 2. Changes in mean-square nuclear charge radii for even mass isotope pairs(fm^2)

| Isotope Pairs | This work | Ref[2] | Ref[3] | Ref[4] |
|---------------------------------------|-----------|-----------|-----------|-----------|
| ^{154}Sm - ^{152}Sm | 0.227(5) | 0.230(12) | 0.234(12) | 0.215(16) |
| ^{152}Sm - ^{150}Sm | 0.420(9) | 0.423(22) | 0.433(32) | 0.409(24) |
| ^{150}Sm - ^{148}Sm | 0.297(6) | 0.303(16) | 0.311(16) | 0.294(15) |
| ^{148}Sm - ^{144}Sm | 0.514(10) | 0.517(27) | 0.527(27) | 0.486(25) |

4 Conclusions

We measured newly the isotope shifts of 20 transition lines in 635 nm - 690 nm region by Doppler-free spectroscopy with a single mode diode laser and a long vapor cell. By using well-known King-plot method, we could analyze the measured isotope shifts into mass shifts and field shifts. We also determined the changes in mean-square nuclear charge radii more accurately from field shifts.

References

1. W. H. King :Comments on the Article "Peculiarities of the Isotope Shift in the Samarium Spectrum". J. Opt. Soc. Am **53**, 638-639 (1963).
2. H. Brand, B. Seibert, and A. Steudel:Laser-Atomic-Beam Spectroscopy in Sm. Z. Phys. A, **296**, 281-286 (1980).
3. Wei-Guo Jin, Takashi Wakui, Kenji Hasegawa, Haruko Uematsu, Tatsuya Minowa, and Hidersugu Katsuragawa: Isotope Shifts in Sm I by atomic beam diode-laser spectroscopy. J. Phys. Soc. Jpn, **88** 2521-2522 (1997).
4. K. Heilig and A. Steudel:Changes in mean-square charge radii from optical isotope shifts. At. Data Nucl. Data Tables **14**, 613-638 (1974).

QND-Like Quantum Measurement with a Photon-Number Squeezed Light Beam

Peng Fanglin¹, Zhang Jing², Dong Ruifang², Zhang Tiancai²

¹ Physics Department, Beijing Normal University, Beijing, 100875 P.R.China

² Institute of Opto-Electronics, Shanxi University, Taiyuan, 030006 P.R. China
e-mail: fipeng@ihw.com.cn

Abstract. A new QND-like measurement experimental scheme with a photon-number squeezed light beam and a beam splitter is proposed. Within the scheme the input signal beam is a modulated coherent beam and the meter beam is a photon-number squeezed light beam coming from a diode laser with optical feedback. The meter beam enters the usual vacuum port of the beam splitter, and then couples with the signal beam at the beam splitter. The calculation shows that if a 50:50 beam splitter is used and the transfer efficiency is 95%, the QND measurement in quantum domain is able to be performed using the meter beam with photon-number squeezing of 12%. For the meter beam of photon-number squeezing of 30%, $T_s + T_m$ and $V_{s/m}$ will be 1.11 and -0.79dB .

Since V. B. Braginski proposed ‘Quantum Non-Demolition (QND)’ measurement [1], the QND measurement draws attentions of scientists due to its potential application in the probe of gravity waves and the precise measurements. Because the limits of the quantum noise in quantum optics is achieved easily and the technique of non-linear optics is matured, the QND research in the fields is developing rapidly. The original QND measurement [2] requires the unitary gain of the observable through a measurement device, and the all criteria introduced by Holland [3] are satisfied. The various QND measurements have been realized in a few laboratories [5]–[8]. On the bases of the QND measurement, cooperating the optical communication technique, ones investigate the ‘QND-like’measurement [2]. The ‘QND-like’measurement satisfies all criteria introduced by Holland [4] but has the nonunitary gain of the observable through measurement device, i.e. the observable may be enlarged or attenuated linearly. The ‘QND-like’ measurement is also called *quantum noiseless optical tap or quantum duplication*. There has been realization of several ‘QND-like’measurements experimentally [8]–[10].

It is well known that the a beam splitter (BS) is one of the simplest coupling device. The quantum measurement experiments using BS have been reported recently [9] [10]. The same technique in the experiments are : a squeezing optical wave (for example, quadrature squeezing fields or quantum correlated twin beams) enters into the usual vacuum port of BS as a meter wave, and then it will be measured after mixing with a signal wave at BS. In principle, the different squeezing optical wave can be used in this

quantum measurements scheme. The photon-number squeezed light beam is conveniently generated by diode laser, so the QND measurement device with the photon-number squeezed light beam and BS will be more convenient and practical. This idea motivated us to exploit a photon-number squeezed light beam in the quantum measurement scheme with BS.

Fig. 1 shows the schematic of the experimental setup with a BS. The signal wave is a modulated coherent light S^{in} and the meter wave is a photon-number squeezed light beam M^{in} coming from diode laser. The putout signal and meter waves denote as S^{out} and M^{out} , respectively. Their respective amplitude quadrature components are $X_s^{in}, X_m^{in}, X_s^{out}, X_m^{out}$. For the coherent light $\langle |\delta X_s^{in}|^2 \rangle = 1$, and for the squeezed light $\langle |\delta X_s^{in}|^2 \rangle < 1$.

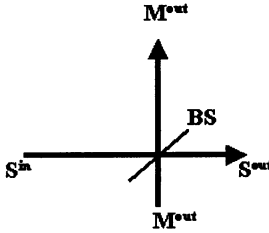


Fig. 1. Schematic of the experimental setup.

The properties of QND measurement are quantified by the signal and meter transfer coefficients T_s and T_m ,^[5] defined as the fraction of signal input SNR transferred to the respective output wave, i.e.

$$T_s = |\langle SNR_s^{out}/SNR_s^{in} \rangle|$$

$$T_m = |\langle SNR_m^{out}/SNR_s^{in} \rangle|$$

where the definition of SNR are

$$SNR_{s(m)}^{in(out)} = \frac{|\langle X_{s(m)}^{in(out)}(\omega) \rangle|^2}{|\langle \delta X_{s(m)}^{in(out)}(\omega)^2 \rangle|}. \quad (1)$$

In addition, the ability for quantum state preparation of the system are characterized by the conditional variance $V_{s/m}$

$$V_{s/m} = V_s^{out}(1 - C_{s,m}^2) \quad (2)$$

where

$$C_{s,m}^2 = \frac{|\langle \delta X_s^{out}(\omega) \delta X_m^{out}(\omega) \rangle|^2}{\langle |\delta X_s^{out}(\omega)|^2 \rangle \langle |\delta X_m^{out}(\omega)|^2 \rangle} \quad (3)$$

is the correlation coefficient between the signal and meter output.

For an ideal QND measurement^[2] the output signal and meter waves are perfectly correlated with the input signal wave at the same time, and

the output signal wave and the output meter wave are perfectly correlated, also. In this case, $T_s = 1$, $T_m = 1$, $V_{s/m} = 0$. For classical measurement $T_s + T_m \leq 1$, $V_{s/m} \geq 1$. The QND measurement in quantum domain requires $T_s + T_m > 1$, $V_{s/m} < 1$.

The relation between output and input quadrature amplitudes at BS can be expressed as

$$\begin{pmatrix} X_s^{out} \\ X_m^{out} \end{pmatrix} = \begin{pmatrix} -\sqrt{R} & \sqrt{T} \\ \sqrt{T} & \sqrt{R} \end{pmatrix} \begin{pmatrix} X_s^{in} \\ X_m^{in} \end{pmatrix} \quad (4)$$

Where T and $R(\equiv 1 - T)$ are the power transmission and reflectivity of BS, respectively. For convenience, we denote $\langle |\delta X_{s(m)}^{in(out)}(\omega)|^2 \rangle$ as $V_{s(m)}^{in(out)}$. Due to the imperfect detection and optical losses of the system the quantum correlation between the input and output quadrature amplitudes must be reduced and the additional noise should be considered. If η stands for the transfer efficiency of the device, considering the losses of system, the corrected relations between the output and input quadrature amplitudes are

$$\begin{aligned} X_s^{out} &= \sqrt{\eta}(-\sqrt{R}X_s^{in} + \sqrt{T}X_m^{in}) + \sqrt{1-\eta}U_s \\ X_m^{out} &= \sqrt{\eta}(\sqrt{T}X_s^{in} + \sqrt{R}X_m^{in}) + \sqrt{1-\eta}U_m \end{aligned}$$

where $U_{s(m)}$ is the excess vacuum fluctuation. Its noise spectra is $\langle |U_{s(m)}|^2 \rangle = 1$.

Following the results above, one has

$$V_s^{out} = \eta(RV_s^{in} + TV_m^{in}) + 1 - \eta \quad (5)$$

$$V_m^{out} = \eta(TV_s^{in} + RT_m^{in}) + 1 - \eta \quad (6)$$

$$C_{s,m} = \frac{\eta^2 RT(V_s^{in} - V_m^{in})^2}{V_s^{out}V_m^{out}} \quad (7)$$

From eqs.(1 - 4) we have

$$T_s = \frac{R}{R + TV_m^{in} + (1 - \eta)/\eta} \quad (8)$$

$$T_m = \frac{T}{T + RV_m^{in} + (1 - \eta)/\eta} \quad (9)$$

$$V_{s/m} = \frac{(1 - \eta) + \eta V_m^{in}}{(T + RV_m^{in})\eta + 1 - \eta} \quad (10)$$

It is clear that $T_s, T_m, V_{s/m}$ are a function of variables V_m^{in}, η and T . Fig. 2 shows QND transfer coefficients $T_s + T_m$ and conditional variance $V_{s/m}$ for $T = 0.5$ as a function of the squeezing degree δx and transfer efficiency η . In this case the transfer efficiency η should be large then 0.67 to perform quantum measurement. Moreover, for $\delta X > 50\%$ the quantum state preparation $V_{s/m}$ will increase evidently. Fig. 3 shows QND transfer coefficients $T_s + T_m$ and conditional variance $V_{s/m}$ for $\delta X = 0.7$ as a

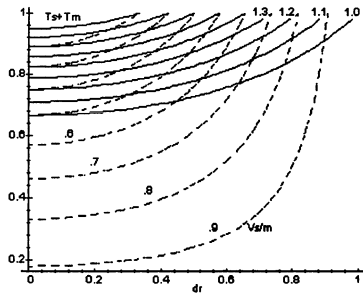


Fig. 2. QND transfer coefficients $T_s + T_m$ and conditional variance V_s/m for $T = 0.5$ as a function of the squeezing degree δx and transfer efficiency η .

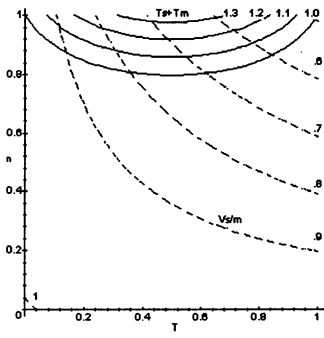


Fig. 3. QND transfer coefficients $T_s + T_m$ and conditional variance V_s/m for $\delta x = 0.7$ as a function of the power transmission T and the transfer efficiency η .

function of the power transmission T and the transfer efficiency η . It shows that maximum of transfer coefficients $T_s + T_m$ is at the point of $T = 0.5$. If a 50:50 beam splitter is used and the transfer efficiency is 95%, the QND measurement is able to be performed using the meter beam with photon-number squeezing of 12%. Experimentally, the meter beam of photon-number squeezing of 30% is available, corresponding $T_s + T_m$ and V_s/m will be 1.11 and -0.79 dB.

References

1. V. B. Braginskii, et al. Sov. Phys. JETP. **46**, 705–718 (1977)
2. J.-Ph. Poizat et al. Ann. Phys. Fr. **19**, 265–297 (1994)
3. M. J. Holland et al. Phys. Rev. A, **42**, 2995–3005 (1990)
4. A. Sinatra, J. F. Rock, K. Vigneron et al. Phys. Rev. A, **57** 2980–2995 (1998)
5. S. F. Pereira et al. Phys. Rev. Lett., **72**, 214–217 (1994)
6. R. Bruckmeier et al. Phys. Rev. Lett., **78**, 1243–1246 (1997)
7. K. Bencheikh et al. Phys. Rev. Lett., **75**, 3422–3425 (1995)
8. J. A. Levenson et al. Phys. Rev. Lett., **70**, 267–270 (1993)
9. R. Bruckmeier et al. Phys. Rev. Lett., **79**, 43–46 (1997)
10. Hai Wang, Changde Xie, Kunchi Peng et al. Phys. Rev. Lett., **82**, 1414–1417 (1999)

The Dynamics of 1D H_2^+ Interacting with Ultrashort Laser Pulse

Weixing Qu, Zhaoyang Chen, Wei Yu, Wenqi Zhang, Shiqi Jin, Zhizhan Xu

Laboratory for High Intensity Optics, Shanghai Institute of Optics and Fine Mechanics, Chinese Academy of Sciences, Shanghai 201800, P. R. China

Abstract. Using a collinear model, we theoretically investigate the dynamic process and the spectrum of high harmonic generation of hydrogen molecular ion (H_2^+) in intense ultrashort laser pulses with intensities of $10^{14} \sim 10^{15} W/cm^2$, the wavelength of 532nm and the duration of 22fs. The results show that: (1) The ionization mainly occurs in the decay-front of the pulse profile when the pulse's peak intensity is low and in the plateau-front when the intensity is high. (2) The dissociation and the dissociative ionization are very smaller and appear later about 5 cycles ($\approx 9 fs$) than the ionization. (3) The spectrum of high harmonic generation demonstrates that the shorter pulse can produce higher order harmonics than the longer one.

With appearing of the chirp-pulse amplifier the intense ultrashort pulse with duration of ten odd femtoseconds can be produced with the table-top laser system. That makes the research of dynamic behavior of the molecule under the ultrashort laser pulse be currently a very active area in an intense-field physics [1]. Compared with the atoms, the molecules in the intense field can exhibit more dynamic behaviors due to more freedom degrees that respond on the very different time scale. A lot of nonlinear phenomena, such as the dissociation through the bond softening and Coulomb explosion [2] and the above threshold dissociation (ATD) [3] et al., have been observed in intense laser-molecule interaction experiments.

TDSE of the collinear H_2^+ in linear polarization laser pulse is (in a.u.)

$$i\frac{\partial\Psi(z,r,t)}{\partial t} = [\hat{H}_0(z,r) + \hat{H}_I(t)]\Psi(z,r,t), \quad (1)$$

$$\hat{H}_0(z,r) = -\frac{1}{2}\frac{\partial^2}{\partial z^2} - \frac{1}{2\mu}\frac{\partial^2}{\partial r^2} + V(z,r), \quad \hat{H}_I(t) = -zE(t) \quad (2)$$

where z and r are the distance from the center of mass of nuclei to the electron and the one of the distance between two nuclei, respectively. $\mu = 918$ is a reduced mass of two nuclei. $V(z,r) = -\frac{1}{\sqrt{(z-0.5r)^2+1.0}} - \frac{1}{\sqrt{(z+0.5r)^2+1.0}} + \frac{1}{\sqrt{r^2+0.03}}$ is a Coulomb potential of H_2^+ system [1].

The wave function $\Psi(z,r,t)$ can be numerically calculated with the second-order split-operator method [4]. The total calculation region is defined by $|z| \leq z_{\max} = 102.4$ a.u. and $0 \leq r \leq r_{\max} = 20.48$ a.u.. We consider the ionization occurring when the distance from the electron to both nuclei is

greater than $z_I = 32$ a.u. and the dissociation occurring when the separation between two nuclei exceeds $r_D = 9.5$ a.u..

The quantum-averaged acceleration of electron

$$a(t) = \int \int \Psi^*(z, r, t) \left(-\frac{\partial V(z, r)}{\partial z} \right) \Psi(z, r, t) dz dr \quad (3)$$

can be calculated in a usual way. Fourier transforming $a(t)$, one gets the spectrum of high-order harmonic.

In our calculating, we assume the electric field of the laser pulse $\mathbf{E}(t) = E_0 f(t) \sin(\omega t) \mathbf{e}_z$ and choose the form of envelope function $f(t)$ as

$$f(t) = \begin{cases} \sin^2\left(\frac{\omega t}{10T}\right), & \text{when } 0 < t \leq 5T \\ 1, & \text{when } 5T < t \leq 7T \\ \cos^2\left[\frac{\pi(t-7T)}{10T}\right], & \text{when } 7T < t \leq 12T, \end{cases} \quad (4)$$

here $T = 73.36$ a.u. (≈ 1.75 fs) is the period of laser field with a wavelength of 532 nm. We choose the steps of space and time as $\delta z = 0.2$ a.u., $\delta r = 0.04$ a.u. and $\delta t = 0.04$ a.u..

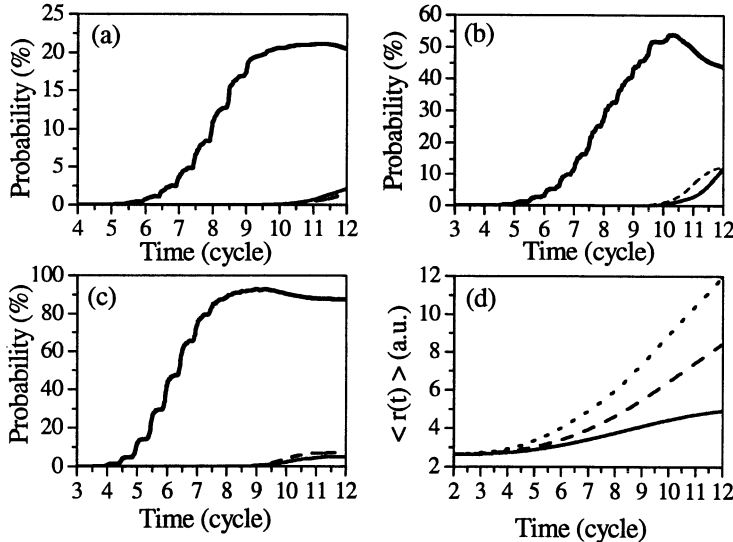


Fig. 1. (a–c) show the probabilities of ionization (bold line), dissociation (thin line) and dissociative ionization (dashed line) of 1D H_2^+ under an intense ultrashort laser pulse with the duration of $T_d = 12$ cycles and peak intensities $I = 2.5 \times 10^{14} W/cm^2$, $4.0 \times 10^{14} W/cm^2$ and $7.5 \times 10^{14} W/cm^2$, respectively; (d) gives average internuclear distance as a function of time for the pulses with different peak intensities: $2.5 \times 10^{14} W/cm^2$ (solid line) and $4.0 \times 10^{14} W/cm^2$ (dashed line), $7.5 \times 10^{14} W/cm^2$ (dot line).

The time-dependent probabilities of ionization, dissociation and dissociative ionization for the pulses with different peak intensities are shown in Fig.1(a-c). Apart from observation that the channels of ionization, dissociation and dissociative ionization turn on at the different moments, similar to the classical simulation [5], we also find that the dissociative ionization exceeds the dissociation when the peak intensity of pulse is $4.0 \times 10^{14} W/cm^2$. This is because both the dissociation and the dissociative ionization compete each other at a given peak intensity I_c between $2.5 \times 10^{14} W/cm^2$ and $4.0 \times 10^{14} W/cm^2$. The dissociation (dissociative ionization) dominates when the peak intensity of pulse is smaller (higher) than I_c .

We present in Fig.1(d) the average separation between nuclei,

$$\langle r(t) \rangle = \frac{\int \int r |\Psi(z, r, t)|^2 dz dr}{\int \int |\Psi(z, r, t)|^2 dz dr} \quad (5)$$

as a function of time for the pulses with different peak intensities. It is easily found that the more intense the pulse intensity is, the higher is the average separating velocity (the slope of curves in Fig.1(d)). This phenomenon can be explained as following: As the total Hamiltonian of system ($H_2^+ +$ laser field) is time-dependent, the system belongs to a non-autonomous one. The energy of H_2^+ is not conservative and the nuclear separation must gradually increase with time during the pulse imposing. Since the pulse with a high intensity ionizes the electron earlier than that with a low intensity, the two nuclei separate apart due to Coulomb potential at the smaller internuclear distance when the high-intensity pulse used. So the nuclei must have the greater kinetic energy in the case of high-intensity pulse.

The spectra of the high-order harmonics for the pulses with the same duration but the different peak intensities are shown in Fig.2. These spectra, like the ones of the high-order harmonics from the atom in the intense laser pulse, have a rapid decrease in intensity for first few harmonics, a plateau where the harmonics have nearly the same intensity and a cutoff where the harmonics quickly vanish. However, the energy of the highest harmonic emitted is not at an energy about $I_p + 3.17U_p$, where $I_p = 0.78$ a.u. is the ionization potential of 1D H_2^+ and $U_p = E^2/(4\omega^2)$ is the ponderomotive energy of electron in the laser pulse, that is the quiver energy of a free electron in the laser field with an amplitude E and a frequency ω . The reason is that the cutoff rule is valid only when the change in the amplitude of the laser field is adiabatic, that is the amplitude of the laser field has few change during the generation of each individual harmonics. If the amplitude of the pulse has significant change before the ionized electron recombines with the parent ion, a maximum energy the ionized electron gets is not equal to $3.17U_p$.

As $U_p(t)$ changes significantly with time for the intense ultrashort pulse, we define the time-average ponderomotive energy $\bar{U}_p = \frac{1}{T_d} \int_0^{T_d} \frac{E^2(t)}{4\omega^2} dt$ (where

T_d is the duration of pulse. Using the \bar{U}_p , we find that the position of the cutoff frequency appears at

$$\omega_{\max} \simeq I_p + 6\bar{U}_p. \quad (6)$$

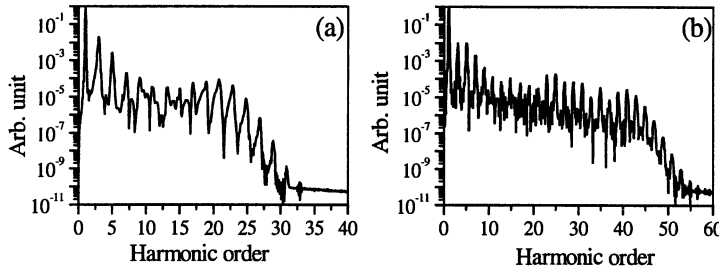


Fig. 2. The high-harmonic generation spectrum of H_2^+ under the intense ultrashort laser pulses with different peak intensities: (a) $2.5 \times 10^{14} W/cm^2$ and (b) $7.5 \times 10^{14} W/cm^2$. The initial state of H_2^+ is the ground state.

We also find that there are more noises between the harmonics peaks in the plateau of spectrum. That indicates the phases of the harmonics in the plateau are random and, therefore, the harmonics in the plateau have poor temporal coherence. However, the spectral peaks of harmonics in the cutoff region have almost the same form and there are few noise between them. So the high-order harmonics in the cutoff region have good temporal coherence. In addition, the broadening of the peaks in the cutoff region also indicates that they are generated during very short time interval. On the temporal coherence of the harmonics from H_2^+ under intense ultrashort laser pulse, we will in detail discuss in forthcoming paper.

References

1. Kulander, K. C., Mies, F. H., Schafer, K. J. (1996) Model for studies of laser-induced nonlinear processes in molecules. *Phys. Rev. A* **53**, 2562-2570
2. Bucksbaum, P. H., Zavriyev, A., Muller, H. G. et al. (1990) Softening of the H_2^+ molecular bond in intense laser fields. *Phys. Rev. Lett.* **64**, 1883-1886
3. Giusti-Suzor, A., He, X., Atacek, O. et al. (1990) Above-threshold dissociation of H_2^+ in intense laser fields. *Phys. Rev. Lett.* **64**, 515-518
4. Hermann, M. R., Fleck, J. A., Jr. (1988) Split-operator spectral method for solving the time-dependent Schrödinger equation in spherical coordinates. *Phys. Rev. A* **38**, 6000-6012
5. Qu, W., Hu, S., Xu, Z. (1998) Classical dynamics of H_2^+ interacting with an ultrashort intense laser pulse. *Phys. Rev. A* **57**, 2219-2222

3D Monte-Carlo Simulation of Zeeman Slower System with Two Level Atoms

Min-Gyu Kim, K.S. Lee, D.Y. Jeong, J.M. Han, Yong-joo Rhee,
Jongmin Lee

Laboratory for Quantum Optics Korea Atomic Energy Research Institute P. O.
Box 105, Yusong, Taejon 305-600, Korea Email: yjrhee@nanum.kaeri.re.kr

Abstract. We report three dimensional numerical simulations of a Zeeman slower system with two level atoms. We choose the magnetic field intensity distribution from experimental data and atomic conditions from population analysis of the transitions between $F=2$ and $F=3$ lines of the Na atom. We use the Monte-Carlo method for simulation. We generate three kinds of random numbers to specify the initial velocity of the atoms and one more random number for the event of the spontaneous emission. We treat the stimulated emission with numerical solution of the Bloch equation for two level atoms. We put atoms into the Zeeman slower system one by one and follow the motion of each atom. Two forces are considered; one is the intensity gradient force caused by stimulated emission and the other is the divergence force caused by spontaneous emission. We employ a parameter related with the atomic states at the exit port of the Zeeman slower. This parameter is related with space distribution and the velocity distribution of the atom at the exit. We analyze three kinds of the laser beam conditions; one is the focusing condition, another being intensity conditions and the last one being intensity shape conditions of the laser beam front.

1 Introduction

MOT(Magneto-Optical Trap) is the most popular method for the trapping and the cooling of atoms. In MOT, it is impossible to cool and trap the atoms which have the velocity above the cooling depth. Further more, the atoms which have high velocity give negative effects on the cooled atoms, like a kicking. This is the reason why we need low velocity atoms for MOT application. There have been some efforts to prepare low velocity atoms for initial atom input into MOT. One of the popular efforts is Zeeman slower system. We do the numerical simulations for analyzing microscopic motions of atoms from the atomic source. Basically, we use Monte-Carlo method for this simulation. We shoot an atom one by one and follow the atomic motion. We consider two kinds of forces generated by laser. The one is divergence force from spontaneous emission, the other is the gradient force from stimulated emission of atom. We test 3 kinds of parameters, which are laser beam focusing condition, laser intensity condition and laser beam shape condition. We wanted to find out the optimal conditions for these three parameters.

2 Light pressure to an atom

The origin of light pressure is the electronic level transition in an atom. For calculating the light pressure, we should follow the level transition of an electron in atom. We considered the transition between F=2 and F=3 of the Na atom. The laser wavelength is tuned to the transition line. We can calculate the stimulated emission probability from rate equations of the atom with detuning. For calculating the event of the spontaneous emission, we use the analytical method as follows. The rate equation of two level atom with detuning is [1]

$$\dot{C}_1 = -i\frac{\Omega}{2}C_0 + \left(-\frac{\gamma}{2} + i\Delta\right)C_1 \quad (1)$$

$$\dot{C}_0 = -i\frac{\Omega}{2}C_1 \quad (2)$$

where C_1 is amplitude of excited state, C_0 for ground state, Ω is Rabi frequency, Δ is detuning and γ is spontaneous emission rate. The solution of this rate equation is as follows

$$C_1(t) = A(\exp \lambda_+ t - \exp \lambda_- t). \quad (3)$$

where

$$\lambda_{\pm} = \frac{1}{2} \left(-\frac{\gamma}{2} + i\Delta \pm \sqrt{\left(\frac{\gamma}{2} - i\Delta\right)^2 - \Omega^2} \right). \quad (4)$$

A is the amplitude of state. We need relaxation time from one spontaneous emission to the next spontaneous emission. We employed another decay rate which represent the probability of the spontaneous emission(γ'). We can write the time derivative of populations of states with γ' such as

$$\frac{d}{dt}(|C_0|^2 + |C_1|^2) \sim -\gamma|A|^2 \exp -\gamma't \quad (5)$$

where

$$\gamma' = \frac{\gamma}{2} - \text{real} \left(\sqrt{\left(\frac{\gamma}{2} - i\Delta\right)^2 - \Omega^2} \right). \quad (6)$$

Finally, we can write the time dependent total population of the atomic state as follow

$$|C_0|^2 + |C_1|^2 = \exp(-\gamma't) \quad (7)$$

As you show, sum of each population is not conserved. When a spontaneous emission occurred, the system loose the energy amount of one photon. We consider the loss amount of populations sum is the probability of the spontaneous emission. We consider two kinds of forces on the atom due to laser

beam. One is the divergence force. This force is related with the spontaneous emission procedure. In every spontaneous emission event, momentum of atom is changed up to $\hbar k$. Force direction is related with direction of the emission. We generate two white random number for treating the emission direction. We can calculate the spontaneous event timing with eqn(7).

The gradient force to the atom is given as follow [2]

$$\mathbf{F} = \hbar \frac{\mathbf{r}}{\omega^2} \Delta \frac{G}{1 + G + \Delta^2/\gamma^2} \quad (8)$$

where $G = I/I_{sat}$. I is the intensity of laser and I_{sat} is the saturation intensity. $\Delta = \omega_0 - \omega + \mu_B B - kv_z$.

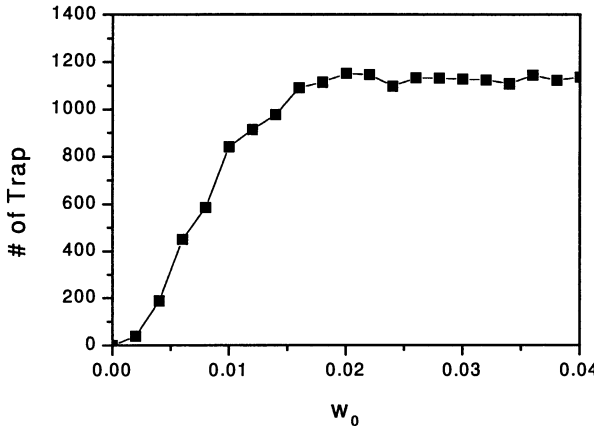


Fig. 1. Number of atoms for various laser beam width

3 The Simulation and Result

We generate four random numbers for three dimensional initial direction of the atom, one Maxwell-Boltzmann distributed random number for initial speed of the inserted atom, one exponential decayed random number for spontaneous emission (γ), one exponential decayed random number for population sum decay rate(γ'), and two white random numbers for emission direction. We use the Runge-Kutta method for following atomic motion. We use the magnetic field shape from experimental data[3]. We use the laser beam with Gaussian beam approximation[4]. In Gaussian beam approximation, spacial characteristics of the laser beam is characterized by two parameter, z_0 and ω_0 . z_0 is related with beam size at the focused point and ω_0 is related with beam divergence. We calculate the result with changing laser parameter of

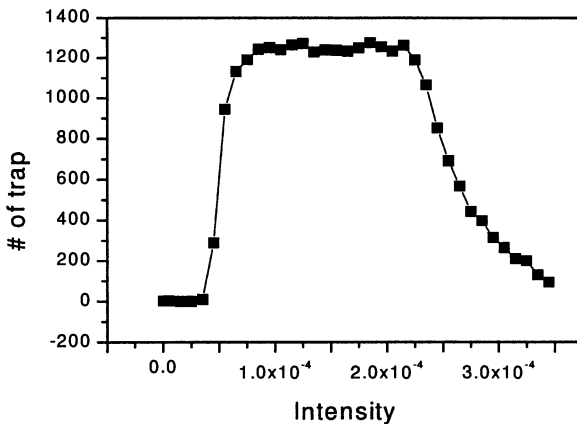


Fig. 2. Number of atoms for various laser intensity

intensity and ω_0 . We use the Zeeman slower with length of 1m. We checked the atom velocity and position at the 1.05 m from atom inlet, another word, 50 mm from Zeeman slower outlet. In Fig(1) We can see the saturation point of slowed atom number with intensity of 1.5×10^{-4} . We put the 2000 atoms per data point into Zeeman slower. We can get around 1200 slowed atoms (with velocity range from 0 to 100 m/s) at the Zeeman slower outlet. In the case of intensity(Fig. 2), We can see the effective range of laser intensity with $\omega_0 = 0.02 \text{ m}$. In the condition of week laser, laser cannot slow the atom effectively. In the condition of strong laser, atoms get too much momentum from laser. So, atoms can not go out of the outlet of the Zeeman slower. From the simulation, we can find out the effective range of slowing beam. High intensity slowing beam gives negative effects to the slowing. In case of focus condition, focusing the slowing beam gives negative effects to the slowing.

References

1. R. Loudon; The Quantum Theory of Light 2nd ed. (Oxford University Press, New York, 1990)
2. V.I.Balykin and V.S.Letkov; Atom optics and laser light, (harwood academic publisher, 1995)
3. Kwang-Hoon Ko, Do-Young Jeong, Jaemin Han, K.S.Lee, Sipyoo Rho, Youngjoo Rhee and Jongmin Lee, J. Kor. Phy. Soc. **35**, 239-243(1999)
4. B.E.A. Saleh, M.C. Teich; Fundamentals of Photonics, (Wiley-interscience, New York, 1991)

The Enhancement of Spontaneous and Stimulated Emission by a Bose-Einstein Condensate

Tan Weihan¹, Yan Kezhu¹, Liu Renhong²

¹ Physics Department, Shanghai University, Shanghai 201800, China

² Shanghai Institute of Optics and Fine Mechanics, Academia Sinica, Shanghai 201800, China

Abstract. In this paper, an exactly solved model for the emission by N atoms is presented. The spontaneous and induced transition rate obtained, are greatly enhanced by a factor which is proportional to the density of atoms n in the volume $\sqrt{\frac{2}{\pi}}\lambda^3$ (λ is the transition wavelength of atom) and dependent on the de-Broglie wavelength λ_B in a more complicated way.

Since the rapid experimental progress made in producing of Bose-Einstein Condensate (BEC), many papers have been published on the optical properties of condensate with large number of Bose atoms in the same quantum state [1, 2]. In this paper, an exactly solved model for the emission by N atoms is presented. The spontaneous and induced transition rate obtained, are greatly enhanced by a factor proportional to the density of atoms n in the volume $\sqrt{\frac{2}{\pi}}\lambda^3$ (λ is the transition wavelength of atom) and dependent on the de-Broglie wavelength λ_B in a more complicated way.

For a single atom, it is easy to evaluate the spontaneous linewidth and energy level shift according to Wigner-Weisskopf theory of natural linewidths [1].

$$\frac{1}{2}\gamma + i \Delta \omega_s = \frac{i}{\hbar^2} \sum_{\lambda,\sigma} \frac{< e, 0 | H' | g, 1_\lambda > < g, 1_\lambda | H' | e, 0 >}{\omega_{eg} - \omega_\lambda + is} \quad (1)$$

In the case of N atoms, the wave function Ψ_n takes the form

$$\Psi_n = \psi_{n_1} \psi_{n_2} \cdots \psi_{n_N}, \quad \psi_{n_i} = e^{-iE_{n_i}t/\hbar} e^{i\mathbf{p}_{n_i} \cdot \mathbf{r}_i / \hbar} \varphi_{n_i}(\mathbf{q}_i) \quad (2)$$

where coordinates \mathbf{q}_i and \mathbf{r}_i , wavefunctions $\varphi_{n_i}(\mathbf{q}_i)$ and $e^{i\mathbf{p}_{n_i} \cdot \mathbf{r}_i / \hbar}$ belong to the internal and center of mass quantum state n_i of i th atom respectively. It is straightforward to generalize Eq.(1) by substituting $\sum_{i=1}^N H'_i$ for H' , thus yields

$$\frac{1}{2}\Gamma_e + i \Delta \omega = \frac{i}{\hbar^2} \sum_{\lambda,\sigma} \sum_{i,j=1}^N \frac{< e, 0 | H'_i | g, 1_\lambda > < g, 1_\lambda | H'_j | e, 0 >}{\omega_{eg} - \omega_\lambda + is} \quad (3)$$

Using Eqs.(1),(2) we can deduce the interaction matrix elements as

$$\langle e, 0 | H'_i | g, 1_\lambda \rangle = \hbar g_\lambda^* r^+(r_i) e^{i\omega_\lambda t - i\mathbf{k}_\lambda \cdot \mathbf{r}_i},$$

$$g_\lambda^* = -ie\sqrt{\frac{2\pi}{\hbar\omega_\lambda L^3}} v_{eg} \cdot \epsilon_{\lambda,\sigma}, \quad r^+(r_i) = e^{-i(\mathbf{p}_e - \mathbf{p}_g) \cdot \mathbf{r}_i / \hbar} \quad (4)$$

$$\langle g, 1_\lambda | H'_j | e, 0 \rangle = \hbar g_{\lambda,\sigma} r^-(r_j) e^{-i\omega_\lambda t + i\mathbf{k}_\lambda \cdot \mathbf{r}_j},$$

$$g_{\lambda,\sigma} = ie\sqrt{\frac{2\pi}{\hbar\omega_\lambda L^3}} v_{ge} \cdot \epsilon_{\lambda,\sigma}, \quad r^-(r_j) = e^{i(\mathbf{p}_e - \mathbf{p}_g) \cdot \mathbf{r}_j / \hbar} \quad (5)$$

and rewrite equation (3) in the form

$$\begin{aligned} \frac{1}{2}\Gamma_e + i\Delta\omega &= i \sum_{\lambda,\sigma} g_\lambda^2 \left[\sum_{i=1}^N \frac{\langle r^+(r_i) r^-(r_i) \rangle}{\omega_{eg} - \omega_\lambda + is} \right. \\ &\quad \left. + \sum_{i=1}^N \sum_{j \neq i}^N \frac{\langle r^+(r_i) r^-(r_j) \rangle}{\omega_{eg} - \omega_\lambda + is} e^{i\mathbf{k} \cdot (\mathbf{r}_i - \mathbf{r}_j)} \right] \end{aligned} \quad (6)$$

where r^+, r^- are the "up" and "down" operators on the energy level, $\langle e | r^+(r_i) r^-(r_i) | e \rangle = 1$, $\langle g | r^+(r_i) r^-(r_i) | g \rangle = 0$. Thus $\sum_{i=1}^N \langle r^+(r_i) r^-(r_i) \rangle$ measures the number of N atoms in the excited state. If we normalize both side by $\sum_{i=1}^N \langle r^+(r_i) r^-(r_i) \rangle$ and use the same notation for $\frac{1}{2}\Gamma_e + i\Delta\omega$ after normalization, yields

$$\begin{aligned} \frac{1}{2}\Gamma_e + i\Delta\omega &= i \sum_{\lambda,\sigma} g_\lambda^2 \frac{1}{\omega_{eg} - \omega_\lambda + is} \\ &\quad + \frac{i \sum_{i=1}^N \sum_{\Delta r_j \neq 0} \langle r^+(r_i) r^-(r_i + \Delta r_j) \rangle}{\sum_{i=1}^N \langle r^+(r_i) r^-(r_i) \rangle} L(\Delta r_j), \\ L(\Delta r_j) &= \sum_{\lambda,\sigma} g_\lambda^2 \frac{1}{\omega_{eg} - \omega_\lambda + is} e^{-i\mathbf{k}_\lambda \cdot \Delta r_j}, \quad \Delta r_j = \mathbf{r}_j - \mathbf{r}_i \end{aligned} \quad (7)$$

The first term is just the linewidth and shift $\frac{1}{2}\gamma + i\Delta\omega_s$ for single atom; the second term shows the modification due to N atoms. The dipole function $L(\Delta r_j)$ can be evaluated through[4]

$$\begin{aligned} L(\Delta r_j) &= 2\gamma(K(\xi) - iW(\xi)), \quad \xi = -\mathbf{k}_\lambda \cdot \Delta r_j, \\ K(\xi) &= \frac{3}{4}[\sin^2 \theta \frac{\sin \xi}{\xi} + (1 - 3\cos^2 \theta)(\frac{\cos \xi}{\xi^2} - \frac{\sin \xi}{\xi^3})], \\ W(\xi) &= \frac{3}{4}[-\sin^2 \theta \frac{\cos \xi}{\xi} + (1 - 3\cos^2 \theta)(\frac{\sin \xi}{\xi^2} + \frac{\cos \xi}{\xi^3})] \end{aligned} \quad (8)$$

From Eqs.(4,5) we derive the correlation function

$$\langle r^+(\mathbf{r}_i)r^-(\mathbf{r}_i + \Delta\mathbf{r}_j) \rangle = \langle r^+(\mathbf{r}_i)r^-(\mathbf{r}_i) \rangle \langle e^{i(\mathbf{p}_e - \mathbf{p}_g) \cdot \Delta\mathbf{r}_j / \hbar} \rangle \quad (9)$$

Therefore, Eq.(7) assumes

$$\frac{1}{2}\Gamma_e + i\Delta\omega = \frac{1}{2}\gamma + i\Delta\omega_s + \sum_{\Delta\mathbf{r}_j} \langle e^{i(\mathbf{p}_e - \mathbf{p}_g) \cdot \Delta\mathbf{r}_j / \hbar} \rangle L(\Delta\mathbf{r}_j) \quad (10)$$

Supposing $\mathbf{p}_e = \langle \mathbf{p}_e \rangle + \Delta\mathbf{p}_e$, $\mathbf{p}_g = \langle \mathbf{p}_g \rangle + \Delta\mathbf{p}_g$, and considering the isotropy of the spontaneous emission, the average momentums may be set equal to each other, $\langle \mathbf{p}_e \rangle = \langle \mathbf{p}_g \rangle$. The following equation holds:

$$\begin{aligned} \langle e^{i(\mathbf{p}_e - \mathbf{p}_g) \cdot \Delta\mathbf{r}_j / \hbar} \rangle &= \langle e^{i(\Delta\mathbf{p}_e - \Delta\mathbf{p}_g) \cdot \Delta\mathbf{r}_j / \hbar} \rangle \\ &\simeq \langle 1 + \frac{i\Delta\mathbf{p}_e \cdot \Delta\mathbf{r}_j}{\hbar} - \frac{(\Delta\mathbf{p}_e \cdot \Delta\mathbf{r}_j)^2}{2\hbar^2} \rangle \langle 1 - \frac{i\Delta\mathbf{p}_g \cdot \Delta\mathbf{r}_j}{\hbar} - \frac{(\Delta\mathbf{p}_g \cdot \Delta\mathbf{r}_j)^2}{2\hbar^2} \rangle \\ &\simeq e^{-\frac{1}{2}(\frac{\Delta\mathbf{p}_e \cdot \Delta\mathbf{r}_j}{\hbar})^2} \cdot e^{-\frac{1}{2}(\frac{\Delta\mathbf{p}_g \cdot \Delta\mathbf{r}_j}{\hbar})^2} = e^{-2\pi(\Delta\mathbf{r})^2/\lambda_B^2} \end{aligned} \quad (11)$$

where $\lambda_B = \sqrt{2\pi\hbar^2/mKT}$.

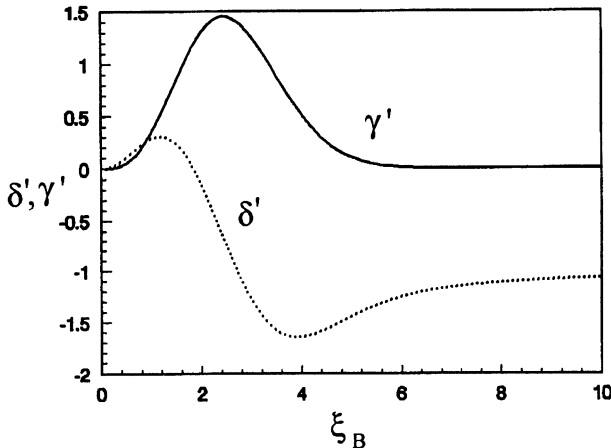


Fig. 1. The coefficients γ' , δ' versus ξ_B

Furthermore, assuming that there are $n = \rho 4\pi (\frac{\lambda}{\sqrt{2\pi}})^3$ atoms in the volume $\sqrt{\frac{2}{\pi}}\lambda^3$, then

$$\sum_{\Delta\mathbf{r}_j} \langle e^{i(\mathbf{p}_e - \mathbf{p}_g) \cdot \Delta\mathbf{r}_j / \hbar} \rangle L(\Delta\mathbf{r}_j) = \rho \int d^3 \Delta\mathbf{r} L(\Delta\mathbf{r}_j) e^{-2\pi(\Delta\mathbf{r})^2/\lambda_B^2}$$

$$= \gamma n \int_0^\infty \xi^2 d\xi \int_0^\pi \sin \theta d\theta e^{-\xi^2/\xi_B^2} [K(\xi) - iW(\xi)] = 2\gamma n(\gamma' + i\delta') \quad (12)$$

$$\frac{1}{2}\Gamma_e + i\Delta\omega = \frac{1}{2}\gamma + i\Delta\omega_s + \gamma n(\gamma' + i\delta') \quad (13)$$

Eq.(13) shows that the spontaneous linewidth and shift $\frac{1}{2}\Gamma_e + i\Delta\omega$ for N atom system is that $\frac{\gamma}{2} + i\Delta\omega_s$ for single atom plus the enhancement $2\gamma n(\gamma' + i\delta')$. The dependence of γ' , δ' on de-Broglie wavelength is depicted in Fig.1. As for the stimulated emission and absorption, we follow the well known Einstein's relation for the coefficients of thermal equilibrium radiation, i.e

$$\begin{aligned} B_{21} \frac{\hbar\omega_\lambda^3}{\pi^2 c^3} n_\lambda N_2 &= A_{21} n_\lambda N_2 = 2[\frac{1}{2}\gamma + i\Delta\omega_s + \gamma n(\gamma' + i\delta')] n_\lambda N_2, \\ B_{12} \frac{\hbar\omega_\lambda^3}{\pi^2 c^3} n_\lambda N_1 &= A_{21} n_\lambda N_1 = 2[\frac{1}{2}\gamma + i\Delta\omega_s + \gamma n(\gamma' + i\delta')] n_\lambda N_1, \end{aligned} \quad (14)$$

where N_1 , N_2 denote the number of atoms in the ground, excited states; n_λ is the average number of photons in mode λ .

Acknowledgment. This work was supported by the National Natural Science Foundation of China under Grant No.697778011.

References

1. J.J. Hope and C.M. Savage, Phys. Rev. A **54** (1996), 3177.
2. H.Huang, D.Z. Wang, L.Chang and Shi-qun Li, Phys. Rev. Lett. **79** (1997), 2923.
3. V.G. Weisskopf and E.Wigner, Phys., **63**, (1930) 54.
4. R.H. Lehmberg, Phys. Rev. A **2** (1970) 883.

The Small Phase Shift Measurement Using Frequency-Degenerated Twin Beams

Hai Wang, Yun Zhang, Xiaoying Li, Jing Jietai, Changde Xie,
Kunchi Peng

Institute of Opto-Electronics, Shanxi University,
Taiyuan, Shanxi, 030006, P. R. China
e-mail: chambers@paris-sud.fr

Abstract. This paper proposed a new method of small phase shift measurement using frequency-degenerated twin beams. The calculation with semi-classical theory shows: when the frequency degenerated twin beams generated by OPA is injected into M-Z interferometer, the small phase shift measurement beyond SNL can be realized. The minimum detectable phase shift is dependent on the average intensity, the quantum noise level of intensity difference between twin beams and the quantum efficiency of homodyne detection. If intensity difference fluctuation between the quantum correlated twin beams approaches to zero, the minimum detectable phase shift will approach to zero too.

1 Introduction

In a standard Mach-Zehnder interferometer, there is actually two input port, one is used as the entrance of input signal and other one usually is empty named “dark port” from which the vacuum noise enters. In this case, the measurement sensitivity of phase is limited by the Shot-Noise-Limit (SNL), that is[1]

$$\delta\phi = 1/\sqrt{N}$$

where N is the amount of photons of the input coherent light in the chosen detection time.

It was found that the SNL can be beaten by injecting the quadrature squeezed vacuum state lights into the “dark” port of interferometers and the sensitivity can be improved to[1] $\delta\phi = \delta\phi_{SNL}e^{-r}$ beyond $\delta\phi_{SNL}$ where r is the squeezing parameter.

The scientists around the world have been interested in exploring applications of twin beams on the sub-shot-noise measurements[2–5]. Based on the semi-classically theoretical analyses, we propose a scheme that quantum correlated twin beams from OPA can be used in sub-shot-noise measurements for small phase shift in Mach-Zehnder interferometers.

2 The principle of measurement

Figure 1 shows sketch of the interferometers measurement of phase shift. The correlation twin beams with orthogonal polarization and degenerate frequency $E_1(t)$ and $E_2(t)$ are generated from an optical nondegenerate parametric amplifier (OPA). The twin beams are injected into the input beam-splitter of interferometer. The field of $E_1(t), E_2(t)$ is written as:

$$E_i(t) = a_i(t) e^{-i\omega_i t - i\theta_i} + a_i^+(t) e^{i\omega_i t + i\theta_i} \quad (i = 1, 2) \quad (1)$$

where, $a_i(t)$, $a_i^+(t)$ are the annihilation and creation operators of $E_1(t)$ and $E_2(t)$. We have assumed that the field of $E_1(t), E_2(t)$ have the same frequency, that is

$$\omega_1 = \omega_2 = \omega \quad (2)$$

To performing the measurement conveniently, we make an initial phase difference of $\pi/2$ between $E_1(t)$ and $E_2(t)$ before entering the interferometer, that is

$$\phi_2 = \phi_1 + \pi/2 \quad (3)$$

For the twin beams, the field of $E_1(t), E_2(t)$ have the same average amplitude α :

$$\langle a_1(t) \rangle = \langle a_1^+(t) \rangle = \langle a_2(t) \rangle = \langle a_2^+(t) \rangle = \alpha \quad (4)$$

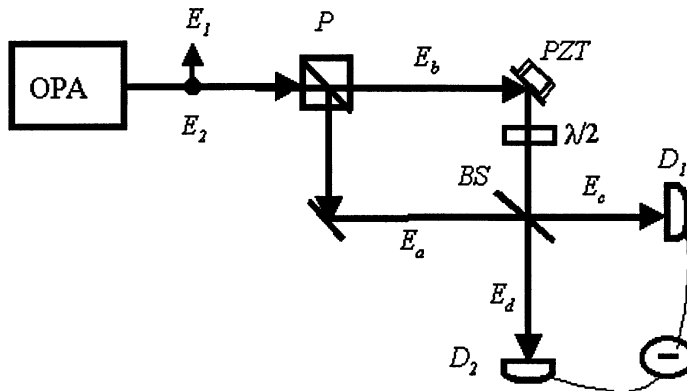


Fig. 1. The sketch of M-Z interferometer

and hence, the same average intensity,

$$\langle I_1(t) \rangle = \langle I_2(t) \rangle = \langle a_1^+(t)a_1(t) \rangle = \langle a_2^+(t)a_2(t) \rangle = \bar{I} = \alpha^2 = \bar{A}^2/4. \quad (5)$$

The M-Z interferometer includes one polarized beam splitter P, two high reflectors and one beam splitter BS with the reflectivity R=50%. The angle between the polarization orientations of P and the polarization of E_1 (or E_2) is 45^0 , so the field of $E_1(t)$, $E_2(t)$ are equally separated into two parts $E_a(t)$, $E_b(t)$ by polarizer P, the annihilation and creation operators of that are written as:

$$a_a(t) = \frac{a_1(t) + a_2(t)e^{-i\pi/2}}{\sqrt{2}}; a_b(t) = \frac{a_1(t) - a_2(t)e^{-i\pi/2}}{\sqrt{2}} \quad (6)$$

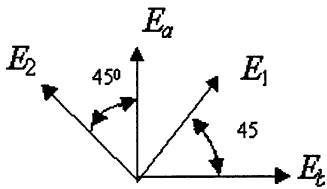


Fig. 2.

The light beam $E_a(t)$ is directly injected into BS and a half-wave plate is placed on the way of $E_b(t)$ before BS to make a polarization rotation of 90^0 and therefore the parallel polarization of $E_b(t)$ and $E_a(t)$ is obtain after BS.

The light beams $E_a(t)$ and $E_b(t)$ are recombined at the 50/50 beam splitter(BS). The annihilation and creation operators of output fields are written as :

$$a_c(t) = \frac{a_a(t) + a_b(t)}{\sqrt{2}} = e^{-i\theta/2}(a_1(t)\cos\frac{\theta}{2} - ia_2(t)e^{-i\pi/2}\sin\frac{\theta}{2}) \quad (7)$$

$$a_d(t) = \frac{a_a(t) - a_b(t)}{\sqrt{2}} = e^{-i\theta/2}(a_2(t)e^{-i\pi/2}\cos\frac{\theta}{2} - ia_1(t)\sin\frac{\theta}{2}) \quad (8)$$

The output fields $E_c(t)$ and $E_d(t)$ are injected into the detector $D1$ and $D2$. The measurement of phase shift q is accomplished by detecting the photocurrent difference between $D1$ and $D2$, that is directly proportional to the intensity difference between light field E_d and E_c

$$I_- = (a_2(t)a_2^+(t) - a_1(t)a_1^+(t))\cos\theta + (a_1(t)a_2^+(t) + a_2(t)a_1^+(t))\sin\theta \quad (9)$$

The average of intensity difference is

$$\langle I_- \rangle = \langle I_d - I_c \rangle = 2\alpha^2\theta \quad (10)$$

The photocurrent noise resulting from quantum fluctuation of light field limited measurement sensitivity. From eq.(7),the variance spectrum of photon number difference between the output fields

$$V(I_-) = \alpha^2 \left\langle |(\delta A_1(\omega) - \delta A_2(\omega))|^2 \right\rangle = 2\alpha^2 \left\langle |\delta r(\omega)|^2 \right\rangle \quad (11)$$

Where $\delta r(\omega)$ is the fluctuation spectrum of amplitude difference between twin beams in the frequency domain, ω is the analyzed noise frequency. To the intensity quantum correlated twin beams the noise power spectrum is less than the SNL:

$$\langle |\delta r(\omega)|^2 \rangle = R < 1 \quad (12)$$

The Signal-to-Noise Ratio(SNR) for phase shift measurement is

$$SNR = \frac{\langle I_- \rangle}{\sqrt{V(I_-)}} = \frac{\theta}{\sqrt{RN}} \quad (13)$$

Where $N = 2\alpha^2$ is the average photons numbers of twin beams. When $SNR = 1$, we get the minimum detectable phase shift:

$$\theta_{\min} = \sqrt{RN}^{-1/2} = \sqrt{R}\theta_{SNL} \quad (14)$$

Where $\theta_{SNL} = N^{-1/2}$ is the shot noise limit for measurement of phase shift.

It is obvious that the minimum detectable phase shift due to using quantum correlated twin beams is reduce a factor \sqrt{R} . For a perfect quantum correlated twin beams $R \rightarrow 0$, therefore $\theta_{\min} \rightarrow 0$ too. The lower the intensity difference fluctuation between twin beams, the higher the sensitivity of measurement.

Acknowledgments. Project supported by the National Nature Science Foundation of China (No.19974021). the Youth Science Foundation of Shanxi Province (No. 981003)

References

1. D. F. Walls, Quantum optics, Spring-verlag, p173 (1994)
2. C. D. Nabors, R. M. Shelby , Phys. Rev. A **42**, 556 (1990)
3. P. R. Tapster , S. F. Seward , J. G. Rarity , Phys. Rev. A **44**, 3266 (1991)
4. J. J. Snyder, E. Gicobino, C. Fabre, J.Opt.Soc.Am., B **7**, 2132 (1990)
5. Hai Wang, Qing Pan, Yun Zhang, Chengyang Xue, Changde Xie, Kunchi Peng, Science in China, A **41**(5), 534-540 (1998)

Quantum Nondemolition Measurements in Degenerate Optical Parametric Oscillator

Wang Kaige, Wang Danling, Yang Guojian

Department of Physics, Beijing Normal University, Beijing 100875, China
e-mail: wangkg@sun.ihep.ac.cn

Abstract. We study the degenerate optical parametric oscillator as a quantum non-demolition (QND) measurement device. We find that in the resonant case, this model can perform a perfect QND measurement at the threshold. In the detuning case, the optimum QND measurement occurs at the nonlinear double resonances.

1 Introduction

In recent years, quantum nondemolition (QND) measurement schemes in optical systems are proposed and developed [1]. It usually involves the coupling of two field modes: one "signal" mode to be measured and one "meter" mode to be directly detected. A QND measurement is performed in such a way that the noise introduced by the measurement does not couple back to measured observable. The coupling can be supplied by a nonlinear medium. The crossed Kerr-type dispersive medium which is $\chi^{(3)}$ nonlinearity provides a favorable QND coupling scheme between two optical modes[2-5]. The QND schemes are also considered in $\chi^{(2)}$ nonlinear medium [6-11]. It has reported that the degenerate optical parametric amplifier (DOPA) can perform QND measurements [8]. In the OPA model, both the signal and the meter couple through the same cavity mode which is actually not excited by the pump field, that is, it works below the threshold.

In this paper, we consider a degenerate optical parametric oscillator (DOPO) as a QND device. There are two main differences between this model and the previous OPA [8]. First, we use the single ended cavity instead of the double ended one. Second, we consider the stationary operation above the threshold, so there are two cavity modes instead of one. Because the model works above the threshold, the semiclassical expectations are much larger than the fluctuations. Therefore the linear approximation theory can be applied. However, the scheme can be considered as a continuous wave operation.

2 Description of DOPO model

We consider a DOPO model, the Hamiltonian in the interaction picture is[12]

$$H = \hbar[\sum_{j=1}^2 \kappa_j \Delta_j a_j^\dagger a_j + (ig/2)(a_1^\dagger a_2 - a_1^2 a_2^\dagger) + i(\varepsilon_2 a_2^\dagger - \varepsilon_2^* a_2)], \quad (1)$$

where the detuning parameters are $\Delta_1 = (\omega_1 - \omega_0)/\kappa_1$ and $\Delta_2 = (\omega_2 - 2\omega_0)/\kappa_2$. a_j and a_j^\dagger are the field operators for the cavity mode j at the frequency ω_j ($\omega_2 \approx 2\omega_1$). ε_2 is the amplitude for the coherent driving field at the frequency $2\omega_0$. g is the nonlinear coupling constant. κ_j is the cavity decay rate for mode j .

We define the normalized variables

$$A_1 \equiv |A_1|e^{i\phi_1} = g \langle a_1 \rangle / \sqrt{2\kappa_1\kappa_2}, A_2 \equiv |A_2|e^{i\phi_2} = g \langle a_2 \rangle / \kappa_1, \quad (2)$$

$$E_2 = g\varepsilon_2 / (\kappa_1\kappa_2), \quad \tau = \kappa_1 t, \quad \kappa = \kappa_2 / \kappa_1,$$

the semiclassical equations read

$$\begin{aligned} (d/d\tau)A_1 &= -(1 + i\Delta_1)A_1 + A_1^*A_2, \\ (d/d\tau)A_2 &= \kappa[E_2 - (1 + i\Delta_2)A_2 - A_1^2]. \end{aligned} \quad (3)$$

where E_2 is real positive as definiteness. The exact steady-state solution above the threshold has been shown in [12]. In the resonant case, $\Delta_1 = \Delta_2 = 0$, the stationary solution is as simple as $A_1 = \sqrt{E_2 - 1}$ and $A_2 = 1$. When $\Delta_1\Delta_2 > 1$, there is bistability between the trivial stationary solution and the nontrivial one. It has proved that in this case the solutions are stable [12].

We assume the single-ended port in the model. The boundary condition for the input and the output fields at the port is

$$E_j^{out} + E_j^{in} = 2A_j \quad (j = 1, 2). \quad (4)$$

In the DOPO model, $E_1^{in} = 0$, so the phase of the first output beam ϕ_1^{out} is always the same as ϕ_1 , that is, there is no phase shift between the internal and the output for beam 1. The phase of the second output beam can be derived from Eq. (4) and the steady-state equation

$$\begin{aligned} \exp(i\phi_2^{out}) &= \arg[(1 - i\Delta_2)A_2 - A_1^2] \\ &= \exp(i\phi_2) \times \arg[|A_2|^2 - |A_1|^2 + i(\Delta_1|A_1|^2 - \Delta_2|A_2|^2)]. \end{aligned} \quad (5)$$

On the other hand, the phase of the second cavity mode can be written as

$$\exp(i\phi_2) = E_2 \cdot [|A_2|^2 + |A_1|^2 + i(\Delta_1|A_1|^2 - \Delta_2|A_2|^2)] / |A_2 E_2^2|. \quad (6)$$

Therefore, when the condition

$$\Delta_1|A_1|^2 = \Delta_2|A_2|^2 \quad (7)$$

is satisfied, the phase shift for the second beam vanishes among the input, the internal and the output. As a matter of fact, this condition becomes the one for the nonlinear double resonance (NDR). According to the NDR condition (7), two detunings must have the same sign. At the input field $E_2 = (1 + \Delta_2/\Delta_1)\sqrt{1 + \Delta_1^2}$, the NDR stationary solution appears as

$$|A_1| = \sqrt{\Delta_1\Delta_2 + \Delta_2/\Delta_1}, e^{2i\phi_1} = (1 - i\Delta_1) / \sqrt{1 + \Delta_1^2}, A_2 = \sqrt{1 + \Delta_1^2}. \quad (8)$$

We will show that the NDR operation is very important for QND measurement.

3 QND performance

The QND performance can be evaluated by three criteria, which are normalized quantum correlations between the input and the output fluctuations [3,13]. Let $\delta a_j \equiv a_j - \langle a_j \rangle$ be the fluctuation operator, the Hermitian quadrature operator is $x_j = [\delta a_j \exp(-i\theta_j) + h.c.]/2$, where θ_j is the quadrature phase of the fluctuation. It is also applied to the input and the output fields. We assume the beam 1 is the meter and the beam 2 the signal, the three correlation coefficients which characterize the QND measurement are $C_1^2 \equiv C^2(x_2^{in}, x_1^{out})$, $C_2^2 \equiv C^2(x_2^{in}, x_2^{out})$, and $C_3^2 \equiv C^2(x_2^{out}, x_1^{out})$. C_1^2 and C_2^2 , as the first two criteria characterize respectively the effectiveness and non-demolition of the measurement. The third criterion is conditional variance of the signal field given the result of a measurement on the meter field. It characterizes the quantum state preparation (QSP) properties of the system, and can be expressed as $V_c(x_2^{out}|x_1^{out}) = V(x_2^{out})(1 - C_3^2)$. To be specific, the two inequalities, $C_1^2 + C_2^2 > 1$ and $V_c < 1$ (shot noise level), are introduced as violation of classical limits of measurement. For a perfect QND measurement $C_1^2 = C_2^2 = 1$ and $V_c(x_2^{out}|x_1^{out}) = 0$. In a linearized treatment of quantum fluctuations, all the three criteria can be calculated by the linear drift and diffusion matrices of the system [5].

For an optimum QND, one has to search the operating parameters and choose the appropriate quadrature phase of the fluctuations. The phase difference between the fluctuation and the expectation is defined for both the input and output fields $\Delta\theta_j = \theta_j - \phi_j$. $\Delta\theta_j = 0$ ($\pm\pi/2$) stands for the amplitude quadrature (phase quadrature). In the following, we will show the stationary working region where the optimum QND measurement can be performed.

(i) the resonant case ($\Delta_1 = \Delta_2 = 0$)

When the phase quadratures (either $\pi/2$ or $-\pi/2$) are chosen for both the meter and the signal, the three criteria at the zero frequency are derived as

$$C_1^2 = \frac{2}{|A_1|^2 + 2}, \quad C_2^2 = \frac{(|A_1|^2 - 1)^2}{|A_1|^4 + 1}, \quad V_c = \frac{|A_1|^2}{|A_1|^2 + 2}. \quad (9)$$

The corresponding squeezings for both the meter and the signal are

$$V_1 = \frac{|A_1|^2(|A_1|^2 + 2)}{(|A_1|^2 + 1)^2}, \quad V_2 = \frac{|A_1|^4 + 1}{(|A_1|^2 + 1)^2}, \quad (10)$$

where the shot noise level is 1. Figures 1a and 1b show respectively the criteria and the squeezings as functions of the meter intensity. A perfect QND performance appears at the threshold, and there is no QND effect far away from the threshold. The effectiveness of the measurement evaluated by C_1^2 is related to the squeezing of the meter, because the noise introduced in the measurement has to be evaded in the conjugate quadrature of the meter. However, the squeezing of the signal will degrade signal itself, and, therefore, demolish the measurement. In Fig. 1 it also shows that when the noise level

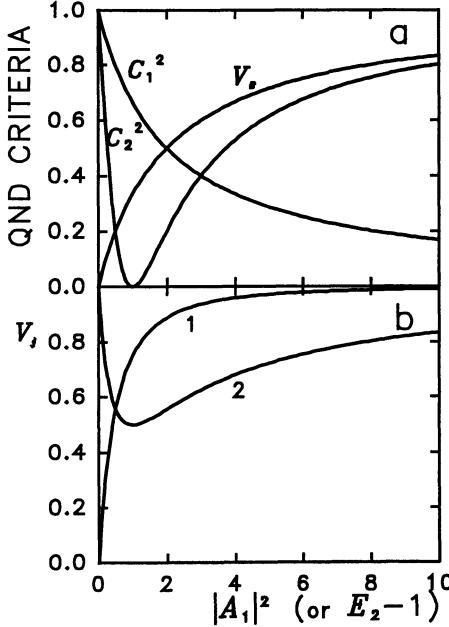


Fig. 1. In the resonant case, $\Delta_1 = \Delta_2 = 0$, (a) QND criteria and (b) squeezings of two modes at the zero frequency as functions of the intensity of mode 1. Phase quadratures are taken for both the meter and signal fluctuations

of the signal has to stay unchanged at the shot noise level as the input, the non-demolition is greatly improved.

(ii) the detuning case

In the detuning case, we focus on the two special steady-states: the down-transition of the bistability and the NDR at which there are no phase shifts in the transmission for two beams. We find that the amplitude quadratures of the meter and the signal are favorite for QND. At the zero frequency, three criteria can be analytically expressed by the detuning parameters as following: at the down-transition of the bistability ($\Delta_1\Delta_2 > 1$)

$$\begin{aligned} C_1^2 = C_2^2 &= \frac{2(\Delta_1\Delta_2 - 1)}{\Delta_2^2 + 2\Delta_1\Delta_2 - 1}, \\ V_c &= \frac{(\Delta_1 + \Delta_2)^2(1 + \Delta_2^2)}{(\Delta_2^2 + 2\Delta_1\Delta_2 - 1)[(\Delta_1 - \Delta_2)^2 + 4]}, \end{aligned} \quad (11)$$

and at the NDR

$$\begin{aligned} C_1^2 &= \frac{2\Delta_1\Delta_2(1 + \Delta_1^2)}{\Delta_1^2 + 2\Delta_1^3\Delta_2 + \Delta_2^2}, \\ C_2^2 &= \frac{\Delta_2(1 + \Delta_1^2)}{2\Delta_1 + \Delta_2 + \Delta_1^2\Delta_2}, \\ V_c &= \frac{(\Delta_1 + \Delta_2)^2}{\Delta_1^2 + 2\Delta_1^3\Delta_2 + \Delta_2^2}. \end{aligned} \quad (12)$$

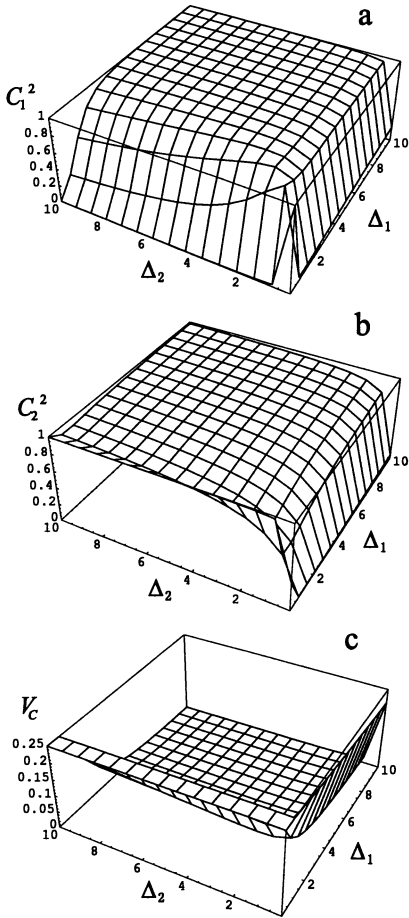


Fig. 2. At NDR, QND criteria at the zero-frequency: (a) C_1^2 , (b) C_2^2 and (c) V_c as functions of parameters Δ_1 and Δ_2 . Amplitude quadratures are taken for both the meter and signal fluctuations

Figure 2 shows 3D-plots of three QND criteria versus two detuning parameters for NDR. Obviously, at the NDR operation, the optimum QND performance can be realized in a large area of the parameter space.

By considering favorite QND for both the down-transition and the NDR, we may set the detunings $\Delta_1 = 10$ and $\Delta_2 = 2$. A comparison between the dynamical features and QND effect is plotted in Fig. 3. In Fig. 3, it shows that at the transition point of bistability (indicated by point P where $C_1^2 = C_2^2$) it has a good QND performance and at the NDR steady-state (indicated by the arrows) the QND measurement reaches the best.

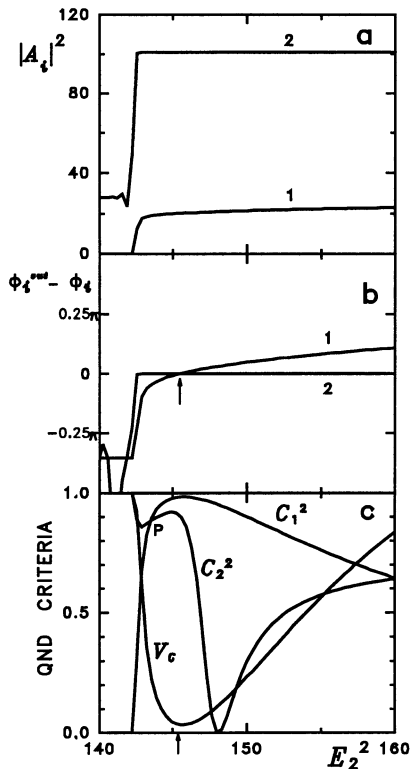


Fig. 3. At $\Delta_1 = 10$ and $\Delta_2 = 2$, (a) stationary intensities, (b) phase differences between the output and the intracavity beams, and (c) QND criteria as functions of the input intensity. Amplitudes quadratures are taken for both the meter and the signal fluctuations

4 Conclusion

We have studied the DOPO model as a QND measurement device. We have found that in the resonant case, this model can perform a perfect QND measurement at the threshold. In comparison with the double-ended OPA model [8], a highly reflecting mirror for the signal port and a highly transmitting mirror for the meter port are not necessary. In the detuning case, the optimum QND measurement occurs at the nonlinear double resonances. This result is consistent with the crossed Kerr-type dispersive model.

Acknowledgment. This research was supported by National Natural Science Foundation of China under Projects No. 19774013.

References

1. See review article, P. Grangier, J. A. Levenson, J-P Poizat: *Nature* **396**, 537-542 (1998)
2. P. Grangier, J.F. Roch, and S. Reynaud: *Opt. Commun.* **72**, 387-391 (1989)
3. C. A. Blockley and D. F. Walls, *Opt. Commun.* **79**, 241-250 (1990)
4. P. Grangier, J.-Ph. Poizat, P. Grelu, F. Castelli, L. A. Lugiato, A. Sinatra: *J. Mod. Opt.* **41**, 2241-2257 (1994)
5. Wang Kaige, Yang Guojian: *Commun. Theor. Phys.* **31**, 347-354 (1999)
6. A. La Porta, R. E. Slusher, B. Yurke: *Phys. Rev. Lett.* **62**, 28-31 (1989)
7. M. Dance, M. J. Collett, D. F. Walls: *Phys. Rev. Lett.* **66**, 1115-1118 (1991)
8. P. Smith, M. J. Collett, D. Walls: *Opt. Commun.* **102**, 105-110 (1993)
9. S. F. Pereira, Z. Y. Ou, H. J. Kimble: *Phys. Rev. Lett.* **72**, 214-217 (1994)
10. K. Bencheikh, J. A. Levenson, Ph. Grangier, O. Lopez, *Phys. Rev. Lett.* **75**, 3422-3425 (1995)
11. R. Bruckmeier, H. Hansen, S. Schiller, *Phys. Rev. Lett.* **79**, 1463-1466 (1997)
12. C. Fabre, E. Giacobino, A. Heidmann, L. Lugiato, S. Reynaud, M. Vadacchino, Wang Kaige, *Quantum Opt.* **2**, 159-187 (1990)
13. M. J. Holland, M. J. Collett, D. F. Walls, *Phys. Rev. A* **42**, 2995-3005 (1990)

Production of Subfemtosecond Pulses Directly through High-order Harmonic Generation

Yingsong Wang and Zhizhan Xu

Laboratory for High Intensity Optics, Shanghai Institute of Optics and Fine Mechanics, P. O. Box 800-211, Shanghai 201800, China

Abstract. Pulses as short as 330 attoseconds generated directly through high-order harmonic generation (HHG) by 785nm driving laser field, without the complicated control of some laser parameters involved in other proposals, is theoretically demonstrated.

High-order harmonics are generated when an atom is irradiated with super-intense laser pulses, which has been attracting much attention in the recent years [1]. HHG paves the way to generate subfemtosecond pulses, while it is a new promising source of coherent XUV and soft X-ray radiation. There have been several proposals to generate subfemtosecond pulses through HHG [2-5]. The impressive manipulation of the driving field or the harmonic signals is needed for the production of the subfemtosecond pulse by these proposals, e.g., the precise control of the time-dependent of the ellipticity of the driving laser pulses [2,3] and the difficult realization of the phase-locking of the harmonics in the plateau regime [4,5]. In addition, there is another type of proposals to produce subfemtosecond pulses through HHG, which is to generate very short harmonic pulse using very short fundamental pulse ($< 25\text{ fs}$) [6-7]. Very recently, Kien *et al* theoretically showed that attosecond pulse could be generated using high harmonics by the driver pulse in the multicycle regime [8]. By means of numerical experiments, we found that the production of subfemtosecond pulse could be realized by HHG if only the driver pulses have a rapid temporal variation and sufficient high intensity, and there was no limit of the width of the driver pulses.

For given atoms and laser pulses, the intensity of harmonic emission of the laser interaction with the ionized atoms is several orders lower than that with neutral ones, and could be relatively neglected [9]. During the interaction of the laser pulse with an atom, the neutral atoms are mainly depleted before the advent of the peak of the pulse, only if the intensity of the laser pulse is strong enough. This requirement could be readily satisfied technologically. Therefore, the harmonic emission from neutral atoms are mainly generated in the leading edge of the laser pulse. If the leading edge of the pulse can be steepen to very short interval, an ultrashort pulse or a train of short pulse composed of harmonic radiation can be obtained. In the present paper, the process of generation of subfemtosecond pulses directly through HHG is investigated.

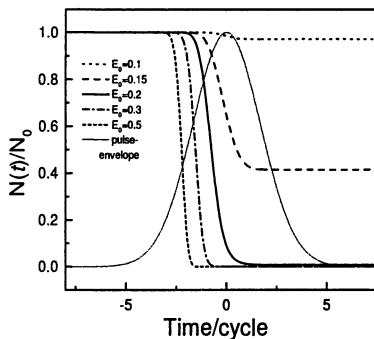


Fig. 1. The time-dependent varying density of the neutral argon atoms at different laser intensity.

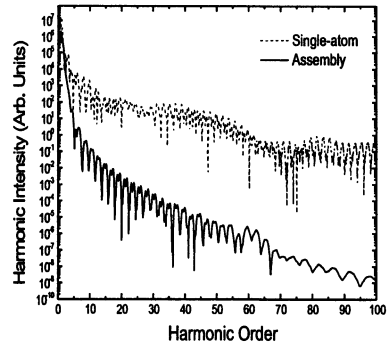


Fig. 2. The harmonic spectra of argon atoms at $E_0 = 0.5$ a.u.: the single atom response (dashed) and the assembly one(solid).

The depletion of the neutral atoms is the main effect during the generation of the subfemtosecond harmonic pulses by the method we proposed. First of all, we will calculate the time-dependent depletion of the medium at different driving laser intensities for illustration. The ionization of an atom in an intense laser field is usually classified into two regimes by Keldysh parameter, $\gamma = \sqrt{I_p/2U_p}$, where I_p is the ionization potential of the atoms concerned and U_p is the ponderomotive potential. For a given atom and a laser frequency, the atom is ionized through multiphoton ionization in the intensity region of $\gamma > 1$ and through the tunneling in the region of $\gamma < 1$. In the present paper, we take argon atom as an example for our illustration, and the interaction between argon atom and Ti:sapphire laser ($\lambda = 785nm$) pulses is considered. The atomic units are used through our calculation, unless otherwise specified. The time profile of the linearly polarized laser pulse $E(t)$ is assumed to be Gaussian with a full width at half maximum (FWHM) of 4 optical cycles. The intensity of 0.1au gives $\gamma < 1$, for neutral argon atom. We take the ionization effect of the medium into account using ADK model[10]. The time-dependent normalized densities of neutral argon atoms at different peak laser intensities are shown in Fig. 1, $N(t)$ and N_0 are the neutral and initial atoms density respectively. E_0 is the peak electric strength. When $E_0 > 0.2$ a.u., almost all of the neutral atoms are ionized before the advent of the peak intensity. Besides, the intensity of harmonic emission from ions is much lower than that from neutral ones. Thus, the harmonic emission from neutral argon atoms could be concentrated into a very small time interval, leading to the production of coherent ultrashort pulses. The ultrashort here means that the harmonic pulses generated could be as short as less than one period of the driving laser.

The high-order harmonic spectra could be obtained with the single-active-electron approximation [11] by Fourier transforming the dipole moment $D(t)$,

and $D(t)$ may be obtained by numerically integrating the one-dimensional time-dependent Schrödinger equation:

$$i\frac{\partial}{\partial t}\psi(x, t) = \left(-\frac{1}{2}\frac{\partial^2}{\partial x^2} + V(x) + xE(t)\right)\psi(x, t). \quad (1)$$

The high-order harmonic spectra of argon at $E_0 = 0.5a.u.$ are shown in Fig. 2. The single-atom response is obtained by Fourier transforming $D(t)$, and the assembly one is by Fourier transforming $D(t)N(t)/N_0$. The intensity of the two harmonic spectra should not be compared directly, since the assembly response is normalized to one atom. The propagation effect are neglected when we obtain the assembly harmonic spectrum. At $E_0 = 0.5a.u.$, harmonic order beyond 100 could be generated in the view of a single atom. However, when the depletion of the neutral atoms is taken into account, the maximum harmonic order with considerable intensity is not larger than 70. And the assembly spectral width of the harmonics is very wide compared with the single-atom response, that is to say, ultrashort harmonic pulse are actually generated. To illustrate this point, the harmonic signal due to the assembly response is examined by the time-frequency analysis method [12], as shown in Fig. 3.

When $E_0 = 0.1a.u.$, all of the pulses at different harmonic order cover more than two optical cycle of the driving laser. This could be attributed to the inefficient depletion of the neutral atoms. Even for this case, however, the harmonic radiation in the plateau or cut-off regime is a train of ultrashort pulses, and all of these pulses are much less than one cycle. For the case of $E_0 = 0.3a.u.$, there is one pulse emerging whose duration is $\sim 200as$ (attosecond, $1as = 10^{-3}fs = 10^{-18}s$), much higher than the others. The duration of this pulse is short down to about 1/10 of the cycle of the driving field, corresponding to $\sim 250as$. At $E_0 = 0.5a.u.$, for the most of the neutral medium are depleted long before the advent of the peak of the driving pulse, the harmonic radiation is mainly concentrated in one cycle. The harmonic pulse are mainly composed by two separated ones whose durations of is both about $330as$ also, and the duration of the whole pulse is half an optical cycle of the driving field. When the signals of given harmonic orders could be filtered out from the whole harmonic radiation, a single subfemtosecond pulse or a train of these is then obtained. Successfully selecting the harmonic radiation at given frequency will be a prerequisite for the stable production of subfemtosecond pulses.

In conclusion, the subfemtosecond pulses could be produced directly by the high-order harmonic generation, if the peak intensity of the driving field is high enough, without the complicated manipulation of the harmonic radiation. An efficient method for selection of the radiation at a specific frequency is the prerequisite.

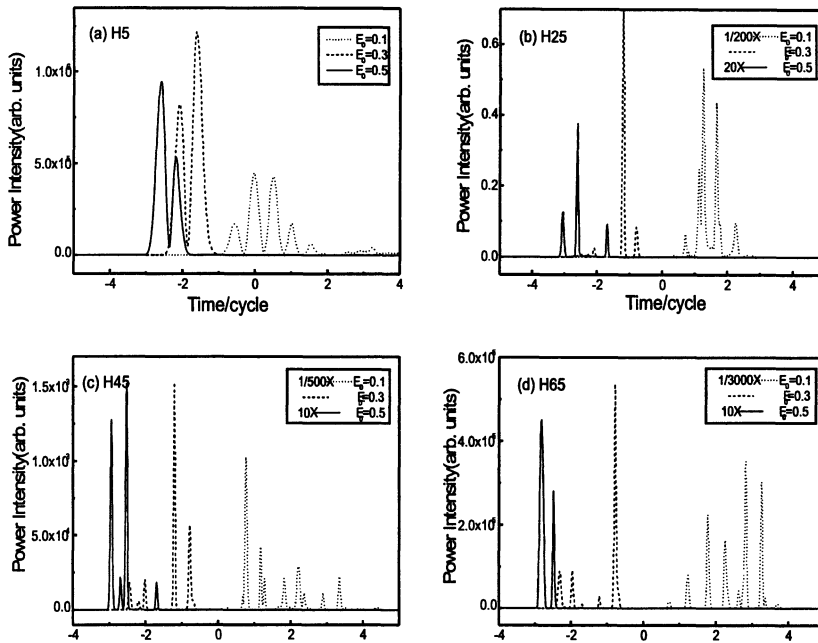


Fig. 3. The time profile of different harmonics using driving laser pulses with different peak intensities, and the harmonic order is (a) 5, (b) 25, (c) 45 and (d) 65, respectively.

References

1. M. Protopapas, C. H. Keitel and P. L. Knight(1997), atomic physics with super-high intensity lasers, *Rep. Prog. Phys.* **60**, 389-486
2. Ph. Antoine, *et al.*(1997), Generation of attosecond pulses in macroscopic media, *Phys. Rev. A* **56**, 4960-4969
3. M. Yu, *et al.*(1995), Routes to control of intense-field atomic polarizability, *Phys. Rev. Lett.* **74**, 2933-2936
4. G. Farkas and C. Toth (1992), Proposal for attoscond light pulses generation using laser induced multiple-harmonic conversion process in rare gases, *Phys. Lett. A* **168**, 447-450; S. E. Harris, J. J. Macklin, and T. W. Hansch(1993), Atomic scal tempral structure inherent to high-order harmonic generation, *Opt. Commun.* **100**, 487-490
5. Ph. Antoine, A. L'Huillier, and M. Lewenstein(1996), Attosecond pulses trains using high-order harmonics, *Phys. Rev. Lett.* **77**, 1234-1237
6. K. J. Schafer and K. C. Kulander(1997), High harmonics from ultrafast pump lasers, *Phys. Rev. Lett.* **78**, 638-641
7. I. P. Christov, M. M. Murnane, and H. C. Kapteyn(1997),High-harmonic generation of attosecond pulses in the "single-cycle" regime, *Phys. Rev. Lett.* **78**, 1251-1254

8. F. Le Kien, K. Midorikawa, and A. Suda(1998), Attosecond pulses generation in the multicycle regime of the driver pulse, Phys. Rev. A **58**: 3311-3319
9. S. G. Preston, *et al.*(1996), High-order harmonics of 248.6nm KrF laser from helium and neon ions, Phys. Rev. A **53**, R31-34
10. M. V. Ammosov, N. B. Delone, and V. P. Kranov(1986), Tunnel ionization of complex atoms of atomic ions in an alternating electromagnetic field, Sov. Phys. JETP **64**, 1191-1194
11. J. L. Krause, K. J. Schafer, and K. C. Kulander(1992), High-order harmonic generation from atoms and ions in the high intensity regime, Phys. Rev. Lett. **68**, 3535-3538
12. Ph. Antoine, *et al.*(1995), Time profiles of harmonics generated by a single atom in a strong electromagnetic field, Phys. Rev. A **51**, R1750-1753

Spontaneous Emission from a Driven Atom Embedded in a Photonic Crystal

Shuangyuan Xie¹, Yaping Yang^{1,2}, Hong Chen¹, Shi-Yao Zhu², Xiang Wu¹

¹ Department of Physics, Tongji University, Shanghai 200092, China

² Department of Physics, Hong Kong Baptist University, HongKong

Abstract. We studied the properties of the spontaneous emission from a three-level atom embedded in photonic crystals with a double-photon external-driving field. As a result of quantum interference and photon localization, the populations in the upper levels display oscillatory or complete decay behavior, which depends on the initial atomic state and the relative position of the two upper levels from the forbidden gap. The external-driving field can also affect the spontaneous emission.

1 Introduction

Photonic crystal is a periodic dielectric structure with the existence of full photonic band gaps(PBG), in which the electromagnetic field propagation is classically forbidden [1-3]. Recently, many efforts have been concentrated on the spontaneous emission from an excited atom embedded in photonic crystals [4-7] because of the novel features of photonic crystals. In present paper, we consider the spontaneous emission from a three-level atom embedded in photonic crystals with a driving field. We found the populations in the upper levels display oscillatory or complete decay behavior. The intensity and the phase of the external driving field can also affect the spontaneous emission.

2 Basic theory

The system depicted in Fig. 1 consists of a three-level atom. The upper levels $|a_1\rangle, |a_2\rangle$ are coupled by the same vacuum modes to the lower level $|a_3\rangle$. The frequency differences between levels $|a_1\rangle, |a_2\rangle$ and $|a_3\rangle$ are, respectively, ω_1 and ω_2 , which are assumed to be near the band edge, and the energy of the lower level is set to be zero. The Hamiltonian for the system, after carrying out the rotating wave approximation(RWA), is

$$\begin{aligned}\hat{H} = & \sum_{j=1,2} \hbar\omega_j |a_j\rangle\langle a_j| + \sum_k \hbar\omega_k b_k^\dagger b_k + i\hbar\Omega^2 [e^{2i(\phi+\nu t)} |a_2\rangle\langle a_1| - H.c.] \\ & + i\hbar \sum_k [g_k^{(1)} b_k^\dagger |a_3\rangle\langle a_1| + g_k^{(2)} b_k^\dagger |a_3\rangle\langle a_2| - H.c.].\end{aligned}\quad (1)$$

where $b_k(b_k^\dagger)$ is the annihilation(creation) operator for the k th vacuum mode with frequency ω_k , and $g_k^{(1,2)}$ are the coupling constants between the k th

mode and the atomic transitions from $|a_1\rangle$, $|a_2\rangle$ to $|a_3\rangle$. The Rabi frequency Ω corresponds to the transition from $|a_2\rangle$ to $|a_1\rangle$, and ϕ, ν represent the phase and frequency of the driving field. The dispersion relation near the PBG edge can be approximated as [3,4] $\omega_k = \omega_c + \frac{\omega_\phi}{k_0^2}(k - k_0)^2$, where ω_c is the cut-off frequency of the band edge. The state vector at arbitrary time t is

$$|\Psi(t)\rangle = \sum_{j=1,2} [A_j(t)e^{-i\omega_j t}|a_j\rangle|0\rangle_f] + \sum_k B_k(t)e^{-i\omega_k t}|a_3\rangle|1_k\rangle_f. \quad (2)$$

where $|0\rangle_f$ and $|1_k\rangle_f$ describes the state vectors corresponding to no photons in reservoir modes and a single photon in k th mode. The dipole vectors between $|a_1\rangle$ and $|a_3\rangle$ and between $|a_2\rangle$ and $|a_3\rangle$ are orthogonal. Here real $g_k^{(1,2)}$ and $2\nu = \omega_1 - \omega_2$ are assumed. We assume the atom is initially excited, i.e., $|A_1(0)|^2 + |A_2(0)|^2 = 1$ and $B_k(0) = 0$. Using Schrödinger equation and with the help of Laplace transform, we get

$$A_1(t) = \sum_j \frac{f_{11}(x_j^{(11)})}{G'_{11}(x_j^{(11)})} e^{x_j^{(11)}t} + \sum_{n=1}^2 \left[\sum_j \frac{f_{1n}(x_j^{(n2)})}{G'_{2n}(x_j^{(n2)})} e^{x_j^{(n2)}t} \right] + R_1(t), \quad (3a)$$

$$A_2(t) = \sum_j \frac{f_{21}(x_j^{(11)})}{G'_{11}(x_j^{(11)})} e^{x_j^{(11)}t} + \sum_{n=1}^2 \left[\sum_j \frac{f_{22}(x_j^{(n2)})}{G'_{2n}(x_j^{(n2)})} e^{x_j^{(n2)}t} \right] + R_2(t). \quad (3b)$$

Where $R_{1,2}(t)$ describe the branch cut contribution and tend to zero as $t \rightarrow \infty$. We defined $\beta = \frac{(\omega_i d_i)^2 k_0^3}{6\pi\epsilon_0\hbar\omega_c^{3/2}}$, $\omega_{1c} = \omega_i - \omega_c$, ($i = 1, 2$) and the functions

$$f_{1m}(x) = K_2^m A_1(0) - \Omega^2 e^{-2i\phi} A_2(0),$$

$$f_{2m}(x) = K_1^m A_2(0) + \Omega^2 e^{2i\phi} A_1(0),$$

$$G_{ml}(x) = K_1^m K_2^n + \Omega^4.$$

where $K_j^1 = (x - \frac{i\beta^{3/2}}{\sqrt{-ix - \omega_{jc}}})$ and $K_j^2 = (x + \frac{\beta^{3/2}}{\sqrt{ix + \omega_{jc}}})$, and $x_j^{(lm)}$ are the roots of the equation $G_{ml}(x) = 0$. Here $x_j^{(11)}$ are all imaginary roots, and $x_j^{(12,22)}$ are all complex roots. The characteristics of the roots depend on the relative position of the two upper levels from the band edge and Ω , and directly related to the populations in the upper levels. It is easy to verify that there is only one imaginary root if $\omega_{1c} \geq \frac{\beta^{3/2}}{\sqrt{\omega_{12}}}$, and there are two imaginary roots if $\omega_{1c} < \frac{\beta^{3/2}}{\sqrt{\omega_{12}}}$.

3 The properties of the population

If the imaginary part of the root is b , the corresponding dressed states splitting from $|a_i\rangle$ are at the frequency $\omega_i - b$ ($i = 1, 2$). The two upper levels split respectively into its own dressed states caused by the interaction between the

atom and its own radiation field. The amount of the dressed states of each upper level are consistent because the splitting is the combined effect of the vacuum Rabi splitting and the Autler-Townes splitting by the external field.

The spontaneous emission is greatly influenced by the external field. This can be observed by examining the populations in the two upper levels, which can be obtained from $P_{1,2}(t) = |A_{1,2}(t)|^2$ and the total population is $P(t) = P_1(t) + P_2(t)$. When $t \rightarrow \infty$, only the first terms in Eqs. (3a) and (3b) remain dominant, and the other terms decay with time and can be neglected. The populations $P_{1,2}$ and P tend to constants $P_{10,20}$ and P_0 .

When $\omega_{1c} \geq \frac{\beta^{3/2}}{\sqrt{\omega_{12}}}$, there is only one imaginary root $i\beta$ yielding one dressed states without decay, and

$$P_{10} \propto [M_i^2 A_1^2(0) + \Omega^4 A_2^2(0) + 2M_i\Omega^2 A_1(0)A_2(0)\sin(2\phi)].$$

where $M_1 = b_1 - \frac{\beta^{3/2}}{\sqrt{b_1 - \omega_{2c}}}$ and $M_2 = b_1 - \frac{\beta^{3/2}}{\sqrt{b_1 - \omega_{1c}}}$. Clearly, the population is dependent on the external field and the initial atomic state. When the initial state is $A_1(0) = 0$ or $A_2(0) = 0$, the population is independent of ϕ , and only Ω can control it. If the initial state is a coherent superposition of the two upper levels, the population can be controlled by changing ϕ and Ω . As a result, a phase-sensitive, optical memory device can be produced because the population keeps the memory of the intensity and the phase of the external field. When $\phi = \pi/4$, The external field can lead to the populations $P_{10,20} = 0$ when $\frac{A_1(0)}{A_2(0)} = -\frac{\Omega^2}{M_1}$. The populations in the two upper levels can be both equal to zero, which means a complete decay of the upper levels and the population will stay in the lower level forever(see Fig. 1). The spontaneous emission can be totally suppressed by the driving field.

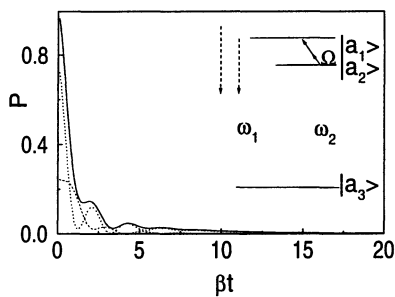


Fig. 1. Atomic population on the upper levels $P_1(t)$ (dashed curve), $P_2(t)$ (dotted curve) and $P(t)$ (solid curve) as a function of the scaled time βt . Here $\Omega^2/\beta = 1$, $\phi = \pi/4$, $\omega_{12}/\beta = 1$, $\omega_{1c}/\beta = 2.4$, $|\Phi(0)\rangle = 0.4991|a_1\rangle - 0.8665|a_2\rangle$. The scheme of the three-level atom is shown in the inset.

When $\omega_{1c} < \frac{\beta^{3/2}}{\sqrt{\omega_{12}}}$, there are two imaginary roots yielding two dressed states without decay. The quantum interference between the two dressed states leads to periodic oscillatory behavior of the population trapping in the upper levels for a long time(see Fig. 2), which indicates the population exchange between the two upper levels always exists. This is caused by

the external field and localized fields and the properties are different from the orthogonal three-level case or two-level case without an external field. If $\Omega = 0$, we can find $A_j(t)$ is related only to $A_j(0)$, ($j = 1, 2$) from Eqs. (3a) and (3b) and the spontaneous emission will reduce into two independent two-level spontaneous emission cases in Ref. [4]. In the orthogonal three-level or two-level case, the photon-atom bound dressed states can lead to the fractionalized steady-state population in the upper level and there is no periodic oscillation of the population. The populations in the two upper levels can not be zero at the same time and no complete decay in the orthogonal three-level system.

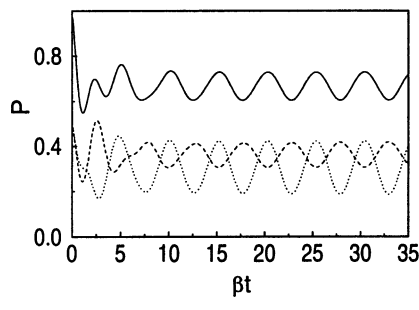


Fig. 2. Atomic population on the upper levels $P_1(t)$ (dashed curve), $P_2(t)$ (dotted curve) and $P(t)$ (solid curve) as a function of the scaled time βt . Here $\Omega^2/\beta = 1$, $\phi = \pi/4$, $\omega_{12}/\beta = 1$, $\omega_{1c}/\beta = 0.4$, $|\Phi(0)\rangle = \frac{1}{\sqrt{2}}(|a_1\rangle + |a_2\rangle)$.

In summary, we found that, in a photonic crystal with an external-driving field, the properties of the spontaneous emission from a three-level atom are different from that either in vacuum or in a photonic crystal without an external-driving field. The populations in the upper levels display oscillatory or complete decay behaviors. The populations in the upper levels reflect the properties of the intensity and the phase of the driving field predicting a phase-sensitive, optical memory device.

Acknowledgment. This work was supported in part by the Shanghai Educational Council and FRG from Hong Kong Baptist University.

References

1. E. Yablonovitch, Phys. Rev. Lett. **58**, 2059 (1987)
2. S. John, Phys. Rev. Lett. **58**, 2486 (1987)
3. S. John and J. Wang, Phys. Rev. Lett. **64**, 2418 (1990)
4. S. John and T. Quang, Phys. Rev. A **50**, 1764 (1994)
5. S. John and T. Quang, Phys. Rev. Lett. **74**, 3419 (1995)
6. S.-Y. Zhu, H. Chen and H. Huang, Phys. Rev. Lett. **79**, 205 (1997)
7. T. Quang and M. Woldeyohannes et al., Phys. Rev. Lett. **79**, 5238 (1997)

AC Magnetic Guide for Cold Atoms in an Ioffe Tube

Lifang Xu¹, Jianping Yin², Yuzhu Wang¹

¹ The Laboratory for Quantum Optics Shanghai Institute of Optics and Fine Mechanics Chinese Academy of Sciences, Shanghai 201800, P. R. China

² 2-Department of Physics, Suzhou University, Suzhou 215006, P. R. China

Abstract. We propose a novel ac magnetic waveguide for cold neutral atoms in an Ioffe tube. The time-averaged magnetic potential and force for the guided atoms in the magnetic guiding tube are calculated, and the results show that it is high enough to collect and guide nearly all of cold atoms from a standard magneto-optical trap with a temperature of $\sim 120\mu K$. We also estimate the atomic losses from background thermal-atom collision, quantum tunneling effect and spin-flip transition in the guiding. Our study shows that a cold and dense atomic beam with a guiding efficiency of $\sim 92\%$ and a beam intensity of about $10^{11} \text{ atoms/cm}^2 \cdot \text{s}$ can be output from the magnetic guide tube, and the guiding scheme proposed here could be used to manipulate spin polarized cold atoms.

The magnetic guiding configuration is shown in Fig.1, which is similar to a vertical *Ioffe* trap [1], but the difference is that the *Ioffe* bars in our magnetic tube are carrying an alternating current, which provides an ac quadrupole magnetic field in the transverse. To avoid *Majorana* transition at any position as the dc magnetic guides, an axial homogeneous field B_0 is added and overlapped with the transverse ac magnetic field. Here the dc field is produced by a dc current I_0 in a pair of *Helmholtz* coils.

To be explicit, we consider the interaction of a magnetic dipole moment μ of ^{87}Rb atoms with both an ac position-dependent magnetic field $\overrightarrow{B_1(r, \phi)} \cos \omega t$ generated by the *Ioffe* bars and a dc bias magnetic field $B_0 \vec{e}_z (B_0 > 0)$ produced by the *Helmholtz* coils (see Fig.1(c)), here ω is the frequency of alternating current. Next, Let us derive the time-averaged trapping potential U of the magnetic fields for the guided ^{87}Rb atoms. For this, we should assume $|B_1| \ll |B_0|$, and choose B_0 as the axis for quantization of total angular momentum p , and atoms are prepared in spin state $|F = 2, m_F = -2\rangle$ at the initial time $t = 0$, which can be done by using optical pumping.

Since there are *Majorana* spin-flip transitions in the magnetic fields, we use $P_{-2,m'}$ to stand for the spin-flip probability from the state $|F = 2, m_F = -2\rangle$ to $|F = 2, m_F = m'\rangle$, which is also the probability of an atom stayed in the state $|F = 2, m_F = m'\rangle$ under the condition $P_{-2,-2}(t = 0) = 1$ after a sufficient long interaction time. We can derive the magnetic potential U when

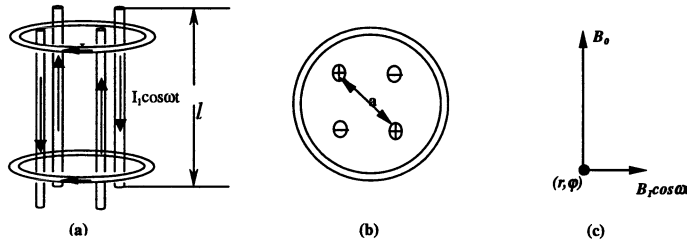


Fig. 1. Proposed Ioffe guide tube composed of four Ioffe bars and a pair of Helmholtz coils, in which the Ioffe bars generate an ac quadrupole magnetic field, whereas the Helmholtz coils provide a dc bias field. The arrows in the Ioffe bars denote the instantaneous direction of alternating current. Both (a) side and (b) end views are shown for Ioffe guide tube. (c) The configuration of the magnetic fields

the atom stays around the center, and under the condition that $|B_1| \ll |B_0|$, which is given by:

$$U = \sum m' g \mu_B P_{-2,m'} B_0. \quad (1)$$

According to Majorana transition formula[3,4], $P_{-2,m'}$ can be expressed as

$$\begin{aligned} P_{-2,-2} &= (1 - P_{1/2,-1/2})^4, \\ P_{-2,-1} &= 4P_{1/2,-1/2}(1 - P_{1/2,-1/2})^3, \\ P_{-2,0} &= 6(P_{1/2,-1/2})^2(1 - P_{1/2,-1/2})^2, \\ P_{-2,1} &= 4(P_{1/2,-1/2})^3(1 - P_{1/2,-1/2}), \\ P_{-2,2} &= (P_{1/2,-1/2})^4. \end{aligned} \quad (2)$$

Where $P_{1/2,-1/2}$ is the transition probability between levels in a two-level atom system with the same γ . From Eq.(2), it is easy to verify that $\sum P_{-2,m'} = 1$.

If assuming that the direction of \vec{B}_1 is paralleled to \vec{e}_x , we have $|B_1| \cos \omega t \vec{e}_x$. In terms of a magnetic resonant model of two-level atomic transition, when the interaction time of an atom with the magnetic field is long enough, the time-averaged transition probability $P_{1/2,-1/2}$ is given by [4]

$$P_{1/2,-1/2} = \frac{(\gamma B_2)^2}{2} [(\omega_0 \pm \omega)^2 + (\gamma B_2)^2], \quad (3)$$

Fig.2 shows the relationship between the probability of a guided atom at each magnetic sublevel m_F and the radial position r . It is clear from Fig.2 that within $r = 50\text{nm}$ (that is, in the transverse-motion range of cold atoms with a temperature of $\sim 120\text{mK}$), the guided atoms of more than 95 % will stay at the trapping state $|F = 2, m_F = -2\rangle$, whereas nearly all of other atoms will stay at the untrapping state $|F = 2, m_F = -1\rangle$, this may result in an atomic loss of less than 5 % due to the spin-flip transition. Using Eq.(1),(2)

and (3), we can derive the trapping potential of the magnetic fields for the guided atoms as follows

$$U = 4g\mu_B B_0 \frac{(\gamma B_2)^2}{2[(\omega_0 \pm \omega)^2 + (\gamma B_2)^2]} - 2g\mu_B B_0. \quad (4)$$

In our case, $B_2(r, \phi) = B_2(r)$, so U is the radial-position dependent. The position-dependent potential due to the Zeeman effect results in a position-dependent gradient force $F[1]$.

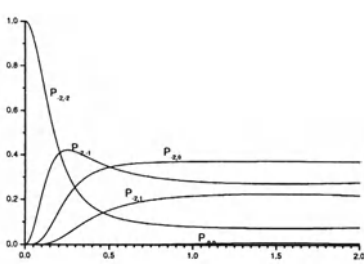


Fig. 2. The probability that a confined atom stays in each five magnetic states verse the radial position.

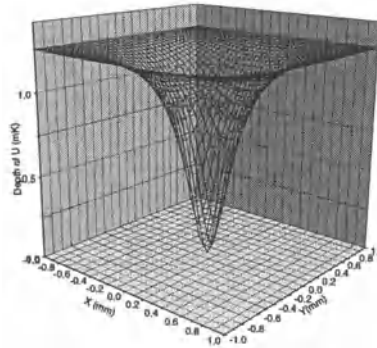


Fig. 3. Time-averaged 2D trapping potential $U(x, y)$ versus the x, y position

When the parameters of our *Ioffe* bars area = 4mm, $\langle I \rangle = 0.4A$, and $B_0 = 5Gauss$ (i.e., $\omega_0 = 87MHz$), and $\omega_0 - \omega = 1.7MHz$, we calculated the trapping potential U and gradient force F for the guided ^{87}Rb atoms in our ac magnetic tube, the results are shown in Fig.3, which show that the guided cold atoms in the *Ioffe* tube are reflected by a centripetal gradient force and tightly confined in a small region ($r \leq 50mm$) around the guiding axis, and the trapping potential around $r = 0$ is like a parabolic one.

Next, we will estimate the guiding loss of cold atoms in our ac *Ioffe* magnetic tube. Through analyses the loaded loss and the atomic loss from spontaneous emission heating can be neglected. Then, There are three main loss mechanisms in our guiding scheme: quantum-tunneling effect of the moving atoms in the potential well, atomic collisions from the background thermal atoms and *spin – flip* transition from the trapping state to untrapping state. Using *WKB* approximation , the tunneling probability T is caculated. The minimum and maximum tunneling probability are about 0.0014% ($\omega_0 - \omega = 1~5MHz$) and 0.08% ($\omega_0 - \omega > 8.5MHz$), respectively. Therefore, the tunneling loss is so small that it can be neglected completely.

When vacuum chamber pressure $p = 10^{-9}torr$,and taking cross section $\sigma_{Rb} \sim 10^{-13}cm^2$ and the background temperature the chamber $T_{back} = 300K$, we obtain collision loss about 1.91% if we take that the mean travelling time of the Rb atoms in the magnetic guiding tube with a length

of 20cm is about $\Delta t = 0.2s$. In this case, the mean velocity of the guided atoms should be 1 m/s, which can be easy to obtain by tilting the guiding direction of the *Ioffe* tube around a horizontal axis. In consideration of the spin-flip-transition induced loss ($\leq 5\%$) mentioned above, the total atomic loss will be less than 8%. In addition, when the loading rate of the cold atoms from the *MOT* into our *Ioffe* tube is $10^7 atoms/s$, the intensity of cold atomic beam output from the magnetic guiding tube will be reached to be about $10^{11} atoms/cm^2.s$. From the analysis mentioned above, it is easy to produce a cold and dense atomic beam with a guiding efficiency of ~92% and a beam intensity of $10^{11} atoms/cm^2.s$ from our ac magnetic guide tube when the pressure in the chamber is kept below $10^{-9} torr$ and the loading rate is about $10^7 atoms/s$.

In conclusions, we have proposed a novel atomic guiding scheme based the interaction between a magnetic dipole moment of the guided atoms and an ac quadrupole magnetic field. We have calculated the transverse trapping potential for the guided ^{87}Rb atoms and estimated the total atomic loss in the guiding. The theoretical study shows that unlike other static magnetic guides, there is no adiabatic limitation in our guiding scheme because *Majarana* spin flip only cause a small loss, and the time-varying field provide a stable and tight confinement [5] for the guided atoms. Therefore, a cold and dense atomic beam with a higher guiding efficiency and a beam intensity can be generated from our ac magnetic guiding tube. Obviously, such a cold and dense atomic beam should be useful in atom interferometers [6], atomic holography [7] and atom lithography [8], and so on.

Acknowledgment. This work was supported by the National Science Foundation of We are grateful for helpful discussions with Long quan, Zeng qinglin and Li This work was supported by National Nature Science Foundation of China under the grant No.19834060, and Ministry of Science and Technique of China under the grant No.95-Yu-34. J. Yin is also grateful to the NSF of Jiangsu province and the NNSF of China for their financial support.

References

1. T. Bergeman, G. Erez, H. J. Metcalf, Phys. Rev. A, **35** (1987) 1535;
2. Ramsey, N. F., *Molecular Beams*. Oxford (1956);
3. Majorana E., Nuovo Cimento, **9** (1932) 43;
4. Yiqiu Wang, et al, *The Principle of Quantum frequency Standard*, (Science Press, Beijing in China, 1986), Chapter3, 4;
5. E. A. Cornell, C. Monroe, and C. E. Wieman, Phys. Rev. Lett., **67** (1991) 2439;
6. D. W. Keith, C. R. Ekstrom, Q. A. Turchette, and D. E. Pritchard, Phys. Rev. Lett., **66** (1991) 2693;
7. J. Fujita, M. Morinaga, T. Kishimoto, M. Yasuda, S. Matsui, and F. Shimizu, Nature (London), **380** (1996) 691;
8. J. J. McClelland, et al, *Science*, **262** (1993) 877; G. Timp, et al, *Phys. Rev. Lett.*, **69** (1992) 163

Bose-Einstein Condensation of Neutral Atoms with Attractive Interaction in a Harmonic Trap

Yan Kezhu and Tan Weihan

Physics Department, Shanghai University, Shanghai 201800, China

Abstract. In this paper we present the numerical solutions of neutral atoms with attractive interaction in a harmonic trap. Very interesting is the bistability curve of condensate atoms versus the energy eigenvalues shown in the calculated results. From which we can deduce a critical number of atoms N_c which is maximum number of atoms of an attractive Bose-Einstein condensate. The critical point divides the eigenstates into condensate and dense state.

After the discovery of Bose-Einstein condensation (BEC) in gases ^{87}Rb [1], ^{23}Na [2], 7Li [3] atoms in trapped, an explosively increasing amount of research is being carried out on the phenomenon of BEC. Unlike the other two species, a uniform system of 7Li atom is usually believed not to form a stable BEC state[4] because the s-wave scattering length \bar{a} is negative and the attractive interaction between the atoms cause the condensate to collapse upon itself. Condensation has been predicted to be stable for a sufficiently small number of particles or sufficiently weak interaction[6-8]. The instability to collapse when these conditions are not obeyed has also discussed by several authors[10-12]. Kagan et al[7] argue that trapped gas with sufficiently large negative scattering lengths are unstable to the formation of clusters using a somewhat different argument, but with the same physical origin, the attraction between particles enables the existence of a much more dense state of atoms, the dense state is strongly compressed compared to the initial state of the trapping potential.

By a direct numerical solution of the Gross-Pitaevskii equation for atoms in a spherical harmonic trap we obtain the bistability curve of the nonlinear coefficient versus the energy eigenvalues. For a given system, the maximum of condensate atoms is limited below the critical value which is calculated from the minimum of the bistability curve. The critical point divides the eigenstates into condensate and dense state.

Mean field theory for a dilute assembly of bosons at $T = 0$ results in an effective nonlinear equation (NLSE) for condensed neutral atoms in a harmonic trap of the form[5]:

$$i\hbar \frac{\partial \Psi(\mathbf{r}, t)}{\partial t} = -\frac{\hbar^2}{2m} \nabla^2 \Psi(\mathbf{r}, t) + \frac{1}{2} m \omega_T^2 \Psi(\mathbf{r}, t) + N U_0 |\Psi(\mathbf{r}, t)|^2 \Psi(\mathbf{r}, t) \quad (1)$$

here $\Psi(\mathbf{r}, t)$ is BEC wave function, m is the mass of a single atom, ω_T is the angular frequency of the trap, N is the number of atoms in the condensate, and $U_0 = 4\pi\hbar^2\bar{a}/m$, the negative scattering \bar{a} length characterizes the attractive interaction.

To find a stationary solution we write $\Psi(\mathbf{r}, t) = e^{-i\mu t/\hbar}\Psi(\mathbf{r})$ (where μ is the chemical potential) inserting this equation into Eq.(1), we find the following equation for $\Psi(\mathbf{r})$:

$$-\frac{\hbar^2}{2m}\nabla^2\Psi(\mathbf{r}) + \frac{1}{2}m\omega_T^2\Psi(\mathbf{r}) + NU_0|\Psi(\mathbf{r})|^2\Psi(\mathbf{r}) = \mu\Psi(\mathbf{r}) \quad (2)$$

The BEC ground-state wave function is spherically symmetric, we transform to dimensionless length unit and dimensionless wave function by setting

$$\begin{aligned} r &= (\hbar/2m\omega_T)^{1/2}x, \quad \beta = \mu/\hbar\omega_T, \\ a &= 2N\bar{a}/(\hbar/2m\omega_T)^{1/2}, \\ \Psi(r) &= (4\pi)^{-1/2}(2m\omega_T/\hbar)^{3/4}\Phi(x) \end{aligned} \quad (3)$$

and yields

$$\left(\frac{d^2}{dx^2} + \frac{2}{x} \frac{d}{dx} + \beta - a\Phi^2(x) \right) \Phi(x) = 0 \quad (4)$$

The norm of $\Phi(x)$ is

$$4\pi \int_0^\infty \Psi^2(r)r^2dr = \int_0^\infty \Phi^2(x)x^2dx = 1 \quad (5)$$

The boundary conditions satisfied by $\Phi(x)$ are

$$\Phi(x)|_{x \rightarrow \infty} = 0, \quad \Phi'(x)|_{x \rightarrow \infty} = 0 \quad (6)$$

and

$$\Phi(x)|_{x=\epsilon} = \Phi(0), \quad \Phi'(x)|_{x=\epsilon} = \epsilon\Phi(0) \quad (\epsilon = 10^{-6}) \quad (7)$$

Using the method of Ref[9], by adjusting β and $\Phi(0)$, such that the conditions Eq.(5,6,7) being satisfied, the numerical solutions of Eq.(1) are depicted in Fig.1 and Fig.2. In Fig.1 we have plotted the variation of nonlinear coefficient a as a function of the ground-state energy β , which has the minimum value at $(0.365, -1.62625)$, from this and Eq.(3) we can deduce a critical number of atoms N_c , that is maximum number of atoms of an attractive BEC can holds. Substituting the experimental data[4] $|\bar{a}| = 1.45nm$, $\omega = (\omega_x\omega_y\omega_z)^{1/3} = 908s^{-1}$, $m_{Li} = 1.16 \times 10^{-23}g$, $\alpha = \sqrt{\hbar/2m\omega} = 2.24\mu m$, we obtain $N_c = 1254$. This is in agreement well with the results of reference[4], "the condensate number to be limited to a maximum value between 650 and 1300 atoms." For every $a > a_{min}$ there are two states with different energy eigenvalues, as shown in Fig.1, wave function curves 1 and 6 correspond

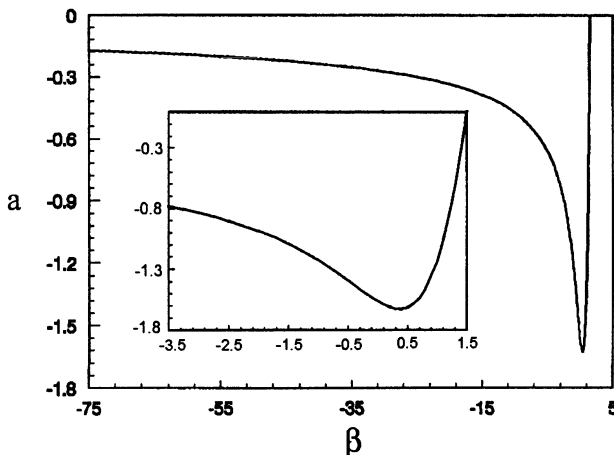


Fig. 1. nonlinear coefficient a as a function of ground-state energy β

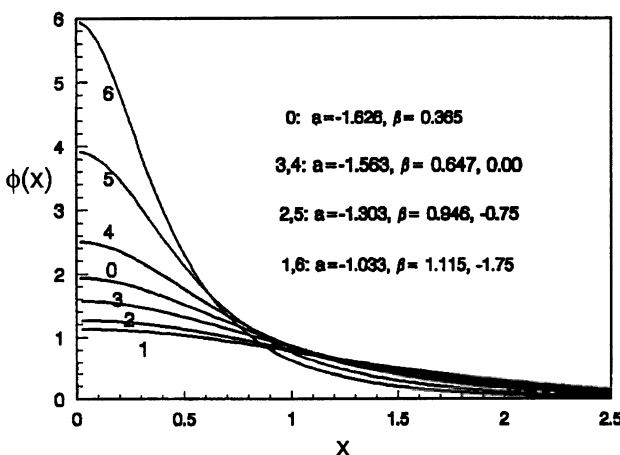


Fig. 2. ground-state wave function $\Phi(x)$ with different a and β

the same nonlinear coefficient $a = -1.033$, but their energy eigenvalues are $\beta = 1.115$ and $\beta = -1.75$ respectively, this is the bistability we mean. For the states, their eigenvalues $\beta > 0.365$, the number of condensate atoms decreases with the increasing of β . The atom spatial distribution are illustrated by the wave function curves 3,2,1 for $\beta = 0.647, 0.946, 1.115$ respectively in Fig.2. These states are Bose-Einstein condensates with attractive interaction. On the other hand, for the states, with eigenvalues $\beta < 0.365$, the number of atoms decreases with the decreasing of β , and the atom spatial distribution are compressed as illustrated by the compressed wave function curves 4,5,6 for $\beta = 0, -0.75, -1.75$ respectively in Fig.2. These compressed wave func-

tions may be related to the dense states as mention in literature[7], but these states are unstable. Therefore the Bose-Einstein condensate with attractive interaction can be formed if it is spatially confined and if the total number of condensate N is below critical value N_c . Nevertheless the transitions between condensates and dense states, especially near the critial point, make BEC with attractive interaction being metastable state.

In conclusion, the numerical solutions for the ground-state energy eigenvalues and wave functions of neutral atoms with attractive interaction are presented. The bistability curve of condensate atoms versus the energy eigenvalues is obtained. The critical point divides the eigenstates into condensate and dense state. The results show that a Bose-Einstein condensate with attractive interaction can be formed if it is spatially confined and if the total number of atoms is below a critical value. Nevertheless the bistability states may make BEC with attractive interaction being metastable state. The property of dense state and stability of BEC with attractive interaction need to study further.

Acknowledgment. This work was supported by the National Natural Science Foundation of China under Grant No.697778011.

References

1. M. H. Anderson, J. R. Ensher, M. R. Methews, C. E. Wieman, and E. A. Cornell, *Science*, **269**, 198 (1995).
2. K. B. Davis, M. -O. Mewes, M. R. Anderson,N. J. van Druten, D. S. Durfee, D. M. Kurn, and W. Ketterle, *Phys. Rev. Lett.*, **75**, 3969 (1995).
3. C. C. Bradley, C. A. Sacket, J. J. Tollett, and R. G. Hulet, *Phys. Rev. Lett.*, **75**, 1687 (1995).
4. C. C. Bradley, C. A. Sacket, and R. G. Hulet, *Phys. Rev. Lett.*, **78**, 985 (1997).
5. P. Nozières and D. Pines, *The theory of quantum liquids*, Addison-Wesley,Reading, MA, 1990,Vol.2.
6. P. A. Ruprecht, M. Edwards, K. Burnett, and C. W. Clark, *Phys. Rev. A* **54**, 4178 (1996).
7. Yu. Kagan, and G. V. Shlyapnikov, and J. T. M. Waltraven, *Phys. Rev. Lett.*, **76**, 2670 (1996).
8. M. Ueda and A. J. Leggett, *Phys. Rev. Lett.*, **80**, 1576 (1998).
9. Yan Kezhu, Tan Weihan, *Acta Physica Sinica*, **48**, 1185 (1999).
10. G. Baym and C. J. Pethick, *Phys. Rev. Lett.*, **76** , 6 (1996).
11. R. J. Dodd, M. Edwards, C. J. Williams, C. W. Clark, M. J. Holland, P. A. Ruprecht, and K. Burnett, *Phys. Rev. A* **54**, 661 (1996).
12. E. V. Shuryak, *Phys. Rev. A* **54**, 3151 (1996).

Influence of Spontaneous Emission on Two-Atom Dark State Inside a Quantized Standing Wave Cavity

Guojian Yang, Weiqiao Zhen, Jian Wang

Department of Physics, Beijing Normal University, Beijing 100875, China
e-mail: guojianyang@bnu.edu.cn

Abstract. We investigate the properties of the entangled two-atom dark states under the influence of the center-of-mass motion of two two-level atoms coupling to a single quantized standing wave mode. We analyze the effects of the dipole-dipole interaction between the atoms and of fluorescence emission from the atoms on these states.

1 Introduction

It is predictable that when a single two-level atom moves in a cavity where it interacts resonantly with a quantized standing-wave cavity mode, the width of its momentum distribution linearly spreads in the Poman-Nath approximation (RNA) or oscillates in the model including the kinetic energy (the full model). While the dissipation due to the damping of the cavity mode or the spontaneous emission will totally erase the pattern of the distribution. What happens if a second atom is injected into the cavity and if the atoms also couple to the electromagnetic vacuum modes? In this paper we try to answer these questions. Throughout the paper we consider the case where only one excitation exists in the atom-cavity system.

2 Two-atom master equation

The model under the consideration is described by the following two-atom master equation in the form suitable for the simulation by Monta-Carlo Wave Function (MCWF) approach[1,2]:

$$\dot{\rho} = -\frac{i}{\hbar} [H_{eff}, \rho] + \mathcal{L}_{feed}\rho, \quad (1)$$

where ρ is the density operator of the reduced atom-cavity system and H_{eff} is the effective Hamiltonian

$$H_{eff} = H_a + H_{ac} + H_{dd} + H_{decay}, \quad (2)$$

composed of the free Hamiltonians of the atoms H_a , the coupling between the atoms and the quantized standing-wave cavity mode H_{ac} , the atomic

dipole-dipole interaction H_{dd} , and the dissipation of the atoms and cavity mode H_{decay} . They are described by

$$H_a = \sum_{j=1}^2 \left(\frac{\hat{P}_j^2}{2M} - \frac{\hbar\delta}{2} \sigma_j^\dagger \sigma_j^- \right), H_{ac} = \sum_{j=1}^2 \hbar \mathcal{R} \cos(qx_j) (\sigma_j^\dagger a + \sigma_j^- a^\dagger), \quad (3)$$

$$H_{dd} = \frac{1}{2} \hbar \sum V_{dd}(qr) (\sigma_i^\dagger \sigma_j^- + \sigma_i^- \sigma_j^\dagger) \quad (4)$$

and

$$H_{decay} = -\frac{i\hbar\gamma}{2} \sum_{j=1,2} \sigma_j^\dagger \sigma_j^- - \frac{i\hbar\gamma}{2} g(qr) (\sigma_1^\dagger \sigma_2^- + \sigma_1^- \sigma_2^\dagger) - \frac{i\hbar\kappa}{2} a^\dagger a, \quad (5)$$

respectively. Here we have modeled j th atom ($j = 1, 2$) as a two-level system with mass M and spontaneous emission rate γ . The definitions of other operators or parameters, such as σ_j^- , x_j , \hat{P}_j and a or \mathcal{R} , q and κ , can be found elsewhere. In addition the functions of the dipole-dipole potential $V_{dd}(qr)$ and the spatial modulation of the atomic decay rate $g(qr)$ are related to spherical functions of the first (second) kind [1,2]. The last term in Eq.(1) has the form:

$$\mathcal{L}_{feed}\rho = \sum_{i,j=1,2} \frac{3\gamma}{2} \int \frac{d\Omega(\mathbf{k})}{4\pi} \sigma_i^-(\mathbf{k}) \rho \sigma_j^\dagger(\mathbf{k}) \quad (6)$$

describing the variation of the population of the atoms in their ground state via spontaneous emission and, obviously, is related to the atomic recoil.

3 Two-atom dark states

In this section we look into the situation in the absence of spontaneous emission[3]. In RNA the dynamic system at present is solvable with one of the eigenvalues equal to zero, which ensures the asymptotic state of the atom-cavity system being *dark*. In the position space, this dark state takes a form:

$$|\Psi(x_1, x_2, t \rightarrow \infty)\rangle = A(x_1, x_2) (\cos(qx_2)|e, g, 0\rangle - \cos(qx_1)|g, e, 0\rangle) \quad (7)$$

where $|\Psi(x_1, x_2, t)\rangle$ denotes the state vector of the system at time t ; $A(x_1, x_2)$ is determined by the initial condition one chooses. In the momentum space the state (7) is transferred to a family of dark states $|d_{m,n}\rangle$

$$|d_{m,n}\rangle = \frac{1}{2} [|(e, m), (g, n), 0\rangle + |(e, m), (g, n+2), 0\rangle - |(g, m+1), (e, n+1), 0\rangle - |g, m-1), (e, n+1), 0\rangle], \quad (8)$$

where the state component $|(e/g, m), (g/e, n), 0\rangle$ with integer momenta m, n multiplying $\hbar q$ is of a probability amplitude $C_{j,m,n}$ ($j = 1, 2$) given by

$$C_{j,m,n} = \frac{q}{2\pi} \int \int_0^{2\pi/q} dx_1 dx_2 e^{-i(mqx_1 + nqx_2)} f_j(x_1, x_2) \quad (9)$$

with $f_1(x_1, x_2) = A(x_1, x_2) \cos qx_2$ and $f_2(x_1, x_2) = -A(x_1, x_2) \cos qx_1$. Obviously, we have the equality of the total probability for the system to settle into the dark state:

$$\frac{q}{2\pi} \int \int_0^{2\pi/q} dx_1 dx_2 \langle \Psi | \Psi \rangle = \sum_{m,n} \sum_{j=1,2,3} |C_{j,m,n}|^2. \quad (10)$$

For the full model, it is easily testified that there are two exact dark states described still by (7), but the function $A(x_1, x_2)$ now takes the forms $A(x_1, x_2) = 1$ and $A(x_1, x_2) = \sin qx_1 \sin qx_2$, respectively.

Let us look an example that initially both atoms are at rest but atom 1 is excited, and no photons are in the cavity mode. From Eq.(9) to (10), we obtain:

$$\begin{aligned} \frac{1}{L_c} \int \int dx_1 dx_2 \langle \Psi | \Psi \rangle &= \frac{1}{2}, C_{1,0,0} = \frac{1}{2}, \\ C_{2,\pm 1,\pm 1} &= \frac{1}{\pi} - \frac{1}{2}, C_{1,\pm 2,0} = -C_{1,0,\pm 2} = \frac{1}{2} - \frac{2}{\pi}, \end{aligned} \quad (11)$$

Figures 1 show the momentum distribution of the first atom $P_m^{(1)}(\tau) = \sum_{i=1,2,3;n} |C_{i,m,n}(\tau)|^2$ without or with the cavity loss ($\kappa/\omega_{rec} = 0$ for Figs.1(a) or $\kappa/\omega_{rec} = 20$ for Figs.1(b)). Two important features can be recognized from these figures, i.e., the center mode and a few nearby sidemodes hold the most probability in the family of the dark states, and the momentum distribution is weakly affected by the cavity loss (Figs.1(b)). Figure 2 shows the long-time behavior of the system by presenting the total probability for finding the excitation in the atom-cavity system $P = \sum P_m^{(1)}$ (curve 1), for sum of the center and its nearby sidemodes $|C_{1,0,0}|^2 + |C_{1,0,\pm 2}|^2 + |C_{1,\pm 2,0}|^2 + |C_{2,\pm 1,\pm 1}|^2$ (curve 2) and for the center mode alone $|C_{1,0,0}|^2$ (curve 3). These coincide with the analytical result (11) and the prediction of the dark states (7,8), and confirm that the presence of the second atom strongly suppresses photon decay from the cavity. For the full model, the state (7) or (8) at present is obviously not *dark*. But the numerical simulations show that the pattern of the distribution for the time concerned is not much different from that in RNA. The states (7,8) are thus *quasidark*.

4 The effects of spontaneous emission on dark state

The interaction between two fluorescent atoms through exchange of spontaneous emission photons leads to the dipole-dipole interaction. Figs. 3 and 4 were plotted to illustrated its influence on the momentum distribution of the first atom. For comparesion, the initial condition, parameters and symbols used in these figures are the same as Figs. 1 and 2. Curve 4 (5) in Fig.4 is denoted as the total probability summed over all modes with integer (non-integer) momenta. We found that the momentum distribution under the action of H_{dd} is transferred from a distinctive diffraction pattern, which mostly concentrates at the center mode ($m = 0$) and a few nearby sidemodes

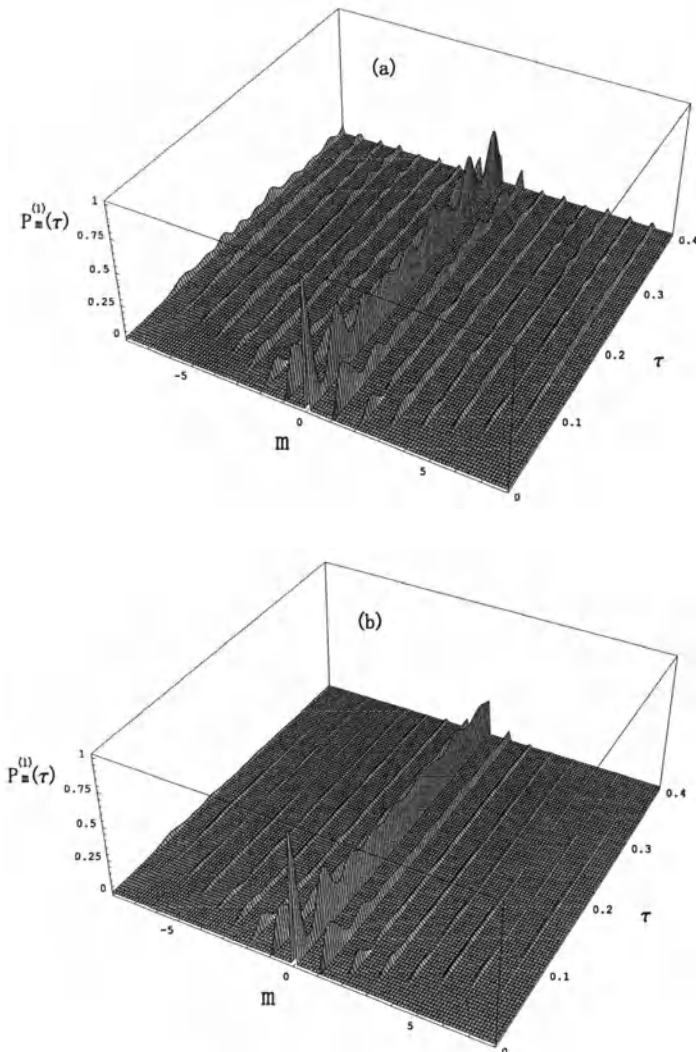


Fig. 1. Time evolution of the momentum distribution of the first atom in RNA for (a) $\kappa/\omega_{rec} = 0$ and (b) $\kappa/\omega_{rec} = 20$. Other parameter values are taken as $\delta = 0$, $\mathcal{R}/\omega_{rec} = 100$. Initially, both atoms are at rest and atom 1 is excited; no photons are in the cavity and the vacuum.

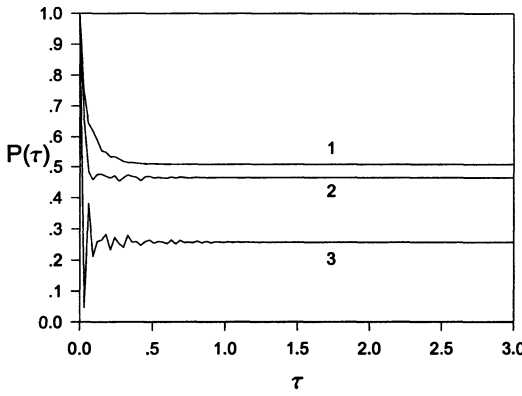


Fig. 2. Long-time view of Fig.1(b) for the total probability $P(\tau)$ to find the excitation in the cavity (curve 1), for $|C_{1,0,0}|^2 + |C_{1,0,\pm 2}|^2 + |C_{1,\pm 2,0}|^2 + |C_{2,\pm 1,\pm 1}|^2$ (curve 2) and for $|C_{1,0,0}|^2$ alone (curve 3).

in the absence of H_{dd} , to a continuous one. This means that the states (8) with integer momenta are now no longer *dark*. However, the total population stored in the whole family of the states (8) is conserved. These features stem from the fact that the state (7) or (8) is not an eigenstate of Hamiltonian H_{dd} , and the coherent action of H_{dd} does not cause the dissipation in the system.

To know the effect of spontaneous emission from the single atoms, we solve the original master equation (1) numerically by adopting MCWF approach. Fig.5 was obtained by averaging the momentum distribution of the first atom over 100 quantum trajectories. The distribution pattern quickly dies out due to the atomic decay, and thus the dissipation due to spontaneous emission destructively dominates the dynamic movement of the system in the time evolution. This property is the same as those found in its one-atom counterpart, where spontaneous emission always erases the patterns of the distribution.

5 Conclusion

We discuss the center of mass motion of two two-level atoms coupling with a single quantized standing-wave cavity mode. In the absence of spontaneous emission the atom-cavity system finally settles into the dark states in RNA. These states are no longer *dark* in the presence of H_{dd} , which transfers the distinctive diffraction pattern of the momentum distribution into a continuous one, but keeps the whole population in these states unchange. Spontaneous emission plays a destructive role in governing the time evolution of atomic momentum distribution.

Acknowledgements. We thank the support of National Natural Science Foundation of China under grant no. 19774013.

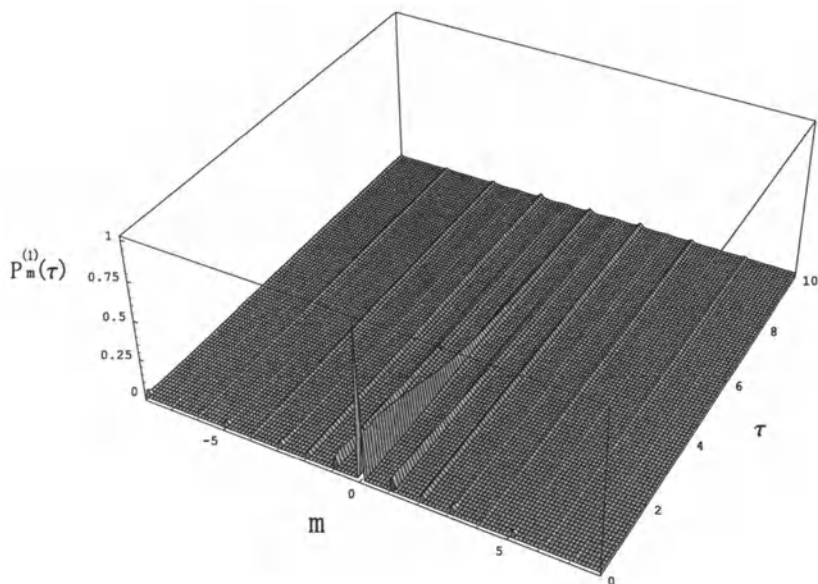


Fig. 3. Time evolution of the momentum distribution of the first atom in RNA under the influence of atomic D-D interaction. The initial and parameter conditions are the same as in Figs.1.

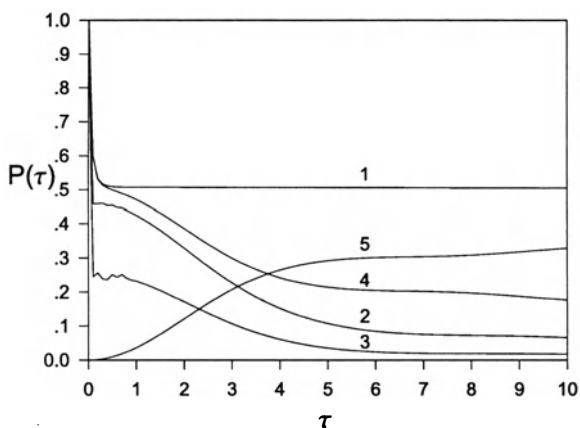


Fig. 4. Long-time view of Fig.3 with the curves 1,2,3 defined similar to Fig 2. Curves 4 and 5 are obtained by summing the probabilities respectively over all integer and non-integer momenta (m,n) .

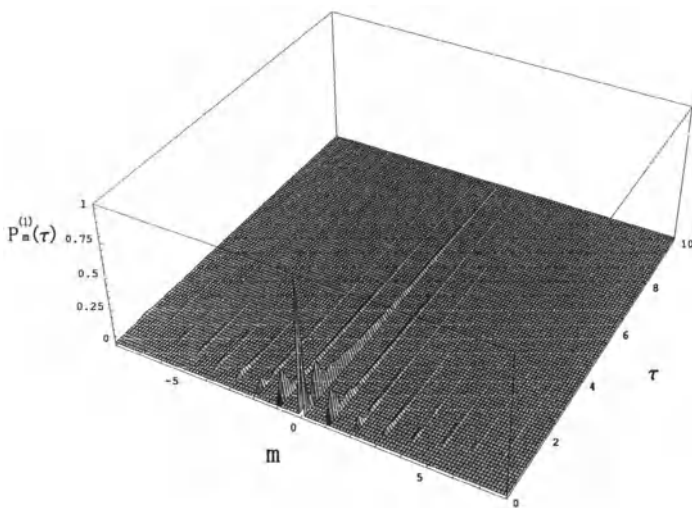


Fig. 5. Time evolution of the momentum distribution of the first atom under the condition same as in Fig.3 except including the SE effect.

References

1. E. Goldstein, P. Pax et al.: Influence of the dipole-dipole interaction on the velocity-selective coherent population trapping. *Appl. Phys.* **B60** 161-167 (1995)
2. P. Pax, G. Lenz, and P. Meystre: Dipole-dipole interaction in the near-resonant Kapitza-Dirac effect. *Phys. Rev.* **A51** 3972-3981 (1995)
3. G. J. Yang, O. Zobay, and P. Meystre: Two-atom dark states in electromagnetic cavities. *Phys. Rev.* **A59** 4012-4020 (1999)

Spectroscopic Study of Gadolinium Energy Levels by Resonant Multi-Photon Ionization

Jonghoon Yi, Jin Tae Kim, Huynmin Park, Jaemin Han, Yongjoo Rhee,
Jongmin Lee

Laboratory for Quantum Optics, Korea Atomic Energy Research Institute
P. O. Box 105, Yusong, Taejon 305-600, Korea.
E-mail: jhlee8@nanum.kaeri.re.kr

Abstract. To find the energy levels of gadolinium (Gd) atoms useful for trace analysis, multi-photon processes have been studied. Transitions with near infra-red wavelengths were investigated in order to use Ti:Sapphire laser for the multiphoton ionization. Several optical paths for resonant multi-photon ionization of Gd were found.

1 Introduction

For the sensitive detection of gadolinium atom in trace analysis where spectroscopic methods are used, energy levels should be studied in advance. To investigate the energy levels of gadolinium atoms, multi-photon processes have been investigated.

Recently, diode-pumped solid-state laser (DPSSL) is gaining popularity in many fields of laser application due to its long lifetime, excellent stability, and high efficiency [1]. For the laser spectroscopy, frequency tunable lasers are needed because many spectroscopic investigations utilize resonant excitation of the transitions between atomic energy levels. Among various tunable lasers which could be pumped by DPSSL, Ti:Sapphire laser might be the most adequate one. Ti:Sapphire laser has a broad tunable range and high energy conversion efficiency comparable to the dye laser [2]. Moreover, solid gain medium provides long-term stability in operation. Stability of the laser system is very important for trace analysis because it determines reliability of the measurement result.

To ionize gadolinium (Gd) atom by three-photon process using Ti:Sapphire lasers, one of the transitions should be excited by UV photons considering ionization potential (IP) of Gd atom ($IP = 49601.45 \text{ } 0.35 \text{ } cm^{-1}$). By frequency doubling the output of Ti:Sapphire lasers, tunable wavelength range can be extended to ultra-violet (UV) region of 320-550 nm. Generally, the transition lines in the UV range have very large transition probabilities compared with the transitions in the visible range for most of the lanthanide element [3]. Thus, energy loss in the frequency doubling process can be compensated effectively.

2 Experiment and Results

Ground state atoms effused from a hole of high temperature oven are excited and ionized through multi-photon process. The photons are emitted from three tunable dye lasers (Lumonics HD-300) pumped by a Nd:YAG laser (Lumonics, HY-750). The Gd ions are detected by time-of-flight mass spectrometer (TOFMS).

The wavelength of the dye laser pumped by third harmonic of Nd:YAG laser was scanned from 410 to 530 nm to obtain single-color multiphoton ionization spectra. In Fig. 1, one of the spectra is shown. An optogalvanic signal from a Gd hollow cathode lamp is simultaneously recorded with the ion signal while scanning the laser wavelength. The energy levels corresponding to ion signal peaks are obtained by calibrating the laser wavelength with help of an argon optogalvanic signal [4].

Most of the strong ion signal peaks are originated from transitions starting from low-lying metastable states. In this investigation, more than 20 strong transition lines excited from several metastable states are found. In some cases, many unidentified small peaks are observed and these are part of a series of Rydberg states. About half of the observed lines could be identified as the states listed in the NBS table of energy levels [5]. To discern peaks by single photon resonant multiphoton ionization process from the peaks by multiphoton resonant transition process, laser intensity dependence of ion signal strength are measured for each peak. In this way, some peaks by two-photon transition could be identified.

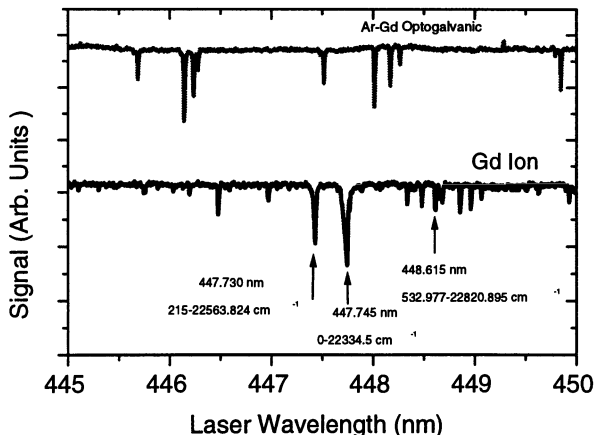


Fig. 1. Typical spectrum obtained from single-color multi-photon ionization experiment.

From the even parity intermediate states determined from a single color experiment, we could reach the odd-parity states located above 37000 cm^{-1} . The second excitation laser wavelength was scanned from 630 to 710 nm. Figure 2 shows the spectrum, which was obtained by scanning the frequency of the second excitation laser from 655 to 670 nm. More than 10 strong peaks are observed in this process and most of them agree well with the states listed in the NBS table [5].

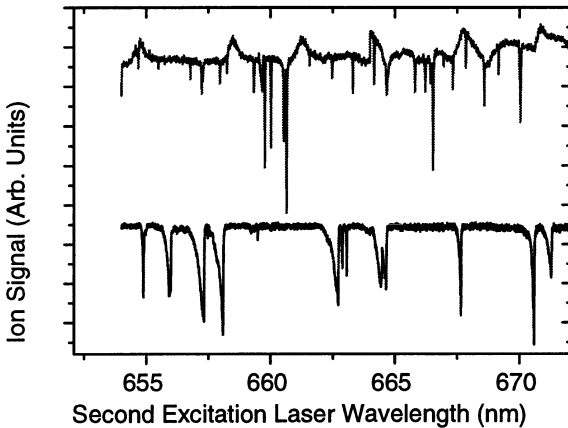


Fig. 2. A photoionization spectrum obtained from two-color multi-photon ionization experiment. The first excitation laser wavelength was fixed at 447.748 nm ($0-22334.5\text{ cm}^{-1}$) and the second excitation laser was scanned from 655 to 670 nm.

Among the states found in the two-color multi-photon ionization experiment, 37529.8 cm^{-1} ($J=2$) level ($\lambda = 658.099\text{ nm}$) was selected as a second excitation level considering both signal strength and wavelength. Finally, we investigated the transition from this state to autoionizing states in order to find efficient resonant three-photon transition pathways. As can be seen in Fig. 3, several autoionizing states above the ionization potential are observed. Among the states found, the 51128.6 cm^{-1} autoionizing state ($\lambda = 735.358\text{ nm}$) showed the strongest signal.

3 Conclusions

To find the ionization pathway of the gadolinium atom adequate for multi-photon ionization by three Ti:Sapphire laser systems, we investigated energy levels by the multi-photon ionization method. From the obtained spectra, we could find the multiphoton ionization pathway starting from ground state. The atoms are excited to 22334.5 cm^{-1} ($J=2$) and then secondly excited

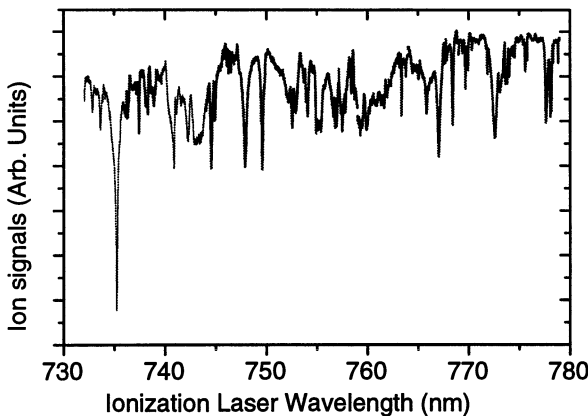


Fig. 3. Three-color photoionization spectrum obtained by scanning the ionizing laser wavelength from 730 to 780 nm. The first excitation laser wavelength was fixed at 447.748 nm ($0-22334.5\text{ cm}^{-1}$) and the second excitation laser wavelength was fixed at 658.099 nm ($22334.5-37529.8\text{ cm}^{-1}$).

to 37529.8 cm^{-1} ($J=2$). The excited atoms are ionized via autoionizing state located at 51128.6 cm^{-1} . For further work, we are going to investigate the second excitation states and autoionizing states accessible by the photons within 780-880 nm wavelength range, which is the most efficient energy conversion range of Ti:Sapphire laser when pumped by frequency-doubled diode-pumped Nd:YAG laser.

References

1. E. J. Lerner : *Laser Focus World*, Nov., **34**, 97 (1998)
2. J. C. Barnes, N. P. Barnes, and G. E. Miller : *IEEE J. Quantum Electron.*, **QE-24**, 1029 (1988)
3. C. H. Corliss and W. R. Bozman : *Experimental Transition probabilities for Spectral Lines of Seventy Elements* NBS Monographs 53 (1962)
4. J. Yi, J. Lee, H. J. Kong : *Phys. Rev.* **A51**, 3053 (1995)
5. W. C. Martin, R. Zabubas and L. Hogan : *Atomic energy levels : the rare earth elements* NSRDS-NBS 60 (1978)

Near-Field Optical Trap by Tapered Fibre Probe

Guoping Zhang¹, Zhuming Huang², Hai Ming³

¹ Department of Physics, Central China Normal University, Wuhan, 430079, China

² Dept. of Basic Course, Wuhan Institute of Chemical and Technology, Wuhan, 430073, China

³ Department of Physics, University of Science and Technology of China, Hefei, 230026, China

e-mail: gpzhang@phy.ccnu.edu.cn

Abstract. We propose a new method for optical trap in this paper. It is based on a tapered fibre probe with a tip size less than a light wavelength. A three-dimension gradient optical field is formed within the optical near field of the fibre probe, and a particle approaching the fibre tip will be trapped. We calculate the evanescent electromagnetic field near the fibre tip and obtain the trapping force for a dielectric particle. The calculating results show the availability of this method.

1 Introduction

Optical trapping by a single-beam gradient force trap was proposed by Ashkin et al. for the first time [1]. Since then, this method has been developed and used extensively for manipulation of various submicron-size dielectric particles and biological structures [2]. However, this type of optical trap has a diffraction-limited trapping volume. In this paper, a novel high-resolution optical trapping scheme is presented by a tapered fibre probe used for the scanning near-field optical microscopy (SNOM). Because the tip diameter of the fibre probe is less than a light wavelength, the near field close to the tip mainly consists of evanescent components [3,4]. Thus a three-dimension gradient optical field is formed within the optical near field of the fibre probe. When one particle approaches the fibre tip, it will be trapped by a three-dimension optical trap. As this kind of optical trapping appears within the optical near field of the fibre tip, it is named as the near-field optical trap.

2 Theory

A laser beam is coupled into the fibre probe from the end opposite to the tip. In order to solve Maxwell's equations in the specific geometry of the tip of the tapered fibre probe and its environment, we employ the multiple multipole method (MMP) which recently has been applied to study near-field

optical phenomena [5]. In terms of scalar fields, the multipolar eigenfunctions $\phi_n(\mathbf{r}, \omega)$ for the eigenvalues q_n satisfy the scalar Helmholtz equation. Three sets of vector eigenfunctions can be obtained by applying the gradient operator to the scalar functions:

$$\mathbf{L}_n(\mathbf{r}, \omega) = C\nabla(\phi_n(\mathbf{r}, \omega)), \quad (1)$$

$$\mathbf{M}_n(\mathbf{r}, \omega) = C\nabla \times (\phi_n(\mathbf{r}, \omega)\mathbf{S}), \quad (2)$$

$$\mathbf{N}_n(\mathbf{r}, \omega) \doteq \frac{1}{k}\nabla \times (\mathbf{M}_n(\mathbf{r}, \omega)), \quad (3)$$

where C is a normalization factor, and \mathbf{S} is a Poynting vector of unit length. The longitudinal eigenfunctions $\mathbf{L}_n(\mathbf{r}, \omega)$ have no physical meaning for our discussion. Therefore, MMP performs the expansion of the electric field in each subdomain only on the sets of transverse eigenfunctions $\mathbf{L}_n(\mathbf{r}, \omega)$ and $\mathbf{M}_n(\mathbf{r}, \omega)$:

$$\mathbf{E}(\mathbf{r}, \omega) = \sum [a_n \mathbf{M}_n(\mathbf{r}, \omega) + b_n \mathbf{N}_n(\mathbf{r}, \omega)]. \quad (4)$$

The coefficients a_n and b_n are then determined from the boundary conditions.

With the electric field distribution near the tip known, the gradient force for a particle can be easily calculated as

$$\mathbf{F} = \frac{\alpha}{2}\nabla(E^2), \quad (5)$$

where α is the polarizability of the particle. The particle tends to move to the higher intensity region where its induced dipole has lower potential energy. The trapping potential U of a particle located at \mathbf{r}_0 is then given by

$$U(\mathbf{r}_0) = - \int_{\infty}^{r_0} \mathbf{F}(\mathbf{r}) \cdot d\mathbf{r}. \quad (6)$$

3 Results and Discussions

The following fibre parameters are chosen in our calculation: $n_1 = 1.4544$, $n_2 = 1.45$, $2a = 8\mu\text{m}$, $2b = 125\mu\text{m}$, and $\lambda = 632.8\text{nm}$ (He-Ne laser).

Figure 1 shows the contours of the near field of the tapered fibre probe. The near field close to the tip is mainly of evanescent components which are mostly concentrated at the axial direction. The field is rotationally symmetric in the vicinity of the tip, and attenuate rapidly with distance from the tip. So a three dimensional gradient optical field is formed near the fibre tip. Figures 2 and 3 give the intensity distributions of the near fields of the tip as functions of the longitudinal and transverse distances (z and x , respectively) from the tip, respectively.

When a particle (of diameter $d=10\text{nm}$) approaches the fibre tip, the trapping force and the potential energy can be calculated from the above equations (5) and (6). Figures 4 and 5 show cross sections of the trapping

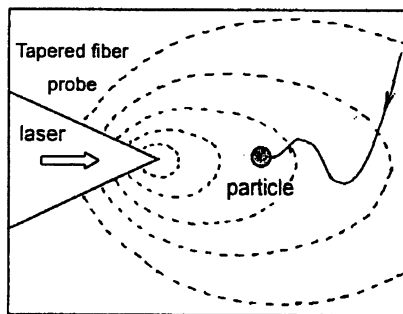


Fig. 1. Contours of the near field of tapered fibre probe

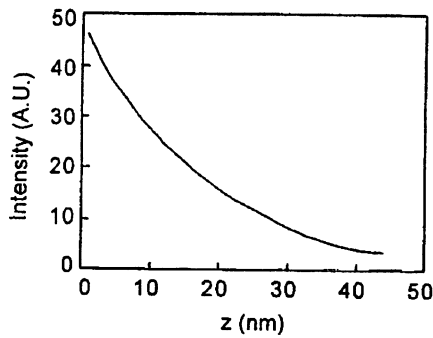


Fig. 2. Intensity distribution of the near field of the tip along the longitudinal direction z

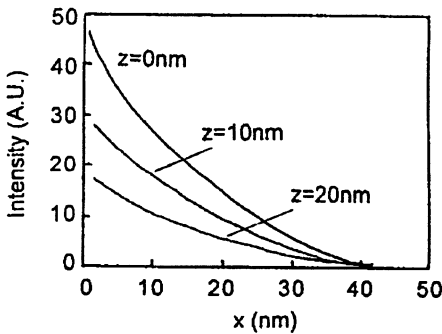


Fig. 3. Intensity distribution of the near field of the tip along the transverse direction x

potential along the axial (z) and lateral (x) directions from the tip, respectively. Since the trapping potential is almost rotationally symmetric, we only show the results for the (x, z) plane.

4 Conclusions

A method performing near-field optical trapping by tapered fibre probe has been presented in this paper. Compared with the optical trap by a highly

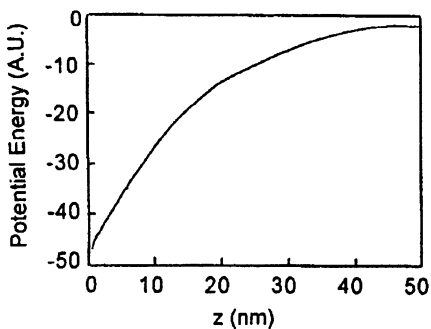


Fig. 4. Potential energy as the function of the longitudinal distance z from the tip

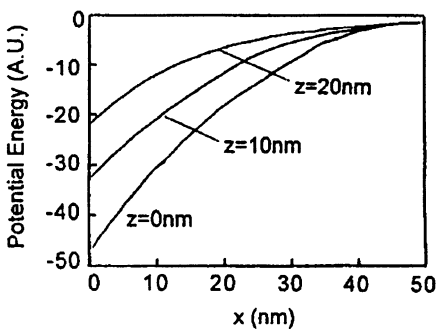


Fig. 5. Potential energy as the function of the transverse distance x from the tip

focused laser beam, the near-field optical trap using a tapered fibre probe exhibits the following advantages: (1) the optical trapping system is simplified without focusing objective lenses; (2) the highly confined evanescent fields significantly reduce the trapping volume; and (3) the trapped particles can be moved precisely and freely when the fibre probe is mounted on the SNOM system.

References

1. A. Ashkin, J. M. Dziedzic, J. E. Bjorkholm, S. Chu: Observation of a single-beam gradient force optical trap for dielectric particles. *Opt. Lett.* **11**, 288–290 (1986)
2. W. H. Wright, G. J. Sonek, Y. Tadir, M. W. Berns: Laser trapping in cell biology. *IEEE J. Quantum Electron.* **26**, 2148–2157 (1990)
3. W. Jhe: Photon scanning tunneling microscope and optical nanotechnology. *AAPPS Bulletin* **5**, 12–14 (1995)
4. Zhang Guoping, Ming Hai, Chen Xiaogang, Wu Yunxia, Xie Jianping: Effect of the Taper Shape upon Transmission Efficiency of Fibre Probes for Scanning Near-field Optical Microscopy. *Chinese J. of Lasers* **B7**, 357–362 (1998)
5. Lukas Novotny, Randy X. Bian and X. Sunney Xie: Theory of nanometric optical tweezers. *Physical Review Letters* **79**, 645–648 (1997)

Frequency Tunable Nonclassical Light Generation

Lingxiang He, Junmin Wang, Tiancai Zhang, Changde Xie, Kunchi Peng

Institute of Opto-Electronics Shanxi University, Taiyuan, Shanxi 030006, China

Abstract. By light injection from the master laser diode, the slave laser diode is injection-locked at the wavelength of 852.356 nm. In the mean time we have obtained amplitude squeezing of 0.9 dB, phase reduction of 5–12 dB, tunable range of 1.7 GHz at the room temperature.

1 Introduction

Squeezed light is a kind of nonclassical light with the noise of one quadrature below the shot noise limit (SNL) and that of the other well above the shot noise limit. It has been proposed in various optical experiments, such as spectroscopy, weak signal measurement and optical communication. In this paper, we report amplitude squeezing is obtained by injection locking. Amplitude squeezing with injection locking method was predicted by Yamamoto in 1986[1]. Recently many groups have carried out the works in injection locking, for example: in 1993 Yamamoto's group obtained intensity squeezing of 0.91 dB with the slave laser mounted on a copper sink in a 77-K cryostat[2]; in 1993 Hailin Wang etc. obtained photon number squeezing of 3 dB with the slave laser held in a closed -cycle cryostat[3]; in 1996 Akirra Furusawa obtained amplitude squeezing of 2.3 dB with the slave laser and its collimating lens held in a liquid nitrogen[4]; in the same year Y.Yamamoto obtained tunable squeezed light of 0.8-1.0 dB[5]. Our group has got tunable squeezed light at the room temperature recently with amplitude squeezing of 0.8 dB, phase reduction of 5–12 dB, tunable range of 1.7 GHz.

2 Theoretical analysis

The Langevin equation for the cavity internal field $\hat{A}(t)$ is given by[2]:

$$\frac{d\hat{A}(t)}{dt} = -\frac{1}{2} \left[\frac{\omega}{Q} + 2i(\omega_r - \omega) - \frac{\omega}{\mu^2} (\tilde{\chi}_i - \tilde{\chi}_r) \right] \hat{A}(t) + \left[\frac{\omega}{\mu^2} \langle \tilde{\chi}_i \rangle \right]^{\frac{1}{2}} \hat{f}_G(t) + \left[\frac{\omega}{Q_0} \right]^{\frac{1}{2}} \hat{f}_L(t) + \left[\frac{\omega}{Q_e} \right]^{\frac{1}{2}} [F_0 + \hat{f}(t)] \quad (1)$$

$$\frac{1}{Q} = \frac{1}{Q_e} + \frac{1}{Q_0} \quad (2)$$

$$\frac{\omega}{\mu^2} \tilde{\chi}_i = \widetilde{E_{cv}} - \widetilde{E_{vc}} \quad (3)$$

The Langevin equation for the total excited-electron-number operator $\widetilde{N}_c(t)$ is given by:

$$\frac{d\widetilde{N}_c(t)}{dt} = p - \frac{\widetilde{N}_c(t)}{\tau_{sp}} - \left(\widetilde{E_{cv}} - \widetilde{E_{vc}} \right) \widehat{n}(t) - \left\langle \widetilde{E_{cv}} \right\rangle + \widetilde{\Gamma_p}(t) + \widetilde{\Gamma_{sp}}(t) + \widetilde{\Gamma}(t) \quad (4)$$

The cavity external phon field $\widehat{r}(t)$, the cavity internal field $\widehat{A}(t)$ and the injection signal $F_0 + \widehat{f}(t)$ have such relationship:

$$\widehat{r}(t) = - \left[F_0 + \widehat{f}(t) \right] + \left[\frac{\omega}{Q_e} \right]^{\frac{1}{2}} \widehat{A}(t) \quad (5)$$

By quasilinearization procedure:

$$\widehat{A}(t) = \left[A_0 + \Delta \widehat{A}(t) \right] \text{Exp}(-i\Delta\widehat{\Phi}) \quad (6)$$

$$\widehat{r}(t) = (r_0 + \Delta \widehat{r}) \text{Exp}(-i\Delta\widehat{\Psi}) \quad (7)$$

$$\widetilde{N}_c(t) = N_{C0} + \Delta \widetilde{N}_c \quad (8)$$

Within the cavity bandwidth, we get the power spectrum of the external field:

$$P_{\Delta r(\Omega)} = \frac{1}{2} \frac{\Omega^2}{\Omega^2 + \left[\frac{\omega}{Q} \right]^2} \quad (9)$$

From the figure we can see the noise drops below the shot noise limit with the increase of the pump level. That is because there is subtle balance between the cooperative force and the fluctuation force. Such balance established the standard quantum limited photon flux. By injection locking, the side modes of the slave laser is further suppressed because of the gain saturation, so is the mode-partition noise. So the noise of the side modes have great correlation to some extent. In this case the noise of the slave laser is suppressed below the shot noise limit.

3 Experimental setup

A laser diode (model SDL 5411-G1) was used as a slave laser. A DBR (distribute bragg reflector) laser diode was used as a master laser, whose wavelength can be tuned continuously. By adjusting the current and the temperature, the master laser oscillates at the wavelength of 852.356 nm, which is the D₂ line of the cesium atoms. About 1.5 mW from the master laser was injected into the slave laser. By matching the mode and the polarization to the slave laser carefully, the slave laser was injection locked.

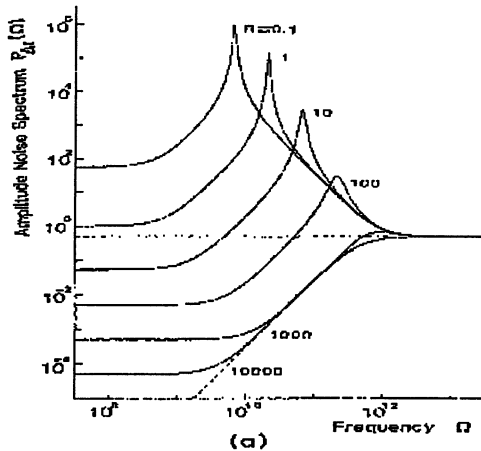


Fig. 1. The dashed line : shot noise limit; R : the pump level($\frac{I}{I_{th}} - 1$), I denotes the operational current, I_{th} denotes the threshold current.

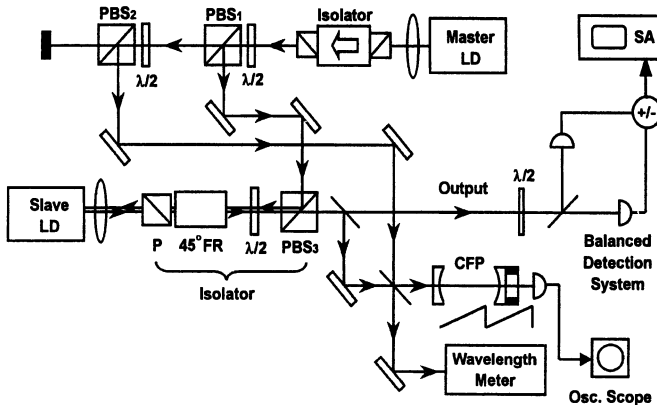


Fig. 2. Experimental setup for injection locking

4 Experimental result

From the figure, there is amplitude squeezing of 0.8–1.0 dB along the whole spectral ranges. Considering the quantum efficiency of 0.88, the squeezing at the output facet of the slave laser is 0.9 dB. With the well known setup, we measure the phase noise of the slave laser. So we get 5–12 dB phase reduction with injection locking.

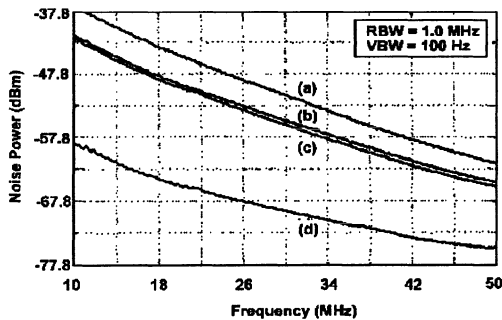


Fig. 3. Observations of the amplitude squeezing along the whole spectrum ranges
 (a) denotes the noise of slave laser without light injection;
 (b) denotes the shot noise limit(SNL);
 (c) denotes the noise of slave laser with injection locking;
 (d) denotes the electronics noise;

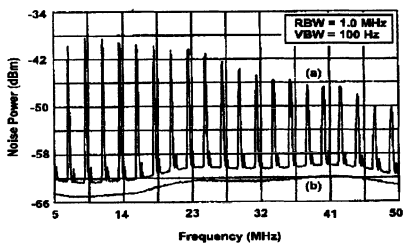


Fig. 4. Observation of phase reduction without injection locking

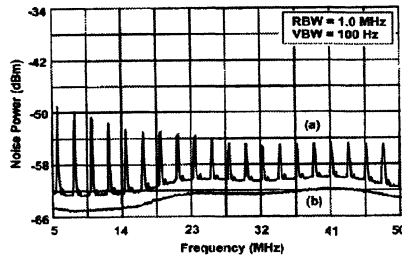


Fig. 5. Phase reduction with injection locking

5 Conclusion

By injection locking, noise of slave laser is 0.8 dB below the shot noise limit. Phase reduction is 5–12 dB. The tunable range is 1.7 GHz. So we can use the tunable squeezed light to interact with Cs atoms in MOT to investigate some characteristics of such nonlinear medium.

Acknowledgements. The project is supported by the National Natural Science Foundation of China under Grant No. 19774039 and 69837010. It is also supported by Young Excellent Teacher Foundation of the Education Department.

References

1. Y.Yamamoto, S.Machida and O.Nilsson Phys. Rev. A **34**, 4025(1986)
2. S.Inote, S.Machida, Y.Yamamoto and H.Ohzu Phys. Rev. A **48**, 2330(1993)
3. Hailin Wang, Michael J.Freeman, and Duncan G.Steel, Phys. Rev. Lett.**71**, 3951(1993)
4. Akira Furusawa, Opt. Lett. **21**, 2014(1996)
5. Steven Kasapi, Seema Lathi, and Y.Yamamoto, Opt. Lett.**22**, 478(1997)

An Analytic Expression of Enhanced Spontaneous Emission in Semiconductor Microcavity Lasers

Xiaoxia Zhang, Wei Pan, Bin Luo, Hongchang Lü, Jianguo Chen

Southwest Jiaotong University, Chengdu 610031, P.R.China

Abstract. Based on the enhanced spontaneous emission caused by microcavity and influence of nonradiative recombination, an analytic resolution of rate equation is derived for microcavity lasers. It is evident that such high spontaneous emission factor value can be used to enhance the efficiency of light-emitting and lower thresholds of lasers. The light output is increased by the enhanced well number and by the decreased width, at the same time the sharpness of those variation depends on spontaneous emission factor. We show that the characteristic curve of a “thresholdless” laser is strongly nonradiative depopulation-dependent. When nonradiative depopulation is no zero even for an ideal closed microcavity, the light-current characteristic is not linearly. The result shows that increasing the coupling of spontaneous emission into the cavity mode causes the lasing properties becoming quite different from those of the conventional laser having cavity dimensions much larger than the lasing wavelength.

1 Introduction

The oxide-confined microcavity structures are being studied in a number of laboratories around the world to optimize their performance for commercial applications. The main advantages of this construction method are superb high efficiency (50-60%) and very low threshold current (ten-100 μA). The progress made in microcavity research has been remarkably rapid on all fronts. The control of the spontaneous emission rate and the spontaneous emission factors has attracted great attention in microcavity lasers for reducing threshold current.[1-4] In this paper we consider another approach to get analytic resolution of rate equation for multi-quantum well microcavity lasers. Based on the concept of spontaneous emission enhancement in a microcavity, we induce the structural parameter of MQW into the rate equation and think about the influence of nonradiative processes, and obtain good agreement with the literature. We demonstrate the first use, to our knowledge, of the enhanced spontaneous emission has been identified and explained using simple analytic expression of models. Some attractive features of microcavity lasers have been predicted.

2 Analytic Resolution of Steady-state Rate Equations

Because of quantum well lasers very sensitive to internal losses, the surface and defect recombination may influence the current-carrier relation, and Auger recombination is the most dominant effect for the high temperature-sensitivity of the threshold current.[5] On the other hand, although enhanced spontaneous emission is not the necessary condition for the lack of a threshold, the consequent increase in the spontaneous emission fact or has some great advantages from the device point of view. To consider the effects of these nonradiative processes and guided by the above analysis, the multi-quantum well microcavity lasers steady-state rate equation can be written as

$$\frac{\eta J}{eML_z} - (1 - \beta)AN - \beta A_c(SV + 1)N - \Lambda N = 0 \quad (1)$$

$$M\Gamma_0\beta A_c(SV + 1)N - \gamma S = 0 \quad (2)$$

Where S is the photon density of intracavity, N is the carrier density, A is the spontaneous emission rate in free space, A_c is the spontaneous emission rate for the cavity mode, Λ is the nonradiative depopulation rate, γ is the damping rate for photons from the passive cavity, V is the cavity volume, J is the injection current density, η is the current-injection efficiency, Γ_0 is the SQW light confinement factor, e is the electron charge. The pair of parameters are introduced in equations for M and L_z (the well number and width of MQW), respectively. Omitting the derivation process, an analysis solutions for the photon density and the carrier density of the MQW microcavity lasers can be given directly.[6] These equations will be used in following partition to discuss by the shown in the figures on the parameters characteristics of microcavity lasers (In the figures S , N and J are normalized as s , n and j). Considering gain-saturation of MQW, with Equation (3) and (4) threshold current density is shown below

$$J_{th} = \frac{eML_z}{\eta\tau_{sp}}N_{tr}\exp\frac{1}{\tau_{ph}M\Gamma_0g_0} \quad (3)$$

and we obtain the optimal well number

$$M_{opt} = \frac{v_g}{\Gamma_0g_0} \left(\alpha_{int} + \frac{1}{L} \ln \frac{1}{R} \right) \quad (4)$$

where g_0 is the gain coefficient per QW, v_g is the group velocity, α_{int} is the internal loss, N_{tr} is the optical transparency, τ_{sp} is the spontaneous emission lifetime, τ_{ph} is the photon lifetime, L is the cavity length and R is the facet reflectivity. This is a remarkably simple expression of optimal well number.

3 Results and Discussions

The influence of spontaneous emission on the properties and structure parameters of microcavity lasers has been investigated. We get the relation

between output properties and structural parameters of multi-quantum wells (MQW). One of the most important consequences of the increased β is the reduction of threshold of a laser. It was found that the characteristic curve of a “thresholdless” laser is strongly nonradiative depopulation-dependent. When the nonradiative depopulation is no zero, the light-current characteristic is not linearly even for an ideal closed microcavity. The light output is increased by the enhanced well number and by the reduced width. The results show that MQW structures exhibit a higher S, which suggests that S have a higher sensitivity to L_z compared with M, and the sharpness of the increment depends on β . However, the relation between N and M and L_z are varied little with β , only while ideal closed microcavity, N varied significantly. In particular, we can also realize that a lower threshold current density for MQW structure in the short cavity, there is an optimal well number for the minimum J_{th} , thus demonstrating good agreement with the experiment results. It is important that device structure optimized to be selected an optimal well and cavity length.

References

1. H. Yokoyama, S. D. Brorson: Rate equation analysis of microcavity lasers. *J. Appl. Phys.* **66**(10), 4801,(1989)
2. G. Bjork, Y. Yamamoto: Analysis of semiconductor microcavity lasers using rate equations. *IEEE J. Quant. Electron.* **QE-27**(11), 2386,(1991)
3. G. Shtengel, H. Temkin: Spontaneous emission factor and its scaling in vertical cavity surface emitting lasers. *Appl. Phys. Lett.* **64**(9), 1062,(1994)
4. T. Baba, T. Hamano, F. Koyama, K. Iga: Spontaneous emission factor of a microcavity DBR surface emitting laser. *IEEE J. Quant. Electron.* **QE-27**(8):1347,(1991)
5. G. P. Agrawal, N. K. Dutta: *Semiconductor Lasers*. 2nd ed. ,New York,(1993)
6. W. Pan, X. Zhang, B. Luo, H. Lu, J. Chen: Vertical cavity surface emitting laser. *Physics (in Chinese)*, **28**(4), 210,(1999)

Quantum Theory of the 3-Level-Atom Mazer

Zhi-Ming Zhang^{1,2}, Xiao-Xia Zhong¹, Chang-Huan Liao³, Ai-Qun Ma⁴, Shi-Kang Zhou²

¹ Department of Applied Physics, Shanghai Jiao Tong University, Shanghai 200240, China

² Université Laser Spectroscopy Laboratory, Anhui Institute of Optics and Fine Mechanics, Academia Sinica, Hefei 230031, China

³ Université Laboratoty for Medico-photonics, Zhongshan Medical University, Guangzhou, 510080, China

⁴ Université Zuhai Polytechnic School, Zuhai 519015, China

Abstract. We report our recent study on the micromaser injected with ultracold cascade three-level atoms, including the general theory, the atomic emission probability in the micromaser cavity, the atomic transmission probability through the cavity, the photon statistics and the spectrum properties of the cavity field. It is shown that the micromaser cavity can be used as a velocity selector for ultracold three-level atoms, the photon statistics of the cavity field can be sub-Poissonian under some conditions, the linewidth can be broadened and the cavity-frequency can be either red-shifted or blue-shifted.

1 Introduction

The micromaser plays an important role in the study on the cavity quantum electrodynamics (cavity QED) . With the development of laser cooling techniques , ultracold atoms have been obtained. In 1996, Scully, Meyer and Walther suggested to use the ultracold atoms in micromasers and proposed the concept of the mazer (Microwave Amplification via Z-motion-induced Emission of Radiation).They and their coworkers have studied various properties, for example, the emission probability, the photon statistics, and the spectrum, of the mazer in a series of papers. In 1998, Löffler, Meyer and Walther proposed to use the micromaser as a velocity selector. However, in all these papers the two-level-atom model was assumed. On the other hand, the two-photon micromaser, which related to three-level atoms, has also been studied theoretically and experimentally. These motivate us to consider the two-photon process and three-level atoms in the study of mazers. We have studied the atomic emission probability in a two-photon mazer by using an effective two-level Hamiltonian [1]; the atomic emission probability [2] and the photon statistics [3] in a Λ -type three-level-atom mazer; the atomic emission probability [4], the photon statistics [5], the atomic transmission probability through the micromaser cavity [6] and the velocity selectivity of the micromaser cavity for the atoms [7] in a cascade three-level-atom mazer. In this paper we briefly review our previous work on the micromaser injected

with ultracold cascade three-level atoms and report our recent study on its spectrum.

2 General Theory

The general theory has been reported in Refs.[4-5]. Suppose that the ultracold atom has a cascade three-level configuration, moves along the z-direction, and enters into a cavity which contains a single-mode quantum radiation field, then we get some quantities R 's and T 's, which have the following meanings: when an atom initially in the upper state $|a\rangle$ enters into a cavity containing n photons, it will be reflected or transmitted while remaining in the state $|a\rangle$ with the amplitudes $R_{a,n}$ and $T_{a,n}$, and be reflected or transmitted while making a transition to the state $|b\rangle$ and emitting one photon with the amplitudes $R_{b,n+1}$ and $T_{b,n+1}$, and be reflected or transmitted while transiting to the state $|c\rangle$ and emitting two photons with the amplitudes $R_{c,n+2}$ and $T_{c,n+2}$, respectively.

3 Emission Probability

The two-photon emission probability is

$$P_{ems}(n, k) = |R_{c,n+2}(k)|^2 + |T_{c,n+2}(k)|^2 \quad (1)$$

The emission probability has been studied in detail in Ref.[4]. In the curves of P_{ems} vs L (the dimensionless cavity length), there are two sets of resonances, one corresponds to the maxima, the other corresponds to the minima. The maxima in the case of large Δ (the detuning) are larger than that in the case of $\Delta = 0$, and the minima in the case of large Δ are smaller than that in the case of $\Delta = 0$. The curves have good periodicity. The period of L is $2\pi(2n+3)^{-1/4}$ in the case of $\Delta = 0$ and is $2\pi\sqrt{\delta/(2n+3)}$ in the case of larger Δ . The resonance peaks become sharper for colder (slower) atoms.

4 Transmission Probability and Velocity Selection

The transmission probability of the atom through the cavity is

$$P_{trans}(n, k) = |T_{a,n}(k)|^2 + |T_{b,n+1}(k)|^2 + |T_{c,n+2}(k)|^2 \quad (2)$$

The transmission probability has been studied in detail in Ref.[6-7]. There are some resonant peaks in the curves of P_{trans} vs r (dimensionless c.m. momentum). It means that the micromaser cavity can select the velocity of incoming atoms. The maximum values of the transmission probability is 1/2 in the two-level atom case and is 1 in the three-level atom case here. This shows that the micromaser cavity has better velocity selectivity for three-level atoms than for two-level atoms.

5 Photon Statistics

The photon statistics of the cavity field in the three-level-atom mazer has been studied in detail in Ref.[5]. The stationary distribution of the photon number involves only the diagonal elements of the master equation and has the following form

$$P_n = P_0 \prod_{m=1}^n X_m, \quad (3)$$

where P_0 is the normalized constant and X_m are some complicated functions. Using Eq.(3) we have calculated the mean number of photons $\langle n \rangle$ and the normalized standard deviation $V = \sqrt{(\langle n^2 \rangle - \langle n \rangle^2) / \langle n \rangle}$. We found: (1) the oscillation amplitudes of $\langle n \rangle$ and V change smaller as the atoms become colder; (2) for some combination of the parameters one can get sub-Poissonian distribution of photon number ($V < 1$).

6 Spectrum

The spectrum linewidth has been studied for the micromaser injected with thermal two-level atoms, for the micromaser injected with thermal three-level atoms, and for the micromaser injected with ultracold two-level atoms. Recently, we get a quantity $\langle \mu_n^{(1)} \rangle$ for the spectrum of the three-level-atom mazer. In general, $\langle \mu_n^{(1)} \rangle$ is a complex number, its real part gives the linewidth and its imaginary part leads to a frequency-shift. We have calculated the dimensionless linewidth $D \equiv \frac{1}{\gamma} \text{Re} \langle \mu_n^{(1)} \rangle$ and the dimensionless frequency-shift $S \equiv \frac{1}{\gamma} \text{Im} \langle \mu_n^{(1)} \rangle$. The main results are as follows: (1) with the increase of L , the oscillations of both D and S become faster, the oscillation amplitude of S decreases; (3) although D is always positive, S can be negative, this means that the linewidth can be broadened and the frequency of cavity field can be blue-shifted or red-shifted.

7 Summary

In summary, we have reviewed our recent work on the micromaser injected with ultracold cascade three-level atoms, including the general theory, the atomic emission probability, the atomic transmission probability through the micromaser cavity and the velocity selectivity of the micromaser cavity for the atoms, the photon statistics and the spectrum of the cavity field.

Acknowledgments. This work was supported by the Chinese Academy of Sciences through the Senior Visiting Scholar Project.

References

1. Z.M.Zhang et al., Phys. Rev. A **59**, 808 (1999).
2. Z.M.Zhang et al., Opt. Commun. **157**, 77 (1998).
3. Z.M.Zhang et al., Acta Physica Sinica (Overseas Edition), **8**, 571(1999).
4. Z.M.Zhang et al., Chin. Phys. Lett. **16**, 26 (1999).
5. Z.M.Zhang et al., J. Phys. B **32**, 4013 (1999).
6. Z.M.Zhang et al., Chin. Phys. Lett. **16**, 568(1999).
7. Z.M.Zhang et al., Phys. Rev. A **60**, No.4(1999).

Optical Wave Mixing of Interacting Charge-Transfer Excitons in Organic Crystalline Films

Ka-Di Zhu^{1,2} and Wai-Sang Li²

¹ Department of Applied Physics, Shanghai Jiao Tong University

² Department of Electronic Engineering, The Hong Kong Polytechnic University

Abstract. The nonlinear optical response of interacting charge-transfer excitons (CTEs) is investigated theoretically by means of pseudospin operators for the model Hamiltonian. The absorption and dispersion response of interacting CTEs associated with a weak probe field in the presence of a strong pump field is calculated in terms of the linear response theory. The numerical results are different from those of a driven two-level system with a weak probe and give a first example of gain without population inversion in a system of interacting CTEs.

1 Introduction

In recent years, there has been an increasing interest in the nonlinear optical properties of excitons confined in low-dimensional molecular geometries such as crystalline organic superlattices grown by organic molecular beam deposition [1-2] and molecular monolayers made by either Langmuir-Blodgett or self-assembly methods. In such structures the bound electron-hole pairs are small and they are usually referred to as charge-transfer excitons (CTEs). A characteristic feature of such complexes is a nonzero static dipole moment which is responsible for their interaction. Recently, the possibility of intrinsic optical bistability due to CTE-phonon interaction in crystalline organic superlattices has been reported [2], which the static dipolar interaction of CTEs has not been considered. The dielectric-metal phase transition due to the strong static dipole-dipole repulsion in a system of interacting CTEs was demonstrated theoretically by Agranovich et al.[3] and Zhu et al.[4]. Yudson and coworkers[5] studied the steady-state nonlinear response of Frenkel excitons in molecular crystals and shown that for a high density of Frenkel excitons their dipole-dipole interaction and finite excitonic bandwidth effects become important, and the interaction of CTEs may have a strong influence on their kinetics which may show itself in nonlinear optics.

2 Theory

In the following, we shall follow the treatment of Boyd [6] who adopted the method of Mollow to treat the problem of a driven two-level system with

a weak field. For the sake of simplicity, we neglect the effect of backward travelling wave and concentrate mainly on the case of optically thin layer. We consider the response of CTEs to the simultaneous presence of a strong optical pump field and a weak probe field. The latter field is considered weak in the sense that it alone cannot saturate the response of the CTE system. For simplicity, we set $w = 2 < s_j^z >$ and $p = \mu < s_j^- >$, where $< s_j^- >$ and $< s_j^z >$ are slowly varying quantities of the CTE operators, μ is a transition dipole moment. Then the generalized optical Bloch equations are given by

$$\frac{dp}{dt} = [i(\Delta + \beta w) - \frac{1}{T_2}]p - i\mu^2 Ew, \quad (1)$$

$$\frac{dw}{dt} = -\frac{1}{T_1}(w + 1) + 4Im(pE^*). \quad (2)$$

where $\Delta = \omega - \omega_0$ is the detuning of the optical field from resonance frequency ω_0 of a constituent molecule, β is the coupling constant, T_1 and T_2 are the longitudinal and transverse relaxation times, respectively. We represent the amplitude of the applied optical field as [6]

$$E = E_0 + E_1 e^{-i\delta t}, \quad (3)$$

where we assume that $|E_1| \ll |E_0|$, δ is the frequency detuning between the pump and probe waves. Eqs.(1) and (2) cannot readily be solved exactly for the field given in Eq.(3). Instead, our strategy will be to find a solution that is exact for an applied strong field E_0 and is correct to the lowest order in the amplitude E_1 of the weak field. We hence require that the steady-state solution of Eqs.(1) and (2) be of the form

$$p = p_0 + p_1 e^{-i\delta t} + p_{-1} e^{i\delta t} \quad (4)$$

and

$$w = w_0 + w_1 e^{-i\delta t} + w_{-1} e^{i\delta t} \quad (5)$$

where p_0 and w_0 denote the solution for the case in which only the pump field E_0 is present, and where the other terms are assumed to be small in the sense that

$$|p_1|, |p_{-1}| \ll |p_0|; \quad |w_1|, |w_{-1}| \ll |w_0|. \quad (6)$$

We now introduce the trial solution Eqs.(4) and (5) into Eqs.(1) and (2) and equate terms with the same time dependence. In accordance with our perturbation assumptions, we drop any term that contains the product of more than one small quantity. Then

$$w_0[1 + \frac{T_1 T_2 \Omega_0^2}{1 + T_2^2(\Delta + \beta w_0)^2}] = -1, \quad (7)$$

$$p_1 = \frac{\mu^2 w_0 E_1}{\Delta' + \delta + \frac{i}{T_2}} \left\{ 1 - \frac{\Omega_0^2}{2} \frac{(\Delta + \frac{i}{T_2})(\delta - \Delta' + \frac{i}{T_2})(\delta + \frac{2i}{T_2})}{D(\delta, \Delta')(\Delta'^2 + \frac{1}{T_2^2})} \right\}, \quad (8)$$

where

$$D(\delta, \Delta') = (\delta + \frac{i}{T_2})(\delta - \Delta' + \frac{i}{T_2})(\delta + \Delta' + \frac{i}{T_2}) - \frac{\Omega_0^2}{2}Q(\delta, \Delta'), \quad (9)$$

$$Q(\delta, \Delta') = \frac{1}{\Delta'^2 + \frac{1}{T_2^2}} \{ (\Delta + \frac{i}{T_2})(\Delta' - \frac{i}{T_2})(\delta - \Delta' + \frac{i}{T_2}) \\ + (\Delta - \frac{i}{T_2})(\Delta' + \frac{i}{T_2})(\delta + \Delta' + \frac{i}{T_2}) \}, \quad (10)$$

where $\Omega_0 = 2\mu E_0$ and $\Delta' = \Delta + \beta w_0$. Since p_1 is the complex amplitude of the dipole moment at frequency $\omega + \delta$ induced by a probe wave at this frequency, the polarization at this frequency is $P(\omega + \delta) = Np_1$, where N is the number density of CTEs. If we set $P(\omega + \delta)$ equal to $\chi^{(1)}(\omega + \delta)E_1$, we find that $\chi^{(1)}(\omega + \delta) = Np_1/E_1$, or through use of Eq.(15) that

$$\chi^{(1)}(\omega + \delta) = \frac{N\mu^2 w_0}{\delta + \Delta' + \frac{i}{T_2}} \left\{ 1 - \frac{\Omega_0^2}{2} \frac{(\Delta + \frac{i}{T_2})(\delta - \Delta' + \frac{i}{T_2})(\delta + \frac{2i}{T_2})}{D(\delta, \Delta')(\Delta'^2 + \frac{1}{T_2^2})} \right\}, \quad (11)$$

In order to obtain the theoretical absorption and dispersion line shapes, we plotted $Im\chi^{(1)}$ (for absorption) and $Re\chi^{(1)}$ (for dispersion) as functions of the probe field detuning δ with a given pump field detuning Δ , Rabi frequency Ω_0 and the coupling constant β of CTE-CTE. .

3 Conclusions

The nonlinear optical response of interacting charge-transfer excitons (CTEs) in a system is investigated theoretically by means of pseudospin operators for the model Hamiltonian. The generalized optical Bloch equations including CTE-CTE transition and static dipolar interaction are derived in terms of Heisenberg equation of motion and the mean-field approximation. The absorption and dispersion response of interacting CTEs associated with a weak probe field in the presence of a strong pump field is calculated under bistable conditions using the linear response theory. For the on-resonance pumping case, the absorption profile of the high excitation branch of the bistable regime consists of two asymmetric dispersionlike features and between the two features there is a amplification for the weak CTE-CTE dipolar couplings. The corresponding dispersion profile consists of a positive and a negative absorptionlike peak and between the two peaks there is a negative absorptionlike profile where the absorption is zero at the frequency of the dispersion peak. The two peaks are asymmetric and the negative profile at line center is enhanced as the CTE-CTE dipolar interaction strength increases. Our results also give a first example of the gain without population inversion in a 2D system of interacting CTEs. We emphasize that the present treatment should be regarded as a guide or a standard of comparison with more refined calculation and experimental data. Finally we hope that this

work will stimulate more theoretical and experimental works which will be helpful for a better understanding of the interacting charge-transfer excitons in low dimensional systems.

Acknowledgement. The part of this work was supported by National Natural Science Foundation of China (No.19874044) and Shuguang Project of Shanghai Education Committee.

References

1. F. F. So, S. R. Forrest, Y. Q. Shi and W. H. Steier, *Appl. Phys. Lett.* **56**, 674(1991).
2. J. F. Lam, S. R. Forrest, and G. L. Tangonan, *Phys. Rev. Lett.* **66**, 1614 (1991).
3. V. M. Agranovich and K. N. Ilinski, *Phys. Lett. A* **191**, 309(1994).
4. K. D. Zhu and T. Kobayashi, *Phys. Lett. A* **201**, 439(1995).
5. V. I. Yudson, Th. Neidlinger and P. Reineker, *Phys. Lett. A* **204**, 313(1995).
6. R. W. Boyd, *Nonlinear Optics* (Academic Press, New York,1992), p225.

Synchronization of Chaos in a Coupled Laser System

Shiqun Zhu¹, Xianfeng Chen¹, Xiang Lu¹, K. Scott Thornburg, Jr.²,
Gregory D. VanWiggeren², Rajarshi Roy²

¹ Department of Physics, Suzhou University, Suzhou, Jiangsu 215006, China

² School of Physics, Georgia Institute of Technology, Atlanta, GA 30332-0430,
U.S.A. e-mail: szhu@suda.edu.cn

Abstract. Synchronization of the chaotic intensity fluctuations of three pump modulated Nd: YAG lasers oriented in a linear array is investigated both experimentally and numerically. It is shown that synchronization only appears between the two outer lasers with little synchrony between outer and inner lasers. The lack of synchrony between outer and inner lasers is mainly due to the asymmetry of the coupling among the lasers.

1 Introduction

Experimental and theoretical investigations of synchronization of chaos in coupled nonlinear systems have attracted much attention in recent years due to the possibility of practical applications of this fundamental phenomenon. Several papers have studied the synchronization of chaotic signals in the context of electronic circuits [1,2], secure communication [3], turbulence in fluids [4], chemical and biological systems [5], and laser dynamics [6,6]. Winful and Rahman have numerically investigated the possibility of synchronization of chaos in semiconductor laser arrays on a nanosecond time scale [6]. To our knowledge, however, the experimental synchronization of chaos in laser arrays with more than two lasers has yet to be performed.

In this paper, the synchronization of three coupled, chaotic, Nd: YAG (trivalent neodymium doped yttrium aluminum garnet) lasers with pump modulations is reported both experimentally and numerically. In a linear array of three lasers, a high degree of synchronization only between outermost pair is seen while little synchronization between outer and inner lasers appears. There is good agreement between numerical and experimental results. The lack of synchronization between outer and inner pairs of lasers is discussed.

2 Theoretical analysis

The equations describing the time evolution of the complex, slowly varying electric field E_j and gain G_j of laser j in an array of three spatially coupled, pump modulated single mode Class B lasers are as follows:

$$\begin{aligned}
\frac{dE_{1,3}}{dt} &= \frac{1}{\tau_c} [(G_{1,3} - \alpha_{1,3}) E_{1,3} - \kappa_{12,32} E_2] + i\omega_{1,3} E_{1,3} \\
\frac{dG_{1,3}}{dt} &= \frac{1}{\tau_f} \{p_{1,3}[1 + M \sin(\Omega t)] - G_{1,3}(1 + |E_{1,3}|^2)\} \\
\frac{dE_2}{dt} &= \frac{1}{\tau_c} [(G_2 - \alpha_2) E_2 - \kappa_{21} E_1 - \kappa_{23} E_3] + i\omega_2 E_2 \\
\frac{dG_2}{dt} &= \frac{1}{\tau_f} \{p_2[1 + M \sin(\Omega t)] - G_2(1 + |E_2|^2)\}
\end{aligned} \tag{1}$$

where the subscript 1, 3 corresponds to lasers 1 and 3. In these equations, τ_c is the cavity round trip time, τ_f is the fluorescence time of the upper lasing level of the Nd^{3+} ion, and p_j , α_j , and ω_j are the pump parameters, losses, and detunings from a common cavity mode respectively. M is the modulation depth of the pump beams, and Ω is the modulation frequency.

The lasers are coupled linearly to one another with strength κ_{jm} , assumed to be small. For laser beams of Gaussian intensity profile and $\frac{1}{e^2}$ beam radius ω_0 the coupling strength is defined as

$$\kappa_{jm} = \exp\left[\frac{-(d_j - d_m)^2}{2\omega_0^2}\right] \tag{2}$$

The experimental measurements [7] are shown in Fig. 1 for a value of the nearest neighbor separation around 0.975 mm and the modulation depth $M = 0.2$. The chaotic intensity time series are shown on the left while the X-Y plots of the laser intensity pairs, plotting $I_j(t)$ vs. $I_m(t)$, are shown on the right. The X-Y plot of the intensities shows that lasers 1 and 3 are synchronized, while other pairs show little synchrony, as predicted by Ref. [6]. The numerical calculations shown in Fig. 2 were calculated by integrating Eqs. (1). It is clear that the theoretical results are in excellent agreement with the experimental measurements.

3 Loss of synchronization

If lasers 1 and 3 are synchronized with $E_1 = E_3$ and $\kappa_{jm} = \kappa$, the equations of motion of electric fields E_1 and E_2 in Eq(1) are reduced to:

$$\begin{aligned}
\frac{dE_1}{dt} &= \frac{1}{\tau_c} [(G_1 - \alpha_1) E_1 - \kappa E_2] + i\omega_1 E_1 \\
\frac{dE_2}{dt} &= \frac{1}{\tau_c} [(G_2 - \alpha_2) E_2 - 2\kappa E_1] + i\omega_2 E_2
\end{aligned} \tag{3}$$

while the equations of gain G_1 and G_2 in Eq. (1) are not changed. From Eq. (3), it is clear that lasers 1 and 2 are not synchronized mainly due to

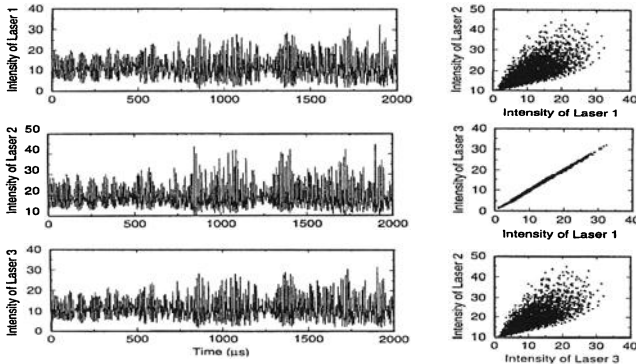


Fig. 1. Experimental measurements of the relative intensities of three coupled lasers. A high degree of intensity synchronization is seen only between lasers 1 and 3.

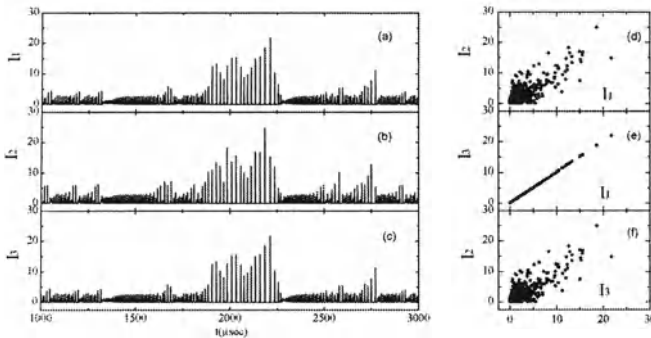


Fig. 2. Numerical simulations of the laser intensities generated by integrating Eqs.(1). The intensity time traces are shown on the left. On the right, only the X-Y plot of lasers 1 and 3 shows significant intensity synchronization.

the asymmetric coupling between lasers 1 and 2. In the equation of E_1 , the coupling is κ while in that of E_2 , the coupling is 2κ .

Assuming $E_1 = x_1 e^{i\phi_1}$ and $E_2 = x_2 e^{i\phi_2}$ with $x = \frac{1}{2}(x_1 - x_2)$ and $y = \frac{1}{2}(x_1 + x_2)$, the numerical results from Eq. (3) are shown in Fig. 3. It is clear that neither $x = 0$ nor $y = 0$. This means that lasers 1 and 2 are never synchronized.

When there is no modulation ($M = 0$), the laser intensity time series are periodic. The X-Y plot of lasers 1 and 3 is still synchronized while that of either lasers 1 and 2 or lasers 2 and 3 are trace out Lissajou-like patterns. The couplings and detunings were chosen such that, in the absence of modulation, the lasers exhibit an instability caused by the resonance of the phase dynamics with the relaxation oscillations; this effect is discussed in Ref. [8].

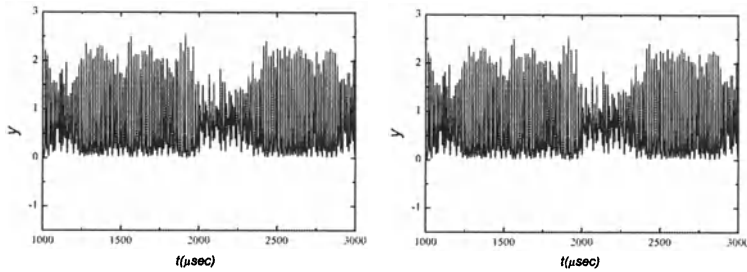


Fig. 3. The numerical results of the difference x and sum y of the amplitudes of lasers 1 and 2.

4 Conclusion

The synchronization of outermost lasers in a linear array of three laser systems is investigated. The numerical calculations reveal that the loss of synchronization of outer and inner lasers is mainly due to the asymmetric coupling among these lasers.

Acknowledgements. It is a pleasure to thank the financial supports from the National Natural Science Foundation of China, Natural Science Foundation of Jiangsu Education Commission(S.Z, X.C., X.L.) and Georgia Institute of Technology(K.S.T.J., G.D.V., R.R.)

References

1. (a)L. M. Pecora and T. L. Carroll, Phys. Rev. Lett. **64**, 821 (1990); (b)L. M. Pecora and T. L. Carroll, Phys. Rev. Lett. **A44**, 2374 (1991).
2. K. M. Cuomo and A. V. Oppenheim, Phys. Rev. Lett. **71**, 65 (1993).
3. L. Kocarev and U. Parlitz, Phys. Rev. Lett. **74**, 5028 (1995).
4. (a)A. V. Gaponov-Grekhov, M. I. Rabinovich, and I. M. Starobinets, Pis'ma v Zh. Eksp. Teor. Fiz. **39**, 561 (1984); (b)V. S. Afraimovich, N. N. Verichev, and M. I. Rabinovich, Izvest. Vyss. Uch. Zavedenii, Radiofizika **29**, 1050 (1986).
5. S. K. Han, C. Kurrer, and Y. Kuramoto, Phys. Rev. Lett. **75**, 3190 (1995).
6. (a)H. G. Winful and Rahman, Phys. Rev. Lett. **65**, 1575 (1990); (b)R. K. DeFreeze et al., in *Nonlinear Dynamics in Optical System*, Ed. by N. B. Abraham, E. M. Garmire, and P. Mandel(Optical Society of America, Washington, D. C., 1991), p.106.
7. (a)R. Roy and K. S. Thornburg, Jr., Phys. Rev. Lett. **72**, 2009 (1994). (b)J. R. Terry, et al, Phys. Rev. **E59**, 4036 (1999).
8. K. S. Thornburg, Jr., et al., Phys. Rev. **E55**, 3865 (1997).

Controlling the Time Evolution of an Atom–Cavity System via Atomic Feedback

X.-L. Feng, S.-Q. Gong, Z.-Y. Wang, Z.-Z Xu

Laboratory for High Intensity Optics, Shanghai Institute of Optics and Fine Mechanics, Chinese Academy of Sciences, Shanghai 201800, China

Abstract. We present a scheme to realize the arbitrary control of the time evolution of an atom-cavity system via atomic feedback for the generation of an arbitrary quantum state. The scheme contains a Ramsey zone, a high- Q cavity and a two-level Rydberg atom. The atom is injected into the Ramsey zone and the cavity successively. After the passage through the cavity, the atom is sent back and injected into the Ramsey zone and the cavity again, instead of being detected. In this way, we repeat the procedure and realize the arbitrary control of the time evolution of an atom-cavity system by controlling the interacting time through the atomic velocity.

The generation of nonclassical states is one of the main tasks of quantum optics and has attracted a great deal of attention in recent years due to their many potential applications. Several schemes have been put forward for the generation of arbitrary quantum states of light fields^[1–4]. In Ref. [1], Vogel, Akulin and Schleich have demonstrated theoretically that a beam of appropriately prepared two-level atoms can drive a vacuum state of a cavity field mode into an arbitrary superposition state, if each atom is measured to be in the ground state after the passage through the cavity. If, however, any one of the atom is measured to be in the excited state, one can't get the desired target state and has to go back to the initial state and start the procedure again. In order to avoid the uncontrollable measurement, Law and Eberly have proposed an ingenious scheme based on a cavity QED interaction [2]. The scheme consists of a quantized cavity and an effective two-level atom driven by a classical field. The atom can make transitions between the two levels through two channels, the classical and the quantum, alternately. By controlling the coupling strength between the atom and the two channels, one can obtain an arbitrary quantum state at a prechosen time. The key question of Law and Eberly's method is to design a Jaynes-Cummings Hamiltonian with arbitrarily variable coupling strength. Although the question has been overcome by using the two-channel Raman interaction, there still exist some technical difficulties in the arbitrary control of quantum field.

In this paper, we present a new scheme to realize the strategy proposed by Law and Eberly [2] via atomic feedback for the generation of an arbitrary quantum state. Our scheme does not need any special requirement either for

the field or for the atom. The scheme contains a classical electromagnetic field (i.e., a Ramsey zone), a high- Q cavity and a two-level Rydberg atom, with the Ramsey zone put in front of the cavity. The atom is injected into the Ramsey zone and the cavity successively. After the passage through the cavity, the atom is sent back and injected into the Ramsey zone and the cavity again, instead of being detected as in Ref. [1] (So the entanglement between the atom and the cavity mode is not destroyed). In this way, we repeat the procedure for predetermined times with one photon emitted to the cavity field mode for each passage. By controlling the interacting time through the atomic velocity, one can obtain an arbitrary superposition of Fock states. We assume our target state of the cavity field mode takes the following form

$$|\Psi\rangle = \sum_{n=0}^M w_n |n\rangle, \quad (1)$$

where w_n is the probability amplitude of finding the cavity field mode in Fock state $|n\rangle$. w_n and M are assumed to be arbitrary.

The initial state of the atom-cavity system is taken to be $|0, g\rangle$, i.e., the atom is initially in the ground state $|g\rangle$ and the cavity field mode in the vacuum state $|0\rangle$. Our goal is to drive the vacuum state of the cavity mode to the state (1) and keep the atom still in the ground state after its last passage through the cavity. The final state of the atom-cavity system can therefore be expressed as

$$|\Psi_{\text{target}}\rangle = \sum_{n=0}^M w_n |n, g\rangle, \quad (2)$$

Obviously, in the final atom-cavity state (2) the atom and the cavity mode are not entangled any more.

Let us elucidate how to achieve the goal in the following. When the atom passes through the Ramsey zone and the cavity each time, it experiences two different interactions, respectively, with the classical field and the quantized cavity mode, this is just as the two channels presented in Ref. [2]. Under the resonant condition the Hamiltonian of the system is given by (in the interaction picture)

$$H_I = \begin{cases} \hbar g_1 (\epsilon \sigma_+ + \epsilon^* \sigma_-), & \text{for atom in the Ramsey zone} \\ \hbar g_2 (a \sigma_+ + a^\dagger \sigma_-), & \text{for atom in the cavity} \end{cases} \quad (3)$$

We suppose that the atom-cavity system is no dissipation, that is, the atomic decay and the photon losses are negligible, which can be achieved by using the Rydberg atom and the high- Q cavity. In this case, the atom-cavity system obeys a unitary time evolution. Therefore, we can perform a unitary time evolution operation on the initial state $|0, g\rangle$ and get

$$|\Psi_{\text{target}}\rangle = U(t) |0, g\rangle, \quad (4)$$

where $U(t)$ is the time evolution operator with the definition

$$U(t) = \exp(-iH_I t/\hbar). \quad (5)$$

In order to get the target state (2), whose maximum photon number is M , the atom should be injected into the cavity for M times, because there is only one photon emitted into the cavity during each passage. Generally, for the j th passage, there are two time intervals τ_j and t_j corresponding, respectively, to the atomic duration through the Ramsey zone and the atomic duration through the cavity. So in our model the whole evolution time t is divided into $2M$ time intervals with unequal lengths, $t = \sum_{j=1}^M (\tau_j + t_j)$, for M passages. Substituting Eq.(3) and $t = \sum_{j=1}^M (\tau_j + t_j)$ into Eq.(5), we obtain

$$U(t) = Q_M C_M Q_{M-1} C_{M-1} \cdots Q_j C_j Q_{j-1} C_{j-1} \cdots Q_2 C_2 Q_1 C_1. \quad (6)$$

Here C_j describes the evolution arising from the interaction between the atom and the classical field and Q_j the evolution arising from the interaction between the atom and the quantized cavity field,

$$C_j = \cos(g_1 \epsilon \tau_j) |e\rangle\langle e| + \cos(g_1 \epsilon \tau_j) |g\rangle\langle g| - i \sin(g_1 \epsilon \tau_j) |e\rangle\langle g| - i \sin(g_1 \epsilon \tau_j) |g\rangle\langle e|, \quad (7)$$

$$\begin{aligned} Q_j = & \cos(g_2 t_j \sqrt{a^\dagger a + 1}) |e\rangle\langle e| + \cos(g_2 t_j \sqrt{a^\dagger a}) |g\rangle\langle g| \\ & - i \frac{\sin(g_2 t_j \sqrt{a^\dagger a + 1})}{\sqrt{a^\dagger a + 1}} a |e\rangle\langle g| \\ & - i a^\dagger \frac{\sin(g_2 t_j \sqrt{a^\dagger a + 1})}{\sqrt{a^\dagger a + 1}} |g\rangle\langle e|, \end{aligned} \quad (8)$$

where $|e\rangle$ is the atomic excited state. g_1 , g_2 and ϵ have been taken to be real.

The main question is to determine each interacting time interval so as to satisfy Eq. (4). Using the technique presented in Ref. [2], we perform a unitary inverse time evolution transformation for Eq. (4) and get

$$\begin{aligned} |0, g\rangle &= U^\dagger(t) |\Psi_{\text{target}}\rangle \\ &= C_1^\dagger Q_1^\dagger C_2^\dagger Q_2^\dagger \cdots C_j^\dagger Q_j^\dagger C_{j+1}^\dagger Q_{j+1}^\dagger \cdots C_M^\dagger Q_M^\dagger |\Psi_{\text{target}}\rangle. \end{aligned} \quad (9)$$

Eq. (9) implies that the inverse time evolution operator $U^\dagger(t)$ eliminates photons from the final state one by one until the final state becomes the ground state $|0, g\rangle$, namely, each combined operator, $C_j^\dagger Q_j^\dagger$, eliminates one photon. Therefore, the following conditions should be satisfied,

$$\langle j, g | Q_j^\dagger | F_{j+1} \rangle = 0, \quad (10)$$

$$\langle j, e | Q_j^\dagger | F_{j+1} \rangle = 0, \quad (11)$$

$$\langle j, g | C_j^\dagger Q_j^\dagger | F_{j+1} \rangle = 0, \quad (12)$$

$$\langle j-1, e | C_j^\dagger Q_j^\dagger | F_{j+1} \rangle = 0, \quad (13)$$

where $|F_{j+1}\rangle = C_{j+1}^\dagger Q_{j+1}^\dagger \cdots C_M^\dagger Q_M^\dagger |\Psi_{\text{target}}\rangle$ and $|F_{M+1}\rangle = |\Psi_{\text{target}}\rangle$. From above conditions, we get

$$\alpha_j \cos(g_2 t_j \sqrt{j}) + i\beta_j \sin(g_2 t_j \sqrt{j}) = 0, \quad (14)$$

$$\mu_j \cos(g_1 \epsilon_1 \tau_j) + i\nu_j \sin(g_1 \epsilon_1 \tau_j) = 0, \quad (15)$$

where

$$\alpha_j = \langle g, j | F_{j+1} \rangle, \quad (16)$$

$$\beta_j = \langle e, j-1 | F_{j+1} \rangle, \quad (17)$$

$$\mu_j = \langle e, j-1 | Q_j^\dagger | F_{j+1} \rangle, \quad (18)$$

$$\nu_j = \langle g, j-1 | Q_j^\dagger | F_{j+1} \rangle. \quad (19)$$

Hence, the time intervals τ_j and t_j can be solved out from Eqs. (14) and (15) and the target state can therefore be determined.

In summary, we have presented a scheme to realize the arbitrary control of the time evolution of an atom-cavity system via atomic feedback for the generation of an arbitrary quantum state. In contrast with Ref. [1], our scheme does not involve the detection of the atomic state, so the uncontrollable measurement can be avoided. In contrast with [2], our scheme does not need any special requirement either for the field or for the atom. This method can also be generalized to the generation of the entangled states of light fields in several cavities, we will discuss it elsewhere.

References

1. Vogel K., Akulin V. M. and Schleich W. P., (1993) Quantum state engineering of the radiation field. *Phys. Rev. Lett.* **71**, 1816-1819.
2. Law C. K. and Eberly J. H., (1996) Arbitrary control of a quantum electromagnetic field. *Phys. Rev. Lett.* **76**, 1055-1058.
3. Parkins A. S., Marte P., Zoller P. and Kimble H. J., (1993) Synthesis of arbitrary quantum states via adiabatic transfer of Zeeman coherence. *Phys. Rev. Lett.* **71**, 3095-3098.
4. Dakna M., Clausen J., Knoll L. and Welsch D.-G., (1999) Generation of arbitrary quantum states of traveling fields. *Phys. Rev. A* **59**, 1658-1661.